Chapter 1
Introduction, Facts and Phenomenology

Extensive air showers are a very unique phenomenon. In the more than six decades since their discovery by Auger and collaborators (Auger, 1938, 1939, 1949; Auger et al., 1938, 1939a, b; Auger and Daudin, 1942, 1945) we have learned a lot about these extremely energetic events and gained deep insight into high energy phenomena, particle physics and astrophysics. However, there remain a number of puzzling questions that are addressed in this volume that cannot yet be fully answered. They remain as a challenge for present and future research in the field.

1.1 Hadron Initiated Air Showers

The bulk of all air showers are initiated by extremely energetic primary cosmic ray hadrons ($E > 10^{13}$ eV or >10 TeV) that enter the atmosphere isotropically from outer space, producing a large number of secondaries in a series of successive collisions with target nuclei of the atmospheric constituents (N_2, O_2, Ar) along their trajectories. Energetic secondaries and particles resulting from higher order generations of interactions behave alike as they propagate deeper and deeper into the atmosphere. The collision processes are hadron dominated and form a hadron cascade that propagates longitudinally, along the direction of the initial momentum vector of the incident primary.

Due to the transverse momentum of the secondaries emerging from the collisions and as a consequence of scattering processes, the cascade spreads out laterally as well. Muons and neutrinos resulting mostly from the decay of charged pions and kaons of the hadron cascade, but also from the decay of charmed particles and other processes, are produced copiously and form a superimposed shower of muons and neutrinos. The latter remain essentially undetected with standard air shower detection instrumentation.

Neutral pions and to a lesser extent muons and other particles open upon decay electromagnetic channels and divert a significant fraction of the energy of the parent hadron cascade into high energy gamma rays and electrons. These generate via repetitive pair creation and bremsstrahlung processes a large number of

P.K.F. Grieder, *Extensive Air Showers,* DOI 10.1007/978-3-540-76941-5_1,

superimposed and intermixed electromagnetic (EM) or photon–electron cascades, that form, so to say, a real *shower* of photons and electrons (negatrons and positrons) that may reach very large proportions if the primary is very energetic.

Air Cherenkov, air fluorescence and radio emission accompany the passage of the cascade shower through the atmosphere. Thus, a single high energy primary can create a giant cascade of particles and photons, as illustrated in Fig. 1.1, that propagates essentially with the velocity of light through the atmosphere and can reach sea level if the event is sufficiently energetic.

The extent of the *longitudinal* and *lateral development* depends chiefly on the energy of the initiating primary. Low energy events reach their maximum development high in the atmosphere and die out slowly with increasing atmospheric depth, leaving only the muon and neutrino components to reach ground level and beyond, whereas extremely high energy events may attain the maximum shower development near sea level.

For moderately energetic events the surviving hadronic and electromagnetic components are readily absorbed in the lower parts of the atmosphere or in the Earth's surface layer, but very energetic muons resulting from various decays or, possibly, from direct production processes, continue to propagate underground and can penetrate to great depths.

Depending on the zenith angle, θ, part or most of the neutrino shower which is co-produced with every air shower and carries away a certain fraction of the total primary energy will penetrate the Earth unaffected and continues its journey into deep space. The large cascades or showers of particles described above are called extensive air showers (EAS) or simply air showers (AS).

The total number of particles that is produced in an extensive air shower at a particular level in the atmosphere is called the shower size, N. It usually includes charged particles only, gamma rays and neutrinos are disregarded in this context, as they escape partly (γ) or completely (ν) detection with common air shower instrumentation. Some authors refer to the shower size as the number of electrons (positrons and negatrons), N_e, since the bulk of charged particles in well developed showers are electrons.

The shower size is chiefly a function of the energy, E_0, the angle of incidence, θ, i.e., the *zenith angle*, and the *height of the first interaction*, h_1, of the primary triggering the event in the atmosphere; it does not depend strongly on primary mass, A.

The characteristic build-up and decay of a shower as it propagates through the atmosphere, i.e., its longitudinal development, is illustrated in Fig. 1.2 for primaries of different energies. Note that the location of the shower maximum in the atmosphere, i.e., the *depth of maximum development*, $X_{\max}$, measured in [g cm^{-2}] from the top of the atmosphere, shifts to greater and greater atmospheric depths as the primary energy increases. This is indicated by the inclined dot-dash line that connects the loci of the shower maxima in Fig. 1.2a, b.

The *height of maximum development* of a shower in the atmosphere, $h_{\max}$, measured in [cm], [m] or [km] from sea level, is moderately sensitive to primary mass. Height, h (or altitude), in the atmosphere is related to atmospheric pressure, P, or

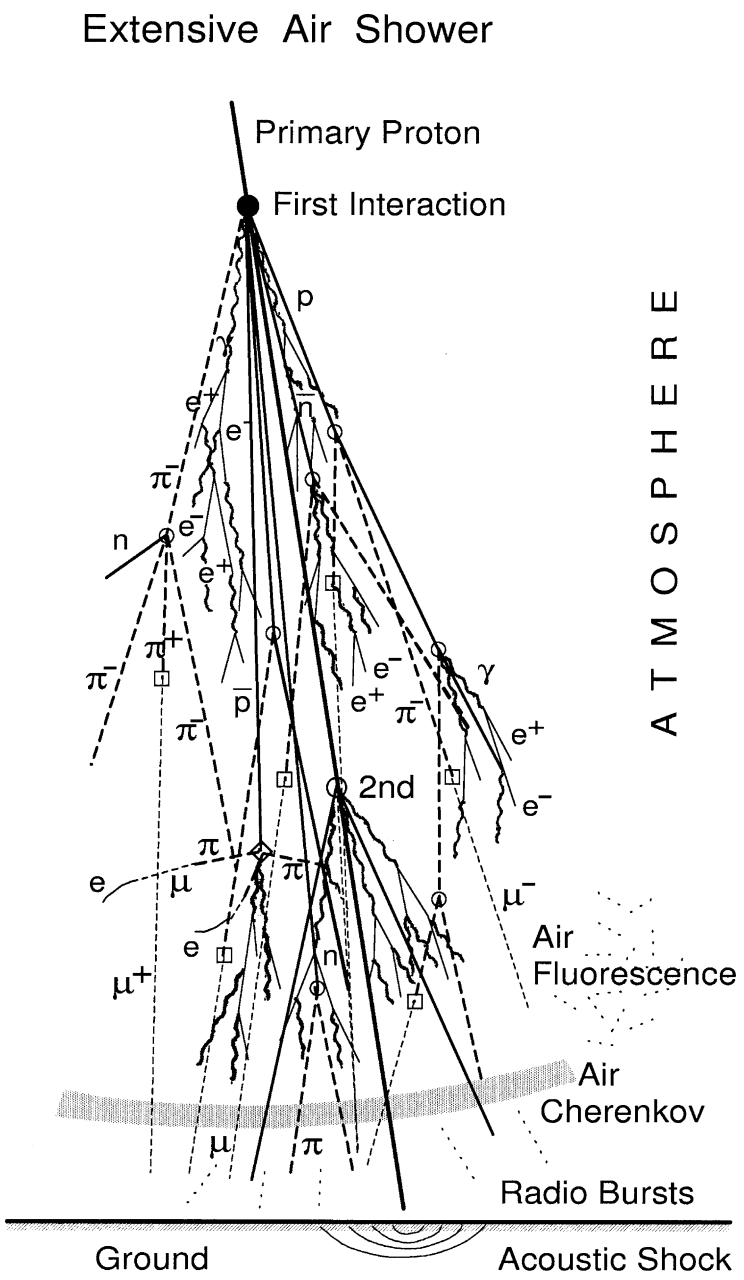

Fig. 1.1 Simplified schematic plot of the longitudinal and lateral development of an extensive air shower in the atmosphere, showing the commonly detectable components. On average a vertically incident high energy proton is subject to about 12 interactions before reaching ground level (neutrinos are not shown)

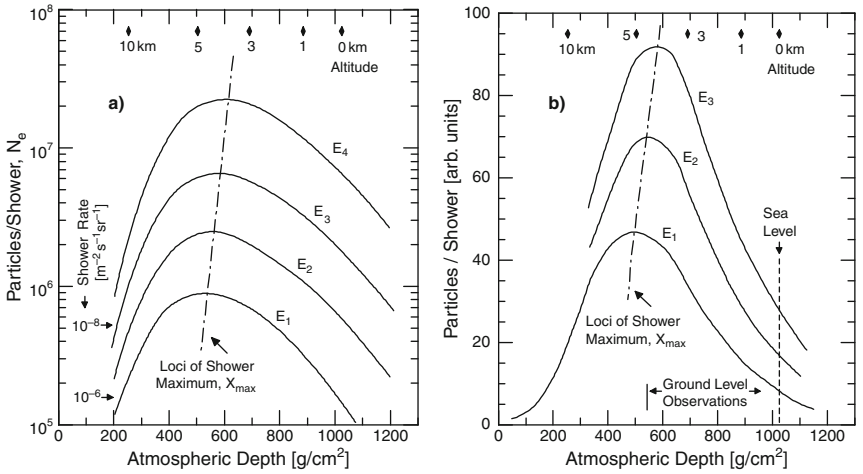

Fig. 1.2 Longitudinal development of an extensive air shower through the atmosphere. Shown is the shower size as a function of atmospheric depth in semi-logarithmic, (**a**), and linear, (**b**), representation for different primary energies ($E_1 < E_2 < E_3 < E_4$) (Grieder, 1979a, b, c)

depth, X, through the so-called *barometer formula* which can be written in its most simple form for a standard isothermal exponential atmosphere as

$$X(h) \;=\; X(h=0)\exp^{-(h/h_s)} \quad [\mathrm{g\,cm^{-2}}], \tag{1.1}$$

where $X(h = 0)$ is the vertical column density of the atmosphere at sea level and h_s the scale height of the atmosphere (for details see Eq. 21.73). Note that the scale height is not a constant, it changes with altitude because the real atmosphere is not isothermal and the pressure does not follow exactly an exponential. However, for many considerations Eq. (1.1) is adequate.

For a given primary energy the height of the first interaction of the primary in the atmosphere as well as the height of maximum development increase with increasing primary mass, A, because the interaction mean free path, λ_{int} (or the inelastic cross section), depends on the projectile mass. This implies a decreasing depth of maximum development with increasing A. X_{max} also exhibits some dependence with respect to the location in the atmosphere where the primary loses a major portion of its energy, i.e., where a large energy transfer takes place between the primary (surviving primary, leading particle or primary fragment) and the secondaries; in other words, where the collision is highly inelastic. This is usually associated with a high multiplicity interaction and does not necessarily have to occur in the first interaction of the primary. The rate of change of the location of the shower maximum in the atmosphere versus primary energy (or shower size) is called the *elongation rate*, ER.

The lateral spread of the particles in the lower regions of the atmosphere, at sea level or mountain altitude, is very large and can cover an area of up to several

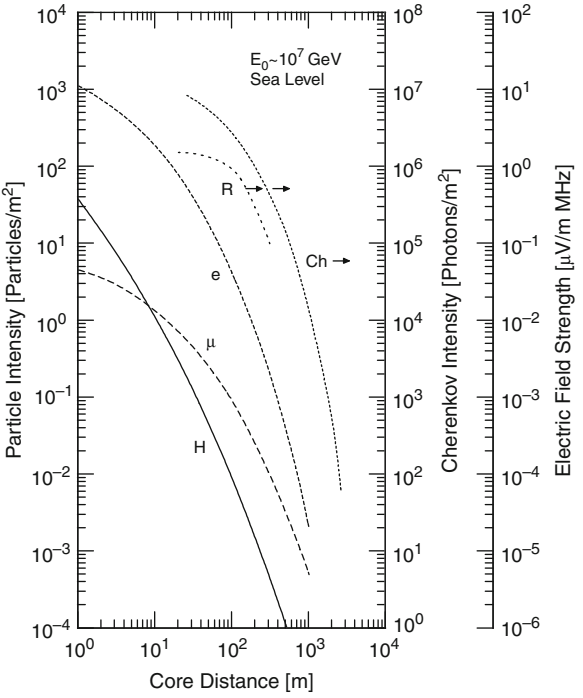

Fig. 1.3 Approximate average radial density distributions of commonly detectable extensive air shower constituents in a simulated 10^7 GeV primary proton initiated shower at sea level (Grieder, 1987). Shown are the hadron ($H \geq 1$ GeV), muon ($\mu^{\pm} \geq 1$ GeV) and electron ($e^{\pm} \geq 10$ MeV) densities (*left hand ordinate*), the atmospheric Cherenkov photon density (Ch) (*right hand ordinate*), and the electric field strength (R) of the radio pulse (*outer right hand ordinate*)

square kilometers, depending on shower size. Figure 1.3 shows the lateral density distributions of the major constituents in a medium size shower. The lateral density distribution in an average air shower is more or less symmetrical about the shower axis, but the geomagnetic field deflects the low energy charged particles and perturbs the symmetry somewhat. This effect, called the *azimuthal asymmetry effect*, is emphasized in strongly inclined showers whose axis is perpendicular to the geomagnetic field lines.

The *shower axis* is defined as the extension of the initial momentum vector of the incident primary in the direction of cascade propagation. Experimentally its intercept with the plane of observation is reconstructed from the measured lateral density distribution of the shower particles. Its direction of incidence, i.e., its *zenith* and *azimuthal angles*, can be determined from measurements of the *arrival time* of the *shower front* of particles on the plane of observation, or by reconstruction of particle trajectories in the shower, using track chambers. The second method is seldom used. An accuracy of about 1–3° can be achieved for the reconstruction of the zenith and azimuthal angles of incidence with many arrays; some authors even claim 0.5 and 0.1° under optimum conditions for very high energy events.

The particle density in the *shower core*, i.e., in the central region, is very high and drops rapidly with increasing distance in a single core shower, as illustrated in Fig. 1.4a. Shower simulations show that the central density depends to some degree on the nature of the primary. It shows a broader and flatter distribution for

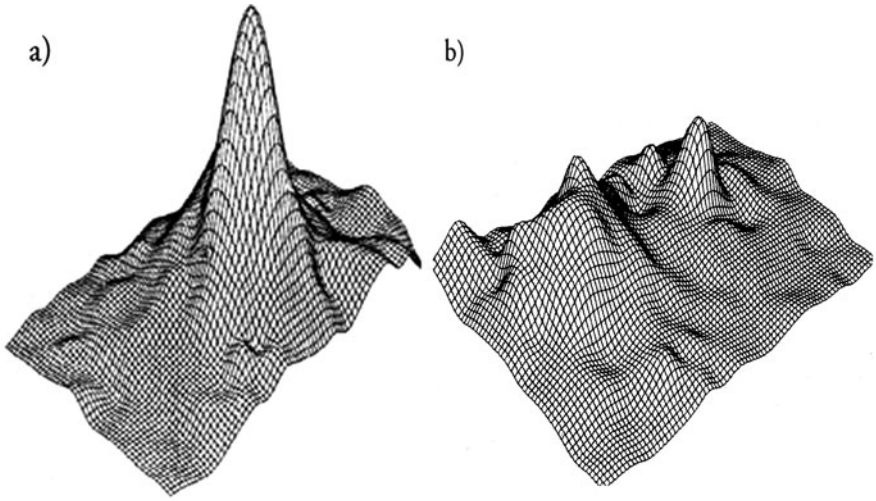

Fig. 1.4 Three-dimensional display of particle density distributions in the central region of small showers recorded at Mount Norikura, Japan with a 54 m^2 spark chamber (Sasaki et al., 1979). (**a**) Shows the typical case of a shower which exhibits a single core structure in the central region. The shower size, N, is $1.43 \cdot 10^5$, the age parameter $s = 0.7$ and the zenith angle $\theta = 14.2^\circ$. (**b**) Shows an example of a shower with a multi-core structure. The shower parameters are $N = 1.28 \cdot 10^5$, $s = 0.8$, $\theta = 15.5^\circ$

heavy primary initiated events in comparison to proton showers. However, large fluctuations are observed and many showers exhibit distinct *sub-core* or *multi-core* structures. This is illustrated in Fig. 1.4b. These can be due to scattered surviving nucleons or nuclear fragments from *fragmented heavy primaries*, to energetic secondaries emerging from interactions at high altitude, or to high energy large *transverse momentum* phenomena of relatively local origin. Thus, multi-core events are not necessarily the signature of heavy primaries.

The *shower front* has the form of a *disk* that shows a slight *curvature* for larger events, as indicated in Fig. 1.5a. The *time profile* of the particles is shown in Fig. 1.5b. The bulk of the particles arrives in a narrow time interval, ranging from only a few nanoseconds in the vicinity of the shower axis to some 10 ns at larger distances from the shower core.

The thickness of the particle disk broadens slightly with increasing radial distance from the shower axis because of larger path length fluctuations due to increased scattering at lower energies, and because of lower Lorentz factors of the parent nucleons, responsible for the local sub-cascades. However, the tail of the arrival time distribution which contains almost exclusively low energy particles, mostly muons but also nucleons, chiefly neutrons, and some antinucleons, can extend beyond one microsecond. Because of the short mean life of pions and kaons there are practically no such particles trailing the shower front by more than 100 ns (Grieder, 1977).

The relative composition of particles in a shower and their respective energy spectra depend on a number of factors, above all on the stage of the shower or

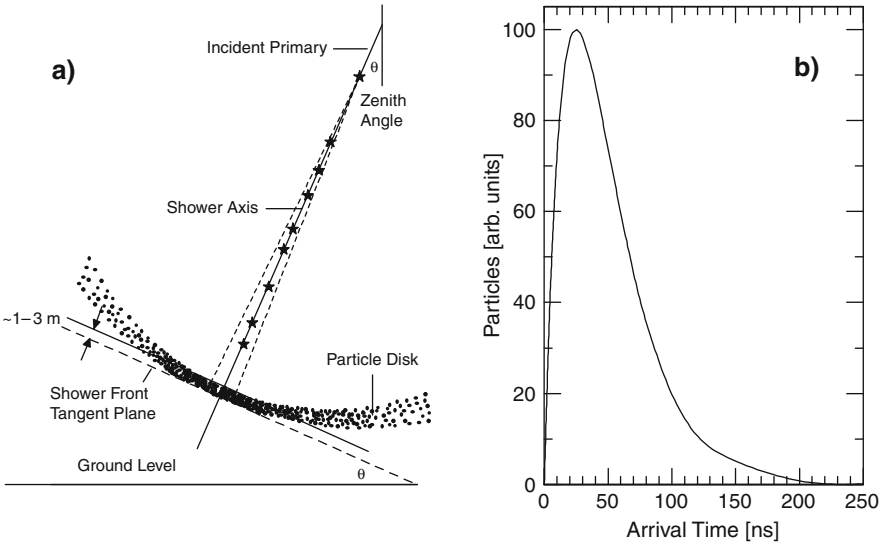

Fig. 1.5 (**a**) Longitudinal profile of an air shower on the *left*. Shown is the curved shower front and thin particle disk of a moderately inclined shower near ground level impact. (**b**) The *right hand figure* shows the approximate time profile of an average shower at ground level, including all particles, with respect to the shower tangent plane

cascade development, often referred to as the *shower age*, characterized by the *age parameter*, s. So called *young showers* ($s < 1$) are those that have not yet reached the maximum development at a particular observation level, *old showers* ($s > 1$) are those that are beyond their maximum. At shower maximum $s = 1$, and when $s = 2$ the shower has died out to a single particle. A more appropriate mathematical definition of the age parameter is given in Chap. 4 (see also Chap. 21).

As a rule of thumb one can say that in an average air shower at sea level, hadrons constitute approximately 1% of the total number of commonly detected particles. About 10% are muons and the overwhelming number, about 90% or more, are electrons and positrons of comparatively low energy.[1] In the older literature the latter together with the associated photons, that are even more abundant, were often referred to as the *soft component*, whereas hadrons and muons used to be called the *hard* or *penetrating component*. Hadrons in showers were sometimes referred to as the *nuclear active* component of a shower or simply *nuclear active particles* (NAP).

The most energetic particles in a shower are found in the shower core, in and around the shower axis, and are usually hadrons. Frequently, as a consequence of the leading particle effect, described in Chap. 3, a nucleon is the most energetic particle

[1] Air shower simulations with the CORSIKA program system yield for 10^{15} eV proton initiated showers at sea level the following percentages for the main shower constituents: 80% photons, 18% $e^{\pm}$, 1.7% $\mu^{\pm}$ and 0.3% hadrons (courtesy of Prof. J. Hörandel, University of Nijmegen, NL). Note that $(\overline{\nu})_{\mu}$ and $(\overline{\nu})_{e}$ are abundantly present in air showers but usually escape detection.

in a shower unless the shower is very old. In this case muons and neutrinos are the only energetic survivors. Strongly *inclined showers*, i.e., showers that subtend a large zenith angle, often referred to as *horizontal air showers* (HAS), are typically old showers. Simulations show that occasionally a pion can be the most energetic particle in a shower (Grieder, 1977).

Typical average integral energy spectra of the major constituents of a vertically incident medium size shower at sea level are shown in Fig. 1.6. Note that in this figure each spectrum includes all particles of the specified kind, irrespective of distance from the shower axis. Local energy spectra depend strongly on the radial distance from the axis, particularly at small distances, as is shown in Fig. 1.7 for muons. This behavior is even more pronounced for hadrons where the very energetic particles cluster in the immediate vicinity of the shower axis. The different locations of the high energy end points of the muon spectra of Figs. 1.6 and 1.7 are due to the fact that the data are from two different simulation runs. The fluctuations from shower to shower in the number of very high energy particles are very significant. Unless the data samples are large one always faces this problem.

Extensive air showers exhibit a *barometric pressure*, a *temperature* and a *zenith angle effect*. For a given set of observations made at a particular level, an increase in barometric pressure is equivalent to the apparatus being placed at greater *atmospheric depth*.

Since more primary energy is required to produce the same size shower at greater depth (cf. Fig. 1.2), and in view of the fact that the primary energy spectrum drops rapidly with increasing energy, the rate of showers of a given size will decrease with increasing depth, and vice versa. Similarly, for analogous reasons a decrease of the

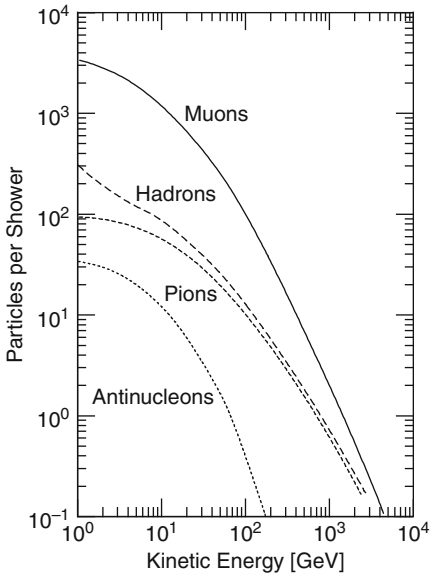

Fig. 1.6 Typical average integral energy spectra of the major components in a simulated 10^6 GeV proton initiated vertically incident air shower at sea level. Each particle type includes all particles summed over the full lateral extent of the shower (Grieder, 1977)

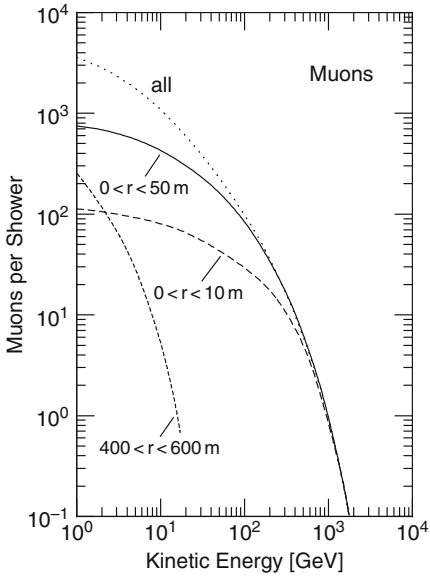

Fig. 1.7 Average integral energy spectra of muons in a 10^6 GeV proton initiated vertical air shower at sea level that fall within annular regions at core distances of $0 \leq r \leq 10\,\text{m}$, $0 \leq r \leq 50\,\text{m}$ and $400 \leq r \leq 600\,\text{m}$, respectively (Grieder, 1977). It is evident from these spectra that the particle populations get less and less energetic with increasing distance from the shower axis. Also shown is the overall muon spectrum (other group of showers than Fig. 1.6)

counting rate of showers of a given size is observed if we select events arriving at larger and larger zenith angles. This is illustrated in Fig. 1.8.

The general form of the composite differential primary energy spectrum is shown in Fig. 1.9. Roughly speaking and disregarding the very low energy part of the spectrum, it can be represented by a power law with a kink around a few times 10^6 GeV, known as the *knee*. The spectrum exhibits some structure around the knee which still remains rather uncertain.

At a few times 10^9 GeV there are indications for the onset of a second rather soft bend, known as the *ankle*, where the spectrum tends to flatten. The statistics are poor in this energy region and the uncertainties large, nevertheless, the data suggest a spectral exponent of about -1.8 at 10^{10} GeV and it appears that the *Greisen-Zatsepin-Kuzmin* (GZK) *cutoff* that should occur around $(3\text{–}5) \cdot 10^{10}$ GeV for protons is being violated (Greisen, 1966; Zatsepin and Kuzmin, 1966; Kuzmin and Zatsepin, 1968). This is illustrated in Fig. 1.10 which shows the high energy portion of the differential primary energy spectrum. Note that the intensity is multiplied by the energy to the power of 2.75 to compress the spectrum and to emphasize the changes of slope.

The cause for the first change of slope, the knee, is uncertain and much debated. It can be interpreted either as a genuine feature of the source spectrum (e.g., a composite spectrum resulting from the superposition of contributions from different sources with different spectral features), or as a change in the primary mass composition. The latter could be the result of a *galactic rigidity confinement effect*, whereby protons begin to leak out of the Galaxy first, followed by heavier and heavier nuclei. A change in the nature of the interactions, which had been proposed at one time as an explanation, seems to be ruled out in the light of recent collider and air shower data.

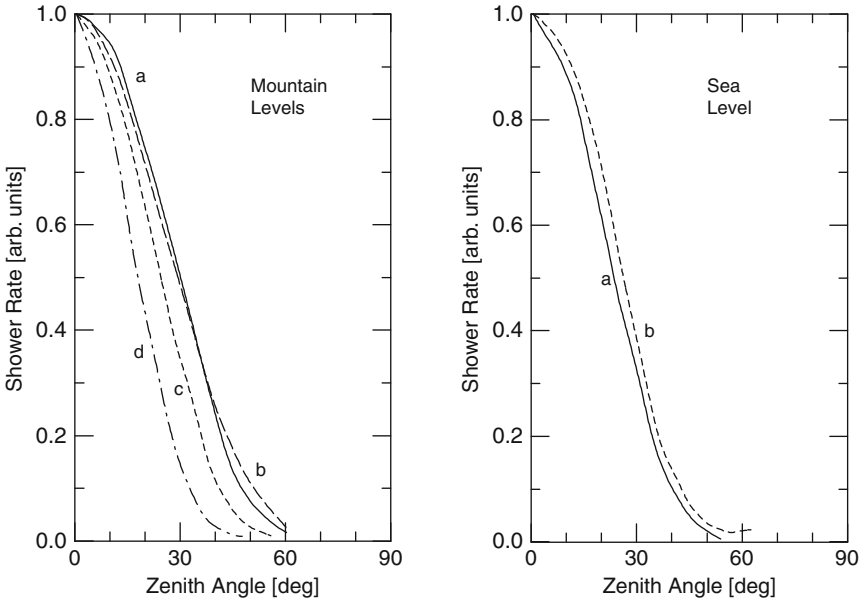

Fig. 1.8 Zenith angle distribution of the rate of air showers of size $\geq N$ at mountain altitudes and sea level (N was not determined experimentally but is estimated by this author to be $\sim 10^4$). Shown is the relative counting rate as a function of zenith angle, θ. *Left hand figure: curve* (*a*) Kraybill (1954) calculated for altitude 3,260 m; (*b*) Brown and McKay (1950) 3,260 m, (*c*) Daudin (1945) 2,000 m, (*d*) Williams (1948) 3,050 m, all experimental. *Right hand figure: curve* (*a*) calculated from altitude dependence (Kraybill, 1954), (*b*) Deutschmann (1947) experimental, both for sea level

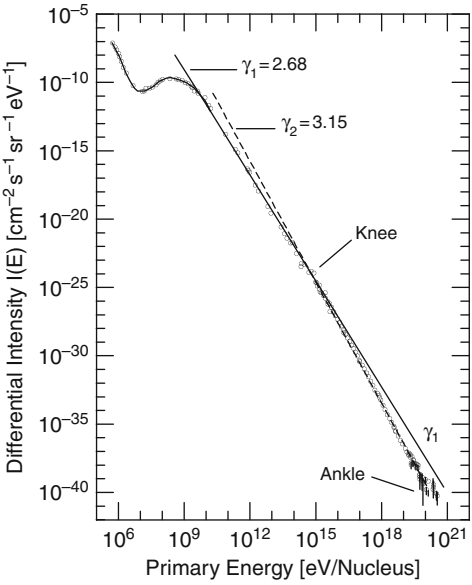

Fig. 1.9 Differential energy spectrum of the composite primary cosmic radiation, also known as the primary all-particle spectrum. Disregarding the very low energy portion, the spectrum exhibits an evident change of slope around a few times 10^6 GeV, known as the *knee*, and some substructure. Each of the two main portions of the spectrum can be approximated by a power law with exponent γ, as indicated. Toward the upper end of the spectrum there is another change of slope, known as the *ankle* where the spectrum appears to flatten (Courtesy of Simon P. Swordy; Cronin et al., 1997; Cronin, 1999)

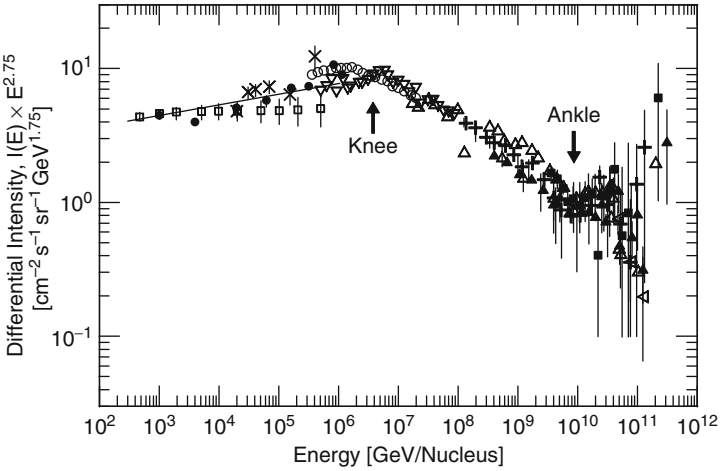

Fig. 1.10 High energy portion of the composite differential primary spectrum. The plot shows along the ordinate the intensity multiplied by the energy to the power of 2.75 to compress the spectrum and emphasize the spectral features and changes of the slope. The knee and ankle of the spectrum are evident (Grieder, 2001)

The reason for the second change of slope, the ankle, is believed to be due to an *extragalactic contribution* to the galactic cosmic radiation which has a flatter spectrum, that becomes the dominating component above 10^{10} GeV.

Air showers have been studied systematically for well over 60 years. Since their discovery by Auger (Auger, 1938; Auger et al., 1938) the motivations for this work arose from different branches of physics. These include high energy particle physics, cosmic ray physics, astrophysics and cosmology. In the first case the interest is focused chiefly on that part of the information that can be extracted from the shower process which is useful to study the phenomenology of ultrahigh energy interactions and to search for new particles and processes. Many of the so-called *elementary particles* were discovered in cosmic ray experiments. They include the e^+, μ^+, μ^-, π^+, π^-, π^0, K^+, K^-, K°, Λ°, Σ^+, Ξ^- and, in fact, charm was first seen by Niu in cosmic ray exposed nuclear emulsion (Niu et al., 1971a, b; Hayashi et al., 1972a, b; Niu, 1979 and references listed therein) before its recognition at the accelerators.

For the remaining fields of cosmic ray physics, astrophysics and cosmology, questions related to chemical and, if possible, isotopic composition, spectral features, time variation, anisotropy of arrival direction and the origin of the most energetic primary cosmic rays are of prime interest.

The air shower process represents the most spectacular but also the most complex phenomenon that we can observe in ultrahigh energy physics. It is a unique source for gathering a great wealth of information over an enormous range of energies, from about 10^4 to well over 10^{10} GeV in the laboratory frame of reference. At present, extensive air showers are the only means to extend the experimentally

accessible energy range for hadron collisions by several orders of magnitude beyond the laboratory energy equivalent of that of the colliders at CERN (European Center for Particle Physics, Geneva, Switzerland), FNAL (Fermi National Accelerator Laboratory, Batavia, IL, USA) and even the future Large Hadron Collider (LHC) at CERN.[2] Moreover, for years to come ultrahigh energy interactions of secondary particles, such as pions, muons, neutrinos, etc., with nuclear targets can only be studied by means of cosmic rays.

In view of the extreme complexity of the shower phenomenon and of the processes involved, and because of the statistical nature and great spatial extension of air showers, the amount of information that is simultaneously accessible by means of conventional detector arrays in individual events is comparatively small. This applies to total absorption shallow lake or pool detectors, too, such as Milagro (McCullough, 1999), that have recently come into operation or are presently in an exploratory phase at various sites.[3] The latter type of detector permits the determination of the total energy flux over a relatively large area and can give some structural details, but it lacks the high resolution of modern hadron calorimeters that should be an integral part of any major air shower array today, as had been demonstrated by the KASCADE detector at Karlsruhe, Germany (Engler et al., 1991; Antoni et al., 2003).

Nevertheless, irrespective of the shower detection system employed, the data thus acquired represent the cascade at a particular level or stage of development. It is, so to say, a *snapshot* of the shower at the plane of observation based on *sampling*.

Apart from the energy and mass of the primary, the stage of shower development depends mostly on the amount of matter that lies between the locations of the first interaction and that of the detector system in the atmosphere, and on the properties of the propagation and interaction characteristics of the particles in the shower that govern the cascade process.

Measurements of *air Cherenkov* and *air fluorescence* (or *air scintillation*) light flashes caused by showers in the atmosphere have proven to be very useful because they yield information on the early history and the longitudinal development of the showers. In principle, the atmosphere can be used in the widest sense as a sort of air Cherenkov or air fluorescence calorimeter.

Unfortunately optical detection methods can only be employed under particular circumstances. Appropriate installations must be located at sites where excellent meteorological conditions prevail (clear cloudless skies, little precipitation), with low dust and aerosol content in the atmosphere, and with low optical background. They can only be operated during clear, moonless nights unless appropriate filters

---

[2] The energy of the LHC at collision will be 7+7 TeV in the CM for *pp*-collisions, corresponding to a proton beam energy of almost 100 PeV (10^8 GeV) in the laboratory on a fixed target.

[3] For historic reasons we should mention the pioneering experiment of this kind, named BATISS (Batavia-Issyk-Kul), that was planned about two decades earlier, basically as a neutrino detector in the Issy-Kul lake in Kyrgyzstan, but had never materialized beyond the prototype stage (Ermatov et al., 1981; Albers et al., 1983; Erofeeva et al., 1987).

and ultraviolet sensitive optical sensors are being used that permit limited operation during nights with the presence of a partial moon in the sky. As a result the duty factor of such installations is very low, on the order of a few percent.

A special feature of air fluorescence is that the light is emitted *isotropically*. Thus, the showers can be viewed from the side, even at large angles and valuable longitudinal information becomes directly accessible. In practice this implies observation from a relatively large distance. Therefore, and because of the omnidirectional emission of fluorescence light, the intensity at a distant detector viewing the same shower side-on is low compared to the intensity of the strongly *polarized* and *forward emitted* Cherenkov light of the same shower falling on a detector within the Cherenkov cone, which is at much closer proximity to the shower axis. For this reason the air fluorescence detection method is only applicable to very large showers, initiated by primaries of energy $\geq 10^8$ GeV.

Arrival time profile measurements of the particles in the shower front can also yield a limited amount of information on the longitudinal development of a shower but the data are rather delicate to analyze and interpret; they are less reliable and cannot be regarded as a substitute in place of atmospheric Cherenkov measurements.

Non-local information on the shower development is in principle also obtainable from radio burst measurements. However the acquisition of radio bursts is very tedious, particularly in industrialized areas, because of the high background level. Moreover, radio data are extremely difficult to interpret because the relative significance of the different mechanisms that are believed to be responsible for producing radio bursts is still uncertain. Today geo-synchrotron radiation is believed to be the main contributor (Falcke and Gorham, 2003). Up to date no relevant new information has been obtained with this technique (for a review of the early work see Allan, 1971).

At present only few detection systems are equipped to acquire simultaneously lateral as well as longitudinal information of the recorded showers, and even fewer installation can carry out such measurements in conjunction with energy or momentum determination of the energetic particles in the shower core. The analysis of the first few ultra energetic interactions ($E > 100$ TeV) near the top of the atmosphere, which hold the relevant and possibly new information on interaction properties, such as cross section, secondary particle multiplicity and the nature of the primaries, remains inaccessible to direct observation by balloon or satellite-borne detectors because of the low primary flux and must therefore be based on observations made many interaction mean free paths deeper in the atmosphere, a truly difficult task.

Detailed shower simulations have shown that in order to improve the reliability and uniqueness of air shower data and their interpretation, each individual shower must be fully assessed by as many simultaneous observables as possible (Grieder, 1977). Large-scale high energy hadron calorimetry and high energy muon spectroscopy in or near the shower core hold some of the most important information and give access to a new generation of data. Combined with standard array data, air Cherenkov and scintillation data, they hold the key for reliable mass composition

measurements in the air shower energy range (Grieder, 1984). Moreover, they permit the study of the properties of ultrahigh energy hadronic collisions at the fringes of the atmosphere, spectral features and composition of the primaries and a wide scope of topics in particle and astrophysics.

For a more extensive introduction to air showers, the reader is referred to the books of Galbraith (1958), Hayakawa (1969), Khristiansen (1980), Sokolsky (1989) and Rao and Sreekantan (1998), and for historic reviews to the articles of Rossi (1948), Cocconi (1961) and Sitte (1961). A treasure chest of important basic theoretical contributions in the form of collected papers is found in Heisenberg (1943, 1953). Specific topics concerning high energy interactions in conjunction with air showers are discussed in the book of Gaisser (1992) and astrophysical aspects in Stanev (2004).

Recent reviews including progress and status reports of the giant Southern Auger Air Shower Observatory, now operating in Argentina[4] are given by Blümer (2003), Abraham et al. (2004), Mantsch (2005) and Dawson (2007) (see also Cronin, 2000, 2001a, b; Zavrtanik, 2000; Olinto, 2007; Cho, 2008), and likewise for the Telescope Array in Utah, USA by Kasahara et al. (2007). For overviews of newly proposed satellite detector systems to study ultrahigh energy cosmic rays and air showers such as JEM-EUSO (EUSO – Extreme Universe Space Observatory) (Ebisuzaki et al., 2007, 2008), OWL-AIRWATCH[5] (Scarsi, 1999; Krizmanic, 1999) and others, the reader is referred to the Proceedings of the International Cosmic Ray Conferences held at Hamburg, Germany in 2001 (Simon et al., 2001), Tsukuba, Japan in 2003 (Kajita et al., 2003), Pune, India in 2005 (Tonwar et al., 2005), Merida, Mexico (UNAM, 2007), Lodz, Poland (2009), and to those of the XII, XIII and XIV. International Symposia on Very High Energy Cosmic Ray Interactions (ISVHECRI) held at CERN, Geneva, Switzerland in 2002 (Pattison et al., 2003), Pylos, Greece in 2004 (Grieder et al., 2006), Weihai, China in 2006 (Cheng et al., 2008), and Paris, France, in 2008.

Another topic worth mentioning is the possibility of high energy primary neutron initiated showers. Energetic neutrons may be a byproduct of various acceleration scenarios, resulting from the dissociation of high energy nuclei in high radiation fields while escaping an acceleration region, or they may result from spallation reactions of nuclei in space. With a mean life of 885 s, a neutron having an energy of 1 EeV (10^{18} eV) has a mean life travel distance of $\simeq 10$ kpc, roughly the distance to Cygnus X-3 (Jones, 1990) (Chap. 11).

[4] The Northern Auger Observatory site that is going to be the counterpart to the Southern Observatory will be built near Lamar, CO, USA. The altitude of the large site ranges from 1,200 to 1,500 m a.s.l.

[5] This proposal was abandoned some time ago.

1.2 Gamma Ray and Electron Initiated Air Showers

1.2.1 Gamma Ray Showers

High energy primary gamma ray initiated air showers ($E_\gamma \geq 1$ TeV) are of particular interest to cosmic ray physicists, astrophysicists and cosmologists because gamma rays are not deflected by the more or less randomly oriented magnetic fields in the Galaxy and beyond as charged particles are. Since the direction of arrival of a shower initiating particle or photon can in principle be determined with ground based installations, such as conventional charged particle detector arrays, air Cherenkov detector arrays, air Cherenkov telescopes or atmospheric fluorescence detectors, provided that the event exceeds the threshold requirements of the detector system, gamma ray showers reveal the direction in space from where the event-initiating gamma rays actually originate. This may possibly lead to the identification of the gamma ray sources which may also be potential sources of hadronic cosmic rays.

Primary gamma rays can be the result of pure electromagnetic processes or may have hadronic parents.[6] In the first case they may be generated as a byproduct of classical electron acceleration in the form of electron bremsstrahlung, resulting from collisions with the surrounding medium (for details see Chap. 4). Low energy photons can also gain significant amounts of energy via *inverse Compton scattering* (IC). This process is important when the density of ambient photons (and electrons) is high. It is an efficient process for boosting photons to high energies and is described in Sect. 4.4.[7]

The classical *synchrotron radiation* mechanism which takes place in curved acceleration scenario is another process that produces electromagnetic radiation. However, it is not suited to generate high energy gamma rays, and environmental conditions in the source region may impose additional limitations (Aharonian and Atoyan, 1995). This process is also outlined in Sect. 4.4.

The classical electromagnetic acceleration mechanism for electrons becomes less and less efficient with increasing energy because more and more energy is lost through synchrotron radiation. This sets practical limits to the asymptotic energy of electrons and consequently of photons, too, from this process.[8]

In the case of hadronic parents, the photons originate chiefly from the decay of neutral pions that are produced in high energy hadronic interactions, most likely in proton–proton or proton–nucleus collisions. Likewise, positive and negative pions are produced that decay to muons and muon neutrinos. In the subsequent decay of

---

[6] We disregard gamma ray lines because they are energetically irrelevant for air shower initiation and likewise radiation of thermal origin.

[7] As an example, IC scattered light from a Ruby laser on 20 GeV electrons boosts the photons to an energy of ∼12 GeV.

[8] The so-called *curvature radiation*, a special process that takes place in extremely high magnetic fields ($\sim 10^{12}$ G), such as in pulsars, is not relevant in the current context.

the muons, electrons which in turn produce gamma rays via bremsstrahlung result and, as important byproducts, electron and muon neutrinos. This sequence of interaction followed by decays is displayed in the following reaction and decay scheme.

$$\begin{aligned} p + p \;\rightarrow\; N + N + n_1\pi^{\pm} + \;\; n_2\pi^0 \\ \pi^0 \;\rightarrow\; 2\gamma \\ \pi^{\pm} \;\rightarrow\; \mu^{\pm} + {}^{(}\overline{\nu}{}^{)}_{\mu} \\ \mu^{\pm} \;\rightarrow\; e^{\pm} + {}^{(}\overline{\nu}{}^{)}_{\mu} + {}^{(}\overline{\nu}{}^{)}_{e} \end{aligned} \tag{1.2}$$

Similar schemes apply to kaons and other particles but their contributions are less relevant.

Because of the large mass of the protons (and nuclei) they can be accelerated more efficiently to high energies than electrons since they do not suffer of synchrotron energy losses in the relevant energy region. This is one of the reasons why it is generally believed that very high energy gamma rays emerge from hadronic and not electromagnetic processes. In principle, however, protons are subject to the same electromagnetic processes as discussed above, but at much higher energies than electrons.

The threshold energy that is required in the center of mass of a pp-reaction, $T_{\mathrm{th,CM}}$, to produce a single new particle of mass m, say a neutral pion, is given by the relation,

$$T_{\mathrm{th,CM}} \;\geq\; 2mc^2\left(1 + \frac{m}{4m_p}\right) \;\; [\mathrm{GeV}], \tag{1.3}$$

where m_p is the proton mass in [GeV/c^2]. Inserting for the mass m of the produced particle the neutral pion mass, $m_{\pi^0} \simeq 0.135\,\mathrm{GeV/c^2}$, one obtains for the threshold energy[9] $T_{\mathrm{th,CM}} \simeq 0.28\,\mathrm{GeV}$.

Cocconi (1960) was one of the first who suggested to search for high energy gamma ray initiated air showers and gamma ray point sources, in an attempt to identify likely sources of cosmic rays. One of the astrophysical objects that was considered to be a likely candidate for high energy gamma ray emission at that time was the Crab Nebula, the remnant of the famous nearby supernova (distance ~ 2 kpc) that exploded 1054 AD, as had been documented by contemporary Chinese astronomers[10] and cited in certain European Church documents (Polcaro, 1993).[11] By 1960 the Crab's highly polarized optical emission which is due to synchrotron radiation had already been observed, which revealed the presence of energetic electrons.

---

[9] Note that all conservation laws of hadronic interactions must be observed.

[10] The records are on display at the ancient astronomical Observatory in Beijing, China.

[11] This author lists specific references found in the Church literature from Rome and Belgium that contain records of a light flash that was observed for approximately half an hour during the day at that time.

Based on contemporary information on the Crab, Cocconi has made a first estimate of the intensity of high energy gamma rays from this object. Subsequent searches to detect this radiation failed initially because the intensity was much lower than predicted, as later successful investigations have proven (for a review of the early history see Weekes, 1988).

For intensity estimates of gamma rays from distant objects one must keep in mind that gamma rays are subject to interactions and scattering processes with the interstellar medium, starlight and the background radiation, that limit their range of undisturbed propagation in space (Wdowczyk et al., 1972) (see Sect. 11.11). The universe is essentially opaque to photons between 10^{14} eV and at least 10^{18} eV because of the interaction with the 2.7 K cosmic microwave background radiation (for details see Sects. 4.4 and 11.4.2). So far the diffuse extragalactic gamma ray spectrum has been explored to $\sim$ 120 GeV. Between 30 MeV and 10 GeV the data can be fitted with a power law spectrum with spectral index -2.10 ± 0.03. The measured integral flux above 100 MeV is $(1.45 \pm 0.05) \cdot 10^{-5}$ ph cm^{-2} s^{-1} sr^{-1} (Smialkowski et al., 1997; Sreekumar et al., 1998; Weekes, 2003b; Aharonian, 2004; Moskalenko et al., 2004).

The basic processes that limit the propagation of high energy gamma rays in space, causing them to lose energy and being scattered are the following:

- Interactions of gamma rays with photons of the radiation field (2.7 K CMBR, starlight, radio waves, etc.) (photon–photon interactions).
- Electron pair production in the Coulomb field of charged particles in the interstellar medium (ISM).
- Muon pair production in the Coulomb field of charged particles.
- Photonuclear interactions with nucleons and nuclei of the ISM.
- Electron pair production in magnetic fields.[12]

Compton scattering, the photo-electric effect, atomic excitation and ionization are irrelevant at this energy regime. Details concerning the different processes are discussed in Sect. 4.4.

The early history of gamma ray astronomy, from the first attempts to detect and identify gamma ray showers to actually finding an acceptable signature from an anticipated or accidentally discovered source to today's impressive catalogue of sources reveals many disappointments and failures. Several reasons are responsible for the great difficulties encountered by the early researchers to detect gamma ray showers.

[12] This process, also known as *magnetic pair production*, occurs only in extremely strong magnetic fields or at ultrahigh energies in weak fields. It has its counterpart in *magnetic bremsstrahlung* of electrons (see Chap. 4).

At first sight gamma ray showers appear to look like hadron initiated showers. However, at a more refined level of investigation one finds that there are some characteristic differences that can be summarized as follows[13]:

- In comparison to hadron showers, gamma ray showers of comparable energy have a significantly different spatial structure. They are more compact, i.e., the particles are strongly beamed in the forward direction and closer to the shower axis than in hadronic showers. This is because the electromagnetic cascade products, i.e., the electrons emerging from pair creation and the photons resulting from electron bremsstrahlung, do not acquire on average the large transverse momenta that are typical for hadrons emerging from production reactions. While propagating the electrons are mainly subject to Coulomb scattering.
- The particles in gamma ray showers are strongly bunched in a thin disk having a thickness of little more than one meter. Their passage through a fast, thin detector yields a rapidly rising narrow pulse of 3–5 ns duration. They lack the tail of late, trailing hadrons and muons.
- Gamma showers lack completely the high energy hadronic core and have a negligible hadron content.
- They are not subject to the large fluctuations in their development that are typical for hadronic air showers. This is evident when comparing simulation results obtained for gamma ray and hadron initiated air showers (see Figs. 4.14 and 6.1).
- The muon content in gamma ray showers is very low, only about a percent of that found in hadron induced showers (Stanev, 1986; Halzen et al., 1997; Boone et al., 2002). The muons are the result of photonuclear reactions, in particular photo-pion production.

In view of these facts it is evident that the crude detection methods with simple air shower arrays have practically no chance to distinguish gamma ray from hadron triggered showers. In Fig. 1.11 we show the longitudinal profile of three simulated air showers across the entire atmosphere that are initiated by different primaries, all having the same total energy of 10^5 GeV. One is a photon, the other a proton and the third an iron nucleus. Plotted are only trajectories of particles that have an energy $\geq$10 GeV.

The lateral spreads are dramatically different, particular between the photon and hadron initiated showers. The widely spread particles of the latter in the lower regions of the atmosphere are mostly muons. If much lower energy particles are included, say down to the air Cherenkov threshold,[14] the spread of the photon shower at sea level would have a radius of about 100 m, whereas the spread of the two hadron showers would have typical radii of about 500 and more than 1,000 m, respectively.[15]

---

[13] Details of hadronic and electromagnetic interactions and cascades are discussed in Chaps. 3 and 4, and in Chaps. 6, 8 and 10.

[14] The Cherenkov threshold is 21 MeV for electrons at atmospheric pressure where the index of refraction is $n = 1.00029$.

[15] Electron initiated showers are essentially identical to gamma ray showers.

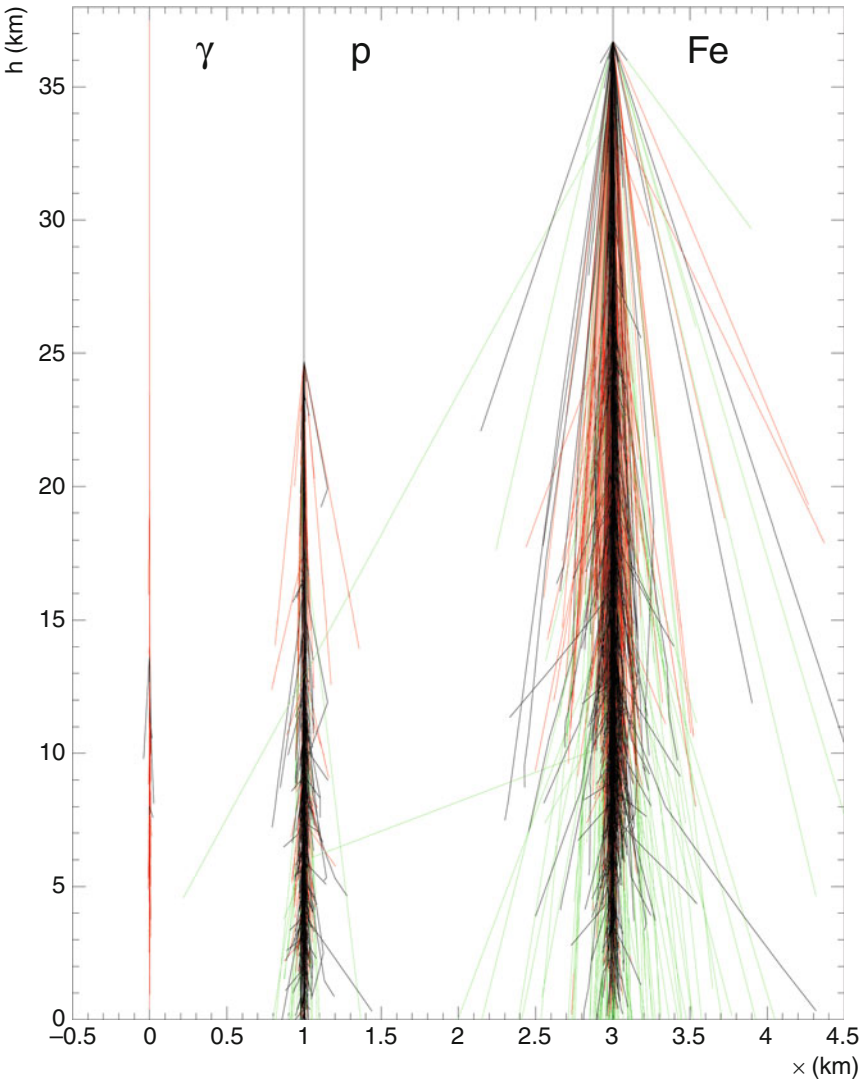

Fig. 1.11 Side view of trajectories of particles of energy $\geq$10 GeV of a photon, a proton and an iron nucleus initiated shower having a total primary energy of 10^5 GeV each. The electromagnetic component is shown in *red*, hadrons are *black* and muons *green*. The widely spread particles in the lower region of the atmosphere in the hadron showers are mostly muons (courtesy of KASCADE group)

A further problem that may arise when searching for point sources is their variability. An exception is the Crab Nebula that was found to be a steady unpulsed (DC) emitter at an energy of $E_\gamma \geq 0.4\,\mathrm{TeV}$ with a flux of $\sim 7 \cdot 10^{-11}\,\mathrm{ph\,cm^{-2}\,s^{-1}}$ and an integral spectrum of the form $E_\gamma^{-1.4\pm0.3}$, that does not show the Crab pulsar periodicity[16] (Vacanti et al., 1991). The Crab is therefore considered as a sort of standard candle for gamma ray astronomy.

The bulk of all air showers that reach ground or even sea level are produced by primary hadrons, predominantly protons in the energy range below the spectral knee and by an increasing admixture of nuclei towards the knee region. These showers produce a very high level of background events that mask the rare gamma showers that account for $\ll 1\%$ of all showers, making it very difficult to filter them out. To optimize the detection of gamma ray showers, it is necessary to select the best suited detection method and instrumentation for a given site and energy regime. In other words, the detection system must be adapted to the distinct properties of the showers to be investigated. For low energy events the altitude is a relevant factor.

We distinguish between the diffuse gamma radiation that cannot be linked directly to a source and gamma rays from point sources. Today, the study of the latter is the domain of gamma ray astronomy, a well established and important field of research (for details see Weekes, 1988, 1996, 2003a, b; Ramana Murthy and Wolfendale, 1993; Schönfelder, 2001; Kifune, 2003; Völk, 2003; Aharonian, 2004). The diffuse radiation is believed to include contributions from collision processes of particles and radiation with the interstellar medium and from unresolved point and extended sources.

Theoretical as well as experimental investigations have shown that for point source studies at low energies ($E \geq 100\,\mathrm{GeV}$) air Cherenkov telescopes with *imaging capability* are best suited (Weekes, 1988). The photons of the atmospheric Cherenkov light flash of gamma ray showers at the detector level fall on a small area compared to hadron showers. Since the optical band of the Cherenkov emission suffers little absorption in the atmosphere, the Cherenkov technique has the advantage that it permits the recording of low energy showers whose particle population has died out in the atmosphere before reaching a detector array on the ground.

The large number of photons that arrive as a relatively compact bundle distributed fairly uniformly over an area of about 100 m in radius[17] in a very short time interval (typically $\sim 5\,\mathrm{ns}$) and the high photon density reduce the inherent fluctuations that are typical for charged particle detection. Shower detection using the optical Cherenkov light flash is therefore *not limited by Poissonian statistics* as is charged particle detection.

During its short occurrence the Cherenkov light flash exceeds the night sky brightness which is on the order of $10^8\,\mathrm{ph\,cm^{-2}\,s^{-1}\,sr^{-1}}$ in the wavelength window between 330 and 450 nm. Night sky brightness fluctuations are crucial for a

[16] Since the angular resolution of detection of a source is seldom better than $\sim 1^\circ$ in the TeV range, one cannot distinguish steady emission from the pulsar and the nebula.

[17] For a primary gamma ray in the TeV energy region (Konopelko, 1997).

good signal to noise ratio.[18] The small time dispersion of the Cherenkov pulse is partly due to the fact that the threshold for producing Cherenkov radiation in air requires highly relativistic particles, particularly at higher altitudes where the index of refraction is small.[19]

The narrow opening angle of the Cherenkov light cone ($\sim 1.3^\circ$ at sea level and less at higher altitudes where the atmospheric density is lower) and the small lateral spread of the electrons yield an angular resolution which is on the order of 0.5–2°. This is comparable to the 1–3° for common shower arrays. In combination with the limited field of view (aperture) of Cherenkov telescopes a high degree of background rejection is achieved with this method. Further details and related topics are discussed in Chap. 16 in conjunction with air Cherenkov phenomena and the detection of common hadron and gamma ray air showers using the atmospheric Cherenkov technique.

At higher energies and for general surveys wide-angle acceptance systems and versatile Cherenkov telescope arrays are more appropriate, as well as compact charged particle detector arrays at higher elevation (Amenomori et al., 1990, 2003; Vernetto et al., 2003; Cao, 2005). To improve hadron shower rejection, additional muon detectors are incorporated to select only so-called muon-poor showers, i.e., showers whose muon content is very low.

For ground based air Cherenkov detection the threshold for gamma ray induced showers is presently between 10 and 100 GeV, for particle arrays it is $\sim$ 100 TeV. For sophisticated arrays at high altitude the threshold is lower (3–10 TeV at 4,300 m a.s.l.) (Amenomori et al., 1990, 1997, 2003, 2005).

Efforts are currently under way to lower the air Cherenkov detection threshold energy down to $\sim$ 5 GeV, to obtain a sufficient overlap with satellite based observations (Merck et al., 2003). Gamma ray detection at lower energies must be carried out with balloon or space borne detectors that employ different techniques (for details see Schönfelder, 2001). Further details on primary gamma rays are given in Sect. 11.4.2.

1.2.2 Electron Initiated Showers

The existence of electrons (positrons and negatrons) in the primary cosmic radiation has been known since the early 1960s (Earl, 1961; Meyer and Vogt, 1961). Additional evidence for the presence of positrons in the Galaxy comes from the observation of the 0.511 MeV e^+e^- annihilation line. The bulk of high energy cosmic ray electrons are thought to be secondaries resulting from high energy collisions

[18] Optical night sky background is discussed in greater detail in connection with the air fluorescence detection method in Chap. 17.

[19] The Cherenkov threshold condition for the velocity of a particle, $\beta \geq n^{-1}$, at sea level ($1{,}033\,\mathrm{g\,cm^{-2}}$, $n = 1.00029$) corresponds to energies of 21 MeV for $e^\pm$, 4.4 GeV for $\mu^\pm$ and 39 GeV for p and $\overline{p}$.

of cosmic rays with the interstellar medium (cf. Eq. 1.2). Generally speaking, electrons beyond 1 TeV cannot travel far distances in space because of synchrotron and inverse Compton energy losses.

Like gamma rays, electrons initiate electromagnetic showers in the atmosphere but they are indistinguishable from each other with ground based equipment. In view of the downward turn of the electron spectrum at relatively low energy ($\geq$ 100 GeV), no significant contribution to the rate of air showers can be expected from cosmic ray electrons. For further details on this subject the reader is referred to Sect. 11.3.2.

1.2.3 Pre-showering Effect

A particular scenario worth mentioning here occurs if an ultrahigh energy photon (gamma ray) approaching the Earth interacts with the geomagnetic field far beyond the fringes of the atmosphere, causing *magnetic electron pair production*. Subsequently, the newly created electrons undergo *magnetic bremsstrahlung*. This sequence of elementary processes may repeat itself several times well before reaching the atmosphere, thus provoking a highly collimated small but very energetic shower.

Upon entry into the atmosphere, the particle group may imitate the arrival of a single heavy primary, such as iron, generating an iron-like shower. This process is known as *pre-showering* and is discussed in more detail in Sect. 4.5. It can cause a major problem for primary mass determination at the highest energies if ultrahigh energy photons ($\geq 10^{18}$ eV) do exist in our Galaxy.

1.3 Neutrino Initiated Air Showers

No very high energy extraterrestrial (non solar) neutrinos have knowingly been detected so far, thus, their intensity is de-facto unknown or at most speculative. Apart from the very successful detection of solar neutrinos, particularly with the Super Kamiokande detector (Koshiba, 1992) which has the capability to determine the approximate direction of arrival of the neutrinos as well, only atmospheric neutrinos (mainly electron and muon neutrinos) and their antiparticles have been observed so far with previous and existing detectors (Washburn et al., 2003, Super Kamiokande), including the large underwater and under ice muon and neutrino detector telescopes (Babson et al., 1990, DUMAND prototype; Ayutdinov et al., 2003, Lake Baikal; Hauschildt et al., 2003, AMANDA-II; Hill, 2005, IceCube; see Montaruli, 2003; Goodman, 2005 for reviews).

The neutrino reactions in air or rock[20] that lead to air showers (Fargion et al., 1999; Fargion, 2001) or those that take place in water or ice and permit the detection

[20] Neutrinos that enter a mountain range under a large zenith angle at a sufficient altitude such that the trajectory can escape the mountain into the lower atmosphere may interact near the point of exit and produce an inclined air shower emerging from the mountain slope.

of the neutrino reaction directly occur on nucleons of nuclei of air, water or rock constituents. The reactions that can take place with the differently flavored neutrinos and their antiparticles are listed in Table 5.1.

Atmospheric neutrinos are predominantly the decay products of charged pions and muons resulting from energetic collisions of the hadronic cosmic radiation with nuclei of the atmospheric constituents, similar to the reaction specified in Eq. (1.2). Their spectrum which follows a power law drops more and more rapidly with increasing energy, reaching a slope of about -3 at 1 TeV (differential), because the decay probability of the parent pions decreases in favor of interaction with increasing energy, thus contributing less and less to the neutrino flux. The situation is similar for kaons but they are less significant (for details see Grieder, 2001, Sect. 5.5). The spectral slope of the rare direct contributions to the atmospheric neutrino (and muon) flux from charm decay remains unaffected.[21] Astrophysical neutrinos are expected to have a hard (flat) spectrum, so that they outnumber the atmospheric component at very high energies (see Sect. 11.5).

As with gamma rays, one usually distinguishes between the diffuse extraterrestrial neutrino flux and neutrinos from point sources. The latter are easier to detect because of a better signal to noise ratio. The projection along the trajectory of each neutrino into the past identifies unambiguously the source region on the celestial sphere, i.e., the direction in space from where the neutrino has arrived.

Because of the scattering angle, θ, between the incident neutrino and the outgoing charged particle, which depends on the neutrino energy, the source direction can only be determined within a certain solid angle. With increasing neutrino energy the scattering angle gets smaller and goes approximately as $\theta \simeq 1.5^\circ/\sqrt{E_\nu}$ for E_ν in [TeV]. For muon neutrinos in the TeV energy range this angle is on the order of $(\sim 1^\circ)^2$ or < 1 msr.

The detection of neutrino point sources is of great importance for cosmic ray and astrophysics as well as cosmology. Muon neutrinos are a unique signature of hadronic processes, such as given in reaction Eq. (1.2). They identify directly a hadron acceleration region and therefore a likely source of hadronic cosmic rays. But also electron neutrinos have hadronic grand parents since they are the decay products of muons. Should a newly discovered neutrino point source overlap with a known source of optical, radio, X- and/or gamma radiation, then, under the assumption that we are dealing with a single object, the combined interpretation of the data from different electromagnetic radiation windows and the neutrinos will give us deep insight into the particular mechanisms that take place within the object and its immediate vicinity. The simultaneous detection of gamma rays and neutrinos from one and the same source would yield direct information on the matter density, ρ [g cm^{-3}], and the column density, X [g cm^{-2}], of the immediate source environment.

However, muon neutrinos do not necessarily trigger-off air showers directly when interacting with a nucleon of a target nucleus in the atmosphere. In a first step the

[21] The competition between interaction and decay of unstable particles is discussed in connection with the nuclear cascade development in Sect. 3.12.

reaction ($\nu_\mu, N \rightarrow \mu, N + kh$)[22] may occur, where N stands for a nucleon (p or n) and kh for k hadrons. The hadronic component, if sufficiently energetic, can initiate a hadron cascade with its byproducts. The resulting muon, while propagating through the atmosphere, may undergo either hard bremsstrahlung or a photonuclear reaction.[23] In the first case the resulting photon creates an electromagnetic shower, in the second, one or several high energy hadrons are produced that can initiate a classical air shower with nuclear and associated electromagnetic cascades interlaced. Recoil effects of neutrino reactions on nuclei are frequently of lesser concern, particularly in dense media, as they are readily absorbed.

On the other hand, electron neutrinos are capable to initiate electromagnetic showers directly after having interacted with a nucleon of a target nucleus, producing an energetic electron, or after quasi-elastic scattering off an (atomic) electron. The probability for an electron or muon neutrino or antineutrino to initiate a shower in the atmosphere is extremely small because of the small cross section and the low density of the atmosphere, particularly at high altitude.[24] High altitude initiation of showers is desirable so that the shower has a chance to develop sufficiently, to be detected.

Another possibility is that a high energy neutrino whose trajectory emerges from beyond the horizon after having traversed part of the Earth undergoes an interaction immediately before surfacing or shortly after entering the atmosphere.[25]

Such events produce upward directed showers. These can be recorded with ground based Fly's Eye type air fluorescence and satellite-borne combined air Cherenkov and fluorescence detectors, such as JEM-EUSO (Scarsi, 2001; Teshima et al., 2003; Ebisuzaki et al., 2007, 2008) and others (Scarsi, 1999; Krizmanic, 1999), if the showers exceed detection threshold. An additional possibility to detect neutrino induced showers may be with ground based antennae that detect the radio bursts that are caused by the showers (Askar'yan, 1961, 1962a, b, 1965a, b; Fujii and Nishimura, 1970; Allan, 1971; Zas et al., 1992; Jelley, 1996; Kalpana and Pranayee, 2001; Horneffer et al., 2003). Radio burst generation of showers is discussed in Chap. 18.

But also so-called *horizontal air showers* (HAS), i.e., showers that have a zenith angle $> 75^\circ$, can occasionally be neutrino induced and may serve as a mean to investigate the high energy astrophysical neutrino flux (Aglietta et al., 1995). Neutrino induced showers are usually *muon-poor showers* because they lack the hadronic component. The Tokyo and Kiel groups were the first to investigate horizontal air showers experimentally (Matano et al., 1968; Böhm et al., 1971; Kiraly et al., 1971; Böhm and Nagano, 1973; Nagano et al., 1986). Further details concerning HAS are discussed in Sect. 19.5.2.

---

[22] Electron neutrinos can initiate an analogous reaction ($\nu_e, N \rightarrow e, N + kh$).

[23] Photonuclear reactions are briefly discussed in Chaps. 4 and 5.

[24] For neutrino cross sections see Chap. 5.

[25] The Earth is opaque to very high energy neutrinos. For details see Chap. 5.

The discovery of neutrino oscillations (Fukuda et al., 1998, 1999, 2000; Ahmad et al., 2001) opens the possibility to investigate the astrophysical neutrino flux with the help of the tau neutrino. This approach is based on the idea that the flavor ratios are

$$\nu_e : \nu_\mu : \nu_\tau \; = \; 1 : 1 : 1 \tag{1.4}$$

because of $\nu_\mu \leftrightarrow \nu_\tau$ oscillations. This opens a window between 10^{15} eV and 10^{18} eV for high energy neutrino astronomy and astrophysics (Beacom et al., 2002). The tau neutrino is expected to have a much higher probability for producing an air shower in an interaction in the Earth's crust or the ocean near the surface that is detectable with a Fly's Eye type fluorescence detector on the ground or with an appropriate space bound detector than the other flavor companions, ν_e or ν_μ.[26] Cao et al. (2003) have carried out a feasibility study for a dedicated experiment using a fluorescence detector.

1.4 Dust Grain Hypothesis

The idea that very energetic cosmic rays may consist of dust grains and that relativistic dust grains may possibly trigger air showers was proposed by several authors in the past and the subject surfaces periodically again. Spitzer (1949) pointed out that interstellar dust grains can be accelerated to velocities near that of light by the pressure of supernova radiation.

Alfvén (1954) noted that cosmic dust will ordinarily be charged, and consequently can be accelerated by the same electromagnetic processes that can produce ordinary cosmic rays. He suggested that the highest energy cosmic rays then known ($\simeq 10^{17}$ eV) might be dust particles having an energy per nucleon on the order of 10^{11} eV. In his analysis, Herlofson (1956) came to the conclusion that the energy per nucleon would have to be about 10^{14} eV N^{-1} to produce showers. He also points out that the grains would begin to evaporate at altitudes around 100 km. Therefore, dust grain initiated showers would have a structure that is different from the commonly observed showers, i.e., the shower would have a much flatter core region as it would be the product of the superposition of many small sub-showers initiated by the numerous nuclei of the evaporated grain.

Hayakawa (1972) has studied the giant air shower event which had been detected by the Tokyo group (Suga et al., 1971a, b) on the basis of the relativistic dust grain hypothesis. The energy of this event had initially been estimated to be $> 10^{21}$ eV but was somewhat reduced in a later evaluation. He argues that a dust grain with a

[26] Large-volume deep-ocean or deep-ice detectors would have a good chance, too, to detect the ν_τ, as proposed by Learned and Pakvasa (1995), and more recently by Bugaev et al. (2003), using the so-called *double-bang* signature.

mass of about 10^{-16} g and a Lorentz factor of $\gamma = 10^3$ can attain an energy as large as 10^{20} eV and produce a huge air shower.

The acceleration due to the radiation pressure from Seyfert galaxies was estimated by Wolfe et al. (1950), taking the Doppler and retardation effects into account. On the basis of these assumptions, a spherical dust grain of radius a and density ρ starting at distance r from the center of a source of luminosity, L, gains velocity βc; therefore

$$\frac{2}{3}\beta^2\gamma^3\left((1+\beta)-\frac{1}{2\gamma(\gamma+1)}\right) = \frac{3}{16\pi}\left(\frac{L}{\rho c^3 a r}\right), \tag{1.5}$$

where $\gamma = 1/\sqrt{(1-\beta^2)}$ is the Lorentz factor, $\beta = v/c$, v being the velocity of the particle and c the speed of light (Hayakawa, 1972). For Seyfert galaxies $L \simeq 10^{46}\,\mathrm{erg\,s^{-1}}$ and for the radius of the nucleus we can take $r \simeq 3 \cdot 10^{17}$ cm. For a typical interstellar dust grain we have $\rho \simeq 3\,\mathrm{g\,cm^{-3}}$ and $a \simeq 3 \cdot 10^{-6}$ cm. The right hand side of Eq. (1.5) is therefore of the order of 10. This is not enough to produce air showers but adequate for injection into a magnetic acceleration process as is generally accepted for protons and nuclei. Ionization caused by the general background radiation field will give the dust particle the necessary electric charge.

In a later paper, Berezinsky and Prilutskiy (1973a, b) argue in their analysis that dust grains would acquire high electric charges while interacting with photons (relic 2.7 K photons and starlight) and the interstellar gas in space. The developing electrostatic forces would eventually break up the particles within the solar system. Grindlay and Fazio (1974) who also studied dust grain acceleration mechanisms came to a similar conclusion.

In another study, Aström (1977) concludes that dust grains would have to be accelerated to energies $\geq 2\,\mathrm{TeV}\,N^{-1}$ to produce the expected muon and electron sizes of air showers at ground level. His estimations indicate that it is unlikely that dust grains of conventional density ($\rho \sim 2$–$3\,\mathrm{g\,cm^{-3}}$) could be accelerated to these energies within a confinement region of heliospheric dimensions and he discards this hypothesis.

Linsley in his analysis (Linsley, 1980) presents a number of arguments and experimental facts, such as the depth of maximum development of showers, that essentially rule out relativistic dust particles for being the agents that generate extensive air showers. More recently, McBreen et al. (1991) argue that relativistic dust grains would melt in the solar radiation field before they reach the Earth.

In a long baseline experiment with air shower arrays at Ootacamund and Gulmarg (India), located some 2,500 km apart, Bhat et al. (1984) searched for correlated showers originating from dust grains which had been fragmented into nuclei in space, however, without success. A similar experiment has been under way in Japan for some time, where eleven air shower arrays that are located up to 1,000 km apart and enclose an area of 130,000 $\mathrm{km^2}$ are looking for time correlated arrivals of local showers (LAAS/ARPEGIO project). The aim of this project is not primarily to look for showers initiated by nucleons or nuclear fragments from nuclei that underwent fragmentation in collisions in space with the interstellar medium or originate from

dust grain fragments, but to focus on topics related to the acceleration mechanisms of cosmic rays (Ochi et al., 1999, 2003a, b).

References

Abraham, J., et al., Auger Collaboration: Nucl. Instr. Meth. A, 523, p. 50 (2004).
Aglietta, M., et al.: PICRC, 1, p. 638 (1995).
Aharonian, F.A., and A.M. Atoyan: Astropart. Phys., 3, p. 275 (1995).
Aharonian, F.A.: Very High Energy Cosmic Gamma Radiation, World Scientific, Singapore (2004).
Ahmad, Q.R., et al.: Phys. Rev. Lett. L, 87, p. 071301 (2001).
Albers, J.R., et al.: PICRC, 11, p. 489 (1983).
Alfvén, H.: Tellus, 6, p. 232 (1954).
Allan, H.R.: Progress in Elementary Particle and Cosmic Ray Physics, 10, p. 171, North Holland Publ. Co., Amsterdam (1971).
Amenomori, M., et al.: Nucl. Instr. Meth. A, 288, p. 619 (1990).
Amenomori, M., et al.: PICRC, 5, p. 249 (1997).
Amenomori, M., et al.: Proceedings of the International Science Symposium "The Universe Viewed in Gamma Rays", University of Tokyo Symposium, September 25–28, 2002, R. Enomoto, et al., eds., Universal Academy Press, Inc., Japan (2003).
Amenomori, M., et al., Tibet Collaboration: PICRC, 4, p. 211 (2005).
Antoni, T., et al.: Nucl. Instr. Meth. A, 513, p. 490 (2003).
Askar'yan, G.A.: Sov. Phys. JETP, 41, p. 616 (1961) (in Russian).
Askar'yan, G.A.: Sov. Phys. JETP, 14, p. 441 (1962a).
Askar'yan, G.A.: J. Phys. Soc. Jpn., 17, Suppl. A III, p. 257 (1962b).
Askar'yan, G.A.: Sov. Phys. JETP, 48, p. 988 (1965a) (in Russian).
Askar'yan, G.A.: Sov. Phys. JETP, 21, p. 658 (1965b).
Aström, K.: Report TRITA-EPP-77-17, Electron and Plasma Physics, Royal Institute of Technology, Stockholm, Sweden (1977).
Auger, P.: Comptes Rendus Acad. Sci. Paris, 207, p. 907 (1938) (in French).
Auger, P., et al.: Comptes Rendus Acad. Sci. Paris, 206, p. 1721 (1938) (in French).
Auger, P.: Rev. Mod. Phys., 11, p. 288 (1939).
Auger, P., et al.: J. de Phys. et Radium, 10, p. 39 (1939a) (in French).
Auger, P., et al.: Comptes Rendus Acad. Sci. Paris, 208, p. 1641 (1939b) (in French).
Auger, P.: J. de Phys. et Radium, 1, p. 173 (1940) (in French).
Auger, P., and J. Daudin: Phys. Rev., 61, p. 91 (1942).
Auger, P., and J. Daudin: J. de Phys. et Radium, 6, p. 233 (1945) (in French).
Ayutdinov, V., et al.: PICRC, 3, p. 1353 (2003).
Babson, J., et al.: Phys. Rev. D, 42, p. 3613 (1990).
Beacom, J.F., et al.: Phys. Rev. D, 66, 021303(R) (2002).
Berezinsky, V.S., and O.F. Prilutskiy: PICRC, 4, p. 2493 (1973a).
Berezinsky, V.S., and O.F. Prilutskiy: Astrophys. Space Sci., 21, p. 475 (1973b).
Bergström, L., and A. Goobar: Cosmology and Particle Astrophysics, Springer, Berlin, 2nd ed. (2004).
Bhat, C.L., et al.: J. Phys. G, 10, p. 1771 (1984).
Blümer, J., Pierre Auger Collaboration: J. Phys. G, 29, p. 867 (2003).
Böhm, E., et al.: PICRC, 4, p. 1438 (1971).
Böhm, E., and M. Nagano: J. Phys. A, 6, p. 1262 (1973).
Boone, L.M., et al.: Astrophys. J., 579, p. L5 (2002).
Brown, W.W., and A.S. McKay: Phys. Rev., 77, p. 342 (1950).
Bugaev, E., et al.: PICRC, 3, p. 1381 (2003).
Cao, Z., et al.: PICRC, 3, p. 1385 (2003).

Cao, Z., ARGO Collaboration: PICRC, 5, p. 299 (2005).
Cheng, K.S., et al.: Nucl. Phys. B (Proc. Suppl.), pp. 175, 176 (2008).
Cho, A.: Science, 319, p. 400 (2008).
Cocconi, G.: PICRC, Moscow 1959, 2, p. 309 (1960).
Cocconi, G.: Handbuch der Physik, S. Flügge, ed., Kosmische Strahlung, XLVI/I, Extensive Air Showers, p. 215, Springer Verlag, Berlin (1961).
Cronin, J., et al.: Sci. Amer., 276, p. 44 (1997).
Cronin, J.W.: Rev. Mod. Phys., 71, p. S165 (1999).
Cronin, J.W.: Nucl. Phys. B (Proc. Suppl.), 80, p. 33 (2000).
Cronin, J.W.: Nucl. Phys. B (Proc. Suppl.), 97, p. 3 (2001a).
Cronin, J.W.: Highlight Talk Presented at the 27th ICRC, Hamburg, Germany, August 7–15, 2001. PICRC, Invited and Rapporteur Volume (CD only), p. 234 (2001b).
Daudin, J.: J. Phys. Rad., 6, p. 302 (1945).
Dawson, B.R., Auger Collaboration: PICRC, pre-conference edition, paper 0976, Merida, Mexico (2007).
Deutschmann, M.: Zeitschr. Naturf., 2a, p. 61 (1947).
Earl, J.A.: Phys. Rev. Lett., 6, p. 125 (1961).
Ebisuzaki, T., et al.: PICRC, pre-conference edition, paper 0831, Merida, Mexico (2007).
Ebisuzaki, T., et al.: Nucl. Phys. B (Proc. Suppl.), 175–176, p. 237 (2008).
Engler, J., et al.: Annual Report on Nuclear Physics Activities, Kernforschungszentrum Karlsruhe, Germany, Report No. KfK 4875, H. Beer and J. Wochele, eds., May (1991).
Ermatov, S.E., et al.: PICRC, 7, p. 121 (1981).
Erofeeva, I.N., et al.: PICRC, 4, p. 355 (1987).
Falcke, H., and P. Gorham: Astropart. Phys., 19, pp. 477–494 (2003).
Fargion, D., et al.: PICRC, 2, p. 396 (1999).
Fargion, D.: PICRC, 3, p. 1297 (2001).
Fujii, M., and J. Nishimura: Acta Phys. Acad. Sci. Hung., 29, S3, p. 709 (1970).
Fukuda, Y., et al.: Phys. Rev. Lett., 81, p. 1562 (1998).
Fukuda, Y., et al.: Phys. Rev. Lett., 82, p. 1810 (1999).
Fukuda, S., et al.: Phys. Rev. Lett., 85, p. 3999 (2000).
Gaisser, T.K.: Cosmic Rays and Particle Physics, Cambridge University Press, Cambridge, 2nd ed. (1992).
Galbraith, W.: Extensive Air Showers, Butterworths Scientific Publishers, London (1958).
Ginzburg, V.L., and S.I. Syrovatskii: The Origin of Cosmic Rays, Pergamon Press, New York (1964).
Goodman, M.: PICRC, 10, p. 303 (2005).
Greisen, K.: Phys. Rev. Lett., 16, p. 748 (1966).
Grieder, P.K.F.: Rivista del Nuovo Cim., 7, p. 1 (1977).
Grieder, P.K.F.: PICRC, 9, p. 167 (1979a).
Grieder, P.K.F.: PICRC, 9, p. 178 (1979b).
Grieder, P.K.F.: PICRC, 9, p. 184 (1979c).
Grieder, P.K.F.: Nuovo Cim. A, 84, p. 285 (1984).
Grieder, P.K.F.: Internal Report, Physikalisches Institut, University of Bern (1987).
Grieder, P.K.F.: Cosmic Rays at Earth, Elsevier Science B.V., Amsterdam, The Netherlands, ISBN 0444507108 (2001).
Grieder, P.K.F., et al., Eds.: Very High Energy Cosmic Ray Interactions. Proceedings of the 13th International Symposium on Very High Energy Cosmic Ray Interactions, NESTOR Institute, Pylos, Greece, September 2004. Nucl. Phys. B (Proc. Suppl.), 151, pp. 3–508 (2006).
Grindlay, J.E., and G.G. Fazio: Astrophys. J., 187, L93 (1974).
Halzen, F., et al.: Phys. Rev. D, 55, p. 4475 (1997).
Hauschildt, T., and D. Steele, AMANDA Collaboration: PICRC, 3, p. 1305 (2003).
Hayakawa, S.: Cosmic Ray Physics, Wiley-Interscience, New York (1969).
Hayakawa, S.: Astrophys. Space Sci., 16, p. 238 (1972).
Hayashi, T., et al.: Progr. Theor. Phys. 47, p. 280 (1972a).

Hayashi, T., et al.: Progr. Theor. Phys. 47, p. 1998 (1972b).
Heisenberg, W.: Kosmische Strahlung (in German), Springer Verlag, Berlin (1943).
Heisenberg, W.: Vorträge über "Kosmische Strahlung" (in German), Springer Verlag, Berlin (1953).
Herlofson, N.: Tellus, 8, p. 268 (1956).
Hill, G., IceCube Collaboration: PICRC, 10, p. 213 (2005).
Horneffer, A., et al.: PICRC, 2, p. 969 (2003).
Jackson, J.D.: Classical Electrodynamics, John Wiley & Sons, New York (1999).
Jelley, V.J.: Astropart. Phys., 5, p. 255 (1996).
Jones, L.W.: PICRC, 2, p. 75 (1990).
Kajita, T., et al., Eds.: Proceedings of the 28th International Cosmic Ray Conference 2003, Tsukuba, Japan. Universal Academic Press, Inc., Tokyo, Japan (2003).
Kalpana, R.S., and D. Pranayee: PICRC, 3, p. 1309 (2001).
Kasahara, K., et al.: PICRC, pre-conference edition, paper 0955, Merida, Mexico (2007).
Khristiansen, G.B.: Cosmic Rays of Superhigh Energies, Verlag Karl Thiemig, München (1980).
Kifune, T.: Invited paper presented at the 28th ICRC, Tsukuba, Japan, July 31–August 7, 2003. Frontiers of Cosmic Ray Science, Universal Academic Press, Inc., Tokyo (Japan), PICRC, 8, p. 17 (2003).
Kiraly, P., et al.: J. Phys. A, 4, p. 367 (1971).
Konopelko, A.K.: Towards a Major Atmospheric Cherenkov Detector – V. Kruger National Park Workshop on TeV Gamma Ray Astrophysics, 8–11 August 1997, Kruger National Park, South Africa, O.C. de Jager ed., Potchefstroom University (1997).
Koshiba, M.: Phys. Rep., 220, 5 & 6, pp. 229–381 (1992).
Kraybill, H.L.: Phys. Rev., 93, p. 1362 (1954).
Krizmanic, J.F.: PICRC, 2, p. 388 (1999).
Kuzmin, V.A., and G.T. Zatsepin: Can. J. Phys., 46, p. S617 (1968).
Learned, J.G., and S. Pakvasa: Astropart. Phys., 3, p. 267 (1995).
Linsley, J.: Astrophys. J., 235, p. L167 (1980).
Mantsch, P.: The Pierre Auger Collaboration. ICRC 2005, Review, Rapporteur and Highlight Papers, published by the Tata Institute of Fundamental Research, Mumbai, India, PICRC, 10, p. 115 (2005).
Matano, T., et al.: Can. J. Phys., 46, p. S369 (1968).
McBreen, B., et al.: PICRC, 1, p. 441 (OG-11.7 Abstract only), (1991).
McCullough, J.-F., Milagro Collaboration: PICRC, 2, p. 369 (1999).
Merck, M., et al.: PICRC, 5, p. 2911 (2003).
Meyer, P., and R. Vogt: Phys. Rev. Lett., 6, p. 193 (1961).
Montaruli, T.: Rapporteur Talk on High Energy Phenomena (Proceedings Papers HE 2.1–5 to HE3.2-4; 139 papers) presented at the 28th ICRC, Tsukuba, Japan, July 31–August 7, 2003. Frontiers of Cosmic Ray Science, Universal Academic Press, Inc., Tokyo (Japan), PICRC, 8, p. 135 (2003).
Moskalenko, I., et al.: Cosmic Gamma-Ray Sources, Kluwer Academic Publishers, Dordrecht, K.S. Cheng and G.E. Romero, eds., 304, p. 279 (2004).
Nagano, M., et al.: J. Phys. G, 12, p. 69 (1986).
Niu, K., et al.: Proc. Theor. Phys., 46, p. 1644 (1971a).
Niu, K., et al.: PICRC, 7, p. 2792 (1971b).
Niu, K.: Cosmic Rays and Particle Physics 1978 (Bartol Conference), T.K. Gaisser, ed., AIP Conference Proceedings No. 49, Particles and Fields Subseries No. 16, p. 181 (1979).
Ochi, N., et al., LAAS group: PICRC, 2, p. 419 (1999).
Ochi, N., et al., LAAS group: PICRC, 1, p. 187 (2003a).
Ochi, N., et al., LAAS group: PICRC, 1, p. 191 (2003b).
Olinto, A., V.: Science, 315, pp. 68–70 (2007).
Pattison, B., et al., Eds.: Very High Energy Cosmic Ray Interactions. Proceedings of the XII International Symposium on Very High Energy Cosmic Ray Interactions (ISVHECRI), CERN, Geneva, Switzerland 15–20 July 2002. Nucl. Phys. B (Proc. Suppl.) 122, pp. 1–487 (2003).

Polcaro, V.F.: The Supernova of 1054 – New Evidence from Previously Unknown European Sources. Proceedings of the 1992 Volcano Workshop, Italian Physical Society Conference Proceedings, 40, p. 289 (1993).
Ramana Murthy, P.V., and A.W. Wolfendale: Gamma Ray Astronomy, Cambridge Astrophysics Series, Cambridge University Press, Cambridge, 2nd ed (1993).
Rao, M.S.V., and B.V. Sreekantan: Extensive Air Showers, World Scientific, Singapore (1998).
Rossi, B.: Rev. Mod. Phys., 20, p. 537 (1948).
Sasaki, H., et al.: PICRC, 8, p. 190 (1979).
Scarsi, L.: PICRC, 2, p. 384 (1999).
Scarsi, L.: Nuovo Cim. C, 24, p. 471 (2001).
Schönfelder, V., Ed.: The Universe in Gamma Rays, Springer Verlag, Berlin, Heidelberg, New York (2001).
Simon, M., et al., Eds.: Proceedings of the 27th International Cosmic Ray Conference 2001, Kaltemburg – Lindau, Germany, ISBN 3-9804862-7-3 (2001).
Sitte, K.: Handbuch der Physik, S. Flügge, ed., Kosmische Strahlung, XLVI/I, Penetrating Showers, Springer Verlag, Berlin, p. 157 (1961).
Smialkowski, A., et al.: Astropart. Phys., 7, p. 21 (1997).
Sokolsky, P.: Introduction to Ultrahigh Energy Cosmic Ray Physics, Frontiers in Physics, Addison-Weskey Publishing Co., New York, Vol. 76 (1989).
Spitzer, L.: Phys. Rev., 76, p. 583 (1949).
Sreekumar, P., et al.: Astrophys. J., 495, p. 523 (1998).
Stanev, T.: Phys. Rev. D, 33, p. 2740 (1986).
Stanev, T.: High Energy Cosmic Rays, Series: Springer Praxis Books. Subseries: Astrophysics and Astronomy, Springer Verlag, Berlin (2004).
Suga, K., et al.: Phys. Rev. Lett. 27, p. 1604 (1971a).
Suga, K., et al.: PICRC, 7, p. 2742 (1971b).
Teshima, M., et al.: PICRC, 2, p. 1069 (2003).
Tonwar, S., et al., Eds.: Proceedings of the 29th International Cosmic Ray Conference 2005, Pune, India. Tata Institute of Fundamental Research, Mumbai, India (2005).
UNAM, Pre-Conference edition of papers submitted for presentation at the 30th International Cosmic Ray Conference, Medida, Mexico, Universidad National Autonoma de Mexico, ISBN 978-970-32-4216-0 (2007).
Uryson, A.V.: PICRC, 2, p. 136 (1993).
Vacanti, G., et al.: Astrophys. J., 377, p. 467 (1991).
Vernetto, S., et al., ARGO-YBJ Collaboration: PICRC, 5, p. 3007 (2003).
Völk, H.J.: Invited paper presented at the 28th ICRC, Tsukuba, Japan, July 31–August 7, 2003. Frontiers of Cosmic Ray Science, Universal Academic Press, Inc., Tokyo (Japan), PICRC, 8, p. 29 (2003).
Washburn, K.; for the Super-Kamiokande Collaboration: PICRC, 3, p. 1285 (2003).
Wdowczyk, J., et al.: J. Phys. A, 5, p. 1419 (1972).
Weekes, T.C.: Phys. Rep., 160, p. 1 (1988).
Weekes, T.C.: Space Sci. Rev., 75, p. 1 (1996).
Weekes, T.C: Very High Energy Gamma-Ray Astronomy, Bristol, Institute of Physics Publishing, XV, p. 221 (2003a).
Weekes, T.C.: Invited paper presented at the 28th ICRC, Tsukuba, Japan, July 31–August 7, 2003. Frontiers of Cosmic Ray Science, Universal Academic Press, Inc., Tokyo (Japan), PICRC, 8, p. 3 (2003b).
Williams, R.W.: Phys. Rev., 74, p. 1689 (1948).
Wolfe, B., et al.: Phys. Rev., 79, p. 1020 (1950).
Zas, E., et al.: Phys. Rev. D, 45, p. 362 (1992).
Zatsepin, G.T., and V.A. Kuzmin: JETP Lett., 4, p. 78 (1966).
Zavrtanik, D., Auger Collaboration: Nucl. Phys. B (Proc. Suppl.), 85, pp. 324–331 (2000).

Chapter 2
Shower Detection Methods and Basic Event Reconstruction

Overview This chapter contains an outline of the different air shower detection methods, many of which are discussed in detail in dedicated chapters later on. Detection techniques that had been explored only briefly in the past or are presently in an exploratory phase, such as radar ranging and acoustic detection, respectively, are not treated in separate chapters but are discussed extensively here. Directly and indirectly accessible shower parameters are introduced and briefly described, followed by the elementary concepts of shower reconstruction and a brief overview of the response of common particle detectors to shower particles, including transition effects. Indirectly accessible parameters are discussed in Chap. 10.

2.1 Introduction

An air shower is characterized by a thin but radially very extended *particle disk* that propagates essentially with the speed of light along the shower axis. The latter is defined theoretically by the direction of the momentum vector of the incident primary. The shower particle disk which exhibits a slightly curved front surface has a high density at the center that decreases approximately exponentially with increasing radial distance. The location of the density maximum defines experimentally the position of the shower axis at impact on the ground. The charged particles produce *highly polarized optical Cherenkov* as well as *radio emission* as they propagate through the atmosphere, and *air fluorescence* along their tracks, leaving a long *column of slowly recombining ionized air*.

Additional but little explored electromagnetic processes such as the interaction of the charged particles with the *geomagnetic* or even the *geoelectric field* in the atmosphere and other processes may also contribute to radio emission. In dense homogeneous media, such as water, extremely energetic and compact showers may produce *acoustic effects*.

Each of the above mentioned phenomena represents a specific signature of an air shower and can in principle be used for detection and classification of an event. In some experiments more than one of these intimately related characteristic effects are being used. However, some of the phenomena caused by the particle disk in

P.K.F. Grieder, *Extensive Air Showers,* DOI 10.1007/978-3-540-76941-5_2,

traversing the atmosphere that are listed above have not yet been explored sufficiently that they can be used as standard tools for air shower investigations.

Today, air showers are mainly detected by means of particle or optical Cherenkov detector arrays, or with one or several Fly's Eye type hemispherical atmospheric fluorescence detectors.[1] Small aperture narrow-angle atmospheric Cherenkov telescopes as they are being used in high energy gamma ray astronomy are not suitable for general all-sky air shower observations. The detection of radio emission from air showers is a long standing topic, still in its infancy, which so far could not be exploited successfully, and likewise RADAR tracking of the ionization column of giant showers in the atmosphere.

In an even more preliminary phase is the technique of acoustic detection of high energy events impacting on a homogeneous medium, such as a large body of water or ice. This method had been pursued during the last three decades mostly with the aim to detect extremely high energy neutrinos in the ocean, as was intended with the pioneering DUMAND (Bosetti et al., 1989; Grieder, 1992) and later follow-up projects (e.g., Anassontzis et al., 1995; Spiering, 2003; Hill, 2005). In the following we briefly describe the different detection methods.

2.2 Particle Detector Arrays

The most common method of shower detection is based on the arrival of the particle disk at ground level with the help of a more or less loosely packed particle detector array.[2] This implies that the particle disk, which contains the full particle mix present in a shower, is only being *sampled* on arrival at ground level. In other words, one obtains only an incomplete two-dimensional picture of the shower at a particular moment and stage of its development with some timing information from the arrival sequence of the current particle generation at the different detectors of the array. The latter yields very limited information on the longitudinal cascade development.

The time structure of the particle disk is outlined in Sect. 1.1. Details are discussed in Chap. 9, where theoretical and experimental data are presented. Temporal properties and data of particular particle groups are discussed in the appropriate chapters of Part II. It is evident that the higher the detector density of an array is the richer the extracted data set is and the more accurate a shower can be reconstructed and analyzed.

The shower particle pattern is circular for vertically incident showers. Besides density fluctuations within the particle disk caused by fluctuations in the shower generating processes that may disturb the symmetry, the particle distribution is more

[1] In some applications only sectors of a hemispherical detector geometry are being used that cover a restricted solid angle of the sky, such as is the case at the *Auger Observatory* (Blümer, 2003).

[2] The layout of a selection of air shower particle detector arrays of the past and present are displayed in Sect. A.1.

or less affected by the geomagnetic field. Depending on the direction of the shower axis with respect to the direction of the geomagnetic field, the particle trajectories exhibit a slight momentum dependent curvature, positively charged particles in one direction and negatively charged particles in the other, causing some degree of lateral *charge separation*, and asymmetry of the particle distribution in the plane of observation may occur (see Fig. 8.17).

With increasing zenith angle the contour of the particle pattern on the ground changes more and more from a circular to an asymmetrical elliptical form, mainly for geometrical reasons. In addition, an increasing *azimuthal asymmetry* of the particle density distribution begins to appear with increasing inclination and radial distance from the shower axis. This is due to differences in the trajectory length and therefore in the degree of development within a shower and affects mainly the electromagnetic component.

The relevant observables that must be acquired by a particle detector array to reconstruct a shower are the *arrival time*, t_i, of the particles at detector i with respect to some reference time, t_0, the *particle density*, ρ_i, and the *detector location* with respect to the reference system, x_i and y_i, or r_i and φ_i. Frequently the instant of arrival and registration of the first particle at the array is taken as the reference time, t_0.

In early experiments the particle detectors consisted of Geiger counters. Today, mainly scintillation and/or water Cherenkov detectors are being used as common shower detectors for fast timing and particle density or energy deposit measurements. However, a number of other detector types are also used for this purpose.

An array may be laid out symmetrically, asymmetrically or in an arbitrary pattern about a predefined array center. An asymmetrical layout permits larger radial coverage of the showers in a particular direction and the detection of larger showers than a symmetrical array for a given site area, number of detectors and for specific trigger conditions. However, because of fluctuations in the lateral distribution of the particles within a shower and the lack of full symmetry, the event interpretation is more subtle with such arrays.

A flat topography is desirable but not a necessity. Frequently the shower detectors are placed closer to each other near the designated array center and spread out more and more with increasing radial distance. This results in a higher lateral resolution in the core region of the showers, where the particle and photon densities and energies are high, for those events whose axis strike near the array center.[3] On the other hand, an increasing separation of the outer detectors with increasing distance from the array center requires larger detectors because of the decreasing particle density.

Shower detection is based on coincidence requirements of the arrival of one or more particles in each of a number of detector units within a predefined time window. The width of the coincidence time window to accept an event for recording

[3] Note that trigger conditions may be set such that event selection can be influenced in many ways to meet special requirements.

depends on the array size, the detector separation and the zenith angular window of shower acceptance desired. Frequently a small number of specially dedicated so-called fast-timing array trigger detectors, usually fast plastic or liquid scintillation detectors, preferentially placed symmetrically at moderate distances from the array center and operated at low threshold levels, are being used for this purpose.

The leading edge of the pulses of the fast-timing array trigger detectors are used to compute the arrival direction of the shower, i.e., the zenith and azimuthal angles. Additional trigger requirements may be imposed on these or the other detectors, such as minimum particle densities, to impose a more restrictive second-level trigger, in order to accept a shower for recording. In this case, a broader time window of acceptance, centered about the initial trigger window, is in general required. In this way one can select the minimum shower size to be accepted. Additional, still more restrictive trigger requirements may be imposed for specific purposes.

The described method selects preferentially showers whose core (axis) lies close to the array center. There, special equipment such as calorimeters or spectrometers to study ultrahigh energy particles and interactions in the shower core (hadronic interactions, muons or delayed particles, etc.) are usually placed. In the past, at rare occasions, cloud chambers were also implemented near the array center.

Well equipped arrays possess a number of large-area muon detectors distributed across the array. Large-area detectors are required for this purpose because of the generally lower density of the muons, particularly at larger distances from the axis. Muon detection is achieved by shielding common charged particle detectors from the bulk of the low energy electromagnetic component with a layer of several centimeters of lead, or by placing them underground. Occasional *punch-throughs* of energetic particles cannot be excluded but are less likely at larger distances from the shower core. The energy thresholds for such muon detectors are usually chosen anywhere between 0.25 GeV to a few GeV. In some cases sophisticated magnet or absorption type muon spectrometers are implemented, in general near the array center, to analyze the energetic muon component in or near the shower core.

A very particular kind of air shower particle detector is the large-area Haverah Park type deep water Cherenkov detector (Tennent, 1967). The typically several square meters large, 1.2 m deep water tanks were spread in clusters of three or four units, widely apart from each other, in particular patterns across the array ground (see Fig. A.20). They record the optical Cherenkov radiation produced by the particle mix that enters the tanks and propagates in the water. With the exception of an occasional direct hit of a detector by a shower core, the detectors are mostly exposed to low energy particles, on average several 100 m from the shower axis.[4]

[4] Mainly low energy muons and electrons, but also photons via conversion processes in the water that produce positron–negatron pairs, Compton scattered and knock-on electrons are being recorded.

Many of the shower muons traverse the water column but some are being stopped as is most of the electromagnetic component of the particle mix.[5] The Cherenkov light flash thus produced is expressed in units of *vertical equivalent muons* and is used as a measure of particle density and energy deposit (Hollows et al., 1969). Because of the fast response of these detectors they yield excellent timing information.

Simple air shower simulations have shown that the all-particle energy density deposit at several hundred meters from the shower axis in deep-water Cherenkov detectors is a rough measure of the primary energy of the shower initiating particle and is fairly independent of its mass (see Chaps. 8, 10 and 11, and Sect. 12.5) (Hillas, 1970; Hillas et al., 1970, 1971). The relatively large thickness (height) of this type of detector extends its applicability to very large zenith angles, since it still exposes a sufficient area to inclined and even horizontal showers.

In some rare cases particle tracking detectors, such as wide-gap spark or discharge chambers, had been used in a more exploratory attempt for shower (axis) direction determination (Heintze et al., 1989a, b; Doll et al., 2002; Poirier et al., 2007), but this method is not very practical for this purpose. Today tracking detectors are sometimes being used in muon telescopes or spectrometers (magnetic or absorption spectrometers) to measure the muon angle with respect to the shower axis in order to estimate the height of origin of high energy muons in showers, or to locate particle trajectories in hadron calorimeters (see Chaps. 13 and 14 for more details).

For completeness we should also mention the large but relatively shallow water pool detector Milagro (Barwick et al., 1993; Yodh, 1996; McCullough, 1999; Atkins et al., 2000). It is used mainly for gamma ray astronomy. The pool measures $80 \times 60\,\mathrm{m}^2$ and has a depth of 8 m. It is located at an altitude of 2,630 m outside of Los Alamos, NM (USA). Two horizontal layers of optical detectors (photomultiplier tubes) arranged in the form of matrices are submerged at depths of 1.5 and 6 m, respectively. The upper layer is used to reconstruct air showers whereas the lower acts as muon detector for hadron shower rejection. A similar detector project was proposed by Russian scientists to be installed at Issyk-Kul lake in Kyrgyzstan but has not yet materialized (Ermatov et al., 1981; Albers et al., 1983; Erofeeva et al., 1987).

A unique instrument which should also be mentioned in this context is the huge *resistive plate detector* ARGO at Yangbajing in Tibet (China), located at an altitude of 4,300 m ($606\,\mathrm{g\,cm}^{-2}$), that covers an area of almost $6{,}000\,\mathrm{m}^2$ (Bacci et al., 2000, 2002; Cao, 2005; Martello, 2007). ARGO is used for air shower studies and gamma ray astronomy.

Details of the sites of many of the arrays of past and present, such as the altitude and average barometric pressure are tabulated in Sect. A.1, where the layouts of some arrays are illustrated. A discussion of the extraction and interpretation of data from particle measurements that are relevant for the shower development, the determination (estimation) of the primary energy spectrum and the mass composition are

[5] Relativistic muons lose about $2\,\mathrm{MeV\,g}^{-1}\,\mathrm{cm}^2$.

discussed in Chap. 10. The results thus obtained yielding primary spectra and mass compositions are presented in Chap. 11.

2.3 Air Cherenkov Detector Arrays

Large aperture, wide-angle acceptance optical detector arrays that record atmospheric Cherenkov emission of air showers are operated essentially in the same manner as particle detector arrays. However, the photon pattern, i.e., the lateral distribution function, is different from that of the charged particles, and the photons are highly polarized. Such arrays may be operated autonomously or in conjunction with a particle detector array.

Unlike Cherenkov telescopes that are used for gamma ray astronomy that use a large light collection mirror with a very narrow field of view that can point in any direction of the night sky and have a very high angular resolution, wide-angle Cherenkov detector arrays cover simultaneously a large fraction of the sky and detect any event that is in their field of view. A modern example of such an array is the installation at the Tunka Valley, near Lake Baikal (Budnev et al., 2005). Suitable climatic, meteorological and environmental site conditions, such as low optical background, a mostly cloudless sky, little precipitation and a dust-free atmosphere with low aerosol contamination are required to operate air Cherenkov detectors and Cherenkov telescopes successfully and with a reasonable duty factor.

Moreover, this kind of detector can only be used during clear moonless nights[6] and the atmospheric conditions (absorption, etc.) must be frequently checked for accurate measurements. The relevant data that must be acquired by a Cherenkov detector array are the *number density* Q_i and *arrival time*, t_i, of the optical photons, and the corresponding *coordinates* of the i detectors, x_i and y_i, or r_i and φ_i, with respect to the reference frame of the array.

The basic event reconstruction procedure is analogous to the one used for particle detector arrays but air Cherenkov data contain more longitudinal shower information. Because of the generally good transparency of the atmosphere for the optical portion of the Cherenkov emission (little absorption and scattering), the light collected by a ground array contains photons from all stages of the shower, along the entire trajectory. Therefore the Cherenkov component carries the history of a shower to the observer at ground level, thus revealing a three-dimensional picture of an event. Hence, Cherenkov measurements represent in fact a sort of *atmospheric Cherenkov calorimetry* of the shower where in principle all stages of development are accessible through the photons. As mentioned in the previous section, this feature is more obscured in the particle time profile, since the recorded particles originate from the last generation of interactions, many generations after the first interaction with many scattering events in between.

---

[6] Using special ultraviolet sensitive photomultiplier tubes and/or appropriate filters in front of the photomultipliers permit to operate an optical atmospheric Cherenkov array at certain times during the presence of the moon.

An important advantage of the atmospheric Cherenkov shower detection method over particle detection is that because of the much larger number of photons of a Cherenkov light burst of a shower arriving at a detector as compared to the number of particles striking a conventional particle detector, the photon burst is *not subject to Poissonian fluctuations* as is the particle count. Fluctuations of Cherenkov signatures are therefore of a different nature. They are caused by fluctuations of the actual physical processes that take place in a shower and the strongly fluctuating superimposed background photon flux. The net shower photon count is then estimated by subtracting the background count from the measured signal.

The longitudinal information is packed partly in a time code and partly in a geometrical code, i.e., the Cherenkov photons from a particular longitudinal section of a shower have a definite time stamp within the light pulse and are deposited within definite annular zones about the shower axis. This information is of course smeared out to some extend by the angular spread (scattering) of the parent particles at any depth, by the changing atmospheric density that affects the index of refraction and therefore the Cherenkov angle, and by fluctuations of the different processes that affect the parent particles.

Theoretical and experimental aspects of air shower induced Cherenkov radiation are discussed in detail in Chap. 16 where a wealth of data from measurements and their interpretation are presented and analyzed. Data related to the primary energy spectrum and the mass composition resulting from atmospheric Cherenkov studies are discussed in Chap. 11.

2.4 Air Fluorescence Detectors

Unlike atmospheric Cherenkov radiation, atmospheric fluorescence produced by air showers is emitted *isotropically*, mainly in the 300–400 nm band, by the excited nitrogen molecules (second positive band) and nitrogen ions (first negative band). The isotropic emission has far reaching consequences for the detection. It implies that in fluorescence light showers can in principle be observed from all directions, in particular also from the side with an appropriate optical detector. There is no need for the shower to point toward the detector as in the case of Cherenkov detection, or even to strike it directly as is required for particle detector arrays. All that is needed is a *hemispherically sensitive imaging kind of detector* that can observe showers all around it and track them.[7] Because of the resemblance of such a detector to a fly's eye this kind of detector is called a *Fly's Eye* type air fluorescence detector (Bergeson et al., 1975a, b).

[7] Note that showers whose axis is directed towards a fluorescence detector or its immediate vicinity are usually excluded from analysis because the intense Cherenkov beam obscures the fluorescence signal.

The relevant observables that must be recorded are the *photon density,* Q, the instantaneous *arrival direction* of the photons, i.e., the *zenith* and *azimuthal angles*, θ and φ, and the *arrival time*, t; thus, one records $Q(\theta, \varphi, t)$.

A Fly's Eye type detector consists in principle of a large number of optical detector modules (large individual photomultiplier tubes or clusters of small tubes) that are arranged on a hemispherical shell. Each module points in a particular direction and views a certain aperture limited element of solid angle of the sky. The entire ensemble is arranged in such a way that it covers in general nearly the full 2π steradian of the sky.

With the exception of the first few designs (Bunner et al., 1967), where the modules were laid out on a hemispherical shell, later designs are quite different in appearance (Hara et al., 1970b). In current practice large mirrors or mirror systems (Schmidt, etc.,) are being used in place of the small diameter modules to collect more light per unit. This new design made it necessary to abandon the compact layout on a hemisphere and to place the individual modules, that have now dimensions on the order of meters, apart from each other, however, still pointing into individual directions each, as before (Baltrusaitis et al., 1985; Cassiday, 1985).

A Fly's Eye detector can monitor a huge volume of atmosphere over a large area and is expected to be an excellent instrument to record rare ultrahigh energy showers that strike far away and would be missed even by a very large array. Another advantage of recording the showers from the side is that one can obtain first hand information of the longitudinal shower development and the location of the shower maximum. This information can only be extracted from array data, mainly from air Cherenkov arrays, in connection with elaborate simulation studies (see Chaps. 7 and 16). A Fly's Eye type detector is therefore expected to be a good tool for $X_{\max}$, primary mass and energy estimations (see Chaps. 11 and 17).

The same very restrictive site requirements apply to fluorescence detectors as are listed above for air Cherenkov detection. Because of the weaker intensity of fluorescence light and the generally larger distances between shower and detector as compared to the situation for Cherenkov arrays, aerosols and dust that cause scattering and absorption require an even more severe surveillance of the atmosphere with frequent monitoring of its parameters. An additional problem arises when showers strike near or directly at a fluorescence detector. In this case portions of the intense forward directed Cherenkov light beam can get scattered into the field of view of the fluorescence detector, or worse even, the detector may get hit by part of the direct Cherenkov beam, which complicates the data analysis significantly.

Another advantage of a fluorescence detector over the more conventional particle detector array is that it can be operated as a quasi single 2π steradian autonomous device from a relatively small site. With two or more units located apart one can get a *stereo view* of the showers that reduces errors and uncertainties significantly. Moreover, in conjunction with a particle detector array a unique set of complementary and redundant data can be acquired.[8] As a matter of fact, a coincident signal of even

[8] The Fly's Eye detector had in fact been operated jointly at times with the CASA-MIA, BLANCA and DICE arrays at Dugway (Utah) (Bird et al., 1995; Cassidy et al., 1997; Swordy and Kieda, 2000).

a single particle detector allows an improved reconstruction of the shower geometry obtained from a fluorescence detector, in a similar way as by the stereo view. This method is employed by the Auger detector and is called *hybrid reconstruction*.

In exceptional cases air fluorescence detectors may be designed to have a restricted zenith and/or azimuthal angular aperture for being placed outside or at the fringes of a particle detector array, to overlook only the air space above the array. This idea had been proposed by Grieder in conjunction with the DUMAND (Deep Underwater Muon And Neutrino Detector) system. The intention was to view from shore that portion of the atmosphere that lies above the submerged detector matrix located at a depth of 5 km some 30 km off shore in the Pacific near Hawaii, in order to investigate the showers that produce ultrahigh energy downward-going atmospheric muons that could have reached the deeply submerged matrix (Grieder, 1980; Elbert et al., 1981). Such a design is now being used by the *Auger* and *Telescope Array* experiments (Mantsch, 2005; Kasahara, 2007).

Chapter 17 is dedicated to the air fluorescence phenomenon and to the fluorescence detection method of showers. There the fluorescence mechanism, the detection technique and related problems such as event reconstruction, background problems and data interpretation are discussed. The achieved scientific results that are related to the primary energy spectrum and the mass composition using the fluorescence method are presented in Chap. 11, cross section and particle physics data in Chap. 3.

2.5 Radio Emission Detection

The detection of radio frequency (RF) pulses produced by air showers is a very old idea. However, the identification of radio frequency shower signatures is difficult because of the so-called electromagnetic smog, i.e., radio noise (static) produced by electric and electronic equipment, particularly in urban areas where large portions of the electromagnetic frequency spectrum are intensely utilized for radio (AM and FM), television and communication services. But there is also a significant natural atmospheric and extraterrestrial electromagnetic noise, particularly of galactic origin (cf. Fig. 18.4). Numerous authors have tackled the problem over the past 50 years but abolished the idea regularly. For a summary of the early work the reader is referred to the comprehensive review of Allan (1971).

The high hopes that accompanied initially the many efforts aimed to determine the energy spectrum and even the mass of the rare ultrahigh energy primary particles that initiate the giant air showers by having a large spatial coverage when using the radio emission from showers as a novel probe did not materialize, so far. Up to date it is not really clear which one of the different mechanisms that are believed to contribute to radio emission from showers is the most relevant[9] and it has not yet been possible to extract any useful information on air showers from radio signatures only (Green et al., 2003), though the situation is improving (Lafebre et al., 2005;

[9] At present geo-synchrotron radiation is believed to be the chief contributor.

Ravel, 2007). Moreover, it has not even been possible so far to definitely associate a radio pulse with the occurrence of a shower without using the information from conventional particle detectors.

Nevertheless, the topic re-surfaces regularly again and again. Major efforts are currently under way to explore the method anew and to exploit it if the attempts prove finally successful, and presently success appears to be tangible (e.g., Falcke and Gorham, 2003; Huege and Falcke, 2003, 2005; Van den Berg, 2007; Saftoiu et al., 2007). In Chap. 18 we review the field in some detail and summarize the different mechanisms that are expected to be responsible for the emission of radio waves in the form of electromagnetic pulses by air showers and present an overview of the available experimental results.

Within the frame of the AMANDA and IceCube neutrino astronomy projects, the possibility to detect radio emission caused by cascades initiated by high energy neutrinos in ice at the surface or even from space is currently being investigated (Hill, 2005; Auffenberg et al., 2007). This method could offer a complementary possibility to optical or acoustic detection of such events in large bodies of ice, such as at Antarctica, if it proves successful.

2.6 RADAR Ranging and Detection

Giant air showers are rare events that require very large and costly surface arrays to be detected at a reasonable rate, to construct reliable shower size and primary energy spectra, and to extract even more subtle information, such as the nature of the primary. At a very early stage of air shower research Blackett and Lovell (1941) suggested that the long and relatively narrow ionization trails produced by distant giant air showers that traverse the entire atmosphere might possibly be detectable by means of *RADAR (RAdio Detecting And Ranging) echo ranging* and they explored the subject theoretically. In the following we briefly summarize their estimation and argumentation for the detectability of showers by RADAR.

Consider a shower at a distance R from a powerful radio transmitter with a wavelength, λ, large compared with the diameter of the column of ionization. Diffraction theory shows that the amplitude of a reflected wave at the location of the transmitter will be approximately equal to that which would be produced by a point cluster of n ions, where n is the number of ions contained in a shower column, whose length L is that of the first Fresnel zone, that is, where

$$L = \sqrt{\lambda R}. \tag{2.1}$$

From the electromagnetic cascade theory (Sect. 4.6), one can calculated the maximum number of ions produced per centimeter of air, n, at a pressure P, expressed as a fraction of an atmosphere, produced by an incident electron of energy E_0. A rough calculation yields

$$n = 5 \cdot 10^{-8} P E_0. \tag{2.2}$$

Thus, the number of electrons in the equivalent point cluster is

$$N_e \;=\; n\,L \;=\; 5\cdot 10^{-8}\,P\,E_0\,\sqrt{\lambda\,R}. \tag{2.3}$$

If the reflection coefficient, κ, is defined as the ratio of the reflected amplitude to that incident on the cluster, then a point cluster of N_e electrons at a distance R from the transmitter will have a reflection coefficient

$$\kappa \;=\; \frac{N_e\,r_e}{R}, \tag{2.4}$$

where r_e is the classical electron radius ($2.8\cdot 10^{-13}$ cm).

Considering Eqs. (2.3) and (2.4), we obtain for the reflection coefficient of a shower of primary energy E_0 at a distance R,

$$\kappa \;=\; 5\cdot 10^{-8} P\,E_0\,r_e\,\sqrt{\frac{\lambda}{R}}. \tag{2.5}$$

If we take $\kappa = 2\cdot 10^{-5}$, $P = 1$, $\lambda = 50$ m, $R = 10$ km, we get $E_0 = 2\cdot 10^{16}$ eV. The conclusion which Blackett and Lovell drew from this analysis was that large extensive air showers can produce measurable radio reflections.

The duration of a radio echo is expected to last for the lifetime of the free ions, and this is governed mainly by the rate of attachment to molecules. Consequently, the duration of the echoes will be roughly inversely proportional to the pressure, and will have a value of $\sim 10^{-5} - 10^{-6}$ s at ground level and of the order of a second at 100 km (Blackett and Lovell, 1941). Thus, though the amplitude of an echo will decrease with the pressure, its duration will increase in the same proportion, leaving the product of amplitude and duration unchanged.

However, the proposal of Blackett and Lovell did not receive much attention, except for a few exploratory experimental attempts in the 1960s and early 1970s. The reason for the lack of interest at that time was mainly that it did not appear to be a very practical method because of background problems, trigger requirements and encouraging new results obtained with the classical particle detector arrays. In addition, it was known that thunderstorms and meteorite trajectories in the atmosphere leave RADAR detectable ionization trails that may confuse the interpretation of RADAR echoes.[10]

In spite of the discouraging outlook, the Tokyo group began to explore the method in the early 1960s, using the echo of pulsed radio waves from a *LORAN (LOng RAnge Navigation)* system to record signals reflected by giant showers of primary energy $> 10^{20}$ eV (Suga, 1962; Matano et al., 1968; Hara et al., 1970a).

[10] Micro meteorites having masses as small as $\sim 1\,\mu$g and diameters $\simeq 0.1$ mm may cause ionization line densities in the atmosphere on the order of $\sim 10^{13}$ electrons m^{-1} which are detectable by RADAR (Gorham, 2001).

In the following we briefly outline as a concrete example the pioneering Tokyo experiment, the assumptions on which it was based and the results obtained.

Consider a shower of size 10^{10} particles. The ionization density produced by such an event is $> 10^4$ [ion pairs cm^{-3}] and comparable to that of the ionosphere. In the column ionized by a shower, however, the collision mean time of electrons is very short, approximately 10^{-9} s. The mean life of electrons due to electron attachment is of the order of 10^{-7} s and the mean life for recombination of the positive and negative ions is several minutes. The power of the echo signal is given by Matano et al. (1968) as

$$2.5 \cdot 10^{-32} \frac{a^2 \mathcal{P} G^2 \lambda^3}{R^3} \left(\frac{m_e}{M}\right)^2 \left(\frac{1}{(4\pi r_M/\lambda^2)+1}\right)\left(\frac{1}{(\nu_c/\pi\nu)^2+1}\right) \text{ [W]}, \quad (2.6)$$

where

a is the number of ions or electrons per meter of shower column,
$\mathcal{P}$ the power of the emitter [W],
G the antenna gain of the emitter and receiver,
r_M the characteristic distance (Molière radius) of the lateral distribution of the shower particles, i.e.,

$$f(r) \propto \left(\frac{1}{r}\right) \exp -(r/r_M), \quad (2.7)$$

λ, ν are the wavelength and frequency of the radio wave,
m_e, M the mass of the electron and air molecule, respectively,
ν_c the collision frequency between the electrons and air molecules ($\sim 10^9$ Hz), and
R is the distance between receiver and air shower.

In a first attempt a pulsed radio wave of 1,850 kHz was transmitted isotropically with a power of more than 100 kW from a LORAN station. The pulse width and the repetition rate were 40 μs and 20–30 Hz, respectively. The experimental configuration is illustrated in Fig. 2.1. The signal-to-noise ratio of the received echo was very low because the sky noise masked the signal. Reflections from the ionosphere disturb the detection beyond a certain distance. In particular, if h is the height of the ionosphere and d the distance of the receiver from the LORAN transmitter, then the shower whose echo pulse has a time delay of Δt with respect to the direct pulse is located on the ellipse with major axis $a = c\Delta t + d$ and minor axis $b = \sqrt{[(c\Delta t + d)^2 - d^2]}$.

Since the first reflected pulse from the ionosphere comes with a time delay of $c\Delta t = \sqrt{[d^2 + (2h)^2]} - d$ after the direct pulse, the detection area with low noise is limited by the ellipse corresponding to this time delay (see Fig. 2.1). When $d \ll h$, the large ellipse tends to a circle with radius h, and the corresponding time delay is $2h/c$ which is almost 400 μs for the D-layer ($h = 70$ km). Therefore only the

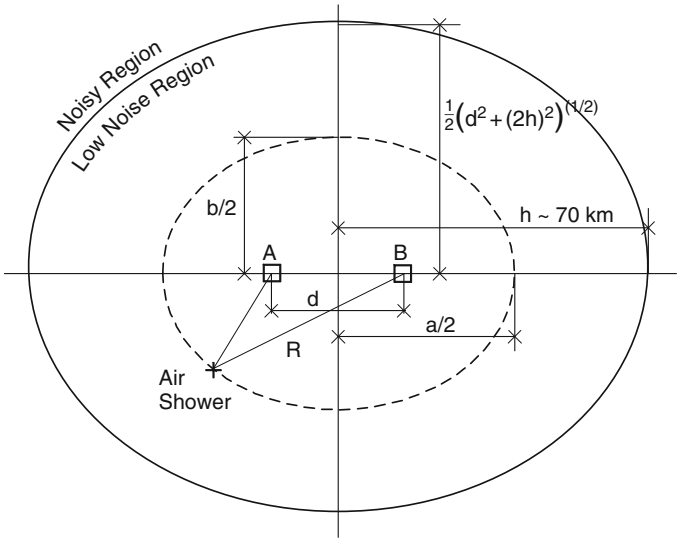

Fig. 2.1 Detection area of air showers for the radio echo (RADAR) method using a LORAN transmitter. d is the distance between the transmitter, A, and the receiver, B, R the distance between the shower axis and the receiver, and h is the height of the ionosphere. The solid ellipse contains the area where the radio echo from the shower precedes the reflection from the ionosphere and shower detection is possible (Matano et al., 1968)

echo pulse which falls within 400 μs after the direct pulse may be detected under low-noise conditions.

A survey of the background noise in the Tokyo area gave a noise level of about $3 \cdot 10^{-6}$ V at the output of the antenna (antenna gain 1.5 and bandwidth of amplifier $1{,}850 \pm 12$ kHz) in the region where no reflected pulse from the ionosphere existed. It was about $3 \cdot 10^{-5}$ V in the reflected pulse region (when $d \ll h$, for the D-layer and in the morning). If one inserts the LORAN pulse amplitude into Eq. (2.6), putting $N = 10^{10}$, $R = 10$ km, $\mathcal{P} = 100$ kW, $G = 1.5$ (for a dipole antenna), and $\lambda = 160$ m (1,850 kHz), then the received echo power is about $3 \cdot 10^{-20}$ W, which corresponds to $3 \cdot 10^{-9}$ V across an input resistor of 300 Ω.

Matano et al. (1968) concluded that due to the fact that the ions in an air shower remain for several minutes, about 10^4 echo pulses can be obtained during that time. By integrating these pulses the signal-to-noise ratio improves by about a factor of 10^4. The echo signal reaches then a level of $\sim 3 \cdot 10^{-5}$ V, which is 10 times the background noise. The observed shower rate was approximately 150 showers per year. If one neglects the scattering losses of the signal, the radius of the effective area increases with energy to ~50 km for $N = 10^{11}$ and to ~200 km for $N = 10^{12}$, thus yielding about 70 showers per year and 30 showers per year, respectively, assuming an integral size spectrum of $I(N) = 10^{-13}(N/10^9)^{-1.6}$ m^{-2} s^{-1} sr^{-1}.

In the latter case ($N = 10^{12}$) only few showers are expected to have a good signal-to-noise ratio (~10) because of ionospheric limitations. The authors conclude from their work that it may therefore be better to use another frequency band or

directional antennae to reduce the background when tackling the ultrahigh energy region (Hara et al., 1970a).

In recent years with the availability of new technologies the RADAR echo detection of extremely large air showers has been revisited by various authors and different projects have been proposed (Wahl et al., 2007). Gorham (2001) has carried out a very detailed feasibility study and came to the conclusion that radar detection of the ionization track of air showers of primary energy $\geq$ 1 EeV (10^{18} eV) can be achieved with common radar trackers operating in the VHF (30–100 MHz) range.

2.7 Acoustic Detection

Large showers impacting on homogeneous media such as large bodies of water (lakes, oceans) or ice are expected to produce a *thermo-acoustic shock wave* that should in principle be detectable. Numerous studies had been conducted in the past and some accelerator experiments were carried out that confirmed the existence of such signatures.

The occurrence of acoustic signals in liquids upon impact of high energy (relativistic) ionizing particle beams was first suggested by Askar'yan (1957) and subsequently confirmed experimentally by Volovik and Popova (1975) and Sulak et al. (1977, 1979). The subject was further explored by Volovik and Khristiansen (1975), Askar'yan and Dolgoshein (1976), Bowen (1976,[11] 1977, 1979a, b, 1980), Hunter et al. (1979, 1980), Jones (1977a, b), and Bowen and Learned (1979), to mention just the pioneers of the field.

Detailed studies revealed that the formation of a thermal shock-like expansion of the liquid caused by the sudden energy deposit of relativistic particles, called a thermo-acoustic shock, governs the process. Subsequently, appropriate theoretical models were developed that describe the process adequately (Askar'yan et al., 1979; Learned, 1979; Tam, 1986).

The basic wave equation for a pressure pulse in a liquid can be written as

$$\nabla^2 \left(P + \frac{1}{\omega_0} \dot{P} \right) - \frac{1}{c_s} \ddot{P} \; = \; - \frac{\beta}{C_p} \frac{\partial E}{\partial t}, \tag{2.8}$$

where P is the pressure, ω_0 the characteristic attenuation frequency ($\approx 2.5 \cdot 10^{10}\,\mathrm{s}^{-1}$) which is in fact a function of frequency itself (Fisher and Simmons, 1977), c_s the speed of sound in the medium ($\approx 1,500\,\mathrm{m\,s}^{-1}$), C_p the specific heat at constant pressure ($\approx 3.8 \cdot 10^3\,\mathrm{J\,kg}^{-1}\,\mathrm{K}^{-1}$), β the bulk coefficient of thermal expansion of the medium, and t is the time. The values specified in parenthesis apply to sea water. For the attenuation coefficient, α, Fisher and Simmons give the following expression,

[11] According to Askar'yan et al. (1979) the acoustic signal estimated by Bowen in this chapter is grossly overestimated by a factor of 10^7–10^8.

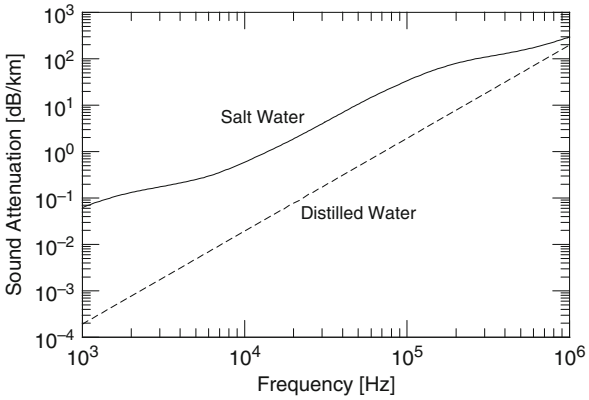

Fig. 2.2 Attenuation coefficient of sound waves in salt and distilled water at a temperature of 25° as a function of frequency (Fisher and Simmons, 1977)

$$\alpha = \frac{10^4}{(2\pi f)^2 \ln(10\omega_0 c_s)}, \tag{2.9}$$

where f if the frequency concerned. This function is plotted in Fig. 2.2.

For simple calculations the heat deposit mechanism is considered to be instantaneous, thus, $E(\vec{r}\,', t) = E(\vec{r}\,')\delta(t)$. The pressure wave can be calculated at the location $\vec{r}$ as a function of time as

$$P(\vec{r}, t) = \int_V E(\vec{r}\,')G(\vec{r} - \vec{r}\,', t)\mathrm{d}^3\vec{r}\,', \tag{2.10}$$

where

$$G(\vec{r}, t) = -\frac{\beta}{4\pi C_p} \cdot \frac{t - r/c_s}{r\tau^3\sqrt{2\pi}} \exp - \left(\frac{(t - r/c_s)^2}{2\tau^2}\right), \tag{2.11}$$

with

$$\tau = \sqrt{\frac{r}{\omega_0 c_s}}. \tag{2.12}$$

The energy deposition region is elongated in the direction of the incident momentum vector of the initiating particle and the acoustic emission is *coherent* in the plane perpendicular to it.

The initial efforts to detect acoustic shocks in large volumes of water were exclusively aimed at the detection of extremely high energy neutrinos ($E_\nu \geq 10^{20}$ eV) in conjunction with the pioneering DUMAND (Deep Underwater Muon And Neutrino Detector) high energy neutrino telescope in Hawaii (Bosetti et al., 1982, 1989; Babson et al., 1990). In this context the intention was to add an acoustic detector matrix in the form of outriggers to the huge optical Cherenkov detector matrix in the deep ocean as a low cost extension, to increase the effective neutrino detection

volume by a large factor and thus to extend the tangible energy range of the telescope far beyond the capabilities of the optical Cherenkov detector matrix. However, this pioneering project, which set the design template and guidelines for all future large neutrino telescopes, had to be discontinued for lack of funding and did not explore acoustic detection.

A project to detect giant air showers impacting on large bodies of water at high altitude was pursued by Kakimoto et al. (1981) and Kaneko et al. (1983) in a series of experiments at Lake Titicaca and Lake Khara Kkota in Bolivia (altitude ~4,080 m).

Today the technique is still in its infancy but numerous feasibility studies are currently under way to develop very large volume neutrino detectors in the oceans and a variety of concrete projects have surfaced in recent years (Dedenko et al., 2001; Lehtinen et al., 2001, 2002; Niess, 2005). The specific aim is the detection of cascades induced by extremely high energy neutrinos in the deep ocean, in major lakes or in large volumes of ice such as at Antarctica, where the *acoustic noise level* is low and therefore the signal to noise ratio for short sharp pulses is optimal (Aynutdinov et al., 2005; Niess and Bertin, 2006; Antipin et al., 2007; Böser et al., 2007a, b). The energy calibration of an acoustic array, too, is a non-trivial problem and requires simultaneous cross checking with other well established methods.

So far no dedicated air shower detector system based on acoustic event detection in the ocean or a lake is operational. The main reason for the lack of interest to employ this method is that an acoustic air shower detector matrix would have to be installed close to the water surface where the shower core dissipates its energy but also a high level of *acoustic background* is present (wind, waves, etc.), not to mention the difficulty to install and operate a near surface array. In addition, the very limited amount of information that such a system yields as compared to other methods and projects currently under construction to explore the highest energy regions of the cosmic ray spectrum are rather discouraging.

2.8 Hybrid Detector Systems and Coupled Experiments

2.8.1 Surface Experiments

At some array sites a combination of different detectors had been used simultaneously, e.g., particle and atmospheric Cherenkov detectors (large aperture and/or narrow angle pointing devices) such as at Yakutsk (Diminstein et al., 1973), at EAS-TOP (Aglietta et al., 1986) and at HEGRA (Aharonian et al., 1991), but also particle detector arrays and fluorescence detectors, or a combination of all three, such as during particular periods at the Akeno (Hara et al., 1970b) and Fly's Eye sites (Bird et al., 1995). In the latter case, several autonomous but synchronized particle and/or atmospheric Cherenkov detector arrays had been operated at times in the vicinity of the fluorescence detector (CASA/MIA, Borione et al., 1994; Bird et al., 1995; DICE, Boothby et al., 1995; CASA-BLANCA, Cassidy et al., 1997), in order to collect as much information as possible from the same simultaneously observed showers.

In later hybrid experiments, e.g., at the Fly's Eye site the HiRes and MIA detectors were operated jointly (Abu-Zayyad et al., 2001). In some cases radio antenna arrays had been incorporated with particle detectors to explore radio pulses generated by air showers, e.g., at Chacaltaya (BASJE experiment, Barker et al., 1967), Haverah Park (Allan, 1971), CASA/MIA (Green et al., 2003) and recently at the KASCADE-Grande experiment in Karlsruhe (Horneffer et al., 2003; Haungs et al., 2007) and at the Auger Observatory (Van den Berg, 2007).

The two very large new experiments that have just come into full operation to explore the highest energy region of the cosmic ray spectrum are the Auger Observatory at Malargüe in Argentina (Camin, 2004; Dawson, 2007), and the Telescope Array in Utah, USA (Kasahara et al., 2007). Both installations are hybrid experiments and use surface particle detectors that are distributed over an area of $\sim$3,000 km^2 and $\sim$680 km^2, respectively, and have several atmospheric fluorescence detectors, each. An Auger counterpart in the northern hemisphere at Lamar (CO, USA) is presently in the planing and design phase. This detector combination, i.e., surface array and fluorescence detectors, yields excellent three-dimensional information of the shower development in the atmosphere and very detailed ground level data.

2.8.2 Special Detector Systems

In order to study specific particles or groups of particles in showers, such as hadrons (nucleons, antinucleons, pions), muons, or electrons and photons, or to search for new hypothetical particles, dedicated detector systems are integrated into the shower arrays. Most frequently used are muon sub-arrays to monitor the low energy muon component, in particular the lateral and temporal distributions of the muons. Sometimes absorption spectrometers and rarely magnet spectrometers had been incorporated at the surface or at shallow depth at specific locations within an array to study the muon spectrum (Vernov et al., 1979) (see Chap. 14 for details).

Only few experiments had been equipped with a hadron calorimeter to analyze the high energy hadron component (e.g., Tien Shan in Kazakhstan, EAS-TOP in Italy, and KASCADE in Germany), and only few air shower arrays had been equipped occasionally with a cloud chamber (e.g., the installations at Tokyo and Mount Norikura in Japan, at Ootacamund in India, and at Sydney in Australia). In an exceptional experiment Hook et al. (1970) have used a magnet spectrometer to record negative pions in showers at Haverah Park (see Chap. 13).

Since the high energy particles are inside the shower core and in its immediate vicinity, the special detector systems to analyze these components are usually placed at or near the array center as defined by the array layout and the trigger requirements that select events where the core strikes the device or its neighborhood. These instruments come in a variety of designs, particularly the hadron calorimeters.

Important properties of hadron calorimeters are high spatial, temporal and energy resolution. Moreover, calorimeters should be sufficiently large, both in area and depth, to record an adequate number of events, to avoid energy leakage in both

directions, in and out, and to absorb the hadron cascades completely in order to analyze them fully.

Muon telescopes and absorption spectrometers are usually placed underground or under a hadron calorimeter, if available, to get a high threshold energy for the muons to study hadron-muon correlations and for obtaining target diagrams. The designs and the operation of the different devices are discussed in the appropriate chapters where the respective particle data are presented (Chaps. 13, 14, 15, 16, 17 and 18 of Part II).

2.8.3 Coupled Surface and Underground Experiments

As mentioned earlier, ultrahigh energy muons play an important role in air shower research. They are extremely difficult to observe because their number is relatively small, they are within the core region and its immediate vicinity, and are therefore accompanied by a large number of other very energetic particles. These must be filtered out to have access to the muons. The only practical way to do this is to have a suitable muon detector buried *deep* underground, under ice or under water, located underneath an air shower array.

Five pairs of experiments, most of which are no longer in operation, offered this unique combination. They included the combined surface and underground installations at the Kolar Gold Fields (KGF) in India (Narasimham, 2004; Acharya et al., 1981), at the Homestake site in Lead, South Dakota, USA (Cherry et al., 1985), the MACRO and LVD underground installations in combination with the EAS-TOP array at Gran Sasso in Italy (Ahlen et al., 1992, 1993; Ambrosio et al., 2002; Bari et al., 1989; Aglietta et al., 1992, 1998, 2004a, b), and the Baksan surface array and underground detector combination in Russia (Alexeyev et al., 1979, 1993). In addition, there was the magnetic muon spectrometer at the Moscow State University (MSU) that was located at the shallow depth of 40 m water equivalent, near the center of the air shower array (Vernov et al., 1979).

The Kolar Gold Fields underground experiments which had been used for this purpose had muon threshold energies of 220 GeV and 1.8 TeV and were located almost perpendicularly below the surface array (see Fig. A.40). The situation at Homestake was similar but the muon threshold was 2.7 TeV. At Gran Sasso the underground experiments were laterally displaced with respect to the EAS-TOP array. The line connecting the centers of the surface and underground experiments subtended an angle of about 35° with respect to the vertical and the muon threshold for coincident events was $\sim$ 1.3 TeV. At Baksan where the installations are still in operation, the underground detector has a threshold of 230 GeV. The rather shallow depth of the MSU muon spectrometer did not affect its usefulness. Background rejection was sufficient, so that actual muon spectra in showers could be measured. The instrument had a maximum detectable momentum for muons of 900 GeV/c.

The problem with all these experiments was the low event rate because of the small aperture, i.e., the small solid-angle-area product of the surface and underground detectors combined. However, the situation for carrying out high energy

muon measurements in air showers will improve dramatically in the near future when the large experimental installations at the South Pole begin to accumulate data. There the IceCube detector, now completed, is a unique giant muon detector embedded deep in the ice, located between 1,450 and 2,450 m under the surface, with an almost congruent well equipped air shower particle detector array at the surface, called IceTop (Klepser, 2007), that is complemented by an array of antennas for the detection of the radio bursts generated by the air showers (Karle, 2007).

A selection of special detector systems that are incorporated in some experiments are described in the appropriate chapters of Part II where we present data on specific shower components. The layouts of a number of arrays of past and present are displayed in Sect. A.1.

2.9 Directly and Indirectly Accessible Shower Parameters

An air shower harbors an enormous amount of information, from the energy and nature of the primary particle to the properties of high energy hadronic, electromagnetic and leptonic interactions, such as cross sections, the type, multiplicity and momentum distributions of secondary particles, their energy and collision partner dependence as well as the specific properties of the different particle groups involved. Different detector systems and detector combinations supply different categories of information. Some yield only very rudimentary, others a wide scope of highly sophisticated shower and particle data.

Some of the basic information that characterizes a shower, such as the arrival time of the charged particles, the associated non-optical photons, and the lateral particle and photon density distributions in the plane of observation at a specific atmospheric depth, is immediately accessible with simple shower particle detector arrays. From the particle arrival time information the *arrival direction of the shower* can be determined directly with simple methods of analysis and event reconstruction.[12]

The particle density distribution in conjunction with a simple fitting procedure using the Nishimura-Kamata-Greisen (NKG) lateral distribution function (LDF) yield the *location of the shower axis* and the *shower size*. Since the shower size at shower maximum is directly related to the primary energy, a rough estimate of the latter can be obtained quickly. However, in general detailed simulations and fitting procedure are required to get a reliable primary energy assignment (for details see Chaps. 8 and 10).

The situation is similar, in principle, for the parameters that can be extracted from measurements of the optical photon component of atmospheric Cherenkov emission that is associated with a shower (Chap. 16), provided appropriate detector systems are being used. Simple information on the composition of the particle population in

[12] Tracking detectors, though only seldom used, reveal directly the direction of propagation of the shower particles. The claimed angular accuracy of this method is $\sim 0.3^{\circ}$.

a shower, such as for instance the approximate determination of the muon fraction, can also be extracted readily with little effort by incorporating comparatively simple (shielded) particle detectors.

Shower parameters and characteristics as listed above can be classified as *directly accessible* since they do not necessarily require complex simulation and analysis procedures. They are discussed in more detail in Sect. 2.10.

On the other hand, to extract information on the hadronic component of a shower (Chap. 13) requires in general the incorporation of a dedicated calorimeter which represents a very significant increase of the instrumental complexity. Such a detector system demands far more sophisticated simulation-based data analysis methods to get at the more subtle specific parameters and distributions. A similar though somewhat less delicate situation exists for the extraction of the relevant shower parameters from measurements of the directly observable atmospheric fluorescence photons recorded with Fly's Eye type detectors (Chap. 17), and likewise for the interpretation of the data from measurements of the presently not fully understood radio wave emission of air showers (Chap. 18).

The signature of the primary particle, in particular of its nature (type, mass and charge) cannot readily be extracted from basic shower data (except for an approximate estimate of the energy as mentioned before). This is also true for most of the relevant and more fundamental interaction and particle physics properties. These as well as the primary mass effects are heavily masked by the multitude of processes that occur in a shower. Many of the processes manifest similar features in the global picture of a shower and are therefore difficult to isolate from each other. This is particularly true for the effects caused by the energy dependence of the hadronic cross sections, the secondary particle multiplicity and the primary mass (see Chap. 3). They all tend to affect a shower alike.

This category of parameters and data must be classified as *indirectly accessible, derived parameters* as they require sophisticated methods of data analysis. Chapter 10 is dedicated to this topic. Further details concerning the extraction of information on specific shower components and parameters from experimental data are discussed in the corresponding chapters of Part II.

2.10 Basic Shower Reconstruction Procedure

In this section we focus the discussion on the basic shower event reconstruction procedure, in particular on the methods that are commonly applied to particle detector arrays. Essentially the same method can be applied to wide-aperture atmospheric Cherenkov detector arrays. Details on optical Cherenkov detection, event reconstruction, results and data interpretation are presented in a separate chapter (Chap. 16). Likewise, event reconstruction based on data from atmospheric fluorescence measurements and radio emission detector (antenna) arrays are discussed in Chaps. 17 and 18, respectively, where a selection of data is presented.

There are many refined procedures to reconstruct the basic shower parameters from timing and particle density measurements acquired with an array (Aglietta et al., 1993). The procedures depend in detail on the array layout, the location of the trigger detectors and the trigger conditions required. Thus, they vary in general from array to array and author to author. For the standard approach see, e.g., Clark et al. (1957, 1961); Tennent (1968); Kakimoto et al. (1996); Ogio et al. (2004).

Usually, before running a full analysis on a recorded shower, certain additional criteria may have to be fulfilled by the raw data beyond the bare trigger condition to accept an event for processing. These may include, for example, the requirement that at least k out of the n array detectors have recorded a predefined minimum number of valid particle density measurements within a given coincidence window. In the following we outline the principle of elementary shower event reconstruction, i.e., the determination of the *direction* of the shower axis, the *axis (core) location* at ground impact, and the *shower size* and *age* on hand of a simple example (see also Chap. 8 for more details).

Consider an array consisting of n particle detectors and five fast-timing array trigger detectors. One of the latter is placed at the array center, the remaining four are located equidistant from the center at the corners of a square. For simplicity let the square be oriented such that its diagonals run east–west (E–W) and north–south (N–S), as shown in Fig. 2.3, and we label the corner detectors accordingly (E, W, N, and S) and the center detector, C.

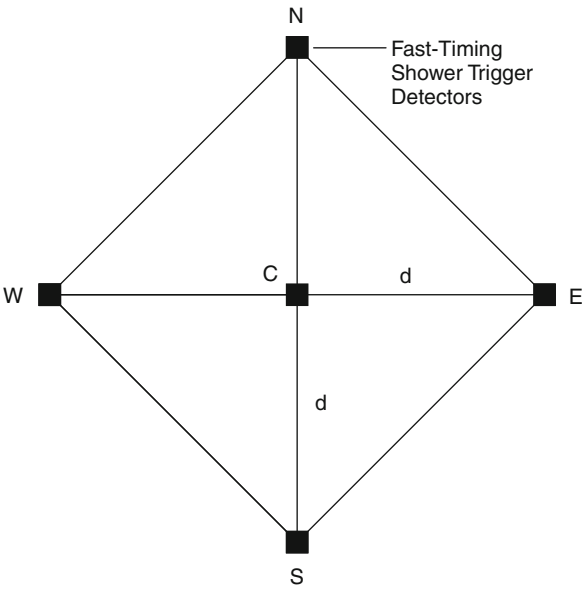

Fig. 2.3 Example of a layout of a simple fast-timing trigger detector arrangement within a shower detection array (not drawn)

2.10.1 Arrival Direction

The arrival direction of the shower is perpendicular to the particle disk[13] and given by the zenith angle, θ, and the azimuthal angle, φ, subtended by the shower axis with respect to a horizontal reference system at the ground. These angles are determined by the arrival time sequence (delay) of the shower front at different locations across the array; in particular, in our example by the arrival of the first particle at each of the 5 fast-timing array trigger detectors. They are obtained using the following relations:

$$\tan\varphi \;=\; -\frac{\Delta t_{\mathrm{N,C}}}{\Delta t_{\mathrm{W,C}}} \tag{2.13}$$

and

$$\sin\theta \;=\; -\frac{c}{d}\,\frac{\Delta t_{\mathrm{N,C}}}{\sin\varphi}, \tag{2.14}$$

where $\Delta t_{i,j}$ is the time difference (delay) [ns] of the arrival signatures between detectors i and j ($i = \mathrm{E, W, N, S};\ j = \mathrm{C}$ in our example), c is the speed of light and d the half-diagonal of the square formed by the 4 outer trigger detectors. In other words, the zenith and azimuthal arrival directions of the axis are determined by an optimized fit of a plane to the particle arrival times recorded by the detectors and taking the perpendicular to this plane.

In more refined procedures and for large showers and arrays the shower front curvature must also be implemented in the reconstruction procedure. Since the thickness of the shower front increases with core distance, the time of the first arriving particle at a detector depends on the density, mainly of electrons, and not on muons at large core distances (Nagano, private communication, 2007). Therefore the particle disc thickness must be taken into account (see Chap. 8).

In this case in a first step the zenith and azimuthal angles, θ' and φ', are determined by the least square method in the so-called *plane front approximation* where the curvature is ignored, as discussed above, imposing only the condition that

$$l^2 + m^2 + n^2 \;=\; 1, \tag{2.15}$$

where $l,\ m,\ n$ are the direction cosines. This leads to a first approximate core position (Aguirre et al., 1973; Nagano, 2007). Subsequently, the *radius of curvature*, r_c, and the disc thickness, Δt, are introduced as parameters. By successive variation, using these parameters and different sets of timing data, the zenith and azimuthal angles, θ and φ, and the core position are calculated anew until finally the errors are reduced to acceptable values. Thus, arrival direction and core location determination are *not independent*.

[13] This is also valid for large showers where the particle disk manifests a curved surface.

Angular errors can be evaluated with the following expressions (Baggio et al., 1977),

$$\delta\theta \;=\; \frac{c}{d}\,\sec\theta\left(\frac{\delta\,\Delta t(\Delta t_{\mathrm{N,C}}+\Delta t_{\mathrm{W,C}})}{(\Delta t^2_{\mathrm{N,C}}+\Delta t^2_{\mathrm{W,C}})^{1/2}}\right), \tag{2.16}$$

$$\delta\varphi \;=\; \delta\,\Delta t\left(\frac{1}{\Delta t^2_{\mathrm{N,C}}}+\frac{1}{\Delta t^2_{\mathrm{W,C}}}\right)^{1/2}\sin\varphi\,\cos\varphi \tag{2.17}$$

and

$$\begin{aligned}\delta\sin\alpha \;=\; &[(\sin\theta_0\,\sin\varphi\,\cos\theta+\cos\theta_0\,\sin\theta)\,\delta\theta\\ &+(\sin\theta_0\,\sin\theta\,\cos\varphi)\,\delta\theta]\cot\alpha.\end{aligned} \tag{2.18}$$

The errors for the arrival direction range from a *few degrees* for small arrays to less than one half of a degree for sophisticated installations (Khristiansen, 1980; Antoni et al., 2003a). In Fig. 2.4 we show as a practical example the variation of the angular resolution of the azimuthal and zenith angles of the MAKET-ANI array as a function of zenith angle (Chilingarian et al., 2007).

Depending on the direction of the shower axis with respect to the direction of the geomagnetic field, the latter must be considered to reconstruct the actual direction of initial incidence of the primary accurately.

For special analyses where the geomagnetic field is of particular importance, such as for shower asymmetry or shower radio emission studies, the angle α between the shower axis and the Earth's magnetic field direction is the relevant parameter.

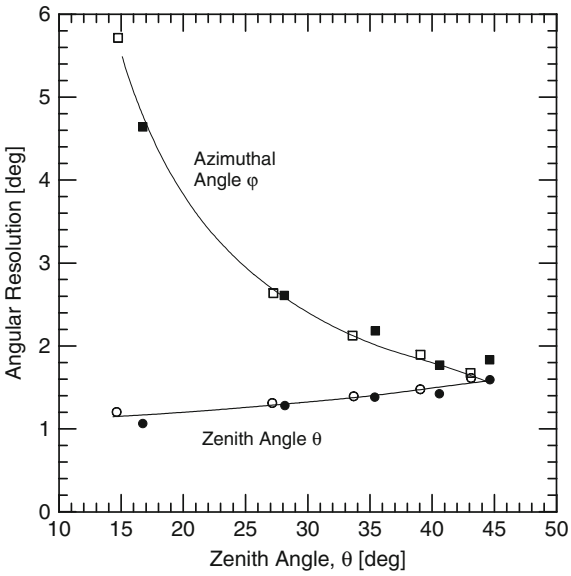

Fig. 2.4 Zenith and azimuthal angular accuracies of the shower axis direction determination as a function of the zenith angle. The example is from the MAKET-ANI experiment on Mt. Aragats, near Yerevan (Armenia). The *square symbols* apply to the azimuthal angles, the *circular symbols* to the zenith angles. The *open symbols* were obtained with the non-parametric method, the *filled symbols* are simulation results (after Chilingarian et al., 2007)

It is determined as a function of θ, θ_0, φ and φ_0, where θ_0 and φ_0 are the angles which define the direction of the geomagnetic field and θ and φ the direction of the shower axis. Thus,

$$\cos\alpha = \sin\theta\ \sin\theta_0(\cos\varphi\ \cos\varphi_0\ +\ \sin\varphi\sin\varphi_0)\ +\ \cos\theta\ \cos\theta_0. \tag{2.19}$$

Further details concerning the influence of the geomagnetic field on the shower particle pattern on the ground are discussed in Chap. 8 and radio emission in Chap. 18.

2.10.2 Shower Core Location

Several procedures had been developed in the course of time that are all similar. The differences are essentially array related. Often a preliminary core location is determined by assuming a power law for the lateral density distribution function of the shower particles. This core position, that may initially be chosen at the location of the highest measured density, is then moved around in a fitting procedure to obtain the best fit of the particle densities, ρ_i, to a simplified Nishimura-Kamata-Greisen (NKG) function or some other, often empirical or experimentally determined distribution function (Greisen, 1956, 1960; Nishimura, 1967), such as

$$\rho(r)\ =\ \left(\frac{A}{r}\right)\exp(-r/B), \tag{2.20}$$

where A and B are obtained by a least-square fit method and r is the distance from the shower axis. In a subsequent procedure the actual NKG function or an array specific lateral distribution function is then used to improve the fit.

Typical errors for the core location amount to a *few meters* for the more sophisticated particle detector arrays if the air shower core falls within the physical boundaries of the array. For large arrays such as Auger with widely spaced detectors the error can be as much as *tens of meters* and more.

As a more specific example for large arrays we outline the method which had been used for the Haverah Park array that is also applicable to other large arrays, such as Auger. There an empirical (experimentally measured) density distribution function (Chap. 8) of the form

$$\rho(r)\ =\ k\,r^{-(\eta+r/a)} = k\cdot f(r),\ [\mathrm{ve}\mu\,\mathrm{m}^{-2}], \tag{2.21}$$

had been used, where r is the radial distance of the detector from the shower axis, a a parameter, k a scale factor, and η the slope parameter which is a function of the zenith angle θ. The expression is claimed to be valid for distances $50 \le r \le 800\,\mathrm{m}$ from the shower axis. η was obtained from simulations and the density $\rho(r)$ depends only weakly on η over the relevant radial core distance range where the density had been used to estimate the primary energy ($r \approxeq 600\,\mathrm{m}$) (for details see Chaps. 8 and 10).

In this procedure both the core position (x, y) and the shower size are fitted by comparing the measured densities with predictions from simulations, using Eq. (2.21), by minimizing χ^2 as follows,

$$\chi^2 = \sum_{i=1}^{n} \frac{1}{\sigma_i^2} (k\, f(r_i) - \rho(r_i))^2 , \tag{2.22}$$

where $\rho(r_i)$ are the measured densities at the location i and σ_i the uncertainties related to the density measurements and particle fluctuations.

By differentiating Eq. (2.22), k, which minimizes χ^2, yields

$$k = \frac{\sum f(r_i)\rho_i/\sigma_i^2}{\sum f(r_i)^2/\sigma_i^2} . \tag{2.23}$$

One of the constraints on Eq. (2.22) is that the distribution of the measurement uncertainties is Gaussian. However, for small densities a Poissonian distribution is more appropriate to calculate the likelihood function. The procedure requires some further refinements to account for fluctuations and uncertainties that are array specific. For further details the interested reader is referred to the papers of Armitage et al. (1987), Ave et al. (2003), Coy et al. (1981, 1997), England (1986), and Lawrence et al. (1989, 1991).

2.10.3 Shower Size, Energy and Age Determination

In principle, the shower size, N, is obtained by integration of the lateral density distribution. However, this procedure is intimately linked to the shower axis (core) position determination and to the fitting of the measured densities of all detectors to an NKG (or other) function of appropriate age, as outlined above, and usually executed jointly (see Chaps. 4, 8 and 10).

In particular, the shower size is determined by looking for the core position which gives the best fit determined from a minimum in normalized χ^2 to the Nishimura-Kamata (NK) function (Kamata and Nishimura, 1958) or an approximated NKG function. The calculation is then made for a series of *age parameter* values, s, defined in Chap. 4, e.g., $s = 0.4$–1.6 in steps of 0.1 or 0.2, and the size for the best fitted s is selected. For a reliable evaluation the shower axis must be located within the boundaries of the array.

The *primary energy* can then be estimated from the *size-energy relation* or from the energy density deposit of the particle mix in a very specific radial zone of the showers in a deep-water Cherenkov detector tank, expressed in units of vertical equivalent muons per unit area [veμ m^{-2}]. This latter method is mainly applicable to larger showers. Under appropriate experimental conditions the primary energy can also be estimated on the basis of the muon size or the so-called *truncated muon size* (Weber, 1997; see also Chaps. 8 and 10).

The size-energy relation was originally based on the photon–electron cascade theory which is summarized in Chap. 4. This theory shows that the shower size at maximum development is nearly proportional to the energy of the shower initiating photon or electron. However, for hadron initiated showers which account for the majority of all events, the parent nuclear cascade must be considered, too, and a full fledged air shower simulations as discussed in Chap. 20 is required to estimate the primary energy from the experimentally determined shower size reliably. This applies even more so to the second method mentioned above, the estimation of the primary energy from the local energy density contents of a shower.

The primary energy determination of air showers is discussed in detail in Chap. 10 (see also Goorevich and Peak, 1975; Takeda et al., 2003; Ave et al., 2003; and Chap. 11). For practical applications a *conversion factor* is frequently used that is obtained from air shower simulations. This factor depends on the altitude of the observation level where the shower size measurement was made and on the zenith angle of the event. Obviously, different calculations yield somewhat different numerical values, however, the deviations are not very large because the result hinges heavily on the well known *photon–electron cascade theory*.

As a thumb rule adequate for rough primary energy estimates one can use the following conversion factors: ≈1 GeV per shower particle for near vertical showers at an altitude of 5,000 m, ≈3 GeV per particle at 2,500–3,000 m and ≈10 GeV per particle at sea level (see also Aglietta et al., 1999). These values apply to smaller size showers (10^{14}–10^{15} eV). For showers of larger size (higher primary energy) the conversion factor in the lower atmosphere must be reduced by about a factor of two to three because the distance between the observer and the shower maximum is reduced, i.e., because the shower maximum moves to greater atmospheric depth.

Folding the particle density distribution of simulated showers with the detector array and detector response, using the *density fluctuations* (Chaps. 8 and 19) derived from the lateral distribution of real showers, one can obtain the approximate overestimation of the shower size for an underestimated value of s, and vice versa. With the help of simulations one can also estimate the core position error, which depends on the shower size, the number of detectors and the geometry of the array.

2.10.4 Array Acceptance and Detection Efficiency

The shower acceptance and the detection efficiency of a particle (or air Cherenkov photon) detector array as a function of shower size, zenith angle and core location depend on many factors and must be carefully explored. This is usually achieved with the help of Monte Carlo simulations of showers, convoluted with the array detector layout and detector response. Cranshaw et al. (1958) and Clark et al. (1961) developed the method initially in connection with the shower size determination (see also the procedures described by Bell et al., 1974; Chiba et al., 1991, 1992; Amenomori et al., 1990, 1993; Chiavassa et al., 2005). Primarily the detection efficiency depends on the array layout, above all on the percentage of detector coverage.

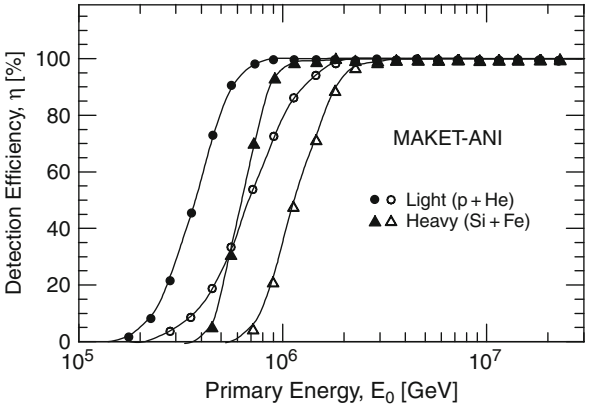

Fig. 2.5 Predicted detection efficiencies obtained from simulations of the MAKET-ANI shower array on Mt. Aragats (Armenia) for light (p, He) and heavy (Si, Fe) primary initiated air showers as a function of primary energy. The *filled symbols* apply to a shower selection criterion for shower sizes $N_e \geq 10^5$, and zenith angles $\theta \leq 30^\circ$, the *open symbols* for $N_e \geq 10^5$, and zenith angles $30^\circ \leq \theta \leq 45^\circ$ (after Chilingaria et al., 2007)

As an example, for the primary energy (or shower size) dependence of the detection efficiency we show in Fig. 2.5 the predicted response of the MAKET-ANI array on Mt. Aragats near Yerevan (Armenia), which is located at an altitude of 3,250 m a.s.l. (695 g cn^{-2}), as a function of primary energy from a simulation of Chilingarian et al. (2007).

Another example showing the simulated detection efficiency of the particle detector array of the University of Kiel at Pic du Midi in France (2,860 m a.s.l., 729 g cm^{-2}) as a function of radial distance of the shower axis from the designated array center is displayed in Fig. 2.6. This rather small and simple array consisted of 13 scintillation detectors of area 0.25 m^2 each. The layout is shown in Fig. A.27.

A very different example is illustrated in Fig. 2.7 which shows the detection efficiency of the far more elaborate and much larger Akeno array as a function of shower age, s, for different shower sizes (Nagano et al., 1984). The array configuration to which this efficiency plot applies is illustrated in Fig. A.5.

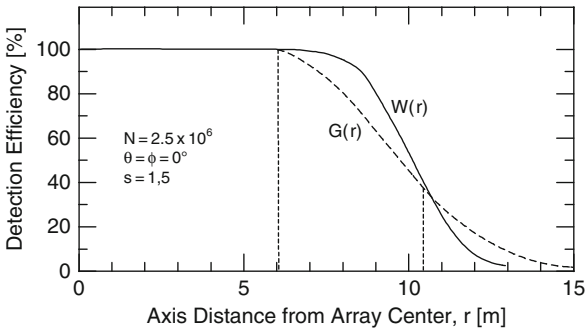

Fig. 2.6 Example of array shower detection efficiency as a function of core location from the array center of the Pic du Midi array (see Fig. A.27, for layout; Böhm and Steinmann, 1979). The curve labeled $W(r)$ shows the theoretical efficiency whereas curve $G(r)$ represents the efficiency if in addition a core position error is included

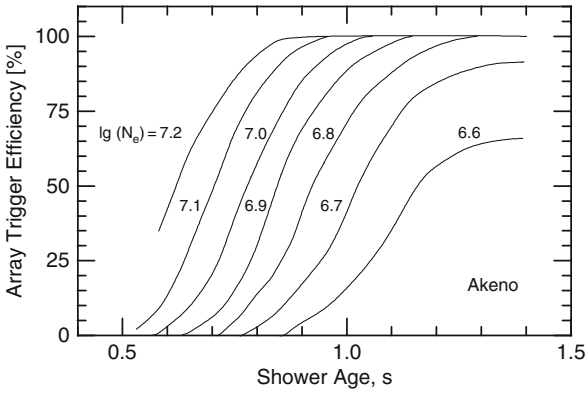

Fig. 2.7 Trigger efficiency as a function of shower age for different shower sizes calculated for the Akeno array layout shown in Fig. A.5 (after Nagano et al., 1984)

The errors and uncertainties adhering to the directly measured observables of a shower affect any subsequently derived indirect observable and the interpretation of an individual event as well as the conclusions drawn for an entire set of events (e.g., the determination of the primary energy spectrum). Consequently, the accuracy of the shower size reconstruction is of fundamental importance for many subsequent steps and must be investigated carefully for every air shower experiment.

The accuracy of the computed shower size depends above all on the recorded particle densities and the number of measured density samples. This implies that it depends on the shower size itself and the array parameters, such as the number and area of the shower detectors and the array layout. In Fig. 2.8 we show the reconstruction uncertainty as a function of shower size for the KASCADE experiment (Antoni et al., 2003a) as it was evaluated on the basis of simulations using the CORSIKA program system, including the detector responses (Antoni et al., 2003b; for KASCADE-Grande see Glasstetter et al., 2003, 2005).

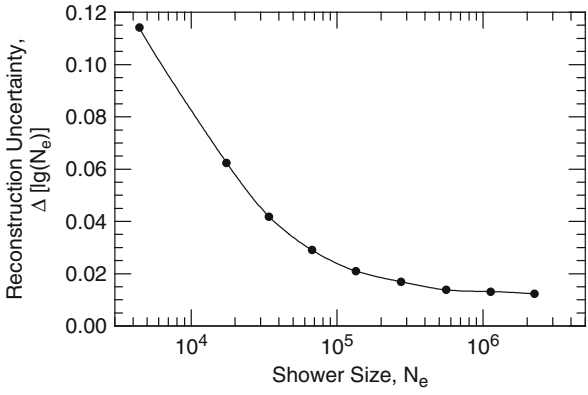

Fig. 2.8 Reconstruction uncertainty of the shower size determination for the KASCADE array as obtained for showers simulated with the CORSIKA program, including detector response (Antoni et al., 2003b). The array layout is shown in Fig. A.22

2.11 Detector Response to Air Shower Particles and Transition Effects

2.11.1 Introductory Comments

A wide variety of detectors had been used in cosmic ray air shower studies, such as Geiger counters, ionization chambers, proportional counters, solid and liquid scintillation detectors, water and air Cherenkov detectors, spark and discharge chambers, transition radiation detectors, time projection chambers and even cloud chambers. In addition combinations of modern electronic detectors are being used in sophisticated calorimeters to analyze the shower cores as well as optical detectors to record atmospheric Cherenkov radiation and air fluorescence associated with air showers. The different particle detectors do not respond alike in similar applications because of *transition effects* that may occur within the detector media and enclosures.

Solid plastic and to a lesser extent liquid scintillators are the most frequently used particle detectors in air shower work because of their fast response, relative linearity, wide dynamic range, high signal to noise ratio, long life, low cost, easy handling, dependable and unproblematic operation. They are used primarily as shower detectors in two different modes of operation.

In conjunction with fast timing circuits and operated at a low threshold level scintillation detectors can be used for arrival time and direction determination. On the other hand, if provided with wide dynamic range circuits they can be used for particle density measurements to determine the lateral distribution (or structure) function, shower age, size, core location and other shower characteristics. In addition there are many other applications in more sophisticated apparatuses, such as muon telescopes, hadron calorimeters, etc.

Signal to noise is inferior in very thin scintillators as compared to thick ones. On the other hand transition effects increase with increasing scintillator thickness, particularly near the shower axis, where the average energy of the particles is high. Thick scintillators are more subject to contributions from electron–photon cascades developing within them and from nuclear interactions of hadrons that are abundantly intermixed with the electromagnetic and muonic components in the vicinity of the shower core. As a result, the relationship between the true particle density and the output pulse height of a thick scintillation detector has a stronger dependence on the energy of the traversing particles than a thin detector and, because of the shower properties, also manifests a dependence on core distance and shower age.

Gas filled detectors are much less subject to transition effects because of the much lower density of the detector medium. There, the main concern is the wall thickness of the envelope of the detector which can cause transition effects. In cloud chambers direct observation of the tracks excludes many of the uncertainties but there are other inherent problems that limit the usefulness of this detector type. Thus, the same measurement made with different detectors may yield different results.

In order to compare a specific kind of data acquired by different air shower arrays, instrumental as well as array layout differences must be properly accounted for besides differences in altitude and the geomagnetic location of the various sites.

This is of particular importance when attempting precision measurements or for studying more subtle topics, such as the kink in the primary spectrum and other aspects.

Numerous authors have compared the response of different detectors under similar or identical conditions in air showers at different core distances and altitudes, and have carried out detector calibrations at accelerators. We present a brief summary of some of this work below to illuminate the significance of the problem. For details concerning particle detectors and their properties the reader is referred to the special literature (Allkofer, 1971; Grupen, 1993; Grupen and Schwartz, 2005, 2008; Leo, 1994; Kleinknecht, 1992, 1998; Rao and Sreekantan, 1998; Sokolsky, 1989).

2.11.2 Comparison of Detector Responses

Early work on this topic had been carried out by the Tokyo group at sea level[14] (Fukui et al., 1960). These authors have made a comparison between a tightly packed thin neon hodoscope consisting of 2 cm diameter cylindrical neon tubes that are oriented with their axis in vertical direction and a 4.5 cm thick scintillator. The result is shown in Fig. 2.9. Saturation effects in a hodoscope with this tube diameter begin to appear at distances of $\leq$1 m from the shower axis in showers of size 10^6. As an example, we show in Fig. 2.10 the photograph of the hodoscope light pattern of a typical single-core shower of size 10^6 from the work of Fukui et al. (1960).

Similar work was undertaken by the Sydney group, also at sea level, but using different kinds of detectors (Bray et al., 1965). These authors have compared the response of a 10 cm thick *plastic scintillation detector* with that of a *cloud chamber* and a *Geiger counter tray*.

Two sets of data are presented of their work. The first shows the ratio of the particle density in the scintillator as determined from its photomultiplier pulse height to that actually observed in the cloud chamber obtained by track counting, as a function of scintillator particle density. One set of data applies to the arrangement where the

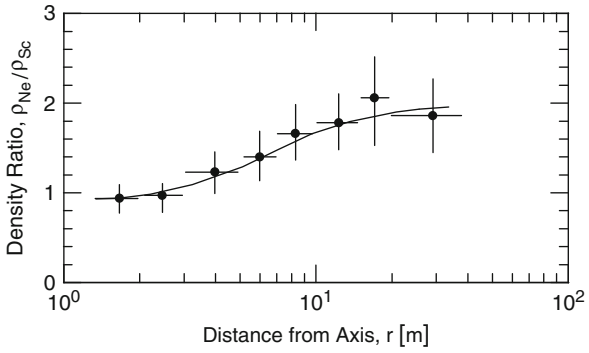

Fig. 2.9 Ratio of particle densities estimated with a neon hodoscope with 2 cm tube diameter and a 4.5 cm thick scintillation detector in showers of size 10^6 as a function of distance from the shower axis at sea level (Fukui et al., 1960)

[14] The altitude is relevant because of the energy of the particles.

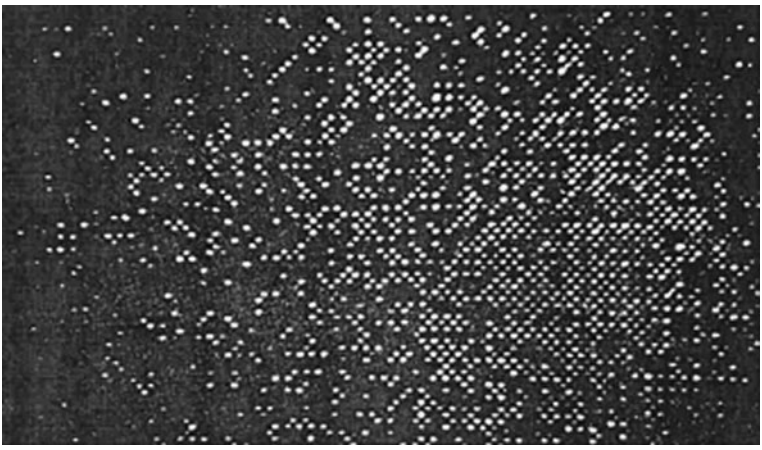

Fig. 2.10 Photograph of a neon tube hodoscope displaying the center of a core of a shower of size 10^6. The hodoscope measures 2 by 3.5 m^2 and consists of 5,040 tightly packed neon tubes measuring 2 cm in diameter (Fukui et al., 1960)

chamber is located directly beneath the scintillator, the other with the chamber on its side, 1 m apart. The results are shown in Fig. 2.11.

The other set of data by the same authors illustrates the core position and shower size dependence of the ratio of scintillator particle density measurements (pulse height) to Geiger tray measurements (number of hits in tray). The Geiger tray had been calibrated separately in earlier measurements. The data are shown in Fig. 2.12 together with results obtained by Kerschenholz et al. (1973) under similar conditions but for a scintillator thickness of only 5 cm.

The increase of the ratio with increasing shower size at a fixed core distance, and the decrease with increasing core distance for a constant shower size are evident. This behavior is in accordance with expectations mentioned above. However, saturation effects in the Geiger tubes, not discussed in this paper, could over emphasize the increase of the ratio at close proximity of the shower axis. The same authors have also studied the effect of lead shielding over the counters and the resulting energy dependence.

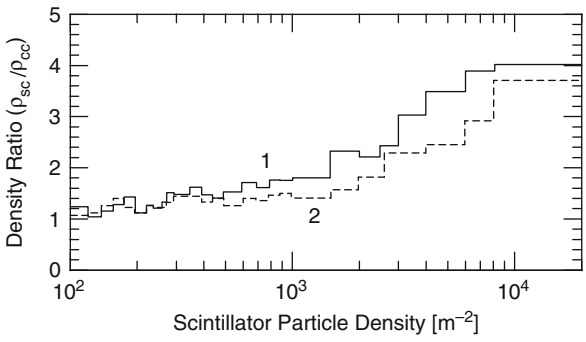

Fig. 2.11 Average ratio of charged particle density measured with a 10 cm thick plastic scintillation detector, ρ_{sc}, to cloud chamber density, ρ_{cc}, at sea level, plotted as a function of scintillator density. The *solid curve*, 1, is for the cloud chamber placed 1 m from the scintillator, the *dashed curve*, 2, for the cloud chamber directly beneath the scintillator (Bray et al., 1965)

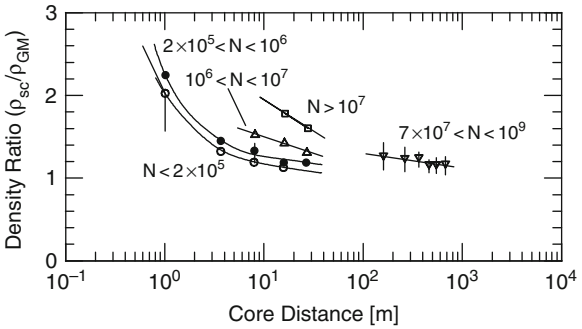

Fig. 2.12 Average charged particle density ratio of plastic scintillation detectors, ρ_{sc}, to tray of Geiger counters, ρ_{GM}, versus core distance for showers of different sizes at sea level. The data points of Bray et al. (1965), ○, ●, △ and □, were obtained at Sydney with a 10 cm thick scintillator, those of Kerschenholz et al. (1973), ▽, at Yakutsk with a 5 cm thick scintillator

Similar measurements comparing scintillators with spark chambers were carried out by Kawaguchi et al. (1971) in Tokyo and Dake et al. (1971) at Mt. Norikura, using scintillators of different thickness. A compilation of their results covering a wide range of core distances and different shower size groups is presented in Fig. 2.13. Additional specifications concerning the measurements are given in the caption.

As an example for a very thick liquid scintillator (30 cm) we present the work of Chudakov et al. (1979), carried out with one of the Baksan detectors. Here the comparison is made with Geiger counters (Fig. 2.14).

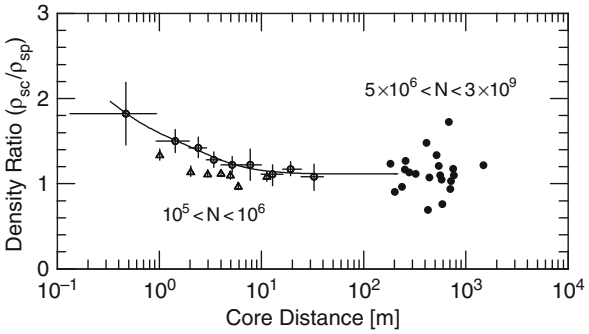

Fig. 2.13 Ratio of charged particle density recorded with a scintillation detector, ρ_{sc}, and a spark chamber, ρ_{sp}, versus distance from the shower axis. Transition effects are evident at distances less than about 10 m from the shower axis and are more pronounced for the thicker scintillator, ○. The measurements at large distances were made with larger showers than those at close proximity, as indicated. The data of Kawaguchi et al. (1971), ○, ●, were obtained in Tokyo (I.N.S.) at sea level with a 5 cm thick scintillator, those of Dake et al. (1971), △, at Mt. Norikura (750 g cm^{-2}) with a 3.5 cm thick scintillator. At distances $\geq$10 m from the axis both scintillator and spark chamber record the same densities up to about 4,000 particles m^{-2}

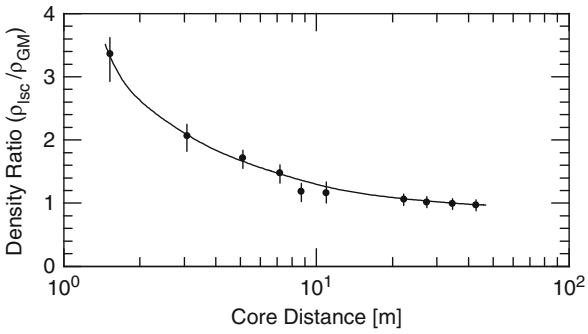

Fig. 2.14 Ratio of particle density determined with a 30 cm thick liquid scintillation detector, ρ_{lsc}, and Geiger counters, ρ_{GM}, as a function of core distance, after Chudakov et al. (1979), at Baksan (840 g cm^{-2}), showing dramatic transition effects in the vicinity of the shower axis

A comparison between scintillators only of very different thickness (3 and 50 mm) was made by Hara et al. (1979, 1981) at the Akeno site (Japan). Their results, shown in Fig. 2.15, are compared with theoretical lateral density distributions.

Very comprehensive work was carried out by Blake et al. (1975, 1978a, 1979) and Towers (1971). These authors have compared density measurements made with a liquid paraffin scintillation detector, a tray of unshielded flash tubes, a 1.2 m deep water Cherenkov detector and a muon (shielded scintillation) detector with a threshold of 0.3 GeV as a function of core distance, in a select group of well defined showers (Blake et al., 1978a). The data are presented in Fig. 2.16. Density ratios

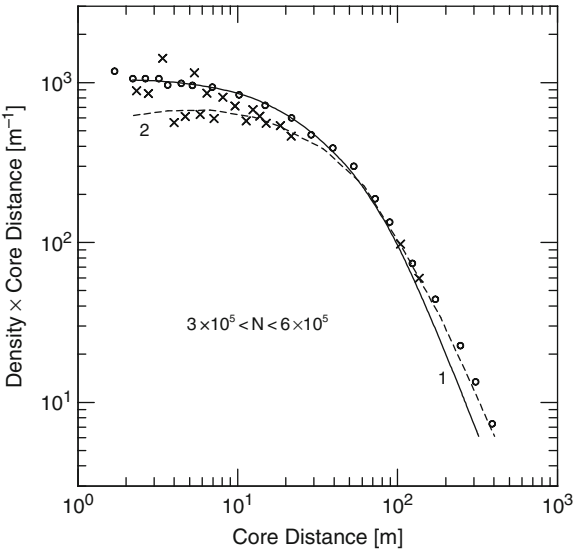

Fig. 2.15 Lateral density distribution of electrons measured with a 3 mm, ×, and a 50 mm, ○, thick plastic scintillation detector at the Akeno site (930 g cm^{-2}). The transition effects of the electromagnetic component in the thick scintillator are clearly seen within 30 m from the shower axis. The *solid* (1) and *dashed* (2) *curves* represents an NKG-functions with a single age parameter, $s = 1.0$ and 1.1, respectively (Hara et al., 1981). The large fluctuations in the thin scintillator are evident. Note that the density along the ordinate is multiplied by the core distance to compress the graph

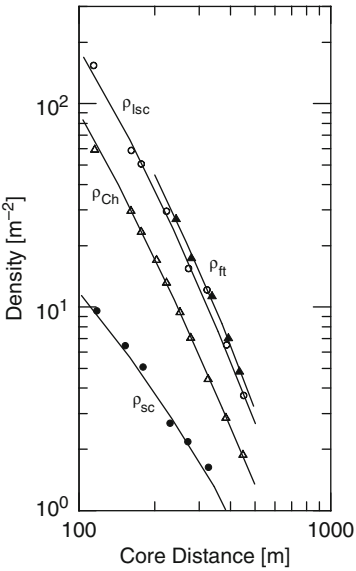

Fig. 2.16 Comparison of the response of various detectors to showers with zenith angles $0^\circ \leq \theta \leq 25^\circ$ and $\rho(500) = 1.2\,\mathrm{ve}\mu\,\mathrm{m}^{-2}$ at Haverah Park (1,018 g cm^{-2}), i.e., for showers that yield a signal corresponding to a vertical equivalent muon density (veμ) of 1.2 m^{-2} in the 1.2 m deep water Cherenkov detector located at a distance of 500 m from the shower axis (Blake et al., 1978a). These showers are initiated by primaries having an energy of approximately $4.7 \cdot 10^{17}$ eV. ρ_{lsc} (○) refers to an unshielded liquid paraffin scintillation detector of thickness 8 g cm^{-2} , ρ_{ft} (▲) to unshielded flash tubes, ρ_{Ch} (△) to the 1.2 m deep water Cherenkov detector, and ρ_{sc} (●) to a plastic muon (shielded) scintillation detector with threshold 0.3 GeV (construction details of the detectors are given in Blake et al., 1978b)

are given in Fig. 2.17 (Blake et al., 1975, 1978a; Towers, 1971). Theoretical energy loss distributions for muons passing through a scintillator are shown in Fig. 2.18 and distribution parameters as a function of muon momentum are given in Fig. 2.19 (Blake et al., 1979).

More recently the problem of transition effects in thin absorbers and plastic scintillators had been studies by Asakimori et al. (1979, 1986) and Asakimori (1988). The measurements were carried out with an arrangement of two plastic scintillators, one located above the other and separated by 10 cm. Scintillators of different thicknesses were used, ranging from 0.3, 1 and 3 cm for the upper, and 2 and 5 cm for the lower. The ratio of the particle densities in the two detectors ($\rho_{\mathrm{lower}}/\rho_{\mathrm{upper}}$) were measured for different combinations of scintillator thicknesses, for showers of different size groups in the age range $0.8 \leq s \leq 1.4$ and zenith angles less than 30°, as a function of core distance. Typically three measurements were carried out for one set of detectors; (a) no shielding, (b) 1 mm of iron and (c) 5 mm of iron in between the two scintillators. Some of their results are presented in Fig. 2.20.

A comparison between the results of Asakimori et al. (1986) discussed above and those of other authors is shown in Fig. 2.21. Included are the density ratios between

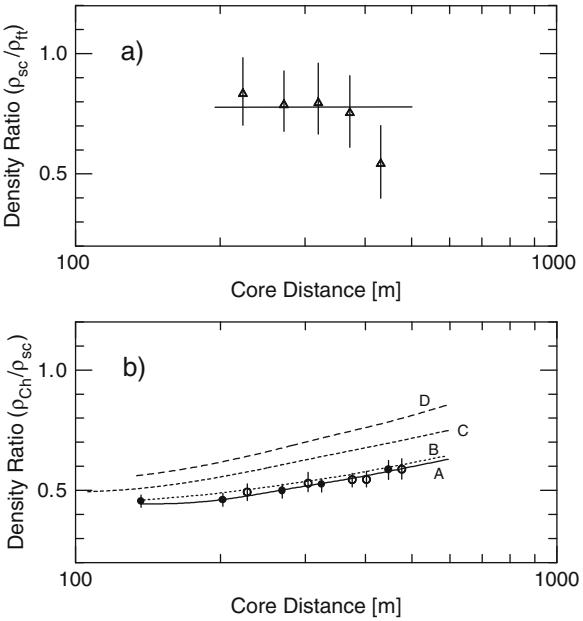

Fig. 2.17 Density ratio versus core distance for two different pairs of detectors, derived from the data presented in the previous figure (Fig. 2.16). (**a**) Shows the density ratio of an 8 g cm^{-2} liquid scintillation detector, ρ_{sc}, to unshielded flash tubes, ρ_{ft}, for showers with $\rho(500) = 0.58$ veμ m^{-2} (vertical equivalent muons m^{-2}) ($E_0 \simeq 2.2 \cdot 10^{17}$ eV) and zenith angles $0^\circ \leq \theta \leq 25^\circ$, $\triangle$ (Blake et al., 1975, 1978a). (**b**) Shows the ratio between a 1.2 m deep water Cherenkov detector, ρ_{Ch}, and the same liquid scintillator as in (**a**), ρ_{sc}, for showers with $\rho(600) = 0.18$ veμ m^{-2} ($E_0 \simeq 1.25 \cdot 10^{17}$ eV). The experimental points, $\bullet$ (Blake et al., 1978a) and $\circ$ (Towers, 1971) as well as *curve A* are for zenith angles $0^\circ \leq \theta \leq 25^\circ$. *Curves B, C and D* are for $25^\circ \leq \theta < 35^\circ$, $35^\circ \leq \theta < 45^\circ$ and $45^\circ \leq \theta < 55^\circ$, respectively, and $\rho(600) = 0.19$ veμ m^{-2}, corresponding to a primary energy of $E_0 \simeq 1.3 \cdot 10^{17}$ eV

10 cm thick scintillators and Geiger-Mueller counters (Bray et al., 1965), two 10 cm thick scintillators, one above the other with a 1/8 inch iron plate in between (Bakich et al., 1970), and spark chambers with unshielded scintillators of different thickness underneath (Shibata et al., 1965, 4.5 cm scintillators; Dake et al., 1971, 3.5 cm; Hara et al., 1970a, 1979, 0.3 and 5 cm).

2.11.3 Response of Deep Water Cherenkov Detectors

The response of the so-called Haverah Park type deep water Cherenkov detectors, originally developed at the Imperial College, London (Allan et al., 1960, 1962; Lillicrap et al., 1963), is of some interest because about 1,600 units of this type of detector are now being used in the Auger experiment (Auger Observatory) in Argentina as surface detectors (Suomijärvi, 2007; Ghia, 2007), in an analogous way

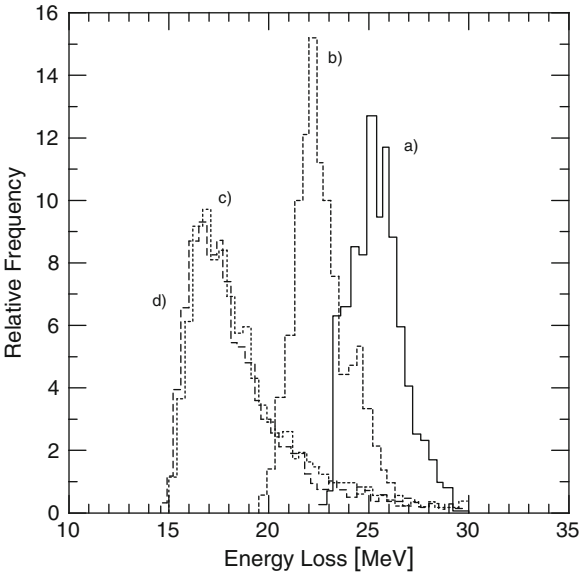

Fig. 2.18 Energy loss distribution of muons passing through 9.2 g cm^{-2} of scintillator, according to Monte Carlo calculations by Blake et al. (1979). The distributions (*a*), (*b*), (*c*) and (*d*) apply to muons having momenta of 0.12, 0.7, 6 and 30 GeV/c, respectively. The enhanced energy loss of low energy muons and the extent of fluctuations are evident

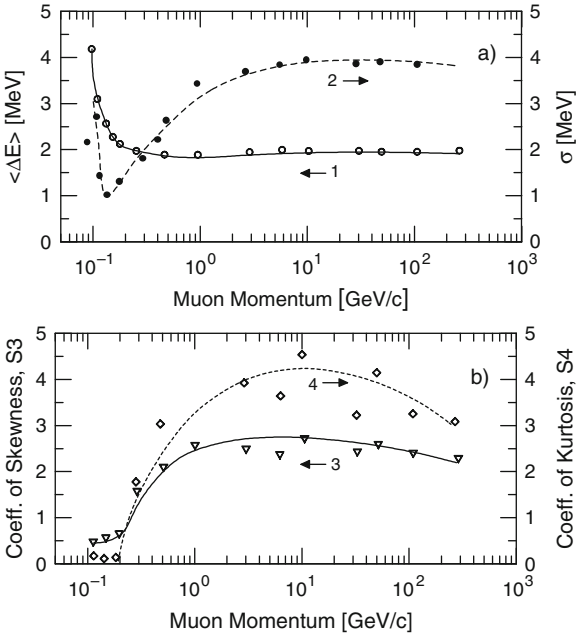

Fig. 2.19 Distribution parameters of energy loss, ΔE, of muons passing through 9.2 g cm^{-2} of scintillator versus incident muon momentum, according to calculations of Blake et al. (1979) (cf. Fig. 2.18). In figure (**a**), *curve* 1 (○) represents the mean energy, ΔE, in MeV, deposited in the scintillator, and *curve* 2 (●) is the standard deviation, σ. In figure (**b**), *curve* 3 (▽) is the coefficient of skewness, $S3$, and *curve* 4 (◇) is the coefficient of kurtosis, $S4$

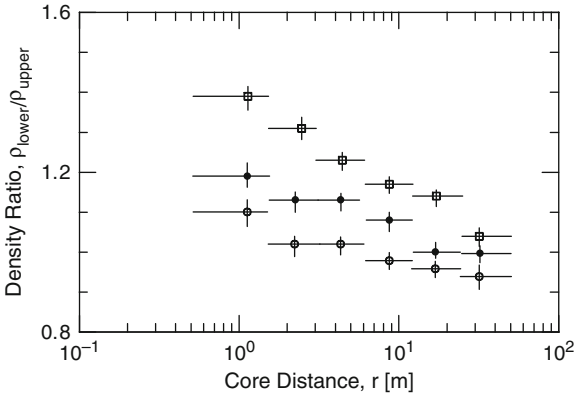

Fig. 2.20 Average ratio of the response of two horizontal scintillators of 5 cm thickness (density 1.05 g cm^{-3}) and area 0.25 m^2, located one above the other and separated by 10 cm, as a function of core distance for showers of size $\geq 7 \cdot 10^4$ and zenith angles $\leq 30°$. ○, no absorber; ●, 1 mm of iron and, □, 5 mm of iron in between scintillators (Asakimori et al., 1986)

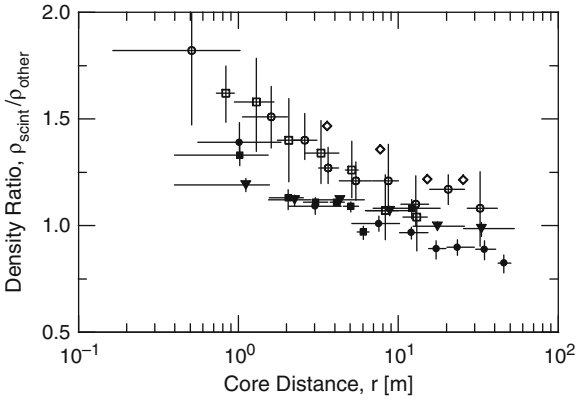

Fig. 2.21 Comparison of particle density ratios measured with scintillation, ρ_{scint}, and other kinds of detectors, ρ_{other}, as a function of distance from the shower axis: ◇ Bray et al. (1965), ● Bakich et al. (1970), ○ Shibata et al. (1965), □ Hara et al. (1970a), ■ Dake et al. (1971), ▼ Asakimori et al. (1986) and Asakimori (1988) (after Asakimori et al., 1986). For details see text

as they had been used decades before at the Haverah Park experiment in England (Wilson et al., 1963).

This kind of detector yields an output signal that is related to the sum of the Cherenkov light produced by the local particle mix in the shower that strikes the water tank. Thus, only those particles whose velocity exceeds the Cherenkov threshold velocity in water contribute to the detector output signal (see Table B.9). The bulk of the electromagnetic component is usually completely absorbed in the first few ten centimeters of the water column unless the shower core happens to hit it directly, which is in general a rare exception. The relative contribution of the different shower constituents, mainly the electromagnetic and muonic components, depends on the radial distance of the detector from the shower axis. At larger distances it is chiefly the muon component that produces the bulk of the signal.

In Fig. 2.22 we show the mean response of such a detector for vertically incident photons, electrons and muons as a function of energy from a simulation of Ave et al. (2003). Very low energy electrons are absorbed in the lid of the tank, whereas energetic muons penetrate the tank and deposit $\approx$ 240 MeV. The response of this detector, in particular the energy deposit recorded at distances around 600 m from

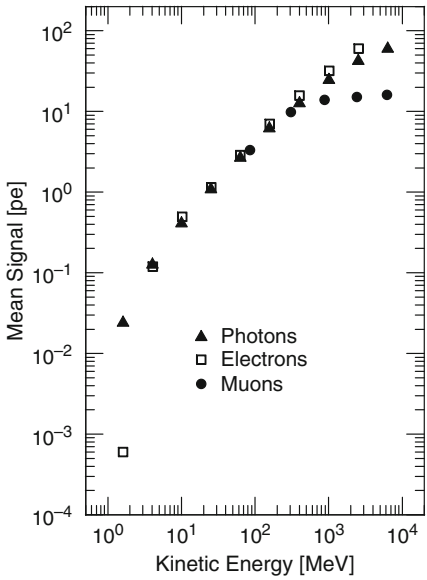

Fig. 2.22 Mean signal in units of photoelectrons [pe] produced in a 1.2 m deep Haverah Park type water Cherenkov detector (DWCD) by vertically incident photons, electrons and muons as a function of energy. Very low energy electrons are absorbed in the lid of the tank, whereas energetic muons penetrate the tank and deposit ≈ 240 MeV (Ave et al., 2003). The calibration of modern DWCD for the Auger experiment is discussed by D'Olivo et al. (1999)

the shower core is an approximate measure of the primary energy of large showers ($E_0 \geq 10^{17}$ eV). Simulations show that this observable is relatively independent of primary mass and hadronic interaction model. Further details related to lateral density and timing measurements of shower particle and the relation of the detector response in showers with respect to primary energy estimation are discussed in Chaps. 8 and 10.

2.11.4 Response of Plastic Scintillation Detectors

The response of plastic scintillation detectors as they had been used for the Akeno and AGASA experiments in Japan (thickness 5 cm) and at many other sites with respect to the different kinds of particles that are present in air showers had been investigated by the AGASA group (Nagano et al., 1984, 1992, 2000; Yoshida et al., 1994; Hayashida et al., 1994, 1999; Sakaki et al., 2001a, b, Takeda et al., 2003). Their study was based mainly on simulations but was also cross checked by experiment. The more recent work was mainly based on the program package GEANT 3.21.

The results are presented in Figs. 2.23, 2.24 and 2.25. The plots show for a wide range of particle kinetic energies and photon energies and for particles traversing the scintillator under different zenith angles, as specified by $\sec\theta$, the detector signal output expressed in equivalent vertically traversing single minimum ionizing particles.

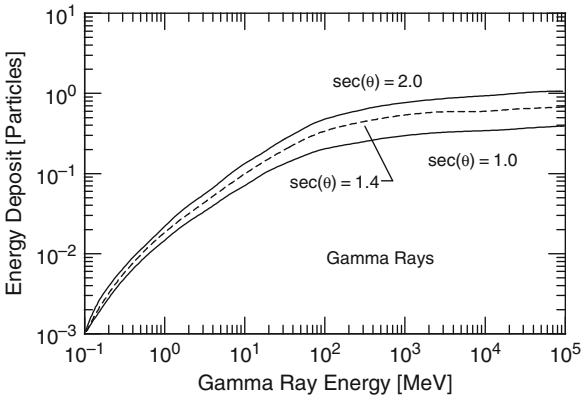

Fig. 2.23 Simulated distribution of energy deposit in a standard AGASA type scintillation detector by gamma rays incident at different zenith angles, as specified by $\sec\theta$. The energy deposit is converted to particle number, using the standard pulse height produced by a single vertically traversing minimum-ionizing particle (Sakaki et al., 2001a)

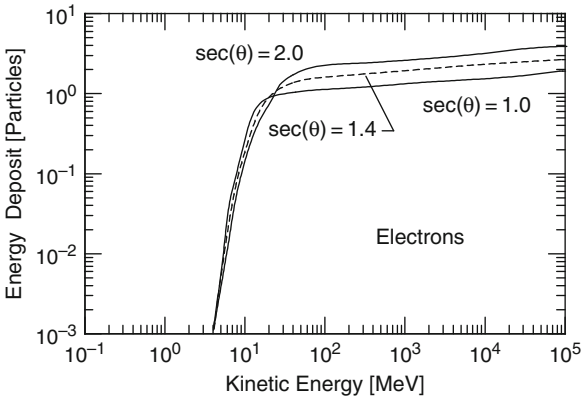

Fig. 2.24 Simulated distribution of energy deposit in a standard AGASA type scintillation detector by electrons incident at different zenith angles, as specified by $\sec\theta$. The energy deposit is converted to particle number, using the standard pulse height produced by a single vertically traversing minimum-ionizing particle (Sakaki et al., 2001a)

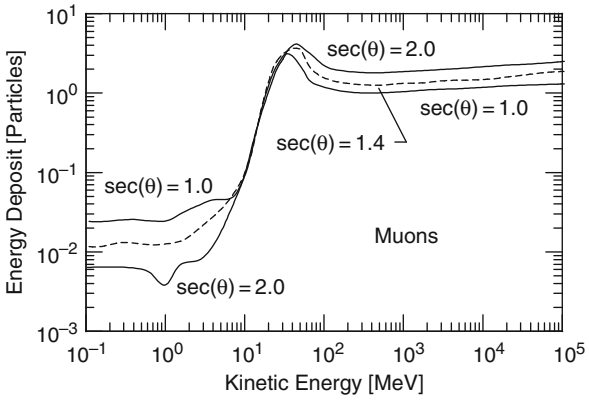

Fig. 2.25 Simulated distribution of energy deposit in a standard AGASA type scintillation detector of muons incident at different zenith angles as specified by $\sec\theta$. The energy deposit is converted to particle number, using the standard pulse height produced by a single minimum-ionizing vertically traversing particle (Sakaki et al., 2001a)

References

Abu-Zayyad, T., et al.: Astropart. Phys., 16, pp. 1–11 (2001).
Acharya, B.S., et al.: PICRC, 11, p. 385 (1981).
Aglietta, C., et al.: Nuovo Cim. C, 9, pp. 262–270 (1986).
Aglietta, M., et al.: Nuovo Cimento, 15C, p. 713–722 (1992).
Aglietta, M., et al.: Nucl. Instr. Meth. A, 336, p. 310 (1993).
Aglietta, M., et al.: Astropart. Phys., 9, p. 185 (1998).
Aglietta, M., et al.: Astropart. Phys., 10, p. 1 (1999).
Aglietta, M., et al.: Astropart. Phys., 20, p. 641 (2004a).
Aglietta, M., et al.: Astropart. Phys., 21, p. 223 (2004b).
Aguirre, C., et al.: PICRC, 4, p. 2576 (1973).
Aharonian, F., et al.: PICRC, 4, p. 452 (1991).
Ahlen, S., et al.: Phys. Rev., D 46, p. 4836 (1992).
Ahlen, S., et al.: Nucl. Instr. Meth., A 324, p. 337 (1993).
Albers, J.R., et al.: PICRC, 11, p. 489 (1983).
Alexeyev, E.N., et al.: PICRC, 10, p. 276 (1979).
Alexeyev, E.N., et al.: PICRC, 2, p. 474 (1993).
Allan, H.R., et al.: Proc. Phys. Soc., 76, p. 1 (1960).
Allan, H.R., et al.: Proc. Phys. Soc., 79, p. 1170 (1962).
Allan, H.R.: Progress in Elementary Particle and Cosmic Ray Physics, North-Holland, Amsterdam, X, pp. 169–302 (1971).
Allkofer, O.C.: Teilchen-Detektoren, Karl Thiemig Taschenbuch Verlag Munich (1971) (in German).
Ambrosio, M., et al.: Nucl. Instr. Meth., A 486, p. 663–707 (2002).
Amenomori, M., et al.: Nucl. Instr. Meth. A, 288, p. 619 (1990).
Amenomori, M., et al., Tibet ASγ Collaboration: Phys. Rev. D, 47, p. 2675 (1993).
Anassontzis, E., et al., NESTOR Collaboration: Proposal for the Construction of NESTOR, A Neutrino Astroparticle Physics Laboratory for the Mediterranean, University of Athens, Athens (1995).
Antipin, K., et al.: PICRC, pre-conference edition, paper 0639, Merida, Mexico (2007).
Antoni, T., et al.: Nucl. Instr. Meth. A, 513, p. 490 (2003a).
Antoni, T., et al.: Astropart. Phys., 19, p. 703 (2003b).
Armitage, R., et al.: J. Phys. G, 13, p. 707 (1987).
Asakimori, K., et al.: PICRC, 8, p. 252 (1979).
Asakimori, K., et al.: Nuovo Cim. A, 91, p. 62 (1986).
Asakimori, K.: J. Phys. G, 14, p. 1167 (1988).
Askar'yan, G.A.: Atomnaya Energia, 3, p. 153 (1957).
Askar'yan, G.A., and B.A. Dolgoshein: Prepr. FIAN N, 160 (1976).
Askar'yan, G.A.: Nucl. Instr. Meth., 164, p. 267 (1979).
Atkins, R., et al.: Nucl. Instr. Meth. A, 449, p. 478 (2000).
Auffenberg, J., et al.: PICRC, pre-conference edition, paper 0293, Merida, Mexico (2007).
Ave, M., et al.: Astropart. Phys., 19, p. 47 (2003).
Aynutdinov, V.M., et al.: PICRC, 8, p. 251 (2005).
Babson, J., et al.: Phys. Rev. D, 42, p. 3613 (1990).
Bacci, C., et al., ARGO-YBJ Collaboration: Nucl. Instr. Meth. A, 443, p. 342 (2000).
Bacci, C., et al., ARGO-YBJ Collaboration: Astropart. Phys., 17, p. 151 (2002).
Baggio, R., et al.: Nuovo Cim., 40, p. 289 (1977).
Bakich, A.M., et al.: J. Phys. A, 3, p. 662 (1970).
Baltrusaitis, R.M., et al.: Nucl. Instr. Meth. A, 240, p. 410 (1985).
Bari, G., et al.: Nucl. Instr. Meth. A, 277, pp. 11–16 (1989).
Barker, P.R., et al.: Phys. Rev. Lett., 18, p. 51 (1967).
Barwick, S., et al.: PICRC, 1, p. 436 (1993).

Bell, C.J., et al.: J. Phys. A, 7, p. 990 (1974).
Bergeson, H.E., et al.: PICRC, 8, p. 3059 (1975a).
Bergeson, H.E., et al.: PICRC, 8, p. 3064 (1975b).
Bird, J.D., et al.: PICRC, 2, p. 760 (1995).
Blackett, P.M.S., and A.C.B. Lovell: Proc. Roy. Soc. (London), 177 A, p. 183 (1941).
Blake, P.R., et al.: PICRC, 8, p. 2778 (1975).
Blake, P.R., et al.: J. Phys. G, 4, p. 617 (1978a).
Blake, P.R., et al.: J. Phys. G, 4, p. 597 (1978b).
Blake, P.R., and C.G. Saltmarsh: PICRC, 8, p. 76 (1979).
Blümer, J.: The Pierre Auger Collaboration. Frontiers of Cosmic Ray Science, Universal Academic Press, Inc., Tokyo (Japan), PICRC, 8, p. 361 (2003).
Böhm, E., and E. Steinmann: PICRC, 8, p. 294 (1979).
Boothby, K., et al.: PICRC, 3, p. 444 (1995).
Borione, A., et al.: Nucl. Instr. Meth. A, 346, p. 329 (1994).
Böser, S., et al.: PICRC, pre-conference edition, paper 1142, Merida, Mexico (2007a).
Böser, S., et al.: PICRC, pre-conference edition, paper 1282, Merida, Mexico (2007b).
Bosetti, P., et al.: DUMAND Proposal 1982, Deptartment of Physics and Astronomy, University of Hawaii, Honolulu, HI, USA (1982).
Bosetti, P., et al.: DUMAND II Proposal, 1989, Deptartment of Physics and Astronomy, University of Hawaii, Honolulu, HI, USA (1989).
Bowen, T.: Proceedings of the DUMAND 1976 Summer Workshop, 6–19 September, 1976, A. Roberts, ed., Hawaii DUMAND Center, University of Hawaii at Manoa, Honolulu, HI (USA), p. 523 (1976).
Bowen, T.: PICRC, 6, p. 277 (1977) (Abstract only).
Bowen, T.: Cosmic Rays and Particle Physics 1978, A.I.P. Conference Proceedings No. 49, Particles and Fields Subseries No. 16, T.K. Gaisser, ed., American Institute of Physics, p. 272 (1979a).
Bowen, T.: PICRC, 11, p. 184 (1979b).
Bowen, T., and J.G. Learned: PICRC, 10, p. 386 (1979).
Bowen, T.: Proceedings of the DUMAND 1979 Summer Workshops at Khabarovsk and Lake Baikal, August 22–31, 1979, J.G. Learned, ed., Hawaii DUMAND Center, University of Hawaii at Manoa, Honolulu, HI (USA), p. 121 (1980).
Bray, A.D., et al.: PICRC, 2, p. 685 (1965).
Budnev, N.M., et al.: PICRC, 8, p. 255 (2005).
Bunner, A.N.: Sky Telescope, 34, p. 204 (October 1967).
Camin, D.V.: Nucl. Instr. Meth., A518, p. 172 (2004).
Cao, Z., ARGO Collaboration: PICRC, 5, p. 299 (2005).
Cassiday, G.L.: Ann. Rev. Nucl. Part. Sci., 35, p. 321 (1985).
Cassidy, M., et al.: PICRC, 5, p. 189 (1997).
Cherry, M.L., et al.: PICRC, 8, p. 246 (1985).
Chiavassa, A., et al.: PICRC, 6, p. 313 (2005).
Chiba, N., et al.: ICRR Report 249-91-18 (July 1991).
Chiba, N., et al.: Nucl. Instr. Meth. A, 311, pp. 338–349 (1992).
Chilingarian, A., et al.: Astropart. Phys., 28, p. 58 (2007).
Chudakov, A.E., et al.: PICRC, 8, p. 217 (1979).
Clark, G., et al.: Nature, Lond., 180, p. 353 (1957).
Clark, G.W., et al.: Phys. Rev., 122, p. 637 (1961).
Coy, R.N., et al.: PICRC, 6, p. 43 (1981).
Coy, R.N., et al.: Astropart. Phys., 6, p. 263 (1997).
Cranshaw, T.E., et al.: Phil. Mag., 3, p. 377 (1958).
Dake, S., et al.: PICRC, 3, p. 948 (1971).
Dawson, B.R., Auger Collaboration: PICRC, pre-conference edition, paper 0976, Merida, Mexico (2007).

Dedenko, L.G., et al.: Proceedings of the First International Workshop on Radio Detection of High Energy Particles (RADHEP) 2000; D. Saltzberg and P. Gorham, eds., A.I.P. Conference Proceedings, 579, p. 277 (2001).
Diminstein, A.S., et al.: PICRC, 5, p. 3232 (1973).
Doll, P., et al.: Nulc. Instr. Meth. A, 488, p. 517 (2002).
D'Olivo, J.C., et al.: PICRC, 2, p. 36 (1999).
Elbert, J., et al.: Proceedings of the 1980 International DUMAND Symposium, Honolulu, Hawaii, 1, p. 203 (1981).
England, D.: Ph.D. Thesis, University of Leeds, Leeds (1986).
Ermatov, S.E., et al.: PICRC, 7, p. 121 (1981).
Erofeeva, I.N., et al.: PICRC, 4, p. 355 (1987).
Falcke, H., and P. Gorham: Astropart. Phys., 19, pp. 477–494 (2003).
Fisher, F.H., and V.P. Simmons: J. Acoust. Soc. Am., 62, p. 558 (1977).
Fukui, S., et al.: Prog. Theor. Phys. Jpn., 16, p. 1 (1960).
Ghia, P.L., Pierre Auger Collaboration: PICRC, pre-conference edition, paper 0300, Merida, Mexico (2007).
Glasstetter, R., et al.: Forschungszentrum Karlsruhe, Wissenschaftliche Berichte, FZKA 6890, p. 9 (2003).
Glasstetter, R., et al.: PICRC, 6, p. 293 (2005).
Goorevich, L., and L.S. Peak: J. Phys. G, 1, p. 762 (1975).
Gorham, P.W.: Astropart Phys., 15, p. 177 (2001).
Green, K., et al.: Nucl. Instr. Meth. A, 498, pp. 256–288 (2003).
Greisen, K.: Progress in Cosmic Ray Physics, North Holland, Vol. 3, p. 1 (1956).
Greisen, K.: Annual Review of Nuclear Science, Annual Reviews, Inc., Palo Alto, CA 10, p. 63 (1960).
Grieder, P.K.F.: Proc. 1980 European Cosmic Ray Symposium, Leningrad, Academy of Sciences USSR, p. 325 (1980).
Grieder, P.K.F.: Europhysics News, 23, 9, p. 167 (1992).
Grupen, C.: Teilchendetektoren, BI – Wissenschaftsverlag, Mannheim, Leipzig, Wien, Zürich, ISBN 3-411-16571-5 (1993) (in German).
Grupen, C., and B. Schwartz: Particle Detectors, Cambridge University Press, 1st ed., ISBN 13: 9783540253129 (2005), 2nd ed., ISBN 13: 9780521840064 (2008).
Hara, T., et al.: Acta Phys. Acad. Sci. Hung., 29, S3, p. 361 (1970a).
Hara, T., et al.: Acta Phys. Acad. Sci. Hung., 29, S3, p. 369 (1970b).
Hara, T., et al.: PICRC, 13, p. 148 (1979).
Hara, T., et al.: PICRC, 6, p. 52 (1981).
Haungs, A., et al.: PICRC, pre-conference edition, paper 0828, Merida, Mexico (2007).
Hayashida, N., et al.: Phys. Rev. Lett., 73, p. 3491 (1994).
Hayashida, N., et al.: PICRC, 1, p. 353 (1999).
Heintze, J., et al.: Nucl. Instr. Meth. A, 277, p. 29 (1989a).
Heintze, J., et al.: Proc. KFK Workshop, Burg Liebenzell, (October 1989b).
Hill, G., IceCube collaboration: PICRC, 10, p. 213 (2005).
Hillas, A.M.: Acta Phys. Acad. Sci. Hung., 29, S3, p. 355 (1970).
Hillas, A.M., et al.: Acta Phys. Acad. Sci. Hung., 29, S3, p. 533 (1970).
Hillas, A.M., et al.: PICRC, 3, p. 1007 (1971).
Hollows, J.D., et al.: J. Phys. A, 2, p. 591 (1969).
Hook, J.R., et al.: Acta Phys. Acad. Sci. Hung., 29, S3, p. 474 (1970).
Horneffer, A., et al.: PICRC, 2, p. 969 (2003).
Huege, T., and H. Falcke: Astron. Astrophys., 412, p. 19 (2003).
Huege, T., and H. Falcke: Astron. Astrophys., 430, p. 779 (2005).
Hunter, S.D., et al.: PICRC, 6, p. 196 (1979).
Hunter, S.D., et al.: Proceedings of the DUMAND 1979 Summer Workshops at Khabarovsk and Lake Baikal, August 22–31, 1979, J.G. Learned, ed., Hawaii DUMAND Center, University of Hawaii at Manoa, Honolulu, HI (USA), p. 128 (1980).

Jones, W.V.: PICRC, 6, p. 271 (1977a).
Jones, W.V.: PICRC, 11, p. 447 (1977b).
Kakimoto, F., et al.: PICRC, 6, p. 27 (1981).
Kakimoto, F., et al.: Nucl. Instr. Meth. A, 373, p. 282 (1996).
Kamata, K., and J. Nishimura: Progr. Theor. Phys. Jpn., 6, Suppl., p. 93 (1958).
Kaneko, T., et al.: PICRC, 11, p. 428 (1983).
Karle, A, IceCube Collaboration: PICRC, pre-conference edition, paper 1180, Merida, Mexico (2007).
Kasahara, K., Telescope Array: PICRC, pre-conference edition, paper 0955, Merida, Mexico (2007).
Kawaguchi, S., et al.: PICRC, 7, p. 2736 (1971).
Kerschenholz, I.M., et al.: PICRC, 4, p. 2507 (1973).
Khristiansen, G.B.: Cosmic Rays of Superhigh Energies, Verlag Karl Thiemig, München (1980).
Kleinknecht, K.: Detektoren für Teilchenstrahlung (in German), Teubner Studienbücher, Stuttgart (1992).
Kleinknecht, K.: Detectors for Particle Radiation, Cambridge University Press, Cambridge (1998).
Klepser, S., et al.: Ice Cube Collaboration: PICRC, pre-conference edition, paper 858, Merida, Mexico (2007).
Lafebre, S., et al.: PICRC, 8, p. 245 (2005).
Lawrence, M.A., et al.: Phys. Rev. Lett., 63, p. 1121 (1989).
Lawrence, M.A., et al.: J. Phys. G, 17, pp. 733–757 (1991).
Learned, J.G.: Phys. Rev. D, 19, p. 3293 (1979).
Lehtinen, N. G., et al.: Astropart. Phys., 17, p. 279 (2002).
Leo, W.R.: Techniques for Nuclear and Particle Physics Experiments. Springer-Verlag, Berlin, Heidelberg, New York, London, Paris, Tokyo, Hong Kong, Barcelona. Budapest (1987) and (1994).
Lillicrap, S.C., et al.: Proc. Phys. Soc., 82, p. 95 (1963).
Mantsch, P., Auger Collaboration: PICRC, 10, p. 115 (2005).
Martello, D., ARGO-YBJ Collaboration: PICRC, pre-conference edition, paper 1029, Merida, Mexico (2007).
Matano, T., et al.: Can. J. Phys., 46, p. S255 (1968).
McCullough, J.-F., Milagro Collaboration: PICRC, 2, p. 369 (1999).
Nagano, M., et al.: J. Phys. G, 10, p. 1295 (1984).
Nagano, M., et al.: J. Phys. G, 18, p. 423 (1992).
Nagano, M., et al.: Astropart. Phys., 13, p. 277 (2000).
Narasimham, V.S.: Proc. Indian Natn. Sci. Acad., 70, p. 11 (2004).
Niess, V., ANTARES Collaboration: PICRC, 8, p. 41 (2005).
Niess, V., and V. Bertin: Astropart. Phys., 26, p. 243 (2006).
Nishimura, J.: Handbuch der Physik, S. Flügge, ed., 46/2, p. 1, Springer Verlag, Berlin (1967).
Ogio, S., et al.: Astrophys. J., 612, p. 268 (2004).
Poirier, J. et al.: PICRC, pre-conference edition, paper 1001, Merida, Mexico (2007).
Rao, M.S.V., and B.V. Sreekantan: Extensive Air Showers, World Scientific, Singapore (1998).
Ravel, O., CODALEMA Collaboration: PICRC, pre-conference edition, paper 0460, Merida, Mexico (2007).
Saftoiu, A., et al.: PICRC, pre-conference edition, paper 0893, Merida, Mexico (2007).
Sakaki, N., et al.: PICRC, 1, p. 329 (2001a).
Sakaki, N., et al.: PICRC, 1, p. 333 (2001b).
Shibata, S., et al.: PICRC, 2, p. 672 (1965).
Sokolsky, P.: Introduction to Ultrahigh Energy Cosmic Ray Physics, Frontiers in Physics, Vol. 76, Addison-Weskey Publishing Co., New York (1989).
Spiering, C.: J. Phys. G, 29, p. 843 (2003).
Suga, K.: 5th Inter-American Seminar on Cosmic Rays, Bolivia, 2, XLIX-1 (1962).
Sulak, L., et al.: PICRC, 11, p. 420 (1977).
Sulak, L., et al.: Nucl. Instr. Meth., 161, p. 203 (1979).

Suomijärvi, T., Pierre Auger Collaboration: PICRC, pre-conference edition, paper 0299, Merida, Mexico (2007).
Swordy, S.P., and D.B. Kieda: Astropart. Phys., 13, p. 137 (2000).
Takeda, M., et al.: Astropart. Phys., 19, p. 447 (2003).
Tam, A.C.: Rev. Mod. Phys., 58, p. 381 (1986).
Tennent, R.M.: Proc. Phys. Soc., 92, p. 622 (1967).
Tennent, R.M.: Can. J. Phys., 46, p. S1 (1968).
Towers, L.: Ph.D. Thesis, University of Leeds (1971).
Van den Berg, A.M., Auger Collaboration: PICRC, pre-conference edition, paper 0176, Merida, Mexico (2007).
Vernov, S.N., et al.: PICRC, 8, p. 129 (1979).
Volovik, V.D., and G.B. Khristiansen: PICRC, 8, p. 3096 (1975).
Volovik, V.D., and G.F. Popova: Sov. Phy., JETP, 1, p. 13 (1975).
Wahl, D., et al.: PICRC, pre-conference edition, paper 0478, Merida, Mexico (2007).
Weber, J.H., KASCADE Collaboration: PICRC, 6, p. 153 (1997).
Wilson, J.G., et al.: PICRC, 4, p. 27 (1963).
Yodh, G.B.: Space Sci. Rev., 75, pp. 199–212 (1996).
Yoshida, S., et al.: J. Phys., G 20, p. 651–664 (1994).

Chapter 3
Hadronic Interactions and Cascades

Overview After a brief introduction we discuss the hadronic cross sections for interactions that are of relevance for air shower and ultrahigh energy physics research, such as cross sections and the corresponding interaction mean free paths of nucleons, pions and nuclei on protons, air and other target nuclei that are encountered in cosmic ray experiments. Their energy dependence is summarized, accelerator and collider data are presented together with the results from cosmic ray and air shower experiments over the entire experimentally accessible energy range up to $\sim 10^{19}$ eV. These topics are followed by a discussion of the projectile and target fragmentation at very high energies and of the basic properties of hadronic interactions, including particle production, secondary particle multiplicity, the nature of the secondaries, kinematic aspects of secondaries, longitudinal and transverse momenta, the phenomenon of large transverse momenta, the leading particle effect, elasticity/inelasticity of hadronic interactions, and correlations among the different observables. Subsequently a large variety of hadronic interaction models are discussed. Some emphasis is given to the early phenomenological-mathematical models that are scarcely documented and difficult to find in the literature, but played a relevant role initially to guide new pioneering experiments. A brief summary of the fast growing number of new models is given in the form of a catalogue, giving some emphasis on the currently relevant so-called event generators. The final part of this chapter is devoted to hadron cascades, outlining the analytical treatment of the problem and the Monte Carlo method for three- and four-dimensional cascade simulations (in space and time). The latter topic is treated in detail in Chap. 20.

3.1 Introduction

As outlined in Chap. 1, an air shower consists of the superposition of two different kinds of cascades, namely a hadronic and an electromagnetic cascade. In addition, there are numerous muons and neutrinos intermixed with the bulk of particles resulting from the two cascades. Neutrinos are usually ignored in air shower experiments and escape detection unless we are dealing with so-called horizontal or upward propagating air showers.

P.K.F. Grieder, *Extensive Air Showers,* DOI 10.1007/978-3-540-76941-5_3,

The hadronic cascade is the parent process that is chiefly responsible for the energy transport within a shower. It is the result of numerous successive collisions of the primary, of primary fragments and of energetic secondary and higher order generation particles that emerge from the collisions with nuclei of nitrogen, oxygen and occasionally with tracer gases along their trajectories through the atmosphere. In each of these high energy hadronic collisions an energy dependent number of new particles is produced until the energy of the projectiles falls below the one-pion threshold.

Below this energy hadrons continue to interact on a nuclear physics level. A large number of scattering processes and reactions take place that affect the low energy neutron flux. These processes are irrelevant for the shower development. They do not affect air shower measurements since the detector thresholds in air shower experiments are usually set to a higher level. Moreover, low energy particles are slow and usually miss the stringent coincidence requirements common for air shower work. For neutron monitors, however, the nuclear physics energy range is relevant but they are rarely used in conjunction with air shower experiments.

The electromagnetic cascades as well as the muons and neutrinos are daughter products of the hadron cascade. They are produced in decay processes of particles that emerge from the hadronic interactions. The electromagnetic cascades are generated mostly by high energy gamma rays resulting from the decay of energetic neutral pions ($\pi^0 \rightarrow 2\gamma$) unless the primary is a high energy gamma ray or an electron. In this more exceptional case we are dealing with a pure photon–electron shower with a small admixture of a few hadrons from photonuclear processes and some muons.

Each of the gamma rays from the decaying neutral pions is building up its own photon–electron cascade through repetitive pair creation and bremsstrahlung processes that are interlaced with the hadron cascade. Pair creation ceases below its threshold energy of 1.02 MeV. Below this energy Compton scattering and the photoelectric effect continue to contribute low energy electrons to the showers.

In view of this picture it is evident that apart from the hadron cascade, an air shower consists of the superposition of a very large number of electromagnetic subcascades of very different energies and sizes, that result from different generations of hadronic interactions in the course of the shower development.

The size of each sub-cascade depends on the energy of the initiating gamma ray and thus on the energy of the neutral parent pion. Some of the electromagnetic subcascades are initiated by electrons (positrons or negatrons) instead of photons. They are the decay products of muons ($\mu^{\pm} \rightarrow e^{\pm} + \overset{(-)}{\nu}_e + \overset{(-)}{\nu}_\mu$) or other unstable particles. There are few very energetic and dominating electromagnetic cascades that originate from the first few interactions and an increasing number of less and less energetic events, that contribute to the shower as it progresses through the atmosphere to greater depths. Eventually the process of growth is stopped when the photon or electron energy gets too low and the shower begins to decline.

Muons within a shower manifest a cascade-like behavior, however, without generating an actual cascade themselves. They are chiefly the decay products of charged pions, but kaons and charmed particles, too, contribute to their number. Due to the relatively long mean life of muons ($\tau_0 = 2.2\,\mu$s at rest) and the comparatively small

energy loss while propagating in a medium,[1] the decay rate is low and a large fraction of the muons produced in a shower penetrate the atmosphere down to sea level and are absorbed in the ground.

The muon flux in a shower is continuously being supplied with new particles from the hadron cascade, as long as the latter is capable of propagating and producing secondary particles. It still grows with diminishing intensity after the hadron cascade has passed its maximum development. Eventually, at large atmospheric depths the muon number declines, too, as more muons decay than are being created, unless the shower is extremely energetic and reaches its maximum development close to ground level.

Over a certain depth range in the atmosphere, which depends on the energy of the shower initiating primary, the muon number grows and grows until finally it reaches a sort of equilibrium, i.e., the number of muons remains constant but the population changes with respect to the generation of interaction in the atmosphere from which the muons originate. In other words, muons of an earlier generation are removed from the cascade in the deeper regions of the atmosphere by decay and replenished by muons resulting from the decay of charged pions of higher order generations of hadronic interactions at greater depth in the atmosphere.

The muon decay rate at this stage of shower development stands so to say in a one to one correspondence with the decay rate of charged pions. This trend is observed in shower simulations and applies to low energy muons. With increasing energy the decay probability for muons decreases rapidly but the probability for muon bremsstrahlung and photonuclear reactions increases, and likewise for ionization losses, due to the relativistic rise of the latter with energy.

Coulomb scattering of muons in conjunction with the initial nuclear scattering of the parent hadrons at production cause the less energetic muons to be deflected significantly from the shower axis. Due to the properties mentioned above, muons are able to travel farther away from the shower axis than the hadronic or electromagnetic components. At the fringes of a shower one observes therefore mostly low energy muons.

It is evident from the previous discussion that in order to fully understand the air shower mechanism the fundamental processes that govern high energy hadron–hadron interactions, i.e., chiefly nucleon–nucleon ($N-N$) and pion–nucleon ($\pi-N$) interactions, and more specific for air showers studies nucleon–nucleus ($N-A$), nucleus–nucleus ($A-A$) and pion nucleus ($\pi^{\pm}-A$) interactions, must be known. If so we can construct a mathematical model, simulate complete air showers and compute all observables. With this knowledge it should be possible to estimate or even determine the nature of the primary, its mass or the mass group it belongs to with reasonable accuracy.

Evidently, this problem is of extreme complexity. Up to date computer simulations have taught us that many parameters and dependencies are required that we do not know adequately or at all. It is therefore one of the goals of air shower

[1] Approximately 2.2 GeV are dissipated per 1,000 g cm^{-2} of air traversed by a relativistic muon.

research to explore the unknown or poorly known quantities and to complement our understanding of high energy interactions well beyond the current accelerator and collider domains.

For a long time, until about 1966, the experience gained from the study of high energy interactions of cosmic ray hadrons, mostly in nuclear emulsion,[2] over many orders of magnitude in energy suggested that there are four relevant *invariants* that govern much of the interaction kinematics, i.e., four observables that appeared to be independent of the energy of the incident hadron when colliding with a target nucleon or nucleus. These include the following:

- The interaction mean free paths of nucleon–nucleon ($\lambda_{\rm int}^{N-N}$), nucleon–nucleus ($\lambda_{\rm int}^{N-A}$) and with somewhat less certainty pion–nucleon ($\lambda_{\rm int}^{\pi-N}$) and pion–nucleus ($\lambda_{\rm int}^{\pi-A}$) encounters, where ($\lambda_{\rm int}^{N-N} \neq \lambda_{\rm int}^{N-A}$), ($\lambda_{\rm int}^{\pi-N} \neq \lambda_{\rm int}^{\pi-A}$) and ($\lambda_{\rm int}^{N-N} \simeq (2/3)\lambda_{\rm int}^{\pi-N}$), ($\lambda_{\rm int}^{N-12C} = 73 \pm 7\,{\rm g\,cm^{-2}}$, measured over the range $10 \leq E \leq 10^3$ GeV).
- The average transverse momenta of secondary pions ($\langle p_t^{\pi} \rangle$) and nucleons ($\langle p_t^{N} \rangle$) emerging from the interactions and their distributions ($\langle p_t^{\pi} \rangle \simeq 0.3\,{\rm GeV/c}$; $\langle p_t^{N} \rangle \simeq 0.4\,{\rm GeV/c}$, measured over the range $10 \leq E \leq 10^6$ GeV). The latter follows the shape of a Boltzmann distribution.
- The average *inelasticity* of nucleon–nucleon ($\langle K_{N-N} \rangle$), nucleon-nucleus ($\langle K_{N-A} \rangle$), pion–nucleon ($\langle K_{\pi-N} \rangle$) and pion–nucleus ($\langle K_{\pi-A} \rangle$) interactions, where $\langle K_{N-N} \rangle \simeq 0.5$, $\langle K_{N-A} \rangle > 0.5$, $\langle K_{\pi-N} \rangle \simeq \langle K_{\pi-A} \rangle \leq 1.0$ (measured over the range $10 \leq E \leq 10^6$ GeV).
- The ratio of γ-rays to charged particles, and the ratio of long-lived charged to neutral strongly interacting particles emerging from high energy interactions.

However, since the early 60s there were first indications from several cosmic ray experiments that there exist very rare events in which extremely high transverse momenta occurred ($> 10\,{\rm GeV/c}$), that the average transverse momenta seemed to increase very slowly with incident energy when observed over many decades, and that the interaction mean free paths of hadronic collisions gets shorter with increasing energy, i.e., that the cross sections increase.

These discoveries were firmly established in subsequent cosmic ray experiments by the early seventies and confirmed afterwards in the first experiments with the *Intersecting Storage Ring* (ISR) at CERN in Geneva (Switzerland).

The debate whether the inelasticity manifests a slight energy dependence or not, whether it increases or decreases with energy, is still going on. Up to date charge symmetry is the only survivor of the former apparent invariants. The energy dependence of the cross sections, the transverse momenta and the inelasticity are discussed in detail in the following subsections, together with the basic concepts that govern high energy hadronic interactions and constitute the elements of the hadron cascade which is the backbone of an air shower.

---

[2] Nuclear emulsion is applicable up to ∼100 TeV. In some cases it had been used at mountain altitude as detector under LiH and carbon targets.

3.2 Hadronic Cross Sections

The hadron cross sections, in particular the inelastic cross sections, play an important role for the development of air showers. The cross section of a given projectile particle to undergo an inelastic collision with a nucleus in a target medium determines on average the location where the collision will take place. Thus, in a hadronic cascade in the atmosphere the cross sections of the involved particles are a major but not the only factor that determines the rate of growth of the cascade. Basically all hadrons must be considered since all are produced in air showers. By far the most relevant are the cross sections for nucleon, pion and kaon initiated interactions with nuclei of air constituents (^{14}N, ^{16}O), as these are the most frequent.

Since the primary cosmic radiation contains the full mass range of known stable isotopes and probably a few unstable ones, too, we also require the cross sections for collisions between any nuclear projectile and all likely atmospheric target nuclei, including noble gases, above all argon, as argon accounts for almost one percent of the atmospheric constituents, to describe and interpret the shower phenomenon.

The energy dependence of the cross sections plays an important role since we are dealing in air shower physics with an enormous energy range, up to 10^{12} GeV in the laboratory frame of reference. This is far beyond the capabilities of present-day accelerators and colliders, and even well above the range of the Large Hadron Collider (LHC) at CERN in Geneva (Switzerland). The latter has a maximum collision energy in the center of mass of 7+7 TeV, corresponding to a fixed target laboratory equivalent energy for protons of $\sim 10^8$ GeV (100 PeV). If operated as a heavy ion collider it will provide Pb-Pb interactions at center of mass energies of ∼1,000 TeV.

It is therefore one of the many tasks of air shower research to extract from the accessible observables in air showers the unknown parameters and properties of particle physics in the energy domain that is inaccessible to accelerator and collider experiments.

Cross sections are usually expressed in units of [cm^2] or *barn* [b] (1 b = 10^{-24} cm^2). As an example, the proton–proton cross section at 30 GeV on a fixed target is $\sim$ 40 mb (millibarn) or $4 \cdot 10^{-26}$ cm^2 (see Fig. 3.1).

In this context we should point out that the total cross section is made up of contributions from the following processes: (1) elastic scattering, (2) diffractive inelastic scattering of the target nucleon or nucleus, (3) diffractive inelastic scattering of the projectile nucleon or nucleus, (4) double diffractive scattering, and (5) the remaining inelastic scattering.

In cosmic ray experiments inelastic cross section measurements generally do not include the inelastic diffraction of the target, as the isobar which is produced in the collision decays into low-energy, isotropically-emitted pions and a nucleon which are not observed and do not contribute to the cascade development. Thus, the inelastic cross section is the sum of items (3), (4) and (5), listed above. On the other hand, accelerator experiments measure (2) and include it in the inelastic cross section. The difference in the definition and interpretation of the term *inelastic* in the two experimental approaches affects the observable *inelasticity*, discussed in detail in

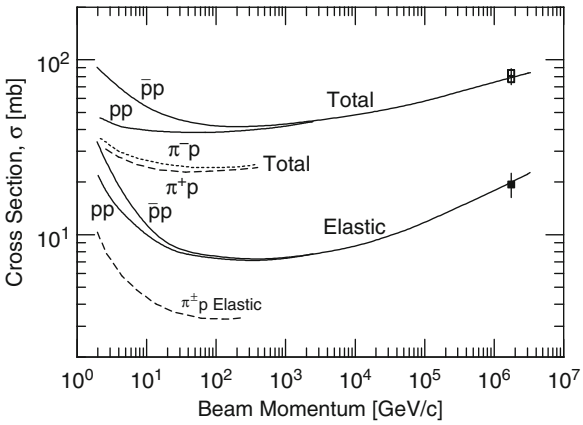

Fig. 3.1 Total and elastic cross sections for proton–proton (pp), antiproton–proton ($\overline{p}p$), and pion–proton ($\pi^{\pm}p$) collisions as a function of beam momentum in the laboratory frame (Hernàndez et al., 1990; see also Caso et al., 1998)

Sect. 3.8, significantly. The cosmic ray definition of the inelasticity of pp-reactions yields $K \sim 0.7$ at a few hundred GeV, and not $K \simeq 0.5$ (Jones, 1982, 1983).[3]

3.2.1 $(N-N)$ and $(\pi-N)$ Cross Sections and Energy Dependence

Prior to 1971 the nucleon–nucleon and more specific the proton–proton (and proton–neutron) cross sections and their energy dependence had been carefully measured in many accelerator experiments up to about 60 GeV and it was generally believed that the cross section was about to approach its asymptotic value at this energy. Likewise, the pion and kaon–nucleon cross sections were determined in similar experiments but to somewhat lower energies.

Since the late fifties of the last century indications were accumulating from cosmic ray experiments that the nucleon–nucleus and pion–nucleus cross sections appeared to be increasing with energy above several hundred GeV incident energy. These observations met initially with much scepticism because of marginal statistics. Since this work was based primarily on nucleon-nucleus interactions we will discuss it later under that heading, together with the proton–proton cross sections derived from high energy proton-air cross sections.

Experiments at the CERN ISR, a proton–proton collider with center of mass energies $\leq$62 GeV (laboratory equivalent energies up to $\approx$ 2 TeV), revealed a significant rise of the pp-cross section beyond about 100 GeV with crushing statistics, thus confirming the cosmic ray claims (Amaldi et al., 1973; Amendolia et al., 1973). This work was continued with the $\overline{p}p$-colliders at CERN ($\sqrt{s}$ = 200–900 GeV, s being the center of mass energy squared) and FNAL ($\sqrt{s}$ = 1,800 GeV) to fixed target laboratory equivalent energies of $\simeq 1.5 \cdot 10^6$ GeV and it was found that the cross

[3] The author is grateful to Prof. Larry Jones for having called his attention to this significant difference.

section continues to rise (Hernàndez et al., 1990). Unfortunately, the pion–nucleon and kaon–nucleon cross sections cannot be explored with colliders, which severely limits the energy range where high statistics data are available.

The energy dependence of the total and elastic cross sections of proton–proton (pp), antiproton–proton ($\overline{p}p$) and of charged pion–proton ($\pi^+ p; \pi^- p$) interactions compiled from accelerator and collider experiments is shown in Fig. 3.1. Above about 1 TeV the pp and $\overline{p}p$ cross sections are essentially identical, and the $\pi^{\pm} p$ cross sections are about 2/3 of the pp cross section,

$$\sigma_{\text{inel}}^{\pi p} \simeq \frac{2}{3} \sigma_{\text{inel}}^{\text{pp}}. \tag{3.1}$$

3.2.2 $(N - Air)$ and $(\pi - Air)$ Cross Sections and Energy Dependence, Glauber Concept

Cross section measurements for hadronic interactions were carried out since about the middle of the last century, using emulsion stacks or ionization calorimeters in the cosmic ray beam. In most events the experimenters were dealing with hadron–nucleus interactions and frequently nucleus–nucleus interactions in balloon-borne experiments. In emulsion stack experiments the target nucleus is a priori unknown and can only be estimated. Frequently specific targets were used in conjunction with emulsion and in calorimeter experiments, such as carbon, iron, etc., to have controlled conditions. The cross sections thus determined were therefore mostly hadron-nucleus or nucleus–nucleus cross sections and the nucleon–nucleon cross section had to be computed on the basis of some model.

The first claim that the inelastic cross section of nucleons in collision with nuclear targets appeared to rise between 20 and 500 GeV with energy was made by Grigorov et al. (1957, 1965, 1968) on the basis of their cosmic ray experiment with a carbon target. Later measurements that covered an energy range from about 100 GeV–10 TeV were made with a larger (10 m^2) 12-layer ionization calorimeter located at an altitude of 3,200 m a.s.l. in conjunction with measurements of the primary proton spectrum that were carried out on board the Proton 1 satellite.

The measurements were made with and without a carbon target above the calorimeter and the intensity of accompanied and unaccompanied hadrons was determined. The combined evaluation of these experiments was interpreted as a significant rise of the inelastic cross section with energy above about 300 GeV. This work was followed by the investigations of Akimov et al. (1970), carrying out experiments on board of the satellites Proton 1, 2 and 3, who came to the same conclusion but their energy range extended only up to 1 TeV.

For some time this work met with much skepticism until finally it was found that an energy dependent increasing number of albedos from the calorimeter which had been used was the cause for the apparently dramatic rise of the cross section at relatively low energies.

It was finally the work of Yodh et al. (1972), that was based on the results of a number of different cosmic ray experiments, that showed that indeed the inelastic proton–proton cross section, extracted from proton-air measurements and evaluated over an energy range from 1 to 30 TeV did increase.

Shortly afterwards, experiments performed at the CERN ISR, mentioned above, confirmed with crushing statistics the rise of the pp-cross section beyond a shadow of doubt. Thus, one of the four long standing apparent invariants of high energy physics mentioned earlier, the constancy of the hadronic cross section (or the interaction mean free path), came to a fall.

The *lower bounds* of the energy dependence of the proton–proton total cross section found by Yodh et al. (1972) is given by the relation

$$\sigma_{\text{total}}^{\text{pp}} \simeq 38.8 + 0.4 \ln^2(s/s_0) \text{ [mb]}, \tag{3.2}$$

where the scale factor s_0 is the value of the square of the total center of mass energy, s, corresponding to an incident energy of 70 GeV. This brings the pp cross section at an incident energy of 10^5 GeV to $\sigma_{\text{total}}^{\text{pp}} \sim 60$ mb (see also Yodh et al., 1973).

In more recent efforts, Tonwar (1979) and Yodh et al. (1983) have investigated the proton–proton and proton-air cross sections at energies from 1 to 100 TeV using ISR as well as cosmic ray data. The same basic approach was used for the latter analysis as in earlier work, i.e., the attenuation of primary cosmic ray protons in the atmosphere. For the proton-air cross section Yodh et al. (1983) obtained the following energy dependence,

$$\sigma_{\text{inel}}^{\text{p-air}}(E) = (267 \pm 8) + (10.1 \pm 2) \ln\left(\frac{E}{200}\right) \text{ [mb]}. \tag{3.3}$$

Using Glauber theory the proton–proton cross section can be extracted[4] (Glauber, 1959).

Hara et al. (1983) made an investigation to extract the proton-air cross section from air shower data obtained with the Akeno array in Japan for the energy range $10^{16} \leq E \leq 10^{18}$ eV. Their result is given as

$$\sigma_{\text{inel}}^{\text{p-air}}(E) = 290 \cdot E_L^{(0.06 \pm 0.01)} \text{ [mb] with } E \text{ in [TeV]} . \tag{3.4}$$

The result is based on the assumption that Feynman scaling (Feynman, 1969) is valid in the fragmentation region (see Sect. 3.10 for details).

Cross section studies on more theoretical grounds, some based on QCD, had been carried out by many authors (Kopeliovich et al., 1989 and references listed therein; see also Gaisser, 1992, for a compact summary).

[4] Glauber theory of hadron–nucleus interactions had been used successfully for many years, yet it is the high energy limit of non-relativistic scattering theory and in fact not valid in the relativistic domain.

3.2.3 $(N - A)$, $(A - A)$, $(\pi - A)$ and $(K - A)$ Cross Sections and Energy Dependence

For air showers of relevance are the cross sections for interactions of hadrons (nucleons, pions, kaons, etc.) with nuclei of air constituents, such as nitrogen, oxygen and argon, as discussed above. However, to treat the first interaction of the primary in the atmosphere correctly, which is by far the most important one, we also need the inelastic cross sections for interactions of incident nuclei with atmospheric target nuclei up to the highest energies. A similar situation may arise for the second and with rapidly diminishing probability for higher generations of interactions, if the projectiles are light nuclear fragments of the primary in place of nucleons or pions, as would be the case if the primary gets fully disrupted in the first collision, which is unlikely. In addition, nucleus–nucleus cross sections are also needed for cosmic ray experiments where special targets are being used, such as C, Fe, Pb, and in nuclear emulsion which consists mainly of Ag, Br, C and O (for the exact chemical composition of Ilford G-5 emulsion see Table B.3).

For a long time accurate and exhaustive data for this class of interactions ($N - A$, $A - A$, $\pi - A$ and $K - A$ collisions) from accelerator experiments were only available up to comparatively low energies ($\leq$ 300 GeV). Systematic investigations of the absorption and interaction cross sections of various hadrons (pions, kaons, protons, neutrons and antiprotons) on complex nuclei (Li, Be, C, Al, Cu, Sn, Pb and U) were undertaken by Denisov et al. (1973) in the momentum range $6 - 60$ GeV/c and Busza et al. (1975) studied pion-nucleus interactions for pion momenta from 100 to 175 GeV/c. Carroll et al. (1974a, b) extended the accelerator measurements of the cross sections for $\pi^{\pm}$, $K^{\pm}$ and $\overline{p}$ on protons and deuterons to momenta of 200 GeV/c, and Bailly et al. (1987) the $(p - Al)$ and $(p - Au)$-cross sections to 360 GeV/c. Neutron cross section measurements on various nuclei were carried out by Murthy et al. (1975) in the momentum range from 30 to 300 GeV/c and by Roberts et al. (1979) over the energy range from 160 to 375 GeV.

More recently a wealth of valuable data on high energy nucleus–nucleus interactions have become available from heavy ion experiments at accelerators, such as the *Super Proton Synchrotron* (SPS) at CERN in Geneva (Switzerland), and colliders, such as the *Relativistic Heavy Ion Collider* (RHIC) at Brookhaven, NY (USA). These data in conjunction with $\overline{p}p$ data permit to crosscheck Glauber theory which is used to link proton–proton to nuclear cross sections (Glauber, 1959).

Nevertheless, valuable information still comes from the study of cosmic ray interactions in various target materials, in combination with calorimeters or nuclear emulsion, that illuminate the physical processes in the ultrahigh energy domain.

The method of extracting hadronic cross sections from *attenuation measurements* of so-called unaccompanied cosmic rays[5] in the atmosphere that are commonly used for cross section estimates harbor many difficulties and yield results with

[5] Caution must be taken when comparing data from different experiments with unaccompanied cosmic rays as the definition of the term "unaccompanied" (within a certain radius) varies from experiment to experiment.

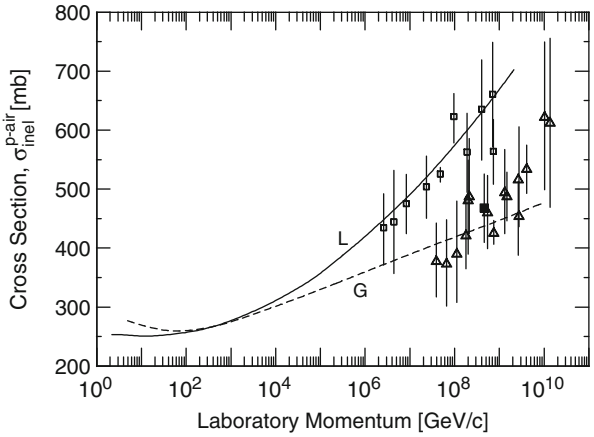

Fig. 3.2 Compilation of inelastic cross sections for proton-air interactions, $\sigma_{\rm inel}^{p-{\rm air}}$, extracted from data obtained with three air shower experiments. □ Volcano Ranch (Linsley, 1985); △ Akeno (Hara et al., 1983); ■ Fly's Eye (Baltrusaitis et al., 1984). The *dashed curve* (G) was calculated with the Glauber model, the *solid* (L) with Liland's parametrization (Liland, 1987) (after Bellandi et al., 1992b)

large errors. The situation worsens with increasing energy (see Sect. 6.3). This is illustrated in Fig. 3.2 where we show a compilation of $\sigma_{\rm inel}^{\rm p-air}$ data that were derived from three different air shower experiments covering the primary energy range from 10^6 to 10^{10} GeV. Part of the errors must be ascribed to the uncertainty of the mass of the primary which is not necessarily a proton.

Another compilation of proton-air cross sections derived from air shower experiments up to 10^{10} GeV that includes mostly recent data is shown in Fig. 3.3. Also shown in this figure are the early data at comparatively low energy obtained by Yodh et al. (1972, 1973, 1983) with unaccompanied hadrons. The curves show the energy dependence of the cross section obtained with four different event generators, using CORSIKA, as listed in the figure.

For lack of detailed knowledge of cross sections for nuclear projectiles on air constituents at high energy, one frequently uses *geometric relations* to estimate numerical values. A frequently used relation to estimate the proton–nucleus cross section from the proton-proton cross section is

$$\sigma_{\rm inel}^{pA} \;=\; \sigma_{\rm inel}^{\rm pp} A^{\alpha} \;\simeq\; \pi (R_0 A^{(1/3)})^2 \;=\; \pi R_A^2 \propto A^{(2/3)} \;, \tag{3.5}$$

where R_0 and R_A are the nucleon and nucleus radii, respectively, and A the mass number of the target nucleus.

Currently accepted values for the inelastic proton–nucleus and pion–nucleus cross sections in the laboratory momentum range $20 \le p \le 50$ GeV/c are (Denisov et al., 1973; Gaisser, 1992)

$$\sigma_{\rm inel}^{pA} \;\approx\; 45 A^{0.691} \;\; [\rm mb] \tag{3.6}$$

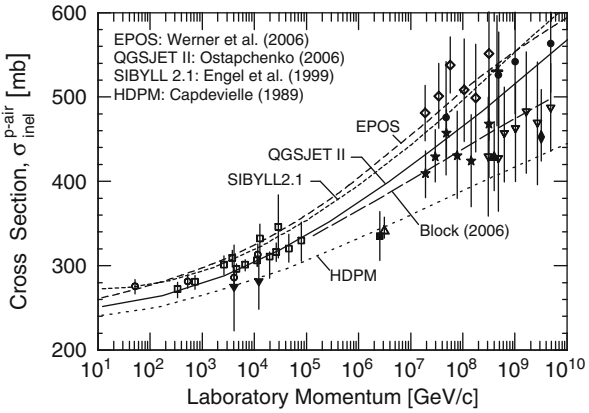

Fig. 3.3 Compilation of inelastic cross sections for proton-air interactions, $\sigma_{\rm inel}^{\rm p-air}$, derived from data of more recent air shower experiments: ○ Mielke et al. (1994) (KASCADE prototype calorimeter); △ Aglietta et al. (1997, 1999) (EAS-TOP); ◇ Honda et al. (1993) (AGASA); + Baltrusaitis et al. (1984) (Fly's Eye); ▽ Dyakonov et al. (1990) (Yakutsk); • Knurenko et al. (1999) (Yakutsk); ⋆ Honda et al. and ▲ Baltrusaitis et al., both re-scaled by Block (2006); ♦ Belov et al. (2006) (Fly's Eye); • De Mitri et al. (2008) and ■ Aglietta et al. (2009), both (EAS-TOP). □ shows the old data of Yodh et al. (1972, 1973) for unaccompanied hadrons. *Curves* show model predictions as listed (see also Hörandel, 2003)

and

$$\sigma_{\rm inel}^{\pi-A} \approx 28A^{0.75} \ \ [\rm mb]. \tag{3.7}$$

Westfall et al. (1979) in their work have parametrized the nucleus–nucleus cross sections and specify the following expression to compute $(A_1 - A_2)$-cross sections, where A_1 and A_2 stand for the mass numbers of the two colliding nuclei (see also Gaisser, 1992),

$$\sigma_{\rm inel}^{A_1-A_2} = \pi R_0^2 (A_1^{1/3} + A_2^{1/3} - \delta)^2 \ \ [\rm mb], \tag{3.8}$$

where $\delta = 1.12$ and $R_0 = 1.47$ fm.

For air shower studies the energy dependence of the hadronic cross sections is only one of the problems. Other closely related questions concern the behavior of the secondary particle multiplicity, kinematic and dynamic properties of interactions between different collision partners (nucleon–nucleon, pion–nucleon, nucleon–nucleus, pion–nucleus, etc.), and many more. Some of these affect the air shower development alike, which makes it often difficult to isolate the different effects. These topics are addressed in Sects. 3.5–3.12.

3.3 Interaction Mean Free Path

In cosmic ray physics one frequently uses the interaction mean free path (i.m.f.p.), $\lambda_{\rm int}$, in place of the interaction cross section, $\sigma_{\rm int}$ (usually the inelastic cross section, $\sigma_{\rm inel}$). This quantity is very practical to compute the location of interactions in the atmosphere or the number of interactions a particle undergoes on average when traversing a certain distance in the atmosphere or in a medium. The two observables are reciprocal and relate as follows.

$$\lambda_{\rm int} = \frac{A}{N_A\,\sigma_{\rm inel}}\ [\mathrm{g\ cm^{-2}}]. \tag{3.9}$$

A stands for the mass number of the target nucleus, N_A is Avogadro's number ($6.022 \cdot 10^{23}\ \mathrm{mol^{-1}}$) and $\sigma_{\rm inel}$ is in [$\mathrm{cm^2}$] (see also Chap. 21).

Saito (1971) in a brief review summarizes the results of interaction mean free path measurements in nuclear emulsion for a variety of projectile nuclei (λ_X) that were obtained in many experiments, including those from other authors, covering an energy range from a few GeV to several hundred GeV. His results are displayed for the usual charge groups in Table 3.1.

Figure 3.4 shows the interaction mean free path for energetic nuclei from hydrogen (protons) to iron (^{56}F) in air.

Table 3.1 Interaction mean free paths of nuclei in emulsion (Saito, 1971)

Nuclear group	Charge group	λ_X [$\mathrm{g\,cm^{-2}}$]
α-particles	$Z = 2$	$\lambda_\alpha = 72.9 \pm 2.5$
L-nuclei	$3 \le Z \le 5$	$\lambda_M = 53.7 \pm 1.3$
H-nuclei	$Z \ge 10$	$\lambda_H = 40.1 \pm 1.6$
LH-nuclei	$10 \le Z \le 15$	$\lambda_{LH} = 43.9 \pm 2.8$
MH-nuclei	$16 \le Z \le 19$	$\lambda_{MH} = 36.7 \pm 3.2$
VH-nuclei	$Z \ge 20$	$\lambda_{VH} = 34.6 \pm 1.2$

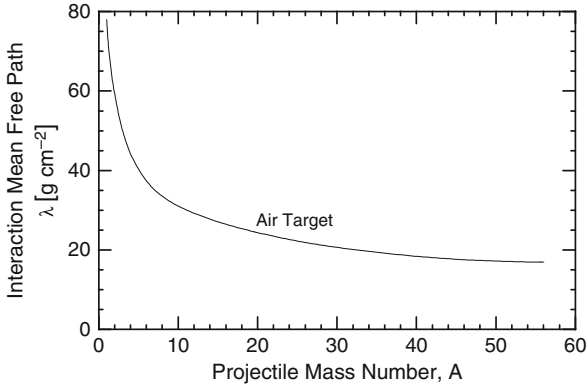

Fig. 3.4 Interaction mean free path of high energy (~ 10 GeV/N$\le E \le \sim 10$ TeV/N) projectile nuclei in air versus projectile mass number

3.4 Projectile and Target Fragmentation

The *fragmentation of relativistic nuclei* in collision with target nuclei is another important topic where our knowledge is rather incomplete. Of particular importance is the projectile fragmentation because it affects the development of a shower. The target fragments are in this case of lesser importance. Many experiments have been carried out so far, yet statistics are still poor, mainly because of the large number of combinations of collision partners and the multitude of the resulting fragments in each case.

For a long time very high energy fragmentation studies could only be carried out with balloon-borne emulsion experiments, using primary cosmic ray nuclei and their fragments as projectiles. A brief review including extensive tabulated results of early work in this field, covering a broad mass spectrum of projectile nuclei in emulsion and air-like targets, is given by Saito (1971). This chapter contains numerous data from other authors, too.

With the coming into operation of the Relativistic Heavy Ion Collider (RHIC) at the Brookhaven National Laboratory (BNL) in the US, a new powerful tool has become available for this kind of work that permits the exploration of nucleus–nucleus collisions to energies as high as 200 GeV/nucleon per beam in the center of mass (Klein, 2003). This correspond in the target frame of gold nuclei to an energy of 4.3 PeV (20 TeV/nucleon) and thus to the energy of the location of the knee in the primary cosmic ray spectrum. So far, the few accelerator facilities that are able to carry out fragmentation studies on nuclear projectiles are fixed target machines and measurements are limited to an energy of $\sim$300 GeV/nucleon.

Fragmentation or spallation is also an important topic in connection with the propagation of cosmic rays in the interstellar space, for their breakup in collisions with the interstellar medium, and to compute the lifetime of the cosmic radiation in the Galaxy.

Some of the earlier accelerator based experimental studies had been focused on the fragmentation of a variety of target nuclei under proton bombardment. The following conclusions were drawn from such measurements on the fragmentation of nuclei such as ^{12}C, ^{16}O, ^{27}Al and ^{56}Fe when bombarded with protons (Shapiro and Silberberg, 1970).

- The cross sections decrease with increasing mass difference, ΔA, between target and product nuclei.
- With decreasing collision energy the cross sections increase for small values of ΔA and decrease for large values of ΔA.
- Many studies claim that the reaction cross sections reach their asymptotic values in proton-nucleus collisions at energies $\geq$2 GeV.
- The neutron excess in nuclei, $(N - Z)$, plays an important role for the breakup in collision.

On the theoretical side, many semi-empirical formulas were constructed (Rudstam, 1966; Silberberg et al., 1982).

Fragmentation studies of nucleus–nucleus collisions with accelerator projectile beams are relatively rare and, as mentioned before, most of this work was carried out at low energies. The application of these data at air shower energies is therefore questionable. Lindstrom et al. (1973) have studied the fragmentation of ^{16}O on C, Cu, Ag and Pb at 2.1 GeV/nucleon, and Westfall et al. (1979) of iron nuclei (^{56}Fe) at 1.88 GeV/nucleon on H, Li, Be, C, S, Cu, Ag, Ta, Pb and U targets. Figure 3.5 shows as an example the charge spectrum obtained in the latter work for the C target.

Extensive studies at higher energies that were aimed to give some guidance for air shower simulations were carried out by Freier and Waddington and are presented in their comprehensive review (Freier and Waddington, 1975 and references listed therein). This work is heavily based on a vast collection of individual interactions in emulsion that was used as a data base for extensive fragmentation simulations. These authors point out that the fragmentation depends to some extent on the mass of the target nucleus.[6]

To account for this fact the emulsion data were separated according to the number of "slow" or heavy tracks, N_h (so-called evaporation tracks), which are a measure for the mass of the target nucleus. Events with $N_h \leq 7$ are likely to have hydrogen, carbon or oxygen nuclei as targets, whereas for $N_h > 7$ the target is frequently silver or bromine. The analysis of Freier and Waddington includes also data from Friedlander et al. (1963) and Badhwar et al. (1965) who used graphite and teflon as target materials. These are quite similar to air, except for the density which is irrelevant in this case. Selecting the appropriate data, the analysis was extended to the fragmentation of primary nuclei on air constituents.

In Table 3.2 the fragmentation parameters of 1,051 interactions of nuclei ranging in mass from the L to the VH class with air (N, O) are given for a variety of fragments. The *fragmentation parameter*, $F_{i,X}$, is defined as follows. Consider an

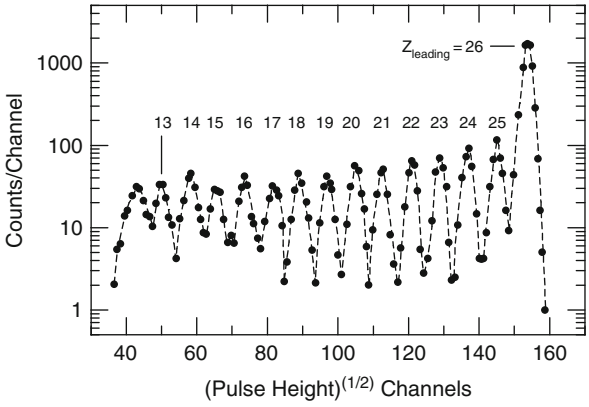

Fig. 3.5 Produced charge spectrum measured for 1.88 GeV/nucleon incident ^{56}Fe nuclei on a C target (Westfall et al., 1979)

[6] According to Lindstrom et al. (1973) the partial cross section for the production of a particular fragment produced in a nucleus–nucleus collision depends strongly on the nature of the target nucleus, but the relative proportions of different fragments are not strongly target dependent.

Table 3.2 Measured fragmentation parameters in air. (Freier and Waddington, 1975)

Fragments Interactions	Group and number of interactions				
	L-nuclei $3 \leq Z \leq 5$ 80	M-nuclei $6 \leq Z \leq 9$ 330	LH-nuclei ≥ 10 146	MH-nuclei ≥ 20 69	VH-nuclei ≥ 30 427
Nucleons	5.81 ± 0.70	6.62 ± 0.40	10.5 ± 0.9	12.8 ± 1.6	18.1 ± 0.9
Helium nuclei	0.61 ± 0.11	0.72 ± 0.06	0.77 ± 0.10	1.17 ± 0.19	1.71 ± 0.10
L-nuclei	0.11 ± 0.04	0.24 ± 0.03	0.21 ± 0.04	0.17 ± 0.05	0.24 ± 0.03
M-nuclei		0.17 ± 0.02	0.39 ± 0.06	0.20 ± 0.06	0.17 ± 0.02
LH-nuclei			0.16 ± 0.04	0.42 ± 0.09	0.22 ± 0.03
MH-nuclei				0.06 ± 0.03	0.20 ± 0.02
VH-nuclei					0.17 ± 0.02
R*	0.38	0.47	0.57	0.62	0.66

R* is the fraction of the mean charge that remains bound in $Z \geq 2$ fragments after an interaction.

interaction between an incident nucleus X and a target nucleus Y. If there are N_T interactions which produce N_i i-type fragments, then $F_{i,X}$ is given by the relation

$$F_{i,X} = \frac{N_i}{N_T} , \tag{3.10}$$

which can exceed unity since N_i can be larger than N_T.

The *fragmentation probability*, $P_{i,X}$, on the other hand, is defined in terms of cross sections. If σ_i is the partial cross section for the production of an i-type nucleus and σ_T is the total interaction cross section, then

$$P_{i,X} = \frac{\sigma_i}{\sigma_T}, \tag{3.11}$$

where $\sigma_i < \sigma_T$ since $P_{i,X} < 1$.

In Figs. 3.6 and 3.7 we display some of the results of this work. The data include simulation results from the work of Cleghorn et al. (1968). Shown are the fragmentation of iron ($Z = 26$) and silicon ($Z = 14$) nuclei in air and the build-up and decay of the fragmentation products as the cascade propagates.

Shown, too, in Fig. 3.7a is the rise and fall of nucleons per gram and square centimeter of air as a function of atmospheric depth that are produced by helium nuclei originating from collisions of iron nuclei in the air (labeled Nucleons from Helium $Z = 26$). Figure 3.7b shows a wider scope of the development of fragmentation products from iron interactions in air (labeled $Z = 26$) and helium only produced by silicon nuclei (labeled $Z = 14$).

More recently several studies of the fragmentation of heavy nuclei on a variety of target nuclei, so-called *charge-changing interactions*, were carried out using accelerator beams of 10 A GeV ^{197}Au at the Alternating Gradient Synchrotron (AGS) at Brookhaven (He and Price, 1994; Waddington et al., 1994; Geer et al., 1995; Hirzebruch et al., 1995) and 158 A GeV ^{207}Pb ion beams at the Super Proton Synchrotron (SPS) at CERN in Geneva (Giaccomelli et al., 1998; Dekhissi et al., 1999; Giaccomelli, 2008).

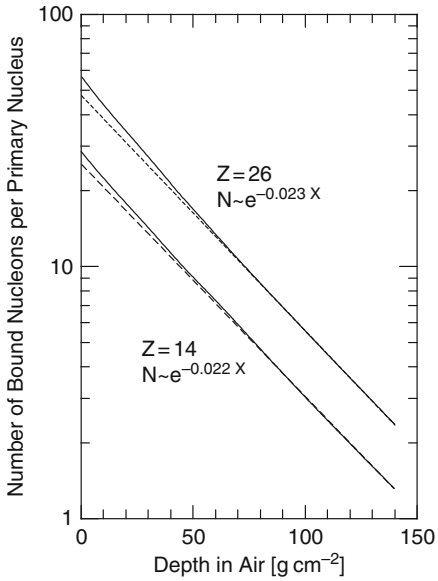

Fig. 3.6 Number of nucleons still bound in helium or heavy nuclei as a function of depth in air for incident nuclei of $Z = 14$ and 26 (*solid curves*) (Freier and Waddington, 1975). The *dashed lines* (drawn by the author) help to visualize the deviation of the distribution from a straight line

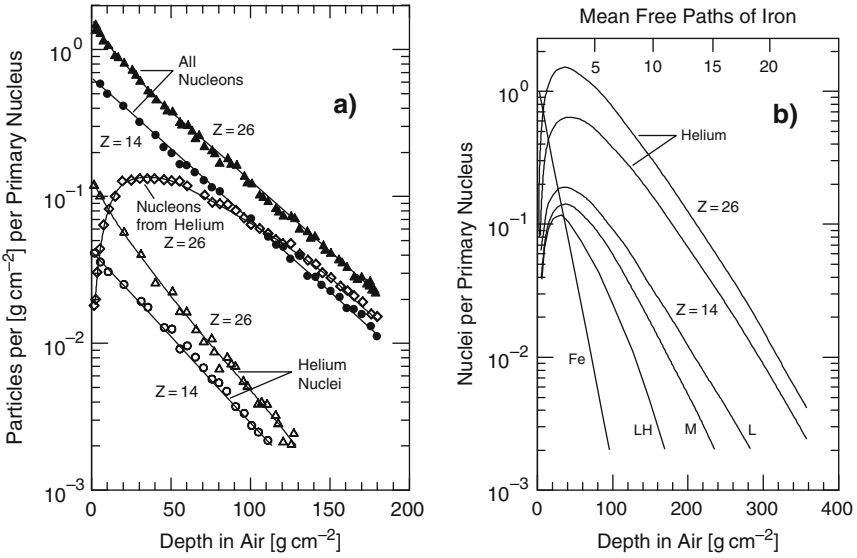

Fig. 3.7 (**a**) The rate of release of nucleons and helium nuclei in air from all heavy nuclei, primary and secondary, both for incident nuclei of $Z = 14$ and 26, and of nucleons from secondary helium nuclei produced by incident nuclei of charge $Z = 26$ (Freier and Waddington, 1975). (**b**) The growth and decay of the various charge components (He, L, M, LH) of simulated cascades initiated by iron ($Z = 26$) and helium resulting from silicon ($Z = 14$) nuclei in air (Freier and Waddington, 1975; Cleghorn et al., 1968). L, M and LH stand for light, medium and light-heavy nuclei. Also indicated is the depth expressed in units of interaction mean free paths of iron in air (for details see text)

Table 3.3 Pb-A collision fragmentation experimental details and results (Dekhissi et al., 1999)

Target	A_T	Z_T	ρ_T[g cm^{-3}]	t_T[cm]	$t_{\mathrm{CR39}(b)}[cm]$	$t_{CR39(a)}$[cm]	σ_{tot}[mb]
H	1	1	–	–	–	–	$1,944 \pm 275$
CH_2	4.67	2.67	0.952 ± 0.002	1.02 ± 0.01	0.73 ± 0.01	1.35 ± 0.01	$2,266 \pm 156$
CH_2+CR39	6.42	3.5	1.19 ± 0.01	3.09 ± 0.01	–	–	$2,515 \pm 81$
CR39	7.41	3.95	1.310 ± 0.003	3.07 ± 0.01	–	–	$2,642 \pm 81$
C+CR39	8.67	4.54	1.44 ± 0.01	3.18 ± 0.01	–	–	$2,726 \pm 84$
Al+CR39	11.49	5.99	1.75 ± 0.01	3.26 ± 0.01	–	–	$2,882 \pm 66$
C	12	6	1.733 ± 0.004	1.01 ± 0.01	0.69 ± 0.01	1.48 ± 0.01	$2,910 \pm 210$
Cu+CR39	22.03	11.25	3.65 ± 0.01	3.22 ± 0.01	–	–	$3,282 \pm 93$
Al	27	13	2.692 ± 0.002	1.04 ± 0.01	0.72 ± 0.02	1.50 ± 0.01	$3,804 \pm 164$
Pb+CR39	30.99	15.86	4.34 ± 0.01	3.23 ± 0.01	–	–	$3,842 \pm 116$
Cu	63.5	29	8.901 ± 0.002	0.99 ± 0.01	0.72 ± 0.01	1.51 ± 0.01	$5,089 \pm 274$
Pb	207	82	11.331 ± 0.003	0.98 ± 0.01	0.72 ± 0.01	1.53 ± 0.01	$12,847 \pm 638$

The symbols represent the following items: A_T Atomic mass, Z_T atomic number, ρ_T density, and t_T the thickness of the target between the CR39 solid state detector packages. σ_{tot} is the measured total cross sections. The quoted uncertainties are statistical only.

There is a systematic disagreement between some of the results of the 10 GeV/n experiments, particularly for the heavy target results, that are discussed by Hirzebruch et al. (1995). In the following we summarize here the results from the 158 GeV/n experiment with lead ion projectiles carried out with the SPS at CERN by Dekhissi et al. (1999) that set valuable anchor points for air shower research.

These authors have used stacks of CR39 ($C_{12}H_{18}O_7$) solid state nuclear track detectors in combination with different target materials, as listed in Table 3.3, where all relevant target details are specified. The last column of this table contains the total so-called *fragmentation charge-changing cross sections*, σ_{tot}. These results are also displayed in the plot of Fig. 3.8a together with the data of He and Price (1994), Geer et al. (1995) and Hirzebruch et al. (1995).

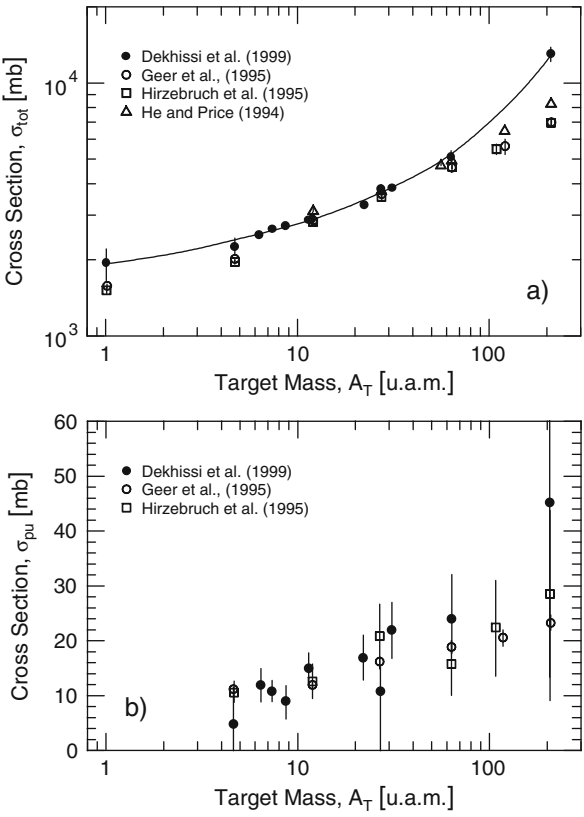

Fig. 3.8 (**a**) Total fragmentation charge-changing cross sections, σ_{tot}, for 158 A GeV ^{207}Pb ion projectiles on various targets of mass A_T measured by Dekhissi et al. (1999) (•). The *solid line* shows the fit of the data to Eq. (3.12). Also shown are the results of 10 A GeV ^{197}Au projectiles from the work of He and Price (1994), Geer et al. (1995) and Hirzebruch et al. (1995). (**b**) Pick-up cross sections, σ_{pu}, for the same projectiles, targets and energy as given in figure (**a**) above from the work of Dekhissi et al. (1999) (•), and the 10 A GeV data from the work of Geer et al. (1995) and Hirzebruch et al. (1995) for comparison

Table 3.4 Measured partial break-up charge-changing cross sections [mb] for Pb-ions at 158 A GeV (Dekhissi et al., 1999)

A_T	σ_{-1}	σ_{-2}	σ_{-3}	σ_{-4}	σ_{-5}	σ_{-6}	σ_{-7}
6.42	297 ± 27	107 ± 10	100 ± 10	67 ± 7	63 ± 7	26 ± 3	21 ± 3
7.41	232 ± 23	126 ± 12	93 ± 9	52 ± 6	50 ± 6	36 ± 5	18 ± 3
8.67	201 ± 19	103 ± 11	98 ± 10	77 ± 8	58 ± 7	32 ± 4	16 ± 3
11.49	258 ± 27	168 ± 16	117 ± 12	68 ± 8	29 ± 4	29 ± 4	38 ± 5
22.03	314 ± 31	161 ± 16	78 ± 9	97 ± 1	76 ± 9	30 ± 4	24 ± 4
30.99	671 ± 60	289 ± 23	139 ± 12	80 ± 8	123 ± 12	80 ± 8	31 ± 3

Dekhissi et al. (1999) have fitted their data to the parametrization proposed by He and Price (1994) and also used by Geer et al. (1995) and Hirzebruch et al. (1995), given here for reference.

$$\sigma_{\text{tot}} = a(A_P^{1/3} + A_T^{1/3} - b)^2 + \alpha Z_T^{\delta} \text{ [mb]} , \tag{3.12}$$

where A_P and A_T are the atomic masses of the projectile and target, respectively, and Z_T is the atomic number of the target. With $a = 54$ mb and $\delta = 1.88$ they obtain $b = (0.96 \pm 0.03)$ and $\alpha = (1.57 \pm 0.17)$ mb with $\chi^2/D.o.F. = 0.7$. For $b = 0.96$ and $\alpha = 1.57$ mb they get $a = (54.0 \pm 0.5)$ mb and $\delta = (1.88 \pm 0.03)$ with $\chi^2/D.o.F. = 0.7$. The solid line in Fig. 3.8a shows the fit of their experimental data to Eq. (3.12). The experimental data include both nuclear and electromagnetic effects. These two effects are discussed in some details in the other papers mentioned above in this context.

The measured partial break-up cross sections are listed in Table 3.4. Figure 3.8b shows the *charge pick-up cross sections*, σ_{pu}, for lead ions together with the data of Geer et al. (1995) and Hirzebruch et al. (1995).

3.5 Secondary Particle Multiplicity

3.5.1 Particle Production and Composition of Secondaries

Another very important observable which characterizes high energy collisions is the secondary particle *multiplicity*, n_s, i.e., the number of secondary particles that are produced. Frequently the charged particle multiplicity, $n_{\pm}$, is specified because in many experiments neutral particles escape undetected, unless special precautions are taken for their detection, as in the case of neutral pions (π^0) that have a very short mean life ($8.4 \pm 0.6 \cdot 10^{-17}$ s) and decay into a pair of photons that can easily be detected.

The energy dependence of the multiplicity is of paramount importance as it affects the rate of growth of the hadron cascade. The fraction of the total center of mass energy of a collision that goes into production of new particles (mass and momentum) is determined by the *inelasticity* of the collision. The remaining energy

is carried away by the *leading particle*, frequently a nucleon in pp collisions or an isobar (N^*).

An important sub-parameter is the *partition* of the inelastic portion of the total center of mass energy that is available for particle production among the different types and mass groups of secondaries (pions, kaons, charmed particles, nucleons and antinucleons, etc.). This is relevant for the subsequent energy transport within the nuclear cascade. Massive particles, such as nucleons and antinucleons, are more effective energy propagators than pions or kaons. The same is basically true for hyperons and antihyperons but their number is significantly smaller. This important topic is discussed in more detail in Sects. 13.4.2 and 13.4.3.

The rather dramatic rise of nucleon-antinucleon pair production with increasing collision energy, which had been predicted by Grieder (1970a, b) on the grounds of air shower simulations, is now well documented by the results of many different accelerator and collider experiments using combinations of protons and nuclei as projectiles and targets.[7] Many of these experiments did also include the investigation of the target and projectile mass dependence of the ratios of the different secondary particle types. This work included from low energy pp and pA-collisions to $\sim 12 \cdot (Z/A)$ GeV/c Au–Au, 400 GeV/c pp and $400 \cdot (Z/A)$ GeV/c Pb–Pb fixed target measurements to $\sqrt{s} = 62$ GeV pp, $\sqrt{s} \sim 600$ GeV $\overline{p}p$ and $\sqrt{s_{NN}} = 200$ GeV Au–Au collider experiments.

In Fig. 3.9 we show as an example from a compilation of Huang (2002) the energy dependence of the $p/\overline{p}$ ratio obtained from pp and central Au(Pb)–Au(Pb) collisions. This figure illustrates very clearly the rapid fall of the $p/\overline{p}$-ratio above the $N\overline{N}$ production threshold energy in the center of mass, implying a rapid rise of the $N\overline{N}$ production, to approach a value of about 2 at ~50 GeV per N, N collision partners and continues to fall then slowly toward the expected asymptotic value of unity at extreme energies. So far the data also indicate that the $p/\overline{p}$-ratio differs very little if at all between pp, pA and A, A collisions. These results are of great significance for extensive air shower studies and simulations.

In this context we must underline the significance of high energy neutrons as well as antineutrons. Like protons and antiprotons, neutrons and antineutrons are produced in pairs in high energy hadronic collisions (conservation laws of strong interactions) and both behave alike at high energy. They are not included in the charged particle multiplicity count but play a significant role in the cascade development, very much like protons and antiprotons, except that they are not subject to ionization losses. They must of course be included in all interaction and air shower models and simulations. An additional contribution of neutrons comes from high energy nucleon–nucleus and nucleus–nucleus collisions as well as from charge exchange reactions.

[7] A similar rise of the production cross section of strange particles, including hyperons was also observed at CERN $\overline{p}p$, Tevatron and RHIC experiments.

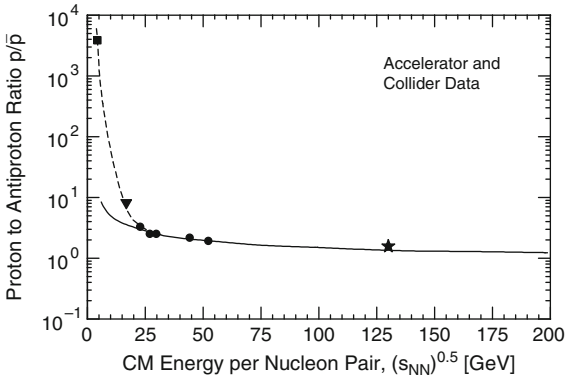

Fig. 3.9 Ratios of $p/\overline{p}$ from pp and central Au(Pb)–Au(Pb) collisions as a function of the center of mass energy. The *curve* is a fit to the pp data (after Huang, 2002). The *dashed line* was added by the author to indicate the sharp increase in the antiproton production. The experimental data are from the following experiments: ■ Ahle et al. (1998); • Rossi et al. (1975) and Aguilar-Benitez et al. (1991); ▼ Bächler et al. (1999); ⋆ Adler et al. (2001) and Huang (2002)

3.5.2 Energy Dependence of Multiplicity

Surprisingly, the energy dependence of the multiplicity is not very well known at high energies, beyond accelerator accessibility. Different investigations yield different dependencies, ranging from an almost logarithmic to a power law dependence. This is due partly to the relatively large width of the multiplicity distribution and associated large fluctuations.

Direct observations of very high energy cosmic ray induced interactions (of pions, nucleons and nuclei) in nuclear emulsion beyond accelerator energies from which useful information can be extracted are not numerous and harbor many uncertainties. At ultrahigh energies the multiplicity can only be extracted indirectly from air shower observables with the help of complex simulations that involve multiparameter correlations, making the task even more difficult. Additional problems arise because rising hadronic cross sections and/or increasing primary mass with energy tend to influence shower observables in the same way as an increasing multiplicity.

Alner et al. (1987) found that the energy dependence of the average number of charged secondaries, i.e., the *average charged particle multiplicity*, $\langle n_{\pm} \rangle$, emerging from a high energy *nucleon–nucleon collision*, can be described with either of the following two relations.

$$\langle n_{\pm} \rangle \; = \; a \; + \; b \ln(s) \; + \; c \, (\ln(s))^2 \, , \tag{3.13}$$

or

$$\langle n_{\pm} \rangle \; = \; a \; + \; b \, s^c , \tag{3.14}$$

Table 3.5 Parameters for energy-multiplicity relation energy range 3–546 GeV in center of mass. (Alner et al., 1987)

Equations	a	b	c
3.13	0.98 ± 0.05	0.38 ± 0.03	0.124 ± 0.003
3.14	-4.2 ± 0.21	4.69 ± 0.18	0.155 ± 0.003

where s is the center of mass energy squared ($s = E_{\mathrm{CM}}^2$). For all inelastic processes Alner et al. (1987) specify for the constants a, b and c the values listed in Table 3.5. Because of charge symmetry it is generally assumed that the ratio for the production of $\pi^+ : \pi^- : \pi^0 = 1 : 1 : 1$ at high energy.

The first term in Eqs. (3.13) and (3.14) represents the diffraction, fragmentation or isobar part, depending on the terminology used. The second and third terms, if applicable, account for the bulk of particles that result mostly from central processes at high collision energies, frequently referred to as *pionization*.

Figure 3.10 shows the center of mass energy dependence of the average secondary particle multiplicity in proton–proton and proton–antiproton collisions obtained from experiments performed at CERN with the Proton Synchrotron (PS), the Intersecting Storage Ring (ISR) and the Proton–Antiproton ($\overline{p}p$) Collider (UA5 experiment, Alner et al., 1987). Relevant for particle production is the energy which is available in the center of mass. At high energies pp and $\overline{p}p$ interactions behave alike (see Fig. 3.1). The solid and dashed curves, A and B, are fits using Eqs. (3.13) and (3.14), respectively, with the parameters listed in Table 3.5.

An earlier study of the energy-multiplicity relation that is based mainly on data from cosmic ray emulsion stack and emulsion chamber experiments at energies up to 10^7 GeV in the laboratory frame, and on air shower simulations was made by Grieder (1972, 1977). This author found the same basic energy dependence as given in Eq. (3.14) but with a larger value for the exponent c. Part of the reason for

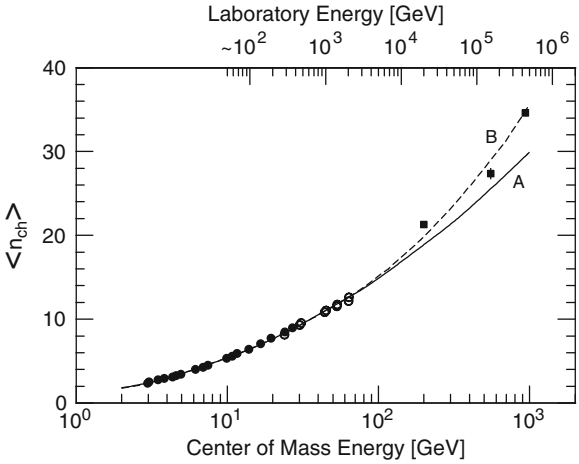

Fig. 3.10 Mean charged multiplicity of inelastic pp or $\overline{p}p$ interactions as a function of center of mass energy, $\sqrt{s}$ (Basile et al., 1980, 1981a; De Angelis, 1996). The *solid curve*, A, is a fit to Eq. (3.13), the *dashed curve*, B, to Eq. (3.14) (after Alner et al., 1987)

the higher value of c resulting from this work is probably due to the fact that the analysis included mostly nucleon–nucleus ($N - A$) collisions which yield higher multiplicities than nucleon–nucleon ($N - N$) collisions at comparable energies.

Pion initiated interactions are less elastic than nucleon initiated collisions and yield a higher multiplicity. Nucleus–nucleus ($A - A$) interactions show the same basic behavior but yield even higher multiplicities. The latter can easily be distinguished from ($N - A$) encounters in emulsion when inspecting the track density of the incident particle.

The curves plotted in Fig. 3.11 show the energy dependence of different multiplicity laws that follow from different partly phenomenological models of particle production mechanisms, ranging from the so-called half-law which represents an absolute upper limit to the simple logarithmic-law (or energy dependence). The latter is predicted by the naive *scaling model* which implies a flat *rapidity distribution* (Feynman, 1969) that yields poor results if applied over a wide energy range with a given set of parameters. Some of the models are discussed in Sect. 3.10 and, in connection with air shower simulations, in Chap. 20.

Of particular interest is the histogram which shows the number of interactions in the different energy bins as they occur in a vertically incident 10^6 GeV primary proton initiated simulated shower (Grieder, 1972). This histogram illustrates very well the reason for the difficulties to extract information on ultrahigh energy hadronic interactions from air showers. It is evident from this histogram that because of the rapid energy degradation in the shower as it propagates deeper and deeper into the atmosphere, the bulk of the produced particles emerge from relatively low energy interactions, making it difficult to find the few relevant high energy signatures.

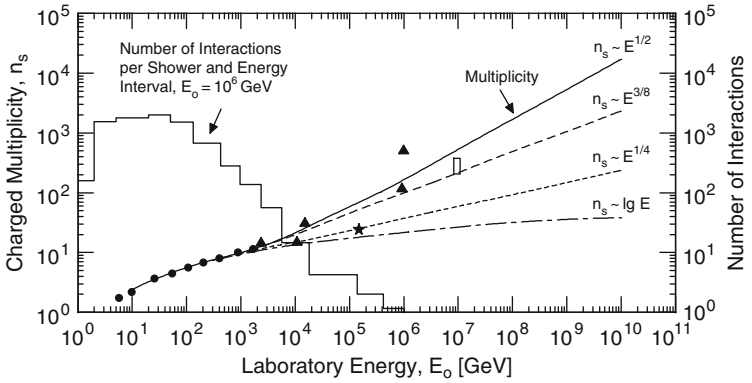

Fig. 3.11 Average charged secondary particle multiplicity in fixed target proton–proton (●) and proton–nucleus (▲, □, ★, emulsion) interactions as a function of energy in the laboratory frame of reference. The *curves* show predicted multiplicities for various multiplicity laws. The histogram shows the number of interactions per energy bin in the hadron cascade in the atmosphere of a 10^6 GeV proton initiated shower (Grieder, 1972)

3.5.3 Projectile and Target Mass Dependence of Secondary Particle Multiplicity

Experiments have shown that at fixed energy the secondary particle multiplicity exhibits a projectile and target mass dependence. This is relevant for air showers where we deal with the full mass spectrum in the primary particle beam, from protons to iron and beyond, which is in collision with nuclei of air constituents, and alike for nuclear fragments in the subsequent hadron cascade process in the atmosphere.

The amount of data that is available on this topic from accelerator experiments is very scarce. The bulk of the data concerns collisions of protons with nuclear targets, such as the precision experiment of Atherton et al. (1980) with 400 GeV/c protons from the CERN Super Proton Symchrotron (SPS) on Beryllium. Most accelerator experiments where nuclear projectiles were aimed at heavy nuclear targets such as Au and Pb were restricted to relatively low energies, approximately 200 GeV/nucleon on fixed targets, and did not measure the total multiplicity. Heavy ion colliders, such as RHIC, are expected to yield data at much higher energies that can serve as guidelines for air shower experiments.

So far the most useful data on the projectile and target mass dependence of the secondary particle multiplicity at high energies have come from cosmic ray emulsion and calorimeter experiments. The most refined data are those from measurements in nuclear emulsion. Babecki (1975) has summarized the results of the early work and arrives at the following general mass dependence of the secondary multiplicity,

$$\langle n_s \rangle = C + D\, A^{(1/3)}, \tag{3.15}$$

This relation was obtained from measurements with protons having energies between 6.2 GeV and about 3,000 GeV and is certainly valid well beyond this value.

The mass dependence of the multiplicity was also studied theoretically (Fishbane and Trefil, 1971, 1973; Gottfried, 1972, 1973a, b, 1974) and with the help of air shower simulations (Grieder, 1973). The early theoretical investigations were based on two different concepts: (a) on intranuclear cascading and (b) on the excitation of intermediate states such as fireballs (Miesowicz, 1971), Nova particles (Jacob and Slansky, 1971) and others. Today such calculations are mainly based on QCD concepts.

3.5.4 Multiplicity Distribution

The multiplicity distribution, $P(n)$, at fixed energy had been studied by many authors. As mentioned earlier, the distribution is very broad and subject to large fluctuations. Different mathematical forms had been proposed to describe it, including

scaling behaviors, such as *KNO-scaling*, Eq. (3.16), (Koba et al., 1972) and others.

$$\langle n\rangle P(n)_{\mathrm{KNO}} \;=\; \psi\left(\frac{n}{\langle n\rangle}\right), \tag{3.16}$$

where ψ is energy independent.

In later experiments, at the $\overline{p}p$-collider it was found that *negative binomials* (NB) describe the charged particle multiplicity for non (single)-diffractive pp and $\overline{p}p$ interactions for center of mass energies from $\sqrt{s} = 10$ to 900 GeV quite well (Adamus et al., 1986). The NB-*distribution* is defined as

$$P_n(\overline{n}, k) \;=\; \frac{(n+k-1)!}{n!(k-1)!}\left(\frac{\overline{n}/k}{1+\overline{n}/k}\right)^n\left(1+\frac{\overline{n}}{k}\right)^{-k}, \tag{3.17}$$

where P_n is the probability for an event with n charged particles (see also Tannenbaum and Kang, 1994). The two parameters, $\overline{n}$, the average charged multiplicity, and k, are related to the dispersion

$$D \;=\; \sqrt{(\overline{n^2}-\overline{n}^2)} \tag{3.18}$$

by the relation

$$\frac{D^2}{\overline{n}^2} \;=\; \frac{1}{k}+\frac{1}{\overline{n}}\;, \tag{3.19}$$

where $\overline{n}$ and k are fitted in a somewhat elaborate procedure (Adamus et al., 1986).

In another analysis, Ammar et al. (1986) found a breakdown of the previously mentioned KNO-scaling in inelastic $\overline{p}p$ reactions without single diffractive events in the range $200 \le \sqrt{s} \le 900$ GeV. On the other hand they found that the following NB-expressions and the energy dependent parameters $\langle n\rangle$ and k, as specified below, describe the distribution well,

$$P(n, \langle n\rangle, k) \;=\; \left(\frac{k(k+1)...(k+n-1)}{n!}\right)\left(\frac{\langle n\rangle^n k^k}{(\langle n\rangle+k)^{(n+k)}}\right), \tag{3.20}$$

where

$$\langle n\rangle \;=\; (2.7\pm 0.7) - (0.03\pm 0.21)\ln(s) + (0.167\pm 0.0162)\ln^2(s) \tag{3.21}$$

and

$$k^{-1} \;=\; -(0.104\pm 0.004) + (0.058\pm 0.001)\ln\sqrt{s}\;. \tag{3.22}$$

3.6 Kinematic Aspects of Secondaries, Longitudinal and Transverse Momenta

The kinematics of high energy hadronic collisions is complex because the secondary particle multiplicity is very large, i.e., a large number of all kinds of newly created particles (pions, kaons, nucleons, antinucleons, antibaryons, charmed particles, etc.) are emerging from an interaction. An instructive method to study the interactions in detail is to display the center of mass momenta of the particles in a so-called *Peyrou plot*, shown in Fig. 3.12 (Peyrou, 1961; see Horn, 1972; Sivers, 1976 for reviews).

The Peyrou plot is a so-called $p_{\ell,\mathrm{CM}} - p_t$ scatter plot. Each particle is represented by a point in a two-dimensional plot with the longitudinal momentum in the center of mass, $p_{\ell,\mathrm{CM}}$, along the abscissa and the transverse momentum, p_t, along the ordinate. Thus, each point is the terminal point of the momentum vector of the particle starting from the origin of the coordinates which is the center of mass. The advantage of such a plot is that it gives a more complete picture of the situation than separate angular and momentum distributions. It enables the ready identification of the different kinematic regions, such as the *fragmentation*, the *central* and the *deep region*.

If displayed for a wide range of different energies the plot illustrates in a striking way the constancy of the leading particle effect and of the transverse momentum distribution of the particles emerging from the interactions. The two phenomena had been discovered in cosmic ray emulsion experiments a long time ago and appeared to be essentially independent of collision energy[8] (Powell et al., 1959; Perkins, 1960).

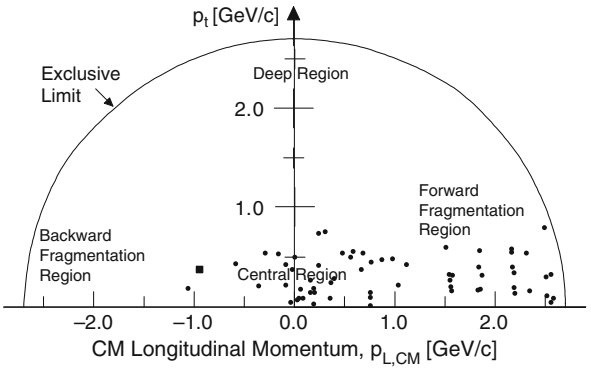

Fig. 3.12 Example of a Peyrou plot ($p_{\ell,CM} - p_t$ plot). The longitudinal momenta of the interaction products in the center of mass are plotted along the abscissa and the transverse momenta along the positive ordinate, with the center of mass at the origin. The *dots* indicate the location of so-called negative prongs from two-prong $\pi^- - p$-collisions (● represent π^-, ■ the only K^-). The *circular contour* shows the exclusive limit. The different kinematic regions are indicated (Peyrou, 1961)

[8] We disregard here the comparatively rare occasional large transverse momentum events that are discussed below.

As mentioned earlier, the transverse momentum distribution can be represented approximately by the Boltzmann law as follows (Cocconi et al., 1966),

$$f(p_t) = \left(\frac{p_t}{p_0^2}\right) \exp\left(-\frac{p_t}{p_0}\right) , \tag{3.23}$$

where $\langle p_t \rangle = 2p_0$ is the average value.[9]

A consequence of the constancy of the p_t-distribution is that a three-dimensional Peyrou representation grows only along the abscissa with increasing energy, i.e., it changes from a near spheroidal shape at low energies to an elongated ellipsoid, as is indicated in Fig. 3.13. Peyrou plots had actually been used for analyzing high energy cosmic ray interactions in nuclear emulsion since the early days of this technique and for the evaluation of accelerator data, too.

Since the introduction of *Feynman Scaling* (Feynman, 1969), which is discussed in Sect. 3.10.4, it has become customary to use a somewhat different representation for comparative interaction studies. In place of the longitudinal momentum of the particles, *rapidity*, y, or *pseudo-rapidity*, η, is now being used[10] (Bøggild and Ferbel, 1974; for a review see Foà, 1975). In this context the Peyrou plots are replaced by rapidity density distributions and *inclusive cross sections*,[11] as shown in Fig. 3.14.

Rapidity and pseudo-rapidity are defined in Sect. 3.10.4 (see also Chap. 21). The advantage of the rapidity picture is that the rapidity distribution is *Lorentz invariant* except for an additive constant when going from one frame of reference to another, say from the center of mass to the laboratory frame, or vice versa. Thus, the character of a distribution plotted in rapidity does not change when changing reference frame. The differences between the Peyrou and rapidity representations are discussed by Horn (1972).

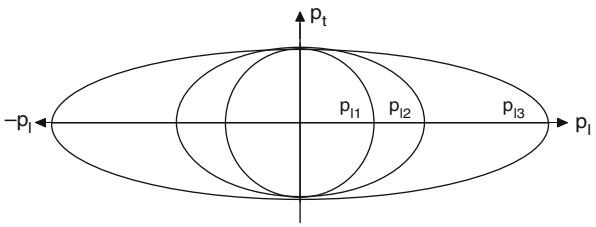

Fig. 3.13 Contour limits of Peyrou plots in the center of mass for different collision energies with corresponding longitudinal momenta ($p_{\ell 1}$, $p_{\ell 2}$, etc.), and an energy independent transverse momentum distribution (p_t)

[9] Cocconi et al. (1966) in their work used a value of $2p_0 \simeq 0.36$ GeV/c.

[10] See Eqs. (3.44) and (3.60), respectively, for definition.

[11] See Chap. 21 for definitions.

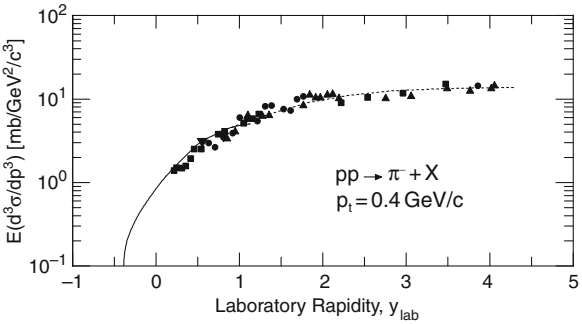

Fig. 3.14 Invariant inclusive cross section of the reaction $pp \rightarrow \pi^- + X$ at $p_t = 0.4$ GeV/c as a function of laboratory frame rapidity obtained in one of the early Intersecting Storage Ring (ISR) experiments at CERN in Geneva, Switzerland (after Bøggild and Ferbel, 1974). The symbols represent different CM energies: ▼ 23 GeV, ■ 31 GeV, ● 45 GeV, ▲ 53 GeV

3.7 Large Transverse Momenta of Secondaries, Energy Dependence

One of the characteristic features of high energy hadronic interactions is the transverse momentum that is imparted to the secondary particles emerging from a collision. For a long time is was believed that the transverse momentum distribution is almost independent of incident energy and has an average value of approximately 350 MeV c^{-1} for nucleons and about 250 MeV c^{-1} for lighter particles, such as pions. This belief was strengthened by the various theories that were popular at that time for describing the interactions such as the multi-peripheral model (Amati et al., 1962) and above all the thermodynamic (or statistical) model of Hagedorn (1965) and Hagedorn and Ranft (1968).

In the early phase of air shower investigations the phenomenon of large transverse momenta was first proposed in connection with the observation of multi-cores in air showers (Heinemann and Hazen, 1953; Goryunov et al., 1960) (for details concerning multi-core events see Sect. 13.7.2). Somewhat later similar phenomena were observed in nuclear emulsion (Akashi et al., 1965a, b; for an early summary see Fowler and Perkins, 1964). In the late 60s it was an established fact that large transverse momenta of up to 10 GeV exist in the multi-TeV energy regime of hadronic interactions in cosmic ray events. Methods for the determination of transverse momenta of high energy interactions in air showers are discussed in Sect. 13.7.3.

Confirmation of the existence of events with large transverse momenta by the accelerator physics community came from one of the first experiments at the ISR at CERN (Alper et al., 1973; Banner et al., 1973; Büsser et al., 1973).[12] In later

[12] At that time Minkowski predicted on the basis of QCD the existence of jets, direct gamma rays and lepton pairs with large transverse momenta that should exhibit a relatively flat distribution that goes asymptotically as p_t^{-4} (Minkowski, 1973, private communication; Fritzsch and Minkowski, 1977).

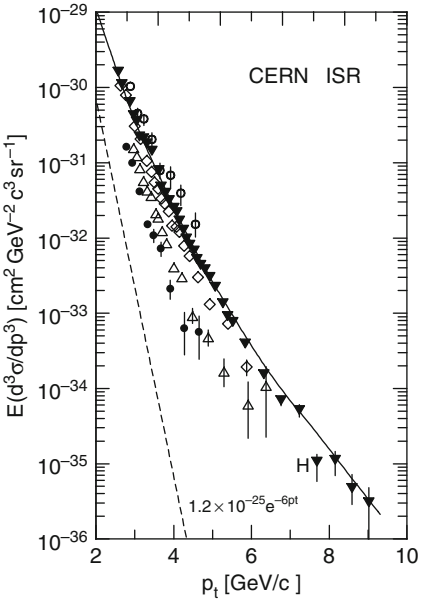

Fig. 3.15 Inclusive cross section $pp \to \pi^\circ + X$ versus transverse momentum for large transverse momenta as measured at different center of mass energies, $\sqrt{s}$, in proton–proton collisions at the CERN Intersecting Storage Rings: • $\sqrt{s} = 23.5$ GeV; △ $\sqrt{s} = 30.6$ GeV; ◇ $\sqrt{s} = 44.8$ GeV; ▼ $\sqrt{s} = 52.7$ GeV; ○ $\sqrt{s} = 62.4$ GeV (Büsser et al., 1973, CERN-Columbia-Rockefeller (CCR) experiment). Also shown is the extrapolation of the Hagedorn thermodynamic model (Hagedorn and Ranft, 1968) which yields a distribution of the form $p_t \propto \exp(-6p_t)$ that applies to the bulk of the interactions

experiments at much higher energies with the colliders at CERN and FNAL it was found that the trend continued. The essential results of this work are summarized in Fig. 3.15. (For details the interested reader is referred to the reviews of Sivers et al., 1976, Jacob and Landshoff, 1978, and Geist et al., 1990; see also Alexopoulos et al., 1993). The energy dependence of the average transverse momentum is illustrated in Fig. 3.16.

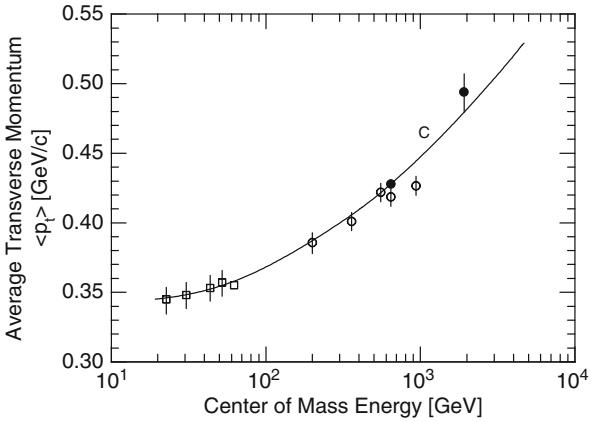

Fig. 3.16 Energy dependence of the average transverse momentum, $\langle p_t \rangle$, obtained from the following experiments. □ CERN ISR, the values are averaged over particle types (Rossi et al., 1975 and references listed therein); ○ CERN UA1, events are averaged over jet and non-jet samples (Ceradini, 1985); • FNAL CDF, Abe et al. (1988) (after Abe et al. 1988)

3.8 Leading Particle Effect, Elasticity and Inelasticity

It has long been known from cosmic ray emulsion and electronic detector experiments that very high energy nucleon as well as nucleus initiated collisions with target nucleons or nuclei manifest a high degree of *elasticity*, η, i.e., the projectile itself or fragments of it in case of a projectile nucleus emerge from a collision while retaining a large fraction of the initial kinetic energy (Guzhavin and Zatsepin, 1957; Peters, 1961, 1962; Grigorov et al., 1965).[13] This phenomenon which is particularly striking when viewed in the laboratory frame is called the *leading particle effect*. One refers therefore often to the *leading nucleon*.[14] This effect is less pronounced in pion initiated collisions with nucleons or nuclei.

The elasticity and the leading particle effect are of prime importance for the development of nuclear cascades and the longitudinal shower development. Without the leading particle effect air showers would look very different than they actually do. At an early stage of theoretical cascade studies, simulations have shown that without a high elasticity, which implies no or only a weak leading particle effect, air showers would build up and decay faster (Grieder, 1970b, c).

If in addition nucleon–antinucleon production would be suppressed and pions, which exhibit a weaker leading particle effect, would be the only kind of secondary particles, showers would grow and decline even faster, leaving mainly muons, neutrinos and part of the electromagnetic component as survivors in the deeper regions of the atmosphere, down to sea level, and would have a deficit in the hadron content.

The observed longitudinal development of air showers implies directly the necessity of a significant nucleon-antinucleon production rate in hadronic collisions at high energies, which enables the hadron cascade to be an efficient energy transport mechanism in the atmosphere since nucleon and antinucleon initiated collisions have a higher elasticity than pion initiated collisions (Grieder, 1970a, b, c, 1977; for further details on this subject see Sect. 13.6.3).

3.8.1 Definition and Direct Determination of Elasticity/Inelasticity

Elasticity is defined as the ratio of the energy carried away by the most energetic particle emerging from an interaction, E_{out}, divided by the energy of the incident projectile, E_{in}. Thus,

$$\eta = \frac{E_{\text{out}}}{E_{\text{in}}}. \tag{3.24}$$

Instead of *elasticity*, many authors prefer to use the *inelasticity*, K, defined as

[13] For an early review see Feinberg (1972), and references listed therein.

[14] It should be noted that in about 25% of all proton–nucleus interactions the most energetic hadron is a neutron (Jones, 1982).

$$K = 1 - \eta, \tag{3.25}$$

which represents that fraction of the total incident energy that is available for the production of secondary particles. Some authors define therefore the inelasticity as

$$K = \frac{\Sigma E_s}{E_{\text{in}}} \quad , \tag{3.26}$$

where ΣE_s is the sum of the total energy of all produced secondary particles.

Considering charge exchange and a classical picture, the emerging leading nucleon may be the surviving incident nucleon itself or the immediate collision partner of the projectile, i.e., a proton or neutron of the target nucleus. A similar though less pronounced effect is observed in pion–nucleon and even less in pion-nucleus interactions. One refers therefore also to the *leading pion* emerging from an interaction. These effects were confirmed later on with high statistics in accelerator experiments, initially at much lower energy and, with increasing capability of the accelerators and colliders, to the TeV energy range (Slansky, 1974; Basile et al., 1981b, 1983; Brenner et al., 1982; Alner et al., 1986; Aguilar-Benitez et al., 1991).

As trivial an observable as it may seem to be, the average inelasticity and its energy dependence still harbor large uncertainties, in spite of decades of work. One of the reasons for this dilemma is that even at fixed energy the inelasticity exhibits large fluctuations that manifest themselves in a very flat and broad distribution. Other problems are due to the fact that K depends on the mass of the collision partners. It can therefore be studied experimentally under well controlled conditions at accelerators only over a comparatively limited energy range, depending on the kind of projectile (pions, nucleons, nuclei, etc.). At colliders the choice of collision partners is even more restricted and the very forward region has so far been ignored in most collider experiments.

On the other hand, in cosmic ray emulsion experiments a wide energy range is available, however, with rapidly diminishing intensity and we are dealing mostly with composite targets, i.e., with nuclei. Moreover, the specific nature of the target is in general unknown.[15] This problem can be avoided in calorimeter experiments where pure targets are used, but the determination of the nature of the incident projectile remains frequently a problem. Theoretical steps using Glauber theory are required to link nucleon-nucleon data with nucleon nucleus data, and vice versa (Glauber, 1959). A comprehensive early review by Jones (1982) which considers accelerator and cosmic ray data illuminates the problems.

More recently, in high energy nucleon–nucleon collisions at accelerators and colliders it was found that the average elasticity appears to be $\langle \eta \rangle < 0.5$, a value that is lower but still compatible with that known for decades from cosmic ray experiments. It also seems to be almost energy independent over many decades, from tens

[15] Rough estimates are possible on the basis of the number of heavy tracks.

of GeV to hundreds of TeV. In pion–nucleon collisions the elasticity distribution is asymmetric and the average elasticity appears to be around 0.2–0.4 over a wide energy range. In pion–nucleus collisions it is even less.

In cosmic ray experiments the direct determination of the inelasticity of high energy interactions is usually achieved by studying individual interactions in nuclear emulsion and emulsion chambers. Measurements with electronic calorimeters as they are commonly used in cosmic ray research are suitable, too, but it is far more difficult to extract reliable data unless the instrument has a high spatial and energy resolution (Mielke et al., 1995; Milke, 1997; Kampert et al., 2001).

New inelasticity studies of hadron–lead interactions ($N-$Pb, $\pi-$Pb) in the energy range around 10^{14} eV using thick lead emulsion chambers exposed at the Pamir mountains in Tadjikistan (4,300 m a.s.l.) were carried out by Barroso et al. (1997). They obtained an average value for the inelasticity of $\langle K_{\pi,p}^{Pb}\rangle = 0.83 \pm 0.17$, consistent with earlier work. From these data the authors infer an average hadron–nucleon inelasticity of $\langle K_{\pi,p}^{p}\rangle \sim 0.5$.

3.8.2 Indirect Methods to Determine the Elasticity/Inelasticity

The inelasticity of hadronic collisions can also be obtained indirectly from hadron spectra measured at different atmospheric depths, by determining the hadron rate attenuation length in the atmosphere, in particular the proton attenuation length, $\Lambda_{\rm att}^{\rm p,air}$ (e.g., Aglietta et al., 1997, 1999; for a recent review see Bellandi et al., 1998, and Fig. 6.13).

If we assume a linear relationship between the rate attenuation length $\Lambda_{\rm att}^{\rm p,air}$ and the interaction mean free path, $\lambda_{\rm int}^{\rm p,air}$, which is inversely proportional to the proton-air cross section, $\sigma_{\rm inel}^{\rm p,air}$ (see Eq. 3.9), we can write

$$\Lambda_{\rm att}^{\rm p,air} \;=\; k\lambda_{\rm int}^{\rm p,air}, \tag{3.27}$$

where the parameter k which is related to the inelasticity $K_{\rm p,air}$ is a proportionality factor. In general $\Lambda_{\rm att}^{\rm p,air}$, $\lambda_{\rm int}^{\rm p,air}$ and k are energy dependent. Furthermore, $\Lambda_{\rm att}^{\rm p,air}$ and k depend on the spectral slope, γ, and k and $\lambda_{\rm int}^{\rm p,air}$ are a priori unknown.

If $\lambda_{\rm int}^{\rm p,air}$ and $K_{p}^{\rm air}$ are assumed to be energy dependent, the analytic solution for the nucleonic diffusion equation in the atmosphere takes the form (Bellandi et al., 1992a, b)

$$F_N(E,X) \;=\; F_N(E,X=0)\exp\left(-\frac{X}{\Lambda_{\rm att}^{\rm p,air}(E)}\right). \tag{3.28}$$

Here, $F_N(E,X)$ [(cm^2 s sr GeV)$^{-1}$] is the differential intensity at atmospheric depth X [g cm^{-2}], $\Lambda_{\rm att}^{\rm p,air}$ [g cm^{-2}] the energy dependent nuclear attenuation length in the atmosphere and

$$F_N(E, X = 0) \;=\; C_0 E^{-(\gamma+1)} \tag{3.29}$$

the primary intensity with C_0 being the normalization constant.

Considering the energy dependence of the quantities of Eq. (3.27) and in addition the spectral slope dependence of the nucleon attenuation length, $\Lambda_{\rm att}^{\rm p,air}(E)$, Bellandi et al. (1992a, b) obtain the following approximate relation between $\Lambda_{\rm att}^{\rm p,air}(E)$, $\lambda_{\rm int}^{\rm p,air}(E)$ and K_p^{air},

$$\Lambda_{\rm att}^{\rm p,air}(E) \;=\; \frac{\lambda_{\rm int}^{\rm p,air}(E)}{1-(1-K_p^{\rm air})^{\gamma}}. \tag{3.30}$$

Recently more elaborate methods, summarized in Sect. 3.9, that are based on correlations between measured cosmic ray intensities or specific air shower signatures and predictions from simulations, using detailed high energy interaction models, had been used to gain better insight.

3.8.3 Energy Dependence of Elasticity/Inelasticity

Since the discussion concerning the energy dependence of the inelastic proton-air cross section, $\sigma_{\rm inel}^{\rm p,air}$, began, the investigation of the energy dependence of the observables Λ, λ, K, n and σ was pursued in air shower experiments to the highest energies. These efforts were intensified after the successful work of Yodh et al. (1972), which showed that $\sigma_{\rm inel}^{\rm p,air}$ is indeed increasing with energy, and are being continued up to date. As mentioned earlier, almost at the same time the cosmic ray results were confirmed by some of the first experiments at the CERN Intersecting Storage Ring (ISR) which showed that the total cross section begins to increase beyond a laboratory momentum of $\simeq 100\,\mathrm{GeV/c}$ in proton–proton collisions (Amaldi et al., 1973; Amendolia et al., 1973; for an early review see Slansky, 1974).

Theoretical studies of the energy dependence of the inelasticity of proton-proton collisions using various interaction models, e.g., statistical (Fowler et al., 1987), mini-jet (Gaisser and Stanev, 1989) and QCD Pomeron model (Kopeliovich et al., 1989), lead to different dependencies (Gaisser et al., 1993; Bellandi et al., 1992b; Hama and Paiva, 1997; Batista and Covolan, 1999).

In Fig. 3.17a,b we show a compilation of Bellandi et al. (1998) of the energy dependence of the proton–air and proton–proton inelasticities, respectively, resulting from different experiments, and theoretical predictions. Inspection of Fig. 3.17a shows a trend for the proton-air inelasticity, K_p^{air}, extracted from proton-air collision data to decrease first, followed by a slow increase with increasing energy. On the other hand, for the proton-proton inelasticity, K_p^p (Fig. 3.17b), no convincing evidence exists for such an increase, the trend is rather the opposite.

The link between proton–proton and proton–air collisions that is necessary to cross check cosmic ray and accelerator or collider data is established with the help of Glauber theory (Glauber, 1959; Glauber and Matthiae, 1970). Accurate elasticity

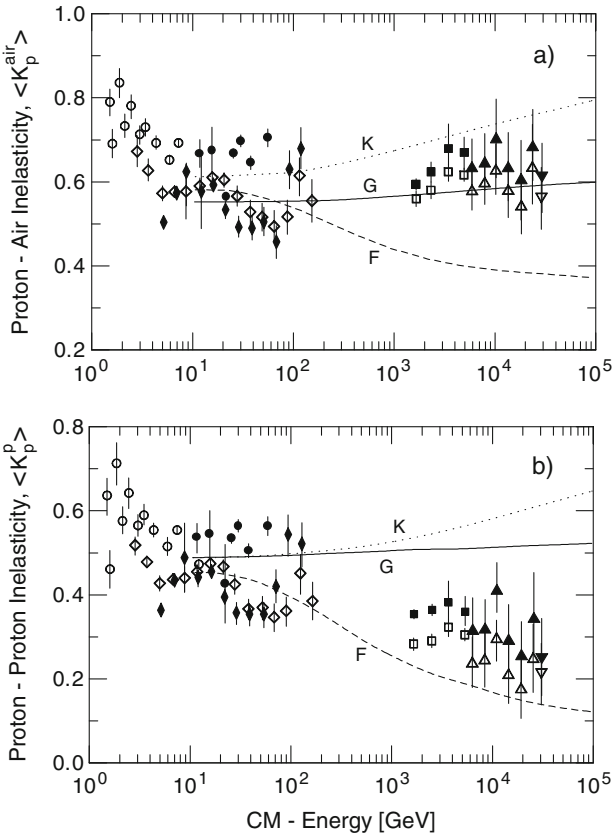

Fig. 3.17 (**a**) Average proton-air and (**b**) proton-proton inelasticities, $K_p^{air}(E)$ and $K_p^p(E)$, respectively, as a function of the center of mass energy (after Bellandi et al., 1998). The experimental data used are from the following authors: ○ Brooke et al. (1964); ●, ♦ Ashton and Coats (1968) and Ashton et al. (1970); ◇ Mielke et al. (1993, 1994); △, ▲ Hara et al. (1983) and Honda et al. (1993); ▽, ▼ Baltrusaitis et al. (1984); and □, ■ Aglietta et al. (1997). At high energies the *open and full symbols* were calculated using the models of Donnachie and Landshoff (1992) and Covolan et al. (1996). The curves K, G and F were obtained using the models of Kopeliovich et al. (1989), Gaisser et al. (1990) and Fowler et al. (1987), respectively

measurements in collider experiments are difficult because of the inaccessibility of the very forward direction in most collider experiments.

From the above analysis it is evident that the problem of the energy dependence of the elasticity/inelasticity is not yet solved. All data so far indicated that the elasticity depends significantly on the mass of the collision partners. Of all the hadronic collisions, nucleon–nucleon collisions are those that show the highest average elasticity, i.e., the lowest inelasticity.

Costa (1998) in his paper reviewed a large number of contributions concerning the energy dependence of K and particle production models. He points out one of

Table 3.6 Particle production and inelasticity models. (After Costa, 1998)

Author(s)	Remarks	Comments	
		Type[1]	Experiment[2]
Decreasing inelasticity			
Ohsawa and Sawayanagi (1992),	Phenomenological model[3]	ES	Fuji/sea level
Bellandi et al. (1994a, b)	–	–	Chacaltaya/Pamir
Fowler et al. (1984, 1985, 1987, 1989)	Interacting gluon model	ID	CERN ISR
He (1993)	pp/e^+e^- similarities	CM	Accelerator
Kadija and Martins (1993)	pp/e^+e^- similarities	ID, CM	Accelerator
Kawasumi et al. (1996)	Proton or heavy	ES, SS	Chacaltaya/Tien Shan
Kempa and Wdowczyk (1983)	Proton dominance	ES	Fuji/JACEE
Ding and Zhu (1992)	Two-component model	$\mathrm{d}N/\mathrm{d}y$	UA5, UA7
Wdowczyk and Wolfendale (1984, 1987)	Scale-breaking model	ES, $\mathrm{d}N/\mathrm{d}\eta$	Fuji/accelerater
Weiner et al. (1992), Wlodarczyk (1993, 1995)	Valon-gluon model	AL, ES, SM	Pamir/Akeno
Constant or slowly increasing inelasticity			
Costa et al. (1995, 1996)	Eq. (2)/model 2	ES, LS	Fuji/Kanbala
	–	–	Chacaltaya/Pamir
Dunaevsky et al. (1991a, b)	Quark-gluon strings	CM, ES, LS	Pamir/Tien Shan
Durães et al. (1993)	Interacting-gluon/mini-jet	ID	Accelerator
Gaisser and Stanev (1989), Gaisser et al. (1993)	Mini-jet model	SM, $\mathrm{d}N/\mathrm{d}\eta$	Fly's Eye/accelerator
Astafiev and Mukhamedshin (1979)	Heavy primary	ES, LS	Pamir
Mukhamedshin (1981)	–	–	–
Fukushima et al. (1989), Saito et al. (1993)	Heavy primary	ES	Mt. Norikura
Ren et al. (1988)	Heavy primary	ES	Fuji/Kanbala

Table 3.6 (continued)

Author(s)	Remarks	Comments	
		Type[1]	Experiment[2]
Increasing inelasticity			
Barshay and Chiba (1986)	Eikonal blackening	CM	Accelerator
Capdevielle (1989)	Dual parton model	SM, $\mathrm{d}N/\mathrm{d}\eta$	Mountain/accelerator
Dias de Deus (1985),	Geometrical model	ES, $\mathrm{d}\sigma/\mathrm{d}x$	Mountain/accelerator
Bellandi et al. (1989, 1992a)	–	–	–
Kaidalov and Ter-Martirosyan (1982)	Quark-gluon strings	CM	Accelerator
Kopeliovich et al. (1989), Nikolaev (1993)	QCD-Pomeron	$\sigma_{\mathrm{total}}^{pp(p\overline{p})}$	CERN $Sp\overline{p}S$
Shabelski (1988), Anisovich et al. (1985)	Additive quark model	CM	Accelerator
Combination of models			
Baradzei et al. (1992)	Proton/Fe dominance	ES, LS	Chacaltaya/Pamir
Capdevielle et al. (1994)	Proton/heavy dominance	ES, SS	Pamir/Tien Shan
Kasahara and Takahashi (1976)	–	–	–
Kasahara et al. (1979a, b)	Proton/Fe dominance	ES, LS	Fuji
Klages et al. (1997)	Several parameters	ES, LS, SS	KASCADE
Shibata (1981)	Several K-A parameters	γ-families	Fuji

[1] AL = attenuation length, CM = charged multiplicity, ES = energy spectra, ID = inelasticity distribution, LS = lateral spread, SM = shower maximum, SS = shower size.
[2] Terms Accelerator and Mountain refer to miscellaneous experiments and data sources.
[3] Ohsawa-Sawayanagi phenomenological scaling violation model.

the causes that is partly responsible for the still prevailing situation that no unique trend of the energy dependence could be found so far, namely the *primary mass-inelasticity uncertainty*. To illuminate the extend of the efforts which had been undertaken by many individuals and groups on this subject we reproduce Costa's summary table of papers that deal with the problem of inelasticity (Table 3.6). However, as we have pointed out earlier, this is only part of the problem as an increase of the hadronic cross sections, of the secondary particle multiplicity, the inelasticity or the primary mass with energy affect the more common shower observables on the ground alike.

3.9 Correlations Between Interaction Observables

The previously discussed observables that characterize high energy hadronic interactions are all correlated in one way or another, mostly via kinematics, i.e., through energy and momentum conservation, as is evident upon inspection. The degree of correlation is readily seen when the observables and their distributions are parametrized, inserted into simulations and calculations are carried out for different parameter values (Engel, 2003).

At low and moderate energies such calculations can be used to compute the cosmic ray counting rate at ground level of a well defined group of particles, using the primary energy spectrum and composition as input over the energy range where these are known. Since the experimentally determined counting rates are well established quantities one can investigate and tune the parameters. Likewise, at much higher energies one can in an analogous way simulate air showers and select specific shower observables to achieve the same goal.

A recent analysis of this kind, shown in Fig. 3.18, had been carried out by the KASCADE group to explore the role of the input parameters of frequently used hadronic interaction models, briefly summarized in the next subsection (for a review see Kampert et al., 2001 and references listed therein). These authors employed both methods mentioned above, i.e., the cosmic ray counting rate and air shower criteria, and demonstrate the degree of fine tuning that can be achieved this way. In particular, they show in conjunction with the so-called QGSJET model (see Sect. 3.10) how sensitive the cosmic ray counting rate at ground level and other critical observables respond to the percentage of diffraction dissociation of the total inelastic cross section, as well as to variations of the total inelastic cross section. The former affects the elasticity of the interactions strongly as is evident from the figures.

In their analysis Kampert et al. (2001) point out the strong correlation between the trigger rates predicted by the different models listed in Fig. 3.18 and the Feynman-x distributions of the leading baryons. This is illustrated in Fig. 3.19. The x-distribution of the leading baryon is directly related to the inelasticity distribution.

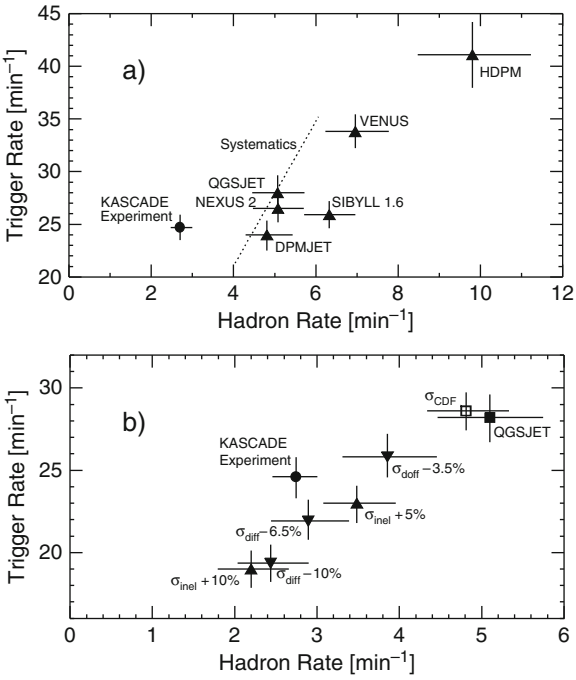

Fig. 3.18 (**a**) Trigger rate vs hadron rate in the KASCADE central detector. Compared are the experimental rates with the predictions of different interaction models for a given set of model parameters. The *dotted line* indicates the systematic uncertainty, mostly given by the absolute flux uncertainty of the experiment (Kampert et al., 2001). (**b**) This plot shows for the QGSJET-98 model the effect of different values of the inelastic cross section and diffraction dissociation (after Kampert et al., 2001)

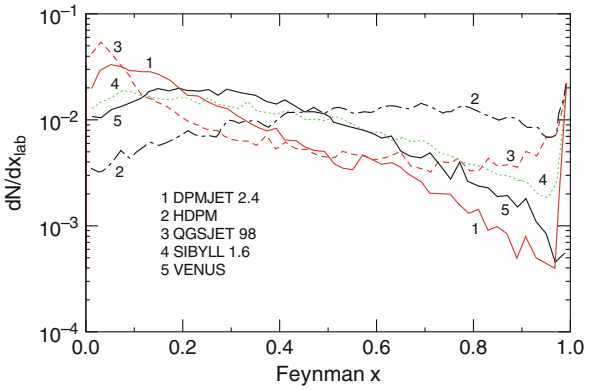

Fig. 3.19 CORSIKA simulations of Feynman-x distributions of the leading baryons from $p-^{14}$N-interactions at 10^{16} eV. Five different interaction models (versions 1997) as listed in the figure are shown (Heck et al., 2001; Kampert et al., 2001; see also Knapp et al., 2003). These authors conclude that the QGSJET model provides the best overall description of extensive air showers in the *knee region*, i.e., around 10^{16} eV. At low energies SIBYLL seems to yield better fits to the muon component of air showers (Tonwar, 2007, private communication)

3.10 Models of High Energy Interactions: I. Early Models

3.10.1 History and Background Information

Hadronic collisions at very high energy are extremely complex. In the air shower energy range that runs from about 100 TeV (10^{14} eV) to 100 EeV (10^{20} eV) and possibly beyond, the multiplicity is huge and the variety of particles and resonances that are produced is very large. Lacking a fundamental self-consistent theory of ultrahigh energy interactions and particle production, a number of phenomenological-mathematical models had been developed over the years to describe these phenomena, in order to simulate hadronic interactions and cascades in extensive air showers, and to interpret air shower data.

At the low energy end the information is taken from experimental data acquired in accelerator and, more recently, in collider experiments. Beyond machine energies information must be extracted from individual interactions of cosmic rays with target nuclei in photographic emulsion and, for the highest energy domain, from air shower experiments (calorimetric and others). Note that data on very high energy interactions of pions and kaons with nucleons and nuclei are only available from cosmic ray experiments.

In emulsion experiments one of the problems is that the projectile beam consists of a mixture of primary and secondary cosmic rays, i.e., nuclei, nuclear fragments, nucleons, pions, kaons, etc., that need to be identified for accurate interpretation of an event, a task that is not always possible.[16] Moreover, the composition and the energy spectrum vary with atmospheric depths (or location where the emulsion stack or chamber is placed). An additional difficulty is that, depending on the nature of the experiment, the target nucleus may be unknown.[17]

Nevertheless, the general features of ultrahigh energy hadronic interactions that are known today emanated from cosmic ray emulsion experiments over decades, some dating back almost 50 years. Many but not all of the phenomena that were discovered in these experiments were subsequently confirmed by ever higher energy machine and eventually collider experiments.[18] The deep insight that we have gained over the past decade on the fundamental processes from contemporary machine experiments have very much enriched our knowledge and understanding

[16] The charge Z can usually be determined but the problem is to distinguish minimum ionizing particles such as charged pions from protons, etc.

[17] The only high energy cosmic ray experiment where a liquid hydrogen (H_2) target had been used was the well known Echo Lake experiment (Jones et al., 1970, 1972).

[18] So far no *Centauro* type events (Lattes et al., 1973; Bellandi et al., 1979) have been discovered in machine experiments (Alner et al., 1987) and neither so-called *co-planar* (*co-linear*) events (Slavatinski, 2003), nor the *long flying* component (Dremin et al., 1990; Yakovlev, 2003, 2005; Dremin and Yakovlev, 2006). Recently, Centauro-I had been re-analyzed by Ohsawa et al. (2004, 2006). A flaw in the initial scanning procedure had been discovered but the essential result, the unique gamma ray deficit, remains.

of hadronic collisions, but it did not really change the overall phenomenological picture at ultrahigh energies significantly.

The *relevant properties* of high energy collisions and of the secondary particles (chiefly pions) emerging from the interactions that were observed in early accelerator experiments ($E \leq 30\,\text{GeV}$), mostly in interactions of *protons* in liquid hydrogen targets or bubble chambers, and the phenomena observed in numerous ultrahigh energy cosmic ray interactions with *light elements* and in *nuclear emulsion* up to the mid 1960s, have led to the first generation of basic phenomenological particle production models. These properties can be summarized as follows (Cocconi et al., 1962, 1966):

- The pion energy spectrum in the laboratory frame has a roughly exponential tail at least up to energies corresponding to about 2/3 of the energy of the incident proton, E_0.
- The transverse momentum distribution for pions follows the Boltzmann law with an average value of $\langle p_t^\pi \rangle = 0.36\,\text{GeV/c}$ at 25 GeV and $\approx 0.4\,\text{GeV/c}$ for incident energies between $100\,\text{GeV} \leq E_0 \leq 10^5\,\text{GeV}$. Thus, it appears to be independent of E_0 beyond about 30 GeV.[19]
- The secondary pion multiplicity, n_π, grows slowly with E_0. The dependence goes approximately as $n_\pi \propto E_0^{0.25}$.
- The total energy fraction carried away by the pions in pp-collisions, i.e., the inelasticity, K_p, is fairly constant and amounts to $0.3 \leq K_p \leq 0.5$.
- The ratio of kaons to pions seems to have reached an asymptotic value of $\approx$0.1 beyond 25 GeV incident proton energy and the average transverse momentum of kaons is similar to that of pions ($p_t^K \approx p_t^\pi$).
- The proton spectrum has a single diffraction inelastic peak at energies just below the elastic peak, but is then very low, and increases with decreasing proton energy toward zero center of mass energy (Jones, 1982). The pion spectrum is peaked towards low momenta in the center of mass.
- The mean energy carried away by the nucleons is about half of the incident energy or less in proton-proton collisions.
- The transverse momentum distribution of the nucleons is similar to that of the pions with a slightly higher average value.
- Nucleon resonances (isobars) are formed that can in their decay yield high momentum pions in the center of mass.
- In many ultrahigh energy cosmic ray interactions observed in nuclear emulsion the bulk of the produced pions appears to emerge from distinct emission centers, sometimes two such centers that are moving in opposite directions away from the center of mass, forming sometimes *jets* of particles. This clustering is evident from Duller-Walker plots of individual interactions shown in Fig. 3.20 (Duller and Walker, 1954; Perkins, 1960). It manifests itself upon transformation to the laboratory frame in the formation of two superimposed cones of particles, one

[19] Large p_t phenomena were unknown at that time.

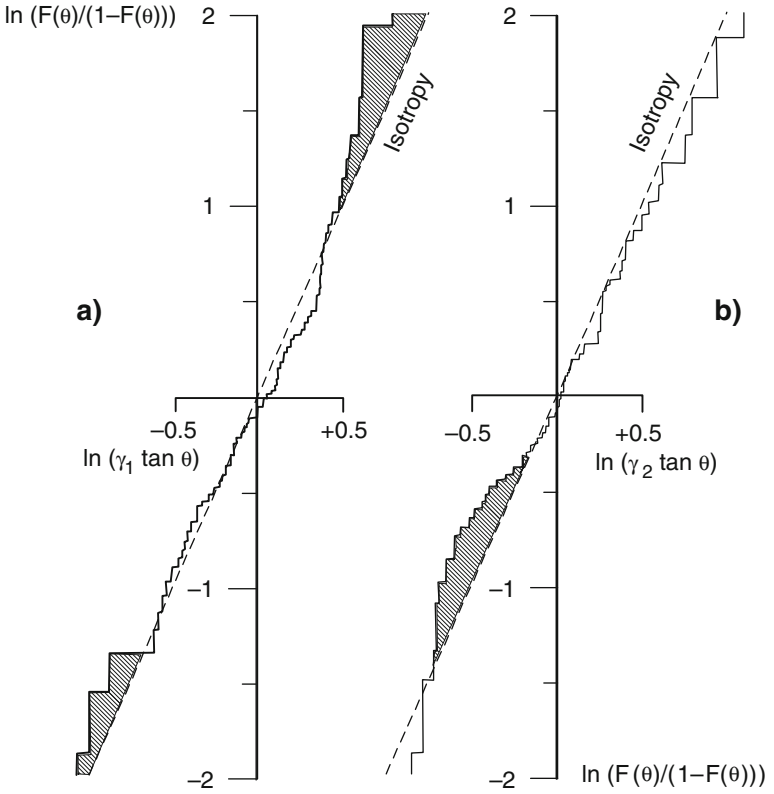

Fig. 3.20 Duller-Walker or F-T-plots of interactions (Duller and Walker, 1954). Shown are the composite integral angular distributions in individual cones of 7 events having a total of 70 tracks with ≤ 5 heavy prongs; (**a**) applies to forward cones, (**b**) to backward cones. $F(\theta)$ is the fraction of secondaries emitted within an angle $\leq \theta$ in the laboratory frame w.r.t. the incident momentum vector. From plots of $\ln(F(\theta)/(1-F(\theta)))$ vs $\ln(\tan\theta)$, the Lorentz factor of the center of mass of the event, γ_{CM}, is found, where $\gamma_{CM} \simeq \langle \ln \tan\theta \rangle$ (Castagnoli et al., 1953). A distribution along the *dashed line* corresponds to isotropic emission of secondaries. The *shaded areas* show regions of clustering. In (**a**) there is a forward and backward clustering, in (**b**) one that is in the backward hemisphere near the central region (after Gierula et al., 1961)

with a narrow the other with a large opening angle, that emerge from the interaction point in the direction of the incident momentum vector. In some cases the cones are directly observable under the microscope in the emulsion. The process of clustered pion production is called *pionization* and led to the concept of *fireballs*.[20]

- Correlation analyses of collider data show that in particular representations the pion distribution has two broad peaks near zero in the center of mass (when plotted versus rapidity or pseudo-rapidity, defined in Sect. 3.10.4), with a dip

[20] In some cases the reconstruction of an event suggested a single emission center.

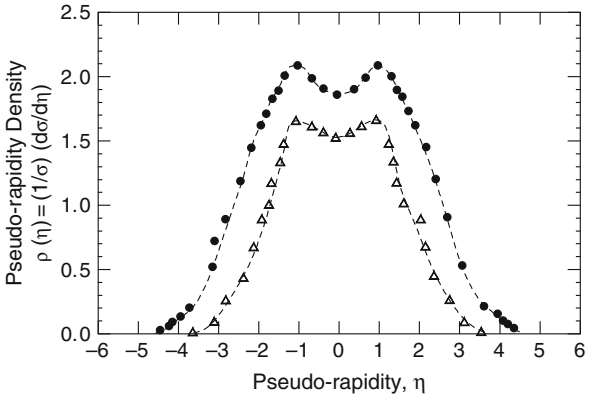

Fig. 3.21 Pseudo-rapidity density distribution obtained from inelastic proton–proton collisions at the CERN ISR at $\sqrt{s} = 23\,\text{GeV}$ (△) and $\sqrt{s} = 63\,\text{GeV}$ (•) (Bellettini et al., 1973). The characteristic shape of the distribution with the two humps and dip in the center is called the *seagull effect* (for details see Foà, 1975)

at zero. This is called the *seagull effect* because of the shape of the distribution profile, as shown in Fig. 3.21 (see also Thomé et al., 1977 for further ISR data at CM-energies of 23.6 and 45.2 GeV; Alner et al., 1986 for $\overline{p}p$-data from the UA-5 experiment at CM-energies from 200 to 900 GeV; Abe et al., 1990 for CDF data at 630 GeV and 1.8 TeV CM-energy). The seagull effect had first been observed at relatively low energies in 10 GeV/c π^- p-reactions by Bardadin-Otwinowska et al. (1966).

The facts listed above were the foundation of the *first generation of interaction models*. The following brief summary is by no means a complete catalog of models. It is simply an overview of some of the more important interaction handling and particle production formulations that were frequently used in the past which reproduce the physical reality with adequate accuracy. Included, too, is a list of latest generation models, often referred to as so-called event or particle generators. These include relevant new phenomena and structures that have been discovered in recent collider experiments.

The last item in the above list of characteristics of high energy interactions, the pionization, led to the early forms of *fireball models* that were not very satisfactory (Ciok et al., 1958; Cocconi, 1958; Gierula et al., 1960a, b, 1961; Miesowicz, 1971). It was the implementation of all the phenomena of the list which eventually led to the famous CKP model and formula of Cocconi et al. (1961, 1962), briefly outlined below. This model (or mathematical formulation) had been widely used in air shower simulations and in the planning of accelerator experiments. It is still being used today mostly for exploratory studies and estimations in extended versions that include the production of different kinds of particles because of its simplicity and relative accuracy.

A contemporary theoretical model describing high energy elastic as well as inelastic scattering processes and *multi-particle production* that should be mentioned but had not been used directly for hadron cascade simulations is the *Multi-Peripheral model* of Amati et al. (1962).

In a next step that included the concept of isobar formation in combination with pionization, Pal and Peters (1964) developed the well known *isobar-fireball model*. This model which can easily be used in a self consistent manner had been widely used in the past in extended versions to account for the production of particles other than just pions, e.g., kaons, nucleons and antinucleons, etc., to generate more realistic hadron cascades in sophisticated air shower simulations (e.g., Grieder, 1977, 1979a–h).

At about the same time the very successful *statistical* or *thermodynamic model*, developed chiefly by Hagedorn (Hagedorn model) for multi-particle production, surfaced.[21] The model evolved significantly over the years and was adapted to new experimental phenomena (Hagedorn, 1965; Hagedorn and Ranft, 1968; Hagedorn, 1980).

In 1969 Feynman proposed his *scaling model*, which found initially wide spread interest among cosmic ray and accelerator physicists because of its simplicity in the formulation and application (Feynman, 1969). It was widely used for the analysis of the CERN ISR data that became available in 1972, and still plays an important role. However, it is far oversimplified, disregards important phenomena and cannot describe the physical reality in its basic form over a wide energy range.

Of some significance is the concept of *limiting fragmentation*, introduced by Benecke et al. (1969), because it considers a rather striking feature which is frequently observed in high energy interactions. However it is not a global description of hadronic interactions. A variety of other models appeared in the late sixties and early seventies of the last century that were of short lived interest because they were oriented too much on specific processes and failed to describe particle production over a sufficient energy range.

In the following we will briefly outline the essence of the CKP and the isobar-fireball models partly for historic reasons and because the original papers are not readily available. We also summarize the Feynman scaling model and the concept of limiting fragmentation. The first three models had been used extensively in the past and can be regarded as landmarks in the evolution of air shower simulations. Limiting fragmentation is implemented in some versions of the isobar fireball model.

3.10.2 CKP-Model of Hadron Production

Until recently, the so-called CKP-model (Cocconi et al., 1961, 1962, 1966) was a very frequently used phenomenological model to handle high energy hadronic

[21] This model was actually first studied by Fermi (1950, 1951, 1953, 1954), Heisenberg (1949a, b), Landau and Pomeranchuk (1953a, b), and Belenkii and Landau (1956).

interactions, to compute the multiplicity of secondaries and the momenta of the produced particles. For years it was one of the backbones of air shower simulations until the new generation of more detailed and sophisticated models were introduced more than a decade ago, that are listed in Sect. 3.10.2 above. But it also played a significant role whenever predictions for experiments with new accelerator or colliders in hitherto unexplored energy domains were needed. The mathematical form is simple and well suited for Monte Carlo simulations. The original work and the basic relations of the CKP model with the arguments in support of it had been summarized in the early seventies in a form that was trimmed specifically for applications at the CERN ISR (Cocconi, 1971).

The CKP-model draws on all the early phenomenological facts that are listed in itemized form in Sect. 3.10.1 above, except that it does not include particular structures. It disregards in its most simple form the production of secondaries other than pions. However, in later expanded versions the production of kaons, nucleons and antinucleons was incorporated. The model has proved to be quite accurate in the description of hadronic interactions over a very wide range of energies.

Nucleon–Nucleon Interactions: Following Cocconi et al. (1961, 1962, 1966), the joint probability, P, of obtaining a pion with a laboratory energy, E, and a transverse momentum, p_t, is given as

$$P(E, p_t) \;=\; f(E)\, g(p_t), \tag{3.31}$$

provided that p_t is independent of E. This applies if $E \gg p_t c$, which applies if $E > 1$ GeV. Inserting for the transverse momentum distribution the Boltzman distribution and fitting $f(E)$ as an exponential, one obtains

$$P(E, p_t)\,\mathrm{d}E\,\mathrm{d}p_t \;=\; \frac{1}{p_0^2 T}\, e^{-(E/T)}\; p_t\, e^{-(p_t/p_0)}\,\mathrm{d}p_t\,\mathrm{d}E\,(E < E_0) \tag{3.32}$$

for 1 GeV$< E < E_0$, and T is the *mean pion energy* [GeV] of a spectrum extending to infinity ($E \to \infty$).

Since $T \ll E_0$, E_0 and p_0 being the incident proton energy and momentum, the pion energy averaged over the entire spectrum ($0 \le E \le E_0$) is about T.[22] In addition, numerous experiments have confirmed that the secondary pion multiplicity, n_π, including all charge states, grows approximately with a power law of the form

$$n_\pi \;=\; a\, E_0^{(1/4)}, \tag{3.33}$$

with $a = 2.7$. Since $n_\pi T = K_p E_0$, where K_p is the *inelasticity* of nucleon initiated interactions, it follows that

$$T \;\propto\; E_0^{(3/4)}. \tag{3.34}$$

[22] In the initial formulation of the CKP model it was assumed that all secondaries are pions.

Under the assumptions stated above ($E,\ pc \gg p_t c$) (high energy approximation) one gets for the emission angle in the laboratory, θ, the following expression,

$$\theta \ \approx \ \sin(\theta) \ = \ \frac{p_t}{p}, \tag{3.35}$$

and since $pc \approx E$

$$p_t \ \approx \ \frac{E}{c}\,\theta. \tag{3.36}$$

From these relations one obtains the expression for the particle flux, N_π,

$$\frac{\mathrm{d}^2 N_\pi(E,\theta)}{\mathrm{d}E\, d\Omega} \ = \ \frac{n'_\pi E^2}{2\pi p_0^2 c^2 T}\ \exp\left(-E\left(\frac{1}{T}+\frac{\theta}{p_0 c}\right)\right)\ , \tag{3.37}$$

where n'_π is the effective pion multiplicity which corresponds to about one half of n_π, i.e.,

$$n'_\pi \ = \ a' E_0^{(1/4)} \ \text{with}\ a' = 1.35\ , \tag{3.38}$$

since only the *pions in the forward region* in the center of mass can contribute to the flux of high energy particles, in accordance with the approximation chosen for this derivation. Equation 3.37 can be rewritten in the form

$$\begin{aligned}\frac{\mathrm{d}^2 N_\pi(E,\theta)}{\mathrm{d}E\, d\Omega} \ &= \ \frac{n'_\pi T}{2\pi p_0^2 c^2}\left(\frac{E}{T}\right)^2 \exp\left(-(E/T)\left(1+\frac{\theta T}{p_0 c}\right)\right) \\ &= \left(n'_\pi\, T\right) f\left(\frac{E}{T}, \theta\, T\right)\ .\end{aligned} \tag{3.39}$$

This expression is a scaling law, which enables the calculation of the flux at one energy from that observed at another.

Pion–Nucleon Interactions: Pion initiated interactions are treated essentially in the same manner, using the same distributions as before for nucleons, except that in the most naive form the inelasticity, K_π, is set to unity ($K_\pi = 1.0$). Because of the large inelasticity the resulting total multiplicity, ν_π, is expected to be somewhat larger, namely

$$\nu_\pi \ = \ b\, E_0^{(1/4)} \ \text{with}\ b \approx 3.2. \tag{3.40}$$

Additional details concerning topics that are related to Monte Carlo simulations such as the handling of fluctuations and the production of secondaries other than pions are given in Chap. 20.

3.10.3 Isobar-Fireball Model

Another early model which, however, has some structure embedded is based on the concepts of isobar and fireball formation. The former concept was borrowed from relatively low energy accelerator experiments, where the formation of isobars was observed, that exhibit leading particle fragmentation (projectile and/or target fragmentation in the center of mass). The latter, the fireball (or pionization) concept, emerged from very high energy cosmic ray emulsion data that manifest an apparent clustering of the bulk of the produced secondaries at or near the center of the rest frame of the collision in many cases, as outlined in (a) above.

In its most simple form as it had been developed by Pal and Peters (1964), the model considers the formation of a single fireball that is essentially at rest in the center of mass, and of one or two isobars in the so-called fragmentation region, i.e., away from the center of mass. After decay into a pion (or pions for heavy isobars) and a nucleon, the one or two isobar system(s) can be regarded as projectile and/or target fragmentation. The energy dependence of the total multiplicity, $n_\pi(E)$, was given by the authors as

$$n_\pi(E) \;=\; 2Pn_B + n_0 E^\rho, \tag{3.41}$$

where P is the probability of baryon excitation (isobar formation) and n_B is the average number of mesons (pions) emitted in the isobar decay. From experiments it was found that in the multi-TeV range the quantity $2Pn_B = 4.75 \pm 0.25$. The term $n_0 E^\rho$ represents the creation of mesons in the pionization process, where the authors claim that $n_0 = 0.25$ and $\rho = 0.5$. Thus,

$$n_\pi \;=\; (4.75 \pm 0.25) + \frac{E^{(1/2)}}{4} \quad [E \text{ in GeV}]. \tag{3.42}$$

In pion initiated interactions only one isobar was expected to be produced and the model fitted to the then available data yields for the total secondary pion multiplicity, ν_π, the expression

$$\nu_\pi \;=\; Pn_B + \nu_0 E^{(1/2)} \quad [E \text{ in GeV}], \tag{3.43}$$

where $\nu_0 = 0.7$ and the pionization term has the same energy dependence as for pp-collisions.

In more elaborate versions of this model, nucleon and antinucleon production were handled via the decay of the central fireball, as a byproduct of pionization and later versions included two moving fireballs (Grieder, 1977).

3.10.4 Feynman Scaling Model

The variable called *rapidity*, briefly mentioned before in Sect. 3.6 in connection with the kinematic properties of produced particles is defined as

$$y = \frac{1}{2}\ln\left(\frac{E+p_\ell}{E-p_\ell}\right) = \ln\left(\frac{E+p_\ell}{\sqrt{p_t^2+m^2}}\right) \tag{3.44}$$

where E is the energy, m the mass and p_ℓ the longitudinal momentum in the direction of the incident momentum of a produced particle, p_t is the transverse momentum and $\sqrt{p_t^2+m^2}$ is sometimes referred to as the *transverse mass*, m_t. Furthermore, $p=\sqrt{p_\ell^2+p_t^2}$, $E=\sqrt{p_\ell^2+p_t^2+m^2}$ and

$$\frac{\partial y}{\partial p_\ell} = \frac{1}{E}. \tag{3.45}$$

Under Lorentz transformation from one inertial frame to another (center of mass to laboratory), where γ, β and E refer to the second frame ($\beta = v/c$), expression 3.44 takes the form

$$\begin{aligned} y' &= \ln\left(\frac{E'+p'_\ell}{\sqrt{p_t^2+m^2}}\right) \\ &= \ln\left(\frac{\gamma(E+\beta p_\ell)+\gamma(p_\ell+\beta E)}{\sqrt{p_t^2+m^2}}\right) = y+\ln\left(\gamma\,(\beta+1)\right). \end{aligned} \tag{3.46}$$

This implies that a rapidity distribution in one Lorentz frame transformed into another, parallel moving frame, remains the same, except that the distribution is simply shifted in rapidity space by the constant

$$\ln\left(\gamma(\beta+1)\right). \tag{3.47}$$

The Lorentz *invariant inclusive cross section* for the production of secondary particles in a high energy hadronic interaction, $d^3\sigma/(dp^3/E)$, after integration of the phase space over the azimuthal angle, is given by the expression

$$\frac{E\,\mathrm{d}^3\sigma_{\mathrm{inel}}}{\mathrm{d}p^{\,3}} = \frac{E\,\mathrm{d}^2\sigma_{\mathrm{inel}}}{\pi\,\mathrm{d}(p_t^2)\,\mathrm{d}p_\ell} = \frac{\mathrm{d}^2\sigma_{\mathrm{inel}}}{\pi\,\mathrm{d}(p_t^2)\,\mathrm{d}y} = f(x,\,p_t,\,s), \tag{3.48}$$

where s is the center of mass energy squared and x, called the Feynman variable or Feynman-x, is the fraction of the maximum available longitudinal momentum in the center of mass, $p_{\ell,\mathrm{CM}}$, defined as

$$x = \frac{p_{\ell,\mathrm{CM}}}{p_{\ell\,\max,\mathrm{CM}}} = 2\left(\frac{p_{\ell,\mathrm{CM}}}{\sqrt{s}}\right). \tag{3.49}$$

The Feynman hypothesis which is the foundation of the Feynman scaling model (Feynman, 1969) states that in the limit, at very high energies ($s \gg M_p$, where M_p is the proton mass), the invariant cross section expressed in the variables x and p_t becomes asymptotically independent of the energy, E. Thus,

$$\lim_{s\to\infty} f(x, p_t, s) = \overline{f}(x, p_t). \tag{3.50}$$

Consequently it follows that

$$\frac{E\,\mathrm{d}^3\sigma_{\mathrm{inel}}}{\mathrm{d}p^{\,3}} = \frac{\mathrm{d}^2\sigma_{\mathrm{inel}}}{\pi\,\mathrm{d}(p_t^2)\,\mathrm{d}y} = \overline{f}(x, p_t). \tag{3.51}$$

This distribution is valid for all particles, however, different kinds of particles have in general different functions $\overline{f}(x, p_t)$. Experimental data show that this function can be written as

$$\overline{f}(x, p_t) \simeq f_x(x) \cdot f_t(p_t), \tag{3.52}$$

but it is a poor approximation.

On the grounds of plausibility arguments, $f_x(x)$ is taken as a constant, C, for small values of x, i.e., $x \le M_p/\sqrt{s}$. This leads to the expression

$$\mathrm{d}^2\sigma_{\mathrm{inel}} = \pi f_t(p_t)\,\mathrm{d}(p_t^2)\,C\,\mathrm{d}y. \tag{3.53}$$

After integration over p_t we get

$$\frac{\mathrm{d}\sigma_{\mathrm{inel}}}{\mathrm{d}y} = \text{const.}, \tag{3.54}$$

which shows that for small x the cross section σ is independent of the rapidity y (see Fig. 3.14). Under this approximation the angular distribution takes the form

$$\frac{\mathrm{d}\sigma_{\mathrm{inel}}}{\mathrm{d}\Omega} = \frac{\mathrm{d}\sigma_{\mathrm{inel}}}{\mathrm{d}y}\left(\frac{\mathrm{d}y}{2\pi\,\sin(\theta_{CM})\,\mathrm{d}\theta_{CM}}\right) \simeq \text{const.}\left(\frac{1}{\sin^2(\theta_{\mathrm{CM}})}\right). \tag{3.55}$$

If $E\,\mathrm{d}^3\sigma_i/\mathrm{d}^3p$ represents the invariant cross section for one kind of particles, then we get upon integration for the total cross section for this kind of particles,

$$n_i\sigma_i = \int \frac{\mathrm{d}^3\sigma_i}{\mathrm{d}p^3}\,\mathrm{d}^3p = \int \overline{f}(x, p_t)\left(\frac{\mathrm{d}^3p}{E}\right), \tag{3.56}$$

and for the total multiplicity we get

$$n_i \;=\; \left(\frac{\pi}{\sigma_i}\right) \int \frac{\overline{f}(x,\, p_t)\, \mathrm{d}^2 p_t\, \mathrm{d}p_\ell\, (1/2)\sqrt{s}}{E\,\sqrt{(s/2)}} \;\simeq\; a\, \ln\left(\frac{s}{m^2}\right) + b. \tag{3.57}$$

Thus, the multiplicity grows logarithmically with energy. The constants a and b are as follows.

$$a \;=\; \left(\frac{\pi}{\sigma_i}\right) \int \overline{f}(0,\, p_t^2)\, \mathrm{d}(p_t^2) \quad \text{and} \tag{3.58}$$

$$b = \frac{\pi}{\sigma_i} \left(\int \left(\overline{f}(x,\, p_t) - \overline{f}(0,\, p_t)\right) \frac{\mathrm{d}x}{x}\, \mathrm{d}p_t^2 - \int \overline{f}(0,\, p_t) \ln\left(1 + \frac{p_t^2}{m^2}\right) \mathrm{d}(p_t^2) \right) \tag{3.59}$$

and m is the mass of the particles under consideration.

The Feynman scaling model relations summarized here had been used frequently in one form or another mostly for simplified air shower simulations (see Chap. 20 for more details concerning Monte Carlo simulation).

Frequently, *pseudo-rapidity*, η, is being used in place of rapidity. It is a convenient variable to approximate rapidity if the mass and momentum of a particle are unknown, a situation that is encountered particularly in the analysis of interactions in nuclear emulsion. It is defined as

$$\eta \;=\; -\ln[\tan(\theta/2)], \tag{3.60}$$

where θ is the scattering angle.

3.10.5 Fragmentation and Limiting Fragmentation

The concepts of *fragmentation* and *limiting fragmentation* grew out of experimental facts that are observed in high energy hadronic collisions, predominantly in nucleon–nucleon collisions, when the multiplicity is relatively low (Wu and Yang, 1965; Benecke et al., 1969; Chou and Yang, 1970). Such events in which few secondary pions are produced that have a very high energy in the laboratory frame and, as is usual for all high energy collision products, have small values of transverse momenta, cannot be well described by fireball or CKP models. It appears rather that the few fast pions are closely correlated with the projectile nucleon, i.e., it looks as if they are *fragments* of the latter. This concept is related to *diffraction dissociation*, mentioned earlier. In the center of mass, for reasons of symmetry, projectile and/or target fragmentation occur, but the target fragments are energetically of no concern in the laboratory frame.

We will not elaborate on this picture as it only describes part of today's understanding of the phenomenology of high energy hadronic interactions. However, the particles in the narrow angle forward cone are of great significance in the

development of air showers as they are the principal carriers of the energy and determine to a good extent the longitudinal development of air showers.

For the target region of a collision and under consideration of Feynman's hypothesis we can write for the invariant cross section,

$$\frac{E_{\mathrm{CM}}\,\mathrm{d}^3\sigma}{\mathrm{d}{p_{\mathrm{CM}}}^3} \;=\; \frac{E_L\,\mathrm{d}^3\sigma}{\mathrm{d}p_L^{\,3}} \;=\; \overline{f}(x,\,p_t), \tag{3.61}$$

where E_{CM} and E_L are the center of mass and laboratory energies, respectively, and p_L is the laboratory momentum. If E_0 is the energy of the incident particle in the laboratory and m_T the target mass, then we can write for the center of mass energy squared

$$s \;=\; 2m_T E_0 + m_T^2 \;\approx\; 2m_T E_0 \tag{3.62}$$

and for the longitudinal momentum of the particle in the laboratory

$$p_{\ell,L} \;=\; \gamma_{\mathrm{CM}}(p_{\ell,\mathrm{CM}} - \beta E_{\mathrm{CM}}) \;=\; \sqrt{\frac{E_0}{2m_T}}\left(p_{\ell,CM} - \beta E_{\mathrm{CM}}\right), \tag{3.63}$$

where γ_{CM} is the Lorentz factor of the center of mass in the laboratory,

$$\gamma_{\mathrm{CM}} \;=\; \frac{E_0}{\sqrt{s}} \;=\; \sqrt{\frac{E_0}{2m_T}}\;. \tag{3.64}$$

For the high energy approximation we can write

$$E_{\ell,\mathrm{CM}} \;\simeq\; p_{\ell,\mathrm{CM}}\left(1 + \frac{m^2 + p_t^2}{2(p_{\ell,\mathrm{CM}})^2}\right) \quad \text{and} \tag{3.65}$$

$$x \;=\; \frac{2p_{\ell,CM}}{\sqrt{2m_T E_0}}\;. \tag{3.66}$$

Inserting Eqs. (3.65) and (3.66) into Eq. (3.64) leads to the following expression,

$$p_{\ell,L} \;\simeq\; \frac{1}{2}\left(x\,m_T - \frac{m^2 + p_t^2}{x\,m_T}\right) \;=\; g(x,\,p_t). \tag{3.67}$$

Solving Eq. (3.67) for x yields $x = x(p_{\ell,L},\,p_t)$, and Eq. (3.61) can be rewritten as

$$\frac{E_L\,\mathrm{d}^3\sigma}{\mathrm{d}p^{\,3}} \;=\; \overline{f}(x(p_{\ell,L},\,p_t),\,p_t) \;=\; \overline{\xi}(p_{\ell,L},\,p_t). \tag{3.68}$$

From this it follows that in the target region, under the postulated approximation, the momentum distribution of the particles, m, is independent of the incident energy

and the nature of the projectile. Analogously, for reasons of symmetry the same arguments apply to the particles in a frame of reference where the projectile is at rest. Bellettini et al. (1973) and other authors carried out experiments at the CERN ISR to test the hypothesis of *limiting fragmentation*.

3.11 Models of High Energy Interactions: II. Modern Models

3.11.1 General Comments

During the last twenty years, partly as a result of new knowledge acquired in experiments with the accelerators and colliders at CERN, FNAL, RHIC, KEK, DESY and SLAC, and partly because of new theoretical ideas and concepts, many new semi-empirical models, so-called *event generators*, had been developed to describe and simulate high energy interactions and particle production. Some of these models are trimmed to handle mainly the high and ultrahigh energy regime, extrapolating interaction physics well beyond collider capabilities while others focus on the well explored low energy domain, in an effort to describe the sub-GeV to a few 100 GeV regime more accurately, and some attempt to cover the entire energy range. These models and the corresponding program packages were designed partly for Monte Carlo based air shower simulations but also for accelerator and collider data interpretation and predictions. They treat the interactions on a more fundamental level than the previous generation of models, accounting for a number of new phenomena and theoretical predictions.

Most of the packages are not stand-alone air shower simulation programs but are intended to be incorporated in such as interchangeable plug-in particle production sub-packages, to compute the parameters of the secondaries emerging from the hadronic interactions. Thus, they can be used in conjunction with programs such as CORSIKA (Heck, 2001; Heck and Knapp, 2002, 2006), its forerunner, ASICO (Grieder, 1977, 1979a), and other code packages that are structured full-fledged air shower simulation program systems. They can replace previously used sets of subroutines that describe particle production mechanisms (Knapp et al., 1996).

3.11.2 Parton, Mini-Jet, Quark-Gluon-String and Gribov-Regge Concepts

Several of the modern high energy interaction and particle production models or event generators, such as the DPMJET, QGSJET, VENUS, NEXUS and EPOS models are quite similar. Most employ in one way or another Gribov-Regge theory (Gribov, 1968, 1969, 1970). They treat soft interactions by the exchange of one or several Pomerons, handle elastic scattering alike but differ in the treatment of inelastic processes. The latter are handled by cutting Pomerons, thus producing two

color strings per Pomeron which subsequently fragment into color-neutral hadrons. Nucleus–nucleus collisions are treated by tracking the participating nucleons (partons) in the projectile as well as in the target particle. The parameters and distributions (amplitudes) used in the different models are chosen such that they describe well the accessible accelerator and collider data to the highest energies and give good fits to the experimental results. Beyond they are used as extrapolations with corresponding uncertainties.

One of the problems with model verification is that the group of the most energetic secondaries escape detection in collider experiments because the forward cones are not instrumented. This lack of detailed knowledge on such an important part of the interaction leaves important questions unanswered and serious uncertainties remain for the complete event reconstruction and interpretation, and hence for model design and formulations. Moreover, it is just this group of particles that plays the most important role in air showers as it contains the main energy carriers in a shower that determine to a great extent the longitudinal development.

In air shower simulations the application of the high energy models is carried many orders of magnitude beyond the "bonafide" energy range where they had been tuned and tested to reproduce accelerator and collider results, into massively extrapolated regions. There, the above mentioned shortcomings trouble the interpretation of experimental air shower data, particularly with respect to primary mass determination.

In comparison to the previous generation of event generators that dealt directly with the full palette of hadrons, the modern models operate on a deeper, more refined level and employ the concepts of *quarks* and *gluons* (*partons*), and *Pomerons* in conjunction with the *optical model* to handle nucleon–nucleus and nucleus–nucleus interactions. They are based on *quantum chromodynamics* (QCD) and include phenomenological aspects, too, such as *mini-jets* and other phenomena.

In spite of the high degree of refinement and the inclusion of the deeper theoretical insights that we have acquired in recent years in the domain of hadronic processes, the modern models are not based on a self consistent theory of hadronic interaction; we are still far from having such a theory. The theoretical details of the current models are very complex and will not be discussed here. A number of outstanding papers and reviews are available that offer any degree of detail concerning the modern physics of high energy hadronic interactions (e.g., Werner, 1993; Ranft, 1995; Kalmykov et al., 1997; Ostapchenko, 2006a, b, c, e; Drescher et al., 2001; Werner et al., 2006, and references listed therein).

Likewise, extensive reports are available where the specific handling of the interactions within the framework of a particular model (event generator) and its construction are discussed. The references are given in Sect. 3.11.3 below, where the most popular current event generators are listed. The computer program packages of the event generators can easily be implemented in an existing air shower simulation program without the need for detailed knowledge of the physics behind them.

3.11.3 Catalogue of Modern Shower and Interaction Models, and Event Generators

Interaction models and event simulation methods are among the fastest evolving branches of air shower research. In the following we list the presently most popular event generators and program packages that are used in air shower studies together with the corresponding references that offer detailed descriptions of the physics involved and instructions for use by third parties. Some of the event generators listed here have evolved in the meantime to actual cascade and air shower simulation code packages and their classification according to the applicable energy range may no longer apply. In view of the rapid development of the field the summary presented here must be regarded as a partial account. The interested reader is therefore referred to the latest conference proceedings and web articles.

For most packages step-by-step descriptions exist to run them. The program packages, some of which are also used by the accelerator physics community, are generally known under their *acronyms*. Note that for air shower simulations most investigators use different hadronic interaction models (event generators) within the frame of an entire shower simulation program structure, each of which handles a particular energy domain, to cover the enormous energy range which hadrons populate within a shower, from the first interaction down to the observation level. In general two models are being used, one that treats the low energy domain from about 0.1 GeV to anywhere between 100 GeV and 10 TeV, and one that covers the region beyond.

Low-Energy Models

- FLUKA – A FORTRAN based Monte Carlo hadronic event generator, originally intended to describe inelastic interactions at laboratory energies below several 100 GeV (FLUKA, 2006). Different interaction sub-models are being used within this package to handle the collisions in the domain below, around and above the nuclear resonances (Aarnio et al., 1987; Fassò et al., 2001; Battistoni et al., 2003a, b, 2004).

  In recent years FLUKA had been generalized and can now be used to simulate hadronic and electromagnetic interactions, and cascades. Photons and electrons from 1 keV to thousands of TeV, neutrinos, muons of any energy, and hadrons of energies up to 20 TeV can be handled. It can be used to study the detector response of particle physics, cosmic ray and space bound experiments, for medical applications, radiation shielding and to investigate low energy air showers.

  The hadronic interaction models are based on resonance production and decay below a few GeV, and on the Dual Parton Model above. For hadron–nucleus interactions at momenta below 3–5 GeV/c an Intra-Nuclear Cascade model (GINC) is used, followed by a pre-equilibrium stage, while the high energy collisions are treated with the Gribov-Glauber multiple collision mechanism. Both

domains are followed by equilibrium processes that include evaporation, fission, Fermi break-up, and gamma de-excitation.

FLUKA can also simulate photonuclear interactions. Ion initiated nuclear interactions are treated through interfaces to external event generators. For neutrons with energy less than 20 MeV down to thermal energies FLUKA uses its own neutron cross section library, derived from recent data (Aiginger et al., 2005; Ballarini et al., 2005).

- GEANT4 – A full C++ Monte Carlo code, originally designed to study calorimeter responses, simulates the hadronic and electromagnetic interactions of particles with matter (GEANT, 1995; Agostinelli et al., 2003). The energy range of validity depends on the physics and particles considered and extends roughly from 250 eV to 10 TeV. Like FLUKA, it had been upgraded and can now also be used to simulate low energy air showers.

  Depending on the simulation needs and the energy range, numerous interaction models are available. For the interactions of hadrons with nuclei at energies above 10 GeV different parton-string models are available, while below Intra-Nuclear Cascade Models can be used. Data driven models based on the GHEISHA package can also be used to simulate hadron–nucleus interactions. Nuclear interactions of ions with nuclei can be treated up to 10 GeV/nucleon. For neutron interactions from thermal energies up to 20 MeV the Neutron High Precision Model based on the evaluated nuclear data files can be used (Aiginger et al., 2005; Ballarini et al., 2005).

- GHEISHA – This event generator (Fesefeldt, 1985) was originally used in the Monte Carlo detector response and test program GEANT, developed at CERN. Its purpose was to simulate interactions of different particle beams in various targets (GEANT3) to help plan and study future experiments (Brun et al., 1987; CERN, 1993, 1994; Allison et al., 2006). GHEISHA 600 had been adapted for applications within the COSRSIKA air shower simulation program in conjunction with different high energy interaction model packages. In the most recent version GHEISHA 2002 (Heck, 2006) some bugs with respect to energy and momentum conservation had been eliminated with correction patches (Cassel and Bower, 2002, private communication to D. Heck).
- UrQMD – An event generator that describes microscopically the projectile transport through an air target in steps of approximately 0.2 fm. It follows collisions and scattering on the hadron level and handles nuclear resonances in detail (Bass et al., 1998; Bleicher et al., 1999). Because of its very refined treatment of the interactions the c.p.u. time requirements diverge at high energies and limit the applicability of this program package. The acronym stands for *Ultra-relativistic Quantum Molecular Dynamics*.

High-Energy Models

- HDPM – A phenomenological model for hadron production based on detailed parameterizations of $\overline{p}p$ collider data for particle production. It is adapted to

handle hadron–nucleus interaction and energies well beyond collider capabilities. The superposition principle is used to handle nucleus–nucleus interactions and Glauber theory for the cross sections (Capdevielle, 1989; Capdevielle et al., 1992 and references listed therein; see also Capella and Krzywicki, 1978; Capella and Tran Thanh Van, 1981; Capella et al., 1994).

- SIBYLL – An efficient event generator for simulating atmospheric cascades at ultrahigh energies. It is based on mini-jets (Gaisser and Halzen, 1985), handles hadron–hadron and hadron–nucleus interactions, and incorporates features of the Lund model (Andersson et al., 1983). Emphasis is given to the fragmentation region and to mini-jet production. For nucleus-nucleus collisions the superposition model is used. SIBYLL is operational up to about 10^{11} GeV (Engel et al., 1992; Fletcher et al., 1994; Engel et al., 1999; Engel, 2001, 2006). It is mainly used in connection with the MOCCA and AIRES codes.
- VENUS – A model to handle *Very Energetic NUclear Scattering*. It handles interactions of hadrons and nuclei based on GRT and accounts for interactions of intermediate strings and secondary hadrons. Charmed particle production is optionally available. It is suited to handle nucleus–nucleus collisions. As it does not contain minijet production, the energy range should be limited to $\leq 2 \cdot 10^7$ GeV (Werner, 1993, and references listed therein).
- NEXUS – An event generator developed partly by the architects of VENUS and QGSJET that supersedes the VENUS and QGSJET packages. It describes high energy interactions from e^+e^- to nucleus–nucleus collisions. The basic interaction mechanisms in NEXUS are parton ladders, calculated as a hard scattering process with corresponding initial and final state evolution of partons. (Drescher, 1999; Drescher et al., 1999; Bossard et al., 2001).
- EPOS – A phenomenological event generator based on the parton model that is essentially a further development of NEXUS model (Werner et al., 2006; Pierog and Werner, 2007).
- DPMJET – A model to handle particle production in hadron–hadron, hadron–nucleus and nucleus–nucleus collisions that is based on GRT. It also accounts for mini-jet production and charmed particles (Ranft, 1995, 1999a, b, and references listed therein).
- QGSJET – Semi-empirical models based on GRT and accounts for mini-jet production. The model is operational up to about 10^{12} GeV (Kaidalov, 1982; Kaidalov and Ter-Martirosyan, 1982; Kalmykov et al., 1997). In a recent update to QGSJET II nonlinear interaction effects – so-called enhanced Pomeron diagrams – are included and proved to be important for a correct extrapolation to the highest energies (Ostapchenko, 2006a, b, d, e).

For completeness we should also mention the *energy splitting algorithm*, sometimes referred to as the HSA model (Hillas, 1981a, b, 1997). It is used by default as low energy model in the AIRES air shower code (Sciutto, 1999a, b, 2001) and had been coupled for test purposes with CORSIKA to compare it with other low energy models (Heck, 2006). This algorithm does not contain any physical processes, it only generates an approximately flat rapidity distribution of the secondaries (usually

pions only) and follows therefore naive Feynman scaling. The method is only useful for exploratory investigations. Because of its simplicity it requires very little computing time and can be used for coarse studies of air showers at the highest energies.

A similar crude code that was designed for speedy computations of ultra high energy showers and meant to be used for rough exploratory work is MOCCA (MOnte Carlo CAscade). It comes in different versions (MOCCA 92, and more recent) and uses the *thin sampling technique* for low energy particles. Newer versions can also be linked with more refined external event generators for more realistic simulations but lose then the only advantage, speedy computation (Hillas, 1981a, b, 1997). Since MOCCA is written in the somewhat more exotic program language PASCAL it had been rewritten by Sciutto (1999a, b) in FORTRAN under the name AIRES.

Very recently, a somewhat similar but more elaborate procedure to handle the hadron cascade very efficiently, using only very few basic average characteristics of hadronic collisions without going into the details of particle physics processes, was proposed by Matthews (2001, 2005). It is a semi-empirical model that is based on the so-called *Heitler splitting approximation* of electromagnetic cascades (Heitler model). According to the author, the model yields reasonable results and can be used to investigate common shower observables at the highest energies.

The merits and deficiencies of the different program packages listed here, in particular for application in complete air shower simulation program packages, such as CORSIKA, were summarized by Heck (1997) and more recently with particular focus on the high energy (Heck et al., 2003) and the low energy models by the same author (Heck, 2006). This author concludes after a careful analysis of the results of the different event generators separately and within the frame of the CORSIKA code that the GHEISHA and HSA codes do not yield satisfactory results.

In an overall investigation involving different combinations of low and high energy models (GHEISHA, FLUKA, DPMJET, SIBYLL and QGSJET) within the framework of CORSIKA in conjunction with a variety of observables of the KASCADE calorimeter (Engler et al., 1999; Antoni et al., 2003). Milke et al. (2006) conclude that the differences resulting from the different low energy models are small compared to those between the high energy models. In particular, these authors note significant discrepancies between the DPMJET 2.55 and SIBYLL 2.1 models on one hand and the QGSJET model on the other.

Some of the event generators (models) mentioned above were also investigated in the context of physics at RHIC (Bass et al., 1999; Drescher, 1999; Drescher et al., 1999; Eskola, 2002). Most packages are frequently updated by their authors. Additional information on these and other program packages is given in Chap. 20 where air shower simulations are discussed.

Irrespective of the details contained in the most recent models and the apparent success which their authors claim they have in the description of the physical processes, there remain major problems. This is not surprising if one considers the disparity in energy where the so-called *anchor points* of the models had been fixed, i.e., the energy where the different parameters which govern the distributions that describe the fundamental processes had been adjusted, usually at the highest

accelerator or collider energies available, and the energy where the models are actually being used.

The degree of extrapolation required to handle the first or first few interactions of an ultrahigh energy primary initiating a shower in the atmosphere with respect to the highest energy where the models had been calibrated is usually very large, frequently many orders of magnitude. The consequences of incorrect treatment of the first few interactions that are of paramount importance for the shower development can be very serious. These surface most seriously when tackling the problem of extracting the primary mass composition from ground based air shower data in conjunction with simulations.

The particular problem that arises is that when correlating different observables, different primary compositions and energy dependencies of the composition result. This problem is discussed in more detail in Sect. 11.7 and in Chap. 20. It has its roots in the earlier mentioned ambiguities owing to the fact that variations in the cross section, the multiplicity, the inelasticity and the primary mass affect ground level shower observables alike.

A large number of phenomenological models had been developed over the years, ranging from the purely analytical one- and three-dimensional versions with ever increasing complexity (see Gaisser, 1992, for a summary) to the modern highly refined and sophisticated multi-dimensional Monte Carlo simulations that require high speed computers. Great progress has been achieved so far, but much work is still required. The remaining problems are summarized in the Collected Contributions to the NEEDS Workshop, held at Karlsruhe (Germany) in April 2002 (NEEDS, 2002) and in the Proceedings of the XII and XIII. International Symposia on Very High Energy Cosmic Ray Interactions (ISVHECRI), held at CERN, Geneva (Switzerland) in July 2002 (Pattison et al., 2003, section "NEEDS Workshop Discussion") and in Pylos (Greece) in September 2004 (Grieder et al., 2006) (see also Costa, 1998; Prague Workshop, 2005).

3.12 Hadron Cascades

3.12.1 Phenomenology of Hadron Cascade Process

A hadron cascade is initiated by a high energy hadron that undergoes a series of successive inelastic collisions while propagating in a target medium, e.g., the atmosphere, producing in each collision an energy dependent number of secondaries of all kinds (pions, kaons, nucleon and antinucleon pairs, hyperons and antihyperons, charmed particles, etc., depending on the energy that is available), until its energy falls below the one-pion threshold. The secondaries emerging from the first and all the subsequent higher generation collisions behave alike until their energy is exhausted.

The transverse momenta acquired by the secondaries cause the particles to spread laterally as they propagate in the target. As the cascade develops longitudinally,

penetrating deeper and deeper into the target, the particles are less and less energetic since the energy of the initiating particle is split and redistributed among more and more participants.

Besides the energy of the initiating particle that is primarily responsible for the longitudinal and lateral growth and decay of a hadron cascade, the geometry, i.e., the spatial extent of the cascade depends strongly on the density of the target (gas, liquid, solid), but also on its composition (chemical, isotopic) and on the evolving projectile particle mix in the cascade. The latter depends on the energy and to some extent on the mass of the initiating particle.

Many of the produced secondaries are unstable particles, such as pions, kaons and charmed particles, that are subject to decay or interaction. Consequently, the composition of the particle population in the cascade changes as it propagates in the target and the different constituents propagate differently. Interlaced with the hadron cascade are a large number of electromagnetic or photon–electron cascades, muons that result from the decay of hadrons and neutrinos which escape detection.

The neutral pions that are co-produced with all the other kind of particles are the main contributors to the electromagnetic channels. They decay almost instantaneously ($\tau_0 = 8.4 \pm 0.6 \cdot 10^{-17}$s at rest) after creation in the hadronic interactions into gamma rays, which initiate the electromagnetic sub-cascades.

In Figs. 3.22 and 3.23 we show photographs of cascades of different energy that were recorded with the large cloud chamber at Ootacamund, India (2,200 m a.s.l., 800 g cm^{-2}). The chamber measures 2 × 1 m and has a height of 1.5 m. It consists of 21 iron plates of 1.8 cm thickness that are arranged in horizontal position, one above the other, and spaced 2.8 cm from each other. For vertical trajectories across the chamber this corresponds to nearly 290 g cm^{-2} of absorber or $\sim$ 2.2 i.m.f.p. for nucleons and to $\sim$ 21 radiation lengths for electromagnetic processes (Vatcha et al., 1972). Each event shows a hadron cascade with the associated electromagnetic shower.

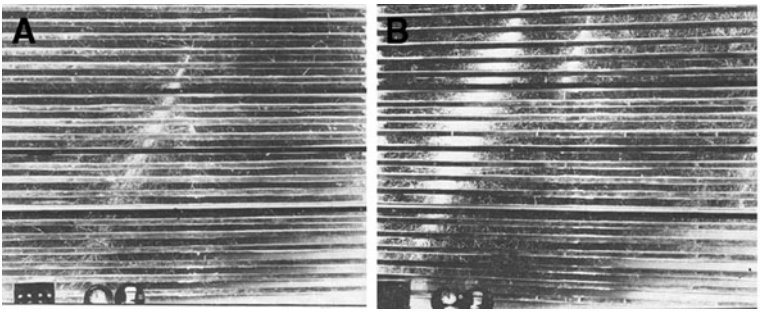

Fig. 3.22 Examples of high energy cascades in a multi-plate Wilson cloud chamber. *Figure A*: A typical cascade which starts in the fourth plate of the chamber. It is often possible to count the number of tracks at all stages of development and absorption and to obtain the integral track length. The energy of the cascade is 200 GeV. *Figure B*: Shown is a cascade which develops from the first plate of the chamber and shows a rapid absorption after its maximum development. The width of the cascade is related to the energy of the initiating particle and is used in one of the methods of energy determination. In this case the energy estimate is 750 GeV (Vatcha et al., 1972)

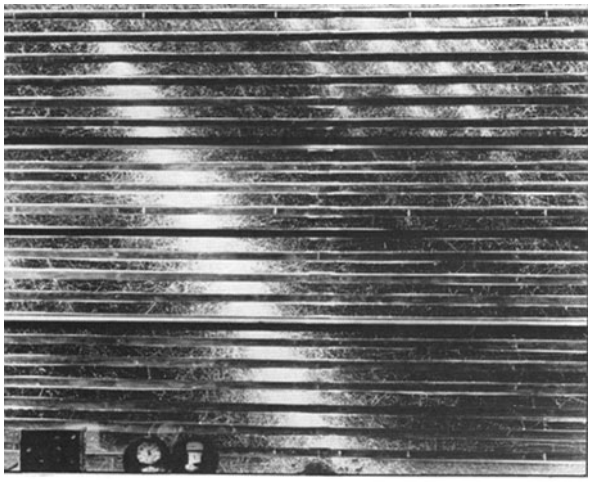

Fig. 3.23 Cascade with an elongated tube-like structure which is not completely absorbed, even after 20 radiation lengths. The estimated energy is 2.4 TeV (Vatcha et al., 1972)

The mean life of an unstable particle in vacuum depends on its kinetic energy or Lorentz factor, γ, and likewise the path length that it can travel on average before decaying. On the other hand, when propagating in a medium the particle has a certain probability per unit path length to undergo an interaction with a target nucleon or nucleus. This situation is illustrated in Fig. 3.24 where we show both, the mean decay length, $L_{X,V}$ [m], in vacuum of charged pions, kaons and some charmed particles as a function of the Lorentz factor, γ, and the corresponding mean interaction length in air, $L_{X,\text{air}}$ [m], as a function of air density, ρ [mg cm^{-2}].

The two processes, decay and interaction, are therefore in competition with each other. More specifically, the competition between interaction and decay of an unstable particle propagating in a medium of matter density ρ [g cm^{-3}] and composition $M(Z, A)$, where Z and A are the electric charge and the mass number, depends on the interaction mean free path, λ_i [g cm^{-2}] (or cross section σ_{inel} [cm^2]), the mean life at rest, τ_0 [s], and the Lorentz factor, γ, of the particle. In the case of an air shower where the propagation takes place in the atmosphere, we are dealing with a medium of changing density, $\rho(h)$. This implies that for a given particle with fixed energy the ratio of the probabilities for decay or interaction is a functions of altitude, h [cm]. In addition, the rate of change of the density along a trajectory in the atmosphere is also a function of zenith angle, θ.

As an example, the probability, $P^{\pi}_{i,d}$, for a charged pion which propagates through a standard isothermal exponential atmosphere to undergo interaction or decay after having traversed X [g cm^{-2}] can be expressed as

$$P^{\pi}_{i,d}(X) \;=\; 1 - \exp\left(-X\left(\frac{1}{\lambda^{\pi}_i} \;+\; \frac{1}{c\rho(h)\tau^{\pi}_0\sqrt{(\gamma^{\pi}_L)^2 - 1)}}\right)\right), \tag{3.69}$$

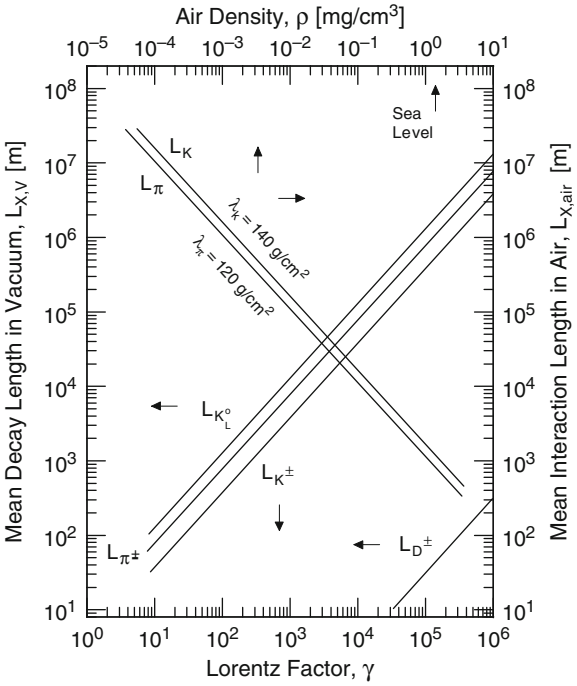

Fig. 3.24 Mean decay length in vacuum of charged pions, kaons and some charmed particles, $L_{X,\mathrm{vac}}$, as a function of the Lorentz factor, γ. The short lived neutral kaons have a negligible branching ratio for muons and are therefore not shown. For comparison we have added the lines labeled λ_π and λ_K (L_π, L_K) which show the relationship between the mean interaction length in air, $L_{X,\mathrm{air}}$, and the density, ρ, for the interaction mean free path of pions (120 g cm^{-2}) and kaons (140 g cm^{-2}) (same for both charge states at high energy), respectively (Grieder, 1986)

where γ_L^π is the Lorentz factor in the lab, λ_i^π the interaction mean free path and τ_0^π the mean life at rest of a charged pion; c is the velocity of light in vacuum.

The critical height in the atmosphere, h_c, defined as the altitude where the probabilities for decay and interaction are equal, is shown for vertically downward propagating particles as a function of energy in Fig. 3.25. The procedure to handle this calculation is outlined in Chap. 20.

If we now formulate mathematically the various hadronic processes discussed above, including the decay of the unstable particles and couple the resulting set of equations in the proper sequence, we can in principle construct an analytic expression in the form of a set of *diffusion* or *transport equation*, that describes the hadron cascade. The solution of these equations should allow us to compute the particle flux in space and time anywhere within the target (atmosphere), i.e., the number, location and energy of the associated particles.

However, this is an extremely difficult task and solutions can only be obtained for the most simple requirements and under severe approximations.

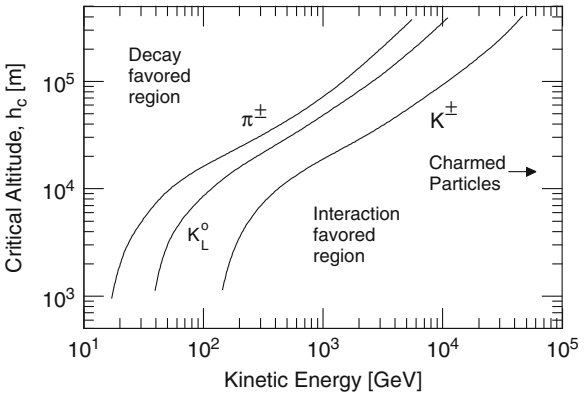

Fig. 3.25 Critical altitude, h_c, of pions, kaons and charmed particles for vertical downward propagation in the atmosphere, defined as that altitude where the probabilities for decay and interaction are equal, plotted as a function of the kinetic energy. In the region above the curves decay is favored, below interaction is more likely. For details see text (Grieder, 1986)

3.12.2 Analytical Treatment of Hadron Cascades

A genuine hadron cascade is a highly complex process. It is the basic energy transport mechanism in an air shower. Until the advent of modern high speed computers the cascade process was studied theoretically, using the previously mentioned transport or diffusion equations. Because of the serious mathematical problems that are encountered when attempting to solve these equations analytically, only very few and simple mechanisms can be incorporated and solutions can only be found with numerical methods. Moreover, the analytical approach can only yield average properties, the important topic of fluctuations is ignored.

Today the properties of hadron cascades are investigated with sophisticated Monte Carlo simulation programs on high speed computers. These allow to include easily every known process as well as distributions of stochastic processes that produce realistic fluctuations, and hypothetical mechanisms that are subject of exploration (see Chap. 20 for details). Limiting factors for the complexity and accuracy of today's simulations are only imposed by our limited knowledge of the processes that we implement, by the capacity of the computers and the available computing time.

Nevertheless, the analytic approach has its merits, too. It permits the overlook of the main functional features of the cascade and the trends of its development. For this reason and for reasons of completeness we present a brief outline of the basic equations, the ingredients and the solutions of the analytical approach of the cascade problem.[23]

[23] For deeper insight the interested reader is referred to the books of Khristiansen (1980); Gaisser (1992), Rao and Sreekantan (1998), and references listed therein.

The basic mathematical approach follows closely the recipe originally developed by the pioneers of the electromagnetic or photon–electron cascade theory[24] which culminated in the work of Rossi and Greisen (1941) and Kamata and Nishimura (1958).

In analogy to the electromagnetic cascade problem, the most simple approach to handle the hadron cascade is to consider a one-dimensional cascade (disregarding transverse momenta) and to limit the multitude of particles to simply nucleons, pions and muons. The basic transport or diffusion equation for nucleons in the atmosphere can then be written as

$$\frac{\partial N_N(E,X)}{\partial X} = -\frac{N_N(E,X)}{\lambda_N(E)} + \int_E^{E_0} \left(\frac{N_N(E',X)}{\lambda_N(E')}\right) G_{N,N}(E',E)\,\mathrm{d}E' + \int_E^{E_0} \left(\frac{N_\pi(E',X)}{\lambda_\pi(E')}\right) G_{\pi,N}(E',E)\,\mathrm{d}E'. \tag{3.70}$$

where $N_N(E,X)\mathrm{d}E$ is the downward flux of nucleons at depth X in the atmosphere within the energy interval E and $E+\mathrm{d}E$, $G_{N,N}(E',E)$ and $G_{\pi,N}(E',E)$ are the number of nucleons and charged pions of energy E in the specified energy interval produced by incident nucleons of energy E', and $\lambda_N(E)$ and $\lambda_\pi(E)$ are the energy dependent interaction mean free paths of nucleons and pions.

The first term of Eq. (3.70) represents the loss of nucleons due to interactions, the second and third terms represent the gain of nucleons from interactions of nucleons and pions, respectively.

The analogous equation for pion initiated interactions is very similar but includes the term which handles the energy dependent competition between interaction and decay of pions.

$$\frac{\partial N_\pi(E,X)}{\partial X} = -N_\pi(E,X)\left(\frac{1}{\lambda_\pi(E)} + \frac{1}{d_\pi(E)}\right) + \int_E^{E_0} \left(\frac{N_N(E',X)}{\lambda_N(E')}\right) G_{N,\pi}(E',E)\,\mathrm{d}E' + \int_E^{E_0} \left(\frac{N_\pi(E',X)}{\lambda_\pi(E')}\right) G_{\pi,\pi}(E',E)\,\mathrm{d}E'. \tag{3.71}$$

Here $G_{N,\pi}(E',E)$ and $G_{\pi,\pi}(E',E)$ are the number of pions of energy E in the specified energy interval produced in interactions of nucleons and charged pions of energy E', and d_π is the air density (altitude) and energy dependent decay mean free path of pions, as discussed previously in Sect. 3.12.1,

$$d_\pi = \gamma_\pi c \tau_\pi \rho(X), \tag{3.72}$$

[24] For details see the brief historical overview given in Sect. 4.6.

where $\rho(X)$ is the air density at atmospheric depth X.

In contrast to Eq. (3.70) the first term on the right hand side of Eq. (3.71) stands for the loss of pions through interaction and decay. The remaining two terms account for pion production in nucleon and pion initiated interactions, respectively.

For muons the diffusion equation takes the form

$$\frac{\partial N_\mu(E,X)}{\partial X} = -\frac{N_\mu(E,X)}{d_\mu(E)} + \frac{N_\pi(E,X)}{d_\pi(E)} + I\,\frac{\partial N_\mu(E,X)}{\partial E} \quad , \tag{3.73}$$

where E_π is the average altitude (air density) dependent energy of the pions for decay,

$$E_\pi = \frac{m_\pi}{m_\mu} E \quad , \tag{3.74}$$

and

$$d_\mu = \gamma_\mu c \tau_\mu \rho(X) \tag{3.75}$$

is the decay mean free path of muons.

The first term on the right of Eq. (3.73) stands for the muon loss through decay, the second represents the muon gain through charged pion decay, and the last term accounts for the energy losses of the muons due to ionization in the atmosphere.

Equations similar to 3.70 can now be assembled to handle the electron and photon components. These are discussed in Sects. 4.6.6 and 4.6.7 where we also outline the methods for solving these equations.

For single incident nucleons, elementary solutions can be found for Eqs. (3.70), (3.71) and (3.73), using numerical methods that yield the growth and decay of the number of participating particles along the cascade axis across the atmosphere. Thus, if plotted we get the so-called hadron cascade curves. Applying the equations to an incident spectrum of primaries leads to the description of the general flux of cosmic ray hadrons and muons in the atmosphere. Adding the results of analogous equations for handling the electromagnetic cascades we could in principle describe an entire shower.

The Monte Carlo approach to simulate extensive air showers, which is a highly technical method, is discussed in Chap. 20. We should also mention that the analytic approach by numerically solving the transport and diffusion equations can be combined with Monte Carlo techniques to save computing time (see Sect. 20.3).

References

Aarnio, P.A., et al.: CERN-TIS-RP-190, CERN, Geneva (1987).
Abe, F., et al.: Phys. Rev. Lett., 61, p. 1819 (1988).
Abe, F., et al.: Phys. Rev. D, 41, p. 2330 (1990). (same author list as Abe et al., 1988).
Adamus, M., et al.: Phys. Lett. B, 177, p. 239 (1986).

Adler, C., et al., STAR Collaboration: Phys. Rev. Lett., 87, p. 262302 (2001).
Aglietta, M., et al.: PICRC, 6, p. 37 (1997).
Aglietta, M., et al.: Nucl. Phys., B (Proc. Suppl.), 75A, p. 222 (1999).
Aglietta, M., et al.: Phys. Rev. D, 79, p. 032004 (2009).
Agostinelli, S., et al.: Nucl. Instr. Meth. A, 506, No. 3, p. 250 (2003).
Aguilar-Benitez, M., et al.: Zeitschr. Phys. C, 50, p. 405 (1991).
Ahle, L., et al., E-802 Collaboration: Phys. Rev. Lett., 81, p. 2650 (1998).
Aiginger, H., et al.: Adv. Space Res., 35, 214 (2005).
Akashi, M., et al.: PICRC, 2, p. 835 (1965a).
Akashi, M., et al.: Progr. Theor. Phys., (Suppl.), 32, p. 1 (1965b).
Akimov, V.V., et al.: Acta Phys. Acad. Sci. Hung., 29, S3, p. 211 (1970).
Alexopoulos, T., et al.: Phys. Rev. D, 48, p. 984 (1993).
Allison, J., et al.: Manchester University, UK; IEEE Trans. Nucl. Sci., 53, No. 1, p. 270 (2006).
Alner, G.J., et al.: Zeitschr. Phys. C, p. 1 (1986).
Alner, G.J., et al., UA5 Collaboration: Phys. Rep., 154, pp. 247–383 (1987).
Alper, B., et al.: Phys. Lett. B, 44, p. 521 (1973).
Amaldi, U., et al.: Phys. Lett. B, 44, p. 112 (1973).
Amati, D., et al.: Nuovo Cim., 26, p. 896 (1962).
Amendolia, S.R., et al.: Phys. Lett. B, 44, p. 119 (1973).
Ammar, R., et al.: Phys. Lett. B, 178, p. 124 (1986).
Andersson, B., et al.: Phys. Rep., 97, p. 31 (1983).
Anisovich, V.V., et al.: Zeitschr. Phys. C, 27, p. 77 (1985).
Antoni, T., et al.: Nucl. Instr. Meth. A, 513, p. 490 (2003).
Ashton, F., and R.B. Coats: J. Phys. A, 1, p. 169 (1968).
Ashton, F., et al.: Acta Phys. Acad. Sci. Hung., 29, S3, p. 25 (1970).
Astafiev, V.A., and R.A. Mukhamedshin: PICRC, 7, p. 204 (1979).
Atherton, H.W., et al.: CERN Yellow Report, CERN 80-07, (22 August 1980).
Babecki, J.: Acta Phys. Polonica B, 6, p. 443 (1975).
Bächler, J., et al., NA49 Collaboration: Nucl. Phys. A, 661, p. 45c (1999).
Badhwar, G.D., et al.: Proc. Ind. Acad. Sci., 61, p. 374 (1965).
Bailly, J.L., et al.: Zeitschr. Phys. C, 35, p. 301 (1987).
Ballarini, F., et al.: AIP Conf. Proc. 769, p. 1197 (2005).
Baltrusaitis, R.M., et al.: Phys. Rev. Lett., 52, p. 1380 (1984).
Banner, M., et al.: Phys. Lett. B, 44, p. 537 (1973).
Baradzei, L.T., et al.: Nucl. Phys. B, 370, p. 365 (1992).
Bardadin-Otwinowska, M., et al.: Phys. Lett., 21, p. 351 (1966).
Barroso, S.L.C., et al.: PICRC, 6, p. 41 (1997).
Barshay, S., and Y. Chiba: Phys. Lett. B, 167, p. 449 (1986).
Basile, M., et al.: Phys. Lett., B, 95, p. 311 (1980).
Basile, M., et al.: Nuovo Cim., A, 65, p. 400 (1981a).
Basile, M., et al.: Lett. Nuovo Cim., 32, p. 321 (1981b).
Basile, M., et al.: Lett. Nuovo C., A, 73, p. 329 (1983).
Bass, S.A., et al.: Progr. Part. Nucl. Phys., 41, p. 255 (1998).
Bass, S.A., et al.: Nucl. Phys. A, 661, pp. 205c–260c (1999).
Batista, M., and R.J.M. Covolan: Phys. Rev. D, 59, 054006(1999).
Battistoni, G., et al.: Astropart. Phys., 19, p. 269 (2003a).
Battistoni, G., et al.: Astropart. Phys., 19, p. 291 (2003b). Erratum to Battistoni et al. (2003a).
Battistoni, G., et al.: hep-ph/0412178 (14 December 2004).
Belenkii, S.Z., and L. Landau: Nuovo Cim., 1, p. 15 (1956).
Bellandi Filho, J., et al.: Cosmic Rays and Particle Physics-1978 (Bartol Conference) T.K. Gaisser, ed., American Institute of Physics, A.I.P. Conference Proceedings, 49, Particles and Fields Subseries, 16, p. 317 (1979).
Bellandi, J., et al.: Nuovo Cim. A, 101, p. 897 (1989).

Bellandi, J., et al.: J. Phys. G, 18, p. 579 (1992a).
Bellandi, J., et al.: Phys. Lett. B, 279, p. 149 (1992b).
Bellandi, J., et al.: Nuovo Cim. A, 107, p. 1339 (1994a).
Bellandi, J., et al.: Phys. Rev., D, 50, p. 6836 (1994b).
Bellandi, J., et al.: Nuovo Cim. A, 111, p. 149 (1998).
Bellettini, G., et al.: Phys. Lett. B, 45, p. 69 (1973).
Belov, K., et al.: Nucl. Phys., B (Proc. Suppl.), 151, p. 197 (2006).
Benecke, J., et al.: Phys. Rev., 188, p. 2159 (1969).
Bleicher, M., et al.: J. Phys., G, 25, p. 1859 (1999).
Block, M.M.: Phys. Rep., 436, p. 71 (2006).
Bøggild, H., and T. Ferbel: Ann. Rev. Nucl. Sci., 24, p. 451 (1974).
Bossard, G., et al.: Phys. Rev. D, 63, p. 054030 (2001).
Brenner, A.E., et al.: Phys. Rev. D, 26, p. 1497 (1982).
Brooke, G., et al.: Proc. Phys. Soc., 83, p. 853 (1964).
Brun, R., et al.: Computer Code GEANT3, CERN Report No. DD/EE/84-1 (1987).
Büsser, F.W., et al.: Phys. Lett. B, 46, p. 471 (1973).
Busza, W., et al.: Phys. Rev. Lett., 34, p. 836 (1975).
Capdevielle, J.N.: J. Phys. G, 15, p. 909 (1989).
Capdevielle, J.N., et al.: The Karlsruhe Extensive Air Shower Simulation Code CORSIKA. Kernforschungszentrum Karlsruhe, Report KfK 4998, (November 1992).
Capdevielle, J.N., et al.: J. Phys. G, 20, p. 947 (1994).
Capella, A., and A. Krzywicki: Phys. Rev. D, 18, p. 3357 (1978).
Capella, A., and J. Tran Thanh Van: Zeitschr. Phys. C, 10, p. 249 (1981).
Capella, A., et al.: Phys. Rep., 236, p. 225 (1994).
Carroll, A.S., et al.: Phys. Rev. Lett., 33, p. 928 (1974a).
Carroll, A.S., et al.: Phys. Rev. Lett., 33, p. 932 (1974b).
Caso, C., et al.: Europ. Phys. J. C, 3, p. 1 (1998).
Castagnoli, C., et al.: Nuovo Cim., 10, p. 1539 (1953).
Ceradini, F.: Proceedings of the International Europhysics Conference on High Energy Physics, Bari, Italy, p. 363 (18–24 July 1985).
CERN W-5013: Detector Description and Simulation Tool, CERN Program Library Long Write-up W5013 (CERN Geneva) (1993).
CERN W-5013: Application Software Group and Network Division. GEANT. Detector Description and Simulation Tool 3.21 (1994).
Chou, T.T., and C.N. Yang: Phys. Rev. Lett., 25, p. 1072 (1970).
Ciok, P., et al.: Nuovo Cim., 8, p. 166 (1958).
Cleghorn, T.F., et al.: Can. J. Phys., 46, p. S572 (1968).
Cocconi, G.: Phys. Rev., 111, p. 1699 (1958).
Cocconi, G.: Handbuch der Physik, S. Flügge, ed., Kosmische Strahlung, Springer Verlag, Berlin, Vol. XLVI/I, p. 215 (1961).
Cocconi, G., et al.: UCRL, 10022, p. 167 (1961). Cocconi, G., et al.: LRL 28, Part 2, VCID-144, (1962).
Cocconi, G., et al.: In 200 BeV Accelerator: Studies on Experimental Use, 1964–1965, Lawrence Radiation Laboratory Report UCRL-16830, Vol. 1, p. 25 (1966).
Cocconi, G.: Nucl. Phys. B, 28, p. 341 (1971).
CORSIKA: http://www-ik.fzk.de/corsika/
Costa, C.G.S., et al.: Phys. Rev., D, 52, p. 3890 (1995).
Costa, C.G.S., et al.: Phys. Rev., D, 54, p. 5558 (1996).
Costa, C.G.S.: Phys. Rev. D, 57, p. 4361 (1998).
Covolan, R.J.M., et al.: Phys. Lett. B, 389, p. 176 (1996).
De Angelis, A.: Proceedings of the XXVI International Symposium on Multiparticle Dynamics, Faro (1996).
De Mitri, I, et al.: PICRC, Merida, Mexico 2007, 4, p. 675 (2008).

Dekhissi, H., et al.: PICRC, 1, p. 1 (1999).
Denisov, S.P., et al.: Nucl. Phys., B, 61, p. 62 (1973).
Dias de Deus, J.: Phys. Rev. D, 32, p. 2334 (1985).
Ding, L., and Q. Zhu: Phys. Lett. B, 297, p. 201 (1992).
Donnachie, A., and P.V. Landshoff: Phys. Lett. B, 296, p. 227 (1992).
Dremin, I.M., et al.: PICRC, 10, p. 166 (1990).
Dremin, I.M., and V.I. Yakovlev: Astropart. Phys., 26, p. 1 (2006).
Drescher, H.J.: in Bass et al. (1999); Nucl. Phys. A, 661, p. 216c (1999).
Drescher, H.J., et al.: Nucl. Phys. A, 661, p. 604c (1999).
Drescher, H.J., et al.: Phys. Rep., 350, p. 93 (2001).
Duller, N., and W. Walker: Phys. Rev., 93, p. 215 (1954).
Dunaevsky, A.M., et al.: PICRC, 4, p. 133 (1991a).
Dunaevsky, A.M., et al.: PICRC, 4, p. 161 (1991b).
Durães, F.O., et al.: Phys. Rev. D, 47, p. 3049 (1993).
Dyakonov, M.N., et al.: PICRC, 9, p. 252 (1990).
Engel, J., et al.: Phys. Rev., D, 46, p. 5013 (1992).
Engel, R., et al.: PICRC, 1, p. 415 (1999).
Engel, R.: PICRC, Invited, Rapporteur, and Highlight papers, p. 181 (2001).
Engel, R.: Nucl. Phys. B (Proc. Suppl.), 122, p. 40 (2003).
Engel, R.: Nucl. Phys. B (Proc. Suppl.), 151, p. 437 (2006).
Engler, J., et al.: Nucl. Instr. Meth. A, 427, p. 528 (1999).
Eskola, K.J.: Nucl. Phys. A, 698, p. 78c (2002).
Fassò, A., et al., Proc. Monte Carlo 2000 Conf., Lisbon, Oct. 23–26 2000, A. Kling et al. Eds.: Springer Verlag Berlin, pp. 159, p. 955 (2001).
Feinberg, E.L.: Phys. Rep., 5, p. 237 (1972).
Fermi, E.: Progr. Theor. Phys. (Kyoto), 5, p. 570 (1950).
Fermi, E.: Phys. Rev., 81, p. 683 (1951).
Fermi, E.: Phys. Rev., 92, p. 452 (1953).
Fermi, E.: Phys. Rev., 93, p. 1434 (1954).
Fesefeldt, H.: PITHA 85/02, RWTH Aachen (1985).
Feynman, R.P.: Phys. Rev. Lett., 23, p. 1415 (1969).
Fishbane, P.M., and J.S. Trefil: Phys. Rev. D, 3, p. 238 (1971).
Fishbane, P.M., and J.S. Trefil: Phys. Rev. Lett., 31, p. 734 (1973).
Fletcher, R.S., et al.: Phys. Rev. D, 50, p. 5710 (1994).
FLUKA code (event-generator), http://www.fluka.org/ (2006)
Foà, L.: Phys. Rep., 22, p. 1 (1975).
Fowler, G.N., et al.: Phys. Lett. B, 145, p. 407 (1984).
Fowler, G.N., et al.: Phys. Rev. Lett., 55, p. 173 (1985).
Fowler, G.N., et al.: Phys. Rev., 35, D, p. 870 (1987).
Fowler, G.N., et al.: Phys. Rev., 40, C, p. 1219 (1989).
Fowler, P.H., and D.H. Perkins: Proc. R. Soc. A, 278, p. 401 (1964).
Freier, Ph. and C.J. Waddington: Astrophys. Space Sci., 38, p. 419 (1975).
Friedlander, M.W., et al.: Phil. Mag., 8, p. 1691 (1963).
Fritzsch, H., and P. Minkowski: CERN Report, CERN-TH-2320, May (1977) and Phys. Lett. B, 69, p. 316 (1977).
Fukushima, Y., et al.: Phys. Rev., D, 39, p. 1267 (1989).
Gaisser, T.K., and F. Halzen: Phys. Rev. Lett., 54, p. 1754 (1985).
Gaisser, T.K., and T. Stanev: Phys. Lett. B, 219, p. 375 (1989).
Gaisser, T.K., et al.: PICRC, 8, p. 55 (1990).
Gaisser, T.K.: Cosmic Rays and Particle Physics, Cambridge University Press, Cambridge 2nd ed. (1992).
Gaisser, T.K., et al.: Phys. Rev. D, 47, p. 1919 (1993).

GEANT: Application Software Group, GEANT, CERN, Geneva, Switzerland, Program Library (1995). http://wwwasdoc.web.cern.ch/wwwasdoc/geant/geantall.html
Geer, L.Y., et al.: Phys. Rev. C, 52, p. 334 (1995).
Geist, W.M., et al.: Phys. Rep., 197, pp. 263–374 (1990).
Giaccomelli, G., et al.: Nucl. Instr, Meth. A, 411, p. 41 (1998).
Giaccomelli, G.: arXiv:0802.2241v1 [hep-ph] (15 February 2008).
Gierula, J., et al.: Acta Phys. Polon., 19, p. 119 (1960a).
Gierula, J., et al.: Nuovo Cim., 18, p. 102 (1960b).
Gierula, J., et al.: Phys. Rev., 122, p. 626 (1961).
Glauber, R.J.: Lectures in Theoretical Physics, W.E. Brittin and L.G. Dunham, eds., Interscience, New York, 1959, Vol. 1, p. 135 (1959).
Glauber, R.J., and G. Matthiae: Nucl. Phys. B, 12, p. 135 (1970).
Goryunov, N.N., et al.: PICRC (Moscow, 1959), 2, p. 70 (1960).
Gottfried, K.: Coherent Nuclear Production of Multibody States, Theory Report, TH.1545-CERN, CERN, Geneva (Switzerland) (1972).
Gottfried, K.: An Introduction to Multiple Production Processes, CERN Lecture Given in the Academic Training Program, November and December, 1972. Theory Report, TH.1615-CERN, CERN, Geneva, Switzerland (1973a).
Gottfried, K.: CERN (Geneva) Theory Preprint, TH.1735-CERN (1973b).
Gottfried, K.: Phys. Rev. Lett., 32, p. 957 (1974).
Gribov, V.N.: Soviet Phys. JETP, 26, p. 414 (1968).
Gribov, V.N.: Soviet Phys. JETP, 29, p. 483 (1969).
Gribov, V.N.: Soviet Phys. JETP, 30, p. 709 (1970).
Grieder, P.K.F.: Acta Phys. Acad. Sci. Hung., 29, S3, p. 563 (1970a).
Grieder, P.K.F.: Acta Phys. Acad. Sci. Hung., 29, S3, p. 569 (1970b).
Grieder, P.K.F.: Institute for Nuclear Study, University of Tokyo, Tokyo, Japan. Report Nr. I.N.S., J, 125 (1970c).
Grieder, P.K.F.: Nuovo Cim., A, 7, p. 867 (1972).
Grieder, P.K.F.: PICRC, 3, p. 2204 (1973).
Grieder, P.K.F.: Rivista del Nuovo Cim., 7, p. 1 (1977).
Grieder, P.K.F.: PICRC, 9, p. 161 (1979a).
Grieder, P.K.F.: PICRC 9, p. 167 (1979b).
Grieder, P.K.F.: PICRC 9, p. 173 (1979c).
Grieder, P.K.F.: PICRC 9, p. 178 (1979d).
Grieder, P.K.F.: PICRC 9, p. 184 (1979e).
Grieder, P.K.F.: PICRC 9, p. 190 (1979f).
Grieder, P.K.F.: PICRC 9, p. 196 (1979g).
Grieder, P.K.F.: PICRC 9, p. 202 (1979h).
Grieder, P.K.F.: Proc. Japan – US Seminar on Cosmic Ray Muon and Neutrino Physics/Astrophysics Using Deep Underground/Underwater Detectors, Institute for Cosmic Ray Research, University of Tokyo, p. 183 (1986).
Grieder, P.K.F., et al., Eds.: Very High Energy Cosmic Ray Interactions. Proceedings of the XIII. Internat. Symposium on Very High Energy Cosmic Ray Interactions (ISVHECRI), Pylos, Greece, 6–12 September 2004, Nucl. Phys. B (Proc. Suppl.), 151, pp. 3–508 (2006).
Grigorov, N.L., et al.: Zh. Eksper. Teor. Fiz., 33, p. 1099 (1957).
Grigorov, N.L., et al.: PICRC, 2, p. 860 (1965).
Grigorov, N.L., et al.: Can. J. Phys., 46, p. S686 (1968).
Guzhavin, V.V., and G.T. Zatsepin: Zurn. Eksp. Teor. Fiz., 32, p. 365 (1957).
Hagedorn, R.: Nuovo Cim., Suppl., 3, p. 147 (1965).
Hagedorn, R., and J. Ranft: Nuovo Cim., Suppl., N. 2, Ser. I, 6, p. 169 (1968).
Hagedorn, R., et al.: Hadronic Matter at Extreme Energy Density, N. Cabbibo and L. Sertorio, eds., Plenum Publishing Corp., New York (1980).
Hama, Y., and S. Paiva: Phys. Rev. Lett., 78, p. 3070 (1997).

Hara, T., et al.: Phys. Rev. Lett., 50, p. 2058 (1983).
He, Y.D.: J. Phys. G, 19, p. 1953 (1993).
He, Y.D., and P.B. Price: Z. Phys. A, 348, p. 105 (1994).
Heck, D., KASCADE Collaboration: PICRC, 6, p. 245 (1997).
Heck, D.: PICRC, 1, p. 233 (2001).
Heck, D., et al.: PICRC, Invited, Rapporteur and Highlight papers, p. 240 (2001).
Heck, D., and J. Knapp: Extensive Air Shower Simulation with Corsika. A User's Guide Forschungszentrum Karlsruhe, Germany. Version 6.018 (October 1 2002).
Heck, D., et al.: Nucl. Phys. B (Proc. Suppl.), 151, p. 127 (2003).
Heck, D., and J. Knapp: Extensive Air Shower Simulation with Corsika: A User's Guide, Forschungszentrum Karlsruhe, Germany; Version 6.500, (March 6 2006). Updated version, see CORSIKA.
Heinemann, R.E., and W.E. Hazen: Phys. Rev., 90, p. 496 (1953).
Heisenberg, W.: Zeitschr. Phys., 126, p. 569 (1949a).
Heisenberg, W.: Nature, Lond., 164, p. 65 (1949b).
Hernàndez, J.J., et al.: Phys. Lett. B, 239, p. 1 (1990).
Hillas, A.M.: PICRC, 1, p. 193 (1981a).
Hillas, A.M.: Proceedings of the Paris Workshop on Cascade Simulations, J. Linsley and A.M. Hillas, eds., p. 39 (1981b).
Hillas, A.M.: Nucl. Phys. B (Proc. Suppl.), 52B, p. 29 (1997).
Hirzebruch, S.E., et al.: Phys. Rec. C, 51, p. 2085 (1995).
Honda, M., et al.: Phys. Rev. Lett., 70, p. 525 (1993).
Hörandel, J.R.: J. Phys. G, 29, p. 2439 (2003).
Horn, D.: Phys. Rep., 4, p. 1 (1972).
Huang, H.Z.: Nucl. Phys. A, 698, p. 663c (2002).
Jacob, M., and R. Slansky: Phys. Lett. B, 37, p. 408 (1971).
Jacob, M., and P.V. Landshoff: Phys. Rep., 48, p. 285 (1978).
Jones, L.W., et al.: Acta Phys. Acad. Sci. Hung., 29, S3, p. 205 (1970).
Jones, L.W., et al.: Nucl. Phys. B, 43, p. 477 (1972).
Jones, L.W.: Proceedings, Workshop on Cosmic Ray Interactions and High Energy Results, C.M.G. Lattes, ed., La Paz, Bolivia (July 19, 1982) and Rio de Janeiro, Brazil, (July 26, 1982), p. 3. (1982).
Jones, L. W.: PICRC, 5, p. 17 (1983).
Kadija, K., and M. Martins: Phys. Rev. D, 48, p. 2027 (1993).
Kaidalov, A.B.: Phys. Lett. B, 116, p. 459 (1982).
Kaidalov, A.B., and K.A. Ter-Martirosyan: Phys. Lett. B, 117, p. 247 (1982).
Kalmykov, N.N., et al.: Nucl. Phys. B (Proc. Suppl.), 52 B, p. 17 (1997).
Kamata, K., and J. Nishimura: Progr. Theor. Phys. Jpn., 6, Suppl., p. 93 (1958).
Kampert, K.H., et al.: PICRC, Invited, Rapporteur and Highlight papers, p. 240 (2001).
Kasahara, K., and Y. Takahashi: Progr. Theor. Phys. 55, p. 1896 (1976).
Kasahara, K., et al.: PICRC, 13, p. 70 (1979a).
Kasahara, K., et al.: PICRC, 13, p. 76 (1979b).
Kawasumi, N., et al.: Phys. Rev. 53, D, p. 3534 (1996).
Kempa, J., and J. Wdowczyk: J. Phys. G, 9, p. 1271 (1983).
Khristiansen, G.B.: Cosmic Rays of Superhigh Energies. Karl Thiemig Verlag, München (1980).
Klages, H.O., et al.: Proceedings of the International Symposium on Very High Energy Cosmic Ray Interactions, Karlsruhe, 1996; Nucl. Phys. B (Proc. Suppl.), 52, p. 92 (1997). (See also Antoni et al., 2003).
Klein, S.R.: Nucl. Phys. B (Proc. Suppl.), 122, p. 76 (2003).
Knapp, J., et al.: A Comparison of Hadronic Interaction Models Used in Air Shower Simulations and their Influence on Shower Development and Observables, Forschungszentrum Karlsruhe, Report FZKA 5828 (1996).
Knapp, J., et al.: Astropart. Phys., 19, p. 77 (2003).

Knurenko, S.P., et al.: PICRC, 1, p. 372 (1999).
Koba, Z., et al.: Nucl. Phys. B, 40, p. 317 (1972).
Kopeliovich, B.Z., et al.: Phys. Rev. D, 39, p. 769 (1989).
Landau, L.D., and I.Ya. Pomeranchuk: Dokl. Akad. Nauk. SSSR, 92, p. 535 (1953a).
Landau, L.D., and I.Ya. Pomeranchuk: Dokl. Akad. Nauk. SSSR, 92, p. 735 (1953b).
Lattes, C.M.G., et al.: PICRC, 4, p. 2671 (1973).
Liland, A.: PICRC, 6, p. 178 (1987).
Lindstrom, P.J., et al.: Paper Presented at the Symposium on Isotopic Composition, Durham, NH, 1973, also LBL-3650 preprint (1973).
Linsley, J.: PICRC, 6, p. 1 (1985).
Matthews, J.: PICRC, 1, p. 261 (2001).
Matthews, J.: Astropart. Phys., 22, p. 387 (2005).
Mielke, H.H., et al.: PICRC, 4, p. 155 (1993).
Mielke, H.H., et al.: J. Phys. G, 20, p. 637 (1994).
Mielke, H.H., et al.: Nucl. Instr. Meth. A, 360, p. 367 (1995).
Miesowicz, M.: Progress in Elementary Particle and Cosmic Ray Physics, North-Holland, Amsterdam, Vol. X, pp. 101–168 (1971).
Milke, J., KASCADE Collaboration: PICRC, 6, p. 97 (1997).
Milke, J., et al.: Nucl. Phys. B (Proc. Suppl.) 151, p. 469 (2006).
Mukhamedshin, R.A.: PICRC, 5, pp. 343, 347 (1981).
Murthy, P.V.R., et al.: Nucl. Phys. B, 92, p. 269 (1975).
NEEDS Workshop: Informal meeting on "Needs for Accelerator Experiments for the Understanding of High Energy Extensive Air Showers", R. Engel, A. Haungs, L. Jones, and H. Rebel, initiators, April 18–20 (2002). Contributions available as PDF-Files at http://www-ik.fzk.de/~needs/
Nikolaev, N.N.: Phys. Rev. D, 48, p. R1904 (1993).
Ohsawa, A., and K. Sawayanagi: Phys. Rev. D, 45, p. 3128 (1992).
Ohsawa, A., et al.: Phys. Rev. D, 70, p. 074028 (2004).
Ohsawa, A., et al.: Nucl. Phys. B (Proc. Suppl.), 151, pp. 227, 231 (2006).
Ostapchenko, S.: Nucl. Phys. B (Proc. Suppl.), 151, p. 143 (2006a).
Ostapchenko, S.: Nucl. Phys. B (Proc. Suppl.), 151, p. 147 (2006b).
Ostapchenko, S.: astro-ph/0610788 (2006c).
Ostapchenko, S.: Phys. Lett. B, 636, p. 40 (2006d).
Ostapchenko, S.: Phys. Rev. D, 74, p. 014026 (2006e).
Pal, Y.A., and B. Peters: Dansk. Vidensk. Selsk., Mat. Fys. Medd., 33, No. 15, p. 1–55 (1964).
Pattison, B., et al., Eds.: Very High Energy Cosmic Ray Interactions. Proceedings of the XIIth International Symposium on Very High Energy Cosmic Ray Interactions (ISVHECRI), CERN, Geneva, Switzerland, 15–20 July 2002, Section "NEEDS Workshop Discussion", Nucl. Phys., B (Proc. Suppl.), 122, pp. 1–487 (2003).
Perkins, D.H.: Progress in Elementary Particle and Cosmic Ray Physics, North-Holland, Amsterdam, Vol. V, pp. 257–363 (1960).
Peters, B.: Nuovo Cim., 22, p. 800 (1961).
Peters, B.: PICRC, Kyoto (1961) 3, p. 522. J. Phys. Soc. Jpn., 17, Suppl. A III (1962).
Peyrou, Ch.: Proceedings of The Aix-en-Provence International Conference on Elementary Particles, 14–20 September 1961, Plenary Sessions, II, p. 103 (1961).
Pierog, T., and K. Werner: PICRC, pre-conference edition, paper 0905, Merida, Mexico (2007).
Powell, C.F., et al.: The Study of Elementary Particles by the Photographic Method, Pergamon Press, London (1959).
Prague Workshop, September (2005). Proceedings of the International Conference From Colliders to Cosmic Rays, Prague (2005), Jan Ridky, ed.:, Czech. J. Phys., 56, Suppl. A, pp. 13–367 (2006).
Ranft, J.: Phys. Rev. D, 51, p. 64 (1995).
Ranft, J.: Siegen Report, SI-99-5 (hep-ph/9911213) (1999a).

Ranft, J.: Siegen Report, SI-99-6 (hep-ph/9911232) (1999b).
Rao, M.S.V., and B.V. Sreekantan: Extensive Air Showers, World Scientific, Singapore (1998).
Ren, J.R., et al.: Phys. Rev. D, 38, p. 1404 (1988).
Roberts, T.J., et al.: Nucl. Phys. B, 159, p. 56 (1979).
Rossi, A.M., et al.: Nucl. Phys. B, 84, p. 269 (1975).
Rossi, B., and K. Greisen: Rev. Mod. Phys., 13, p. 240 (1941).
Rudstam, G.: Z. Naturforschung, 21a, p. 1027 (1966).
Saito, T.: J. Phys. Soc. Jpn., 30, p. 1243 (1971).
Saito, T.: Astropart. Phys., 1, p. 257 (1993).
Sciutto, S.J.: PICRC, 1, p. 411 (1999a).
Sciutto, S.J.: Preprint, astro-ph/9911331 (1999b).
Sciutto, S.J.: PICRC, 1, p. 237 (2001).
Shabelski, Yu.M.: Zeitschr. Phys. C, 38, p. 569 (1988).
Shapiro, M.M., and R. Silberberg: Ann. Rev. Nucl. Sci., 20, p. 323 (1970).
Shibata, M.: Phys. Rev. D, 24, p. 1847 (1981).
Silberberg, R., et al.: Composition and Origin of Cosmic Rays, p. 321, NATO ASI Series. Series C. Mathematical and Physical Sciences No 107, M.M. Shapiro, ed., D. Reidel Publishing Co., Dordrecht (1982).
Sivers, D., et al.: Phys. Rep., 23, p. 1 (1976).
Slansky, R.: Phys. Rep., 11, p. 99 (1974).
Slavatinski, S.A.: Nucl. Phys. B (Proc. Suppl.), 122, pp. 3–11 (2003).
Tannenbaum, M.J., and J. Kang: Nucl. Phys. A, 566, p. 423c (1994).
Thomé, W., et al.: Nucl. Phys. B, 129, p. 365 (1977).
Tonwar, S.C.: J. Phys. G, 5, p. L193 (1979).
Vatcha, R.H., et al.: J. Phys. A, 5, p. 859 (1972).
Waddington, C.J., et al.: Nucl. Phys. A, 566, p. 427c (1994).
Wdowczyk, J., and A.W. Wolfendale: J. Phys. G, 10, p. 257 (1984).
Wdowczyk, J., and A.W. Wolfendale: J. Phys. G, 13, p. 411 (1987).
Weiner, R.M., et al.: Phys. Rev. D, 45, p. 2308 (1992).
Werner, K.: Phys. Rep., 232, p. 87 (1993).
Werner, K., et al.: Phys. Rev. C, 74, p. 044902-11 (2006).
Westfall, G.D., et al.: Phys. Rev. C, 19, p. 1309 (1979).
Wlodarczyk, Z.: J. Phys. G, 19, p. L133 (1993).
Wlodarczyk, Z.: J. Phys. G, 21, p. 281 (1995).
Wu, T.T., and C.N. Yang: Phys. Rev., 137, p. B708 (1965).
Yakovlev,V.I.: Nucl. Phys. B (Proc. Suppl.), 122, pp. 417–421 (2003).
Yakovlev,V.I.: PICRC, 9, p. 251 (2005).
Yodh, G.B., et al.: Phys. Rev. Lett., 28, p. 1005 (1972).
Yodh, G.B., et al.: Phys. Rev. D, 28, p. 3233 (1973).
Yodh, G.B., et al.: Phys. Rev. D, 27, p. 1183 (1983).

Chapter 4
Electromagnetic Interactions and Photon–Electron Cascades

Overview After a brief introduction and the presentation of a list of the fundamental electromagnetic processes we first define frequently used quantities, relations and concepts. We then review the processes that are relevant for the development of electromagnetic (photon–electron) cascades such as bremsstrahlung by electrons, pair production by photons, Coulomb scattering, energy loss of electrons by ionization, and Compton and inverse Compton scattering. Subsequently we discuss miscellaneous processes that are of lesser or no relevance for cascade development, such as photonuclear reactions and photon–photon interactions, but also processes that play a significant role for the detection of photons and electrons, like the photo effect, and processes that occur only under extreme conditions, such as the Landau-Pomeranchuk-Migdal effect, magnetic bremsstrahlung, magnetic pair production and the pre-showering effect. These topics are followed by an introduction to cascade theory that is worked out to some degree of detail. The solution of the diffusion equations under different approximations are outlined. The longitudinal shower development profile, the energy spectra and the lateral density distributions of the participating particles and photons are discussed, and the characteristic parameters like the shower age and Molière radius are introduced and defined. A collection of formulae for practical applications is given at the end.

4.1 Introduction

All charged particles are subject to electromagnetic (EM) interactions. Of particular significance for the development of extensive air showers are the interactions of *photons* and *electrons* (positrons and negatrons) with the medium in which they propagate (e.g., air), as they are responsible for the phenomenon of the electromagnetic or photon–electron cascade. Generally speaking, the fundamental electromagnetic processes include the following.

Photon initiated Processes:
- Rayleigh Scattering
- Photo-electric Effect
- Compton Effect

P.K.F. Grieder, *Extensive Air Showers,* DOI 10.1007/978-3-540-76941-5_4,

– Pair Production (Coulomb)
– Photonuclear Interactions
– Photon–Photon Interactions
– Magnetic Pair Production

Electron initiated Processes:

– Coulomb Scattering
– Ionization, Excitation, Knock-on Process
– Bremsstrahlung (Coulomb)
– Cherenkov Radiation
– Radio Emission
– Transition Radiation
– Synchrotron Radiation
– Inverse Compton Scattering
– Positron Annihilation

Most relevant for the development of electromagnetic cascades and air showers are *electron pair production* by photons and *bremsstrahlung* by electrons in the Coulomb field of a nucleus. *Compton scattering* plays a certain role at the later stage of the cascade development, at locations away from the shower axis, toward the fringes of the shower and at atmospheric depths beyond maximum development. There, low energy photons are abundant and produce a significant number of low energy electrons via this process. *Ionization (collision) losses* are of course present whenever charged particles are propagating in a medium other than vacuum, however, they are frequently disregarded in cascade problems when dealing with high energy phenomena only, to simplify the mathematical treatment.

On the other hand, some of the other processes listed above play a rather significant role for the detection of particles and radiation, such as the *photoelectric effect, Cherenkov* and *transition radiation, radio emission* and, of course, *ionization*, too. Others are important for the generation of cosmic gamma rays, such as the classical *synchrotron radiation* and *inverse Compton scattering*. In addition there are higher order processes, such as direct pair creation by electrons, or processes that become important only at very high energies, such as muon bremsstrahlung, the Landau-Pomeranchuk-Migdal (LPM) effect (Landau and Pomeranchuk 1953a, b; Migdal, 1956), or muon pair production by photons, that can often be ignored.

Furthermore, the phenomenon known as *magnetic bremsstrahlung* or *curvature radiation*, a form of synchrotron radiation of electrons that occurs in the ultra-relativistic domain and the quantum phenomenon of *magnetic pair production* by photons can occur in an environment of extremely high magnetic fields (Erber, 1966; Sturrock, 1971; Manchester and Taylor, 1977; Aharonian, 2004), but also at ultrahigh energies in very weak magnetic fields, such as the geomagnetic field. These two phenomena become relevant for ultrahigh energy primary photons ($E_\gamma \geq 10^{19}$ eV) entering the geomagnetic field while approaching the Earth. They may cause so-called pre-cascading or pre-showering well before entering the

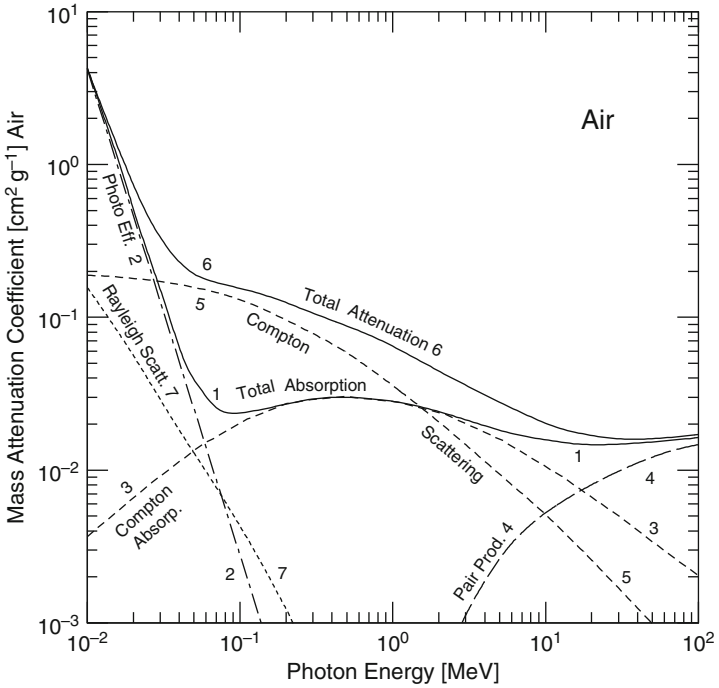

Fig. 4.1 Mass attenuation coefficients of photons in air (Evans, 1955). *Curve* 1, labeled *Total Absorption*, is the sum of the linear coefficients for photoelectric absorption, *curve* 2, Compton absorption, *curve* 3, and pair production, *curve* 4. Adding Compton scattering, *curve* 5, yields the *Total Attenuation*, *curve* 6. Elastic Rayleigh scattering, *curve* 7, is irrelevant and shown for completeness. The plots apply for the following air composition: 78.04% by volume of N_2, 21.02% O_2 and 0.94% A at 0°C, 760 mm Hg and density $\rho = 0.001293$ g cm^{-3}

Earth's atmosphere (Nikishov and Ritus, 1979; Akhiezer et al., 1994; Anguelov and Vankov, 1999) and could fake heavy nuclei initiated showers.

Finally, *photon–photon* and *photonuclear interactions* of ultrahigh energy primary gamma rays and hadronic cosmic rays, respectively, with the cosmic microwave background radiation affect their energy and limit their range of propagation in space.[1] Likewise, synchrotron radiation of electrons propagating in our Galaxy limits their range. In addition, photonuclear processes play also a certain yet minor role in the development of air showers. Some of these processes are also discussed in Chap. 11 that deals with the primary radiation and related topics that affect the propagation of the latter in galactic and extragalactic space. In Fig. 4.1 we show the energy dependence of all the common photon initiated processes in air at low

[1] This phenomenon is known as the Greisen-Zatsepin-Kuzmin (GZK) cutoff or effect, discussed later.

energies (10 keV–100 MeV). All the processes mentioned in this section are part of modern *quantum electrodynamics* (QED).

In Fig. 4.2 we show the energy dependence of the interaction lengths of common electromagnetic processes of electrons and photons in air at low energies (1 MeV–3 GeV).

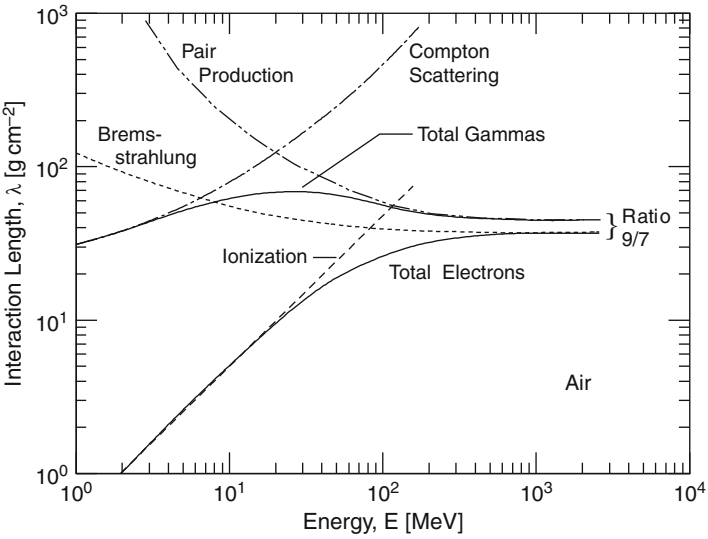

Fig. 4.2 Interaction lengths of photons for Compton scattering and pair production, and of electrons for bremsstrahlung at low energies in air. Also shown is the electron range with respect to ionization (after Evans, 1955)

4.2 Definition of Frequently Used Terms

In the theory of electromagnetic interactions the terms *screening energy, radiation length, critical energy*, and *scattering energy* are frequently used. They are defined as follows:

4.2.1 Screening Energy

The screening effect which is observed in radiation processes is due to the atomic electrons that screen the nuclear Coulomb field. It is discussed in detail by Rossi and Greisen (1941) and Rossi (1952). At very low energies screening is not effective and can be neglected. It becomes more and more effective with increasing energy (intermediate screening) and can be considered to be complete if the particle energy is $E \gg E_{\mathrm{scr}}$, where E_{scr} is called the *screening energy*. It is defined as

$$E_{\rm scr} = \frac{m_e c^2}{\alpha\, Z^{(1/3)}} \quad [\mathrm{MeV}]\,, \tag{4.1}$$

where $m_e c^2$ is the rest mass energy of the electron (0.51 MeV), Z the atomic number of the medium, and α the fine-structure constant (1/137). In air, if we take for $\langle Z\rangle \simeq 7.4$, we get for $E_{\rm scr} = 36.5$ MeV. The Z-dependence of the screening energy is plotted in Fig. 4.3.

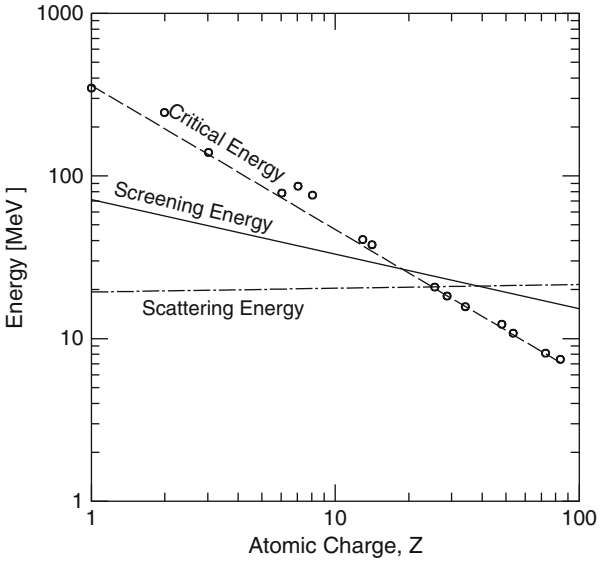

Fig. 4.3 Variation of the screening, the critical and the scattering energy of electrons as a function of atomic number (after Nishimura, 1967)

4.2.2 Radiation Length in Matter

The radiation length, χ_0, (*radiation unit*, (ru), or *cascade unit*, (cu)), is an important characteristic of electron and photon interactions with matter. It is the scale length, measured in [g cm^{-2}], for the energy loss of these particles and quanta.

For *bremsstrahlung* it is the mean distance traversed in a medium over which a high energy electron loses all but the $(1/e)$-th fraction of its energy by bremsstrahlung. In air shower studies the expression given by Tsai (1974) and stated here for *complete screening* is now generally used today,

$$\begin{aligned}\chi^{-1}_{0,\ \rm brems} = \quad & \alpha \left(\frac{N_A}{A}\right) r_e^2 \left\{ Z^2 \left[\varphi_1(0) - \left(\frac{4}{3}\right) \ln(Z) - 4 f(z) \right] \right. \\ & \left. + Z \left[\psi_1(0) - \left(\frac{8}{3}\right) \ln(Z) \right] \right\} \qquad [\mathrm{g\,cm^{-2}}],\end{aligned} \tag{4.2}$$

where $\alpha = (1/137)$ is the fine-structure constant, $r_e = 2.817 \cdot 10^{-13}$ [cm] the classical radius of the electron, $N_A = 6.022 \cdot 10^{23}$ [mol^{-1}] Avogadro's number, and Z and A are the charge (atomic number) and mass number of the medium. In addition,

$$\varphi_1(0) = 4 \ln\left(\frac{Z^{(1/3)}}{2\eta_\varphi \alpha}\right) + \left(\frac{13}{3}\right), \tag{4.3}$$

$$\psi_1(0) = 4 \ln\left(\frac{Z^{(2/3)}}{2\eta_\psi \alpha}\right) + \left(\frac{23}{3}\right). \tag{4.4}$$

η_ϕ and η_ψ represent form factors,

$$\eta_\phi = Z^{(1/3)} \exp\left(\frac{(13/12)}{2\alpha 184.15}\right), \tag{4.5}$$

$$\eta_\psi = Z^{(2/3)} \exp\left(\frac{(23/12)}{2\alpha 1194}\right), \tag{4.6}$$

and $f(z)$ is the Coulomb correction,

$$f(z) = z \sum_{n=1}^{\infty} n(n^2 + z), \tag{4.7}$$

where

$$z = (\alpha\, Z)^2 . \tag{4.8}$$

Equation 4.2 can be written in the compact form (Tsai, 1974) as

$$\chi_0 = \frac{716.405\, A}{Z^2[(L_{\text{rad}} - f(z)] + Z L'_{\text{rad}}} \quad [\text{g cm}^{-2}]. \tag{4.9}$$

The quantities $f(z)$ and the resulting *unit radiation lengths*, χ_0, for all atoms from $Z = 1 - 92$ and $A = 1.0080 - 238.03$ [g mol^{-1}] are given in Table B.4. The quantities L_{rad} and L'_{rad} stand for the expressions

$$L_{\text{rad}} = \ln(184.15\, Z^{-(1/3)}) \tag{4.10}$$

and

$$L'_{\text{rad}} = \ln(1, 194\, Z^{-(2/3)}). \tag{4.11}$$

Their derivation is discussed in the article of Tsai (1974), where further details are given.

Equation 4.2 yields for air, assuming a composition of 76.9% nitrogen ($Z = 7$), 21.8% oxygen ($Z = 8$) and 1.3% argon ($Z = 18$) by weight a value of $\chi_{0,\,\mathrm{air}} = 36.664$ [g cm^{-2}] (Tsai, 1974).

Slightly different expressions are given by other authors that yield modestly deviating values for $\chi_{0,\,\mathrm{air}}$ (Wheeler and Lamb, 1939; Rossi and Greisen, 1941; Rossi, 1952; Dovzchenko and Pomanski, 1963, 1964; Nishimura, 1967; Eidelman et al., 2004).[2] The differences are mainly due to different handling of the effect of atomic electrons, screening and molecular effects, if included.

For *pair production* by a high energy photon the corresponding e-folding distance, $\chi_{0,\mathrm{pair}}$, is

$$\chi_{0,\,\mathrm{pair}}^{-1} = \left(\frac{9}{7}\right)\alpha\left(\frac{N_A}{A}\right)r_e^2\left\{Z^2\left[\varphi_1(0) - \left(\frac{4}{3}\right)\ln(Z) - 4f\right] + Z\left[\psi_1(0) - \left(\frac{8}{3}\right)\ln(Z)\right]\right\} \quad [\mathrm{g\,cm^{-2}}]. \tag{4.13}$$

This expression is almost the same as the one for the radiation length of bremsstrahlung (Eq. 4.2). The two are related as

$$\chi_{0,\mathrm{pair}} = \left(\frac{9}{7}\right)\chi_{0,\mathrm{brems}}, \tag{4.14}$$

which implies that on average a photon traverses a longer track in a medium before creating an electron-positron pair than an electron to undergo bremsstrahlung.

Frequently, for convenience of notation, it is customary to express the thickness x of a medium in units of radiation length, t, thus,

$$t = \frac{x}{\chi_0}\ \ [\mathrm{rl}]. \tag{4.15}$$

For a *mixture of substances* or a compound the radiation length can be approximated by the expression

$$\chi_0^{-1} = \sum f_i\,\chi_i^{-1}\ \ [\mathrm{g\,cm^{-2}}]. \tag{4.16}$$

where f_i is the fraction by weight and χ_i^{-1} the radiation length of the i-th element.

Molecular Effects: Genannt and Pilkuhn (1973) have considered the effect of the molecular nature of the air constituents on the radiation length and obtained a value of $\chi_{0,\mathrm{air}} = 34.6$ g cm^{-2}. Tsai (1974) whose calculation is based entirely on

[2] Rossi and Greisen (1941) have used the simplified expression

$$\chi_0^{-1} = 4\alpha\left(\frac{N_A}{A}\right)r_e^2 Z^2\ln(183\,Z^{-(1/3)})\ \ [\mathrm{g\,cm^{-2}}]\ . \tag{4.12}$$

the Thomas-Fermi model specifies a value of $\chi_{0,\mathrm{air}} = 36.66\ \mathrm{g\,cm^{-2}}$ which is also listed in the Particle data Booklet (Eidelman et al., 2004).

Linsley (1985) criticized these calculations and points out an error in the work of Genannt and Pilkuhn. The calculation of Linsley leads to a value of $\chi_{0,\mathrm{air}} = 37.15\ \mathrm{g\,cm^{-2}}$. Bourdeau et al. (1975a, b), Procureur et al. (1975), and other authors have studied the effect of different values of $\chi_{0,\mathrm{air}}$ on the development of air showers (for details see Sect. 6.2 and Chap. 21).

Values of the radiation length of other materials are tabulated in Appendix B.

4.2.3 Critical Energy of Electrons

At low energy, an electron propagating in a medium of atomic number Z loses energy mainly by ionization, which increases approximately logarithmically with energy. On the other hand, a fast electron loses energy predominantly by radiation (bremsstrahlung), which increases nearly proportional with energy. The energy at which the two losses are equal is called the *critical energy*, E_{crit}. More specific, at critical energy an electron loses equal amounts of energy per unit radiation length, χ_0 [$\mathrm{g\,cm^{-2}}$], by ionization, $(\mathrm{d}E/\mathrm{d}x)_{\mathrm{ion}}$, and radiation, $(\mathrm{d}E/\mathrm{d}x)_{\mathrm{br}}$.[3]

Below the critical energy the particle multiplication process takes place mainly via Compton scattering and collision processes that produce very low energy electron-ion pairs. At shower maximum almost 75% of all electrons are below the critical energy (Richards and Nordheim, 1948; Nishimura, 1967, p. 37, Table 11).

In a *gaseous medium* of atomic number Z, the critical energy is given by the approximate relation,

$$E_{\mathrm{crit}} \approx \frac{710}{Z + 0.92}\ [\mathrm{MeV}], \tag{4.17}$$

in *solids* by

$$E_{\mathrm{crit}} \approx \frac{610}{Z + 1.24}\ [\mathrm{MeV}]. \tag{4.18}$$

For the derivation of the accurate expression the reader is referred to the article by Rossi and Greisen (1941).

The critical energy is a characteristic property of the medium in which an electron propagates. In air $E_{\mathrm{crit}} \simeq 84\,\mathrm{MeV}$. Values of other media are listed in Table B.1. For energies small compared to the critical energy, both the Compton effect and collision processes contribute considerably to the absorption, whereas the production of shower particles declines rapidly.

For *gamma rays* the critical energy is where Compton scattering begins to be more important than pair production. In air, for instance, a photon of 24 MeV has

[3] A different definition of the critical energy is used by Rossi and Greisen (1941, p. 271).

equal probabilities for Compton scattering or pair production. At lower energies collision losses become important and at still smaller energies the Compton effect must be taken into account. The Z-dependence of the critical energy is displayed in Fig. 4.3.

4.2.4 Scattering Energy

Analogous to the radiation length and screening energy, the scattering energy, too, was introduced for practical reasons to lump together constants (see Sect. 4.3.3, Eq. 4.36). It is a characteristic energy that is approximately a constant (Rossi, 1952) and defined as

$$E_{\text{scatt}} = m_e c^2 \sqrt{\frac{4\pi}{\alpha}} \simeq 21.2 \text{ [MeV]}, \tag{4.19}$$

where $\alpha = (1/137)$ is the fine-structure constant. Figure 4.3 shows the Z-dependence of the scattering energy, E_{scatt}, the critical energy, E_{crit}, and the screening energy, E_{scr}.

4.3 Electromagnetic Interactions Relevant for Cascade and Shower Development

4.3.1 Bremsstrahlung by Electrons

Above the so-called *critical energy*, E_{crit}, the main energy loss of an electron (e^+, e^-) is by common bremsstrahlung in the Coulomb field of a nucleus, also referred to as *Coulomb bremsstrahlung*, in contrast to *magnetic bremsstrahlung*, which is relevant only in certain cases, discussed later (Sect. 4.5). According to the classical theory of radiation, a moving particle having unit electric charge e, passing a nucleus of charge Z at a given distance of approach (impact parameter), d, emits radiation whose intensity is proportional to

$$\left(\frac{N_A Z^2}{A m^2}\right) E, \tag{4.20}$$

where N_A and A are Avogadro's number and the mass number, respectively, i.e., N_A/A is the number of atoms per unit mass of the medium in which the particle is propagating, m is the mass of the projectile particle and E its energy. From this equation it is evident that in most cases the emission of bremsstrahlung by heavy particles can be neglected.

In the radiation process described above the atomic electrons can *screen* the Coulomb field of the nucleus as seen by the projectile, depending on the impact

parameter, d, which must be taken into account. In general one must distinguish between *no (ineffective) screening, intermediate* or *complete screening*. It can be shown that screening is complete if the energy of the particle is large (Rossi, 1952; Kamata and Nishimura, 1958, 1960; Nishimura, 1967; Marmier and Sheldon, 1969). This condition is fulfilled if

$$E \gg E_{\rm scr}, \tag{4.21}$$

where E is the particle energy and $E_{\rm scr}$ the screening energy as defined in Sect. 4.2.1, Eq. (4.1). Since for air $E_{\rm crit} > E_{\rm scr}$, *complete screening* applies.[4] In this case the differential probability, $\varphi_{\rm br}$, for an electron to undergo bremsstrahlung *per unit radiation length*, χ_0, is

$$\varphi_{\rm br}(v)\mathrm{d}v = \left[1 + (1-v)^2 - (1-v)\left(\frac{2}{3} - 2b\right)\right]\frac{\mathrm{d}v}{v}, \tag{4.23}$$

where v is the *fractional energy* carried away by the photon and the parameter b is

$$b = \frac{1}{18\ln\left(184.15\,Z^{-(1/3)}\right)}. \tag{4.24}$$

For air, $b = 0.0122$. Note that $\varphi_{\rm br}$ does not depend explicitly on the energy of the process initiating electron or the emitted photon, but only on the fractional energy, v, taken by the photon.

The average energy loss of an electron by bremsstrahlung per gram per centimeter square [$\mathrm{g}^{-1}\,\mathrm{cm}^2$] of matter traversed is given by the expression,

$$-\left\langle\frac{\mathrm{d}E}{\mathrm{d}x}\right\rangle\Bigg|_{\rm br} = N\int_0^{v_{\max}} h\nu \sum\left(\frac{\mathrm{d}\nu}{\nu}\right) = \chi_0^{-1} h\nu_{\max} = \chi_0^{-1}E. \tag{4.25}$$

where $h\nu$ is the energy of the emitted photon, ν being its frequency, and χ_0 the radiation length, as defined in Sect. 4.2. In a more explicit approximate form it can be written as

$$-\left\langle\frac{\mathrm{d}E}{\mathrm{d}x}\right\rangle\Bigg|_{\rm br} \approx 4Z^2\frac{e^2}{\hbar c}\left(\frac{e^2}{m_e c^2}\right)^2\frac{N_A}{A}E\left(\ln\left(184.15Z^{-(1/3)}\right) + \frac{1}{18}\right). \tag{4.26}$$

[4] The expression for no screening is (Rossi and Greisen, 1941),

$$\varphi(E,v)\mathrm{d}v = 4\alpha\frac{N_A}{A}Z^2r_e^2\left(1 + (1-v)^2 - \frac{2}{3}(1-v)\right)\left(\frac{\mathrm{d}v}{v}\right) \cdot\left[\ln\left(\frac{2E(1-v)}{m_e v}\right) - \frac{1}{2}\right] \tag{4.22}$$

Thus, the amount of energy loss by radiation is proportional to the particle energy. Note that this expression applies only to media where the condition

$$Z\left(\frac{e^2}{\hbar c}\right) \ll 1 \tag{4.27}$$

is fulfilled, which is the case for air.

4.3.2 Electron Pair Production

Common electron pair production by photons in the Coulomb field of a nucleus, also referred to as *Coulomb pair production*, in contrast to *magnetic pair production*, discussed later (Sect. 4.5), occurs when the energy of a photon exceeds the $(e^+ + e^-)$ pair creation threshold of 1.052 MeV. It is the main energy loss mechanism of photons at energies above the critical energy, $E_{\rm crit}$ (see Fig. 4.1).

The differential probability for an incident photon of energy $E_{\rm in} = h\nu$ to produce an electron pair *per unit radiation length*, $\chi_{0,\rm pair}$, in air with energy fractions $uE_{\rm in}$ and $(1-u)E_{\rm in}$, respectively, for *complete screening* is given by Rossi (1952) as

$$\psi_{\rm pair}(u)\mathrm{d}u = \left[u^2 + (1-u)^2 + \left(\frac{2}{3} + 2b\right)u(1-u)\right]\mathrm{d}u, \tag{4.28}$$

where b is given by Eq. (4.24). The condition for complete screening is the same as for bremsstrahlung and Eq. (4.1) can be rewritten as

$$h\nu \gg \frac{m_e c^2}{\alpha\, Z^{(1/3)}}\ [\mathrm{MeV}]. \tag{4.29}$$

Note that in Eq. (4.28) $\psi_{\rm pair}$ is independent of the photon energy and depends only on the *energy fraction* taken by one of the electrons of the pair.

The probability that a photon of energy E produces an electron pair per gram per centimeter square [$\mathrm{g}^{-1}\,\mathrm{cm}^2$] of matter traversed is given by the expression,

$$\frac{\mathrm{d}P_{\rm pair}}{\mathrm{d}x} \approx 4Z^2\frac{e^2}{\hbar c}\left(\frac{e^2}{m_e c^2}\right)^2\frac{N_A}{A}E\left(\ln\left(184.15Z^{-(1/3)}\right) - \frac{1}{54}\right). \tag{4.30}$$

According to Tsai (1974) the *differential* cross section for pair production is approximately given by

$$\frac{\mathrm{d}\sigma_{\rm pair}}{\mathrm{d}E} = \frac{A}{\chi_0 N_A}\left(1 - \frac{4}{3}u(1-u)\right), \tag{4.31}$$

where u is the fractional energy transfer to the created negatron or positron, $u = E/E_{\rm in}$. In the high energy limit, $h\nu \gg m_e c^2$, the total pair production cross section is given by

$$\sigma_{\text{pair}} = \frac{7}{9}\left(\frac{A}{\chi_0 N_A}\right) \text{ [cm}^2\text{]}. \tag{4.32}$$

In air this corresponds to ≈ 500 mb.

4.3.3 Coulomb Scattering of Electrons

As mentioned earlier, *multiple Coulomb scattering* is the dominating process that is responsible for the lateral spread of the electrons and, consequently, of the photons, when propagating in a column of matter.[5] When traversing a layer of thickness 1 [g cm^{-2}], the *number of deflections*, k, an electron suffers is approximately given by the expression

$$k \approx \frac{N_A}{A} d^2, \tag{4.33}$$

where N_A is Avogadro's number, A the atomic number of the medium, and d is the diameter of the scattering center (the atom). Therefore, in a dense medium there are about 10^7 to 10^8 scattering events per g cm^{-2}.

From the theory of *multiple scattering* (Rossi and Greisen, 1941; Molière, 1948a, b; Snyder and Scott, 1949; Scott, 1950, 1951, 1963; Rossi, 1952; Nigam et al., 1959; Nishimura, 1967; Tsai, 1974), the *mean square scattering angle* $\langle\theta^2_{\text{scatt}}\rangle$ in an infinitesimal layer of thickness dx [cm] is obtained as

$$\langle\theta^2_{\text{scatt}}\rangle \text{d}x = 16\pi N_A \left(\frac{Z^2}{A}\right) r_e^2 \left(\frac{m_e^2 c^4}{p^2\beta^2 c^2}\right) \ln\left(184.15\, Z^{-(1/3)}\right) \text{d}x, \tag{4.34}$$

where p and β are the particle momentum and velocity, N_A is Avogadro's number, Z and A are the atomic (charge) and mass number of the scattering center, and m_e and r_e are the rest mass and classical radius of the electron, respectively.

If the thickness dx is expressed in units of radiation length, t, and if we disregard the small difference caused by the difference in the numerical factor of Eqs. (4.2) and (4.13), then Eq. (4.34) can be rewritten in a form independent of the atomic number, and we get the simple expression

$$\langle\theta^2_{\text{scatt}}\rangle \text{d}t = \frac{4\pi}{\alpha}\left(\frac{m_e^2 c^4}{p^2\beta^2 c^2}\right) \text{d}t. \tag{4.35}$$

[5] The opening angle of the electron pair in pair production and the angles of emission of the photon and electron in the radiation process are irrelevant compared to Coulomb scattering.

Introducing now the substitution,

$$E_{\text{scatt}} = m_e c^2 \sqrt{\frac{4\pi}{\alpha}}, \tag{4.36}$$

where E_{scatt} is the *scattering energy* as defined previously in Eq. (4.19) ($E_{\text{scatt}} \simeq 21.2\,\text{MeV}$), we obtain

$$\langle \theta^2_{\text{scatt}} \rangle \mathrm{d}t = \left(\frac{E^2_{\text{scatt}}}{p^2 \beta^2 c^2} \right) \mathrm{d}t. \tag{4.37}$$

Including the process of multiple Coulomb scattering of electrons in the treatment of the EM-cascade extends the theory to three dimensions, which eventually yields the lateral structure function, from which the lateral density distribution of the shower particles can be obtained.

As indicated earlier, there are different treatments of the scattering process. The approach taken by Molière is the most detailed and accurate (Molière, 1953).

4.3.4 Ionization and Excitation by Electrons

All charged particles are subject to energy losses by ionization while propagating in a medium. The term "ionization losses" includes beside the ionization of atoms also *atomic excitation, knock-on electrons* (*delta-rays*[6]). At very low energy the energy losses decrease with increasing energy, reaching a minimum value called *minimum ionization*. Beyond this minimum, at highly relativistic energies, the ionization loss manifests a *slow logarithmic rise* with increasing energy.

For incident electrons knock-on electrons do not play a major role, however, they are often relevant for incident muons. As an example, Fig. 4.4, which is from the

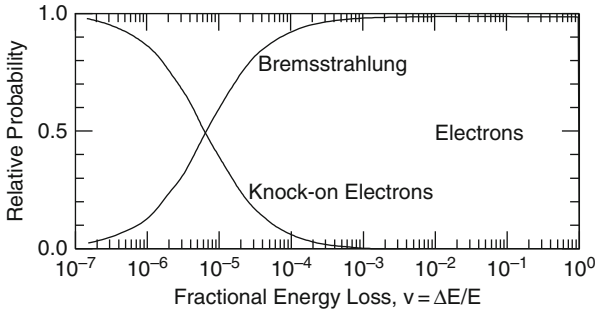

Fig. 4.4 Relative probabilities of fractional energy losses, $v = \Delta E_e / E_e$, per interaction per radiation length for 180 GeV electrons in iron, after Amaral et al. (2001)

[6] When an ejected electron has sufficient energy to produce its own trail of ionization it is termed a δ-*ray* and the ionization which is associated with it is called *secondary ionization*.

work of Amaral et al. (2001), shows the relative probabilities of fractional energy losses, $v = \Delta E_e / E_e$, per interaction and radiation length in iron for 180 GeV electrons for bremsstrahlung and knock-on electrons. The companion figure for muons is shown in Fig. 5.10.

The derivation of the ionization loss formula is complicated. Inspection of the literature shows that different authors obtained different expressions because different approximations had been used. Moreover, the energy loss depends on the velocity, mass and spin of the particle under consideration. One usually distinguishes between *heavy* and *light particles*, and whether we deal with highly relativistic velocities or not.

In their article Rossi and Greisen (1941) treat the problem of collision losses by charged particles in great detail. A very comprehensive overview that deals with all the aspects of ionization is given by Evans (1955) where the relevant original papers are listed. For the electromagnetic cascade problem and the study of the photon–electron component of extensive air showers we are dealing mainly with high energy electrons, which simplifies the problem somewhat. We therefore restrict the discussion to this category of particles and use the expressions given by Rossi and Greisen (1941).

The energy loss by ionization of an electron per unit path length, x, measured in [g cm^{-2}], in a medium of nuclear charge, Z, and mass number, A, is given by Rossi (1952) as

$$-\frac{\mathrm{d}E}{\mathrm{d}x} = 2\pi N_A \frac{Z}{A} r_e^2 m_e c^2 \left(\ln \left(\frac{\pi^2 m_e^2 c^2}{(1-\beta^2)^{(3/2)} I^2(Z)} \right) - \delta \right) \ [\mathrm{eV\ g^{-1}\,cm^2}] \quad (4.38)$$

where $\beta = v/c$ is the velocity of the electron in units of the velocity of light, c, and $I(Z)$ is the average ionization potential in eV of an atom of the traversed medium with atomic charge Z. For air $I(Z) = 80.5$ eV.[7] The constant δ, which accounts for part of the above mentioned logarithmic rise which is due to the *density effect* is $\delta = 2.9$ for negatrons, and $\delta = 3.6$ for positrons.

The density effect had been studied in great detail by Sternheimer and is discussed in his articles (Sternheimer, 1952, 1953, 1954a, b, 1956, 1971; Sternheimer et al., 1984; see also Tsai, 1974).

4.3.5 Compton Effect

Even though the Compton effect plays a minor role in the cascade development, we will briefly summarize the basic relations. Compton scattering and Compton absorption are relevant at low energies, below the critical energy, E_{crit}, where pair creation can be disregarded (Fig. 4.1).

[7] For media with $Z > 1$ the thumb rule $I(Z) \simeq 16(Z)^{0.9}$ eV is frequently used.

For Compton scattering of an incident photon of wavelength λ and outgoing photon of wavelength λ' with scattering angle θ, the well known expression for the wavelength shift is

$$\lambda' - \lambda \;=\; \frac{h}{m_e c}(1 - \cos\,\theta). \tag{4.39}$$

The cross section for Compton scattering depends on the polarization of the incident photon beam. For *polarized* photons it is

$$\frac{\mathrm{d}\sigma_{\mathrm{Comp}}}{\mathrm{d}\Omega} \;=\; \frac{r_0^2}{4}\left(\frac{\nu'}{\nu}\right)^2\left(\frac{\nu}{\nu'} + \frac{\nu'}{\nu} - 2 + 4\cos^2\theta\right) \;\; [\mathrm{cm}^2\,\mathrm{sr}^{-1}\,\mathrm{electron}^{-1}]\,, \tag{4.40}$$

where ν and ν' are the corresponding photon frequencies and θ is the angle between the electric vectors of the two photons.
For *unpolarized* photons it is

$$\frac{\mathrm{d}\sigma_{\mathrm{Comp}}}{\mathrm{d}\Omega} \;=\; \frac{r_0^2}{2}\left(\frac{\nu'}{\nu}\right)^2\left(\frac{\nu}{\nu'} + \frac{\nu'}{\nu} - 2 - \sin^2\theta\right) \;\; [\mathrm{cm}^2\,\mathrm{sr}^{-1}\,\mathrm{electron}^{-1}]\,. \tag{4.41}$$

At very low energies ($\lim E_\gamma \rightarrow 0$) the Compton cross section reduces to the Thomson cross section, σ_{Th}, if integrated over all solid angle elements, $\mathrm{d}\Omega$, thus

$$\sigma_{\mathrm{Th}} \;=\; \frac{8\pi\alpha^2}{3m_e^2}. \tag{4.42}$$

At high energies the Compton cross section is described by the Klein–Nishina formula (Klein and Nishina, 1929), which yields the Klein–Nishina cross section, $\sigma_{\mathrm{K-N}}$,

$$\sigma_{\mathrm{K-N}} \;=\; \frac{2\pi\alpha^2}{E_{\mathrm{CM}}^2}\left(\ln\left(\frac{E_{\mathrm{CM}}^2}{m_e^2}\right) + \frac{1}{2}\right), \tag{4.43}$$

where E_{CM} stands for the center of mass energy. This equation shows that $\sigma_{\mathrm{K-N}}$ is roughly inversely proportional to the photon energy.

The probability for a photon of energy E_{ph} to undergo Compton scattering is given by the relation

$$P_{\mathrm{Comp}}(E) \;=\; \chi_0\left(\frac{Cm_e c^2}{E_{\mathrm{ph}}}\right)\left(\ln\left(\frac{2E_{\mathrm{ph}}}{m_e c^2}\right) + \frac{1}{2}\right) \tag{4.44}$$

where

$$C \;=\; \pi N_A\left(\frac{Z}{A}\right) r_e^2 \;=\; 0.15\left(\frac{Z}{A}\right) \;\; [\mathrm{g}^{-1}\,\mathrm{cm}^2] \tag{4.45}$$

and χ_0 is the radiation length of the medium, defined by Eq. (4.2), in which the process takes place.

4.4 Miscellaneous EM-Interactions of Lesser or No Relevance for Cascades

4.4.1 Photo-Electric Effect

In the photoelectric process an incident photon removes an electron from the shell of an atom and transfers all but the binding energy, necessary to remove the electron from the atom, to the electron in the form of kinetic energy. This process is only important at very low energy, on the order of the binding energy of the outer electrons of atoms. It is irrelevant for air shower development as its cross section drops off rapidly with increasing energy (see Fig. 4.1). It is usually disregarded in most air shower studies, and likewise Rayleigh scattering. However, the photoelectric effect plays an important role in air shower detection techniques and particle detectors.

4.4.2 Photonuclear Reactions

This type of interaction has a very small cross section. For photons of energy 120 GeV on protons the cross section, $\sigma(\gamma p \rightarrow p\pi)$, amounts to about 100 μb. On air nuclei ($A \simeq 14.5$) the cross section is $\sigma(\gamma A \rightarrow A'\pi) \simeq 1.5$ mb. In comparison to common pair production the cross section ratio is

$$\frac{\sigma(\gamma p \rightarrow p\pi)}{\sigma(\gamma p \rightarrow pe^+e^-)} \simeq 3 \cdot 10^{-3}. \tag{4.46}$$

This is also representative for the low muon content in photon initiated showers.

However, photonuclear processes play an important role for the propagation of ultrahigh energy cosmic ray hadrons (protons and nuclei) in space. These particles may interact along their trajectories through galactic and intergalactic space with the 2.7 K background radiation and with starlight, producing nucleon resonances and subsequently decay pions. In this process the cosmic rays can lose a significant fraction of their energy that may result in a *rapid drop* of the high energy tail of the cosmic ray spectrum toward 10^{20} eV and above, and could cause at the same time a *pile-up* of particles around 10^{18}–10^{19} eV. This phenomenon is generally known as the Greisen-Zatsepin-Kuzmin (GZK) cutoff (Greisen, 1966; Zatsepin and Kuzmin, 1966; Kuzmin and Zatsepin, 1968). It is discussed in connection with the primary cosmic radiation in Chap. 11.

On the nuclear physics level, nuclei are expected to undergo *spallation* and *dissociation* because of photonuclear interactions. These topics are discussed in more detail in Chap. 11.

Photonuclear processes play a minor yet non-negligible role in the development of air showers. McComb et al. (1979) were among the first to carry out a series of simulations to explore the significance of photo–pion production in common hadron initiated showers and the contribution to the muon content in the showers through these processes. On the other hand the same processes are relevant for primary photon initiated showers as they may lead to a small muon component in initially pure electromagnetic cascades. These are then referred to as *muon-poor showers*.

Likewise photonuclear processes play a certain role when high energy neutrinos enter the atmosphere under very inclined trajectories, where they can penetrate great slant depths and may interact with a nucleon of a target nucleus. In the case of a muon neutrino, a high energy muon can be produced. The latter may undergo catastrophic bremsstrahlung and the resulting high energy photon will trigger an electromagnetic cascade.

Subsequently, in rare cases photo–pion production may occur that can initiate a local hadron cascade with the associated muons from charged pion decay and the accompanying photon–electron shower from neutral pion decay. Note that in a neutrino reaction on a nucleon of a target nucleus the recoil nucleon (nucleus) may acquire a sufficient amount of energy to generate a small hadron cascade, which can produce a number of muons.

In Fig. 4.5 we show a prediction of the total photon–proton cross section as a function of the center of mass energy, based on a so-called Reggeon-Reggeon-Pole model from the recent theoretical work of Cudell et al. (2000), together with some experimental data points.

In photon–nucleus interactions, such as may occur in air showers with atmospheric target nuclei, the cross section scales approximately as $A^{0.91}$, thus,

$$\sigma(\gamma A) \simeq A^{0.91}\,\sigma(\gamma\, p)\,. \tag{4.47}$$

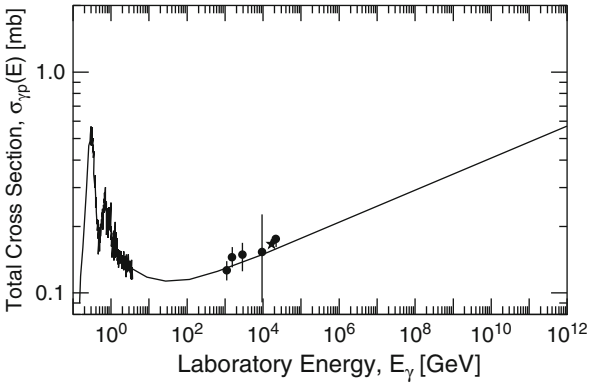

Fig. 4.5 Total cross section of photon–proton (γp) interactions over a wide range of energies. In the resonance-rich low energy region the curve shows a crude average over the numerous experimental points. The data are after Eidelman et al. (2004). The curve represents a theoretical prediction based on the RRP (Reggeon-Reggeon-Pole) model (Cudell et al., 2000, 2002). For further details concerning the ultrahigh energy region see Risse et al. (2006)

For a comprehensive review of this topic, the reader is referred to the article of Weise (1974).

As one out of many essays to estimate the photonuclear cross section at high energy we mention the work of Halzen and Zas (1990). In their attempt of investigating likely mechanisms that could enrich the muon content of very high energy gamma ray initiated showers via photonuclear processes, these authors constructed an expression to compute the photonuclear cross section via hadron production in jets, using the gluon structure function of the photon, which they claim to have calculated conservatively. They obtain for the photon–nucleon cross section the following formula,

$$\sigma(\gamma N) = \int_{p_t} \mathrm{d}p_t'^2 \int \mathrm{d}x_1 \mathrm{d}x_2 g_\gamma(x_1) g(x_2) \left(\frac{\mathrm{d}\hat{\sigma}}{\mathrm{d}p_t^2} \right), \tag{4.48}$$

where p_t stands for the transverse momentum and the $g(x)$ are the gluon structure functions ($g_\gamma(x_1)$ is the gluon structure function of the photon). The result of Eq. (4.48) was adapted to handle gamma-air interactions and parameterized to account for the expected logarithmic rise of the cross section, for subsequent application in Monte Carlo simulations. However, the rather dramatic rise of the production cross section which this equation predicts above 1 TeV for $p_{t\,\mathrm{min}} > 1\,\mathrm{GeV}$ appears to be unrealistic.

High energy muon induced photonuclear interactions are discussed separately in Chap. 5.

4.4.3 Photon–Photon Interactions

If a gamma ray of energy E_{γ_1} interacts with another gamma ray of energy E_{γ_2} a pair of particles of mass m each will be created, provided that the energy E_{γ_1} is greater than the threshold energy, E_{th}, for the process, thus

$$E_{\gamma_1} \geq E_{\mathrm{th}} = \frac{2m^2c^4}{E_{\gamma_2}(1 - \cos\theta)}, \tag{4.49}$$

where θ is the angle between the trajectories of the colliding photons.

For head-on collisions ($\theta = 180^\circ$) and the production of an *electron pair* relation 4.49 yields

$$E_{\gamma_1} = \frac{m_e^2c^4}{E_{\gamma 2}} = \frac{2.6 \cdot 10^{11}}{E_{\gamma_2}}\ [\mathrm{eV}] \tag{4.50}$$

and for the production of a *muon pair* we get for the threshold

$$E_{\gamma_1} = \frac{1.15 \cdot 10^{16}}{E_{\gamma_2}}\ [\mathrm{eV}]\,. \tag{4.51}$$

In the extreme relativistic case the cross section for the production of pairs of particles of equal mass, m, is

$$\sigma(\gamma\gamma)_{\text{pair}} = \pi r_e^2 \left(\frac{m}{\omega}\right)^2 \left(2\ln\left(\frac{2\omega}{m}\right) - 1\right) \ [\text{cm}^2] \,, \tag{4.52}$$

where $\omega = (E_{\gamma_1} \cdot E_{\gamma_2})^{1/2}$ and r_e is the classical radius of the electron.

In the non-relativistic classical domain ($\omega \sim m$) Eq. (4.52) reduces to

$$\sigma(\gamma\gamma)_{\text{pair}} = \pi r_e^2 \left(1 - \frac{m^2}{\omega^2}\right)^{1/2} \ [\text{cm}^2] \,. \tag{4.53}$$

For additional details see Jauch and Röhrlich (1955).

Photon–photon interactions play an important role for the propagation of gamma rays in the Universe. It is in fact the processes that limits their range of undisturbed propagation in space by causing them to lose energy by scattering (see Sect. 11.4.2).

4.4.4 Cherenkov and Transition Radiation, Radio and Fluorescence Emission

Cherenkov radiation, transition radiation, fluorescence and radio emission are electromagnetic processes that appear as bulk effects. They occur during the passage of charged particles (and photons) through a refractive medium. In addition, in the geomagnetic field radio emission is enhanced by an additional component due to interaction of the moving charges with the geomagnetic field. These processes cause very minor, for practical purposes negligible energy losses to the charged particles and to an air shower while propagating in the atmosphere. With the exception of radio emission, these phenomena are widely used as basic principles in the design of particle detectors.

On the other hand Cherenkov radiation as well as air fluorescence and radio emission, caused by the passage of radiation through the atmosphere, are directly detected and measured as such with ground based equipment, and are used for the analysis and interpretation of air showers. Because of their relevance, separate chapters are devoted to these topics (Chaps. 16, 17 and 18, respectively).

As mentioned before, transition radiation finds its application in special particle detectors. The theory and mathematical relations can be found in the fundamental paper of Ginzburg and Frank (1946) (see also Ter-Mikaelian, 1972; Bell, 1976; Ginzburg and Tsytovich, 1979, 1990; for some recent experimental work see Castellano et al., 1995; Barbarito et al., 1995, and references therein).

4.4.5 Synchrotron Radiation

The classical *synchrotron radiation* mechanism which takes place in curved acceleration scenario is not suited to generate high energy gamma rays and environmental conditions in the source region may impose additional limitations (Aharonian and Atoyan, 1995). The *critical frequency*, $\nu_{\rm crit}$, beyond which the synchrotron emission spectrum drops rapidly is (Jackson, 1999)

$$\nu_{\rm crit} \;=\; \frac{3eH\,\sin(\theta)}{4\pi m_e c}\left(\frac{E_e}{m_e c^2}\right)^2, \tag{4.54}$$

where e is the electric charge of the electron, H is the magnitude of the magnetic field strength, θ the angle between the field and the velocity vector of the electron, E_e and m_e are the energy and rest mass of the electron, and c the velocity of light.[8]

The maximum emission occurs at a frequency of

$$\nu_{\rm max} \;\simeq\; 1.2\cdot 10^6 H_\perp \left(\frac{E_e}{m_e c^2}\right)^2 \;\;[{\rm s}^{-1}], \tag{4.55}$$

or

$$\nu_{\rm max} \;\simeq\; 4.6\cdot 10^{-6} H_\perp E_e^2 \;\;[{\rm s}^{-1}], \tag{4.56}$$

which corresponds to an energy of

$$E_{\rm max} \;=\; h\nu_{\rm max} \;\simeq\; 1.9\cdot 10^{-20} H_\perp E_e^2 \;\;[{\rm eV}], \tag{4.57}$$

where $H_\perp$ is the component of the magnetic field strength perpendicular to the velocity vector of the electron in units of Oersted [Oe] and E_e the energy of the electron in [eV] (for details see Ginzburg and Syrovatskii, 1964, 1969; Ramana-Murthy and Wolfendale, 1993).

For a relativistic particle of charge e, relative velocity $\beta = v/c$, Lorentz factor γ and energy E moving in a circular orbit of radius ρ [m] the energy loss per revolution, ΔE, is given by the equation,

$$-\,\Delta E \;=\; \frac{4\pi}{3}\left(\frac{e^2}{\rho}\right)\beta^3\,\gamma^4 \;\;[{\rm MeV\,rev}^{-1}]. \tag{4.58}$$

Evaluating the constants in Eq. (4.58), one obtains for a relativistic particle of energy E [GeV] and $\beta \simeq 1$, moving in a circular orbit of radius ρ [m] an energy loss by synchrotron radiation per revolution of approximately

---

[8] The compact expression $\omega_c = 2\pi\nu_{\rm crit} = 3\gamma_e^3(c/\rho)$ is frequently used in place of Eq. (4.54), where c is the velocity of light [m s^{-1}], γ_e the Lorentz factor of the electron and ρ the radius of curvature [m] of the electron orbit.

$$-\Delta E \simeq 0.0885 \left(\frac{E^4}{\rho}\right) \ [\mathrm{MeV\,rev^{-1}}]\,. \tag{4.59}$$

4.4.6 Inverse Compton Scattering

This process is important in environments where photons of comparatively low energy interact with high energy electrons. The latter transfer part of their energy in the interaction to the photons, thus boosting their energy. In particular, an ambient photon of energy E_{ph} in the laboratory frame appears to be moving with an energy $\gamma_e E_{\mathrm{ph}}$ in the rest frame of a relativistic electron with Lorentz factor γ_e. In this inertial frame of reference, however, the *inverse Compton* (IC) *scattered* photon has an energy $< \gamma_e E_{\mathrm{ph}}$ and, when transformed back to the laboratory frame, its energy is $\sim \gamma_e^2 E_{\mathrm{ph}}$. The energy of an IC boosted photon, E_γ, is therefore given by (for details see, e.g., Ramana-Murthy and Wolfendale, 1993; Aharonian, 2004).

$$E_\gamma \approx \gamma_e^2 E_{\mathrm{ph}} \quad \text{when} \quad \gamma_e E_{\mathrm{ph}} \ll m_e c^2, \tag{4.60}$$

where m_e is the rest mass of the electron and c the velocity of light, or,

$$E_\gamma \sim E_e \quad \text{when} \quad \gamma_e E_{\mathrm{ph}} \gg m_e c^2, \tag{4.61}$$

where E_e is the energy of the electron.

The condition of expression 4.60 is commonly experienced in connection with interactions of electrons with the photons of the 2.7 K cosmic microwave background radiation (CMBR).[9]

At low energy the cross section for the inverse Compton process approaches asymptotically the Thomson cross section (see Eq. 4.42) and at high energy in the so-called Klein-Nishina regime, Eq. (4.43) (Bergström and Goobar, 2004).

4.4.7 Positron Annihilation

Positrons are produced in the pair production process and are subject to annihilation with electrons. At low energy the positron–negatron pair first forms the quasi atom called positronium. About 25% of the positroniums are in the $^1S_0$ state and 75% in the $^3S_1$ state. The former decay with a mean lifetime of $1.25 \cdot 10^{-10}$ s into two 0.511 MeV gamma rays, whereas the rest decay with a mean lifetime of $1.5 \cdot 10^{-7}$ s into three photons. The latter produce a continuum with a maximum energy of 0.511 MeV.

[9] The mean energy of a CMBR photon is $\langle E_{\mathrm{ph}} \rangle \approx 6 \cdot 10^{-4}$ eV. Thus, the condition of expression 4.60 is satisfied for Lorentz factors $\gamma_e < 10^9$, corresponding to electron energies $< 5 \cdot 10^{14}$ eV.

Annihilation can also take place as so-called free annihilation with the particles in flight. In this case the resulting gamma rays will have a continuous energy distribution instead of a line. In the highly relativistic case the cross section for positron–negatron annihilation (Stecker, 1971) is given by

$$\sigma_{\text{ann}}(E) = \left(\frac{\pi\, r_e^2}{\gamma}\right)[\ln(2\gamma) - 1]\,, \tag{4.62}$$

where γ is the Lorentz factor of the positron ($\gamma = E_e/(m_e c^2)$), r_e and m_e are the classical radius of the electron and its rest mass, respectively. In the case of forward-backward emission of the gamma rays, the forward going photon takes almost the entire energy of the positron while the recoil photon gets $m_e c^2/2 = 0.256\,\text{MeV}$. The cross section as given by Eq. (4.62) is rather low. For a 100 MeV positron it amounts to

$$\sigma_{\text{ann}}(100\,\text{MeV}) = 6 \cdot 10^{-27}\ \text{cm}^2. \tag{4.63}$$

For the development of extensive air showers positron annihilation plays a minor role. However, annihilation causes a negative charge excess which contributes to radio emission of showers. This subject is discussed in Chap. 18.

4.5 Processes Under Extreme Conditions

Some processes and phenomena occur only under very extreme conditions, such as at extremely high energies or in unusual environments, such as in extremely high magnetic fields, or in a combination of both. Three processes that are particularly relevant for ultrahigh energy photons and electrons comprise the Landau-Pomeranchuk-Migdal (LPM) effect, magnetic bremsstrahlung and magnetic pair production.

The LPM effect which is enhanced in dense media had been studied intensely for a long time by cosmic ray physicists experimentally and theoretically (Ivanenko et al., 1977; Kasahara, 1985; Bielawska et al., 1987; Okamoto and Shibata, 1987; Anthony et al., 1993; Misaki, 1993 and references listed therein), whereas the two latter processes were mostly a subject for astrophysicists in connection with studies of pulsars and similar objects, where very high magnetic fields ($\approx 10^{13}$ G) can occur (see, e.g., Ramana-Murthy and Wolfendale, 1993; Schönfelder, 2001). However, in recent years in connection with questions related to ultrahigh energy primary gamma rays the subjects of magnetic pair production and magnetic bremsstrahlung have attained a certain significance.

4.5.1 Landau-Pomeranchuk-Migdal (LPM) Effect

The Landau-Pomeranchuk-Migdal effect is due to quantum mechanical interference between amplitudes from different scattering centers that suppresses both the pair production and bremsstrahlung cross sections at very high energies (Landau and Pomeranchuk, 1953a, b; Migdal, 1956, 1957a, b). As a consequence it causes the initial phase of an electromagnetic cascade (shower) initiated by an ultrahigh energy photon or electron to develop at a slower rate, i.e., it penetrates deeper into the medium and the cascade is stretched at the beginning.

The phenomenon is linked to the fact that bremsstrahlung is not a point-like interaction. The effective region for bremsstrahlung and pair production in the vicinity of a nucleus that is given by

$$r_{\rm eff} \sim \frac{\hbar c}{q_\parallel} \sim \frac{2E(E-E')}{m_e c^2\, E'} \left(\frac{\hbar}{m_e c}\right), \tag{4.64}$$

where $r_{\rm eff}$ is the effective average collision distance (impact parameter) from the nucleus, E and E' are the energy of the incident electron and outgoing photon, respectively, in the case of bremsstrahlung, and

$$q_\parallel \sim \frac{m_e^2 c^4 E'}{2E(E-E')} \quad \text{for} \quad E,\ (E-E') \gg m_e c^2 \tag{4.65}$$

is the parallel component of the product $(\boldsymbol{q} \cdot \boldsymbol{r})$ in the exponent of the expression for the matrix element $\boldsymbol{V}_{f,i}$ of the Coulomb field, V, in the derivation of the Bethe-Heitler formula,

$$\boldsymbol{V}_{f,i} = \int \psi_f V \psi_i \mathrm{d}\tau \simeq \int \frac{e^{[i(\boldsymbol{q} \cdot \boldsymbol{r})/\hbar c]}}{r} \boldsymbol{r}^2 \mathrm{d}r. \tag{4.66}$$

The longitudinal momentum transfer between the electron and the nucleus in the bremsstrahlung process, $q_\parallel$, is small.

If E is so large or E' so small that $r_{\rm eff} > r_{\rm ave}$, the average radius between neighboring atoms, an interference effect occurs in aligned media, such as crystals, and the radiation is expected to be strongly collimated in a specific direction (diffraction scattering).

In amorphous media the interference is related to the mean square angle of multiple scattering, $\langle \theta^2_{\rm scatt} \rangle$, of an electron of energy E after passing a distance r in the medium which is given by (see also Eq. 4.37)

$$\langle \theta^2_{\rm scatt} \rangle \sim \left(\frac{E_{\rm scatt}}{E}\right)^2 \left(\frac{r}{\chi_0}\right). \tag{4.67}$$

It can be shown (Landau and Pomeranchuk, 1953a, b; Nishimura, 1967) that the interference becomes predominant if

$$\langle \theta^2_{\text{scatt}} \rangle^{1/2} > \left(\frac{m_e c^2}{E} \right), \tag{4.68}$$

which implies that

$$E_{\text{scatt}} \left(\frac{\hbar c}{q_{\parallel} \chi_0} \right)^{1/2} > m_e c^2. \tag{4.69}$$

This leads to the following criterion for the process to become relevant,

$$\frac{E(E - E')}{E'} > \left(\frac{m_e c^2}{E_{\text{scatt}}} \right)^2 m_e c^2 \left(\frac{m_e c}{\hbar} \right) \chi_0. \tag{4.70}$$

Thus, because of χ_0 in the expression it is evident that the LPM effect is most significant in heavy elements at very high energies. Numerically Eq. (4.70) yields

$$\frac{E(E - E')}{E'} > 4 \cdot 10^{12} \chi_0 \text{ eV} \tag{4.71}$$

for χ_0 given in units of [cm]. For the medium Pb and $E' \sim (E/2)$, the LPM effect becomes relevant at $E > 2 \cdot 10^{12}$ eV.

In the quantum mechanical treatment Migdal (1956) introduces a quantity that we call s_{Mig}, which represents the effect of multiple scattering, as a measure for the onset criterion of the LPM effect.

$$s_{\text{Mig}} = \frac{m_e c^2}{2E} \frac{1}{\langle \theta^2_{\text{scatt}} \rangle^{1/2}} = 10^6 \sqrt{\left(\frac{E' \chi_0}{E(E - E')} \right)} \left[\text{eV cm}^{-1} \right]^{1/2}. \tag{4.72}$$

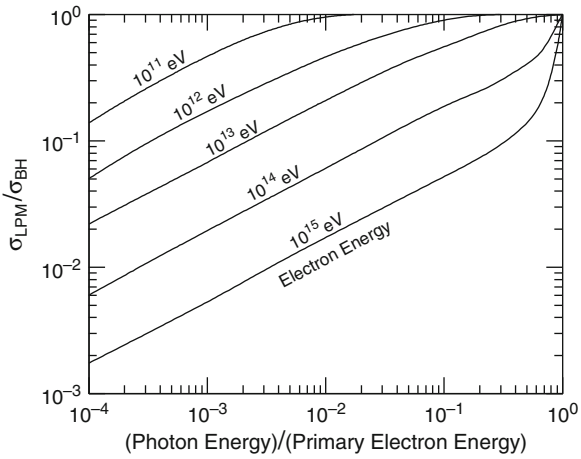

Fig. 4.6 Deviations from the Bethe-Heitler radiation cross section in Pb due to the Landau-Pomeranchuk-Migdal (LPM) effect. σ_{LPM} is the cross section calculated by Migdal (1956), σ_{BH} the one calculated by Bethe and Heitler (1934) (after Nishimura, 1967)

If $s_{\text{Mig}} > 1$ the effect is essentially negligible, if $s_{\text{Mig}} < 1$ it becomes predominant. Note that *the LPM effect scales with the fourth power of the projectile mass* (see Eq. 4.70).

The difference between the radiation cross section calculated according to Landau, Pomeranchuk and Migdal, and with the standard Bethe-Heitler formula disregarding the LPM effect is illustrated in Fig. 4.6, taken from Nishimura (1967). Shown is the ratio of the two cross section as a function of the energy fraction in Pb.

4.5.2 Magnetic Bremsstrahlung, Magnetic Pair Production and Pre-showering

Analogous to common bremsstrahlung and pair production in the high Coulomb field of a nucleus (Coulomb bremsstrahlung), magnetic bremsstrahlung (sometimes called *curvature radiation* or quantized synchrotron radiation) and magnetic pair production are processes that occur in high magnetic fields (Erber, 1966; Sokolov and Ternov, 1986). Apart from studies concerning electromagnetic effects in high magnetic field scenarios like in pulsars (Sturrock, 1971), the two latter effects have received little attention by cosmic ray physicists until recently when the phenomenon of *pre-showering* in connection with ultrahigh energy primary gamma rays has been recognized and became an issue of concern (McBreen and Lambert, 1981; Stanev and Vankov, 1997; Bertou et al., 2000; Anguelov and Vankov, 1999; Aharonian and Plyasheshnikov, 2003; Vankov et al., 2003; Homola et al., 2003, 2006).

Magnetic bremsstrahlung and pair production are essentially governed by a single parameter, Υ, which determines the threshold condition of the process (Erber, 1966),[10] namely

$$\Upsilon = \left(\frac{E}{m_e c^2}\right)\left(\frac{H_\perp}{H_{\text{crit}}}\right). \tag{4.73}$$

Here, E is the energy of the projectile electron, $H_\perp$ the strength of the ambient magnetic field perpendicular to the direction of motion of the electron, $m_e c^2$ the rest mass energy of the electron, and H_{crit}, referred to as the *critical field strength*, is the natural quantum mechanical measure of the magnetic field,

$$H_{\text{crit}} = \frac{m_e^2 c^3}{e\hbar} = 4.414 \cdot 10^{13} \text{ [G]}. \tag{4.74}$$

[10] The author wants to acknowledge the excellent lectures given by Prof. Thomas Erber in electrodynamics which he could enjoy as one of his students at the Illinois Institute of Technology in Chicago during the academic year 1957/1958.

Thus, the total probabilities in terms of cross sections for the two processes, magnetic radiation and pair production, for a given value of the magnetic field strength, H, depend only on the energy, E, of the particle or photon.

Equation 4.73 can be rewritten in terms of the *critical energy*, E_{Mcrit}, which a particle must exceed for the process to become effective, i.e., the threshold energy. Hence,

$$E \; > \; E_{\mathrm{Mcrit}} \; = \; mc^2 \left(\frac{H_{\mathrm{crit}}}{H_{\perp}} \right). \tag{4.75}$$

Here, the critical energy plays essentially the same role as the critical energy in ordinary electromagnetic cascade theory for ordinary matter, below which the multiplication process ceases.

Akhiezer et al. (1994) formulated the electromagnetic cascade theory in magnetic fields in vacuum in analogy to the one developed by Kamata and Nishimura (1958) for shower development in ordinary matter. We will not present any details of the derivation but give only the simplified expressions for the probabilities of magnetic bremsstrahlung, $P_{\mathrm{mag,br}}$ and magnetic pair production, $P_{\mathrm{mag,pair}}$, per unit path length. Using Anguelov and Vankov's notation, these are

$$P_{\mathrm{mag,br}}(\epsilon, \omega)\mathrm{d}\omega \; = \; \frac{q}{\epsilon^{(1/3)}} \left(\frac{(1-u)^{(5/3)}}{u^{(2/3)}} + \frac{1}{(1-u)^{(1/3)} u^{(2/3)}} \right) \mathrm{d}u \tag{4.76}$$

and

$$P_{\mathrm{mag,pair}}(\omega, \epsilon)\mathrm{d}\epsilon \; = \; \frac{q}{\omega^{(1/3)}} \left(\frac{(1-u)^{(5/3)}}{u^{(1/3)}} + \frac{u^{(5/3)}}{(1-u)^{(1/3)}} \right) \mathrm{d}u, \tag{4.77}$$

where in Eq. (4.76) $u = \omega/\epsilon$ and in Eq. (4.77) $u = \epsilon/\omega$ (Anguelov and Vankov, 1999). The variables ϵ and ω are the energy of the electron and photon, respectively. The parameter q follows from the derivation of the probability functions. After inserting the numerical values for the different constants, q can be expressed as

$$q \; = \; 3.9 \cdot 10^6 \left(\frac{H_{\perp}}{H_{\mathrm{crit}}} \right) \; [\mathrm{cm}^{-1} \; \mathrm{GeV}^{(1/3)}]. \tag{4.78}$$

Equations 4.76 and 4.77 correspond to Eqs. (4.23) and (4.28), respectively, for ordinary bremsstrahlung and pair production.

One can also define an *effective radiation length* for electrons, L_{e}, and for photons, L_{ph}, for magnetic bremsstrahlung and pair production, respectively. However, it turns out that these quantities are energy dependent and vary proportional to the third root of the energy. Numerically, L_{e} and L_{ph} are given by the relations

$$L_{\mathrm{e}} \; = \; 2.093 \left(\frac{E_0^{(1/3)}}{q} \right) \tag{4.79}$$

and

$$L_{\mathrm{ph}} \;=\; 4.091 \left(\frac{E_0^{(1/3)}}{q} \right). \tag{4.80}$$

With the above equations the growth of an electromagnetic cascade in a magnetic field in vacuum can be computed and analyzed in analogy to the cascades in gaseous or solid media, as discussed in Sect. 4.6 (e.g., Homola et al., 2003, 2006). However, the *thickness of the medium*, x, expressed in units of the radiation length L, i.e., $t = x/L$, is now energy dependent, too.

In Table 4.1, taken from Akhiezer et al. (1994), some values of L and $\overline{L}$, given in units of [cm], and $\overline{E}/E_0$ are listed for two energy regimes and four magnetic field ratios, H/H_{crit}. The average energy after an interaction, $\overline{E}$, is given by

$$\overline{E} = \frac{E_0}{t_{\mathrm{max}}} = \frac{E_0 \ln 2}{\ln(E_0 H_\perp / mc^2 H_{\mathrm{crit}})}, \tag{4.81}$$

and

$$t_{\mathrm{max}} \;=\; \left(\frac{1}{\ln 2} \right) \ln \left(\frac{E_0 H_\perp}{mc^2 H_{\mathrm{crit}}} \right). \tag{4.82}$$

The cross sections for these processes were calculated by Anguelov and Vankov (1999) and are shown in Fig. 4.7.

The main characteristics of a shower initiated in a strong magnetic field in vacuum are described by formulae that are entirely analogous to those for showers in ordinary matter. However, the characteristic difference is that the radiation length in a magnetic field in vacuum is *energy dependent* and *extremely small (short)*. The multiplication process takes place as long as the energy of the participating particles (electrons, photons) exceeds the critical energy, E_{Mcrit}.

Table 4.1 Values of L, $\overline{L}$ and $\overline{E}/E_0$ for two energy regimes and several magnetic field strength (after Akhiezer et al., 1994)

$H_\perp/H_{\mathrm{crit}}$	$E_0 = 100\,\mathrm{GeV}$			$E_0 = 10^6\,\mathrm{GeV}$		
	L [cm]	$\overline{L}$ [cm]	$\overline{E}/E_0$	L [cm]	$\overline{L}$ [cm]	$\overline{E}/E_0$
10^{-4}	$5.5{\cdot}10^{-4}$	$3.4{\cdot}10^{-4}$	0.2330	$1.2{\cdot}10^{-2}$	$4.6{\cdot}10^{-3}$	0.0569
10^{-3}	$1.2{\cdot}10^{-4}$	$6.0{\cdot}10^{-5}$	0.1310	$2.6{\cdot}10^{-3}$	$9.3{\cdot}10^{-4}$	0.0478
10^{-2}	$2.6{\cdot}10^{-5}$	$1.2{\cdot}10^{-5}$	0.0915	$5.5{\cdot}10^{-4}$	$1.9{\cdot}10^{-4}$	0.0413
10^{-1}	$5.5{\cdot}10^{-6}$	$2.3{\cdot}10^{-6}$	0.0701	$1.2{\cdot}10^{-4}$	$3.9{\cdot}10^{-5}$	0.0363

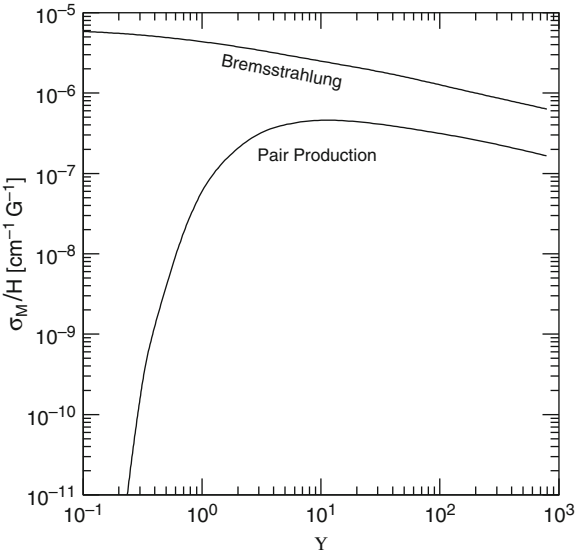

Fig. 4.7 Total cross sections for magnetic bremsstrahlung, σ_{Mbr}, and pair production, σ_{Mpair}, as a function of Υ (after Anguelov and Vankov, 1999)

4.6 Photon–Electron Cascade Theory

4.6.1 General Comments

Electrons (positrons and negatrons) account for about 90% of all the particles in a well developed hadron initiated air shower in the lower half of the atmosphere and photons are even more abundant.[11] Consequently, electromagnetic processes play an important role in the development and study of air showers. The bulk of the electrons are produced in *electromagnetic (EM) sub-cascades* (or sub-showers) that are interlaced with the hadron cascade and are initiated by high energy gamma rays originating from neutral pion decays via successive pair creation and bremsstrahlung processes. The neutral pions are products of the hadronic collisions that build up the mixed hadronic and electromagnetic showers (see Sect. 3.12).

Minor contributions to the electromagnetic channels in the form of electrons (positrons and negatrons) come mainly from the decay of muons and others unstable particles. Basically the photons as well as the electrons are subject to all electromagnetic processes provided that they are energetically possible. However, relevant for the growth of an EM cascade are the processes of *pair creation* by photons and *bremsstrahlung* by electrons. With the development of the cascade the energy of the participating components declines. As mentioned earlier, toward the fringes of the shower, beyond the shower maximum, *Compton scattering* of the more abundant low energy photons contributes to the flux of low energy electrons and an even less significant contribution comes from the *photoelectric effect*.

[11] The number of low energy photons is a multiple of that of electrons.

Apart from the above mentioned mechanisms that control the growth of an EM cascade and eventually its degradation through energy repartition among the cascade particles and quanta in each interaction, ionization and excitation of the atmospheric constituents are the ultimate causes for the energy dissipation and the decline of a shower.[12]

Similarly as in the case of the hadron cascade, the spatial development of an EM cascade (longitudinal and lateral) depends on the energy of the initiating agent (photon or electron) and on the properties of the medium in which it propagates. In the following, after a brief review of the development of the photon–electron cascade theory, we focus our discussion on the shower development in the atmosphere.

4.6.2 Historical Overview

The theory of the fundamental electromagnetic processes is well established and extensively documented in numerous articles and text books (Schiff, 1949; Rossi, 1952; Heitler, 1956; Jackson, 1999). The basic theory of the processes of photon emission or pair creation in the Coulomb field of a scattering center (nucleon or nucleus) had been worked out by Bethe and Heitler (1934). The foundations of the photon–electron shower or cascade theory were laid by Bhabha and Heitler (1937) and Carlson and Oppenheimer (1937).

In the early approaches scattering and ionization losses of the electrons were ignored and complete screening was assumed (Landau and Rumer, 1938).[13] This approximation was later on called *Approximation A*. Snyder (1938) and Serber (1938) introduced ionization losses, using the complete screening cross sections in the Bethe-Heitler formula. This approximation was later on called *Approximation B*. The two approximations are discussed in greater detail in Sect. 4.6.6. In subsequent work Snyder (1949) and Scott (1950) extended the theory further. In this context and for completeness we must also mention the early work of the Russian group of Tamm and Belenky (1939).

In these calculations the cascade problem was treated as a one-dimensional phenomenon. However, pair creation as well as bremsstrahlung and above all Coulomb scattering[14] provoke a lateral spread of the cascade participants and it was soon realized that the cascade problem had to be dealt with in three dimensions.

---

[12] Geomagnetic interactions, the production of Cherenkov radiation and radio frequency emission cause additional but essentially negligible energy losses.

[13] As pointed out by Nishimura (1967, p. 23, 2007, private communication), the importance of the Landau-Rumer theory is that it yields the exact analytic solution under approximation A in the form of complex integrals. The treatments of Bhabha and Heitler, and Carlson and Oppenheimer yield approximate series solutions.

[14] Single, plural and multiple Coulomb scattering occur, however, single large-angle scattering events are relatively rare whereas narrow-angle multiple scattering accounts for the bulk of the events.

Euler and Wergeland (1940) were the first to tackle the three-dimensional problem, followed by Bagge et al. (1943). However, some of the most significant work in this context was carried out by Rossi and Greisen (1941), Molière (1942, 1943, 1946, 1947,1948a, b, 1949, 1950 1952, 1953, 1954), Pomeranchuk (1944a, b), Migdal (1945a, b), Molière and Ott (1953), and by Guzhavin and Ivanenko (1958), (see also the book by Rossi, 1952). Additional and refined treatments of the problem followed by Roberg and Nordheim (1949), Eyges and Fernbach (1951), Green and Messel (1952), Nishimura and Kamata (1950, 1951a, b, 1952, 1954), and by Kamata and Nishimura (1958). For an outstanding review of the theory of electromagnetic cascade showers the interested reader is referred to the article of Nishimura (1967). Up to this point the cascade problem was treated purely analytically.

In view of the great mathematical complexity, Butcher and Messel (1958, 1960) and Messel et al. (1962a, b) (see also Messel and Crawford 1970, 1977) approached the solution of the problem with the help of the Monte Carlo (MC) method, using electronic computers. This method which employs the step by step application of the basic processes has been perfectioned through the years and is now common practice to compute all aspects of electromagnetic cascades. The program package called EGS4 is now accepted as a standard for three-dimensional electromagnetic cascade simulations that require a high degree of precision, whereby essentially all observables are accessible (Nelson et al., 1985).

However, the package is not very suitable for ultrahigh energy EM cascade simulations such as are needed in the air shower energy regime beyond 10^{18} eV. The very large number of particles and quanta that are typical at these energies cause the computation time to diverge. This applies even more if one wants to compute the *air Cherenkov* or *air fluorescence* photon flux associated with large showers.

For such cases the so-called *thinning* or *sampling methods* are more appropriate (Hillas, 1981), or a *hybrid* approach, using analytic relations in combination with the Monte Carlo procedures (Pierog et al., 2003, 2006; Drescher and Farrar, 2003; Drescher, 2006, and references listed therein). These methods were developed chiefly to simulate entire hadron initiated air showers, including the electromagnetic and optical components at the highest energies ($E \geq 10^{18}$ eV) (see Chap. 20 for details).

4.6.3 Basic Cascade Process and Phenomenology

The main ingredients for any EM cascade theory are the two fundamental processes outlined above that are responsible for the growth of the cascade, namely pair production by photons and bremsstrahlung by electrons. Considering for the time being only these two processes, disregarding any kind of scattering and energy dissipation, we can quickly overlook the two basic properties of cascade development in *one dimension*, namely the growth of the number of participating particles and quanta, and the energy degradation of the particle population by energy partition as the cascade develops.

If we assume that in this strongly simplified cascade picture a primary photon of energy E_0 propagating in the atmosphere will undergo pair creation after having penetrated on average a column of air of thickness χ_0 [g cm^{-2}], the two newly created electrons will subsequently propagate and undergo bremsstrahlung after having penetrated on average another column of unit radiation length of air. This sequence of alternating processes continues whereby the number of particles and photons increases and their energy decreases.

If we now assume that in each interaction the available energy is split into equal parts among the participating particles, i.e., each member of the first electron pair obtains an energy fraction $E_0/2$, and that in the bremsstrahlung process the initiating electrons split their energy among the outgoing scattered electrons and the created photons, one quickly sees that after n successive steps of the cascade process there are a total of $N = 2^n$ particles and quanta combined. The energy of each of the particles or photons of the n-th generation is

$$E_n = E_0/2^n. \tag{4.83}$$

The mathematical treatment of this repetitive process as outlined here is usually stopped when the energy of an electron or photon reaches the so-called *critical energy*, E_{crit}, defined in Sect. 4.2, to avoid an unrealistic diverging growth of the number of particles because of the lack of energy dissipation. It must also be remembered that in reality the available energy is not split into equal fractions among the particles and quanta that emerge from these processes as had been assumed above, but derives from a spectrum as determined by the fundamental processes described in Sect. 4.3.

4.6.4 Longitudinal Shower Development, Simple Picture

In the following we will summarize the qualitative description of Sect. 4.6.3 of the cascade development more quantitatively. For this, we consider a pure electromagnetic cascade and assume that after every radiation length each particle splits into two. After t radiation lengths of penetration in a medium the particle number in a shower, N, is

$$N = 2^t. \tag{4.84}$$

This expression holds irrespective of the approximations chosen for bremsstrahlung, pair production and even Compton scattering, if included.

The number of particles in the shower increases up to a depth X [g cm^{-2}], or T [rl], where $T = X/\chi_0$, defined by the integral

$$\int_0^T 2^t \mathrm{d}t = \frac{E_0}{E_{\text{crit}}} \tag{4.85}$$

and is assumed to drop to zero for $t > T$. We therefore get for T the value

$$T \simeq \frac{\ln(E_0/E_{\rm crit})}{\ln(2)}, \tag{4.86}$$

which represents essentially the depth of the shower maximum, $T_{\rm max}$ [rl] (or to $X_{\rm max}$ [g cm^{-2}], if converted). Thus, we see that $T_{\rm max}$ is proportional to the logarithm of the ratio $(E_0/E_{\rm crit})$. At this depth in the medium (atmosphere) the particle number is

$$2^{T_{\rm max}} \simeq \frac{E_0}{E_{\rm crit}}. \tag{4.87}$$

From this relation it is seen that the particle number in a shower, called the *shower size*, N, is proportional to the incident energy,[15]

$$N \propto \frac{E_0}{E_{\rm crit}}. \tag{4.88}$$

The basic trends of these results are essentially the same as those obtained with the full analytic treatment discussed below. In this simplified picture, it is usually assumed that the particle number in a shower is subject to exponential absorption of the form

$$N(t) \simeq N_{\rm max} \exp(-\lambda_{\rm abs} t_a) \tag{4.89}$$

beyond the shower maximum. Here, $t_a = t - t_{\rm max}$, and $\lambda_{\rm abs}$ is the *particle absorption length* in a shower, discussed in Chap. 6. The general longitudinal behavior of a shower as outlined here is essentially the same as shown in Fig. 4.8 that was obtained in the rigorous solution of the diffusion equation, discussed in Sect. 4.6.8.

4.6.5 Track Length Integral

If the energy dissipation of the particles occurs only through constant ionization and atomic excitation losses, energy conservation leads to the total *track length integral* as a measure of the shower (primary) energy, i.e.,

$$\int_0^\infty N_e(E_0, E = 0, t) {\rm d}t = \frac{E_0}{E_{\rm crit}}, \tag{4.90}$$

where N_e is the total number of shower electrons at depth t.

[15] We use N for the total number of particles and photons and N_e for the number of electrons (negatrons and positrons) only.

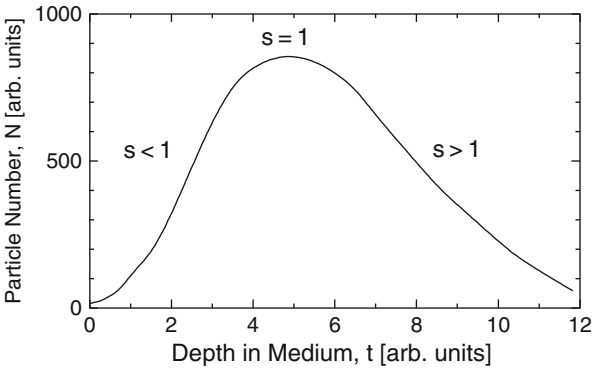

Fig. 4.8 Relation between the longitudinal shower development and the age parameter, *s* (after Nishimura, 1967)

4.6.6 Analytical Treatment, Assumptions, Approximations and Limitations

Today the standard analytic representation of the electromagnetic cascade theory as it is still being used in many cases in extensive air shower studies and very recently anew in hybrid approximations at ultrahigh energies (Drescher and Farrar, 2003; Drescher, 2006; Pierog et al., 2003, 2006) is the one developed by Nishimura, Kamata and Greisen, generally known as the NKG-theory (Greisen, 1956, 1960; Kamata and Nishimura, 1958; Nishimura, 1967). This theory yields the shower structure function, usually referred to as the *NKG-function* or *NKG-distribution*, i.e., analytic expressions for the longitudinal, lateral and angular distributions of the particles and quanta, and the energy spectra as a function of depth of penetration in the medium. In the course of time other authors have developed *structure functions* that are claimed to yield better fits to specific experimental data sets (Dedenko, 1977; Dedenko and Khristiansen, 1977; Hillas and Lapikens, 1977; Lagutin et al., 1979a, b, 1981; Uchaikin, 1979; Plyasheshnikov et al., 1979a, b; Capdevielle and Gawin, 1982, and others).

The main problem one is faced with when attempting to formulate the cascade process is to find a way to combine the equations of the fundamental processes such that the cascade can be treated analytically with simple expressions suitable for direct practical applications. This goal can only be achieved by the introduction of a number of approximations. Depending on the degree of accuracy desired more or less crude approximations are chosen. In the following we briefly illuminate the most common approximations.

If the photon and electron energies are large compared to the critical energy, ionization losses can be neglected. If in addition pair production and bremsstrahlung are the only processes considered and complete screening is assumed for the cross sections of these processes, the procedure is called *Approximation* A. Under this approximation the number of particles in the cascade grows indefinitely unless an energy cutoff is introduced, usually at the level of the critical energy.

The analogous procedure which, however, includes constant (energy independent) ionization losses but disregards Compton scattering, is called *Approximation* B. Under this approximation the cascade growth is limited because of the energy losses and likewise the maximum number of particles. In these two approximations any lateral spread of particles and quanta is ignored. Thus, the treatments yield *one-dimensional* cascade descriptions only.

However, extensive air showers are *three-dimensional* phenomena. The lateral spread of the particles and photons is due to (a) the opening angle of the electron pairs produced in pair production, (b) to the emission angle of the photons and scattered electrons in the bremsstrahlung process and, above all, (c) due to Coulomb scattering of the electrons. A careful analysis shows that in general the opening and emission angles of pair production and bremsstrahlung, respectively, can be neglected compared to the scattering angle, except at the very beginning of an electron shower.

The two standard treatments of the three-dimensional cascade theory are the one using the *Fokker-Planck approximation* for multiple scattering (Fokker, 1914; Planck, 1917) (called treatment in *Landau approximation*), and the one where the *Molière scattering theory* (Molière, 1953; Budini, 1953; Budini and Molière, 1953) is being used (called treatment *without* Landau approximation).

The treatment of the individual fundamental processes is based on quantum electrodynamics and radiation theory, as outlined in Sect. 4.3. These yield the probabilities for bremsstrahlung by an electron, φ_{br}, and for electron pair creation by a photon, Ψ_{pair}, which can be written in approximate form as

$$\varphi_{\mathrm{br}} \frac{\mathrm{d}E'}{E} \simeq \chi_0^{-1} \frac{\mathrm{d}E'}{E'}, \tag{4.91}$$

and

$$\Psi_{\mathrm{pair}} \frac{\mathrm{d}E'}{E} \simeq \left(\frac{7}{9}\right) \chi_0^{-1} \frac{\mathrm{d}E'}{E}, \tag{4.92}$$

where in Eq. (4.91), E is the energy of the electron in the initial state and E' the energy of the emitted photon. In Eq. (4.92), E is the energy of the initial photon and E' the energy of an electron. χ_0 is the radiation length as defined in Sect. 4.2.

From these equations we see that in the radiation process mostly low energy photons (gamma rays) are emitted, while in the pair production process the electrons are distributed uniformly, from zero to the full energy of the parent gamma ray.

4.6.7 Diffusion Equations

On the basis of the equations of the fundamental processes outlined in Sect. 4.3, the cascade structure function can now be constructed. This is being achieved by assembling diffusion equations that account for the rate of change of the population

of particles and photons in number and energy per path increment in the medium of propagation.

For convenience, one uses here the variable t, defined in Eq. (4.15), which represents the path length in the medium of propagation, measured in units of radiation length, χ_0, thus simplifying Eq. (4.25) to read

$$-\left\langle \frac{\mathrm{d}E}{\mathrm{d}x} \right\rangle \Big|_{\mathrm{br}} = \chi_0^{-1} E \;\rightarrow\; -\frac{\mathrm{d}E}{\mathrm{d}t} = E. \tag{4.93}$$

Following Nishimura (1967) and using partly his notation, the *one-dimensional diffusion equation* for electrons under approximation A, where energy dissipation is ignored, has the form

$$\frac{\partial n_e}{\partial t} = -A' n_e + B' n_\gamma, \tag{4.94}$$

and for the photons

$$\frac{\partial n_\gamma}{\partial t} = -\sigma_0 n_\gamma + C' n_e, \tag{4.95}$$

where n_e and n_γ are functions of the energy, E, and depth, t, in the medium. Moreover, $n_e(E,t)\mathrm{d}E$ and $n_\gamma(E,t)\mathrm{d}E$ are the average number of electrons and photons, respectively, in the energy interval E to $E + \mathrm{d}E$ in a shower at depth t.

A', B' and C' are *integral operators* relating to the radiation and pair creation processes, and σ_0 is the total probability (cross section) for pair creation. In particular, in Eq. (4.94) $A'n_e$ represents the loss of electrons within a specified energy interval due to bremsstrahlung and $B'n_\gamma$ is the gain from pair production by photons. In Eq. (4.95) $\sigma_0 n_\gamma$ is the loss of photons within the specified energy interval due to electron pair creation, and $C'n_e$ the gain of photons from electron bremsstrahlung.

For approximation B where ionization losses are included for electrons, represented by the constant ϵ_{ion}, we get the following modified form of the diffusion equation for the electrons (Eq. 4.94), namely

$$\frac{\partial n_e}{\partial t} = -A' n_e + B' n_\gamma + \epsilon_{\mathrm{ion}} \frac{\partial n_e}{\partial E}. \tag{4.96}$$

Equation 4.95 for the photons remains unaffected.

Finally, for the *three-dimensional* case in approximation B, n_e and n_γ become now functions of E, $\mathbf{r}$, and $\boldsymbol{\theta}$, where $\boldsymbol{\theta}$ stands for θ_1 and θ_2 which are the angles in two perpendicular planes that intersect in a line parallel to the z-axis of propagation of the shower. We then have $n_e(E, \boldsymbol{r}, \boldsymbol{\theta})\mathrm{d}E\,\mathrm{d}\boldsymbol{r}\,\mathrm{d}\boldsymbol{\theta}$ and $n_\gamma(E, \boldsymbol{r}, \boldsymbol{\theta})\mathrm{d}E\,\mathrm{d}\boldsymbol{r}\,\mathrm{d}\boldsymbol{\theta}$, which represent the average number of electrons and photons having energy between E and $(E + \mathrm{d}E)$, within the lateral range $\boldsymbol{r}$ and $\boldsymbol{r} + \mathrm{d}\boldsymbol{r}$, and angular range $\boldsymbol{\theta}$ and $\boldsymbol{\theta} + \mathrm{d}\boldsymbol{\theta}$ with respect to the shower axis.

The problem of multiple scattering which must now be considered can be handled either according to Landau and Rumer (1938) or Molière (1953). The resulting diffusion equations are then as follows (for details see Kamata and Nishimura, 1958; Misaki, 1964; Nishimura, 1967).

(i) Diffusion equations in Landau approximation:

$$\left(\frac{\partial}{\partial t} + \boldsymbol{\theta}\,\frac{\partial}{\partial \boldsymbol{r}}\right) n_e \;=\; -A' n_e + B' n_\gamma + \epsilon_{\text{ion}}\,\frac{\partial n_e}{\partial E} + \frac{E_s^2}{4E^2}\left(\frac{\partial^2}{\partial \theta_1^2} + \frac{\partial^2}{\partial \theta_2^2}\right) n_e \tag{4.97}$$

for the electrons and

$$\left(\frac{\partial}{\partial t} + \boldsymbol{\theta}\,\frac{\partial}{\partial \boldsymbol{r}}\right) n_\gamma \;=\; -\sigma_0 n_\gamma + C' n_e \tag{4.98}$$

for the photons.

(ii) Diffusion equations using Molière's scattering theory (without Landau approximation):

$$\left(\frac{\partial}{\partial t} + \boldsymbol{\theta}\,\frac{\partial}{\partial \boldsymbol{r}}\right) n_e \;=\; -A' n_e + B' n_\gamma + \epsilon_{\text{ion}}\,\frac{\partial n_e}{\partial E} + \int \left(n_e(\boldsymbol{\theta} - \boldsymbol{\theta'}) - n_e(\boldsymbol{\theta'})\right) \sigma(\boldsymbol{\theta'})\,\mathrm{d}\boldsymbol{\theta'} \tag{4.99}$$

for the electrons and

$$\left(\frac{\partial}{\partial t} + \boldsymbol{\theta}\,\frac{\partial}{\partial \boldsymbol{r}}\right) n_\gamma \;=\; -\sigma_0 n_\gamma + C' n_e \tag{4.100}$$

for the photons. Here, the variables $\boldsymbol{\theta}$, $\boldsymbol{\theta'}$ and $\boldsymbol{r}$ are the angles and the radial distance in the x-y-plane, and $\sigma(\boldsymbol{\theta'})\mathrm{d}\boldsymbol{\theta'}$ is the probability of deflection of the particle by an angle between θ' and $\theta' + \mathrm{d}\theta'$ in an infinitesimal layer of thickness $\mathrm{d}x$, i.e., $2\pi\sigma(\theta')\theta'\mathrm{d}\theta'\mathrm{d}x$.

Solving these equations is a rather elaborate task and requires the introduction of approximations and substitutions as well as *Laplace* and *Mellin transforms*. In the following we will only outline the general approach and summarize some of the essential and useful results. For details the interested reader is referred to the review article of Nishimura (1967) and the original publications (Rossi and Greisen, 1941; Rossi, 1952; Nishimura and Kamata, 1950, 1951a, b, 1952, 1954; Greisen, 1956, 1960; Kamata and Nishimura, 1958; Nishimura, 1964).

However, to illuminate the general technique of the solution of the diffusion equations, we discuss in the following the most simple problem, the solution under approximation A, to some degree of detail. For deeper insight or for the solution under approximation B, or for the three-dimensional cascade problem, the inter-

ested reader is referred to the original articles as listed above, and the work of Molière (1953, 1954) and references listed therein.

4.6.8 Solutions of the Diffusion Equations: Approximation A

The integral operators in approximation A are represented by *fractional forms* of the energy of the shower particles. This implies that shower particles of energy $E = 10^9$ eV in a shower initiated by a primary electron of energy $E_0 = 10^{12}$ eV are described by the same function as particles of energy $E = 10^{10}$ eV in a shower triggered by a primary of energy $E_0 = 10^{13}$ eV. Thus, the shower is described by a function which depends on the ratio E_0/E and t only. Following Rossi and Greisen (1941), and Nishimura (1967) we introduce as *Ansatz* for the solutions of the diffusion equations the expressions

$$n_e(E,t)\,\mathrm{d}E \;=\; a1\left(\frac{E_0}{E}\right)^s \frac{\mathrm{d}E}{E} e^{(-\mu t)} \tag{4.101}$$

and

$$n_\gamma(E,t)\,\mathrm{d}E \;=\; b1\left(\frac{E_0}{E}\right)^s \frac{\mathrm{d}E}{E} e^{(-\mu t)}. \tag{4.102}$$

Substituting these into the basic diffusion equations, Eqs. (4.94) and (4.95), one obtains

$$\mu \;=\; A(s) - \left(\frac{b1}{a1}\right) B(s) \quad \text{and} \tag{4.103}$$

$$\left(\frac{b1}{a1}\right)\mu \;=\; \left(\frac{b1}{a1}\right)\sigma_0 - C(s), \tag{4.104}$$

and expressions for $A(s)$, $B(s)$ and $C(s)$ as follows,

$$A(s) = \int_0^1 [1-(1-v)^s]\varphi_0(v)\mathrm{d}v$$

$$= 1.3603\left(\frac{\mathrm{d}}{\mathrm{d}s}\right)\ln\Gamma(s+2) - \frac{1}{(s+1)(s+2)} - 0.07513, \tag{4.105}$$

$$B(s) = 2\int_0^1 u^s \psi_0(u)\mathrm{d}u = 2\left(\frac{1}{s+1} - \frac{1.3603}{(s+2)(s+3)}\right), \tag{4.106}$$

$$C(s) = \int_0^1 u^s \phi_0(u)\mathrm{d}u = \frac{1}{s+2} + \frac{1.3603}{s(s+1)}, \tag{4.107}$$

and

$$\sigma_0 \;=\; 0.7733. \tag{4.108}$$

Combining 4.103 and 4.104 leads eventually to the following equation,

$$[\mu + \lambda_1(s)]\,[\mu + \lambda_2(s)] \;=\; 0, \tag{4.109}$$

Equation 4.109 can now be solved for λ_1 and λ_2, which are both functions of s that can be evaluated numerically for s.

$$\lambda_{1,2}(s) \;=\; -\left(\frac{A(s)+\sigma_0}{2}\right) \pm \frac{1}{2}\left([A(s)-\sigma_0]^2 + 4B(s)C(s)\right)^{1/2} \tag{4.110}$$

λ_1 and λ_2 correspond to the two parameters,

$$\frac{b1_{1,2}}{a1_{1,2}} \;=\; \frac{C(s)}{\sigma_0+\lambda_{1,2}} \text{ for } \mu_{1,2} \;=\; -\lambda_{1,2}. \tag{4.111}$$

Two sets of elementary solutions are now obtained, namely

$$n_{e_{1,2}}(E,t)\mathrm{d}E \;=\; \left(\frac{a1_{1,2}\,E_0^s\,\mathrm{d}E}{E^{(s+1)}}\right) e^{\lambda_{1,2}(s)t} \tag{4.112}$$

and

$$n_{\gamma_{1,2}}(E,t)\mathrm{d}E \;=\; \left(\frac{a1_{1,2}\,C(s)}{\sigma_0+\lambda_{1,2}(s)}\right)\left(\frac{E_0^s\,\mathrm{d}E}{E^{(s+1)}}\right) e^{\lambda_{1,2}(s)t}. \tag{4.113}$$

The general form of the solution is a linear combination of the solutions for n_{e_1}, n_{e_2} and n_{γ_1}, n_{γ_2}, respectively and the numerical values of A, B, C, λ_1, and λ_2 can now be obtained and are given in Table 4.2.

Since λ_2 is always negative, and as Eq. (4.110_2) shows,[16] $|\lambda_2| > \sigma_0$, the coefficient $(\sigma_0+\lambda_2)^{-1}$ of Eq. (4.113_2) should always be < 0. Consequently, a solution of Eq. (4.113_2) can only be obtained in combination with a solution of Eq. (4.112_2) for n_{e_2}. On the other hand, λ_1 is positive for $s < 1$, zero for $s = 1$, negative for $s > 1$, and approaches $-\sigma_0 = -0.7733$ for large s (see Table 4.2).

The spectrum $\mathrm{d}E/E^{(s+1)}$ for $s < 1$ represents the growing phase of the shower, for $s = 1$ the shower maximum and for $s > 1$ the declining phase. Thus, the parameter s which is the spectral index is a measure of the *shower age* along its path through the medium. This is illustrated in Fig. 4.8.

[16] The subscript $_2$ attached to equation number (4.110), and to (4.112) and (4.113) refers to the expression for λ_2 with the negative second term of Eq. (4.110).

Table 4.2 Numerical values of the functions $A(s)$, $B(s)$, $C(s)$, $\lambda_2(s)$, $\lambda_1(s)$, $\lambda_{1'}(s)$, and $\lambda_1''(s)$. (Rossi and Greisen, 1941; Nishimura, 1967)

s	$A(s)$	$B(s)$	$C(s)$	$\lambda_2(s)$	$\lambda_1(s)$	$\lambda_1'(s)$	$\lambda_1''(s)$
0.0	0.0000	1.547	∞	$-\infty$	$+\infty$	$-\infty$	$+\infty$
0.1	0.1522	1.400	12.84	–4.715	3.789	25.01	355.8
0.2	0.2865	1.280	6.123	–3.340	2.280	–9.457	65.43
0.3	0.4067	1.180	3.923	–2.749	1.569	–5.415	24.69
0.4	0.5154	1.095	2.846	–2.414	1.126	–3.655	12.48
0.5	0.6147	1.022	2.214	–2.201	0.8125	–2.693	7.418
0.6	0.7062	0.9593	1.802	–2.055	0.5754	–2.092	4.878
0.7	0.7909	0.9041	1.514	–1.952	0.3877	–1.684	3.428
0.8	0.8699	0.8554	1.302	–1.878	0.2348	–1.389	2.550
0.9	0.9439	0.8121	1.140	–1.825	0.1075	–1.166	1.965
1.0	1.014	0.7733	1.014	–1.787	0.0000	–0.9908	1.653
1.1	1.079	0.7383	0.9115	–1.761	–0.0917	–0.8497	1.276
1.2	1.142	0.7067	0.8278	–1.744	–0.1708	–0.7332	1.059
1.3	1.201	0.6778	0.7580	–1.735	–0.2391	–0.6358	0.8910
1.4	1.257	0.6515	0.6990	–1.732	–0.2984	–0.5532	0.7607
1.5	1.311	0.6273	0.6485	–1.734	–0.3501	–0.4824	0.6614
1.6	1.363	0.6049	0.6048	–1.741	–0.3952	–0.4216	0.5733
1.7	1.413	0.5843	0.5666	–1.751	–0.4347	–0.3691	0.4901
1.8	1.460	0.5651	0.5331	–1.764	–0.4693	–0.3236	0.4275
1.9	1.506	0.5473	0.5033	–1.780	–0.4996	–0.2840	0.3684
2.0	1.550	0.5360	0.4767	–1.797	–0.5263	–0.2498	0.3201
2.2	1.634	0.5004	0.4313	–1.837	–0.5704	–0.1943	0.2391
2.4	1.713	0.4737	0.394	–1.882	–0.6049	–0.1523	0.1823
2.6	1.787	0.4499	0.3627	–1.929	–0.6320	–0.1205	0.1375
2.8	1.857	0.4289	0.3362	–1.977	–0.6536	–0.0963	0.1079
3.0	1.924	0.4093	0.3134	–2.026	–0.6709	–0.0777	0.0974
4.0	2.213	0.3352	0.2349	–2.265	–0.7206	–0.0306	–
5.0	2.449	0.2848	0.1882	–2.480	–0.7419	–0.0145	–

Thus, s is related to the rate of growth and decay of the particle number in a shower as

$$\frac{\partial \ln(N_e)}{\partial t} = \lambda(s), \tag{4.114}$$

and to the energy spectrum of the photons and electrons approximately as

$$I(E) \propto E^{-(s+1)}\mathrm{d}E. \tag{4.115}$$

In summary, in a shower initiated by a photon or electron, s increases as the shower develops and the spectrum becomes softer and follows approximately Eq. (4.115). Moreover, the *rate of growth and decay* of the shower size, N_e, is related to s as described by Eq. (4.114). It is 0 when $s = 1$, i.e., at the shower maximum.

In showers initiated by a power law spectrum of photons or electrons, we have

$$n_0(E)\mathrm{d}E \sim E^{-(\alpha+1)}\mathrm{d}E \tag{4.116}$$

and s would be a constant, equal to α (Greisen, 1960, p. 71).

The general form of the solutions for n_e and n_γ (Eqs. 4.112 and 4.113) can be written as

$$n_e(E,t)\mathrm{d}E \;=\; \frac{\mathrm{d}E}{E^{s+1}}\left(a1_1\, e^{\lambda_1(s)t} + a1_2\, e^{\lambda_2(s)t}\right) \tag{4.117}$$

and

$$n_\gamma(E,t)\mathrm{d}E \;=\; \frac{\mathrm{d}E}{E^{s+1}}\left(\frac{a1_1 C}{\sigma_0+\lambda_1}\, e^{\lambda_1(s)t} + \frac{a1_2 C}{\sigma_0+\lambda_2}\, e^{\lambda_2(s)t}\right). \tag{4.118}$$

These equations are now solved with the help of Mellin transforms and corresponding boundary conditions. Details of this procedure can be found in the original article of Rossi and Greisen (1941), in Kamata and Nishimura (1958), or in the review of Nishimura (1967).

Without going into further details, a simple solution of the diffusion equations under approximation A leads eventually to the following results for the average *differential* number of electrons and photons, n_e and n_γ, respectively, and the *integral number* of electrons, $N_e(E_{0,e}, E, t)$, of energy $\geq E_e$ at a given location, t, in the medium due to an *incident electron* of energy $E_{0,e}$. Thus, for electrons of energy E_e we get

$$n_e(E_{0,e}, E_e, t)\mathrm{d}E_e \;=\; \frac{H_1(s)}{\sqrt{2\pi\,\lambda_1''(s)t}}\left(\frac{E_{0,e}}{E_e}\right)^s \frac{\mathrm{d}E_e}{E_e}\, e^{\lambda_1(s)t}, \tag{4.119}$$

where

$$t \;=\; -\frac{1}{\lambda_1'(s)}\,\ln\left(\frac{E_{0,e}}{E_e}\right), \tag{4.120}$$

and for photons of energy E_γ

$$n_\gamma(E_{0,e}, E_\gamma, t)\mathrm{d}E_\gamma \;=\; \frac{L(s)}{\sqrt{2\pi s\left(\lambda_1''(s)t + \frac{1}{2s^2}\right)}}\left(\frac{E_{0,e}}{E_\gamma}\right)^s \frac{\mathrm{d}E_\gamma}{E_\gamma}\, e^{\lambda_1(s)t}, \tag{4.121}$$

where

$$t \;=\; -\frac{1}{\lambda_1'(s)}\left(\ln\left(\frac{E_{0,e}}{E_\gamma}\right) - \frac{1}{2s}\right). \tag{4.122}$$

For the integral number of electrons we get

$$N_e(E_{0,e}, E_e, t) \;=\; \frac{H_1(s)}{s\sqrt{2\pi\left(\lambda_1''(s)t + \frac{1}{s^2}\right)}}\left(\frac{E_{0,e}}{E_e}\right)^s e^{\lambda_1(s)t}, \tag{4.123}$$

where

$$t \;=\; -\frac{1}{\lambda_1'(s)}\left(\ln\left(\frac{E_{0,e}}{E_e}\right)-\frac{1}{s}\right). \tag{4.124}$$

The corresponding equations for an *incident photon* of energy $E_{0,\gamma}$ read

$$n_e(E_{0,\gamma},E_e,t)\mathrm{d}E_e \;=\; \frac{M(s)\sqrt{s}}{\sqrt{2\pi\left(\lambda_1''(s)t-\frac{1}{2s^2}\right)}}\left(\frac{E_{0,\gamma}}{E_e}\right)^s\frac{\mathrm{d}E_e}{E_e}\,e^{\lambda_1(s)t}, \tag{4.125}$$

where

$$t \;=\; -\frac{1}{\lambda_1'(s)}\left(\ln\left(\frac{E_{0,\gamma}}{E_e}\right)+\frac{1}{2s}\right), \tag{4.126}$$

and

$$n_\gamma(E_{0,\gamma},E_\gamma,t)\mathrm{d}E_\gamma \;=\; \frac{H_2(s)}{\sqrt{2\pi\lambda_1''(s)t}}\left(\frac{E_{0,\gamma}}{E_\gamma}\right)^s\frac{\mathrm{d}E_\gamma}{E_\gamma}\,e^{\lambda_1(s)t}, \tag{4.127}$$

where

$$t \;=\; -\frac{1}{\lambda_1'(s)}\ln\left(\frac{E_{0,\gamma}}{E_\gamma}\right). \tag{4.128}$$

For the integral number of electrons we get

$$N_e(E_{0,\gamma},E_e,t) \;=\; \frac{M(s)}{\sqrt{2\pi s\left(\lambda_1''(s)t+\frac{1}{2s^2}\right)}}\left(\frac{E_{0,\gamma}}{E_e}\right)^s e^{\lambda_1(s)t}, \tag{4.129}$$

where

$$t \;=\; -\frac{1}{\lambda_1'(s)}\left(\ln\left(\frac{E_{0,\gamma}}{E_e}\right)-\frac{1}{2s}\right). \tag{4.130}$$

In these expressions $\lambda_1'(s) = \mathrm{d}\lambda_1(s)/\mathrm{d}s$. $H_1(s)$, $H_2(s)$, $L(s)$ and $M(s)$ are slowly varying functions of s.

$$H_1(s) = \frac{\sigma_0 + \lambda_1(s)}{\lambda_1(s) - \lambda_2(s)}, \tag{4.131}$$

$$H_2(s) = -\frac{\sigma_0 + \lambda_2(s)}{\lambda_1(s) - \lambda_2(s)}, \tag{4.132}$$

$$L(s) = \frac{C(s)\sqrt{s}}{[\lambda_1(s) - \lambda_2(s)]}, \tag{4.133}$$

$$M(s) = \frac{B(s)}{\sqrt{s}[\lambda_1(s) - \lambda_2(s)]}. \tag{4.134}$$

The numerical values of A, B, C, λ_1, λ_1', λ_1'', λ_2, $H_1(s)$, $H_2(s)$, $L(s)$ and $M(s)$, given in Tables 4.2 and 4.3, were originally tabulated for a range of s-values by Rossi and Greisen (1941) and Nishimura (1967). An extended discussion on the different approximations and their limitations can be found in the articles of these authors.

An estimate of the location of the shower maximum, $X_{\max}$, of electron initiated showers can be obtained from Eq. (4.124) by rearranging the equation, setting $\lambda_1(s = 1) = 0$, $\lambda_1'(1) \approx -1$, and it follows that

$$X_{\max} = \ln\left(\frac{E_{0,e}}{E_e}\right) - 1. \tag{4.135}$$

Table 4.3 Numerical Values of the Functions $H_1(s)$, $H_2(s)$, $L(s)$ and $M(s)$ (Rossi and Greisen, 1941; Nishimura, 1967)

s	$H_1(s)$	$H_2(s)$	$L(s)$	$M(s)$	s	$H_1(s)$	$H_2(s)$	$L(s)$	$M(s)$
0.0	0.5000	0.5000	0.4689	0.5333	1.4	0.3312	0.6688	0.5768	0.3840
0.1	0.5365	0.4635	0.4776	0.5207	1.5	0.3057	0.6943	0.5737	0.3700
0.2	0.5433	0.4567	0.4872	0.5093	1.6	0.2809	0.7191	0.5684	0.3554
0.3	0.5424	0.4576	0.4975	0.4989	1.7	0.2572	0.7428	0.5612	0.3404
0.4	0.5364	0.4636	0.5084	0.4891	1.8	0.2348	0.7653	0.5523	0.3253
0.5	0.5263	0.4737	0.5195	0.4799	1.9	0.2138	0.7862	0.5419	0.3102
0.6	0.5128	0.4872	0.5306	0.4709	2.0	0.1944	0.8057	0.5304	0.2952
0.7	0.4962	0.5038	0.5412	0.4619	2.2	0.1602	0.8398	0.5050	0.2663
0.8	0.4771	0.5229	0.5511	0.4527	2.4	0.1319	0.8681	0.4781	0.2395
0.9	0.4559	0.5442	0.5599	0.4428	2.6	0.1090	0.8910	0.4511	0.2152
1.0	0.4327	0.5673	0.5672	0.4328	2.8	0.0905	0.9096	0.4251	0.1935
1.1	0.4083	0.5917	0.5728	0.4218	3.0	0.0755	0.9244	0.4005	0.1744
1.2	0.3830	0.6171	0.5763	0.4100	4.0	0.0341	0.9659	0.3039	0.1085
1.3	0.3571	0.6429	0.5777	0.3974	5.0	0.0181	0.9819	0.2421	0.0733

There, the shower size is given by

$$N_{e,\max} = \frac{H_1(1)\left(\frac{E_{0,e}}{E_e}\right)}{\sqrt{2\pi(1.56X_{\max}+1)}} \approx \frac{H_1(1)\left(\frac{E_{0,e}}{E_e}\right)}{\sqrt{2\pi\left(1.56\ln\left(\frac{E_{0,e}}{E_e}\right)-0.56\right)}}. \tag{4.136}$$

From this it follows that the maximum shower size is proportional to the primary energy, a result obtained before with the simple picture (Sect. 4.6.4, Eq. 4.88).

We should point out that a primary photon penetrates a depth of about σ_0^{-1} [rl] before undergoing pair production. Therefore a photon initiated shower reaches its maximum development at *greater depth* than an electron initiated event of equal primary energy. Numerically this amounts to a depth difference of

$$\Delta t = \sigma_0^{-1} - \ln(2) \simeq 0.6 \text{ [rl]} \tag{4.137}$$

for equipartition of the energy among the electron pair.

The evaluation of Eq. (4.123) in terms of the number of electrons, N_e, as a function of depth, t, measured in units of radiation lengths in a medium is plotted in Fig. 4.9. At shower maximum ($s = 1$) the energy spectrum is proportional to $(1/E)$.

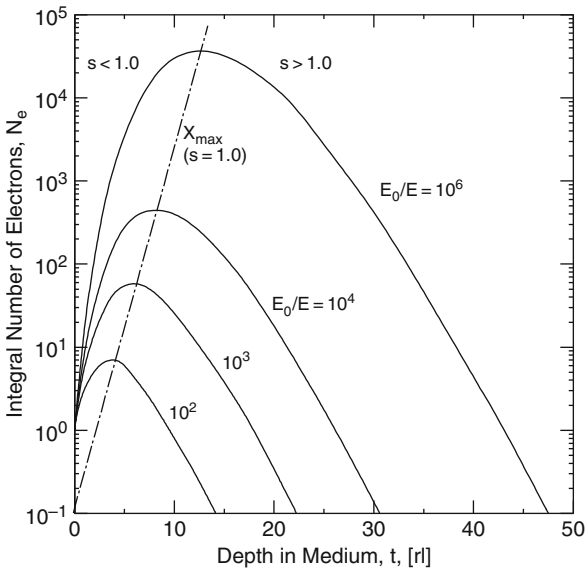

Fig. 4.9 Longitudinal shower development obtained from the shower function given by Eq. (4.123) (approximation A), after Rossi and Greisen (1941). Shown are the integral electron spectra, $N_e(E_0, E, t)$, for electron initiated showers. The loci of maximum development (at $s = 1.0$) are connected by the *dot-dash line*, labeled $X_{\max}$

4.6.9 Comments to Approximation B

As briefly mentioned before, in approximation B the situation is more complicated. The ionization term, $\epsilon_{\rm ion}(\partial n_e/\partial E)$ in Eq. (4.96) *destroys* the *fractional form* with respect to the energy of the solution. The problem is circumnavigated at high energy simply by avoiding this term as it is irrelevant there. However, at low energy the ionization losses reduce the number of particles.

The spectral shape of the electrons and photons in the low energy region can be predicted by introducing restrictions on the electron spectrum and by assuming that the absorption coefficient of the photons is energy independent. One obtains then an expression for the spectrum of low energy photons. These produce electron pairs of energy $E' \leq E_{\rm crit}$, having a spectrum which is similar to that of the photons. Since these electrons are stopped immediately, the electrons are in equilibrium with the source function. This leads to the low energy spectrum of photons and electrons of the form

$$n_\gamma {\rm d}E \;\sim\; \frac{{\rm d}E}{E} \tag{4.138}$$

and

$$n_e {\rm d}E \;\sim\; \ln\left(\frac{\epsilon_{\rm ion}}{E}\right){\rm d}E. \tag{4.139}$$

These expressions must be properly adapted if Compton scattering is to be included. Details of the calculation are given in Rossi and Greisen (1941), Kamata and Nishimura (1958) and Nishimura (1967).

4.6.10 Three-Dimensional Treatment and Energy Flow Distribution

For the three-dimensional case scattering must be included. Major scattering occurs among the low energy electrons. The *average lateral spread* is on the order of

$$\langle\, r \,\rangle \;\sim\; \frac{E_{\rm scatt}}{E}, \tag{4.140}$$

where $E_{\rm scatt}$ is the scattering energy (Eq. 4.19) and the average lateral distribution function of the electrons of energy $E \geq E_{\rm scatt}$ in electromagnetic cascades of age s can be described by

$$\frac{{\rm d}E}{E^{(s+1)}} \;\sim\; \frac{r{\rm d}r}{r^{(2-s)}}. \tag{4.141}$$

The angular spread about the cascade axis follows essentially the same behavior. For photons slightly different expressions apply because high energy photons are located closer to the cascade axis than energetic electrons.

The lateral distribution of the *energy flow* in an electromagnetic cascade at a given depth in the medium in which the cascade propagates is of considerable interest as it is linked to the primary energy of the initiating photon or electron, to the stage of the shower development (or shower age), and because it reveals physical properties of the cascade mechanism and the medium. The energy passing through an annular ring with radii r and $(r + \mathrm{d}r)$ about the shower axis is obtained in an analogous procedure as the lateral spread and leads to the relation

$$\frac{E\,\mathrm{d}E}{E^{(s+1)}} \sim \frac{r\,\mathrm{d}r}{r^{(3-s)}}. \tag{4.142}$$

Thus, the *energy flow distribution* is $(1/r)$-times steeper than the lateral spread of the particle number in the cascade. This is rather evident since particles of higher energy are scattered through smaller angles and are therefore located closer to the shower axis than low energy particles.

4.6.11 Lateral Spread of Electrons and Photons

Including the process of multiple Coulomb scattering in the diffusion equation for the electrons leads to the *lateral density distribution* of the shower particles. This is achieved by solving the diffusion equations for the three-dimensional treatment (Eqs. 4.97 and 4.98, or 4.99 and 4.100). The general result is of the form

$$\rho(r) = \left(\frac{N_e}{r_M^2}\right) f\left(s, \frac{r}{r_M}\right). \tag{4.143}$$

In this expression, N_e is the total number of electrons, r the perpendicular radial distance from the shower axis, r_M is the *Moliére radius* (or *Moliére unit*) defined below, and s is the shower age parameter, discussed previously.

For the age parameter range $0.5 \leq s \leq 1.5$, the second term of Eq. 4.143 can be written more explicitly in approximate form as

$$f\left(s, \frac{r}{r_M}\right) = \left(\frac{r}{r_M}\right)^{s-2} \left(1 + \frac{r}{r_M}\right)^{s-4.5} \left(\frac{\Gamma(4.5-s)}{2\pi\,\Gamma(s)\Gamma(4.5-2s)}\right) \tag{4.144}$$

in place of the complicated expression of Nishimura and Kamata (1952; Kamata and Nishimura, 1958), without impairing the result (Greisen, 1956, 1960) (Γ is the common gamma function). This expression is known as the *Nishimura-Kamata-Greisen or NKG function*.

Typical lateral density distributions of electrons in pure electromagnetic cascades in terms of the lateral structure function, $f(r)$, normalized as

$$2\pi \int f\left(\frac{r}{r_M}\right) \frac{\mathrm{d}r}{r_M} \;=\; 1 \tag{4.145}$$

are plotted as a function of r/r_M for three different stages of cascade development, characterized by the age parameter, s, in Fig. 4.10.

The quantity r_M of Eqs. (4.143) and (4.144) is the *Molière radius*, which is the characteristic unit of length in the scattering theory of Molière (1953).[17] It is defined as

$$r_M \;=\; \chi_0 \frac{E_{\mathrm{scatt}}}{E_{\mathrm{crit}}} \;\; [\mathrm{g\,cm^{-2}}]. \tag{4.146}$$

It amounts to $r_M \simeq 9.5\ \mathrm{g\,cm^{-2}}$ in air and can also be expressed in units of radiation lengths [rl]. Converted to units of meters the Molière radius, Eq. (4.146), is rewritten as

$$r_M \;=\; \frac{73.5}{P} \frac{T}{273} \;\; [\mathrm{m}], \tag{4.147}$$

where P [atm] is the pressure and T [K] the absolute temperature of the atmosphere at the observation level. At sea level it corresponds to a length of $r_M \simeq 79\ \mathrm{m}$.

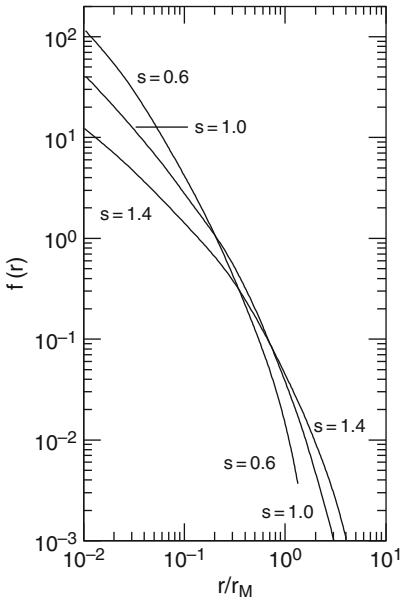

Fig. 4.10 Typical lateral distributions of electrons in an air shower under approximation B at different stages of its development, characterized by different age parameters, s. Shown is the structure function, $f(r)$, as a function of the ratio r/r_M for three values of s. The quantity r_M is called the characteristic or *scattering length*, often also referred to as the Molière radius (Molière, 1942, 1950, 1953) (after Nishimura and Kamata, 1950, 1951a, b, 1952)

[17] For further details concerning the Molière unit see Chap. 21.

The analogous angular characteristic unit of scattering is the *Molière angle*, θ_M, defined as

$$\theta_M = \frac{E_{\text{scatt}}}{E_{\text{crit}}} \text{ [rad]}, \tag{4.148}$$

which amounts to almost 1/4 radian (Molière, 1953).

The geometrical value of r_M [m] is inversely proportional to the density of the medium in which the cascade propagates. Because air showers propagate in a medium of varying density, one should use for computations that are related to experimental applications a value of r_M that corresponds to an altitude which is about two radiation length (approx. 75 g cm^{-2}) above the observation level, i.e., where the pressure is $P' = (P - 0.07)$ [atm]. Hence, Eq. (4.147) takes the form

$$r_{M'} = \frac{73.5}{P - 0.07}\left(\frac{T}{273}\right) \text{ [m]}. \tag{4.149}$$

The dependence of the corrected value of the Molière radius, $r_{M'}$, is plotted in Fig. 4.11.

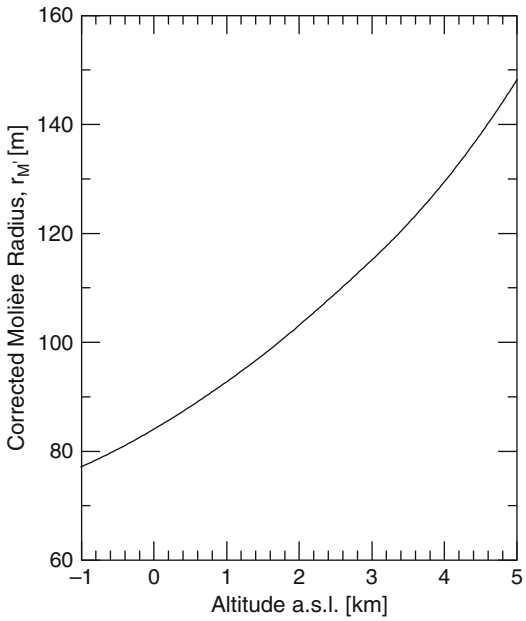

Fig. 4.11 Molière radius, $r_{M'}$, as a function of altitude above sea level corrected according to Greisen (1956) for the inhomogeneous atmosphere (International Standard Atmosphere) (after Cocconi, 1961)

4.6.12 Additional Results of Classical Cascade Theory

It had been shown in Sect. 4.6.8 that in the classical analytic treatment of the cascade problem some of the solutions can be obtained or expressed readily in terms of the fractional energy. Without going deeper into the mathematical details of the treatment of the problem (for details see Nishimura and Kamata, 1952; Greisen, 1956, 1960; Kamata and Nishimura, 1958, Nishimura, 1967) we present in Fig. 4.12a the integral energy spectra of photons and electrons at the shower maximum from the detailed cascade calculations of Richards and Nordheim (1948). The spectra are given in terms of the fractional energy E/E_{crit} and are normalized per one particle. Similarly, in Fig 4.12b are plotted the mean square radial displacements of electrons, averaged over the total length of a shower, as a function of the fractional energy E/E_{crit} for the differential and integral spectra obtained by Roberg and Nordheim (1949) (see also Greisen, 1956).

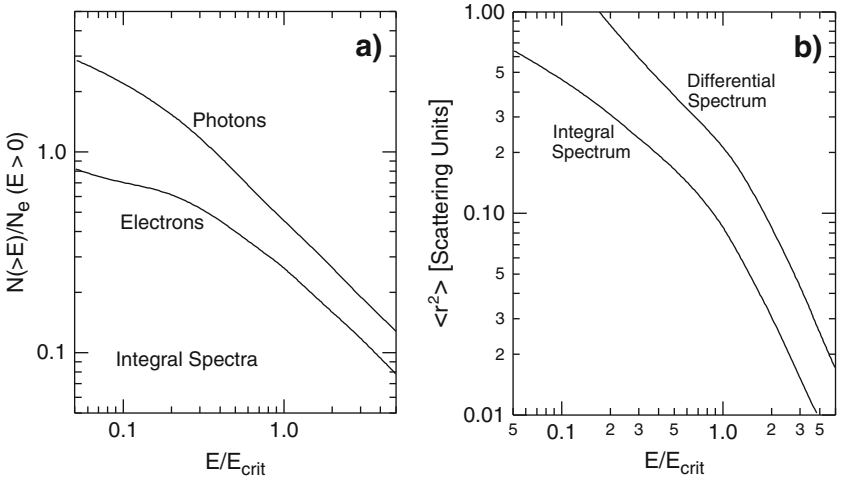

Fig. 4.12 (**a**) Normalized integral energy spectra of electrons and photons at shower maximum in terms of the fractional energy (after Richards and Nordheim, 1948). (**b**) Mean square radial displacement of the electrons as a function of fractional energy, averaged over the length of a shower for the differential and integral spectra. Single scattering and the variation of the air density are neglected (after Roberg and Nordheim, 1949)

4.6.13 Multi-Dimensional Descriptions of Electromagnetic Cascades Using Monte Carlo Simulations

Today, three-dimensional electromagnetic cascades are usually generated by simulations using Monte Carlo (MC) methods of numerical calculations. This method allows to include any kind of process very easily, including geomagnetic

deflection, air fluorescence (scintillation) as well as atmospheric Cherenkov radiation, radio emission and other effects. Moreover the calculations can be performed in *space and time* and yield the energy spectra of the electrons and photons as well.

The procedure which is outlined in more detail in Chap. 20 allows to calculate the superimposed electromagnetic component within primary hadron initiated air showers. However, as mentioned earlier, the computing time required by the photon–electron part of the shower simulation begins to diverge at ultrahigh energies and regress must be taken to analytical or hybrid approaches (Hillas, 1981; Drescher and Farrar, 2003; Drescher, 2006; Pierog et al., 2003, 2006). The situation gets worse if atmospheric Cherenkov and air fluorescence photon production are included.

4.6.14 Special Longitudinal Shower Profiles

In the following we illustrate how the Landau-Pomeranchuk-Migdal (LPM) effect and the pre-showering phenomenon affect the longitudinal profile of ultrahigh energy photon initiated electromagnetic showers. This topic is of great importance for the estimation of the primary mass and the distinction between primary photon and hadron initiated showers on the basis of the depth of maximum development of showers in the atmosphere.

As discussed in Sect. 4.5.1, the LPM effect reduces the cross section of electromagnetic interactions in a medium and thus retards the shower development. Since the process becomes important only at very high energies in the atmosphere, it applies only to the largest showers. However, it can lead to misinterpretation of the primary energy.

On the other hand, the effect of pre-showering, discussed in Sect. 4.5.2, occurs in the geomagnetic field well outside the Earth's atmosphere. It causes a rapid succession of electromagnetic interactions as long as the energy of the involved particles are above the required threshold energy. Consequently, instead of a single photon a tightly packed group of photons and electrons can enter the atmosphere. These may fake heavy primary initiated showers if one does not apply adequate experimental criteria to distinguish the two kinds of events, i.e., hadron from photon initiated showers.

In Fig. 4.13 we show the results obtained by Risse et al. (2004) in a modern Monte Carlo simulation of $3 \cdot 10^{20}$ eV photon initiated showers. Shown are three events each for (a) the common electromagnetic cascade process with the LPM and pre-showering processes deactivated, (b) the LPM and pre-showering processes activated, and (c) only the LPM process activated and pre-showering turned off. Inspection of this figure shows that in case (b) the LPM effect does not manifest itself. The reason for this is that the energy of the particle swarm produced in the pre-showering process has been degraded too much before entering the atmosphere, so that the LPM effect cannot become effective.

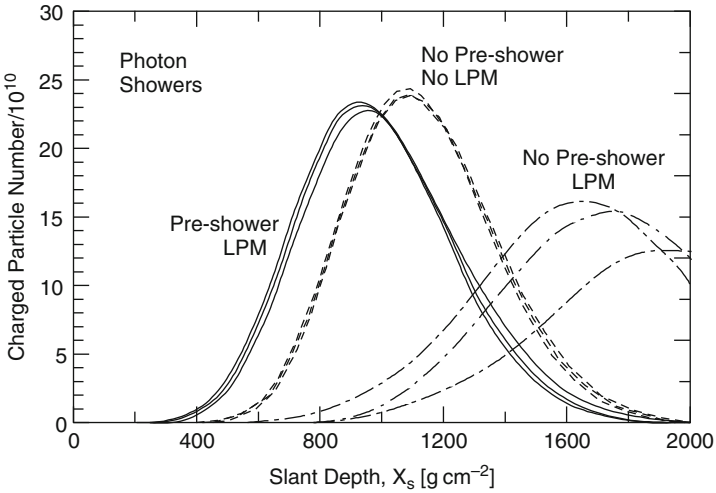

Fig. 4.13 Examples of simulated longitudinal profiles of $3 \cdot 10^{20}$ eV photon initiated showers. Shown are distributions of events having been subject to pre-showering and the LPM effect activated, normal cascades without pre-showering and LPM effect turned off, and normal cascades without pre-showering but LPM effect activated (for details see text) (after Risse et al., 2004)

4.7 Expressions for Practical Applications

4.7.1 Longitudinal Development, Shower Size and Age

To avoid evaluating the complicated expressions that describe the longitudinal development of an electromagnetic cascade for computing the location of the shower maximum, $t_{\max}$ [rl] (or $X_{\max}$ [g cm^{-2}]), and $N_{e,\max}$, or the shower size as a function of primary energy, E_0, and atmospheric depth, t (or X), $N_e(E_0, t)$, for the different approximations, several authors have developed approximate expressions that can be used readily to compute the shower size anywhere in the atmosphere.

Under *approximation* A, the depth, t, at which the shower size reaches its maximum is obtained as

$$t_{\max} = 1.01 \left[\ln\left(\frac{E_0}{E_{\text{cut}}}\right) - n \right], \tag{4.150}$$

where $n = 1$ for electron initiated showers and $n = 0.5$ for photon initiated showers, and E_{cut} is the so-called cutoff energy, i.e., the low energy limit of the fractional representation. The reason for $t_{\max}$ to be larger for photon initiated showers than for electron initiated showers is because of the larger effective radiation length for pair production by photons.

The number of electrons at shower maximum is given by

$$N_{e,\max} = \left(\frac{0.137}{\sqrt{[\ln(E_0/E_{\rm cut}) - 0.37]}}\right)\frac{E_0}{E_{\rm cut}} \tag{4.151}$$

and the number of photons amounts to

$$N_{\gamma,\max} = \left(\frac{0.137}{\sqrt{[\ln(E_0/E_{\rm cut}) - 0.18]}}\right)\frac{E_0}{E_{cut}} \ . \tag{4.152}$$

Under *approximation* B the expression for the location of the shower maximum is basically the same, except that now the critical energy $E_{\rm crit}$ is replaced by the cutoff energy, $E_{\rm cut}$, thus

$$t_{\max} = 1.01\left[\ln\left(\frac{E_0}{E_{\rm cut}}\right) - n\right], \tag{4.153}$$

In his review Greisen (1956) proposes the following expression to compute the shower size as a function of E_0 and t when N_e is large, i.e., at several radiation lengths from the starting point of the shower,

$$N_e(E_0, E_{\rm crit}, t) \simeq \left(\frac{0.31}{\sqrt{[\ln(E_0/E_{\rm crit})]}}\right)\exp\left[t\left(1 - \frac{3}{2}\ln(s)\right)\right], \tag{4.154}$$

where s stands for the approximate expression

$$s \approx 3t\left[t + 2\ln\left(\frac{E_0}{E_{\rm crit}}\right)\right]^{-1}. \tag{4.155}$$

In Fig. 4.14 we show the so-called shower curves, i.e., the shower size as a function of atmospheric depth, calculated by Snyder (1949) for primary gamma rays from 10^2 to 10^{10} GeV under approximation B. Also shown are the loci of constant age for different values of s.

Considering the basic solution for the shower size N_e in terms of $\lambda_1(s)t$ (Eq. 4.123), one obtains for the rate of change of N_e with respect to t Eq. (4.114). Beyond the shower maximum this equation describes the absorption of the shower, a topic discussed in detail in Chap. 6.

The link between the rate of change of the shower size with respect to t can be illuminated more by taking the logarithm of both sides of Eq. (4.154) and differentiating the expression with respect to t, which yields

$$\frac{\partial \ln(N_e)}{\partial t} = 1 - \left(\frac{3}{2}\right)\ln(s) + t\left(\frac{\partial}{\partial s}\right)\left(1 - \frac{3}{2}\ln(s)\right)\frac{{\rm d}s}{{\rm d}t}. \tag{4.156}$$

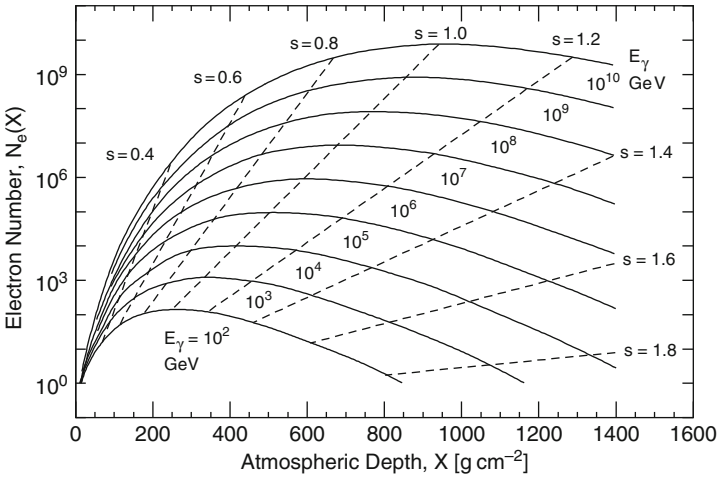

Fig. 4.14 Average shower development curves for gamma ray initiated electromagnetic cascades in the atmosphere. Shown are the electron number as a function of atmospheric depth for gamma ray energies from 10^2–10^{10} GeV obtained under approximation B. The loci of equal stages of shower development, i.e., of equal shower age of the different *cascade curves*, characterized by the age parameter, s, are connected by *dashed lines*. At $s = 1.0$ the shower is at its maximum development (after Snyder, 1949)

Substituting for t in terms of s from Eq. (4.155) into Eq. (4.156) simplifies the latter and leads to

$$\frac{\partial \ln(N_e)}{\partial t} = \frac{1}{2}\left[s - 1 - 3\ln(s)\right] . \tag{4.157}$$

4.7.2 Lateral Distribution of Particles, NKG-Function and Shower Age

For a pure electromagnetic cascade, the lateral distribution function of the shower particles had been derived by Nishimura and Kamata (1952).[18] This function is given in approximated form by Eq. (4.144). In compact form the Nishimura-Kamata-Greisen (NKG) function can be written as (Greisen, 1956, 1960)

$$\rho(r) = N_e\, C_1(s) \left(\frac{r}{r_M}\right)^{(s-\alpha)} \left(1 + \frac{r}{r_M}\right)^{(s-\beta)} . \tag{4.158}$$

Greisen found that setting $\alpha = 2$ and $\beta = 4.5$ gave the best fits to the experimental data. Thus, rewriting Eq. (4.158) more explicitly we get

[18] See also Kamata and Nishimura (1958). For a review see Nishimura (1967).

$$\rho(r) \;=\; N_e\, C_1(s) \left(\frac{r}{r_M}\right)^{(s-2)} \left(1+\frac{r}{r_M}\right)^{(s-4.5)}, \tag{4.159}$$

where the parameters and variables are as defined before. At sea level the appropriate Molière radius is $r_M = 79\,\mathrm{m}$.[19] $C_1(s)$ includes the normalizing factor such that

$$\frac{1}{N_e}\int_0^\infty 2\pi r\rho(r)\mathrm{d}r \;=\; 1. \tag{4.160}$$

Values of $C_1(s)$ for a range of s values valid for $0.01 \le (r/r_M) \le 10$ are given in Table 4.4 (Greisen, 1956; Cocconi, 1961).

Table 4.4 Values of $C_1(s)$ for Eq. 4.159 and given s

s	0.6	0.8	1.0	1.2	1.4	1.6	1.8
$C_1(s)$	0.22	0.31	0.40	0.44	0.43	0.36	0.25

The expression for $C(s)$ can be approximated with gamma functions as follows,

$$C(s) \;=\; \frac{1}{2\pi r_M^2}\left(\frac{\Gamma(4.5-s)}{\Gamma(s)\Gamma(4.5-2s)}\right), \tag{4.161}$$

where Γ represents the common gamma function.

The explicit form of Eq. (4.159) can then be written as

$$\rho(N_e, r) = \frac{N_e}{2\pi r_M^2}\left(\frac{r}{r_M}\right)^{(s-2)}\left(1+\frac{r}{r_M}\right)^{(s-4.5)}\left(\frac{\Gamma(4.5-s)}{\Gamma(s)\Gamma(4.5-2s)}\right)\;[\mathrm{m}^{-2}]. \tag{4.162}$$

It should be noted that the age parameter changes very slowly with shower size over a wide size range at large atmospheric depth. However, detailed studies have shown that there are discrepancies between theory and experiment. It was also found that in many cases the age parameter depends on r and accurate measurements have shown that in some cases two age parameters are needed to obtain a good fit with the experimental data (Chudakov et al., 1979).

Part of this discrepancy between theory and experiment is of course due to the fact that an air shower is not a pure electromagnetic cascade but consists of a superposition of a very large number of electromagnetic sub-cascades, initiated chiefly by the gamma rays resulting from neutral pion decay along the hadron cascade. The π^0 mesons are products of the parent hadron cascade which is chiefly responsible for the energy transport within a shower and for part of the lateral spread of the particles.

[19] For the definition of the Moliére radius see Sect. 4.6.11.

Other authors use some of their own slightly modified formulae, or simply different parameters to account for the hadronic origin of the showers to get a better fit to the experimental data, e.g., the KASCADE-Grande collaboration uses Eq. (4.158) with the following modified parameters for the normalizing factor,

$$C(s) = \frac{1}{2\pi r_M^2} \left(\frac{\Gamma(\beta - s)}{\Gamma(s - \alpha + 2)\Gamma(\alpha + \beta - 2s - 2)} \right), \tag{4.163}$$

where N_e and s are the shower size and age parameter, respectively, and for distances $r < 300$ m they use $\alpha = 1.5$, $\beta = 3.6$ and $r_M = 40$ m (Glasstetter et al., 2005).

It is found that at a given observation level the following empirical expression gives a good fit to experimental data and is frequently used.

$$f(r) = \frac{r_M^2 \rho(r)}{N_e}, \tag{4.164}$$

where r is the radial distance from the shower axis, r_M the characteristic Molière radius which depends on the atmospheric depth or altitude of the observation level, $\rho(r)$ the particle density at r, and N_e is the shower size.

References

Aharonian, F.A., and A.M. Atoyan: Astropart. Phys., 3, p. 275 (1995).
Aharonian, F.A., and A.V. Plyasheshnikov: Astropart. Phys., 19, p. 525 (2003).
Aharonian, F.A.: Very High Energy Cosmic Gamma Radiation, World Scientific, Singapore (2004).
Akhiezer, A.I., et al.: J. Phys. G, 20, p. 1499 (1994).
Amaral, P., et al.: ATLAS TileCal Collaboration: Eur. Phys. J., C 20, p. 487 (2001).
Anguelov, V., and H. Vankov: J. Phys. G, 25, p. 1755 (1999).
Anthony, P., et al.: PICRC, 4, p. 175 (1993).
Bagge, E., et al.: Kosmische Strahlung, W. Heisenberg, ed., Springer Verlag, Berlin (1943).
Barbarito, E., et al.: Nucl. Instr. Meth. A, 357, p. 588 (1995).
Bell, J.S.: Nucl. Phys. B, 112, p. 461 (1976).
Bergström, L., and A. Goobar: Cosmology and Particle Astrophysics, Springer, Berlin, 2nd ed. (2004).
Bertou, X., et al.: Astropart. Phys. 14, p. 121 (2000).
Bethe, H., and W. Heitler: Proc. Roy. Soc. A, 146, p. 83 (1934).
Bhabha H.J., and W. Heitler: Proc. Roy. Soc. A, 159, p. 432 (1937).
Bielawska, H., et al.: PICRC, 5, p. 399 (1987).
Bourdeau, M.F., et al.: J. Phys. G, 1, p. 821 (1975a).
Bourdeau, M.F., et al.: PICRC, 8, p. 2878 (1975b).
Budini, P.: Vorträge über Kosmische Strahlung, 2. Auflage (in German), W. Heisenberg, ed., Springer, Berlin, p. 418 (1953).
Budini, P., and G. Molière: Vorträge über Kosmische Strahlung, 2. Auflage (in German), W. Heisenberg, ed., Springer, Berlin, p. 438 (1953)
Butcher, J.C., and H. Messel: Phys. Rev., 112, p. 2096 (1958).
Butcher, J.C., and H. Messel: Nucl. Phys. B, 20, pp. 15–128 (1960).
Capdevielle, J.N., and J. Gawin: J. Phys. G, 8, p. 1317 (1982).
Carlson, J.F., and J.R. Oppenheimer: Phys. Rev., 51, p. 220 (1937).

Castellano, M., et al.: Nucl. Instr. Meth. A, 357, p. 231 (1995).
Chudakov, A.E., et al.: PICRC, 8, p. 217 (1979).
Cocconi, G.: Handbuch der Physik, S. Flügge, ed., Kosmische Strahlung, XLVI/I, Extensive Air Showers, Springer Verlag, Berlin, p. 222 (1961).
Cudell, J.R., et al.: Phys. Rev. D, 61, p. 034019 (2000).
Cudell, J.R., et al.: Phys. Rev. D, 65, p. 074024 (2002).
Dedenko, L.G.: PICRC, 8, p. 466 (1977).
Dedenko, L.G., and G.B. Khristiansen: PICRC, 8, p. 474 (1977).
Dovzchenko, O.J., and A.A. Pomanski: J. Exptl. Theoret. Phys. (USSR), 45, p. 268 (1963).
Dovzhenko, O.J., and A.A. Pomanski: Sov. Phys. JETP, 18, p. 187 (1964).
Drescher, H.J., and G. Farrar: Phys. Rev. D, 67, p. 116001 (2003).
Drescher, H.J.: Nucl. Phys. B (Proc. Suppl.), 151, p. 151 (2006).
Eidelman, S., et al.: Particle Physics Booklet, Particle Data Group, Springer, Berlin (available from LBNL and CERN) (2004), and Phys. Lett. B, 592, p. 1 (2004).
Erber, T.: Rev. Mod. Phys. 38, p. 626 (1966).
Euler, H., and H. Wergeland: Astrophys. Norw., 3, p. 163 (1940).
Evans, R.D.: The Atomic Nucleus, McGraw-Hill, New York (1955).
Eyges, L., and S. Fernbach: Phys. Rev., 82, p. 23 (1951).
Fokker, A.D.: Ann. Phys. 13, p. 810 (1914).
Genannt, R., and H. Pilkuhn: PICRC, 4, p. 2434 (1973).
Ginzburg, V.L., and I.M. Frank: Zh. Eksp. Teor. Fiz., 16, p. 15 (1946).
Ginzburg, V.L., and S.I. Syrovatskii: The Origin of Cosmic Rays, Pergamon Press, New York (1964).
Ginzburg, V.L. and S.I. Syrovatskii: The Origin of Cosmic Rays, Gordon and Breach, New York (1969).
Ginzburg, V.L., and V.N. Tsytovich: Phys. Rep., 49, pp. 1–89, (1979).
Ginzburg, V.L., and V.N. Tsytovich: Transition Radiation and Transition Scattering, Adam Hilger, Bristol (1990).
Glasstetter, R., et al.: PICRC, 6, p. 293 (2005).
Green, H.S., and H. Messel: Phys. Rev., 88, p. 331 (1952).
Greisen, K.: Progress in Cosmic Ray Physics, North Holland, Co., Amsterdam, Vol. 3, p. 1 (1956).
Greisen, K.: Annual Review of Nuclear Science, Annual Reviews, Inc., Palo Alto, California, USA, 10, p. 63 (1960).
Greisen, K.: Phys. Rev. Lett., 16, p. 748 (1966).
Guzhavin, V.V., and I.P. Ivanenko: Nuovo Cimento, Suppl. 8, p. 749 (1958).
Halzen, F., and E. Zas: Nucl. Phys. B (Proc. Suppl.) 14A, p. 60 (1990).
Heitler, W.: Quantum Theory of Radiation, Oxford University Press, London (1956).
Hillas, A.M., and J. Lapikens: PICRC, 8, p. 460 (1977).
Hillas, A.M.: PICRC, 1, p. 193 (1981).
Homola, P., et al.: astro-ph/0311442 (2003).
Homola, P., et al.: Nucl. Phys. B (Proc. Suppl.), 151, p. 119 (2006).
Ivanenko, I.P., et al.: PICRC, 7, p. 292 (1977).
Jackson, J.D.: Classical Electrodynamics, John Wiley & Sons, New York (1999).
Jauch, J.M., and F. Röhrlich: The Theory of Photons and Electrons, Addison-Wesley, Cambridge, MA (1955).
Kamata, K., and J. Nishimura: Progr. Theor. Phys. Jpn., 6, Suppl., p. 93 (1958).
Kamata, K., and J. Nishimura: J. Phys. Soc. Jpn., 15, p. 1565 (1960).
Kasahara, K.: Phys. Rev. 31, D, p. 2737 (1985).
Klein, O., and Y. Nishina: Zeitschr. f. Physik, 52, p. 853 (1929).
Kuzmin, V.A., and G.T. Zatsepin: Can. J. Phys. 46, p. S617 (1968).
Lagutin A.A., et al.: PICRC, 7, p. 7 (1979a).
Lagutin A.A., et al.: PICRC, 7, p. 18 (1979b).
Lagutin A.A., et al.: PICRC, 6, p. 260 (1981).

Landau, L., and G. Rumer: Proc. Phys. Soc., 166, p. 531 (1938).
Landau, L.D., and I.Ya. Pomeranchuk: Dokl. Akad. Nauk. SSSR, 92, p. 535 (1953a).
Landau, L.D., and I.Ya. Pomeranchuk: Dokl. Akad. Nauk. SSSR, 92, p. 735 (1953b).
Linsley, J.: PICRC, 7, p. 163 (1985).
Manchester, R.N., and J.H. Taylor: Pulsars, Freeman Press, San Francisco (1977).
Marmier, P., and E. Sheldon: Physics of Nuclei and Particles, Academic Press, New York, Vol. 1 (1969).
McBreen, B., and C.J. Lambert: Phys. Rev. D, 24, p. 2536 (1981).
McComb, T.J.L., et al.: J. Phys. G, 5, p. 1613 (1979).
Messel, H., et al.: J. Phys. Soc. Jpn., 17, Suppl. A III, p. 444 (1962a).
Messel, H., et al.: Nucl. Phys., 39, p. 1 (1962b).
Messel, H., and D.F. Crawford: Electron-Photon Shower Distribution Function, Tables for Lead, Copper and Air Absorbers, Pergamon Press, Oxford (1970).
Messel, H. and D.F. Crawford: Electron-Photon Shower Distribution Functions, Pergamon Press, Oxford (1977).
Migdal, A.B.: Zu. Eksper. Teor. Fiz., 15, p. 313 (1945a).
Migdal, A.B.: J. Phys. USSR, 9, p. 183 (1945b).
Migdal, A.B.: Phys. Rev., 103, p. 1811 (1956).
Migdal, A.B.: JETP 32, p. 633 (1957a) (in Russian).
Migdal, A.B.: Sov. Phys. JETP 5, p. 527 (1957b).
Misaki, A.: Progr. Theor. Phys. Suppl., 32, p. 82 (1964).
Misaki, A.: Nucl. Phys. B (Proc. Suppl.), 33AB, p. 192 (1993).
Molière, G.: Naturwissenschasten, 30, p. 87 (1942).
Molière, G.: Kosmische Strahlung, W. Heisenberg, ed., Springer Verlag, Berlin (1943).
Molière, G.: Cosmic Radiation, W. Heisenberg, ed., Dover Publications, New York, 1st ed., (1946).
Molière, G.: Z. Naturforschung, 2a, p. 133 (1947).
Molière, G.: Z. Naturforschung, 3a, p. 78 (1948a).
Molière, G.: Zeitschr. f. Physik, 125, p. 250 (1948b).
Molière, G.: Nuovo Cim., 6, Suppl., p. 374 (1949).
Molière, G.: Phys. Rev., 77, p. 715 (1950).
Molière, G.: Zeitschr. f. Naturforschung, 7a, p. 280 (1952).
Molière, G.: Vorträge über Kosmische Strahlung, 2. Auflage (in German), W. Heisenberg, ed., Springer, Berlin, pp. 446, 524 (1953).
Molière, G., and K. Ott: Vorträge über Kosmische Strahlung, 2. Auflage (in German), W. Heisenberg, ed., p. 412, Springer, Berlin (1953).
Molière, G.: Phys. Rev. Lett., 93, p. 636 (1954).
Nelson, W.R., et al.: The EGS4 Code System, Report No. SLAC-265, Stanford Linear Accelerator Center, Stanford, California (December 1985).
Nigam, B.P., et al.: Phys. Rev., 115, p. 491 (1959).
Nikishov, A.I., and V.I. Ritus: Proc. FIAN 111, p. 3 (1979).
Nishimura, J., and K. Kamata: Progr. Theor. Phys., 5, p. 899 (1950).
Nishimura, J., and K. Kamata: Progr. Theor. Phys., 6, p. 262 (1951a).
Nishimura, J., and K. Kamata: Progr. Theor. Phys., 6, p. 628 (1951b).
Nishimura, J., and K. Kamata: Progr. Theor. Phys., 7, p. 185 (1952).
Nishimura, J., and K. Kamata: Progr. Theor. Phys., 11, p. 608 (1954).
Nishimura, J.: Progr. Theor. Phys. Suppl., 32, p. 72 (1964).
Nishimura, J.: Handbuch der Physik, S. Flügge, ed., 46/2, p. 1, Springer Verlag, Berlin (1967).
Okamoto, M., and T. Shibata: NIM A, 257, p. 155 (1987).
Pierog, T., et al.: Nucl. Phys. A, 715, p. 895 (2003).
Pierog, T., et al.: Nucl. Phys. B (Proc. Suppl.), 151, pp. 159 (2006).
Planck, M.: Berl. Ber., p. 324 (1917).
Plyasheshnikov, A.V., et al.: PICRC, 7, p. 1 (1979a).
Plyasheshnikov, A.V., et al.: PICRC, 7, p. 13 (1979b).

Pomeranchuk, J.: Zu. Eksper. Teor. Fiz., 14, p. 1252 (1944a).
Pomeranchuk, J.: J. Phys. USSR, 8, p. 17 (1944b).
Procureur, J., et al.: PICRC, 8, p. 2878 (1975).
Ramana-Murthy, P.V., and A.W. Wolfendale: Gamma Ray Astronomy, Cambridge University Press Cambridge, 2nd ed. (1993).
Richards, J.A., Jr., and L.W. Nordheim: Phys. Rev., 74, p. 1106 (1948).
Risse, M., et al.: Astropart. Phys. 21, p. 479 (2004).
Risse, M., et al.: Czechoslovak J. Phys. 56, p. A327 (2006).
Roberg, J., and L.W. Nordheim: Phys. Rev., 75, p. 444 (1949).
Rossi, B., and K. Greisen: Rev. Mod. Phys. 13, p. 240 (1941).
Rossi, B.: High Energy Particles, Englewood Cliffs, New Jersey (1952).
Schiff, L.I.: Quantum Mechanics, McGraw Hill, New York (1949).
Schönfelder, V., Ed.: The Universe in Gamma Rays, Springer Verlag, Berlin, Heidelberg, New York (2001).
Scott, W.T.: Phys. Rev., 80, p. 611 (1950).
Scott, W.T.: Phys. Rev., 82, p. 893 (1951).
Scott, W.T.: Rev. Mod. Phys. 35, p. 231 (1963).
Serber, R.: Phys. Rev., 54, p. 317 (1938).
Snyder, H.S.: Phys. Rev., 53, p. 960 (1938).
Snyder H.S.: Phys. Rev., 76, p. 1563 (1949).
Snyder H.S., and W.T. Scott: Phys. Rev., 76, p. 220 (1949).
Sokolov, A.A., and I.M. Ternov: Radiation form Relativistic Electrons, Springer Verlag, Berlin (1986).
Stanev, T., and H.P. Vankov: Phys. Rev. D, 55, p. 1365 (1997).
Stecker, F.W.: Cosmic Gamma Rays, NASA SP-249 US GPO, Washington, DC, USA (1971).
Sternheimer, R.: Phys. Rev., 88, p. 851 (1952).
Sternheimer, R.: Phys. Rev., 89, p. 1309 (1953), erratum.
Sternheimer, R.: Phys. Rev., 93, p. 351 (1954a).
Sternheimer, R.: Phys. Rev., 93, p. 1434 (1954b).
Sternheimer, R.: Phys. Rev., 103, p. 511 (1956).
Sternheimer, R.M., and R.F. Peierls: Phys. Rev. B, 3, p. 3681 (1971).
Sternheimer, R.M., et al.: The Density Effect for the Ionization Loss of Charged Particles in Various Substances, At. Nucl. Data Tables, 30, p. 261 (1984). See also Groom, D.E., N.V. Mokhov, and S.I. Striganov, At. Nucl. Data Tables 78, p. 183 (2001) and Ivanov, D.Yu., et al.: Phys. Lett., B 442, p. 453 (1998) for corrections.
Sturrock, P.A.: Astrophys. J., 164, p. 529 (1971).
Tamm, Ig., and C. Belenky: J. Phys. USSR, 1, p. 177 (1939).
Ter-Mikaelian, M.L.: High Energy Electromagnetic Processes in Condensed Media, Wiley, New York (1972).
Tsai, Y.S.: Rev. Mod. Phys. 46, p. 815 (1974).
Uchaikin, V.V.: PICRC, 7, p. 24 (1979).
Vankov, H.P., et al.: Phys. Rev. D, 67, p. 043002 (2003).
Weise, W.: Phys. Rep., 13, p. 53 (1974).
Wheeler, J.A., and W.E. Lamb, Jr.: Phys. Rev., 55, p. 858 (1939).
Zatsepin, G.T., and V.A. Kuzmin: JETP Lett., 4, p. 78 (1966).

Chapter 5
Muon and Neutrino Interactions

Overview The first part of this chapter is devoted to muon physics. After a brief introduction to the subject the main muon production channels are summarized and photoproduction of muon pairs is outlined. Muon energy loss mechanisms and reactions are discussed at some length, including ionization losses, muon bremsstrahlung, direct electron pair production by muons, direct muon pair and muon trident production, and photonuclear reactions of muons. A summary of muon reaction probabilities, energy losses and a brief account of recent developments in muon physics end the muon part.

The second part of this chapter is devoted to neutrinos. We present first a general overview of neutrino production and neutrino induced reactions. Subsequently we discuss neutrino cross sections and present a data summary of experimentally determined cross sections at accelerators. This is followed by a compilation of theoretically derived cross sections for the different kinds of neutrinos that extends over the full energy range to ultrahigh energy neutrinos as are expected from astrophysical objects, such as active galactic nuclei. The chapter ends with an outline of the opacity of the Earth to ultrahigh energy neutrinos.

5.1 Introduction

Muons and neutrinos are leptons and therefore weakly interacting particles, having correspondingly small cross sections. This implies that in principle, once created in a high energy interaction, they can penetrate dense columns of matter without being much affected. Their subsequent influence on the average shower development is therefore insignificant. This is particularly true for neutrinos that do not carry electric charge.

On the other hand, muons which carry electric charge are subject to electromagnetic (EM) interactions that limit their range. However, their much larger mass defers the onset of bremsstrahlung and other EM-processes to much higher energies than is the case of electrons, leaving ionization as the principal energy loss mechanism over a wide energy range in the mid relativistic region while propagating through the atmosphere. These properties qualify the muons to be the ideal test particles for investigating the regions of early shower development at great heights

P.K.F. Grieder, *Extensive Air Showers,* DOI 10.1007/978-3-540-76941-5_5,

from ground level. They are, so to say, the messengers carrying at least part of the shower history directly to the observer.

In most air shower experiments neutrinos remain unobserved and are ignored because they escape recognition with common air shower detection instrumentation. Nevertheless, they are basically of importance because a certain fraction of the total energy of each shower is diverted into the neutrino component. Neglecting their existence falsifies calorimetric and other shower energy measurements and leads to incorrect primary energy estimates.

Neutrino induced showers, though very rare, are a special topic and play a certain role for strongly *inclined* and *horizontal air showers* (HAS), penetrating to great depth in the atmosphere, but also for showers emerging from steep mountain slopes and *upward directed air showers*, emerging from the ground or water surfaces (Fargion, 2001). The latter two categories of events are caused by high energy neutrino interactions taking place inside a mountain flank or in the Earth or a body of water, at relatively shallow depth. This subject is briefly discussed in Sect. 1.3 and more extensively in Sect. 19.5.2.

5.2 Muons

5.2.1 Muon Production: Main Channels

Muons are copiously produced in showers, in particular in the hadron cascade, and contribute about 10% to the total particle flux in an average air shower at ground level. They are mainly the decay products of a variety of unstable secondary particles like pions, kaons and others, emerging from high energy collisions, such as

$$\begin{aligned} p + N\ (\text{or } A) &\rightarrow p + N\ (\text{or } A) + n\pi^{\pm,0} + X \\ \pi^{\pm} &\rightarrow \mu^{\pm} + {}^{(}\overline{\nu_{\mu}}{}^{)} \\ \mu^{\pm} &\rightarrow e^{\pm} + {}^{(}\overline{\nu_{e}}{}^{)} + {}^{(}\overline{\nu_{\mu}}{}^{)}\,, \end{aligned} \tag{5.1}$$

where X stands for anything, including additional hadrons.

Many of the produced secondaries have several branches into different decay modes. Some, particularly the high-mass particles, may decay via other unstable particles and exhibit entire decay chains.[1]

The main contributors to the muon component in air showers are charged pions ($\pi^+,\ \pi^-$) and kaons ($K^+,\ K^-,\ K_L^0$), but also charmed particles, such as $D^{\pm}$, D^0, J/ψ and others. The bulk of the decay processes that yield muons are two-body

[1] For further details concerning decay channels of the different unstable particles consult the "Particle Physics Booklet" or the "Review of Particle Physics", assembled by the Particle Data Group; Eidelman et al. (2004).

decays with a *muon–neutrino* (or *muon–antineutrino*) associated to satisfy the conservation laws. Consequently, a significant neutrino component is co-produced and continuously building up in a shower together with the muon component as the shower propagates in the atmosphere and develops in age.

The mean life of charmed particles is $\leq 10^{-12}$ s. Hence, charmed particle decays are *prompt decays* and yield so-called *prompt or direct muons* that are in general energetic for kinematic reasons. All long-lived unstable particles ($10^{-8} \leq \tau \leq 10^{-10}$ s) are subject to competition between interaction and decay as they propagate in the atmosphere. The probability for either process to occur depends on the mean life of the particle and is a function of its kinetic energy and the local atmospheric density, which is a function of altitude.

This interrelationship is responsible for the zenith angle enhancement of the bulk of the muons in air showers, a phenomenon which muons from charmed particle decays do not exhibit. This problem is discussed in detail in Sect. 3.12.1. In Table 5.1 we list the particles and decay schemes that are the most relevant contributors to muons in air showers.

Table 5.1 Major muon and muon–neutrino parent particles and decay schemes relevant for air showers. The $\tau^{\pm}$ decay yields in addition a tau neutrino ($^{(}\overline{\nu_\tau}^{)}$)

Particle symbol	Partial decay modes	Branching fraction [%]	Mean life [s]
$\pi^{\pm}$	$\rightarrow \mu^{\pm} + {}^{(}\overline{\nu_\mu}^{)}$	99.99	$2.603 \cdot 10^{-8}$
$K^{\pm}$	$\rightarrow \mu^{\pm} + {}^{(}\overline{\nu_\mu}^{)}$	63.43	$1.238 \cdot 10^{-8}$
	$\rightarrow \pi^0 + \mu^{\pm} + {}^{(}\overline{\nu_\mu}^{)}$	3.27	
$\tau^{\pm}$	$\rightarrow \mu^{\pm} + {}^{(}\overline{\nu_\mu}^{)} + {}^{(}\overline{\nu_\tau}^{)}$	17.36	$2.906 \cdot 10^{-13}$
$D^{\pm}$	$\rightarrow {}^{(}\overline{K^0}^{)} + \mu^{\pm} + {}^{(}\overline{\nu_\mu}^{)}$	7.0	$1.040 \cdot 10^{-12}$
D^0	$\rightarrow \mu^+ +$ Hadrons	6.5	$4.103 \cdot 10^{-13}$
	$\rightarrow K^- + \mu^+ + \nu_\mu$	3.19	
J/ψ	$\rightarrow \mu^+ + \mu^-$	5.88	$\sim 10^{-20}$
etc.			

Due to the energy degradation of the hadron cascade in a shower as it penetrates into deeper regions of the atmosphere, the hadronic collisions become less energetic and likewise the secondaries, emerging from the collisions, some of which are prospective parent particles of the muons. Therefore, muons resulting from later generations of interactions that occur at greater depth in the atmosphere are less energetic than those from the first few generations originating from great heights.

5.2.2 Photoproduction of Muon Pairs

Photoproduction of a muon pair by a photon in the Coulomb field of a proton or nucleus can be calculated analogously to electron pair production on the basis of quantum-electrodynamics (QED) (see Chap. 4) and under the assumption that the muon is a heavy Dirac particle (Bethe and Heitler, 1934; Heitler, 1956; Akhiezer and Berestetskii, 1965; Källén, 1972). Symbolically the reaction can be represented

in its most simple form without target excitation as

$$\gamma \; + \; p \,(\text{or } Z) \rightarrow p \,(\text{or } Z) \; + \; \mu^+ \; + \; \mu^- \;\; , \tag{5.2}$$

where γ, p and Z represent the incident photon, the target proton or the target nucleus, respectively.

Evaluating the corresponding Feynman graphs for the Bethe-Heitler and Compton diagrams for pair production (one of each is shown in Fig. 5.1), and using Feynman notation convention, one obtains for the average *differential* cross section for the γ, p case

$$\mathrm{d}\sigma = \left(\frac{\alpha^3 M_p}{4\pi^2 k}\right) \delta^{(4)}(k - p_+ - p_- - q) \left(\frac{\mathrm{d}^3 Q'}{E'} \frac{\mathrm{d}^3 p_+}{E_+} \frac{\mathrm{d}^3 p_-}{E_-}\right) (\lambda_{11} + \lambda_{12} + \lambda_{22}) \;\; , \tag{5.3}$$

where α is the fine-structure constant, M_p the proton mass, k and q are the 4-momenta of the incident and virtual photon ($q = Q' - Q = k - p_+ - p_-$), Q and Q' are the 4-momenta of the incident and recoil proton (or nucleus), p_+, E_+ and p_-, E_- the 4-momenta and energies of the outgoing μ^+ and μ^- ($E_+ = p_+ \cdot \omega/\omega_0$, $E_- = p_- \cdot \omega/\omega_0$), $\omega = Q + k - p_+$, $\omega_0 = (\omega^2)^{1/2}$), and $\delta^{(4)}$ is the delta function relating to the 4-vectors. The λ-terms are complicated expressions; λ_{11} stands for the contribution from the Bethe-Heitler graph, (a), λ_{22} from the Compton graph, (b), and λ_{12} results from the interference of the two. λ_{12} vanishes because of charge conjugation and λ_{22} is very small for small proton recoil energies (for further details see Adair, 1977).

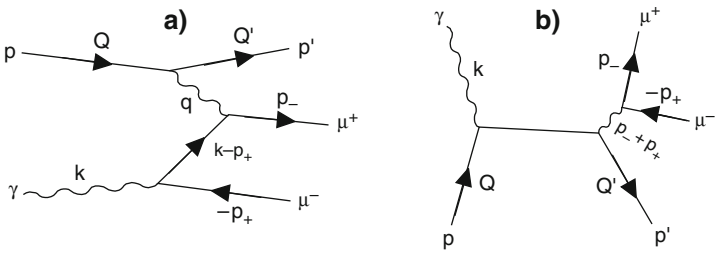

Fig. 5.1 Feynman graphs representing photoproduction of muon pairs. Shown are the Bethe-Heitler (**a**), and one of the Compton diagrams (**b**)

5.2.3 Muon Energy Losses, Overview

Muons propagating in matter (solids, liquids or gases) are subject to the following energy loss mechanisms: *ionization* (including *atomic excitation* and *knock-on electrons*) (Rossi, 1952; Sternheimer, 1956; Sternheimer and Peierls, 1971), *bremsstrahlung* (Bethe and Heitler, 1934; Petrukhin and Shestakov, 1968; Kelner and Kotov, 1968a), *direct electron pair production* (Kelner and Kotov, 1968b;

Kokoulin and Petrukhin, 1971; Wright, 1973), and *photonuclear interactions* (Heitler, 1956; Murota and Ueda, 1956; Kessler and Kessler, 1956, 1960; Daiyasu et al., 1962; Kobayakawa, 1967; Kobayakawa and Miono, 1968; Kobayakawa, 1973; Bezrukov et al., 1971; Borog and Petrukhin, 1975; Bezrukov and Bugaev, 1981a,b). In addition, higher order effects from ionization (Jackson and McCarthy, 1972) and direct muon pair production (Kokoulin and Petrukhin, 1970) make rare contributions to the energy loss.

The references listed above are those of the basic papers where the models and computational approaches to treat the particular process are discussed. Reviews of these subjects are found in Crispin and Fowler (1970), Bugaev et al. (1970), Kotov and Logunov (1970), Bergamasco and Picchi (1971), Vavilov et al. (1974), Grupen (1976), Lohmann et al. (1985), and Bugaev et al. (1993, 1994). Direct muon pair production and other higher order processes are usually disregarded unless specific aims are pursued.

The total energy loss formula for muons can be written as

$$-\frac{\mathrm{d}E}{\mathrm{d}x} = a_{\mathrm{ion}}(E) + [b_{\mathrm{br}}(E) + b_{\mathrm{pp}}(E) + b_{\mathrm{ni}}(E)]E \quad . \tag{5.4}$$

The term $a_{\mathrm{ion}}(E)$ in Eq. (5.4) stands for energy losses due to *ionization, atomic excitation* and *knock-on electrons*. It has a weak logarithmic energy dependence and is therefore sometimes regarded as quasi-constant for approximate range calculations and energy loss estimates in the mid relativistic energy range.

The terms $b_{\mathrm{br}}(E)$, $b_{\mathrm{pp}}(E)$ and $b_{\mathrm{ni}}(E)$ represents the energy losses resulting from *bremsstrahlung, pair production* and *photonuclear interactions*, respectively. Each of these mechanisms is energy dependent and the mathematical expressions are relatively complex. Different approaches and approximations were chosen by different authors. In the following sections we summarize the different processes based on the work of the references listed above and use in parts the notation of Kokoulin and Petrukhin (1970).

In Table 5.2 we give as an example the values of the different terms listed in Eq. (5.4) for 6 energies of muons propagating in iron. The values are taken from the tables of Lohmann et al. (1985). Additional data to this topic are given in Appendix B.

Table 5.2 Energy loss, $\mathrm{d}E/\mathrm{d}x$, of muons in iron [GeV g^{-1} cm^2]. (After Lohmann et al., 1985)

E [GeV]	a_{ion}	b_{br}	b_{pp}	b_{ni}	Total
1	$1.56 \cdot 10^{-3}$	$5.84 \cdot 10^{-7}$	$1.77 \cdot 10^{-7}$	$4.14 \cdot 10^{-7}$	$1.56 \cdot 10^{-3}$
10	$1.93 \cdot 10^{-3}$	$1.40 \cdot 10^{-5}$	$1.49 \cdot 10^{-5}$	$4.23 \cdot 10^{-6}$	$1.96 \cdot 10^{-3}$
100	$2.16 \cdot 10^{-3}$	$2.24 \cdot 10^{-4}$	$3.17 \cdot 10^{-4}$	$3.85 \cdot 10^{-5}$	$2.74 \cdot 10^{-3}$
300	$2.25 \cdot 10^{-3}$	$7.72 \cdot 10^{-4}$	$1.13 \cdot 10^{-3}$	$1.14 \cdot 10^{-4}$	$4.27 \cdot 10^{-3}$
1,000	$2.45 \cdot 10^{-3}$	$2.87 \cdot 10^{-3}$	$4.19 \cdot 10^{-3}$	$3.88 \cdot 10^{-4}$	$9.78 \cdot 10^{-3}$
10,000	$2.50 \cdot 10^{-3}$	$3.17 \cdot 10^{-2}$	$4.52 \cdot 10^{-2}$	$4.33 \cdot 10^{-3}$	$8.38 \cdot 10^{-2}$

In the past, several authors have given approximate expressions for $a_{\rm ion}(E)$, $b_{\rm br}(E)$, $b_{\rm pp}(E)$ and $b_{\rm ni}(E)$ for quick computation of the average energy loss of muons for everyday use (Kobayakawa, 1967; Adair, 1977). However, the deviations with respect to modern Monte Carlo simulations are large and we recommend to use the tabulated energy losses of Lohmann et al. (1985) instead for quick reference.

5.2.4 Ionization Losses of Muons

The ionization cross section of a muon incident on an atom of atomic number Z can be written as (Rossi, 1952)

$$\left(\frac{{\rm d}\sigma}{{\rm d}v}\right)_{\rm ion} = Z\left(\frac{2\pi r_e^2}{\beta^2 v^2}\right)\left(\frac{m_e}{E_\mu}\right)\left[1-\beta^2\left(\frac{v}{v_{\rm max}}\right)+\frac{v^2}{2}\right], \tag{5.5}$$

where Z is the atomic number of the target medium, r_e the classical radius of the electron, m_e its rest mass, v the fractional energy of the muon transferred to the electron, E_μ the energy of the incident muon and $\beta = v/c$ is its velocity in terms of the velocity of light, c. The units for mass, energy and momentum are GeV and $c = 1$. This equation is valid provided that the momentum transfer to the atomic electron is large enough that it can be considered to be free of all bound state and screening effects.

The maximum fractional energy transfer is

$$v_{\rm max} = \frac{\beta^2}{1+\left(\frac{m_\mu^2+m_e^2}{2m_e E_\mu}\right)}, \tag{5.6}$$

where m_μ is the muon mass.

The average incremental energy loss by ionization per unit path length in a medium is given by the Bethe-Bloch formula (Rossi, 1952; Fano, 1963) that can be written as

$$\begin{aligned} -\left(\frac{{\rm d}E}{{\rm d}x}\right)_{\rm ion} = \; & 2\pi r_e^2\left(\frac{N_A Z}{A}\right)\left(\frac{m_e}{\beta^2}\right) \\ & \cdot\left[\ln\left(\frac{2m_e E_\mu \beta^2 v_{\rm max}}{(1-\beta^2)I^2(Z)}\right)-2\beta^2+\left(\frac{v_{\rm max}^2}{4}\right)-\delta\right], \end{aligned} \tag{5.7}$$

where x is the path length expressed in [g cm^{-2}], i.e., the mass per unit area or the *column density*, r_e the classical electron radius (2.817^{-13} cm), N_A Avogadro's number ($6.023 \cdot 10^{23}$), Z and A are the atomic number and weight of the target, m_e and m_μ the mass of the electron and muon, respectively, $\beta = p/E_\mu$ where p is the muon momentum, $\gamma = E_\mu/m_\mu$ the Lorentz factor of the muon, $I(Z)$ the mean ionization potential of the target ($I(Z) \sim 16Z^{0.9}$ [eV] for $Z \geq 1$), and δ is the density effect which approaches $2\ln(\gamma)$ (Sternheimer, 1956; Sternheimer et al., 1984). Note that

the high energy tail of the distribution yields high energy knock-on electrons that initiate electromagnetic cascades (see Fig. 4.4).

Equation (5.7) can be rewritten in a somewhat more explicit form as

$$-\left(\frac{\mathrm{d}E}{\mathrm{d}x}\right)_{\text{ion}} = 2\pi N_A \alpha^2 \lambda_e^2 \left(\frac{Z}{A}\right)\left(\frac{m_e}{\beta^2}\right) \cdot \left[\ln\left(\frac{2m_e\beta^2\gamma^2 E'_{\max}}{I^2(Z)}\right) - 2\beta^2 + \left(\frac{E'^2_{\max}}{4E_\mu^2}\right) - \delta\right], \tag{5.8}$$

where α is the fine-structure constant (1/137), λ_e the Compton wavelength of the electron ($3.86 \cdot 10^{-11}$ cm), and $E'_{\max}$ is the maximum energy transferable to the electron,

$$E'_{\max} = 2m_e\left(\frac{p^2}{m_e^2 + m_\mu^2 + 2m_e\sqrt{(p^2 + m_\mu^2)}}\right) . \tag{5.9}$$

For more accurate calculations the following expressions should be used for δ:

$$\delta(X) = 4.6052X + a(X_1 - X)^m + C \quad \text{for } X_0 < X < X_1 \text{ and} \tag{5.10}$$

$$\delta(X) = 4.6052X + C \quad \text{for } X > X_1 . \tag{5.11}$$

Here, $X = \lg(\beta\gamma)$. The values of $X_0,\ X_1,\ a,\ m, C$ and $I(Z)$ are given in the tables of Sternheimer (1956) and Sternheimer et al. (1984).

5.2.5 *Muon Bremsstrahlung*

This process, symbolically written in expression (5.12) below, had first been calculated by Bethe and Heitler (1934) and is very similar to electron bremsstrahlung.

$$\mu + p\ (\text{or } Z) \rightarrow \mu' + p\ (\text{or } Z) \tag{5.12}$$

Since the emission of photons by muons takes place at much smaller impact parameters from the nucleus than in the case of electrons, the screening of the nuclear Coulomb field by the outer electrons can be neglected to a greater extent than for electrons. At distances less than the nuclear radius the field cannot be regarded as a point charge and the spin of the particles becomes significant. According to Christy and Kusaka (1941a, b) the differential radiation probability for muons (spin 1/2 particles) per gram per square centimeter [$\mathrm{g}^{-1}\mathrm{cm}^2$], $P(E_\mu, v)_{\mu\text{br}}$, where v is the fractional energy of the emitted photon, is given by the expression (see also Rossi and Greisen, 1941),

$$P(E_\mu, v)_{\mu\mathrm{br}}\mathrm{d}v = \alpha \frac{N_A}{A} Z^2 r_e^2 \left(\frac{m_e}{m_\mu}\right)^2 \frac{16}{3}\left(\frac{3v}{4} + \frac{(1-v)}{v}\right)\mathrm{d}v \cdot \left[\ln\left(\frac{12}{5}\,\frac{(1-v)}{v}\,\frac{E_\mu}{m_\mu Z^{\frac{1}{3}}}\right) - \frac{1}{2}\right] . \quad (5.13)$$

Here, E_μ is the total energy of the incident muon, m_μ its rest mass and m_e the rest mass of the electron. The remaining symbols are as defined earlier. Except for the mass ratio term that suppresses the probability for radiation by the factor $(m_e/m_\mu)^2$, which amounts to more than four orders of magnitude, and the second part of the equation, the expression resembles Eq. (4.22). From Eq. (5.13) the cross section for bremsstrahlung of a muon in the Coulomb field of a proton or nucleus can be computed. Note that Eq. (5.13) is valid only for $E \gg m_\mu$.

Several authors have chosen different approaches and approximations to derive the cross section of muon bremsstrahlung. In the following we present the expression obtained by Petrukhin and Shestakov (1968) which is widely used today (Lohmann et al., 1985; Sakumoto et al., 1992).

$$\left(\frac{\mathrm{d}\sigma}{\mathrm{d}v}\right)_{\mathrm{br}} = \alpha\left(2Zr_e\frac{m_e}{m_\mu}\right)^2 \frac{1}{v}\left[1 + (1-v)^2 - 2\left(\frac{1-v}{3}\right)\right]\phi(q_{\min}) , \quad (5.14)$$

where

$$\phi(q_{\min}) = \ln\left[f_n\left(\frac{m_\mu}{m_e}\right)\left(\frac{RZ^{-1/3}}{1 + (q_{\min}/m_e)\sqrt{e}RZ^{-1/3}}\right)\right] \quad (5.15)$$

and

$$f_n = \left(\frac{2}{3}\right) Z^{-1/3} \quad (5.16)$$

is the nuclear form factor correction, $e = 2.7182...$, and $R = 189$. Furthermore,

$$q_{\min} = \frac{m_\mu^2 v}{2E_\mu(1-v)} \quad (5.17)$$

is the minimum momentum transfer to the proton or nucleus. The range of the fractional energy transfer, v, is

$$0 < v \leq \left(1 - \frac{m_\mu\sqrt{e}}{2f_n E_\mu}\right) . \quad (5.18)$$

The Petrukhin-Shestakov cross section (Eq. 5.14) is an analytic approximation to the Bethe-Heitler cross section with arbitrary screening. Sakumoto et al. (1992) find in their work that the f_n of Petrukhin and Shestakov (1968) underestimates the

numerical calculation by about 10% and propose to use in its place the expression $f_n = \exp(-0.128 R_{0.5})$ with $R_{0.5} = (1.18 A^{1/3} - 0.48)$ [fm].

As an example, we show in Fig. 5.2 the energy dependence of the two major processes that are responsible for the energy loss of muons over the range $0.1 \leq E_\mu \leq 10^4$ GeV in standard rock ($\langle Z \rangle = 11$, $\langle A \rangle = 22$, $Z/A = 0.5$, $Z^2/A = 5.5$, $\rho = 2.650\ \mathrm{g\,cm^{-3}}$), and the sum of both (for details see Grieder, 2001, Chap. 4; Eidelman et al., 2004).

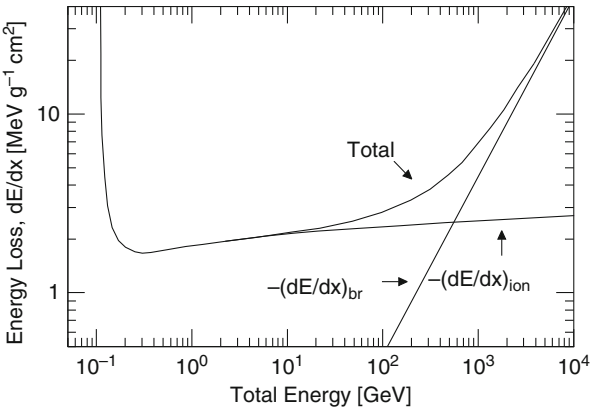

Fig. 5.2 Energy loss of muons versus total energy in standard rock ($Z = 11$), due to ionization and bremsstrahlung

The photon resulting from bremsstrahlung of a high energy muon in the Coulomb field of a nucleus can initiate an electromagnetic cascade that accompanies the muon trajectory over a certain track length, depending on its energy and the medium in which it propagates. Such EM-cascades as well as photonuclear reaction products of high energy muons can regenerate horizontal air showers at great atmospheric depth. They also contaminate a pure muon beam and are of particular relevance for highly shielded deep underground experiments that require low background, or measurements of high energy muons under thick absorbers or in calorimeters in the shower core. In the latter case so-called *punch-throughs* pose an additional problem.

The mean energy loss is obtained by evaluating the expression

$$\frac{\mathrm{d}E}{\mathrm{d}x} = E_\mu \left(\frac{N_A}{A}\right) \int_{v_{\min}}^{v^{\max}} \left(\frac{\mathrm{d}\sigma}{\mathrm{d}v}\right) \mathrm{d}v \tag{5.19}$$

where the range of v is given by Eq. (5.18), i.e., $v_{\min} = 0$ and for $v_{\max}$ we can write

$$v_{\max} = 1 - \left(\frac{3}{4}\right) \sqrt{e} \left(\frac{m_\mu}{E}\right) Z^{1/3} \ . \tag{5.20}$$

To account for bremsstrahlung on atomic electrons one usually replaces Z^2 by $Z(Z+1)$ (Kelner and Kotov, 1968a, b).

5.2.6 Direct Electron Pair Production by Muons

The differential cross section for the direct production of electron pairs by muons in the Coulomb field of a proton or nucleus, as shown symbolically below,

$$\mu^{\pm} + p \text{ (or } Z) \;\rightarrow\; \mu^{\pm'} + p \text{ (or } Z) + e^{+} + e^{-} \tag{5.21}$$

can be calculated under the assumption that all particles are relativistic, and that the Thomas-Fermi model can be used to compute the effect of screening of nuclei by atomic electrons. Kelner and Kotov (1968a, b) derived expressions for the two extreme cases, *no screening* and *complete screening*.

The diagrams (a) (a1 and a2) and (b) (b1 and b2) of Fig. 5.3 represent the pair production process in the lowest order of perturbation theory. From these and on the basis of the earlier work of Kelner (1967), these authors derived the following expression for the *differential* cross section of the process shown in (a),

$$\begin{aligned} \mathrm{d}\sigma_a = \quad & \frac{2(Z\alpha r_e)^2}{\pi}\,\frac{1}{E_\mu^2}\,\frac{\mathrm{d}t}{t^2}\,\frac{\mathrm{d}\epsilon_+\mathrm{d}\epsilon_-}{\omega^2}\cdot\left\{-l_{\alpha\alpha}\left(t\left[E_\mu(E_\mu-\omega)+\frac{\omega^2}{2}\right]-m_\mu^2\omega^2\right)\right. \\ & \left. +\; l_{00}\frac{t^2}{\omega^2}\left(t\left[3E_\mu(E_\mu-\omega)+\frac{\omega^2}{2}\right]-m_\mu^2\omega^2\right)\right\}\;, \end{aligned} \tag{5.22}$$

where E_μ is the energy of the muon, m_μ its mass, ϵ_+ and ϵ_- are the energy of the positron and negatron, respectively, $\omega = (\epsilon_+ + \epsilon_-)$, $t = \kappa^2$ the square of the 4-momentum transferred to the muon, r_e the classical electron radius, Z the charge of the target nucleus, and $h = c = m_e = 1$. The tensor $l_{\alpha\beta}$ describes the creation of pairs by the virtual photon (for details see Kelner and Kotov, 1968b).

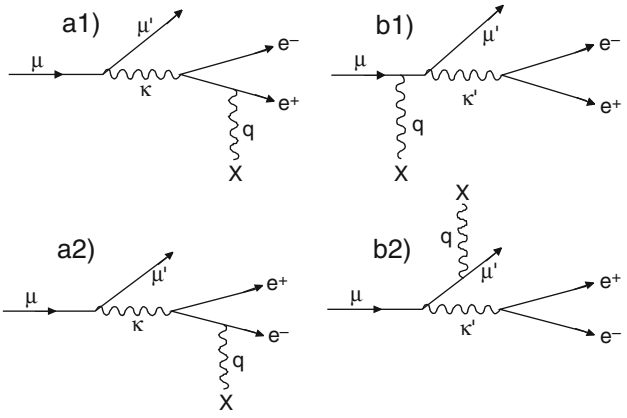

Fig. 5.3 Feynman graphs to compute direct electron pair production by muons

Using the Thomas-Fermi model and following the steps of Kelner (1967) in conjunction with the interpolation formulas of Petrukhin and Shestakov (1966), one obtains the following expression for the differential cross section for diagram (a),

$$\mathrm{d}\sigma_a = \left(\frac{16}{\pi}\right)(Z\alpha r_e)^2\, F_a(E_\mu, v)\frac{\mathrm{d}v}{v} \quad . \tag{5.23}$$

For $v \sim 1$ the contribution of diagram (b) is of the same order of magnitude as diagram (a) and one obtains an equation for $\mathrm{d}\sigma_b$ analogous to Eq. (5.23) for (b) with $F_b(E_\mu, v)$. The functions $F_a(E_\mu, v)$ and $F_b(E_\mu, v)$ are evaluated by integration over x and t, where $x_\pm = \epsilon_\pm/\omega$, and the interference between (a) and (b) becomes zero.

This calculation is valid provided that the energies of the particles in the initial and final states are much larger than their masses, i.e., when $E_\mu \gg m_\mu$, $x_\pm \gg 1/E_\mu v$, where v and $(1 - v)$ are the energy fractions of the electrons, $v \gg 2/E_\mu$, and $(1 - v) \gg m_\mu/E_\mu$.

Finally the complete differential cross section for direct electron pair production by muons can be written as

$$\mathrm{d}\sigma = \left(\frac{16}{\pi}\right)(Z\alpha r_e)^2\, F(E_\mu, v)\frac{\mathrm{d}v}{v} \quad , \tag{5.24}$$

where $F(E_\mu, v) = F_a + F_b$. The function $F(E_\mu, v)$ is plotted in Fig. 5.4.

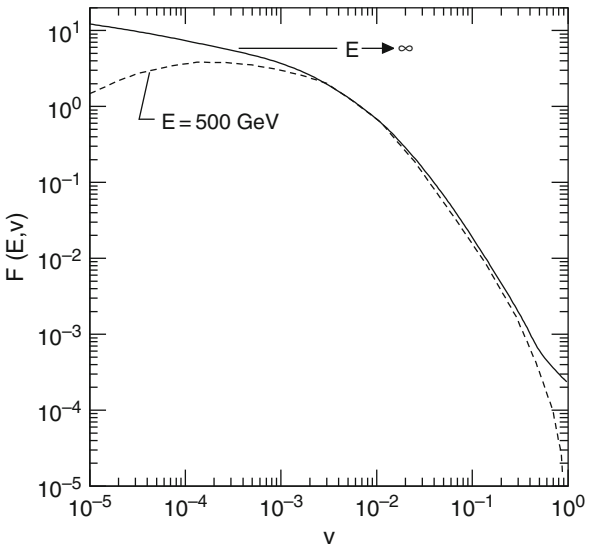

Fig. 5.4 Example of the function $F(E_\mu, v)$ for standard rock ($Z = 11$) plotted as a function of v for muon energies $E_\mu = 500$ GeV and $E_\mu \to \infty$. For the detailed calculation and tabulated values see Kelner and Kotov (1968b)

From Eq. (5.24) the formula for the energy loss of muons for $e^+ + e^-$ pair production can now be obtained,

$$-\frac{1}{E_\mu}\frac{\mathrm{d}E_\mu}{\mathrm{d}x} = \left(\frac{16}{\pi}\right)(Z\alpha r_e)^2 n \cdot \chi(E_\mu) \ , \tag{5.25}$$

where

$$\chi(E_\mu) = \int_{v_{\min}}^{v_{\max}} F(E_\mu, v)\,\mathrm{d}v \tag{5.26}$$

and n is the number of atoms per unit volume. Kelner and Kotov have computed the values of $\chi(E_\mu)$ for a wide range of energies and present tabulated data in their paper.

For the two extreme cases, *negligible screening* and *complete screening*, the following simple equations result:

$$\left(-\frac{1}{E_\mu}\frac{\mathrm{d}E_\mu}{\mathrm{d}x}\right)_{\text{pair}} = n\left(\frac{19\pi}{9m_\mu}\right)(Z\alpha r_e)^2 \cdot \left[0.965 \ln\left(\frac{E_\mu}{4m_\mu}\right) - 1.771\right] \tag{5.27}$$

and

$$\left(-\frac{1}{E_\mu}\frac{\mathrm{d}E_\mu}{\mathrm{d}x}\right)_{\text{pair}} = n\left(\frac{19\pi}{9m_\mu}\right)(Z\alpha r_e)^2 \cdot \left[0.965 \ln(189Z^{1/3}) + 0.605\right] \ . \tag{5.28}$$

For muons complete screening applies if their energy is $\geq 10^{13}$ eV. In this case and for $Z = 11$ (standard rock) one obtains the following simple approximate expression for the energy loss,

$$\left(-\frac{1}{E_\mu}\frac{\mathrm{d}E_\mu}{\mathrm{d}x}\right)_{\text{pair}} = 2.40 \cdot 10^{-6} \ [\mathrm{g}^{-1}\,\mathrm{cm}^2] \ . \tag{5.29}$$

Figure 5.5 shows a plot of the energy loss due to electron pair production by muons in standard rock.

In a different approach, based on the work of Kelner and Kotov (1968a, b), Kokoulin and Petrukhin (1970) derived another approximate expression for the *differential* cross section of the processes shown in Fig. 5.3 and obtained the following formula which is frequently used.

$$\left(\frac{\mathrm{d}\sigma}{\mathrm{d}v\,\mathrm{d}\rho}\right)_{\text{pair}} = \frac{2}{3\pi}(Z\alpha r_e)^2 \left(\frac{1-v}{v}\right) \cdot \left[\Phi_e(E_\mu, \rho, v) + \left(\frac{m_e}{m_\mu}\right)^2 \Phi_\mu(E_\mu, \rho, v)\right] , \tag{5.30}$$

where ρ is the e^+e^- energy asymmetry and v the energy fraction transferred to the electron pair,

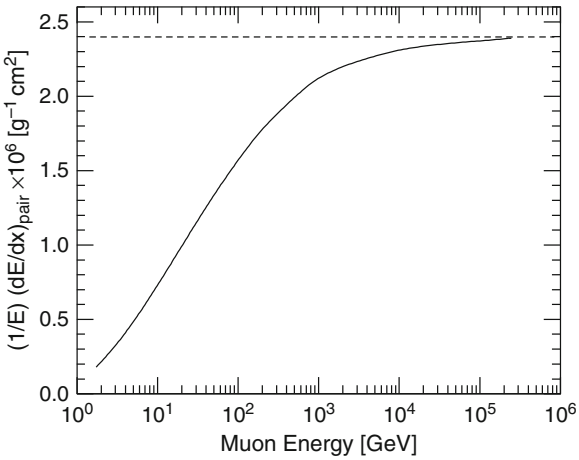

Fig. 5.5 Energy loss of muons through direct electron pair production in standard rock ($Z = 11$) as a function of muon energy (Kelner and Kotov 1968b)

$$\rho = \frac{\epsilon_+ - \epsilon_-}{\epsilon_+ + \epsilon_-} \ , \tag{5.31}$$

$$v = \frac{\epsilon_+ + \epsilon_-}{E_\mu} \ , \tag{5.32}$$

where ϵ_+ and (ϵ_-) are the energy of the positron and negatron, respectively. The functions $\Phi_{e,\mu}(E_{\mu,\rho,v})$ are complicated expressions that are discussed by Kokoulin and Petrukhin (1970). They are given below (see also Sakumoto et al., 1992).

$$\begin{aligned}\Phi_e(E_\mu, \rho, v) = \quad & \left\{\left[(2+\rho^2)(1+\beta) + \xi(3+\rho^2)\right]\right. \\ & \left.\cdot \ln\left(1+\frac{1}{\xi}\right) + \left(\frac{1-\rho^2-\beta}{1+\xi}\right) - (3+\rho^2)\right\} L_e\end{aligned} \tag{5.33}$$

$$\begin{aligned}\Phi_\mu(E_\mu, \rho, v) = \quad & \left\{\left[(1+\rho^2)\left(1+\frac{3\beta}{2}\right) - \left(\frac{(1+2\beta)(1-\rho^2)}{\xi}\right)\right]\right. \\ & \left.\cdot \ln(1+\xi) + \xi\left(\frac{1-\rho^2-\beta}{1+\xi}\right) + (1+2\beta)(1-\rho^2)\right\} L_\mu\end{aligned} \tag{5.34}$$

$$L_e = \ln\left[\left(\frac{2}{3}\right)\left(\frac{m_\mu}{m_e}\right)\left(\frac{R}{D_e}\right)Z^{-2/3}\right] - \frac{1}{2}\ln\left\{1+\left[\left(\frac{2}{3}\right)\left(\frac{m_\mu}{m_e}\right)Z^{-1/3}\right]^2\left(\frac{1}{(1+\xi)(1+Y_e)}\right)\right\} \tag{5.35}$$

$$L_\mu = \ln\left[\left(\frac{2}{3}\right)\left(\frac{m_\mu}{m_e}\right)\left(\frac{R}{D_\mu}\right)Z^{-2/3}\right] \tag{5.36}$$

$$D_{e,\mu} = 1+\sqrt{e}\left(\frac{q_{\min}}{m_e}\right)RZ^{-1/3}\left(1+Y_{e,\mu}\right) \tag{5.37}$$

$$Y_e = \frac{5-\rho^2+4\beta(1+\rho^2)}{2(1+3\beta)\ln(3+1/\xi)-\rho^2-2\beta(2-\rho^2)} \tag{5.38}$$

$$Y_\mu = \frac{4+\rho^2+3\beta(1+\rho^2)}{(1+\rho^2)(3/2+2\beta)\ln(3+\xi)+1-(3/2)\rho^2} \tag{5.39}$$

The remaining symbols used in the equations above are as follows: $e = 2.7162\ldots$, $R = 189$, and the parameters β, ξ, and $q_{\min}$ are

$$\beta = \frac{v^2}{2(1-v)}\ , \tag{5.40}$$

$$\xi = \left(\frac{m_\mu v}{2m_e}\right)^2\left(\frac{1-\rho^2}{1-v}\right) \quad \text{and} \tag{5.41}$$

$$q_{\min} = \left(\frac{2m_e^2}{vE_\mu}\right)\left(\frac{1+\xi}{1-\rho^2}\right)\ . \tag{5.42}$$

The limits on the fractional energy transfer and the energy asymmetry are

$$\left(\frac{4m_e}{E_\mu}\right) \le v \le \left[1-\frac{3}{4}\left(Z^{1/3}\sqrt{e}\right)\left(\frac{m_\mu}{E_\mu}\right)\right] \tag{5.43}$$

and

$$0 \le |\rho| \le \left[1-\left(\frac{6m_\mu^2}{E_\mu^2(1-v)}\right)\right]\left[1-\left(\frac{4m_e}{vE_\mu}\right)\right]^{1/2}\ . \tag{5.44}$$

Equation (5.30) includes form factor corrections and applies to an arbitrary Thomas-Fermi atom. This formula can in principle also be used to compute the direct $\mu^+\mu^-$ pair production that can reach approximately 10% of the direct e^+e^- pair production.

The energy loss is obtained by solving the following equation in an analogous manner as Eq. (5.19), and by replacing Z^2 by $Z(Z+1)$, to account for the effect of atomic electrons.

$$\frac{\mathrm{d}E}{\mathrm{d}x} = 2E_\mu \left(\frac{N_A}{A}\right) \int_{v_{\min}}^{v_{\max}} v \cdot \int_0^{\rho_{\max}} \left(\frac{\mathrm{d}^2\sigma}{\mathrm{d}v\,\mathrm{d}\rho}\right) \mathrm{d}\rho\,\mathrm{d}v \ , \tag{5.45}$$

5.2.7 Direct Muon Pair Production by Muons, Muon Trident Events

Direct production of muon pairs by high energy muons in the Coulomb field of a proton or nucleus in reactions such as shown below,

$$\mu^\pm + p\ (\text{or } Z) \ \rightarrow \ \mu^{\pm'} + p\ (\text{or } Z) + \mu^+ + \mu^- \tag{5.46}$$

had been observed in cosmic ray and accelerator experiments (Morris and Stenerson, 1968; Barton and Rogers, 1970; Russell et al., 1971). The energy loss mechanism of this process had been studied by several authors and had been accounted for in muon range calculations (Kokoulin and Petrukhin, 1970; Lohmann et al., 1985; Sakumoto et al., 1992). The procedure consists of replacing the electron mass, m_e, by the muon mass, m_μ, in all formulas, parameter definitions and limits, except in the expressions for $L_{e,\mu}$ and $D_{e,\mu}$ (Eqs. 5.35, 5.36 and 5.37). In addition, the classical electron radius, r_e is re-scaled by (m_e/m_μ), and in the L_e-function (Eq. 5.35) R is replaced by $R(m_\mu/m_e)$.

The cross section obtained by Russell et al. (1971) in their accelerator experiment with a positive and negative muon beam of 10.5 GeV on a Pb target is

$$\sigma(\mu^\pm, Pb) = 51.7 \pm 7 \cdot 10^{-33} \ [\mathrm{cm}^2/\mathrm{Nucleus}] \ , \tag{5.47}$$

in agreement with QED.

5.2.8 Photonuclear Interactions of Muons

Nuclear interactions of muons (or electrons) with nucleons or nuclei, i.e., inelastic reactions where hadrons are being produced, are so-called *photonuclear interactions* where virtual photons are involved. An example of such a reaction is shown below,

$$\mu^\pm + p\ (\text{or } A) \ \rightarrow \ \mu^{\pm'} + p\ (\text{or } A) + X \ , \tag{5.48}$$

where X stands for hadrons (pions, etc.).

These processes are theoretically not so well understood as the processes where real photons are involved. Photonuclear processes initiated by muons play an important role in highly shielded deep underground experiments where they cause problematic background, and occasionally in thick calorimeters.

A summary of the results of early measurements of photonuclear interaction cross sections of muons obtained from accelerator and cosmic ray experiments on nuclear targets, expressed per nucleon, is given in Fig. 5.6.

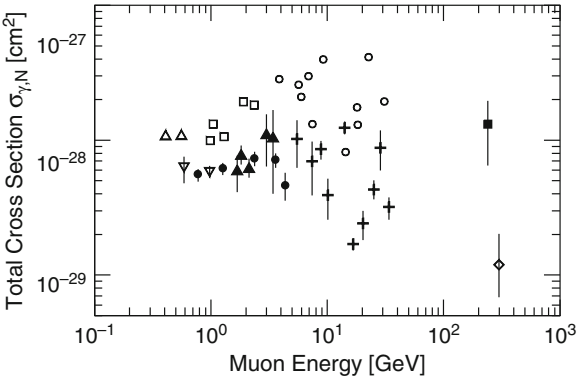

Fig. 5.6 Data summary of early measurements of the energy dependence of the photonuclear interaction cross section of muons (Borog et al., 1968; see also Borog and Petrukhin, 1975 and references listed therein). The plot includes accelerator gamma ray data by Chasan et al. (1960) and Crouch et al. (1964) (●); accelerator muon data by Kirk et al. (1965) interpreted using the Weizsäcker-Williams (WW)-theory (△) and the Kessler-Kessler (KK)-theory for the same data (▽). The cosmic ray muon data include the analysis of Fowler and Wolfendale (1958) using the WW-theory (□) and the KK-theory (▲). The *symbols* ○ and + are data from different experiments evaluated according to the WW and KK theories, respectively, and likewise for points ■ and ◇ which are from the work of Borog et al. (1968) using cosmic ray muons

The theoretical treatment of these interactions are based on the exchange of a virtual photon (Weizsäcker, 1934; Williams, 1933, 1935; Murota and Ueda, 1956; Murota et al., 1956; Kessler and Kessler, 1956, 1957, 1960; Daiyasu et al., 1962). Using Lorentz and gauge invariance only, the cross section for hadron production by muons (or electrons) can be expressed by two Lorentz-invariant functions where the character of the strong interaction is confined (Higashi et al., 1965; Kobayakawa, 1967; see also Adair, 1977).[2]

Following Kobayakawa (1967) and using his notation (not the Feynman notation convention), then, when an incident muon (electron) with 4-momentum $Q_1(\vec{p}_1, E_1)$ collides with a nucleon at rest ($Q(0, M)$) and has a 4-momentum $Q_2(\vec{p}_2, E_2)$ in the final state, emitting a virtual photon with 4-momentum $q(\vec{q}, \epsilon)$, the *differential* cross section, expressed as a function of the transferred energy ϵ and the square of 4-momentum transfer, $q^2 = |\vec{q}\,|^2 - \epsilon^2 > 0$, is

[2] In the early work of Higashi et al. (1965) the criterion for hadron production was the production of a hadronic cascade of energy $\geq E$ by a muon.

$$\frac{\mathrm{d}^2\sigma}{\mathrm{d}q^2\,\mathrm{d}\epsilon} = \frac{\alpha}{8\pi^2}\frac{1}{(E_\mu^2 - m_\mu^2)}\frac{1}{q^4} \cdot \left[L_N\left((E_\mu^2 + (E_\mu - \epsilon)^2)q^2 - 2m_\mu^2\epsilon^2 - \frac{q^4}{2}\right) + L'_N(2m_\mu^2 - q^2)q^2\right] \tag{5.49}$$

where α is the fine-structure constant and m_μ the muon mass. L_N and L'_N are functions of q^2, $p^2(= -M^2)$ and $qp(= -M\epsilon)$, and the contribution of the strong interaction is confined to these functions. With the assumptions of the forms of the L and L' functions, a practical expression of the differential cross section can be obtained. For the detailed treatment the reader is referred to the paper of Kobayakawa (1967) and references listed therein.

More recently, Bezrukov and Bugaev (1981a, b) derived the following expression for the photonuclear cross section which is now used frequently.

$$\begin{aligned}\left(\frac{\mathrm{d}\sigma}{\mathrm{d}v}\right)_{\mathrm{ni}} = \frac{\alpha}{2\pi}A\sigma_{\gamma,N}(v, E_\mu)v\Bigg\{&0.75G(x) \cdot \left[\kappa\ln\left(1 + \frac{m_1^2}{t}\right) - \frac{\kappa m_1^2}{m_1^2 + t} - \frac{2m_\mu^2}{t}\right] \\ &+ 0.25\left[\kappa\ln\left(1 + \frac{m_2^2}{t}\right) - \frac{2m_\mu^2}{t}\right] \\ &+ \frac{m_\mu^2}{2t}\left[0.75G(x)\left(\frac{m_1^2}{m_1^2 + t}\right) + 0.25\frac{m_2^2}{t}\ln\left(1 + \frac{t}{m_2^2}\right)\right]\Bigg\}.\end{aligned} \tag{5.50}$$

Here, v is the fraction of the energy transferred by the muon to the nucleon or nucleus,

$$t = \frac{m_\mu^2 v^2}{1 - v}\ , \tag{5.51}$$

$$\kappa = 1 - \frac{2}{v} + \frac{2}{v^2}\ , \tag{5.52}$$

$m_1^2 = 0.54\ \mathrm{GeV}^2$, and $m_2^2 = 1.8\ \mathrm{GeV}^2$.

The remaining symbols represent the following functions:

$$\sigma_{\gamma,N}(E) = 114.3 + 1.647\ln^2(0.0213E)\ \mu\mathrm{b}\ , \tag{5.53}$$

where $\sigma_{\gamma,N}$ is the nucleon-photonuclear cross section and E the energy in GeV. Furthermore,

$$G(x) = \frac{3}{x^2}\left[\frac{x^2}{2} - 1 + e^{-x}(1+x)\right] \ , \tag{5.54}$$

$$x = 0.00282 A^{1/3} \sigma_{\gamma,N}(v, E_\mu) \ , \tag{5.55}$$

and the range of v is taken as

$$\frac{m_\pi}{E_\mu} < v < \left(1 - \frac{m_\mu}{E_\mu}\right) \tag{5.56}$$

with m_π being the pion mass.

5.2.9 Summary of Muon Reaction Probabilities and Energy Loss

Figure 5.7 shows the energy loss probability of muons for different processes in standard rock obtained from an early calculation of Adair (1977).

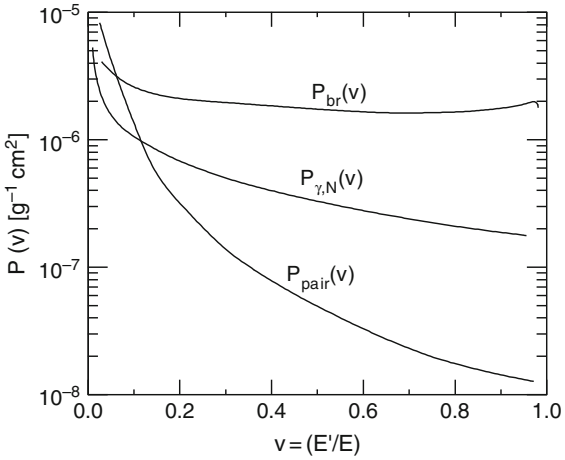

Fig. 5.7 Probability of a muon of energy E_μ losing a fraction of its energy $v = E'_\mu / E_\mu$ per gram of *standard rock* traversed through bremsstrahlung, $P_{\rm br}(v)$, photonuclear reaction, $P_{\gamma,N}(v)$, and direct electron pair production, $P_{\rm pair}(v)$ (after Adair, 1977). The *curves* apply to 2 TeV muons but are valid over a wide range of energies

A very comprehensive set of muon energy loss data for many different elements and compounds, including standard rock and water, are given in tabulated form in the report of Lohmann et al. (1985), covering the energy range from 1 to 10^4 GeV. Bhattacharyya (1986) presents in his paper plots of the energy loss of muons in the range from 50 to 1,000 GeV in sea water that are compared with experimental data.

The energy loss of cosmic ray muons in iron covering the energy range from 40 to 1200 GeV had been measured by Sakumoto et al. (1992) in a precision experiment.

Their work had been complemented by detailed calculations using the equations given in the previous subsections. The results are shown in Fig. 5.8.

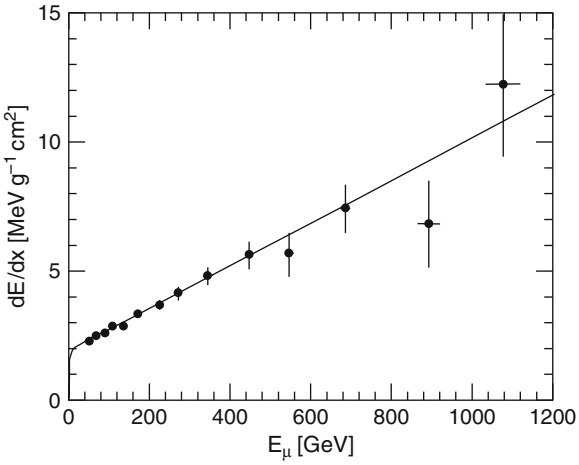

Fig. 5.8 The dE_μ/dx-plot for muons in iron as a function of energy. The *solid curve* is the prediction from a calculation (adopted from Sakumoto et al., 1992)

Additional results from the theoretical work of Sakumoto et al. (1992) that are of interest for many applications are reproduced in Fig. 5.9. In Table 5.3 we list some cross sections obtained from cosmic ray experiments.

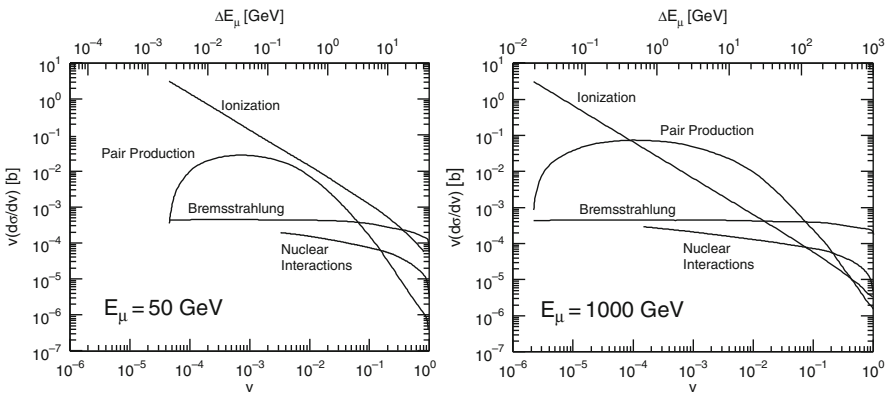

Fig. 5.9 Ionization, bremsstrahlung, direct electron pair production and photonuclear cross sections (in units of barns) of 50 and 1,000 GeV muons incident on an iron atom. The scale on *top* of the figure gives the energy loss, ΔE_μ which corresponds to the fractional energy loss, v. Note that the ordinate is the logarithmic derivative $d\sigma/d(\ln v) = d\sigma/d(\ln \Delta E_\mu)$ (after Sakumoto et al., 1992)

Table 5.3 Photonuclear reaction cross sections of Muons from cosmic ray experiments

Experimental	E_μ [GeV]	References
$\sigma(\mu^\pm, \text{Pb})^a = (2.58 \pm 0.36) \cdot 10^{-31}$ [cm^2]	≥ 100	Higashi et al. (1965)
$\sigma(\mu^\pm, \text{Fe})^a = (3.62 \pm 0.76) \cdot 10^{-31}$ [cm^2]	≥ 100	
Experimental [g^{-1} cm^2 GeV^{-1}] in standard rock (SR)		
$\sigma(\mu^\pm, \text{SR}) = (1.9 \pm 0.1) \cdot 10^{-10}$	≥ 190	Enikeev et al. (1983)
$\sigma(\mu^\pm, \text{SR}) = (7.6 \pm 0.6) \cdot 10^{-11}$	≥ 270	
$\sigma(\mu^\pm, \text{SR}) = (8.1 \pm 1.4) \cdot 10^{-12}$	≥ 550	
$\sigma(\mu^\pm, \text{SR}) = (2.2 \pm 0.6) \cdot 10^{-12}$	≥ 780	
$\sigma(\mu^\pm, \text{SR}) = (5.3 \pm 2.3) \cdot 10^{-13}$	$\geq 1,320$	
$\sigma(\mu^\pm, \text{SR}) = (1.5 \pm 1.1) \cdot 10^{-13}$	$\geq 1,860$	

[a] Cross sections refer to penetrating shower-producing events.

5.2.10 Recent Work and Developments

For a long time high energy muon physics had been of interest almost exclusively to cosmic ray physicists (Higashi et al., 1965; Chin et al., 1973; Matsuno et al., 1984; Mitsui, 1992), and more recently to the neutrino astronomy community. However, in view of the coming into operation of the Large Hadron Collider (LHC) at CERN, in Geneva (Switzerland) in 2009, where TeV muons will be available, the accelerator physics community began to explore the field of high energy muon interactions. They carried out precision experiments with cosmic ray muons up to 1,200 GeV (Sakumoto et al., 1992) and, using the most energetic accelerator muon beams (Amaral et al., 2001, 180 GeV; Antonelli et al., 1997, 300 GeV), extracted data on the nuclear elastic form factor and other parameters. This work dealt almost exclusively with the study of interactions and energy loss of muons in iron and lead.

In recent years several authors have made substantial theoretical contributions, exploring the consequences of a number of refinements and corrections to the treatment of the interaction of muons in the Coulomb field of nuclei and with atomic electrons in order to improved the accuracy of energy loss predictions. Kelner et al. (1995, 1997) and Kelner (1998) showed that the radiative corrections to knock-on electron production and muon bremsstrahlung on atomic electrons increase the probability of energy losses. Similarly, Tannenbaum (1991) pointed out that uncertainties in the computation of bremsstrahlung of muons are caused by different theoretical predictions of the nuclear size correction (see also Kelner and Fedotov, 1999). Because of the small mass of electrons this effect is irrelevant for electrons.

In this context some authors did also carry out detailed calculations to check theory against experiment. Instructive, too, are the results of calculations by Amaral et al. (2001), displayed in Fig. 5.10, that accompanied their experimental work, which show the relative probabilities of the fractional energy losses of muons of 180 GeV in iron for knock-on electrons, bremsstrahlung, electron pair production and photonuclear interactions. An analogous plot for electrons obtained by the same authors is shown in Fig. 4.4.

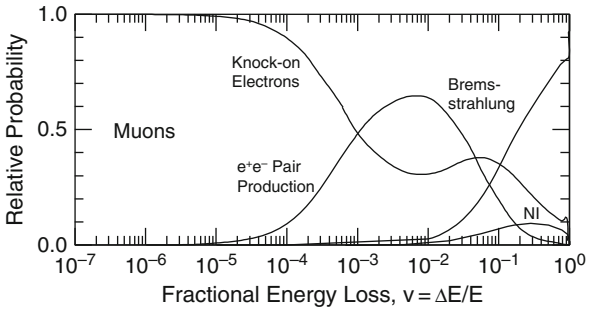

Fig. 5.10 Relative probability of fractional energy loss $v = \Delta E_\mu / E_\mu$ per interaction and per unit of radiation length in iron for 180 GeV muons. The *curve* labeled NI represents nuclear interactions (after Amaral et al., 2001)

A comparison of the two plots is quite instructive. It illustrates nicely the differences in the degree of significance of the various processes of the energy loss of muons and electrons.

A plot similar to Fig. 5.7 showing the v-dependence of the different energy loss mechanisms for muons of 300 GeV in Pb using the most recent muon interaction models that was obtained by Battistoni et al. (1995) is shown in Fig. 5.11.

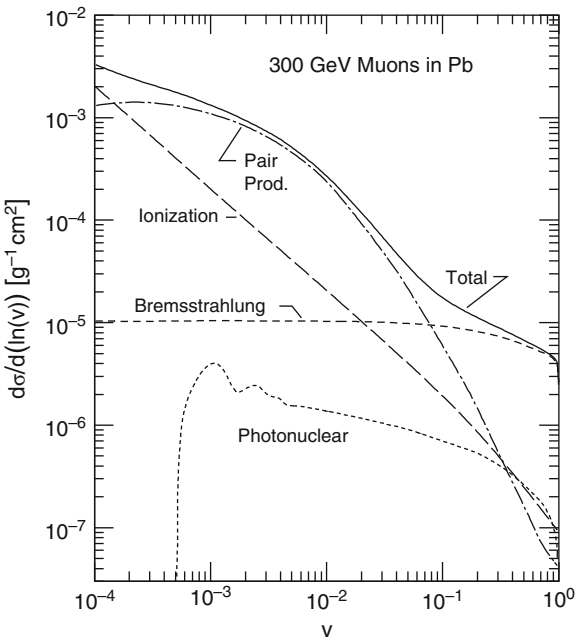

Fig. 5.11 Differential cross sections as a function of v for 300 GeV muons in Pb (after Battistoni et al., 1995)

5.3 Neutrinos

In this section we discuss only high energy neutrino topics that are relevant for air showers. Low energy neutrinos such as solar neutrinos and neutrinos from common radioactive decays as well as neutrino oscillations are ignored.[3]

5.3.1 Neutrino Production

Like muons, neutrinos are the decay products of unstable particles, such as charged pions and other particles. In the case of charged parent pions (π^+, π^-), *muon–neutrinos* and *muon antineutrinos* (ν_μ, $\overline{\nu_\mu}$) are co-produced with the muons, as discussed in Sect. 5.2.1. The decay channels that produce the bulk of muons listed in Table 5.1 are at the same time the major producers of muon–neutrinos and antineutrinos).

But also unstable leptons, such as muons ($\mu^\pm$) produce neutrinos, whereby the decay products of the latter are electrons ($e^\pm$), *electron–neutrinos* or *electron–antineutrinos* (ν_e, $\overline{\nu_e}$) and *muon–antineutrinos* or *muon–neutrinos* ($\overline{\nu_\mu}$, ν_μ), depending whether we deal with the decay of a μ^- or a μ^+. Considering only charged pions and muons as the sources of the two different kinds of neutrinos, the ratio of electron to muon neutrinos should be 0.5. It was this ratio which eventually led to the discovery of neutrino oscillations (Koshiba, 1992; Suzuki et al., 2000). In particular it was the ratio of the predicted to the measured ratio of electron to muon neutrinos, known as *the ratio of ratios* that was the key to this puzzle.

In addition to the electron and muon neutrinos there is a third kind of neutrino, the *tau-neutrino* and its anti-particle, the *tau-antineutrino* (ν_τ, $\overline{\nu_\tau}$).[4] These result from the decay of another lepton, called the *tau meson* whose mean life is $2.906 \cdot 10^{-13}$ s (Barish and Stroynowski, 1988). It has numerous two, three and more particle decay modes (for details see Eidelman et al., 2004).

In view of the enormous energy that is available in the interactions of ultra-high energy primary cosmic rays with nuclei of atmospheric constituents, practically all known and presumably some as yet unknown processes occur. However, energetically and from an air shower investigators point of view, only few are of concern for neutrino production. In Table 5.4 we list the most relevant electron-neutrino producing decay processes that occur in air showers. Of these the muon decays are the main contributors. The $\tau^\pm$-decay is also listed which produces $(\overline{\nu_\tau})$.

[3] An excellent and broad coverage of neutrino physics is given by Schmitz (1997).

[4] The existence of the tau (anti)-neutrino has not yet been confirmed experimentally.

Table 5.4 Major electron- and tau-neutrino producing decay schemes relevant for air showers

Particle symbol	Partial decay modes	Branching fraction [%]	Mean life [s]
μ^-	$\rightarrow e^- + \overline{\nu_e} + \nu_\mu$	≈ 100	$2.197 \cdot 10^{-6}$
μ^+	$\rightarrow e^+ + \nu_e + \overline{\nu_\mu}$	≈ 100	$2.197 \cdot 10^{-6}$
$K^\pm$	$\rightarrow \pi^0 + e^\pm + (\overline{\nu_e})$	4.87	$1.238 \cdot 10^{-8}$
$\tau^\pm$	$\rightarrow e^\pm + (\overline{\nu_e}) + (\overline{\nu_\tau})$	17.84	$2.906 \cdot 10^{-13}$
	$\rightarrow \mu^\pm + (\overline{\nu_\mu}) + (\overline{\nu_\tau})$	17.36	$2.906 \cdot 10^{-13}$
$D^\pm$	$\rightarrow (\overline{K^0}) + e^\pm + (\overline{\nu_e})$	4.5	$1.040 \cdot 10^{-12}$
D^0	$\rightarrow e^+ +$ Hadrons	6.87	$4.103 \cdot 10^{-13}$
	$\rightarrow K^- + e^+ + \nu_e$	3.58	
etc.			

5.3.2 Neutrino Reactions

Neutrinos are subject to a variety of reactions that open a number of other channels. In other words, an initially pure beam of neutrinos of a particular kind (flavor) propagating in a dense medium becomes contaminated with other particles as a result of neutrino induced interactions. However, because of the small cross section the rate of neutrino reactions is small.

We distinguish between *charged-current (CC) reactions* and *neutral-current (NC) reactions*. In the former a W^+ or a W^- is exchanged and the leptons before and after the reaction are different. Typical examples of charged-current reactions are

$$\begin{aligned} \nu_\mu + N &\rightarrow \mu^- + X \\ \overline{\nu_\mu} + N &\rightarrow \mu^+ + X \end{aligned}$$

where N stands for a nucleon (p or n), and X for $hadron(s) + anything$.

On the other hand, in neutral-current reactions a Z^0 is exchanged and the lepton kind (*flavor*) does not change, such as in the reactions

$$\begin{aligned} \nu_\mu + N &\rightarrow \nu_\mu + X \\ \overline{\nu_\mu} + N &\rightarrow \overline{\nu_\mu} + X \end{aligned}$$

where the symbols are as defined above.

The neutrino reactions in air that lead to air showers or those that take place in water or ice and permit the detection of the neutrino reaction directly through the Cherenkov radiation caused by the produced charged secondary particles occur on nucleons of nuclei of the target medium. For the different neutrino flavors and their antiparticles the reactions shown in Table 5.5 can take place. Energetic reaction products may subsequently generate an electromagnetic or hadronic cascade, or both. Analogous reactions can be listed for elastic and inelastic neutral-current reactions, whereby the same lepton stands on either side of the arrow.

Table 5.5 Charged-current neutrino reactions

Quasi-elastic reactions	Inelastic reactions
$\overline{\nu_e} + p \rightarrow e^+ + n$	$\overline{\nu_e} + N \rightarrow e^+ + \text{Hadrons}$
$\nu_e + n \rightarrow e^- + p$	$\nu_e + N \rightarrow e^- + \text{Hadrons}$
$\overline{\nu_\mu} + p \rightarrow \mu^+ + n$	$\overline{\nu_\mu} + N \rightarrow \mu^+ + \text{Hadrons}$
$\nu_\mu + n \rightarrow \mu^- + p$	$\nu_\mu + N \rightarrow \mu^- + \text{Hadrons}$
$\overline{\nu_\tau} + p \rightarrow \tau^+ + n$	$\overline{\nu_\tau} + N \rightarrow \tau^+ + \text{Hadrons}$
$\nu_\tau + n \rightarrow \tau^- + p$	$\nu_\tau + N \rightarrow \tau^- + \text{Hadrons}$

5.3.3 Neutrino Cross Sections

The total cross section for neutrino reactions on nucleons (p or n), $\sigma(\nu, N)$, is proportional to the neutrino laboratory energy, $E_{\nu,\text{lab}}$, below the $W^\pm$ and Z° production thresholds. Figure 5.12 shows a compilation of early measurements of muon neutrino and antineutrino cross sections on nucleons up to laboratory energies of about 14 GeV (Eichten et al., 1973; Barish et al., 1975; Perkins, 1975). The plot shows that the energy dependence of the cross section goes approximately as $0.74 \cdot 10^{-38}$ cm$^2 \cdot E_\nu$/GeV for (ν, N) reactions and as $0.28 \cdot 10^{-38}$ cm$^2 \cdot E_\nu$/GeV for $(\overline{\nu}, N)$ reactions at these energies.

The event rate, I, for (ν, N) reactions is therefore

$$I \;=\; N_t \cdot I_i \cdot \sigma_{\nu,N}(E) \;\; [\text{s}^{-1}] \;\; , \tag{5.57}$$

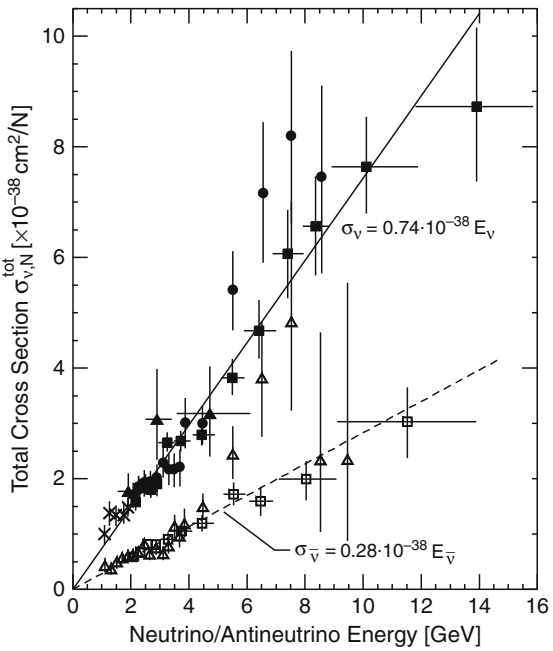

Fig. 5.12 Total neutrino and antineutrino cross sections as a function of energy (Eichten et al., 1973 ×, •, △; Barish et al., 1975 ▲; and Perkins, 1975 □, ■). The *solid line* indicates the linear energy dependence of the cross section for neutrinos and the *dashed line* for antineutrinos

where N_t is the number of target nucleons per square centimeter and I_i the intensity of the neutrino beam in neutrinos per second and square centimeter.

As a thumb rule we can say that for neutrino reactions on nucleons at a cross section of $\sim 2 \cdot 10^{-38}$ cm^2 one obtains about 1 reaction per 10^{15} incident neutrinos in a target of thickness 1 g cm^{-2}. This figure must be multiplied by the factor A/Z for neutrino reactions on electrons, where A is the mass number of the target nucleus and Z its electronic charge.

In Table 5.6 we list neutrino–nucleon cross sections from different experiments and in Table 5.7 we list the neutrino–electron cross sections predicted by the Glashow-Weinberg-Salam (GWS) theory (Glashow, 1961, 1980; Weinberg, 1967, 1971, 1980; Salam, 1964, 1968, 1980) together with some experimental cross sections.

More recent data are summarized in Fig. 5.13 which also shows a point that was extracted from HERA[5] data that were converted to a ν, N cross section, corresponding to an equivalent fixed target energy of ~50 TeV (Ahmed et al., 1994).

Figure 5.14 shows the energy dependence of cross sections for a variety of neutrino reactions, as indicated, from threshold to 1,000 GeV from a compilation of Eisele (1986). Note that no experimental data on high energy electron-neutrino and

Table 5.6 Neutrino-nucleon scattering cross sections

Experimental [cm^2]	References
$\sigma(\nu_\mu, p) = (0.474 \pm 0.030) \cdot 10^{-38} \cdot (E_\nu/\text{GeV})$	Aderholz et al. (1986)
$\sigma(\overline{\nu_\mu}, p) = (0.500 \pm 0.032) \cdot 10^{-38} \cdot (E_\nu/\text{GeV})$	
$\sigma(\nu_\mu, n) = (0.84 \pm 0.07) \cdot 10^{-38} \cdot (E_\nu/\text{GeV})$	Allasia et al. (1984)
$\sigma(\overline{\nu_\mu}, n) = (0.22 \pm 0.02) \cdot 10^{-38} \cdot (E_\nu/\text{GeV})$	
$\sigma(\nu_\mu, p) = (0.40 \pm 0.04) \cdot 10^{-38} \cdot (E_\nu/\text{GeV})$	
$\sigma(\overline{\nu_\mu}, p) = (0.44 \pm 0.03) \cdot 10^{-38} \cdot (E_\nu/\text{GeV})$	
Experimental average [cm^2]	
$\sigma(\nu_\mu, N) = (0.682 \pm 0.012) \cdot 10^{-38} \cdot (E_\nu/\text{GeV})$	Schmitz[a] (1997, p. 134)
$\sigma(\overline{\nu_\mu}, N) = (0.338 \pm 0.007) \cdot 10^{-38} \cdot (E_\nu/\text{GeV})$	

[a] average of data from MacFarlane et al. (1984), Berge et al. (1987) and Allaby et al. (1988)

Table 5.7 Neutrino-electron scattering cross sections

Theoretical (Glashow-Weinberg-Salam) [cm^2]	References
$\sigma(\nu_e, e) = 9.49 \cdot 10^{-42} \cdot (E_\nu/\text{GeV})$	
$\sigma(\overline{\nu_e}, e) = 3.97 \cdot 10^{-42} \cdot (E_\nu/\text{GeV})$	
$\sigma(\nu_\mu, e) = 1.56 \cdot 10^{-42} \cdot (E_\nu/\text{GeV})$	
$\sigma(\overline{\nu_\mu}, e) = 1.33 \cdot 10^{-42} \cdot (E_\nu/\text{GeV})$	
Experimental (mean values) [cm^2]	
$\sigma(\nu_\mu, e) = (1.49 \pm 0.24) \cdot 10^{-42} \cdot (E_\nu/\text{GeV})$	Myatt (1982)
$\sigma(\overline{\nu_\mu}, e) = (1.69 \pm 0.33) \cdot 10^{-42} \cdot (E_\nu/\text{GeV})$	Myatt (1982)

[5] HERA (ep-collider) experiment at DESY in Hamburg, Germany.

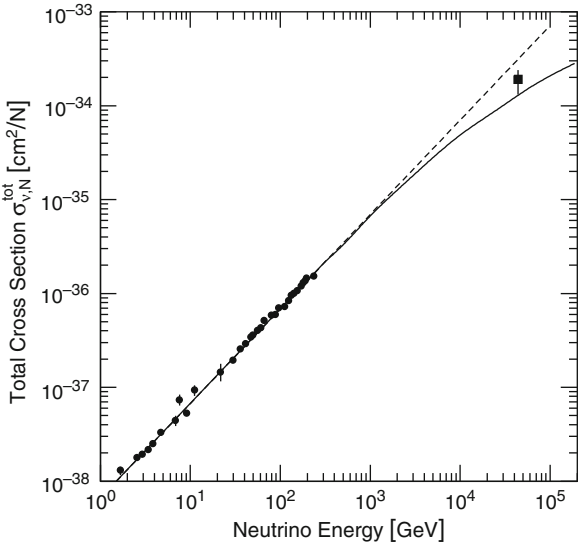

Fig. 5.13 Summary of neutrino–nucleon (ν, N) total cross sections to 300 GeV (Haidt and Pietschmann, 1988 •) and one data point at ∼50 TeV equivalent fixed target energy extracted from HERA data (Ahmed et al. 1994)

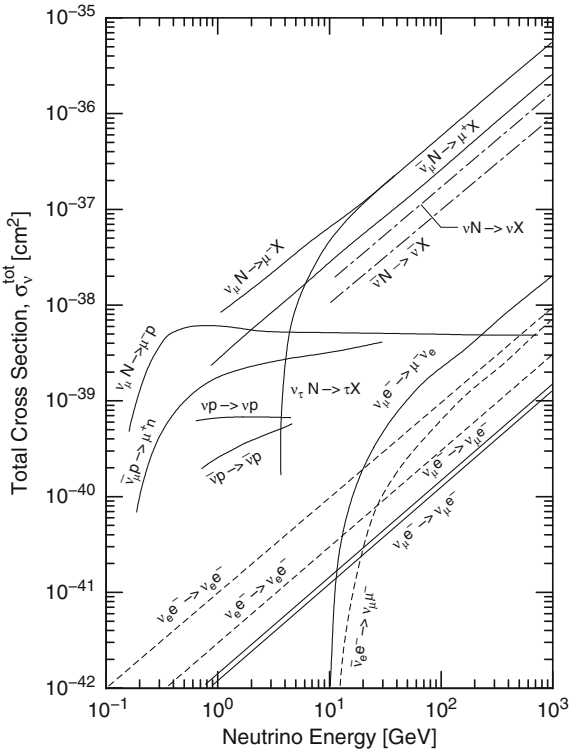

Fig. 5.14 Total cross sections of different neutrino reactions as a function of neutrino energy (Eisele, 1986)

antineutrino cross sections are available since present-day accelerator facilities cannot produce such beams with adequate intensity.

The theoretical predictions of ultrahigh energy neutrino cross sections have been greatly influenced in recent years by the *deep inelastic scattering* (DIS) results of the HERA experiments at Hamburg, starting in 1992 (Reno, 2006). The HERA experiments did not measure neutrino cross sections but yielded improved *parton distribution functions* (PDFs) from negatron and positron collisions on protons. At an energy equivalent to a neutrino energy of 54 TeV, the HERA results have aided our understanding of the parton distribution functions in new kinematic regimes. These have led to different extrapolations of the ultrahigh energy neutrino cross section than was obtained in earlier work.

5.3.4 Predicted High Energy Neutrino Cross Sections

For the cross section of the reaction

$$\nu_\mu(k)\, N(p) \;\rightarrow\; \mu(k')\, X \tag{5.58}$$

with an isoscalar nucleon[6] N, the charged-current *differential* cross section in terms of $x = Q^2/(2p \cdot q)$, where $Q^2 = -q^2$, $q = k - k'$, $y = p \cdot q/(p \cdot k)$, Q being the 4-momentum transfer, y the relative energy transfer (inelasticity), p, q, k and k' are the 4-momenta of the initial and final particles, and M_p the nucleon mass, is

$$\begin{aligned}\frac{\mathrm{d}^2\sigma}{\mathrm{d}x\,\mathrm{d}y} &= \frac{2G_F^2 M_p E_\nu}{\pi(1 + Q^2/M_W^2)^2} \\ &\quad \cdot \left\{q(x, Q^2) + (1 - y)^2 \bar{q}(x, Q^2)\right\}\,,\end{aligned} \tag{5.59}$$

where E_ν is the neutrino energy and G_F the coupling constant. The parton distribution functions for the relevant quark and antiquark distributions are functions of (x, Q^2) and labeled as $q(x, Q^2)$ and $\bar{q}(x, Q^2)$.

At low energies, where $Q^2 \ll M_W^2$, M_W being the $W^\pm$ mass, the PDFs are nearly Q^2 independent, and the neutrino-nucleon cross section scales with incident neutrino energy, E_ν. At high energies, the increase in the PDFs with increasing Q^2 is more than offset by the decrease in the cross section due to the W-boson propagator. As a result, using the relation

$$xy(2M_p E_\nu) = Q^2 \tag{5.60}$$

[6] Average nucleon, mean between proton and neutron.

and the approximation that $Q^2_{\max} \sim M^2_W$, one is led to the relation

$$x \sim \frac{10^4}{(E_\nu/\mathrm{GeV})} \,. \tag{5.61}$$

At the highest energies of interest, on the order of $E_\nu \sim 10^{12}$ GeV, this translates to $x \sim 10^{-8}$. HERA measurements made a significant improvement in the range of (x, Q^2) compared to fixed target measurements. At HERA energies for $y \leq 1$, $x \geq 10^{-5} \cdot Q^2$ is accessible (Reno, 2006).

Apart from fixed target experiments, there are PDF measurements at colliders. The Tevatron experimental results are limited to $x > 10^{-3}$, however, these measurements were done at large Q^2 values (for details see Pumplin, 2002; Martin et al. 2003a, 2004).

Parton distribution function parametrizations are extracted from fits to the experimental data (for details see Devenish and Cooper-Sarkar, 2004). An important difference between the older and the modern fits is that at the reference value of $Q = Q_0$, at which the PDFs were parametrized, steeper distributions are now being used at small x. This has an influence on the extrapolation to even smaller x values. Small-x PDFs are important at ultrahigh energies where sea quarks dominate. This is evident when inspecting Fig. 5.15, where the (ν, N) and $(\bar{\nu}, N)$ charged-current cross sections are equal at $E \sim 10^6$ GeV.

The small-x behavior of the PDFs has implications in neutrino astrophysics for more than the neutrino–nucleon cross section. At lower energies, the small-x PDFs are inputs to $c\bar{c}$ and $b\bar{b}$ production by cosmic ray interactions with air nuclei. The semi-leptonic heavy quark decays are responsible for the prompt lepton fluxes which should dominate the atmospheric flux in the range of 100 TeV (Martin et al., 2003b; Gelmini et al., 2000, 2001; Pasquali et al., 1999). Measurements of the prompt lepton flux may help constrain small-x physics.

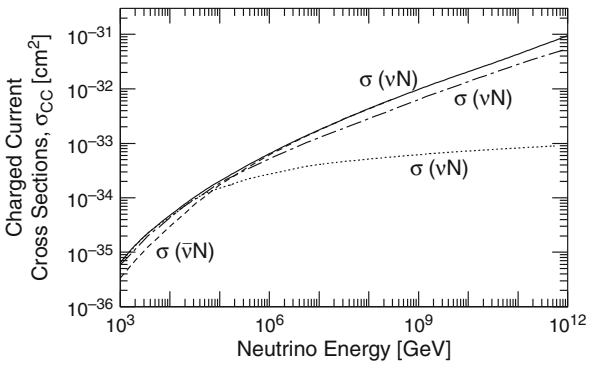

Fig. 5.15 Charged-current νN (*solid curve*) and $\bar{\nu} N$ (*dashed curve*) cross sections as a function of incident neutrino or antineutrino energy, using the CTEQ6 (Pumplin, 2002) PDFs. Also shown is the νN cross section using the EHLQ (Eichten et al., 1984) PDFs (*dot-dashed line*) and EHLQ PDFs, frozen at the scale of $Q^2 = 5\,\mathrm{GeV}^2$ (*dotted line*) (after Reno, 2006)

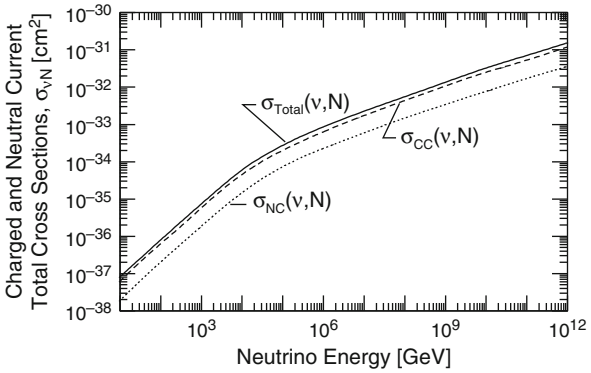

Fig. 5.16 Total neutrino–nucleon (νN) cross section (*solid curve*), and charged-current (CC) (*dashed curve*) and neutral-current (NC) (*dotted curve*) cross sections as a function of the neutrino laboratory energy (after Kwiecinski et al., 1999)

We should mention that ultrahigh energy theoretical cross sections obtained by other authors using modified approaches are only slightly different, as shown in Fig. 5.16 (see Kutak and Kwiecinski, 2003).

5.3.5 Neutrino-Opaque Earth

At 10^{17} eV the neutrino cross section is $\sigma_{\nu,\text{total}} \simeq 10^{-33}$ cm^2 and the attenuation length of the Earth is $\simeq 4 \cdot 10^6$ meters water equivalent [m w.e.] while its diameter is $3.4 \cdot 10^7$ [m w.e.] (Reno and Quigg, 1987; Reno, 2006). Thus, upward going neutrino induced showers at this energy can be expected to emerge from the Earth at nadir angles between $0^\circ \leq \theta \leq 25^\circ$, corresponding to zenith angles in the range of $90^\circ \leq \theta \leq 115^\circ$ above ground, i.e., moderately upward directed showers. Kwiecinski et al. (1999) have estimated rates for different nadir (zenith) angles for estimated spectra from active galactic nuclei (AGN).

References

Adair, R.K.: Muon Physics I, Electromagnetic Interactions. V.W. Hughes, and C.S. Wu, eds., Academic Press, New York (1977).
Aderholz, M., et al., BEBC WA59 Collaboration: Phys. Lett. B, 173, p. 211 (1986).
Ahmed, T., et al., HERA H1 Collaboration: Phys. Lett. B, 324, p. 241 (1994).
Akhiezer, A.I., and V.B. Berestetskii: Quantum Electrodynamics, Wiley (Interscience), New York (1965).
Allaby, J.V., et al.: Zeitschr. f. Phys. C, 38, p. 403 (1988).
Allasia, D., et al., Amsterdam-Bergen-Bologna-Padova-Pisa-Saclay-Torino Collaboration: Nucl. Phys. B, 239, p. 301 (1984).
Amaral, P., et al., ATLAS TileCal Collaboration: Eur. Phys. J. C, 20, pp. 487–495 (2001).

Antonelli, M., et al.: Proceedings of 6th International Conference on Calorimetry in High Energy Physics, 1996, Frascati, Italy, p. 561 (1996), and Design Report, CERN/LHCC 96-40, p. 150 (1997).
Barish, B.C., et al.: Phys. Rev. Lett., 34, p. 538 (1975).
Barish, B.C., and R. Stroynowski: Phys. Rep., 157, p. 1 (1988).
Battistoni, G., et al.: PICRC, 1, p. 597 (1995).
Barton, J.C., and I.W. Rogers: Acta Phys. Acad. Sci. Hung., 29, S4, p. 259 (1970).
Bergamasco, L., and P. Picchi: Nuovo Cim. B, 3, p. 134 (1971).
Berge, P., et al.: Zeitschr. f. Phys. C, 35, p. 443 (1987).
Bethe, H., and W. Heitler: Proc. Roy. Soc. A, 146, p. 83 (1934).
Bezrukov, L.B., et al.: PICRC, 6, p. 2445 (1971).
Bezrukov, L.B., and E.V. Bugaev: Yad. Phys., 33, p. 1195 (1981a)
Bezrukov, L.B., and E.V. Bugaev: Sov. J. Nucl. Phys., 33, p. 635 (1981b).
Bhattacharyya, D.P.: Nuovo Cim. C, 9, p. 404-413 (1986).
Borog, V.V., et al.: Can. J. Phys., 46, p. S381 (1968).
Borog, V.V., and A.A. Petrukhin: PICRC, 6, p. 1949 (1975).
Bugaev, E.V., et al.: Cosmic Muons and Neutrinos (in Russian) (Atomizdat) (1970).
Bugaev, E.V., et al.: Proceedings of Nestor Workshop, p. 268 (1993).
Bugaev, E.V., et al.: Università degli Studi di Firenze, Dipartimento di Fisica and Instituto Nationale di Fisica Nucleare Sezione di Firenza, Preprint DFF 204/4/1994 (1994).
Chasan, B.M., et al.: Phys. Rev., 119, p. 811 (1960).
Chin, S., et al.: PICRC, 3, p. 1971 (1973).
Christy, R.F., and S. Kusaka: Phys. Rev., 59, p. 405 (1941a).
Christy, R.F., and S. Kusaka: Phys. Rev., 59, p. 414 (1941b).
Crispin, A., and G.N. Fowler: Rev. Mod. Phys., 42, p. 290 (1970).
Crouch, H.R., Jr., et al.: Phys. Rev. Lett., 13, p. 636 (1964).
Daiyasu, K., et al.: J. Phys. Soc. Jpn., 17, Suppl. A-III, p. 344 (1962).
Devenish, R., and A. Cooper-Sarkar: Deep Inelastic Scattering, Oxford University Press, Oxford (2004).
Eichten, T., et al.: Phys. Lett. B, 46, p. 274 (1973).
Eichten, E., et al.: Rev. Mod. Phys., 56, p. 579 (1984). [Addendum-ibid. 58, p. 1065 (1986)]. See also Duke, D.W., and J.F. Owens: Phys. Rev. D, 30, p. 49 (1984).
Eidelman, S., et al.: Particle Physics Booklet, Particle Data Group, Springer, Berlin (available from LBNL and CERN) (2004), and Phys. Lett. B, 592, p. 1 (2004).
Eisele, F.: Rep. Prog. Phys., 49, p. 233 (1986).
Enikeev, R.I., et al.: PICRC, 7, p. 82 (1983).
Fano, U.: Ann. Rev. Nucl. Sci., 13, p. 1 (1963).
Fargion, D.: PICRC, 3, p. 1297 (2001).
Fowler, D., and A. Wolfendale: Progr. Elem. Particle Cosmic Ray Phys., 4, p. 107 (1958).
Gelmini, G., et al.: Phys. Rev. D, 61, p. 056011 (2000).
Gelmini, G., et al.: Phys. Rev. D, 63, p. 036001 (2001).
Glashow, S.L.: Nucl. Phys., 22, p. 579 (1961).
Glashow, S.L.: Rev. Mod. Phys., 52, p. 539 (1980).
Grieder, P.K.F.: Cosmic Rays at Earth (Rsearcher's Reference Manual and Data Book), Elsevier Science B.V., Amsterdam, The Netherlands, ISBN 0444507108 (2001).
Grupen, C.: Fort. d. Phys., 23, p. 127 (1976).
Haidt, D., and H. Pietschmann: Landolt-Börnstein New Series, I/10, Springer, Berlin (1988).
Heitler, W.: Quantum Theory of Radiation, Oxford University Press, Oxford (1956).
Higashi, S., et al.: Nuovo Cim., 38, p. 107 (1965).
Jackson, J.D., and R.L. McCarthy: Phys. Rev. B, 6, p. 4131 (1972).
Källén, G.: Quantumelectrodynamics, Springer Verlag, New York (1972).
Kelner, S.R.: Yadernaya Fiz., 5, p. 1092 (1967).
Kelner, S.R., and Yu.D. Kotov: Sov. J. Nucl. Phys., 7, p. 237 (1968a).

Kelner, S.R., and Yu.D. Kotov: Can. J. Phys., 46, p. S387 (1968b).
Kelner, S.R., et al.: preprint 024-95, Moscow Technical University, Moscow (1995).
Kelner, S.R., et al.: Phys. Atom. Nucl., 60, p. 657 (1997).
Kelner, S.R.: Phys. Atom. Nucl., 61, p. 448 (1998).
Kelner, S.R., and A.M. Fedotov: Phys. Atom. Nucl., 62, p. 307 (1999).
Kessler, D., and P. Kessler: Nuovo Cim., 4, p. 601 (1956).
Kessler, D., and P. Kessler: Comptes Rendus, 244, p. 1896 (1957).
Kessler, D., and P. Kessler: Nuovo Cim., 17, p. 809 (1960).
Kirk, J.A., et al.: Nuovo Cim., 40, p. 523 (1965).
Kobayakawa, K.: Nuovo Cim., B, 47, p. 156 (1967).
Kobayakawa, K., and S. Miono: Can. J. Phys., 46, S212 (1968).
Kobayakawa, K.: PICRC, 5, p. 3156 (1973).
Kokoulin, R.P., and A.A. Petrukhin: Acta Phys. Acad. Sci. Hung., 29, S4, p. 277 (1970).
Kokoulin, R.P., and A.A. Petrukhin: PICRC, 6, p. 2436 (1971).
Koshiba, M.: Phys. Rep., 220, 5 & 6, pp. 229–381 (1992).
Kotov, Y.P., and V.M. Logunov: Acta Phys. Acad. Sci. Hung., 29, S4, p. 73 (1970).
Kutak, K., and J. Kwiecinski: Eur. Phys. J. C, 29, p. 521 (2003).
Kwiecinski, J., et al.: Phys. Rev. D, 59, p. 093002 (1999).
Lohmann, W., et al.: CERN Yellow Report 85-03 (1985).
MacFarlane, D.B., et al.: Zeitschr. f. Phys. C, 26, p. 1 (1984).
Martin, A.D., et al.: Eur. Phys. J. C, 28, p. 455 (2003a).
Martin, A.D., et al.: Acta Phys. Polon. B, 34, p. 3273 (2003b).
Martin, A.D., et al.: Eur. Phys. J. C, 35, p. 325 (2004).
Matsuno, S., et al.: Phys. Rev. D, 29, p. 1 (1984).
Morris, M.L., and R.O. Stenerson: Nuovo Cim. B, 53, p. 494 (1968).
Mitsui, K.: Phys. Rev. D, 45, p. 3051 (1992).
Murota, T., and A. Ueda: Prog. Theor. Phys., 16, p. 497 (1956).
Murota, T., et al.: Prog. Theor. Phys., 16, p. 482 (1956).
Myatt, G.: Rep. Prog. Phys., 45, p. 1 (1982).
Pasquali, L., et al.: Phys. Rev. D, 59, p. 034020 (1999).
Perkins, D.H.: In 1975 International Symposium on Lepton and Photon Interactions at High Energies, Stanford (1975).
Petrukhin, A.A., and V.V. Shestakov: Physics of Elementary Particles, Atomizdat, Moscow (1966).
Petrukhin, A.A., and V.V. Shestakov: Can. J. Phys., 46, part 1, p. S377 (1968).
Pumplin, J.: JHEP, 0207, p. 012 (2002).
Reno, M.H., and C. Quigg: Fermilab-Pup-87/66-T (1987).
Reno, M.H.: Nucl. Phys. B (Proc. Suppl.), 151, p. 255 (2006).
Rossi, B., and K. Greisen: Rev. Mod. Phys., 13, p. 240 (1941).
Rossi, B.: High Energy Particles, Prentice-Hall, Englewood Cliffs, NJ, (1952).
Russell, J.J., et al.: Phys. Rev. Lett., 26, p. 46 (1971).
Salam, A., and J.C. Ward: Phys. Lett., 13, p. 168 (1964).
Salam, A.: Elementary Particle Theory, p. 367, N. Swarthohn, ed., Almquist and Wiksell, Stockholm (1968).
Salam, A.: Rev. Mod. Phys., 52, p. 525 (1980).
Sakumoto, W.K., et al.: Phys. Rev. D, 45, p. 3042 (1992).
Schmitz, N.: "Neutrinophysik" (in German), Teubner Studienbücher, Physik, B.G. Teubner Stuttgart (1997).
Sternheimer, R.: Phys. Rev., 103, p. 511 (1956).
Sternheimer, R.M., and R.F. Peierls: Phys. Rev. B, 3, p. 3681 (1971).
Sternheimer, R.M.: "The Density Effect for the Ionization Loss of Charged Particles in Various Substances", Atomic Nucl. Data Tables, 30, p. 261 (1984). See also Groom, et al.: Atomic Nucl. Data Tables, 78, pp. 183–356 (2001) and Ivanov, D.Yu., et al.: Phys. Lett. B, 442, p. 453 (1998) for corrections.

Suzuki, Y., et al., ed.: Proceedings of First Workshop on Neutrino Oscillations and their Origin, Feb. 11–13 (2000). Frontiers in Science Series No 35 (2000).
Tannenbaum, M.J.: Report CERN-PPE/91-134, 19 August 1991.
Vavilov, Yu.N., et al.: Sov. J. Nucl. Phys., 18, p. 434 (1974).
Weinberg, S.: Phys. Rev. Lett., 19, p. 1264 (1967).
Weinberg, S.: Phys. Rev. Lett., 27, p. 1688 (1971).
Weinberg, S.: Rev. Mod. Phys., 52, p. 515 (1980).
Weizsäcker, C.F.: Zeitschr. f. Phys., 88, p. 612 (1934).
Williams, E.J.: Proc. Roy. Soc. A, 139, p. 163 (1933).
Williams, E.J.: K. Dan. Vidensk. Selsk. Math. Fys. Medd., 13, p. 4 (1935).
Wright, A.G.: J. Phys. A, 6, p. 79 (1973).

Chapter 6
Longitudinal Development and Equal Intensity Distributions

Overview In this chapter we discuss the general aspects of the longitudinal development of air showers and the effects of the primary energy and mass. These are based on the fundamental processes treated in detail in Chaps. 3, 4 and 5. However, the current chapter can in principle be studied without the full knowledge of the contents of the previous chapters, but some knowledge of hadronic and electromagnetic interactions is useful. Examples of simulated longitudinal shower profiles and the effect of the radiation length are presented. We then outline the longitudinal and lateral energy deposit profile of the different shower constituents in the atmosphere. This is followed by the definition of the shower rate attenuation and shower particle absorption. The absorption and attenuation lengths and coefficients are introduced, the relation of these quantities to the nucleon spectrum in the atmosphere and the mathematical expressions that link the observables are explained. Subsequently, the altitude and zenith angle dependence, and the influence of environmental parameters on the shower rate and the particle flux in showers are summarized. Experimental methods to access these quantities are discussed and data of the shower attenuation rate, the absorption of shower particles, the zenith angle dependence and of the environmental effects are discussed at some length. Finally, the concept of equal intensity cuts and distributions which offer deeper insight into the longitudinal development of showers are introduced and data samples presented.

6.1 Introduction

After the discovery of extensive air showers by Auger and Kohlhörster independently (Auger, 1938; Auger et al., 1938, 1939a, b; Auger, 1940; Kohlhörster et al., 1938), the altitude dependence of the showers was one of the first characteristics which had been studied by numerous researchers. Within a decade of the discovery a large number of measurements had been carried out from sea level to mountain altitudes of 4,300 m. Because of the initial lack of understanding of the physical processes that govern the shower development, some of the early data are rather difficult to compare because of the different detection criteria and particle groups which had been selected at that time for the investigation. Some authors focused more on the so-called *penetrating* or *hard component* or *penetrating*

P.K.F. Grieder, *Extensive Air Showers,* DOI 10.1007/978-3-540-76941-5_6,

showers whereas others were more interested in the *soft component* and in general shower phenomena (for the definition of hard and soft component see Chap. 21). In spite of this problem many of the early data are fairly consistent.

With the availability of large high flying aircraft after 1945 a much wider range of altitudes, up to 12 km, became readily accessible for exploring air showers at their early stage of development with small counter arrangements in coincidence and mini arrays, similar to the layouts used for the early density measurements at ground level. In a few cases mini arrays were flown with balloons. This work was restricted to small showers because of the limited geometry of the arrays, the size of the aircraft and the duration of the flights.

Parallel to this work the *zenith angle dependence* of showers was studied intensively with ground based equipment. This permitted the extension of the measurements of the longitudinal development of showers significantly because of the $\sec\theta$ dependence of the shower path length in the atmosphere. Moreover, larger arrays could be used and more sophisticated equipment, which also allowed to extend the measurements to larger size showers. Analogous measurements using exclusively the muon component in showers were also carried out and are discussed below. Subsequently, improved data and better statistics imposed the need for analyzing also the environmental influences, such as the barometric pressure and temperature dependence of the shower development, from which valuable shower properties can be extracted. These are discussed in Sect. 6.5.

With the improved understanding of the physics of air showers, ground based experiments grew in size and became more and more sophisticated. Part of this work eventually developed into the important branch of *equal intensity* (or *constant intensity*) measurements of air showers which yield unique data on the *longitudinal shower development*, the primary energy spectrum, some information on the chemical composition and on other aspects. The topic of equal intensity distributions is discussed separately in Sect. 6.7.

The longitudinal development of an air shower, i.e., the variation of the number of particles in a shower as a function of altitude or atmospheric depth or, more generally, as a function of path length or column density traversed in the atmosphere, is an important characteristic. It is directly accessible in individual showers only by the observation of air fluorescence caused by the charged particle flux, viewed side-on, preferentially at an angle $\geq 30^\circ$ with respect to the direction of the shower axis. A Fly's Eye type detector employs this principle (Bergeson et al., 1975a, b). Chapter 17 is devoted to topics concerning the air fluorescence detection method. However, air Cherenkov and to a lesser extent shower particle front rise time measurements also yield information on the longitudinal development of individual showers (see Chaps. 7, 9, 10 and 16).

6.2 Physical Processes and Concepts

6.2.1 Phenomenological Aspects

The principal processes that govern the longitudinal development of an air shower are above all the hadronic but also the electromagnetic interactions and the respec-

tive cascades. With respect to the hadronic processes there are the interaction cross sections,[1] σ_{int} [cm^2], or the reciprocal, the interaction mean free paths (i.m.f.p.), λ_{int} [g cm^{-2}] of the participating particles, the secondary particle multiplicity, n_s, its partition among the different kinds of secondaries emerging from an interaction, i.e., the ratio of pions to kaons to nucleons and antinucleons, etc., and the kinematics of the interactions that are primarily responsible for the energy transport in the hadron cascade and its longitudinal development and lateral spread. All these quantities are *energy dependent* and subject to *large fluctuations*. Details concerning the different hadronic processes involved are discussed in Chap. 3.

The electromagnetic processes are initiated chiefly by gamma rays that are the decay products of the neutral pions that are produced in the hadronic interactions, but also from gamma rays and electrons resulting from the decay of other unstable particles. Repeated pair production, bremsstrahlung and Compton scattering are the relevant processes that build up the photon-electron cascade which can reach very large sizes. Scattering processes such as Coulomb scattering add to the spread of the cascade, and ionization and excitation losses dissipate part or all of the energy of the electromagnetic component in the atmosphere or, if the event is very energetic, eventually in the ground. But also Cherenkov, fluorescence, and radio emission remove a tiny fraction of the energy and all charged particles are subject to geomagnetic deflection. There exists a *roughly linear* relationship between shower size at maximum development and the primary energy over a large energy range. This linear relationship is essentially valid down to ground level over a wide range of primary energy with correspondingly adapted scale factors.

To get a rough estimate of the primary energy of an average shower from its size, one can use as a thumb rule the following energy conversion factors per particle: $\sim$3 GeV at an observation level of 5,000 m, $\sim$5 GeV at 2,500 m and $\sim$10 GeV at sea level (cf. Fig. 6.2a). Thus, multiplying the shower size at the corresponding level with the appropriate energy factor yields the approximate primary energy (for details see Sect. 10.2).

The cross sections determine the intervals at which interactions take place in the atmosphere. Consequently, at the early stage of the shower development, before the complete break-up of a projectile nucleus, a shower initiated by a heavy primary shows a longitudinal behavior which is significantly different from that of a proton shower. In the former, the first interaction takes place at much higher altitude and the shower develops more rapidly, reaching its maximum development at greater height than a proton initiated shower. But even at large depths there remain some differences between proton and heavy primary initiated showers, such as the muon number, though the differences are frequently masked because of large fluctuations in the longitudinal and lateral developments. In addition, an energy dependent primary mass composition complicates the interpretation of ground based measurements even more.

[1] Of particular interest are the energy dependent *inelastic cross sections* for collisions of nucleons, pions and other hadrons, such as nuclei, with nuclei of air constituents, $\sigma_{\text{inel}}^{N,A}$, $\sigma_{\text{inel}}^{\pi,A}$, etc., where A stands for ^{14}N or ^{16}O.

The energy dependence of the hadronic cross sections, too, manifests a similar though much lesser effect. A rising cross section with increasing energy causes a slipping of the height of the first interaction and of the shower maximum to higher altitudes with increasing energy. This applies particularly to proton initiated showers, that tend to resemble more and more light nuclei initiated showers at extremely high energies, as had been demonstrated by simulations (Grieder, 1984, 1986).

The secondary particle multiplicity which is a function of energy is mostly responsible for the growth rate of the hadron cascade.[2] It also affects the location of the height of maximum development of a shower in the atmosphere and a number of other observables (Grieder, 1977; Wdowczyk and Wolfendale, 1972). The nature of the secondaries, chiefly their mass but also their mean life if they are subject to decay such as pions, kaons, etc., and kinematics affect the propagation of the cascade.

Since the average energy of the particles decreases and the density of the atmosphere increases as the shower propagates to greater atmospheric depth, the particle population, too, changes because of the changing competition between decay and interaction of unstable particles such as pions and kaons, but also because of the energy dependence and threshold requirements of the processes involved (see Figs. 3.24 and 3.25).

Of great significance is the *elasticity*, η, or its counterpart, the *inelasticity*, K, of hadronic collisions ($K = 1 - \eta$). The so-called *leading particle effect*, particularly dominant in baryon and antibaryon initiated collisions, reflects the relatively high degree of elasticity which is typical for this kind of collisions. It plays an important role for the propagation of a shower and for the energy transport within it, and shows little energy dependence.[3]

The large widths of the elasticity and multiplicity distributions at any energy folded with the probability distribution of the interaction length and the height of the first interaction are the main causes for the large *fluctuations* which shower observables manifest at any altitude. In addition, the wide range of primary masses introduces further uncertainties. As a result, the distribution of the height of maximum development of showers of fixed primary energy is smeared over a rather wide range of altitudes. This is illustrated in Fig. 6.1 where we show four sets of proton initiated showers having primary energies of 10^4, 10^5, 10^6 and 10^7 GeV, respectively (Grieder, 1979a, 1984).

The figure shows very clearly that, with the exception of the fluctuations of the height of the first interaction, the fluctuations of the general shower development diminish with increasing primary energy. This is chiefly due to the secondary particle multiplicity of the first few interactions that get very large at high energy, provoking rapid growth of the shower. The large average number of secondaries emerging from these interactions reduces the effect of fluctuations of individual subsequent interactions on the general shower development.

---

[2] The energy dependence of the secondary particle multiplicity is discussed in Sect. 3.5.

[3] For a detailed discussion on the *leading particle effect, elasticity* and *inelasticity* see Sect. 3.8.

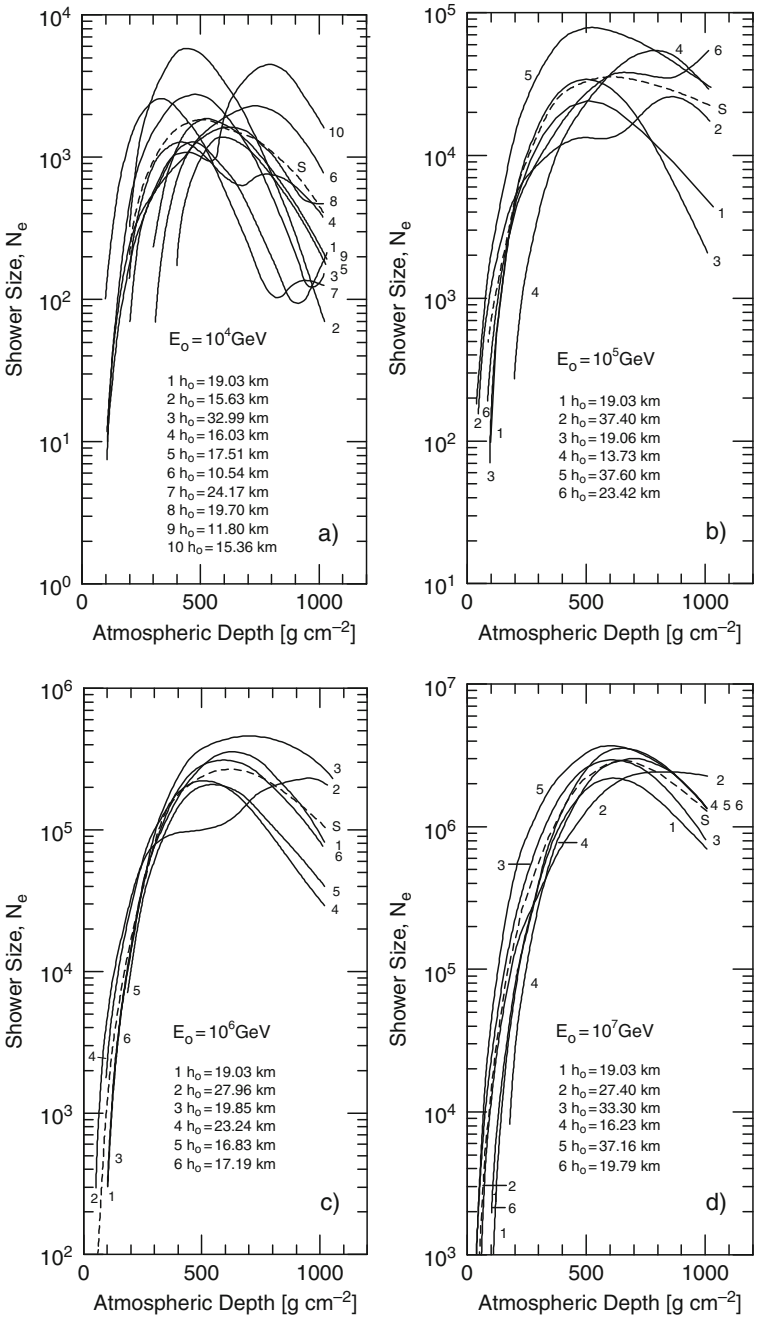

Fig. 6.1 Longitudinal development of the electromagnetic component (negatrons and positrons only) in proton initiated air showers (Grieder, 1979a, 1984). The primary energies for the data displayed in Figs. (**a**), (**b**), (**c**) and (**d**) are 10^4, 10^5, 10^6 and 10^7 GeV, respectively

For analogous reasons heavy primary initiated showers manifest less fluctuations in their development than proton showers. Nevertheless, significant fluctuations remain because of the randomness of the height of the first interaction in the atmosphere and because of the fragmentation of the heavy primaries. Heavy primaries may be but are not necessarily the cause of multi-core showers. Large transverse momenta imparted on very energetic secondary hadrons at high altitude may also cause multi-core showers.

Generally speaking, hadronic showers initiated deep in the atmosphere develop more rapidly and contain a smaller fraction of high energy muons because pions which constitute the bulk of unstable secondaries emerging from a hadronic interaction are more likely to interact than decay while propagating in the lower and denser regions of the atmosphere, and vice versa.

The pure electromagnetic (EM) cascade development shows a far more steady growth and decline profile and is subject to much less fluctuations than the hadronic cascade if we disregard the ultrahigh energy regime. There the Landau-Pomeranchuk-Migdal effect (LPM effect), discussed in Sect. 4.5, can stimulate additional fluctuations in the photon–electron cascade development (Landau and Pomeranchuck, 1953a, b; Migdal, 1956; Konishi et al., 1991).

However, since an air shower is a superposition of a hadron–muon and photon–electron cascade[4] and because the former is the latter's parent process, the shower size, too, exhibits large fluctuations. Moreover, the photon-electron component of an air shower consists of the superposition of thousands and thousands of electromagnetic sub-cascades, initiated mostly by gamma rays from neutral pion decays and to a much lesser extent by electrons from the decay of muons and other particles (Grieder, 1977).

Because of the direct genetic relationship of the electromagnetic cascade's parent particles, chiefly the π^0, with the hadron cascade, the initial conditions of the electromagnetic cascades are subject to all inherent fluctuations of the former in space, time and energy within a shower. The large number of interlaced electromagnetic sub-cascades attenuates the effect of the hadronic fluctuations somewhat, yet amazing fluctuations still remain and are observed at great atmospheric depths.

It is evident from the above discussion that precise knowledge of the longitudinal development of air showers yields profound insight into ultrahigh energy hadronic processes. It reveals information on the energy dependence of the inelastic cross section, on the primary energy and composition, the secondary particle multiplicity and on other important observables, however, the information is masked.

[4] In spite of the fact that muons do not generate a cascade themselves, but represent so-to-say an extension of the history of the hadron cascade into the deeper atmosphere where they exhibit a shower like behavior when analyzed with a detector array, we use the term hadron–muon cascade in place of hadron cascade and associated muon shower.

6.2.2 Theoretical Studies and Simulation Results

Extensive theoretical studies on the longitudinal development of the showers using full Monte Carlo simulations in space and time were carried out by numerous authors (see Chap. 20).

Examples of the longitudinal development of the electromagnetic component (negatrons and positrons only) of simulated proton initiated showers of different primary energies are illustrated in the previously mentioned Fig. 6.1. These curves, sometimes referred to as *transition curves*, are the result of a highly sophisticated four-dimensional Monte Carlo calculation which includes all relevant hadronic processes and generates all components (hadrons, muons and electrons) in space and time, together with a wealth of other, so-called genetic information (Grieder, 1977, 1984 and references listed therein).[5]

Figure 6.2a shows average shower development curves obtained from the same calculation as the curves shown in the previous figure (Fig. 6.1). The systematic shift of the location of the maximum development of the showers to greater atmospheric depth with increasing primary energy, indicated by the dashed line labeled $X_{\max}$ [g/cm^2] is evident. The change of the location of the depth of maximum development with primary energy is called the *elongation* and its rate of change per decade of primary energy the *elongation rate* (Linsley, 1977).

New hadronic processes at ultrahigh energies, though unlikely, could influence the shower development. Frequently such processes were suggested in the past as the cause for the apparent disagreement between the results of shower simulations based on heavily approximated and extrapolated interaction models that were derived from accelerator observations at much lower energies and from experimental air shower and emulsion data. Extensive studies in this respect had been made by many authors in the past and remain an important research topic today. For details the reader is referred to Chap. 20 and to the Collected Contributions to the "NEEDS Workshop 2002" at Karlsruhe, Germany, that was dedicated to these problems (NEEDS, 2002). Likewise, the Proceedings of the "XII. International Symposium on Very High Energy Cosmic Ray Interactions (ISVHECRI) 2002" held at CERN, Geneva, Switzerland, that represented a first attempt to link the common interests of the Large Hadron Collider (LHC) community at CERN and the cosmic ray community, offer valuable new information (Pattison et al., 2003) (see also Proceedings of the ISVHECRI, Paris, 2008).

A relevant parameter for the development of the electromagnetic component of a shower is the radiation length, χ_0, of electrons in air. Genannt and Pilkuhn (1973) pointed out that the radiation length of electrons in air has never been accurately verified experimentally. In their calculation they show that if the molecular binding

[5] This program system, called ASICO, was the forerunner of today's widely used CORSIKA program (Capdevielle et al., 1992; Heck et al., 1998a, b; Heck and Knapp, 2002). The two programs have essentially identical structures, however, an extended choice of modern interaction models (event generators) is now available with CORSIKA (for details see Chap. 20).

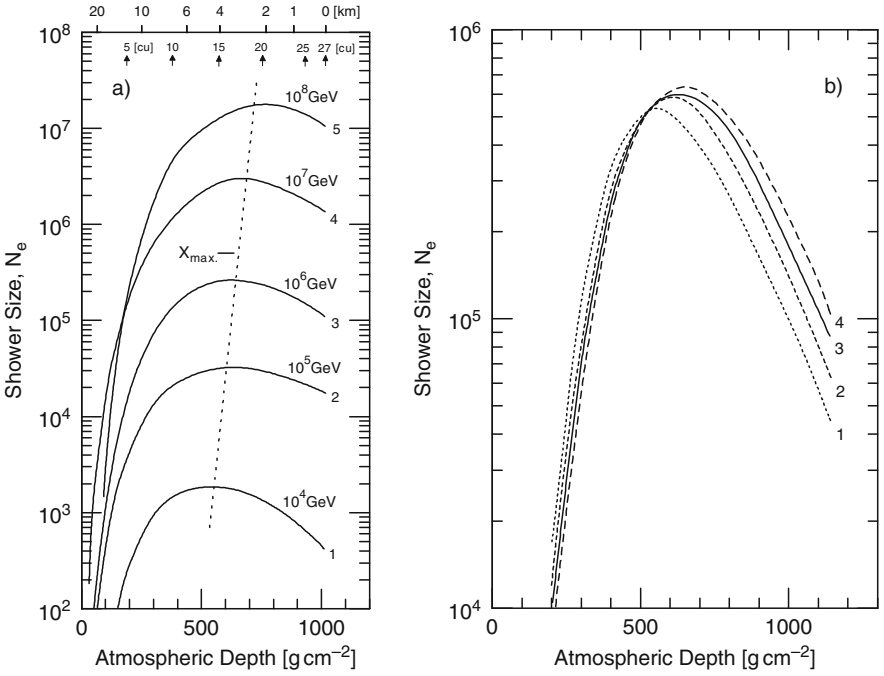

Fig. 6.2 (**a**) Average longitudinal development of vertically incident proton initiated showers having primary energies of 10^4, 10^5, 10^6, 10^7 and 10^8 GeV (*curves* 1–5). The displacement of the height of maximum development, $X_{\max}$ [g cm^{-2}], indicated by the *dotted line* is evident (Grieder, 1979b). The labels on top of the figure indicate the altitude in [km] and the atmospheric depth in cascade units [cu] (inside figure frame) corresponding to the column density in [g cm^{-2}] given along the abscissa. (**b**) Longitudinal development of 10^6 GeV proton initiated showers (Bourdeau et al., 1976). An interaction mean free path of 80 g/cm^2 and an average elasticity of 0.5 were used. The different curves apply to different values of the electron radiation length, χ_0: (1) $\chi_0 = 30$ g cm^{-2}; (2) $\chi_0 = 34.6$ g cm^{-2}; (3) $\chi_0 = 37.7$ g cm^{-2}; (4) $\chi_0 = 40$ g cm^{-2}

of the air constituents is considered, one obtains for the radiation length instead of the commonly used value of $\chi_0 = 37.1$ g cm^{-2} a reduced value of $\chi_0 = 34.6$ g cm^{-2} (see Sect. 4.2.2, Tsai, 1974).[6]

Linsley (1981, 1985) has shown that the calculation of Genannt and Pilkuhn (1973) is incorrect and that χ_0 for molecular nitrogen is only $\sim$1% greater than for atomic nitrogen, giving as best value the Thomas-Fermi value without any molecular binding correction. Procureur et al. (1975) and Bourdeau et al. (1976) have investigated the effect which different values of the radiation length have on electromagnetic showers. Their results are shown in Fig. 6.2b.

In Fig. 6.3 we show longitudinal shower development curves for proton and iron primary initiated events of total energy 10^{19} eV from a simulation of Sakaki (2003).

[6] Different authors use different values for χ_0. In older work 36.66 g cm^{-2} was frequently used; today a value of 37.1 g cm^{-2} is recommended.

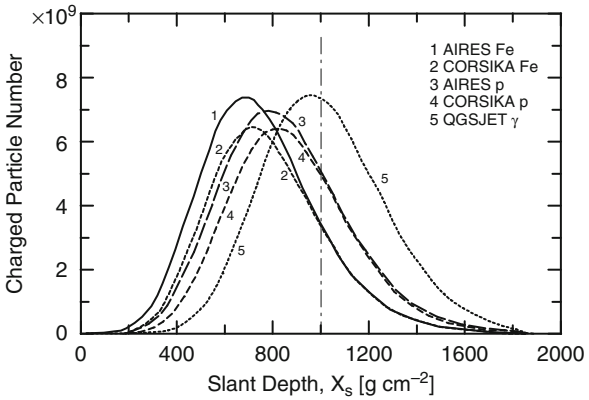

Fig. 6.3 Average longitudinal development of 10^{19} eV proton and iron initiated showers using the QGSJET event generator with the AIRES and CORSIKA codes, respectively, as indicated in the figure. Also shown is the development of gamma ray triggered showers using the AIRES program. A thinning level of 10^{-6} had been applied. The *vertical chain-line* at 1,000 g cm^{-2} marks the approximate vertical atmospheric depth at sea level (after Sakaki, 2003)

This author used the modern QGSJET event generator (Kalmykov et al., 1997; Ostapchenko, 2006a, b, c, d) in conjunction with the simulation programs CORSIKA (Heck and Knapp, 2002, 2006) and AIRES (Sciutto, 2002, 2005).

This figure is very instructive. It illustrates that the two program systems do not yield identical results for identical initial primary conditions, i.e., for the same primary particle (mass) and energy. It is seen that respective shower maxima are at nearly the same location in the atmosphere, though AIRES yields slightly higher locations, but the total number of particles generated by the two programs deviate significantly at shower maximum.

Such differences impede the accuracy of primary mass and energy estimates (see Chap. 11). Remedy of this problem is expected when the data from the Large Hadron Collider (LHC) at CERN in Geneva (Switzerland) become available, that offer a new anchor-point to tune hadronic interaction models near 100 PeV.

Also shown in Fig. 6.3 is the average longitudinal profile of pure electromagnetic showers initiated by photons of energy 10^{19} eV. Such events reach their maximum development at significantly larger depth than hadronic showers, even without invoking the LPM effect, because of the low multiplicity of electromagnetic interactions (see Chaps. 4 and 7).

An observable that is rarely discussed explicitly but is of great relevance for the shower development, in particular for the atmospheric fluorescence detection method, discussed later (Chap. 17), as well as for general cascade theory (Chap. 4), is the energy release or energy deposit per unit column density [g cm^{-2}] of the shower as it penetrates the atmosphere, i.e., the track length energy integral per gram per centimeter square.

To get a feeling of this quantity we display in Fig. 6.4 the results obtained by Risse and Heck (2004) from a simulation using the CORSIKA code for a 10^{19} eV

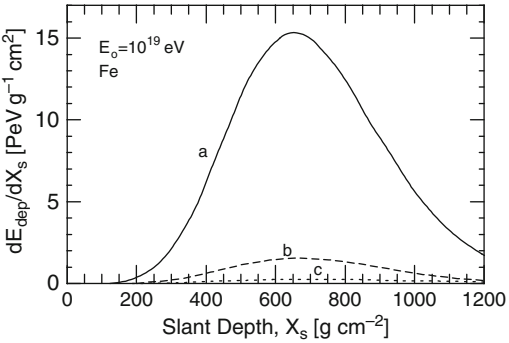

Fig. 6.4 Differential energy deposit, dE_{dep}/dX_s, of positrons + negatrons of energy $\geq$0.1 MeV (*curve* a), and of muons + hadrons combined (*curve* c) versus atmospheric slant depth, X_s, of an iron nucleus initiated shower of primary energy 10^{19} eV. Also shown is the energy deposit of the electronic component below the energy threshold of 0.1 MeV (*curve* b) (after Risse and Heck, 2004)

primary iron initiated shower, incident under a zenith angle of 45°. The figure shows separately the overwhelming contributions from positrons and negatrons combined and the minute contribution from the muonic and hadronic components combined. Also indicated is that part that results from the electromagnetic component below the simulation threshold of 0.1 MeV. This calculation includes the additional track length of the involved particles due to scattering by an angle δ with respect to an inclined shower axis. The energy spectrum of the dominating electromagnetic component (negatrons and positrons) that was obtained from the same calculation at shower maximum is shown in Fig. 6.5 for different radial zones about the inclined shower axis.

Another topic of relevance is photoproduction (photonuclear reactions) which is briefly discussed in Sect. 4.4. It had been shown by McComb et al. (1979a, b) that

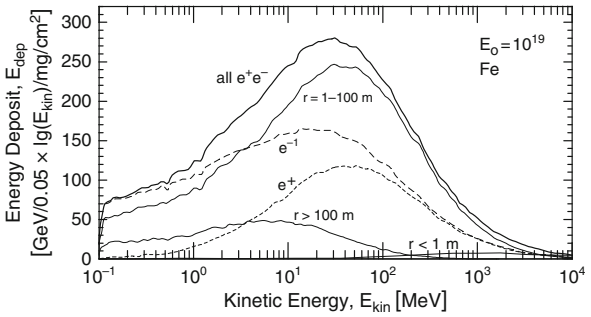

Fig. 6.5 Differential energy deposit of positrons + negatrons per unit column density (in [mg cm^{-2}]) in air at maximum development of a 10^{19} eV iron primary initiated shower as a function of the kinetic energy of the particles. Shown, too, are the contributions at three different radial zones ($r < 1$ m, $1 \leq r \leq 100$ m, $r > 100$ m) (after Keilhauer et al., 2005; see also Risse and Heck, 2004)

photoproduction affects the low energy component of muons in very high energy showers to some extent.

6.3 Attenuation of Shower Rate and Absorption of Shower Particles

6.3.1 General Comments and Historic Aspects

During the early stages of air shower research it was assumed that showers were initiated by primary electrons or gamma rays. Initial theoretical considerations were therefore based on this assumption and a number of fundamental concepts and relations were introduced at that time, which ignore the existence and role of the parent hadron cascade, that are still used today for convenience.

However, it must be pointed out that (a) due to the fact that the radiation length in air, χ_0 (37.1 g cm^{-2}), and the interaction mean free path of hadrons, $\lambda_{\rm int}^{\rm air}$ ($\lambda_{\rm int}^{N,{\rm air}} \simeq 80\,{\rm g\,cm^{-2}}$ for nucleons, $\lambda_{\rm int}^{\pi,{\rm air}} \simeq 120\,{\rm g\,cm^{-2}}$ for pions, etc.), differ only by roughly a factor of two to three and, (b) because the electromagnetic sub-cascades are fully interlaced and superimposed with the hadron cascade and the accompanying muons, the early concepts of *shower frequency* or *rate attenuation length*, $\Lambda_{\rm att}$ [g cm^{-2}], and *particle number absorption length* in a shower, $\lambda_{\rm abs}$ [g cm^{-2}], are still useful for analyzing and interpreting showers.

Evidently, the terms attenuation and absorption of the shower rate and the shower particles, respectively, is only applicable to showers in the lower regions of the atmosphere, beyond their maximum development. Disregarding extremely energetic events this applies to the lower third of the atmosphere. The two observables, $\Lambda_{\rm att}$ and $\lambda_{\rm abs}$, and their reciprocals, the corresponding *attenuation* and *absorption coefficients*, $\mu_{\rm att}$ [cm^2 g^{-1}] and $\mu_{\rm abs}$ [cm^2 g^{-1}], respectively, are defined below.

Many articles that deal with these quantities are frequently confusing, partly because of the terminology and partly because some authors have interchanged the meaning of the symbols[7] Λ and λ. In the following we will summarize the most relevant facts and relations concerning these two observables and present the available data. Detailed discussions on these topics can be found in the articles of Greisen (1956, 1960), Miyake (1958, 1968), Cocconi (1961), Hayakawa (1969) and in the books of Galbraith (1958), Wolfendale (1973), Khristiansen (1980), Sokolsky (1989), and Rao and Sreekantan (1998).

[7] In the literature there is no clear-cut terminology. *Attenuation length* as well as *absorption length* are used for shower rate attenuation and/or shower particle absorption, and likewise for Λ and λ.

6.3.2 Energy Spectrum of Nucleons in the Atmosphere

At high energies and for a general discussion the differential energy spectrum of the primary cosmic ray nucleons can be approximated by the following expression,[8]

$$I(E, X = 0)\mathrm{d}E \;=\; S_0 E^{-(\gamma+1)}\mathrm{d}E \;\;, \tag{6.1}$$

where $I(E, X = 0)\mathrm{d}E$ is the intensity of primary nucleons in the energy interval between E and $E + \mathrm{d}E$ at atmospheric depth $X = 0$, $(\gamma + 1)$ is the differential spectral index ($\gamma = 1.75$), and S_0 is a scale factor.

Upon entry into the atmosphere the primary nucleons are subject to collisions as they propagate. The probability that a nucleon has suffered j collisions by the time it has reached an atmospheric depth of X [g cm^{-2}] is given by the Poissonian distribution,

$$P(j) \;=\; e^{-(X/\lambda_{\mathrm{int}}^N)} \left(\frac{X}{\lambda_{\mathrm{int}}^N}\right)^j \frac{1}{j!} \;\;, \tag{6.2}$$

where λ_{int}^N [g cm^{-2}] is the interaction mean free path for nucleons in air.

Experiment has shown that when emerging from a collision the nucleons retain on average a large fraction, η_N, of their energy, namely $\eta_N E$. Consider now a nucleon of energy E at atmospheric depth X that has suffered j nuclear collisions on its way, then, $E = \eta_N^j E_0$, where E_0 is the primary energy, and the differential energy spectrum of the nucleons at depth X is

$$\begin{aligned} I(E, X)\mathrm{d}E &= \sum_{j=0}^{\infty} S_0 \left(\frac{E}{\eta_N^j}\right)^{-(\gamma+1)} \left(\frac{\mathrm{d}E}{\eta_N^j}\right) P(j) \\ &= S_0 E^{-(\gamma+1)}\, \mathrm{d}E\; e^{-(X/\lambda_{\mathrm{int}}^N)} \sum_{j=0}^{\infty} \left(\frac{X}{\lambda_{\mathrm{int}}^N}\right)^j \left(\frac{\eta_N^{j\gamma}}{j!}\right) \\ &= I(E, 0)\, \mathrm{d}E\; e^{-(X/\Lambda_{\mathrm{att}}^N)} \;\;, \end{aligned} \tag{6.3}$$

where

$$\Lambda_{\mathrm{att}}^N \;=\; \frac{\lambda_{\mathrm{int}}^N}{1 - \eta_N^{\gamma}} \;\; [\mathrm{g\,cm^{-2}}] \tag{6.4}$$

is called the *attenuation length* of the rate of nucleons in air and η_N is the *average elasticity* of nucleons (Schopper, 1967).

[8] We disregard the steepening of the spectrum beyond the so-called knee.

6.3.3 Attenuation of Shower Rate

It has been found in many experiments that the intensity (or rate, or frequency) of showers of given size N, $I(N)$, manifests an *exponential attenuation* with increasing atmospheric depth, X [g/cm^2], measured along the shower axis.[9] Therefore the *shower rate attenuation coefficient*, $\mu_{\rm att}$, can be expressed as

$$-\frac{\partial \ln I(N)}{\partial X} = \mu_{\rm att} = \frac{1}{\Lambda_{\rm att}} \ [\mathrm{cm}^2\,\mathrm{g}^{-1}] \ . \tag{6.5}$$

$\Lambda_{\rm att}$ is called the *attenuation length of the shower rate*. This relation is linked to the slopes of the shower size and density spectra that exhibit essentially the same exponents and are approximately linearly related to the primary energy spectrum. $\mu_{\rm att}$ can also be expressed in units of reciprocal radiation lengths [(rl)$^{-1}$]. The quantity $\Lambda_{\rm att}$ can be determined from measurements of the altitude variation, the zenith angle distribution, or from the barometric effect.

6.3.4 Absorption of Shower Particles

It was also found that the size spectrum of showers can be represented approximately by a power law of the form

$$I(N)\mathrm{d}N = kN^{-(\gamma+1)}\mathrm{d}N \ , \tag{6.6}$$

where N is the shower size. Hence, we can write

$$I(N)\mathrm{d}N = k_0 \exp\left(-\frac{X}{\Lambda_{\rm att}}\right) N^{-(\gamma+1)}\mathrm{d}N \ . \tag{6.7}$$

This equation applies if we suppose that all the particles in the showers are being absorbed *exponentially* with an absorption length, $\lambda_{\rm abs}$. From this relation it follows that

$$-\frac{\partial \ln N}{\partial X} = \frac{1}{\gamma\,\Lambda_{\rm att}} = \frac{1}{\lambda_{\rm abs}} = \mu_{\rm abs} \ [\mathrm{cm}^2\,\mathrm{g}^{-1}] \ . \tag{6.8}$$

Thus, the *particle absorption length*, $\lambda_{\rm abs}$, can be determined by measuring γ and $\Lambda_{\rm att}$. The quantity $\mu_{\rm abs}$ is called the *particle absorption coefficient*. Note that Eq. (6.8) merely defines $\lambda_{\rm abs}$.

---

[9] We write N instead of N_e in this case since experimentally the distinction between the electron size, N_e, and the total shower size, N, which includes all particles, is made only in a few experiments, e.g., in KASCADE (Antoni et al., 2003).

6.3.5 Spectral Aspects of Particle Absorption and Rate Attenuation

Due to the prolonged paths of inclined showers with respect to vertical showers to reach a given observation level at altitude h [m] a.s.l., corresponding to a vertical atmospheric depth, X [g cm^{-2}], a higher energy is required for a primary of a given kind, say a proton, incident under a zenith angle $\theta \geq 0^\circ$ to overcome the additional absorption, in order to produce a shower of the same size as a vertically incident primary.

Consequently, at a fixed location in the atmosphere, the rate of showers of a given size declines with increasing zenith angle, θ, because of the rapidly falling primary spectrum with increasing energy.

If the particle number in a given vertical shower, i.e., the shower size N, decreases with increasing atmospheric depth X according to the relation

$$N(X) \;=\; N(X_m) \exp\left(-\frac{X - X_m}{\lambda_{\rm abs}}\right) \;, \tag{6.9}$$

where $N(X_m)$ is the size at depth X_m below which the shower absorption is exponential and $X > X_m$, and if we assume that the primary spectrum can be described by a simple power law of the form

$$I(> E_0) \;=\; A E_0^{-\alpha} \;, \tag{6.10}$$

where E_0 is the primary energy and α the spectral exponent, and if the shower size produced by a primary of energy E_0 at depth X follows the relation

$$N(E_0, X) \;=\; B E_0^{\delta} \exp\left(-\frac{X - X_m}{\lambda_{\rm abs}}\right) \;, \tag{6.11}$$

then the resulting rate of showers of size $> N$ is

$$I(> N, X) \;=\; A B^{\alpha/\delta} N^{-\alpha/\delta} \exp\left(-\frac{(X - X_m)/\lambda_{\rm abs}}{\alpha/\delta}\right) \;. \tag{6.12}$$

Introducing the substitutions $\gamma = (\alpha/\delta)$ and $\Lambda_{\rm att} = (\lambda_{\rm abs}/\gamma)$, and since experiment shows that $\delta \simeq 1$, we obtain the expression

$$\begin{aligned} I(> N, X) &= A B^{\gamma} N^{-\gamma} \exp\left(-\frac{X - X_m}{\Lambda_{\rm att}}\right) \\ &= C N^{-\gamma} \exp\left(-\frac{X - X_m}{\Lambda_{\rm att}}\right) \;\; [\mathrm{g\,cm^{-2}}] \;. \end{aligned} \tag{6.13}$$

Note that in the absence of fluctuations the relation

$$\lambda_{\rm abs} \;=\; \gamma \Lambda_{\rm att} \;\; [\mathrm{g\,cm^{-2}}] \tag{6.14}$$

would have a simple interpretation: all vertical showers of one size at one point in the atmosphere would be at the same stage of development, i.e., would have the same *age parameter*, s. In reality this relation is a complicated average of absorption lengths over showers that are still growing and others that are dying out at various rates. Fluctuations in the height of the first interaction are to a good extent responsible for this situation. Likewise primaries of different mass and the knee in the spectrum add to the problem and mask the overall picture.

If it is assumed that the shower development depends only on the amount of matter (atmosphere) traversed and not on the matter density of air, $\rho_{\mathrm{air}}(h)$ [g cm^{-3}], the *rate of showers* of size $> N$ at vertical depth X under a zenith angle θ is given by

$$I(>N, X, \theta) \;=\; CN^{-\gamma} \exp\left(-\frac{X}{\Lambda_{\mathrm{att}}}(\sec\theta \;-\; 1)\right) \;\propto\; (\cos\theta)^{(X/\Lambda_{\mathrm{att}})} \quad . \qquad (6.15)$$

Disregarding the *changing density* of the atmosphere with altitude implies that we ignore its *effect on the population of unstable particles*, such as pions, kaons and charmed particles,[10] as we change the geometric length of the shower trajectory in the atmosphere when going from vertical to inclined showers at a given observation level.

It must be pointed out that for a given group of showers the results of attenuation or absorption measurements, i.e., shower rates or particle numbers, may vary from experiment to experiment because of detector differences, in particular if the detectors have different responses to the various kinds of particles in a shower and are subject to transition effects (see Sect. 2.11). Normally the full mix of particles is used, nevertheless the results show large spreads.

Some authors have also determined the absorption lengths (or coefficients) for individual shower constituents, e.g., electrons, muons and so-called nuclear active particles (NAP), i.e., hadrons (Hodson, 1952; Miyake, 1962), as listed below.

6.3.6 Methods of Measurement

There are several experimental methods to determine the attenuation and absorption coefficients or lengths of the shower rate and shower size, respectively.

Disregarding Fly's Eye type fluorescence and modern air Cherenkov experiments, ground based direct observations of the longitudinal development of individual showers to carry out particle absorption measurements at different stages of development along the shower path are difficult.

On the other hand, early investigations of the 1950s that were based on the method of the altitude dependence of the density spectrum, measured with small

[10] Charmed particles are little affected by the changing density because of their very short mean life.

detector arrangements on board of aircraft that were flown at different altitudes, have proven to be quite successful. Similarly successful were the methods based on the zenith angle and barometric pressure dependence of showers, discussed below (Sects. 6.4 and 6.5), as well as the method of *equal intensity cuts* outlined in Sect. 6.7.

In a forerunner experiment of modern air Cherenkov measurements, Chudakov et al. (1960) compared the atmospheric Cherenkov light flux with the size of individual showers at ground level and attempted to correlate the two observables, however, with very marginal success.

Rather unsuccessful was the method pioneered by Greisen (1960) that was based on the azimuthal asymmetry of the particle density in a horizontal plane in inclined showers. Somewhat more promising was the method which consisted of measuring the average radius of curvature of the shower front via time delay and the direction of propagation of the muons with respect to the shower axis. The essential results of these studies are that the showers originate very high in the atmosphere and reach their maximum development at altitudes around 10 km, a value, as we know today, that applies to low energy showers only.

Further details concerning the different methods that are summarized below can be found in Bennett et al. (1962), Wolfendale (1973); Ashton and Parvaresh (1975), Ashton et al. (1975), Popova and Wdowczyk (1975), Hochart (1976), Bourdeau et al. (1980), Khristiansen (1980), Nagano et al. (1984a, 1992), Aglietta et al. (1999), and Antoni et al. (2003).

6.4 Altitude and Zenith Angle Dependence

6.4.1 Altitude Dependence

When discussing the altitude dependence of air showers we distinguish between the altitude dependence or variation of the *rate of showers* and of the *number of particles in a given shower*. Both are linked directly to the longitudinal development of the showers.

The variation of the rate of showers of fixed size with altitude (or column density) reflects above all the features of the primary spectrum, chiefly its slope.[11] On the other hand, when we are dealing with the variation of the number of particles in an individual shower as a function of altitude, we are dealing with an event of given primary energy. Its variation with altitude is essentially a consequence of the longitudinal development of the cascade and, thus, of the physical processes involved.

The lateral development, too, plays an important role. It is not only a function of the longitudinal development but is also affected by the nature and properties of the interactions, by decay processes and the matter density profile of the atmosphere.

[11] It is assumed that the primary composition remains constant; if energy dependent it affects the shower development.

The latter affects the *Molière radius*. These topics are reviewed in Chap. 4. Corresponding observational data and complementary information are given in Chaps. 8 and 10.

Besides the quantities already mentioned, the exponent of the density spectrum, γ, discussed in Sect. 12.4, and the particle composition of a shower, i.e., the relative fractions of the electromagnetic, hadronic and muonic components, too, manifest an altitude dependence. The second topic illuminates chiefly the changing nature of the processes involved in the hadron cascade development as the shower propagates and dissipates its energy along its path. Details and data of the different shower constituents are presented in Chaps. 13, 14, 15, 16, 17 and 18 and their correlations are discussed in Chap. 19.

The principal aim of the early work on the altitude dependence of air showers was to study the nature and general development of the showers, their build-up, attenuation and absorption characteristics in the atmosphere, and to determine the rate attenuation and particle absorption lengths or the corresponding coefficients.

Shower development data were initially analyzed under the assumption that the showers were initiated by primary electrons or photons and then compared with predictions of the electromagnetic cascade theory, the only cascade theory then fully understood (see Nishimura, 1967, for a review). Even today many shower properties are still compared with the general properties of electromagnetic cascades, and quantities are expressed in terms and units introduced in these days.

The early measurements were based on small and very simple counter arrangements operated in a fixed configuration in coincidence at different altitudes, to determine the altitude dependence of the shower frequency and its slope. A remarkable experiment of this kind was carried out by Hilberry (1941). He had a small counter arrangement installed under the roof of a station wagon which he operated at many different altitudes, from Chicago (91 m a.s.l.) to Mt. Evans (4,300 m a.s.l.).

From these and similar data it had been found that the shower rate attenuation in terms of the density spectrum is exponential. Therefore the attenuation coefficient, μ_{att}, can be written as

$$\mu_{\mathrm{att}} \;=\; -\frac{\partial \ln G(\geq \rho, X)}{\partial X} \;\; [\mathrm{cm}^2\,\mathrm{g}^{-1}] \;\; . \tag{6.16}$$

Its reciprocal yields the shower rate attenuation length, Λ_{att}. $G(\geq \rho, X)$ is the rate of showers $[\mathrm{s}^{-1}]$ of density $\geq \rho$ $[\mathrm{m}^{-2}]$, and X $[\mathrm{g\,cm}^{-2}]$ is the vertical atmospheric depth of the observer. In Sect. 6.3 we have defined these quantities in a somewhat different way, expressing them in terms of the shower size spectrum, Eq. (6.5), instead of the density spectrum.

Unfortunately the capabilities of such small apparatuses as had been used by Hillberry are very limited. The same is true, of course, for the early airborne shower experiments, mentioned before. However, the later work of Antonov and collaborators (Antonov, 1974; Antonov and Ivanenko, 1974; Antonov et al., 1974 and subsequent papers) included detectors not only in the fuselage of a giant airplane

but also in the wings, which permitted to fly mini arrays measuring 44 m by 33 m across. (For details of the layout see Fig. A.4).

One of the problems with this kind of measurements is that if larger, stationary arrays are being used that are located at different sites and altitudes, they are usually not identical in layout and geometry. This introduces instrumental uncertainties and errors that can lead to partial incompatibilities of the data.

6.4.2 Zenith Angle Dependence

Initially the zenith as well as the azimuthal angular distributions of air showers were of interest in connection with questions related to the origin of the primaries and the search for anisotropies in the arrival direction. Early experiments revealed that the zenith angle distribution of the arrival rate of showers *changes with altitude*, a fact that was fully understood on theoretical grounds only when it became known that unstable particles, such as pions, play a dominating role in the shower development.[12]

However, the variation of the shower intensity with zenith angle is also of interest because it permits to extend the measurements on the longitudinal development of the showers considerably and yields valuable additional and complementary information. It is also directly related to the shower attenuation length $\Lambda_{\rm att}$ and permits to identify the contribution of prompt muons from charmed particle decays. The fact that values of $\Lambda_{\rm att}$ ranging from 80 to over 160 g cm^{-2} had been reported during the early days of air shower research by different authors indicates that $\Lambda_{\rm att}$ is not a trivial observable.

The amount of matter a shower must penetrate to reach a given observation level, h, under a zenith angle, θ, i.e., the total column density, can be expressed by the slant depth, $X_s(h,\theta)$ as

$$X_s(h,\theta) \;=\; X(h,\theta=0)\cdot\sec\theta \;\;[\mathrm{g\,cm^{-2}}]\;, \tag{6.17}$$

where

$$X(h,\theta=0) \;=\; X(0,0)\cdot e^{-(h/h_s)} \;=\; X_0\cdot e^{-(h/h_s)} \;\;[\mathrm{g\,cm^{-2}}]\;. \tag{6.18}$$

h [m] is the altitude or height above sea level, h_s the scale height of the atmosphere ($h_s \simeq 7,300$ m a.s.l., changing slowly with altitude) and X_0 is the vertical column density of the atmosphere at sea level ($X_0 \simeq 1,030$ g cm^{-2}).

At large zenith angles the *curvature of the Earth* must be considered, requiring the *Chapman function* to compute the column density of a given path in the

[12] Kaons affect the shower development alike but play an inferior role because they are much less abundant. Because of the very short mean life of charmed particles and the high production threshold energy their contribution to the high energy muon flux at ground level is essentially independent of zenith angle.

atmosphere (Chapman, 1931). The Chapman function is discussed in Sect. B.4 (Eq. B.10). In horizontal direction, i.e., for $\theta = 90^\circ$, the column density or atmospheric thickness of the real atmosphere at sea level is approximately 40 times larger than for $\theta = 0^\circ$; it is infinite under the flat Earth approximation (Eq. 6.17 given above).[13]

The zenith angle dependence of the arrival rate of showers of size $> N$, $I(> N, X, \theta)$, was found in many experiments to follow the relation

$$I(> N, X, \theta) = I(> N, X, 0) \cos^n \theta \ \ [\mathrm{m}^{-2}\mathrm{s}^{-1}\mathrm{deg}^{-1}] \ . \tag{6.19}$$

Here, X is the vertical depth in the atmosphere where the measurement is being carried out and θ the zenith angle of the shower axis. The above expression is linked to the attenuation length of showers discussed in Sect. 6.3 (see Eq. 6.15).

For showers of moderate size ($10^5 \leq N \leq 10^6$) a good fit is obtained at sea level with an exponent $n = 8^{+1.4}_{-1.2}$ for local particle densities of $\rho > 20\,\mathrm{m}^{-2}$. The exponent n increases with increasing particle density (or shower size) and reaches $n = 9.3^{+1.0}_{-0.8}$ for $\rho > 80\,\mathrm{m}^{-2}$ and $n = 10.0^{+1.9}_{-0.9}$ for $\rho > 250\,\mathrm{m}^{-2}$. On the other hand, the value of n decreases with increasing altitude. (Ashton et al., 1975).

The accurate measurement of the zenith and azimuthal angles, θ and ϕ, of a shower is important to determine its arrival direction. The former is relevant to determine the atmospheric column density a shower has penetrated and both are needed to account for *geomagnetic effects*, but also for astronomical and astrophysical reasons.

In the overwhelming number of experiments this is achieved by timing the arrival of the shower front at the different detectors of an array. Only few shower arrays employ complementary or exclusively particle tracking to determine the angle of incidence of the events. In general the directional accuracy is between 1° and 5° for most installations (see Sect. 2.10). Some researchers claim to achieve $< 0.5^\circ$ with particle tracking (De Beer et al., 1962; Heintze, 1989a, b).

6.5 Environmental Effects

6.5.1 Introduction

In the following we will briefly discuss the effects of changes of the environmental parameters, such as the *barometric pressure, air temperature, air density* and *humidity*, on the shower development.

The dependence of the stage of development of air showers and the counting rate on altitude, zenith angle, barometric pressure, air temperature and air density are closely related. A variation of any one of these five parameters results in a change

[13] For zenith angles $\theta \geq (70^\circ$–$80^\circ)$, depending on the accuracy required, the Chapman function must be used to compute the atmospheric column density along the trajectory correctly.

of the atmospheric column density [g cm^{-2}] along the shower trajectory between the fringes of the atmosphere and an observer's location and, hence, in a change of the stage of development of a given kind of showers at that particular location with all its consequences.

6.5.2 Barometric Pressure Dependence

Changes in the barometric pressure at a given altitude of observation in the atmosphere imply a change in the overlaying column of air and therefore affect the shower development, and the rate of events at the location of measurement. An increase in pressure is equivalent to a greater atmospheric depth, and vice versa. The barometric coefficient β is defined as

$$\beta \;=\; -\frac{\partial \ln G(\geq \rho)}{\partial P} \;\; [\mathrm{cm}^{-1}\,\mathrm{Hg}] \;\; \text{or} \;\; [\mathrm{hPa}] \tag{6.20}$$

where $G(\geq \rho)$ is the rate of showers of density $\geq \rho$ [m^{-2}] and P is the atmospheric pressure [cm Hg] or [hPa].

The barometric pressure dependence of the counting rate of air showers can therefore also be used to determine the shower rate attenuation length, Λ_{att}, in the atmosphere. In comparison to the altitude dependence method mentioned above, where large changes in the overlaying air column can easily be achieved, but normally with different shower arrays, the barometric pressure dependence method has the great advantage that the measurements can be carried out with the same array at the same place, though over a smaller pressure range. Hence, instrumental differences are therefore eliminated.

The barometric effect (and its coefficient, β), is in fact made up of two effects: (a) the true *mass absorption* of the showers due to the matter above the detectors (with coefficient, β_{mass}), and (b) the variation of the counting probability of showers due to a *change of density* which affects the lateral spread of the showers. The *density effect* manifests itself as a *temperature effect* (*temperature coefficient*), discussed below. The former also affects the Molière radius (Eq. 4.146) (Molière, 1953; Greisen, 1956, 1960; Janossy et al., 1958). If one assumes that the temperature coefficient α of the counting rate is entirely due to the density effect, one may subtract its influence on the barometric coefficient β by the use of Eq. (21.17), to obtain the *pure pressure (absorption) dependence*, β_{mass} (see Sect. 6.5.3). Thus,

$$\beta_{\mathrm{mass}} \;=\; \beta - \left(\frac{T}{P}\right)\alpha \;\;, \tag{6.21}$$

where T [K] is the absolute temperature of the atmosphere, P the atmospheric pressure and α the temperature coefficient.

6.5.3 Air Temperature, Density and Humidity Dependence

The temperature dependence of the shower rate can be expressed in terms of the *temperature coefficient*, α. The latter is defined as

$$\alpha = \frac{\partial \ln G(\geq \rho, X)}{\partial T} \approx \frac{\partial \ln N(X)}{\partial T} \ [\mathrm{cm}^{-1}\mathrm{Hg}] \ , \tag{6.22}$$

where $G(\geq \rho, X)$ is the rate of showers of density $\geq \rho$ [m^{-2}] at depth X [$\mathrm{g\,cm}^{-2}$] in the atmosphere (see Sect. 12.4), T [°C] the temperature of the atmosphere and $N(X)$ the shower size.

As mentioned in Sect. 6.5.2 above, a change in air temperature at a given site causes a change in air density. Under the assumption of an isothermal atmosphere this results in a change of atmospheric pressure with its consequences for the shower development.

In a homogeneous atmosphere the root mean square lateral spread of a cascade shower is proportional to the length of the cascade unit (radiation length) which in turn is inversely proportional to the air density, ρ_{air} [$\mathrm{g\,cm}^{-3}$] (Blatt, 1949). This implies that a change in temperature of the atmosphere causes a *geometric effect* which influences the lateral spread of a shower.

Since, according to Janossy (1948, 1958), most of the lateral spread of a shower observed at a given atmospheric depth is due to the scattering in the previous one or two cascade units, the spread at a given depth is therefore more correctly given by taking the density, ρ_{air}, equal to that at one cascade unit above the detectors. Hodson (1951) presents the arguments and shows that at constant pressure the shower rate, $G(\geq \rho, X)$, is therefore expected to depend on the (absolute) temperature T at one cascade unit above the detectors roughly as $T^{-(2\gamma-2-\kappa)}$, i.e., the temperature coefficient is of the order of

$$\alpha = \frac{1}{G(\geq \rho, X)} \left(\frac{\partial G(\geq \rho, X)}{\partial T} \right) = -(2\gamma - 2 - \kappa) \frac{100}{T}$$

$$\alpha = -\left(\frac{2\gamma - 2 - \kappa}{2.8} \right) \ [\%\ ^{\circ}\mathrm{C}^{-1}] \tag{6.23}$$

where γ is the exponent of the density spectrum and κ the exponent of the *decoherence rate* distribution, $G(\geq \rho, X) \propto d^{\kappa}$, d being the distance between the counters (see Khristiansen, 1980).

The effect of the *humidity*, $\mathcal{H}$, on air shower development is not well known. However, atmospheric humidity is strongly non-linear with temperature which led Bennett et al. (1962) to represent the *overall temperature effect*, expressed by the temperature coefficient α, as a sum of a *constant temperature coefficient*, α_T, and a *humidity term*, $b(\mathrm{d}\mathcal{H}/\mathrm{d}T)$, b being a scale factor and T the temperature, as follows.

$$\alpha = \alpha_T + b\left(\frac{\mathrm{d}\mathcal{H}}{\mathrm{d}T}\right) . \tag{6.24}$$

We should point out that the temperature effect also influences the pion and muon decays because of the geometric effect mentioned above, and thus the hadron and muon counting rates in the atmosphere (see Braun et al., 2008, p. 481).

6.6 Data on Attenuation and Absorption, Altitude and Zenith Angle Dependence, Environmental Effects

6.6.1 General Data on Shower Rate Attenuation and Shower Particle Absorption

(a) Shower Rate Attenuation

In the following we summarize briefly the results of measurements of the shower rate attenuation and shower particle absorption lengths and/or coefficients, carried out by different authors using the various methods mentioned above.

A compilation of the results of early shower rate attenuation measurements made by Bennett et al. (1962) covering a wide range of shower sizes is shown in Fig. 6.6. The figure shows along the left hand ordinate the shower rate attenuation coefficient, μ_{att} $[(\mathrm{rl})^{-1}]$ (in units of reciprocal radiation lengths), and on the right hand ordinate the shower rate attenuation length, Λ_{att} $[\mathrm{g\,cm^{-2}}]$. Another compilation made by the author shows in Fig. 6.7 the shower rate attenuation lengths resulting from the work of other groups of researchers on showers of similar size range, and in Fig. 6.8 we have displayed the results of measurements made by Hara et al. (1981a) at Akeno. The curves in this latter figure represent predictions from simulations of Hara et al. (1981a) and Bourdeau et al. (1980).

A further compilation made by Nagano et al. (1984a) which includes various data derived from more recent measurements made at Akeno under different trigger conditions is presented in Fig. 6.9 (see also Tan et al., 1982). In addition, attenuation length data derived from optical Cherenkov measurements are indicated in the figure by the shaded area. Shown, too, are some sea level data from other experiments for comparison. The figure also contains the results of several predictions. The two dashed curves, 1 and 2, are from a calculation of Capdevielle and Procureur (1984), the three solid curves, A, B and C are from the work of Nagano et al. (1984a). The latter have used basically the so-called Maryland spectrum (Goodman et al., 1982) with some modifications and two different interaction models, one a scaling type model, the other a fireball model with similarities to the CKP model.

Shower rate attenuation length determinations of newest date from near sea level measurements (106 m a.s.l., $\langle X_0 \rangle = 1{,}022\,\mathrm{g\,cm^{-2}}$) using different methods had been carried out by the KASCADE group at Karlsruhe (Antoni et al., 2003). Figure 6.10 shows the results of shower rate measurements in terms of frequency as a function of atmospheric depth that were obtained by these authors using

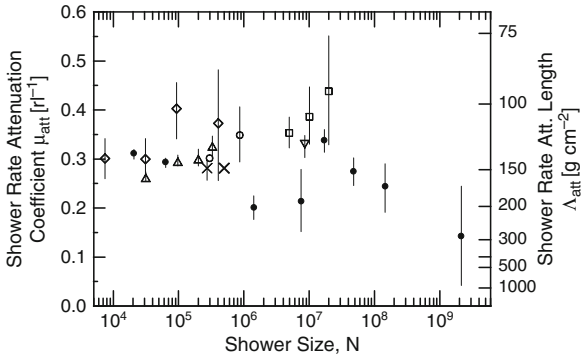

Fig. 6.6 Compilation of shower rate attenuation coefficients, μ_{att}, and shower rate attenuation lengths, Λ_{att}, versus shower size (after Bennett et al., 1962). Included are data from the following authors: × Hodson (1952, 1953a, b); ◇ Farley and Storey (1954); △ Citron and Stiller (1958); ▽ Clark et al. (1958); □ Cranshaw et al. (1958a, b); ● Greisen (1960); ○ Bennett et al. (1962)

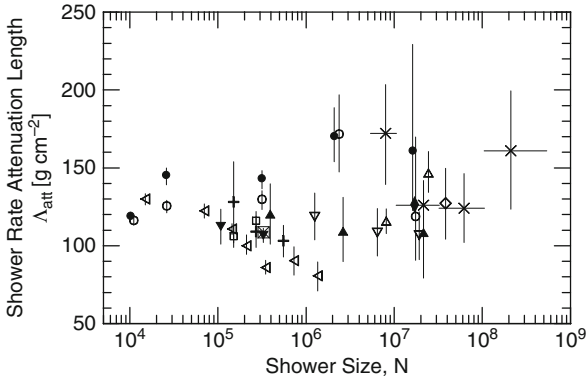

Fig. 6.7 Compilation of shower rate attenuation length measurements, Λ_{att}, based on (a) zenith angle, (b) barometric pressure and (c) altitude variation, versus shower size. The symbols refer to the following authors: ▼ (a) and ▲ (a) Clark (1957, 1961); ○ (b), ● (b), × (a) and ◇ (a) Delvaille et al. (1960); ▽ (a) Rossi (1960); △ (a), (b) and (c) Bennett et al. (1962); ◁ (a) Efimov et al. (1967); ♦ (a) Kozlov et al. (1973); □ (b), + (a) Ashton et al. (1975); ⊠ (a) Hochart (1976)

atmospheric ground pressure variations at five different zenith angle intervals. Figure 6.11 shows the shower rate attenuation length as a function of shower size for the same five zenith angle intervals, using the barometric method.

These measurements are based on the differential shower size spectra recorded by Antoni et al. (2003), at different zenith angles, that are shown in Fig. 12.19 from which also the equal intensity plots, discussed later and shown in Fig. 6.44 of this chapter, were derived. One of the more novel methods that was employed in this work makes use of the assumption that the spectral knee, located at about 4 PeV, is of astrophysical nature and can therefore be used as an energy reference point. However, one of the problems that arises when applying this method is that the

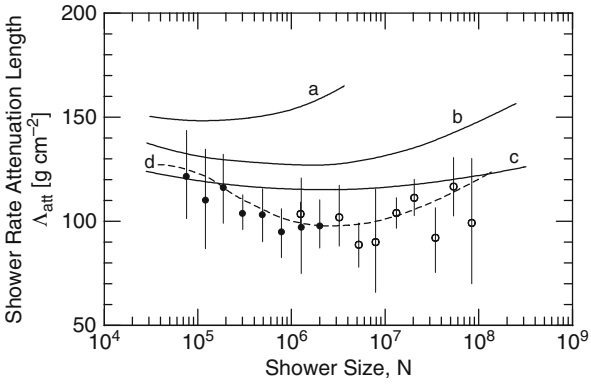

Fig. 6.8 Shower rate attenuation length, Λ_{att}, versus size determined with the Akeno installation (Hara et al., 1981a). • and ○ identify different trigger conditions. *Curves* (a), (b) and (c) show expected dependencies from calculations based on the scaling, CKP and half-law models, respectively, by the same authors. The *dashed curve* (d) is from a calculation of Bourdeau et al. (1980)

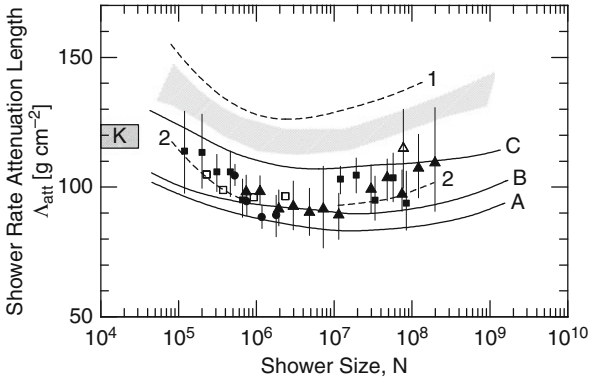

Fig. 6.9 Shower rate attenuation lengths, Λ_{att}, versus shower size for different trigger conditions at Akeno, ▲, ■, • (Nagano et al., 1984a). Shown for comparison are the sea level data of Clay and Gerhardy (1981a) □, Kozlov et al., (1973) △, and Böhm and Nagano (1973) cross-hatched square with K. Curves 1 and 2 are predictions after Capdevielle and Procureur (1984). Curves A, B and C are for different spectral assumptions and interaction models, the shaded area was obtained from optical measurements (Nagano et al., 1984a). For details see text

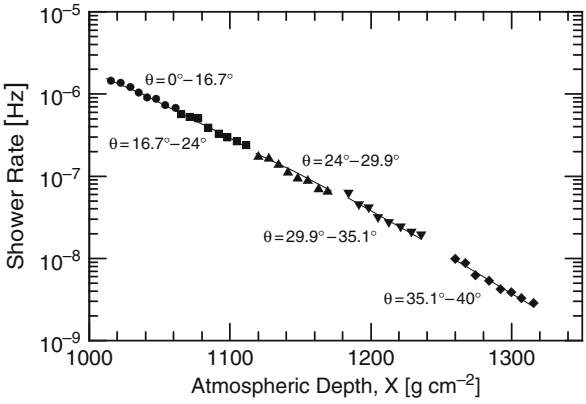

Fig. 6.10 Variation of the shower rate in terms of frequency with atmospheric ground pressure for different zenith angle intervals and showers of size $N_e > 2.5 \cdot 10^5$ measured with the KASCADE array. The *lines* indicate fits with exponential functions (Antoni et al., 2003)

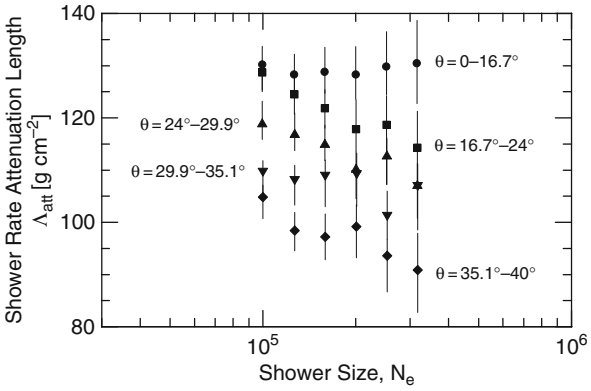

Fig. 6.11 Shower rate attenuation length, Λ_{att}, determined with the barometric method by the KASCADE array for showers of different zenith angles (Antoni et al., 2003)

resulting attenuation and absorption lengths depend on the procedure used to locate the position of the knee.

The shower size range where the shower rate attenuation length measurements were carried out by the KASCADE group covers the entire knee region of the primary energy spectrum. Figure 6.12 shows the resulting attenuation length, Λ_{att}, as a function of shower size over the entire investigated range. A significant systematic size dependence of Λ_{att} is evident. The decline with increasing shower size is linked to the moving knee position outlined in Fig. 12.19 and the changing slopes and biases of the angular method. This region is marked by the hatched area in Fig. 6.12. The increase of the attenuation length beyond a size of about 10^6 is partly related to a similar effect visible in Fig. 6.17 which shows the particle absorption length, λ_{abs}, discussed in (b) below. The reason for this rise is that with increasing shower size the observations are made closer and closer to the shower maximum.

One of the most recent compilations of data on the energy dependence of the *proton-air attenuation length*, $\Lambda_{att}^{p,air}$ that is based on a wide spectrum of measurements was made by Bellandi et al. (1998). It is displayed in Fig. 6.13. In this context we should also mention the new proton-air attenuation length determination by

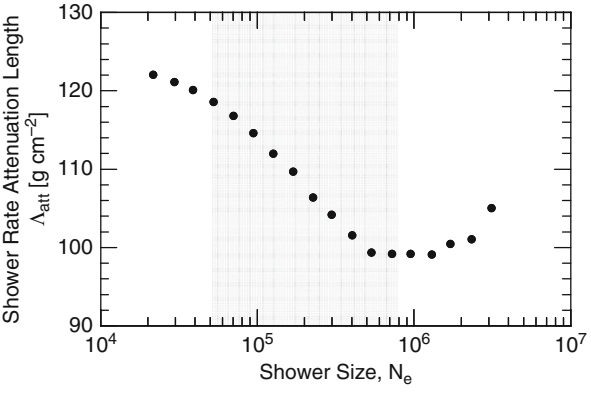

Fig. 6.12 Shower rate attenuation length, Λ_{att}, as a function of electron shower size determined by the variation of the zenith angle. The *cross-hatched area* identifies the region affected by the changing slopes of the spectra in the knee region (see Fig. 12.19, Sect. 12.2) (Antoni et al., 2003)

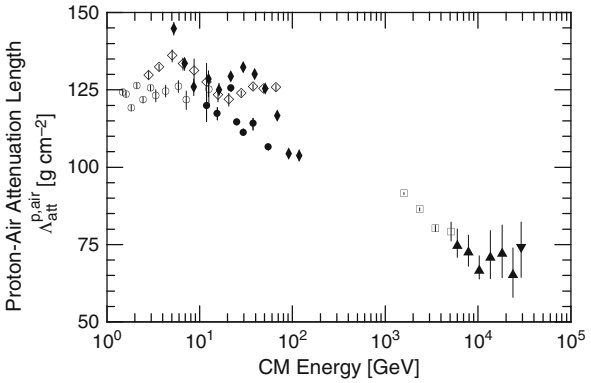

Fig. 6.13 Proton rate attenuation length in the atmosphere as a function of the center of mass (CM) energy (after Bellandi et al., 1998). The experimental data that were used in this compilation include: ○ Brooke et al. (1964); ●, ♦ Ashton and Coats (1968) and Ashton et al. (1970); ▲ Hara et al. (1983a) and Honda et al. (1993); ▼ Baltrusaitis et al. (1984); ◇ Mielke et al. (1993, 1994); □ Aglietta et al. (1997) (see also Aglietta et al., 1999)

Aglietta et al. (1999) using EAS-TOP data that are not listed in Bellandi's compilation. These authors have used several different event generators in conjunction with the CORSIKA code and have also determined proton-air cross sections listed in Chap. 3. Tabulated data of shower rate attenuation length measurements at different shower sizes that were obtained with different methods are compiled in the various tables of this section together with environmental parameters that affect the shower development. These are discussed in dedicated subsections below.

(b) Shower Particle (or Size) Absorption

Figure 6.14 shows a compilation of Bennett et al. (1962) of the *all-particle absorption coefficient*, μ_{abs} [(rl)$^{-1}$] (in units of reciprocal radiation lengths on the left hand ordinate), as a function of shower size resulting from many experiments. On the opposite ordinate of the same plot the corresponding particle absorption lengths, λ_{abs} [g cm^{-2}] are indicated. In spite of the fact that different apparatuses with different geometries had been used by the various groups that are bound to yield deviating results, the general agreement is fair. One must keep in mind that the *age* of the electron–photon component may vary with core distance as well as the fraction of the gamma and muon content. Moreover, the measurements are subject to large fluctuations.

Particular care had been taken by Bennett et al. (1962) to deduct the muon contamination and to compute the absorption of the electrons only. The solid curve in Fig. 6.14 indicates the best guess as to the variation of the all particle absorption coefficient (left hand ordinate) and the corresponding absorption length (right hand ordinate) with shower size near sea level. The dashed curve shows the computed absorption coefficient (absorption length) for showers initiated by primary electrons

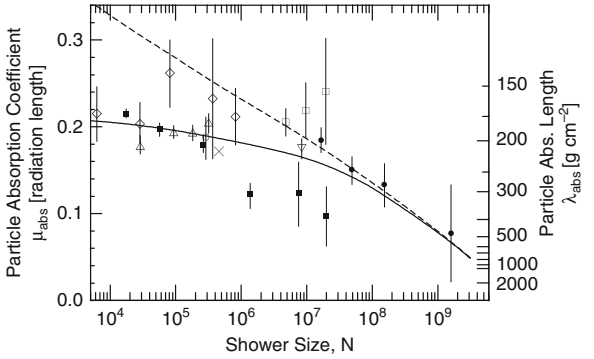

Fig. 6.14 Compilation of particle absorption coefficients, μ_{abs}, and particle absorption lengths, λ_{abs}, in showers versus shower size obtained from barometric effect and zenith angle distributions (after Bennett et al., 1962). The data include: • and ■ Greisen (1960), ○ Bennett et al. (1962), *solid line* is best fit to these data; × Hodson (1952, 1953a, b); ◇ Farley and Storey (1954); □ Cranshaw et al. (1958a, b); ▽ Clark et al. (1958); △ Citron and Stiller (1958). The *dashed curve* represents the computed particle absorption for showers initiated by single electrons at the top of the atmosphere

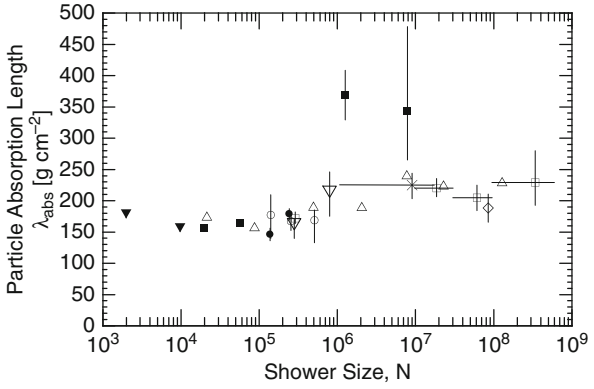

Fig. 6.15 Compilation of results of particle absorption length measurements, λ_{abs}, based on the barometric pressure effect, and on the zenith angle and altitude variations versus shower size. The different symbols refer to the following authors: ▼ Citron and Stiller (1958), ▽ Malos (1960), × Rossi (1960); □ zenith angle and ■ barometric effects Bennett et al. (1962); △ altitude variation Bradt et al. (1965) and La Pointe et al. (1968) interpreted by Ashton et al., (1975), ◇ Kozlov et al. (1973); ○ zenith angle and • barometric effects Ashton et al. (1975)

at the top of the atmosphere. Another set of data which includes some more recent measurements of λ_{abs} is plotted in Fig. 6.15.

In Fig. 6.16 we have reproduced distributions of shower particle absorption lengths of early measurements made at Mt. Norikura in Japan (2,770 m a.s.l.) by Miyake et al. (1968) on individual showers belonging to three different size groups, having average zenith angles of $\langle\theta\rangle = 22^\circ$. The absorption was measured across a 2 m deep water target in the form of a water tank, covering an area of $6 \times 5.5\,m^2$,

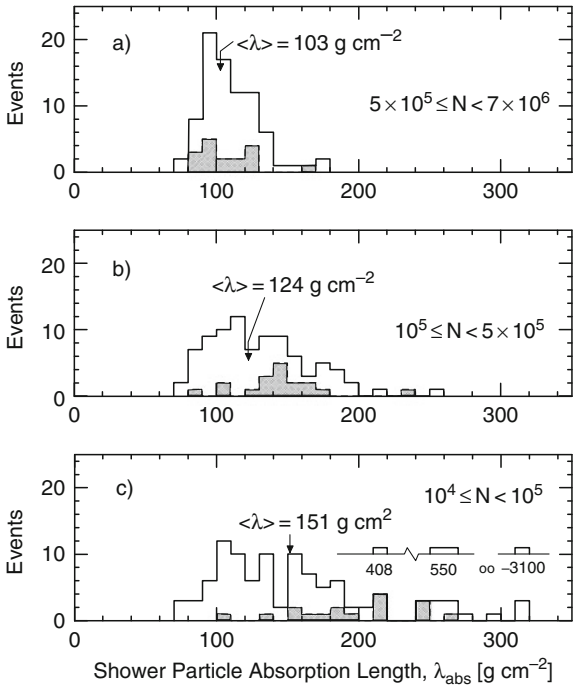

Fig. 6.16 Distribution of shower particle absorption lengths, λ_{abs}, for showers of different size groups observed at Mt. Norikura (Miyake et al., 1968). The number of events that are included in this analysis are for (**a**) 102 (16), (**b**) 88 (18) and (**c**) 83 (17). The figures in parentheses give the number of double core showers. Their distribution is indicated by the *shaded area* in the graphs. One single core event had a negative attenuation length (see inset in **c**), i.e., it was a young, growing shower

with a carpet of plastic scintillators above and below the tank. The distributions reveal large variations of the absorption lengths from shower to shower.

Some of the most recent data on shower particle absorption length were obtained by Antoni et al. (2003), using equal intensity cuts from the Karlsruhe experiment, mentioned before. The data are plotted in Fig. 6.17 as a function of integral shower intensity. Also shown on this plot is the absorption length determined by the knee position, outlined in (a) above, at the weighted mean value of the intensity at the spectral knee.

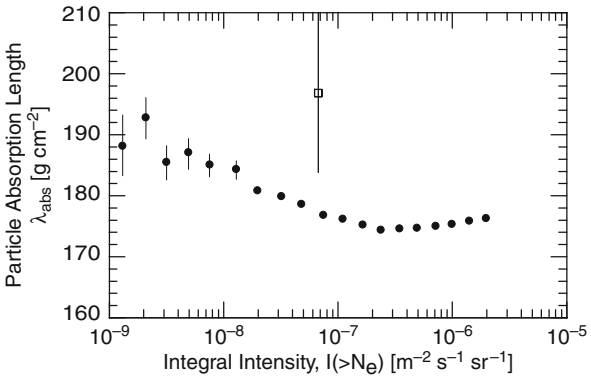

Fig. 6.17 Shower particle absorption length, λ_{abs}, determined by the method of constant intensity (•), and by the spectral knee position (□). The latter is placed at the weighted mean flux at the knee of the differential spectrum $I(N_{e,\mathrm{knee}}) = (6.75 \pm 0.13) \cdot 10^{-8}$ [$m^{-2}s^{-1}sr^{-1}$] of Fig. 12.19, Sect. 12.2) (Antoni et al., 2003)

An interesting aspect that was explored by Antoni et al. (2003) in the context of their work is the influence of fluctuations of different nature on the particle absorption length that was determined using constant (or equal) intensity cuts. These authors considered intrinsic shower fluctuations, event trigger efficiency, and reconstruction accuracy of the electron shower size. The results of this work are shown in Fig. 6.18 and illustrates that fluctuations increase the particle absorption length by about 15–30 g cm^{-2}.

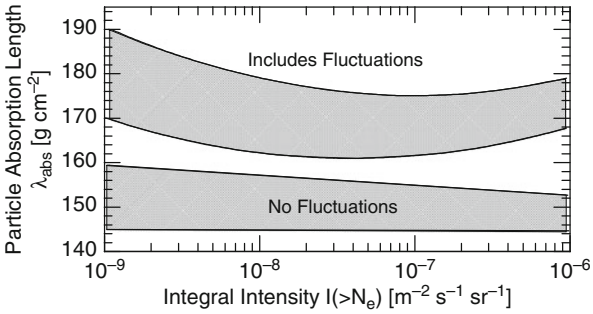

Fig. 6.18 Effect of fluctuations on the shower particle absorption length, λ_{abs}, as a function of integral shower intensity obtained from Monte Carlo spectra, determined with the method of constant intensity. The *shaded areas* indicate the range of uncertainties. The lower area is the result of average shower size spectra without any fluctuations nor detector effects, the upper includes all three kinds of fluctuations mentioned in the text (Antoni et al., 2003)

(c) Muon Absorption in Showers

The absorption length of muons, $\lambda_{\mu,abs}$, in mid-size showers at sea level was determined by Firkowski et al. (1965, 1967) and Hochart et al. (1975). The latter used the air shower array at Verrières, near Paris, France. Bell et al. (1973, 1974) have carried out similar measurements on large showers at Narrabri (260 m a.s.l.) and Diminstein et al. (1979) at Yakutsk (105 m a.s.l.). The data of Bell et al. are shown in Fig. 6.19. More recently Kakimoto et al. (1981) and Hara et al. (1983a, b) have

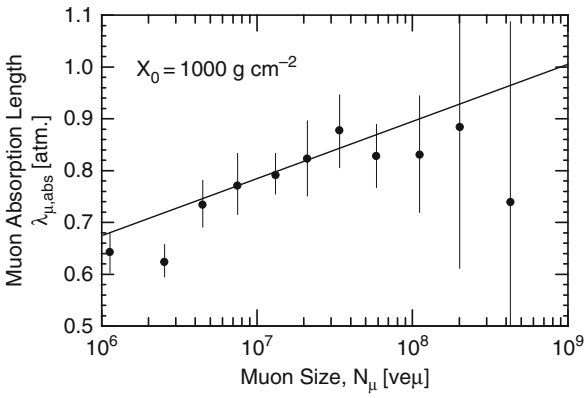

Fig. 6.19 Muon absorption length, $\lambda_{\mu,abs}$, in showers in units of atmospheres versus muon size, obtained at Narrabri (NSW, Australia, 260 m a.s.l.) (Bell et al., 1973, 1974). X_0 is the vertical atmospheric depth of the array. See also Diminstein et al. (1979)

determined the muon absorption length from a set of muon equal intensity distributions, shown in Fig. 6.49, that were derived from muon size spectra measured at Chacaltaya (5,230 m a.s.l.) and Akeno (900 m a.s.l.), respectively. Their results which cover a wide range of shower intensities, i.e., primary energies, are shown in Fig. 6.20. Mathematical fits are given in Sect. 6.6.5.

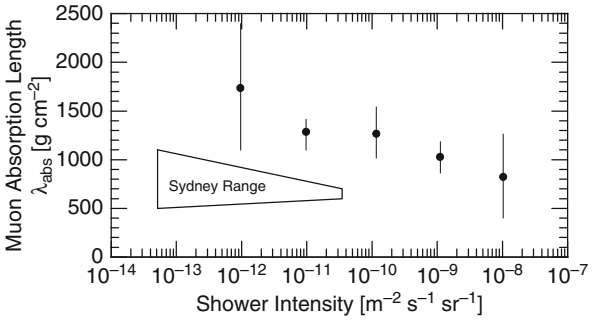

Fig. 6.20 Muon absorption length, $\lambda_{\mu,abs}$, in showers as a function of shower intensity (Hara et al., 1983b). Also indicated is the range of the results of the Sydney group obtained from data recorded at Narrabri that are shown in Fig. 6.19 above as a function of muon shower size

The results of many early shower rate attenuation length and shower particle absorption length measurements based on different methods are summarized in chronological order in the following tables (Tables 6.1, 6.2 and 6.3).

6.6.2 Data on Altitude Dependence

In this subsection we present chiefly early work on the altitude dependence of the shower rate which is based on coincidence requirements of a few small counters, distributed over a small area. This work is not only of historic value but reveals basic features of air showers that are valid to this date.

As mentioned before, among the first to study the altitude dependence of the shower rate with ground based equipment were Auger et al. (1939a, b), Auger and Daudin (1945) [Paris (50 m a.s.l.), Bagnères de Bigorre (980 m) and Pic du Midi (2,860 m), France], Broadbent et al. (1950) [Manchester, GB (50 m)], Cocconi et al. (1946) [Passo Sella (2,200 m), Italy], Cocconi (1949a, b), Cocconi Tongiorgi (1949), Cocconi et al. (1949) [Ithaca, NY (260 m) and Echo Lake, CO (3,260 m), USA], Hilberry (1941) [Chicago, IL (91 m) to Mt. Evans, CO (4,320 m), USA], Loverdo and Daudin (1948) [Pic du Midi], Treat and Greisen (1948) [Echo Lake and Mt. Evans]. The locations in brackets are the sites where the measurements were carried out.

Some of the initial data on the slope of the frequency versus altitude dependence of the shower rate were contradictory. However, it was soon established that the slope changes very little with altitude. This fact was in contradiction with predictions from the electromagnetic cascade theory and was an early indication that the primaries could not be predominantly photons or electrons. This conclusion was

Table 6.1 Summary of all-particle shower rate attenuation and shower particle absorption lengths. (Sea level unless specified otherwise)

Experiment	Size or rate or energy	Λ_{att} [g cm^{-2}]	λ_{abs} [g cm^{-2}]
Greisen (1956, 1960)	$3 \cdot 10^8$	164 ± 40	–
Clark (1957)	10^5	107 ± 11	–
Clark et al. (1957)	10^6	98 ± 5	–
	10^7	90 ± 5	–
Delvaille et al. (1960)	$3 \cdot 10^7 - 10^8$	141 ± 12	200 – 300
	10^4	$\sim$125	
	10^8	$\sim$150	
Fukui et al. (1960)	10^6	102 ± 15	–
Malos (1960)	$3 \cdot 10^5$	125^{+19}_{-17}	–
	$8.5 \cdot 10^5$	107^{+16}_{-19}	–
Rossi (1960)	$1.2 \cdot 10^6 - 1.8 \cdot 10^7$	113 ± 9	214 ± 20
Clark et al. (1961)	$6 \cdot 10^5$	121	–
	$5 \cdot 10^6$	111	–
Bennett (1962)	$\langle 5 \cdot 10^5 \rangle$	$\langle 135 \rangle$	–
	$> 10^7$	121 ± 7	–
	$(1 - 3) \cdot 10^7$	111 ± 7	–
	$(3 - 10) \cdot 10^7$	137 ± 13	–
	$(1 - 6) \cdot 10^9$	153^{+34}_{-23}	–
	$>6 \cdot 10^9$	263^{+560}_{-106}	–
Hersil (1962)[a]	$2 \cdot 10^8$	–	160 ± 20
Hasegawa et al. (1962)	–	–	150 – 170
Miyake (1962)[b]	10^{-11} [1 cm^{-2}s^{-1} sr^{-1}]	100	140
	10^{-12} [1 cm^{-2}s^{-1} sr^{-1}]	125	170
	10^{-13} [1 cm^{-2}s^{-1} sr^{-1}]	94	200
Suri (1965)[c]	$>10^{17}$ [eV]		240 ± 20
Miyake et al. (1968)[b,c]	$10^4 - 10^5$	–	103
	$10^5 - 5 \cdot 10^5$	–	124
	$5 \cdot 10^5 - 7 \cdot 10^6$	–	151
La Point et al. (1968)[d]	$2.3 \cdot 10^5$	104 ± 2	–
	$4 \cdot 10^5$	100 ± 6	–
	10^6	97 ± 2	–
	$2.5 \cdot 10^6$	98 ± 3	–
Catz (1971)	$\geq 10^5$	104	–
Kozlov et al. (1973)	$5 \cdot 10^7 - 5 \cdot 10^8$	126 ± 15	–

Measurements made at [a] El Alto, 4,200 m; [b] Mt. Norikura 2,770 m;
[c] in water tank at Haverah Park (212 m a.s.l.); [d] Chacaltaya, 5,230 m.

further strengthened when it was established that local cascades could be initiated in thick absorber material.

In the late forties the first measurements were carried out to high altitudes with small arrays on board of airplanes by Maze et al. (1948), Biehl et al. (1949) and Kraybill (1948, 1949). Other airborne experiments by Hodson (1952, 1953a, b), Kraybill (1954a, b) and a long series of measurements by Antonov and co-workers (Antonov et al., 1957, 1960, 1963, 1964a, b, c, 1971; Antonov, 1974; Antonov and Ivanenko, 1974; Antonov et al., 1973, 1974; Antonov and Ivanenko, 1975a, b; Antonov et al., 1975, 1977, 1979a, b, c, 1981, 1983, 1984) followed. Hodson in

Table 6.2 Summary of all-particle shower rate attenuation and shower particle absorption lengths. (Sea level unless specified otherwise)

Experiment	Size	γ (integral)	Λ_{att} [g cm^{-2}]	λ_{abs} [g cm^{-2}]
Ashton et al. (1975)	$1.5 \cdot 10^5$ [f]	1.38[j]	128 ± 26	177 ± 35
	$1.5 \cdot 10^5$ [g]	1.38[j]	106 ± 7	146 ± 10
	$2.7 \cdot 10^5$ [f]	1.53[j]	109 ± 10	167 ± 15
	$2.7 \cdot 10^5$ [g]	1.53[j]	116 ± 6	178 ± 9
	$5.5 \cdot 10^5$ [f]	1.64[j]	103^{+10}_{-20}	169^{+16}_{-33}
Hochart (1976)	$5 \cdot 10^5$	–	108.5 ± 3	–
Miyake (1979)[a]	$5 \cdot 10^6$	1.92 ± 0.03	119 ± 7	–
	$7 \cdot 10^6$	1.92 ± 0.03	116 ± 9	–
	10^7	1.92 ± 0.03	119 ± 7	–
	$2 \cdot 10^7$	1.92 ± 0.03	110 ± 10	–
	$5 \cdot 10^7$	1.92 ± 0.03	105 ± 17	–
Ohta et al. (1979)[b]	$10^5 - 10^7$	–	86 ± 5	–
Clay and Gerhardy (1981a)	$2.3 \cdot 10^5$	~2	104 ± 2	–
	$4 \cdot 10^5$	~2	100 ± 6	~200
	10^6	~2	97 ± 2	–
	$2.5 \cdot 10^6$	~2	98 ± 3	–
Clay and Gerhardy (1982)	10^6	~2.0	100	185 ± 5
Experiment	Size	γ (differential)	Λ_{att} [g cm^{-2}]	λ_{abs} [g cm^{-2}]
Aglietta et al. (1999)[c]	$\sim 3 \cdot 10^5$ [h]	2.54 ± 0.02	–	
	$-\sim 3 \cdot 10^6$ [h]	3.04 ± 0.10	–	222 ± 3
Chilingarian et al. (1999)[d]	$\sim 3 \cdot 10^5$ [h]	2.54 ± 0.012	–	
	$\sim 3 \cdot 10^6$ [c)]	2.94 ± 0.042	–	278 ± 76
Antoni et al. (2003)	$\sim 3.2 \cdot 10^4$ [h]	2.7	130	175
	$> 3.2 \cdot 10^5$ [h]	Rising to	–	Rising to
	$\sim 3.2 \cdot 10^6$ [h]	3.1	90–100	194
Experiment	Rate [m^{-2}s^{-1}sr^{-1}]	γ (integral)	Λ_{att} [g cm^{-2}]	λ_{abs} [g cm^{-2}]
Nagano et al. (1992)[e]	10^{-10} [i]	2.83 ± 0.01	–	203 ± 21
	10^{-11} [i]	2.83 ± 0.01	–	193 ± 12
	10^{-12} [i]	2.83 ± 0.01	–	216 ± 16

Measurements made at [a] Mt. Norikura, 750 g cm^{-2}; [b] Chacaltaya, 530 g cm^{-2};
[c] Gran Sasso, 820 g cm^{-2}; [d] Mt Aragats, 695 g cm^{-2}; [e] Akeno, 920 g cm^{-2}.
[f] zenith angle method; [g] Barometric method; [h] combined method using spectral knee location;
[i] various detector arrangements and/or trigger requirements; [j] Special evaluation of γ.

his early experiments had also investigated the altitude dependence of the penetrating component (Hodson, 1953b). Theoretical results on the altitude variation of the shower counting rate were obtained by Kalmykov et al. (1973) from Monte Carlo simulations.

A compilation of early data on the altitude dependence of the shower rate which includes ground based as well as airborne data is presented in Fig. 6.21. In addition, using the *Gross transformation* (Gross, 1933; see Eq. B.13, Sect. B.5) Greisen (1956) computed the intensity distribution for vertical showers which is indicated by the curve labeled (c). Some of the more recent work of Antonov (Antonov, 1974; Antonov and Ivanenko, 1974; Antonov et al., 1973, 1974), who

Table 6.3 Muon size attenuation and absorption lengths. (Sea level unless specified otherwise)

Experiment	Size	γ (integral)	E_μ [GeV]	$\Lambda_{\mu,\mathrm{att}}$ [g cm^{-2}]	$\lambda_{\mu,\mathrm{abs}}$ [g cm^{-2}]
De Beer et al. (1962)	$N_e 10^7$	1.85 ± 0.1	>0.7	–	571
Hinotani et al. (1963)[a,b]	–	1.96 – 2.04	>1	$\sim$170	362 ± 46
	–	1.86 – 1.94	>2	$\sim$170	320 ± 34
Firkowski et al. (1965)[a]	–	2.1 ± 0.1	>0.6	–	640^{+180}_{-110}
Firkowski et al. (1967)[a]	–	2.1 ± 0.1	>0.6	–	690
Bell et al. (1974)	$N_\mu 10^7$	–	>0.75	–	813 ± 51
Goorevich et al. (1974)	$N_\mu 10^7$	–	>0.75	–	803
Hochart et al. (1975)	$N_e \sim 5 \cdot 10^5$	–	>5	108.5 ± 3	750

[a] Used density spectrum, [b] measurements made at 200 m and 2,200 m a.s.l.

did the most extensive experimental work in this field using aircraft, covering almost 80% of the atmosphere measured from sea level, is shown in Fig. 6.22 together with some ground based data by Aminjeva et al. (1969), Chudakov et al. (1960) and Vernov et al. (1968). These two figures are forerunners of the more modern equal intensity curves that are discussed in Sect. 6.7. Details of Antonov's aircraft array layout are given in Fig. A.4.

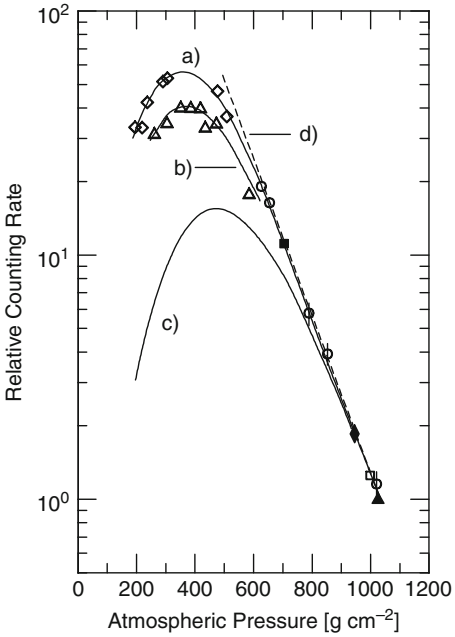

Fig. 6.21 Compilation of early data on the altitude dependence of the counting rate of showers recorded with Geiger counters, after Greisen (1956). Included are showers with particle densities $\leq 50\,\mathrm{m}^{-2}$ from the following authors: ◇ Kraybill (1949) normalized to the curve at ◆, △ Hodson (1953a) normalized to ▲, □ and ■ Cocconi and Cocconi Tongiorgi (1949b), Cocconi et al. (1949), and ○ Hilberry (1941) normalized at point ■. The *curve* labeled (c) is for vertical showers and was inferred by means of a Gross transformation from a smooth curve going midway between points ◇ and ◆ at high altitudes (Gross, 1933). *Curves* (a), (b) and (d) are fits to the data points

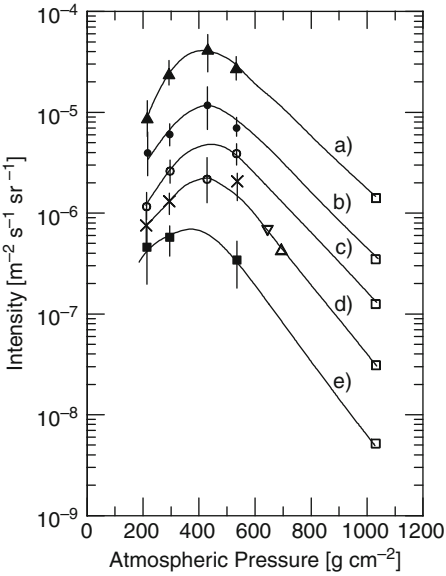

Fig. 6.22 Altitude dependence of the intensity of showers of fixed size. The data points ▲, ●, ○, × and ■ have been recorded with an array mounted on board of an airplane (Antonov, 1974; Antonov and Ivanenko, 1974; Antonov et al., 1974) and identify the different shower size groups as $N > 1.2 \cdot 10^5$ (*curve* a), $N > 3 \cdot 10^5$ (*curve* b), $N > 6 \cdot 10^5$ (*curve* c), $N > 1.2 \cdot 10^6$ (*curve* d) and $N > 3 \cdot 10^6$ (*curve* e), respectively. Points □, △ and ▽ are from the work of Vernov et al. (1968) at sea level, Aminjeva et al. (1969) and Chudakov et al. (1960) at mountain altitudes, respectively

In Fig. 6.23 we show another compilation of results on the altitude variation of the shower rate, after Antonov et al. (1979b), which includes data obtained from airplane and balloon-borne experiments as well as some ground based data points. The details are given in the figure caption. The layout of the balloon-borne array is shown in Fig. A.8. Theoretical studies based on simulations were made by Antonov et al. (1975, 1983, 1984). A re-analysis of these data by Antonov and co-workers (Antonov et al., 1984) affected the results significantly, as is shown in Fig. 6.24.

In the lower third of the atmosphere the altitude dependence of the shower counting rate can be described fairly well by a power law with exponent γ. Measurements show that γ changes only very slowly with altitude. These measurements are difficult to perform because of the low counting rate and poor statistics. The shower size spectrum, discussed in Sect. 12.2, and the shower density spectrum, discussed in Sect. 12.4, are closely related, and so are the respective spectral exponents (see Sect. 12.4.1).

Hodson (1953a) has made extensive studies on the exponent γ of the density spectrum and determined its value over a wide range of altitudes for particle densities between 5 and 500 m^{-2}. He obtained $\gamma = 1.445 \pm 0.014$ at sea level and $\gamma = 1.549 \pm 0.018$ at 26,000 ft (7,925 m a.s.l.). The results are presented in Fig. 6.25 together with earlier data of Kraybill (1949, 1952).

The results of an early theoretical analysis by Mills (1948) , based on the assumption that air showers are initiated by electrons, is shown by the dashed line in Fig. 6.25. Mills was aware of the disagreement between his data and the early experimental results of Kraybill (1948) on the altitude dependence of the shower development. He comments in his paper that multiple production of secondaries by primary

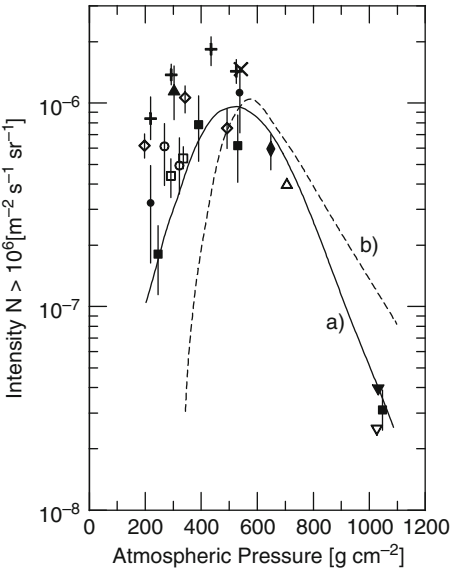

Fig. 6.23 Altitude dependence of the intensity of showers of size $N \geq 10^6$ (Antonov et al., 1979b). The high altitude data ◇ and + are from airplane experiments by Antonov et al. (1963, 1964a, b, c, 1974), Antonov (1974), and Antonov and Ivanenko (1974). Points ○, ●, □, ■ and ▲ are from balloon experiments carried out in 1976 and 1978 by Antonov and collaborators. ○ and □ are for zenith angles $\theta < 30°$, ● and ■ for $30° \leq \theta \leq 60°$, and ▲ is the result of an individual shower analysis (Antonov et al., 1979a). Additional data are presented to extend the distribution down to sea level: ♦ Chudakov et al. (1960), △ Aminjeva et al. (1969), ▽ and ▼ Vernov et al. (1968), and × Bradt et al. (1965). *Curves* a and b are predictions from simulations by Kalmykov et al. (1971, 1973) and Capdevielle and Cachon (1975), respectively. (For theoretical aspects see Antonov et al., 1979c)

protons, as proposed by Lewis (1948), should lead to an altitude dependence in better agreement with experiment; the correct conclusion as we know today.

6.6.3 Data on Zenith Angle Dependence

Some of the pioneering measurements on the zenith angle distribution of air showers were carried out by Hilberry (1941) at different altitudes, by Daudin (1945) at 2,900 m, Cocconi and Tongiorgi (1946) at 2,200 m, Deutschmann (1947) at sea level, Williams (1948) at 3,050 m and Cocconi and Cocconi Tongiorgi (1949a) at 260 m. A remarkable experiment was made by Brown and McKay (1949) who have used a cloud chamber at Echo Lake (altitude 3,260 m) to determine the arrival direction of the showers. Biehl et al. (1949) and Kraybill (1954b) made measurements with detectors installed in airplanes at altitudes up to 9,100 m.

Further measurements, listed in chronological order, were made by Bassi et al. (1952, 1953) at the Agassiz site (altitude 183 m), Hazen et al. (1954), MacLeod (1956) at sea level, Clark (1957) at Agassiz; Guseva et al. (1959) at the old Pamir

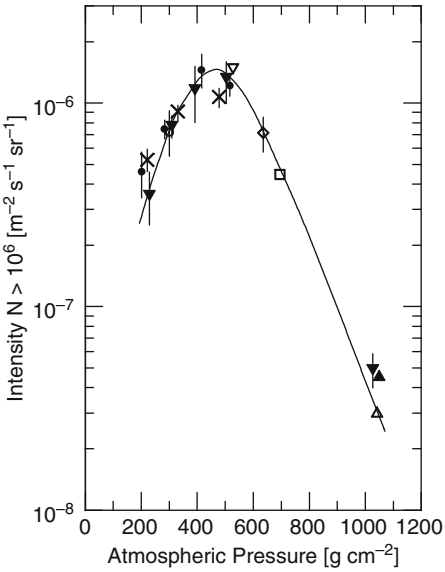

Fig. 6.24 Revised results of the altitude dependence of the intensity of air showers of size $N \geq 10^6$ (Antonov et al., 1984). The re-analyzed data are from the following references: • Antonov (1974), Antonov and Ivanenko (1974) and Antonov et al. (1974); × Antonov et al. (1963, 1964a); ▼ and ○ Antonov et al. (1980), balloon and airplane data. In addition the following results are also shown for comparison: ◇ Kulikov et al. (1960), Pamir Mountains; □ Danilova et al. (1977), Tien Shan; ▲ and △ Vernov et al. (1968), Moscow and ▽ Bradt et al. (1965), Chacaltaya. The *curve* is the result from a rather detailed calculation of Nikolsky (1981a, b)

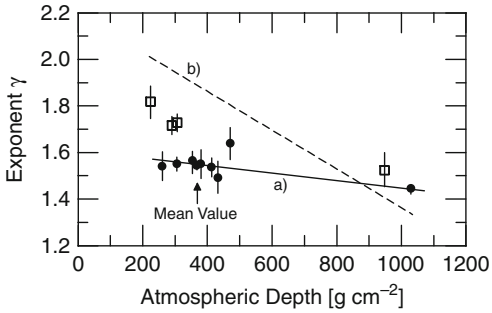

Fig. 6.25 Altitude variation of the exponent γ of the density spectrum of air showers. The *full circles*, •, are from the work of Hodson (1953a), the *squares*, □, after Kraybill (1949, 1952). The density range covered was from 50 to 500 particles m^{-2}. The *dashed line*, (b), is from an early calculation of Mills (1948), assuming electrons to initiate the showers and *line* (a) is a fit to Hodson's data

station (3,860 m); Fukui et al. (1960) at Tokyo (s.l.), Clark et al. (1961) at Agassiz, Delvaille et al. (1960) and Bennett et al. (1962) at Ithaca, NY (260 m), and Coxell et al. (1963) at Durham (65 m) and Silwood Park (∼200 m) in England. Bradt et al. (1965) have used the same array in Bolivia initially at the El Alto site (4,200 m) and later on at Mt. Chacaltaya (5,230 m).

The data of the extensive work of Delvaille et al. (1960) who determined the shower rate attenuation length, Λ_{att}, for different size groups from the zenith angle distribution measured at the Ithaca site (1,006 g cm^{-2}) and the corresponding attenuation coefficient, μ'_{att}, are summarized in Table 6.4.

Additional data are available from Haverah Park (s.l.) (Tennent, 1967), Moscow (altitude 192 m) (Efimov, 1967), Yakutsk (105 m) (Kozlov et al., 1973), Durham (65 m) (Ashton et al., 1979), Mt. Norikura (2,770 m) (Miyake et al., 1979) and Adelaide (s.l.) (Ciampa and Clay, 1988). Ashton et al., (1975) have also studied the size dependence of the zenith angle distribution. In the following we present a limited selection of the extensive data mentioned above.

The results of the zenith angle measurements of Bassi et al. (1953) are shown in Fig. 6.26 together with a smooth curve derived from the altitude variation of the shower rate obtained by Greisen (1956). The early work of Fukui et al. (1960) for moderate size showers ($N \geq 10^5$) near sea level is summarized in Fig. 6.27. These data like many others do not show absolute counting rates. The reason for this is that an exact calibration is rather difficult and to obtain the functional relationship of the angular distribution, relative counting rates are fully adequate. The abscissa shows on top the zenith angle and at the bottom the excess of atmospheric thickness with respect to the vertical column of air, overlaying the array, which a shower trajectory inclined at an angle θ must traverse to reach the array.

The data obtained by Kozlov et al. (1973) at Yakutsk for relatively large showers are shown in Fig. 6.28a. They are presented as the logarithm of the ratio of the counting rates at zenith angle θ to vertical incidence versus $\sec\theta$. The resulting attenuation length, Λ_{att}, is listed in the figure caption.

The more recent measurements of Miyake et al. (1979) at Mt. Norikura, altitude 2,770 m, are given in Fig. 6.28b. These authors subdivided their data into four different size groups. Statistics does not allow to draw any conclusions concerning the size dependence of the zenith angle distribution. In Fig. 6.29 we show a set of data obtained with the extended Chacaltaya array (5,230 m) (Ohta et al., 1979).

Table 6.4 Shower rate attenuation deduced from zenith angle dependence at sea level. (Delvaille et al., 1960)

Shower size	Number of showers	Average $\sec\theta$	$\mu'_{att} = 1,006/\Lambda_{att}$	Λ_{att} [g cm^{-2}]
$5 - 10 \cdot 10^6$	56	1.1218	5.8 ± 1.1	174 ± 32
$1 - 3 \cdot 10^7$	113	1.0961	7.9 ± 1.0	128 ± 16
$3 - 10 \cdot 10^7$	55	1.0957	7.9 ± 1.4	127 ± 22
$1 - 5 \cdot 10^8$	35	1.1161	6.2 ± 1.4	164 ± 38
Total	259	1.1039	7.1 ± 0.6	141 ± 12

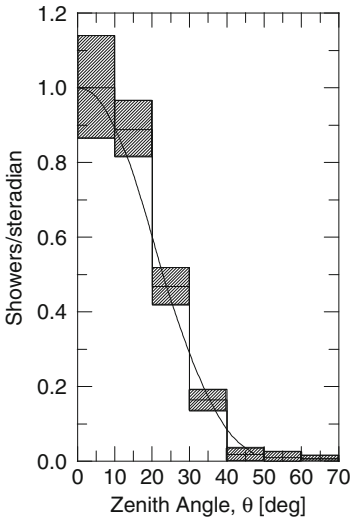

Fig. 6.26 Histogram of the frequency of showers with zenith angle θ per unit solid angle as a function of θ, measured at sea level in showers of size $10^5 - 10^6$ (Bassi et al., 1953). The *shaded area* represents the error band. The *smooth curve* is derived from the altitude variation of the number of showers with density $\simeq 50\,\mathrm{m}^{-2}$, after Greisen (1956)

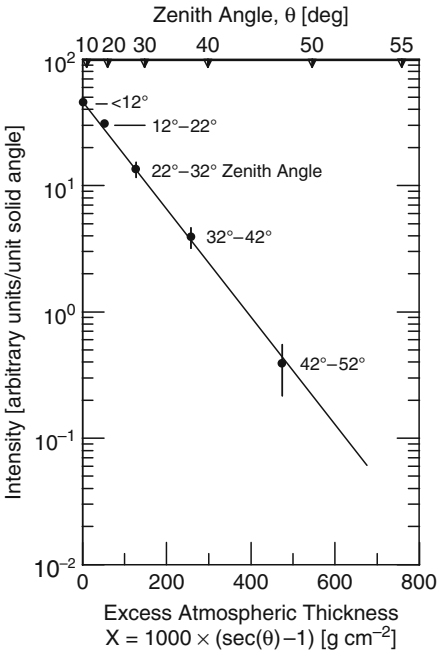

Fig. 6.27 Zenith angle distribution of extensive air showers of size $\geq 10^5$ at sea level. Plotted is the relative intensity as a function of X, the excess amount of atmosphere a shower incident under a zenith angle θ has to traverse to reach the observation level as compared to vertical incidence; thus $X = X_0(\sec\theta - 1)$, where $X_0 = 1,000\,\mathrm{g\,cm}^{-2}$. The zenith angle ranges indicated in the figure represent the bin widths of the measurements. The shower rate attenuation length, Λ_{att}, resulting from this measurement is $102 \pm 15\,\mathrm{g\,cm}^{-2}$ (Fukui et al., 1960)

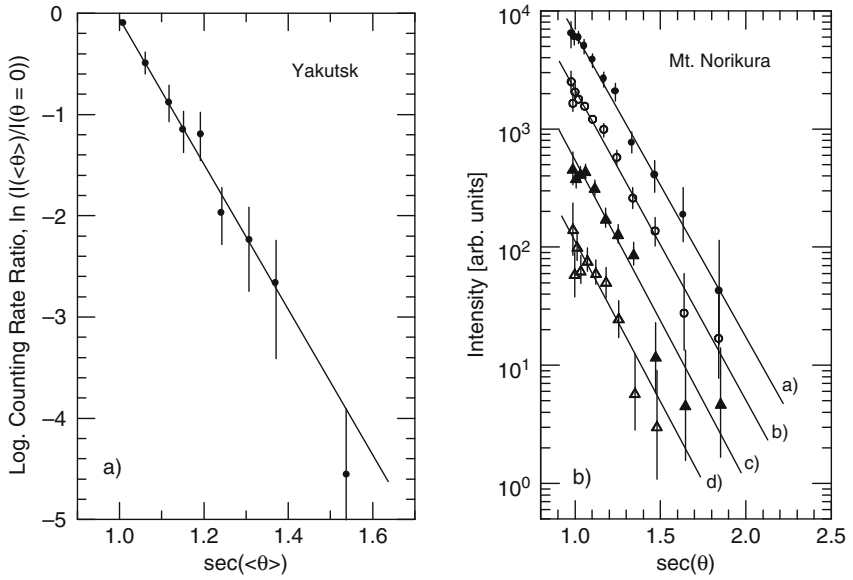

Fig. 6.28 (**a**) Logarithm of the ratio of the counting rates of showers at zenith angle θ to vertical incidence plotted as a function of $\sec\theta$ for showers of average size $8.5 \cdot 10^7$ ($5 \cdot 10^7 \leq N \leq 5 \cdot 10^8$), recorded at Yakutsk (1,020 g cm^{-2}) (Kozlov et al., 1973). The shower rate attenuation length obtained from the raw data is $\Lambda_{att} = 140 \pm 15$ g cm^{-2}, after corrections it is 126 ± 15 g cm^{-2}. (**b**) Zenith angle dependence of showers of different size groups recorded at Mt. Norikura, 2,770 m (750 g cm^{-2}). The intensity is plotted as a function of $\sec\theta$, where θ is the zenith angle (Miyake et al., 1979). The *lines* are fits to the data points. The shower groups comprise (a) •, $N > 5 \cdot 10^6$, (b) ○, $N > 10^7$, (c) ▲, $N > 2 \cdot 10^7$, and (d) △, $N > 5 \cdot 10^7$

Catz et al. (1971) and Maze (1970) have measured the zenith angle distribution over a wide angular range, up to zenith angles $\theta \simeq 80^\circ$, at Verrières le Buisson (France) and Lodz (Poland) to study mainly *muon-poor* showers[14] and their angular distribution in conjunction with questions related to the hypothesis of a *long-flying component* (Bazarov et al., 1981; Dremin et al., 1985; Yakovlev, 2003). The data are presented in Fig. 6.30 and include showers with particle densities ≥ 26 m^{-2}. The timing accuracy at Verrières was about 2 ns, at Lodz about 7 ns, which resulted in a more accurate angular resolution at Verrières that was about 2°.

The results of one of the more recent measurements carried out at sea level is from the work of Ciampa and Clay (1988) made at Buckland Park in Adelaide, South Australia, shown in Fig. 6.31. These authors have used different particle densities as trigger criterion, as specified in the caption. The criterions were software selected and the threshold size corresponding to the least stringent criterion (6-particles in any two of nineteen detectors) is about $3 \cdot 10^4$. The array is described

[14] The muon content in muon-poor showers amounts to about 1% or less of all the particles.

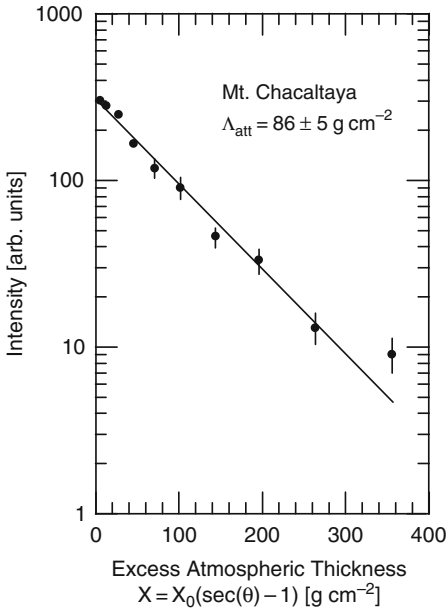

Fig. 6.29 Zenith angle distribution of showers with size $10^5 \leq N \leq 10^7$ recorded at Mt. Chacaltaya, 530 g cm^{-2}. The intensity is plotted as a function of X, the excess amount of atmosphere a shower incident under zenith angle θ has to traverse to reach the observation level as compared to vertical incidence (Ohta et al., 1979). X_0 is the vertical atmospheric column density at the observation level. The resulting shower rate attenuation length is $\Lambda_{att} = 86 \pm 5$ g cm^{-2}

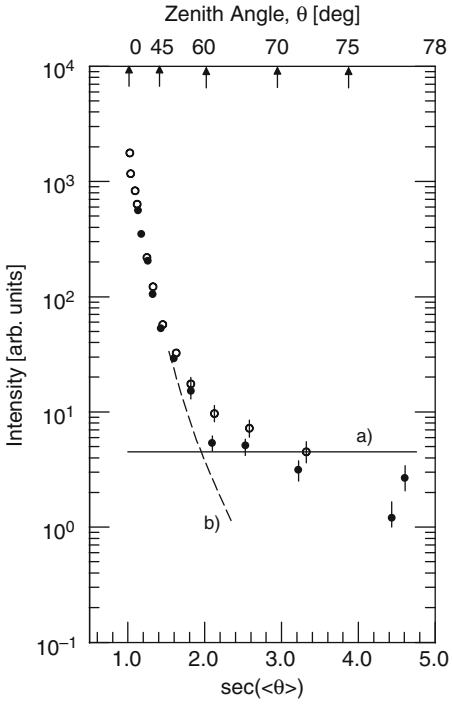

Fig. 6.30 Zenith angle distribution of muon-poor showers near sea level, recorded at Verriéres, France, ○ (Catz et al., 1971) and Lodz, Poland, • (Gawin et al., 1970). The intensity is plotted as a function of sec θ, θ being the zenith angle. *Line* a corresponds to an isotropic, *curve* b to the theoretically expected angular distribution for a constant attenuation length (Maze, 1970)

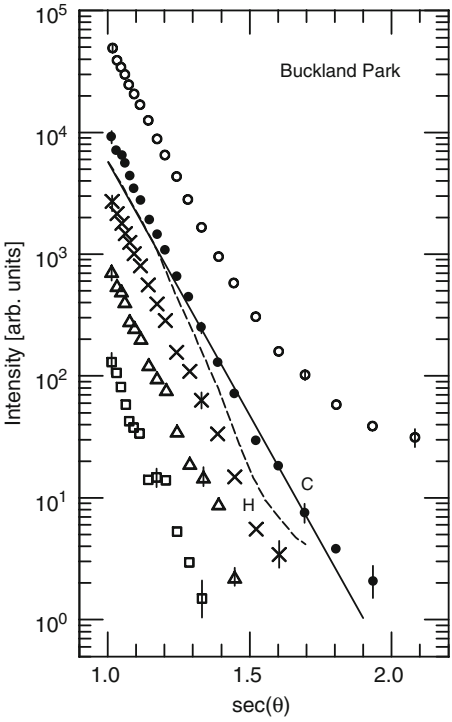

Fig. 6.31 Zenith angle distributions of shower rates measured with the Buckland Park array. The intensity is plotted as a function of sec θ, θ being the zenith angle. The five distributions correspond to different trigger thresholds in any two of nineteen detectors: ○ 6, ● 20, × 40, △ 80 and □ 160 particles (Ciampa and Clay, 1988). These authors compare their results with distributions from calculations of Kalmykov et al. (1973) using a conventional (*solid line*, C) and a high multiplicity model (*dashed line*, H), and primary protons to simulate the showers

in Ciampa et al. (1986) and the layout is shown in Fig. A.9. A comparison is made with some theoretical results by Kalmykov et al. (1973).

The zenith angle distribution of showers using the muon component in place of electrons was measured by Bell et al. (1974) with the SUGAR array in Australia. These data are discussed in more details together with other zenith angle distributions in the context of equal intensity distributions in Sect. 6.7 of this chapter.

6.6.4 Data on Environmental Effects

(a) Data on Barometric Pressure Dependence

Measurements of the *all-particle* barometric pressure dependence of the shower rate were carried out by Auger and Daudin (1942), Daudin and Daudin (1949, 1953a, b), Hodson (1953a), Daudin et al. (1956), Greisen (1956), Citron and Stiller (1958), Cranshaw et al. (1958a, b), Bennett et al. (1962), and Ashton et al. (1975). The results of these authors are summarized in Table 6.5. In Fig. 6.32 we show the very consistent data obtained by Hodson (1953a). A compilation due to Bennett et al. (1962) which shows the barometric pressure coefficient as a function of shower size is presented in Fig. 6.33.

Table 6.5 Barometric coefficients, β

Author	Altitude	β [% cm^{-1} Hg]
Auger and Daudin (1942)	Sea level	9.0
Millar (1951)	Sea level	11.1
Hodson (1953a)	Sea level	9.0 ± 1.1
Ashton et al. (1975)	Sea level	8.3[a]
Citron (1952)	280 m	11.8
Daudin and Daudin (1949)	550 m	8.9 ± 0.9[b]
	550 m	8.5 ± 0.5[b]
Citron (1952)	1,230 m	9.0
Daudin and Daudin (1949)	2,860 m	9.2 ± 2[c]
Daudin and Daudin (1953a)	2,860 m	10.2 ± 0.1[d]
	2,860 m	10.4 ± 0.2[e]
Castagnoli et al. (1950)	3,500 m	9.8

[a] calculated by the author.
[b] applies to counter separations of 5 m and different epochs.
[c] average value over several measurements.
[d] applies to counter separations of 5 m and a total of $2 \cdot 10^7$ showers.
[e] applies to counter separations of 80 m and a total of $3 \cdot 10^6$ showers.

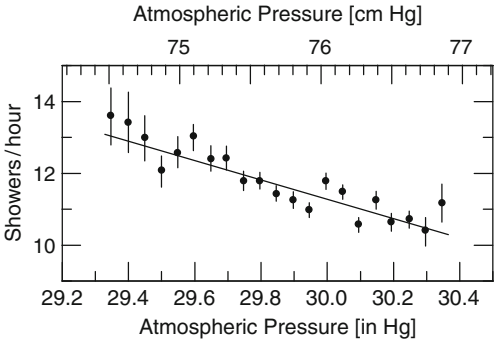

Fig. 6.32 Barometer effect on the shower rate at sea level (Hodson, 1953a). The apparatus was the same that had been used to get the data presented in Fig. 6.24. The analysis includes showers in the density range from 50 to 500 particles per m^2. The *line* is a fit to the data

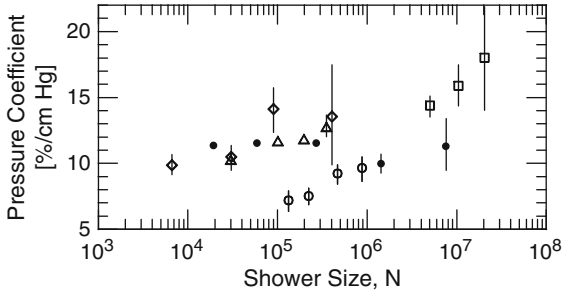

Fig. 6.33 Barometric pressure coefficient in percent per centimeter of mercury of extensive air showers as a function of shower size, near sea level, after Bennett et al. (1962). The different data are from the work of the following authors: •, Greisen (1956); △, Citron and Stiller (1958); □, Cranshaw et al. (1958a); ◇, Farley and Storey (1957), and ○, Krasilnikov after Bennett et al. (1962)

From their work, Bennett et al. (1962) conclude that the barometric coefficient β is approximately 11% per cm Hg and essentially the same for all shower sizes. In their analysis these authors consider the fact that the barometric effect is in part a geometric effect, as mentioned before (Sect. 6.5.2). They assume that the temperature coefficient α of the counting rate is entirely due to the density effect and subtract its influence on the barometric coefficient β by the use of Eq. (6.21) to obtain the *pure pressure dependence*, β_{mass}. The results of this work that includes a wide range of shower sizes are listed in Table 6.6, including a background run with single particles. A similar analysis was carried out by Delvaille et al. (1960). Their results are given in Tables 6.7 and 6.8.

In a relatively recent study Aglietta et al. (1995) determined the dependence of the barometric coefficient on the zenith angle at the site of the EAS-TOP experiment (2,005 m a.s.l.). The result of this work is illustrated in Fig. 6.34.

Firkowski and collaborators have measured the barometric pressure dependence β of the *muon component* in air showers with their installation in Lodz, Poland, near sea level (Firkowski et al., 1965). These authors disregard the temperature effect and claim that it can be neglected for muons. The threshold energy of the muons was 0.6 GeV. Their data are shown in Fig. 6.35. The resulting barometric coefficient is $\beta_{\text{mass}} \simeq \beta = 5.4 \pm 1.2\%\,\text{cm}^{-1}\,\text{Hg}^{-1}$.

Table 6.6 Barometric pressure and temperature coefficients, and shower attenuation length for different shower sizes at sea level (Bennett et al., 1962)

Median size N	β [% cm^{-1} Hg^{-1}]	α_T [%/°C]	sec θ	Λ_{att} [g cm^{-2}]
1[a]	-2.86 ± 0.7	-0.03 ± 0.02	1.268	580 ± 27
$2 \cdot 10^4$	-11.4 ± 0.2	-0.27 ± 0.02	1.091	120 ± 2
$6 \cdot 10^4$	-11.6 ± 0.2	-0.06 ± 0.03	1.095	127 ± 3
$3 \cdot 10^5$	-11.7 ± 0.3	$+0.12 \pm 0.05$	1.099	133 ± 5
$1.4 \cdot 10^6$	-10.1 ± 0.7	$+0.46 \pm 0.10$	1.127	185 ± 20
$8 \cdot 10^6$	-11.4 ± 2.0	$+0.66 \pm 0.30$	1.121	172^{+70}_{-40}

[a] Background measurement.

Table 6.7 Barometric pressure and temperature coefficients, pressure dependence of mass attenuation coefficient and shower rate attenuation length. Weighted averages of 24 half-month periods at sea level (Delvaille et al., 1960)

Median shower size	Pressure coefficient β [% cm^{-1} Hg^{-1}]	Temperature coefficient α [%/°C]	Mass absorption β_{mass} [% cm^{-1} Hg^{-1}]	Shower rate attenuation Λ_{att} [g/cm^2]
10^4	-11.4 ± 0.25	-0.070 ± 0.023	-11.6 ± 0.27	117 ± 3
$2.5 \cdot 10^4$	-11.1 ± 0.34	$+0.065 \pm 0.032$	-10.8 ± 0.36	126 ± 4
$3 \cdot 10^5$	-11.3 ± 0.45	$+0.248 \pm 0.041$	-10.4 ± 0.48	131 ± 6
$2 \cdot 10^6$	-9.0 ± 1.03	$+0.310 \pm 0.093$	-7.8 ± 1.09	174 ± 25
$1.5 \cdot 10^7$	-12.2 ± 3.12	$+0.268 \pm 0.281$	-11.2 ± 3.3	121^{+51}_{-27}
Single particles	-3.03 ± 0.12	-0.013 ± 0.011	–	–

Table 6.8 Barometric pressure and temperature coefficients, pressure dependence of mass attenuation coefficient and shower rate attenuation length. Full year analysis at sea level. (Delvaille et al., 1960)

Median shower size	Pressure coefficient β [%/cm Hg]	Temperature coefficient α [%/°C]	Mass absorption β_{mass} [%/cm Hg]	Shower rate attenuation Λ_{att} [g/cm^2]
10^4	-11.0 ± 0.21	-0.078 ± 0.010	-11.3 ± 0.21	120 ± 2
$2.5 \cdot 10^4$	-10.2 ± 0.29	$+0.237 \pm 0.013$	-9.3 ± 0.29	146 ± 5
$3 \cdot 10^5$	-10.7 ± 0.37	$+0.324 \pm 0.017$	-9.5 ± 0.38	144 ± 6
$2 \cdot 10^6$	-9.5 ± 0.81	$+0.416 \pm 0.037$	-7.9 ± 0.82	173 ± 18
$1.5 \cdot 10^7$	-10.7 ± 2.45	$+0.626 \pm 0.113$	-8.4 ± 2.5	163^{+68}_{-38}
Single particles	-2.98 ± 0.12	-0.016 ± 0.005	–	–

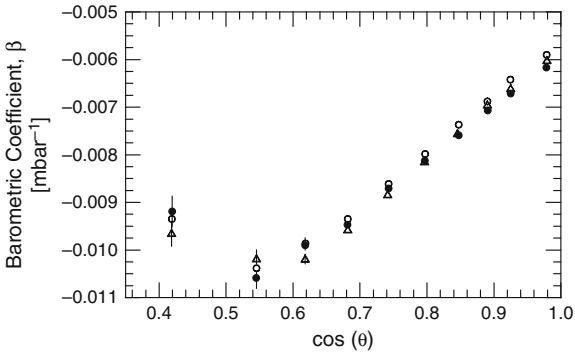

Fig. 6.34 Dependence of the barometric coefficient, β, on the zenith angle as measured by the EAS-TOP experiment at Gran Sasso (2,005 m a.s.l., 820 g cm^{-2}). The expected $\cos\theta$ dependence is evident. The deviation occurs only at $\theta > 60°$. The three data points correspond to different experimental epochs (• 1992, ○ 1993, △ 1994) (Aglietta et al., 1995)

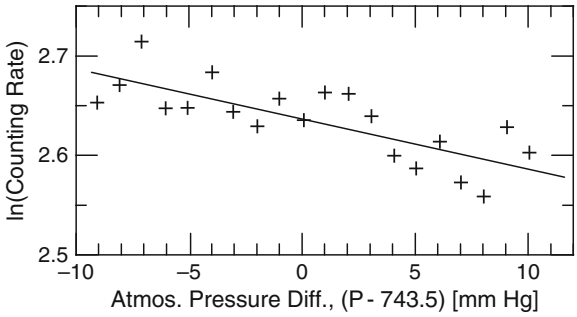

Fig. 6.35 Dependence of the frequency of the muon component of showers on barometric pressure, P, measured at Lodz (Poland) (Firkowski et al., 1965). The resulting barometric coefficient thus obtained is $\beta = (5.4 \pm 1.2)\%$ per cm Hg. The abscissa shows the pressure variation with respect to the normal pressure (743.5 mmHg) at the experimental site

(b) Data on Air Temperature, Density and Humidity Dependence

The dependence of the lateral spread and related consequences on air density and thus on air temperature leads one to expect a seasonal variation of the rate of extensive air showers in the lower atmosphere. Such an effect had been suggested by Euler (1940) and Daudin and Daudin (1949, 1953a). Hodson (1951) was one of the first to demonstrate the existence of the temperature effect of air showers. Later work by Daudin and Daudin (1953a, b) and Daudin et al. (1956) followed.

Hodson (1951) and Janossy et al. (1958) have measured the seasonal variation of the shower rate. The results of Hodson (1951) are illustrated in Fig. 6.36 together with the mean monthly air temperatures. He obtained a temperature coefficient at a level of 950 mb of $-(0.38 \pm 0.11)\%$ per K with a counter arrangement having separations of 0.38 and 2.16 m, respectively. Such small counter separations select predominantly small showers on the order of $N \simeq 10^4$ particles near the core.

In measuring both the temperature coefficient α and the barometric pressure coefficient β Bennett et al. (1962) noticed that the description of atmospheric effects in terms of only two parameters was an oversimplification, since the values for α and β obtained for different intervals of time were not fully consistent with each other. For the pressure coefficient this effect was small, but in the case of α the percentage variation was large.

In addition Bennett et al. (1962) found that the temperature coefficient appeared to vary with temperature itself. Thus, the variation of the counting rate with atmospheric temperature seems to be *strongly non-linear*. The fact that the temperature

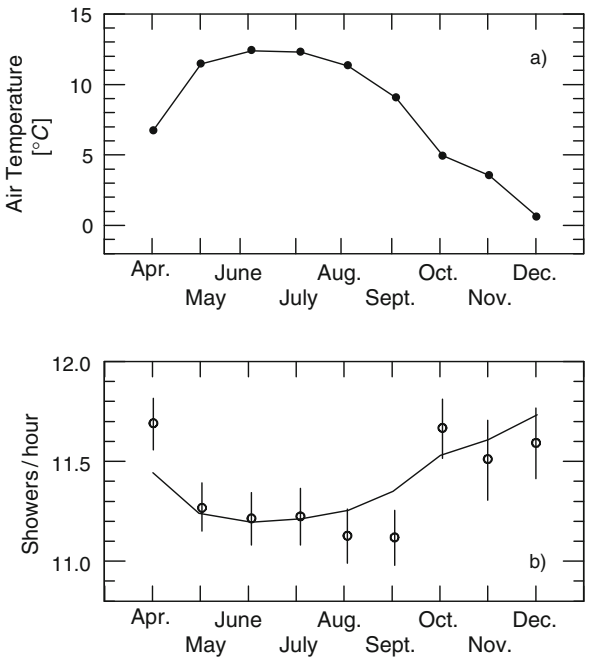

Fig. 6.36 Seasonal variation of mean outside air temperature shown in the upper figure, (**a**), and corresponding hourly rate of extensive air showers shown in the lower figure, (**b**). The data points with the error bars were recorded by Hodson (1951) at Liverpool and the curve indicates the expected rate computed on the basis of the curve of, (**a**) for a temperature coefficient of -0.38% per °C

coefficient appears to be different at different core positions was interpreted by these authors to deliver proof that it is chiefly a geometric effect that reduces the lateral extension of the shower with increasing temperature.

The measurements of Bennett et al. (1962) that consider the humidity as well yield values for α_T (Eq. 6.24) ranging from $-(0.27 \pm 0.02)\%$ per K for counter separations of a few meters, and therefore for small showers of size $N \simeq 2 \cdot 10^4$ particles, to $+(0.66 \pm 0.30)\%$ per K at counter separations of 600 m, corresponding to large showers ($N \simeq 8 \cdot 10^6$), with values near zero at about 10 m ($N \simeq 6 \cdot 10^4$). These results are also included in Table 6.6. Results from a very similar analysis made somewhat earlier by Delvaille et al. (1960) are given in Tables 6.7 and 6.8.

In conclusion we can say that there is agreement between the results of Hodson (1951) and Bennett et al. (1962) at small counter separations, implying small core distances and small showers, and good general agreement between the results of, Delvaille et al. (1960) and Bennett et al. (1962) over the full range of their investigations.

Based on measurements carried out more recently with the EAS-TOP array, Aglietta et al. (1989) determined the temperature and barometric coefficients at an altitude of 2,005 m a.s.l. for showers of energy around 10^{14} eV. The data are displayed in Table 6.9. Inspection of these data reveals that the temperature coefficient is of much lesser importance than the barometric effect, a conclusion also reached by the early investigators.

Table 6.9 Barometric and temperature coefficients at altitude 2,005 m. EAS-TOP array (Aglietta et al., 1989)

Energy [eV]	Rate [s^{-1}]	Barometric coefficient β [% $mbar^{-1}$]	Temperature coefficient α [% deg^{-1}]
$3 \cdot 10^{13}$	5.3	-0.71 ± 0.01	0.1 ± 0.05
10^{14}	1.1	-0.73 ± 0.02	0.24 ± 0.08
$2 \cdot 10^{14}$	0.11	-0.79 ± 0.07	-0.03 ± 0.02

Finally, in Table 6.10 we show a summary of very early basic shower data.

6.6.5 Mathematical Expressions and Fits

Khristiansen et al. (1977) give the following simple relationship for the zenith angle dependence of the intensity $I(\theta)$ of showers in the size range $10^5 \leq N \leq 10^6$ at sea level,

$$I(\theta) \;=\; I(\theta = 0) \cos^n \theta \;\;, \tag{6.25}$$

where $I(\theta = 0)$ is the vertical intensity and $n = 9 \pm 1$. The expression holds for $0 \leq \theta \leq 40^\circ$.

Table 6.10 Summary of basic shower parameters (Early measurements). (Cranshaw et al., 1958b)

Experiment	Size	γ (int.)	Barometer coeff. β [% (cm Hg)$^{-1}$]	Temperature coeff. α [% ^{o}C^{-1}]	Mass abs. effect. [% cm^{-1}]	Λ_{att} [g cm^{-2}]	λ_{abs} [g cm^{-2}]
Millar (1951)	$5 \cdot 10^4$	1.54	11.1 ± 1.0	~ -0.3	12.3 ± 1.5	120	185 ± 25
Hodson (1951)	–	–	–	-0.38 ± 0.11	–	–	–
Hodson (1953a, b)	$5 \cdot 10^4$	1.54	9.0 ± 1.1	–	10.5 ± 1.5	140	216 ± 30
Farley and Storey (1957)	10^4	1.45	9.9 ± 0.7	-0.89 ± 0.24	13.0 ± 1.5	114	164 ± 23
	$3 \cdot 10^4$	1.51	10.5 ± 0.8	-0.37 ± 0.26	12.0 ± 1.7	122	185 ± 25
	$9 \cdot 10^4$	1.57	14.2 ± 1.8	-0.37 ± 0.60	15.6 ± 2.5	94	148 ± 30
	$3 \cdot 10^5$	1.65	13.6 ± 3.7	-2.10 ± 1.3	14.6 ± 4.5	100	168 ± 50
Citron and Stiller (1958)	$2 \cdot 10^3$	1.36	–	-0.12 ± 0.03	10.6 ± 0.4	138	188 ± 6
	$8 \cdot 10^3$	1.44	–	-0.28 ± 0.02	11.9 ± 0.3	123	178 ± 4
	10^4	1.45	–	-0.34 ± 0.03	12.1 ± 0.4	121	175 ± 5
	$2 \cdot 10^4$	1.49	–	-0.37 ± 0.04	12.9 ± 0.6	114	170 ± 7
Cranshaw et al. (1958a, b)	$3 \cdot 10^5$	1.65	13.0 ± 0.6	~ 0	13.0 ± 1	114	187 ± 15
	$8 \cdot 10^5$	1.70	13.5 ± 1.0	~ 0	13.5 ± 1.5	110	185 ± 20
	$2 \cdot 10^6$	1.75	13.3 ± 2.0	~ 0	13.3 ± 2.5	111	195 ± 30
Culham (1958, unpublished)	$5 \cdot 10^6$	1.80	13.6 ± 0.6	0.08 ± 0.04	13.3 ± 0.7	110	199 ± 11
	10^7	1.84	14.5 ± 1.3	0.24 ± 0.17	13.8 ± 1.5	106	195 ± 20
	$2 \cdot 10^7$	1.88	14.2 ± 2.6	0.54 ± 0.35	13.4 ± 2.8	106	200 ± 34

Ashton et al. (1975) obtained for the same relation applied to the density spectrum of showers the exponents $n = 8.0^{+1.4}_{-1.2}$, $n = 9.3^{+1.0}_{-0.8}$, $n = 10^{+1.9}_{-0.9}$ for densities > 20, > 80, and $> 250\,\mathrm{m}^{-2}$, respectively.

Hodson (1952) gives the following expression for the intensity of "fast nucleons", i.e., of showers, at depth X [g cm^{-2}] in the atmosphere at an angle θ with respect to the vertical, assuming exponential attenuation,

$$I(X, \theta) \;=\; I(X, \sec\theta) \;=\; A \exp\left(\frac{-\mu_{\mathrm{att}} X}{\cos\theta}\right) \quad . \tag{6.26}$$

A is the scale factor and μ_{att} the attenuation coefficient (Cranshaw et al., 1957).

If the detector has an angular dependence of the sensitivity, $S(\theta)$, for penetrating particles incident under an angle θ with respect to the vertical, the rate of showers, $I(X)$, recorded at depth X is

$$I(X) \;=\; \int_0^{\pi/2} \exp\left(\frac{-\mu_{\mathrm{att}} X}{\cos\theta}\right) S(\theta) \sin\theta \, \mathrm{d}\theta \quad . \tag{6.27}$$

Kraybill (1954b) has derived similar expressions to deduce the angular variation of the shower intensity from the altitude dependence and the relative counting rates for differently shaped detectors, including detector directional sensitivity functions.

The simple general relationship given below (Kozlov et al., 1973; Bourdeau et al., 1980) can be used to describe the zenith angle dependence of the integral size spectrum $I(\theta)$ in terms of the vertical spectrum $I(\geq N, X_0)$ at vertical depth X_0, provided that the zenith angle θ is not too large.

$$I(\geq N, X_0, \theta) \;=\; I(\geq N, X_0, \theta = 0) e^{-(X_0/\Lambda_{\mathrm{att}})(\sec\theta - 1)} \tag{6.28}$$

where N is the shower size and Λ_{att} the shower rate attenuation length.

Bell et al. (1974) obtained the following expression for the muon size, N_μ, dependence of the muon absorption length, $\lambda_{\mu,\mathrm{abs}}$, in large vertical showers, expressed in units of atmosphere,

$$\lambda_{\mu,\mathrm{abs}} \;=\; (0.79 \pm 0.05) + (0.144 \pm 0.068) \ln\left(\frac{N_\mu}{10^7}\right) \;\; [\mathrm{atm}] \;\; . \tag{6.29}$$

The same authors obtained for the longitudinal development curves of muons a relation of the form

$$N_\mu(X, \theta) \;=\; N_\mu(X, \theta = 0) \cdot (\sec\theta)^{-\beta} \;\; , \tag{6.30}$$

where

$$\beta \;=\; (1.71 \pm 0.08) - (0.116 \pm 0.052) \ln\left(\frac{N_\mu(X, \theta = 0)}{10^7}\right) \;\; . \tag{6.31}$$

6.7 Equal Intensity Distributions

6.7.1 Introduction

The topic which is presented here is intimately related to the topics discussed in Sects. 6.2, 6.3, 6.4, 6.5 and 6.6. These deal so to say with the old classical aspects of the longitudinal development of air showers, whereas in Chap. 7 we outline the more modern concepts of the *height of maximum development* and the *elongation rate*, introduced by Linsley (1977), that yield deeper insight into the physics of cascade development. To appreciate the principle of equal intensity cuts or equal (constant) intensity distributions the reader is advised to consult the previous sections of this chapter.

In these the *average* longitudinal development of showers was studied by exploiting the various effects and dependencies of the showers on altitude, zenith angle,

barometric pressure and air temperature. In this section we discuss a particular aspect of the zenith angle distribution combined with properties of the primary radiation to access information on the longitudinal development of showers and related data.

Many authors have attempted to extract relevant information by the previously discussed methods, however, it was not until the method of equal intensity cuts in conjunction with the large high altitude installations such as the one at Chacaltaya (5,230 m a.s.l.) and airborne experiments came into operation that our knowledge on the longitudinal development of air showers has increased significantly.

6.7.2 Method of Equal Intensity Cuts

This method is based on the assumption that the high energy primary radiation that initiates air showers upon entry into the atmosphere is isotropic, i.e., it arrives from all directions at the same intensity and manifests the same spectral features. This assumption is supported by a large number of experiments over a wide range of primary energies which all indicate that the anisotropy is very small. It seems to increase slightly toward the highest energies, however, this is irrelevant for the present discussion.

Under the assumption stated above it is evident that showers initiated by primaries of a given energy and mass (or mass mix) must arrive at the same rate at all zenith angles. However, at a fixed vertical depth (or altitude) in the atmosphere the size of showers initiated by primaries of fixed energy will vary with zenith angle because they must traverse different path lengths in the atmosphere to reach the observer. If, for *fixed primary conditions*, the observations are made with an array located at high altitude, well above the maximum development of the considered vertically incident showers, the shower size will increase with increasing zenith angle until the slant depth corresponding to the depth of maximum development is reached, beyond which the size declines, and vice versa. Since the majority of all ground based experiments are located below shower maximum, even for very energetic vertically incident showers, this method can be applied by these installations only over the declining portion of the shower development curve. The accuracy of the method is infringed by varying density and temperature profiles of the atmosphere which affect the altitude-zenith angle relation of the slant depth in a non-trivial way.

Nevertheless, it is possible to study the average longitudinal development of showers over a restricted range by recording showers at a given altitude arriving from all directions and at all zenith angles. From these data the corresponding size spectra can be obtained for different zenith angle intervals, from which *equal intensity distributions* can be constructed. This is achieved by executing equal intensity cuts on the size spectra, computing the air column along the shower trajectory for every zenith angle interval and displaying the data on an atmospheric depth versus shower size plot, using intensity (event rate) as parameter

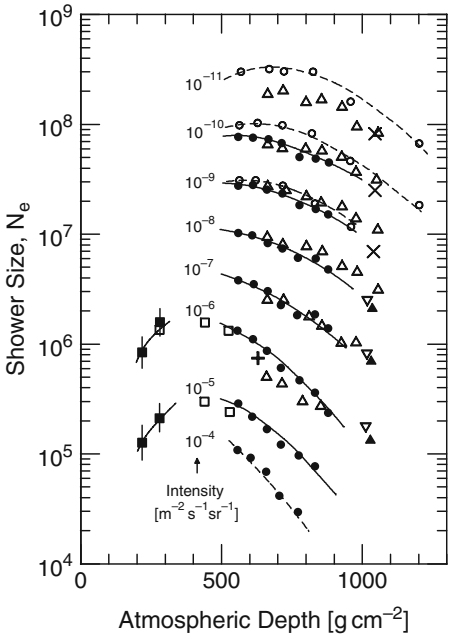

Fig. 6.37 Compilation of early equal intensity data: • represent data from Chacaltaya (5,230 m) (Bradt et al., 1965), ○ are the later, so-called improved Chacaltaya data (La Pointe et al., 1968) and △ show the combined data recorded by Hersil et al. (1962) and Clark et al. (1963) at El Alto (4,200 m). ■ are data from airplane measurements by Antonov and Ivanenko (1974) and Antonov et al. (1973, 1974), and □ are after Antonov (1974). The single data point + is from the Pamir experiment of Kulikov et al. (1960). ×, ▽ and ▲ are from measurements at Agassiz (Clark et al., 1961), Verrières (Hochart, 1976) and Moscow (Khristiansen, 1973), respectively. The *curves* are drawn to fit the data points

(cf Figs. 6.37, 6.38, 6.39, 6.40, 6.41, 6.42, 6.43 and 6.44). However, equal intensity curves are not exactly the same as longitudinal development curves and the interpretation of the former requires caution. This problem is discussed in more detail in Sect. 6.7.3 and in Chap. 10.

The same procedure applies for studying the longitudinal development of the muon component in showers. In this case one uses in place of unshielded shower detectors which record all particles an array of shielded detectors that records muons only. But here a quite different picture emerges as is illustrated in Figs. 6.47, 6.48 and 6.49. Such data are complementary to the longitudinal development of the electromagnetic component and offer an additional key to solve the complex problems and the interrelations outlined above.

In Sect. 12.2 we discuss shower size spectra and present numerous data that are the base for constructing equal intensity distributions. The same aspects concerning the muon component are discussed in Sect. 12.3 where numerous data on muon size spectra are given.

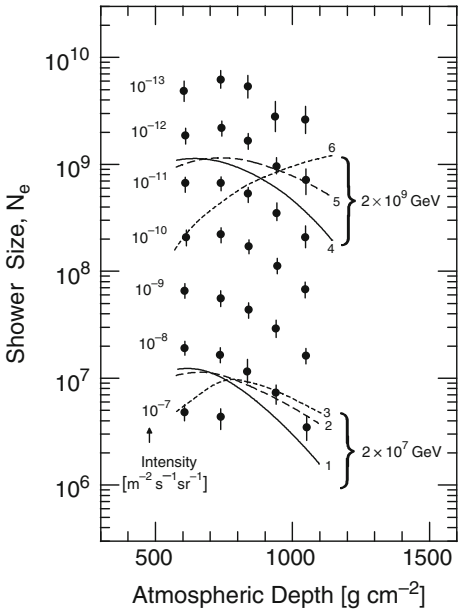

Fig. 6.38 Equal intensity distributions from measurements carried out at Mt. Chacaltaya, • (Aguirre et al., 1977a, 1979a). The two sets of three curves, 1, 2, 3 and 4, 5, 6 represent theoretical distributions based on high energy particle production models with multiplicities that follow the half (1 and 4), quarter (2 and 5) and log laws (3 and 6), respectively, for primary energies as indicated at the right hand side in the figure (Mizumoto et al., 1979)

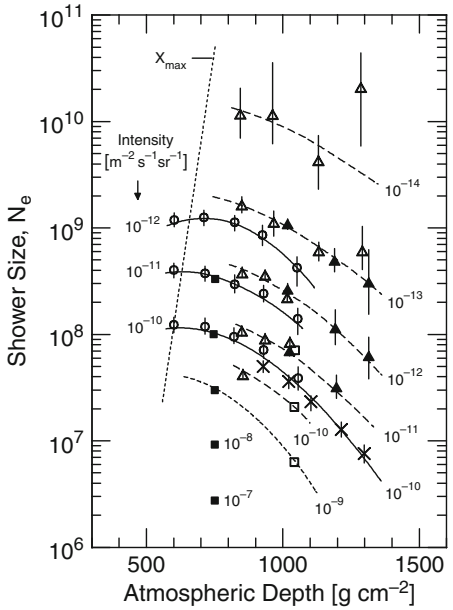

Fig. 6.39 Compilation of equal intensity distributions. The following data are included: ▲ Yakutsk (100 m a.s.l.) (Diminstein et al., 1975), △ Volcano Ranch (1,768 m a.s.l.) (Linsley, 1973), ○ Mt. Chacaltaya (5,230 m a.s.l.) (Kakimoto et al., 1981), × Akeno (900 m a.s.l.) (Hara et al., 1981b), □ Agassiz (183 m a.s.l.) (Clark et al., 1961) multiplied by the factor 0.95, and ■ Mt. Norikura (2,770 m a.s.l.) (Miyake et al., 1971, 1979). The *dashed* and *solid curves* link corresponding experimental data points. The *dotted straight line* labeled X_{max} connects the estimated locations of maximum shower development. For details see text

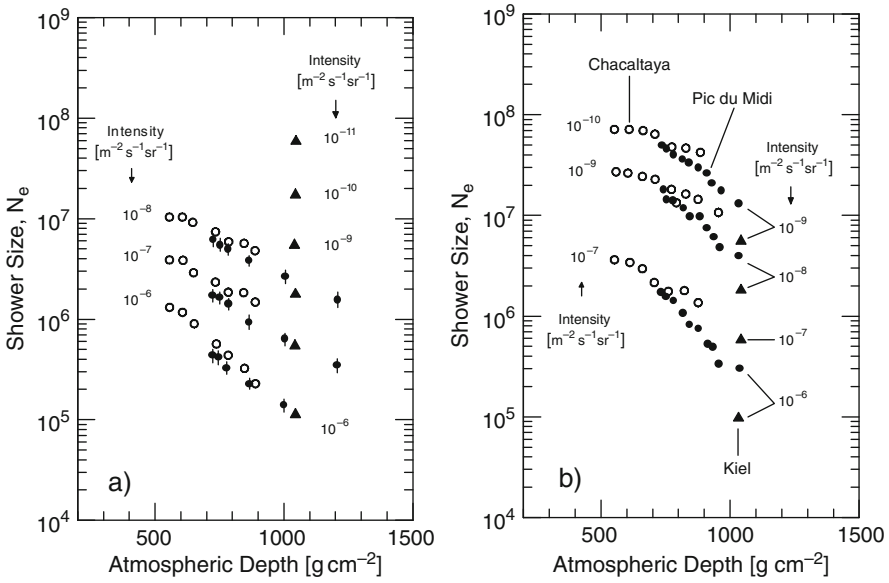

Fig. 6.40 (**a**) Equal intensity distributions from measurements at Tien Shan (3,340 m a.s.l.), • (Kirov et al., 1981) are compared with corresponding distributions from Mt. Chacaltaya, ○ (Bradt et al., 1965). In addition we have included the data from the Moscow group, ▲ (Vernov et al., 1968). (**b**) Equal intensity distributions obtained at Mt. Chacaltaya, ○ (5,230 m a.s.l.) (Bradt et al., 1965) and Pic du Midi, • (2,855 m a.s.l.) (Böhm and Steinmann, 1979). The data points from the measurements at Kiel, ▲ (s.l.) (Samorski, 1973), are also shown for comparison

6.7.3 Data of Equal Intensity Distributions and Primary Mass Effects

In this subsection we present a summary of the most significant contributions concerning the longitudinal development of air showers based on equal intensity distributions. The data are subdivided into three groups: (a) older and (b) recent measurements with unshielded detectors that represent mainly the longitudinal development of the electromagnetic component, since 90% or more of all the particles in well developed showers are electrons (negatrons and positrons) and photons, and (c) measurements with shielded detectors that give access to the longitudinal development of the muon component. Note that most data presented here were derived from *integral* shower size spectra.

(a) Older Measurements with Unshielded Detectors

A large number of measurements had been carried out through the years with arrays located at altitudes ranging from sea level through half of the atmosphere to Mt. Chacaltaya (5,230 m a.s.l.). The most valuable measurements are those that are made at high altitude which can cover a wide range of zenith angles or atmospheric

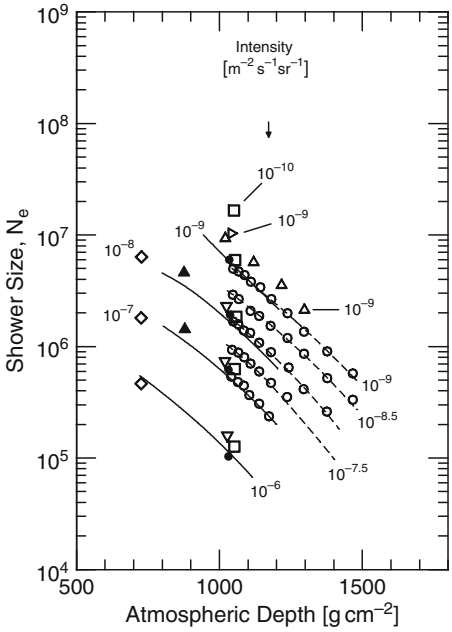

Fig. 6.41 Compilation of equal intensity distributions. The figure includes data from the following authors with installations located at or near sea level: ○ Clay and Gerhardy (1981b), ▽ Catz et al. (1975), ● Samorski (1973), and □ Vernov et al. (1968). In addition we have added the following data from higher altitudes to extend the distributions: △ Hara et al. (1981b) and ◇ Kirov et al. (1981) which represent the data from Akeno (900 m) and Tien Shan (3,340 m), respectively, and some data points from Mt. Chacaltaya, ▷ (5,230 m) Kakimoto et al. (1981) and ▲ Bradt et al. (1965) that were recorded at different zenith angles

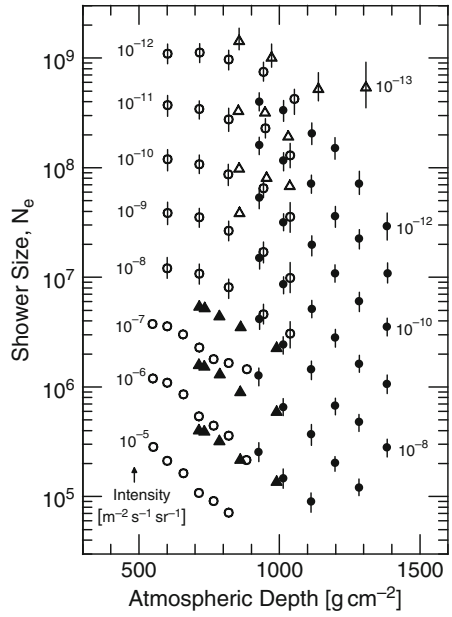

Fig. 6.42 Compilation of more recent equal intensity distributions derived from shower size spectra measured at different zenith angles with the installations at Akeno, ● (900 m) (Nagano et al., 1984b, 1992), Mt. Chacaltaya, ○ (5,230 m) (Kakimoto et al., 1981), and Tien Shan, ▲ (3,340 m) (Kirov et al., 1981). In addition a set of data from Volcano Ranch, △ (1,768 m) (Linsley, 1973) is also shown for comparison (after Nagano et al., 1984b)

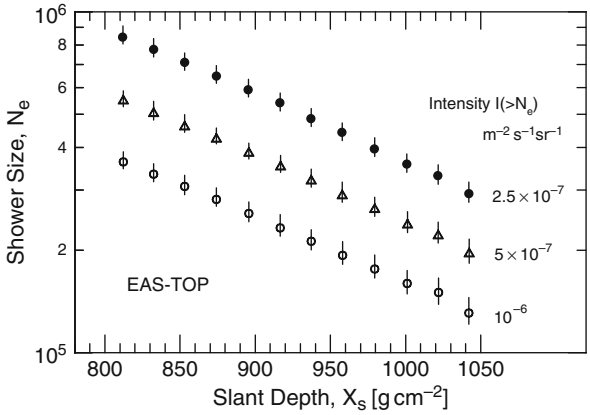

Fig. 6.43 Equal intensity distributions obtained with the EAS-TOP array at Gran Sasso, Italy (2,005 m a.s.l., 810 g cm^{-2}. Shown is the electron number as a function of atmospheric slant depth, X_s, for three different rates of constant intensity, as indicated on the right hand side of the plot (Navarra, 1998)

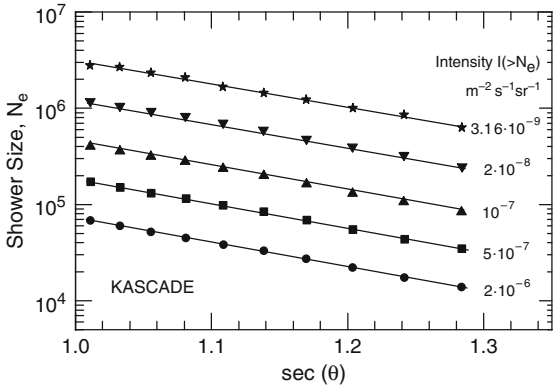

Fig. 6.44 Equal intensity distributions obtained with the KASCADE array at Karlsruhe, Germany (110 m a.s.l., 1,022 g cm^{-2}). Shown is the electron number as a function of sec θ for different values of constant intensity, as indicated on the right hand side of the plot. The *lines* are exponential fits to the data points. Error bars are less than the symbol size. (Antoni et al., 2003)

depths because they allow to study the shower development over a relatively large longitudinal range. Of particular interest are, of course, the data from Chacaltaya because they include measurements on showers near their maximum development and possibly even slightly above the maximum for the most energetic category of vertical events.

At low primary energies the data from individual experiments have small statistical errors, however, when comparing the results from different experiments, significant deviations are evident. These must be due to systematic errors and differences or incompatibilities in the calibration procedures, or to deviations in the detector responses. Similarly, differences also occur when comparing data from an array before and after modification or renewal, without changing the location. With increasing primary energy the statistical errors increase because of the rapidly decreasing event rate; they are very large for the most energetic group of showers.

In Fig. 6.37 we present a compilation of four sets of outstanding early integral equal intensity distributions. The first three sets of data, • △ and ○, are from measurements carried out with two different arrays, one located at El Alto (altitude 4,200 m) (Clark et al., 1963; Hersil et al., 1962), the other at Mt. Chacaltaya

(5,230 m) (Bradt et al., 1965; La Pointe et al., 1968). The data of Clark et al. (1963) and Hersil et al. (1962) are compiled into one set. The results of La Pointe et al. (1968) are referred to by the authors as the improved Chacaltaya data because of improved statistics since the work of Bradt et al. (1965). The high altitude data of Antonov and Ivanenko (1974) and Antonov et al. (1974) are from airplane measurements. They allow a smooth fit with the results of Bradt et al. (1965).

A comparison of the data reported by Aguirre et al. (1979a, b) with simulated development curves, using three different interaction models for the hadron cascade that follow for the secondary particle multiplicity an energy dependence that is proportional to the so-called half-, quarter- and log-law (Mizumoto et al., 1979), is shown in Fig. 6.38. The conclusion from this comparison is that the so-called *half-law* gives the best fit to the experimental data. Close inspection of the two sets of experimental data by Aguirre et al. (1979a, b) and Kakimoto et al. (1981) (Fig. 6.42) reveals that shape and slope of the curves agree well but that there is a difference in absolute rate.

A wealth of data is presented in Fig. 6.39. The compilation includes above all the results from the very large arrays at Yakutsk (Diminstein et al., 1975) and Volcano Ranch (Linsley, 1973). For comparison we have added three distributions from Chacaltaya (Kakimoto et al., 1981) and one from Akeno (Hara et al., 1981b), taken from the previous graph. Data for vertically incident showers at Mt. Norikura (Miyake et al., 1971, 1979) and Agassiz (Clark et al., 1961) are also shown. The Volcano Ranch and Agassiz data include a correction made by Linsley (1973). Disregarding the data for the largest showers from Volcano Ranch which have very large error bars, we conclude that the results from the two large arrays (Volcano Ranch and Yakutsk) agree rather well.

With the exception of the data point for the most inclined set of showers belonging to the most energetic group of primaries recorded at Chacaltaya, which seems to lay too low, and ignoring an apparent but not very serious calibration problem, fair general agreement with respect to the Chacaltaya data must also be acknowledged. The data from the two sets of vertical showers recorded at Mt. Norikura and Agassiz which yield only one point on each equal intensity curve indicate that their calibrations are compatible with the other arrays. This is remarkable since calibration is not a very trivial matter and the configurations of most arrays are very different. The inclined straight line intercepts the estimated loci of maximum shower development (Diminstein et al., 1975, 1977).

Data from the Tien Shan (Kirov et al., 1981) and Pic du Midi installations (Böhm and Steinmann, 1979) are presented in Figs. 6.40a, b, respectively. In both figures we have added corresponding data from Bradt et al. (1965) for comparison. In addition we also show the rates for vertical showers obtained by Vernov et al. (1968) in Fig. 6.40a and those of Samorski (1973) in Fig. 6.40b. A minor calibration difference is evident between the data of Fig. 6.40a. However, the disagreement between the data shown in Fig. 6.40b is more serious.

A rich set of data obtained by Clay and Gerhardy (1981b) at Adelaide (sea level) is shown in Fig. 6.41. For comparison we have added a corresponding set of data from the work of Hara et al. (1981b) recorded at Akeno (900 m a.s.l.). Furthermore

the rates of vertical showers from the installations at Verrières le Buisson (Catz et al., 1975), Kiel (Samorski, 1973) and Moscow (Vernov et al., 1968), all at sea level, and from Tien Shan (3,340 m) (Kirov et al., 1981), together with three points from Chacaltaya, two for inclined showers traversing a column density of about $880\,\mathrm{g\,cm^{-2}}$ (Bradt et al., 1965) and one point at a column density of $1{,}000\,\mathrm{g\,cm^{-2}}$ (Kakimoto et al., 1981), are also included.

Three more recent sets of equal intensity distributions acquired with the arrays at Mt. Chacaltaya, Tien Shan and Akeno, covering a wide range of measurements each and having good statistics, are shown in Fig. 6.42. (Kakimoto et al., 1981; Kirov et al., 1981; Nagano et al., 1984a, b, respectively). The Akeno data are derived from the shower size spectra measured at different zenith angles that are displayed in Fig. 12.21. Apart from a relatively small systematic deviation that is evident in the overlap region of the Akeno and Chacaltaya data, probably due to problems with the absolute calibration, these two sets of data match a smooth curve (not drawn) very well.

The dimensions of the two arrays, Akeno and Chacaltaya, at the time of the experiment were similar and could be classified as being of medium size but the detector density at Akeno was considerably larger, particularly in the central area. An earlier set of data from Akeno, not shown here, obtained by Hara et al. (1981b) agrees very well with those of Nagano et al. (1984b) (see Sect. 12.2). The data of Kirov et al. (1981) are about a factor of two or less lower. Some data points from the Volcano Ranch array (Linsley, 1973) are also shown for comparison.

(b) Recent Measurements with Unshielded Detectors

In Fig. 6.43 we have reproduced three equal intensity distributions that were obtained with the EAS-TOP installation at Gran Sasso, Italy (2,005 m a.s.l., $810\,\mathrm{g\,cm^{-2}}$). Included are showers of size $\leq 10^6$ (Navarra, 1998). Corresponding electron and muon size spectra are displayed and discussed in Sects. 12.2 and 12.3, respectively.

Antoni et al. (2003) have constructed a set of equal (or constant) intensity distributions, shown in Fig. 6.44, using integral *electron* shower size spectra obtained with the KASCADE array at Karlsruhe, using the zenith angular method.[15] They have grouped the data into a total of 10 angular bins covering the range from 0° to 40° (only every other data bin is shown here). The differential size spectra of this experiment are shown in Fig. 12.19. A total of $37 \cdot 10^6$ showers had been analyzed in this experiment which implies very high statistics data and consequently very small errors.

These data had been used to derive the shower rate attenuation length, Λ_{att}, and the particle absorption length, λ_{abs}, as a function of shower size that are presented in Figs. 6.11 and 6.17, respectively. The authors have also carefully studied fluctuations and their influence on the accuracy of the derived quantities. Likewise, they

[15] Note that in this experiment the electron component can be separated from the bulk of all-charged particles.

have analyzed the effect of a mixed primary composition as compared to a pure primary proton beam on the derived observables.

In a recent analysis of data from the small air shower array (MAS) at Mt. Chacaltaya (see Fig. A.12) (Kakimoto et al., 1996), Ogio et al. (2004) have measured integral shower size spectra for different zenith angle intervals that are presented in Fig. 12.24. From these they produced equal intensity distributions that are plotted in Figs. 6.45 and 6.46 together with results from simulations, using CORSIKA with QGSJET for a variety of primary mass mixes, as listed in the captions of the figures.

These authors underline the fact, briefly mentioned before, that equal intensity curves and longitudinal development curves cannot be compared directly. They point out that the zenith angle variations of the size spectra depend on the longitudinal development of the showers in a non-trivial way because hadronic and electromagnetic interactions, both present in hadron initiated showers, behave differently. Moreover, attention must be payed to the detector response with respect to the particle mix in the showers, and to the array layout.

They show that the depth of maximum development of proton initiated showers resulting from their simulations depends not only on the primary energy, as expected, but also on the shape (and slope) of the particular section of the primary energy spectrum. The simulated data show a clear maximum at $N_e \simeq 3 \cdot 10^6$ around $\sim 660\,\mathrm{g\,cm^{-2}}$ at a shower rate of about $10^{-7}\,\mathrm{m^{-2}\,s^{-1}\,sr^{-1}}$, i.e., at a depth that is significantly larger than the vertical overburden of $550\,\mathrm{g\,cm^{-2}}$ (5,230 m a.s.l.). Also in accordance with expectations is the corresponding distribution for iron primaries which shows a maximum at a lesser atmospheric depth, around about $550\,\mathrm{g\,cm^{-2}}$.

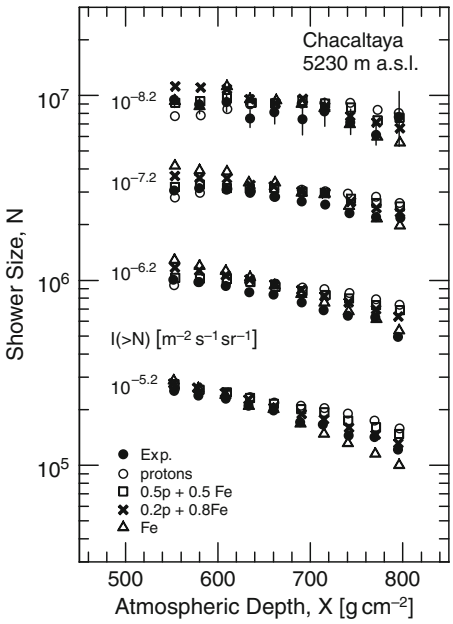

Fig. 6.45 Experimentally determined equal intensity distributions for fixed integral intensity $I(>N)$ [$\mathrm{m^{-2}s^{-1}sr^{-1}}$] as indicated (•), recorded at Mt. Chacaltaya, compared with simulation data (*open symbols*, not normalized) for different primary masses and mass mixes as listed in the plot, obtained with the CORSIKA program using the QGSJET event generator (Ogio et al., 2004)

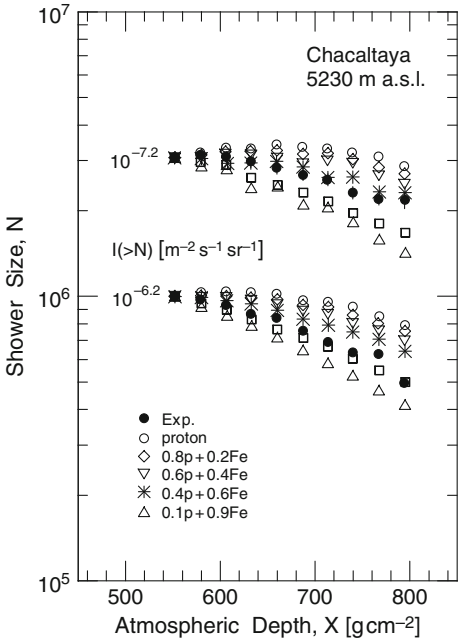

Fig. 6.46 Experimentally determined equal intensity distributions for fixed integral intensity $I(> N)$ [$m^{-2}s^{-1}sr^{-1}$] (•) recorded at Mt. Chacaltaya, compared with simulation data normalized to the measurements at 578 g cm^{-2} (*open symbols*) for protons and different primary mass mixes, as indicated in the plot, obtained with the CORSIKA program using the QGSJET event generator (Ogio et al., 2004)

This behavior is illustrated in Figs. 6.45 and 6.46. On the other hand the experimentally measured distribution for the same shower rate which is also plotted in these figures appears to have its maximum around 550–600 g cm^{-2}, thus suggesting an intermediate primary mass mix with an average mass laying between that of protons and iron nuclei. The other distributions shown for lower and higher event rates follow the expected trends. These results have far reaching consequences for the interpretation of the primary mass, as will be explained in Chaps. 7, 10 and 11.

(c) Measurements with Shielded Detectors, Muon Data

Few researchers only have attempted to acquire data on the longitudinal development of the muon component in air showers and data are scarce. This is probably because of the relatively big instrumental effort that is needed to determine the muon size of a shower with sufficient accuracy. In comparison to regular shower detectors, muon detectors should be larger and must be distributed over a larger area because of the wider spread and much lower density of the muon component in a shower as compared to electrons. In addition adequate shielding must be provided to remove electromagnetic *punch-throughs* that falsify the measurements.

One set of data for very large showers recorded at sea level with the giant SUGAR array at Narrabri (Aus.) (Bell, 1976) is presented in Fig. 6.47. The threshold for vertical muons is 0.75 GeV; it increases with increasing zenith angle θ as

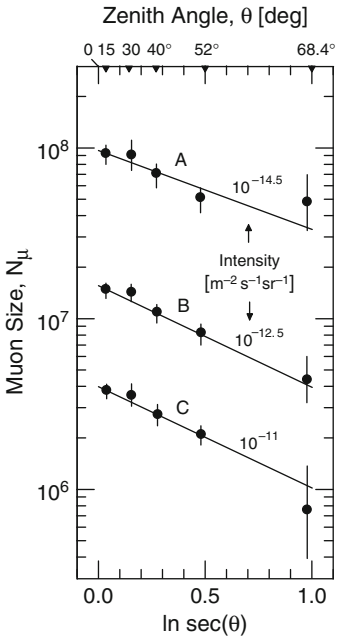

Fig. 6.47 Muon equal intensity distributions derived from integral muon size spectra, ($E_\mu \geq 0.75$ GeV), recorded near sea level with the SUGAR array at Narrabri (Aus.), (Bell, 1976) (see also Bell et al., 1974). Shown is the muon size versus the natural logarithm of sec θ in place of atmospheric depth. The approximate zenith angle is indicated at the *top* of the figure. The resulting muon attenuation lengths for the three fits are as follows: (A) $\lambda_{\mu,\mathrm{abs}} = 1.63 \pm 0.63$; (B) $\lambda_{\mu,\mathrm{abs}} = 1.14 \pm 0.17$; and (C) $\lambda_{\mu,\mathrm{abs}} = 0.99 \pm 0.08$, in units of atmosphere

$0.75 \cdot \sec\theta$ [GeV]. At greater atmospheric depth the constant intensity curves become essentially straight lines when plotted as a function of sec θ. An even better fit to a straight line is obtained when plotted against ln(sec θ), except for the highest intensity group, where sec θ gives a closer fit.

A compilation of the results of several measurements carried out with arrays located at different altitudes and having different muon thresholds is shown in Fig. 6.48. Included are the results from Chacaltaya (Aguirre et al., 1977b, 1979c; Suga et al., 1979), Tien Shan (Kirov et al., 1981), Akeno (Hara, 1981b) and those for vertical showers from the SUGAR array (Bell et al., 1974; Bell, 1976). The muon threshold energies are given in the figure caption. Generally speaking the different data agree fairly well.

We have also added some theoretical longitudinal development curves of the muon size in air showers to the experimental data shown in Fig. 6.48. Curves 1, 2 and 3 are from the work of Mizumoto et al. (1979), mentioned above, that yielded the corresponding curves for electrons, shown in Fig. 6.38. The data include muons of energy ≥ 0.6 GeV and apply to proton initiated showers. Curves 1 and 2 are for a primary energy of $2 \cdot 10^8$ GeV, curve 3 for 10^7 GeV. Curves 4 and 5 are predictions from calculations of Dedenko (1975) for a muon threshold of 0.75 GeV and Capdevielle (1972) for muons of energy ≥ 1 GeV, respectively, both for proton showers of energy 10^8 GeV. Dedenko had been using a CKP model with isobars, Capdevielle a similar quarter law multiplicity model.

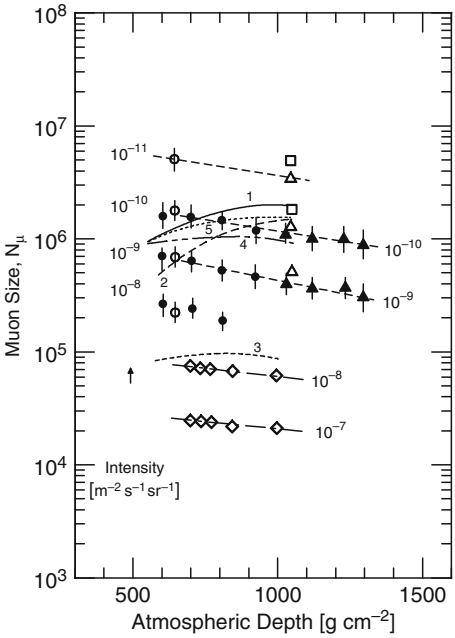

Fig. 6.48 Muon equal intensity distributions from observations made at Mt. Chacaltaya for $E_\mu \geq 0.6$ GeV, •, ○ (Aguirre et al., 1977b, 1979a; Suga et al., 1979); Tien Shan for $E_\mu \geq 5$ GeV, ◇ (Kirov et al., 1981); Akeno for $E_\mu \geq 1$ GeV, ▲ (Hara, 1981b); Narrabri (SUGAR) for $E_\mu \geq 0.75$ GeV, □ and △ (Bell et al., 1974; Bell, 1976). Note that the threshold energies given apply to vertically incident showers, they have to be multiplied by the factor $\sec\theta$, θ being the zenith angle, for inclined showers. The *dashed lines* connect equal intensities. Curves 1, 2 and 3 ($E^{0.5}$, $E^{0.25}$ and ln E models, respectively) are predictions from the same calculations that produced the corresponding curves for the electrons in Fig. 6.38 (curves 1 and 2, $E_0 = 2 \cdot 10^8$ GeV; curve 3, $E_0 = 10^7$ GeV) (Mizumoto et al., 1979). The muon threshold is ≥ 0.6 GeV. Curves 4 and 5 (CKP + isobar and $E^{0.25}$ models, resp.) are after Dedenko (1975) for $E_\mu \geq 0.75$ GeV and Capdevielle (1972) for $E_\mu \geq 1$ GeV, respectively, both for proton showers and $E_0 = 10^8$ GeV

The more recent work of Kakimoto et al. (1981) and Hara et al. (1983b) that were carried out at the Chacaltaya and Akeno sites, respectively, are shown in Fig. 6.49. The Sydney group data from their work at Narrabri are also indicated for comparison.

6.7.4 Mathematical Expressions and Fits

Simulations were carried out by numerous authors to study the longitudinal development of air showers. In this context particular interest was frequently focused on questions related to the properties of the first few very energetic interactions of the primaries in the atmosphere, such as the energy dependence of the cross sections, of the secondary particle multiplicity as well as the elemental composition of the

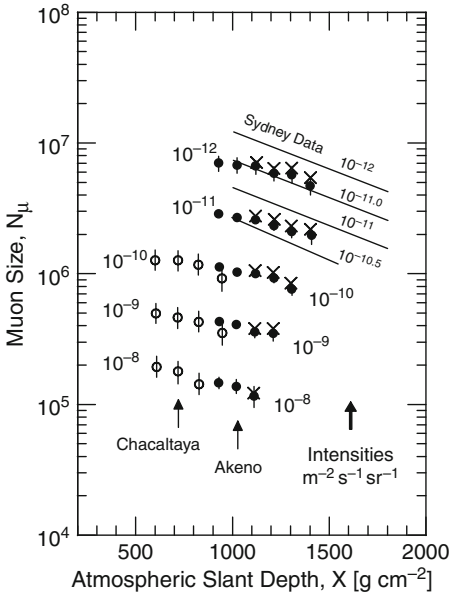

Fig. 6.49 Muon equal intensity distributions from measurements carried out at Mt. Chacaltaya for $E_\mu = 0.6 \cdot \sec\theta$ GeV, ○ (Kakimoto et al., 1981), at Akeno for $E_\mu = 1.0 \cdot \sec\theta$ GeV, •, and × at Akeno for muons of energy ≥ 1 GeV after accounting for the zenith angle absorption effect (Hara et al., 1983b). Also shown for comparison are the Sydney group data (*solid lines*) from Narrabri shown in Fig. 6.47 for muons of energy $E_\mu \geq 0.75 \cdot \sec\theta$ GeV

primary radiation. A brief introduction to the architecture of complex air shower simulation programs and the methods of shower simulation is given in Chap. 20.

Mathematical fits to equal intensity distributions are given by various authors. Bell (1976) finds that the muon data points that are presented in Fig. 6.47 can be approximated fairly well by a straight line of the form

$$\ln N_\mu(\theta) \;=\; \ln N_\mu(0) \;-\; (\sec\theta - 1) \quad , \tag{6.32}$$

or

$$N_\mu(\theta) \;=\; N_\mu(0) \exp\left(\frac{1 \;-\; \sec\theta}{\lambda_{\mu,\mathrm{abs}}}\right) \tag{6.33}$$

where $N_\mu(\theta)$ and $N_\mu(0)$ are the muon sizes of the showers at zenith angles θ and 0, respectively, and $\alpha = 1/\lambda_{\mu,\mathrm{abs}}$ is the absorption length of a muon shower. Values of $\lambda_{\mu,\mathrm{abs}}$ for different intensities are given in the caption of Fig. 6.47.

References

Aglietta, M., et al.: Nucl. Instr. Meth., A 277, p. 23 (1989).
Aglietta, M., et al.: EAS-TOP Collaboration: PICRC, 2, p. 800 (1995).
Aglietta, M., et al.: PICRC, 6, p. 37 (1997).
Aglietta, M., et al.: Nucl. Phys. B (Proc. Suppl.), 75A, p. 222 (1999).
Aguirre, C., et al.: PICRC, 8, p. 208 (1977a).

Aguirre, C., et al.: PICRC, 8, p. 213 (1977b).
Aguirre, C., et al.: PICRC, 8, p. 107 (1979a).
Aguirre, C., et al.: J. Phys. G, 5, p. 139 (1979b).
Aguirre, C., et al.: J. Phys. G, 5, p. 151 (1979c).
Aminjeva, T.P., et al.: Izv. Akad. Nauk SSSR, Ser. Fiz., 33, p. 1508 (1969) (in Russian).
Antoni, T., et al.: Astropart. Phys., 19, p. 703 (2003).
Antonov, Yu.N., et al.: Sov. Phys. JETP, 5, p. 172 (1957).
Antonov, R.A., et al.: PICRC, 2, p. 96 (1960).
Antonov, R.A., et al.: Zh. Eksp. Teor. Fiz., 45, p. 1865 (1963).
Antonov, R.A., et al.: Sov. Phys. JETP, 18, p. 1279 (1964a).
Antonov, R.A., et al.: Sov. Phys. JETP, 19, p. 20 (1964b).
Antonov, R.A., et al.: Trudi, FIAN 26, p. 142 (1964c) (in Russian).
Antonov, R.A., et al.: PICRC, 6, p. 2194 (1971).
Antonov, R.A., et al.: Yadernaya Fiz., 18, p. 554 (1973) (in Russian).
Antonov, R.A.: Yadernaya Fiz., 19, p. 1053 (1974) (in Russian). Sov. J. Nucl. Phys., 19, p. 540 (1974).
Antonov, R.A. and I.P. Ivanenko: Yadernaya Fiz., 19, p. 869 (1974) (in Russian). Sov. J. Nucl. Phys., 19, p. 443 (1974).
Antonov, R.A., et al.: Sov. J. Nucl. Phys., 18, p. 285 (1974).
Antonov, R.A. and I.P. Ivanenko: PICRC, 8, p. 2708 (1975a).
Antonov, R.A. and I.P. Ivanenko: PICRC, 8, p. 2714 (1975b).
Antonov, R.A., et al.: PICRC, 9, p. 3360 (1975).
Antonov, R.A., et al.: PICRC, 8, p. 137 (1977).
Antonov, R.A., et al.: PICRC, 9, p. 258 (1979a).
Antonov, R.A., et al.: PICRC, 9, p. 263 (1979b).
Antonov, R.A., et al.: PICRC, 9, p. 269 (1979c).
Antonov, R.A., et al.: Izv. AN SSSR, Ser. Fiz., 44, p. 547 (Bull. USSR Acad. Sci. Phys. Ser.) (1980).
Antonov, R.A., et al.: PICRC, 6, p. 225 (1981).
Antonov, R.A., et al.: PICRC, 6, p. 52 (1983).
Antonov, R.A., et al.: Yadernaya Fiz., 40, p. 1222 (1984) (in Russian). Sov. J. Nucl. Phys., 40, p. 775 (1984).
Ashton, F., and R.B. Coats: J. Phys., A 1, p. 169 (1968).
Ashton, F., et al.: Acta Phys. Acad. Sci. Hung., 29, S3, p. 327 (1970).
Ashton, F., and A. Parvaresh: PICRC, 8, p. 2719 (1975).
Ashton, F., et al.: PICRC, 8, p. 2831 (1975).
Ashton, F., et al.: PICRC, 13, p. 238 (1979).
Auger, P.: Comptes Rendus Acad. Sci. Paris, 207, p. 907 (1938) (in French).
Auger, P., et al.: Comptes Rendus Acad. Sci. Paris, 206, p. 1721 (1938) (in French).
Auger, P., et al.: J. de Phys. et Radium, 10, p. 39 (1939a) (in French).
Auger, P., et al.: Comptes Rendus Acad. Sci. Paris, 208, p. 1641 (1939b) (in French).
Auger, P.: J. de Phys. et Radium, 1, p. 173 (1940) (in French).
Auger, P., and J. Daudin: Phys. Rev., 61, p. 91 (1942).
Auger, P., and J. Daudin: J. de Phys. et Radium, 6, p. 233 (1945) (in French).
Baltrusaitis, R.M., et al.: Phys. Rev. Lett., 52, p. 1380 (1984).
Bassi, P., et al.: Nuovo Cim., 9, p. 1037 (1952) (in Italian).
Bassi, P., et al.: Phys. Rev., 92, p. 441 (1953).
Bazarov, E.V., et al.: PICRC, 5, p. 32 (1981).
Bell, C.J., et al.: PICRC, 4, p. 2519 (1973).
Bell, C.J., et al.: J. Phys. A, 7, p. 990 (1974).
Bell, C.J.: J. Phys. G, 2, p. 867 (1976).
Bellandi, J., et al.: Nuovo Cim., 111 A, p. 149 (1998).
Bennett, S., et al.: J. Phys. Soc. Jpn., 17, Suppl. A III, p. 196 (1962).
Bergeson, H.E., et al.: PICRC, 8, p. 3059 (1975a).

Bergeson, H.E., et al.: PICRC, 8, p. 3064 (1975b).
Biehl, A.T., et al.: Phys. Rev., 76, p. 914 (1949).
Blatt, J.M.: Phys. Rev., 75, p. 1584 (1949).
Böhm, E., and M. Nagano: J. Phys. A, 6, p. 1262 (1973).
Böhm, E. and E. Steinmann: PICRC, 8, p. 294 (1979).
Bourdeau, M.F., et al.: J. Phys. G, 2, p. 57 (1976).
Bourdeau, M.F., et al.: J. Phys. G, 6, p. 401 (1980).
Bradt, H., et al.: PICRC, 2, p. 715 (1965).
Braun, I., et al.: Adv. Space Res., 43, p. 480 (2008).
Broadbent, D., et al.: Proc. Phys. Soc. A, 63, p. 864 (1950).
Brooke, G., et al.: Proc. Phys. Soc., 83, p. 853 (1964).
Brown, W.W., and A.S. McKay: Phys. Rev., 76, p. 1034 (1949).
Capdevielle, J.N.: Ph.D. Thesis, University of Paris, Paris (1972).
Capdevielle, J.N., and A. Cachon: J. Phys. G, 1, p. 120 (1975).
Capdevielle, J.N., and J. Procureur: J. Phys. G, 10, p. 705 (1984).
Capdevielle, J.N., et al.: The Karlsruhe EAS simulation code CORSIKA, KFK Report 4998 (1992).
Castagnoli, C., et al.: Nuovo Cim., 7, p. 307 (1950).
Catz, Ph., et al.: PICRC, 3, p. 1030 (1971).
Catz, Ph., et al.: PICRC, 12, p. 4329 (1975).
Chapman, S.: Proc. Roy. Soc. (Lond.), 43, p. 483 (1931).
Chilingarian, A., et al.: PICRC, 1, p. 240 (1999).
Chudakov, A.E., et al.: PICRC, 2, p. 50 (1960).
Ciampa, D., et al.: Proc. Astron. Soc. Aust., 6, p. 336 (1986).
Ciampa, D., and R.W. Clay: J. Phys. G, 14, p. 787 (1988).
Citron, A.: Zeitschrift für Naturforschung, 7a, p. 712 (1952).
Citron, A., and G. Stiller: Nuovo Cim., Suppl. 8, p. 675 (1958).
Clark, G.W.: Phys. Rev., 108, p. 450 (1957).
Clark, G., et al.: Nature, 180, p. 353 (1957).
Clark, G., et al.: Nuovo Cim., Suppl. 8, p. 623 (1958).
Clark, G.W., et al.: Phys. Rev., 122, p. 637 (1961).
Clark, G., et al.: PICRC, 4, p. 65 (1963).
Clay, R.W., and P.R. Gerhardy: J. Phys. G, 7, p. L33 (1981a).
Clay, R.W., and P.R. Gerhardy: Nuovo Cim., 4 C, p. 26 (1981b).
Clay, R.W., and P.R. Gerhardy: Aust. J. Phys., 35, p. 59 (1982).
Cocconi, G. and V. Tongiorgi: Phys. Rev., 70, p. 850 (1946).
Cocconi, G., et al.: Phys. Rev., 70, p. 846 (1946).
Cocconi, G.: Phys. Rev., 76, p. 984 (1949a).
Cocconi, G.: Phys. Rev., 75, p. 1074 (1949b).
Cocconi Tongiorgi, V.: Phys. Rev., 76, p. 192 (1949).
Cocconi, G., and V. Cocconi Tongiorgi: Phys. Rev., 76, p. 318 (1949a).
Cocconi, G., and V. Cocconi Tongiorgi: Phys. Rev., 75, p. 1058 (1949b).
Cocconi, G., et al.: Phys. Rev., 75, p. 1063 (1949).
Cocconi, G.: Handbuch der Physik, S. Flügge, ed., Kosmische Strahlung, XLVI/I, p. 215, Springer Verlag, Berlin (1961).
Coxell, H., et al.: Proc. Phys. Soc., 81, p. 604 (1963).
Cranshaw, T.E., et al.: Phil. Mag., 2, p. 891 (1957).
Cranshaw, T.E., et al.: Phil. Mag., 3, p. 811 (1958a).
Cranshaw, T.E., et al.: Nuovo Cim., Suppl. 8, p. 567 (1958b).
Danilova, T.V., et al.: PICRC, 8, p. 129 (1977).
Daudin, J.: J. Phys. et Radium, 6, p. 302 (1945) (in French).
Daudin, J., and A. Daudin: J. de Phys. et Radium, 10, p. 394 (1949) (in French).
Daudin, A., and J. Daudin: J. Atmos. Terr. Phys. 3, p. 245 (1953a) (in French).
Daudin, A., and J. Daudin: Bagneres-de-Bigorre Conf. J. Phys. Radium 14, p. 169 (1953b) (in French).

Daudin, A., et al.: Nuovo Cim., 3, p. 1017 (1956) (in French).
De Beer, J.F., et al.: Phil. Mag., 7, p. 499 (1962).
Dedenko, L.G.: PICRC, 8, p. 2857 (1975).
Delvaille, J., et al.: PICRC, 2, p. 79 (1960).
Deutschmann, M.: Z. Naturforschung, 2a, p.61 (1947).
Diminstein, O.S., et al.: PICRC, 12, p. 4325 (1975).
Diminstein, O.S., et al.: PICRC, 8, p. 154 (1977).
Diminstein, O.S., et al.: PICRC, 8, p. 122 (1979).
Dremin, I.M., et al.: PICRC, 8, p. 314 (1985).
Efimov, N.N.: Ph.D. Thesis, Moscow State University, Moscow (1967).
Euler, H.: Z. Phys., 116, p. 73 (1940).
Farley, F.J.M., and J.R. Storey: Proc. Phys. Soc. A, 67, p. 996 (1954).
Farley, F.J.M., and J.R. Storey: Proc. Phys. Soc. Lond. B, 70, p. 840 (1957).
Firkowski, R., et al.: PICRC, 2, p. 694 (1965).
Firkowski, R., et al.: Inst of Nucl. Research, Warsaw, Poland, Report No. 803/VI-PH (1967).
Fukui, S., et al.: Prog. Theor. Phys. Jpn., 16, p. 1 (1960).
Galbraith, W.: Extensive Air Showers, Butterworths Scientific Publications, London (1958).
Gawin, J., et al.: Proceeding VI. Interamerican Seminar on Cosmic Rays, La Paz, Bolivia 3, p. 723 (1970).
Genannt, R., and H. Pilkuhn: PICRC, 4, p. 2434 (1973).
Goodman, J.A., et al.: Phys. Rev. D, 29, p. 1043 (1982).
Goorevich, L., and L.S. Peak: J. Phys. A, 7, p. 1777 (1974).
Greisen, K.: Progress in Cosmic Ray Physics, North Holland, Amsterdam, Vol. 3, p. 1 (1956).
Greisen, K.: Annual Review of Nuclear Science, Annual Reviews Inc., Palo Alto, CA, 10, p. 63 (1960).
Grieder, P.K.F.: Rivista del Nuovo Cim., 7, p. 1 (1977).
Grieder, P.K.F.: PICRC, 9, p. 184 (1979a).
Grieder, P.K.F.: PICRC, 9, p. 178 (1979b).
Grieder, P.K.F.: Nuovo Cim., 84 A, p. 285 (1984).
Grieder, P.K.F.: Proceedings of Japan – US Seminar on Cosmic Ray Muon and Neutrino Physics/Astrophysics Using Deep Underground/Underwater Detectors, Institute for Cosmic Ray Research, University of Tokyo, Tokyo, p. 183 (1986).
Gross, B: Zeitschr. f. Physik, 83, p. 214 (1933).
Guseva, V.V., et al.: Sov. Phys. JETP, 35(8), p. 577 (1959).
Hara, T., et al.: PICRC, 6, p. 52 (1981a).
Hara, T., et al.: PICRC, 11, p. 250 (1981b).
Hara, T., et al.: Phys. Rev. Lett., 50, p. 2058 (1983a).
Hara, T., et al.: PICRC, 11, p. 281 (1983b).
Hasegawa, H., et al.: J. Phys. Soc. Jpn., 17, Suppl. A-III, p. 189 (1962).
Hayakawa, S.: Cosmic Ray Physics, Wiley – Interscience, New York (1969).
Hazen, W.E., et al.: Phys. Rev., 93, p. 578 (1954).
Heck, D., et al.: Report FZKA 6019, Forschungszentrum Karlsruhe (1998a).
Heck, D., et al.: Report FZKA 6097, Forschungszentrum Karlsruhe (1998b).
Heck, D., and J. Knapp: Extensive Air Shower Simulation with CORSIKA: A User's Guide, Forschungszentrum Karlsruhe, Germany. Version 6.018 October 1 (2002).
Heck, D., and J. Knapp: Extensive Air Shower Simulation with CORSIKA: A User's Guide, Forschungszentrum Karlsruhe, Germany; Version 6.500, March 6, (2006). Updated version, see CORSIKA.
Heintze, J., et al.: Nucl. Instr. Meth., A277, p. 29 (1989a).
Heintze, J., et al.: Proceedings of KFK Workshop, Burg Liebenzell, October (1989b).
Hersil, J., et al.: J. Phys. Soc. Jpn., 17, Suppl. A-III, p. 243 (1962).
Hilberry, N.: Phys. Rev., 60, p. 1 (1941).
Hinotani, K., et al.: PICRC, 4, p. 277 (1963).

Hochart, J.P., et al.: PICRC, 8, p. 2822 (1975).
Hochart, J.P.: Ph. D. Thesis, University of Paris, Paris VI (1976).
Hodson, A.L.: Proc. Phys. Soc. A, 64, p. 1061 (1951).
Hodson, A.L.: Proc. Phys. Soc. A, 65, p. 702 (1952).
Hodson, A.L.: Proc. Phys. Soc. A 66, p. 49 (1953a).
Hodson, A.L.: Proc. Phys. Soc. A 66, p. 65 (1953b).
Honda, M., et al.: Phys. Rev. Lett., 70, p. 525 (1993).
Proceedings, ISVHECRI (International Symposium on Vey High Energy Cosmic Ray Interactions), Paris, France, September 1–6 (2008).
Janossy, L.: Cosmic Rays, Oxford University Press, Oxford (1948).
Janossy, L., et al.: Nuovo Cim., Suppl., VIII, p. 701 (1958).
Kakimoto, F., et al.: PICRC, 11, p. 254 (1981).
Kakimoto, F., et al.: Nucl. Instr. Meth. A, 373, p. 282 (1996).
Kalmykov, N.N., et al.: PICRC, 6, p. 2074 (1971).
Kalmykov, N.N., et al.: PICRC, 4, p. 2633 (1973).
Kalmykov, N.N., et al.: Nucl. Phys. B, (Proc. Suppl.), 52, p. 17 (1997).
Keilhauer, B., et al.: Preprint, FZK, November (2005).
Khristiansen, G.B., et al.: PICRC, 8, p. 148 (1977).
Khristiansen, G.B.: Cosmic Rays of Superhigh Energies. Verlag Karl Thiemig, München (1980).
Kirov, I.N., et al.: PICRC, 2, p. 109 (1981).
Kohlhörster, W., et al.: Naturwissenschaften, 26, p. 576 (1938).
Konishi, E., et al.: J. Phys. G, 17, p. 719 (1991).
Kozlov, V.I., et al.: PICRC, 4, p. 2588 (1973).
Krasilnikov, D.D.: after Bennett, (1962).
Kraybill, H.L.: Phys. Rev., 73, p. 632 (1948).
Kraybill, H.L.: Phys. Rev., 76, p. 1092 (1949).
Kraybill, H.L.: Phys. Rev., 86, p. 590 (1952).
Kraybill, H.L.: Phys. Rev., 93, p. 1360 (1954a).
Kraybill, H.L.: Phys. Rev., 93, p. 1362 (1954b).
Kulikov, G.V., et al.: PICRC, 2, p. 85 (1960).
Landau, L.D., and I.Ya. Pomeranchuck: Dokl. Akad. Nauk. SSSR, 92, p. 535 (1953a).
Landau, L.D., and I.Ya. Pomeranchuck: Dokl. Akad. Nauk. SSSR, 92, p. 735 (1953b).
La Pointe, M., et al.: Can. J. Phys., 46, p. 68 (1968).
Lewis, H.W.: Phys. Rev., 73, p. 1341 (1948).
Linsley, J.: PICRC, 5, p. 3207 (1973).
Linsley, J.: PICRC, 12, p. 89 (1977).
Linsley, J.: PICRC, 6, p. 246 (1981).
Linsley, J.: PICRC, 7, p. 163 (1985).
Loverdo, A., and J. Daudin: J. de Phys. et Radium, 9, p. 134 (1948).
MacLeod, G.R.: Nuovo Cim., 3, p. 118 (1956).
Malos, J.: PICRC, 2, p. 84 (1960).
Maze, R., et al.: Phys. Rev., 73, p. 418 (1948).
Maze, R.: Acta Phys. Acad. Sci. Hung., 29, S3, p. 685 (1970).
McComb, T.J.L., et al.: PICRC, 9, p. 126 (1979a).
McComb, T.J.L., et al.: J. Phys. G, 5, p. 1613 (1979b).
Mielke, H.H., et al.: PICRC, 4, p. 155 (1993).
Mielke, H.H., et al.: J. Phys. G, 20, p. 637 (1994).
Migdal, A.B.: Phys. Rev., 103, p. 1811 (1956).
Millar, D.D.: Proc. Roy. Irish Acad., 54, p. 115 (1951).
Mills, M.M.: Phys. Rev., 74, p. 1555 (1948).
Miyake, S.: Prog. Theor. Phys., 20, p. 844 (1958).
Miyake, S.: J. Phys. Soc. Jpn., 17, Suppl. A-III, p. 291 (1962).
Miyake, S., et al.: Can. J. Phys., 46, p. S21 (1968).

Miyake, S., et al.: PICRC, 7, p. 2748 (1971).
Miyake, S., et al.: PICRC, 13, p. 171 (1979).
Mizumoto, Y., et al.: PICRC, 9, p. 116 (1979).
Molière, G.: Vorträge über Kosmische Strahlung, 2. Auflage (in German), ed. W. Heisenberg, p. 446 Springer, Berlin (1953).
Nagano, M., et al.: J. Phys. G, 10, p. L235 (1984a).
Nagano, M., et al.: J. Phys. G, 10, p. 1295 (1984b).
Nagano, M., et al.: J. Phys. G, 18, p. 423 (1992).
NEEDS Workshop: Informal meeting on "Needs for Accelerator Experiments for the Understanding of High Energy Extensive Air Showers", R. Engel, A. Haungs, L. Jones, and H. Rebel, initiators, April 18–20 (2002). Contributions available as PDF-Files at http://www-ik.fzk.de/ needs/needs_1c.htm
Nikolsky, S.I.: Usp. Fiz. Nauk 135, p. 545 (1981a).
Nikolsky, S.I.: Sov. Phys. Uspekhi 24, p. 925 (1981b).
Nishimura, J.: Handbuch der Physik, 46/2, p. 1, Springer Verlag, Berlin (1967).
Ogio, S., et al.: Astrophys. J., 612, p. 268 (2004).
Ohta, K., et al.: PICRC, 13, p. 177 (1979).
Ostapchenko, S.: Nucl. Phys. B (Proc. Suppl.), 151, p. 143 (2006a).
Ostapchenko, S.: Nucl. Phys. B (Proc. Suppl.), 151, p. 147 (2006b).
Ostapchenko, S.: astro-ph/0610788 (2006c).
Ostapchenko, S.: Phys. Lett. B, 636, p. 40 (2006d).
Pattison, B., et al. (Eds.): Very High Energy Cosmic Ray Interactions. Proceedings of the 12th International Symposium on Very High Energy Cosmic Ray Interactions, Geneva, Switzerland 15–20 July 2002. Nuclear Physics B (Proc. Suppl.) 122 (2003) (487p.).
Popova, L., and J. Wdowczyk: PICRC, 8, p. 2883 (1975).
Procureur, J., et al.: PICRC, 8, p. 2878 (1975).
Rao, M.S.V., and B.V. Sreekantan: Extensive Air Showers, World Scientific, Singapore (1998).
Risse, M., and D. Heck: Astropart. Phys., 20, p. 661 (2004).
Rossi, B.: PICRC, 2, p. 18 (1960).
Sakaki, N.: Ph.D. Thesis, Department of Physics, University of Yamanashi , Kofu, Japan (2003).
Samorski, M.: Dissertation, University of Kiel, Kiel (1973).
Schopper, E.: Handbuch der Physik, S. Flügge, ed., 46/2, p. 372, Springer Verlag, Berlin (1967).
Sciutto, S.J.: http://www.fisica.unlp.edu.ar/auger/aires/ AIRES, version 2.6.0 (2002).
Sciutto, S.J.: PICRC, 7, p. 9 (2005).
Sokolsky, P.: Introduction to Ultrahigh Energy Cosmic Ray Physics, Frontiers in Physics, Vol. 76, Addison-Weskey Publishing Co., New York (1989).
Suga, K., et al.: PICRC, 13, p. 142 (1979).
Suri, A.N.: PICRC, 2, p. 751 (1965).
Tan, Y.H., et al.: ICR-Report 99-82-2, Institute for Cosmic Ray Research, University of Tokyo, Tokyo (1982).
Tennent, R.M.: Proc. Phys. Soc., 92, p. 622 (1967).
Treat, J.E., and K.I. Greisen: Phys. Rev., 74, p. 414 (1948).
Tsai, Y.S.: Rev. Mod. Phys., 46, p. 815 (1974).
Vernov, S.N., et al.: Can. J. Phys., 46, p. 197 (1968).
Wdowczyk, J. and A.W. Wolfendale: Nature 236, p. 29 (1972).
Williams, R.W.: Phys. Rev., 74, p. 1689 (1948).
Wolfendale, A.W.: Cosmic Rays at Ground Level. The Institute of Physics, London (1973).
Yakovlev, V.I.: Nucl. Phys. B (Proc. Suppl.), 122, p. 201 (2003).

Chapter 7
Depth of Shower Maximum and Elongation Rate

Overview We outline the role of the location of the shower maximum in the atmosphere for the interpretation of the primary particle parameters, its dependence on primary energy and mass, and illuminate the different possibilities that air shower observables offer to estimate the depth of the shower maximum. These are explained on the basis of measurements of ground level observables such as atmospheric Cherenkov or fluorescence photons, shower particles, and on combined data from hybrid experiments. The essentials of the associated theoretical work are discussed and results from simulations that are needed for the interpretation of the measurements are summarized. The discussion is kept on a more general level, details are to be found in the chapters that deal with the specific observables (Chaps. 10, 16 and 17). Subsequently, the influence of different atmospheric effects such as seasonally changing density profiles, or the use of different atmospheric models on the height of the shower maximum and the consequences for the interpretation of the data with respect to primary mass are analyzed. The concept of the elongation rate is introduced and its interpretation discussed. Numerous experimental and theoretical data are presented.

7.1 Introduction

The location of the maximum development of an air shower in the atmosphere, the so-called *depth of maximum development*,[1] $X_{\max}$, measured in [g cm^{-2}], or the less frequently used *height of maximum development*, $h_{\max}$ [cm, m or km], depends on the processes that govern the longitudinal development of a shower (see Sect. 6.7). The latter are functions of the energy and mass of the primary, and of the properties of the hadronic and associated electromagnetic interactions involved.

Extensive theoretical studies on the influence of these effects on shower development, based upon computer simulations, had been carried out by many authors through the years (for details see Chaps. 3, 4 and 6). A very comprehensive early

[1] Note that some authors refer to the *depth of shower maximum* as the *elongation*, not to be confused with the *elongation rate*.

P.K.F. Grieder, *Extensive Air Showers,* DOI 10.1007/978-3-540-76941-5_7,

overview concerning the influence of the various processes on the depth of maximum development is given by Bourdeau et al. (1975). In their analysis these authors find that apart from the primary energy the secondary particle multiplicity law and the primary mass affect the average location of the depth of the shower maximum in the atmosphere strongest, followed by variations of the hadronic cross sections and the radiation length,[2] and least by the inelasticity of the interactions (see also Bourdeau et al., 1976).

In view of the remoteness of the location of the shower maximum from the majority of the observers, it is evident that data from common air shower arrays that yield access to this observable are rather indirect and rely heavily on the interpretation via computer simulations. This is not necessarily the case for the few high altitude arrays, e.g., Chacaltaya and Tibet, whose location corresponds approximately to an atmospheric depth where a particular class of showers reaches its maximum development, and for fluorescence detectors that yield more direct information on the longitudinal development of the showers. Large fluctuations, irrespective of their nature, that are typical of air shower development, reduce the relevance of averages and impose the necessity to search for unique signatures of $X_{\max}$ to determine this quantity reliably in individual showers.

The rate of change of the location of shower maximum versus primary energy (or shower size) is called the *elongation rate* (Linsley, 1977). Section 7.8 deals with this quantity in greater detail. The determination of the absolute value of the primary mass, A, is difficult because it is strongly model dependent, however, changes in the composition, ΔA, are quite model independent as long as the elongation rates are equal for different pure compositions.

7.2 Methods of $X_{\max}$ Determination

The following methods have been explored and can in principle be used to determine the location of the depth of the shower maximum in the atmosphere, however, restrictions with respect to shower size may apply to some of them:

- Direct determination
- Equal intensity distributions
- Air Cherenkov Signatures:
  - Cherenkov photon lateral distribution
  - Cherenkov light pulse time profile
  - Cherenkov light front curvature
- Particle Signatures:
  - Particle arrival time distribution
  - Muon core angle

[2] Molecular effects that influence the radiation length in air are discussed in Sect. 4.2.2, 6.2, and in Chap. 21.

- Hybrid Signatures:
  Arrival delay between Cherenkov light and particle fronts
- Air fluorescence tracking of longitudinal shower profile.

Direct and therefore *model independent* determination of the shower maximum is a very difficult task. Such measurements must be carried out in-situ at very high altitude by means of air-borne equipment (balloon or aircraft) and are severely limited for practical reasons (Antonov et al., 1981). Direct observation of upper limits of X_{max} of very large showers is also possible with ground based equipment, using *equal intensity distributions* or *equal intensity cuts* (Sect. 6.7), if the installation is located at high altitude, such as at Chacaltaya or in the Tibet (Bradt et al., 1965; Kakimoto et al., 1981; Xu et al., 2003; Böhm and Steinmann, 1979). One of the difficulties which the experimenter faces when using these two methods is that the shower maximum is a slowly varying function of atmospheric depth (or altitude) and, hence, difficult to localize. In addition, large fluctuations increase the uncertainty of its location.

Direct measurements and the method of equal intensity distributions are described in Sect. 6.7 and will not be discussed here. However, the results obtained with these methods are included in Table 7.3.

As mentioned before, the bulk of the measurements that yield data that are related in one way or another to the depth of the shower maximum are carried out in the lower regions of the atmosphere, where most showers are well beyond their maximum development. Analysis and interpretation of such measurements can only be carried out in conjunction with complex computer simulations of air showers. In the following sections we will briefly outline the various methods, their merits and shortcomings, and present a data summary.

7.3 Air Cherenkov Signatures of X_{max}

7.3.1 General Comments

The basic properties of Cherenkov light emission of extensive air showers are summarized in Chap. 16. Some of the more specific topics discussed here that are related to X_{max} are based on facts and results that are discussed there. In addition Chap. 9 contains important complementary information on temporal features of shower constituents that are relevant for the subjects treated here.

Computer simulations show that atmospheric Cherenkov light measurements at ground level represent a quasi direct method for determining the location of the shower maximum in individual events. After the pioneering work in England, Russia, Australia, and the US (Jelley, 1958; Brennan et al., 1958; Chudakov et al., 1960; Zatsepin and Chudakov, 1962; Boley et al., 1962),[3] Boley (1964) and Fomin

[3] For a more complete list of references concerning the Cherenkov technique and measurements, see Chap. 16.

and Khristiansen (1971, 1972) indicated that the longitudinal development of air showers is mapped in detail into the shape of the optical Cherenkov light pulse, produced mostly by the shower electrons in the atmosphere. The results of these early explorations which illustrate that both the amplitude and time of arrival are closely linked with the cascade development are shown in Fig. 7.1a, b, respectively, for the case of large showers at large distances from the axis (Kalmykov et al., 1971).

The quantities most easily accessible to measurement are the lateral density distribution of the Cherenkov photons at a given observation level and the arrival time and shape of the local Cherenkov light pulse, i.e., its time profile. It should be noted that contrary to particle measurements in showers, Cherenkov light measurements are *not limited by Poissonian statistics* because of the large number of photons that are recorded in each event.

Early work in this field consisted largely of studies of the lateral distribution function of the light intensity at ground level (Smith and Turver, 1973a, b; Efimov

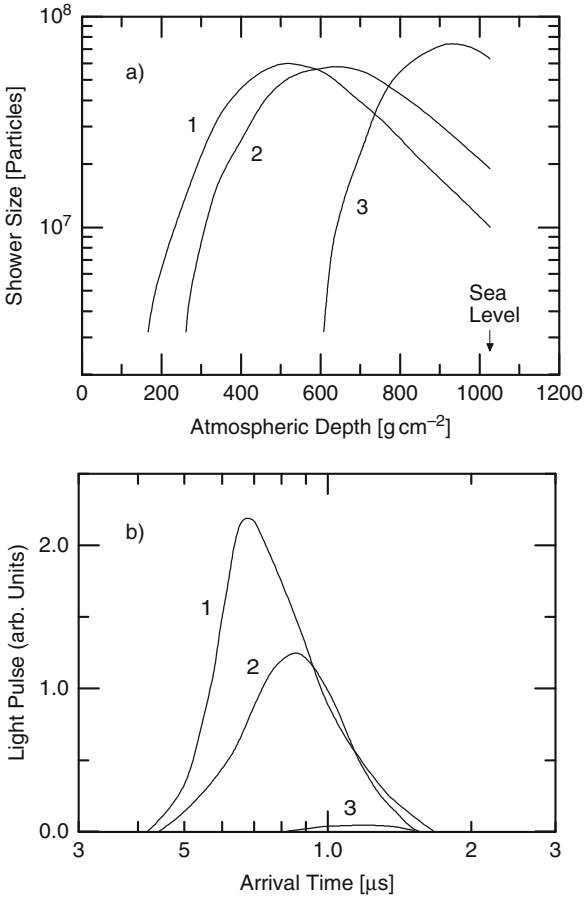

Fig. 7.1 Relation between the longitudinal cascade development of a shower (**a**), and the temporal properties of the Cherenkov light pulse in big showers ($E_0 = 10^8$ GeV) at large distance (2 km) from the shower axis (**b**). The correlation between the location of the cascade maximum and the arrival time and amplitude of the light pulse is evident. (**b**) Illustrates the effect of the superposition of the angle of emission of the Cherenkov light and of the particle scattering angle. Corresponding curves in (**a**) and (**b**) have equal numbers (Kalmykov et al., 1971)

et al., 1973). More recently it was chiefly the Durham, Moscow and Yakutsk groups (Orford et al., 1975a, b; Orford and Turver, 1976; Protheroe, 1977, Thesis, University of Dusham, unpublished; Protheroe and Turver, 1979; Kalmykov et al., 1979; Berezhko et al., 1979) followed by the Adelaide group (Kuhlmann et al., 1977; Kuhlmann and Clay, 1981a, b) who have explored the correlation between the different Cherenkov parameters and the depth of the shower maximum very systematically (for a summary see Turver, 1992).

There are basically *three* not necessarily uncorrelated Cherenkov observables that manifest a unique dependence on the depth of the shower maximum. They comprise

- the Cherenkov photon lateral density distribution function,
- the Cherenkov pulse time profile and arrival time, and
- the Cherenkov light front curvature.

Berezhko et al. (1979) concluded from their work that the combined use of experimental data on the duration of the Cherenkov pulses and on the spatial distribution of Cherenkov light at large distances from the shower axis makes it possible, in principle, to determine uniquely the angular distribution function of the electrons, and the depth of the shower maximum in the atmosphere. McComb and Turver (1981a, 1982a, 1982c) drew essentially the same conclusions from their simulation calculations.

In addition McComb and Turver have found the important result that the transformation of each of the above listed Cherenkov light observables to X_{max} is *single valued* and essentially independent of primary mass, primary energy or model of hadronic interaction for a fixed zenith angle. This is because the Cherenkov observables depend primarily on the broad features of the electron cascade and not on details of the hadronic interactions and cascade from which the former is generated. Of course, X_{max} itself is a function of primary energy and depends on primary mass.

The electron cascade is essentially the product of the neutral pions emerging from the forward fragmentation regions of the first few interactions of the primary in a shower. Up to date this portion of the rapidity distribution remains unexplored by collider experiments but it had been studied in cosmic ray experiments, mainly in emulsion experiments, that offer some guidance for interaction model design.

However, the properties of the fragmentation region are strongly bounded by arguments related to the elasticity of hadronic collisions, to the leading particle effect, and therefore to the attenuation of the cosmic radiation in the atmosphere and the cosmic ray spectrum in the lower portions of the atmosphere, leaving little room for model adjustments there. Major interaction model differences are usually found in the treatment of the central region of rapidity that affect chiefly the abundance of low to medium energy muons in showers and much less the electromagnetic component.

Many of the experimental installations can produce data that allow to apply all three methods mentioned above simultaneously, and many workers in the field have explored them all. Nevertheless, for clarity we will discuss the details of the different methods in separate subsections.

7.3.2 Cherenkov Photon Lateral Distribution Function

In their work based on computer simulations and confirmed by experiment, Smith and Turver (1973a, b) have shown that the *optical Cherenkov photon density* at about 250–300 m from the shower axis varies little with the stage of development of 10^{17} eV proton initiated showers. It is nearly independent of the height at which the shower originates and/or reaches its maximum development. Figure 7.2a illustrates this result. These authors also show that the photon density at this particular core distance reflects accurately the primary particle energy and is a good and cheap measure of primary energy for showers in the energy range 10^{15}–10^{18} eV (see also Egorov et al., 1971; Diminstein et al., 1972; Dyakonov et al., 1973a, b, and Chap. 16).[4] However, the *total flux of Cherenkov photons* in a shower depends on the height of the first interaction, but it is largely independent of shower (interaction) model. The same trend exists for a wide range of primary energies.

Smith and Turver (1973a, b) thus suggested on the basis of their theoretical work that the *ratio R* of the Cherenkov photon density at small and large core distances,

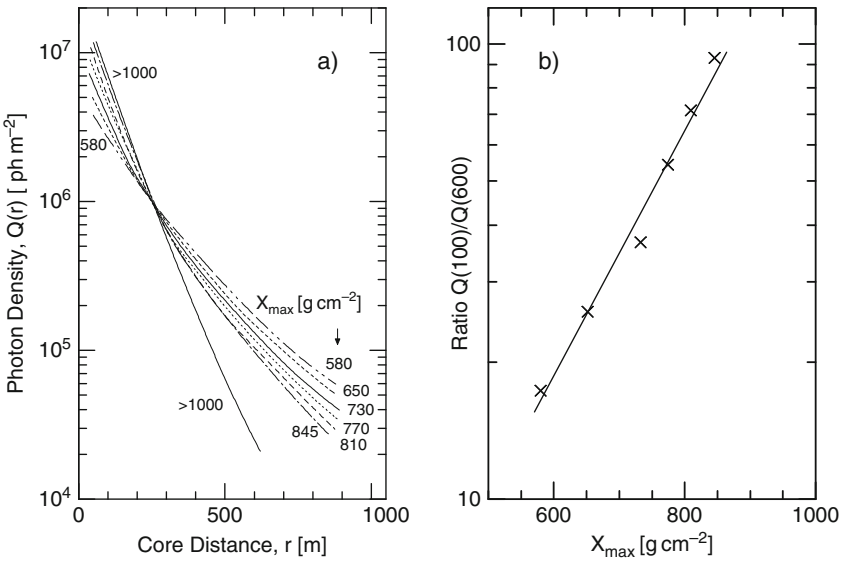

Fig. 7.2 (**a**) Computed lateral distributions of the Cherenkov photon density in the wavelength window between 350 and 500 nm at sea level in vertical 10^{17} eV proton initiated showers, having their maximum of development, X_{max}, at different depths in the atmosphere (Smith and Turver, 1973a, b). (**b**) Ratio, R, of the optical Cherenkov photon density at 100 m, $Q(100)$, to that at 600 m from the shower axis, $Q(600)$, at sea level as a function of depth of maximum development, X_{max}, of the 10^{17} eV showers shown in Fig. 7.2a (Smith and Turver, 1973a, b)

[4] For showers of much lower primary energy a smaller core distance is more suitable. This is discussed in greater detail in Chap. 16.

$Q(r_1)$ and $Q(r_2)$, respectively, may serve as a measure for the stage of development of a shower and may be used to locate the depth, X_{max} [g cm^{-2}] or height, h_{max} [cm, m, km] of maximum development in the atmosphere. Thus,

$$Q(r_1)/Q(r_2) \;=\; R(r_1, r_2) \;=\; f(X_{max}) \tag{7.1}$$

This is illustrated in Fig. 7.2b. They also proposed that this observable may be used as a *primary mass indicator*. This latter topic is discussed in Sect. 11.7 and Chap. 16.

It is important to note that the only assumptions made in these calculations that are relevant for the Cherenkov light component are that the light originating from the position of maximum Cherenkov intensity propagates as a spherical wave front, and that the temporal structure of the light pulses at the observation level maps the longitudinal development.

These assumptions are supported by various arguments (Orford et al., 1975a; Orford and Turver, 1976), by simulations (Hammond et al., 1978; Protheroe and Turver, 1979) and by the fact that deviations of the timing data from spherical fits show no correlation with core distance. Initially these workers have used a power law of the form

$$Q(r) \;=\; C \cdot r^{-\gamma} \;\; [\text{photons m}^{-2}]. \tag{7.2}$$

to describe the *photon lateral density distribution*, $Q(r)$, over the core distance interval 100 m $\leq r \leq$ 500 m at Haverah Park. Theoretical values for the parameters C and γ of Eq. (7.2) to describe the Cherenkov photon lateral density distribution obtained by Hammond et al. (1978) from simulations are listed in Tables 7.1 and 7.2.

Subsequent work confirmed that the *ratio* $R(r_1, r_2)$ between the Cherenkov light densities $Q(r_1)$ and $Q(r_2)$ at core distances r_1 and r_2 is sensitive to the depth of the cascade maximum of a shower, and relatively independent of the model of high energy hadronic interactions. In a very detailed later analysis McComb and Turver (1982a) point out that there is *no unique* core distance where the optical Cherenkov density is totally independent of the depth of maximum for all zenith angles and depends only on primary energy. This is illustrated in Fig. 7.3 for two different zenith angles and observation levels.

Table 7.1 Parameters for Cherenkov lateral distribution function, Eq. (7.2), for sea level (Hammond et al., 1978)

Energy [eV]	Constant	Primary mass		
		p	He	Fe
10^{16}	C	$8.88 \cdot 10^{10}$	$5.84 \cdot 10^{10}$	$1.37 \cdot 10^{10}$
	γ	-2.39	-2.30	-2.07
10^{17}	C	$1.63 \cdot 10^{12}$	$1.34 \cdot 10^{12}$	$4.31 \cdot 10^{11}$
	γ	-2.54	-2.46	-2.24
10^{18}	C	$2.44 \cdot 10^{13}$	$2.03 \cdot 10^{13}$	$9.03 \cdot 10^{12}$
	γ	-2.65	-2.59	-2.41

Table 7.2 Parameters for Cherenkov lateral distribution function, Eq. (7.2), for atmospheric depth 835 g cm^{-2} (Hammond et al., 1978)

Energy [eV]	Constant	Primary mass		
		p	He	Fe
10^{16}	C	$2.15 \cdot 10^{11}$	$1.61 \cdot 10^{11}$	$5.37 \cdot 10^{10}$
	γ	-2.63	-2.54	-2.32
10^{17}	C	$2.69 \cdot 10^{12}$	$2.68 \cdot 10^{13}$	$1.24 \cdot 10^{12}$
	γ	-2.75	-2.68	-2.47
10^{18}	C	$3.24 \cdot 10^{13}$	$3.06 \cdot 10^{13}$	$2.00 \cdot 10^{13}$
	γ	-2.85	-2.80	-2.63

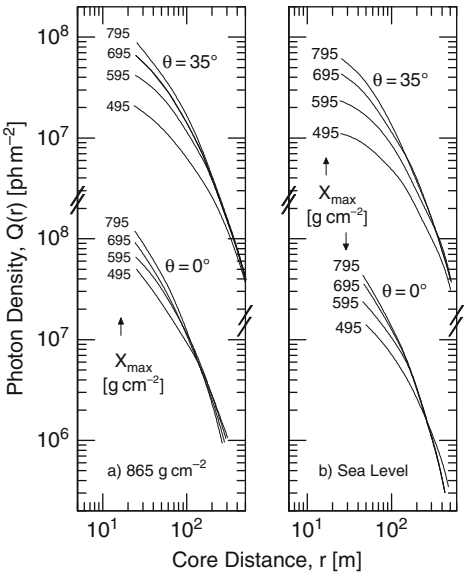

Fig. 7.3 Variation of the optical Cherenkov photon density, $Q(r)$, with core distance, r, for two zenith angles, θ, and different depths of electron cascade maximum, X_{max}, at observation levels of 865 g cm^{-2} (**a**), and at sea level (**b**), in 10^{17} eV showers (McComb and Turver, 1982a)

To improve the accuracy of the method, the distances r_1 and r_2 must be chosen appropriate to each array and shower size range (Chantler et al., 1981; Andam et al., 1982).[5] The essence of this analysis is illustrated in Figs. 7.4 and 7.5 where measured ratios of $Q(r_1)/Q(r_2)$ are included in the plots and compared with simulation results of showers having different heights of maximum development, zenith angles and primary energies.

Theoretical studies, mostly based on simulations, and measurements show that the lateral photon density distribution function broadens with increasing distance between observer and shower maximum. This includes also showers recorded at larger zenith angles and developing at increased distances above the detection area (Hammond et al., 1977a). Hammond et al. (1978) find that the exponent γ of the

[5] Further details concerning the primary energy dependence of the lateral density distribution of Cherenkov photons are given in Chap. 16.

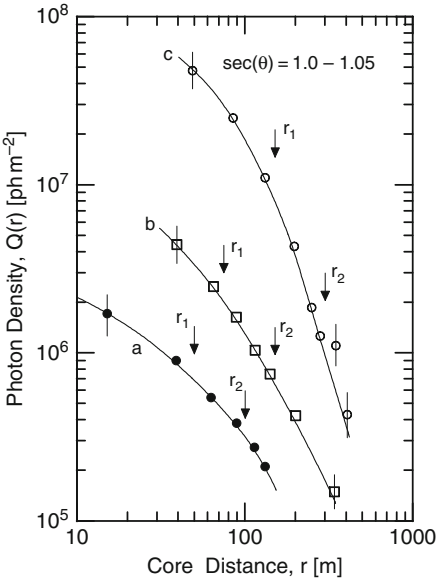

Fig. 7.4 Lateral density distributions of atmospheric Cherenkov light recorded at Dugway in near vertical showers (Chantler et al., 1981; Andam et al., 1982). The three distributions were obtained from showers belonging to three different primary energy groups, E_0, as stated below, using the same array pattern but different array dimensions, i.e., different distances, R, of the outer detectors from the array center, implying different array scale factors. The *curves* represent fits to the function $f(r) = (r + r_0)^{-\eta}$

Curve	E_0 [eV]	R [m]
a	$6.5 \cdot 10^{15}$	100
b	$2.3 \cdot 10^{16}$	200
c	$2.0 \cdot 10^{17}$	400

structure function, Eq. (7.2), depends on the zenith angle θ of the shower and its energy, expressed in terms of the ground parameter, $\rho_{(500)}$ [veμ] (see Sect. 12.5), as follows[6]:

$$\gamma \;=\; 1.20 + 0.27 \cdot \lg(\rho_{(500)}) - 3.55 \cos\theta \tag{7.3}$$

They estimate that γ decreases by approximately 0.32 for every additional 100 g cm^{-2} of atmosphere between the cascade maximum and the observation level. Equation (7.3) implies an increase of γ of 0.27 per one decade of primary energy since $\rho_{(500)}$ increases approximately *linearly* with energy. Its application is restricted to core distances 100 m $\leq r \leq$ 500 m and to zenith angles less than about 60°. The change in the mean depth of shower maximum is about 85 g cm^{-2} per decade of primary energy.

[6] A different expression is given by these authors in an earlier paper (Hammond et al., 1977a).

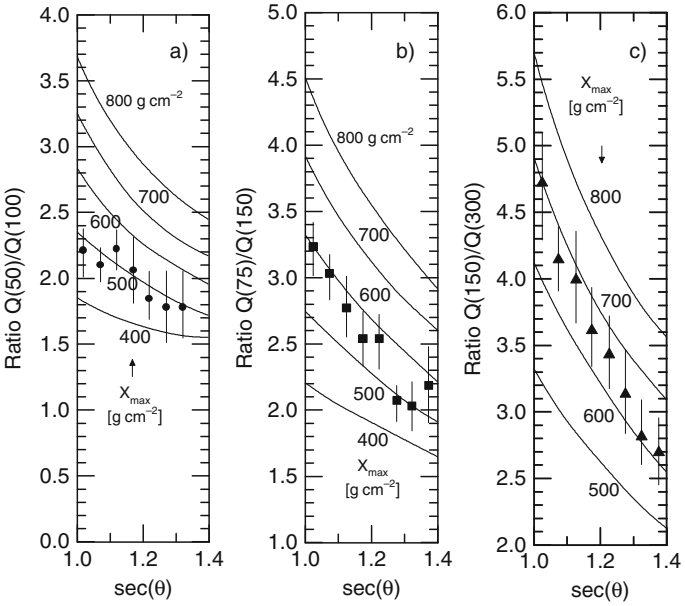

Fig. 7.5 Dependence of the structure function parameter, $R(r_1, r_2) = Q(r_1)/Q(r_2)$, versus $\sec\theta$, θ being the zenith angle (Chantler et al., 1981; Andam et al., 1982). The experimental points are from Dugway for the three sets of data presented in Fig. 7.4. The curves are simulation results of showers with the indicated depths of electron cascade maxima, X_{max}. The three figures, (**a**), (**b**) and (**c**) apply to the following sets of array parameters and primary energy intervals:

(**a**) array size	$100\,\text{m}, 3 \cdot 10^{15} \le E_0 \le 6 \cdot 10^{15}\,\text{eV}$
	$r_1 = 50\,\text{m}, r_2 = 100\,\text{m}$
(**b**) array size	$200\,\text{m}, 6 \cdot 10^{15} \le E_0 \le 2 \cdot 10^{16}\,\text{eV}$
	$r_1 = 75\,\text{m}, r_2 = 150\,\text{m}$
(**c**) array size	$400\,\text{m}, 3 \cdot 10^{16} \le E_0 \le 10^{18}\,\text{eV}$
	$r_1 = 150\,\text{m}, r_2 = 300\,\text{m}$

r_1 and r_2 are the two radii which had been used to fit the lateral distribution function, i.e., $f(r_1 + r_2)^{-\eta}$. The continuous curves are from simulations of McComb and Turver (1981a). For details see text

Andam et al. (1979) and McComb and Turver (1982a, b) have shown that for the primary energy range from about 10^{15} to 10^{18} eV a somewhat better fit to the experimental lateral Cherenkov photon density distribution can be obtained with the expression

$$Q(r) \;=\; A(r + r_0)^{-\eta} \;\; [\text{photons}\,\text{m}^{-2}] \tag{7.4}$$

than with Eq. (7.2), allowing for greater curvature at core distances near 100 m. Here, r is the core distance and r_0 a constant set to 50 m. The fit can be used over the core distance range $100\,\text{m} \le r \le 350\,\text{m}$ and was applied initially to the

Dugway data (vertical atmospheric depth 835 g cm^{-2}).[7] Simulation results indicate a universal relationship between structure function shape and depth of maximum, irrespective of model of high energy interactions. This is attributed to the fact that the Cherenkov lateral distribution represents the integral of the electron cascade through the atmosphere. The finer details of the cascade are lost and only the absolute position of the shower maximum is relevant.

In their later work McComb and Turver (1982a) obtain a decrease of η (Eq. 7.4) of only 0.2–0.25 per 100 g cm^{-2} decrease of X_{max}. In an earlier paper Andam et al. (1979) specify a value for η of about 0.3 per 100 g cm^{-2}. It is evident that the exponent η of Eq. (7.4) has a very similar behavior as γ. The previously mentioned dependence of the exponent of the lateral density distribution function of the optical Cherenkov photons and the depth of the detector with respect to the depth of production of the Cherenkov light is plotted in Fig. 7.6.

The high degree of model independence is illustrated in Fig. 7.7 by the many data points representing individual simulated showers that were obtained for a wide range of models and primary masses, incident at a zenith angle of 35°, observed at sea level. Corresponding data for the other observation level (865 g cm^{-2}) and zenith angles manifest similar model insensitivities, as is shown in Fig. 7.8. The scatter of the data points of individual showers about the respective average curve is slightly less under vertical incidence, and vice versa for more inclined showers.

Energy and zenith angle dependencies of the photon lateral density distribution, $Q(r)$, had also been measured by Kuhlmann et al. (1977, 1981), Kuhlmann and

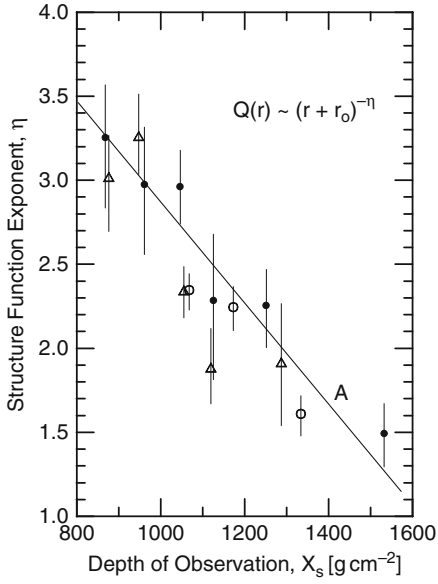

Fig. 7.6 Variation of the optical Cherenkov photon lateral structure function exponent η of Eq. (7.4) as a function of (slant) depth, X_s, of the detector location in the atmosphere. The measurements • apply to small ($\sim 10^{16}$ eV) and △ to large ($\sim 10^{17}$ eV) showers at Dugway (835 g cm^{-2}), and ○ to Haverah Park (1,018 g cm^{-2}), respectively, after adapting the γ of Eq. (7.2) actually determined at Haverah Park to η of Eq. (7.4) (Andam et al., 1979). The measurements include showers with zenith angles $< 60°$

[7] The authors frequently give 865 g cm^{-2} for the atmospheric depth for average zenith angles.

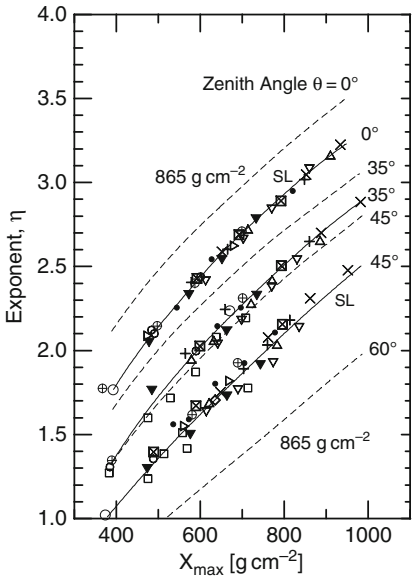

Fig. 7.7 Variation of the optical Cherenkov photon lateral structure function exponent, η, Eq. (7.4), with depth of electron cascade maximum, $X_{\max}$. The *dashed curves* apply to an observation level of 865 g cm^{-2} (Dugway, Utah, USA) and showers of energy $10^{15} \leq E_0 \leq 10^{18}$ eV, the *solid curves* to sea level (Haverah Park, 1,016 g cm^{-2}) and showers of energy $10^{17} \leq E_0 \leq 10^{18}$ eV. The different symbols apply to a wide range of different primary masses and models (McComb and Turver, 1982a)

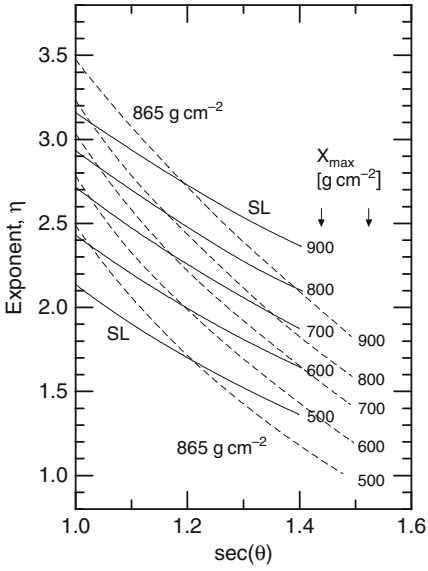

Fig. 7.8 Variation of the optical Cherenkov photon lateral structure function exponent, η, Eq. (7.4), with the secant of the zenith angle, θ. The *dashed curves* apply to an observation level at 865 g cm^{-2} (Dugway, Utah, USA), the *solid curves* to sea level (Haverah Park, 1,016 g cm^{-2}) for the same respective shower energy groups as specified for Fig. 7.7 (McComb and Turver, 1982a)

Clay (1981a, b) and Dawson et al. (1989) on somewhat smaller showers, covering a size range between $2 \cdot 10^5$ and $3 \cdot 10^6$ particles (see Chap. 16). These authors found that the exponential function

$$Q(r) \;=\; C \cdot \exp(-b \cdot r) \;\; [\text{photons m}^{-2}] \tag{7.5}$$

is an adequate representation for the Cherenkov photon lateral density distribution over the core distance range $25\,\text{m} \leq r \leq 125\,\text{m}$. b is a scale parameter and a function of shower development, whereas C is a measure of the flux of Cherenkov photons close to the shower core and depends on shower size. These authors claim that Eq. (7.5) is more suitable at shorter core distances than Eq. (7.4) which seems to be a better approximation at larger distances.

Since the distance between the shower maximum and an observer, L_{max}, depends on the depth (or *slant depth*) of the shower maximum, X_{max}, measured from the top of the atmosphere, and the shower zenith angle, θ, a given height, h_{max}, above the observation level (or distance L_{max} from the observer) may be obtained for a number of combinations of depth of maximum and zenith angle. Kuhlmann and Clay (1981a) conclude from the analysis of the data of Andam et al. (1979), Dyakonov et al. (1973b), Tornabene (1979a), and their own experimental work, that the following relationship between the quantity b, as defined above, and the distance to shower maximum, L_{max} (or height of maximum development, h_{max}), holds,

$$b \cdot L_{max} \;=\; D \;\; . \tag{7.6}$$

For b in units of $[\text{m}^{-1}]$ and L_{max} in [km], D is a constant of the order of 550 $[\text{m}^{-1}\text{km}]$. The relationship between b and L_{max} is shown in Fig. 7.9. Berezhko et al. (1979) find a similar relationship.

Patterson and Hillas (1983) have carried out extensive simulation studies, investigating the relationship between the parameter b and the height of maximum development, L_{max}, and that between the exponent γ and h_{max}. These authors use different values for the exponent γ in Eq. (7.2), one for the near-core region out to 100 m where the distribution is relatively flat, and one for the outer region after the marked change of slope. They have come to the conclusion that near the axis and in smaller showers ($\sim 10^{15}$ eV) the slope of the lateral photon distribution expressed by the ratio $R = Q(50)/Q(150)$, fitted to an exponential graph for $r \sim (30\text{–}50)\,\text{m}$ in the shower plane, shows good sensitivity to L_{max}, particularly in vertical showers (Hartman et al., 1979).

On the other hand, for high energy showers observed at larger core distances ($100\,\text{m} \leq r \leq 500\,\text{m}$), the power law parameter η of Eq. (7.4) is a more suitable quantity to obtain the L_{max} or h_{max}-sensitive lateral distribution shape.

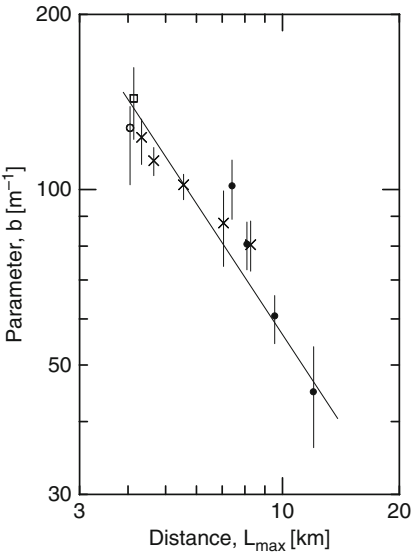

Fig. 7.9 Relationship between parameter b, Eqs. (7.5) and (7.6), of the Cherenkov lateral density distribution function, $Q(r)$, and the *distance* of the shower maximum from the observation site, L_{max}. The data are derived from the following published lateral distributions covering a zenith angular range from 0° to 40° and primary energies from $2 \cdot 10^{13}$ to 10^{18} eV: ○ Andam et al. (1979) as interpreted by Kuhlmann and Clay (1981b); □ Dyakonov et al. (1973b); • Tornabene (1979a) and Kuhlmann and Clay (1981b); × Kuhlmann and Clay (1981b). The *straight line* is an approximation (after Kuhlmann and Clay, 1981a)

7.3.3 Cherenkov Light Pulse Time Profile

It has been suggested by Fomin and Khristiansen (1972) and Efimov et al. (1973) that the *time profile of the Cherenkov light pulse* may offer another rather independent and relatively sensitive approach to determine the position of maximum development, X_{max} or h_{max}, of a shower in the atmosphere.

Theoretical investigations based on computer simulations have revealed that other measures of pulse time structure are also sensitive to cascade development, such as pulse rise time, pulse top time, and pulse fall time (Kalmykov et al., 1975a, b; Orford et al., 1975b; Orford and Turver, 1976; Protheroe and Turver, 1977, 1979; Hammond et al., 1977a, b, 1978; and others). The exact definitions of some of these quantities may vary slightly from author to author, however, the average properties of these observables can be summarized as follows.[8]

[8] For complementary aspects concerning the temporal structure of Cherenkov light pulses the reader is referred to Chaps. 9 and 16.

- *Pulse rise time*, t_r (10–90% pulse amplitude) [ns]:
  The average Cherenkov pulse rise time shows a monotonic variation with the depth of cascade maximum. The rise time reflects the growth of the cascade and shows little sensitivity to the primary energy since the development of the showers (for constant primary mass) changes very slowly, and also because the proton – air cross section changes slowly with energy. Hammond et al. (1977a, 1978) found that typically for a core distance of 350 m the rise time increases by approximately 3 ns per 100 g cm^{-2} increase in depth of maximum for 10^{17} eV showers, and that the dependence on core distance can be expressed as

$$t_r(r) \;=\; A + B \cdot r^{\kappa} \tag{7.7}$$

  where A and B are constants.
- *Pulse top time*, t_t (90–90% pulse amplitude) [ns]:
  The average value of the width of the relatively flat top portion of the light pulse depends principally upon the location of the electron cascade depth of maximum. However, at certain core distances it shows a somewhat non-monotonic behavior.
- *Pulse fall time*, t_f (90–50% pulse amplitude) [ns]:
  The fall time of the Cherenkov light pulse shows little sensitivity with respect to core distance out to about 400 m from the shower axis, and to primary mass. Beyond this distance it manifests a non-monotonic behavior with respect to changes in the location of the depth of shower maximum. This may be due to contributions from scattered light or from light emitted by scattered low energy particles, originating in the lower regions of the atmosphere.

Subsequent studies have revealed that the behavior of the *full width at half maximum (FWHM)*, τ [ns], of the optical Cherenkov pulse versus core distance relates in an unique, monotonic and model independent way to the depth of the electron maximum of a shower. The relationship is somewhat more complicated than that between the photon lateral distribution function, $Q(r)$, and $h_{\max}$. However, the $FWHM$ is an easily accessible practical observables. It characterizes the pulse profile at a given core distance and observation level (Andam et al., 1981c). Typically, in a $5 \cdot 10^{17}$ eV shower the $FWHM$ increases $\sim$10 ns per 100 g cm^{-2} increase in depth of maximum when measured at a core distance of 350 m. Its dependence on core distance is of central importance (Hammond et al., 1978). Figure 7.10 shows a typical lateral distribution of the rise time (Fig. 7.10a) and of the $FWHM$ (Fig. 7.10b), observed in large showers.

To underline the reliability of these results, the authors emphasize that the general average properties of the simulated showers that constitute the sample for the above analysis agree well with measurements.

Further theoretical studies have shown that in the near-core region of large showers the variation of the $FWHM$ with core distance, zenith angle, and depth of maximum development is quite different from that far from the core. At distances of about 70–100 m the $FWHM$ is practically invariant to depth of maximum in $10^{15} - 10^{17}$ eV showers (Thornton and Clay, 1979b; Thornton et al., 1979; Protheroe

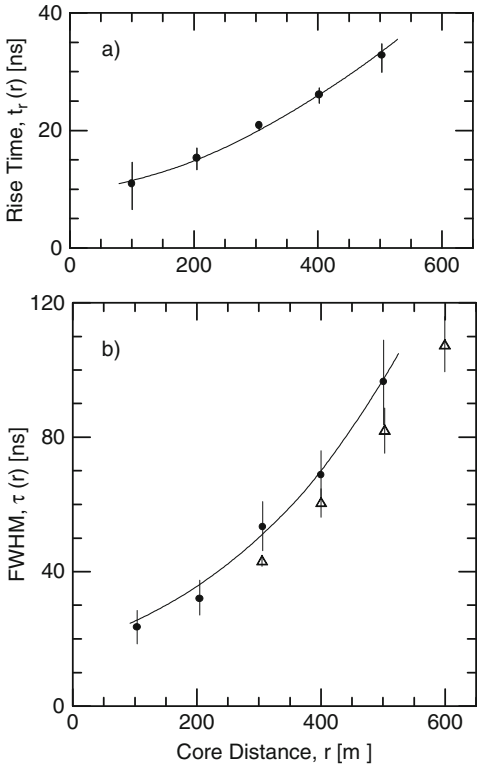

Fig. 7.10 Observed average rise time, $t_r(r)$ (**a**), and average full width at half maximum (FWHM), $\tau(r)$ (**b**), of the atmospheric Cherenkov light pulse as a function of core distance, r, in vertical showers of energy $\sim 2 \cdot 10^{17}$ eV at Haverah Park, • (no bandwidth correction) and Yakutsk, △ (with bandwidth correction). The mathematical expressions for the fits (*solid lines*), and their zenith angle and primary energy dependencies (in units of [veμ]) are given in Sect. 7.10, Eqs. (7.30), (7.31), (7.32) and 7.33, (Hammond et al., 1978; Kalmykov et al., 1976, unpublished)

and Turver, 1979; Galkin et al., 1979). However, beyond this zone the sensitivity increases with distance faster than $r^{1.0}$ (Thornton and Clay, 1981). The rise time manifests similar properties with respect to the depth of the electron maximum.

For strongly inclined showers ($\theta \sim 60^\circ$) the region of insensitivity increases out to ~200 m. On the other hand, at small core distances ($r \leq 100$ m) a broadening of the $FWHM$ is indicated in showers with $X_{\max} \leq 700\,\mathrm{g\,cm^{-2}}$. Thus a *reversal* of the normal pulse behavior is observed close to the core for large zenith angles. Moreover, at core distances <100 m the $FWHM$ increases slowly with increasing zenith angle and decreases with increasing depth of maximum. Figures 7.11a and 7.12 show the influence of different parameters on the relationship between the $FWHM$ and $X_{\max}$ in simulated showers ($10^{15} \leq E_0 \leq 10^{18}$ eV) (McComb and Turver, 1982a).

In their analysis of experimental data from Dugway and Haverah Park, in conjunction with simulated data, Andam et al. (1979) note that changes in the $FWHM$ at 300 m due to changes in the position of the depth of maximum in vertical showers could *not* be related to changes in the position of depth of maximum due to changes in zenith angle, in spite of proper accounting for differences in system bandwidth. It appears that the $FWHM$ recorded at Dugway for showers incident at 38° is less

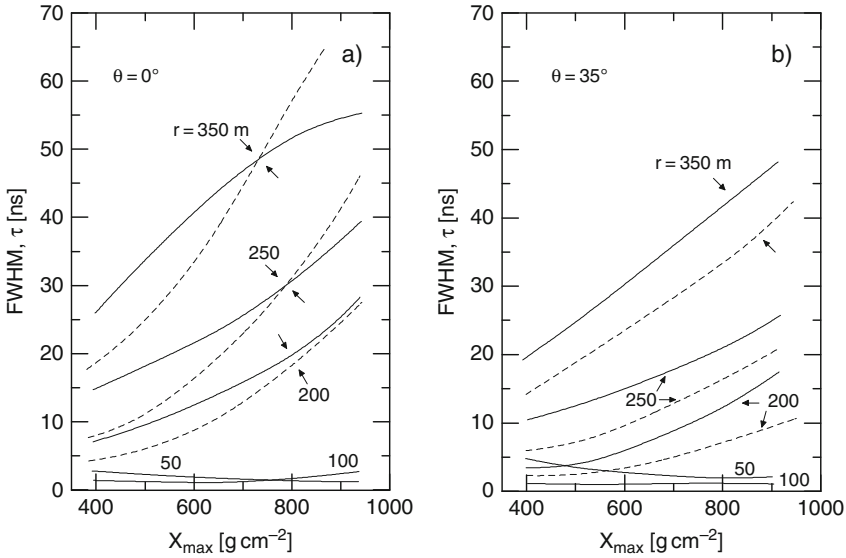

Fig. 7.11 (**a**) Variation of the full width at half maximum (*FWHM*), of the atmospheric Cherenkov light pulse width, τ, in nanoseconds for a recording system with infinite bandwidth as a function of depth of the electron cascade maximum, X_{max}, at the indicated core distances, r, for a zenith angle of $\theta = 0°$. The *solid curves* apply to an observation level of 865 g cm^{-2}, the *dashed curves* to sea level (McComb and Turver, 1982a). (**b**) Variation of the full width at half maximum (*FWHM*), of the atmospheric Cherenkov light pulse width, τ, in nanoseconds for a recording system with infinite bandwidth as a function of depth of the electron cascade maximum, X_{max}, at the indicated core distances, r, for a zenith angle of $\theta = 35°$. The solid curves apply to an observation level of 865 g cm^{-2}, the dashed curves to sea level (McComb and Turver, 1982a)

than for comparable vertical showers at Haverah Park, having traversed the same amount of atmosphere *but not the same track length*.

The response (bandwidth) of the recording system is an important factor and must be accounted for to obtain the actual pulse profile. It is usually assumed that the full width half maxima of *system response and signal add in quadrature* (Protheroe et al., 1975; Kalmykov et al., 1978a, b; Thronton et al., 1979). Problems that may arise as a consequence of such corrections are discussed by Patterson and Hillas (1983).

Distortions of the Cherenkov light pulse at small distances from the shower axis due to the curvature of the particle front, the finite thickness of the particle disk, and the influence of the Cherenkov emission angle had been studied by Galkin et al. (1981). Similar theoretical studies for inclined showers and *geomagnetic effects*, had been carried out by Orford et al. (1975b), Makarov et al. (1981) and Chantler et al. (1982). Detailed Cherenkov pulse shape studies in smaller showers ($5 \cdot 10^5 \leq N_e \leq 5 \cdot 10^6$) were also carried out by Thornton et al. (1979).

It had been pointed out in Sect. 7.3.2 above that the radial photon density distribution function broadens with increasing zenith angle and increasing distance

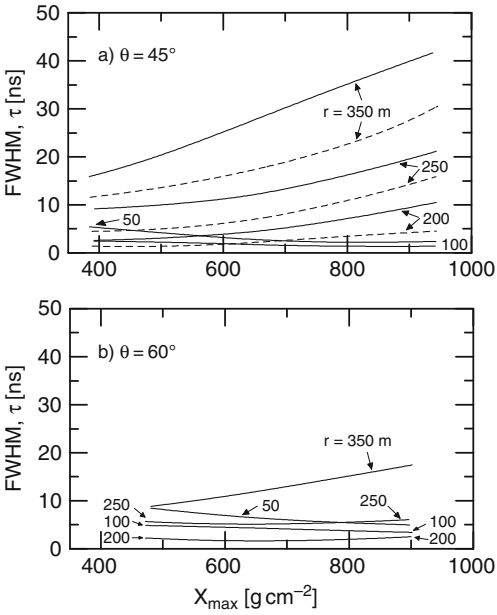

Fig. 7.12 Variation of the full width at half maximum (*FWHM*), of the atmospheric Cherenkov light pulse width, τ, in nanoseconds for a recording system with infinite bandwidth as a function of depth of the electron cascade maximum, $X_{\max}$, at the indicated core distances, r, for zenith angles of $\theta = 45^\circ$ (**a**), and $\theta = 60^\circ$ (**b**). The *solid curves* apply to an observation level of 865 g cm^{-2}, the *dashed curves* to sea level (McComb and Turver, 1982a)

between observer and shower maximum. On the other hand, it had been found that the pulse time profile spreads in time with decreasing distance between observer and shower maximum (Figs. 7.11a and 7.12) and increasing core distance (Protheroe and Turver, 1979; McComb and Turver, 1982a, b). Thus, broad lateral distributions are correlated with narrow light pulses, and vice versa.

For normalization of the $FWHM$ to a specific core distance two expressions are frequently used to relate the functional form of the dependence of the $FWHM$, expressed as $\tau(r)$, to core distance, r, namely

$$\tau(r) \;=\; C \cdot r^{\delta} \tag{7.8}$$

or

$$\tau(r) \;=\; A + B \cdot r^{\alpha} \;\; . \tag{7.9}$$

The exponents δ and α depend on primary energy or shower size range and therefore on the height of maximum development, $h_{\max}$. Kalmykov et al. (1978b, 1979) estimated δ using the expression

$$\delta \;\simeq\; 1.5 + 0.1\;[\mathrm{km}^{-1}] \cdot h_{\max}\;\;[\mathrm{km}] \;\; . \tag{7.10}$$

Different values are used by different authors. The Adelaide and Moscow groups seem to prefer the simple power law, Eq. (7.8) (Thornton and Clay, 1979a), whereas the Durham group gives preference to Eq. (7.9), inserting $\alpha = 2.0$ (Hammond

et al. 1978). In their earlier work Hammond et al. (1977a) used for the radial dependence of the rise time $t_r(r)$ and the FWHM $\tau(r)$ basically the same exponential expression but with different constants

At higher energies and larger core distances, showers seem to be flatter in structure and/or broader in time than an extrapolation of the theory would predict.

On the basis of their simulations Berezhko et al. (1979) and Kalmykov et al. (1978b, 1979) have derived the following relationship between the $FWHM$ measured at a distance of 300 m from the shower axis, $\tau(300)$ [ns], and $h_{\max}$ [km] with respect to ground level, measured along the shower axis, for $E_0 > 2 \cdot 10^{16}$ eV,

$$h_{\max}(\tau) \;=\; 17.05 - 9.17 \lg(\tau(300)) \;\; [\mathrm{km}] \;\; . \tag{7.11}$$

The derivation of this expression implies a power law relationship of the form given in Eq. (7.8), with $1.7 \leq \delta \leq 2.4$ for core distances in the range $300\,\mathrm{m} \leq r \leq 600\,\mathrm{m}$. Kalmykov et al. (1979) also offer an expression for $h_{\max}(\tau)$ for any core distance r (see Sect. 7.10).

Similarly, Liebing et al. (1984) constructed an expression to fit their simulations which includes in addition a pulse recording system response of 5 ns for $FWHM$ measurements, τ [ns], at a distance from the shower axis of 200 m,

$$h_{\max}(\tau) \;=\; 52.5 - 71.0 \lg(\tau) + 25.2 \cdot (\lg(\tau))^2 \;\; [\mathrm{km}] \;\; . \tag{7.12}$$

These authors give for the standard deviation of the residuals $\Delta h \sim 0.3$ km or $\sim 15\,\mathrm{g\,cm^{-2}}$.

Thornton and Clay, (1978a,1978b,1979b) have determined $X_{\max}$ with the help of $FWHM$ measurements of air Cherenkov pulses. Their results are given in Table 7.3. The rapid change of $X_{\max}$ around a few times 10^{15} eV primary energy found by these authors (Thornton and Clay, 1979b) and criticized by Orford and Turver (1980) had been revised in a later publication (Thornton and Clay, 1980), where a larger value for the scale height of the atmosphere, 8 km in place of 7.1 km, had been used.

$$\tau(r) \;=\; A \cdot \exp(B \cdot r) \;\propto\; t_r(r) \;\; . \tag{7.13}$$

7.3.4 *Cherenkov Light Front Curvature, Arrival Time and Event Reconstruction*

Detailed computer simulations, outlined in Chap. 16 (Protheroe et al., 1975; Orford et al., 1975a; Orford and Turver, 1976; Protheroe and Turver, 1977; Hammond et al., 1977a, b, 1978), have shown that the light recorded in specific small regions of the Cherenkov pulse of a shower by an array of widely spaced ground based detectors originates from a small volume in the sky. Moreover, different parts of

Table 7.3 Depth of shower maximum, X_{max} early epoch

Energy [eV]	X_{max} [g cm^{-2}]	References
$1.6 \cdot 10^{15}$	450±50	Antonov et al. (1975, 1979)[a]
$1.73 \cdot 10^{15}$	452±14	Thornton and Clay (1979b, 1980)[a]
$2.4 \cdot 10^{15}$	487±22	Chantler et al. (1981)
$4 \cdot 10^{15}$	530±14	Thornton and Clay (1979b, 1980)[a]
$4.25 \cdot 10^{15}$	490±8	Thornton and Clay (1979b, 1980)[a]
$5 \cdot 10^{15}$	509±11	Chantler et al. (1981)
$8.5 \cdot 10^{15}$	553±12	Chantler et al. (1981)
$1.35 \cdot 10^{16}$	568±8	Thornton and Clay (1979b, 1980)[a]
$2.9 \cdot 10^{16}$	564±13	Chantler et al. (1981)
$3 \cdot 10^{16}$	675±15	Kalmykov et al. (1979)[a]
$3.35 \cdot 10^{16}$	628±16	Thornton and Clay (1979b, 1980)[a]
$5 \cdot 10^{16}$	533±16	Andam et al. (1981a)
$6.7 \cdot 10^{16}$	675±15	Kalmykov et al. (1979)[a]
$7 \cdot 10^{16}$	649±17	Chantler et al. (1981)
$\geq 10^{17}$	684±30	Gibson et al. (1981)
$1.2 \cdot 10^{17}$	706±36	Thornton and Clay (1979b, 1980)[a]
$1.7 \cdot 10^{17}$	730±35	Andam et al. (1981b)
$2 \cdot 10^{17}$	681±20	Protheroe and Turver (1979)[a]
$2.2 \cdot 10^{17}$	708±59	Chantler et al. (1981)
$3 \cdot 10^{17}$	710±20	McComb and Turver (1982c)
$5.6 \cdot 10^{17}$	712±20	Kalmykov et al. (1979)[a]
10^{18}	775±20	McComb and Turver (1982c)
$2 \cdot 10^{18}$	766±30	Protheroe and Turver (1979)[a]
10^{19}	840±20	McComb and Turver (1982c)
10^{19}	805±30	Walker and Watson (1981a)[a]
10^{20}	845±80	Walker and Watson (1981a)

[a] After a compilation by Linsley and Watson (1981b).

locally observed Cherenkov pulses can be related directly to distinct longitudinal portions (and sub-cascades) of the electromagnetic cascade of a shower. It has also been shown that despite refractive index and other effects the earliest observed light originates high in the atmosphere and *the pulse shape is clearly a direct measure of the cascade development*. On the other hand, light close to the shower core originates low in the atmosphere (Orford and Turver, 1976).

Thus, the possibility exists to locate the origin in the atmosphere of the light recorded at various positions in the light pulse and so to estimate directly the electron cascade longitudinal development as well as the depth or height of maximum development of a shower. The early light in a pulse at large core distances originates at large distance above the array and seems to be produced *quasi-isotropically*, i.e., the light is produced by scattered electrons in a volume which is small relative to the extent of the detector array.

The propagation of the light from a particular source element produces a spherical light front at large distances. Thus, the Cherenkov light front of a shower at ground level is of approximately spherical shape. Hence, its time lag with respect to the tangent plane of the shower front that intersects the shower axis perpendicularly, increases with increasing radius from the shower axis.

By considering the very beginning of the leading edge of the light pulse, say at the 3%, 5% or 10% level, one can construct the *extreme light front* of the shower. Protheroe and Turver (1977) computed the depth of origin of this portion of the light by fitting a parabolic approximation of a spherical front to the arrival times at distances in the range between 100 and 500 m from the core, a procedure well justified when inspecting the data they have used (Fig. 7.13a). According to these authors the deviation from sphericity arises due to the increasing importance of Coulomb scattering of the electrons, to light produced low in the atmosphere, and because of bandwidth limitations of the recording system.

The chief advantage of using Cherenkov light in place of particles to determine the shower front curvature is that the copiously present optical photons in a Cherenkov pulse sample are *not subject to statistical limitations* as are the few electrons or sparse muons, even in very large detectors, and permit therefore accurate measurements. Of course, detector and system response (rise time, delay, etc.,) must be properly accounted for. A best fit to the arrival times of the first light at

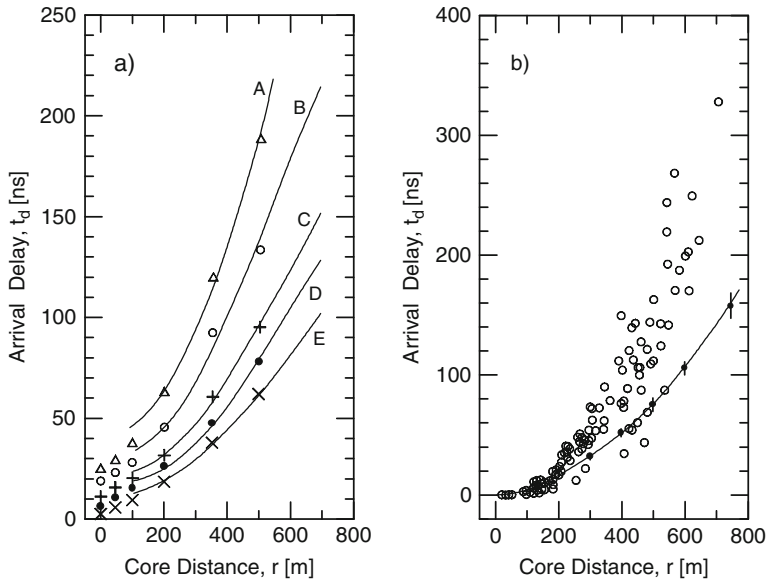

Fig. 7.13 (**a**) Arrival delay, t_d, of the Cherenkov light with respect to the tangent plane of the shower front at the axis in simulated 10^{17} eV showers as a function of core distance, r. The delays are given for the 10% (×); 50% (•) and 90% (+) levels of the full height on the rising edge, and for the 90% (○) and 50% (△) levels on the falling edge. The *solid lines* are parabolic fits for core distances 100–500 m. (Hammond et al., 1978). (**b**) Arrival delay, t_d, versus core distance , r, of the Cherenkov light front with respect to the shower front tangent plane. The *open circles*, ○, represent measurements made on 19 showers at Haverah Park ($5 \cdot 10^{16} \leq E_0 \leq 10^{18}$ eV). The large scatter of the points is due to inaccuracies in the core position determination with the water Cherenkov counters. The mean radius of curvature of the fitted sphere is 2.99 km (Orford et al., 1975a). The *full circles*, •, with error bars and the *curve* are the result of a simulation of Protheroe et al. (1975) for primary protons of 10^{17} eV

the different detectors can be obtained by simultaneously optimizing the spherical radius of curvature, and zenith and azimuthal angles that specify the arrival direction of the shower. A representative example is given in Fig. 7.13b that includes 19 showers with six or seven optical measurements per shower. It should be pointed out that for precise work the *geomagnetic effects* on the shower must be considered (Orford et al., 1975a).

For each fractional amplitude level (10, 50, 90%, etc.) of the rising and/or falling edge (90, 50%, etc.) of any locally observed Cherenkov light pulse one can construct the arrival delay with respect to the tangent plane as a function of core distance. Curves fitted to loci of equal fractional amplitude yield parabolas (Fig. 7.13a) that can be approximated by circles out to moderate distances from the shower core, whose radii can be computed. Figure 7.14 shows the corresponding results (Protheroe and Turver, 1977; Hammond et al., 1978).

From a large sample of simulated showers one can show the relationship between the depth of maximum development, $X_{\max}$, and the arrival delay of the different fractional amplitude levels of the Cherenkov pulse with respect to the tangent plane. This is illustrated in Fig. 7.15. Conversely one can estimate the depth of shower maximum from the radius of curvature of the Cherenkov light front of a shower.

Hammond et al. (1977a) find that for vertical showers with a primary energy of $3 \cdot 10^{17}$ eV the radius of curvature of the Cherenkov light front is 7.25 ± 0.5 km. This corresponds to a depth of origin of the light at the 10% level of 360 ± 30 g cm^{-2} for showers of all zenith angles.

From precision measurements of the arrival time of the 100% level of the Cherenkov photon pulse of large showers ($\simeq 10^{17}$ eV) recorded by several detectors spread over a radial distance between 100 and 500 m from the shower axis at Dugway, Andam et al. (1979) have determined the radius of curvature of the Cherenkov

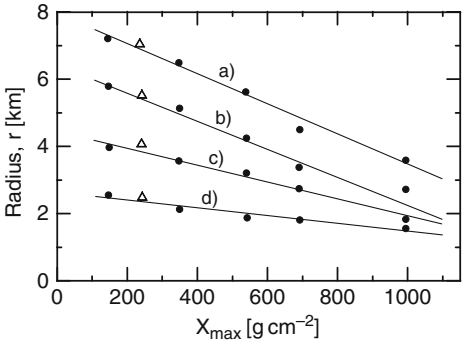

Fig. 7.14 Radii of curvature of Cherenkov shower fronts, r, obtained for loci of different delays, t_d, on the rising and falling edges of the Cherenkov pulse with respect to the pulse beginning as a function of depth of maximum development, $X_{\max}$, of 10^{17} eV proton, •, and iron, △, initiated showers. (a) 10%, (b) 50%, (c) 95% level of full pulse height on rising edge, (d) 10% level on falling edge. (Protheroe et al., 1975)

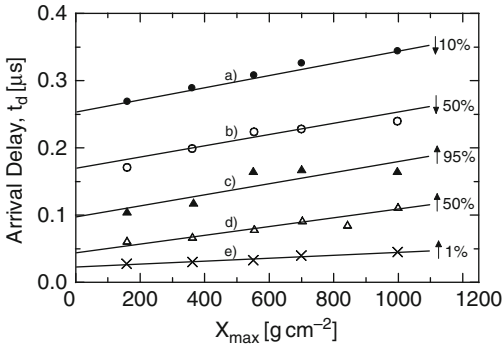

Fig. 7.15 Dependence of the delay, t_d, of loci of different amplitude levels, in percent, of the Cherenkov pulse, determined at 400 m from the shower core, on depth of shower maximum development, X_{max}, in the atmosphere. (Protheroe et al., 1975). ↑ refer to the rising edge, ↓ to the falling edge of the pulse

light front. From these data they find the origin of the Cherenkov light cascade maximum to be at a depth of 609±47 g cm^{-2}. Hammond et al. (1978) obtained for similar showers recorded at Haverah Park which is located 180 g cm^{-2} deeper in the atmosphere a depth of cascade maximum of 608±14 g cm^{-2}. The two results indicate that the two sets of showers develop alike in the atmosphere but, when viewed from different observation levels, they have correspondingly different heights of origin above the respective ground levels, as expected.

For a given primary mass the curvature of the shower front depends on primary energy since the longitudinal development and therefore the depth of shower maximum, too, depend on primary energy. Several authors have explored the relationship between the shower front curvature and the primary energy and mass. Likewise there is a correlation between the curvature and the exponent of the lateral density distribution of the Cherenkov photons. These topics are discussed in greater detail in conjunction with primary energy and mass determination in Sects. 11.6 and 11.7, respectively, and in Chap. 16.

7.3.5 Fluctuations of Air Cherenkov Light Flux

We have pointed out before that fluctuations observed in air Cherenkov measurements are not of the same nature as in the case of particle measurements, where low particle densities cause statistical fluctuations, since the photon number recorded by Cherenkov counters in showers is usually quite large, unless measurements are made at large distances from the shower axis, at the fringes of the showers. Simulations have revealed that fluctuations observed by atmospheric Cherenkov detectors are directly related to fluctuations in the number of shower particles and thus to fluctuations in the shower development. The latter manifest themselves in many ways, in particular in fluctuations of the height of the first interaction and of the height of maximum development of the showers. However, the location of the shower maximum is also strongly dependent on the nature of the primary and can in fact be used to estimate its mass. This topic is discussed in Sect. 11.7.

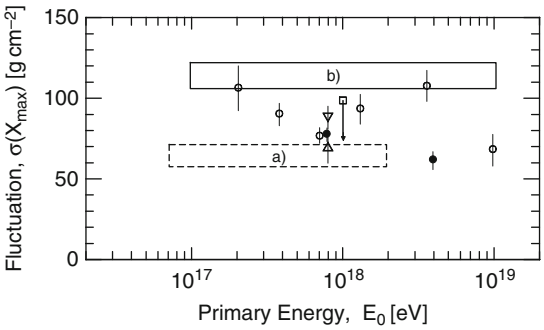

Fig. 7.16 Fluctuations of the depth of shower maximum, $\sigma(X_{\max})$, resulting from atmospheric Cherenkov and particle measurements in large showers versus primary energy. The compilation is due to Dyakonov et al. (1981b). The different points and fields represent the following data. Air Cherenkov measurements: • Dyakonov et al. (1981b); (a) Berezhko et al. (1979). Particle measurements: ○ Lapikens et al. (1979); □ Craig et al. (1979); △ Barrett et al. (1977) and Barrett et al. (1978), ▽ same, corrected; (b) England et al. (1979)

Several authors have studied the fluctuations of the atmospheric Cherenkov component in common showers (Hammond et al., 1978; Berezhko et al., 1979; Protheroe and Turver, 1979; Dyakonov et al., 1981b). A compilation by Dyakonov et al. (1981b) is shown in Fig. 7.16. Browning and Turver (1975) have also made a careful analysis of fluctuations in low energy (100 GeV) gamma ray initiated showers. They point out that in such showers the geomagnetic deflection, too, can cause significant fluctuations, particularly if the opening angle of the Cherenkov detector is small.

7.4 Particle Signatures of $X_{\max}$

In analogy to the previously discussed air Cherenkov techniques, numerous efforts were made to link particle observables of air showers with the height of their origin or the depth of maximum development of a shower in the atmosphere, in an attempt to identify the nature of the primary initiating a shower. The observables considered include the particle lateral distribution function (Craig et al., 1979), the spatial angle with respect to the direction of the shower axis (De Beer et al., 1962, 1970; Earnshaw et al., 1968, 1973; Dixon et al., 1973; Gibson et al., 1979), the distortion of the muon charge ratio at a given position with respect to the axis direction and location as a consequence of the geomagnetic deflection (see Sect. 8.8) (Somogyi, 1966), equal intensity distributions (see Sect. 6.7), fluctuations (Walker and Watson, 1974; Lapikens, 1977; Craig et al., 1979), as well as local temporal features of the particles (Turver 1975a, b; Walker and Watson, 1981a).

However, because of the much lower density of particles in the shower front as compared to the photon density in the Cherenkov burst of a shower, Poissonian statistics applies. Consequently particle observables are much more subject

to fluctuations than Cherenkov signatures. It is therefore more difficult to extract the desired information. In the following we present a brief summary of the essential results of this work.

7.4.1 Particle Lateral Distribution

Computer simulations show that the lateral distribution function of the particle front of air showers manifests similar properties with respect to the longitudinal shower development and the location of the depth of maximum as the atmospheric Cherenkov light burst. This is not surprising as the two are intimately related.

Several experimental investigations were carried out to study the correlation between the lateral distribution function, the depth of maximum development of a shower and the primary energy for different groups of particles. The latter were mostly selected by the type of detector that was used to sample the showers, i.e., unshielded scintillators, shielded muon counters employing flash tubes or scintillators, and Haverah Park type deep-water Cherenkov detectors (Edge et al., 1977; Lapikens et al., 1979). The evaluation and interpretation of the data hinges completely on detailed computer simulations.

In Fig. 7.17 we show the result of this work as it had been summarized by McComb and Turver (1981b, 1982b) who carried out extensive and very detailed simulations. Details concerning the lateral distribution of shower particles are discussed in Chap. 8.

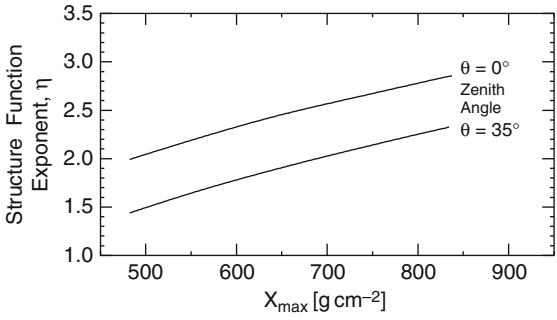

Fig. 7.17 Predicted variation of the deep-water Cherenkov detector lateral distribution structure function exponent, η, as used at Haverah Park in the Durham-Leeds experiment, with depth of shower maximum development for two zenith angles in showers of primary energy $\simeq 10^{18}$ eV (McComb and Turver, 1981b, 1982b)

7.4.2 Muon Core Angle

Gibson et al. (1979, 1981) and McComb and Turver (1981b, 1982c) have found a correlation between the core angle of muons and the depth of the electron cascade maximum with the help of scaling model based computer simulations. They have measured the core angle of muons of energy ≥ 0.3 GeV and ≥ 0.8 GeV in showers of primary energy $\geq 10^{17}$ eV at Haverah Park and noted that there is good agreement

with their predictions for low energy muons. However, these authors point out that the correlation may be model dependent and hinges on the validity of scaling in the fragmentation region, which is sufficiently fulfilled. They find for the depth of the shower maximum a value of $684 \pm 30\,\mathrm{g\,cm^{-2}}$ for the above specified primary energy. Their work is summarized in Fig. 7.18. Muon production height, core angle and tracking are discussed in detail in Chap. 14.

7.4.3 Particle Arrival Time Profile

It can be shown on the basis of computer simulations that *temporal features* such as the particle arrival time profile (*rise time, FWHM, fall time*) are correlated with the longitudinal development of a shower and the location of the depth of shower maximum, in analogy to the corresponding Cherenkov light observables, discussed above. (For the more basic temporal properties of the particles associated with air showers and a discussion of the early work the reader is referred to Chap. 9).

In a pioneering effort, Turver (1975a, b) has carried out theoretical and experimental studies of the correlation of the time spread between the arrival of the first muon and 50% of the muons of the shower disk in deep-water Cherenkov detectors at fixed distances from the shower axis at Haverah Park, t_{d50}, with the depth of maximum development of the showers. Likewise, he investigated the correlation between t_{d50} and the height of the first interaction of the primary in the atmosphere, h_0. The results of this work are illustrated in Fig. 7.19.

Whereas the depth of maximum development shows a fairly good correlation with the t_{d50} time the correlation with h_0 is rather poor. This is not too astonishing since $X_{\max}$ is several interaction mean free paths deeper in the atmosphere, allowing large initial fluctuations in h_0 to be smoothed out by the subsequent interactions and the large secondary particle multiplicities contributing to the flux of neutral pions that are chiefly responsible for producing the electromagnetic cascade.

These efforts eventually established the rise time of the pulse of appropriately positioned particle detectors as a useful and unambiguous observable to estimate the depth of maximum development of a shower in the atmosphere. Figure 7.20 taken from McComb and Turver (1981b, 1982b) shows the sensitivity of such measurements for 305 MeV muons at 300 m from the shower axis in showers having a primary energy $\geq 10^{17}$ eV (see also Blake et al., 1979b).

Some authors have gone one step further and have attempted to estimate the mass of the primary initiating the shower from the $X_{\max}$ distribution. Others have tried to fix in an iterative process relevant properties and parameters of ultrahigh energy interaction models (Suga et al., 1979). These topics are discussed in Sect. 11.7.

It has been shown by several authors (Lapikens et al., 1979; Linsley and Watson, 1981b) that the *depth of maximum development* and the *elongation rate* of air showers can be determined unambiguously from measurements of the rise time of the pulse produced by the particle front of showers in large particle detectors, such as the Haverah Park deep-water Cherenkov detectors.

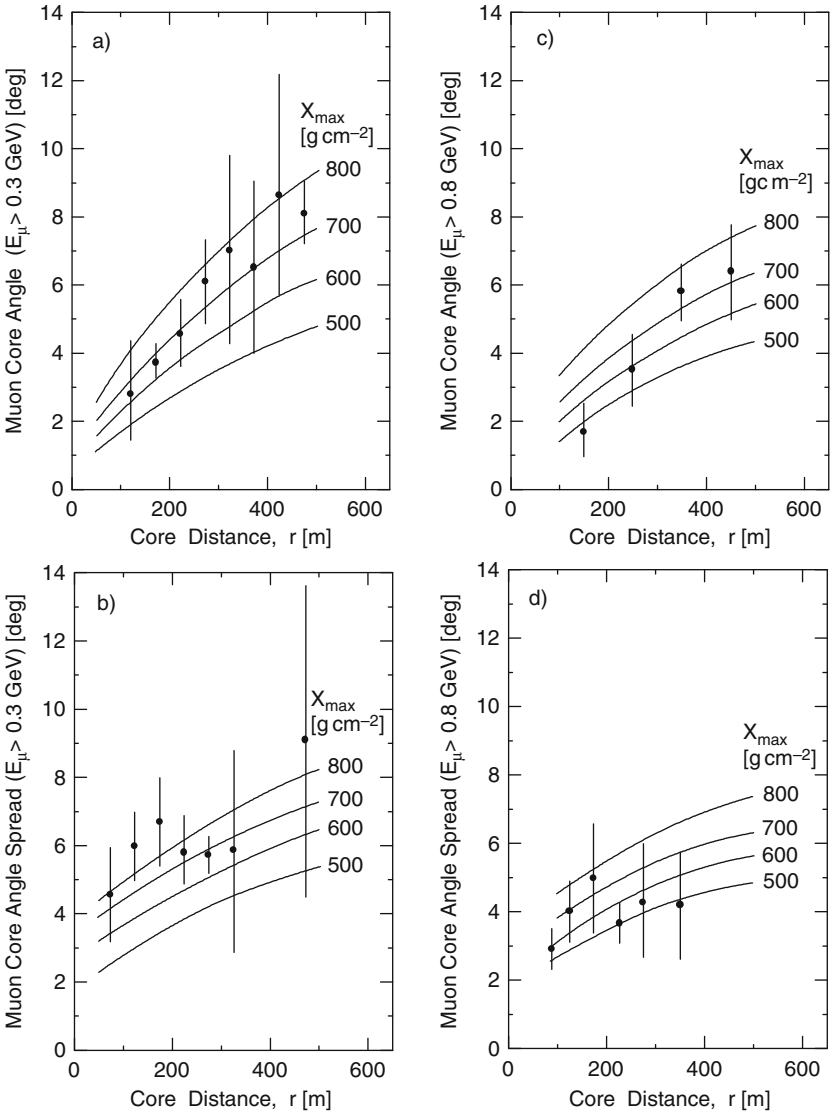

Fig. 7.18 Variation of the muon core angle (**a** and **c**) and spread of the muon core angle (**b** and **d**) (defined as the standard deviation of the muon core angle distribution) as a function of core distance for muons of energies $\geq$0.3 GeV (**a** and **b**) and $\geq$0.8 GeV (**c** and **d**), measured at Haverah Park in $\sim 3 \cdot 10^{17}$ eV showers, •. The *curves* labeled X_{max} 500–800 g cm^{-2} show the predicted dependence of the muon core angle – core distance distribution on depth of shower maximum development (after Gibson et al., 1981)

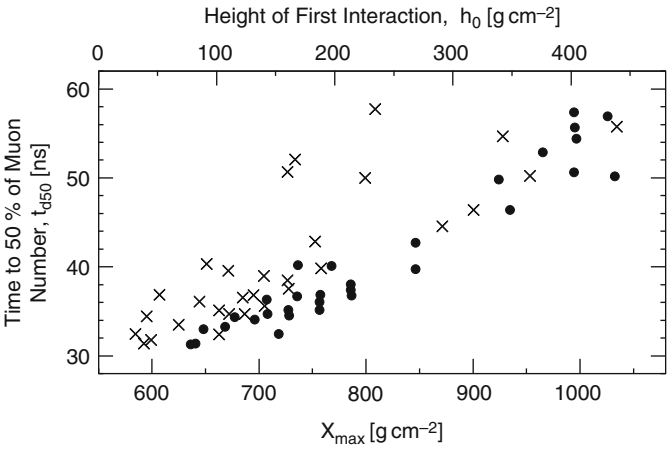

Fig. 7.19 Predicted correlation of the time spread (delay) between the arrival of the first muon and the arrival of 50% of the muons of a shower in a deep-water Cherenkov detector at a core distance of 500 m in 10^{17}–10^{18} eV showers at Haverah Park, t_{d50}, with the height of the first interaction of the primary in the atmosphere, h_0 (×), and the depth of maximum development of the shower, X_{max} (•) (Turver, 1975a, b)

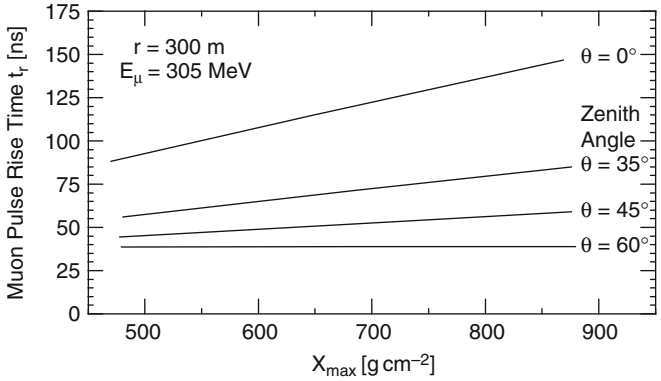

Fig. 7.20 Predicted correlation of the rise time, t_r (10–70% levels) of the muon pulse of the University of Nottingham muon detector used at Haverah Park (Blake et al., 1979b) with the depth of maximum development of the showers for muons of energy $E_\mu = 305$ MeV recorded at a core distance of $r = 300$ m and different zenith angles in 10^{17}–10^{18} eV showers (McComb and Turver, 1981b, 1982b)

7.4.4 Particle Shower Front Curvature

Linsley and Scarsi (1962) were among the first to apply temporal features of shower particles, particularly at large core distances (200–1,500 m), to *estimate the height at which certain processes begin to occur and cease to occur*, to use their words. Using muons and electrons they determined the particle front curvature. They found

that the particle surfaces are approximately spherical with the center of curvature located at an atmospheric depth of $320 \pm 70\,\mathrm{g\,cm^{-2}}$ for the muons, and that the average median surface for the electrons has a radius of curvature of about 1 km at a distance of 450 m from the core.

The radius of curvature of the electron front increases at greater core distances. Measurements indicate that the center of a spherically shaped electron front may be as high as $320\,\mathrm{g\,cm^{-2}}$. The authors point out that muons are less suitable for this kind of measurement because of their relatively small number, yielding large fluctuations and inaccurate results. They have also made the first estimation of the height of maximum development of individual showers.

Andam et al. (1979) and Chantler et al. (1983) have carried out similar work at the Dugway site ($865\,\mathrm{g\,cm^{-2}}$) and at Haverah Park (s.l.).

7.4.5 *Fluctuations of the Particle Shower Front*

Another individual shower signature for comparing the state of the longitudinal development among different showers in the atmosphere is the fluctuation of the rise time of the pulse produced by the particle front in a fast detector, such as a scintillation or deep-water Cherenkov detector, located at a distance of a few hundred meters from the shower core (Walker and Watson, 1974; Edge, 1976; Barrett et al., 1975a, b, 1977). The interpretation of these data, however, requires detailed simulations.

Barrett et al. (1977) found the following fit to describe the observed rise time, which they defined as $t_{(0.5)}$, the time required by the signal to rise from the 10% to the 50% level,

$$t_{(0.5)} \;=\; 51.8 + \left(0.281\cos\theta \;+\; 0.02\lg\left(\frac{E_0}{10^{17}}\right) - 0.118\right) r \;\;[\mathrm{ns}] \qquad (7.14)$$

where θ is the zenith angle, E_0 the primary energy [eV] and r the distance from the shower axis [m]. The energy determination of the showers is based on the density $\rho(500)$ or $\rho(600)$, described in Sects. 8.5, 10.2, and 11.6, respectively (Lapikens, 1977). For a typical shower of $5 \cdot 10^{17}$ eV having a zenith angle of 20° a rise time of 132 ± 3 ns[9] had been measured at a core distance of 500 m and the following expression is given for the standard deviation of the fluctuations (Barrett et al., 1977).

$$\sigma_f(t_{0.5}, r) \;=\; 2.24 - 1.29 \cdot 10^{-2} r + 6.26 \cdot 10^{-5} r^2 \;\;[\mathrm{ns}]\;. \qquad (7.15)$$

[9] Due to the finite size of the $34\,\mathrm{m^2}$ detectors an additional uncertainty of about 10 ns must be added.

For a given kind of showers incident at small deviations from the vertical the *depth of shower development*, D [g cm^{-2}], as it was called by Barrett et al. (1977), meaning the *depth* [g cm^{-2}] (or *height* [m]) of the *first interaction* in the atmosphere, is nearly independent of zenith angle, θ.[10] Therefore the reduction of the rise time $t_{(0.5)}$ [ns] of the shower front with increasing zenith angle arises because of the increase in the path length, X [g cm^{-2}], along the inclined shower axis between the location of the shower maximum and the observer. Thus,

$$X + D \;=\; X_0 \cdot \sec\theta \;\;, \tag{7.16}$$

where X_0 is the vertical depth of the atmosphere at the observation level and $X_0 \cdot \sec\theta$ is called the slant depth, X_s.

From this relationship one finds easily that

$$\frac{\partial t_{(0.5)}}{\partial X} \;=\; \frac{\partial t_{(0.5)}}{\partial \cos\theta} \cdot \frac{\partial \cos\theta}{\partial X} \;\;. \tag{7.17}$$

If one identifies $\sigma_f(t_{(0.5)})$ with $\partial t_{(0.5)}$ and $\sigma(X)$ with ∂X, fluctuations in X can be estimated. It follows from the results of Barrett et al. (1977) that at a core distance of 500 m

$$\frac{\partial t_{(0.5)}}{\partial X} \;=\; -(0.138 \pm 0.004)\cos^2\theta \;\; [\text{ns g}^{-1}\,\text{cm}^2] \;\;. \tag{7.18}$$

The work summarized here yields for the fluctuation in X of the degree of shower development the weighted mean value of $\sigma(X) = 88 \pm 7$ g cm^{-2}. This value must be considered an overestimation because of the large number of late developing showers of much lower primary energy. Considering this fact and the absorption length of showers together with the spectral slope, Barrett et al. (1977) obtain for the fluctuation of the depth of maximum the value $\sigma(X_{\max}) = 70 \pm 10$ g cm^{-2} for showers of mean energy $8{\cdot}10^{17}$ eV. The results of this work are plotted in Fig. 7.16 together with comparative date from other particle and some atmospheric Cherenkov measurements discussed earlier.

From the fluctuations $\sigma(X)$ only one cannot directly identify the depth of maximum development of a shower, $X_{\max}$. However, one can go one step further and try to correlate $\sigma(X)$ with the primary mass composition in a given primary energy window. This topic is discussed in Sect. 11.7.

The energy dependence of $X_{\max}$ resulting from different particle measurements is displayed in Fig. 7.21 together with some results from atmospheric Cherenkov measurements, for comparison.

---

[10] In the early papers that deal with this topic, D [g cm^{-2}] is interpreted as the depth (or height h_0 [m]) of the first interaction in the atmosphere. However, it was soon realized that the depth (or height $h_{\max}$ [m]) of maximum development, $X_{\max}$ [g cm^{-2}], as defined earlier manifests a stronger correlation with the rise time of the shower front than h_0 (see Fig. 7.19) and is therefore a more reliable signature of the degree of longitudinal development of a shower.

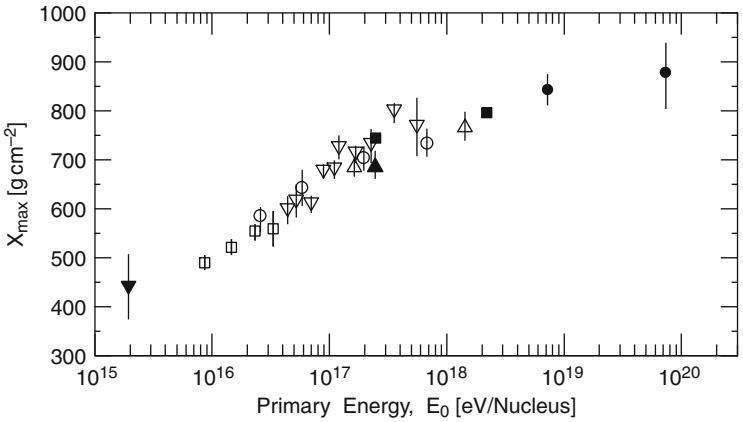

Fig. 7.21 Depths of maximum development of the electron cascade of air showers as a function of primary energy resulting from measurements of different particle observables in conjunction with computer simulations (*solid symbols*: ● Walker and Watson, 1981a; ■ Craig et al., 1979, interpreted by Andam et al., 1982; ▲ Gibson et al., 1981; ▼ Antonov et al., 1979, interpreted by Linsley and Watson, 1981b), and some air Cherenkov measurements for comparison (*open symbols*: □, ▽ Chantler et al., 1981; ○ Andam et al., 1981c; △ Hammond et al., 1978) (after Andam et al., 1982)

7.5 Hybrid Signatures of X_{max}

7.5.1 Arrival Delay Between Cherenkov Light and Particle Front

The arrival time difference between the atmospheric Cherenkov light front and the associated particle front is another measure of the cascade development that arises from the different heights of origin and velocities of propagation for light and particles. The light is subject to refractive index delays and particles are subject to increases in transit time due to path length differences, caused by Coulomb scattering effects and *geomagnetic deflection*, as well as velocity dispersion. Malos (1955) was one of the first to study the arrival time difference between the particle and Cherenkov light fronts.

This time difference is correlated with the distance between the location of the shower maximum and the observer. A shower developing earlier in the atmosphere is expected to manifest a larger time difference between the arrival of the Cherenkov front and the particle front than an average developing shower, the *Cherenkov component arriving earlier*. On the other hand, for showers developing low in the atmosphere, having their maximum closer to the observer, the Cherenkov – particle time separation is expected to be smaller. The sensitivity depends on the separation of the observer (detector) from the shower axis.

Pioneering work of theoretical and experimental nature in this field was carried out by Hammond et al. (1977a) and Chantler et al. (1979b) at Haverah Park and later on by Chantler et al. (1979b) at Dugway. They find that in showers of energy 10^{16} eV to 10^{18} eV the delay of the particle front with respect to the tangent plane is

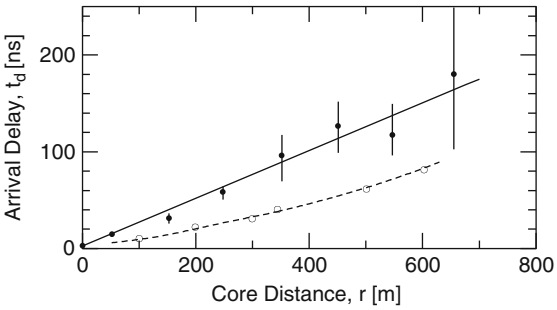

Fig. 7.22 The measured time delay behind the tangent plane as a function of core distance for particles, •, and Cherenkov light, ○, in showers of primary energy of approximately $5 \cdot 10^{17}$ eV at Haverah Park (Chantler et al., 1979b)

on the order of 30–40 ns at a core distance of 150 m. The delay increases by about 30 ns for each 100 m increase in core distance. For the initial work at Haverah Park 34 m^2 deep-water Cherenkov detectors and a 0.4 m^2 fast plastic scintillator were used as particle detectors; for the work at Dugway a 1 m^2 plastic scintillator (see also Chantler et al., 1979a).

Figure 7.22 illustrates the phenomenology (Chantler et al., 1979b). On axis the separation of particles and light is close to zero. Caution is recommended for measurements near the core in small showers where the light originates low in the atmosphere and the particles may precede the light by a few nanoseconds, governed by the local development of the cascade at low altitudes.

Evaluation of the data presented in Fig. 7.22 leads to the conclusion that the delay of the particle front with respect to the *tangent plane* of the shower increases linearly with core distance, whereas the light front delay follows approximately with the square of the distance. These features are expected for particles emitted from a line source with constant transverse momentum and for photons emitted pseudo-isotropically from a point source.

At moderate core distances (approx. 80 m) the arrival delay between Cherenkov light and particle front, $t_d(80)$ also shows a correlation with the *exponent of the lateral structure function* of the Cherenkov light distribution, η of Eq. (7.4), introduced in Sect. 7.3.2 above (Chantler et al., 1979a, b).

A direct regression of the time delay, $t_d(80)$, between the two fronts versus $(\sec\theta - 1)$, θ being the zenith angle of the shower, and the primary energy indicates a sensitivity of $t_d(80)$ to changes in the depth of maximum of $\sim$5 ns/100 g cm^{-2}.

The arrival time difference shows a broad sensitivity to cascade development by a clear correlation with an established *depth of maximum indicator*, the *lateral Cherenkov light structure function shape*, given by Eq. (7.4) (Orford et al., 1981; Chantler et al., 1981).

7.6 Air Fluorescence Tracking of Shower Development and X_{max}

Air shower observations by means of a Fly's Eye type air fluorescence detector is a very ingenious technique. It allows to observe directly the longitudinal as well as the lateral development of a shower as it passes through the atmosphere. Moreover,

it permits to determine in a most direct way the depth of maximum development of a shower. However, this method is only suited for large showers of primary energy $E_0 \geq 5 \cdot 10^{16}$ eV.

The method of air shower detection by means of air fluorescence observation and the subsequent event reconstruction are discussed in detail in Chap. 17, including the optical problems encountered in the atmosphere caused by optical absorption, scattering and background light.[11] In this section we restrict the discussion exclusively to the location of the depth of maximum development, X_{max}, of the showers resulting from fluorescence measurements with the Fly's Eye detector at Dugway (Utah) as an example.

It will be evident from the discussion of the technique, given in Chap. 17, that in spite of the fact that air fluoresce observations yield an image of the longitudinal development of an air shower which facilitates reconstruction of the shower profile and the location of the shower maximum, the interpretation of the acquired data hinges heavily on computer simulations, and therefore on interaction and air shower models. In Fig. 7.23 we present the results of Bird et al. (1994a), showing X_{max} as a

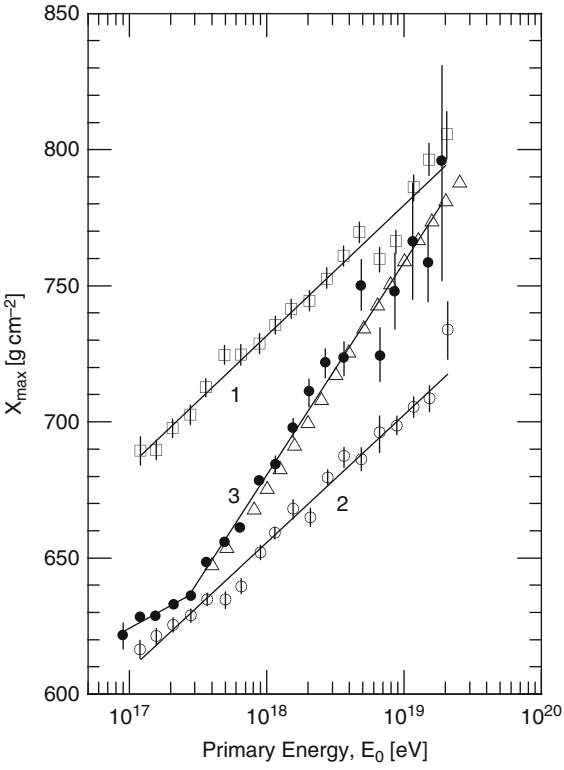

Fig. 7.23 Depth of maximum development, X_{max}, of showers as a function of primary energy. The *full circles*, •, are the results of the evaluation of measurements made with the Fly's Eye detector, the *open squares*, □, and *open circles*, ○, represent simulation results that are based on the KNP model (Kopeliovich et al., 1989) for proton and iron initiated showers, respectively. The *open triangles*, △, show simulation results based on a two-component primary composition model in which the composition changes continuously from predominantly iron around $3 \cdot 10^{17}$ eV to protons above 10^{19} eV (after Bird et al., 1994a). The *lines* are fits to the data points

[11] Note that for fluorescence measurements the air Cherenkov component of the showers can present a disturbing background contribution that must be accounted for.

function of primary energy over an energy range from about 10^{17} eV to a few times 10^{19} eV, the energy range best suited for measurements with the Fly's Eye.

Shown, too, are predictions based on computer simulations carried out on the basis of the hadron interaction model of Kopeliovich et al. (1989) by Bird et al. (1994a). The results include three sets of data that consist of (1) showers initiated by primary protons only, (2) primary iron only, and (3) an energy dependent primary mixture of protons and iron. The latter consists mostly of iron nuclei at about $3 \cdot 10^{17}$ eV, changing slowly to protons with increasing energy, reaching an almost pure proton composition at a few times 10^{19} eV. Inspection of Fig. 7.23 shows clearly that data set (3) is in good agreement with the experimental $X_{\max}$ energy dependence extracted from the Fly's Eye measurements, thus implying an energy dependent primary mass composition that gets lighter with increasing energy over the investigated primary energy range.

A similar analysis though much less exhaustive had been carried out by Hara et al. (1981) using air Cherenkov data from the Akeno site in Japan with a somewhat different detector layout. However, these authors focused their interest more on hadronic interaction model aspects at lower primary energies.

7.7 Atmospheric Effects

In recent years with the improving accuracy of air shower measurements it was realized that local atmospheric conditions, such as local density profiles and other relevant atmospheric parameters may vary significantly with respect to standard atmospheres, such as the widely used US Standard Atmosphere. Moreover, significant differences in the characteristic variations of local atmospheres have been discovered recently that are of relevance for the interpretation of air shower data and must be considered in simulations. These local atmospheric deviations from the standard affect all kinds of air shower studies but particularly air fluorescence experiments, such as the Auger project in Argentina where besides a large array of Haverah Park type surface detectors (deep water Cherenkov detectors) several widely spaced Fly's Eye type air fluorescence detectors[12] are being used.

Several research groups have therefore undertaken extensive studies of the local atmospheric profiles and parameters, and of the seasonal variations using a variety of modern techniques, some of which are outlined in Chaps. 16 and 17, including also common meteorological balloon-borne radiosondes.

In Fig. 7.24a–f we have compiled the essential results of this work (Keilhauer et al., 2003, 2004). Figure 7.24 shows the deviation of the column density across the atmosphere of the real Argentine atmosphere from the US Standard Atmosphere during different seasons. The same measurements carried out at Stuttgart (Germany)

[12] These detectors do not have omnidirectional sensitivity, i.e., they do not have a true Fly's Eye geometry, but cover only a limited solid angle, adequate to overlook the air space above the surface array.

are displayed in Fig. 7.24b. The differences between the two plots are evident (see also Appendix B.3.3).

Applying these data to simulations of 60° inclined 10^{19} eV proton and iron initiated showers reveals rather disturbing effects that are evident when inspecting Fig. 7.24c–f. The conclusion one must draw from this study is that air shower data collected over a year and interpreted without properly accounting for the seasonal atmospheric effects lead to serious misinterpretation of the primary mass.

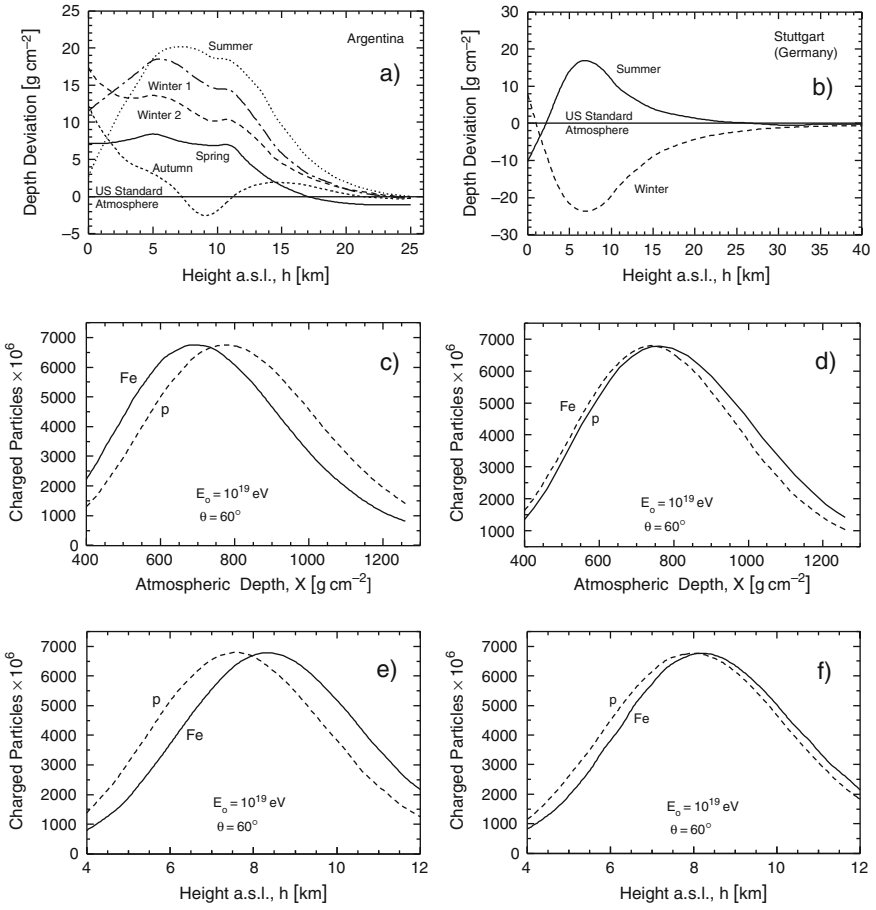

Fig. 7.24 (**a**) Deviation of the average seasonal atmospheric depth profiles measured at the Auger site (Pampa Amarilla, Argentina) from the US Standard Atmosphere (NASA, 1976). Winter 1 and winter 2 refer to two different atmospheric models, depending on the pressure conditions. (**b**) Same plot for summer and winter at Stuttgart, Germany. (**c**) Average longitudinal development of 10^{19} eV iron and proton initiated showers incident at a zenith angle of 60° in a US Standard Atmosphere. (**d**) Same primary conditions as for (**c**) but for iron showers in the Argentine summer and proton showers in the Argentine winter atmosphere. (**e**) and (**f**) correspond to (**c**) and (**d**), respectively, and show the same data plotted as a function of height above sea level (Keilhauer et al., 2003, 2004)

7.8 Elongation and Elongation Rate

7.8.1 Original Linsley Definition and Interpretation

The terms *elongation* and *elongation rate* had been introduced by Linsley (1977) (see Linsley and Watson, 1981b). The *elongation* denotes the increase in atmospheric depth of the maximum development, $X_{\max}$ [g cm^{-2}], of a shower in the atmosphere that results from increased primary energy, for showers of a given type. By extension, it refers also to the corresponding increase in depth at which showers attain a given *age*, s. Here "type" refers to the nature (mass number A) of the primary particle.

The *elongation rate, ER,* denotes the derivative

$$ER = \frac{\mathrm{d}X_{\max}}{\mathrm{d}\ln(E_0)} \ , \tag{7.19}$$

where $X_{\max}$ is the depth of maximum development of an average shower of primary energy E_0. Note that the elongation rate depends explicitly on particle physics, including the nature of the primary.

Linsley (1977) has shown that, with few assumptions about particle physics, for a constant primary particle composition the elongation rate is bounded from above by the characteristic length of cascade theory, the radiation length χ_0 (37.1 g cm^{-2} in air[13]), and is very nearly equal to $(1 - B) \cdot \chi_0$, where B is the exponent of the energy in the formula for the pion multiplicity (more generally, the logarithmic derivative of the secondary particle multiplicity with respect to the energy).

The elongation rate has proved to be very useful to study primary composition as well as aspects of interaction properties at very high energies in the early stages of shower development.

For convenience the elongation rate is usually expressed as the rate of change of the location of the shower maximum, $X_{\max}$ [g cm^{-2}], per decade of primary energy, E_0 [eV or GeV] (or per decade of shower size, N_e). Thus,

$$ER_{10} = \frac{\mathrm{d}X_{\max}}{\mathrm{d}\lg(E_0)} \ \text{[g cm}^{-2}\text{/decade of energy]} \ . \tag{7.20}$$

Frequently, when analyzing showers with respect to $X_{\max}$, the latter is averaged over the fluctuations and, in the case of mixed composition considerations, over the *equal-energy mass spectrum* (Walker and Watson, 1981a, b).

In a more refined interpretation of the *elongation rate theorem* we must also consider the energy dependence of the cross section, of the secondary particle

[13] Some authors use slightly different values for χ_0; see Sects. 4.2.2, 6.2.2, Table B.2, and Tsai (1974).

multiplicity and possibly of other phenomena, such as the energy dependence of the primary mass (Linsley and Watson, 1981a; Walker and Watson, 1981a). In this case the expression for the elongation rate can be written as

$$ER = (1 - B)\chi_0 \left(1 - \frac{\mathrm{d}\ln(A)}{\mathrm{d}\ln(E_0)}\right) , \tag{7.21}$$

where A is the atomic mass number of the primary particle and B can be written as a series of terms. As a first step in this direction we write for B

$$B \simeq B_n + B_\lambda , \tag{7.22}$$

where

$$B_n = \frac{\mathrm{d}\ln(n)}{\mathrm{d}\ln(E)} , \tag{7.23}$$

n being the secondary particle multiplicity and E the energy, and

$$B_\lambda = \frac{-\beta \mathrm{d}(\lambda_N + \lambda_\pi)}{\mathrm{d}\ln(E)} . \tag{7.24}$$

β is a dimensionless constant and λ_N and λ_π are the mean free paths in air of nucleons and pions, respectively. B is on the order of 0.25.

7.8.2 Extension of the Elongation Theorem

Assuming now that the *superposition model* of shower description is valid (total fragmentation of projectile nucleus after first interaction), the elongation rate, ER, can be related to a mass A as follows,

$$\frac{\mathrm{d}X_{\max}}{\mathrm{d}\ln(E_0)} = a\left(1 - \frac{\mathrm{d}\ln(A)}{\mathrm{d}\ln(E_0)}\right) \tag{7.25}$$

or

$$X_{\max} = a\ln\left(\frac{E_0}{A}\right) + b . \tag{7.26}$$

Thus, we can write for $X_{\max}$

$$X_{\max} = X_{\mathrm{init}} + ER_{10}\lg\left(\frac{E_0}{A}\right) , \tag{7.27}$$

and averaged for a mixed composition

$$\langle X_{\max} \rangle \;=\; X_{\text{init}} + ER_{10}(\lg(E_0) - \langle \lg(A) \rangle) \;. \tag{7.28}$$

Here, X_{init} is the depth of the first interaction. As long as ER_{10} depends only weakly on energy, $X_{\max}$ exhibits practically a linear dependence on $\lg(E_0)$. Consequently, by definition any change of this dependence indicates a change in ER_{10}, which implies a change in ($\langle \lg(A) \rangle$), i.e., in the composition (or a change in the nature of hadronic interactions, which we exclude).

The above concept can now be further extended and applied to other parameters that are not explicitly dependent on primary energy, but depend on the depth of observation, X_{obs}, and on $X_{\max}$, and thus offer access to information on primary composition. Several authors followed this idea and investigated temporal features (Badea et al., 1999), or distribution parameters of specific particle groups in showers, e.g., muons (Hayashida et al., 1995). Hillas (1997) studied the elongation principle in hadronic cascades and analyzed the $X_{\max}$ behavior of the different hadronic shower constituents to gain deeper insight.

7.9 Data Summary of $X_{\max}$, Its Fluctuations, $\sigma(X_{\max})$, and the Elongation Rate

We present here in tabulated and graphic form compilations of results of measurements of the depth of maximum development, of fluctuations of the depth of maximum development and of elongation rates for a wide range of primary energies obtained by many different groups. Essentially all the methods discussed above are represented in the data given below.

7.9.1 Data on Depth of Shower Maximum, $X_{\max}$

(a) Early $X_{\max}$ Data

As pointed out before, initial work by Linsley and Scarsi (1962), using fast timing at the Volcano Ranch array, yielded a *source depth* for the different particles which they derived from the curvature of the shower front. It was $320 \pm 70\,\text{g cm}^{-2}$ for the muons and $\leq 320\,\text{g cm}^{-2}$ for the electrons in showers of size $8 \cdot 10^8$–$2 \cdot 10^9$ particles.

Later data of $X_{\max}$ are shown in Table 7.3 that were taken from a compilation of Linsley and Watson (1981b) which had been extended by the author. Linsley and Watson have estimated the primary energies for the $X_{\max}$ values from corresponding sea level shower sizes, N_e, as given in the references listed in the right hand column of Table 7.3, using the relationship

$$E_0 = 10^6 \left(\frac{N_e}{10^5}\right)^{0.922} \text{ [GeV]} \ . \tag{7.29}$$

The absolute depth of maximum determination hinges on air shower simulations. The results of these simulations are heavily influenced by the type of interaction model employed as well as model details, the primary mass and the hadronic cross sections. Details of the break-up mechanism of the primary nucleus are of lesser significance.

In Figs. 7.25 and 7.26 we have summarized the data of the depth of maximum development of air showers as a function of primary energy from early work. Included are experimentally determined values of $X_{\max}$ that were obtained with the different methods discussed in this section as well as predicted values. The latter are mostly for proton and iron nuclei initiated showers and in one case for mass number $A = 10$. A more refined distinction is worthless because of the large uncertainties that are mostly due to fluctuations of the measured parameters, to the experimen-

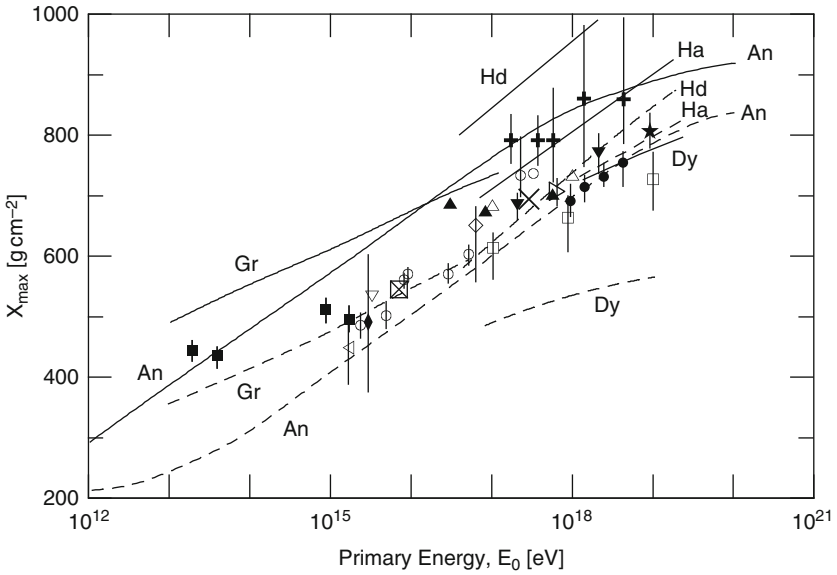

Fig. 7.25 Compilation of older theoretical and experimental data of the depth of maximum development, $X_{\max}$, of showers in the atmosphere as a function of primary energy, E_0. The *curves* represent results from work based on air shower simulations. The *solid lines* are for proton, the *dashed* for iron initiated showers. Gr, Grieder (1979a, b,1984); Dy, Dyakonov et al. (1978); Ha, Hara et al. (1977), Hd, Hammond et al. (1978) and An, Andam et al. (1981b). The experimental points include the work of the following authors: ◁, Antonov et al. (1979); +, Glushkov et al. (1979); ×, Grigoryev et al. (1978); ♦, Kuhlmann et al. (1981); ★, Linsley and Watson (1981a); ■ Tornabene (1979a); □, Kaneko et al. (1971); ▽, Andam et al. (1981a); ▲, Kalmykov et al. (1979); ⊠, Thornton and Clay (1978a, 1981); ●, Dyakonov et al. (1981a); ○, Chantler et al. (1981); ▼, Protheroe and Turver (1979); ◇, Andam et al. (1982); ▷, Craig et al. (1979); and △, Berezhko et al. (1979)

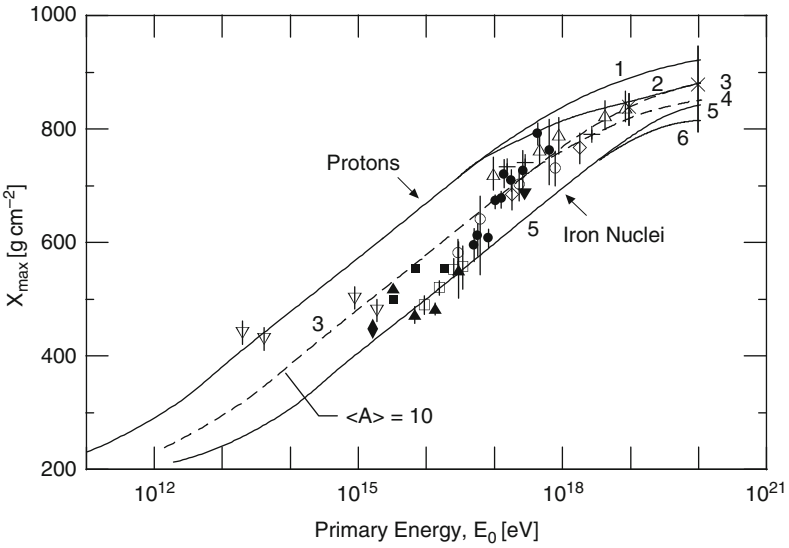

Fig. 7.26 Compilation of depth of shower maximum data versus estimated primary energy (Andam et al., 1981a, b; Turver, Private Communication, 1982). The various points are based on particle or air Cherenkov measurements carried out by the following authors: ♦ Antonov et al. (1974) and Antonov and Ivanenko (1974) interpreted by Linsley and Watson (1981a, b); ◇ Hammond et al. (1978) after Andam et al. (1981a); + Craig et al. (1979); × Linsley and Watson (1981a, b); ▼ Gibson et al. (1981); △ Blake et al. (1979b, 1982) interpreted by Andam et al. (1981b); ▽ Tornabene (1979a, b) interpreted by Andam et al. (1981b); ▲, □, • Andam et al. (1981b) and Turver (Private Communication 1982); ○ Andam et al. (1981c) and Turver (Private Communication 1982); ■ Aguirre et al. (1969) (see also Andam et al., 1982). For computational aspects see Protheroe and Turver (1979), McComb and Turver (1981a, b), and Grieder (1984). The proton, mass A = 10 and iron nuclei curves labeled 1, 3 and 5 apply to calculations carried out for an energy dependence of the cross section that goes as $\sigma(E) \propto \ln(E)$, curves 2, 4 and 6 for $\sigma(E) \propto \ln^2(E)$

tal methods, but also to the uncertainties embedded in the shower and interaction models, and the atmospheric profiles that had been used in the simulations.

(a) Recent X_{max} Data

Considering now recent data, we point out the remarkable results of the Fly's Eye experiment (Bird et al., 1994a), mentioned previously when discussing the fluorescence method in Sect. 7.6, that are displayed in Fig. 7.23, and the results of the hybrid experiment HiRes-MIA shown in Fig. 7.27 (Abu-Zayyad et al., 2001). These data show that the primary composition appears to get lighter above a few times 10^{17} eV, a trend which is confirmed by other experiments. This is evident upon inspection of Figs. 7.28 and 7.29. These two figures that are due to Hörandel (2003) and Abraham et al. (2007), respectively, are compilations of data on the depth of shower maximum, X_{max}, as a function of primary energy that had been acquired

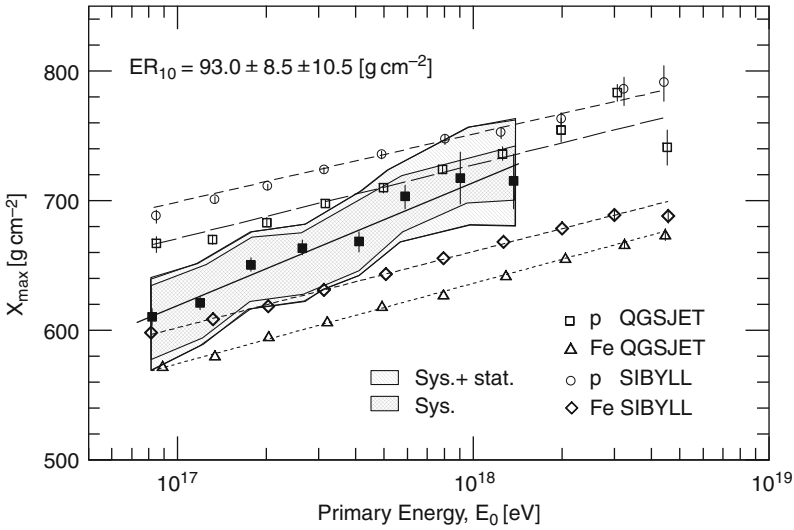

Fig. 7.27 Average depth of maximum development, X_{max}, as a function of primary energy obtained from measurements with the HiRes detector at Utah. The *solid line* is a fit to the experimentally determined data. The *two shaded* surfaces represent the error regions and the *dashed* and *dotted lines* show the X_{max} values as obtained for protons and iron nuclei from simulations using the two event generators QGSJET and SIBYLL, as identified in the plot. The measured elongation rate, ER_{10} over the investigated energy range is 93 g cm^{-2} (after Abu-Zayyad et al., 2001)

by different experiments using a variety of different techniques, as described in the previous sections.

Also shown in these two figures are model predictions of the energy dependence of X_{max} for proton and iron nuclei initiated showers, using different event generators (QGSJET and SIBYLL) as listed in the figures, that set upper and lower bounds for X_{max}. The simulations show that the difference between the average X_{max} of proton initiated showers compared to iron initiated showers having the same total energy is about 100 g cm^{-2} and almost independent of primary energy.

Of particular relevance for current investigations that focus on questions related to the origin of ultrahigh energy cosmic rays, more specifically for testing the different models of origin (bottom-up or top-down, see Sect. 11.11), is the curve showing the primary energy dependence of X_{max} for photon initiated showers in Fig. 7.29 (Abraham et al., 2007). Very high energy photon initiated showers are expected to have a *larger* depth of shower maximum than hadron triggered showers and contain fewer muons. The reasons are the low multiplicity of electromagnetic interactions, the Landau-Pomeranchuk-Migdal (LPM) effect (Chap. 4), and the mean free path for photonuclear reactions and direct muon pair production that are more than two orders of magnitude larger than the radiation length. At these high photon energies the process of *pre-showering* in the geomagnetic field becomes relevant and must be considered as it affects the shower development and can imitate heavy primaries (see Sect. 4.5.2 for details).

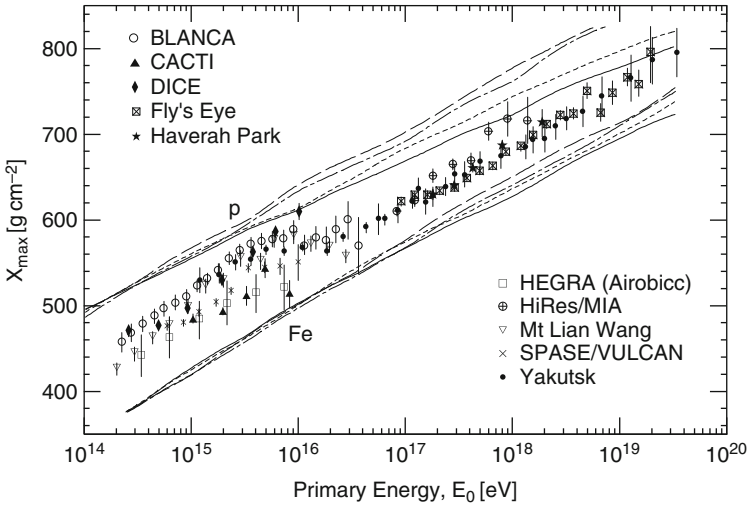

Fig. 7.28 Compilation of recent and/or revised older experimental data of the depth of maximum development, $X_{\max}$, of showers in the atmosphere as a function of primary energy, E_0. The *symbols* represent the experiments as listed in the figure and refer to the following papers: ○ Fowler et al. (2001); ▲ Paling et al. (1997); ♦ Swordy and Kieda (2000); ☒ Bird et al. (1994a); ★ Watson (2000); □ Arqueros et al. (2000); ⊕ Abu-Zayyad et al. (2000a, b); ▽ Cha et al. (2001); × Dickinson et al. (1999); and • Dyakonov et al. (1993), Knurenko et al. (2001). Also shown are predictions from air shower simulations for proton (*upper set of curves*) and iron primary initiated showers (*lower set of curves*), using different versions of the QGSJET interaction model. The *solid curves* apply to the original QGSJET model (after Hörandel, 2003). Comparison of this figure with the two previous figures (Figs. 7.25 and 7.26) shows the vast increase in the number of experimental date over the last decade, the improvement in the quality and consistency of the data, and the significant progress achieved in the phenomenological-mathematical description of the high energy hadronic processes with the modern models

Table 7.4 shows the depth of shower maximum, $X_{\max}$, as a function of primary energy over the range $0.4 \leq E_0 \leq 15\,\text{PeV}$ measured with the DICE double imaging atmospheric Cherenkov experiment (Boothby et al., 1997; Swordy and Kieda, 2000). The width of the $X_{\max}$ distribution for the different energy bins of the measurements made with this experiment, i.e., the fluctuations, are given in Table 7.7. The DICE detector system was located at the same site as the CASA-MIA-BLANCA experiments at Dugway, Utah.

In Table 7.5 we show the $X_{\max}$ distribution that was obtained with the combined CASA-BLANCA particle and air Cherenkov arrays, mentioned before (Fowler et al., 2001). Also given in the table is the exponential inner slope parameter, s_{Ch}, of the Cherenkov photon distribution that was used among other parameters and two empirical mathematical distributions to extract the $X_{\max}$ parameter in conjunction with simulations (for details see the original publication). The layouts of the CASA, MIA, BLANCA and DICE experiments, all located at the same site, are displayed in Fig. A.10.

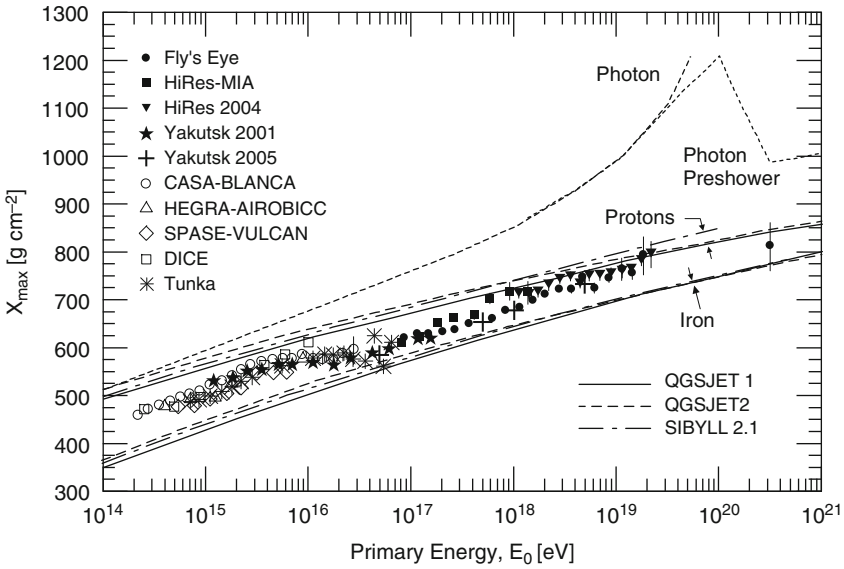

Fig. 7.29 Comparison of predicted and experimentally determined average depth of shower maximum, X_{max}, as a function of primary energy, E_0. The three *curves* each for protons and iron nuclei are predictions resulting from simulations with the three different event generators as listed in the figure. The *short dashed* and the *dotted line* apply to primary photons. Their X_{max}-distribution splits near $5 \cdot 10^{19}$ eV where pre-showering begins to occur and X_{max} becomes not only energy dependent but depends also on the direction of the photon trajectory with respect to the orientation of the magnetic field, as is discussed in Sect. 4.5.2 (after Abraham et al., 2007; see also Knapp et al., 2003). ● Abu-Zayyad et al. (2000a, b); ■ Abu-Zayyad et al. (2001); ▼ Sokolsky (2005); ⋆ Knurenko et al. (2001); + Ivanov et al. (2005); ○ Fowler et al. (2001); △ Arqueros et al. (2000); ◇ Dickinson et al. (1999); □ Swordy and Kieda (2000); ⁕ Budnev et al. (2005)

Table 7.4 Depth of Shower Maximum, X_{max}, Determined with DICE. (Boothby et al., 1997; see also Swordy and Kieda, 2000)

Energy bin [PeV]	Event number	$\langle X_{max} \rangle$ Raw [a] [g cm^{-2}]	δ [b] [g cm^{-2}]	Median energy [c] [PeV]	$\langle X_{max} \rangle$ [g cm^{-2}]
0.2 – 0.4	6132	474	−12	0.25	462 ± 2
0.4 – 0.7	3708	479	−1	0.5	478 ± 2
0.7 – 1.5	2279	501	+2	1.0	503 ± 2
1.5 – 3.0	740	534	+3	2.0	537 ± 3
3.0 – 5.0	212	549	+3	4.0	552 ± 4
5.0 – 8.0	70	587	+3	6.0	590 ± 10
8.0 – 15.0	37	628	+3	10.0	631 ± 14

[a] Before trigger correction. [b] Trigger correction, not commented here, is discussed in original paper.
[c] The energy scale has an estimated systematic error of ±20%.

Table 7.5 Mean cherenkov inner slope, s_{Ch}, measured by CASA-BLANCA and the corresponding mean depth of shower maximum, $\langle X_{\mathrm{max}} \rangle$ (after Fowler et al., 2001)

Energy range lg(E) [eV]	Mean slope s_{Ch} 10^{-3} [m^{-1}]	$\langle X_{\mathrm{max}} \rangle$ ± Stat± Sys Errors [a] [g cm^{-2}]
14.3 – 14.4	11.4 ± 0.0	458 ± 0.3 ± 12
14.4 – 14.5	11.9 ± 0.0	469 ± 0.3 ± 10
14.5 – 14.6	12.5 ± 0.0	479 ± 0.4 ± 9
14.6 – 14.7	12.9 ± 0.0	488 ± 0.4 ± 9
14.7 – 14.8	13.4 ± 0.0	497 ± 0.5 ± 9
14.8 – 14.9	13.7 ± 0.0	504 ± 0.6 ± 9
14.9 – 15.0	14.1 ± 0.0	511 ± 0.8 ± 8
15.0 – 15.1	14.7 ± 0.0	523 ± 1 ± 7
15.1 – 15.2	15.2 ± 0.1	532 ± 1 ± 7
15.2 – 15.3	15.6 ± 0.1	542 ± 1 ± 7
15.3 – 15.4	16.3 ± 0.1	555 ± 2 ± 7
15.4 – 15.5	16.8 ± 0.1	565 ± 2 ± 7
15.5 – 15.6	17.2 ± 0.1	573 ± 3 ± 7
15.6 – 15.7	17.3 ± 0.2	576 ± 4 ± 8
15.7 – 15.8	17.4 ± 0.2	578 ± 4 ± 8
15.8 – 15.9	17.5 ± 0.2	579 ± 5 ± 8
15.9 – 16.0	17.9 ± 0.3	588 ± 6 ± 9
16.0 – 16.1	17.0 ± 0.4	570 ± 8 ± 9
16.1 – 16.2	17.5 ± 0.4	579 ± 10 ± 9
16.2 – 16.3	17.4 ± 0.6	576 ± 12 ± 10
16.3 – 16.4	18.1 ± 0.5	589 ± 11 ± 11
16.4 – 16.5	18.5 ± 0.8	600 ± 19 ± 11
16.5 – 16.6	17.2 ± 1.5	570 ± 31 ± 12

[a] The first column of errors given for each quantity is statistical; the standard deviation divided by $\sqrt{N}$. For X_{max} a systematic error is given which is due to a combination of effects. These results use the QGSJET-derived X_{max} transfer function.

As pointed out at the beginning of this chapter, there is a relevant correlation between the depth of maximum development of a shower and the primary mass. This topic and the methods to estimate the primary mass from X_{max} data are extensively discussed in Chap. 10. The corresponding results are presented in Sect. 11.7.

7.9.2 Data on Fluctuations of Depth of Shower Maximum, $\sigma(X_{\mathrm{max}})$

(a) Predicted X_{max} Distributions and Fluctuations

In a recent study of the effect of atmospheric profile changes on the depth of shower maximum of very energetic showers, Keilhauer et al. (2004, 2006) have carried out extensive simulations using the CORSIKA code with the QGSJET01 event generator to establish the shape of the X_{max} distributions of 10^{19} eV proton and iron initiated showers with good reliability. Their results are reproduced in Figs. 7.32a, b and apply to the Standard US Atmosphere.

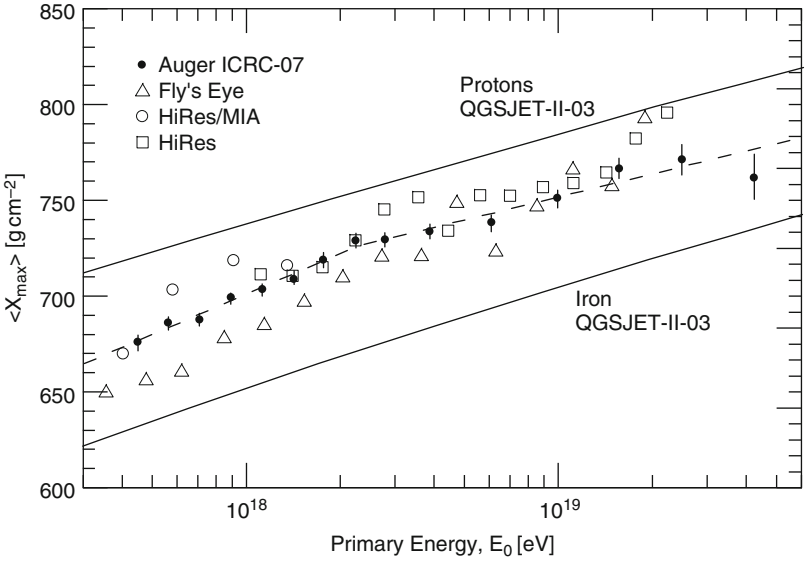

Fig. 7.30 Average depth of maximum distribution, $\langle X_{max} \rangle$, from measurements of the Auger, Fly's Eye, HiRes/MIA and HiRes experiments. Shown, too, are the theoretically expected X_{max} values for protons and iron primaries, using the QGSJET-II-03 event generators (Watson, 2009; and http://www.auger.org/technical_info/)

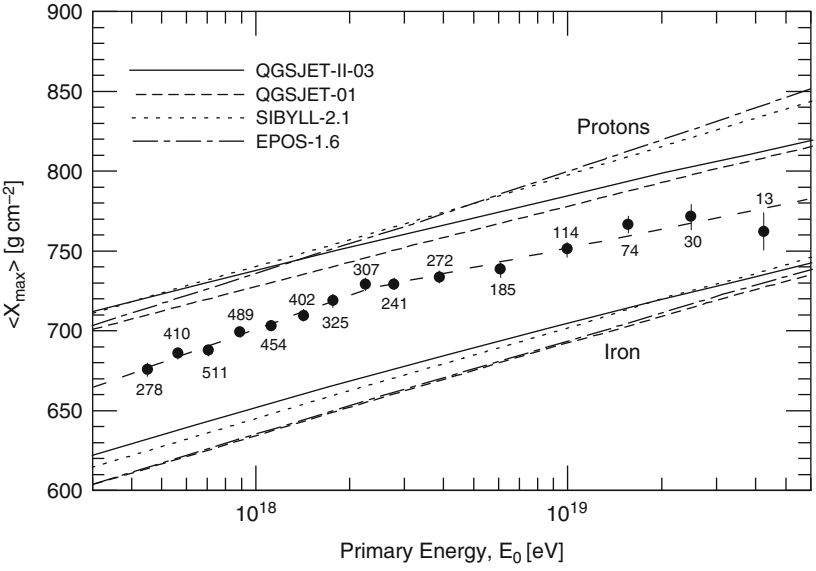

Fig. 7.31 Average depth of maximum distribution, $\langle X_{max} \rangle$, from measurements of the Auger experiments. The numbers indicate the events recorded. Shown, too, are theoretically expected X_{max} values for protons and iron primaries according to the models as listed (Watson, 2009; and http://www.auger.org/technical_info/)

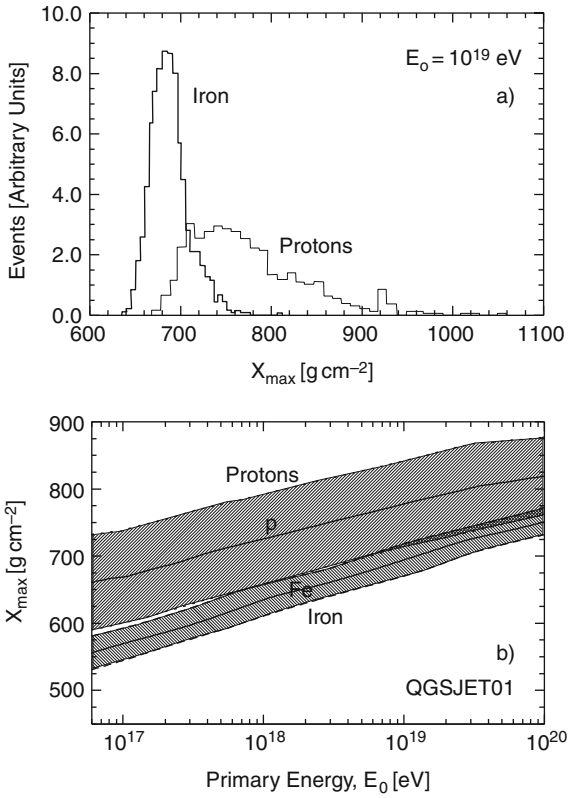

Fig. 7.32 (**a**) Distribution of the depth of maximum development, X_{max}, of 500 proton and 1,000 iron initiated showers of 10^{19} eV primary energy in the Standard US Atmosphere (Keilhauer et al., 2004). (**b**) Primary energy dependence of the mean value and the fluctuations of the depth of shower maximum of 500 proton and 200 iron primary initiated showers using the CORSIKA simulation code and the QGSJET01 event generator (Heck et al., 1998). The width of the distributions represent one standard deviation (Keilhauer et al., 2004)

The distribution for proton primaries shown in Fig. 7.32a contains a total of 500 events, that for iron primaries shown in the same figure 1,000 events. The energy dependence of the mean value of X_{max} of the two types of showers are displayed in Fig. 7.32b by the corresponding center lines in the shaded areas. The widths of the latter represent one standard deviation.

The conclusion from these two plots underlines that not only the mean value of the depth (or height) of maximum development for a given total primary energy is clearly related to the primary's mass, but also the width of the distribution of X_{max}.

(b) Measured X_{max} Fluctuations

Table 7.6 is a compilation of results of fluctuations from several experiments. In their paper Walker and Watson (1982) discuss the measurements of some of the

Table 7.6 Measured fluctuations of depth of shower maximum, $\sigma(X_{max})$. early epoch

Energy [eV]	Number of events	$\sigma(X_{max})$ [g cm^{-2}]	References
$2 \cdot 10^{16} - 2 \cdot 10^{18}$	96	66±7	Berezhko et al. (1979)[a]
$5.0 \cdot 10^{16}$	40	80±12	Andam et al. (1981d)
$2 \cdot 10^{17} - 10^{19}$	–	60.5±4	Walker and Watson (1982)
$2 \cdot 10^{17} - 10^{20}$	–	88±3	Lapikens et al. (1979)
$4.9 \cdot 10^{17}$	519	71±6	Coy et al. (1981)[a]
$5.0 \cdot 10^{17}$	432	44±14	Walker and Watson (1974)[a]
$7.5 \cdot 10^{17}$	300	79±4	Dyakonov et al. (1981b)[a]
$8.0 \cdot 10^{17}$	–	70±10	Barrett et al. (1977)
10^{18}	550	≤100	Craig et al. (1979)
$1.5 \cdot 10^{18}$	75	72±16	Walker and Watson (1974)[a]
$4.0 \cdot 10^{18}$	201	63±5	Dyakonov et al. (1981b)[a]

[a] After a compilation by Walker and Watson (1982).

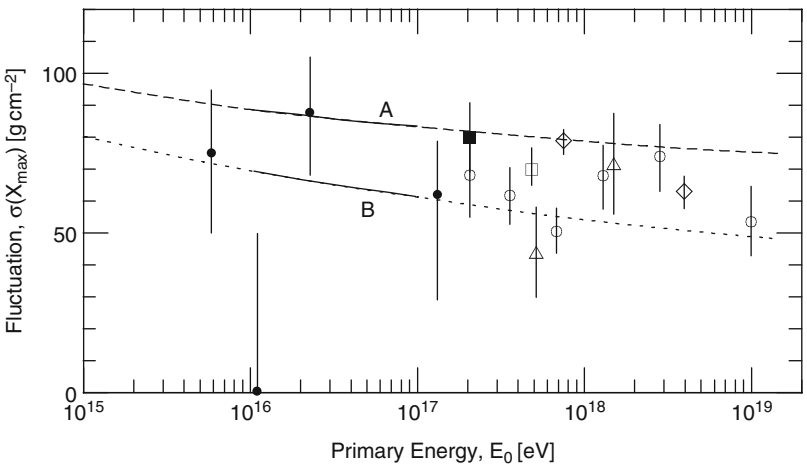

Fig. 7.33 Observed dependence of the fluctuations of the height of maximum development, $\sigma(X_{max})$, of showers on primary energy (Chantler et al., 1983). The *symbols* apply to the following techniques and sites: • lateral distribution, ■ pulse shape, both Dugway Cherenkov array. The *open symbols* are from a compilation of Walker and Watson (1982) and references therein. The *solid lines* are simulation results for proton primaries, the *dashed* and *dotted* are extrapolations. *Curves* A and B apply to an energy dependence of the cross section that goes as $\ln(s)$ and $\ln^2(s)$, respectively, s being the center of mass energy squared

references listed here. In Fig. 7.33 we show the results of a fluctuation analysis by Chantler et al. (1983) using atmospheric Cherenkov measurements carried out at Dugway and Haverah Park on high energy hadron initiated showers. The figure also includes data obtained with other methods.

The measured widths of the $\langle X_{max} \rangle$ distributions measured by the more recent DICE experiment that are given in Table 7.4 for a range of primary energies are listed in Table 7.7 together with simulated widths for pure proton and iron initiated showers.

Table 7.7 Width of X_{max} distribution, $\sigma(X_{max})$, measured by DICE compared with simulations for protons and iron nuclei. (Boothby et al., 1997)

Median energy[a] [PeV]	DICE $\sigma(X_{max})$ [g cm^{-2}]	Simulations σ(p) [g cm^{-2}]	Simulations σ(Fe) [g cm^{-2}]
1.0	73 ± 1	87	66
2.0	66 ± 2	83	49
4.0	58 ± 4	82	41
6.0	82 ± 12	81	40
10.0	85 ± 20	79	40

[a] Only energies at which the trigger bias is small are included.

7.9.3 Data on Elongation Rate, ER_{10}

A compilation of elongation rate data derived from experimental observations in conjunction with computer simulations are summarized in Table 7.8 for a wide range

Table 7.8 Measured elongation rates per decade of energy, ER_{10}. (Early data)

Energy [eV]	ER_{10} [g cm^{-2}/dec]	References	Method
$10^{15} - 7 \cdot 10^{16}$	102±32	Thornton and Clay (1979a)[a]	(a), (b)
$10^{15} - 10^{16}$	60	Thornton and Clay (1979b)[a]	(a), (b)
$5 \cdot 10^{15} - 5 \cdot 10^{16}$	300	Thornton et al. (1979)[a]	(a), (b)
$10^{15} - 10^{17}$	> 100	Thornton and Clay (1981)[a]	(a), (b)
$10^{15} - 10^{18}$	101±8	Andam et al. (1981a)	(a), (b), (c)
$10^{15} - 10^{18}$	100±50	Aguirre et al. (1979)[b]	(g)
$2 \cdot 10^{16} - 3 \cdot 10^{18}$	30±18	Kalmykov et al. (1979)[b]	(c)
$10^{17} - 10^{18}$	105±30	England et al. (1979)[b]	(d)
$10^{17} - 10^{18}$	75±25	Craig et al. (1979)[b]	(d)
$10^{17} - 5 \cdot 10^{18}$	60±30	Glushkov et al. (1979)[b]	(b)
$10^{17} - 10^{19}$	65±15	McComb and Turver (1982c)[c]	(d)
$2 \cdot 10^{17} - 2 \cdot 10^{18}$	79±14	Coy et al. (1981)	(d), (h)
$2 \cdot 10^{17} - 2 \cdot 10^{18}$	85±37	Hammond et al. (1978)[b]	(a), (b), (c)
$3 \cdot 10^{17} - 3 \cdot 10^{18}$	85±40	Linsley (1977)[b]	(e)
$3 \cdot 10^{17} - 3 \cdot 10^{18}$	120±75	Dyakonov et al. (1979)[b]	(b)
$2 \cdot 10^{17} - 5 \cdot 10^{18}$	70±5	Walker and Watson (1981a)[b]	(f)
$2 \cdot 10^{17} - 5 \cdot 10^{18}$	90±10	Barrett et al. (1977)	(f)
$2 \cdot 10^{17} - 10^{20}$	105±7	Lapikens et al. (1977)	(f)
$10^{18} - 5 \cdot 10^{18}$	90±25	Dyakonov et al. (1981a)	(b)
$10^{18} - 10^{19}$	90±40	Lapikens (1977)	(f)
$5 \cdot 10^{18} - 10^{20}$	40±20	Walker and Watson (1981a)	(f)

(a) air Cherenkov full width at half maximum, *FWHM*. (b) air Cherenkov lateral structure function, $Q(r)$. (c) air Cherenkov pulse rise time, t_r. (d) lateral structure function using deep-water Cherenkov detectors. (e) lateral structure with scintillation detector. (f) rise time of deep-water Cherenkov pulse. (g) equal intensity cuts. (h) density fluctuations using deep-water Cherenkov detectors.

[a] Used 10^{10} eV per particle at sea level for conversion to primary energy.

[b] After a compilation by Walker and Watson (1981a).

[c] Data of Blake et al. (1979a).

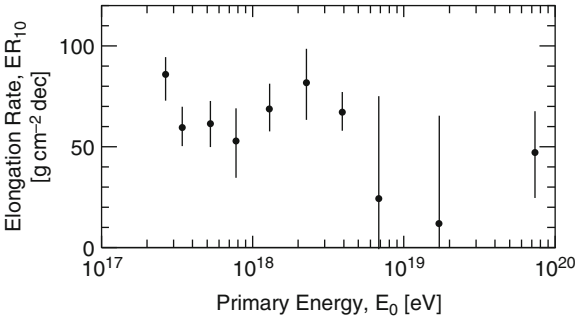

Fig. 7.34 Elongation rate per decade of energy, ER_{10}, as a function of estimated primary energy. The data are based on rise time measurements of pulses from the large water Cherenkov counters at Haverah Park. Averaged over the energy range shown, $ER_{10} = 70 \pm 5\,\mathrm{g\,cm^{-2}}$ per decade. Above $5 \cdot 10^{18}$ eV, $ER_{10} = 40 \pm 20\,\mathrm{g\,cm^{-2}}$ per decade based on 35 events (Lapikens et al., 1979; Walker and Watson, 1981a)

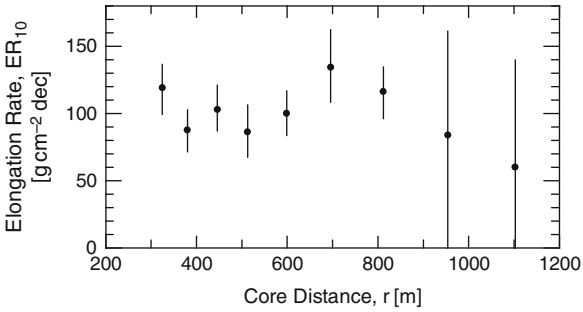

Fig. 7.35 Elongation rate per decade of energy, ER_{10}, as a function of core distance, r, for showers with primary energy E_0 between $2{\cdot}10^{17}$ and 10^{20} eV. The data are derived from rise time measurements carried out with water Cherenkov counters at Haverah Park (Lapikens et al., 1979)

of primary energies. The experimental methods employed are also listed together with the references. Some of the data are presented in Figs. 7.34 and 7.35. The latter shows the elongation rate as a function of core distance in large showers ($2 \cdot 10^{17} \leq E_0 \leq 10^{20}$ eV) (Lapikens et al., 1979).

In several papers Thornton and Clay (1979a, b, 1980) and Thornton et al. (1979) stress the fact that they observe a rapid increase of the depth of shower maximum over the size range from about $2 \cdot 10^5$ to about $2 \cdot 10^7$ particles measured at sea level and a correspondingly large elongation rate. Their results depend on details of the analysis, as is evident from Table 7.8. Revised data are presented and discussed in a later paper (Thornton and Clay, 1981).

It should be noted that simulations show that the elongation rates are almost the same for proton and iron initiated showers and nearly independent of (modern) interaction models. For the QGSJET model the respective values are $58.5 \pm 1.3\,\mathrm{g\,cm^{-2}}$ and $60.9 \pm 1.1\,\mathrm{g\,cm^{-2}}$ per decade of primary energy (Abu-Zayyad et al., 2001).

In Table 7.9 we list some more recent values of elongation rates of energetic showers that had been determined using different techniques. These comprise data from fluorescence measurements with the Fly's Eye detector (Bird et al., 1993, 1994a, b), the HiRes-MIA hybrid experiment (fluorescence and muon detectors)

Table 7.9 Measured elongation rates per decade of energy, ER_{10}. (Recent data)

Energy [eV]	ER_{10} [g cm^{-2} dec^{-1}]	References	Method
$< 3 \cdot 10^{17}$	~ 50	Bird et al. (1994b)	(a)
$3 \cdot 10^{17} - 10^{19}$	78.9 ± 3.0	Bird et al. (1993)	(a)
$10^{17} - 10^{19}$	69 ± 1.9	Bird et al. (1994b)	(a)
$1.6 \cdot 10^{17} - 3.2 \cdot 10^{18}$	$93.0 \pm 8.5 \pm 10.5$	Abu-Zayyad et al. (2001)	(b)
$< 3 \cdot 10^{18}$	62 ± 6	Dyakonov et al. (1993)	(c)
$> 3 \cdot 10^{18}$	74 ± 7	Dyakonov et al. (1993)	(c)
$2 \cdot 10^{17} - 3 \cdot 10^{18}$	85 ± 10	Hinton et al. (1999)	(d)
$3 \cdot 10^{17} - 3 \cdot 10^{18}$	90 ± 12	Hinton et al. (1999)	(d)
$> 5 \cdot 10^{18}$	40 ± 20	Hinton et al. (1999)	(d)

(a) air fluorescence; (b) air fluorescence and muon hybrid; (c) air Cherenkov; (d) arrival time distribution of particles in water Cherenkov detectors.

(Abu-Zayyad et al., 2001), all located at Dugway (Utah), the atmospheric Cherenkov experiment at Yakutsk (Siberia) (Dyakonov et al., 1993), and from a re-analysis of the old data from the Haverah Park experiment that used particle arrival time distributions measured with the deep water Cherenkov detectors, using modern simulations (Hinton et al., 1999).

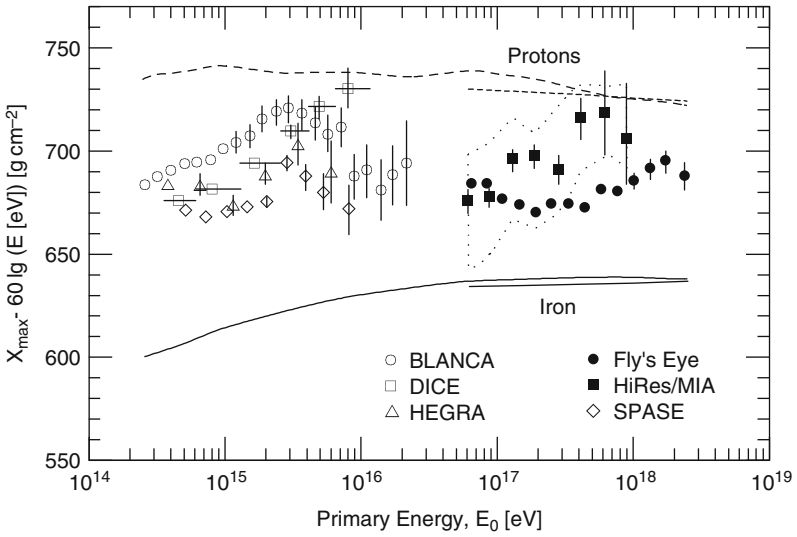

Fig. 7.36 Average depth of shower maximum as a function of primary energy from a variety of experiments (BLANCA, Fowler et al., 2001; DICE, Swordy and Kieda, 2000; HEGRA-AIROBICC, Cortina et al., 1997, Arqueros et al., 2000; Fly's Eye, Bird et al., 1993, 1994, 1999; HiRes-MIA, Abu-Zayyad et al., 2000a, b; SPASE-VULCAN, Dickinson et al., 1999). An arbitrary elongation rate of 60 g cm^{-2} is subtracted for reasons explained in the text. The full width *solid* and *dashed lines* are model predictions according to Fortson et al. (1999a, b), the *short lines* after Abu-Zayyad et al. (2001)

Finally, in Fig. 7.36 we show a compilation of data on the energy dependence of $X_{\max}$ from several modern experiments, assembled by Abu-Zayyad et al. (2001). Shown, too, are the proton and iron bounds from a simulation of Fortson et al. (1999a, b) and Abu-Zayyad, as explained in the figure caption. Note the special representation of the data to emphasize the energy dependence.

7.10 Mathematical Expressions and Fits

7.10.1 Air Cherenkov Related Expressions

Hammond et al. (1978) use the following expressions to fit their data of the rise time, $t_r(r)$ [ns], and full width at half maximum (FWHM), $\tau(r)$ [ns], versus core distance, r [m] over the range $150\,\text{m} \leq r \leq 600\,\text{m}$ in showers of mean primary energy $3 \cdot 10^{17}$ eV:

$$t_r(r) \;=\; 11.6 + 0.87(r/100)^2 \;\; [\text{ns}] \tag{7.30}$$

$$\tau(r) \;=\; 21.7 + 2.97(r/100)^2 \;\; [\text{ns}] \tag{7.31}$$

For the zenith angle θ and primary energy E_0 (expressed in terms of $\rho_{(500)}$) dependence of these two quantities Hammond et al. (1978) give the following expressions valid for a core distance of 400 m:

$$t_r(400) \;=\; -16.55 + 43.75\cos\theta \;+\; 0.12\lg(\rho_{(500)})[\text{ve}\mu] \;\; [\text{ns}] \tag{7.32}$$

$$\tau(400) \;=\; -45.14 + 120.3\cos\theta + 9.92\lg(\rho_{(500)})[\text{ve}\mu] \;\; [\text{ns}] \tag{7.33}$$

A more general expression for the FWHM, τ, is given by Thornton and Clay (1979a). It includes shower size, N_e, zenith angle, θ, and radial distance, r, from the shower axis.

$$\tau(N_e, r, \theta) \;=\; C N_e^{\alpha} (\cos\theta)^{\beta} \left(\frac{r}{100}\right)^{\gamma} \;\; [\text{ns}] \;\; . \tag{7.34}$$

Here $\alpha = 0.2 \pm 0.03$, $\beta = 1.8 \pm 0.5$, $\gamma = 1.4 \pm 0.2$, and C is a scale factor.

Kalmykov et al. (1979) use several similar formulae to calculate the height of maximum development, $h_{\max}$, from the FWHM, τ, measured at any distance r from the shower axis. One of the more recent is given below.

$$h_{\max}(\tau) \;=\; \frac{17.05 - 9.17\lg(\tau) + 13.75\lg(r/300)}{1 - 0.92\lg(r/300)} \;\; [\text{km}] \;\; , \tag{7.35}$$

where r is measured in meters [m] and τ in nanoseconds [ns].

Dyakonov et al. (1981a) compute the primary energy dependence of the depth of maximum development, $X_{\max}(E_0)$, using the relation

$$X_{\max}(E_0) \;=\; (690 \pm 20) + (90 \pm 25)\lg\left(\frac{E_0[\mathrm{eV}]}{10^{18}}\right) \;\; [\mathrm{g\,cm^{-2}}] \;. \tag{7.36}$$

A similar expression by Kalmykov et al. (1979) reads

$$X_{\max}(E_0) \;=\; (690 \pm 10) + (33 \pm 18)\lg\left(\frac{E_0[\mathrm{eV}]}{10^{17}}\right) \;\; [\mathrm{g\,cm^{-2}}] \tag{7.37}$$

7.10.2 Particle Related Expressions

Various authors have developed fits to describe the dependence of the deep-water Cherenkov tank rise time, t_r [ns], produced by the shower particle disk on zenith angle θ, core distance r [m] and primary energy E_0 [eV] (Barrett et al., 1977; Lapikens et al., 1979). We give here the more complicated expression used by the latter.

$$t_r(\theta, r, E_0) \;=\; \left(c_1 + c_2 \sec\theta \;+\; c_3 \lg(E_0/10^{17})\right) r + c_4 \sec\theta \;+$$

$$c_5 \lg(E_0/10^{17}) + c_6 \;\; [\mathrm{ns}] \;, \tag{7.38}$$

where $c_1 = 0.545 \pm 0.002$, $c_2 = -0.377 \pm 0.019$, $c_3 = 0.04 \pm 0.002$, $c_4 = 85.2 \pm 10.3$, $c_5 = -9.3 \pm 1.7$, and $c_6 = -38.8 \pm 0.6$.

For the primary energy dependence of the fluctuations of the depth of the shower maximum Walker and Watson (1982) find from rise time measurements of the water Cherenkov detector pulse for showers in the energy range $1.5 \cdot 10^{17} \le E_0 \le 10^{19}$ eV with zenith angles $\theta \le 40^\circ$ the following expression

$$\sigma(X_{\max}, E_0) = (64 \pm 7.5) - (5 \pm 4.5)\lg(E/10^{17}) \;\; [\mathrm{g\,cm^{-2}}] \;, \tag{7.39}$$

where E is in eV. For a somewhat broader data base they find the slightly different expression that describes the data well.

$$\sigma(X_{\max}, E_0) = (78 \pm 5) - (12 \pm 3)\lg(E/10^{17}) \;\; [\mathrm{g\,cm^{-2}}] \;. \tag{7.40}$$

References

Abraham, J., et al., Auger Collaboration: Astropart. Phys., 27, p. 155 (2007).
Abu-Zayyad, T., et al.: Phys. Rev. Lett., 84, p. 4276 (2000a).
Abu-Zayyad, T., et al.: Phys. Rev. Lett., 85, p. 1347 (2000b).
Abu-Zayyad, T., et al.: Astrophys. J., 557, p. 686 (2001).

Aguirre, C., et al. (1969), after Andam et al. (1982).
Aguirre, C., et al.: PICRC, 8, p. 107 (1979).
Andam, A., et al.: PICRC, 9, p. 48 (1979).
Andam, A.A., et al.: PICRC, 6, p. 57 (1981a).
Andam, A.A., et al.: PICRC, 11, p. 281 (1981b).
Andam, A.A., et al.: PICRC, 6, p. 125 (1981c).
Andam, A.A., et al.: PICRC, 6, p. 129 (1981d). (Abstract only).
Andam, A.A., et al.: Phys. Rev. D, 26, p. 23 (1982).
Antonov, R.A., and I.P. Ivanenko: Yadernaya Fiz. 19, p. 869 (1974) (in Russian). Sov. J. Nucl. Phys., 19, p. 443 (1974).
Antonov, R.A., et al.: Sov. J. Nucl. Phys., 18, p. 285 (1974).
Antonov, R.A., et al.: PICRC, 9, p. 3360 (1975).
Antonov, R.A., et al.: PICRC, 9, p. 258 (1979).
Antonov, R.A., et al.: PICRC, 6, p. 229 (1981).
Arqueros, F., et al., HEGRA-Collaboration: Astron. Astrophys., 359, p. 682 (2000).
Auger Web Site (2008).
Badea, A.F., et al.: PICRC, 1, p. 502 (1999).
Barrett, M.L., et al.: PICRC, 8, p. 2753 (1975a).
Barrett, M.L., et al.: PICRC, 8, p. 2758 (1975b).
Barrett, M.L., et al.: PICRC, 8, p. 172 (1977).
Barrett, M.L.: Ph. D. Thesis, University of Leeds, England (1978).
Berezhko, I.A., et al.: Yad. Fiz., 30, p. 415 (1979). Sov. J. Nucl. Phys., 30, p. 215 (1979).
Bird, J.D., et al.: Phys. Rev. Lett., 71, p. 3401 (1993).
Bird, J.D., et al.: Astrophys. J., 424, p. 491 (1994a).
Bird, D.J., et al.: PICRC, Calgary 1993, Invited, Rapporteur and Highlight Papers, p. 447, World Scientific, Singapore (1994b).
Bird, D.J., et al.: Astrophys. J., 511, p. 739 (1999).
Blake, P.R., et al.: PICRC, 8, p. 67 (1979a).
Blake, P.R., et al.: PICRC, 8, p. 82 (1979b).
Blake, P.R., et al.: J. Phys. G, 8, p. 1605 (1982).
Böhm, E., and E. Steinmann: PICRC, 8, p. 294 (1979).
Boley, F.I., et al.: Phys. Rev., 126, p. 734 (1962).
Boley, F.I.: Rev. Mod. Phys., 36, p. 792 (1964).
Boothby, K., et al.: Astrophys. J. Lett., 491, p. L35 (1997).
Bourdeau, M.F., et al.: J. Phys. G, 1, p. 821 (1975).
Bourdeau, M.F., et al.: J. Phys. G, 2, p. 57 (1976).
Bradt, H., et al.: PICRC, 2, p. 715 (1965).
Brennan, M.H., et al.: Nuovo Cim., Suppl. 8, p. 662 (1958).
Browning, R., and K.E. Turver: PICRC, 8, p. 3002 (1975).
Budnev, N.M., et al.: PICRC, 6, p. 257 (2005).
Cha, M., et al.: PICRC, 1, p. 132 (2001).
Chantler, M., et al.: PICRC, 9, p. 42 (1979a).
Chantler, M., et al.: PICRC, 9, p. 56 (1979b).
Chantler, M.P., et al.: PICRC, 6, p. 121 (1981).
Chantler, M.P., et al.: J. Phys. G, 8, p. L51 (1982).
Chantler, M.P., et al.: J. Phys. G, 9, p. L27 (1983).
Chudakov, A.E., et al.: PICRC, 2, p. 50 (1960).
Cortina, J., et al., HEGRA Collaboration: PICRC, 4, p. 69 (1997).
Coy, R.N., et al.: PICRC, 6, p. 43 (1981).
Craig, M.B.A., et al.: PICRC, 8, p. 180 (1979).
Dawson, B.R., et al.: J. Phys. G, 15, p. 893 (1989).
De Beer, J.F., et al.: Phil. Mag., 7, p. 499 (1962).
De Beer, J.F., et al.: Acta Phys. Acad. Sci. Hung., 29, S3, p. 657 (1970).

Dickinson, J.E., et al.: PICRC, 3, p. 136 (1999).
Diminstein, O.S., et al.: Paper presented at the 3rd. European Symposium on Air Showers, Paris (1972).
Dixon, H.E., et al.: PICRC,4, p. 2556 (1973).
Dyakonov, M.N., et al.: PICRC, 4, p. 2384 (1973a).
Dyakonov, M.N., et al.: PICRC, 4, p. 2389 (1973b).
Dyakonov, M.N., et al.: Bulleten NTI Yakutsk, Izv. YaF So Akad. Nauk. SSSR, aprel (1978).
Dyakonov, M.N., et al.: PICRC, 8, p. 174 (1979).
Dyakonov, M.N., et al.: PICRC, 6, p. 106 (1981a).
Dyakonov, M.N., et al.: PICRC, 6, p. 110 (1981b).
Dyakonov, M.N., et al.: PICRC, 4, p. 303 (1993).
Earnshaw, J.C., et al.: Can. J. Phys., 46, p. S115 (1968).
Earnshaw, J.C., et al.: J. Phys. A, 6, p. 1244 (1973).
Edge, D.M.: J. Phys. G, 2, p. 433 (1976).
Edge, D.M., et al.: PICRC, 9, p. 137 (1977).
Efimov, N.N., et al.: PICRC, 4, p. 2378 (1973).
Egorov, T.A., et al.: PICRC, 6, p. 2164 (1971).
England, C.D., et al.: PICRC, 8, p. 88 (1979).
Fomin, Yu.A., and G. Khristiansen: Yad. Fiz., 14, S3, p. 642 (1971).
Fomin, Yu.A., and G. Khristiansen: Sov. J. Nucl. Phys., 14, p. 360 (1972).
Fortson, L.F., et al.: PICRC, 3, p. 125 (1999a).
Fortson, L.F., et al.: PICRC, 5, p. 336 (1999b).
Fowler, J.W., et al.: Astropart. Phys., 15, p. 49 (2001).
Galkin, V.I., et al.: PICRC, 9, p. 79 (1979).
Galkin, V.I., et al.: PICRC, 11, p. 285 (1981).
Gibson, A.I., et al.: PICRC, 8, p. 101 (1979).
Gibson, A.I., et al.: PICRC, 6, p. 16 (1981).
Glushkov, A.V., et al.: PICRC, 8, p. 158 (1979).
Grieder, P.K.F.: PICRC, 9, p. 161 (1979a).
Grieder, P.K.F.: PICRC, 9, p. 167 (1979b).
Grieder, P.K.F.: Nuovo Cim., 84 A, p. 285 (1984).
Grigoryev, V.M., et al.: Izv. Akad. Nauk. SSSR, Ser. Fiz., 42, 7, p. 1445 (1978), Sov. J. Nucl. Phys., 27, p. 225 (1978).
Hammond, R.T., et al.: PICRC, 8, p. 281 (1977a).
Hammond, R.T., et al.: PICRC, 8, p. 287 (1977b).
Hammond, R.T., et al.: Nuovo Cim., 1 C, p. 315 (1978).
Hara, T., et al.: PICRC, 8, p. 308 (1977).
Hara, T., et al.: PICRC, 11, p. 277 (1981).
Hartman, D.H., et al.: Nuovo Cim., 51 A, p. 131 (1979).
Hayashida, N., et al.: J. Phys. G, 21, p. 1101 (1995).
Heck, D., et al.: Report FZKA 6019, Forschungszentrum Karlsruhe (1998).
Hillas, A.M.: Nucl. Phys. B (Proc. Suppl.), 52B, p. 29 (1997).
Hinton, J., et al.: PICRC, 3, p. 288 (1999).
Hörandel, J.R.: J. Phys. G, 29, p. 2439 (2003).
Ivanov, A.A., et al.: PICRC, 6, p. 241 (2005).
Jelley, J.V.: Cherenkov Radiation and Its Applications, Pergamon, London (1958).
Kakimoto, F., et al.: PICRC, 11, p. 254 (1981).
Kalmykov, N.N., et al.: PICRC, 6, p. 2074 (1971).
Kalmykov, N.N., et al.: PICRC, 8, p. 3034 (1975a).
Kalmykov, N.N., et al.: JETP Lett., 21, p. 30 (1975b).
Kalmykov, N.N., et al.: Izv. Akad. Nauk. Ser. SSSR, Fiz. 42, p. 1445 (1978a).
Kalmykov, N.N., et al.: Preprint of paper presented at the European Cosmic Ray Symposium, Kiel (1978b).

Kalmykov, N.N., et al.: PICRC, 9, p. 73 (1979).
Kaneko, T., et al.: PICRC, 7, p. 2720 (1971).
Keilhauer, B., et al.: PICRC, 2, p. 879 (2003).
Keilhauer, B., et al.: Astropart. Phys., 22, p. 249 (2004).
Keilhauer, B., et al.: Astropart. Phys., 25, p. 259 (2006).
Knapp, J., et al.: Astropart. Phys., 19, pp. 77–99 (2003).
Knurenko, S., et al.: PICRC, 1, p. 177 (2001).
Kopeliovich, B.Z., et al.: Phys. Rev. D, 39, p. 769 (1989).
Kuhlmann, J.D., et al.: PICRC, 8, p. 239 (1977).
Kuhlmann, J.D., and R.W. Clay: J. Phys. G, 7, p. L183 (1981a).
Kuhlmann, J.D., and R.W. Clay: PICRC, 6, p. 96 (1981b).
Kuhlmann, J.D., et al.: J. Phys. G, 7, p. L13 (1981).
Lapikens, J.: PICRC, 8, p. 178 (1977).
Lapikens, J., et al.: PICRC, 8, p. 95 (1979).
Liebing, D.F., et al.: J. Phys. G, 10, p. 1283 (1984).
Linsley, J., and L. Scarsi: Phys. Rev., 128, p. 2384 (1962).
Linsley, J.: PICRC, 12, p. 89 (1977).
Linsley, J., and A.A. Watson: Phys. Rev. Lett., 46, p. 459 (1981a).
Linsley, J., and A.A. Watson: PICRC, 2, p. 137 (1981b).
Makarov, V.V., et al.: PICRC, 11, p. 289 (1981).
Malos, J.: Ph. D. Thesis University of Sydney, Australia (1955).
McComb, T.J.L., and K.E. Turver: PICRC, 6, p. 130 (1981a).
McComb, T.J.L., and K.E. Turver: PICRC, 6, p. 234 (1981b).
McComb, T.J.L., and K.E. Turver: Nuovo Cim., C 5, p. 131 (1982a).
McComb, T.J.L., and K.E. Turver: J. Phys. G, 8, p. 871 (1982b).
McComb, T.J.L., and K.E. Turver: J. Phys. G, 8, p. 1119 (1982c).
NASA, National Aeronautics and Space Administration, U.S. Standard Atmosphere 1976, NASA-TM-X-74335 (1976).
Orford, K.J., et al.: PICRC, 8, p. 3014 (1975a).
Orford, K.J., et al.: PICRC, 8, p. 3019 (1975b).
Orford, K.J., and K.E. Turver: Nature, 264, p. 727 (1976).
Orford, K.J., and K.E. Turver: Phys. Rev. Lett., 44, p. 959 (1980).
Orford, K.J., et al.: PICRC, 6, p. 118 (1981).
Paling, S., et al.: PICRC, 5, p. 253 (1997).
Patterson, J.R., and A.M. Hillas: J. Phys. G, 9, p. 1433 (1983).
Protheroe, R.J., et al.: PICRC, 8, p. 3008 (1975).
Protheroe, R.J., and K.E. Turver: PICRC, 8, p. 275 (1977).
Protheroe, R.J., and K.E. Turver: Nuovo Cim., 51 A, p. 277 (1979).
Smith, G.J., and K.E. Turver: J. Phys. A, 6, p. L121 (1973a).
Smith, G.J., and K.E. Turver: PICRC, 4, p. 2369 (1973b).
Sokolsky, P., HiRes Collaboration: PICRC, 7, p. 381 (2005).
Somogyi, A.J.: Ann. Physik, 17, p. 221 (1966).
Suga, K., et al.: PICRC, 13, p. 142 (1979).
Swordy, S.P., and D.B. Kieda: Astropart. Phys., 13, p. 137 (2000).
Thornton, G.J., and R.W. Clay: J. Phys. G, 4, p. L193 (1978a).
Thornton, G.J., and R.W. Clay: J. Phys. G, 4, p. L251 (1978b).
Thornton, G.J., and R.W. Clay: J. Phys. G, 5, p. L137 (1979a).
Thornton, G.J., and R.W. Clay: Phys. Rev. Lett., 43, p. 1622 (1979b).
Thornton, G.J., et al.: PICRC, 9, p. 103 (1979).
Thornton, G.J., and R.W. Clay: Phys. Rev. Lett., 45, p. 1463 (1980).
Thornton, G., and R. Clay: Phys. Rev. D, 23, p. 2090 (1981).
Tornabene, H.: PICRC, 9, p. 94 (1979a).
Tornabene, H.: PICRC, 9, p. 99 (1979b).

Tsai, Y.S.: Rev. Mod. Phys., 46, p. 815 (1974).
Turver, K.E.: PICRC, 8, p. 2851 (1975a).
Turver, K.E.: J. Phys. G, 1, p. 134 (1975b).
Turver, K.E.: Nucl. Phys. B (Proc. Suppl.), 28B, p. 16 (1992).
Walker, R., and A.A. Watson: J. Phys. G, 7, p. 1297 (1981a).
Walker, R., and A.A. Watson: PICRC, 6, p. 31 (1981b).
Walker, R., and A.A. Watson: J. Phys. G, 8, p. 1131 (1974).
Watson, A.A., and J.G. Wilson: J. Phys. A, 7, p. 1199 (1974).
Watson, A.A.: Phys. Rep., 333–334, p. 309 (2000).
Watson, A.A.: PICRC, 6, p. 67 (2009).
Xu, X.W., et al.: J. Phys. G, 29, p. 719 (2003).
Zatsepin, V.I., and A.E. Chudakov: Zh. Eksp. Teor. Fiz., 42, p. 1622 (1962). JETP, 15, p. 1126 (1962).

Chapter 8
Lateral Structure of Showers and Energy Flow

Overview In this chapter we summarize mainly properties of the lateral structure of all shower particles combined, as recorded by conventional surface array detectors. The data that are presented here are a selection from different experiments that are operated at atmospheric depths ranging from sea level to the altitude of Mt. Chacaltaya (5,230 m), and from simulations that are representative for the various observation levels. The distributions and properties of the individual shower components such as hadrons, muons, photons and electrons as well as optical (Cherenkov and fluorescence) and radio emission, are discussed separately in Chaps. 13–18, where a wealth of data is presented.

8.1 Introduction

Air showers are usually characterized by shower size. At and near the shower maximum the latter is closely related to the energy of the primary particle. The size of an individual shower is determined by sampling the particle density distribution at ground level with an array of suitable detectors over the struck area. The shower axis should be contained within the array for reliable size determination.[1] To compute the shower size, N, from the data sample the *lateral (density) distribution function* (LDF) of the particles, $\rho(r)$, is required to carry out the integration over the entire shower impact area. Thus,

$$N = 2\pi \int_0^\infty \rho(r)\, r\, \mathrm{d}r \quad . \tag{8.1}$$

The particle density, $\rho(r)$, represents the flux of shower particles integrated over the event time, t, and solid angle, Ω, at distance r from the shower axis. It includes the full particle mix. Axial symmetry is in general assumed but large fluctuations,

[1] A similar procedure is applied for common air Cherenkov measurements with an array of wide-aperture optical detectors.

P.K.F. Grieder, *Extensive Air Showers,* DOI 10.1007/978-3-540-76941-5_8,

zenith angle and geomagnetic effects, and at rare occasions large electrostatic fields in the atmosphere can disturb this symmetry considerably.

The density distribution can be obtained experimentally from measurements or derived theoretically with the help of cascade theory. However, the original classical and theoretically well founded cascade theory to describe air showers considers electromagnetic processes only[2] (see Sect. 4.6). It consists basically of an assembly of the fundamental electromagnetic interactions that are applied sequentially to build up the cascade. Depending on the approximation used (approximation A, B or other), energy losses and/or scattering processes are disregarded or included, thus yielding non-dissipating or dissipating one or three-dimensional photon–electron cascades (Kamata and Nishimura 1958; Nishimura, 1967; Misaki 1970, 1993).

8.2 Shower Development and Particle Spread

Since, as we know today, most air showers are initiated by primary hadrons and not by gamma rays or electrons, hadronic interactions and the resulting hadron cascade are the fundamental processes. The *transverse momentum* imparted on the secondary particles emerging from hadronic interactions is the primary cause for the *lateral spread* of the hadrons. But also muons resulting mainly from the decay of charged pions and to a lesser extent from the decay of kaons and charmed particles[3] acquire part of their parent's momentum in addition to their proper decay momentum, thus increasing the lateral spread.

The hadron cascade plays a significant role for the energy transport in a shower and thus for its longitudinal but also lateral development. It also implants the countless superimposed electromagnetic sub-cascades that make up the shower. These are initiated chiefly by the photons of the decaying neutral pions and to a lesser extent by electrons from muon decays, but also occasionally through branching from charged pion and kaon decays.

The different interactions that occur in the electromagnetic cascade (pair production, bremsstrahlung, Compton and multiple Coulomb scattering, excitation and ionization) cause additional *scattering* and energy loss of the photons and electrons, and enhance the *lateral spread* of the electromagnetic component. Therefore, the lateral distribution of the shower particles is the product of the *superposition* of the hadronic as well as the electromagnetic processes in a shower. Compton and above all Coulomb scattering are the *principal causes* for the wide lateral spread of the electromagnetic component of a shower. In addition, due to the different path lengths of the particle trajectories caused by the scattering processes and because of Lorentz factor differences, the particles in the shower front are subject to time dispersion

[2] At the time, when the theory was developed, it was assumed that air showers are initiated by primary gamma rays or electrons.

[3] Charmed particle decays yield so-called *prompt muons* because of their short mean lifetime.

and the particle disc of larger showers manifests a *curvature* (Bassi et al., 1953a, b; Wilson et al., 1963).

In view of the complexity of an air shower, it is evident that its real lateral structure function is different from that of a plain photon or electron initiated pure electromagnetic shower. Unfortunately we still lack a viable general theory of hadronic interactions to compute the relevant experimental observables in a cascade accurately. However, theoretical distribution functions and spectra can be obtained from full-fledged Monte Carlo simulations of entire showers where all processes, hadronic, electromagnetic and leptonic, are considered. But we have to keep in mind that the current hadronic interaction models are to a good extent phenomenological and carefully tuned to describe accelerator results properly. There, inclusive data in the forward region are only available to energies of about 1 TeV. At collider energies our knowledge is at present confined to the central region of the available rapidity range because so far no measurements were made in the forward region. The reliability of the models diminishes rapidly with increasing degree of extrapolation as is needed to handle ultrahigh energy cosmic ray interactions, several orders of magnitude beyond accelerator and collider energies.[4]

Modern simulations permit to generate realistic air showers in four dimensions (space and time) that yield not only lateral distributions but all the observables of all particles and photons in a shower that are of interest, including optical and radio emission, at any observation level. However, for many back of the envelope considerations, distribution functions obtained from the classical electromagnetic cascade theory, and modified versions, are fully adequate as long as we deal with vertical events. In addition, since electrons make up the bulk of all the particles in a shower ($\sim$90%) the all-particle size, N, is an acceptable substitute for the electron size, N_e, for many analyses, and it is easily accessible. The situation, however, changes dramatically for strongly inclined showers because of the increasing importance of the muon component with increasing zenith angle.

Figure 8.1 shows examples of lateral density distributions of photons, electrons and muons of different threshold energies near sea level, obtained by Nagano et al. (1998) with the current state of the art air shower simulation code called CORSIKA, using the QGSJET hadronic interaction model.

In a recent study based on air shower simulations, Drescher and Farrar (2003) have investigated the lateral distribution of the electromagnetic and muonic components in large showers in an attempt to isolate the most relevant causes that affect these distributions. They arrive at the conclusion that outside the core the bulk of the muons originate from pions that emerge from relatively low energy interactions that take place at intermediate altitudes, and that the electrons at large distances are predominantly the product of low energy neutral pions that are being produced at low altitude and large distances from the core, subtending large angles with respect to the shower axis.

[4] New data from the Large Hadron Collider (LHC) at CERN in Geneva, Switzerland, will allow us to fix the hadronic interaction model parameters at an energy of about 100 PeV (10^8 GeV).

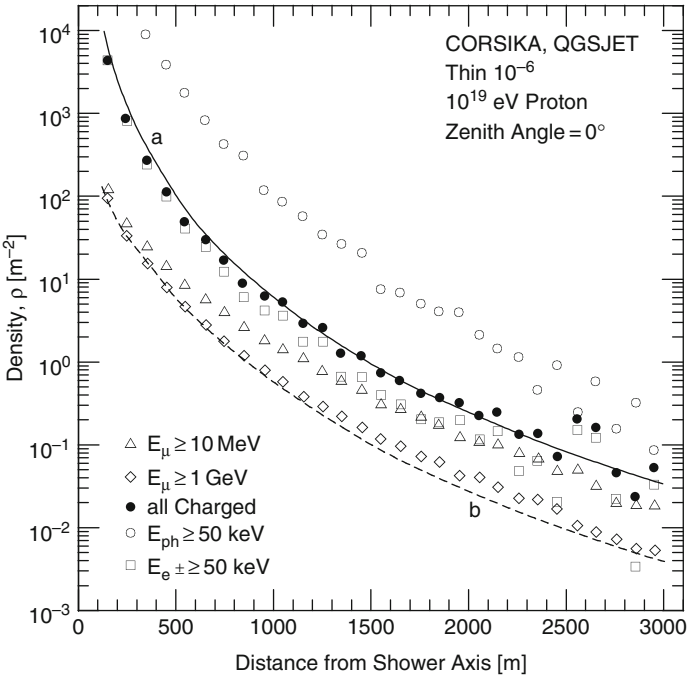

Fig. 8.1 Lateral density distribution of photons, electrons and muons of different energy groups as indicated by the symbols, obtained from simulations with the CORSIKA code using the QGSJET hadronic interaction model (Kalmykov and Ostapchenko, 1993; Kalmykov et al., 1997) for a proton primary of 10^{19} eV, using a thinning factor of 10^{-6} (Nagano et al., 1998). The *solid* and *dashed curves* show the distribution of charged particles and muons of energy $\geq$ 1 GeV, respectively, described by the empirical formulae determined experimentally from AGASA data (900 m a.s.l.) (Yoshida et al., 1994)

These conclusions agree with the very extensive much earlier analysis of Grieder (see Grieder, 1977 for a review and references listed therein). This author studied the height of origin of muons and of their parent particles as well as the generation of interactions from which the muon parents originate for different energy groups in showers using the ASICO program system, which is the parent program of CORSIKA.[5] Genetic data[6] on muons in showers are given in Chap. 14 (see also Rebel et al., 1995).

[5] ASICO, described in Chap. 20 as an example of a very comprehensive shower simulation program system, uses 12-parameters per particle, including four so-called genetic parameters which are included in some versions of CORSIKA, that permit to extract information on the origin of particles in showers.

[6] Genetic data include the generation and height of interaction or decay from which the particles originate.

8.3 Radial Dependence of Particle Composition and Particle Energy

The particle composition in a shower and the energy of the different constituents vary with distance from the shower axis. Generally speaking the energy of the particles and therefore the *energy flow* across unit area in a shower, i.e., the energy flow density, decreases rapidly with increasing distance from the shower axis within the core region. Moreover, the relative contributions of the different shower constituents (hadrons, muons, photons and electrons) to the total energy flow depend on the distance from the shower axis.

Energetic hadrons are clustered in the immediate core region. They manifest a very sharp drop in density and energy within the first few meters from the shower axis, leaving mostly low energy neutrons as the sole hadronic component at moderate core distances (details are given in Chap. 13). In and near the core the electromagnetic component is very energetic and the bulk of this component consists of direct cascade products. From the core area outward to intermediate distances the electromagnetic component is the dominating one and at large distances low energy muons are the most abundant charged particles.

At moderate distances from the shower core, from about 100 m to many 100 m in large showers ($E_0 \geq 10^{18}$ eV) the average energy of the shower particles changes little (Nishimura, 1967). This is partly because photons can travel outward up to several hundred meters from the shower axis whereas electrons in this region are mostly secondaries of the photons, have relatively low energies and travel only short distances (Kellermann and Towers, 1970). The same basic shower properties were discovered earlier by Fukui et al. (1960) for small showers ($N_e \simeq 10^5$).

With the exception of the shower core and the near-core region where energetic hadrons, multi-core events and large fluctuations may complicate the picture, the bulk of the particles in an average shower shows a *monotonic* but particle type specific decline of the density with increasing distance from the shower axis (cf. Fig. 8.1). At large distances the muon density exceeds the electron density and eventually muons are the only remaining component of a shower except for very low energy electrons ($\leq$ 10 MeV) resulting from Compton scattering of photons. The photons may be as much as *ten times* more abundant than electrons.

The long range of the muons in the atmosphere is because ionization is essentially their only kind of energy loss while propagating in a medium,[7] and many muons even at large distances from the shower axis are still relativistic. Note that slow (non-relativistic) muons have a short range and decay rapidly. Typical energies of photons, electrons and muons at distances from the shower axis ranging from about 100 to 1,000 m in $3 \cdot 10^{17}$ to 10^{18} eV showers are 10 MeV, 40 MeV and 1 GeV, respectively (Ave et al., 2003).

In a relatively recent study, Honda et al. (1997) have analyzed the particle composition at large distance in proton, iron and gamma ray initiated showers of primary

[7] Unless they are extremely energetic and subject to bremsstrahlung (see Chap. 5 for details).

energy 10^{19} eV theoretically and experimentally. In particular, they have determined the energy spectra of photons, electrons ($e^{\pm}$) and muons ($\mu^{\pm}$) at a distance of 1,410 m from the shower axis using sandwiches of unshielded and Pb-shielded scintillators, one on top of the other. Their results are shown in Fig. 8.2. These data are extremely valuable for exploring the response of the different kinds of particle detectors to shower particles, and to determine conversion relations for comparing

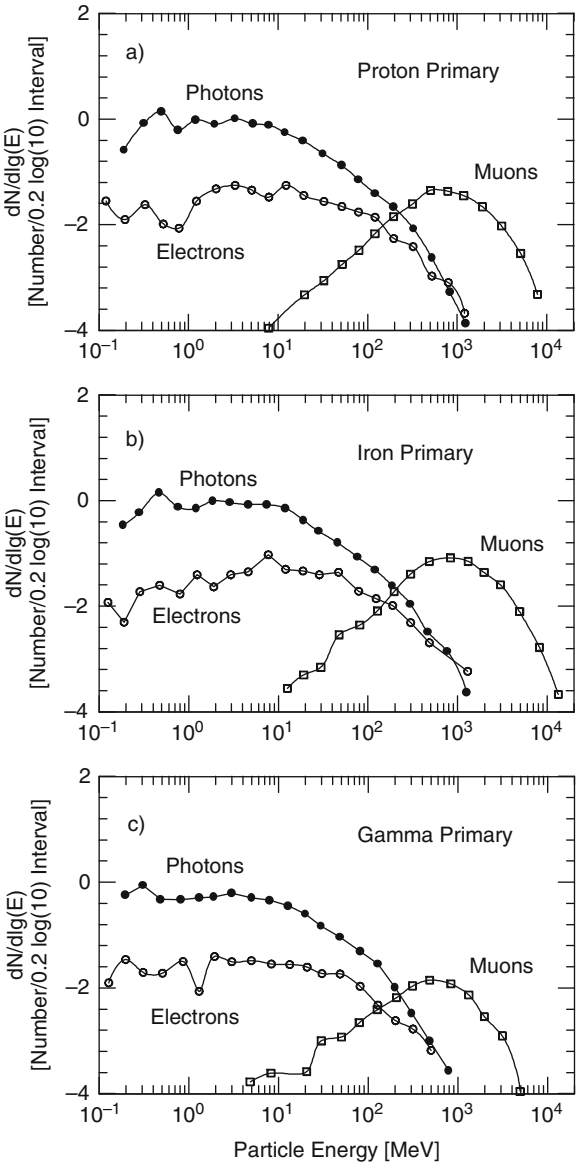

Fig. 8.2 Energy spectra of photons, electrons ($e^{\pm}$) and muons ($\mu^{\pm}$) at a core distance of 1,410 m in proton, iron and gamma ray initiated showers of primary energy 10^{19} eV (Honda et al., 1997)

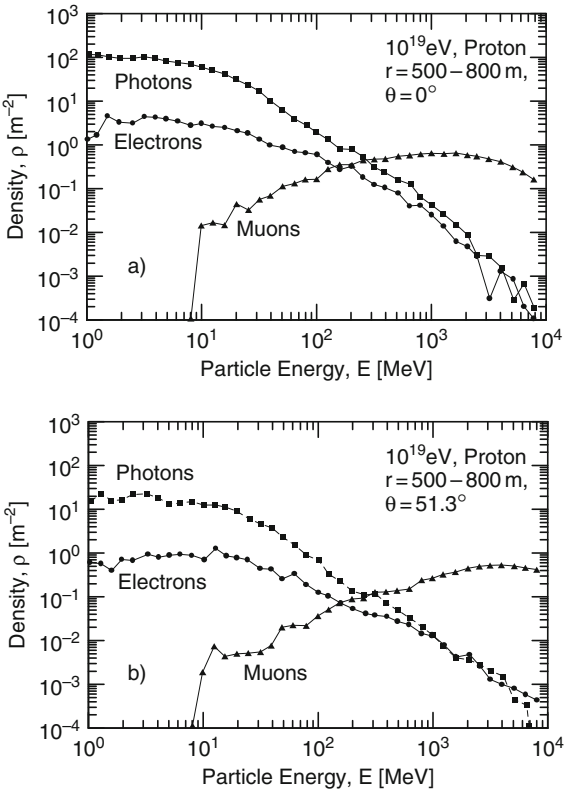

Fig. 8.3 Energy spectra of photons, electrons ($e^{\pm}$) and muons ($\mu^{\pm}$) in 10^{19} eV primary proton initiated showers in the core distance interval between 500 and 800 m for primaries incident at zenith angles of 0° (**a**), and 51.3° (**b**), after Nagano et al. (2000)

the results of deep water Cherenkov and scintillation detectors. Since the hadrons account for only about 1% of all the shower particles the shower size detectors that are distributed over a wide area in a particular pattern record mainly electrons and muons. The latter account for about 10% of all shower particles in the lower atmosphere.

A similar set of data from the work of Nagano et al. (2000) is displayed in Fig. 8.3. There the energy spectra of the same kinds of particles are plotted for vertically incident (Fig. 8.3a) and 51.3° inclined (Fig. 8.3b) 10^{19} eV proton initiated showers at the core distance interval between 500 m and 800 m. Apart from the higher particle and photon densities and a stronger presence of the more energetic particles the distributions of the two figures are similar, as must be expected.

The facts outlined above imply that for accurate work the detector response to air shower particles must be carefully considered when carrying out and interpreting particle density measurements across the shower impact area, or energy flow measurements, discussed below. In many experiments the instrumentation and calibration of the detector is such that particle density measurements yield via integration the total shower size, N, that includes all particles.

To obtain the pure electromagnetic component to get the electron size, N_e, one needs a combination of an all-particle detector and a shielded (muon) detector underneath, to subtract the latter count from the former (Honda et al., 1997). The extremely well equipped KASCADE experiment at Karlsruhe (Germany) uses this technique (Antoni et al., 2003). For either kind of shower size measurements the central density, i.e., the density in the immediate core region, requires special attention because of *detector saturation*. Another important topic to be considered is *transition effects* in the detectors, including γ-e conversion, that are discussed in Sect. 2.11.

8.4 Energy Release of Particles in the Atmosphere

Risse and Heck (2004) have calculated the energy release in the atmosphere of different air shower constituents, using the CORSIKA simulation code. This work is of relevance to compute the fluorescence photon yield of showers in the atmosphere, treated in detail in Chap. 17. The authors have come to the conclusion that the bulk of the contribution to the total energy deposit comes from the electrons and positrons populating the sub-MeV to the few hundred MeV region in a shower. Figure 8.4, taken from the work of these authors, shows the percentage of released energy contained within a given radial distance from the shower axis of the total integral energy release as a function of radial distance from the shower axis of a 10^{19} eV iron nucleus initiated shower at two different stages of development.

It is interesting to note that particles in the immediate vicinity of the shower core, at distances up to $\sim$1 m, contribute a very small fraction, in spite of their very high energy and high density, because their total number is small compared to the rest of the shower population. This work also reveals that quantitatively about 80% of the total energy release occurs in the radial range between 1 and 100 m from the axis and is due to particles in the energy range $10 \leq E \leq 50$ MeV.

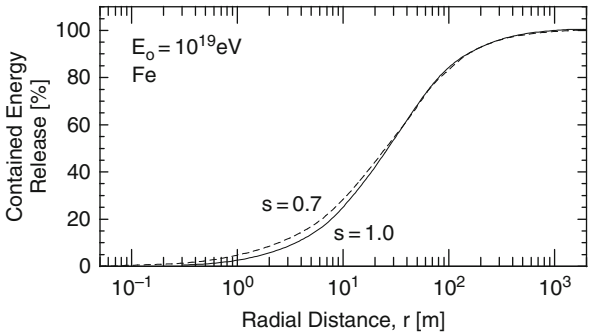

Fig. 8.4 Percentage of integral energy release as a function of radial distance from the shower axis of a 10^{19} eV primary iron nucleus initiated shower at two different stages of development characterized by the age parameters, $s = 0.7$ and 1.0, respectively (after Risse and Heck, 2004)

8.5 Density Measurements and Detector Response, Zenith Angle Dependence

8.5.1 General Aspects

For particle density measurements to determine the shower size mainly scintillation detectors are being used today, but in some older experiments ionization chambers, proportional or Geiger counters had been used instead. Another option to achieve the same ultimate goal, i.e., the determination of the primary energy of a shower, is to use so-called deep water Cherenkov detectors, known today as *Haverah Park type deep water Cherenkov detectors*. This type of detector had been developed originally for the Haverah Park experiment (220 m a.s.l., 1,018 g cm^{-2}), located near Leeds, England, many years ago (Lillicrap et al., 1963; Tennent, 1967, 1968). The standard version consisted of a rectangular tank of area 2.29 m^2 that was filled to a height of 1.2 m with water, corresponding to about 3.2 rl. Other units and assemblies measuring 9, 13.5 and even 34 m^2 having the same depth were also used (Lawrence et al., 1991). In the Pierre Auger experiment a large number of this type of detectors is being used (Pierre Auger Design Report, 1997; Bertou, 2005).

The different detector types listed here record in principle all charged particles whose energy exceeds the detector threshold, however, they exhibit different specific properties when exposed to the particle mix and energy flow in an air shower. In the following we outline the relevant features of these detectors. A more specific comparison of different detector types is given in Sect. 2.11. Since scintillation and deep water Cherenkov detectors are the most frequently used devices we will focus on these in the following outline.

8.5.2 Density Measurements and Detector Response

Scintillation detectors, ionization chambers and proportional counters measure basically *ionization*, i.e., the ionization losses the particles suffer along their track in the detector medium. The threshold energy of these detectors is very low and depends mainly on the detector enclosure and, for scintillation detectors, in addition on the light collection and photoelectron conversion efficiency. Figure 8.5 shows the energy deposit of all major shower constituents separately, expected in a standard unshielded scintillation detector, designed to be used to determine the density of the electromagnetic shower component in the KASCADE experiment as a function of distance from the shower axis over a rather moderate radial range (Weber, 1997). The plot applies to a 10^{15} eV proton initiated shower having a zenith angle of 22°.

Deep water Cherenkov detectors record the *Cherenkov photons* produced along the tracks of charged particles whose kinetic energy exceeds the Cherenkov threshold

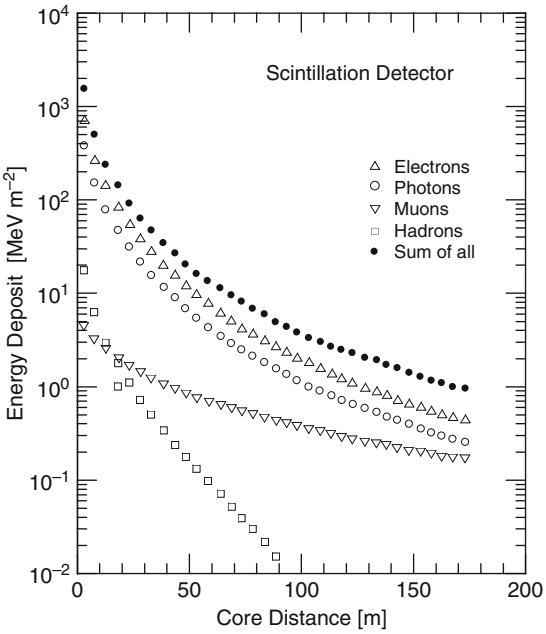

Fig. 8.5 Simulated energy deposit per square meter of the major shower constituents separately in a 5 cm deep liquid scintillation detector of the KASCADE array (110 m a.s.l.). The plot applies to a 10^{15} eV primary proton initiated shower, incident under a zenith angle of 22° (after Weber, 1997)

in water.[8] The optical photon number is nearly proportional to the energy deposited in the water, i.e., to the *energy loss* of the particles. This kind of detector is insensitive to very low energy particles.

Because of the large depth of the water column of the Haverah Park detectors the typical electromagnetic component of a shower outside the core region is completely absorbed whereas vertical muons of energy >250 MeV penetrate the detector. The detector response is therefore quite different from that of a scintillator, particularly at larger core distances; it acts partly as a calorimeter. Figure 8.6 shows the energy deposit of the major shower components in a deep water Cherenkov detector as had been used at the Haverah Park array and is now being used at the Auger Observatory over a wide radial range from the shower axis.

The signal amplitude of deep water Cherenkov detectors, i.e., the apparent particle density, $\rho(r)$, is usually expressed in terms of *vertical equivalent muons per square meter*, [veμ m^{-2}]. This corresponds to an energy deposit of $\simeq$250 MeV. An obvious advantage of deep water Cherenkov detectors over thin scintillation detectors is that the projected area of the former exposed to inclined and even to horizontal showers remains large because of the great thickness (height) of the active detector medium (water).

[8] For electrons the Cherenkov threshold energy in water is $\sim$ 0.257 MeV, for muons $\sim$ 53 MeV, for pions $\sim$ 70 MeV and for protons $\sim$ 475 MeV.

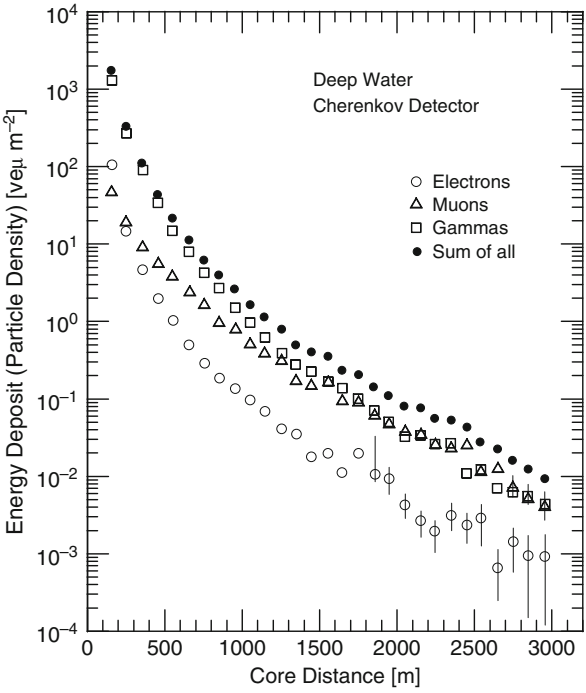

Fig. 8.6 Simulated energy deposit (or vertically penetrating muon equivalent density) [veμ m^{-2}] of the major shower constituents separately in a 120 cm deep water Cherenkov detector of a 10^{19} eV vertically incident primary proton initiated shower (after Dova et al., 2003). Thresholds are ≥ 90 keV for $e^{\pm}$, γ and > 10 MeV for $\mu^{\pm}$. A similar plot based on a different calculation is shown in Fig. 8.19

Figure 8.7 which is from a simulation of Dova et al. (2003) shows how the relative contributions from the muon and electromagnetic components to the total signal of a deep water Cherenkov detector vary with core distance in a vertical 10^{19} eV proton initiated shower. Additional properties of deep water Cherenkov detectors, are summarized in Sect. 2.11.

Simulations have shown that for large showers the energy loss in a deep water Cherenkov detector, i.e., the *energy loss density*, can be related directly to the primary energy without the need of getting first the classical shower size provided that the measurement is made outside the shower core, in the mid range of the lateral

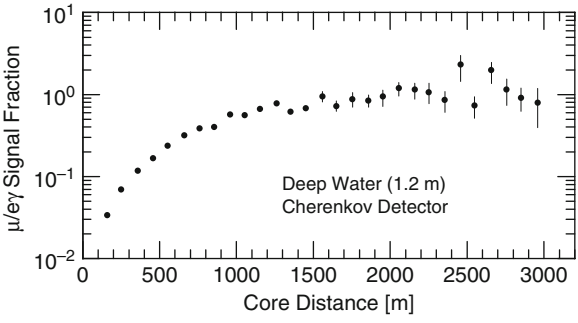

Fig. 8.7 Dependence of the relative contributions from the muon and electromagnetic components to the total signal of a deep water Cherenkov detector as a function of core distance of a vertical 10^{19} eV primary proton initiated shower (after Dova et al., 2003)

particle spread of a shower. This is at a distance of typically 600 m from the axis of showers of $\sim 10^{18}$ eV primary energy. The ideal location depends slightly on primary energy (or shower size) and zenith angle.[9] The relationship between the quantity $\rho(600)$ [veμ m^{-2}] and the primary energy is almost independent of primary mass and hadronic interactions (Hillas et al., 1970, 1971).

The reason for this rather amazing detector response is that at this location in the shower the energy flow as measured by the deep water detector is fairly independent of the details of the hadronic interactions and the mass of the primaries. As mentioned previously, this lateral region is the domain of relatively low energy photons and muons, typically $\sim$1 GeV (Honda et al., 1997; Ave et al., 2003). Additional details concerning the interpretation of the detector response and its relation to primary energy are discussed in Sects. 10.2 and 12.5.

In connection with the operation of the deep water Cherenkov detectors at the Haverah Park experiment Kellermann and Towers (1970) have carried out extensive studies of the response of this type of detector and of lead shielded and unshielded scintillation detectors to shower particles in large air showers, away from the core area, and as a function of core distance. The aim of this work was to analyze the detector differences and to find a correlation between the two kinds of measurements (scintillator and water Cherenkov) for direct comparison of the data recorded with shower arrays using the other kind of detectors.

Besides their own data, Kellermann and Towers have used the energy spectra of photons at medium and large core distances (400–1,000 m) reported by Baxter (1969), and the muon data of Allan et al. (1960, 1968), Earnshaw et al. (1968) and Vernov et al. (1968) to interpret the detector responses. At a later epoch a problem arose in the interpretation of the most energetic events recorded by the large experiments (Bower et al., 1983a and references listed therein). Bower et al. (1983b) added scintillation detectors to the Haverah Park experiment to cross check the earlier measurements and for comparison with the Yakutsk data. Their results agree well with the earlier work, with the work of Fukui et al. (1960) and Fukui (1961) using scintillators, neon hodoscopes and spark chambers at Tokyo for similar purposes, and with the previously mentioned results from the more recent work of Honda et al. (1997).

The ultimate goal of this work was to prove that the so-called *ground parameter* $\rho(600)$ (or $S(600)$ for scintillation detectors), i.e., the detector signal expressed in units of [veμ m^{-2}] (or in units of *single minimum ionizing particles for scintillators*) at a core distance of 600 m, is a reliable primary energy estimator (see also Chap. 10). In addition the work of these authors confirmed that the density measurements at this distance range made with deep water Cherenkov detectors are not subject to large fluctuations as are scintillator measurements of the predominantly electromagnetic component, in agreement with the prediction of Hillas et al. (1970).

[9] Note that deep water Cherenkov detectors are not suitable to measure the usual shower size, N or N_e in individual showers (Bower et al., 1983b).

8.5.3 Zenith Angle Dependence

Because of the zenith angle dependence of the column density (or slant depth) of the atmosphere with respect to a given observation level, showers are subject to increasing absorption with increasing zenith angle. Consequently, the stage of development and therefore the size of a shower of given primary energy manifest a zenith angle dependence and likewise for the same reason the intensity of showers of fixed size.[10] This implies that the particle and photon density of showers of fixed primary energy decrease with increasing zenith angle (if observed below the shower maximum) and the average path length of the particles in the detectors increases.

Moreover, the particle mix, too, is a function of zenith angle because the absorption of the different components follow different dependencies. Therefore different detector types respond differently to zenith angle variations and yield different shower particle absorption lengths, λ_{abs}. All these effects must be considered when converting a measured density at a particular zenith angle to vertical incidence. Different experiments must therefore use appropriately adapted relations.

For the AGASA experiment the zenith angle dependence for the scintillator density, $S(r)$, in particular for the parameter, $S(600)$, which specifies the particle density at the reference core distance of 600 m that is used for the primary energy determination, as outlined in Sect. 2.10.3 and discussed in detail in Sect. 10.2, is given for zenith angles $\theta \leq 45^\circ$ ($\sec\theta \sim 1.4$) and primary energies up to $5 \cdot 10^{19}$ eV as

$$S_\theta(600) \;=\; S_0(600)\exp\left(-\frac{X_{obs}}{\lambda_{abs}}(\sec\theta - 1)\right) \;\; [\text{part. m}^{-2}]\,. \tag{8.2}$$

Here, λ_{abs} is the particle absorption length and X_{obs} the vertical atmospheric depth [g cm^{-2}] of the observation level (920 g cm^{-2} for Akeno) (Yoshida et al., 1994). The same expression applies to other experiments using different detectors as listed below, however, the parameter λ_{abs} is detector specific.

For zenith angles $\theta \leq 45^\circ$ the particle absorption lengths λ_{abs} required to convert the densities measured at zenith angle θ to $\theta = 0$ are specified for the following experiments as (Nagano and Watson, 2000)

AGASA for $S(600)$	$\lambda_{abs} = 500 \pm 50$ g cm^{-2}	(Nagano et al., 1992)
Yakutsk for $S(600)$	$\lambda_{abs} = 500 \pm 40$ g cm^{-2}	(Glushkov et al., 1987)
Haverah Park for $\rho(600)$	$\lambda_{abs} = 760 \pm 40$ g cm^{-2}	(Edge et al., 1973)

where $\rho(600)$ applies to the density measured by the deep water Cherenkov detectors and $S(600)$ to 5 cm thick scintillators. The much longer absorption length for the water Cherenkov detectors is because comparative measurements are dominated by the muon component.

[10] For details concerning the shower rate attenuation length, Λ_{att}, and shower particle absorption length, λ_{abs}, see Chap. 6.

The particle absorption length, λ_{abs}, of $S_0(600)$ can be determined from integral $S_\theta(600)$ spectra at various zenith angles by assuming that $S_\theta(600)$ at constant intensity and different zenith angles is due to primaries of the same energy group (Nagano et al., 1992) (see Chap. 6 for details on absorption and Sect. 2.11 for complementary information on detector response).

For larger zenith angles, up to 55°, expression 8.2 takes the form

$$S_\theta(600) \;=\; S_0(600)\exp\left(-\frac{X_0}{\lambda_1}(\sec\theta-1)-\frac{X_0}{\lambda_2}(\sec\theta-1)^2\right)\;\;[\text{part.m}^{-2}]\;. \tag{8.3}$$

Here, $\lambda_1 = \lambda_{abs} = 500\,\text{g cm}^{-2}$, as before for scintillators, and $\lambda_2 = 594^{+270}_{-120}\,\text{g cm}^{-2}$ (Yoshida et al., 1994). The second term with λ_2 is a correction term because the muon to electron ratio changes in favor of the muons at large zenith angles which affects the absorption measurements. For special studies where events with even larger zenith angles are required Eq. (10.8), discussed in Sect. 10.2.3b, should be used.

8.5.4 Fluctuations and Accuracy of Measurements

Density measurements are subject to fluctuations. These must be taken into account when fitting the data from each detector to the average distribution for a particular shower group. The overall fluctuation, σ_{tot}, is the sum of contributions from different sources but depends mainly on the average particle density. The sources comprise: (1) the detector response, σ_{det}, that depends on the detector type, its resolution, the fluctuations of the ionization energy losses, the actual particle number entering and/or penetrating the detector, the particle energy and distribution (because of detector inhomogeneity), and on their angular distribution; (2) shower process inherent fluctuations that affect the lateral distribution, σ_{stat}; and (3) other possible fluctuations, σ_{res}. This situation can be expressed mathematically as follows,

$$\sigma^2_{tot} \;=\; \sigma^2_{det} + \sigma^2_{stat} + \sigma^2_{res}\;\;. \tag{8.4}$$

σ_{det} amounts to about 100% of the mean pulse height for one shower particle. Using a fitting procedure, the AGASA group found the following empirical relation to account for the contributions from the different sources of fluctuations to the density measurements,

$$\sigma^2_{\rho,tot} \;\sim\; \rho + (a\,\rho)^2 + \rho\;\;, \tag{8.5}$$

where the parameter $a = 0.25 \pm 0.05$ had been fitted to the experimental data at high densities (Hatano et al., 1979; Teshima et al., 1986).

8.6 Lateral Distribution of Shower Particles

8.6.1 Experimental Considerations

Since the discovery of air showers the lateral density distribution is one of the most intensely studied shower properties. The fundamental theoretical background concerning the lateral spread of the particles in a shower or cascade is discussed in detail in Chaps. 3 and 4. Here we summarize general results of predictions from simulations and of typical experimental lateral distributions of all shower particles as they are recorded with common unshielded detectors, unless specified otherwise. The data cover the altitude range from sea level to Mt. Chacaltaya (5,230 m a.s.l.). Measurements carried out over such a wide span of atmospheric depth sample the showers over a wide range of stages of development and shower ages.

Experimental lateral density distributions are constructed from particle density measurements obtained with the array detectors that sample the shower. The geometry of an array, i.e., the area it covers, the percentage of active detector surface, detector separation, the kind and the number of detectors an array has are important parameters that determine the size range that can be investigated with sufficient efficiency, reasonable accuracy and adequate statistics. Shower detection methods, techniques and simple shower reconstruction procedures are discussed in some detail in Chap. 2. More elaborate procedures to estimate the primary energy and other more subtle shower parameters are discussed in Chap. 10.

One of the problems that are encountered with density measurements is detector *saturation* in the presence of high particle densities and *transition effects* that are caused by energetic particles, particularly in thick plastic scintillators, faking a higher density. Both phenomena occur chiefly in the near-core area where the particle densities and energies are high. On the other hand, at large distances from the shower axis where the photon–electron component carries little energy and particle densities are low, muons are the relevant contributors to the energy deposit in thick detectors, such as deep water Cherenkov detectors.

As a practical example to illustrate detector saturation and transition effects we show in Fig. 8.8 the average lateral density distribution of particles in showers of size 10^6 at sea level, recorded by Fukui et al. (1960) at Tokyo. Shown are particle density measurements made with 4.5 cm thick scintillation detectors of 1 m^2 area, each consisting of 4 sub-units of 0.25 m^2, that sample the showers over the radial distance range from 2 to 100 m from the axis, and measurements made in the shower core region with a tightly packed neon tube hodoscope consisting of 5,040 tubes of diameter 2 cm each.[11]

This figure shows that the scintillation detectors measure too high a particle density beginning at distances of less than about 10 m from the core because of transition effects. Saturation effects in the neon hodoscope begin to appear in the

[11] The response of a single neon tube is similar to that of a Geiger counter of comparable dimensions, except that the read-out is optical.

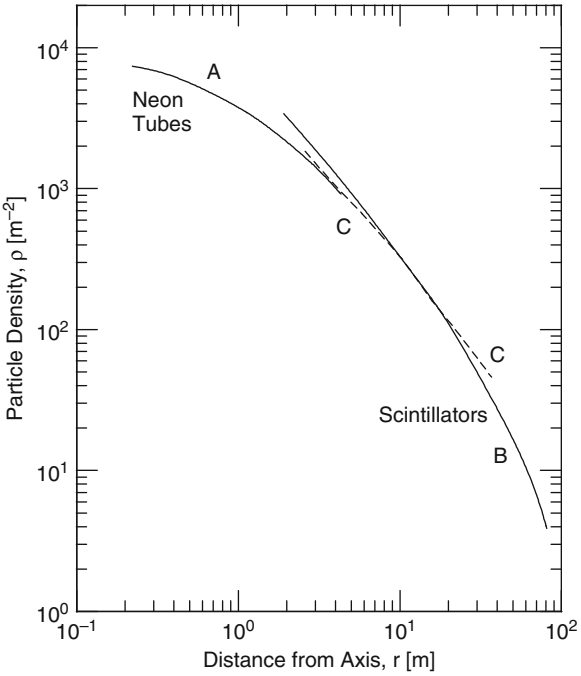

Fig. 8.8 Average lateral density distribution of particles in a shower of size 10^6 determined with two different kinds of detectors at Tokyo (s.l.). Curve A which covers the core region was obtained with a neon tube hodoscope consisting of 5,040 tubes (diameter 2 cm each), measuring 2 by 3.5 m^2, curve B with 4.5 cm thick scintillation counters of 1 m^2 area each that sample an area out to 100 m. The *dashed curve*, C, shows the best estimate after correcting for saturation and transition effects near the axis and inefficiency because of lack of energy of the particles at large distances (Fukui et al., 1960)

proximity of the shower axis,[12] at ∼1 m. A photograph of the light pattern of the neon hodoscope produced by a typical single-core shower of size 10^6 recorded by Fukui et al. (1960) is shown in Fig. 2.10 of Sect. 2.11, and illustrates this effect. The radial boundaries specified here where the two effects begin to be noticeable increase slowly outward with increasing shower size or primary energy.

8.6.2 Measured Charged Particle Distributions

Average lateral density distributions of charged particles, mainly of electrons, in small showers belonging to three different age groups that are normalized to a size of $N_e = 10^5$, recorded at Tokyo (59 m a.s.l., 1,020 g cm^{-2}), are plotted in Fig. 8.9 (Fukui, 1961). The broadening of the distribution with increasing shower age is evident. These measurements are of particular interest because they also cover the immediate core region. In Fig. 8.10 we show very recent lateral distributions of all charged particles in showers belonging to five larger energy groups, covering the range from $\geq 10^{16}$ to 10^{18} eV, recorded by the KASCADE-Grande array located at 110 m a.s.l. (Glasstetter et al., 2005).

[12] See also Chap. 15 where the lateral density distribution of the photon–electron component is discussed.

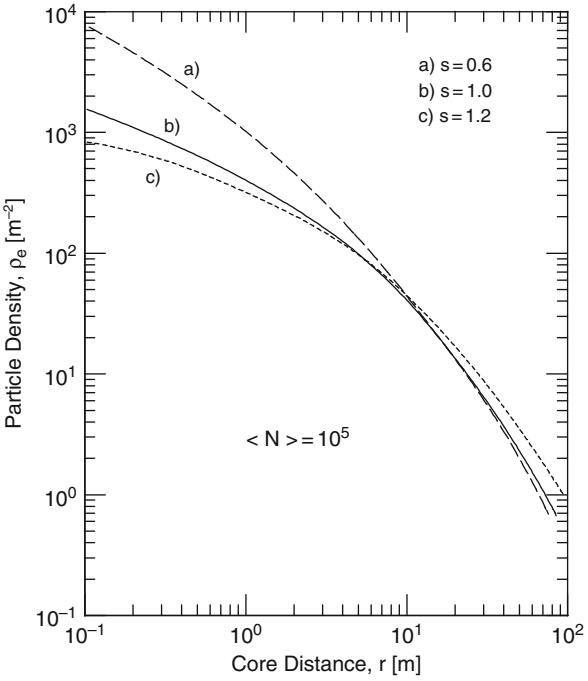

Fig. 8.9 Average lateral density distributions of charged particles, chiefly electrons, in showers of different age, s, normalized to a size of 10^5. The data are from the experimental work of Fukui (1961) carried out at Tokyo

An interesting compilation due to Hara et al. (1979) is shown in Fig. 8.11 where the data of six different experiments from sea level to Mt. Chacaltaya (5,230 m a.s.l., 530 g cm^{-2}) are summarized. The measurements from arrays at altitudes higher than sea level were made at appropriate zenith angles such that the slant depth corresponds to the vertical depth at sea level. The data cover a wide range of shower sizes ($5 \cdot 10^4 \leq N \leq 10^8$) and were normalized at about 1.5 Molière radii for comparison. Hara et al. (1979) offer some explanation for the deviations, in particular the lack of a sufficient number of density measurements within one Molière radius of the shower axis. But also the wide range of shower sizes, the greater physical lengths of inclined trajectories and the increased probability for pion decays in inclined showers may contribute to the deviations. Figure 12.1, shows a compilation of the size spectra obtained by some of these experiments and shows the degree of compatibility.

The twin figures shown in Fig. 8.12 are from the Akeno experiment (900 m a.s.l., 920 g cm^{-2}) (Hara et al., 1983). Figure 8.12a shows the density readings of the many charged particle detectors and also the muon detectors as recorded in a representative individual shower, and Fig. 8.12b the corresponding average distributions for the size group $3.15 \cdot 10^8 \leq N \leq 3.15 \cdot 10^9$.

Distributions at higher altitudes are shown in Fig. 8.13a, b. The data of Fig. 8.13a are from measurements made with the EAS-TOP array at the Gran Sasso site (2,005 m a.s.l., 810 g cm^{-2}) and include all charged particles. The four curves and

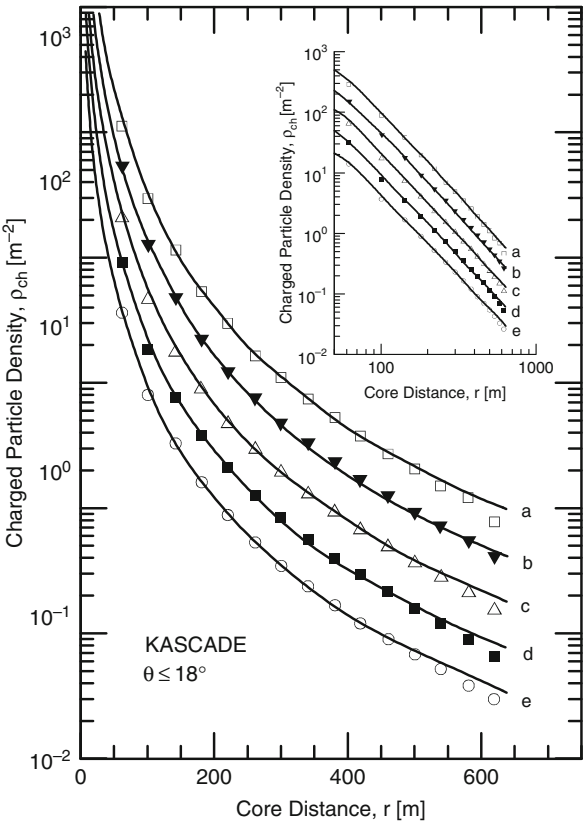

Fig. 8.10 Lateral density distribution of all charged particles measured with the KASCADE-Grande array (110 m a.s.l.) for five primary energy groups and average ages as listed below (Glasstetter et al., 2005). The large semi-logarithmic plot shows the originally published data, the insert a double-logarithmic display made by the author for comparison with similar plots from other experiments. The threshold energies are ≥ 3 MeV for the electrons ($e^{\pm}$) and ≥ 230 MeV for the muons ($\mu^{\pm}$). (Note that $\langle s \rangle$ applies to a modified NKG function.)
$\circ$ $10^7 - 2 \cdot 10^7$ GeV $\langle s \rangle$ 0.816;
$\blacksquare$ $2 \cdot 10^7 - 4 \cdot 10^7$ GeV $\langle s \rangle$ 0.817; $\triangle$ $4 \cdot 10^7 - 8 \cdot 10^7$ GeV $\langle s \rangle$ 0.824;
$\blacktriangledown$ $8 \cdot 10^7 - 1.6 \cdot 10^8$ GeV $\langle s \rangle$ 0.836;
$\square$ $(1.6 - 3.2) \cdot 10^8$ GeV $\langle s \rangle$ 0.849

sets of data points apply to four shower size groups covering the range $6.3 \cdot 10^4 \leq N_e \leq 10^6$ (Aglietta et al., 1999). Three average experimental lateral distributions obtained from measurements at Mt. Chacaltaya (5,230 m a.s.l., 530 g cm^{-2}) of very large showers covering the size range $10^8 \leq N \leq 2.4 \cdot 10^9$ are presented in Fig. 8.13b (Aguirre et al., 1973; Kaneko et al., 1975).

Finally, Fig. 8.14 shows a comparison of Aguirre et al. (1979) of distributions from Chacaltaya, the Tien Shan site in Kazakhstan (former U.S.S.R., 3,340 m a.s.l., 690 g cm^{-2}) and Yakutsk in Siberia (105 m a.s.l., 1,020 g cm^{-2}). The densities are normalized with the corresponding Molière radius to account for the different atmospheric depths.

8.6.3 Comments on Classical Theoretical and Refined Lateral Distribution Functions

As explained at the beginning of this chapter and outlined in Chap. 2, it is customary to use for the description of the lateral density distribution (LDF) of *all shower*

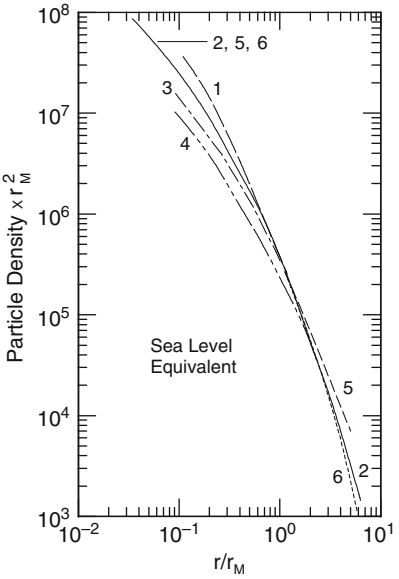

Fig. 8.11 Compilation of lateral density distributions of charged particles, chiefly electrons, obtained with different experimental installations as listed below. The data are normalized to the same density at a core distance of about 1.5 Molière units and multiplied by the Molière radius squared, at sea level. Data from elevated sites were selected from inclined showers incident under a zenith angle θ such that they had to penetrate the same atmospheric depth (or column density) as vertical showers at sea level, as is indicated by the $\sec\theta$ values, for comparison. The data cover the size range from $5 \cdot 10^4 \leq N_e \leq 10^8$. The Molière radius is $r_M = 80$ m for Moscow and $r_M = 91.6$ m for the Akeno level. The *curves* apply to the following sites: 1, Chacaltaya ($\sec\theta = 1.9$); 2, Akeno ($\sec\theta = 1.1$); 3, Moscow (s.l.); 4, Yakutsk (s.l.); 5, I.N.S. Tokyo (s.l.); and 6, Volcano Ranch ($\sec\theta = 1.2$) (Hara et al., 1979)

particles combined distribution functions that have their roots in the electromagnetic cascade theory. Frequently a common or modified Nishimura-Kamata-Greisen (NKG) function (Eq. 4.162) is used (see also Chap. 15). This is partly justified because the electromagnetic component is so dominating in well developed air showers and represents the bulk of all the particles.

NKG-like functions give a good description of the particle distribution of common vertically incident air showers in the radial mid range of the distribution ($100 \leq r \leq 1,500$ m for larger showers), outside the immediate core region. Near the shower core ($r \ll 100$ m) the particle densities and energies are so large that transition effects and saturation in the detectors, and the hadronic contamination become so important that conventional density measurements are impractical and the distribution functions invalid.

Many investigators have noticed discrepancies between theory and experiment at large radii in vertical showers. In particular, it was observed that even in pure electromagnetic (photon or electron initiated) showers the lateral spread of the

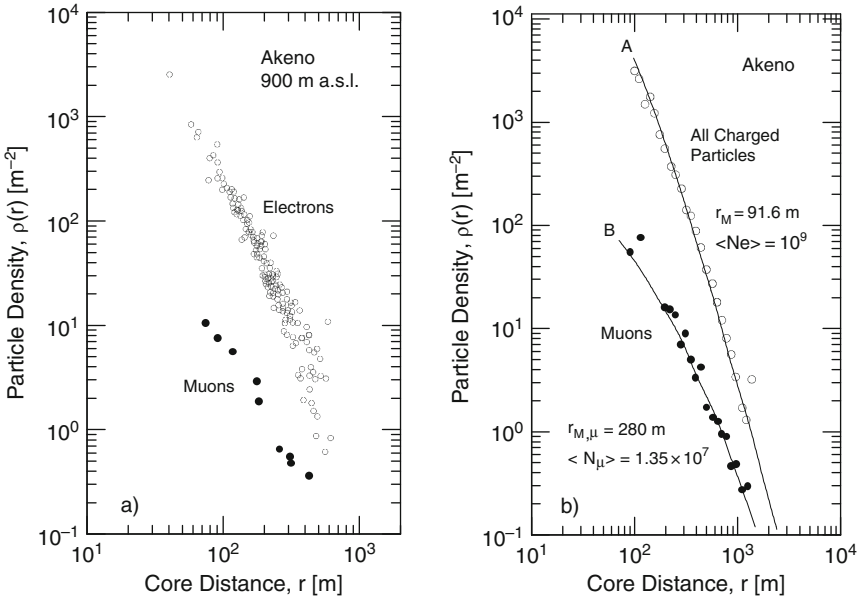

Fig. 8.12 (**a**) Example of the lateral density distribution of electrons, ○, and muons, •, in a typical shower detected at Akeno (900 m a.s.l., 920 g cm^{-2}). The shower specifications are: $N_e = 6.4 \cdot 10^7$; $N_\mu = 1.8 \cdot 10^6$ and zenith angle $\theta = 34^\circ$ (Nagano et al., 1984). (**b**) Average lateral density distribution of electrons, ○, and muons, •, in showers belonging to the size group $3.15 \cdot 10^8 \leq N_e \leq 3.15 \cdot 10^9$, detected at Akeno (900 m a.s.l.). The *curves* represent fits to the average distributions of the two particle groups for normalized showers of size of 10^9. r_M is the Molière radius for the electron distribution, $r_{M,\mu}$ is the corresponding radius of the muon distribution (Hara et al., 1983)

electrons is less than predicted by the NKG theory (Allan et al., 1975). This fact was also confirmed by Monte Carlo simulations (Hillas and Lapikens, 1977). Additional problems arise when we deal with extremely energetic and *strongly inclined showers*, where marked azimuthal asymmetries in the particle distribution at ground level occur for reasons addressed in Sect. 8.7.

A major part of the deviation between theory and experiment in vertical showers is due to the fact that common showers are initiated by energetic primary hadrons and not photons or electrons. All the products originating from hadronic interactions are subject to transverse momenta and likewise their decay products that feed the electromagnetic cascade, thus causing additional scattering which is superimposed on the electromagnetic scattering processes. The history of the hadronic parents of the electromagnetic cascade implants itself in the parameters used to describe the latter, where the age parameter s and the Molière radius, r_M, play an important role.

The deficiency of the NKG function to describe the observed particle distribution over the entire lateral range has occupied many authors through the years (Linsley, 1973; Aguirre et al., 1973; Porter, 1973; Kawaguchi et al., 1975; Nagano et al., 1984), and even in recent times (Yoshida et al., 1994; Glushkov

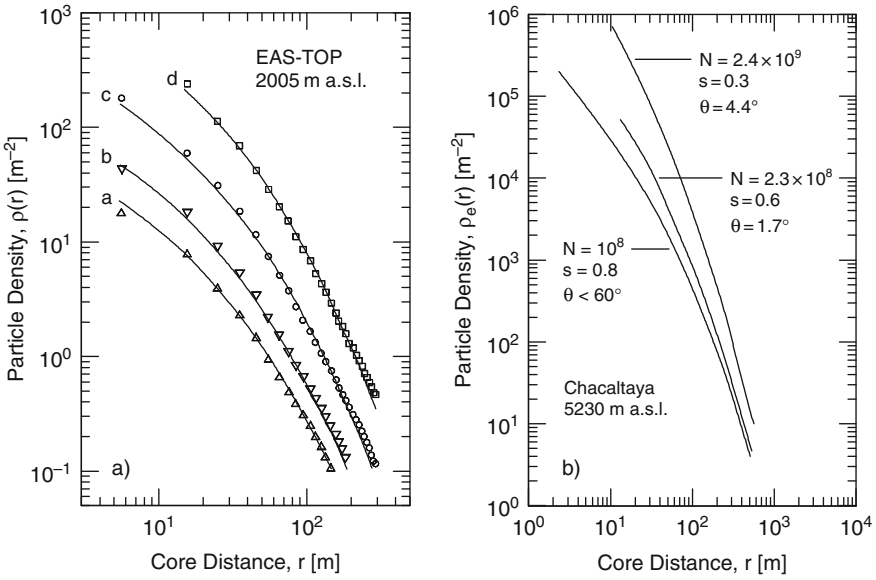

Fig. 8.13 (**a**) Experimental average lateral density distributions of charged particles in showers of different size groups measured at an altitude of 2,005 m a.s.l. (810 g cm^{-2}) at Gran Sasso and the fits to the NKG function. The symbols apply to the following shower sizes: $\triangle\ 6.3 \cdot 10^4 \leq N_e \leq 10^5$, $\triangledown\ 10^5 \leq N_e \leq 3.2 \cdot 10^5$, $\circ\ 3.2 \cdot 10^5 \leq N_e \leq 6.3 \cdot 10^5$, $\square\ 6.3 \cdot 10^5 \leq N_e \leq 10^6$ (after Aglietta et al., 1999). (**b**) Measured average lateral density distribution of charged particles in large and relatively young showers at Mt. Chacaltaya (5,230 m, 530 g cm^{-2}) (Aguirre et al., 1973; Kaneko et al., 1975)

et al., 1997; Coy et al., 1997; Nagano et al., 2000; Sakaki et al., 2001a, b; Takeda et al., 2003). Many have proposed modified forms of the distribution function and different mathematical approaches to solve the cascade problem analytically (Bourdeau et al., 1980; Lagutin et al., 1997a, b; Plyasheshnikov et al., 1979; Uchaikin et al., 1979) or proposed correction terms to improve the fits (Lagutin et al., 1979). Others have developed array and detector specific empirical distributions to fit their data for subsequent analysis. The most relevant are discussed in Sects. 8.10, 10.2, and 15.2.

For hadron initiated showers described by NKG-like functions some authors have tried to improve the fits by modifying or refining the expression for the age parameter, s (cf. Eq. 4.155), e.g., Dova et al. (2003), writing

$$s = \frac{3}{1 + (2\beta/t)}\ , \tag{8.6}$$

where β is a free parameter and accounts for the difference between a hadron initiated air shower and a pure electromagnetic shower.

Antoni et al. (2001) have investigated the lateral distribution of the electromagnetic, muonic and hadronic components with the KASCADE array. This experiment

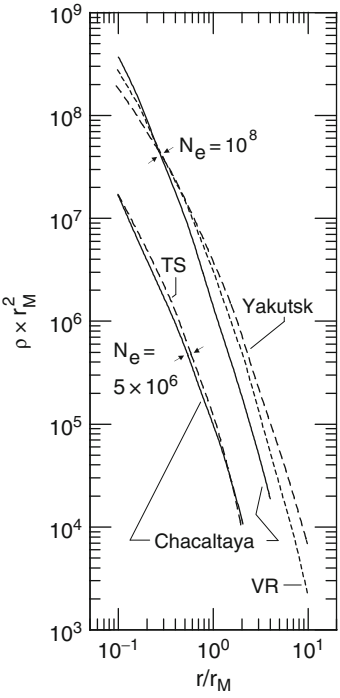

Fig. 8.14 Comparison of the lateral density distribution of shower particles recorded at the high altitude laboratory Chacaltaya (5,230 m a.s.l., 530 g cm^{-2}) with corresponding distributions measured at Yakutsk (105 m a.s.l., 1,020 g cm^{-2}) (Diminstein et al., 1977), Volcano Ranch (VR) (834 g cm^{-2}) (Linsley, 1977b), for a shower size of 10^8, and Tien Shan (TS) (3,340 m a.s.l., 690 g cm^{-2}) for a size of $5 \cdot 10^6$ (Aseikin et al., 1977). The densities and core distances are normalized with the characteristic scattering length, r_M (Molière radius) to account for the different atmospheric depths (after Aguirre et al., 1979)

allows to separate the electromagnetic and muonic components outside the core region so that fairly pure distributions of the two components become available for analysis. With the large central hadron calorimeter they are also able to obtain the distribution of the hadron component. These authors have also studied the correlation between the *scale* (Molière) *radii* of the distributions of the different components and the age parameter and arrive at the conclusion that all distributions, including that of the hadrons are well described by the NKG function, provided that the characteristic scale radii are adapted and the age parameter s properly fitted. Their work yields for the electron data $r_M = 30$ m, for the *hadron* data $r_h = 10$ m and for the *muon* data $r_\mu = 420$ m. Lateral distribution functions specifically for muons and for electrons are discussed in Chaps. 14 and 15, respectively.

8.7 Azimuthal Asymmetries of Particle Distribution

Even in vertically incident showers where one would expect an azimuthally symmetric distribution of the shower particles one observes asymmetries. These are partly due to the stochastic nature of the cascade process that causes fluctuations

of kinematic and other nature that result in locally different lateral and longitudinal developments. The more systematic patterns of the asymmetry of the lateral and azimuthal distributions of the particles in vertical showers are of geomagnetic nature and discussed in Sect. 8.8.

Inclined showers are subject to the same processes and fluctuations as vertical showers but manifest more pronounced asymmetries. Apart from the direction of propagation dependent geomagnetic effects that are emphasized in very inclined showers, the particles are spread over larger areas. In a first approximation, disregarding fluctuations and geomagnetic effects, very inclined showers produce an elongated asymmetric elliptical particle distribution pattern for geometrical reasons.

For inclined showers the stage of development at ground impact depends on the radial distance from the shower axis, on the azimuthal orientation and on the zenith angle, because of the different trajectory lengths (L_0, L_1, L_2, L_3, L_4) and corresponding column densities traversed by the different particles, from the point of production, ultimately from the point of the first interaction, h_0, down to the location of detection, r_0 to r_4, as is illustrated in Fig. 8.15. Thus, the shower age, s, is different at the different locations indicated (s_0 to s_4), whereby $s_1 > s_0 > s_2$. These effects are much emphasized in very large and strongly inclined showers. They lead to marked azimuthal asymmetries and affect the density distribution and composition of the local particle population significantly.

Figure 8.16, which is from the work of Dova et al. (2003), illustrates these effects, in particular plots (c) and (d) which show the azimuthal distributions of electrons and muons, respectively. Note that the slant depths to which the data sets of the two particle groups apply are somewhat different which, however, does not affect the arguments. These facts are important for large arrays like Auger (Dawson, 2007) and the Telescope Array (Kasahara et al., 2007) and must be considered in the data analysis. Properties of extremely inclined and horizontal air showers are discussed in Sect. 19.5.2.

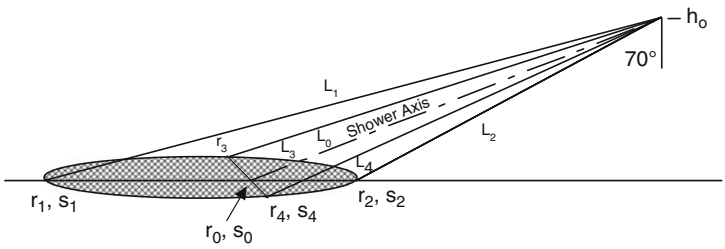

Fig. 8.15 Geometry of very inclined air shower whose axis subtends a zenith angle of 70°. h_0 marks the height and location of the first interaction in the atmosphere. The figure illustrates the very different particle trajectory lengths, e.g., L_1 and L_2, at the extreme points of ground impact at r_1 and r_2 where the shower has different local ages

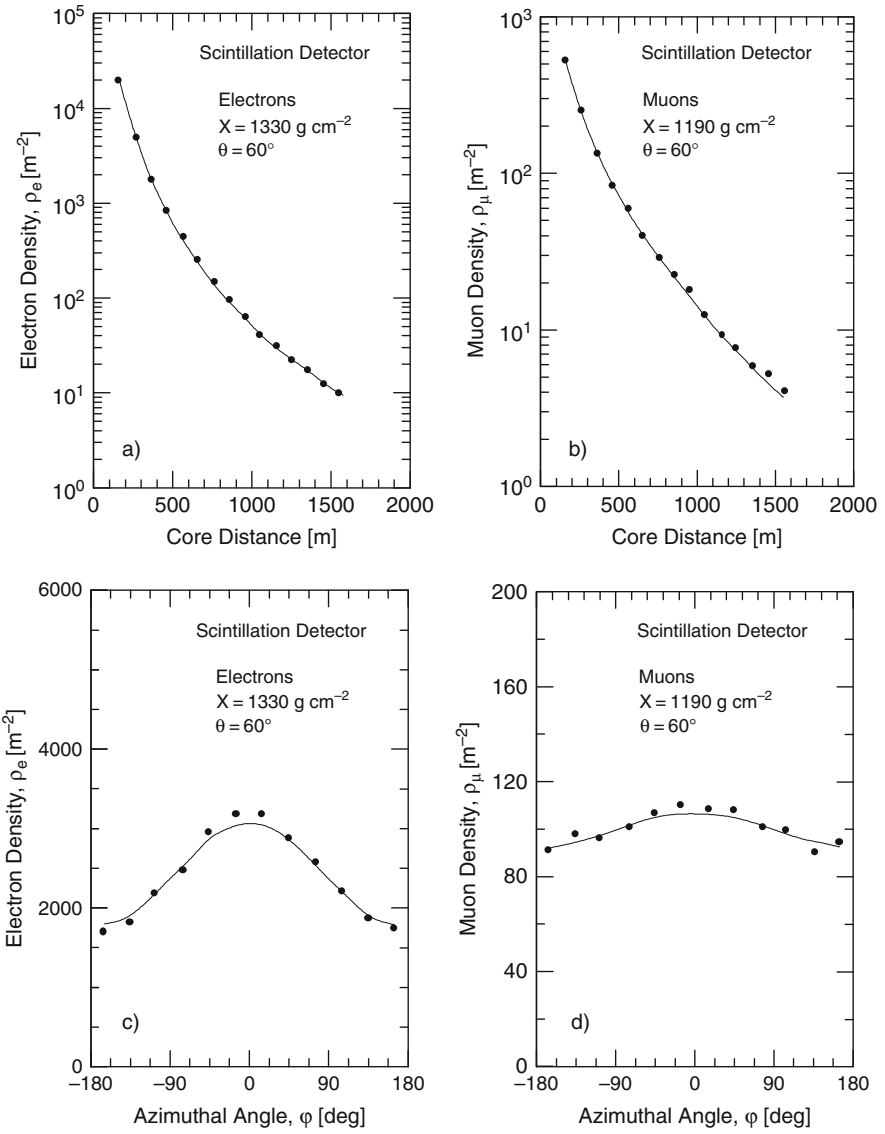

Fig. 8.16 Example of lateral density distribution of electrons (**a**) and muons (**b**), integrated over all azimuthal angles ϕ, in a 10^{19} eV simulated primary proton initiated shower having a zenith angle of 60° at altitudes corresponding to a slant depth of 1,330 g cm^{-2} (electrons) and 1,190 g cm^{-2} (muons), respectively, and azimuthal distributions of electrons (**c**) and muons (**d**), integrated over the entire fitted radial range, of the same event and at the two respective atmospheric depths (after Dova et al., 2003)

8.8 Geomagnetic Effects

Disregarding the geomagnetic field, a vertically incident primary causes a shower that exhibits on average a fairly symmetrical circular pattern of particles around the shower axis at ground level, whose density decreases with increasing radius. The symmetry is due to the randomness of the various scattering processes that are responsible for the lateral distribution of the shower particles. However, large fluctuations and asymmetries are observed from shower to shower.

The geomagnetic field affects the propagation of the particles and their trajectories through the atmosphere. The deflection of the particles depends on their velocity vector, the charge sign, on the magnitude of the geomagnetic field, and on the angle between the field and velocity vectors, i.e., referring to a shower as an entity at a particular geographic location the deflection depends on the zenith and azimuthal angles.

The deflection of a particle of mass m with charge e moving with velocity $\boldsymbol{v}$ in a given magnetic field of strength $\boldsymbol{B}$ is governed by the Lorentz force according to the equation

$$m\,\gamma\,\frac{\mathrm{d}\boldsymbol{v}}{\mathrm{d}t} \;=\; e\,(\boldsymbol{v}\times\boldsymbol{B})\;, \tag{8.7}$$

where γ is the Lorentz factor of the particle. It should be noted that γ is a rather complicated function of the particle path in the atmosphere because of the energy loss through ionization which must be considered for the less energetic particles.

The geomagnetic deflection causes not only curved particle trajectories with changing radii of curvature because of the continuous energy losses through ionization, affecting low momentum particles stronger than very energetic ones, but also provokes electric charge separation. Consequently, the azimuthal symmetry of a shower is disturbed and can lead to significant asymmetries in the density and charge distribution of the particles.

With increasing zenith angle the shower pattern begins to take on an increasingly elliptical shape. Electrons and muons are being affected differently because of the dominating effect of Coulomb scattering on the electron trajectories that dilutes the magnetic deflection effects, as explained below, which does not manifest itself alike for muons. For very inclined and quasi-horizontal showers the muon pattern deteriorates from an ellipsoidal to a double-lobe shape, with the lobes located symmetrically about the perpendicular magnetic field vector. This feature had been carefully studied by Ave et al. (2000). Other authors focused their interest on the muon charge ratio in showers (Rebel et al., 2007a, b; Xue and Ma, 2007).

Figure 8.17 illustrates the charge separation effect on the muon component in a highly inclined shower as specified in the caption. The simulation from which the results presented in this figure were obtained is based on a very simplified, naive interaction and shower model. Nevertheless, it shows beautifully the effects caused by the presence of the geomagnetic field. Beside the dislocation of the particles from the otherwise symmetric azimuthal distribution, the interaction of the moving

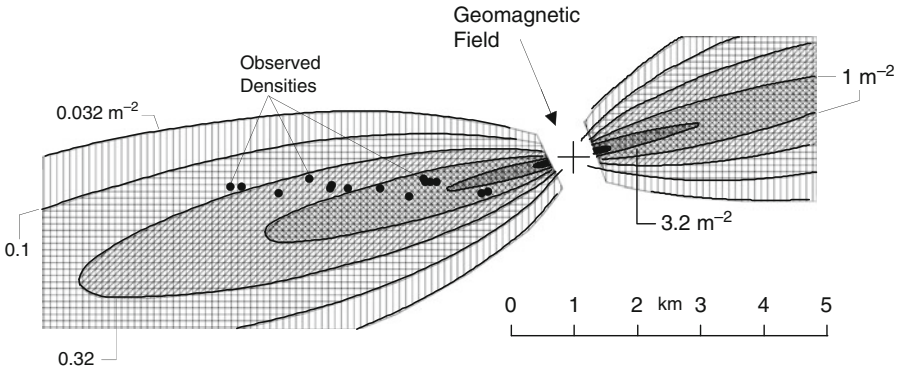

Fig. 8.17 Example of the geomagnetic deflection of the shower particles in a simulated shower. The calculation is based on a rudimentary shower model (Hillas C). Shown is the lateral density distribution of the muons in the plane normal to the shower axis projected onto the array at sea level in a 10^{20} eV proton initiated shower, incident at a zenith angle of 85° from a direction 52°E of geomagnetic north at Haverah Park. The geomagnetic field strength is 0.466 G, the typical median muon energy at the array is 100 GeV. The *dots* (•) indicate densities measured with the Haverah Park deep water Cherenkov detectors in an actual shower with the stated specifications (Hillas et al., 1970)

charges with the magnetic field also generates radio emission. This topic is discussed in Chap. 18.

The electron component manifests basically an analogous behavior as the muons, however, Coulomb scattering usually plays a more effective role over a path length on the order of one radiation unit, χ_0, for the lateral spread of the electrons than magnetic deflection. In addition, occasional large-angle scattering at high altitude of a neutral pion at production can disturb the usual symmetry of the lateral distribution significantly. Irrespective of these effects, under extreme conditions (very inclined showers with long trajectories in the geomagnetic field and the shower axis perpendicular to the field orientation) two separated density peaks may occur within a single shower which consist predominantly of low energy electrons, containing positive and negative charge excesses, respectively.

As a rule of thumb we can characterize the displacements of electrons from the initial trajectory due to Coulomb scattering, d_{scatt}, and magnetic deflection, d_{magn}, by the following expressions.

$$d_{\text{scatt}} = \frac{E_{\text{scatt}}}{E}\chi_0 \tag{8.8}$$

and

$$d_{\text{magn}} = \frac{\chi_0}{R}\chi_0 \ , \tag{8.9}$$

where E is the energy of the particle, $R = E/(300H \sin\psi)$ with H the geomagnetic field strength and ψ the angle between the directions of the field and the

momentum vector of the particle. Inserting for the radiation length $\chi_0 = 310\,\mathrm{m}$, $E_{\mathrm{scatt}} = 21\,\mathrm{MeV}$ and $H \sin\psi \approx 0.2\,\mathrm{Oe}$, one gets for the ratio

$$\frac{d_{\mathrm{magn}}}{d_{\mathrm{scatt}}} \sim 0.1 \ . \tag{8.10}$$

Thus, under average conditions Coulomb scattering is more relevant for electrons than geomagnetic deflection. For muons, however, where the trajectory may be on the order of one atmosphere, the geomagnetic deflection can cause a displacement of the same order of magnitude as Coulomb scattering.

Dedenko et al. (1995) have calculated the effect of the geomagnetic deflection on the lateral distribution function of muons in large and inclined showers using detailed Monte Carlo simulations. They have come to the conclusion that the degree of asymmetry must be considered for muon size evaluations since local densities at larger core distances may deviate by as much as a factor of two. Geomagnetic effects on extremely inclined and horizontal air showers are discussed in Sect. 19.5.2.

8.9 Lateral Distribution of Energy Flow

8.9.1 Concept of Energy Flow

The energy flow in the particle disc of a shower as it propagates through the atmosphere and its radial distribution across the disc is of interest because it contains the signatures of a variety of processes that characterize the shower development and the energy transport within a shower. Total energy flow measurements are usually based on calorimetric measurements. More tricky are energy flow measurements of individual components and particularly the determination of the energy spectrum of high energy hadrons and muons in or near the shower core because of very serious background problems. Such measurements require special detector systems that are discussed in Chaps. 13, 14 and 15.

8.9.2 Energy Flow Data

Here we present as an example the results of the pioneering energy flow measurements of Fukui et al. (1960) that can be regarded as representative for medium size showers ($N \simeq 10^6$). These authors have made extensive studies of the energy flow of the electron component ($e^{\pm}$) from the near-core region out to about 100 m from the axis in showers of size $N_e \simeq 10^6$ at sea level. The measurements were carried out with two different types of Cherenkov detectors that were designed as total absorption calorimeters.

One type consisted of a cylindrical block of optical lead glass measuring 53 cm in diameter and 30 cm in height, corresponding to a thickness of 12 radiation lengths;

the other of a lead nitrate solution in a container having a diameter of 56 cm and a height of 80 cm, corresponding to 6 radiation lengths. A total of fifteen units, distributed across the detector array out to 60 m from its center were used.

Electrons and photons that strike the detectors initiate electromagnetic showers within the Cherenkov radiator. The intensity of the Cherenkov radiation is proportional to the path length integral of all cascade electrons and, hence, is proportional to the energy dissipated in the radiator. These detectors give approximate data on the amount of energy carried by the electron–photon component. If the energy of the cascade initiating photon or electron is less than several GeV, at least 90% of their energy is deposited in the lead glass radiator, or at least 60% in the lead nitrate solution. Occasionally accompanying muons added their track length integral to the total energy deposit, but their contribution is negligible for this study. Figure 8.18, taken from the work of Fukui et al. (1960), shows the superposition of a large number of individual energy flow sampling measurements. The energy flow measured by each detector is shown with a point whose abscissa is the distance of the detector from the shower axis, and the ordinate is the energy density normalized to a shower size of 10^6. The data are corrected for the zenith angle of incidence.

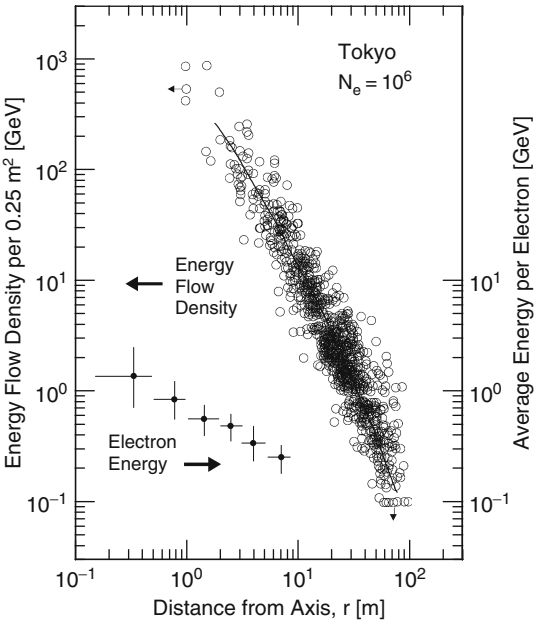

Fig. 8.18 Lateral density distribution of the energy flow of the electron-photon component in air showers at sea level, normalized to a shower size of 10^6. The *solid curve* shows the average distribution. The ordinates of the points in the superimposed scatter plot represent the energy density measured by the Cherenkov calorimeters and the abscissa the distance to the shower axis. The data are corrected for the incident zenith angle. The *tiny arrows* attached to the *upper most left* and *right side bottom points* indicate detector saturation and no count, respectively. The average energy of the electrons (*right hand ordinate*) as a function of distance from the shower axis is shown in the *lower left* of the plot (Fukui et al., 1960)

The authors have also carefully analyzed a variety of error sources. For the underestimation of the energy deposit due to leakage because of the finite thickness of the calorimeters a correction of 20% is needed. On the other hand hadrons are estimated to contribute an excess of about 20%.

The average energy of the electrons was also determined in this experiment by dividing the energy deposit in the calorimeters by the local particle density. The energy dependence of the average energy per electron is plotted in the lower left of Fig. 8.18. The energy of the electrons decreases with increasing distance from the shower axis, as expected. Additional experimental and theoretical data on the energy of the electrons in showers as a function of core distance are summarized in Fig. 15.26.

8.10 Array Specific Lateral Particle Distribution Functions

Since the measured average lateral density distribution function depends on altitude, environmental parameters, detector type and thickness, each work group has developed its own structure function to describe the lateral density distribution of the particles to fit their experimental data in order to determine the axis location of the showers, the shower size or energy, and the age parameter. Particular attention must be paid to the detector type that is being used for the shower detection, i.e., scintillation detectors (used at Volcano Ranch, Yakutsk, Akeno and AGASA) or deep water Cherenkov detectors (used at Haverah Park and at the Pierre Auger experiment[13]), since they respond very differently to shower particles, as pointed out before.

Some authors find that rather simple parameterizations in the form of a power law describe their measured distributions adequately. However, in general when working out a distribution function, most authors start with some form of NKG (Nishimura-Kamata-Greisen) function as given by Eq. (4.144) (Sect. 4.6) and adapt it to the local situation of the particular experiment.

In the following we discuss a few distribution functions that were specifically adapted to handle the data of the large arrays mentioned before. We should point out that some of the functions and/or parameters as specified here for particular experiments were subject to slight modifications in the coarse of time, as inspection of earlier publications reveals. They may be subject to modification in the future, as experience has shown, to further improve the fits. Note that many authors use for shower size the symbol N_e (electron size) instead of N (all-particle size), in spite of the fact that in most experiments the particle count includes all charged particles recorded.

In their pioneering work at the Volcano Ranch experiment (Linsley et al., 1962; Linsley, 1963) that was designed to investigate very large showers of size $5 \cdot 10^7 \leq N \leq 5 \cdot 10^{10}$ where most of the measurements were made at core distances between 700 and 1,000 m, these authors have used the following lateral structure function,

[13] The Auger experiment uses also fluorescence detectors.

$$\rho(N,r) = \frac{N}{2\pi r_{\mathrm{M}}^2}(\eta-2)\left(\frac{r}{r_{\mathrm{M}}}\right)^{-1}\left(1+\frac{r}{r_{\mathrm{M}}}\right)^{-(\eta-1)}, \tag{8.11}$$

where

$$\eta \;=\; \eta(N,\theta)\;. \tag{8.12}$$

Later, Linsley (1973, 1977a) adopted the following modified NKG structure function to fit the particle density measurements,

$$\rho(N,r) = \frac{N}{2\pi r_{\mathrm{M}}^2}\left(\frac{r}{r_{\mathrm{M}}}\right)^{-\alpha}\left(1+\frac{r}{r_{\mathrm{M}}}\right)^{-(\eta-\alpha)}\left(\frac{\Gamma(\eta-\alpha)}{\Gamma(2-\alpha)\Gamma(\eta-2)}\right), \tag{8.13}$$

where N is the all-particle shower size, r_{M} the Molière radius, adapted to account for the altitude of 1,768 m a.s.l. (834 g cm^{-2}) to a value of $r_{\mathrm{M}} = 100$ m, Γ is the common gamma function and $\alpha = (2-s)$, s being the age parameter. The logarithmic slope of this distribution approaches $-\alpha$ for $r \ll r_{\mathrm{M}}$ and $-\eta$ for $r \gg r_{\mathrm{M}}$. In addition the exponent η is a function of shower size and zenith angle, θ.

In a careful analysis using a large number of density measurements in each shower (up to 50 for large showers) and classifying the showers according to size and zenith angle, Linsley (1977a) obtained the following general expression for the zenith angle dependence of η,

$$\langle\eta\rangle \;=\; b_0 + b_1(\sec\theta\;-1) + b_2\lg(N/10^8). \tag{8.14}$$

In an elaborate fitting procedure he fixed the constants b_0, b_1, b_2, thus yielding for Eq. (8.14)

$$\langle\eta\rangle \;=\; (3.88\pm0.05)-(0.64\pm0.07)(\sec\theta\;-1)+(0.07\pm0.03)\lg(N/10^8). \tag{8.15}$$

This distribution function was used by Linsley to determine the *shower size*, not the core location. The procedure consisted of simply fitting the measured particle densities to the distribution. An accurate distribution function is important to reduce the uncertainty of the shower size from which the *primary energy* is estimated. The core location can readily be found with sufficient accuracy using even a relatively simple distribution function and applying the fitting procedure described in Sect. 2.10, or by interpolation.

For *primary energy estimates* derived from the 1.2 m deep water Cherenkov detectors operated at Haverah Park, data of measurements made at core distances between 400 and 800 m (usually 600 m) had been used.[14] At these distances the

[14] Details for the choice of the core distance for these measurements and the relation between particle density and primary energy are discussed in Sect. 10.2.

electromagnetic component is absorbed in the water column but most of the muons still penetrate the full depth of the water tanks.

Because of the large thickness of these detectors, the fraction of the energy dissipated by the two components (electromagnetic and muonic) varies with core distance and primary energy (cf. Fig. 8.7), and was determined experimentally and by simulations.[15] In the course of time slightly different functions and parameter values had been used to describe the lateral density distribution (Kellermann and Towers, 1970; Andrews et al., 1970a, b, 1971; Edge et al., 1973; Lawrence et al., 1991). In a re-assessment of the old Haverah Park work (Ave et al., 2003) it was confirmed that the lateral density distribution, $\rho(r)$, deduced from the water Cherenkov signal, expressed in units of vertical equivalent muons per square meter [veμ m^{-2}], can best be described by the function

$$\rho(r) \;=\; k\, r^{-(\eta + r/a)} \;\; [\mathrm{ve}\mu\ \mathrm{m}^{-2}] \;\;, \tag{8.16}$$

where r is the radial distance of the detector from the shower axis in meters, a is a parameter set to 4,000, k is a scale factor, and η is given by

$$\eta \;=\; 3.49 - 1.29\, \sec\theta + 0.165\, \ln\left(\frac{E}{10^{17}}\right) \quad , \tag{8.17}$$

where θ is the zenith angle and E the primary energy in [eV]. These equations are applicable for $50 \le r \le 800$ m (Coy et al., 1997).

However, it was found that for very energetic events ($E_0 \ge 10^{19}$ eV) Eq. (8.16) underestimates the density at distances $\ge$800 m, i.e., the lateral distribution gets *flatter*. Coy et al. (1997) who investigated the problem came to the conclusion that good fits to very large showers could be obtained with the modified expression that reads

$$\rho(r) \;=\; k \left(\frac{1}{800}\right)^{\beta} r^{-(\eta + r/a) + \beta} \;\; [\mathrm{ve}\mu\ \mathrm{m}^{-2}] \;\;, \tag{8.18}$$

where the authors specify $\beta = 1.03 \pm 0.05$

Figure 8.19 shows the response of a deep water Cherenkov detector as a function of core distance to photons, electrons and muons, expressed in units of [veμ m^{-2}] (corresponding to an energy deposit of $\approx$ 250 MeV), exposed to a 10^{19} eV proton initiated shower (Pierre Auger Project Design Report, 1997; Nagano and Watson, 2000). (A similar plot is shown in Fig. 8.6 from another simulation using a different shower model.)

As mentioned before, plastic scintillators had been used as shower detectors in many arrays, in particular at Volcano Ranch, Akeno and AGASA. They are being

[15] In large showers, beyond about 1 km from the axis, muons contribute on average about 50% to the total detector signal.

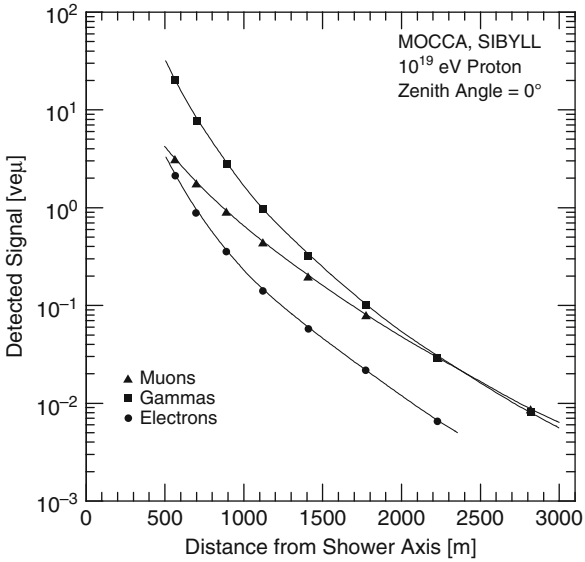

Fig. 8.19 Lateral distributions of energy deposited by photons, electrons and muons in a 1.2 m deep water Cherenkov detector in units of energy loss of vertically penetrating muons, [veμ], of energy ≥ 250 MeV, obtained from simulations with the MOCCA code (Hillas, 1981a, b, 1997) using the SIBYLL hadronic interaction model (Fletcher et al., 1994) for a proton primary of 10^{19} eV (Pierre Auger Project Design Report, 1997; after Nagano and Watson, 2000)

used at KASCADE and Yakutsk among other detectors, and at many other arrays for timing and particle density measurements. These detectors measure not actually the number of particles but ionization and therefore the energy deposit (loss) of charged particles, including low energy particles, and also the energy loss of charged interaction products of photons and neutral particles (transition effects) produced within the relatively thin detectors ($\sim$5 cm) (cf. Fig. 8.5). The scintillation detector signal, labeled $S(r)$ to distinguish it from the $\rho(600)$ signal of the deep water Cherenkov detectors, is usually expressed in units of *vertically penetrating minimum ionizing particles per square meter* (e.g., muons), from which the shower size is determined.

In order to be able to compare measurements of scintillators expressed by $S(r)$ [particles m^{-2}] with deep water Cherenkov detector data that yield $\rho(r)$, and in particular the primary energy estimator $\rho(600)$, expressed in [veμ m^{-2}], the two kinds of data must be brought to a common denominator. This had been achieved by cross calibration of the two detector types at different levels that led to conversion factors, and the quantity $S(600)$ had been adapted to the different experiments for reasons of compatibility with deep water Cherenkov detector measurements, (see Sect. 10.2 for additional details). $S(r)$ and therefore $S(600)$, too, depend on altitude and scintillator thickness.

At the Akeno array the following all-particle density distribution function, $\rho(r, N)$, had been used to fit the density measurements, expressed in charged particles per square meter, to determine the shower size (Nagano et al., 1984),

$$\rho(r, N) = \frac{N}{2\pi r_{\mathrm{M}}^2}\, C \left(\frac{r}{r_{\mathrm{M}}}\right)^{s-2} \left(1 + \frac{r}{r_{\mathrm{M}}}\right)^{s-4.5} \left(1 + \beta \frac{r}{r_{\mathrm{M}}}\right)^{v} \quad [\mathrm{m}^{-2}]. \qquad (8.19)$$

N is the total charged particle shower size, r, r_M and C have the usual meaning, $\beta = 0.2$ and $\nu = 1.3$.

For the AGASA array the distribution function had been modified only very slightly. It reads, using $S(r, N)$ in place of $\rho(r, N)$ (Yoshida et al., 1994; Doi et al., 1995; Takeda et al., 2003),

$$S(r, N) = N\,C \left(\frac{r}{r_M}\right)^{-\alpha} \left(1 + \frac{r}{r_M}\right)^{-(\eta-\alpha)} \left[1 + \left(\frac{r}{a}\right)^2\right]^{-0.6} . \tag{8.20}$$

Here, N is the shower size, C the normalizing constant that depends on shower size, $r_M = 91.6$ m is the Molière radius at a height of two radiation lengths above the Akeno site[16] (900 m a.s.l.), a is a parameter set to $a = 1000$, $\alpha = 1.2$ and

$$\eta = 3.97 - 1.79(\sec\theta - 1) . \tag{8.21}$$

According to Hayashida et al. (1999) and Sakaki et al. (2001a) Eq. (8.20) applies to a radial range of $500 \le r \le 3,000$ m from the shower axis for showers up to primary energies of 10^{20} eV and zenith angles $\theta \le 45^\circ - 50^\circ$. Note that the constants in the expression for η are frequently slightly modified, depending on the authors, to optimize the analysis.

Nagano et al. (2000) in operating the Akeno and later on the AGASA experiment noticed that at very large distances from the shower axis *the density appears to drop more rapidly*. This conclusion contradicts an earlier statement by Hara et al. (1979).

The corresponding relation for the Yakutsk array is given by (Afanasiev et al., 1996) as

$$S(r) = N\,C \left(\frac{r}{r_M}\right)^{-\alpha} \left(1 + \frac{r}{r_M}\right)^{-(\eta-\alpha)} \left[1 + \left(\frac{r}{2,000}\right)\right]^{-g} , \tag{8.22}$$

where $r_M = 70$ m, corresponding to the altitude of 100 m a.s.l. for Yakutsk,[17] $\alpha = 1.3$, C is the scale factor, and

$$\eta = 1.38 + 2.16\cos\theta + 0.15\lg[S_\theta(600)] . \tag{8.23}$$

The exponent g is a function of primary energy. It is 1.6 at $1.26 \cdot 10^{18}$ eV and 3.5 at $1.26 \cdot 10^{19}$ eV, and $S_\theta(600)$ is the $S(600)$ value at zenith angle θ.

Some additional expressions that had been used in older experiments to describe the lateral density distribution are given in Sect. 8.13.

---

[16] The reason for taking a Molière radius one or two radiation lengths above the observation level is because of the density effect, discussed in Sects. 6.5.2 and 6.5.3 (see also Molière, 1953; Greisen, 1956, 1960; Janossy, 1948, 1958).

[17] At the Yakutsk site r_M must be seasonally adapted because of the large temperature and air density changes between summer and winter.

8.11 Effects of Shower Front Structure, Time Dispersion and Delayed Particles on Density Measurements

In order to extend the dynamic range of particle density measurements it is customary to use logarithmic amplifiers and a time over threshold detector to convert the pulse height from the photomultiplier of a scintillation detector to pulse width. The output pulse width increases logarithmically with the input pulse height, thus expanding the range of the density measurement significantly. Other detector types may use this kind of device, too.

Because the particles in the shower disc manifest a time dispersion, the arrival of the particles in a shower burst at any detector of an array is in general not instantaneous but spread over an interval on the order of ∼100 ns in large showers at several 100 m from the axis. Since the resulting pulse width at the output of the pulse height to time converter depends not only on the input pulse height but also on the temporal spread of the pulse sequence caused by the particles (and on the system integration time constant), the signal is not unique for a given number of particles in a burst.

A similar and sometimes even worse effect is caused by delayed particles that trail the shower front by several microseconds, particularly when they deposit large ionization losses in the scintillator, and by accidental coincidences. Time dispersion and delayed particles can therefore lead to erroneous particle density interpretations and to wrong estimates of the primary energy of a shower. Caution is therefore required in the interpretation of density measurements that employ pulse height to pulse width converters.

Temporal aspects of the particles in the shower disc and the disc curvature are discussed in Chap. 9. Topics related to time dispersion and delayed particles, and their effect on particle density measurements are summarized in Sect. 9.6.

8.12 Lateral Distribution of Air Cherenkov Photons

A separate chapter (Chap. 16) is dedicated to optical Cherenkov emission of air showers where all the details are discussed and many data are presented. We therefore list here simply for reasons of completeness and as an example a lateral density distribution function of Cherenkov photons, $Q(r)$ (Eq. 8.24), and present in Fig. 8.20 a corresponding experimental distribution in showers of average size $3.1 \cdot 10^7$, both from the work of the Yakutsk group (Egorov et al., 1971). Also shown in this figure are lateral density distributions of optical Cherenkov photons from simulated 10^{17} and 10^{18} eV primary gamma ray initiated showers and, for comparison, a particle density distribution of showers of size $1.5 \cdot 10^8$ from the same experiment. The simulations lead to an optical photon lateral distribution function that can be described by the following relation

$$Q(r, N) \propto r^{(-1.6 \pm 0.15)} \ [\mathrm{ph\,m^{-2}}] \,. \tag{8.24}$$

This relation gives a good fit to the measured photon distribution.

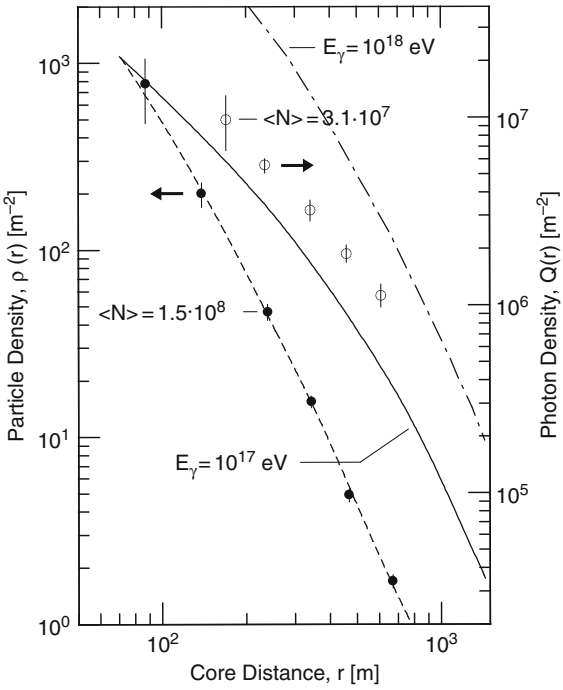

Fig. 8.20 Lateral density distribution of particles (•), $\rho(r)$, and of optical Cherenkov photons (○), $Q(r)$, observed in showers incident at zenith angles $\theta \leq 30^\circ$ at Yakutsk (100 m a.s.l.). The particle measurements apply to showers of average size $\langle N \rangle = 1.5 \cdot 10^8$, the photon measurements to showers of average size $3.1 \cdot 10^7$. For comparison, the *dot-dash* and *solid curves* are theoretical distributions of $Q(r)$ obtained from calculations for primary gamma rays of energy 10^{18} and 10^{17} eV, respectively. The *dashed curve* is a fit obtained by Linsley (1963) (after Egorov et al., 1971)

8.13 Mathematical Expressions and Fits

In the following we list for reference some additional lateral density distribution functions of shower particles that had been used in the past in some experiments to describe and interpret measurements.

For historic reasons we should mention the LDF which Greisen introduced in the early days of air shower research (Greisen, 1960), given below.

$$\rho(r, N) = \frac{0.4N}{r_M^2} \left(\frac{r_M}{r}\right)^{0.75} \left(\frac{r_M}{r + r_M}\right)^{3.25} \left(1 + \frac{r}{11.4 r_M}\right) , \qquad (8.25)$$

where N is the shower size, and r and r_M are the core distance and Molière radius, respectively. It must be pointed out that here the term shower particles includes all charged particles, i.e., electrons, muons and hadrons. This implies that the true electron density runs about 5–10% below the actually measured density.

This formula which is an empirical analytic function is claimed to be valid for core distances from 5 cm to 1,500 m in showers of size ranging from $2 \cdot 10^3$ to $2 \cdot 10^9$ particles and atmospheric depths from 537 g cm^{-2} (5,200 m a.s.l.) to 1,800 g cm^{-2} (zenith angle at sea level of 55°) (Greisen, 1960, p. 71). The formula resembles strongly the NKG function (Kamata and Nishimura, 1958) but *does not depend* on the age parameter, s.

Hasegawa et al. (1962) have used the relation

$$f\left(\frac{r}{r_{\mathrm{M}}}\right) \propto \frac{r_{\mathrm{M}}^2}{2\pi\sqrt{120\pi}}\left(\frac{\exp(r/120)}{r^{1.5}}\right) , \tag{8.26}$$

where r is the distance from the shower axis and $r_{\mathrm{M}} = 80\,\mathrm{m}$ for the Molière radius at sea level.

Egorov et al. (1971) obtained a good fit for their data of large showers ($10^{17} \leq E_0 \leq 10^{18}$ eV) over the core distance range from 100 to 600 m at Yakutsk with the expression

$$\rho(r, N) = \frac{N}{r_{\mathrm{M}}^2}\left(\frac{\eta - 2}{2\pi}\right)\left(\frac{r}{r_{\mathrm{M}}}\right)^{-1}\left(1 + \frac{r}{r_{\mathrm{M}}}\right)^{-(\eta-1)} \quad [\mathrm{m}^{-2}] , \tag{8.27}$$

where $r_{\mathrm{M}} = 71.5\,\mathrm{m}$ at the Yakutsk level at an atmospheric depth of $1{,}005\,\mathrm{g\,cm}^{-2}$ ($\sim$100 m a.s.l.) and a temperature of -10°C. The parameter η is 3.35, 3.5 and 4.0 for showers of size $5 \cdot 10^7$, 10^8 and 10^9, respectively, and zenith angles $\theta \leq 30^{\circ}$ at sea level.

Kaneko et al. (1975) found in a careful analysis of the data from the array at Mt. Chacaltaya (5,230 m a.s.l.) by optimizing various parameters using χ^2-tests the following LDF,

$$\rho(r, N) = \frac{C_1 N}{2\pi r_{\mathrm{M}}^2}\left(\frac{r}{r_{\mathrm{M}}}\right)^{(s-2)}\left(1 + \frac{r}{r_{\mathrm{M}}}\right)^{(s-4.5)}\left[1 + C_2\left(\frac{r}{r_{\mathrm{M}}}\right)^{2.0}\right] [\mathrm{m}^{-2}] , \tag{8.28}$$

where

$$C_1 = \left(\frac{\Gamma(s)\Gamma(4.5 - 2s)}{\Gamma(4.5 - s)} + C_2\frac{\Gamma(2.0 + s)\Gamma(2.5 - 2s)}{\Gamma(4.5 - s)}\right)^{-1} , \tag{8.29}$$

and

$$C_2 = 0.100 + 0.125(\sec\theta - 1) . \tag{8.30}$$

These relations are valid for $3 \cdot 10^6 < N < 3 \cdot 10^9$, $0 < \theta < 60^{\circ}$, $0.1 < r_{\mathrm{M}} < 3r_{\mathrm{M}}$ and for the locally valid Molière radius, $r_{\mathrm{M}} = 155\,\mathrm{m}$.

At a somewhat later epoch Aguirre et al. (1979) introduced the following distribution function that appears to be better adapted to the Chacaltaya altitude (5,230 m a.s.l.).

$$\rho_{\mathrm{ch}}(r, N) = \left(\frac{1.03 \cdot C_1 N}{2\pi r_{\mathrm{M}}^2}\right)\left(\frac{r}{r_{\mathrm{M}}}\right)^{(s-2.0)}\left(1+\frac{r}{r_{\mathrm{M}}}\right)^{(s-4.5)} \cdot \left(1 + C_2\left(\frac{r}{r_{\mathrm{M}}}\right)^{2.0}\right) \cdot \left(1 - 0.20 \cdot \exp\left[-2\left(\ln\left(\frac{r}{r_{\mathrm{M}}}\right) + 0.3\right)^2\right]\right) \quad [\mathrm{m}^{-2}] \tag{8.31}$$

where C_1 and C_2 are given by Eqs. (8.29) and (8.30).

References

Afanasiev, B.N., et al.: Proceedings of the International Symposium on Extremely High Energy Cosmic Rays: Astrophysics and Future Observatories, M. Nagano, ed., Institute for Cosmic Ray Research, University of Tokyo, p. 32 (1996).
Aglietta, M., et al.: Astropart. Phys., 10, p. 1 (1999).
Aguirre, C., et al.: PICRC, 4, p. 2592 (1973).
Aguirre, C., et al.: J. Phys. G, 5, p. 139 (1979).
Allan, H.R., et al.: Proc. Phys. Soc., 76, p. 1 (1960).
Allan, H.R., et al.: Can. J. Phys., 46, p. S234 (1968).
Allan, H.R., et al.: PICRC, 8, p. 3071 (1975).
Andrews, D., et al.: Acta Phys. Acad. Sci. Hung., 29, S3, p. 343 (1970a).
Andrews, D., et al.: Acta Phys. Acad. Sci. Hung., 29, S3, p. 349 (1970b).
Andrews, D., et al.: PICRC, 3, p. 995 (1971).
Antoni, T., et al.: Astropart. Phys., 14, pp. 245–260 (2001).
Antoni, T., et al.: Nucl. Instr. Meth., A 513, p. 490 (2003).
Aseikin, V.S., et al.: PICRC, 8, p. 98 (1977).
Ave, M., et al.: Astropart. Phys., 14, p. 91 (2000).
Ave, M., et al.: Astropart. Phys., 19, p. 47 (2003).
Bassi, P., et al.: Phys. Rev., 91, p. 432 (1953a). (Abstract A.P.S. Spring meeting.)
Bassi, P., et al.: Phys. Rev., 92, p. 441 (1953b).
Baxter, A.J.: J. Phys. A, 2, p. 50 (1969).
Bertou, X., Pierre Auger Collaboration: PICRC, 7, p. 1 (2005).
Bourdeau, M.F., et al.: J. Phys. G, 6, p. 901 (1980).
Bower, A.J., et al.: J. Phys. G, 9, p. L53 (1983a).
Bower, A.J., et al.: J. Phys. G, 9, p. 1569 (1983b).
Coy, R.N., et al.: Astropart. Phys., 6, p. 263 (1997).
Dawson, B.R., Telescope Array Collaboration: PICRC, pre-conference edition, paper 0976, Merida, Mexico (2007).
Dedenko, L.G., et al.: PICRC, 4, p. 309 (1995).
Diminstein, O.S., et al.: PICRC, 8, p. 154 (1977).
Doi, T., et al.: PICRC, 2, p. 764 (1995).
Dova, M.T., et al.: Astropart. Phys., 18, p. 351 (2003).
Drescher, H.-J., and G.R. Farrar: Astropart. Phys., 19, p. 235 (2003).
Earnshaw, R.A., et al.: Can. J. Phys., 46, p. S5 (1968).
Edge, D.M., et al.: J. Phys. A, 6, p. 1612 (1973).
Egorov, T.A., et al.: PICRC, 6, p. 2059 (1971).
Fletcher, R.S., et al.: Phys. Rev., D 50, p. 5710 (1994).
Fukui, S., et al.: Prog. Theor. Phys. Jpn., 16, p. 1 (1960).

Fukui, S.: J. Phys. Soc. Jpn., 16, p. 604 (1961).
Glasstetter, R., et al.: PICRC, 6, p. 293 (2005).
Glushkov, A.V., et al.: PICRC, 5, p. 494 (1987).
Glushkov, A.V., et al.: PICRC, 6, p. 233 (1997).
Greisen, K.: Progress in Cosmic Ray Physics, North Holland, Amsterdam, Vol. 3, p. 1 (1956).
Greisen, K.: Ann. Rev. Nucl. Sci., 10, p. 63 (1960).
Grieder, P.K.F.: Rivista del Nuovo Cim., 7, p. 1 (1977).
Hara, T., et al.: PICRC, 13, p. 148 (1979).
Hara, T., et al.: PICRC, 11, p. 276 (1983).
Hasegawa, H., et al.: J. Phys. Soc. Jpn., 17, Suppl. A-III, p. 189 (1962).
Hatano, Y., et al.: PICRC, 11, p. 161 (1979).
Hayashida, N., et al.: PICRC, 1, p. 353 (1999).
Hillas, A.M., et al.: Acta Phys. Acad. Sci. Hung., 29, S3, p. 533 (1970).
Hillas, A.M., et al.: PICRC, 3, p. 1007 (1971).
Hillas, A.M., and J. Lapikens: PICRC, 8, p. 460 (1977).
Hillas, A.M.: PICRC, 1, p. 193 (1981a).
Hillas, A.M.: in Proceedings of the Paris Workshop on Cascade Simulations, J. Linsley and A.M. Hillas, eds., Texas Center for the Advancement of Science and Technology College Station, TX, p. 39 (1981b).
Hillas, A.M.: Nucl. Phys. B (Proc. Suppl.), 52B, p. 29 (1997).
Honda, K., et al.: Phys. Rev. D, 56, p. 3833 (1997).
Janossy, L.: Cosmic Rays, Oxford University Press, London (1948).
Janossy, L., et al.: Nuovo Cim., Suppl. VIII, p. 701 (1958).
Kalmykov, N.N., and S.S. Ostapchenko: Phys. Atom. Nucl., 56-3, p. 346 (1993).
Kalmykov, N.N., et al.: Nucl. Phys. B (Proc. Suppl.), 52B, p. 17 (1997).
Kamata, K., and J. Nishimura: Prog. Theor. Phys. Jpn., 6, Suppl., p. 93 (1958).
Kaneko, T., et al.: PICRC, 8, p. 2747 (1975).
Kasahara, K., et al.: PICRC, pre-conference edition, paper 0955, Merida, Mexico (2007).
Kawaguchi, S., et al.: PICRC, 8, p. 2826 (1975).
Kellermann, E.W., and L. Towers: J. Phys. A, 3, p. 284 (1970).
Lagutin, A.A., et al.: PICRC, 7, p. 18 (1979).
Lagutin, A.A., et al.: PICRC, 6, p. 285 (1997a).
Lagutin, A.A., et al.: PICRC, 6, p. 289 (1997b).
Lawrence, M.A., et al.: J. Phys. G, 17, p. 733 (1991).
Lillicrap, S.C., et al.: Proc. Phys. Soc., 82, p. 95 (1963).
Linsley, J., et al.: J. Phys. Soc. Jpn., 17, Suppl. A-III, p. 91 (1962).
Linsley, J.: PICRC, 4, p. 295 (1963).
Linsley, J.: PICRC, 5, p. 3212 (1973).
Linsley, J.: PICRC, 12, p. 56 (1977a).
Linsley, J.: PICRC, 8, p. 206 (1977b).
Misaki, A.: Acta Phys. Acad. Sci. Hung., 29, S3, p. 593 (1970).
Misaki, A.: Nucl. Phys. B (Proc. Suppl), 33AB, p. 192 (1993).
Molière, G.: Vorträge über Kosmische Strahlung, 2. Auflage (in German), W. Heisenberg, ed., Springer, Berlin, p. 446 (1953).
Nagano, M., et al.: J. Phys. G, 10, p. 1295 (1984).
Nagano, M., et al.: J. Phys. G, 18, p. 423 (1992).
Nagano, M., et al.: Report FZKA 6191, Forschungszentrum Karlsruhe, Germany (1998).
Nagano, M., and A.A. Watson: Rev. Mod. Phys., 72, p. 689 (2000).
Nagano, M., et al.: Astropart. Phys., 13, p. 277 (2000).
Nishimura, J.: Handbuch der Physik, S. Flügge, ed., Vol. 46/2, p. 1, Springer Verlag, Berlin (1967).
Pierre Auger Project Design Report, 1997, Auger Collaboration, Fermi National Accelerator Laboratory (FNAL) (1997).
Plyasheshnikov, A.V., et al.: PICRC, 7, p. 1 (1979).

Porter, N.A.: PICRC, 5, p. 3657 (1973).
Rebel, H., et al.: J. Phys. G, 21, p. 451 (1995).
Rebel, H., et al.: Forschungszentrum Karlsruhe, Report FZKA 7294 (2007a).
Rebel, H., et al.: PICRC, pre-conference edition, paper 0861, Merida, Mexico (2007b).
Risse, M., and D. Heck: Astropart. Phys., 20, p. 661 (2004).
Sakaki, N., et al.: PICRC, 1, p. 329 (2001a).
Sakaki, N., et al.: PICRC, 1, p. 333 (2001b).
Takeda, M., et al.: Astropart. Phys., 19, p. 447 (2003).
Tennent, R.M.: Proc. Phys. Soc., 92, p. 622 (1967).
Tennent, R.M.: Can. J. Phys., 46, p. S1 (1968).
Teshima, M., et al.: J. Phys. G, 12, p. 1097 (1986).
Uchaikin, V.V.: PICRC, 7, p. 24 (1979).
Vernov, S.N., et al.: Can. J. Phys., 46, p. S197 (1968).
Weber, J.H., KASCADE Collaboration: PICRC, 6, p. 153 (1997).
Wilson, J.G., et al.: PICRC, 4, p. 27, (1963).
Xue, B.K., and B.-Q. Ma: Astropart. Phys., 27, p. 286 (2007).
Yoshida, S., et al.: J. Phys. G, 20, p. 651 (1994).

Chapter 9
Temporal Structure of Showers and Front Curvature

Overview In this chapter we summarize mainly properties of the temporal structure of all shower particles combined, as recorded by conventional surface array detectors. The data that are presented here are a selection from different experiments that are operated at atmospheric depths ranging from sea level to the altitude of Mt. Chacaltaya (5,230 m), and from simulations that are representative for the various observation levels. The temporal distributions and properties of the individual shower components such as hadrons, muons, photons and electrons as well as optical (Cherenkov and fluorescence) and radio emission, are discussed separately in Chaps. 13, 14, 15, 16, 17 and 18, where a wealth of data is presented.

9.1 Introduction

In this section we give an overview of the general temporal properties of air showers, in particular of the electrons ($e^{\pm}$) and muons ($\mu^{\pm}$) that make up the bulk of the particles in the so-called *shower disc*. Temporal features that concern specific shower components, such as hadrons, muons, electrons, atmospheric Cherenkov and fluorescence photons, or specific results that follow from temporal investigations are discussed in the corresponding chapters that deal with these components (Chaps. 13, 14, 15, 16 and 17).

To an observer a shower appears as a disc of particles and photons having a certain thickness that propagates in the atmosphere essentially with the speed of light along the shower axis. Figure 9.1 illustrates the situation in a cut-away snapshot view in a vertical plane containing the shower axis, immediately before ground impact.

The shower disc extends radially outward with decreasing particle and photon density. The reason why the shower disc has a finite thickness is because of the time dispersion of the particles and photons which has two causes. One is due to the different Lorentz factors of the particles which depend on the particle energy, the other and more relevant one is the path length differences of the particle and photon trajectories that are caused by the numerous scattering processes (interactions,

P.K.F. Grieder, *Extensive Air Showers,* DOI 10.1007/978-3-540-76941-5_9,

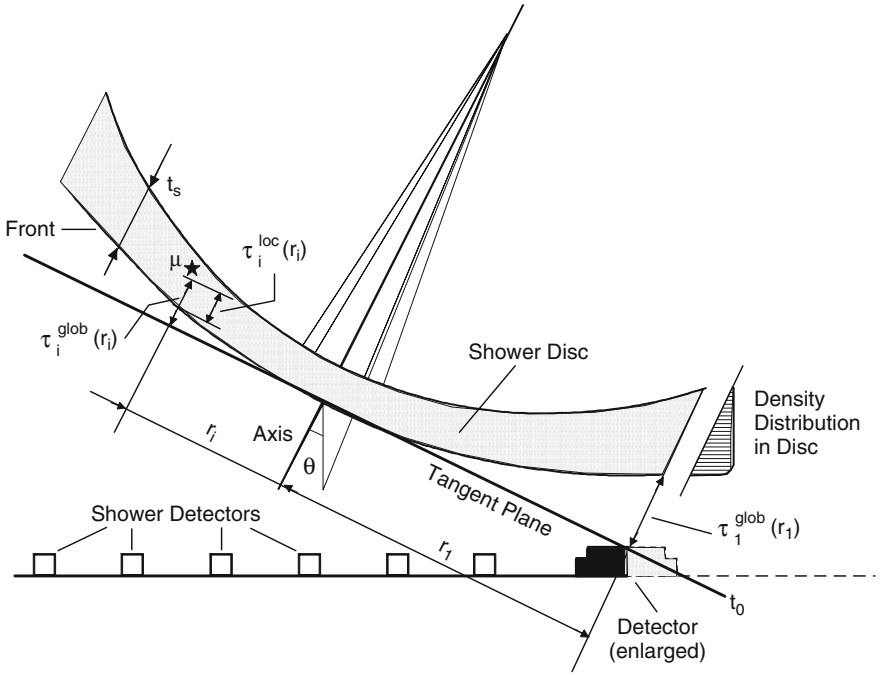

Fig. 9.1 Cut-away view of a shower before ground impact in a vertical plane containing the shower axis. θ is the zenith angle, t_s the particle disc thickness (the dispersion), t_1 the arrival time of the first particle of the shower at a timing detector and also the time lag of the shower front with respect to the tangent plane at location r_1 from the axis. t_i is the arrival time of particle i at distance r_i from the shower axis w.r.t. the shower front. The detached hatched area to the right of the disc symbolizes the particle density distribution across the disc

transverse momenta, Coulomb scattering, etc., including geomagnetic deflection), that are responsible for the lateral spread of the particles and photons away from the shower axis.

For Cherenkov light the emission angle of the photons, the scattering of the photons in the air and the changing index of refraction across the atmosphere cause additional delay and time dispersion that must be added to the one acquired by their parent particles. However, once created, optical photons suffer little scattering and absorption in the atmosphere and are excellent messengers to reveal the history of an air shower to the observer at ground level (see Chap. 16).

In larger showers the front of the particle disc describes a *curved surface* that can be approximated roughly by a *spherical shell* or, more accurately, by a *parabolic surface*, centered about the shower axis, that extends symmetrically outward.[1] With respect to a plane perpendicular to the shower axis that lies tangent to the shower

[1] Geomagnetic and other effects, including fluctuations in shower development can disturb this symmetry.

front surface, the so-called *tangent plane*, the particles and photons at the shower front and in the disc manifest an increasing delay with increasing radial distance from the shower axis because of the front curvature.

The particle disc in the immediate vicinity of the axis, in the shower core region, contains a high density of highly relativistic particles of all sorts and is very narrow, measuring only a few meters, or nanoseconds if expressed in transit time. With increasing radial distance from the axis the average energy of the particles decreases and the thickness of the shower disc increases because of increasing time dispersion due to larger scattering angles and lower Lorentz factors. The shower front is trailed by slower, less energetic particles, mostly low energy muons and locally produced scattered electrons. In addition multiply scattered low energy hadrons, mainly neutrons and occasionally antinucleons populate the tail of the temporal distribution and can accumulate delays with respect to the front of the order of microseconds.

Timing information of the arrival of the particle swarm of an air shower is a basic and relatively easily accessible observable. The time sequence of the arrival of the shower particles at the detectors of a classical array permits to locate the direction of the shower axis and thus the direction of incidence of the primary particle. The temporal and spatial structure of the particle disc hold information on the longitudinal development of a shower, in particular on the height (or depth) of origin of the shower constituents and the location of the shower maximum. The latter is linked through the inelastic cross section to the mass of the primary. Similar information is carried by the atmospheric Cherenkov component of the shower particles that is discussed in Chap. 16.

9.2 Basic Definitions of Timing Observables

The arrival time of particle i at distance r_i from the shower axis, $t_i(r_i)$, is in general specified with respect to an experimentally defined *reference time zero*, t_0. The latter is usually defined by the arrival of the leading edge of the center of the shower core, at $r = 0$ (axis), which also fixes the location of the so-called *tangent plane*, a fictive plane perpendicular to the shower axis, as shown in Fig. 9.1.

The arrival time of the particles, $t_i(r_i)$, is then expressed with respect to the arrival time of the tangent plane, t_0, in terms of the *time delay*, $\tau_i(r_i)$, with respect to that plane. This time is often referred to as the *global time* ($\tau_i^{\mathrm{glob}}(r_i)$), thus,

$$\tau_i^{\mathrm{glob}}(r_i) \;=\; t_i(r_i) \;-\; t_0(r=0) \;\; [\mathrm{ns}]\;. \tag{9.1}$$

To study local temporal distributions of particles at distance r_i from the shower axis, i.e., to investigate the disc thickness, the time delay, $\tau_i^{\mathrm{loc}}(r_i)$ is measured with respect to a *local reference time*, $t_0^{\mathrm{loc}}(r_i)$, e.g., with respect to the front of the curved shower shell at r_i, hence,

$$\tau_i^{\mathrm{loc}}(r_i) \;=\; t_i(r_i) \;-\; t_0^{\mathrm{loc}}(r_i) \;\; [\mathrm{ns}]\;. \tag{9.2}$$

In practice the reference time zero is fixed by the arrival time of the first particle of a shower, t_1, at a timing detector located at r_1 from the shower axis. Therefore,

$$\tau_1^{\text{glob}}(r_1) \;=\; t_1(r_1) \;-\; t_0(r=0) \;\; [\text{ns}]\;. \tag{9.3}$$

This time fluctuates slightly ($\sim$2 ns) with respect to the tangent plane time (t_0, the global time zero), or the shell front time, The fluctuation of t_1 and the mean value of the delay depend on the particle multiplicity recorded per event (Woidneck and Böhm, 1975; de Villiers et al., 1986; Agnetta et al., 1997; Ambrosio et al., 1997a; Antoni et al., 2001). In simulations a *fictive spherical light front* is initiated at the point of the first interaction of the primary in the atmosphere that propagated into space with the speed of light, c. It serves to keep track of the timing of all particles of a simulation throughout the shower.

In simulated showers the arrival delay of particle i in the k-th event, τ_i^k, is usually defined with respect to the tangent plane (global time) as

$$\tau_i^k(r_i) \;=\; t_i^k(r_i) \;-\; t_0^k \;\; [\text{ns}] \;\;, \tag{9.4}$$

or with respect to the spherical light front, depending on the subsequent analysis. t_0^k is the arrival of the tangent plane of the k-th event.

The mean value of the time delay at different core distances r in an event, $\langle\tau\rangle(r)$, is

$$\langle\tau\rangle(r) \;=\; \left(\frac{1}{N}\right)\sum_{i=1}^{N}\tau_i \;\; [\text{ns}] \tag{9.5}$$

and the standard deviation, $\sigma(r)$, is

$$\sigma(r) \;=\; \sqrt{\left(\frac{1}{N-1}\right)\sum_{i=1}^{N}(\tau_i - \langle\tau\rangle)^2} \;\;, \tag{9.6}$$

where N is the total number of particles in the distribution. The observable $\langle\tau\rangle(r)$ is the *space-time profile* of the shower disc and $\sigma(r)$ the *disc thickness*.

9.3 Early Work, Basic Results and Front Curvature

9.3.1 Experimental Aspects, Timing and Curvature

The earliest measurements of the temporal characteristics of particles in extensive air showers were made by McCusker et al. (1950), Mezzetti et al. (1951), Officer (1951), Bassi et al. (1953a, b), Jelley and Whitehouse (1953), Officer and Eccles (1954), and Eccles (1960), using a single scintillation counter. This

work showed that air shower particles do not arrive simultaneously but are distributed over a narrow time interval, thus revealing a disc structure with a certain thickness.

It was soon realized by the early investigators that arrival time measurements of shower particles with an array of like detectors could be used to determine the arrival direction of the showers and thus reveal the location of the source. It was only at a later time, after the discovery that most air showers are initiated by hadrons which carry electric charge, that it was realized that the projection of the shower axis back into space could not necessarily point at the source because of the more or less randomly oriented magnetic fields in the interstellar space which deflect the particles from straight trajectories, unless the primary is a neutral particle, such as a neutron or a gamma ray.

The technique of using a number of separated detectors arranged to form a matrix-like array to conduct timing measurements was first introduced by Bassi et al. (1953a, b) who also produced the first evidence that the *shower front* has a *curvature*. Subsequent experiments by other authors confirmed this discovery (Sugarman and DeBenedetti, 1956; Wilson et al., 1963).

Systematic exploration and subsequent exploitation of the temporal features of the particles of the shower front to determine the arrival direction of the showers was begun by Chitnis et al. (1960), Delvaille et al. (1960), Fukui et al. (1960), Clark et al. (1961), Hersil et al. (1961), Linsley et al. (1961) and Bennett et al. (1962). Today this method is the backbone for the arrival direction determination of showers that are recorded by surface arrays. It yields an angular accuracy for the zenith and azimuthal angle determination of at best 0.1° for densely packed arrays, and on the order of several degrees for loosely packed arrays. Other methods, such as particle tracking, are seldom used (Heintze et al., 1989).

Linsley and Scarsi (1962) were the first to study temporal features of shower particles at larger core distances in order to extract information on the *longitudinal development* of the showers. In their work they have used the arrival times of single muons of energy ≥ 100 MeV to determine the curvature of the shower front and from that the *height of origin* of the muons and their parent particles.

Since that time many more investigations of the temporal features of showers were carried out that pursued a variety of goals. Some were simply aimed at the exploration of the space-time structure of the particle disc (Armitage et al., 1973a, b; Barrett, 1976; Baxter et al., 1965, Blake et al., 1978, 1982; Earnshaw et al., 1968) whereas others attempted to correlate the temporal data with the longitudinal development of the showers to locate the shower maximum in the atmosphere with the ultimate goal to estimate the mass of the shower initiating primary particle (Lapikens et al., 1979; Watson and Wilson, 1974; Blake et al., 1990). It is worth noting that Watson and Wilson (1974) deduced from their measurements that the muon component arrives *ahead* of the electromagnetic component.

Similar experiments were trimmed to use the time dispersion and the arrival delay of the particles as a criterion to select particular kinematic regions in the shower process by selecting appropriate time windows behind the shower front, to search for specific delayed (massive) particles, such as in the early quark-hunt experiments

(Damgaard et al., 1965a, b; Bjornboe et al., 1968), to determine the antinucleon content in showers (Tonwar and Sreekantan, 1971), or to search for tachyons (Ramana Murthy, 1971; Ashton et al., 1977; Bhat et al., 1979; MacNeill and Fegan, 1983). In this context Armitage et al. (1981) have carried out a careful re-appraisal of the temporal properties of the different detector types, such as the rise time, to minimize timing errors.

Kozlov et al. (1973), using the data of the large air shower array at Yakutsk, measured the arrival delay of the shower particles with respect to the tangent plane as a function of core distance of a large shower (size $3 \cdot 10^8$) that was incident under a large zenith angle ($\theta = 75^\circ$). From these data they determined the radius of curvature of the shower front, using a spherical fit. The result is shown in Fig. 9.2a where the delay is plotted as retardation, expressed in meters. The lateral distribution of this particular shower is shown in Fig. 15.8.

A similar analysis was made by Hara et al. (1983) with data taken at Akeno at large core distances (0.5–1.5 km) and for different particle densities in the detectors. Their results are displayed in Fig. 9.2b, where three spherical fits with different radii of curvature are shown. The time dispersion, i.e., the delay fluctuations, σ_τ, obtained from this work are shown in Fig. 9.3. A similar set of data was obtained with the SUGAR array at Narrabri (Australia) by Brownlee et al. (1970), recording muons. The dispersion plot of Fig. 9.4 is from a compilation of Linsley (1986) that includes older data, mostly from unusually large showers, but also from some smaller events that were recorded at Volcano Ranch over a wide range of impact parameters, and one data point at ground zero from the work of Woidneck and Böhm (1975). Finally, Fig. 9.5 shows the shower size dependence of the radius of curvature determined from data taken with the Chacaltaya array by Aguirre et al. (1973).

9.3.2 Simulations and Primary Mass Signatures

Parallel to the experimental work several authors investigated the temporal properties of shower particles (and optical Cherenkov photons) theoretically, using Monte Carlo simulations (Baxter et al., 1968; Baxter, 1969; Dixon and Turver, 1974; Dixon et al., 1974a, b; Grieder, 1977 and references listed therein). Some tried to explore the primary mass dependence of the temporal distribution of the shower particles, others to study properties of hadronic interactions in showers (Pal and Tandon, 1965; Murthy et al., 1968a, b, c; Grieder, 1970a, b) using models of different degree of refinement. Grieder was the first to use a highly structured shower simulation code, the forerunner of the ASICO program system (see Chap. 20), which later on became the presently widely used CORSIKA air shower simulation program. He used a very refined interaction model that was based on the thermodynamic (Hagedorn) model and produced a wealth of simultaneous observables that allowed to carry out extensive correlation analyses (Grieder, 1977).

Of the different topics listed above the search for a reliable primary mass signature remained the primary objective of temporal studies. It was known from

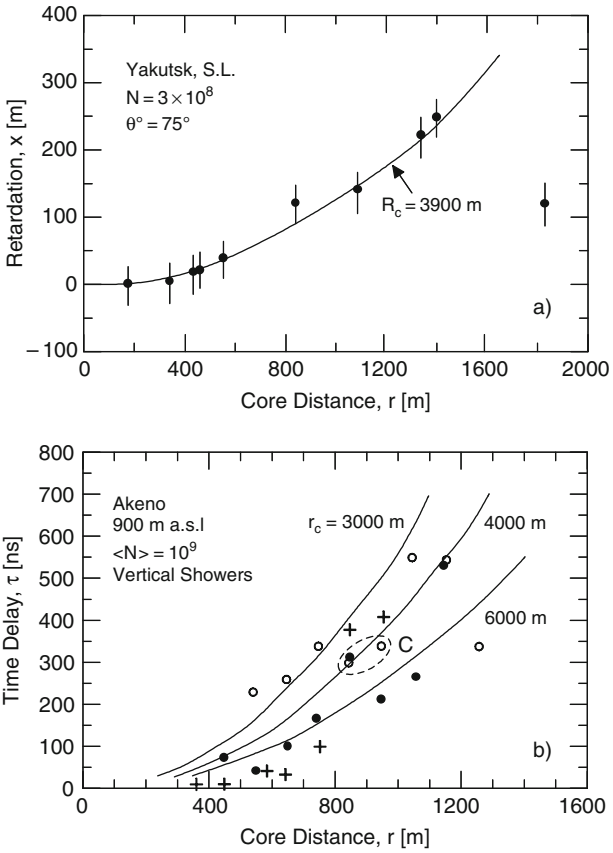

Fig. 9.2 (**a**) Shower front curvature of an individual shower of very large size ($N = 3 \cdot 10^8$), incident at a zenith angle of 75° at Yakutsk. Plotted is the retardation of the front as a function of distance from the axis, expressed in meters behind the tangent plane (perpendicular to the shower axis). The all-particle lateral density distribution of this event is displayed in Fig. 15.8 (Kozlov et al., 1973). (**b**) Average arrival time delay of the fastest particles in the shower front with respect to the tangent plane of the shower detected at Akeno, plotted as a function of core distance. The *symbols* ○, • and + signify 1–3, 3–10 and 10–30 particles per counter (2.25 m^2). The *solid curves* labeled $r_c = 3,000$ m, 4,000 m and 6,000 m represent radii of curvature of the shower front. The *dashed contour*, C identifies the fastest group of particles. (Hara et al., 1983)

simulations that the height (or depth) of the shower maximum is the key to reach this goal and that apart from optical Cherenkov photons, muons offer the best and most direct access into the past of the longitudinal development of a shower for an observer at ground level. Moreover, muons offer a 100% duty factor as compared to atmospheric Cherenkov measurements that reach at best a duty factor of ∼10%. Thus, the problem was to identify the relevant messengers in a sea of less relevant particles that mask the desired signatures.

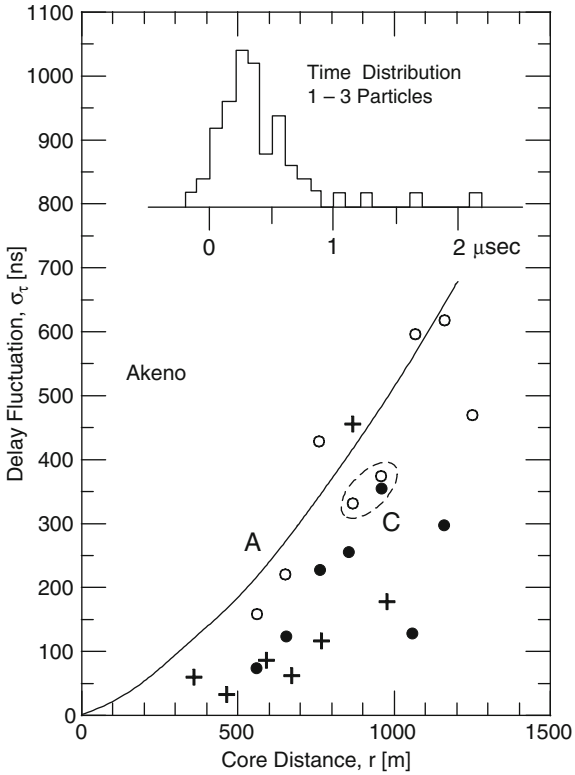

Fig. 9.3 Fluctuations of the arrival delay, σ_τ, of the fastest shower particles with respect to the tangent plane, as a function of core distance. The *symbols* ○, ● and + signify 1–3, 3–10 and 10–30 particles per counter (2.25 m^2) (see Fig. 9.2b). The inserted histogram shows as an example the time distribution of the fastest particles of the encircled data points (*dashed contour*, C) (Hara et al., 1983). The *solid curve* labeled A shows σ_τ as a function of core distance from the work of Linsley (1986)

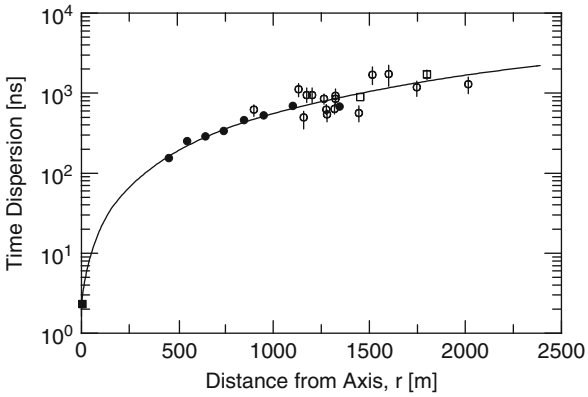

Fig. 9.4 Time dispersion of the shower disc as a function of radial distance from the shower axis in very large showers recorded at Volcano Ranch (Linsley, 1986)

Simulations have shown that the rise time of the photomultiplier output pulse of large deep water Cherenkov detectors and thus of the arrival time of local groups of shower particles depends on the zenith angle, θ, of the shower axis, on primary energy, E_0, and on the radial distance, r, from the shower axis where the measurement is being made. Lapikens et al. (1979) have used these features to determine

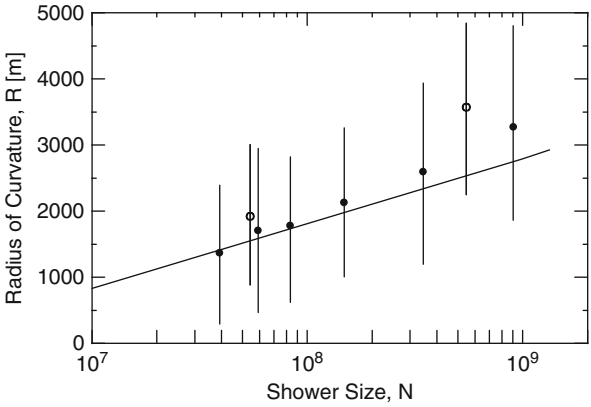

Fig. 9.5 Mean radius of curvature of shower front, R, as a function of shower size, N, recorded at Mt. Chacaltaya (530 g cm^{-2}, 5,230 m a.s.l.). Included are events in the size range $3 \cdot 10^7 \leq N \leq 3 \cdot 10^9$. The *straight line* is an approximate fit to the data (Aguirre et al., 1973)

from the zenith angle dependence of the pulse rise time of the Haverah Park detectors the *change* of the depth of the shower maximum and thus the *elongation rate* as a function of primary energy.

Figure 9.6a shows the zenith angle dependence of the rise time at different radial distances from the shower axis and in Fig. 9.6b the primary energy dependence as measured by Lapikens et al. (1979). The measurements were made with the large

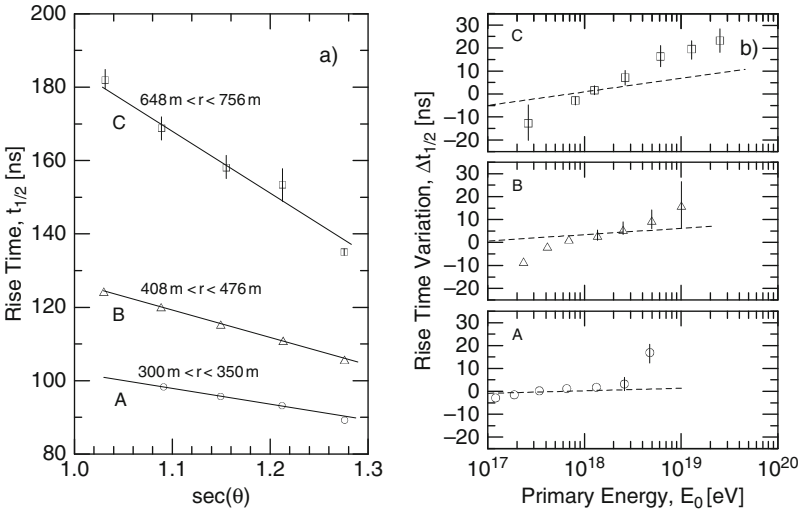

Fig. 9.6 (**a**) Rise time $t_{1/2}$ (10–50% level) of the particle shower front versus secant of the zenith angle θ at different radial distances, r, from the shower axis, in showers of primary energy $2 \cdot 10^{17} < E_0 < 10^{20}$ eV at Haverah Park (Lapikens et al., 1979). (**b**) Rise time variation, $\Delta t_{1/2}$ of the particle shower front at different radial distances from the shower axis as a function of primary energy. The data are from the same experiment and for the same core distance ranges as those of Fig. 9.6a (A, $300 \leq r \leq 350$ m; B, $408 \leq r \leq 476$ m; C, $648 \leq r \leq 756$ m). The *dashed lines* show the trend if $\partial \langle \Delta t \rangle / \partial lg(E_0) = 0$ (Lapikens et al., 1979)

($34\,m^2$) Haverah Park deep water Cherenkov detectors. It should be noted that for a sample of showers recorded by an array, the variables r, θ, and E_0 are correlated because the collecting area of a given array depends on θ, the zenith angle, and the primary energy, E_0.

Similar initiatives had been started by several groups working with large aperture atmospheric Cherenkov detector arrays. It was mostly the Durham (GB) and Yakutsk groups who expanded the work initiated previously by Jelley and collaborators in England and Chudakov in the former Soviet Union (see Chap. 16 for details), who showed that atmospheric optical Cherenkov photons are extremely well suited to explore the longitudinal development of air showers because of small scattering and little absorption of optical photons in the atmosphere. Since Chap. 16 is fully dedicated to this topic it will not be discussed here.

9.4 Recent Experimental Work and Simulations

Temporal studies on shower particles were continued for decades by different groups but did not get much attention because of the very modest progress that was achieved. However, in recent years interest arose from the primary mass composition study groups to explore the subject with present day instrumentation and improved analysis methods. This initiative is partly the consequence of a deadlock in the progress of primary composition identification and in the interpretation of numerous correlation analyses that yield an amazing multitude of results with sometimes quite diverging conclusions, depending on the choice of the observables.

Some of the new studies consider all charged particles, but most are focused at particular muon groups and are carried out in conjunction with dedicated simulations. The main interest concerns the question whether a select temporal feature or a particular *space-time-energy window* can yield additional information which in combination with other primary mass indicating or discriminating observables and/or correlations can strengthen the conclusions. In the following we summarize some of the results and conclusions from recent simulations and experimental investigations.

The integral arrival time distribution of muons, photons and electrons resulting from a simulation of Honda et al. (1997) for large showers ($E_0 \geq 10^{18}$ eV) at large core distance is displayed in Fig. 9.7 which shows that the first component to arrive are the muons ($\mu^{\pm}$), followed by the photons and last the electrons ($e^{\pm}$). This result is confirmed by measurements with the KASCADE muon facilities and by simulations of Haeusler et al. (1999) displayed in Fig. 9.8 and is in agreement with much earlier findings of Watson and Wilson (1974) and Woidneck and Böhm (1975). A very recent and detailed study concerning this topic was carried out by Apel et al. (2008) using the KASCADE-Grande array.

Agnetta et al. (1997) and Ambrosio et al. (1997a, b) have carried out extensive experimental and theoretical studies of the arrival time distribution of muons in air showers in connection with the GREX/COVER-PLASTEX experiment at Haverah Park. Figure 9.9 illustrates the arrival delay distribution of four groups of shower particles that comprise (a) all-charged particles, (b) electrons, (c) muons and (d)

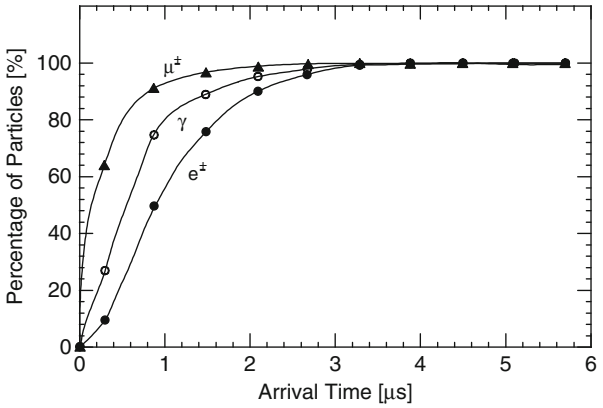

Fig. 9.7 Integral arrival time distributions of muons, photons and electrons at a core distance of 900 m in showers of primary energy $>10^{18}$ eV (Honda et al., 1997)

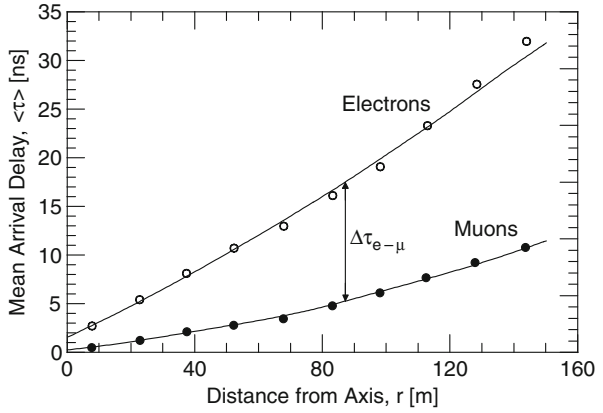

Fig. 9.8 Mean arrival delay of the electromagnetic component and of muons of energy ≥ 2 GeV as a function of distance from the axis in showers of about $2 \cdot 10^{15}$ eV, measured with the KASCADE installation (Haeusler et al., 1999)

charged hadrons in 10^{15} eV vertically incident proton initiated showers at the radial interval between 100 and 110 m from the shower axis.[2]

These authors found that the local delay distributions of the different particle groups are substantially different, yet the general shape which is given by the dominating electrons at this radial interval can be fitted to a Γ-probability distribution function of the form

$$f(\tau) = \Gamma(\tau) = a\tau^b e^{-c\tau} \quad , \tag{9.7}$$

[2] Similar plots were obtained by Grieder (1970a, b, 1977) for muons, pions, nucleons and antinucleons, and by Tonwar and Sreekantan (1971) for hadrons only in their search for antinucleons in air showers.

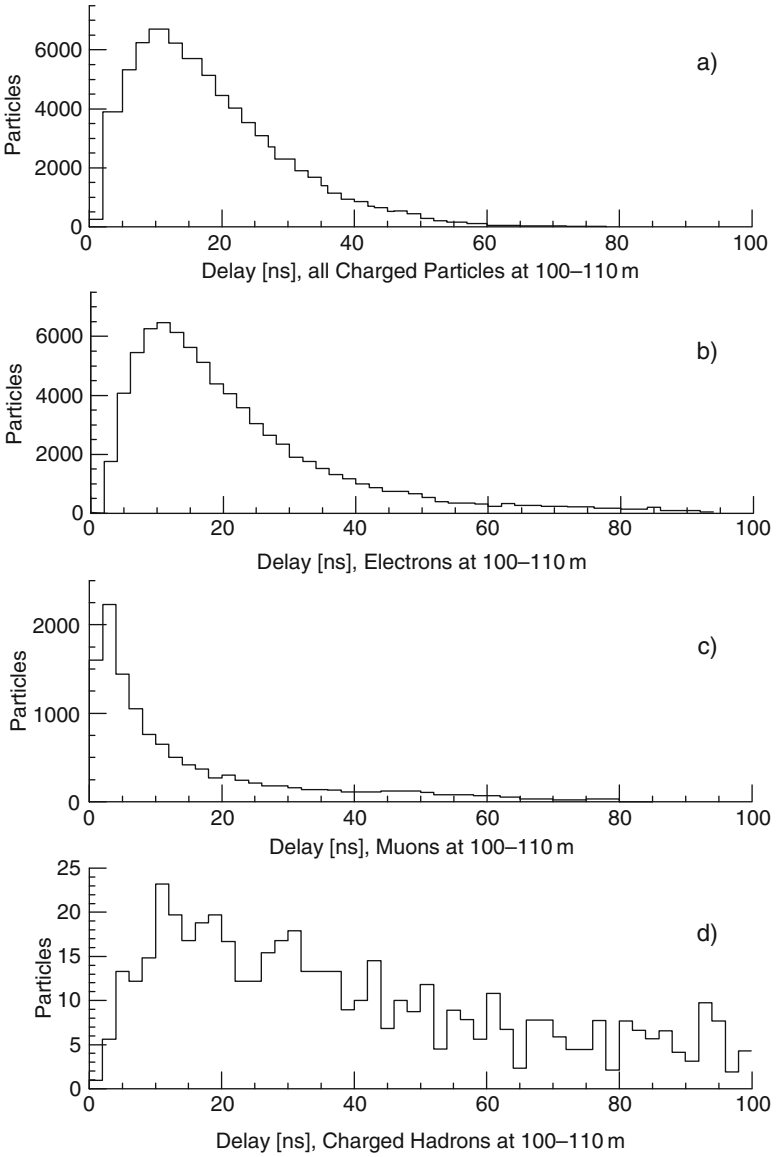

Fig. 9.9 Arrival time distribution of different particle groups in a vertical 10^{15} eV proton initiated shower arriving at the radial distance interval $100 \leq r \leq 110$ m from the axis. The hadron distribution extends far beyond the plot limit into the microsecond region. The CORSIKA code was used for the simulation (Ambrosio et al., 1997a)

where, a, b, and c are adjustable parameters. It is worth noting in this context that in their early work Woidneck and Böhm (1975) have arrived at the same conclusion and have used Eq. (9.7) to describe their experimental data. We should remind the

reader of our earlier remark that the distributions have long, thinly populated tails, particularly the hadron component, that extend well beyond the optimum fits.

To get a general parametrization of the average shower disc profile, $\langle\tau\rangle$, and thickness, σ, the following generalized parabolic function is frequently used (Agnetta et al., 1997; Ambrosio et al., 1997a),

$$\langle\tau\rangle\,,\sigma \;=\; f + g\left(\frac{r}{r_{\mathrm{M}}}\right)^{h} \quad . \tag{9.8}$$

Here, f is given by Eq. (9.7), r is the core distance and r_{M} the Molière radius. Figure 9.10 shows as an example the shower disc profile (Fig. 9.10a) and thickness (Fig. 9.10b) as measured by Ambrosio et al. (1997a) with the GREX/COVER-PLASTEX experiment at Haverah Park. Referring to Eq. (9.8) and to Fig. 9.10, and inserting for the Molière radius the appropriate value for Haverah Park ($r_{\mathrm{M}} = 79$ m), these authors get the best fit using the following values for the different parameters,

$$\begin{array}{lllll} \text{for } \langle\tau\rangle\text{:} & f_\tau = 1.18 \pm 0.02\,\text{ns} & g_\tau = 20.33 \pm 0.05\,\text{ns} & h_\tau = 1.43 \pm 0.06 \\ \text{for } \sigma\text{:} & f_\sigma = 1.18 \pm 0.02\,\text{ns} & g_\sigma = 20.33 \pm 0.05\,\text{ns} & h_\sigma = 1.43 \pm 0.06 \end{array}$$

Haeusler et al. (2002) have studied various distortions of the experimental muon arrival time distribution in air showers that are due to interrelated effects such as the time resolution of timing detectors, fluctuations of the reference time and to the muon multiplicity. They note that the distortions are relevant and decrease with increasing core distance (>250 m) and increasing muon energy. In addition, they find that *local* arrival time distributions which refer to the arrival time of the first locally recorded muon are less sensitive to primary mass, whereas distributions expressed in terms of the so-called *global* arrival time have a stronger mass signature because they include the shower front curvature.

Of the numerous investigations which had been conducted during the last few years the general consensus is that timing data contribute only marginally to primary mass determination or discrimination, in particular when attempting to isolate a particular mass group, in contrast to the relatively strong and robust primary mass dependent ratio N_μ/N_e, at least in the carefully analyzed zone out to radii of ~100 m from the shower axis (Antoni et al., 2003) (for details see Sects. 10.3, 11.7, and Chap. 19).

On the other hand, Rebel et al. (1995) and Brancus et al. (2003a, b) state that global as well as local arrival time distributions of the muons at larger core distances ($r \geq 100$ m) have a potential to improve primary mass discrimination, a conclusion that does not seem to apply to smaller showers at lower primary energies, as some studies suggest.

Some authors have also tried to correlate the muon arrival angle measured with respect to the shower axis with the local arrival time of the particular muon with respect to the tangent plane, a concept originally introduced by Linsley (1992, 1995) and referred to as *time-track complementarity* (TTC) (Danilova et al., 1994; Brancus et al., 1997; Ambrosio et al., 1997b). Danilova et al. (1994) claim that including the

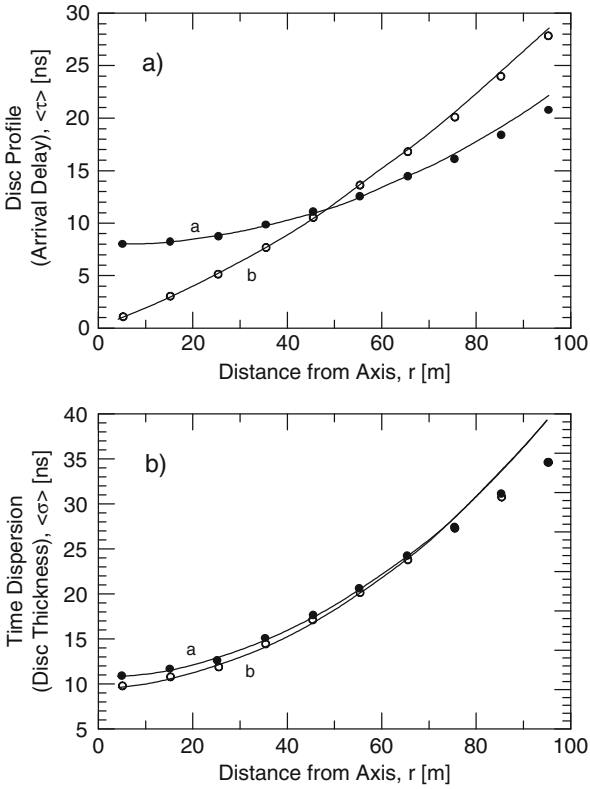

Fig. 9.10 Average shower disc profile $\langle\tau\rangle$ (**a**), and disc thickness (time dispersion) $\langle\sigma\rangle$ (**b**), measured by the GREX/COVER-PLASTEX experiment at Haverah Park. The *symbols* • are the uncorrected, ○ the corrected data, taking into account systematic errors. *Curves* (a) and (b) follow the parametrization of Eq. (9.8) given in the text (Ambrosio et al., 1997a)

angular information reduces the uncertainty of the location of the height of origin of muons by about $10\,\mathrm{g\,cm^{-2}}$ from 45 to about $35\,\mathrm{g\,cm^{-2}}$. Other studies indicate that the muon angular information, if used in conjunction with other analyses, improves the primary mass resolution only insignificantly (Antoni et al., 2003).

9.5 Special Analysis Methods

In an attempt to extract more information from temporal shower data, in particular with respect to the nature and mass of the shower initiating primary, several authors have explored new, more elaborate and refined methods of analysis. This work had been focused mainly on the muon component because muons, like optical atmospheric Cherenkov photons, carry information of the early shower development almost undisturbed to an observer at ground level.[3]

[3] The properties of optical atmospheric Cherenkov photons in air showers are discussed in Chap. 16.

The methods comprise correlation studies of experimental arrival times and arrival time distributions with *multidimensional distributions* consisting of several other simultaneous observables and their distributions. The analyses are carried out partly on an *event by event* (shower by shower) basis in conjunction with shower simulations, employing *non-parametric statistical methods* and *Bayes error estimations*. These methods are sometimes referred to as *multivariate distribution analyses* or *multivariate approaches* (Chilingarian, 1989; Chilingarian and Zazian, 1991; Rebel et al., 1995; Brancus et al., 1997, 2003b; Antoni et al., 2001, 2003; Rebel, 2001).

Some of this work consists of careful analyses of specific regions (quartiles) (Antoni et al., 2001; Brancus et al., 2003a, b) of the global and local temporal distributions in an attempt to resolve subtle differences between the leading and trailing portions of the distributions, and likewise of the shower disc profile with respect to the radial distance from the shower axis, for specific groups of particles, mainly muons.

Since these topics are intimately related to primary mass identification they are discussed in Chap. 10. However, we will briefly list some characteristic temporal properties of shower particles that have emanated from this work that are of general interest. Some of these reveal new aspects, others confirm earlier findings.

One of the results obtained by the KASCADE group using the novel methods mentioned here is that the thickness of the muon disc of rather energetic muons ($E_\mu \geq 2.4\,\mathrm{GeV}$) is significantly narrower than that of the bulk of the accompanying comparatively low energy electron component ($E_e \geq 4\,\mathrm{MeV}$) (Haeusler et al., 1999; Antoni et al., 2003). This suggests that very likely the bulk of the particular muons originates from the same region of the longitudinal shower profile or range of altitudes, and probably from the same or neighboring generations of interactions.

Furthermore, this work confirms once more that the mean delay and the thickness of the particle disc increase with increasing core distance. It was also found that the space-time disc containing the selected muon group is flatter than the electron disc (Antoni et al., 2001) and that the disc can be fairly well approximated by a quasi-parabolic shape in a limited radial range, a property which probably scales with energy. The dependence of the shower time profile on primary energy and zenith angle appears to be weak, yet significant, e.g., the shower particle disc gets flatter and thinner with increasing primary energy (Antoni et al., 2003).

9.6 Time Dispersion and Delayed Particle Effects on Density Measurements

The time dispersion of the particles in the shower front can affect particle density measurements, particularly when logarithmic amplifiers are being used (see also the previous section, Sect. 8.11). The influence of the time dispersion on the measurement depends on the degree of dispersion and the integration time of the electronic system employed for the measurement. Delayed particles that are associated with

the shower as well as accidental coincidences can introduce additional signal components that can lead to serious errors in the interpretation of the particle density, which subsequently affects the primary energy estimation. The AGASA group has carried out detailed studies on this topic in order to reduce the errors of the primary energy estimation (Takeda et al., 2003). In view of the relevance of the problem we summarize in the following the essence of their work.

Figure 9.11 shows the output pulse height distribution as registered by a waveform recorder at the output of a 30 m^2 and 5 cm thick scintillation detector of the AGASA array that is located at 1,920 m from the core of a $2 \cdot 10^{20}$ eV shower (Honda et al., 1987, 1993, 1997). The delayed arrivals are evident. The average shape of the arrival time distribution can be expressed by the relation

$$f(t,r) = \frac{t}{t_0(r)} \exp\left(\frac{-t}{t_0(r)}\right) , \tag{9.9}$$

where the scaling factor, t_0, is 168, 212 and 311 ns at distances $r = 534$ m, 750 and 1,050 m, respectively, accounting for the increase of the disc thickness with increasing core distance. For large distances where the event rate is too low to determine averages, the authors used extrapolated values, as given in Fig. 9.12. Using t_0 and the number of incident particles on the detector, N_i, one can estimate the density due to the broadening of the shower front structure and determine the ratio of this density to that resulting for zero front thickness, $t_0 = 0$. This ratio, called the *overestimation factor*, F, is plotted in Fig. 9.13. One can extend this procedure to delayed particles associated with the shower. Studies have shown that it appears that these trailing particles may be neutrons having energies between 30 and 40 MeV (Teshima et al., 1986; Takeda et al., 2003).

In large showers the number of delayed particles, N_d, amounts to a few percent between 1 and 3 km from the shower core. A single delayed particle can produce a pulse height that may correspond to several standard unit particle pulses, i.e., vertical minimum ionizing particles, as had been defined for the detector calibration.

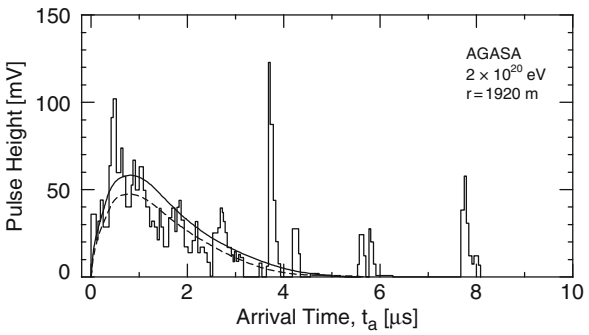

Fig. 9.11 Arrival time distribution of charged particles in a 30 m^2 plastic scintillation detector at 1,920 m from the core of a $2 \cdot 10^{20}$ eV shower registered with a waveform recorder at Akeno (AGASA array). The *dashed* and *solid curves* show expected system responses to 10^{19} eV showers. The areas under the *curves* are normalized to 87 and 115 particles, respectively, within 2.5 μs (Honda et al., 1993; Hayashida et al., 1994; Takeda et al., 2003)

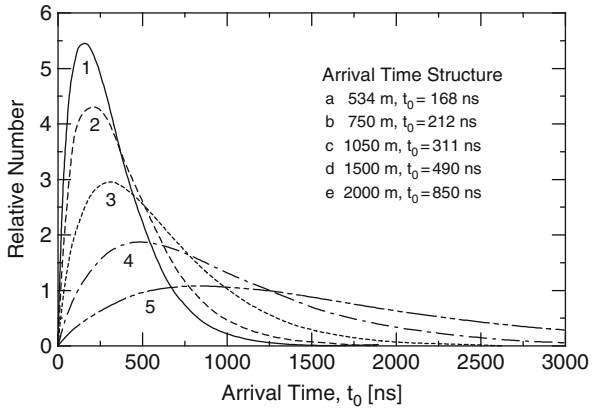

Fig. 9.12 Arrival time distribution of shower particles. The t_0 scale parameter for 534, 750 and 1,050 m were determined experimentally (Honda et al., 1987), those for 1,500 and 2,000 m are extrapolated values assuming lg $t_0 \propto r$ (Takeda et al., 2003)

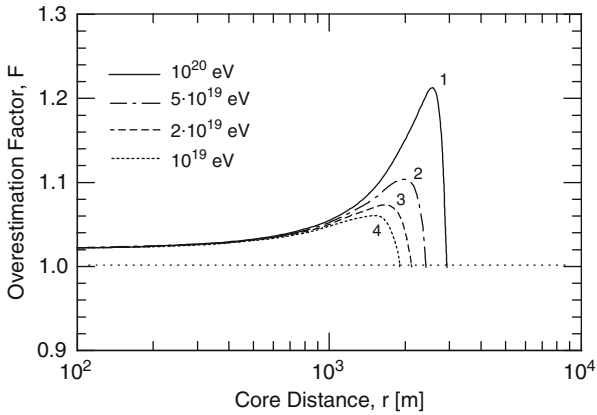

Fig. 9.13 Density overestimation due to the effect of shower front thickness estimated by considering the LDF profile for different primary energies. The sharp drop at large core distance, r, occurs where the particle count is unity (Takeda et al., 2003)

Figure 9.14 shows the measured fraction of delayed particles as a function of core distance from different arrays. A similar plot (Fig. 9.15) from more recent measurements carried out at Akeno (AGASA) shows this ratio for two primary energy groups. It appears that this phenomenon is largely independent of primary energy.

Figure 9.16 shows that the actual delay of the trailing particles (○) is almost independent of core distance, except possibly at very large distances, and likewise for their energy deposit (or signal level) produced in the scintillator (●). This suggests that the delayed particles are of the same nature at all radial distances from the core and are probably nucleons and antinucleons, as was shown many years earlier by Grieder (1970a, b, 1977), Murthy et al. (1968a, b, c) and Pal and Tandon (1965) on the basis of simulations, and by Tonwar and Sreekantan (1971) experimentally.

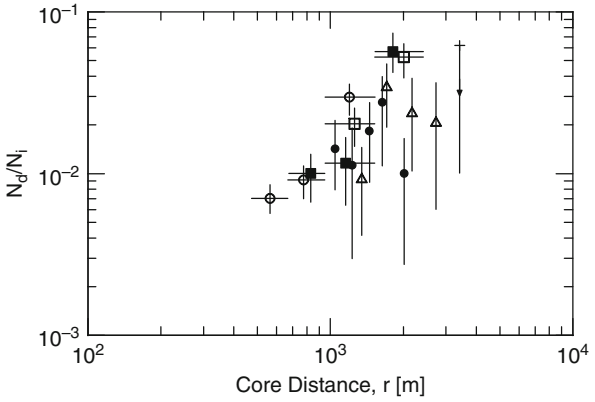

Fig. 9.14 Radial dependence of the fraction of delayed particles (delay $t_d \geq 3\,\mu$s, pulse height corresponding to $N_d \geq 1$ particle), to all shower particles recorded, N_i, in showers of energy $3.16 \cdot 10^{18} \leq E_0 < 10^{19}$ eV (○), $10^{19} \leq E_0 \leq 2.5 \cdot 10^{19}$ eV (□), and $> 2.5 \cdot 10^{19}$ eV (■). Earlier measurements from Akeno (△) (Teshima et al., 1986) and Volcano Ranch (●) (Linsley, 1963) for $t_d \geq 4\,\mu$s and $N_d \geq 3$ at primary energies around 10^{18} eV are also shown (Takeda et al., 2003)

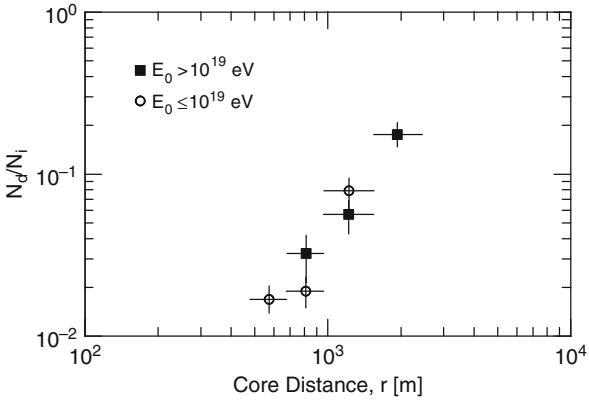

Fig. 9.15 Radial dependence of the ratio N_d/N_i for delays $t_d \geq 3\,\mu$s and pulse heights corresponding to $N_d \geq 1$ unit particle signatures in showers of energy $< 10^{19}$ eV (○) and $\geq 10^{19}$ eV (■) (Takeda et al., 2003)

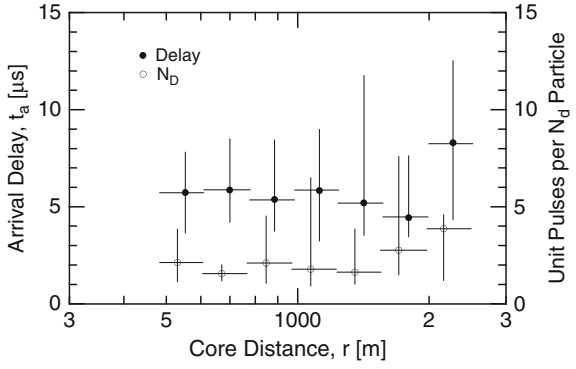

Fig. 9.16 Delay time (*left*) and number of delayed particles, N_d (*right*), as a function of distance from shower axis. Error bars show 68% confidence limits. First 6 bins contain 15–30 data points, most distant bin only 3 (Takeda et al., 2003)

References

Agnetta, M., et al.: Astropart. Phys., 6, p. 301 (1997).
Aguirre, C., et al.: PICRC, 4, p. 2576 (1973).
Ambrosio, M., et al.: Astropart. Phys., 7, p. 329 (1997a).
Ambrosio, M., et al.: J. Phys. G., 23, p. 219 (1997b).
Antoni, T., et al.: Astropart. Phys., 15, p. 149 (2001).
Antoni, T., et al.: Astropart. Phys., 18, p. 319 (2003).
Apel, W.D., et al.: Astropart. Phys., 29, p. 317 (2008).
Armitage, M.L., et al.: PICRC, 4, p. 2539 (1973a).
Armitage, M.L., et al.: PICRC, 4, p. 2545 (1973b).
Armitage, R., et al.: PICRC, 6, p. 35 (1981).
Ashton, F., et al.: PICRC, 7, p. 370 (1977).
Barrett, M.L.: J. Phys. G, 2, p. L73 (1976).
Bassi, P., et al.: Phys. Rev. 91, p. 432 (1953a). (Abstract A.P.S. Spring meeting.)
Bassi, P., et al.: Phys. Rev., 92, p. 441 (1953b).
Baxter, A.J., et al.: PICRC, 2, p. 724 (1965).
Baxter, A.J., et al.: Can. J. Phys., 46, p. S9 (1968).
Baxter, A.J.: J. Phys. A, 2, p. 50 (1969).
Bennett, S., et al.: J. Phys. Soc. Jpn., 17, Suppl. A III, p. 196 (1962).
Bhat, P.N., et al.: J. Phys. G, 5, p. L13 (1979).
Bjornboe, J., et al.: Nuovo Cim., 53 B, p. 241 (1968).
Blake, P.R., et al.: Nuovo Cim., 1 C, p. 360 (1978).
Blake, P.R., et al.: J. Phys. G, 8, p. 1605 (1982).
Blake, P.R., et al.: J. Phys. G, 16, p. 755 (1990).
Brancus, I.M., et al.: Astropart. Phys., 7, p. 343 (1997).
Brancus, I.M., et al.: PICRC, 1, p. 41 (2003a).
Brancus, I.M., et al.: J. Phys. G, 29, p. 453 (2003b).
Brownlee, R.G., et al.: Acta Phys. Acad. Sci. Hung., 29, S3, p. 645 (1970).
Chilingarian, A.A.: Comput. Phys. Commun., 54, p. 381 (1989).
Chilingarian, A.A., and G.Z. Zazian: Nuovo Cim., 14, p. 555 (1991).
Chitnis, E., et al.: PICRC, 2, p. 18 (1960).
Clark, G.W., et al.: Phys. Rev., 122, p. 637 (1961).
Damgaard, G., et al.: PICRC, 2, p. 808 (1965a).
Damgaard, G., et al.: Phys. Lett., 17, p. 152 (1965b).
Danilova, T.V., et al.: J. Phys. G, 20, p. 961 (1994).
Delvaille, J., et al.: PICRC, 2, p. 101 (1960).
de Villiers, et al.: J. Phys. G, 12, p. 547 (1986).
Dixon, H.E., and K.E. Turver: Proc. R. Soc. A, 339, p. 171 (1974).
Dixon, H.E., et al.: Proc. R. Soc. A, 339, p. 133 (1974a).
Dixon, H.E., et al.: Proc. R. Soc. A, 339, p. 157 (1974b).
Earnshaw, R.A., et al.: Can. J. Phys., 46, p. S5 (1968).
Eccles, P.J.: Proc. Phys. Soc. (Lond.), 76, p. 449 (1960).
Fukui, S., et al.: Prog. Theor. Phys. Jpn., 16, p. 1 (1960).
Grieder, P.K.F.: Acta Phys. Acad. Sci. Hung., 29, S3, p. 563 (1970a).
Grieder, P.K.F.: Acta Phys. Acad. Sci. Hung., 29, S3, p. 569 (1970b).
Grieder, P.K.F.: Rivista del Nuovo Cim., 7, p. 1 (1977).
Haeusler, R., et al.: PICRC, 1, p. 325 (1999).
Haeusler, R., et al.: Astropart. Phys., 17, p. 421 (2002).
Hara, T., et al.: PICRC, 11, p. 276 (1983).
Hayashida, N., et al.: Phys. Rev. Lett., 73, p. 3491 (1994).
Heintze, J., et al.: Nucl. Instr. Meth., A277, p. 29 (1989).
Hersil, J., et al.: Phys. Rev. Lett., 6, p. 22 (1961).

Honda, K., et al.: PICRC, 6, p. 83 (1987).
Honda, K., et al.: PICRC, 4, p. 311 (1993).
Honda, K., et al.: Phys. Rev. D, 56, p. 3833 (1997).
Jelley, J.V., and W.J. Whitehouse: Proc. Phys. Soc. (Lond.), A66, p. 454 (1953).
Kozlov, V.I., et al.: PICRC, 4, p. 2588 (1973).
Lapikens, J., et al.: PICRC, 8, p. 95 (1979).
Linsley, J., et al.: Phys. Rev. Lett., 6, p. 485 (1961).
Linsley, J., and L. Scarsi: Phys. Rev., 128, p. 2384 (1962).
Linsley, J.: J. Phys. G, 12, p. 51 (1986).
Linsley, J.: Nuovo Cim. C, 15, p. 743 (1992).
Linsley, J.: PICRC, 1, p. 352 (1995).
MacNeill, G.C., and D.J. Fegan: PICRC, 5, p. 110 (1983).
McCusker, C.B.A., et al.: Nature, 166, p. 400 (1950).
Mezzetti, L., et al.: Phys. Rev., 81, p. 629 (1951).
Murthy, G.T., et al.: Can. J. Phys., 46, p. S147 (1968a).
Murthy, G.T., et al.: Can. J. Phys., 46, p. S153 (1968b)
Murthy, G.T., et al.: Can. J. Phys., 46, p. S159 (1968c).
Officer, V.C.: Phys. Rev., 83, p. 458 (1951).
Officer, V.C., and P.J. Eccles: Aust. J. Phys., 7, p. 410 (1954).
Pal, Y., and S.N. Tandon: PICRC, 2, p. 802 (1965).
Ramana Murthy, P.V.: Lett. Nuovo Cim., 1(22), p. 908 (1971).
Rebel, H., et al.: J. Phys. G, 21, p. 451 (1995).
Rebel, H.: Progr. Part. Nucl. Phys., 46, p. 109 (2001).
Sugarman, R., and S. DeBenedetti: Phys. Rev., 102, p. 857 (1956).
Takeda, M., et al.: Astropart. Phys., 19, p. 447 (2003).
Teshima, M., et al.: J. Phys. G, 12, p. 1097 (1986).
Tonwar, S.C., and B.V. Sreekantan: J. Phys. A, 4, p. 868 (1971).
Watson, A.A., and J.G. Wilson: J. Phys. A, 7, p. 1199 (1974).
Wilson, J.G., et al.: PICRC, 4, p. 27 (1963).
Woidneck, C.P., and E. Böhm: J. Phys. A, 8, p. 997 (1975).

Chapter 10
Derived Shower and Interaction Parameters, Refined Event Reconstruction

Overview In this chapter we discuss some of the hidden air shower and hadronic interaction parameters that cannot be extracted reliably directly from experimental data but require detailed simulations for the interpretation. We present experimental methods and the handling of the acquired data to access the relevant parameters, such as the energy and mass of the primary, and the shower age. In this context we also discuss the relationship of the data from the two kinds of surface detectors that are frequently used, the deep water Cherenkov and the plastic scintillation detectors, to the shower parameters under investigation. The complex interrelations of the derived parameters that often lead to ambiguous results are outlined and the methods that include detailed simulations and correlation studies to obtain unique results are summarized. The problem of the height of the first interaction and its effect on shower development is briefly touched. The results that have emerged from these investigations that concern the primary radiation are summarized in Chap. 11. Parameters related to atmospheric Cherenkov, air fluorescence and radio detection of showers are discussed in separate chapters.

10.1 Introduction

Of the many parameters that specify the characteristics of an air shower a certain number can easily be determined directly from observables recorded with simple measurements, however, some are only indirectly accessible. The former are discussed in Sects. 2.9 and 2.10 whereas the latter, referred to here as *derived parameters* and discussed in this chapter, can only be extracted reliably from experimental data with the help of air shower simulations. Included in this category of parameters are above all the energy and mass of the primary (E_0 and M_0), the shower age (s), the depth or height of maximum development of the shower ($X_{\max}$ or $h_{\max}$), and the elongation rate (ER), but also key parameters that characterize the interactions, such as the inelastic hadronic cross sections or the interaction mean free paths (σ_{inel} or λ_{int}), the secondary particle multiplicity (n), the elasticity or inelasticity of the interactions (η or K, where $K = 1 - \eta$), and many more. The aim of this chapter is to illuminate mainly the accessibility of the different indirectly observable or derived

P.K.F. Grieder, *Extensive Air Showers,* DOI 10.1007/978-3-540-76941-5_10,

parameters and their effects on shower development. The most relevant are treated more extensively in separate chapters.

Of the derived parameters those that are sensitive to the properties and nature of the primary, i.e., to its energy, E_0 and mass, M_0 (if we consider hadronic primaries), are of paramount interest. For hadron initiated showers all the complex processes that are discussed in Chap. 3 as well as those of Chaps. 4 and 5 are involved in the cascade and shower process and play an important role. They determine the shower completely. On the other hand, the processes that are discussed in Chaps. 16, 17 and 18 that deal with atmospheric Cherenkov, fluorescence and radio emission, respectively, are irrelevant for the shower development but play an important role for the shower detection, the event analysis and the interpretation.[1]

Closely linked to the primary mass and primary energy are the depth or height of maximum development of a shower in the atmosphere, $X_{\max}$ [g cm^{-2}] or $h_{\max}$ [cm], respectively, and the elongation rate, ER [g cm^{-2}per decade of energy], that are in principle experimentally accessible (see Chap. 7), and the essentially inaccessible height of the first interaction of the primary, h_1. These observables, i.e., $X_{\max}$, $h_{\max}$, ER and h_1, are not only functions of M_0 and E_0 but are also affected by the fundamental interaction processes that govern the shower development.[2] Of these the hadronic interactions harbor the most uncertainties, including of course the interaction models and the relevant model parameters that we use in simulations for the analysis. These are also subject to investigation in this context. They all belong to the category of indirectly accessible and derived parameters.

Many of these parameters and their functional dependencies are interrelated. As an example, the inelasticity which plays an important role for the energy transport in a shower and the longitudinal development is also a measure of the energy fraction of a collision that is converted to particle production. It is therefore related to the secondary particle multiplicity, n. Of relevance, too, are the kind of secondaries emerging from an interaction because different particles affect the shower development differently, e.g., heavy particles (nucleons, antinucleons) are more effective energy transport agents than pions or kaons (see Chaps. 3 and 13 for details). Thus, the *partition* of the center of mass energy that is available for particle creation among the different kinds of secondaries is relevant, too.

A rough inspection based on air shower simulations has revealed that the variation of any one of the derived parameters listed above causes a similar effect on the common ground level shower observables, except for the elasticity which is complementary to the inelasticity and behaves therefore in the opposite sense. In

[1] Optical Cherenkov and fluorescence emission account for a fraction of about 10^{-5} to 10^{-4} each of the total shower energy, and radio emission for a fraction of about 10^{-4}.

[2] Note that atmospheric (barometric) conditions affect the shower development, too, (see Chaps. 6, 7 and 17) but we disregard this aspect here.

other words, an increase of the primary mass causes a similar overall effect as does an increase of the inelastic cross section, or an increase of the secondary particle multiplicity or the inelasticity, at a fixed total primary energy. Moreover, studies have shown that the energy dependence of these parameters tends to affect ground level observables alike. These findings illustrate how masked and interrelated the effects of the *primary mass*, of the *interaction model*, the *model parameters* and their *energy dependence* are, and how difficult it is to isolate any one of them for specific investigations. Differences appear, of course, on a more refined level of multi-parameter analyses.

The procedure to disentangle the different contributions is essentially based on a *trial and error method*, whereby experimental data are compared with simulation results for specific primary parameters (E_0, M_0), a given shower and interaction model, and a particular set of model parameters. The primary parameters, the model and the model parameters are then varied, one by one, until the simulated results fit the experimental data best.

Besides a simple comparison of experimental and theoretical spectra and distributions, *multi-parameter correlation analyses* that include several simultaneous observables are a necessity since they are a far more sensitive tool of analysis and disclose model differences and inadequacies readily and more pronounced, particularly in *event by event analyses*. Of great importance is, of course, the uniqueness of the result, i.e., that only one model and set of simulation parameters yield a particular result. In view of the large number of parameters that are involved, this is a difficult task. This is also the reason why several different (independent) experimental observables must be acquired simultaneously for each individual shower to conduct a reliable analysis which hopefully yields a unique and conclusive answer. With an adequate number of observables an event by event analysis can yield valuable insight.

The above discussion illuminates why it is so difficult to extract the mass of the shower initiating primary from individual shower data and thus to determine the composition of the primary cosmic radiation and its energy dependence from ground-based observations. The results are not much improved when we attempt to determine the *average mass* from a large set of experimental data of a group of showers belonging to a particular primary energy range. Irrespective of the approach that we choose, it is difficult to investigate any one aspect without getting involved with the others. The primary composition and its energy dependence are of great astrophysical interest. They are closely coupled with the nature of the sources of the cosmic radiation and with the acceleration and propagation mechanisms.

In the following we will focus the discussion mainly on particle aspects and methods based on ground level shower particle measurements to derive information on indirectly accessible shower parameters and only skim methods using atmospheric Cherenkov, fluorescence and radio phenomena. These topics are discussed separately in Chaps. 16, 17 and 18, respectively.

10.2 Primary Energy Estimation

10.2.1 Energy Related Observables

The energy of an air shower and therefore the energy of the initiating primary particle (or photon) can be estimated from a variety of ground based observables (parameters). These comprise the shower size, N (N_{ch} for all charged particles, or N_e for the electron size only), the muon size, N_μ (or N_μ^{tr} for the *truncated muon size*), the atmospheric Cherenkov or the fluorescence photon flux, Q_{ph}. These observables are obtained from particle or photon density measurements, respectively. In addition, the energy density deposit in terms of the quantity $\rho(xxx)$ expressed in units of *vertical equivalent muons per square meter* [veμ m^{-2}] in a particular target, e.g., the water column of a deep water Cherenkov detector, or the charged particle density in terms of $S(xxx)$ in a relatively thin scintillator ($\leq$5 cm thick) expressed in units of *minimum ionizing particles per square meter*, both recorded within a specific distance range from the shower axis, (xxx), offer an alternative direct method of primary energy estimation that is commonly used today at large air shower arrays. Radio frequency measurements are not yet at the stage of development where they can be used as stand-alone method for primary energy estimation.

In contrast to a gamma ray or electron initiated pure electromagnetic shower[3] where in principle the primary energy of the initiating photon (or electron) can be computed readily and fairly reliably with the help of the photon–electron cascade theory, once the electron shower size, N_e, is known (see Chap. 4), the estimation of the energy of a shower initiating primary hadron (proton or nucleus) is more delicate and less reliable.

The reliability of the primary energy determination depends on many factors. Apart from the quality of the measurements it is above all the choice of the observables, the method of analysis and the quality of the shower and interaction models that are being used in the simulation for the analysis of hadron initiated showers that are of prime importance. As pointed out in the previous section, the largest uncertainties in the analysis are embedded in the hadronic interaction models at very high energies, where the validity of the models hinges on the validity of massive extrapolations that are carried many orders of magnitude beyond the so-called *highest energy anchor point*, i.e., the highest energy point where the models were fitted to accelerator and (pre-LHC) collider data.[4]

---

[3] Gamma ray or electron initiated showers may contain some muons that originate from low cross section photonuclear processes.

[4] Note that there are still no data available from the high rapidity forward region of collider experiments. Forward beam experiments are planned with the Large Hadron Collider (LHC) at CERN, such as CASTOR, LHCf and TOTEM.

Besides the uncertainties that surround the elementary hadronic interactions, an additional difficulty arises from the fact that we must deal with hadron–light–nucleus interactions ($N - A$, $\pi - A$, etc.) in the atmosphere, and that the nature (mass) of the primary is a priori unknown and can be a composite nucleus. In the case of primary nuclei, nucleus–nucleus interactions must be considered for the first few interactions of the primary and its fragments in the atmosphere, until the fragments are broken up into nucleons.

The primary mass dependence of the (electron) shower size of a primary of given total energy (not energy per nucleon) is illustrated in Fig. 10.1. The plot shows the electron shower size as a function of the total primary energy obtained by Antoni et al. (2002) from a simulation carried out with the program package CORSIKA, using different event generators, for primary protons and iron nuclei (see also Antoni et al., 1999a). Irrespective of the fact that the different event generators used within the same shower program yield somewhat deviating results, it is obvious that not knowing a priori the primary mass introduces a considerable uncertainty for the estimation of the primary energy from the shower size only.

The common shower size, N (or N_{ch}), recorded by most experiments includes all the particles of a shower at a specified level in the atmosphere. These exhibit a typical lateral density distribution. The local particle densities recorded by the majority of the array detectors are subject to large fluctuations and obey in general Poissonian statistics because of the low particle density. This statement does

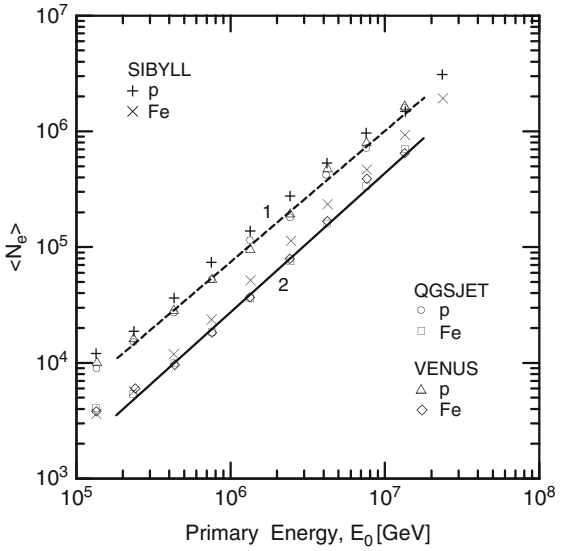

Fig. 10.1 Mean value of the electron number (size), N_e, at 110 m a.s.l. as a function of total primary energy, E_0, (not E_0/A) for primary proton and iron nuclei initiated showers as predicted by CORSIKA using the particle production models (event generators) as indicated in the figure (after Antoni et al., 2002)

not apply to atmospheric Cherenkov and air fluorescence measurements where the recorded optical photon density is usually large.[5]

As discussed in Chap. 8, different shower constituents manifest different radial density distributions. Muons are much less abundant than electrons and are spread out to larger distances from the shower axis than electrons. In other words, the local density ratio of electrons to muons is a function of core distance, and likewise for other particle ratios (cf Fig. 8.1). Furthermore, the different shower constituents exhibit different local energy spectra (cf Figs. 8.2 and 8.3).

On the other hand, different kinds of detectors respond differently to a given particle mix at a specific location in a shower. Many are not able to distinguish between different (charged) particles (electrons, muons, etc.,) and measure simply ionization over the track length of the particles in the detector medium, such as scintillators, ionization chambers or proportional counters. In thin detectors the signal can be interpreted as charged particle count. The response of scintillation detectors to the major shower constituents and the energy dependence is presented in Sects. 2.11.4, 8.5 and 8.10.

Other detector types may be sensitive preferentially to muons, such as the Haverah Park type deep water Cherenkov detectors which have a more calorimetric behavior. Their response depends on the particle mix and the respective particle energy spectra (for details see Sects. 2.11.3, 8.5 and 8.10). The detector signal is proportional to the optical Cherenkov photon count and is a measure of the energy loss (energy deposit) of the particles in the detector medium.

In summary, plain scintillation detectors record all charged particles, including gamma ray conversion products, from which the common all-particle shower size is obtained, whereas deep water Cherenkov detectors record energy loss of all charged particles above the Cherenkov threshold, including adequately energetic gamma conversions, and require a different procedure to estimate the primary energy. In either case, for specific applications as outlined below, conversion coefficients can be obtained for both detector types to get the primary energy from the detected signal amplitudes.

Thus, the *kind of detectors* that are being used in an array and the *array layout pattern* must be carefully considered when determining the shower size, the muon size, or equivalent observables, such as the energy loss density or similar observables from array measurements to determine the primary energy and other relevant shower and interaction parameters.

The determination of the *arrival direction* and of the *core location* is described in Sect. 2.10. The two observables are intimately related and should not be determined independently for reasons explained in Chaps. 2 and 8. Note that accurate core position and arrival direction determination are of paramount importance for a reliable primary energy estimation. A rudimentary primary energy estimation based

[5] The main source of fluctuations of optical Cherenkov measurements is the superimposed fluctuating night sky background brightness.

on shower size determination from particle density measurements and fits of these to a simple Nishimura-Kamata-Greisen (NKG) function is also discussed there.

Today, the most frequently used method to estimate the primary energy of a shower using particle measurements, which is also believed to be the most reliable method, is based on the comparison and matching of the results of full fledged air shower event simulations including detector response with the measured experimental data from the shower array detectors. Obviously, the quality of the result hinges heavily on the quality of the simulations. For this reason many authors use two or three different shower program packages and insert various hadronic event generators to check the results and investigate the differences.

As mentioned earlier, for particle detection at ground level mainly two quite different kinds of detectors are being used. Their particularities are discussed in the following subsections (see also Chap. 8 for further details). Analogous studies using atmospheric Cherenkov photons are only briefly mentioned in this chapter; they are discussed extensively in Chap. 16.

10.2.2 Energy Estimation Using Deep Water Cherenkov Detectors

An important observation due to Hillas et al. (1970), briefly mentioned in Chap. 8, who carried out air shower simulations using a very naive phenomenological shower model was that the apparent particle density (more specifically the energy loss density) at several hundred meters from the shower axis in large showers as recorded at Haverah Park with a specific kind of deep water Cherenkov detector is *almost independent* (within about 20% according to the authors) of the particle production mechanism[6] and the primary mass at fixed primary energy (Hillas et al., 1971a, b). Moreover, this particular behavior is claimed to persist over a wide primary energy range, as is illustrated in Fig. 10.2 for a set of primary energy normalized lateral particle density distributions, $\rho(r)$, expressed in units of vertical equivalent muons per square meter [veμ m^{-2}]. This detector feature can therefore be used as a *primary energy estimator*.

The particle mix at the specified core distance, say 600 m, is shown in Fig. 10.3a. It consists of low energy electrons and photons, and moderately energetic muons (see Figs. 8.2 and 8.3). The response of the deep water Cherenkov detector to the particle mix of Fig. 10.3a is shown in Fig. 10.3b. In Sect. 2.11 where detector responses to shower particles are compared, we show in Fig. 2.22 the energy dependence of the response of a Haverah Park type deep water Cherenkov detector to photons, electrons and muons. A compilation of energy loss and $\rho(r = xxx)$

[6] This is true only if the models are such that particle production remains within reasonable bounds of extrapolated accelerator data. Simulations with realistic models show that actually the location of the quasi mass independent energy loss density within a shower varies slowly with primary energy.

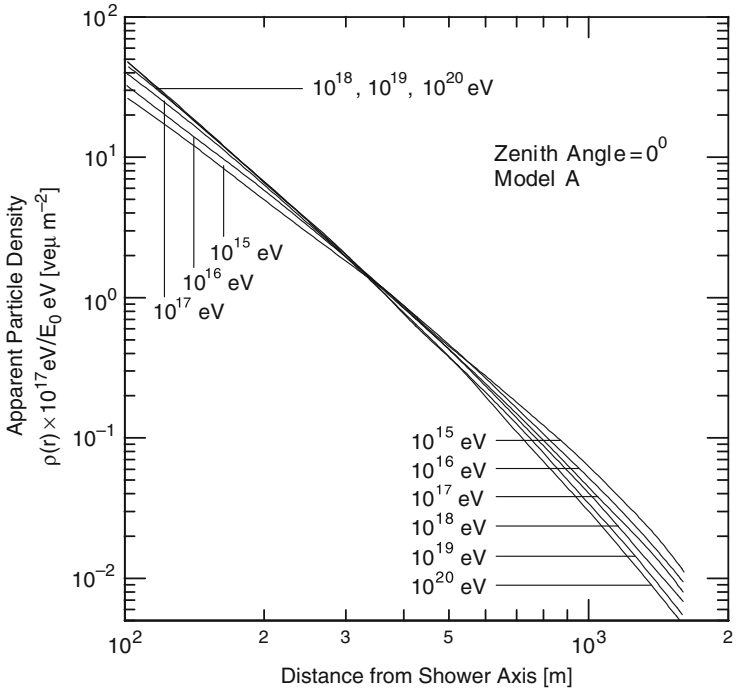

Fig. 10.2 Lateral density distributions calculated for a 1.2 m deep water Cherenkov detector for vertical showers of primary energy $10^{15} \leq E_0 \leq 10^{20}$ eV/nucleon. To get the actual density multiply the reading of the ordinate by the factor (E_0[eV]/10^{17}) (after Hillas et al., 1970)

differential and integral density spectra of showers in units of vertical equivalent muons per square meter of large showers is presented in Sect. 12.5.

(a) Lateral Density Distribution

The lateral distribution of the shower particles is discussed at length in Chap. 8, where also a number of array specific distribution functions and the corresponding detector responses are presented (Sect. 8.10). For the interpretation of the deep water Cherenkov detector data the Haverah Park group had used the experimentally established lateral distribution function given by Eq. (8.16), repeated here for convenience (Edge et al., 1973; Coy et al., 1981, 1997; Lawrence et al., 1991),

$$\rho(r) \;=\; k\, r^{-(\eta + r/a)} \;\; [\mathrm{ve}\mu\ \mathrm{m}^{-2}] \;\; . \tag{10.1}$$

Here, r [m] is the distance from the shower axis, a is a constant equal to 4,000, k is the size specific normalizing constant, and the slope parameter, η, is given by the relation

$$\eta \;=\; 3.78 - 1.44 \sec\theta \;\; . \tag{10.2}$$

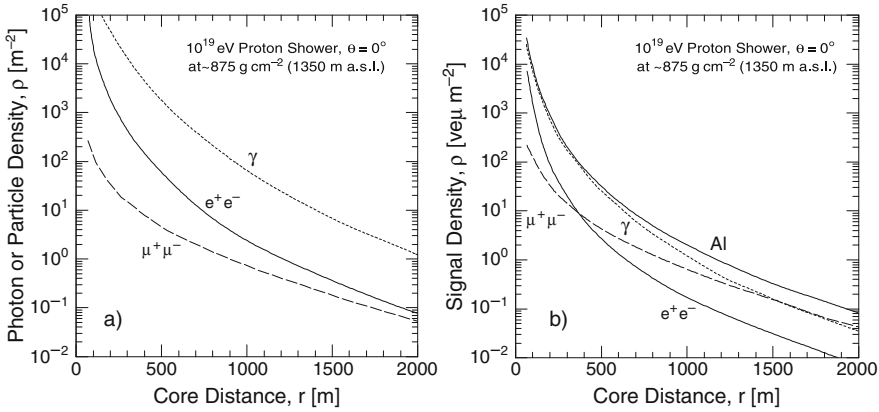

Fig. 10.3 (**a**) Radial density distribution of gamma rays, positrons and negatrons, and muons of both charge signs in a vertical 10^{19} eV proton initiated shower at an altitude of ~1, 350 m a.s.l.; (**b**) the signal level produced by these particles in a 1.2 m deep water Cherenkov detector, expressed in vertical equivalent muons [veμ m^{-2}] (after Dova, 2003)

This expression which applies for 50 m $\leq r \leq$ 800 m and primary energies $10^{17} \leq E_0 \leq 10^{20}$ eV is claimed to be in good agreement with simulation results. The energy dependence of η is small, approximately 0.165 ± 0.022 per decade (Ave et al., 2003).

(b) Zenith Angle Dependence and Correction

In comparison to vertical showers of local particle density $\rho(r = 600, \theta = 0^\circ)$ at 600 m from the core, the particle density of inclined showers having identical primary parameters but arriving at zenith angle $\theta > 0$, $\rho(600, \theta)$, observed at the same site, is reduced because inclined showers pass through more atmosphere, i.e., through a larger column density or slant depth, X_s [g cm^{-2}]. Hence, the shower size is smaller because more particles are subject to absorption.[7] At the same time the particle mix changes slowly in favor of an increasing fraction of muons with increasing zenith angle.

As discussed in Chaps. 6 and 7, the particle absorption length can be determined from constant intensity cuts. In Fig. 10.4 we show the zenith angle dependence of the particle density, $\rho(600)$, as recorded by the deep water Cherenkov detectors in terms of the natural logarithm of the density plotted as a function of sec θ as measured at Haverah Park at two different epochs. From the lines connecting the respective data points one gets the particle absorption lengths, λ_{abs}, as stated in the figure. The disagreement between the two absorption lengths is claimed by the authors

[7] This applies to observations beyond the shower maximum, where the additional interactions contribute fewer new particles than are removed by absorption.

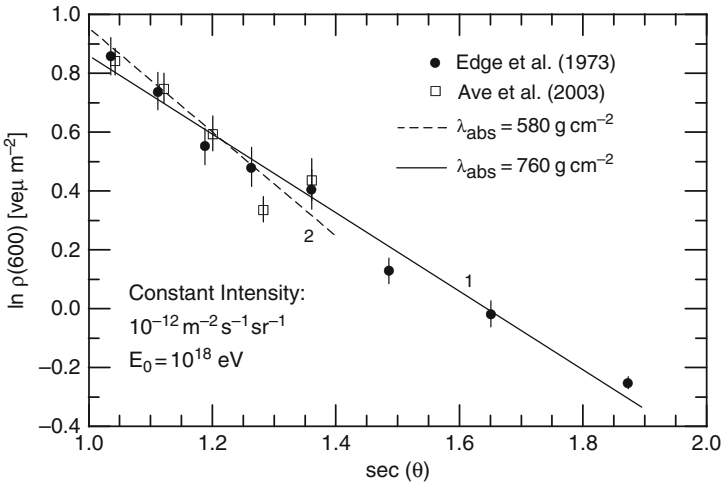

Fig. 10.4 Absorption of the density, $\rho(600)$, as a function of the zenith angle in terms of $\sec\theta$, obtained by the method of constant intensity cuts, measured at two epochs with water Cherenkov detectors (after Ave et al., 2003)

to be mainly due to the different zenith angle intervals used by Edge et al. (1973) ($0^\circ \leq \theta \leq 60^\circ$) and Ave et al. (2003) ($0^\circ \leq \theta \leq 45^\circ$).

For showers of equal primary energy (and mass) that are incident under different zenith angles, θ, the particle densities $\rho(r, \theta)$ at location r are related to the vertical particle density $\rho(r, 0^\circ)$ as follows,

$$\rho(r, 0^\circ) \;=\; \rho(r, \theta) \exp\left(\frac{X_{\rm obs}}{\lambda_{\rm abs}}(\sec\theta \;-\; 1)\right) \;\; [\text{ve}\mu\,\text{m}^{-2}]\,. \qquad (10.3)$$

Here, $X_{\rm obs}$ is the vertical atmospheric depth of the observation level and $\lambda_{\rm abs}$ the absorption length (for further details see Sect. 8.5.3).

An analogous plot constructed from simulated data is shown in Fig. 10.5 where $\rho(600)$ is displayed on a logarithmic scale as a function of $\sec\theta$ for proton and iron nuclei initiated showers. The simulation was carried out with the COSRIKA program system, using the modern QGSJET event generator and the program package known as GEANT to simulate the detector response.

(c) Primary Energy Estimation

The estimation of the primary energy, E_0, is based on the correlation of the observable $\rho(600)$ with E_0, which is obtained from shower simulations. This correlation is illustrated in Fig. 10.6 which shows the response of a standard Haverah Park type deep water Cherenkov detector in terms of $\rho(600)$ to proton and iron initiated showers, incident at $\theta = 26^\circ$, at a core distance of 600 m as a function of primary energy, as obtained by Ave et al. (2003), using CORSIKA with QGSJET98 and

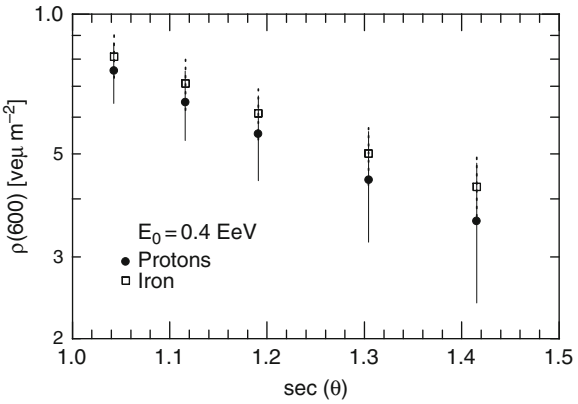

Fig. 10.5 Predicted absorption using CORSIKA with QGSJET for the shower simulation and GEANT for the detector response. The error bars correspond to the spread of $\rho(600)$, illustrating the shower fluctuations (after Ave et al., 2003)

GEANT. Also shown in this figure is the particle density versus primary energy calibration curve for such detectors at 600 m from the shower axis obtained by Hillas et al. (1970), using their simple shower model. In either case the particle density is expressed in terms of the so-called *ground parameter*, $\rho(600)$ [veμ m^{-2}].[8]

The Haverah Park group used for reference and calibration the data obtained from a set of simulated showers having zenith angles of $\theta = 26^\circ$, which is close to the median angle of the detected showers. Therefore, the observed densities $\rho(600, \theta)$ had to be converted to $\rho(600, \theta = 26^\circ)$ to estimate the primary energy, using the following relation with the appropriate absorption length, $\lambda_{\rm abs}$,

$$\rho(r, 26^\circ) \;=\; \rho(r, \theta) \exp\left(\frac{X_{\rm obs}}{\lambda_{\rm abs}}(\sec\theta \;-\; \sec 26^\circ)\right) \;\; [\text{veμ m}^{-2}]\,, \qquad (10.4)$$

where $X_{\rm obs}$ is the vertical atmospheric depth of the observation level (1,018 g cm^{-2}, 212 m a.s.l. at Haverah Park) and $\lambda_{\rm abs}$ the absorption length (580 ± 50 g cm^{-2} for the recent value). The simulations mentioned before yield absorption length for $\rho(600)$ in proton initiated showers of 512 g cm^{-2} and 581 ± 20 g cm^{-2} for iron showers at $E_0 = 4 \cdot 10^{17}$ eV for the particle mix recorded with deep water Cherenkov detectors.

It is important to note that the value of $\lambda_{\rm abs}$ depends significantly on the kind of detector that is being used, such as the Haverah Park type deep water Cherenkov detector, which is also being used at the Auger experiment, or the relatively thin scintillation detectors that had been used in many arrays of the past, including Akeno and AGASA, that are currently being used at Yakutsk, and will be used partly at the

[8] The original calculations show as least mass dependent radial distance from the shower axis a distance of 350–400 m. Subsequent work at higher primary energy suggested that a distance of 500–600 m appears to be more appropriate, and for very large showers core distances $\geq$ 600 m. Recent work shows that for the Auger surface array at $E_0 > 10^{19}$ eV, the measurements should be made at a core distance of $\approx 1,000$ m.

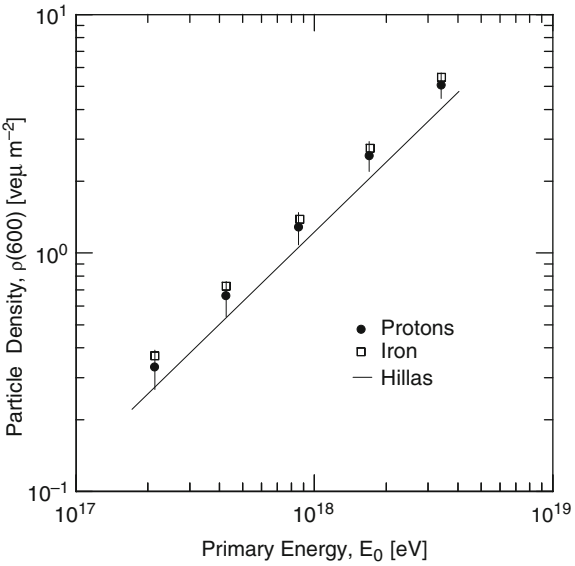

Fig. 10.6 $\rho(600)$ ground parameter-primary energy conversion plot for Haverah Park type deep water Cherenkov detectors. Shown is the vertical equivalent muon density per square meter at 600 m from the shower axis, $\rho(600)$ [veμ m^{-2}], as a function of primary energy for proton and iron initiated showers incident under a zenith angle of 26° obtained with the CORSIKA code using the QGSJET98 event generator (Ave et al., 2003). The *solid straight line* shows the conversion as it was used for the Haverah Park experiment. This relation is the result of simulations using a very naive phenomenological shower model (Hillas et al., 1970, 1971a, b)

future Telescope Array (Kasahara et al., 2007). Since the deep water Cherenkov detectors respond preferentially to muons, the absorption length of showers determined with this kind of detector is larger than the one obtained with scintillators that respond efficiently even to the low energy electromagnetic component for which water Cherenkov detectors yield very low signal levels, if any.

The conversion formula to compute the primary energy from the density $\rho(600, \theta = 26^\circ)$ values that results from this work is given by

$$E_0 \;=\; C\,\rho(600, \theta = 26^\circ)^b \;\; [\mathrm{EeV}]\,. \tag{10.5}$$

The parameters C and b were determined from data obtained from simulations of proton and iron initiated showers using CORSIKA and QGSJET98 (Ave et al., 2003). Their values are listed in Table 10.1.

Table 10.1 Parameters for Eq. (10.5) based on CORSIKA and QGSJET-98. (Ave et al., 2003)

Primary	b	C
p	0.998 ± 0.008	0.616 ± 0.006
Fe	1.011 ± 0.004	0.574 ± 0.003

(d) Optimization of Density Measurements

It had been pointed out in Sect. 2.10, and earlier in this chapter that the layout pattern of the detectors of an array is of importance and must be considered carefully to correctly interpret the measured particle densities and the detection efficiency. This is particularly relevant for very large arrays where the detector spacing is large to record giant air showers.

Newton et al. (2007) have investigated this problem in the context of the Auger surface array that uses Haverah Park type deep water Cherenkov detectors. We will not discuss the analysis of these authors but point out that the problem is linked to core position errors. They show that the optimum core distance to measure the density and to determine the shower size can be calculated for each shower and is mainly determined by the array geometry, with no significant dependence on zenith angle, primary energy or lateral distribution function chosen. The result which is of practical relevance is plotted in Fig. 10.7.

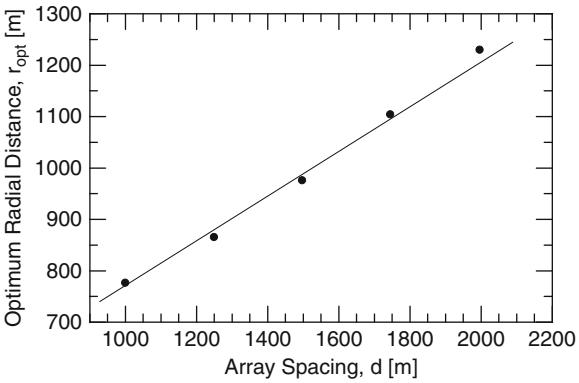

Fig. 10.7 Optimum core distance to minimize the errors in the measurement of the particle density in order to determine the shower size and/or primary energy as a function of surface array detector separation (after Newton et al., 2007)

10.2.3 Energy Estimation Using Unshielded Scintillation Detectors

In a separate careful and detailed study carried out by the Akeno/AGASA group (Nagano et al., 1984, 1992, 2000; Hayashida et al., 1994, 1999; Sakaki et al., 2001a, b; Takeda et al., 2003) the response of scintillation detectors to shower particles as a function of distance from the shower axis, the primary energy and mass, and the interaction models was investigated, analogously to the work of Hillas et al. (1970, 1971a, b) earlier. The simulations of the Akeno/AGASA group have revealed that at approximately the same radial distance from the shower axis (∼600 m) where the insensitivity of the response of the Haverah Park type deep water Cherenkov detectors with respect to hadronic interaction models and primary

mass composition for fixed primary energy was found for large showers, the scintillation detectors manifest similar features.

These authors have used for their simulations initially their own program, called COSMOS (Kasahara et al., 1979), with the QGSJET event generator (Ding et al., 1984). They arrived essentially at the same conclusion for their relevant observable, $S(600,\ 0^\circ)$ [part. m^{-2}], the charged particle density as measured by a scintillation detector, the objective oriented equivalent of $\rho(600, 0^\circ)$ [veμ m^{-2}] of the deep water Cherenkov detectors, as the Haverah Park group, in spite of using a different simulation code (Dai et al., 1988).

According to simulations of Nagano et al. (2000), the radial zone where the relative independence of the density of air shower particles, $S(r, \theta = 0^\circ)$, with respect to interaction model and primary mass applies, extends actually from a few hundred meters out to at least 2,000 m from the shower axis, when recorded with scintillation detectors. In addition, the *functional dependence* of the lateral distribution does not depend significantly on primary energy between $10^{17.5} \leq E_0 \leq 10^{20}$ eV, as measurements have confirmed. The agreement was further strengthened by cross checking the results of the Akeno/AGASA scintillator array with data from a deep water Cherenkov detector which had been incorporated into the Akeno array and was operated at a core distance comparable to that used at Haverah Park, for comparison (Nagano et al., 2000).

For the muon lateral distribution (using shielded detectors, frequently shielded proportional counters) a similar independence of the *functional dependence* of the lateral distribution function (LDF) with respect to interaction models and primary mass had been observed over the radial distance range from near the shower core out to about 1,000 m, for the same primary energy range. However, in this case the *absolute values* of the densities are model and primary mass dependent.

In the following we describe briefly the method which had been outlined by Sakaki et al. (2001a) and Takeda et al. (2003) that had been used to estimate the primary energy of the showers recorded by the Akeno/AGASA array as an example. The details of the method had been slightly varied in the coarse of time to improve it, to reduce the errors, and also to extend the zenith angular acceptance to larger angles, but the general procedure remained the same. The relevant steps are described below.

(a) Lateral Density Distribution

The particle density observed at each detector is fitted to the empirical lateral density distribution function given by Eq. (8.20), repeated here for convenience (Takeda et al., 2003),

$$S(r) \propto \left(\frac{r}{r_M}\right)^{-1.2} \left(1 + \frac{r}{r_M}\right)^{-(\eta-1.2)} \left[1 + \left(\frac{r}{1000}\right)^2\right]^{-0.6} , \qquad (10.6)$$

where, r [m] is the distance from the shower axis, r_M the Molière radius (91.6 m at Akeno) and the parameter η is a function of the zenith angle, θ, given by the expression,

$$\eta = (3.84 \pm 0.11) - (2.15 \pm 0.56)(\sec\theta - 1) \ . \tag{10.7}$$

Equation (10.7) is an improved expression as compared to older ones and, according to the authors, valid to the highest energies since, contrary to Ave et al. (2003) (see Sect. 10.2.2), no energy dependence of η had been observed. The parameter η which depends on θ is relevant for the accuracy of the subsequent energy estimation. Various investigations have shown that the energy uncertainty using this expression is about $\pm 7\%$ (Takeda et al., 2003; Yoshida et al., 1994). For $r = 600$ m and zenith angles of incidence of the showers $\theta \leq 45^\circ$, Eq. (10.6) yields the local density, $S(600, \theta)$, at 600 m from the axis, if properly normalized.

(b) Zenith Angle Dependence and Correction

The AGASA group has used $S(600, 0)$ as an energy estimator. The zenith angle dependence of particle density measurements in air showers carried out with scintillation detectors manifests basically the same behavior as the measurements made with deep water Cherenkov detectors discussed in Sect. 10.2.2b). However, the detector specific response to the zenith angle dependent changing particle population must be accounted for.

Figure 10.8 shows the decline of the particle density in the scintillation detectors, $S(600, \theta)$, and of the total number of charged particles, N_{ch}, i.e., of the shower size, at ground level as a function of $\sec\theta$. The fluctuations of $S(600, \theta)$ are smaller than those of N_{ch} and $S(600, \theta)$ declines more slowly than N_{ch} with increasing $\sec\theta$. This is the reason for using $S(600, \theta)$ instead of N_{ch} as an energy estimator. As mentioned earlier, this feature was first pointed out by Hillas et al. (1971a, b). Dai et al. (1988) have shown that the fluctuations of the density at 600 m is actually rather small.

For further event processing, the density $S(600, \theta)$ is converted to the corresponding $S(600, 0)$ value, using the shower particle absorption length, λ_{abs}. The latter is determined experimentally from constant (equal) intensity cuts as for the observable $\rho(600)$, and is described in Chap. 6. Details concerning the conversion of $S(600, \theta)$ to $S(600, 0)$ are discussed in Sect. 8.5b. An important fact is that over the primary energy range investigated the absorption length λ_{abs} as defined for the observable $S(600, \theta)$ is independent of energy. The error introduced by the conversion of $S(600, \theta)$ to $S(600, 0)$ is estimated to amount to about 5% (Takeda et al., 2003).

In order to increase the rate of recording ultrahigh energy showers ($E_0 \geq 3 \cdot 10^{18}$ eV) with the AGASA array, Sakaki et al. (2001b) increased the zenith angular acceptance of the array to 60°. They continued using the lateral distribution function as given by Eq. (10.6) but refined Eq. (8.3) to convert the density $S(600, \theta)$ to the vertical density, $S(600, 0)$ as follows,

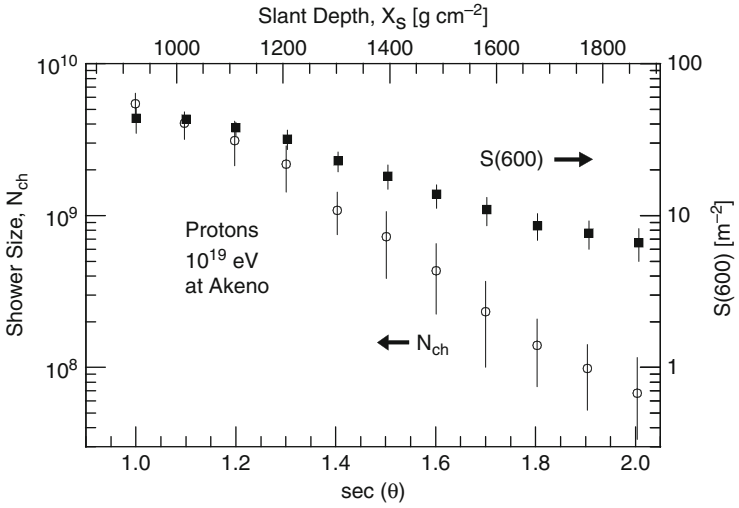

Fig. 10.8 Absorption of the total number of charged particles, N_{ch} and $S(600)$ as a function of $\sec\theta$ for proton initiated showers of 10^{19} eV primary energy, obtained with the AIRES program (after Sakaki et al., 2001a)

$$S(600,\theta) = S(600,0)\exp\left[-\left(\frac{X_0'}{\lambda_1'}(\sec\theta-1)\right)-\left(\frac{X_0'}{\lambda_2'}(\sec\theta-1)\right)^2 + \left(\frac{X_0'}{\lambda_3'}(\sec\theta-1)\right)^3\right] \text{ [particles m}^{-2}\text{]} . \tag{10.8}$$

This step required the extension of shower particle absorption and shower rate attenuation length measurements using equal intensity cuts to account accurately for the atmospheric effects at large zenith angles.

For this analysis Sakaki et al. (2001b) assumed circular symmetry of the particle density distribution around the shower axis for all showers, which in fact does not really apply to inclined showers. For very large and also very inclined showers the absorption length of the shower particles, λ_{abs}, depends on the radial distance from the shower axis and on the azimuthal location at larger core distances, due to the different trajectory lengths and column densities traversed by the particles, from the point of the first interaction down to the location of detection (cf. Sect. 8.7). The same applies to the shower age parameter. These facts are important for large arrays like Auger and the Telescope Array.

(c) Primary Energy Estimation

The primary energy is estimated using the relation between $S(600, 0)$ [m^{-2}] and the primary energy, which is obtained from Monte Carlo simulations. The conversion factor from $S(600, 0)$ to the primary energy at the Akeno level was derived

from simulations of Dai et al. (1988) based on the COSMOS program of Kasahara et al. (1979). The following relation was obtained and had been used for the AGASA experiment until about 2001.

$$E_0 \;=\; a \cdot 10^{17} \cdot (S(600,0))^b \;\; [\mathrm{eV}] \;, \tag{10.9}$$

where $a = 2.03$ and $b = 1.0$. The accuracy of this expression was estimated to be within 20%, irrespective of the type of interaction model or primary composition considered (Dai et al., 1988; Sakaki et al., 2001a).

In the simulation, the density was calculated by adding the densities from electron sub-showers, which had been approximated by an NKG function. The observed (experimental) density was converted to electron density for direct comparison with the simulated densities (Nagano et al., 2000). The layout pattern of the AGASA detector array was accounted for in the Monte Carlo simulation for the evaluation of the scintillator densities, which can then be compared directly with the experimental data.

(d) Comments on Spectrum

The primary energy spectrum when determined with Eq. (10.9) using the AGASA data lies ∼10% higher in the 10^{18} eV range than when using the 1 km^2 Akeno array data (Nagano et al., 2000). Thus, to interpret the AGASA data the following modified equation must be used to get a smooth fit with the lower energy region of the primary spectrum that was determined with the Akeno array,

$$E_0 \;=\; 1.8 \cdot 10^{17}\, S(600,0)^{1.0} \;\; [\mathrm{eV}] \;. \tag{10.10}$$

On the other hand, simulations carried out with the MOCCA program and the SIBYLL hadronic event generator suggest that the AGASA energy spectrum should be about 30% higher for the Akeno altitude (Cronin, 1997).

It was suggested that the *disagreement* is probably due to a significant contribution of low energy photons to the detector signal (Kutter, 1998). In support of this hypothesis is the fact that, irrespective of the independence of the energy loss of photons and electrons on scintillator thickness, the apparently measured scintillator particle density in the photon contaminated environment of a shower, ρ_{sci}, expressed in units of *vertically penetrating minimum ionizing particles per square meter* [m^{-2}] (or fast vertical muons [vμ m^{-2}]), the ratio R of the actual scintillator signal, ρ_{sci} [m^{-2}] (or S [m^{-2}]), to the signal produced by charged minimum ionizing particles only, ρ_{min} [m^{-2}], at fixed zenith angle, i.e., $R(\rho_{\mathrm{sci}}/\rho_{\mathrm{min}})$, depends on core distance. The obvious reason for this dependence is the change of the particle population, i.e., the composition and energy of the particles in the shower, with core distance (see Sect. 8.3).

According to Nagano et al. (2000) this ratio is $R \simeq 1.1$ within 100 m from the core (Shibata et al., 1965) and agrees with the Akeno measurements.[9] The ratio increases to $R \simeq 1.2$ at a core distance of ∼600 m according to calculations with MOCCA using SIBYLL. Calculations with CORSIKA using QGSJET yield a ratio of 1.4 at the same distance. The increase of the ratio R with increasing core distance r is due to an increasing fraction of low energy particles with growing core distance that produce more specific ionization in the scintillators. The difference between the two simulation programs appears to be due to differences in the low energy photon and electron contents and energy spectra, far from the shower axis. The quantity $\rho_{\rm sci}$ is also sensitive to the cutoff energy of the electromagnetic component in the simulation.

Figure 10.9 shows the relation between $S(600, 0)$ [part. m^{-2}] (or $\rho_{\rm sci}(600)$) and the primary energy obtained by Nagano et al. (2000) from a simulation for primary proton and iron nuclei induced showers, using CORSIKA with QGSJET and SIBYLL, respectively. These authors have also carefully studied the relation between the pure muon component ($E_\mu \geq 1$ GeV), characterized by $\rho_\mu(600, 0)$, and the shower particle parameter $S(600, 0)$ (or $\rho_{\rm sci}(600, 0)$ as defined before), which includes the full particle mix, i.e., photons, electrons and muons, for a 5 cm thick scintillator. Figure 10.10 shows their results for the same primary conditions and interaction model selection as before. The zenith angle dependence of the scintillator signal $S(600, \theta)$ is discussed in Sect. 8.5.3 and is given by Eqs. (8.2) and (8.3).

In the numerous efforts made by the AGASA group to resolve the differences between their primary spectrum and the spectra of the other large experiments, and in order to reduce errors in the interpretation of the lateral distribution, the scintillation detector response, the conversion of the observable $S(600, 0)$ to primary energy, and to improve the accuracy of the primary energy estimation, different simulation program packages and interaction models had been explored for two slightly different altitudes of observation. One was the level of the central Akeno laboratory (900 m a.s.l.), the other the average altitude of the AGASA array (667 m a.s.l.). The various studies yielded different values for the parameters a and b of Eq. (10.9), ranging from 2.03 to 2.34 for a and 1.00 to 1.04 for b (for details see Sakaki et al., 2001a; Takeda et al., 2003).

After accounting for all experimental effects, including fluctuations, the Akeno /AGASA group recommends to use the following relation to convert the $S(600, 0)$ [m^{-2}] particle density measured with a 5 cm thick scintillator at the Akeno altitude to the primary energy of a shower,

$$E_0[\text{eV}] \;=\; 2.17 \cdot 10^{17} \cdot (S(600, 0))^{1.0} \;\; [\text{m}^{-2}] \;, \tag{10.11}$$

and for the average AGASA altitude

[9] The density calibration at Akeno and AGASA was based on the electron density measured with a spark chamber, and the density ratio between scintillator and spark chamber was found to be 1.1 at ∼ 100 m from the core (Takeda et al., 2003).

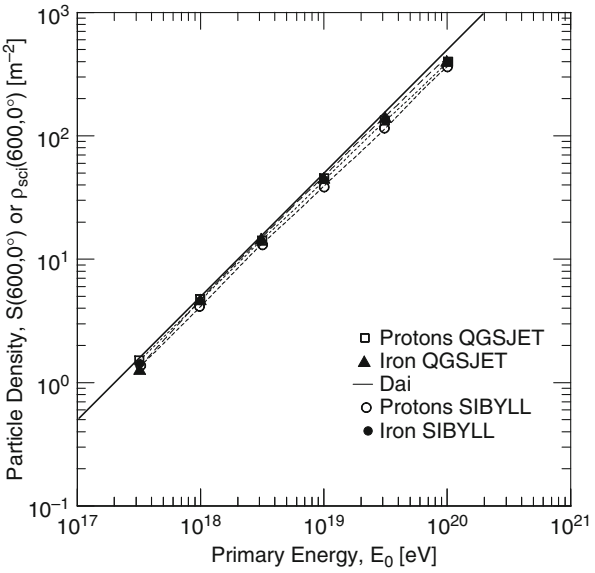

Fig. 10.9 Scintillator density $S(600, 0^\circ)$ or $\rho_{\rm sci}(600, 0)$ [m^{-2}] as a function of energy estimated from the QGSJET and SIBYLL models for proton and iron primaries (after Nagano et al., 2000; see also Takeda et al., 2003)

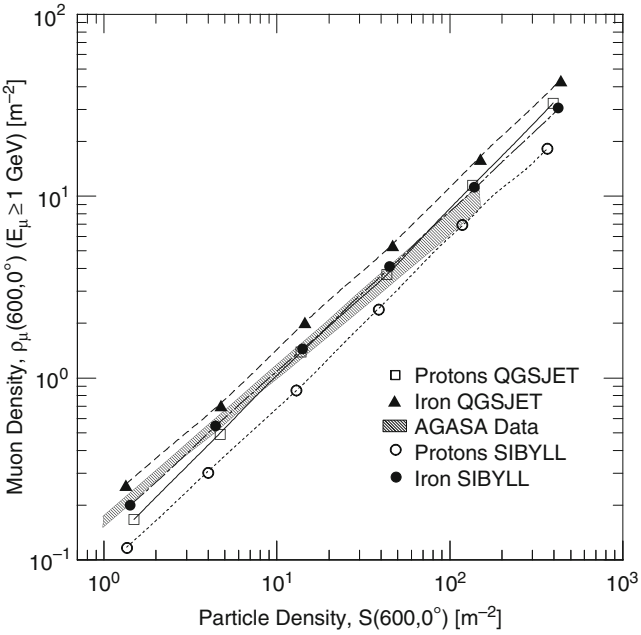

Fig. 10.10 Comparison of experimental $\rho_\mu(600)$ [m^{-2}] muon density versus $S(600, 0)$ (or $\rho_{\rm ch}(600, 0)$) [m^{-2}] charged particle density relation (AGASA data) with the simulation results obtained with CORSIKA (after Nagano et al., 2000)

$$E_0[\text{eV}] \;=\; 2.21 \cdot 10^{17} \cdot (S(600, 0))^{1.03} \;\; [\text{m}^{-2}] \;. \qquad (10.12)$$

The accuracy of these expressions was analyzed in detail by Takeda et al. (2003) and estimated to be within 18%.

(e) Effects of Temporal Structure of Shower Front and Delayed Particles on Density Measurements

When using logarithmic amplifiers (pulse height to pulse width converters) to expand the dynamic range of scintillation and other detectors, the arrival time spread of the particles, delayed particles and accidental coincidences may cause particle density and primary energy overestimation errors that may be as large as 20% of the true particle density and primary energy. Caution is therefore required in the interpretation of density measurements that employ pulse height to pulse width converters. This problem is discussed in more detail in Chap. 8.

(f) Shower Size-Primary-Energy Conversion Factors

For completeness we also mention that in an earlier study Nagano et al. (1984) determined a conversion factor, U, to estimate the primary energy from the shower size based on $S(600)$ density measurements, which had been used at Akeno. The factor is size (and altitude) dependent and is given in the graph of Fig. 10.11 for vertical showers. It is expressed in units of GeV per shower particle, i.e., the shower size must be multiplied by the corresponding factor U to get the approximate primary energy in GeV. Note that a larger factor is needed for small showers as compared to large showers because these are well beyond their maximum development at the Akeno site, and vice versa for large showers.

10.2.4 Energy Estimation Using the Muon or Truncated Muon Number (Size)

Like the total electron or the total charged particle number (size) of an air shower, the muon number or size, too, can in principle be used as a measure of the primary energy. Basically the procedure to determine the muon size is the same as for the determination of the total charged particle or electron size with the exception that appropriately shielded detectors are now being used that respond only to muons that exceed the required energy threshold.

An assumed or a more or less empirical or theoretically founded *muon lateral distribution function*, $\rho_\mu(r)$, (for detailed expressions see Chap. 14) is then fitted to the densities measured by the muon detectors that sample the muon distribution across the shower as predetermined by the layout of the detectors within the air shower array. The integration is then carried out over the entire radial range, $0 \leq r \leq \infty$, that yields the muon size, N_μ,

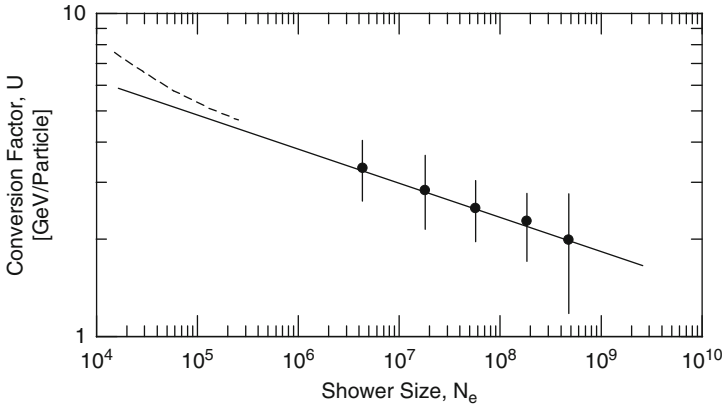

Fig. 10.11 Conversion factor, U, to determine the primary energy, E_0, from the shower size of vertical showers at Akeno. The *straight solid line* is a simple fit to the data points. The *dashed line* is an extrapolation to small size showers (low primary energies), considering the effect of slowly rising cross sections with increasing energy. This factor is determined with the help of simulations in conjunction with combined equal intensity distributions measured at Akeno (900 m a.s.l., 920 g cm^{-2}) and Mt. Chacaltaya (5,230 m a.s.l., 530 g cm^{-2}) (Nagano et al., 1984, 2000; see also Hara et al., 1983; Hillas, 1983)

$$N_\mu \;=\; 2\pi \int_0^\infty r\rho_\mu(r)\mathrm{d}r \;, \tag{10.13}$$

and the result is interpreted with the help of simulation data.

However, this procedure has a major drawback. Since the muons are distributed over a larger area than the electrons in a given shower and since their density is much lower, requiring in general larger detectors, reliable muon size measurements are in general more difficult. Because the integration must be carried out over a large area using a distribution function that may deviate at large radii from the actual density distribution, this approach harbors major uncertainties.

A careful study based on detailed simulations has revealed that the so-called *truncated muon number (size),* N_μ^{tr}, i.e., the muon number determined by integrating the density distribution only over a restricted radial zone from the shower axis (an annular ring $a \le r \le b$),

$$N_\mu^{\mathrm{tr}} \;=\; 2\pi \int_{r=a}^{r=b} r\rho_\mu(r)\mathrm{d}r \;, \tag{10.14}$$

is a more reliable measure of the primary energy than the total muon size. The parameters a and b are chosen such that a is outside the immediate shower core, thus avoiding saturation, transition effects, electromagnetic *punch-through* and massive hadronic contributions, and b is given by the fiducial area of the array, i.e., the most distant array detectors. This method had been developed by the KASCADE group (Weber et al., 1997; Antoni et al., 2001a; Haungs et al., 2003; van Buren et al., 2005).

In this way the interpretation stays clear of the un-sampled extended radial tail of the shower and minimizes biases introduced by inaccuracies of the distribution function at large distances. In addition simulations have shown that the quantity $N_\mu^{\rm tr}$ is relatively *insensitive to primary mass* and can therefore be used as an energy estimator. Thus, the behavior of this observable has similar properties as the quantity $\rho(600)$ discussed in Sect. 10.2.2 in connection with deep water Cherenkov detectors.

In Fig. 10.12 we show the energy dependence of the truncated muon size, $N_\mu^{\rm tr}$, as a function of the primary energy, E_0, for proton and iron nuclei initiated air showers, as predicted by CORSIKA using different event generators, as indicated in the figure, from the work of Antoni et al. (2002). The figure is the companion to Fig. 10.1 which shows the $N_e - E_0$ correlation. Note that for a given primary energy the truncated muon number is significantly less sensitive to the mass of the shower initiating primary than the electron number.

10.2.5 Energy Estimation Using Atmospheric Cherenkov, Fluorescence and Radio Emission

Atmospheric Cherenkov, fluorescence and radio emission are the result of secondary processes initiated by the shower particles from all stages of shower development

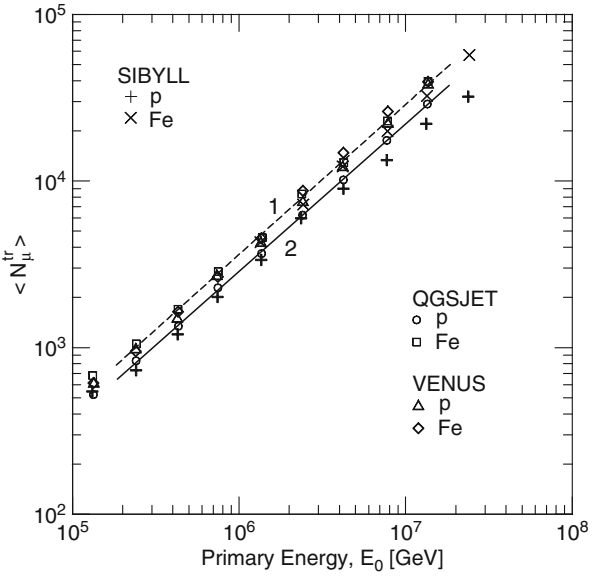

Fig. 10.12 Mean values of the *truncated* muon number (size), $N_\mu^{\rm tr}$ ($E_\mu \geq 230$ MeV$\cdot\sec\theta$), as a function of total primary energy, E_0, (not E_0/A) for primary proton and iron nuclei initiated showers as predicted by CORSIKA using the indicated particle production models (Antoni et al., 2002). Note the small difference between proton and iron events here. This is because the truncated muon number and not the usual full muon size is being used (cf. Fig. 10.16 where N_μ is used)

and require very different detection methods and techniques. Contrary to particles, these shower agents yield information on the longitudinal development of a shower that particles detected at ground level cannot supply, or at most only in a very diluted and masked form. These topics are only skimmed in this chapter. They are discussed separately in detail in Chaps. 16, 17 and 18, respectively, where we also present the basic mechanisms of the three phenomena, together with related theoretical aspects, including the information that can be extracted from the data. The interested reader is referred to these chapters to study the subjects.

In spite of a roughly 50 year history of activities, the field of radio emission and detection is only now getting out of its infancy. Recent contributions to the field look very promising but it will take some time before radio bursts associated with air showers can be interpreted properly and used for practical applications.

10.3 Primary Mass Estimation

10.3.1 Mass Related Observables

From the scope of problems outlined in the previous sections it is evident that only a realistic simulation of the entire air shower process can possibly reveal reliable primary mass signatures. The reliability depends not only on the type, number, quality and properties of the experimental observables, but just as much on the accuracy and completeness of the entire air shower simulation, in particular on the hadronic interaction model, and very significantly on the kind of analysis. However, many of the fundamental processes and their energy dependence are not well known and make it difficult to decode primary mass signatures from the wealth of experimentally accessible data. An additional complexity arises from the circumstance that the atmospheric target particles are nuclei. Moreover, new processes or new particles, if they should occur in ultrahigh energy collisions, which at present cannot be ruled out completely, could falsify current event interpretations at the highest energies.

10.3.2 Basic Differences Between p and Fe Showers and Kinematically Related Mass Signatures

Early simulations have shown that the high energy portion of the hadron spectrum in air showers exhibits the most marked primary mass signature. This is evident when comparing the hadron spectra of proton and iron initiated showers having the *same total primary energy*. This behavior is illustrated in Fig. 10.13 and is not unexpected since the leading particle effect is well pronounced in nucleon–nucleon and nucleon–nucleus collisions, and even in collisions between nuclei (see Chap. 3 and Grieder, 1977).

The situation is similar when inspecting the high energy portion of the muon spectra of proton and iron nuclei initiated showers of the same total primary energy.

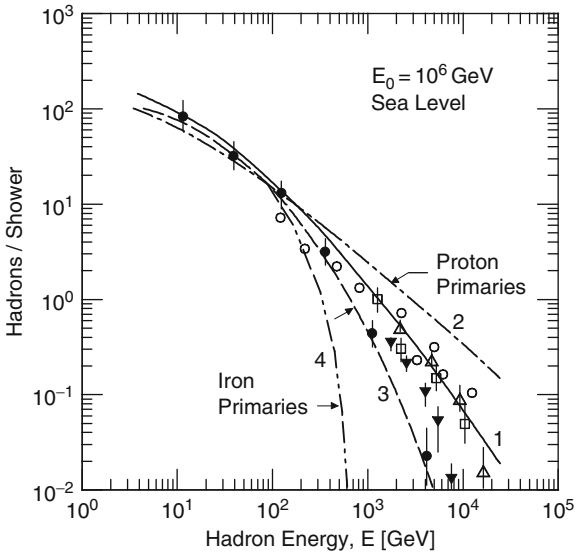

Fig. 10.13 Example of integral energy spectra of hadrons in vertically incident 10^6 GeV primary proton (curves 1–3) and iron nuclei (curve 4) initiated air showers at sea level. Curves 1 and 4 were obtained with the same basic interaction model using the superposition principle for the iron primaries, both for constant cross sections. Curves 2 and 3 are the result of a moderately different model, yielding a slightly lower multiplicity, for fixed and rising cross sections, respectively (after Grieder, 1977). The experimental points are from the work of the following authors: • Tanahashi (1965), ○ Kameda et al. (1965), △ Böhm et al. (1968), ▼ Matano et al. (1970), and □ Baruch et al. (1975)

There, some ultrahigh energy muons are present in proton showers that are lacking in iron showers (Grieder, 1977, 1986; Danilova et al., 1989; Forti et al., 1990). The reason for this behavior is that the energy of a proton–nucleon collision occurring on a light nuclear target is approximately A-times higher than in a nucleus initiated collision per nucleon for the same incident total energy if we consider the simple *superposition model*.

Figure 10.14 illustrates the kinematic aspects of this situation schematically. The figure shows the initial stages of proton and iron initiated showers having total primary energies of 10^5 GeV, plot a, and 10^8 GeV, plot b, respectively. The plots illustrate symbolically in the vertical, which represents altitude, h, the location of the first two interactions, $h_{1,2}$, p and $h_{1,2}$, Fe of the respective showers, where the subscript identifies the generation of interaction.

The interactions are characterized by the *rapidity density* distributions, $\mathrm{d}N/\mathrm{d}y$. The two stacked distributions shown for the iron initiated showers symbolize multiple interactions occurring in the iron-air and heavy iron fragment-air collisions. The zones where the most energetic muon parent pions are likely to originate are marked by the shaded areas. The primary energy dependent rising hadronic cross

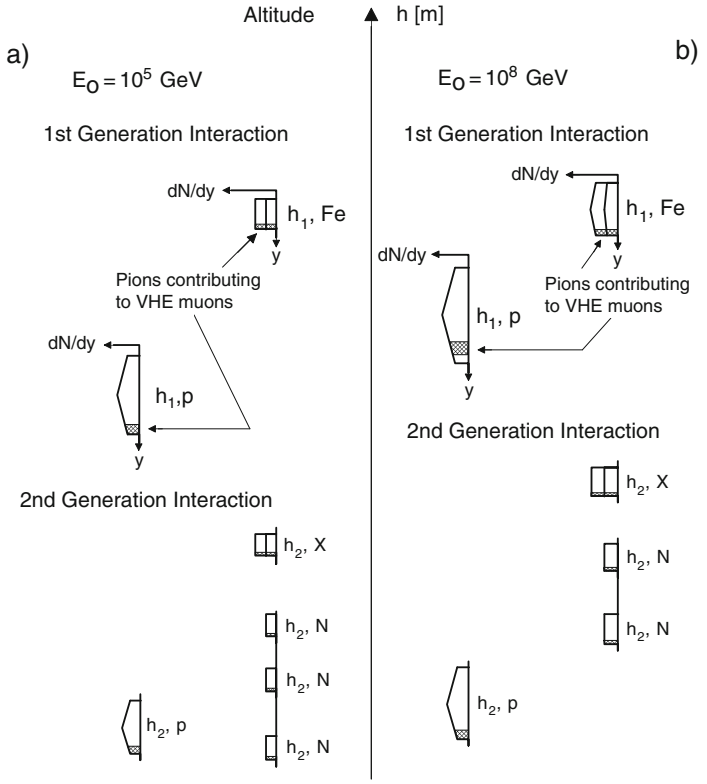

Fig. 10.14 Symbolic representation of the rapidity distributions of secondary particles resulting from the first and second generation proton and iron initiated collisions in the atmosphere, for two different primary energies, figures a and b, respectively. The *dotted areas* represent those regions of rapidity that contribute chiefly to the most energetic muons via normal processes, i.e., via pion and kaon decays. Charmed particles populate the central as well as the fragmentation regions of rapidity. Those from the latter are expected to dominate the production of the most energetic muons in very high energy collisions since pions have an increasing probability to interact rather than decay. The *vertical line* which separates figure **a** from **b** represents the altitude. h_1 and h_2 refer to the heights of the first and second interactions of the primary proton, p, and iron nucleus, Fe, and the heavy fragments, X, and nucleons from fragmented nuclei, N, respectively (after Grieder, 1986)

section effect is also indicated by the higher altitude location of the 10^8 GeV proton initiated shower as compared to the 10^5 GeV companion event.

Consequently, the rapidity range is much larger in the first case (proton primaries), resulting in a number of much higher energy secondaries (pions, kaons and charmed particles) that have no counterpart in the iron initiated shower. Even though the decay probability of these particles is much reduced as compared to the probability for interaction because of their large Lorentz factor, a few will decay and yield ultrahigh energy muons.

This trend slowly reverses with increasing primary energy as the kinematic limit is reached where the probabilities for pion and kaon decay get very small and the

asymptotic muon production rate is reached. There the content of high energy muons in heavy primary initiated showers begins to surpass the production rate in proton showers and becomes dominating. This is illustrated in Figs. 10.15a, b where the contribution from charmed particles is ignored. On the other hand, the total number of muons that includes mainly low energy muons is significantly larger in heavy primary (Fe) initiated showers at all primary energies as compared to proton showers because of the larger number of hadronic interactions.

Note that charmed particles with their extremely short mean life are not affected by this kinematic effect. Charmed particles originating from the forward fragmentation region will keep on contributing a few ultrahigh energy muons beyond the kinematic limit for the production via pions and kaons, whereby the contribution from primary proton initiated collisions yields correspondingly higher energy muons than primary iron interactions under the conditions stated above.

Unfortunately high energy hadron and muon spectroscopy is extremely difficult because the hadrons and muons of interest are within the shower core that contains

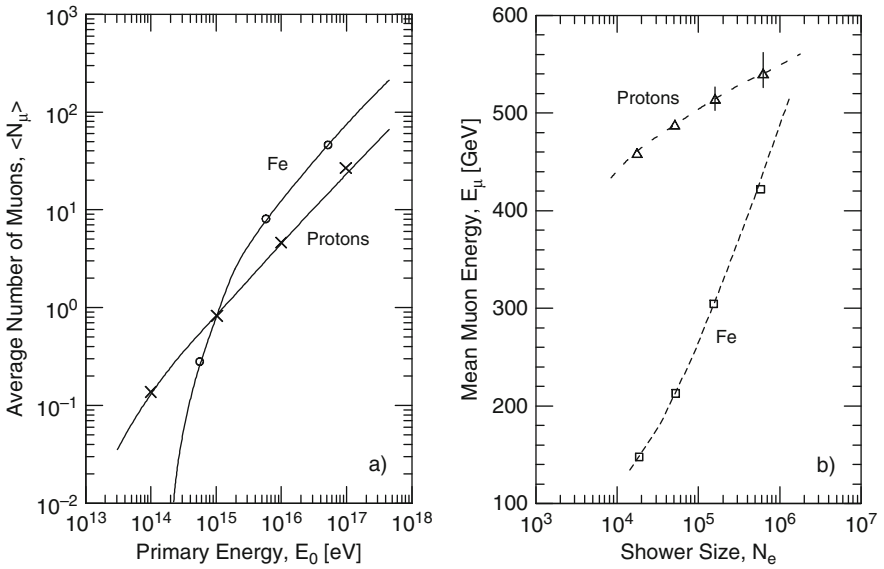

Fig. 10.15 (**a**) Average muon multiplicity in vertical proton and iron nuclei initiated showers at a depth of 4,000 hg cm^{-2} underground ($E_\mu^{\text{top}} > 2.2$ TeV) as a function of primary energy from a simulation of Forti et al. (1990). This work was aimed at the interpretation of muon data obtained with the MACRO detector in combination with surface shower data from the EAS-TOP experiment. (**b**) Predicted mean muon energy at a rock depth of 3,000 m w.e. (LVD experimental level at Gran Sasso Laboratory) as a function of shower size, N_e, at the EAS-TOP level (2,005 m a.s.l.) above LVD for primary proton and iron initiated showers. The data were sampled over a spectral range $10^{14} \leq E_0 \leq 10^{16}$ eV for protons and $2.1 \cdot 10^{14} \leq E_0 \leq 1.4 \cdot 10^{16}$ eV for iron and a differential spectral index of $\gamma = 2.7$ (after Aglietta et al., 1998). These data are the key to primary mass identification using high energy muons in conjunction with surface detector data, as is discussed in Sect. 10.3.4

a high density of very energetic particles of all sorts. One possibility, however, is to combine observables acquired by surface and suitable deep underground experiments, a condition that is fulfilled only at a very few sites. This topic is discussed below. Hadron and muon spectra in showers are discussed in detail in Chaps. 13 and 14, respectively, where data summaries are presented.

10.3.3 Low Energy Muon–Electron Correlation

Air shower simulations clearly show that of the *relatively easily accessible particle observables* the muon to electron number (or size) ratio, N_μ/N_e, is that parameter which exhibits the most significant and reliable primary mass signature (Hillas, 1971a; Grieder, 1977, 1986; Gaisser et al., 1978; Blake and Nash, 1998; Antoni et al., 1999a, b, 2002; Gupta et al., 2003). The general trend is illustrated in Fig. 10.16 which shows the average number of muons, $\langle N_\mu \rangle$, as a function of primary energy, E_0, per particle (not energy per nucleon) for proton and iron initiated showers.

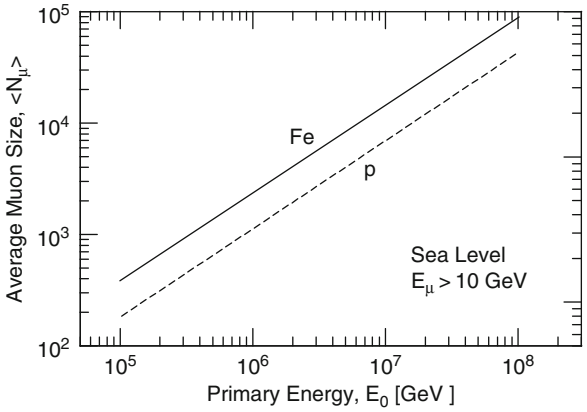

Fig. 10.16 Average number of muons, N_μ, as a function of total primary energy per particle, E_0, (not E_0/A) in proton and iron initiated showers from a calculation by Grieder (1986) using the ASICO program system

The difference between the two extreme primary mass groups (light and heavy) is rather modest as is evident from Fig. 10.16. It is on average about a factor of two to three for low energy muons and depends on the muon energy and on experimental conditions. The latter are influenced by the quality and scope of the muon sampling, and on the muon lateral distribution function from which the muon size (or truncated muon size) is computed. This leads to deviations from the true muon size of the shower and thus individualizes the N_μ/N_e ratio to some degree, making it somewhat array specific. At higher muon energies the ratio appears to increase and around $E_\mu = 200\,\text{GeV}$ it appears to be as high as about four to five (Acharya et al., 1981b).

N_μ/N_e is expected to decrease again at TeV energies where the ratio eventually reverses (cf. Fig. 10.15).

The rather complex behavior of the muon component itself is partly a kinematic effect, manifesting itself also as a function of the primary energy per nucleon (Grieder, 1986). Forti et al. (1990) have studied the properties of high energy muons in showers as a function of primary energy and mass in view of combined surface and deep underground experiments, such as EAS-TOP and MACRO or LVD, discussed later, in an attempt to determine the primary mass.

As stated before, in practice one observes the electron and muon sizes and not directly the primary energy, and both of these observables are subject to large fluctuations. Their interpretation with respect to primary mass is therefore more difficult than can be anticipated from Fig. 10.16 and does not yield a precise answer, and even less so in an event by event analysis unless additional observables are included in the analysis. Thus, the method is far from allowing a clear-cut mass assignment to the shower initiating primary and can at best distinguish between different mass groups, such as light (protons, He), medium (CNO, Al) and heavy (iron) components.

The degree to which fluctuations impede the interpretation of N_μ/N_e data becomes evident when inspecting Fig. 10.17 which is the result of a simulation by Capdevielle et al. (1990). This figure shows contour plots of the density distribution of the loci of the N_μ–N_e data points of individual simulated showers of three sets each of proton and iron initiated showers, belonging to three different primary energy groups, as stated in the caption. Higher level multi-parameter correlations with additional observables improve the sensitivity further but run into conflict with the inadequacies of the hadronic interaction models used in present-day simulations (Ulrich et al., 2005).

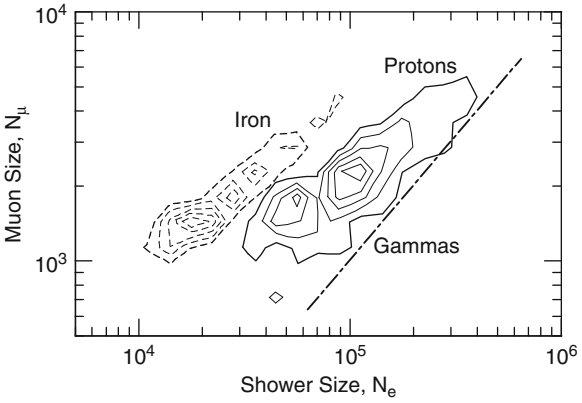

Fig. 10.17 Contours of equal event density of the distribution of the muon number, N_μ ($E_\mu \geq 1$ GeV) versus electron number, N_e, in proton and iron nuclei initiated groups of simulated showers of primary energy $5 \cdot 10^{14}$, 10^{15} and $2 \cdot 10^{15}$ eV. The correlation of the muon number with primary mass is obvious, however, the fluctuations are large, particularly for proton showers. The calculation was carried out with the CORSIKA simulation program package. Also shown is the $N_\mu - N_e$ correlation for gamma ray initiated showers (after Capdevielle et al., 1990)

These problems arise because different high energy interaction models (event generators) yield deviating N_μ/N_e values, though they manifest the same general feature, i.e., heavy primary initiated showers produce more mainly low energy muons and less electrons than showers initiated by light primaries of comparable total energy. This situation is well illustrated in Fig. 10.18 which shows the $N_e - N_\mu^{\mathrm{tr}}$ correlation obtained by Antoni et al. (2002) from an extensive analysis. These authors explored three of the currently popular event generators (QGSJET, VENUS and SIBYLL) using CORSIKA and compare the results with experimental data from the KASCADE experiment.

A similar analysis had been carried out with the EAS-TOP experiment, using the charged particle shower size and the average muon density $\langle \rho_\mu(180) \rangle$ in the distance range from the shower axis of $180 \leq r \leq 210\,\mathrm{m}$ (Aglietta et al., 2004c). The measurements are compared with simulation data for pure primary beams of protons, He, CNO, Mg and Fe nuclei. The results are displayed in Fig. 10.19.

Another interesting primary mass study which is based on an event by event analysis employing the low energy muon to electron ratio was carried out by Antoni et al. (1999b) using data from the KASCADE experiment (Klages et al., 1997) and

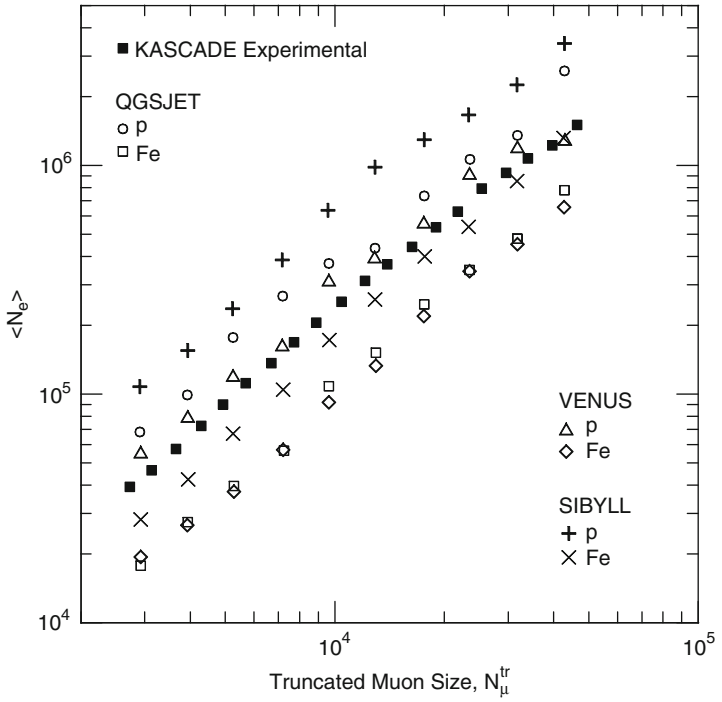

Fig. 10.18 Mean electron shower size, N_e, versus truncated muon shower size, N_μ^{tr}. The *full symbols* (■) are from measurements with the KASCADE array, the other symbols are predictions from simulations for primary protons and iron nuclei initiated showers using CORSIKA and the event generators as indicated in the figure (after Antoni et al., 2002)

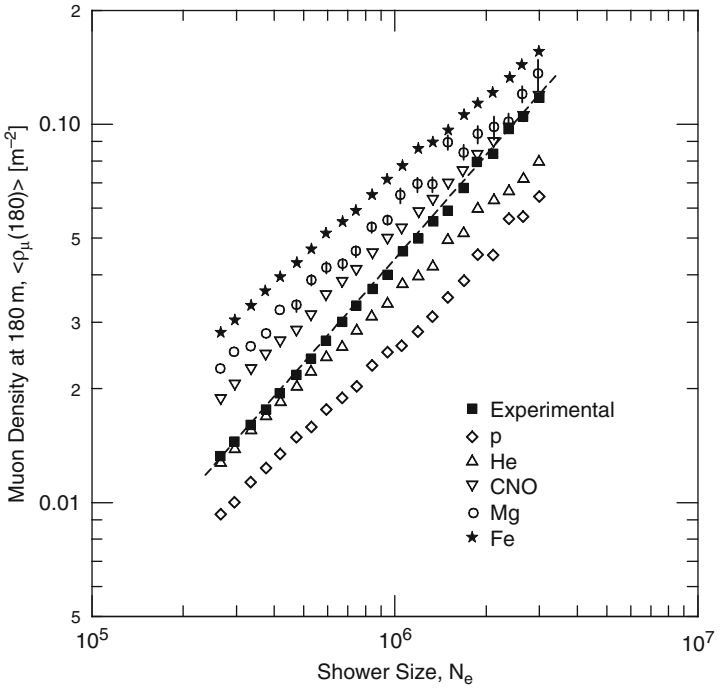

Fig. 10.19 Predicted average muon densities ($E_\mu \geq 1$ GeV) in the radial distance range $180 \leq r \leq 210$ m from the shower axis ($\langle \rho_\mu(180) \rangle$) for vertically incident primaries ($0^\circ \leq \theta \leq 17^\circ$) of distinct mass as indicated, as a function of shower size at EAS-TOP (Aglietta et al., 2004c). The *dashed line* is a hand drawn fit added by the author to help guide the eye

comparing these with appropriate simulation data. Approximately $6 \cdot 10^7$ events were recorded. From these about 580,000 remained after reconstruction, screening and applying the required cuts. The analysis was carried out using 5,000 simulated showers of each of the three considered primary mass groups, light (p, He), medium (O) and heavy (Fe) nuclei, that were generated with different event generators and a spectral slope of E^{-1}. The data were then properly weighted with a slope proportional to $E^{-1.7}$.

For the evaluation a four parameter maximum likelihood fit was applied to the muon–electron ratio distributions for narrow primary energy bins and a restricted zenith angle range. We show in Fig. 10.20a, b the result obtained with the QGSJET event generator for two primary energy bins and in Fig. 10.21 the corresponding fractions of primaries.

An excellent study had been carried out quite recently by the GRAPES group (Tanaka et al., 2007a, b), using the closely packed array at Ootacamund (2,200 m a.s.l.) in southern India (see Fig. A.19) to estimate the primary mass composition in the knee region of the primary spectrum ($10^{15} - 10^{16}$ eV). This array is equipped with the presently largest muon tracking detector system having a threshold of $\geq$1 GeV (Hayashi et al., 1999, 2005; Gupta et al., 2005).

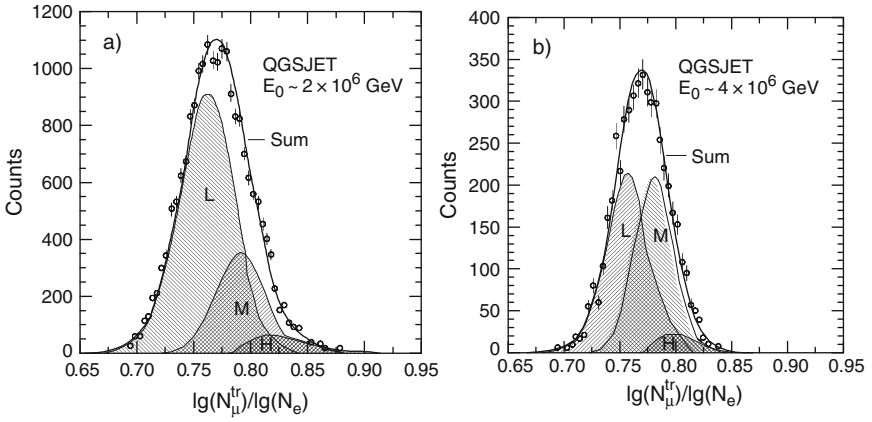

Fig. 10.20 Muon to electron ratio distributions for an energy of $\sim 2 \cdot 10^{15}$ eV (**a**) and $\sim 4 \cdot 10^{15}$ eV (**b**), from an analysis of Antoni et al. (1999b) of data acquired by the KASCADE experiment. L, M and H identify the distributions of light, medium and heavy primaries

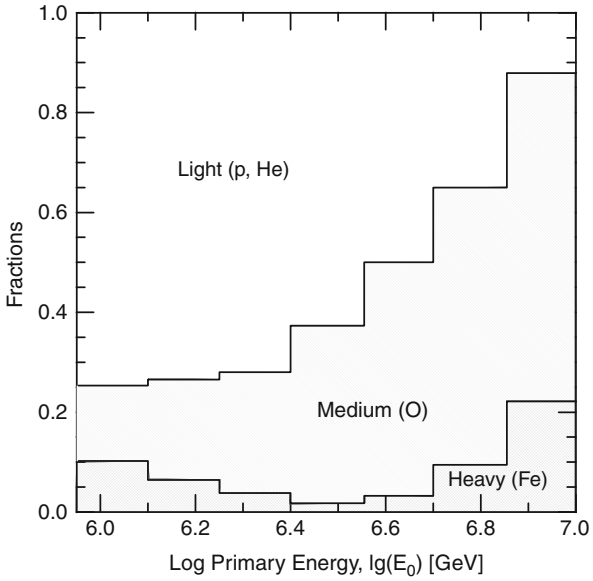

Fig. 10.21 Fraction of the three mass groups as a function of primary energy (after Antoni et al., 1999b)

The analysis is based on two data sets, one includes showers having an electron size $N_e < 1.58 \cdot 10^5$, the other $N_e \geq 1.58 \cdot 10^5$, both for zenith angles $\theta \leq 25^\circ$, with restrictions on the core location for accurate measurements. In addition, the events were classified in subgroups of shower size intervals of 0.2 $\lg(N_e)$. The muon multiplicity distributions of the recorded event classes were determined and

corresponding shower simulations carried out for proton, He, N, Al and Fe initiated showers, using CORSIKA with the SIBYLL and QGSJET event generators. The simulated events were subject to the same selection and classification conditions as the recorded experimental events.

Subsequently the muon multiplicity distributions of the simulated events were fitted to the observed distributions to estimate the abundance of each primary nuclear group in each size bin. For this procedure the ratio Al/Fe was fixed to a value of 0.8, which corresponds to the value established by direct measurements, to avoid an endless loop of trials. Some of the results of this work are plotted in Fig. 10.22a, b for the two shower size groups, $1.6 \cdot 10^4 \leq N_e < 2.5 \cdot 10^4$ and $10^5 \leq N_e < 1.6 \cdot 10^5$ (Tanaka et al., 2007a, b). With data like these from all the shower size intervals, the authors constructed primary energy spectra for the four primary mass groups that are presented in Chap. 11.

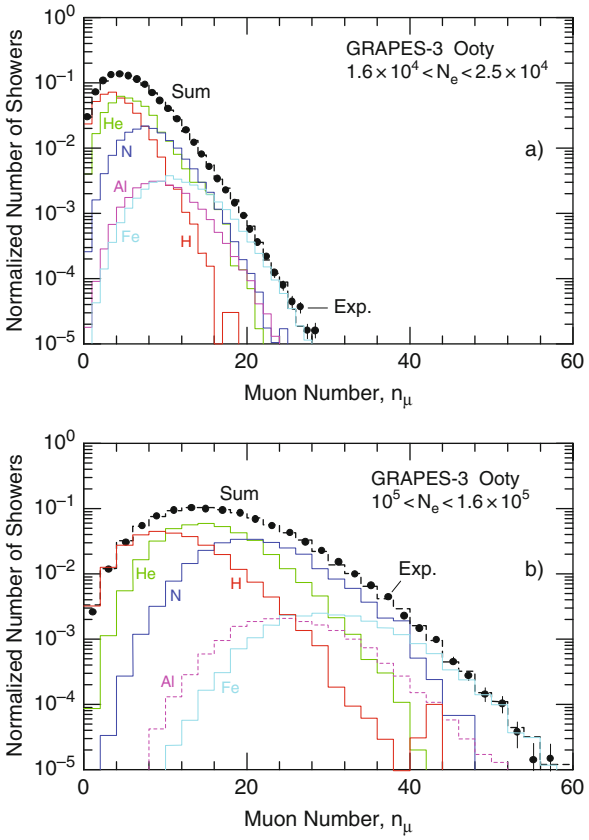

Fig. 10.22 Observed and simulated (SIBYLL-2.1) distributions of multiple muons in two different shower size ranges, figures (**a**) and (**b**), as indicated. The measurements were made with the GRAPES-3 array at Ootacamund (2,200 m a.s.l.) in India (Tanaka et al., 2007a, b)

10.3.4 High Energy Muon, Surface Electron and Atmospheric Cherenkov Photon Correlations

Another approach which had been tackled by several authors with the aim to include additional observables to better corner the problem of mass determination of the primary radiation is to use *simultaneously multiple observables*. An excellent example of this approach is the inclusion of the high energy (TeV) muon component of air showers in the analysis. This endeavor requires the simultaneous availability of a sufficiently sophisticated deep underground detector of sufficient size to achieve an adequate solid angle-area product, ideally located underneath a well equipped surface array.

These conditions were best fulfilled at the Gran Sasso site in Italy with the EAS-TOP air shower experiment at Campo Imperatore (2,005 m a.s.l., 820 g cm^{-2}) (Aglietta et al., 1986) in combination with the MACRO or LVD detector, located in the Gran Sasso deep underground laboratory (altitude 963 m a.s.l.; 930 g cm^{-2}). EAS-TOP and MACRO (both now shut-down) were separated by a rock thickness ranging from 1,100 m (3,100 m w.e.) to 1,300 m, depending on the location within the surface array. The line connecting the centers of the array and the MACRO detector had an inclination with respect to the zenith of 35°. The atmospheric overburden at the EAS-TOP array under this inclination was 930 g cm^{-2} and the corresponding muon threshold energy at the surface to reach MACRO was, $1.3 \leq E_{\mu}^{\mathrm{th}} \leq 1.6$ TeV (Ahlen et al., 1993; Ambrosio et al., 2002), and similarly for the LVD detector (Aglietta et al., 1998; Aglietta et al., 2004b).

Another suitable set of installations for a comparable experiment was the combination of the AMANDA under-ice detector at the South Pole (Andres et al., 2000), the SPASE-2 scintillator array (Dickinson et al., 2000a) and the VULCAN air Cherenkov array at the surface (Dickinson et al., 2000b; Andeen et al., 2007) (see also Swordy et al., 2002). Earlier combined surface-underground experiments that are listed in Sect. 2.8.3 where similar attempts had been made, that are no longer in operation, were too small to yield statistically significant useful results.

The EAS-TOP experiment was equipped with charged particle shower detectors (scintillators), air Cherenkov detectors, and a muon telescope that was combined with a hadron calorimeter. Event selection could in principle be made with any of the detector systems or, to be more stringent, by a combination of criteria. We will discuss here briefly the experiment where the high energy muons detected by MACRO were used as the principal event trigger criterion (Aglietta et al., 2004b; Bertaina et al., 2005).

The primary mass identification hinges on the pion production in the forward fragmentation region of the first interaction and on the energy per nucleon. As an example, a 40 TeV primary proton has a non-negligible probability to produce a muon with a kinetic energy $E_{\mu} \geq 1.5$ TeV that can reach the MACRO detector. Analogously a primary of mass A requires the A-fold energy to attain the same rapidity range to produce muons of comparable energy, and so on for the even heavier masses, up to iron and beyond.

The simulations of Forti et al. (1990) show that primary protons and helium nuclei in the $40 \leq E_0 \leq 100\,\text{TeV}$ range contribute mainly to the ≥ 1 TeV muon group, whereas the CNO-group begins to contribute only at primary energies $E_0 > 100\,\text{TeV}$. This is illustrated in Fig. 10.23.

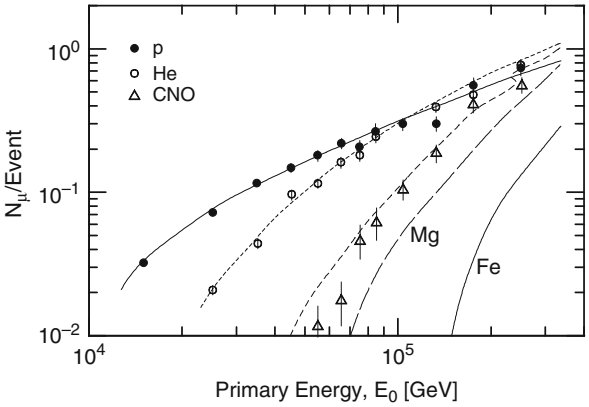

Fig. 10.23 Number of muons per event from proton (•), He (○) and CNO (△) initiated showers reaching the MACRO depth ($E_\mu \geq 1.3\,\text{TeV}$) as a function of primary energy, E_0 (after Aglietta et al., 2004b). The *curves* show the simulation results of Forti et al. (1990) for a muon threshold of $E_\mu^{\text{th}} = 1.6\,\text{TeV}$ ($\theta = 35^\circ$)

Since the Cherenkov photon density at distances $r > 100\,\text{m}$ is a measure of the primary energy, as is explained in Chap. 16, by selecting the primary energy of the shower events according to the conditions outlined above, one selects at a primary energy of $E_0 \simeq 80$ TeV mainly proton and Helium initiated showers, whereas at $E_0 \simeq 250$ TeV p, He and CNO nuclei initiated events.

From the shower rate in conjunction with the applied event selection criteria one gets the intensities of (p+He) and (p+He+CNO) initiated showers. Together with the data of the proton spectrum in the atmosphere obtained from unaccompanied hadron intensity measurements, one can get the relative weights of the proton, He and CNO components in the primary radiation. Details of the procedure to extract the desired information are given in the paper of Aglietta et al. (2004b). The results of this work together with results from many other experiments that employ the various methods outlined in this section are presented in Sect. 11.7 where the primary composition is discussed.

We should also mention that a similar experiment, not discussed here, using the high energy muon data from MACRO and in place of the optical Cherenkov photons the data from the shower particle detectors of the EAS-TOP array to estimate the primary composition, had been carried out by the same authors (Aglietta et al., 2004a).

10.3.5 Primary Mass Sensitivity of Temporal Observables and Shower Front Structure

In this section we will focus only on temporal properties of observables that can be related to the mass of the shower initiating primary and predominantly on rather recent work. General temporal features of air shower particles are discussed at length in Chap. 9 where mass related aspects are only briefly touched in Sects. 9.3.2 and 9.4. Specific temporal properties of distinct shower constituents that are of broader interest are discussed in the chapters that deal with the particular constituents.

It is obvious and had been known for a long time that the arrival time distribution of the shower particles is linked to the longitudinal development of a shower. Many authors have therefore investigated the temporal structure of the particles in the shower disc (or shell) in an attempt to isolate specific properties that can be related to the mass of the shower initiating primary (Rebel et al., 1995; Brancus et al., 1997, 2003; Blake and Nash, 1998; Antoni et al., 2001b, 2003a; Haeusler et al., 2002). Energetic muons are obviously the most likely candidates for this purpose since they originate from charged pions of the first or first few interactions and can propagate relatively freely through the atmosphere to the observer on the ground.[10]

Muons reveal their production height in the atmosphere by the intermediary of the time of flight from the point of creation (or from the location of the interaction where the parent pions are created) to the point of detection at ground level, as illustrated symbolically in Fig. 10.24. For simplicity we consider in this plot a forward pion–muon decay, yielding τ_μ. The reference time, τ_c, is taken as the time of a hypothetical spherical light shell originating at the location of the first interaction in the atmosphere (for details see Chap. 9). It is therefore evident that muons originating from iron primaries that are released at higher altitudes are expected to have smaller delays with respect to the reference light front than muons from proton showers at the same point of impact.

Two factors affect the time required for a muon to reach an observer from the instant of the creation of its parent pion, namely the Lorentz factors of the two particles and the actual geometrical length of the combined trajectories of the pion and muon. The former are linked to the kinematics of the interaction creating the pion and to the subsequent pion–muon decay, the latter depend on the scattering processes that occur along the trajectories (that may of course affect the Lorentz factors, too), including the pion–muon decay. Ionization losses can be ignored in this context as well as rare catastrophic interactions that essentially remove the particles under investigation from the particular energy group.

Detailed studies to investigate the mass dependence of temporal observables in recent years had been carried out by the KASCADE group (Rebel et al., 1995;

[10] Similar arguments and additional mass sensitive features apply also to the optical photons from the Cherenkov light burst caused by air showers that are briefly mentioned below and in Chap. 7, and discussed in detail in Chap. 16.

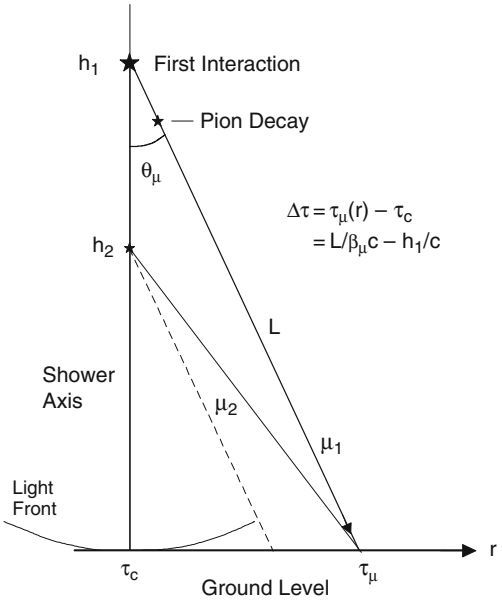

Fig. 10.24 Symbolic pion–muon trajectories emerging from the first interaction of a primary iron and proton in the atmosphere at locations h_1 and h_2, respectively, illustrating the propagation time, τ_μ, and delay, $\Delta\tau$, with respect to the light front reference time, τ_c. Note that the scattering angle, θ_μ is grossly exaggerated

Brancus et al., 1997, 2003; Antoni et al., 2001b, 2003a) using mainly muons of energy $\geq$230 MeV and $\geq$2.4 GeV. These authors have carried out a very detailed analysis, employing *multivariate distributions* and *non-parametric statistical techniques* (Chilingarian, 1989; Chilingarian and Zazian, 1991). We will not discuss the subtle details of the method but summarize the essential results and conclusions that follow from this work.

Figure 10.25 shows some of the basic results that have emanated from the theoretical investigation. Part a of this figure shows the average *global arrival time delay* distributions, $\Delta\tau^{\text{global}}$, of muons of energy $\geq$230 MeV in vertically incident simulated 10^{15} eV primary proton and iron initiated showers at a core distance of $r = 150$ m, and in part b the analogous distributions for a primary energy range of $(3.16 - 5.62) \cdot 10^{17}$ eV and a zenith angle range of $0 \leq \theta \leq 30^\circ$ at a core distance of $r = 310$ m (Brancus et al., 2003). The global arrival time delay is defined in Chap. 9 (see Fig. 9.1) as the time delay of a particle with respect to the shower tangent plane. In other words, for a vertical shower the *global arrival time zero* is the time of impact of the shower axis (core) at the plane of observation (Antoni et al., 2001b).

When considering arrival times of locally detected muons at some core distance, r, one usually refers to global time zero for reference. However, because of fluctuations of the muon multiplicity and other difficulties that arise in the determination

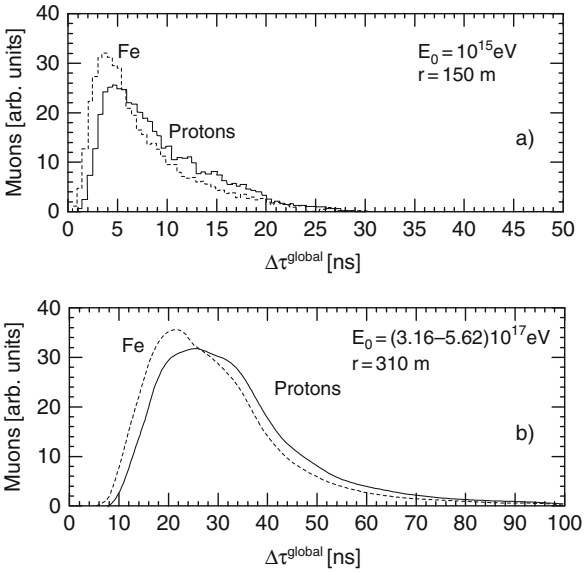

Fig. 10.25 Predicted average global muon arrival time distributions. (**a**) Shows a histogram of the delay distribution obtained for proton and iron initiated showers of primary energy 10^{15} eV at a distance of 150 m from the shower axis, (**b**) the analogous average distributions for the primary energy range $(3.16 - 5.62) \cdot 10^{17}$ eV at a core distance of 310 m (after Brancus et al., 2003)

of the global reference time, τ^{global}, which is fixed by the first particle triggering a detector in the core region, one frequently uses *local time* only instead of global time for reference. This reference time is fixed by the arrival of the foremost locally detected muon. Unfortunately local measurements using local reference times yield only local depth profiles of the shower front and no information of the front curvature.

Inspection of Fig. 10.25 shows that the temporal differences that are observable between proton and iron initiated showers having the same primary energy must be classified as marginal. They can at best be part of a multidimensional analysis where they may be useful to assist in the process of primary mass selection or discrimination.

Brancus et al. (2003) and Antoni et al. (2003a) have carried out event by event analyses of local time profiles. Such measurements are subject to muon multiplicity fluctuations. The individual arrival time distributions were characterized by the mean value of the delays, $\Delta\tau_{\text{mean}}$, and by various so-called *quantiles*, $\Delta\tau_q$, like the median, $\Delta\tau_{0.5}$, the first *quartile*, $\Delta\tau_{0.25}$, and the third quartile, $\Delta\tau_{0.75}$, in their attempt to extract useful information from different portions of the delay distributions (Brancus et al., 1999; Antoni et al., 2001b). Figure 10.26 shows some of the results of this work that confirm earlier results and show that iron initiated showers produce a faster rising, more compact muon burst.

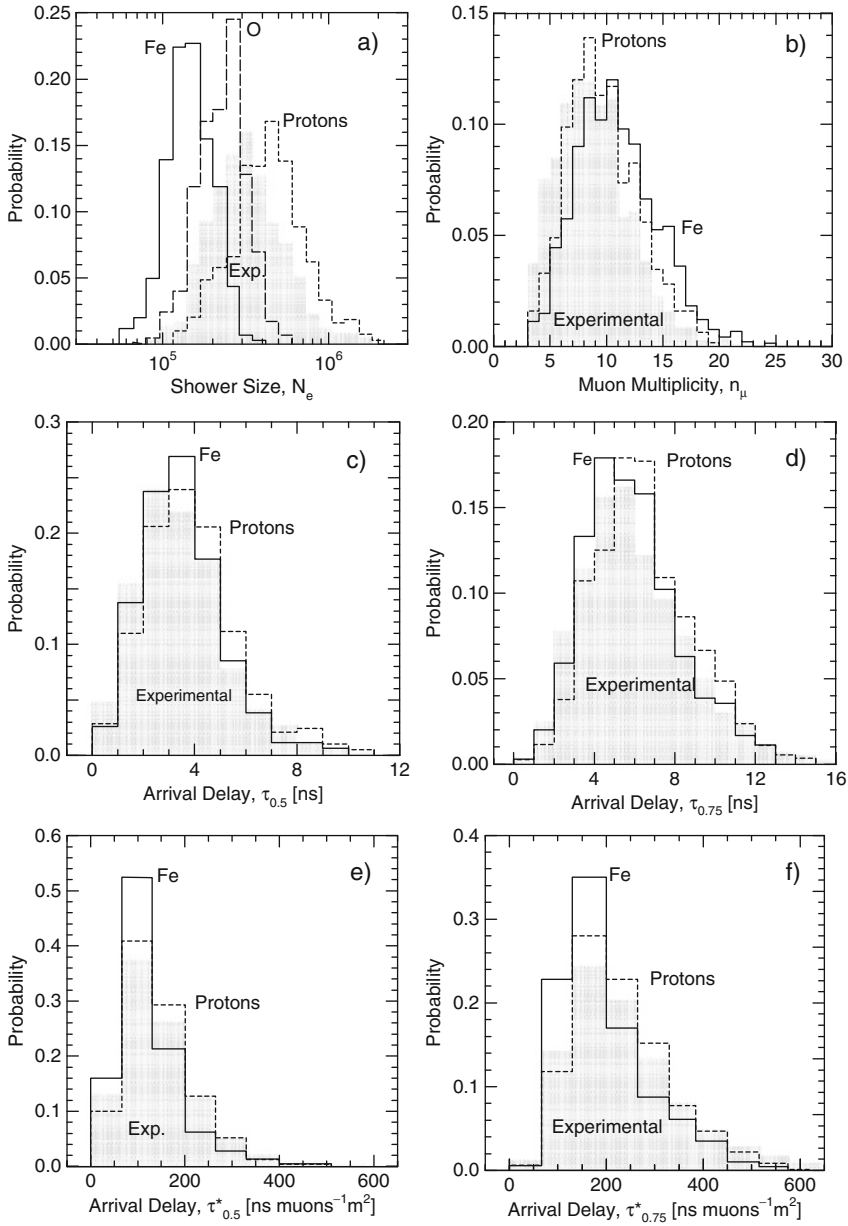

Fig. 10.26 Probability (frequency) distributions of various observables within the radial range of $80 \le r \le 90\,\mathrm{m}$ from the axis in simulated showers having truncated muon sizes in the range $10^4 \le N_\mu^{\mathrm{tr}} \le 2 \cdot 10^4$ and zenith angles $0 \le \theta \le 24^\circ$, initiated by different primaries as indicated, and experimental distributions for comparison. Plot (**a**) shows the corresponding electron size, (**b**) the muon multiplicity, (**c**) and (**d**) the local arrival delay and (**e**) and (**f**) the so-called reduced local arrival delay distributions of muons of energy $E_\mu \ge 2.4\,\mathrm{GeV}$ ($\Delta\tau_q^* = \Delta\tau_q/\rho_\mu$, where ρ_μ is the local muon density) (after Antoni et al., 2003a; for details see text)

From their extensive analysis these authors arrive at the following conclusions. The local time observables as studied here over a limited lateral range ($r < 100\,\mathrm{m}$) offer only a marginal contribution to primary mass identification or mass discrimination. This statement does not apply to global muon arrival time distributions, i.e., to distributions expressed with respect to the arrival time of the shower core. Such measurements include the effects of the shower front curvature and manifest an enhancement of the mass discrimination at larger core distances and higher primary energies (Rebel et al., 1995; Antoni et al., 2003a). This point, however, should not be overstressed, though a potential for improving the primary mass discrimination exists but it is far inferior compared to the muon–electron correlation.

10.3.6 Additional Primary Mass Related Observables

The *height of the first interaction*, h_1, discussed more extensively in Sect. 10.5, which depends on the mass of the primary via the inelastic hadronic cross section, would be a useful mass identifier, but it is essentially inaccessible to measurement and subject to very large fluctuations.

Another, more tangible primary mass sensitive observable is the *depth of maximum development*, $X_{\max}$, (or the corresponding *height of maximum development*, $h_{\max}$) of a shower in the atmosphere, and the *elongation rate*, ER. The latter is derived from the variation of the shower maximum with primary energy, since $X_{\max}$ is a function of primary energy, but also of primary mass. In addition, for theoretical considerations $X_{\max}$ is interaction model and parameter dependent and one must keep in mind that the inelastic hadronic cross sections, $\sigma_{\mathrm{inel}}^{A,\mathrm{air}}(E)$, $\sigma_{\mathrm{inel}}^{\pi,\mathrm{air}}(E)$, etc., too, are slowly increasing with energy, most likely with the square of the logarithm of the energy (Block, 2006), and affect the shower development and subsequently the interpretation of experimental data. Both, the depth of maximum development and the elongation rate of a shower are discussed in detail in Chap. 7. They are difficult to determine on the basis of ground level particle measurements. Air Cherenkov and fluorescence measurements offer a more direct access to $X_{\max}$.

Related to the depth of the shower maximum are the *equal intensity distributions*. An interesting study was carried out by Ogio et al. (2004) in this context. These authors studied the dependence of the equal intensity distributions on primary mass. This subject was briefly touched in Sect. 6.7 where experimental equal intensity distributions recorded by these authors at Mt. Chacaltaya (5,230 m a.s.l.) had been compared with simulated distributions for different primaries and primary mass mixes (cf. Figs. 6.45 and 6.46). By fitting sets of simulated showers initiated by different primaries to experimental equal intensity distributions one can obtain a best fit primary mass mix for different primary energy intervals and thus get an estimate of the composition and its energy dependence. The results obtained by Ogio et al. (2004) are presented in Fig. 10.27.

Simulations have revealed that *optical atmospheric Cherenkov emission* of showers offers a better, more direct possibility to determine the location of the shower

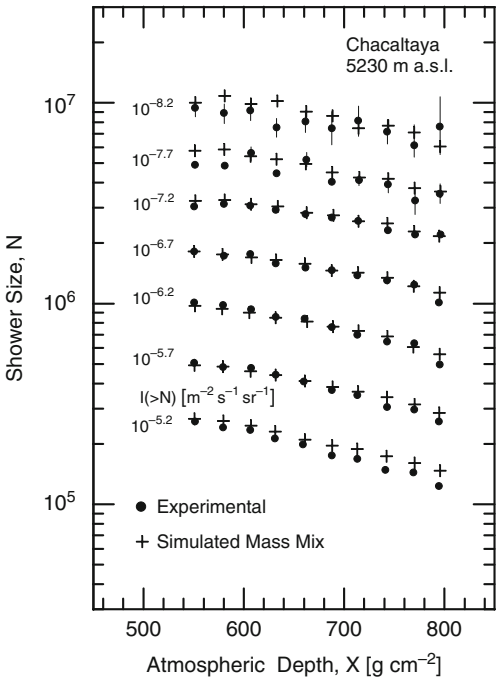

Fig. 10.27 Experimentally determined equal intensity distributions for fixed integral intensity $I(> N)$ [m^{-2} s^{-1} sr^{-1}] as indicated (•), recorded at Mt. Chacaltaya, compared with simulation data consisting of a primary mass mix as listed in Table 11.4, to optimize a fit with the experimental distribution. The simulation was carried out with the CORSIKA program using the QGSJET event generator (after Ogio et al., 2004)

maximum than particle measurements and is therefore a useful approach to derive the primary mass. But the poor duty factor of optical detection and the fact that the shower must point at the array make this approach rather unattractive. Nevertheless, many air Cherenkov experiments had been carried out in recent years such as BLANCA (Fowler et al., 2001) and DICE (Boothby et al., 1997) in Utah, SAS at Chacaltaya (Shirasaki et al., 1997; Ogio et al., 2004), Tunka in Russia (Gress et al., 1997) and others. Details concerning this method are discussed in Chap. 16 which treats atmospheric Cherenkov emission and detection of showers. Results related to the longitudinal shower development are discussed in Chap. 7, and implications for the primary radiation are presented in Chap. 11.

Finally, *air fluorescence* is the most promising method because the shower maximum can be determined usually unambiguously and directly. Furthermore, the longitudinal development can be inspected over a major portion of the shower trajectory.[11] This ability reduces the ambiguities and uncertainties that are typical

[11] For fluorescence detection the shower axis should not strike too close to the detector to avoid an interfering contribution of Cherenkov light.

for conclusions drawn from measurements with particle detectors at ground level. All aspects of fluorescence generation, detection and interpretation are discussed in Chap. 17. The method is subject to the same duty factor limitations as the optical Cherenkov detection method.

The data on the primary mass composition and its energy dependence that are currently available from air shower experiments reflect clearly the difficulties and limitations we are presently facing. On one side we have the problem to extract an initial parameter from a cascade process ten or twelve generations of interactions downstream from local cascade products. In view of the many complex processes that are involved in the entire shower process in which the initiating agent is modified significantly in the first few interactions, unless it is a proton or a gamma ray, it is evident that its signature is heavily masked when arriving at the observation level.

On the other hand the problem of mass identification is further impeded by the fact that we do not have adequate knowledge of the hadronic mechanisms at the highest energies to make precise predictions. The diverging and sometimes contradictory results that we get from refined multi-parameter correlation analyses of data from the different experiments in our attempt to untangle the primary mass composition puzzle are at least partly the consequence of the inadequacy of our contemporary models.

Moreover, we deal with stochastic processes that are subject to very large fluctuations. These facts set definite limits to the interpretation of ground level observables and it is evident that contrary to atmospheric Cherenkov and fluorescence experiments, particle experiments aimed at the extraction of primary mass or high energy interaction parameters yield more reliable data when carried out at high altitude.

Section 11.7 is dedicated to primary mass composition and its energy dependence. There we present results obtained by the many experiments that employ the different methods and principles that we have outlined here.

Correlation studies concerning all relevant observables that play a key role to disentangle the primary mass puzzle and other delicate aspects of high energy interactions and air shower phenomena are summarized in Chap. 19. This chapter offers complementary information and includes numerous experimental data.

10.4 Shower Age

10.4.1 Introduction

The *common age parameter*, s, is a measure of the degree of shower development of pure electromagnetic cascades, i.e., of showers that are initiated by a photon or an electron. It is related to the growth and decline of the number of particles in a shower and to the energy spectrum of the photons and electrons. The age parameter grew out of the electromagnetic cascade theory that was developed by Rossi and Greisen (1941), and Kamata and Nishimura (1958, 1960), and is summarized in Chap. 4 (see also Nishimura, 1967).

Since the overwhelming number of particles ($\simeq$90%) in common primary hadron initiated showers consists of electrons (positrons and negatrons) and photons, the age parameter is used as a convenient observable to describe the showers as if they were pure electromagnetic events. For many considerations and analyses this is fully adequate. However, as will be evident from more detailed studies discussed below and in other chapters, the age parameter must be treated in a more subtle way in a number of cases because of the parent hadron cascade from which the electromagnetic component originates. In addition in very inclined and/or very large showers the age parameter may vary over larger radial distances and can exhibit an azimuthal dependence, as is explained in Sect. 8.7. In Eq. (4.155), Sect. 4.7.1, the relation for s is written in its most simple form for the one-dimensional case in approximation B.

As briefly described in Sect. 2.10.3, the age parameter of an experimentally observed shower, s, is obtained by fitting the measured *lateral* particle density distribution function (LDF) to a standard Nishimura-Kamata-Greisen (NKG) function (Eq. (4.144), Sect. 4.6.11) by minimizing χ^2.

10.4.2 Experimental Facts and Theoretical Aspects

Many measurements and investigations have shown that the situation is in fact more complex than suggested by the pure electromagnetic cascade theory. In particular, it appears that one must distinguish under certain circumstances between the lateral or transverse (perpendicular) and the longitudinal (parallel) age parameters, s_{lat} (or $s_{\perp}$) and s_{long} (or $s_{\parallel}$), respectively.

Dedenko et al. (1975) have shown that, within the framework of their calculations that are based on a CKP plus isobar model for the hadronic interactions, which yields a so-called quarter-law multiplicity of secondaries, the two age parameters of the associated electromagnetic shower obtained with the NKG formula for some age parameter s_{lat} and Molière radius r_{M} have the same value, i.e., $s_{\mathrm{long}} = s_{\mathrm{lat}}$, at atmospheric depths $X \geq 200\,\mathrm{g\,cm^{-2}}$, over the investigated primary energy range from 10^{14} to 10^{16} eV.

There is no direct way to measure s_{long} in air showers except, in principle, by the fluorescence method, but it is experimentally possible to evaluate whether $s_{\mathrm{long}} \leq 1$ or $s_{\mathrm{long}} \geq 1$ using the correlation of the shower intensities at different zenith angles, θ. From their work at the Tien Shan site (3,340 m a.s.l.), Dedenko et al. (1975) find the following ratio for the intensities, $I(N, \theta)$, of showers in the size range $10^5 < N < 10^6$ incident under a zenith angle of $\theta < 30^\circ$ and $\theta > 30^\circ$, respectively,

$$\frac{I(> N, \theta < 30^\circ)}{I(> N, \theta > 30^\circ)} \sim 2 \ . \tag{10.15}$$

The authors therefore conclude that the showers are beyond their maximum development and, hence, the experimentally determined value of the longitudinal age parameter must be $s_{\mathrm{long}} > 1$. Since the experimentally determined value of $s_{\mathrm{lat}} \approx 0.85$, it follows that $s_{\mathrm{long}} \neq s_{\mathrm{lat}}$, as predicted theoretically. Moreover, from the

relation of Eq. (10.15) it is conceivable that s_{lat} does not directly reflect the actual age of a shower but is simply a parameter.

Comparing their theoretical results with lateral age parameter values from actual measurements made over a wide range of atmospheric depths (Fig. 10.28), these authors find the following empirical relationship,

$$s_{\mathrm{long}} = s_{\mathrm{lat}} + \Delta s \quad , \tag{10.16}$$

where $\Delta s \approx 0.15 - 0.20$ (Dedenko et al., 1979). The authors point out that the calculations for this analysis were made for proton initiated vertical showers and constant primary energy. For showers of fixed size the resulting s_{long} would be smaller, and vice versa for a spectrum of primary masses and a range of zenith angles. In addition, lower multiplicity models, such as a scaling model, lead to smaller values of s_{long}. By substituting the Molière radius r_{M} by kr_{M} in the NKG formula with the coefficient $k = 0.6$, the two age parameters can be brought to equality.

An interesting effect was noticed by Chudakov et al. (1979), who observed that for about half of all the showers of size $\geq 2 \cdot 10^5$ recorded at the Baksan site (1,700 m a.s.l.), the *common shower age* determined from density measurements made close to the shower core ($1.0 \leq r \leq 15$ m), s_1, is different from that derived from density samples collected over a more distant annular region of the same event ($6.0 \leq r \leq 45$ m), s_2. Moreover, the correlation between the two age values, shown in Fig. 10.29, was found to be rather small. More than 50% of the events shown in

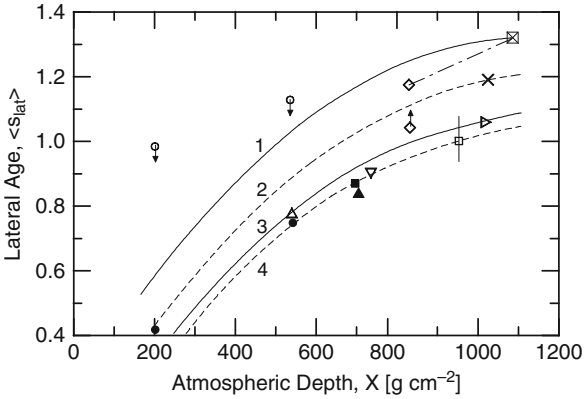

Fig. 10.28 Atmospheric depth dependence of the lateral age parameter, s_{lat}. The data points are a compilation from different experiments and the curves are from a calculation of Dedenko et al. (1975). Included are showers having a primary energy of approximately 10^{15} eV. Curves 1–4 are from model calculations of Dedenko et al. (1975); curves 2, 3 and 4 are normalized to the experimental data of Vernov et al. (1968), Aguirre et al. (1977), and Aseikin et al. (1977), respectively. The experimental points are: ○ Antonov et al. (1973); ● Antonov et al. (1973), data readjusted by Stamenov and Ushev (1977), taking into account the fact that the longitudinal age parameter, s_{long}, differs from the lateral age parameter, s_{lat}, in a shower. ▲ and △ Aguirre et al. (1977); ■ and □ Aseikin et al. (1977); ⊠ and ◇ Alexeyev et al. (1977); ▽ Miyake et al. (1977); ▷ Sakuyama and Suzuki (1977), and × Vernov et al. (1968) (after Dedenko et al., 1979)

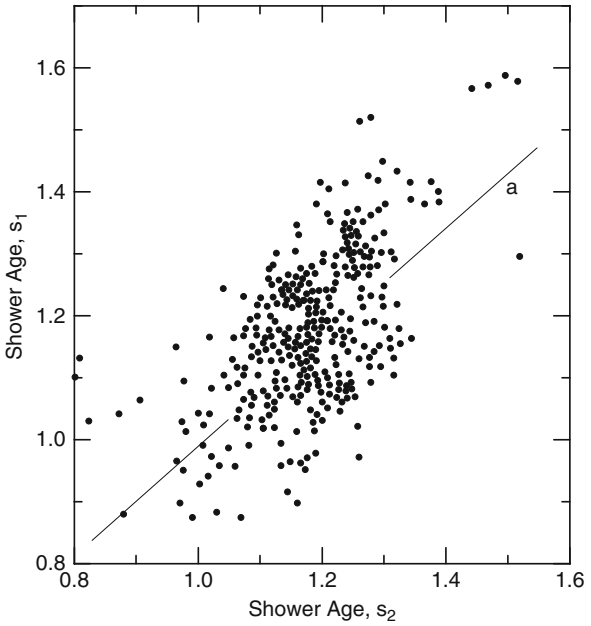

Fig. 10.29 Scatter plot of two independent age determinations, s_1 and s_2, of showers of size $\geq 2{\cdot}10^5$ recorded at Baksan (North Caucasus, Russia, 1,700 m a.s.l.; 820 g cm^{-2}) (Chudakov et al., 1979). s_1 had been determined at a distance between 1 and 15 m, s_2 between 6 and 45 m from the shower axis. The small correlation coefficient of 0.62 between s_1 and s_2 is not due to experimental inaccuracies, but is attributed to truly different shower structures. More than 50% of the events are lying outside the limits of $\pm 2\sigma$ of the *straight line* labeled *a*, corresponding to $s_1 = s_2$. Figure 10.30 is the companion figure showing the lateral structures needed to explain the experimental scatter plot shown here

this figure are lying outside the $\pm 2\sigma$ limit of the $s_1 = s_2$ line. For that particular half of all the observed showers the measured LDF could not be described by an NKG function, though the mean LDF of all showers could be well fitted to a single NKG function.[12]

For 35% of the particular events s_1 is larger than s_2 ($s_1 \geq s_2$) and these show a remarkable flattening in the central region that is ascribed to effects due to the parent nuclear cascade of the showers. On the other hand it was found that for about 15% of the select group s_1 is less than s_2 ($s_1 \leq s_2$), implying that the LDF is steeper near the axis than at larger distances as compared to a standard shower. This situation is illustrated in Fig. 10.30 where two examples are shown. The plots show that the data points of each of the two separate showers can be well fitted with *two different NKG functions* each, having different s-values.

[12] This effect was also noticed by other authors.

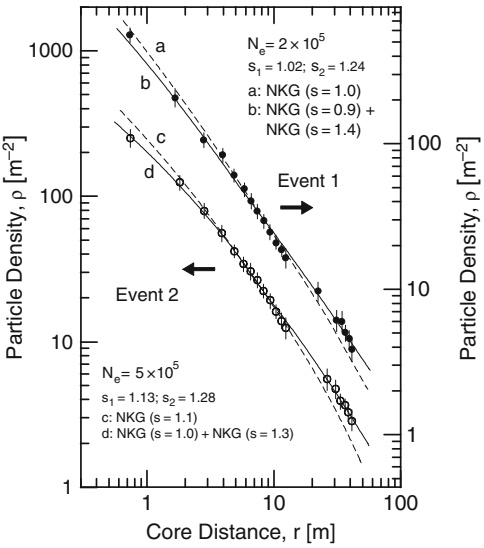

Fig. 10.30 Lateral density distribution of shower particles in two showers, • and ○, having a lateral structure that can only be fitted with two superimposed NKG functions having different age parameters, s_1 and s_2 (Chudakov et al., 1979). About 15% of all showers observed at Baksan have $s_1 < s_2$. These show a significantly steeper distribution near the core. Showers with $s_1 > s_2$ account for about 35% and exhibit a rather flat distribution near the core. The *dashed curves*, *a* and *c*, represent fits to the experimental data with a single NKG function whereas the *solid curves*, *b* and *d*, consist of two functions with different s, as indicated. Note the different scales on the left and right hand sides of the plot, applying to the lower and upper data sets, respectively

If one assumes that the shower consists of two sub-cascades, each contributing one half of the total shower size, one can compute the respective heights of origin, h_{orig}. Under approximation B of the cascade theory the corresponding heights can be obtained from Eq. (4.155), repeated here for convenience,

$$s = \frac{3t}{t + 2\ln(E_0/E_{\text{crit}})} \quad . \tag{10.17}$$

Here, t is the atmospheric depth expressed in units of radiation length. Following Chudakov et al. (1979) one obtains for the first event of Fig. 10.30 for the two sub-showers initiation heights of $h_{\text{orig},1} = 8.5\,\text{km}$ and $h_{\text{orig},2} = 24\,\text{km}$, and for the second event for $h_{\text{orig},1} = 6.5\,\text{km}$ and $h_{\text{orig},2} = 30\,\text{km}$, respectively. The extraction of such details from individual shower measurements is indeed remarkable.

In the following we present a summary of age parameter data from a variety of measurements carried out across the atmosphere, from airplane and mountain altitudes down to sea level, on showers of widely different sizes.

10.4.3 Age Parameter Determination, Data and Implications

In their pioneering work, Antonov and collaborators have carried out a series of air shower measurements with a small array installed on board of a large aircraft (Antonov et al., 1979) (for the layout see Fig. A.4). They have determined the age parameter distribution and the average ages for different radial regions around the shower axis at different altitudes. The data are summarized in Fig. 10.31 which shows the average age of showers of different size groups at different atmospheric depths. The unusual behavior of some of the data shown in this figure is difficult to explain; it could be due to core location errors. Also shown are a selection of data from several ground based experiments that are located at various altitudes, as indicated, for comparison.

The two curves that are plotted in this figure show predictions from the theoretical work of Kalmykov et al. (1975) that were obtained for two different shower models, one a highly dissipative, the other a more conservative model that is based

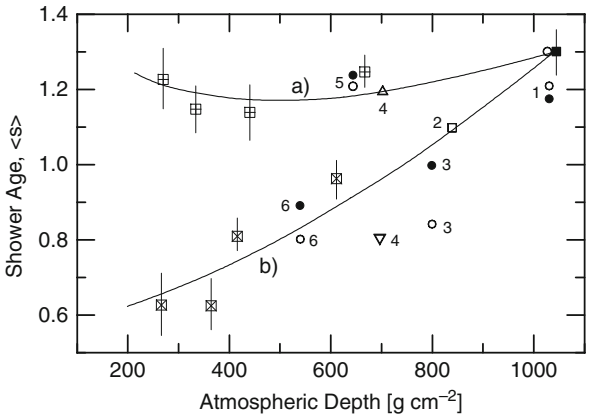

Fig. 10.31 Average age, $\langle s \rangle$, of showers of different size groups versus atmospheric depth (Antonov et al. 1979). The data are grouped into different radial intervals over which particle densities were recorded. The data of Antonov et al. (1977, 1979) cover the full range of atmospheric depth, from sea level to 11.8 km with the same instrument and installation. The *solid lines* (*a*) and (*b*) represent theoretical results from the work of Kalmykov et al. (1975). Both are for $1 < r < 10$ m. (*a*) is for a highly dissipative model, (*b*) for one adapted to extrapolated accelerator data. Evidently (*a*) is a much better fit to points ⊞ than (*b*). Consequently, the authors (Antonov et al. 1979) conclude that two NKG functions are needed to describe the lateral distribution of shower particles in the range $1 \le r \le 100$ m. Additional data from other authors as listed below are included for comparison. ⊞, $r \le 15$ m; $3 \cdot 10^5 \le N \le 10^6$ (Antonov et al., 1979); ⊠, $20 \le r \le 50$ m; $7 \cdot 10^5 \le N \le 2 \cdot 10^6$ (Antonov et al., 1979); ■, overlapping point for both distance intervals, ⊞ and ⊠, at sea level (Antonov et al., 1977, 1979); △, $r \le 10$ m; $2 \cdot 10^5 \le N \le 3.7 \cdot 10^5$ (Aseikin et al., 1976); ▽, $20 \le r \le 80$ m; $2.6 \cdot 10^5 \le N \le 2 \cdot 10^6$ (Aseikin et al., 1976); □, $3 \le r \le 40$ m; $N \ge 2 \cdot 10^5$ (Alexeyev et al., 1977); •, Various data with $N \simeq 10^5$ as identified by number below; ○, Various data with $N \simeq 10^6$ as identified by number below; (1) Agassiz (USA), Moscow (Russia); (2) Baksan (Caucasus, Russia); (3) Ootacamund (India); (4) Tien Shan (Kazakhstan); (5) Pamir (Tajikistan); (6) Chacaltaya (Bolivia)

on extrapolations from accelerator data. Similar but balloon borne experiments by Antanov and collaborators are discussed in Chaps. 6 and 7, in connection with the longitudinal development of the showers.

A more refined analysis of the earlier data of Antonov et al. (1973) was carried out by Stamenov and Ushev (1977). These authors introduced a variety of corrections for systematic distortions caused by the airborne experimental arrangement and conclude that the average age parameter, $\langle s \rangle$, of the showers were overestimated in previous papers by a value of about 0.43–0.48.

Of particular interest are the shower age data obtained by Kaneko et al. (1975) with the Mt. Chacaltaya array (5,230 m a.s.l., 550 g cm^{-2}) because there large vertical showers are expected to be near their maximum development ($s \simeq 1.0$) or possibly still growing (young showers, $s < 1.0$) at that altitude. The layout of the old Chacaltaya array[13] that was used for this study is displayed in Fig. A.11. The data of Kaneko et al. are presented in Fig. 10.32. Shown are five sets of data that apply to five different zenith angle intervals, covering the range from $1.0 \leq \sec\theta \leq 2.0$, in steps of 0.2, corresponding to an angular range of $0^\circ \leq \theta \leq 60^\circ$. Included are showers of size $10^7 \leq N \leq 7 \cdot 10^9$.

The analysis of Miyake et al. (1971, 1973) carried out with early data from Mt. Norikura in Japan (2,770 m a.s.l.), illustrated in Fig. 10.33, shows very clearly the general trend over the mid-range of shower sizes that is also expected on theoretical grounds, namely that the average age, $\langle s \rangle$, of the showers decreases with increasing shower size or primary energy at a given observation level, i.e., at a fixed atmospheric depth. This is well understood because the location of the shower maximum moves to greater depth with increasing primary energy. Consequently the showers get *younger*.

The later data set from the same experimental site but acquired with a modified layout of the 100 detector array (see Fig. A.25) that is plotted in the same figure shows the same trend but most of the data points lay about 0.2 $\langle s \rangle$-units lower (Miyake et al., 1977, 1979). This difference is due to a re-normalization of the data, as is pointed out by the authors in the 1977 paper.

The trend reversal of the data shown in Fig. 10.33 beyond a size of $\sim 10^7$, where the showers appear to get *older*, can be understood in terms of a change in the primary composition, the latter getting heavier with increasing shower size. In comparison to proton initiated showers, higher primary masses at the same total primary energy result in a lower energy per nucleon. Because of the larger inelastic cross section of heavy primaries the height of the first interaction in the atmosphere increases and the shower maximum occurs at greater height. In addition, the secondary particle multiplicity of the first interaction increases, too, even though the energy per nucleon is now A-times lower, because we now deal with nucleus–nucleus interactions. All these factors cause the shower age at a given observation level in the

[13] More recent Chacaltaya array layouts are described by Shirasaki et al. (2001); Ogio et al. (2004) and Furuhata et al. (2005).

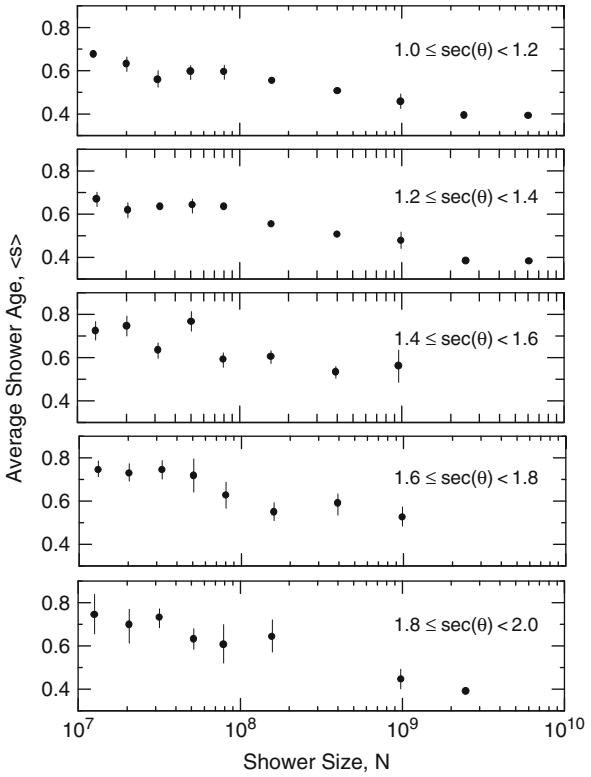

Fig. 10.32 Average age, $\langle s \rangle$, versus shower size for showers of size $10^7 \leq N \leq 10^9$ and different zenith angle intervals. The data are from Mt. Chacaltaya (5,230 m a.s.l.) (Kaneko et al., 1975)

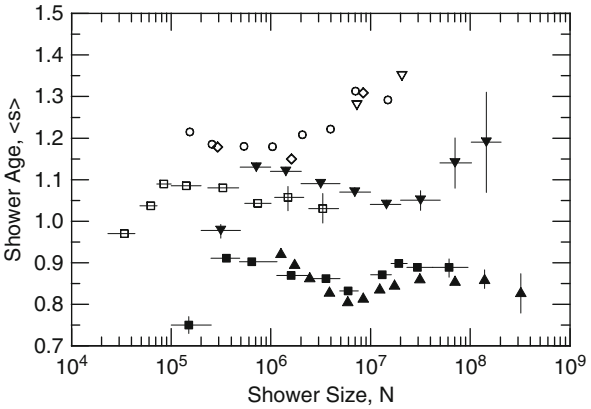

Fig. 10.33 Compilation of average age parameters, $\langle s \rangle$, as a function of shower size, N, determined at Mt. Norikura, 2,770 m a.s.l. (*full symbols*): ▼ Miyake et al. (1971, 1973); ■ Miyake et al. (1977) and ▲ Miyake et al., (1979), both re-normalized. Also included are the following sea level data for comparison (*open symbols*): ◇ Abdullah et al. (1981); □ Sakuyama and Suzuki (1977); ▽ Khristiansen et al. (1971, 1973, 1980), and ○ Vernov et al. (1970)

deeper atmosphere to increase in comparison to proton initiated showers of the same total energy and can thus explain the observed behavior of the average shower age.

At a size of about $5 \cdot 10^7$ the trend of the more recent data of Miyake et al. (1977, 1979) reverses again and the showers appear to get *younger* with increasing size, suggesting that the compositional change has ceased or possibly even reversed. The older data set discussed earlier exhibits a similar trend but the $\langle s \rangle$-distribution depicted by the corresponding data points in the plot is shifted to the right, i.e., towards higher shower sizes, and the falling trend beyond a shower size of $\sim 10^8$ exhibited by the newer data set is not observed.

The sharp dip toward low values of $\langle s \rangle$ for very small size showers that exhibit the opposite trend (decreasing age with decreasing shower size) is probably due to a combination of two effects. One is ascribed to large fluctuations that are typical for low energy showers because of the low secondary particle multiplicity in the first interaction. Events with low multiplicities have fewer but more energetic secondaries, and vice versa for events with a high multiplicity. Therefore, showers with high multiplicities in the first interaction are likely to die out or decline to sizes below detection threshold at the array level whereas the former are subject to a retarded development, reach their maximum at greater depth and are likely to be detected as relatively young small size showers.

In addition, the large event rate at low primary energies increases the number of late starters, i.e., events where the primary may skip one or several interaction mean free paths before undergoing the first interaction that initiates the shower, thus faking a more energetic primary. This situation changes rapidly with increasing primary energy because of the rapidly falling event rate, causing the showers to reach the more classical development regime at sizes approaching 10^6 at the Mt. Norikura level. To produce this shower size at that level requires a primary whose energy approaches the neighborhood of the spectral knee.

For reasons of comparison we have added some data sets from sea level measurements to Fig. 10.33 (open symbols) (Abdullah et al., 1981; Sakuyama and Suzuki, 1977; Khristiansen et al., 1971, 1973, 1980; Vernov et al., 1970). These data show a similar behavior except that now the average shower ages have larger values at comparative shower sizes and greater atmospheric depth but larger primary energy, and the average age versus size distribution plots are shifted to the left, i.e., to lower shower sizes. This, too, follows the expected trend, as the shower size of an event of given primary energy has a lower size and higher age at sea level than at higher altitude.

An additional set of data from Mt. Norikura showing the average age as a function of zenith angle for $0^\circ \leq \theta \leq 48^\circ$ ($1.0 \leq \sec\theta \leq 1.5$) is plotted in Fig. 10.34 for showers belonging to the narrow size group $10^7 \leq N \leq 2 \cdot 10^7$. There the expected trend of a rising $\langle s \rangle$ with $\sec\theta$ is well demonstrated.

Shower age distributions from measurements carried out with the array at the Kolar Gold Fields (KGF) site in India (for the array layout see Fig. A.23), located at an altitude of approximately 920 m (920 g cm^{-2}), are shown in Fig. 10.35 for six shower size groups, ranging from $N = 10^4$ to $N = 10^8$ (Acharya et al., 1981a). The previously mentioned trend of the average age variation with shower size is confirmed.

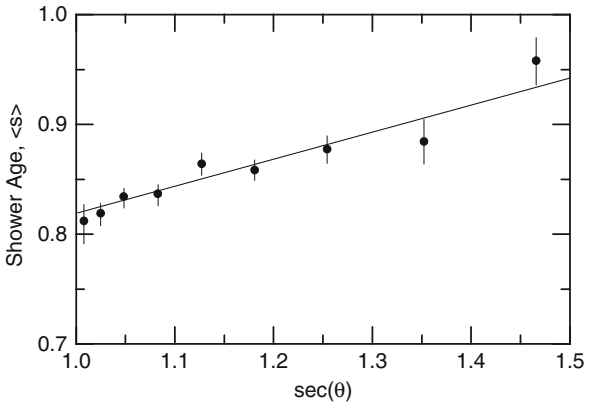

Fig. 10.34 Average age, $\langle s \rangle$, of group of showers belonging to the narrow size interval between 10^7 and $2{\cdot}10^7$ versus sec θ, where θ is the zenith angle. The data were taken at Mt. Norikura (Miyake et al., 1979)

The results from an extensive analysis of shower age data from the Akeno site (900 m a.s.l., 920 g cm^{-2}) in Japan (for the array layout see Fig. A.5) are illustrated in Fig. 10.36a for near vertical showers (Hara et al., 1979b, 1981a). Different conditions had been employed for the evaluation of the measured lateral density distributions, as stated in the figure caption. We have added the data of Acharya et al. (1981a), mentioned before, that were acquired at nearly the same altitude, for comparison. Figure 10.36b shows the standard deviation of the data.

A set of sea level data obtained by Clay et al. (1981) with the Buckland Park array at Adelaide, Australia (for the array layout see Fig. A.9), showing the lateral age parameter as a function of shower size over a relatively narrow size range is shown in Fig. 10.37 for three zenith angle intervals.

Recent data on the shower size dependence of the age parameter from measurements with the MAKET-ANI array located at Mt. Aragats (3,200 m a.s.l.) in Armenia are presented in Fig. 10.38. Shown, too, are results from simulations showing the expected age dependence that would result for a primary beam of pure iron and pure protons, and for the common normal and a rigidity dependent normal composition from the work of Chilingarian et al. (2007).

An interesting plot is shown in Fig. 10.39 where the shower age is plotted as a function of the muon size for fixed shower sizes, recorded at Akeno (Hara et al., 1981b). The general trend showing a rising shower age with an increasing muon number at fixed shower size is evident and is probably correlated with the primary mass and/or the secondary particle multiplicity and collision elasticity in the first (few) interactions.

For showers of fixed size no significant correlation was found between the radius of curvature of the shower front and the age parameter over the size range from $3 \cdot 10^7$ to $3 \cdot 10^9$ (Aguirre et al., 1973). Additional data on correlations between the shower age and other observables are given in Chap. 19.

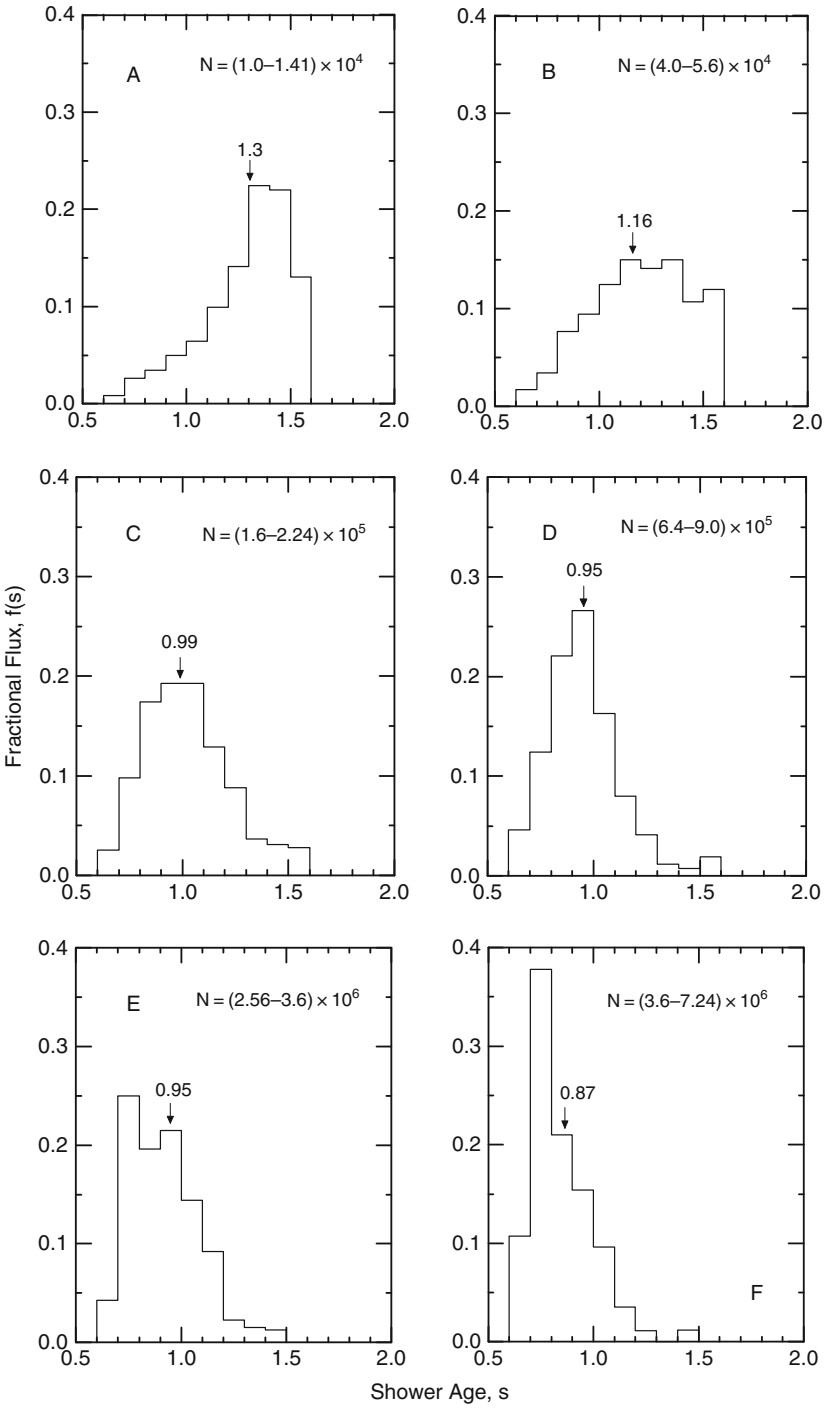

Fig. 10.35 Age parameter distributions of showers of different size groups recorded at the Kolar Gold Fields (Acharya et al., 1981a). The *arrows* show the location of the average value of each distribution

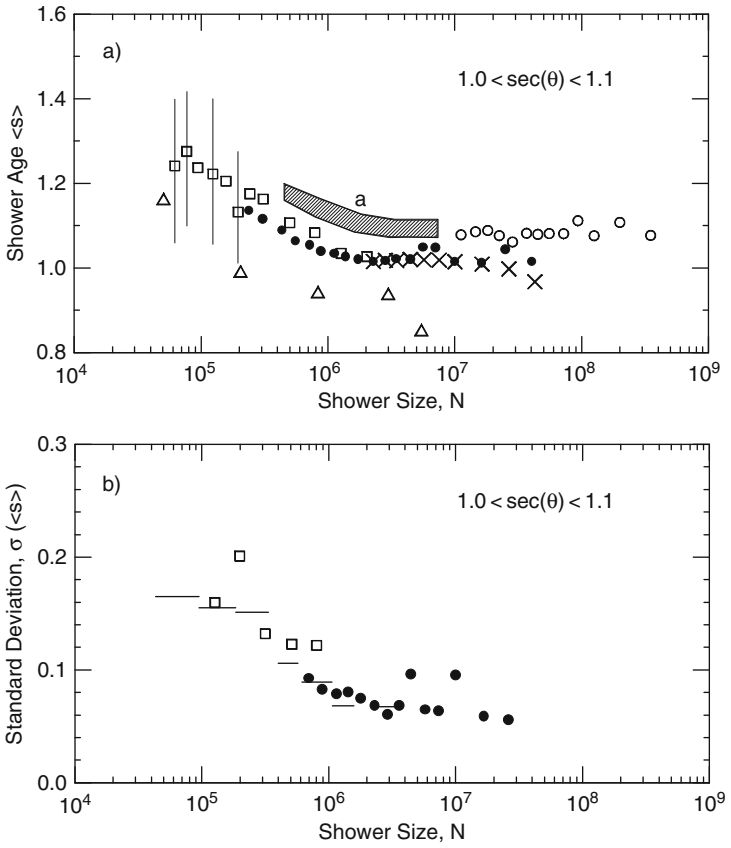

Fig. 10.36 Size dependence of average value of age parameter, $\langle s \rangle$, of showers detected at Akeno (**a**), and standard deviation, $\sigma \langle s \rangle$ (**b**) (Hara et al., 1979b, 1981a). The data points • apply to vertical showers of medium size and × to showers determined within one Molière unit from the axis. In either case 5 cm thick scintillators had been used. The *symbols* ○ represent large showers where most of the detectors are beyond one Molière unit, and □ are the data presented at the Kyoto conference (Hara et al., 1979b). We have also added the results of Acharya et al. (1981a) △ from the Kolar Gold Fields for comparison. This installation was located at about the same altitude as Akeno. The *hatched area, a*, in (**a**) represents measurements made with 3 mm thick scintillators. The fluctuation results of (**b**) have been obtained with 5 cm thick scintillators and the lines are the corresponding results from earlier measurements by Hara et al. (1979a)

10.5 Additional and Hidden Parameters

10.5.1 Height of First Interaction

The height of the first interaction of an incident primary initiating an air shower in the atmosphere, h_1, or the corresponding depth of the first interaction, X_1, are practically intangible. They depend on the interaction cross section of the primary

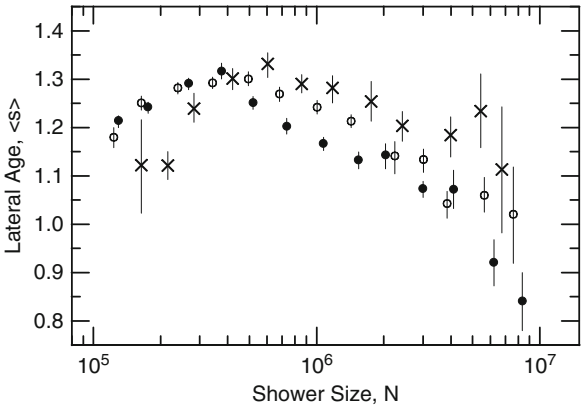

Fig. 10.37 Lateral age parameter, s_{lat}, versus shower size, N, obtained at sea level for 1,060 g cm^{-2} and different zenith angles, θ: •, $\theta < 20°$; ○, $20° \leq \theta < 30°$; × $30° \leq \theta < 45°$ (Clay et al., 1981)

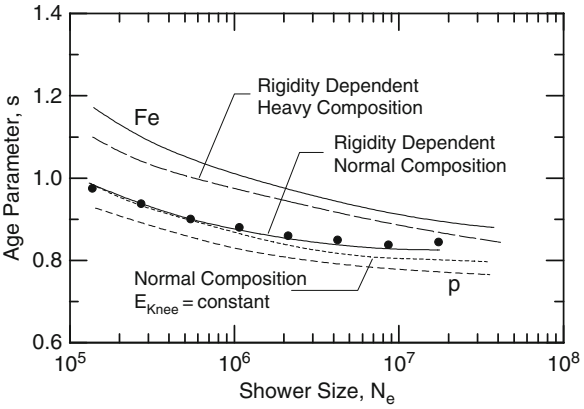

Fig. 10.38 Shower size dependence of the age parameter, s, as determined from the lateral distribution function, measured by the MAKET-ANI experiment located at 3,200 m a.s.l. (•). The *curves* show the size dependence of the shower age for a pure iron and pure proton primary beam, for a common normal and a rigidity dependent normal composition, and a rigidity dependent heavy composition (after Chilingarian et al., 2007)

with the atmospheric target nuclei. Thus, for a primary hadron of mass A the inelastic cross section, $\sigma_{\mathrm{inel}}^{A,\mathrm{air}}(E)$, is the relevant parameter. It depends on the projectile and target mass and manifests a slow energy dependence. h_1 and therefore X_1 are subject to *very large fluctuations*.

In addition, the location of the first interaction of a primary of given initial parameters (mass, energy) in the atmosphere (i.e., the height above sea level or the altitude) depends also on the zenith angle of incidence. Since after traversing a column of air corresponding to one interaction mean free path, $\lambda_{\mathrm{int}}^{A,\mathrm{air}}$ [g cm^{-2}], along an inclined trajectory, characterized by the *slant depth*, X_s [g cm^{-2}], the primary arrives at a higher altitude than when it penetrates the same column density along a vertical

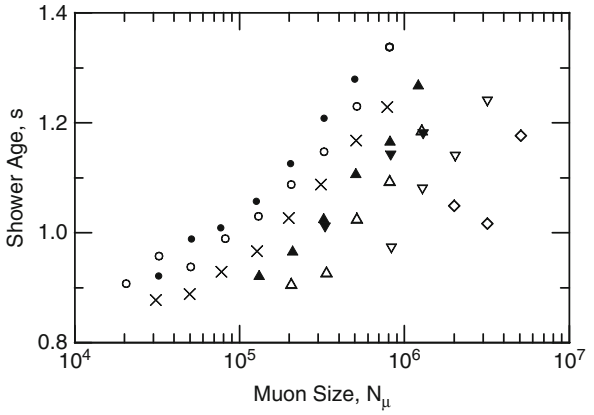

Fig. 10.39 Scatter plot of age parameter, s, of individual showers versus muon size, N_μ, obtained at Akeno (Hara et al., 1981b). The *symbols* identify the center values of the electron shower size bins (N_e) into which the events had been grouped: ● $7.95{\cdot}10^6$, ○ $1.26{\cdot}10^7$, × $2{\cdot}10^7$, ▲ $3.16{\cdot}10^7$, △ $5{\cdot}10^7$, ▼ $7.95{\cdot}10^7$, ▽ $1.26{\cdot}10^8$, and ◇ $2{\cdot}10^8$

trajectory.[14] Consequently, for a primary of given energy and mass the height of the first interaction increases with increasing zenith angle of incidence, and likewise the heights of the higher generations of interactions, too.

It must also be noted that in comparison to vertical showers, inclined showers having otherwise identical primary parameters develop differently. Since an inclined trajectory of given column density is physically longer than a vertical trajectory of equal column density because it extends in a medium of lower average density, due to the exponential altitude dependence of the density of the atmosphere. Thus, it takes more time to traverse the inclined trajectory and the competition between interaction and decay of unstable particles, such as pions and kaons changes in favor of decay[15] (cf. Figs. 3.24 and 3.25). Consequently, with increasing zenith angle this trend continues and affects the particle population. After having traversed an equal number of interaction mean free paths (equal column densities) the inclined shower will contain more muons and less pions than an otherwise comparable vertical shower.

(a) Estimation of the Height of the First Interaction

So far there has been no practical way to determine the height of the first interaction in air showers, neither by direct measurement nor could it be estimated with

[14] This applies to the height (or depth) of maximum development of a shower as well.

[15] Due to the very short mean life of charmed particles ($\approx 10^{-13}$ s), their decay probability is not affected.

reasonable reliability via indirect observables in conjunction with air shower simulations. However, very recently the H.E.S.S. collaboration has shown that the trajectories of heavy primaries in the atmosphere, such as iron nuclei, can be identified by their Cherenkov signature prior to the first interaction (Bühler, 2007). If further developed and refined, this technique bears the potential to become a method to determine the altitude of the first interaction, at least for multiply charged primaries aiming at the detector.

Instinctively one might think of the possibility to use core-angle measurements of high and ultrahigh energy muons that originate from almost instantly decaying charmed particles, or possibly from the decay of charged pions emerging from the first interaction. The less energetic charged pions of the backward hemisphere in the center of mass of the first interaction are more likely to decay than the fast forward going ones that are much more likely to interact because of their large Lorentz factor, even in the low density environment of the upper atmosphere.

The likelihood that this method is successful must be discarded because that particular group of muons is located within the shower core and its immediate proximity. Appropriate measurements would have to be carried out at adequate depth underground to remove the accompanying energetic non-muonic shower core constituents and the abundant low energy muon component that could impede the measurement. Because of the small angle which the high energy muons subtend with respect to the shower axis, extreme precision measurements would be required for both, the direction and location of the shower axis and the muon trajectories at ground impact.

However, along their trajectories to the detector, muons are subject to scattering processes which pose an insurmountable problem so that this method must be discarded. A target diagram showing the ground impact locations of ultrahigh energy muons with *genetic tags* attached is displayed in Fig. 14.67 from a simulation of Grieder (1977) for a 10^6 GeV proton initiated shower. The genetic tags indicate the *generation of interaction* from which the parent pions originate and the *height of origin* of each muon, i.e., the location of the decay of the parent pion in the atmosphere. In addition the muon energy is also listed.

Only six pairs of experiments, most of which are no longer in operation, would have been suitable, in principle, to carry out simultaneous combined surface and underground measurements. These comprise the Kolar Gold Fields (KGF) air shower array in combination with the KGF deep underground detectors in India, (Acharya et al., 1981b), the EAS-TOP array on top of Gran Sasso (Aglietta et al., 1986) in combination with the large underground detectors MACRO (Ahlen et al., 1992, 1993; Ambrosio et al., 2002) and LVD (Aglietta et al., 1992) in Italy, the surface array and underground detector at Baksan, Russia (Chudakov et al., 1979), the Homestake surface and underground installations (Cherry et al., 1985), and the SPASE-VULCAN-AMANDA detector combination at the South Pole (Andres et al., 2000; Dickinson et al., 2000a, b).

The KGF underground detector that was used for this work was located almost directly underneath the surface array, at a vertical depth of 266 m in the rock (muon

threshold $\simeq$220 GeV),[16] whereas MACRO and LVD, discussed in Sect. 10.3.4, were laterally displaced with respect to the EAS-TOP array by an inclination of $\sim 35^\circ$ and had a muon threshold of $\geq$1.3 TeV.

Apart from the relatively small aperture each of these combined experiments had, the core location accuracy and, as mentioned before, the scattering of the muons in the rock excluded a priori useful core angle measurements.

Nevertheless, the two twin experiments, EAS-TOP and MACRO, and the KGF surface and underground installations, were the only ones that yielded valuable high energy muon data of the immediate core region of air showers of well defined primary energy, particularly the EAS-TOP and MACRO combination. These data had been interpreted in terms of primary mass composition. The results are discussed in Sect. 11.7 (Acharya et al., 1981b; Aglietta et al., 2004a, b, respectively).

In this context we should mention that a few other authors have carried out experiments to measure the core angle of relatively low energy muons, on the order of 10 GeV, recorded with shallow underground and even surface installations to determine the height of origin of muons (Dixon et al., 1973; Earnshaw et al., 1973; Böhm et al., 1977; Gibson et al., 1979; Brancus et al., 1997; Büttner et al., 2003). This work is summarized in Chap. 14 where all aspects of muons in showers are discussed.

(b) Effects of the Height of the First Interaction on Shower Development

In a recent Monte Carlo study Antoni et al. (2003b) have investigated the effect of fluctuations of the first interaction on the shower size. The result of this work is shown in Fig. 10.40. Inspection of this figure reveals that the effect is not very dramatic, however, other observables may be affected more seriously by fluctuations of h_1.

10.5.2 Hadronic Interaction Parameters

Hadronic interaction models and model parameters used in simulations affect the interaction products and their kinematic properties. They have far reaching consequences for the development of simulated showers and, therefore, for the interpretation of experimental data using simulation results. Extracting information on quantities like the secondary particle multiplicity, the energy partition among the different newly created particles (pions, kaons, nucleons, antinucleons, charmed particles, etc.) and other *hidden* interaction details is extremely difficult since these parameters are hidden and masked by other effects. These aspects are discussed in Chaps. 3, 13, 14 and 19.

[16] At that time there were all-together three underground experiments in operation at KGF (see Chatterjee et al., 1965 and Fig. A.40).

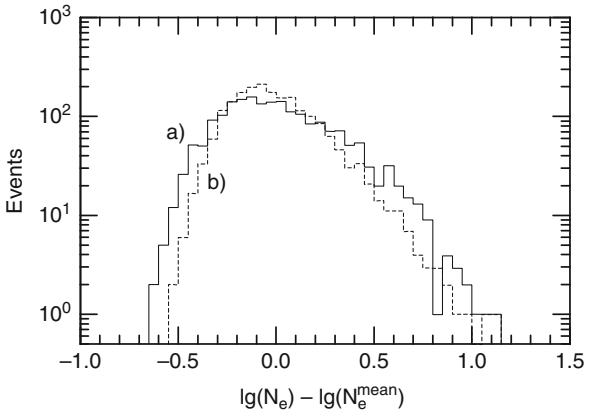

Fig. 10.40 Histogram (*a*) (*solid line*) shows intrinsic shower size fluctuations of 10^{15} eV proton initiated showers, incident under a zenith angle of 22°, resulting from a simulation with the CORSIKA code using Monte Carlo selected heights of the first interaction ($\sigma = 0.24$). The *dashed curve* (*b*) shows a comparative set of showers with a prefixed height of the first interaction set to an altitude of 23.9 km ($\sigma = 0.20$). The distributions refer to their mean value of $N_e \approx 3.98 \cdot 10^4$ and apply to Karlsruhe (110 m a.s.l.) (after Antoni et al., 2003b)

References

Abdullah, M.M., et al.: PICRC, 6, p. 151 (1981).
Acharya, B.S., et al.: PICRC, 9, p. 162 (1981a).
Acharya, B.S., et al.: PICRC, 11, p. 385 (1981b).
Aglietta, M., et al.: Nuovo Cim., C 9, p. 262 (1986).
Aglietta, M., et al.: Nuovo Cim., 105A, p. 1793 (1992).
Aglietta, M., et al.: Astropart. Phys., 9, p. 185 (1998).
Aglietta, M., et al.: Astropart. Phys., 20, p. 641 (2004a).
Aglietta, M., et al.: Astropart. Phys., 21, p. 223 (2004b).
Aglietta, M., et al.: Astropart. Phys., 21, p. 583 (2004c).
Aguirre, C., et al.: PICRC, 4, p. 2576 (1973).
Aguirre, C., et al.: PICRC, 8, p. 208 (1977).
Ahlen, S., et al., MACRO Collaboration: Phys. Rev. D, 46, p. 4836 (1992).
Ahlen, S., et al., MACRO Collaboration: Nucl. Instr. Meth. A, 324, p. 337 (1993).
Alexeyev, E.N., et al.: PICRC, 8, p. 52 (1977).
Ambrosio, M., et al.: Nucl. Instr. Meth. A, 486, p. 663 (2002).
Andeen, K.G., et al., IceCube Collaboration: PICRC, pre-conference edition, paper 1285, Merida, Mexico (2007).
Andres, E., et al.: Astropart. Phys., 13, pp. 1–20 (2000).
Antoni, T., et al.: J. Phys. G, 25, p. 2161 (1999a).
Antoni, T., et al.: Nucl. Phys. B (Proc. Suppl.), 75A, p. 234 (1999b).
Antoni, T., et al.: Astropart. Phys., 14, p. 245 (2001a).
Antoni, T., et al.: Astropart. Phys., 15, p. 149 (2001b).
Antoni, T., et al.: Astropart. Phys., 16, p. 245 (2002).
Antoni, T., et al.: Astropart. Phys., 18, p. 319 (2003a).
Antoni, T., et al.: Astropart. Phys., 19, p. 703 (2003b).
Antonov, R.A., et al.: Yadernaya Fiz. 18, p. 554 (1973) (in Russian).
Antonov, R.A., et al.: PICRC, 8, p. 137 (1977).
Antonov, R.A., et al.: PICRC, 9, p. 258 (1979).

Aseikin, V.S., et al.: Preprint No 142, FIAN Moscow (1976).
Aseikin, V.S., et al.: PICRC, 8, p. 98 (1977).
Ave, M., et al.: Astropart. Phys., 19, p. 47 (2003).
Baruch, J.E.F., et al.: PICRC, 8, p. 2949 (1975).
Bertaina, M., et al.: PICRC, 6, p. 41 (2005).
Blake, P.R., and W.F. Nash: J. Phys. G, 24, p. 217 (1998).
Block, M.M.: Czechoslovak J. Phys., 56, Suppl. A, p. A77 (2006).
Böhm, E., et al.: Can. J. Phys., 46, p. S50 (1968).
Böhm, E., et al.: PICRC, 8, p. 25 (1977).
Boothby, K., et al.: PICRC, 5, p. 193 (1997).
Brancus, I.M., et al.: Astropart. Phys., 7, p. 343 (1997).
Brancus, I.M., et al.: PICRC, 1, p. 345 (1999).
Brancus, I.M., et al.: J. Phys. G, 29, p. 453 (2003).
Bühler, R., H.E.S.S. Collaboration: PICRC, pre-conference edition, paper 0284, Merida, Mexico (2007).
Büttner, C., et al.: Nucl. Phys. B (Proc. Suppl.), 122, p. 289 (2003).
Capdevielle, J.N., et al.: PICRC, 10, p. 275 (1990).
Cherry, M.L., et al.: PICRC, 8, p. 246 (1985).
Chilingarian, A.A.: Comput. Phys. Commun., 54, p. 381 (1989).
Chilingarian, A.A., and G.Z. Zazian: Nuovo Cim., 14, p. 555 (1991).
Chilingarian, A., et al.: Astropart. Phys., 28, p. 58 (2007).
Chudakov, A.E., et al.: PICRC, 8, p. 217 (1979).
Clay, R.W., et al.: Nuovo Cim., 4 C, p. 668 (1981).
Coy, R.N., et al.: PICRC, 6, p. 43 (1981).
Coy, R.N., et al.: Astropart. Phys., 6, p. 263 (1997).
Cronin, J.W.: GAP-97-034 (Auger Technical Note) (1997).
Dai, H.Y., et al.: J. Phys. G, 14, p. 793 (1988).
Danilova, T.V., et al.: J. Phys. G, 15, p. 509 (1989).
Dedenko, L.G., et al.: PICRC, 8, p. 2731 (1975).
Dedenko, L.G., et al.: PICRC, 8, p. 320 (1979).
Dickinson, J.E., et al.: Nucl. Instr. Meth. A, 440, p. 95 (2000a).
Dickinson, J.E., et al.: Nucl. Instr. Meth. A, 440, p. 114 (2000b).
Ding, L.K., et al.: Proceedings of International Symposium on Cosmic Rays and Particle Physics, Institute for Cosmic Ray Research, University of Tokyo, Tokyo, p. 142 (1984).
Dixon, H.E., et al.: PICRC, 4, p. 2556 (1973).
Dova, M.T.: Nucl. Phys. B (Proc. Suppl.), 122, p. 170 (2003).
Earnshaw, J.C., et al.: Department of Physics Report, University of Durham, Durham (1973).
Edge, D.M., et al.: J. Phys. A, 6, p. 1612 (1973).
Forti, C., et al.: Phys. Rev. D, 42, p. 3668 (1990).
Fowler, J.W., et al.: Astropart. Phys., 15, p. 49 (2001).
Furuhata, A., et al., BASJE Collaboration: PICRC, 6, p. 329 (2005).
Gaisser, T.K., et al.: Rev. Mod. Phys., 50, p. 859 (1978).
Gibson, A.I., et al.: PICRC, 8, p. 101 (1979).
Gress, O.A., et al.: PICRC, 4, p. 129 (1997).
Grieder, P.K.F.: Rivista del Nuovo Cim., 7, p. 1 (1977).
Grieder, P.K.F.: Proceedings of Japan – US Seminar on Cosmic Ray Muon and Neutrino Physics/Astrophysics Using Deep Underground/Underwater Detectors, Institute for Cosmic Ray Research, University of Tokyo, p. 183 (1986).
Gupta, S., et al.: Phys. Rev. D, 68, p. 052005 (2003).
Gupta, S., et al.: Nucl. Instr. Meth. A, 540, p. 311 (2005).
Haeusler, R., et al.: Astropart. Phys., 17, p. 421 (2002).
Hara, T., et al.: PICRC, 8, p. 135 (1979a).
Hara, T., et al.: PICRC, 13, p. 148 (1979b).
Hara, T., et al.: PICRC, 6, p. 52 (1981a).

Hara, T., et al.: PICRC, 11, p. 231 (1981b).
Hara, T., et al.: Phys. Rev. Lett., 50, p. 2058 (1983).
Haungs, A., et al.: Rep. Prog. Phys., 66, p. 1145 (2003).
Hayashi, Y., et al.: PICRC, 1, p. 276 (1999).
Hayashi, Y., et al.: Nucl. Instr. Meth., A 545, p. 643 (2005).
Hayashida, N., et al.: Phys. Rev. Lett., 73, p. 3491 (1994).
Hayashida, N., et al.: PICRC, 1, p. 353 (1999).
Hillas, A.M., et al.: Acta Phys. Acad. Sci. Hung., 29, S3, p. 533 (1970).
Hillas, A.M., et al.: PICRC, 3, p. 1001 (1971a).
Hillas, A.M., et al.: PICRC, 3, p. 1007 (1971b).
Hillas, A.M.: Proceedings of Cosmic Ray Workshop, University of Utah, Utah, p. 16 (1983).
Kalmykov, N.N., et al.: PICRC, 8, p. 3034 (1975).
Kamata, K., and J. Nishimura: Prog. Theor. Phys. Jpn., 6, Suppl., p. 93 (1958).
Kamata, K., and J. Nishimura: J. Phys. Soc. Jpn., 15, p. 1565 (1960).
Kameda, T., et al.: PICRC, 2, p. 681 (1965).
Kaneko, T., et al.: PICRC, 8, p. 2747 (1975).
Kasahara, K., et al.: PICRC, 13, p. 70 (1979).
Kasahara, K., et al.: PICRC, pre-conference edition, paper 0955, Merida, Mexico (2007).
Khristiansen, G.B., et al.: Izv. Akad. Nauk SSSR, Ser. Fiz., 35, p. 2107 (1971).
Khristiansen, G.B.: JETP Lett., 18, p. 207 (1973).
Khristiansen, G.B.: Cosmic Rays of Superhigh Energies. Karl Thiemig Verlag, München (1980).
Klages, H.O., et al.: Nucl. Phys. B (Proc. Suppl.), 52, p. 92 (1997).
Kutter, T.: GAP-98-048, Auger Technical Note (1998).
Lawrence, M.A., et al.: J. Phys. G, 17, p. 733 (1991).
Matano, T., et al.: Acta Phys. Acad. Sci. Hung., 29, S3, p. 451 (1970).
Miyake, S., et al.: PICRC, 7, p. 2748 (1971).
Miyake, S., et al.: PICRC, 5, p. 3220 (1973).
Miyake, S., et al.: PICRC, 12, p. 36 (1977).
Miyake, S., et al.: PICRC, 13, p. 171 (1979).
Nagano, M., et al.: J. Phys. G, 10, p. 1295 (1984).
Nagano, M., et al.: J. Phys. G, 18, p. 423 (1992).
Nagano, M., et al.: Astropart. Phys., 13, p. 277 (2000).
Newton, D., et al.: Astropart. Phys., 26, p. 414 (2007).
Nishimura, J.: Handbuch der Physik, S. Flügge, ed., 46/2, p. 1, Springer Verlag, Berlin (1967).
Ogio, S., et al.: Astrophys. J., 612, p. 268 (2004).
Rebel, H., et al.: J. Phys. G, 21, p. 451 (1995).
Rossi, B., and K. Greisen: Rev. Mod. Phys., 13, p. 240 (1941).
Sakaki, N., et al.: PICRC, 1, p. 329 (2001a).
Sakaki, N., et al.: PICRC, 1, p. 333 (2001b).
Sakuyama, H., and N. Suzuki: PICRC, 8, p. 18 (1977).
Shibata, S., et al.: PICRC, 2, p. 672 (1965).
Shirasaki, Y., et al.: PICRC, 4, p. 53 (1997).
Shirasaki, Y., et al.: Astropart. Phys., 15, p. 357 (2001).
Stamenov, J.N., and S.Z. Ushev: PICRC, 8, p. 133 (1977).
Swordy, S.P., et al.: Astropart. Phys., 18, p. 129 (2002).
Takeda, M., et al.: Astropart. Phys., 19, p. 447 (2003).
Tanahashi, G.: J. Phys. Soc. Jpn., 20, p. 883 (1965).
Tanaka, H., et al.: PICRC, pre-conference edition, paper 1233, Merida, Mexico (2007a).
Tanaka, H., et al.: PICRC, pre-conference edition, paper 1235, Merida, Mexico (2007b).
Ulrich, H., et al.: PICRC, 6, p. 129 (2005).
van Buren, J., et al.: PICRC, 6, p. 301 (2005).
Vernov, S.N., et al.: Izv. Akad. Nauk. SSSR, Ser. Fiz., 32, p. 458 (1968).
Vernov, S.N., et al.: Acta Phys. Acad. Sci. Hung., 29, S3, p. 429 (1970).
Weber, J.H., KASCADE Collaboration: PICRC, 6, p. 153 (1997).
Yoshida, S., et al.: J. Phys. G, 20, p. 651 (1994).

Chapter 11
Primary Cosmic Radiation and Astrophysical Aspects

Overview In this chapter we briefly summarize the current situation of our knowledge of the primary cosmic radiation in the vicinity of the Earth. We outline the essential properties of the low energy components of the radiation that is accessible to direct measurements and present spectra of hadrons (protons and nuclei), electrons, gamma rays and antimatter from balloon and satellite experiments, and predictions for neutrinos of anticipated galactic and extragalactic origin. Subsequently we discuss the high energy radiation that is responsible for air shower phenomena, whose composition and spectral features are still subject of debate. Much emphasis is given to the exploration of the dominating primary hadronic component, to the determination of the mass and energy of the shower initiating agents, that are at present only indirectly accessible via ground based observations, from which the relevant parameters are derived or estimated. We then discuss spectral features and irregularities, such as the knee(s), the ankle and the Greisen-Zatsepin-Kuzmin (GZK) cutoff. Data from many different experiments are presented. The techniques employed are only outlined, as they are discussed in detail in the specific chapters as mentioned in the text. Topics like anisotropy, the Compton-Getting effect, time variation, propagation and sources of the radiation are outlined but not discussed at depth as they go well beyond the intended scope of this book. The vast field of gamma ray astronomy, which is originally a spin-off of air shower research, has rapidly developed into a separate fast growing discipline of its own. It is therefore only briefly touched on the side.

11.1 Introduction

The primary cosmic radiation offers a vast and highly complex field of research. Much is known about the properties of the radiation in the vicinity of the Earth, in particular of the low energy component. However, our knowledge is diminishing rapidly with increasing energy because of the rapidly falling intensity and increasing technical difficulties of measurements. Relatively little is known about the nature and properties of the high and ultrahigh energy (UHE) radiation beyond about 10^{14} eV, whose spectrum is known to extend to 10^{20} eV, and possibly beyond.

P.K.F. Grieder, *Extensive Air Showers,* DOI 10.1007/978-3-540-76941-5_11,

Moreover, comparatively little is known about the origin of the particles and quanta, about the nature of the sources, the acceleration mechanisms, the properties of space in which the cosmic radiation propagates and interacts with matter and fields contained within it. It is generally believed that the radiation below 10^{16}–10^{17} eV is of galactic origin whereas the component beyond about 10^{18} eV is believed to be of extragalactic origin.

High energy primary gamma radiation is a domain of its own. Originally discovered with common air shower arrays that have established the existence of a diffuse (unresolved) gamma ray background as well as distinct point sources, this branch of primary cosmic ray research has developed into a fast growing new field of its own, called *high energy gamma ray astronomy*. Densely packed dedicated air shower particle or wide aperture atmospheric Cherenkov detector arrays as well as imaging Cherenkov telescopes (H.E.S.S., MAGIC, VERITAS) and special detectors such as the water pool detector Milagro and the resistive plate detector ARGO are now mainly being used for this purpose. In this discipline the interest today is focused chiefly on gamma ray point sources.

Many of the important topics mentioned above concerning the primary cosmic radiation go far beyond the scope of this book. In the following sections, after briefly reviewing the low energy cosmic radiation that cannot initiate air showers which reach ground level, we restrict the discussion and the data that we present to the nature and properties of the high and ultra high energy component. This part of the spectrum can only be explored with large ground based detector systems that record air shower observables and from future satellite based instruments that will record the fluorescence tracks of giant air showers in the atmosphere and ground-reflected atmospheric optical Cherenkov radiation.

Much emphasis is given to primary hadrons which, according to our present knowledge, constitute the bulk of all the agents that initiate air showers. We present a very limited selection of spectra and distributions from numerous experiments that use a wide variety of different techniques, methods and shower observables. The many comparative compilations that are presented in the subsequent sections permit to cross-check the different methods of investigations that are discussed in more detail in Chap. 10.

11.2 Nature of the Primary Radiation

11.2.1 Brief Summary

Observations have revealed that the radiation outside the Earth's atmosphere that we call the *primary cosmic radiation*, consists of particles and quanta whose spectra cover an enormous energy range. Of particular interest for air shower studies are *hadrons, gamma rays*, and *neutrinos*, and possibly hitherto unidentified agents having energies in excess of about 10^{13}–10^{14} eV. Because of heavy energy losses of energetic electrons by synchrotron radiation, the spectrum of primary electrons

drops rapidly, preventing them from producing large air showers in significant number. Another consequence of this situation is that primary electrons are of rather local origin. No extra-terrestrial non-solar neutrinos have so far been identified and no *dark matter* agents either – as of early 2009 (Bernabei et al., 2008, 2009).

On their way from the source to the fringes of the atmosphere the different kinds of radiation are subject to interactions with matter (gas and dust), radiation (particles and photons) and local and large-scale magnetic fields.[1] This implies that the spectra and composition of the cosmic radiation at the source must be different from what we observe at the fringes of the atmosphere. Accurate knowledge of the local, near Earth properties of the cosmic radiation leads to a better understanding of the properties of the interstellar and intergalactic space, and of the nature of likely cosmic ray sources and acceleration processes.

Measurements with balloon borne instruments flown at the fringes of the atmosphere or on board of satellites in outer space permit to investigate the different components of the cosmic radiation *directly*. However, because of the rapidly falling spectra of all cosmic ray constituents and because of the size, weight and power limitations for on-board equipment, direct measurements cannot yield useful data beyond certain instrumentally imposed cutoff energies where the counting rate becomes statistically irrelevant.

The high energy limit for *direct measurements*, i.e., the energy region where measurements run out of statistics, depends not only on the detector size and the duration of the exposure, but also on the specific kind of radiation under investigation. Presently, it lies around 100 TeV per particle for hadrons, at about 1 TeV for electrons and a few 10 GeV for gamma rays. Beyond these approximate cutoff energies only ground based *indirect measurements* can be carried out that are based on the evaluation and interpretation of air shower observables. Unfortunately, the bulk of the particles and quanta that have energies around the instrumental cutoff of direct measurements cause only very small air showers when entering the atmosphere. They die out long before even reaching mountain altitudes and remain undetectable with conventional particle detector arrays. Only the atmospheric Cherenkov light bursts of these events are near, at, or above the threshold of optical detection by ground based atmospheric Cherenkov telescopes and Cherenkov detector arrays.

Most conventional air shower particle detector arrays have thresholds for events initiated by primaries having energies > 100 TeV. The threshold depends on altitude, array layout and detector coverage. Thus, there exists a gap between the spectral ranges covered by direct measurements and conventional air shower arrays of the order of 1–2 decades in energy where we have lacked reliable data for many years. Fortunately, in recent years with many long flying balloon missions in the Earth's polar regions, where the balloons can remain afloat for days because of continuous exposure to the Sun, the spectral range covered by direct measurements could be extended significantly to higher energies.

[1] Electric fields and gravitational effects are usually disregarded when studying propagation.

Likewise, heavily instrumented and tightly packed particle detector arrays of recent date located at higher altitudes (e.g. the GRAPES array at Ootacamund in India, 2,200 m a.s.l., the ARGO detector system and the Tibet array, both located at Yangbajing, 4,300 m a.s.l.) could extend air shower investigations to lower primary energy thresholds, so that the gap between the directly and indirectly accessible spectral regions is in the process of being closed to form a single broad spectrum. However, much work remains to be done because indirect primary energy and above all indirect primary mass determination remain a major problem, as had been outlined in Chap. 10 and will become evident in this chapter.

11.2.2 Classification of Nuclei

Primary nuclei are frequently grouped according to their atomic (nuclear electric) charge, Z, that identifies the chemical element. The classification or grouping had been introduced originally by the nuclear emulsion community. Several classifications and sub-classifications are used, depending on the particular project orientation, and not all authors follow the same rules. A frequently used classification is given in Table 11.1 (see also Table 3.1).

Table 11.1 Classification of primary nuclei

Particle, element	Group	Atomic charge	Element
Protons	–	1	H
Helium nuclei	–	2	He
Light nuclei	L	$3 \leq Z \leq 5$	Li, Be, B
Medium nuclei	M	$6 \leq Z \leq 9$	C, N, O, F
Heavy nuclei	H	$10 \leq Z \leq 19$	Ne – K
Very heavy nuclei	VH	$20 \leq Z \leq 30$	Ca – Zn
Ultra-heavy nuclei	VVH	$Z > 30$	Ga – U
Super-heavy nuclei	SH	$Z > 92$	
Other occasionally used subgroups			
Light group	L	$1 \leq Z \leq 5$	H – B
Light-heavy (Silicone) group	LH	$10 \leq Z \leq 14$	Ne – Si
Iron group	–	$15 \leq Z \leq 26$	P – Fe

11.3 Low Energy Primary Radiation

The low energy primary cosmic radiation is in principle irrelevant for air shower studies only, however, it is of great significance for astrophysical reasons. Because of atmospheric absorption the low energy component can only be investigated at the fringes of the atmosphere with balloon-bound instruments or with the help of detectors on board of satellites. The different components of the low energy radiation can

thus be studied *directly* in-situ with comparatively small detectors because of the relatively high intensity.

Today *direct measurements* of the energy spectrum and composition of the hadronic primary radiation can be carried out to energies as high as about 100 TeV per particle. For photon, electron and antimatter measurements much lower upper bounds exist. The limits are imposed by the rapidly falling spectra which are typical of all components, and the physical limitations of balloon and space bound instruments. At higher energies only *indirect measurements* using large ground-based detector systems, preferentially located at higher elevations, particularly for studying the hadronic component, are required to get adequate statistics.

The interpretation of observables from indirect measurements require in general mathematical models and complex computer simulations to extract the relevant information, such as the nature, energy and mass of the primary. The different indirect methods are discussed in Chap. 10. For completeness we present in the following section a brief summary of data of the low energy (air shower irrelevant) primary radiation.

11.3.1 Hadronic Spectra and Composition

One of the important questions is, for example, what is the energy dependence of the primary mass composition, and how does the composition obtained from direct measurements compares with that deduced by indirect methods from air shower observables at very high energies. Of particular interest in this context is how well the upper end of the directly measured all particle spectrum matches on to the very low energy all-particle spectrum deduced from air shower analyses, and likewise the spectra of individual mass groups in the overlapping energy region.

We must point out here that only very recently has it become possible to more or less bridge the gap between the two experimentally very different energy regimes, as will be evident when inspecting the data presented in Sect. 11.6. This could be achieved by refining the experimental methods that eventually allowed extending the respective energy ranges towards and into the neighboring domains.

In Fig. 11.1 we present the very low energy ($E \simeq 1$ GeV/N) primary mass abundances as it is measured at the top of the atmosphere. Many individual experiments and a large number of measurements were required to collect these data (for a data summary see, e.g., Grieder, 2001; Wefel, 2008).

As mentioned before, direct measurements of the primary cosmic ray spectrum and composition are currently practicable up to energies of about 100 TeV. Major relatively recent contributions to this field had been made by the JACEE emulsion experiment (Asakimori et al., 1998), by the RUNJOB calorimeter-type emulsion chamber (Furukawa et al., 2003a, b, c; Kopenkin, 2007), by the ATIC calorimeter experiments (Ahn et al., 2007; Wefel et al., 2005), and by CREAM (Seo et al., 2007) and TRACER (Müller et al., 2007; Boyle et al., 2007). Figure 11.2 shows a compilation of data from direct measurements carried out with balloon and satellite bound

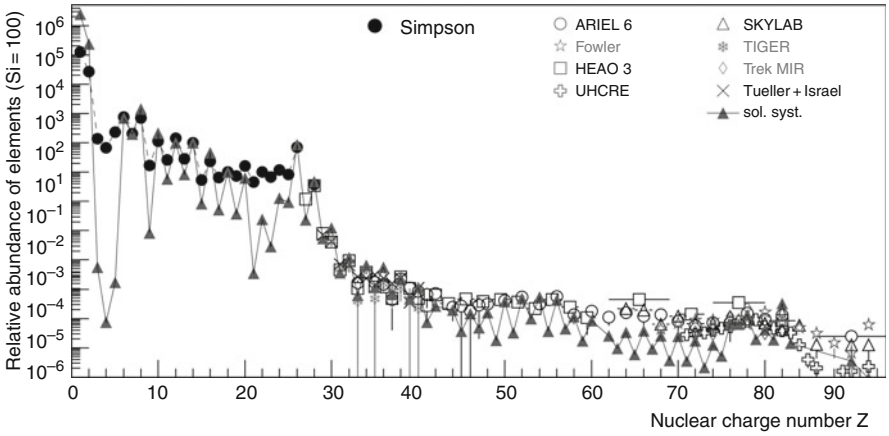

Fig. 11.1 Low energy primary abundances of the elements at an energy of $\simeq 1$ GeV/nucleon in the cosmic radiation, normalized to Si = 100. The plot is assembled from data by Simpson (1983) for $Z \leq 28$, Fowler et al. (1977) for $Z \geq 34$, and the following experiments: ARIEL-6 (Fowler et al., 1987), HEAO-3 (Binns et al., 1981, 1989), SKYLAB (Shirk and Price, 1978), TIGER (Lawrence et al., 1999), TREK/MIR (Weaver and Westphal, 2001; Tueller et al., 1981), and UHCRE (Donelly et al., 1999). The abundances in the solar system are according to Lodders (2003) (courtesy of J.R. Hörandel, 2003a, b)

instruments. Many more data from direct measurements are included in the plots showing the indirectly determined high energy spectra, to illustrate how well the two kinds of data join in the overlapping energy region.

A comprehensive table of the abundance of the elements in the energy range around 1 TeV/Nucleus had been assembled by Hörandel (2003b) and is reproduced in Table 11.2. It contains much of the data from the earlier compilation made by Wiebel-Sooth et al. (1998) and many more data from recent measurements. The latter had been made with large and sophisticated detector systems. These mainly balloon-bound experiments had been carried out in the Arctic and Antarctic regions, during the local summers. The high latitude flights have the great advantage that the balloons which encircle the poles remain continuously exposed to the Sun, which allows very long-duration flights.

11.3.2 Electrons (Negatrons and Positrons) (e^+, e^-)

Since the first observation of cosmic ray negatrons by Earl (1961) and Meyer and Vogt (1961) and the discovery of cosmic ray positrons in the early sixties by De Shong et al. (1964), many experiments using balloon-borne magnetic spectrometers had been carried out to investigate these two components. The general belief is that charged pions produced in high energy collisions of cosmic ray nucleons with the interstellar gas are the principal source of positrons and electrons via the pion–muon decay channels, $\pi^+ \rightarrow \mu^+ + \nu_\mu$, $\mu^+ \rightarrow e^+ + \nu_e + \overline{\nu}_\mu$, and the analogous processes,

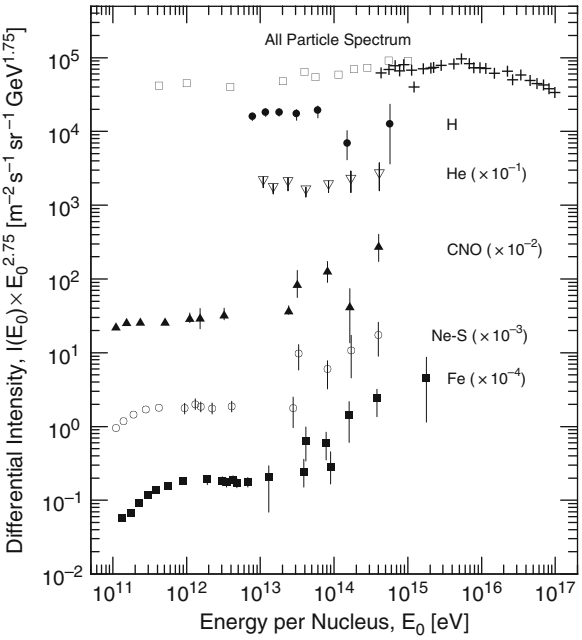

Fig. 11.2 Summary of data from direct measurements of the spectral distribution of the different charge groups of the primary hadronic cosmic radiation over a wide energy range to the present *upper limit* of direct experimental accessibility. Shown are results from the HEAO spacecraft, the CRN experiment on Spacelab-2 and the JACEE balloon emulsion packages, as well as the all particle spectrum at the *top* of the figure. Note that each charge group is offset vertically by 1 decade in intensity from the preceding charge group for reasons of display to avoid overlapping of spectra (Galactic Origin and Acceleration Limit Workshop, 1993). Results from recent direct measurements are included in the plots of Sects. 11.6 and 11.7 where we discuss the mass composition at high energies

$\pi^- \rightarrow \mu^- + \overline{\nu_\mu}$, $\mu^- \rightarrow e^- + \overline{\nu_e} + \nu_\mu$. Based on this hypothesis the expected fraction of positrons in the framework of the Leaky Box model (Peters, 1960; Cesarsky, 1980) appears to be consistent with observations in the energy range from 1 to 10 GeV.

A calculation of Uryson (1993), using the quark-gluon-string model of Kaidalov et al. (1987), shows that over the investigated energy range from 10 to 10^6 GeV the expected production spectra for positrons and electrons have slopes that are identical to the initial proton spectrum. Because of charge conservation in the reactions the positron–electron ratio of secondaries obtained by Uryson is $e^+/e^- \approx 1.3 - 1.4$.

Nevertheless, additional contributions from other processes must be considered, too, such as pair production in high magnetic fields (Grimani, 1996), the annihilation of super-symmetric particles (Tylka, 1989), and photon-photon collisions (Mastichiadis et al., 1991a, b). These sources contribute equal numbers of negatrons and positrons and do not affect their ratio.

Table 11.2 Absolute vertical differential intensity, $I_v(Z)$ [$(m^2\,s\,sr\,TeV)^{-1}$)] at $E_0 = 1$ TeV/nucleus and spectral index γ_z of cosmic ray elements (Hörandel, 2003)

Z		$I_v(Z)$	$-\gamma_z$	Z		$I_v(Z)$	$-\gamma_z$
1[a]	H	$8.73 \cdot 10^{-2}$	2.71	47[c]	Ag	$4.54 \cdot 10^{-7}$	2.42
2[a]	He	$5.71 \cdot 10^{-2}$	2.64	48[c]	Cd	$6.30 \cdot 10^{-7}$	2.41
3[b]	Li	$2.08 \cdot 10^{-3}$	2.54	49[c]	In	$1.61 \cdot 10^{-7}$	2.40
4[b]	Be	$4.74 \cdot 10^{-4}$	2.75	50[c]	Sn	$7.15 \cdot 10^{-7}$	2.39
5[b]	B	$8.95 \cdot 10^{-4}$	2.95	51[c]	Sb	$2.03 \cdot 10^{-7}$	2.38
6[b]	C	$1.06 \cdot 10^{-2}$	2.66	52[c]	Te	$9.10 \cdot 10^{-7}$	2.37
7[b]	N	$2.35 \cdot 10^{-3}$	2.72	53[c]	I	$1.34 \cdot 10^{-7}$	2.37
8[b]	O	$1.57 \cdot 10^{-2}$	2.68	54[c]	Xe	$5.74 \cdot 10^{-7}$	2.36
9[b]	F	$3.28 \cdot 10^{-4}$	2.69	55[c]	Cs	$2.79 \cdot 10^{-7}$	2.35
10[b]	Ne	$4.60 \cdot 10^{-3}$	2.64	56[c]	Ba	$1.23 \cdot 10^{-6}$	2.34
11[b]	Na	$7.54 \cdot 10^{-4}$	2.66	57[c]	La	$1.23 \cdot 10^{-7}$	2.33
12[b]	Mg	$8.01 \cdot 10^{-3}$	2.64	58[c]	Ce	$5.10 \cdot 10^{-7}$	2.32
13[b]	Al	$1.15 \cdot 10^{-3}$	2.66	59[c]	Pr	$9.52 \cdot 10^{-8}$	2.31
14[b]	Si	$7.96 \cdot 10^{-3}$	2.75	60[c]	Nd	$4.05 \cdot 10^{-7}$	2.30
15[b]	P	$2.70 \cdot 10^{-4}$	2.69	61[c]	Pm	$8.30 \cdot 10^{-8}$	2.29
16[b]	S	$2.29 \cdot 10^{-3}$	2.55	62[c]	Sm	$3.68 \cdot 10^{-7}$	2.28
17[b]	Cl	$2.94 \cdot 10^{-4}$	2.68	63[c]	Eu	$1.58 \cdot 10^{-7}$	2.27
18[b]	Ar	$8.36 \cdot 10^{-4}$	2.64	64[c]	Gd	$6.99 \cdot 10^{-7}$	2.25
19[b]	K	$5.36 \cdot 10^{-4}$	2.65	65[c]	Tb	$1.48 \cdot 10^{-7}$	2.24
20[b]	Ca	$1.47 \cdot 10^{-3}$	2.70	66[c]	Dy	$6.27 \cdot 10^{-7}$	2.23
21[b]	Sc	$3.04 \cdot 10^{-4}$	2.64	67[c]	Ho	$8.36 \cdot 10^{-8}$	2.22
22[b]	Ti	$1.14 \cdot 10^{-3}$	2.61	68[c]	Er	$3.52 \cdot 10^{-7}$	2.21
23[b]	V	$6.31 \cdot 10^{-4}$	2.63	69[c]	Tm	$1.02 \cdot 10^{-7}$	2.20
24[b]	Cr	$1.36 \cdot 10^{-3}$	2.67	70[c]	Yb	$4.15 \cdot 10^{-7}$	2.19
25[b]	Mn	$1.35 \cdot 10^{-3}$	2.46	71[c]	Lu	$1.72 \cdot 10^{-7}$	2.18
26[a]	Fe	$2.04 \cdot 10^{-2}$	2.59	72[c]	Hf	$3.57 \cdot 10^{-7}$	2.17
27[b]	Co	$7.51 \cdot 10^{-5}$	2.72	73[c]	Ta	$2.16 \cdot 10^{-7}$	2.16
28[b]	Ni	$9.96 \cdot 10^{-4}$	2.51	74[c]	W	$4.16 \cdot 10^{-7}$	2.15
29[c]	Cu	$2.18 \cdot 10^{-5}$	2.57	75[c]	Re	$3.35 \cdot 10^{-7}$	2.13
30[c]	Zn	$1.66 \cdot 10^{-5}$	2.56	76[c]	Os	$6.42 \cdot 10^{-7}$	2.12
31[c]	Ga	$2.75 \cdot 10^{-6}$	2.55	77[c]	Ir	$6.63 \cdot 10^{-7}$	2.11
32[c]	Ge	$4.02 \cdot 10^{-6}$	2.54	78[c]	Pt	$1.03 \cdot 10^{-6}$	2.10
33[c]	As	$9.99 \cdot 10^{-7}$	2.54	79[c]	Au	$7.70 \cdot 10^{-7}$	2.09
34[c]	Se	$2.11 \cdot 10^{-6}$	2.53	80[c]	Hg	$7.43 \cdot 10^{-7}$	2.08
35[c]	Br	$1.34 \cdot 10^{-6}$	2.52	81[c]	Tl	$4.28 \cdot 10^{-7}$	2.06
36[c]	Kr	$1.30 \cdot 10^{-6}$	2.51	82[c]	Pb	$8.06 \cdot 10^{-7}$	2.05
37[c]	Rb	$6.93 \cdot 10^{-7}$	2.51	83[c]	Bi	$3.25 \cdot 10^{-7}$	2.04
38[c]	Sr	$2.11 \cdot 10^{-6}$	2.50	84[c]	Po	$3.99 \cdot 10^{-7}$	2.03
39[c]	Y	$7.82 \cdot 10^{-7}$	2.49	85[c]	At	$4.08 \cdot 10^{-8}$	2.02
40[c]	Zr	$8.42 \cdot 10^{-7}$	2.48	86[c]	Rn	$1.74 \cdot 10^{-7}$	2.00
41[c]	Nb	$5.05 \cdot 10^{-7}$	2.47	87[c]	Fr	$1.78 \cdot 10^{-8}$	1.99
42[c]	Mo	$7.79 \cdot 10^{-7}$	2.46	88[c]	Ra	$7.54 \cdot 10^{-8}$	1.98
43[c]	Tc	$6.98 \cdot 10^{-8}$	2.46	89[c]	Ac	$1.97 \cdot 10^{-8}$	1.97
44[c]	Ru	$3.01 \cdot 10^{-7}$	2.45	90[c]	Th	$8.87 \cdot 10^{-8}$	1.96
45[c]	Rh	$3.77 \cdot 10^{-7}$	2.44	91[c]	Pa	$1.71 \cdot 10^{-8}$	1.94
46[c]	Pd	$5.10 \cdot 10^{-7}$	2.43	92[c]	U	$3.54 \cdot 10^{-7}$	1.93

[a] Hörandel (2003).
[b] Wiebel-Sooth et al. (1998).
[c] Hörandel (2003), extrapolation for ultra-heavy elements.

However, at energies >10 GeV the observed positron flux exceeds the expected secondary contribution and it is assumed that at least part of the excess may be due to other sources (Golden et al., 1996). Some authors suggest that part of the observed positrons could be from the decay of energetic radioactive isotopes, e.g., Co56→Fe56 + β^+, that get accelerated in pulsars and young supernova remnants and could account for the excess flux (Harding and Ramaty, 1987; Ramaty et al., 1993; Skibo and Ramaty, 1993).

Electrons beyond 1 TeV cannot travel far distances in space because of energy losses due to synchrotron radiation and inverse Compton scattering. In the energy range between 10 and 100 GeV the observed spectrum bends downward because of synchrotron energy losses. This yields a clue to estimate the confinement time of the electrons in the Galaxy, which is believed to be $(0.7 - 2.2) \cdot 10^7$ years (Taira et al., 1993). Figure 11.3 shows an experimentally determined spectrum of cosmic ray electrons (negatrons only) assembled from data of many different experiments (Wiebel-Sooth, 1998; Wiebel-Sooth et al., 1998) and a theoretical spectrum that relates to a confinement time of 10^7 years. We show this spectrum in the uncompressed form to emphasize its steepness. Above 100 GeV the spectral slope goes

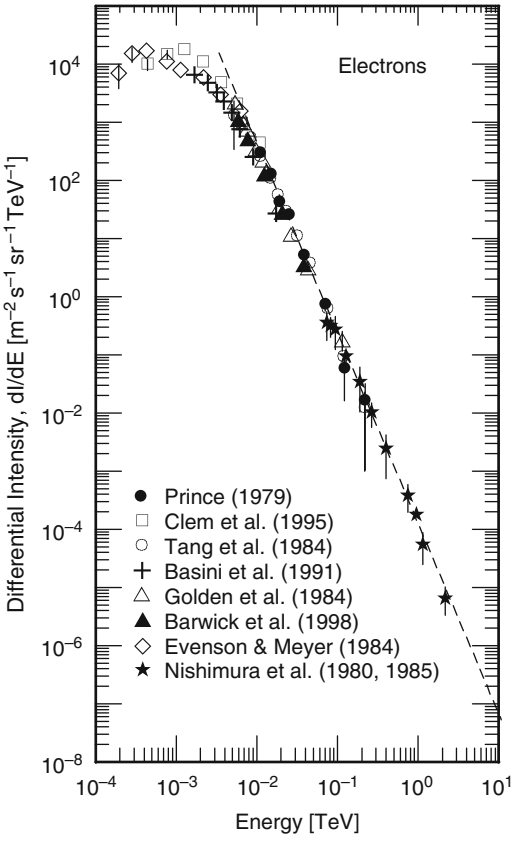

Fig. 11.3 Compilation of data on the primary electron spectrum from eight experiments (after Wiebel-Sooth, 1998, Wiebel-Sooth et al., 1998). The *dashed line* follows the relation $dI/dE = I_0 \cdot E^{-\gamma}$ $[(m^2 s\,sr\,TeV)^{-1}]$ with $I_0 = (0.95 \pm 0.19) \cdot 10^{-4}$, $\gamma = 3.26 \pm 0.06$ and E in TeV

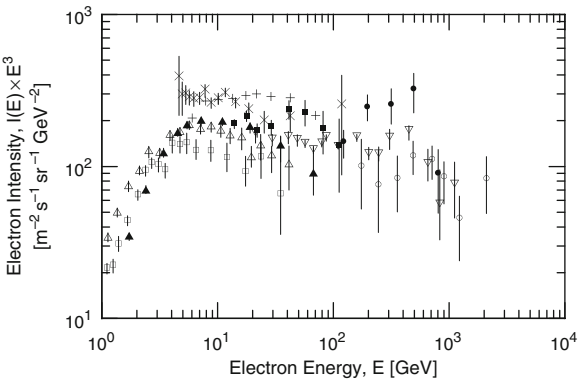

Fig. 11.4 Electron energy spectra of mostly recent measurements. Included are the data from the following experiments: + Tang (1984), × Golden et al. (1984a, b), □ Boezio et al. (2000), ▲ DuVernois et al. (2001), ■ Torii et al. (2001), △ Aguilar et al. (2002), ○ Kobayashi et al. (2004), ▽ Chang et al. (2005), and • Yoshida et al. (2007), (after Yoshida et al. 2007)

approximately as $E^{-3.3}$. A compilation in compressed form with the intensity multiplied by the energy to the third power including mostly recent measurements is displayed in Fig. 11.4.

The principal electron sources are expected to be relatively nearby. Since synchrotron radiation from high energy electrons is observed in *Super Nova Remnants*, it is likely that at least a fraction of the observed electrons may be produced by these objects.

The differential energy spectrum of cosmic ray positrons assembled from a variety of rather recent measurements is illustrated in Fig. 11.5 (Grimani, 2005). The curves show the result of theoretical studies for certain assumptions (Moskalenko and Strong, 1998; Harding and Ramaty, 1987; after Grimani, 2005).

11.3.3 Antimatter

The question concerning the presence of antimatter in the cosmic radiation, in particular of antiprotons and their spectral features are of relevance for astrophysical reasons, for cosmology and for questions that are related to the propagation of the cosmic radiation and the matter density in space. One of the fundamental questions in this context is whether cosmic ray antiparticles are of primordial origin or the result of high energy collisions of the primary cosmic radiation with the interstellar gas and dust.

Numerous balloon-borne experiments had been carried out in the past. However, this work was restricted for technical reasons, such as physical size, payload limitations and the duration the experiment was operational, to energies below 100 GeV. Figure 11.6 shows a compilation of low energy antiproton data from direct measurements carried out with balloon experiments at the fringes of the atmosphere.

A few attempts had been made in the low energy air shower domain using the shadow effect of the Sun and the Moon in conjunction with the geomagnetic field. We outline here very briefly the nice work carried out by the Tibet air shower group (Amenomori 1993; Amenomori et al., 1995, 2005, 2007), using this technique.

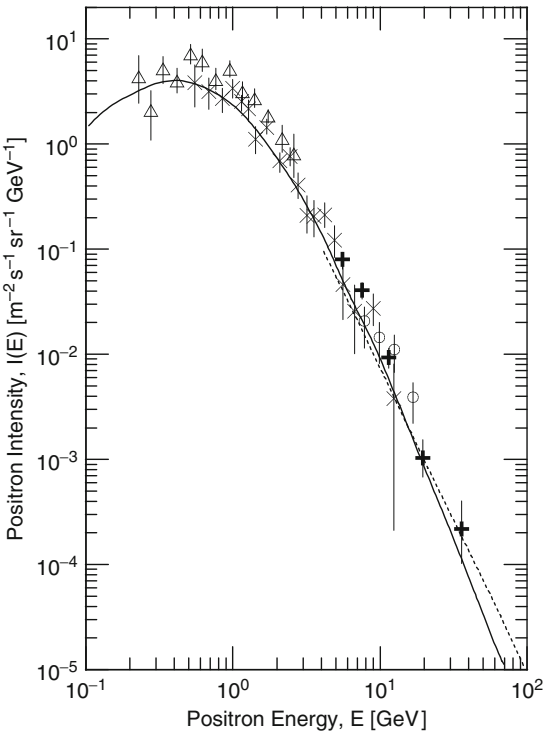

Fig. 11.5 Differential energy spectrum of cosmic ray positrons. The data are from the following authors: ○ Grimani et al. (2002); △ Alcaraz et al. (2000a); × Boezio et al. (2000); + Barwick et al. (1998) (after Grimani, 2005)

The Moon shadow of all cosmic rays as observed on Earth is given by the relation

$$f_1(\theta) \;=\; \sum_{i=1}^{4} A_{\mathrm{all},i} \exp\left(-\frac{4\ln 2\cdot(\theta - M_{\mathrm{all},i})^2}{\sigma^2_{\mathrm{all},i}}\right) , \tag{11.1}$$

and for protons only by

$$f_2(\theta) \;=\; \sum_{i=1}^{4} A_{p,i} \exp\left(-\frac{4\ln 2\cdot(\theta - M_{p,i})^2}{\sigma^2_{p,i}}\right) , \tag{11.2}$$

where θ is the angular distance from the center of the Moon in the *west-east direction*, and A, M and σ are the fitting parameters for the distribution function for all cosmic rays and for protons only, respectively.

The observed Moon shadow is expressed by the function

$$f_3(\theta) \;=\; a\, f_1(\theta) + b\, f_2(\theta) , \tag{11.3}$$

where the first term is the deficit in cosmic rays and the second term the deficit in antiprotons.

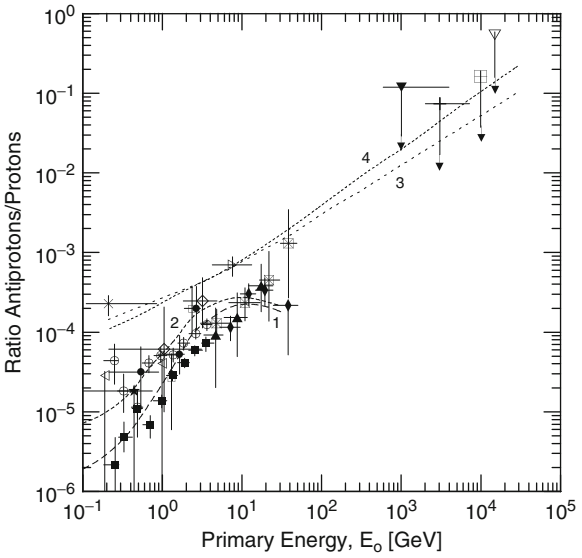

Fig. 11.6 Antiproton to proton ratio on *top* of the atmosphere and in the vicinity of the Earth. The symbols represent the following experiments: × Buffington et al. (1981); ▷ Golden et al. (1984a, b); ◇ Bogomolov et al. (1987); ⋆ LEAP, Streitmatter et al. (1990); ◁ PBAR, Salamon et al. (1990); • IMAX, Mitchell et al. (1996); □ CAPRICE 1997, Boezio et al. (1997); ▲ Basini et al. (1999); ■ BESS 1999 and ○ BESS 2000, Asaoka et al. (2002); ⊠ CAPRICE 2001, Boezio et al. (2001); ♦ HEAT 2001, Beach et al. (2001); ▽ MACRO 2003, Ambrosio et al. (2003); ▼ L3+C, Achard et al. (2005); ⊞ Tibet-I 1990-1993, Amenomori (1995); + Tibet-II 1999-2004, Amenomori (2007). The *dashed lines 1 and 2* represent leaky box model *upper* and *lower limits* from calculations by Simon et al. (1998). The *lines 3 and 4* are for a model that includes leaky box and the presence of anti-stars. The rigidity dependent confinement of the cosmic radiation in the Galaxy is assumed to be $\propto R^{-\delta}$ and *curves 3 and 4* apply to $\delta = 0.7$ and $\delta = 0.6$ (Stephens and Golden, 1987). (After Amenomori, 2007; see also Yoshida et al., 2005)

From their simulations that include the geomagnetic field distribution, Amenomori (2007) estimate the fraction of protons to all cosmic rays to be $62 \pm 1\%$. Thus, the ratio $b/0.62a$ corresponds to the $\overline{p}/p$ ratio and the observed antiproton deficit can be fitted by the function $f_3(\theta)$ with the parameters $a = 1.64 \pm 0.10$ and $b = -0.10 \pm 0.08$ (for $\chi^2/d.o.f. \sim 1.50$), for the boundary condition that the integral of $af_1(\theta)$ must be smaller than the total number of observed events.

The result of this work is given in Fig. 11.6 together with a data point from earlier work at the same site using the shadow of the Sun (Amenomori, 1995). Also shown are the multi-TeV results from a similar measurement with MACRO (Ambrosio et al., 2003) and the L3 + C experiment at CERN (Achard et al., 2005). These data together with the previously mentioned results from the direct measurements reveal our current knowledge on antiprotons in the cosmic radiation.

The ratio of antihelium to helium had also been investigated by various authors as well as the presence of heavier antinuclei. Figure 11.7 summarizes the anti-helium data.

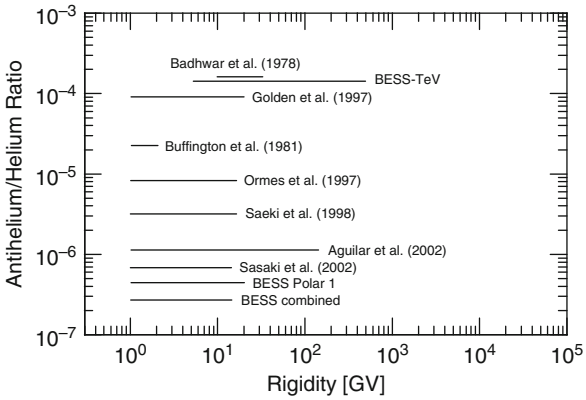

Fig. 11.7 Antihelium flux limits from many experiments, as listed. The BESS data are after Hams et al., 2007

11.4 Gamma Radiation

The spectrum of energetic primary photons is divided into the *X-ray* and *gamma ray* domains. The division between the two domains does not necessarily reflect the usual physical process of origin of the radiation but is drawn more arbitrarily according to photon energy. Radiation up to 100 or 200 keV is usually referred to as X-rays, sometimes the domain boundary is taken at 0.5 MeV, and the more energetic radiation is called gamma rays.

Referring to the gamma radiation, we distinguish basically between gamma rays from *point sources* and the *diffuse gamma radiation*. In particular regions of the sky enhanced radiation is observed that is often referred to as *extended sources*. Point sources are well defined and localized gamma ray emitters that can frequently but not necessarily be associated with astronomical objects that had been known before as emitters in other wavelength windows, such as the optical or radio bands.

Because of the atmospheric absorption and the atmospheric gamma ray background, low energy extra-terrestrial gamma ray measurements can only be made with balloon or satellite bound instruments. However, very high energy gamma rays initiate extensive air showers that have specific characteristics that permit to identify them as such. Moderately energetic events where the particles of the gamma ray initiated electromagnetic cascade do not reach ground level can be observed with suitable ground based atmospheric optical Cherenkov detector telescopes or large aperture Cherenkov detector arrays, preferentially at elevated (mountain) altitudes to lower the detection threshold energies. Cherenkov detector arrays require higher threshold energies to detect an event than telescopes that use large mirrors for the light collection. However, high energy photon initiated air showers can be detected with particle detector arrays at ground level. These are usually combined with muon detectors to improve the discrimination against hadron initiated showers to prevent misinterpretation.

The first gamma ray telescope in a terrestrial orbit was on board of the Explorer-XI satellite in 1961. The results of these measurements suggested an omnidirectional, uniform gamma ray background. The existence of energetic gamma rays in and

from space had been discovered by Kraushaar et al. (1972). These authors noted that emission from the Galactic Plane is the main feature of the high energy gamma ray sky, but that there is a general low level omnidirectional background. Since the late sixties and in the seventies many satellite-based measurements were made with a variety of instruments that led to the discovery of numerous point sources that initiated the rapidly growing field of gamma ray astronomy.

Because the Galaxy is essentially transparent to gamma rays up to energies of about 10^{14} eV (see Sect. 11.11.6) and because the gamma ray production mechanisms are well known, and similarly the interstellar gas distribution, a variety of quantitative calculations can be made readily about the cosmic ray distribution in space, and vice versa, if we assume a homogeneous cosmic ray density (Bertsch et al., 1993, and references therein).

11.4.1 Diffuse Gamma Radiation

The conventional theory of the diffuse gamma ray production considers mainly three mechanisms. These comprise *bremsstrahlung, inverse Compton scattering of electrons*, and the *decay of neutral pions* that originate from collisions of nucleons and nuclei of the cosmic radiation with the interstellar gas, dust and radiation. In addition there is an extragalactic contribution, presumably from a large number of unresolved distant point sources (Smialkowski et al., 1997). Figure 11.8 shows spectra obtained from calculations considering the conventional model and assumptions

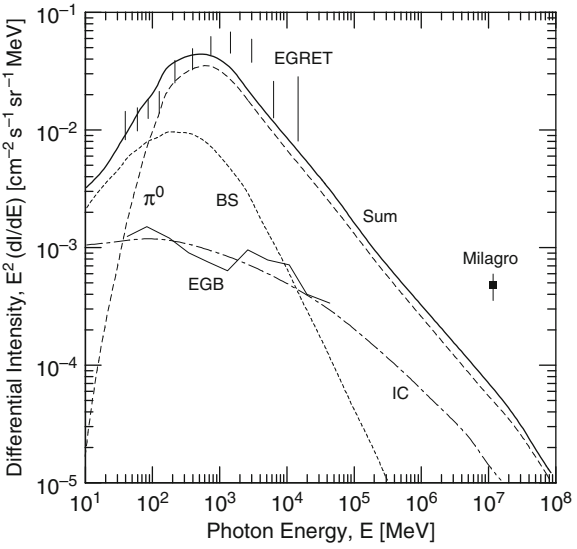

Fig. 11.8 Diffuse gamma ray spectrum showing the sum resulting from the different contributing processes according to the conventional theory that comprise neutral pion decay (π_0), bremsstrahlung of electrons (BS), inverse Compton scattering (IC), and the extragalactic background component (EGB). Also shown are the results obtained from the satellite experiment EGRET and a high energy data point from measurements with the Milagro detector (Smith, 2005) of the Cygnus region which manifests an enhanced intensity (after Abdo et al., 2007)

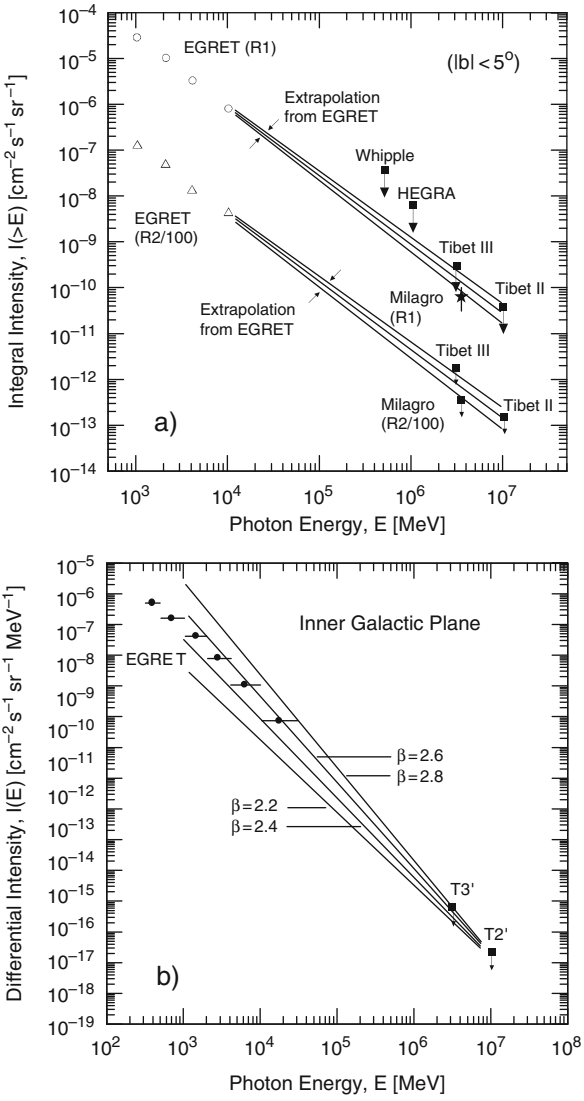

Fig. 11.9 (**a**) Integral intensity of diffuse gamma rays as measured by the Milagro (Atkins et al., 2005) and EGRET (Hunter et al., 1997) detectors from two regions having galactic longitudes $R1\,[l \in (40°, 100°)]$ and $R2\,[l \in (140°, 200°)]$, both with latitude $|b| < 5°$. Also shown are *upper limits* from measurements made by Whipple $[l \in (38.5°, 41.5°), |b| < 2°]$ (LeBohec et al., 2000), HEGRA $[l \in (38°, 43°), |b| < 5°]$ (Aharonian et al., 2001), and two data sets from the Tibet array $[l \in (20°, 55°), |b| < 5°]$, (Amenomori et al., 2002, Amenomori, 2006). Note that the data of the R2 region are divided by a factor of 100 to prevent overlapping. (**b**) Analogous data showing recent Tibet array results from the inner Galactic Plane (Amenomori, 2006) and old EGRET data. The *lines* show power law spectra with different slopes β for comparison

(Strong et al., 2004). Also shown are data from the EGRET satellite experiment and the Milagro detector.

A compilation of diffuse gamma ray data from different ground-based experiments that extend over a wide energy range is displayed in Fig. 11.9a which shows the integral energy spectrum. The data are from two different celestial regions, R1 and R2, as specified in the caption. The high energy data points ($E_\gamma > 10^5$ MeV) had been obtained using the atmospheric Cherenkov technique. Note that the data of the R2 region are divided by a factor of 100 to prevent overlapping. Included, too, are the corresponding data from EGRET satellite measurements.

The two revised data points from the Tibet experiment (Amenomori, 2006) using the air shower array as illustrated in Fig. A.31 of Appendix A are plotted in the

differential energy spectrum shown in Fig. 11.9b. The lines that emerge from point T2' at 10 TeV represent extrapolated power law spectra towards the EGRET data points and have spectral indices, β, as indicated. They serve as guide lines and suggest the spectral trend.

Among others, Amenomori (2006) have investigated the gamma ray emission above 1 TeV from the inner and outer Galactic Plane with the high altitude Tibet air shower array. Their results together with the data from other experiments as listed in the caption are reproduced in Figs. 11.10a, b. Also shown are predicted spectra due to inverse Compton scattering (IC) from the theoretical work of Porter and Protheroe (1997) and Tateyama and Nishimura (2003).

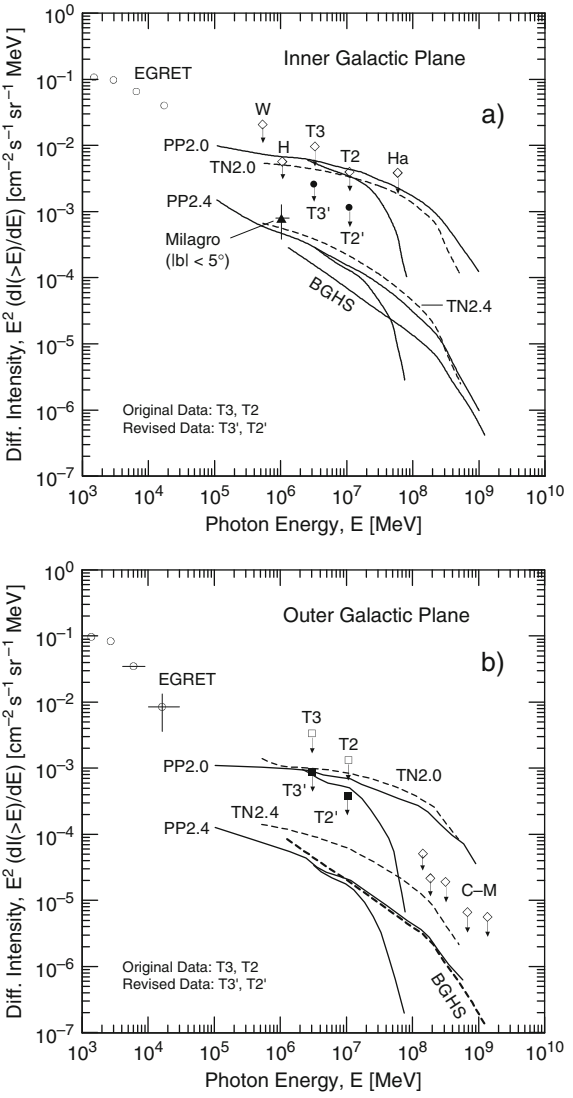

Fig. 11.10 Diffuse differential gamma ray spectral data of the inner (**a**) and outer (**b**) Galactic Plane obtained by EGRET and *upper limit* data points from other experiments: W, Whipple (LeBohec et al., 2000); H, HEGRA (Aharonian et al., 2001); Ha, HEGRA-AIROBICC (Aharonian et al., 2002); C-M, CASA-MIA (Borione et al., 1998); Milagro (Fleysher et al., 2005); T2 and T3 Tibet array II and III, respectively (Amenomori et al., 2002), and T2' and T3' Tibet array II and III, respectively (Amenomori, 2006). The *curves* are from model calculations for the IC process: PP2.0 and PP2.4 (Porter and Protheroe, 1997), TN2.0 and TN2.4 (Tateyama and Nishimura, 2003), where 2.0 and 2.4 stand for the source electron spectral indices. *Curve BGHS* identifies contribution of hadronic origin (π_0) (Berezinsky et al., 1993) (after Amenomori, 2006)

11.4.2 Gamma Ray Point Sources

The search and investigation of gamma ray point sources is the vast field of gamma ray astronomy which is beyond the scope of this book. The interested reader is referred to the excellent reviews of Weekes (1988) and Ong (1998), the rapporteur papers presented at cosmic ray conferences and specialized conferences, e.g., Weekes et al. (2003), Ong (2005), and the books by Schönfelder (2001) and Aharonian (2004), just to mention a few.

As an example of an integral energy spectrum of a gamma ray source we present in Fig. 11.11 a compilation of data from measurements made by several different atmospheric Cherenkov telescopes of the Crab Nebula (see cover picture) (Konopelko et al., 1996). This object (catalogue designations M1, NGC 1952, Taurus A) is at an estimated distance of 2 ± 0.5 kpc (6.5 ± 1.6 kly) from the Earth and is the remnant of the supernova SN-1054 that was observed in the year 1054 AD in China, as old records prove (Brecher et al., 1983). Recently some old European records were discovered in Belgium and independently in Italy that confirm the occurrence of the supernova at that time (Guidoboni et al., 1992).

The Crab Nebula is a steady emitter of TeV gamma rays in our own Galaxy. It is considered the *standard candle* of TeV gamma ray astronomy. In addition, we

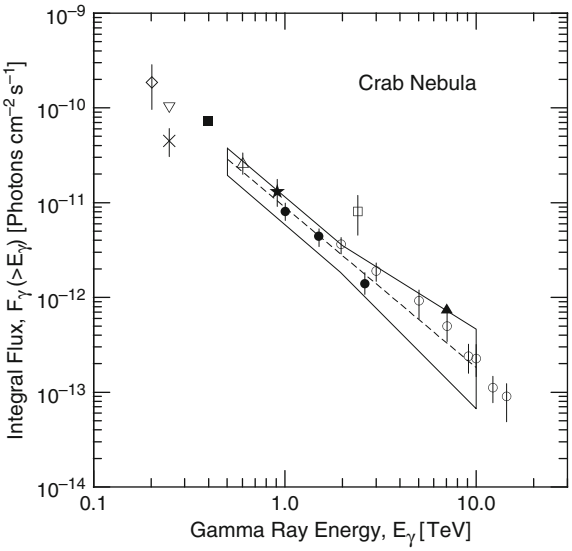

Fig. 11.11 Integral gamma ray flux from the Crab Nebula, $F_\gamma(> E_\gamma)$ [ph cm^{-2} s^{-1}], measured with the second HEGRA telescope during the 1994/1995 observation period. The fluxes reported by other groups are also shown for comparison: ◇ Akerlof et al. (1989, 1990); ▽ Whipple (Lessard et al., 1995); × Smithsonian group (Fazio et al., 1972); ■ Whipple (Vacanti et al., 1991); △ ASGAT (Goret et al., 1993); ⋆ CrAO (Stepanian, 1995); ● HEGRA (Konopelko et al., 1996); ○ Themistocle (Goret, 1994); □ HEGRA (Krennrich, 1995, Ph. D. Thesis Unpublished); ▲ CANGAROO (Tanimori et al., 1994). The *dashed line* indicates the best fit spectrum of the Whipple spectral analysis (Lewis et al., 1993) with the corresponding error box (*solid line*) (after Konopelko et al., 1996)

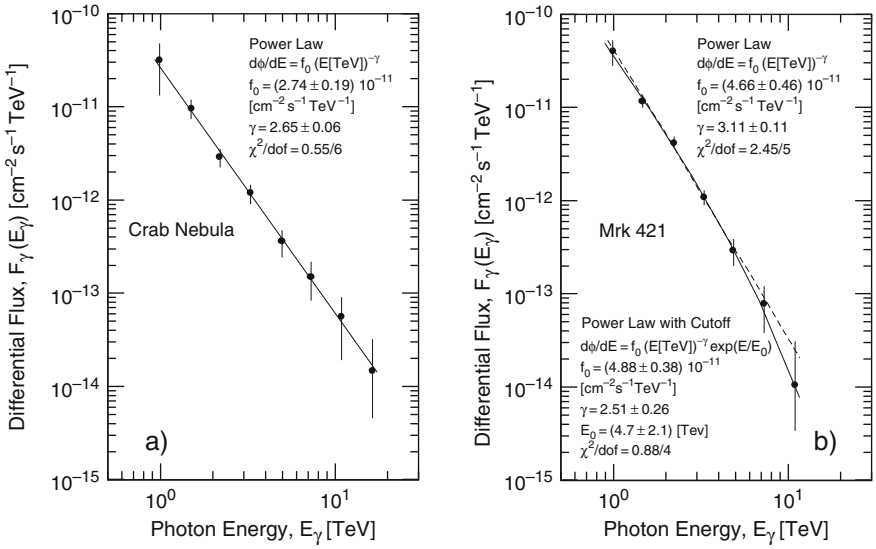

Fig. 11.12 Differential gamma ray energy spectrum of the Crab Nebula (**a**) and Markarian Mrk-421, (**b**), when the latter was in a high state, obtained by the TACTIC telescope at Mt. Abu (1,300 m a.s.l.), in India (Yadav et al., 2007)

show in Fig. 11.12 the differential energy spectrum of the Crab Nebula and of the extragalactic source Markarian Mrk-421. These spectra were obtained from measurements made with the atmospheric Cherenkov detector installation TACTIC in India (Acharya, 2005). Both of these sources and many others are intensely studied by many groups.

Besides the steady (dc-like) emission from the Crab Nebula, there appears to be also a pulsed TeV and PeV gamma ray emission from the Crab Pulsar (PSR B0531+21) (Rao and Sreekantan, 1992) which is a relatively young neutron star. This pulsed high energy gamma ray emission is not so firmly established (Acharya et al., 2007). The pulsar is located in the center of the nebula and is a remnant of the supernova SN-1054. It was discovered in 1968 and was the first pulsar that could be linked with a supernova remnant (Zeilik and Stephen, 1998).

11.5 Established and Predicted Neutrino Spectra

Our present knowledge of the extra-terrestrial neutrino flux at Earth is very limited. Experimentally confirmed are only the solar neutrinos (Bahcall, 2000) and the unique neutrino burst from the supernova SN-1987a (Schramm, 1987). The corresponding spectra are plotted in the compilation of Koshiba (1992) reproduced in Fig. 11.13.

Up to date no other extra-terrestrial neutrinos have been detected knowingly. However, we expect to detect neutrino fluxes from a variety of astrophysical objects,

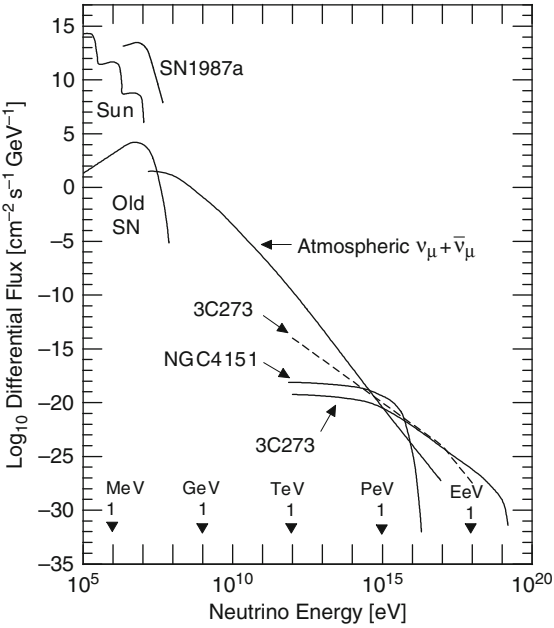

Fig. 11.13 Predicted differential energy spectra of neutrinos of some point sources. The predicted and measured atmospheric flux applies to 2π steradian (Volkova, 1980; Koshiba, 1992). The ν_μ ($\overline{\nu}_\mu$) spectra of the two point sources, NGC4151, the brightest radio-quiet AGN, and 3C273, the brightest radio-loud AGN, (*solid curves*) are from a calculation of Stecker et al. (1991, 1992a, b). The calculation is based on assumed X-ray luminosities of $L_X = 3 \cdot 10^{43}$ erg s^{-1} and $L_X = 10^{47}$ erg s^{-1}, and distances of $4.5 \cdot 10^{25}$ and $3 \cdot 10^{27}$ cm for NGC4151 and 3C273, respectively. The ν_e , $\overline{\nu}_e$ intensity is half of that of the ν_μ , $\overline{\nu}_\mu$ intensity. The *dashed line* labeled 3C273 is a predicted neutrino spectrum of this object from the work of Szabo and Protheroe (1994) using different assumptions. The measured solar and SN1987a fluxes are taken from Koshiba (1992)

such as active galactic nuclei (AGN), binary systems, quasars, blazers, and others with suitable detectors. These sources should manifest themselves as high energy neutrino point sources.

In addition to neutrino point sources we expect to see a *diffuse* neutrino background from unresolved distant sources as well as from the decay of collision products resulting from the interactions of the cosmic radiation with matter and radiation in galactic and extragalactic space (Stecker, 1979). Lacking any experimental guidance we must rely at present on predictions that are based on different theoretical models and assumptions.

11.5.1 Atmospheric Background

The detection of neutrinos from beyond the solar system is difficult because of the large background of cosmic ray induced atmospheric neutrinos, mainly ν_μ and $\overline{\nu_\mu}$

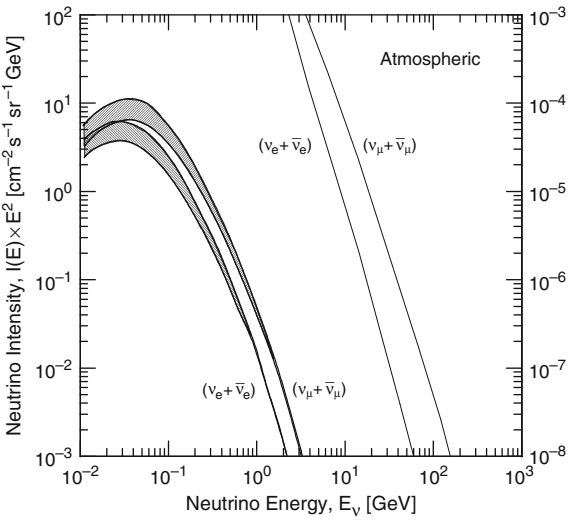

Fig. 11.14 Differential energy spectrum of atmospheric neutrinos as labeled in the figure. The *upper curve* of the shaded regions is for solar minimum, the *lower* for solar maximum (after Gaisser et al., 1988; see also Gaisser, 2006)

from pion and kaon decays, and to a lesser extend ν_e and $\overline{\nu_e}$ from muon decays. Figure 11.14 shows the energy spectra of the vertical atmospheric neutrino components (($\nu_e + \overline{\nu_e}$) and ($\nu_\mu + \overline{\nu_\mu}$)) from 10 MeV to over 100 GeV. The hatched areas show how the spectra change from solar minimum to solar maximum due to the solar modulation of the primary hadronic cosmic radiation (Volkova and Zatsepin, 1999).

The reason for the lower intensity of the electron neutrino background is that twice as many muon neutrinos (antineutrinos) are produced in the pion-muon decay chain than electron neutrinos (antineutrinos),

$$\begin{aligned} \pi^+ &\rightarrow \mu^+ + \nu_\mu \\ \mu^+ &\rightarrow e^+ + \nu_e + \overline{\nu_\mu} \\ \pi^- &\rightarrow \mu^- + \overline{\nu_\mu} \\ \mu^- &\rightarrow e^- + \overline{\nu_e} + \nu_\mu . \end{aligned}$$

The ratio R of muon to electron neutrinos and antineutrinos,

$$R = \frac{\nu_\mu + \overline{\nu_\mu}}{\nu_e + \overline{\nu_e}} \tag{11.4}$$

increases with increasing energy above about 1 GeV because muons begin to reach the ground before they decay, which reduces their contribution to the neutrino flux (Gaisser, 2006). Recent predictions for the flavor ratio had been carried out by Battistoni et al. (2003a, b), Honda et al. (2004) and Barr et al. (2004).

Besides the atmospheric neutrino background there is another purely terrestrial background of electron neutrinos and antineutrinos from the decay of radioactive

isotopes in the Earth. However, this background is of very low energy and of no concern for the detection of high energy neutrinos of all flavors of astrophysical origin.

Since the spectra of neutrinos of atmospheric origin drop rapidly, except for the small contribution of *prompt neutrinos*, and because neutrinos from astrophysical sources are expected to have a *harder spectrum*, the search for neutrinos from beyond the solar system must be focused on high energy neutrinos that should become the dominating component in the multi-TeV region, according to predictions of current model calculations (c.f. Fig. 11.13).

11.5.2 Model Predictions

Several authors have carried out calculations and simulations to estimate neutrino fluxes and energy spectra from specific astrophysical objects that are likely sources, and the intensity of the diffuse neutrino background (e.g., Stecker et al., 1991, 1992a, b; Szabo and Protheroe, 1994). The result of some of these calculations showing the differential neutrino *flux* of two particular AGNs, NGC4151 and 3C273, are plotted in Fig. 11.13.

The estimates that we have presently available on the intensity of the *diffuse (isotropic)* flux of extra-terrestrial neutrinos from all sources combined, e.g., active galactic nuclei, gamma ray bursters (GRB), cosmological sources, including *super massive particles (top-down mechanisms)*, *Z-bursts* (Weiler, 1999) and cosmic ray interactions in space range from between 3 and 100 times less than the cosmic ray intensity (Stecker et al., 1991, 1992a; Stecker and Salamon, 1996; Waxman and Bahcall, 1997; Sigl et al., 1999; Yoshida et al., 1998). All predictions of the intensity and the spectral shape are based on a variety of assumptions and theoretical considerations, most of which hinge in one way or another on data from observations made in other radiation windows.

In Fig. 11.15 we show a summary of the available experimental data on high energy neutrinos from measurements with the AMANDA II detector (Münich et al., 2005) and the highest energy point of the spectrum measured by the Fréjus experiment (Daum et al., 1995). Shown, too, are upper limits from the MACRO (Ambrosio et al., 2002) and the Lake Baikal experiments (Aynutdinov et al., 2006; Antipin et al., 2007). In addition, upper limits from predictions of various models as listed in the figure caption are also indicated, and the Baikal limit for the so-called Glashow resonance ($\star$) (Glashow, 1960), i.e., the electron antineutrino resonance reaction

$$\overline{\nu_e} + e^- \rightarrow W^- \rightarrow \text{anything}$$

Obviously high energy neutrino point sources are the most likely to be detected first with large neutrino detectors, such as Ice Cube (Ishihara et al., 2007) or the

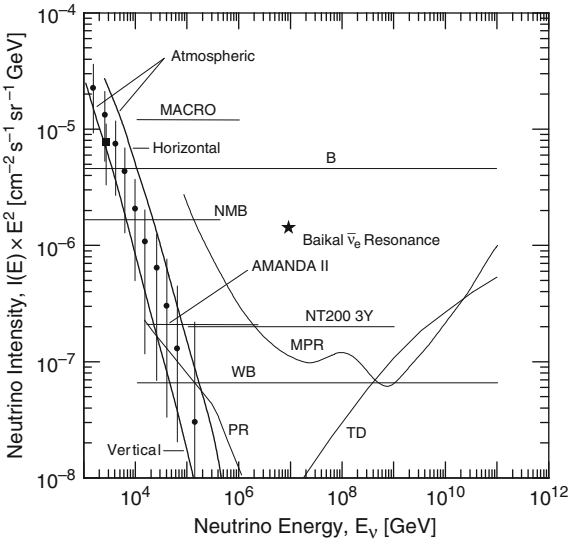

Fig. 11.15 Differential all-flavor diffuse neutrino intensity predictions for different models of neutrino sources compared to experimental *upper limits: B* (Berezinsky et al., 1990; model independent), NMB (Nellen et al., 1993; diffuse intensity from AGNs), MPR (Mannheim et al., 2002; superposition of extragalactic sources), TD (Semikoz and Sigl, 2003; topological defects), WB (Waxman and Bahcall, 1999). Shown, too, are the conventional atmospheric neutrino intensities for vertical and horizontal directions and the contribution from prompt neutrinos, PR, by Volkova and Zatsepin (1999). The symbols • show the measurements of AMANDA II (Münich et al., 2005) and ■ is the highest energy point from the Fréjus experiment (Daum et al., 1995). *Upper limits* are indicated for MACRO (Ambrosio et al., 2002) AMANDA II and for the Baikal NT-200 experiment after a 3 year run (Aynutdinov et al., 2006; Antipin et al., 2007). The symbol ⋆ indicates the model independent limit on $\overline{\nu_e}$ at the W-resonance (Glashow resonance, Glashow, 1960)

various proposed giant deep ocean detector matrices such as the pioneering but later on discontinued DUMAND detector (Babson et al., 1990; Grieder, 1993), because of a more favorable signal to noise ratio than for the diffuse component. If we detect a neutrino point source and if this source is at the same time a gamma ray emitter we can deduce important astrophysical properties of the source and its surroundings.

11.5.3 Neutrino Induced Air Showers

High energy neutrinos of all sorts, including ν_τ and $\overline{\nu_\tau}$, can occasionally initiate extensive air showers that can be detected with conventional detector arrays. They are expected to initiate most likely in the deeper regions of the atmosphere, preferentially as inclined or horizontal showers. Neutrinos that penetrate the Earth may

also trigger upward or sideways going showers that emerge from the ground or from a mountain side as a result of neutrino interactions in the soil, the deep atmosphere, or in rock, as briefly discussed in Sect. 1.3. Upward and sideways going showers can easily be detected with Fly's Eye type air fluorescence detectors.

An important point to remember in this context is that at $E_\nu \sim 40\,\text{TeV}$, the neutrino interaction length is approximately equal to the diameter of the Earth (see Fig. 5.15). At higher energies, neutrino fluxes having trajectories that cross the Earth's core are significantly attenuated (Kwiecinski et al., 1999).

Cocconi was the first to suggest that neutrinos could be the most energetic cosmic rays (Cocconi, 1967; Berezinsky and Zatsepin, 1969; Domokos et al., 1993; Domokos and Kovesi-Domokos, 2006). Ultrahigh energy neutrinos can contribute to the flux of the most energetic air showers and are not subject to the Greisen-Zatsepin-Kuzmin (GZK) cutoff like the hadronic component (Greisen, 1966; Zatsepin and Kuzmin, 1966; Domokos and Kovesi-Domokos, 2003). Very recently the Auger collaboration has made a first analysis of data from near horizontal air showers (Bigas et al., 2007). The results are presented in Fig. 11.16 together with a recent summary of astrophysical neutrino flux limits from different experiments.

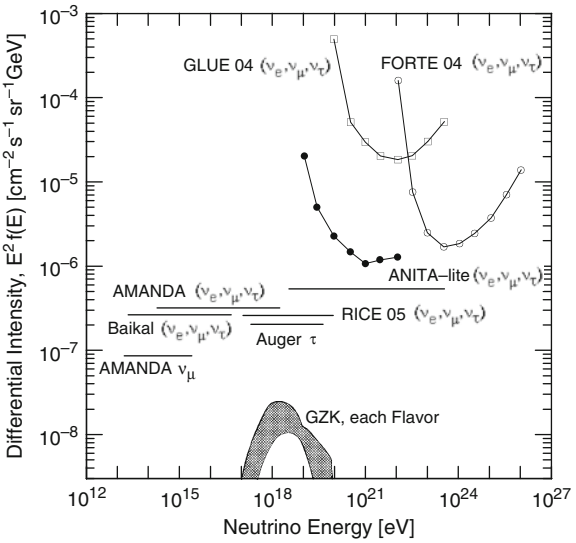

Fig. 11.16 Limit at 90% C.L. to an E^{-2} diffuse flux of ν_τ at EeV energies obtained from Auger Observatory measurements, and limits from other experiments: Auger (ν_τ) (Blanch-Bigas et al., 2007); AMANDA-B10 (ν_e, ν_μ, ν_τ) (Ackermann et al., 2005); AMANDA (ν_τ) (Achterberg et al., 2007); ANITA-lite (ν_e, ν_μ, ν_τ) (Barwick et al., 2006); Baikal (ν_e, ν_μ, ν_τ) (Aynutdinov et al., 2006); FORTE-04 (ν_e, ν_μ, ν_τ) (Lehtinen et al., 2004); GLUE-04 (ν_e, ν_μ, ν_τ) (Gorham et al., 2004); RICE-05 (ν_e, ν_μ, ν_τ) (Kravchenko et al., 2006). Also shown is the intensity expected from GZK neutrinos (Berezinsky and Zatsepin, 1969; Allard et al., 2006; Engel et al., 2001; after Blanch-Bigas et al., 2007)

11.6 High Energy All-Particle Primary Spectrum

11.6.1 Introduction

One of the principal aims of high energy cosmic ray research today is to determine the *nature* and *energy* of the incident primary particles or quanta (photons) and their arrival direction. For hadronic primaries that initiate the bulk of all air showers the *mass* of the incident particle is of importance, too. These parameters are needed to construct the all-particle primary spectrum as measured with air showers, to resolve it into the component or mass-specific spectra, and to search for anisotropies in the arrival direction. They are also of relevance to resolve the questions related to the origin, acceleration and propagation of the cosmic radiation.

On the other hand, to study the air shower process in order to extract global or specific information on high energy hadronic interactions from air shower observables reliably, knowing the parameters that specify the shower initiating primary is a fundamental prerequisite.

Because of the rapidly falling spectrum with increasing energy, primary particles (hadrons) with energies in excess of about 1 PeV have such low intensities that they can no longer be detected directly, outside the atmosphere, with any reasonable effort.[2] The same statement applies to electrons and photons as well, except that in this case the energy limits are about 1 TeV and 100 GeV, respectively (see Sect. 11.3). Thus, indirect observations of effects caused by these particles and photons in the atmosphere, in particular of air shower phenomena, with ground based detectors offer the only possibility to study the high energy portions of the respective spectra.

However, extracting the parameters of the primary from air shower observables is an extremely difficult task. The numerous interactions that occur in the shower process during the development and propagation of an air shower in the atmosphere mask these parameters heavily. Moreover, our accurate knowledge of high energy hadronic interactions that control the cascade process in common air showers is confined to the accelerator and collider energy range. Beyond that domain we depend on guidance from theoretical models, from observations of high and ultrahigh energy interactions of cosmic ray particles in emulsion chambers, and on information extracted from air showers in conjunction with shower simulations in a sort of trial and error approach.

In these simulations we use mainly phenomenological-mathematical models for the description of the hadronic interactions and parent processes that are carefully trimmed to reproduce existing accelerator and collider data correctly (see Chap. 3). Beyond the domain of machine particle physics, appropriate scaling of accelerator

[2] The event rate at 1 PeV is $\sim 1\,\mathrm{km^{-2}\,s^{-1}\,sr^{-1}}$ and at 1 EeV $\sim 0.1\,\mathrm{km^{-2}\,day^{-1}\,sr^{-1}}$.

and collider data must be performed by the interaction models. Thus, our predictions of the shower properties that we obtain from the simulations and use for comparison and interpretation of experimental shower observables hinge heavily on massive extrapolations that we push far beyond the energy regime of machine physics, as of early 2009. Consequently the predictions get less and less reliable with increasing energy.

In the preceding chapters, in particular in Chaps. 3, 4 and 5, we have discussed the fundamental processes that govern the development of air showers and outlined the different interaction models. In Chap. 2 we have presented the detection methods for air showers and the determination of the directly accessible elementary shower parameters. In Chaps. 8 and 10 we have given a detailed account of the many different methods that allow to extract the so-called indirectly accessible or hidden parameters that can be derived from the different shower observables with the help of more or less sophisticated air shower simulations. There we have also outlined the different techniques of analysis and correlations that play a key role to get at hidden parameters and distributions that allow eventually the determination of the energy of the primaries, the construction of the all-particle spectrum, to estimate the mass or mass group of the shower initiating primaries and the energy dependence of the mass composition.

The chapters mentioned above deal chiefly with the particle component of the showers. On the other hand, the detection, evaluation and interpretation of *optical* and *radio* emission of air showers, i.e., of the effects that do not affect the shower development noticeably, such as the shower accompanying *Cherenkov*, *fluorescence* and *radio* bursts, are discussed in the specific chapters that deal exclusively with these topics (Chaps. 16, 17 and 18, respectively).

In view of the contents of the above mentioned chapters, we restrict the discussion in this chapter and in particular in this and the next section to the presentation of spectral and compositional data which had been acquired by many different experiments without discussing details of the employed procedures and analyses, pointing out only the methods used and peculiarities of interest.

The problems of energy and mass determination essentially converge to a single problem because both, the energy and the mass of the primary affect the shower development process. This becomes evident when comparing average proton and iron nuclei initiated showers that have the same total primary energy. In other words the effects of energy and mass of the primary on shower development are intimately coupled whereby the template of a shower gets fixed after the first few interactions within the boundaries of primary mass and energy specific fluctuations (Edge, 1976).

Moreover, the parameters of the initiating primary and those that characterize the hadronic interactions and cascade process are also intimately coupled and control essentially the entire air shower process. Disentangling and separating the effects of the different parameters is extremely difficult. We should note that apart from the aspects of shower development, knowing the properties of the primary radiation in the vicinity of the Earth is also essential for investigating the origin and propagation of the cosmic radiation.

11.6.2 Derived All-Particle Spectrum: Early Work

Irrespective of the nature of the primary one can estimate the total energy of a shower-initiating agent from the common shower size, N (N_{charged}) or N_e, and can thus construct a primary energy spectrum. Such a spectrum must therefore be expected to consist of a mix of particles, from protons to heavy nuclei and may include primary photons as well. It is therefore called the *all-particle primary energy spectrum*. Likewise, in place of the shower size one can use the muon shower size, N_μ, or the truncated muon size, N_μ^{tr}, but the conversion to primary energy is in this case more tricky.

It became clear at a very early stage of air shower research that the cosmic ray spectrum is very steep and extends to extremely high energies, in excess of 10^{18} eV (Clark et al., 1961). At that time Kulikov and Khristiansen (1958, 1959) made a discovery that still puzzles cosmic ray researchers today and is a steady topic at present-day conferences. While studying the shower size spectrum with their array at Moscow, these authors noticed that the size spectrum exhibits a kink, changing its slope from -2.5 ± 0.1 to -3.2 ± 0.3 at a size of about $8 \cdot 10^5$ (cf. Sect. 12.2). Likewise, Fukui et al. (1960) found from their measurements carried out at Tokyo a spectral slope change from -2.4 ± 0.1 below a size of about 10^6 to -3.0 ± 0.2 above. Similarly, Allan et al. (1962) working at Silwood (GB) near sea level found a *rapid change of slope* from -2.3 ± 0.1 to -3.0 ± 0.15 at a size of $6 \cdot 10^5$.

Thus, there appeared to be no doubt that the size spectrum is subject to a change of slope in the shower size range $10^5 \leq N_e \leq 10^6$ when measured at sea level. This kink is now called the *knee* of the primary spectrum. It is centered around ~ 3 PeV. Later on a similar kink (knee) was discovered in the muon size spectrum (Miura and Hasegawa, 1962; Stamenov et al., 1979), and much later a less significant *second knee* centered around a shower size of $\sim 10^8$, corresponding to a primary energy of roughly $5.0 \cdot 10^{17}$ eV. There the spectral index changes from about -3.0 to -3.2 (Yoshida and Dai, 1998).

Since the primary energy spectrum did not seem to show a cutoff, larger and larger arrays were built in order to accumulate better statistics and to search for a possible cutoff. However, instead of finding a cutoff the new large arrays of the sixties and early seventies of the last century revealed that the primary spectrum gets harder, exhibiting a decrease of slope from about -3.2 ± 0.1 to -2.75 ± 0.25 of the differential spectrum at a size between a few times 10^8 and 10^9, corresponding to an energy of $\sim 3 \cdot 10^{18}$ to 10^{19} eV. This decrease is called the *ankle* of the spectrum (see Figs. 11.17, 11.18, 11.19, 11.20 and 11.21).

From there on the spectrum appeared initially to continue towards the 10^{21} eV mark without giving an indication of the existence of the Greisen-Zatsepin-Kuzmin (GZK) cutoff (Greisen, 1966; Zatsepin and Kuzmin, 1966) (see Sect. 11.11). This phenomenon should begin to attenuate the intensity of the radiation at about 50–70 EeV ($5 - 7 \cdot 10^{19}$ eV) very heavily (Olinto, 2000; Stecker and Scully, 2005) because of the interaction of the particles with the Cosmic Microwave Background Radiation (CMBR) (Penzias and Wilson, 1965). The knees and the ankle in the shower size spectrum manifest themselves, too, in the all-particle energy spectrum,

which is evident because the shower size is closely correlated with the primary energy.

The apparent lack of an end of the spectrum triggered major experimental efforts for further exploration of the spectrum beyond the ankle. The status of spectral research at that time, i.e., in the sixties and seventies of the last century, is illustrated in Figs. 11.17, 11.18, 11.19, 11.20 and 11.21, which show all-particle primary energy spectra as they were derived from shower size and muon size measurements of the large arrays of the early epoch.

Figure 11.17 shows the spectrum over a wide energy range and includes data from low energy direct measurements, too. The portion beyond the knee shows the spectra as determined with the high altitude array at Mt. Chacaltaya in Bolivia (5,230 m a.s.l.) and the Volcano Ranch array in New Mexico (USA) (1,768 m a.s.l.). Also indicated are some data points from the large muon array (SUGAR) at Narrabri in Australia (260 m a.s.l.). The full spectrum as determined with this array which

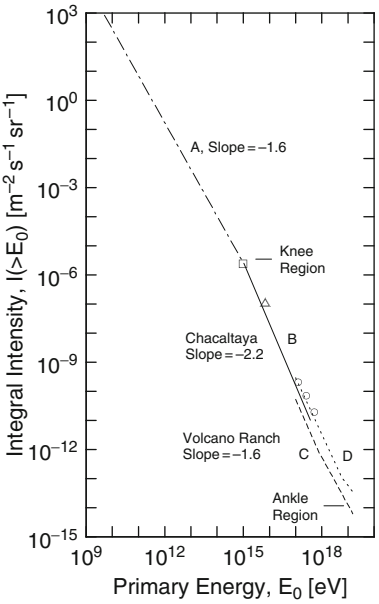

Fig. 11.17 Compilation of data of the all-particle integral primary energy spectrum obtained from early measurements at various altitudes. The *chain line, A*, with slope −1.6 indicates approximately that portion of the spectrum which covers the range from direct particle measurements to the small and medium air shower domain. The *solid line labeled B* was obtained from the Chacaltaya array (5,230 m a.s.l.) and has slope -2.2 ± 0.15 (Bradt et al., 1965), the *dashed portion, C*, with slope −1.6 shows the spectrum derived from measurements with the Volcano Ranch array (1,768 m a.s.l.) (Linsley, 1963) and *curve D* shows the result of Brownlee et al. (1970) from the SUGAR array in Australia. The symbols □, △ and ○ are data points from the work of Nikolsky (1962), Greisen (1960) (Cornell) and Egorov et al. (1971) (Yakutsk), respectively. The two regions where changes of the slope of the spectrum occur, the knee region and the ankle region are also indicated

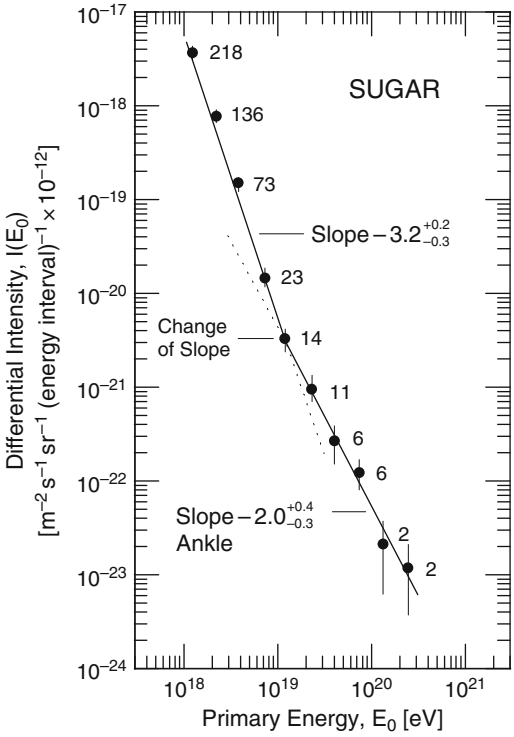

Fig. 11.18 All-particle differential primary energy spectrum derived from the muon size data obtained with the Sydney University's giant SUGAR array at Narrabri (Aus.) (260 m a.s.l.), interpreted for proton primaries (•). The *solid line* with the kink is a fit to the data. The change of slope is evident; the *dashed lines* are extrapolations of the two power law approximations, drawn to emphasize the change of slope (Brownlee et al., 1970)

had a muon threshold of 0.75 GeV is plotted in Fig. 11.18 and shows the ankle very well. Another comparison of the SUGAR data with other data that illustrates the smoothness of the spectrum over a very large energy range is displayed in Fig. 11.19.

Sea level data from the large arrays at Yakutsk in Siberia (105 m a.s.l.) and Haverah Park in England (212 m a.s.l.) are presented in Fig. 11.20 together with the near sea level data from SUGAR. We close this summary of early data with a comparison of the spectra from Chacaltaya, Haverah Park and Yakutsk plotted in Fig. 11.21. Shown, too, in this figure are some data points from atmospheric Cherenkov measurements made at Yakutsk.

Several causes were proposed to explain the existence of the first knee, ranging from the superposition of contributions from different sources of cosmic rays (Kulikov and Khristiansen, 1958) to rigidity dependent confinement of the charged hadronic component in the frame of the *leaky box model* (Peters, 1960, 1961; Cesarsky, 1980). Some authors even raised the question whether a change of the properties of ultrahigh energy hadronic interactions may possibly take place and be the cause for the knee. With respect to the ankle, the generally accepted belief was, and still is, that it is caused by the ultrahigh energy extragalactic component of the cosmic radiation that appears to have a harder spectrum, that takes over beyond about 10 EeV (10^{19} eV).

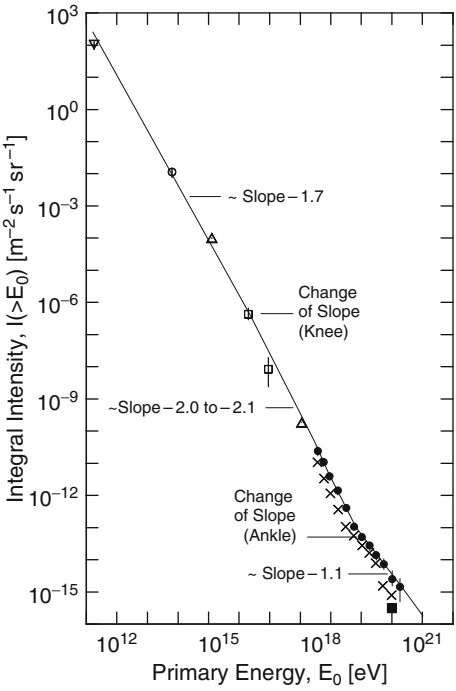

Fig. 11.19 Compilation of data of the all-particle integral primary energy spectrum from different altitudes. The experimental points • are the interpretation of the SUGAR array muon data, assuming proton primaries and × Cu primaries. The other data points are as follows: ▽ McDonald (1958), ○ McCusker and Peak (1964), both primary protons from direct measurements; △ Greisen (1965) (Cornell), □ Jauncey (1965) (Sydney array) and ■ Linsley (1963) (Volcano Ranch array), all air showers, proton interpretation. The *solid line* is an approximate fit to the proton data (after Brownlee et al., 1970)

11.6.3 Derived All-Particle Spectrum: Recent Work

With the coming into operation of a new generation of large air shower arrays, such as Akeno, CASA, MIA, AGASA , including the expanded and improved older array at Yakutsk, and the conceptually new Fly's Eye type fluorescence detectors, the exploration of the ultrahigh energy region of the primary all-particle cosmic ray spectrum continued and is continuing with the new giant cosmic ray observatories Auger and Telescope Array.

Beside these large installations a number of highly instrumented and sophisticated multipurpose experiments of medium size, such as the EAS-TOP on top of Gran Sasso in Italy (2,005 m a.s.l.), KASCADE (KASCADE Grande) at Karlsruhe in Germany (110 m a.s.l.) (both now shut-down) began operation in the eighties and nineties of the last century, and more recently GRAPES in Ootacamund, India (2,200 m a.s.l.) and GAMMA at Mt. Aragats, Armenia (3,250 m a.s.l.), to mention the most relevant. These experiments measured simultaneously a multitude of different shower observables which comprise the acquisition of hadron, muon, and electron data as well a atmospheric Cherenkov and radio emission. The detector systems were trimmed to determine not only the primary all-particle spectrum with high precision but also to go one step further and extract detailed information on the nature, in particular on the mass composition of the primaries that initiate air showers.

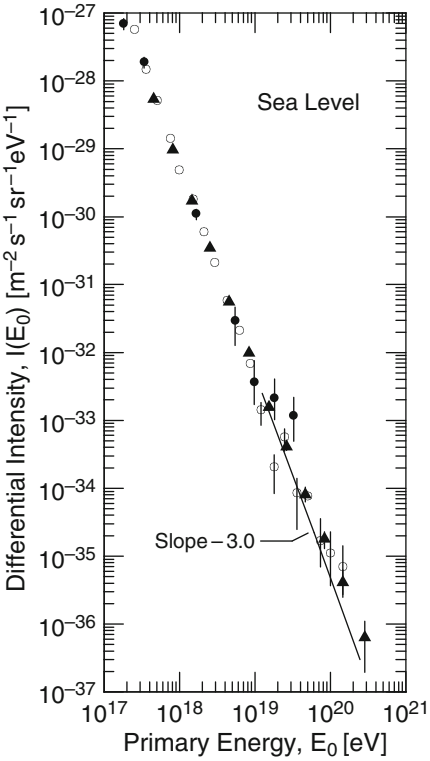

Fig. 11.20 Compilation of all-particle differential primary energy spectra derived from shower size measurements carried out near sea level with the arrays at Yakutsk (105 m a.s.l.) • (Krasilnikov et al., 1975) and Haverah Park (212 m a.s.l.) ○ (Edge et al., 1973), and from muon size measurements with SUGAR (Narrabri, Aus., 260 m a.s.l.) ▲ (Bell et al., 1971, 1973, 1974). The size spectra were converted to energy spectra using a very simple shower model (Hillas, 1971) and equal intensity cuts. The *solid line* indicates a slope of −3.0 of a power law spectrum, drawn for comparison (Krasilnikov et al., 1975)

These unique experiments and a selection of other, less spectacular experiments are briefly discussed below and in Sect. 11.7 where we discuss the composition. The layouts of many arrays are displayed in Appendix A, where many more experiments of the past and present that are not particularly mentioned in this section are listed in Table A.1. Note that the spectra plotted in this section have the ordinate which represents the intensity multiplied by the energy to some power, as indicated in each plot, in order to compress the scale and emphasize the details.

In Fig. 11.22 we show the comparison of two older spectra of the more recent era obtained with data from the Haverah Park (Cunningham et al., 1980a, 1989b; Linsley, 1980) and Yakutsk (Diminstein et al., 1982, b, Unpublished) experiments, made by Bower et al. (1983). The energy estimation at Haverah Park is based on the conversion of the $\rho(600)$ [veμ m^{-2}] energy deposit of the shower particle mix measured at 600 m from the shower axis in the deep water Cherenkov detectors, as explained in Chaps. 8 and 10. The Yakutsk energy estimate is based on both, $S(600)$ scintillator particle density and $Q(400)$ [ph m^{-2}] Cherenkov light photon density measurements (Dyakonov et al., 1979). In their analysis, the authors of the comparison have included the Volcano Ranch data (Linsley, 1973a) and have carefully considered the different methods of measurement and the density-energy conversions for the energy estimate. They conclude that the different methods are

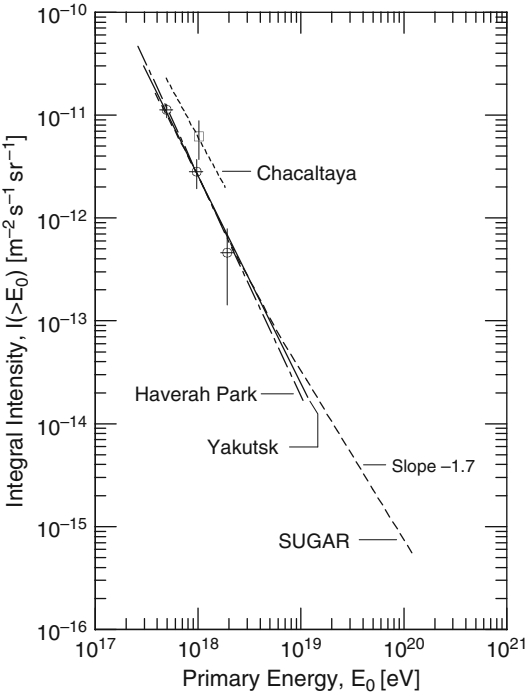

Fig. 11.21 Three data points of the all-particle integral primary energy spectrum obtained from air Cherenkov measurements at 400 m from the shower axis at Yakutsk (105 m a.s.l.) ○. The *solid line* is a power law fit to these data. Also shown are corresponding spectra from the Haverah Park (212 m a.s.l.) (Edge et al., 1973) and SUGAR (260 m a.s.l.) (Bell et al., 1973) arrays. Point □ and the short *dashed line* indicate the high altitude Chacaltaya (5,230 m a.s.l.) spectrum (La Point et al., 1968; Aguirre et al., 1973) which deviates significantly from the other spectra (after Krasilnikov et al., 1975; see also Watson, 1975)

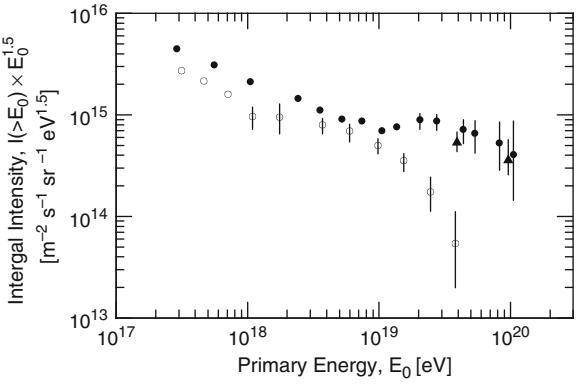

Fig. 11.22 Comparison of all-particle primary integral energy spectra above $2 \cdot 10^{17}$ eV obtained with the Haverah Park (●) (Cunningham et al., 1980a, b; Linsley, 1980) and Yakutsk arrays (○) (Diminstein et al., 1982, b). The two symbols ▲ indicate updated averaged intensities for energies $\geq 4 \cdot 10^{19}$ eV and $\sim 10^{20}$ eV, respectively, using the combined data from Volcano Ranch and Haverah Park (after Bower et al., 1983)

in excellent agreement, and that the only explanation that remains for the spectral disagreement beyond 10^{19} eV is that for some reason or other the Yakutsk array must have missed ultrahigh energy events.

A comparison of primary all-particle spectra obtained by several more recent experiments that cover the lower primary energy range from 10^{15} to 10^{18} eV is shown in Fig. 11.23. Included in this compilation are data from the classical particle detector arrays at Moscow (192 m a.s.l.) (Fomin et al., 1991), Akeno (900 m a.s.l.) (Nagano et al., 1992) and Tien Shan (3,340 m a.s.l.) (Vildanova et al., 1994), and from the air Cherenkov array Tunka (680 m a.s.l.) (Gress et al., 1999). Included, too, are results from the very novel experiment called SPHERE (Antonov et al., 1999, 2008).

This experiment (SPHERE-1) which uses an old suggestion of Chudakov (1972) consists of a cluster of 19 photomultiplier tubes that view a 1.2 m diameter spherical mirror (SPHERE-2 has 1.5 m mirror; Anokhina et al., 2007; Chernov et al. 2007). The assembly is attached to a tethered balloon with the mirror facing downward, collecting air shower induced Cherenkov light that is reflected from the frozen and snow covered Lake Baikal (elevation 455 m a.s.l.). The angular aperture of the optical detector system is about 50° and the altitude above ground is 1 km. The determination of the spectrum which involves extensive simulations hinges on the fact that the Cherenkov light is proportional to the shower energy. A wavelength shifter had been used. The authors specify a background light count of $(5.7 \pm 1.4) \cdot 10^{12}$ photons $m^{-2}\,s^{-1}\,sr^{-1}$.

In Fig. 11.24 we show the short section of the revised Haverah Park spectrum after the old data from the period 1974 to 1987 had been re-evaluated for two different assumed primary compositions and much improved shower simulations using the QGSJET-98 event generator with CORSIKA and the GEANT package for the detector response (Ave et al., 2003a). These data have some relevance for comparison with the Auger data resulting from the surface array which uses similar detectors and methods.

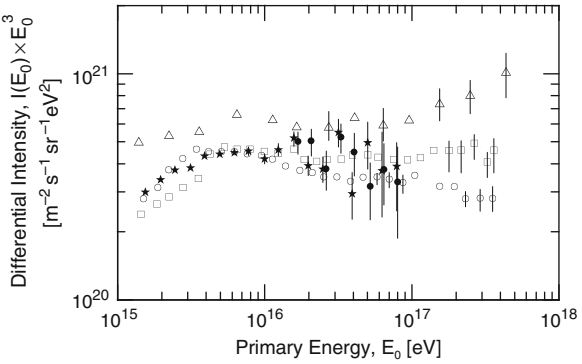

Fig. 11.23 Compilation of differential all-particle primary energy spectra of the knee region obtained by the following experiments: • SPHERE (Antonov et al., 1999; see also Antonov et al., 2008); ○ Moscow (Fomin et al., 1991); □ Akeno (Nagano et al., 1992); △ Tien Shan (Vildanova et al., 1994); and ⋆ TUNKA (Gress et al., 1999) (after Antonov et al., 1999)

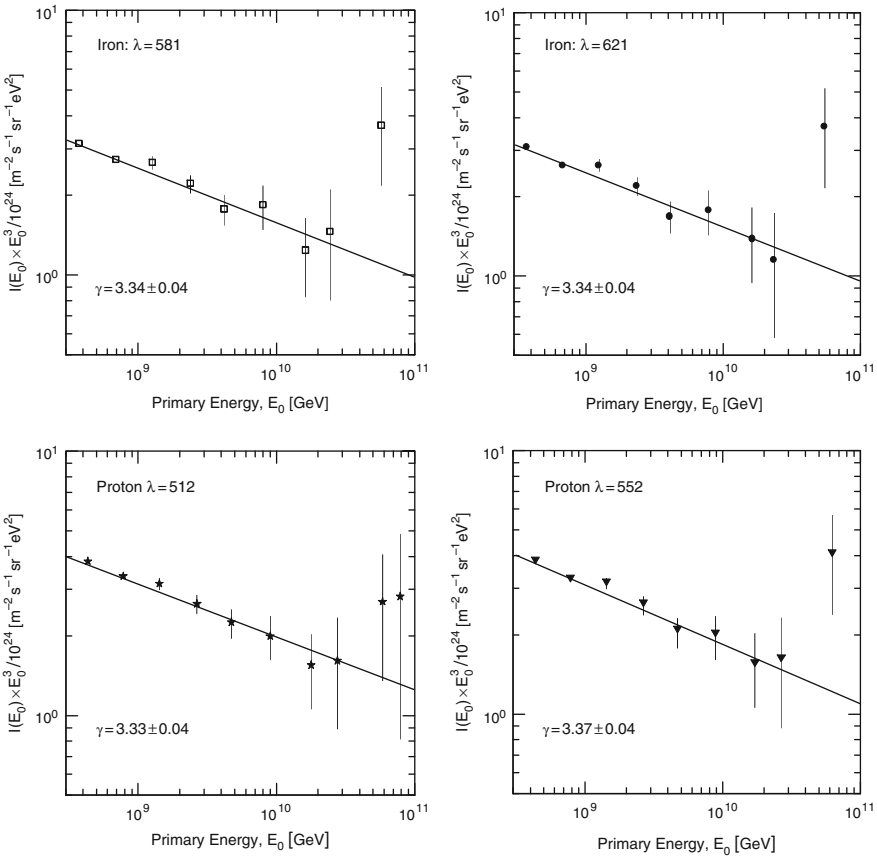

Fig. 11.24 Revised primary energy spectra estimated for different assumptions of the primary mass and the shower attenuation length as obtained in the re-analysis of Ave et al. (2003a) of data from Haverah Park acquired in the years 1974–1987. Earlier Haverah Park spectra that are based essentially on the same data but on different analyses are given in Fig. 11.22 (Cunningham et al., 1980a, b) and Fig. 11.33 (Lawrence et al., 1991). The old and new Haverah Park spectra are also indicated in Fig. 11.35 for comparison with the HiRes Fly's Eye data

Figure 11.25 shows the all-particle spectrum obtained from measurements with the large AGASA array in Japan (Takeda et al., 1998, 2003). This spectrum is also given in tabulated form in Table 11.3. In Fig. 11.25a) two sets of data are displayed, one showing all events, the other only well contained events. The solid curve shows the spectrum as predicted under the assumption that the sources are uniformly distributed and that the GZK cutoff occurs as expected. However, the experimental data suggests that the GZK cutoff does not exist. Figure 11.25b shows the result of an earlier data summary by Sakaki et al. (2001b), showing the spectrum obtained from showers collected within the zenith angle interval $0^\circ \leq \theta \leq 40^\circ$ ($1.0 \leq \sec\theta \leq 1.3$) and $40^\circ \leq \theta \leq 60^\circ$ ($1.3 \leq \sec\theta \leq 2.0$).

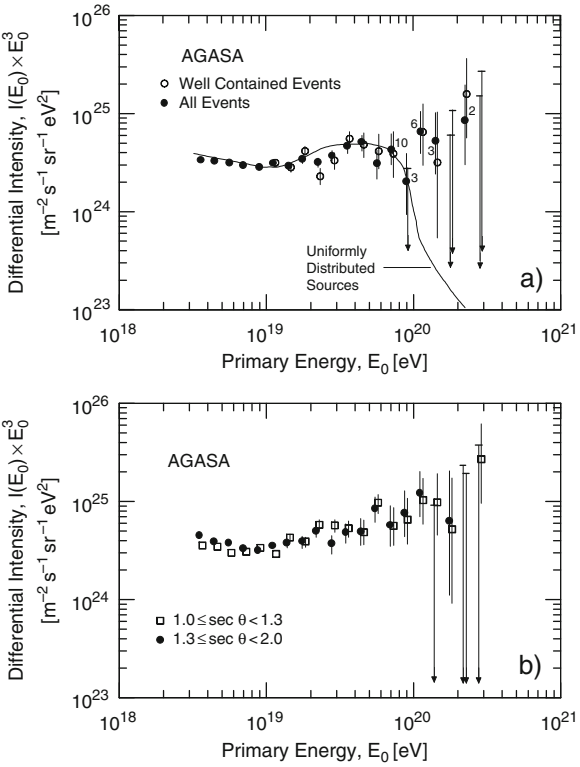

Fig. 11.25 (**a**) Differential primary all-particle energy spectrum obtained from AGASA measurements for zenith angles $\theta \leq 45^\circ$ and data collected until July 2002, multiplied by E_0^3 (Takeda et al., 2003). The error bars are Poissonian *upper and lower limits* at 68% c.l., and the *arrows* at 90% c.l. *upper limits*. The *numbers* indicate the number of events per bin. The *solid curve* shows the expected spectrum for a uniform universal source distribution, including the Greisen-Zatsepin-Kuzmin cutoff, after Takeda et al. (1998). (**b**) An earlier data summary compiled by Sakaki et al. (2001b) shows the spectra obtained for two different zenith angle intervals ($\square, \theta \leq 40^\circ$; $\bullet, \theta \leq 60^\circ$)

Here, too, the same trend is observed, the spectrum seems to continue and no sign of the GZK cutoff is seen. The shower measurements at AGASA are based on scintillation detectors, measuring the common shower size. The particle density versus primary energy conversion for vertically incident proton and iron initiated showers is given in Fig. 11.26 for two different sets of simulations. The close agreement between the event generators and the small primary mass dependence of the conversion relations is evident.

The spectrum obtained with the EAS-TOP array at Gran Sasso (810 g cm^{-2}, 2,005 m a.s.l.) which had been derived from shower size measurements using the electron component in conjunction with shower simulations using the CORSIKA program system together with the HDPM event generator (Capdevielle et al., 1992) is plotted in Fig. 11.27 (Navarra, 1998; Aglietta et al., 1999). Also shown in this figure for comparison are the spectra resulting from measurements with the arrays at Moscow (192 m a.s.l.) (Fomin et al., 1991), Akeno (900 m a.s.l.) (Nagano et al., 1984a) and Tibet (4,300 m a.s.l.) (Amenomori et al., 1996), and a few points from direct measurements as listed in the figure caption. Aglietta et al. (1999) specify for the change of slope from the asymptotic value of the branch before the knee, which is located near 3–5 PeV, and the asymptotic value of the branch after the knee a value of $\Delta\gamma = 0.40 \pm 0.09$. Their expressions to describe the spectrum before and

Table 11.3 Differential primary intensities from AGASA for $\theta \leq 45^\circ$. Errors are poissonian upper and lower limits at 68% confidence limit. Data accumulated until July 2002 (Takeda et al., 2003)

Energy bin $\lg(E_0)$ [eV]	$\lg(I(E_0) \cdot E_0^3)$ [$m^{-2}\ s^{-1}\ sr^{-1}\ eV^2$]
18.55	$24.528^{+0.009}_{-0.009}$
18.65	$24.519^{+0.010}_{-0.011}$
18.75	$24.497^{+0.013}_{-0.013}$
18.85	$24.473^{+0.016}_{-0.017}$
18.95	$24.449^{+0.021}_{-0.022}$
19.05	$24.492^{+0.025}_{-0.026}$
19.15	$24.460^{+0.032}_{-0.034}$
19.25	$24.530^{+0.038}_{-0.041}$
19.35	$24.496^{+0.041}_{-0.054}$
19.45	$24.568^{+0.056}_{-0.064}$
19.55	$24.664^{+0.062}_{-0.073}$
19.65	$24.702^{+0.074}_{-0.089}$
19.75	$24.484^{+0.146}_{-0.153}$
19.85	$24.633^{+0.154}_{-0.161}$
19.95	$24.304^{+0.294}_{-0.340}$
20.05	$24.814^{+0.203}_{-0.219}$
20.15	$24.711^{+0.294}_{-0.340}$
20.25	24.779 (90% C.L. upper limit)
20.35	$24.924^{+0.364}_{-0.449}$
20.45	25.177 (90% C.L. upper limit)

after the knee are given in Section 11.6.5 where we list mathematical fits to describe the spectrum.

An interesting compilation of data of the all-particle spectrum from many experiments that spans the wide primary energy range from 10^{14} eV to over 10^{20} eV due to Takeda et al. (2003) is presented in Fig. 11.28. Included are besides the classical Grigorov data (Grigorov et al., 1971b) relatively recent data from other direct measurements, as listed in the caption, and the results from eight indirect measurements, using air shower observables. These comprise data from the Tibet (Amenomori et al., 1996), KASCADE (Ulrich et al., 2001), Akeno (Nagano et al., 1992) and AGASA (Takeda et al., 2003) particle detector arrays, from the DICE double imaging atmospheric Cherenkov experiment (Swordy and Kieda, 2000), from BLANCA which is a non-imaging, large wide-aperture optical Cherenkov detector array (Fortson et al., 1999; Fowler et al., 2001), from the combined particle and Cherenkov detector installation HEGRA-AIROBICC (Röhring et al., 1999;

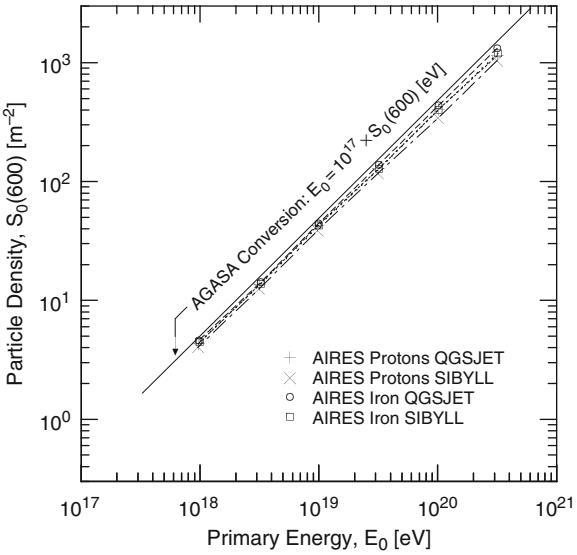

Fig. 11.26 The relation between the $S_0(600)$ ($S(600, \theta = 0^\circ)$) ground parameter and the primary energy for proton and iron nuclei initiated showers obtained from simulations with the AIRES program, using the QGSJET and SIBYLL event generators, as indicated in the figure (after Sakaki et al., 2001a)

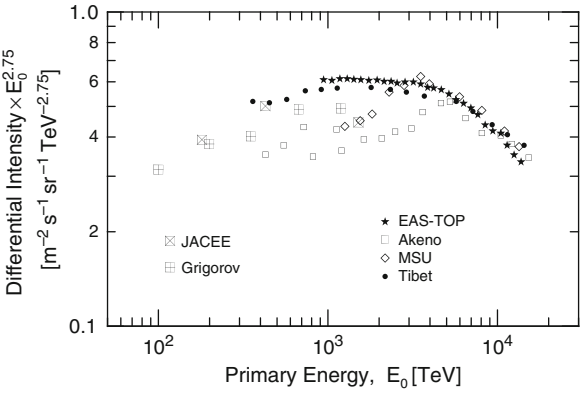

Fig. 11.27 All-particle spectrum obtained by EAS-TOP at Gran Sasso, Italy (2005m a.s.l.) (⋆) (Navarra, 1998, 2006; Aglietta et al., 1999). Note that the intensity is multiplied by the factor $E_0^{2.75}$. Also shown for comparison are the spectra from the Akeno (□), Moscow (◇) and Tibet (●) arrays, and from the direct measurements of Grigorov (1971a) (⊞) and Asakimori et al. (1998) (⊠)

Aharonian et al., 1999), and from the air fluorescence detector HiRes at Dugway in Utah (Abu-Zayyad et al., 2001). This figure demonstrates clearly the disagreement that exists among the relatively low energy spectra obtained from atmospheric Cherenkov measurements. It also illustrates that the directly measured spectra match fairly well onto the higher energy spectra derived from air shower particle measurements.

The spectra presented in Fig. 11.29 illustrate the lingering problem that we face with the hadronic interaction models (or event generators) that surfaces when interpreting a given set of observables with different simulations. The two primary energy spectra obtained from one and the same very comprehensive multiple observable data set collected with the KASCADE array and interpreted using the program system CORSIKA with the event generators QGSJET and VENUS are quite different, reflecting the model differences (Antoni et al., 2002). In this analysis the

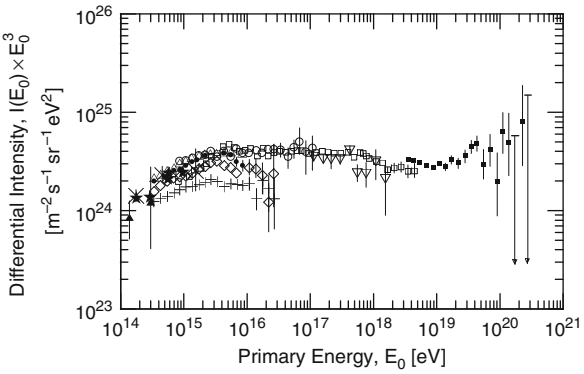

Fig. 11.28 Compilation of differential primary all-particle energy spectra obtained from different air shower experiments and some spectra from direct measurements, as listed below. See the caption of Fig. 11.25a for details concerning the *error bars and arrows* (after Takeda et al., 2003). *Air Shower Experiments*: △, Tibet (Amenomori et al., 1996); ◇, DICE (Kieda and Swordy, 1999); +, BLANCA (QGSJET) (Fortson et al., 1999; Fowler et al., 2001); ●, HEGRA (Röhring et al., 1999; Aharonian et al., 1999); ○, KASCADE (Ulrich et al., 2001); ▽, HiRes-MIA (Abu-Zayyad et al., 2001); □, Akeno 1 km^2 (Nagano et al., 1992); ■, AGASA (Takeda et al., 1998, 2003). *Direct Measurements*: ★, Proton satellite (Grigorov et al., 1971b); ▲, RUNJOB (Ichimura et al., 1993); ×, JACEE (Asakimori et al., 1993a, b)

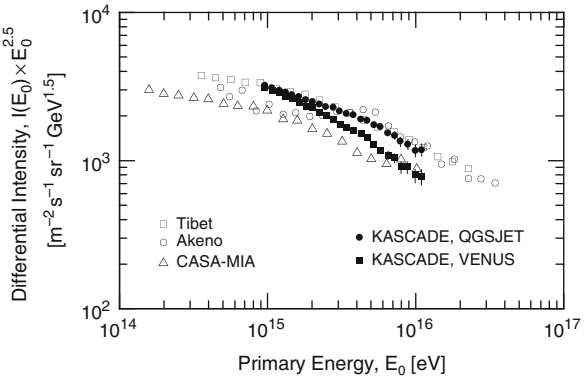

Fig. 11.29 All particle differential primary cosmic ray spectra as determined by different work groups. The two solid symbols, ● and ■, show the spectra obtained from measurements with the KASCADE experiment (Antoni et al., 2002) using the event generators QGSJET and VENUS, respectively, in their simulation for the interpretation of the data, illustrating the model differences. The other symbols show the results of the Tibet (Amenomori et al., 1996), Akeno (Nagano et al., 1984a) and CASA-MIA (Glasmacher et al., 1999a, c) experiments

QGSJET model interpretation is in quite good agreement with the Tibet and Akeno spectra that are also shown together with the CASA-MIA results. The same problem that is encountered here appears also when attempting the delicate extraction of the heavily masked primary mass of the shower initiating particle from the experimental data. This topic is addressed in Sect. 11.7.

Similarly, different results and different features manifest themselves in the derived primary spectrum when the latter is investigated on the basis of the electron, muon or hadron component of the showers, or of different combinations of the shower constituents using the same simulation (Kakimoto et al., 1981; Antoni et al., 2002).

These problems are evidently due in parts to our inadequate knowledge of the properties of hadronic interactions at very high energies. There, no accelerator or collider data offer guidance to construct a correct phenomenological-mathematical model describing the interactions and the entire shower that we use in our simulations. The problem is most likely nested in the *forward physics domain*. But also because of the uncertainty of the nature (mass) of the primaries that initiate the showers. Last but not least experimental inadequacies may also be responsible for part of this problem.

A similar plot, partly redundant with respect to the previous one, showing again some of the classical spectra from direct measurements together with indirectly derived spectra from air shower measurements, presented in Fig. 11.30, shows the striking agreement of the Akeno (900 m a.s.l.) (Nagano et al., 1984a), Tibet (Yangbajing, 4,300 m a.s.l.) (Amenomori, 1996) and the KASCADE (110 m a.s.l.) (Ulrich et al., 2001) data that are based on all charged particle shower size and electron size only (KASCADE) measurements. They agree amazingly well in spite of the fact that the arrays are located a quite different altitudes. The relatively recent BASJE spectrum was derived from data collected with a new array (Ogio et al., 2004). The BASJE spectrum is also given in tabulated form in Table 11.4. Also shown for comparison is the CASA-MIA spectrum (Glasmacher et al., 1999a, c).

Rather impressive is the compilation and comparison of relatively recent data displayed in Fig. 11.31. Besides the nicely matching data from the direct

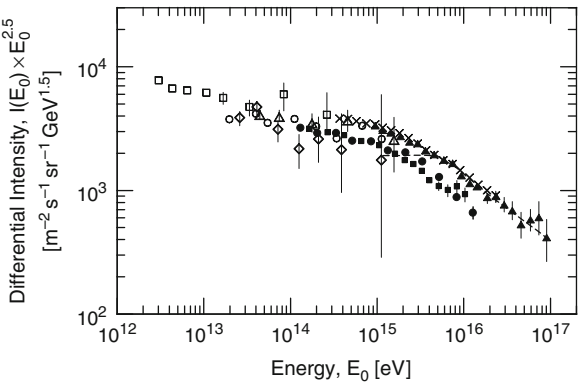

Fig. 11.30 Differential all-particle primary energy spectrum recorded by the BASJE-MAS experiment at Mt Chacaltaya (5,230 m a.s.l.), • (Ogio et al., 2004). Also shown for comparison are the spectra obtained by the following experiments: △ JACEE (Asakimori et al., 1995, 1998); ◇ RUNJOB (Apanasenko et al., 2001); □ SOKOL (Ivanenko et al., 1993); ○ Proton satellite (Grigorov et al., 1971a, b); ▲ KASCADE, electrons (Ulrich et al., 2001); ■ CASA-MIA (Glasmacher et al., 1999a, c); × Tibet array (Amenomori et al., 1996). The *dashed line* shows the Akeno spectrum (Nagano et al., 1984a; after Ogio et al., 2004)

Table 11.4 Best fit $n_p/(n_p + n_{Fe})$ values for cosmic ray integral intensities at corresponding primary energies, E_0, recorded at Mt. Chacaltaya by the BASJE experiment (Ogio et al., 2004)

$I(>N)$ $[m^{-2}\,s^{-1}\,sr^{-1}]$	$\lg E_0^a$ [eV]	$(E_{0,center})^b$ [eV]	$n_p/(n_p + n_{Fe})$ p-fraction
$6.31 \cdot 10^{-6}$	14.55 ± 0.10	$(3.55 \cdot 10^{14})$	0.444 ± 0.029
$3.55 \cdot 10^{-6}$	14.70 ± 0.09	$(5.01 \cdot 10^{14})$	0.369 ± 0.021
$2.00 \cdot 10^{-6}$	14.85 ± 0.07	$(7.08 \cdot 10^{14})$	0.334 ± 0.023
$1.12 \cdot 10^{-6}$	15.00 ± 0.06	$(1.00 \cdot 10^{15})$	0.260 ± 0.026
$6.31 \cdot 10^{-7}$	15.15 ± 0.05	$(1.41 \cdot 10^{15})$	0.291 ± 0.024
$3.55 \cdot 10^{-7}$	15.29 ± 0.04	$(1.95 \cdot 10^{15})$	0.286 ± 0.028
$2.00 \cdot 10^{-7}$	15.42 ± 0.02	$(2.63 \cdot 10^{15})$	0.259 ± 0.027
$1.12 \cdot 10^{-7}$	15.54 ± 0.01	$(3.47 \cdot 10^{15})$	0.284 ± 0.039
$6.31 \cdot 10^{-8}$	15.65 ± 0.00	$(4.47 \cdot 10^{15})$	0.312 ± 0.034
$3.55 \cdot 10^{-8}$	15.76 ± 0.01	$(5.75 \cdot 10^{15})$	0.220 ± 0.080
$2.00 \cdot 10^{-8}$	15.87 ± 0.02	$(7.41 \cdot 10^{15})$	0.148 ± 0.080
$1.12 \cdot 10^{-8}$	15.98 ± 0.05	$(9.55 \cdot 10^{15})$	0.077 ± 0.110
$6.31 \cdot 10^{-9}$	16.08 ± 0.04	$(1.20 \cdot 10^{16})$	0.095 ± 0.101

[a] Systematic errors only. Another error of $\pm$ 0.10 in terms of $\lg(E_0)$, the primary energy, is due to the size determination error.
[b] Energy center values of previous column (author inserted column).

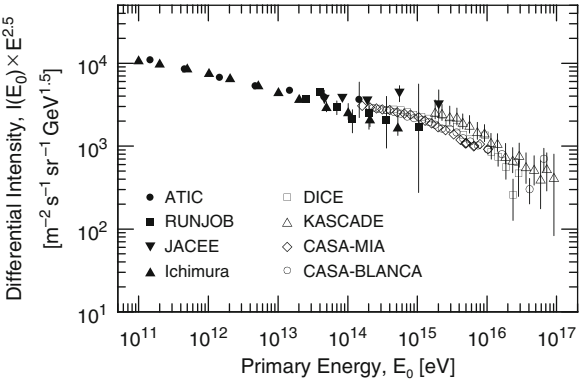

Fig. 11.31 All-particle differential primary energy spectra, multiplied by $E^{2.5}$. Full symbols are direct measurements: ● ATIC (Ahn et al., 2005, 2006); ■ RUNJOB (Apanasenko et al., 2001); ▼ JACEE (Takahashi, 1998); ▲ (Ichimura et al., 1993). Open symbols are from air shower experiments: □ DICE (Swordy and Kieda, 2000); △ KASCADE (Antoni et al., 2005); ◇ CASA-MIA (Glasmacher et al., 1999a, c); ○ CASA-BLANCA (Fowler et al., 2001; after Ahn et al., 2007)

measurements and the smooth fit of these onto the indirectly derived spectra into and over the knee region, the higher energy data fit into a relatively narrow band. These data comprise the results from the dual imaging atmospheric Cherenkov experiments DICE (Swordy and Kieda, 2000), the particle (mainly electrons) and wide aperture atmospheric Cherenkov detector arrays CASA-BLANCA (Fowler et al., 2001), the combined electron and muon detector arrays CASA-MIA (Glasmacher et al., 1999a, c), and the complex KASCADE experiment (Antoni et al., 2005). The CASA-BLANCA spectrum is also given in tabulated form in Table 11.5.

Table 11.5 Primary energy spectrum measured by CASA-BLANCA (after Fowler et al., 2001)

Energy range[a] $\lg(E_0)$ [eV]	Differential intensity $I(E_0)$ [$m^{-2}\ s^{-1}\ sr^{-1}\ GeV^{-1}$]
14.3–14.4	$(12.12 \pm 0.04) \cdot 10^{-11}$
14.4–14.5	$(6.68 \pm 0.02) \cdot 10^{-11}$
14.5–14.6	$(3.58 \pm 0.02) \cdot 10^{-11}$
14.6–14.7	$(1.91 \pm 0.01) \cdot 10^{-11}$
14.7–14.8	$(1.03 \pm 0.01) \cdot 10^{-11}$
14.8–14.9	$(5.42 \pm 0.04) \cdot 10^{-12}$
14.9–15.0	$(2.90 \pm 0.03) \cdot 10^{-12}$
15.0–15.1	$(1.57 \pm 0.02) \cdot 10^{-12}$
15.1–15.2	$(8.18 \pm 0.12) \cdot 10^{-13}$
15.2–15.3	$(4.36 \pm 0.08) \cdot 10^{-13}$
15.3–15.4	$(2.21 \pm 0.05) \cdot 10^{-13}$
15.4–15.5	$(1.22 \pm 0.03) \cdot 10^{-13}$
15.5–15.6	$(6.2 \pm 0.2) \cdot 10^{-14}$
15.6–15.7	$(2.9 \pm 0.1) \cdot 10^{-14}$
15.7–15.8	$(1.5 \pm 0.1) \cdot 10^{-14}$
15.8–15.9	$(7.7 \pm 0.5) \cdot 10^{-15}$
15.9–16.1	$(2.9 \pm 0.2) \cdot 10^{-15}$
16.1–16.3	$(8.1 \pm 0.8) \cdot 10^{-16}$
16.3–16.5	$(2.1 \pm 0.3) \cdot 10^{-16}$
16.5–16.7	$(3.1 \pm 1.0) \cdot 10^{-17}$
16.7–16.9	$(2.3 \pm 0.7) \cdot 10^{-17}$

[a] Bin widths rise with increasing energy so that $E_{max}/E_{min} = 10^{0.1}$ at lower energies, while $E_{max}/E_{min} = 10^{0.2}$ for the five highest bins. Errors represent only the Poisson uncertainty in each bin. There is an additional instrumental systematic uncertainty of 18%. These results use the QGSJET-derived energy transfer function.

A similar plot (Fig. 11.32) showing the higher energy range ($3 \cdot 10^{15}$–$3 \cdot 10^{18}$ eV) includes also the hybrid data from the combined Fly's Eye (HiRes) and MIA muon array experiments (Abu-Zayyad et al., 2001).

A comparison of the primary spectra derived on the basis of data from the five large experiments that employed the three established methods, i.e., particle, atmospheric Cherenkov and fluorescence detection separately or in some combination, including AGASA, Akeno (mainly scintillation detectors), Haverah Park (deep water Cherenkov detectors), Yakutsk (scintillation and atmospheric Cherenkov detectors), and the Stereo Fly's Eye (air fluorescence) had been carried out by Nagano et al. (2000). The results from these experiments are displayed in Fig. 11.33. It is evident from this plot that we cannot draw a decision whether we see the GZK cutoff or not.

The primary all-particle spectrum determined with the Tibet III array, shown in Fig. 11.34, covers the region of the *knee* (the first and principal knee near ~ 3 PeV) very nicely. This spectrum is possibly one of the best and most realistic in this energy range because the array is located at an almost ideal atmospheric depth for

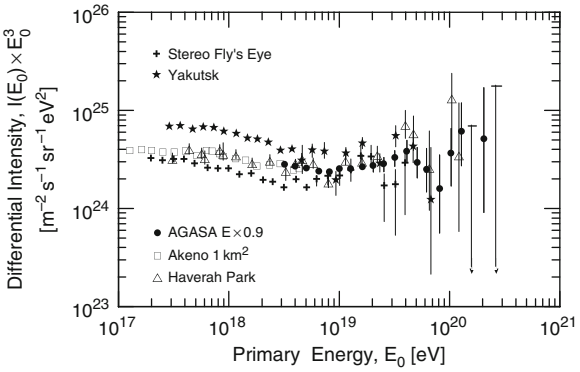

Fig. 11.32 Differential primary energy spectrum obtained by the hybrid measurements including the Fly's Eye (HiRes) detector and the MIA muon array at Dugway. Included, too, are the results from the Akeno (Nagano et al., 1984b), BLANCA (Fortson et al., 1999; Fowler, 2000), CASA-MIA (Glasmacher et al., 1999a), DICE (Kieda and Swordy, 1999), and Tibet (Amenomori et al., 1996) experiments. The ordinate is multiplied by E_0^3 to emphasize spectral details (after Abu-Zayyad et al., 2001)

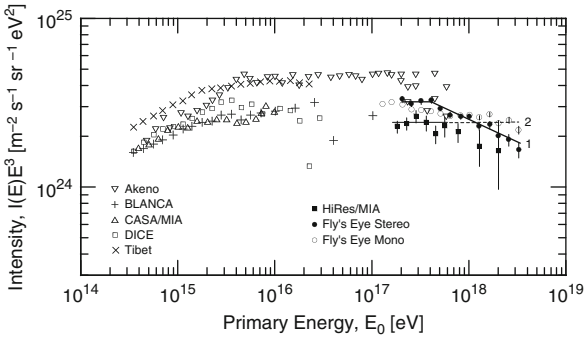

Fig. 11.33 Comparison of the ultrahigh energy portion of the primary spectra obtained with the AGASA (Nagano et al., 2000), Akeno (Nagano et al., 1984b), Haverah Park (Lawrence et al., 1991), and Yakutsk (Afanasiev et al., 1993) arrays, and the Stereo Fly's Eye (Bird et al., 1994) fluorescence detector (after Nagano et al., 2000)

this energy and is highly instrumented. Shown are three spectra. One is from an older publication, whereas the other two are from very recent work. The spectra had been obtained using different simulations (CORSIKA v. 6.204 with QGSJET-01c + HD, and CORSIKA v. 6.204 with SIBYLL-2.1 + HD) for the data interpretation, as listed in the caption. The label HD refers to their *heavy dominant* primary spectrum (Amenomori et al., 2000a). The spectra lie all very close together. Shown, too are several other spectra and points from direct measurements, as listed in the table attached to the figure, for comparison.

Of particular interest is the recent announcement of the Fly's Eye (HiRes) group of the *first observation* of the Greisen-Zatsepin-Kuzmin (GZK) suppression (or cutoff) (for details see Sect. 11.11.5) with a statistical significance of 5 standard deviations (Abbasi et al., 2008a). The HiRes measurements show that the intensity of ultrahigh energy cosmic rays makes a sharp dip at an energy of $\sim 6 \cdot 10^{19}$ eV that is consistent with the predictions of the GZK cutoff. The same measurements show the spectral ankle at an energy of $4 \cdot 10^{18}$ eV. The HiRes-1 and HiRes-2 monocular

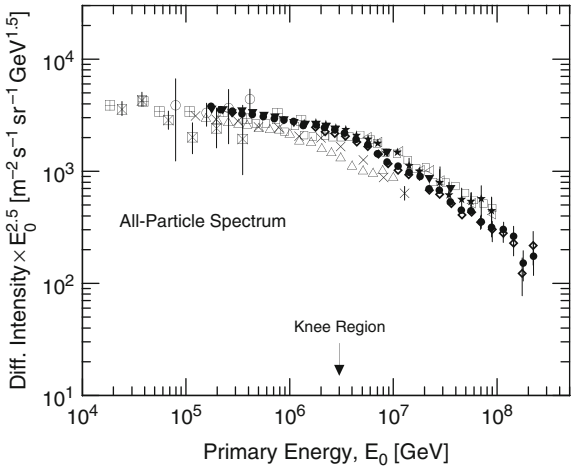

Fig. 11.34 Differential all-particle primary cosmic ray energy spectrum determined with the Tibet array, using different high energy interaction models in the simulations for the interpretation of the data, as listed below. Note that the intensity is multiplied by $E_0^{2.5}$. Also shown are the spectra obtained by other experiments, including data from three direct measurements (after Amenomori et al., 2008a). *Air Shower Experiments*: ●, Tibet III (CORSIKA QGSJET + HD) (Amenomori et al., 2008a); ◇, Tibet III (CORSIKA SIBYLL + HD) (Amenomori et al., 2008a); ▼, Tibet III (Amenomori et al., 2003b); △, CASA-MIA (Glasmacher et al., 1999a); □, Akeno (Nagano et al., 1984a); ×, Chacaltaya BASJE-MAS (Ogio et al., 2004); ⋆, KASCADE (QGSJET) (Antoni et al., 2005); ◁, KASCADE (SIBYLL) (Antoni et al., 2005). *Direct Measurements*: ⊞, PROTON (Grigorov et al., 1971a); ○, JACEE (Asakimori et al., 1998); ⊠, RUNJOB (Apanasenko et al., 2001)

spectra as obtained by these measurements are plotted in Fig. 11.35 together with the AGASA results that do not observe the cutoff. We have also added the old and the revised Haverah Park spectrum for comparison (Ave et al., 2003a). For the latter we have plotted the average spectrum between the one resulting for primary protons

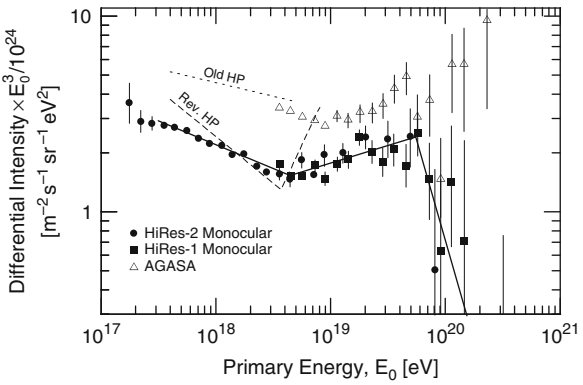

Fig. 11.35 Cosmic ray primary energy spectrum measured by the HiRes detectors operating in monocular mode. The spectra of HiRes-I and HiRes-II are shown. The highest two energy bins of the detector are empty, with the 68% confidence level bounds shown (Abbasi et al., 2008a). The AGASA and the old and revised Haverah Park (Rev. HP) spectra are also shown (Ave et al., 2003a)

Table 11.6 Differential primary intensities at Haverah Park (Ave et al., 2003a)

Energy $\langle E_0 \rangle$ [EeV]	Intensity $I \cdot 10^{30}$ [m^{-2} s^{-1} sr^{-1} eV^{-1}]	Number of events
Assuming proton primaries for interpretation		
0.36	78.5 ± 1.7	2,052
0.53	22.8 ± 0.8	860
0.76	7.05 ± 0.36	384
1.10	1.97 ± 0.16	155
1.54	0.55 ± 0.07	63
2.29	0.16 ± 0.03	27
3.49	0.042 ± 0.01	10
4.52	0.014 ± 0.006	5
7.07	0.008 ± 0.004	4
8.60	0.0028 ± 0.002	2
Assuming iron primaries for interpretation		
0.34	80.9 ± 1.8	1,986
0.49	22.9 ± 0.8	815
0.70	7.31 ± 0.39	378
1.03	2.00 ± 0.17	150
1.44	0.52 ± 0.07	57
2.15	0.177 ± 0.03	28
3.33	0.039 ± 0.01	9
4.19	0.015 ± 0.007	5
7.04	0.0124 ± 0.005	6

Table 11.7 Haverah Park differential spectral indices for different composition assumptions: revised analysis (Ave et al., 2003a)

Primary mass	Spectral index	Intensity $I \cdot 10^{30}$ at 10^{18} eV [m^{-2} s^{-1} sr^{-1} eV^{-1}]
Protons	3.33 ± 0.04	2.66 ± 0.09
Iron	3.34 ± 0.04	2.14 ± 0.09
Mixed (34%p + 66%Fe)	3.33 ± 0.04	2.35 ± 0.09

and for iron nuclei. The tabulated data of the two spectra and the primary mass dependent slopes are given in Tables 11.6 and 11.7, respectively.

Very recent results of measurements in the ultrahigh energy region of the cosmic ray spectrum obtained by the Auger Observatory are shown in Fig. 11.36 (Bleve, 2008; Facal, 2007; Perrone, 2007; Yamamoto, 2007). This spectrum, too, shows the sharp drop at about the same location on the energy scale. In Fig. 11.37 we show the same spectrum in the more common undistorted double logarithmic representation, where the drop looks less dramatic. Nevertheless the evidence for the onset of the GZK cutoff is very strong (for further details see the recent review by Nagano, 2009).

So far we have not given particular emphasis to the causes for the spectral knees nor the ankle. These features are established spectral properties. The ankle is believed to be due to the appearance of the ultrahigh energy extragalactic component

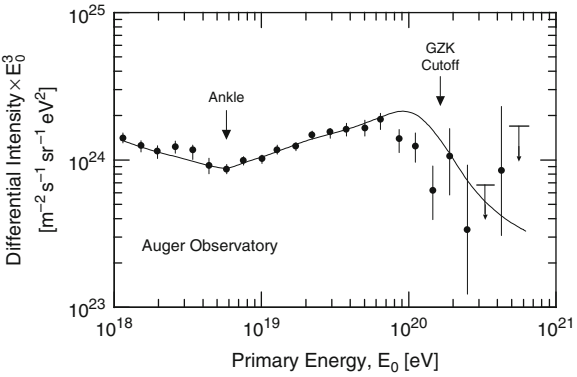

Fig. 11.36 Differential primary energy spectrum multiplied by E_0^3, obtained by the Auger Observatory, showing the significant drop in intensity above $\sim 4 \cdot 10^{19}$ eV. The plot shows the combined spectrum using the different detector systems (after Bleve, 2008; see also Facal, 2007; Perrone, 2007; Yamamoto, 2007)

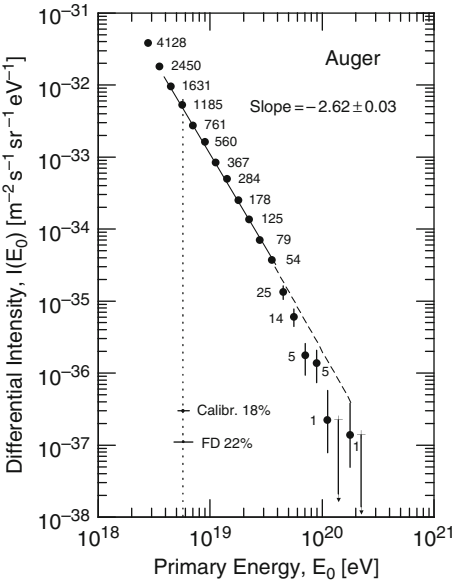

Fig. 11.37 Differential primary energy spectrum at ultrahigh energies in common double-logarithmic representation, recorded by the Auger detector. Included are showers with zenith angles $\theta \leq 60^\circ$. The numbers attached to the data points represent the number of events per bin. Calibr. 18% and FD 22% represent the calibration uncertainty of the array and the fluorescence detectors. The sharp drop of the intensity above $\sim 4{\cdot}10^{19}$ eV is evident The expected event numbers for no GZK are 132 ± 9 at $> 4 \cdot 10^{19}$ and 30 ± 2.5 at $> 10^{20}$ eV, the observed numbers are 51 and 2, respectively (after Auger web site)

of the cosmic radiation. The nature of the particles that carry this energy is still highly speculative. The *first* and the *second* (less pronounced) *knee* will be discussed in more detail in Sect. 11.7.

Today the general belief is that the first knee in the all-particle spectrum (and most likely the less marked second knee, too) is caused by the different mass (charge) components whose spectra exhibit a slow rigidity dependent cutoff that is linked either to the limitations of the *diffusive shock acceleration* process, resulting from supernova explosions, or to *rigidity dependent leakage* from the Galaxy, or possibly both. Such mechanisms lead to power law spectra for the different constituents that reach charge dependent maximum energies on the order of $Z \cdot 10^{15}$ eV (Drury, 1983; Kirk and Dendy, 2001).

Hörandel et al. (2003a, b), Hörandel (2008) has studied these mechanisms in detail and offers plausible explanations for the knee structures in the multi PeV range of the spectrum. We conclude this section of the all-particle spectrum with a plot of the outstanding analysis of Hörandel (2008), shown in Fig. 11.38. In this paper that we will not discuss further but highly recommend to the interested reader, the author discusses the cosmic ray composition and its relation to shock acceleration by supernova remnants. The figure shows the spectra that result in this context for the different hadronic constituents of the cosmic radiation and the resulting spectrum with its wiggles and knees. Hörandel terms this model the *poly-gonato model*, which in Greek means the many-knee model (Hörandel, 2003b). The contribution of the extragalactic component, too, is plotted in the figure.

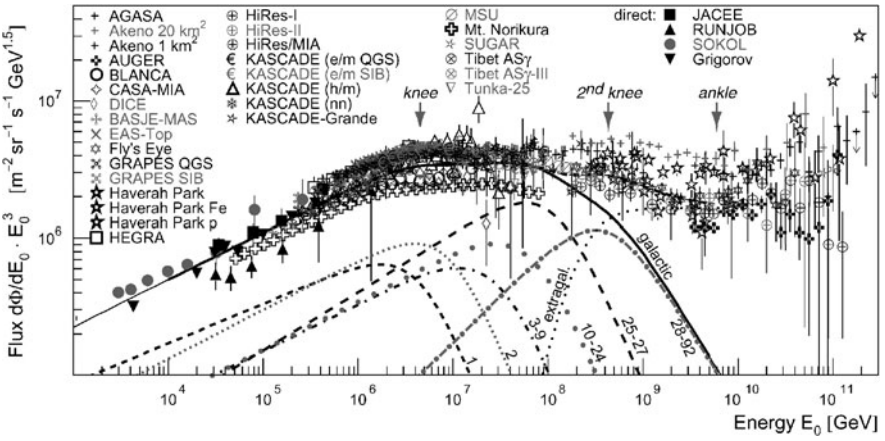

Fig. 11.38 Compilation of all-particle primary energy spectra. Shown are data points deduced from many different air shower experiments and data from direct measurements, as listed. The *curves* show a fit to the overall data, including the presumed extra-galactic component, the expected galactic contribution and predicted spectra of different mass groups. Indicated, too, are the locations of the first and second knee, and of the ankle (Hörandel, 2008). For details see Comments and References to Fig. 11.38, next page and Hörandel, 2003a, b, 2008 (courtesy of J.R. Hörandel)

Comments and References to Figure 11.38

Note that the flux of the all-particle primary energy spectrum is multiplied by E^3. Included in the plot are results from direct measurements by Grigorov et al. (1999), JACEE (Asakimori et al., 1995), RUNJOB (Derbina et al., 2005), and SOKOL (Ivanenko et al., 1993) as well as from the air shower experiments AGASA (Takeda et al., 2003), Akeno 1 km^2 (Nagano et al., 1984a), and Akeno 20 km^2 (Nagano et al., 1984b), Auger (Sommers et al., 2005), BASJE-MAS (Ogio et al., 2004), BLANCA (Fowler et al., 2001), CASA-MIA (Glasmacher et al., 1999b), DICE (Swordy and Kieda, 2000), EAS-TOP (Aglietta et al., 1999), Fly's Eye (Corbato et al., 1994), GRAPES-3 interpreted with two hadronic interaction models (Hayashi, 2005), Haverah Park (Lawrence et al., 1991; Ave et al., 2003a), HEGRA (Arqueros et al., 2000), HiRes-MIA (Abu-Zayyad et al., 2001), HiRes-I (Abbasi et al., 2004), HiRes-II (Abbasi et al., 2005a), KASCADE electrons and muons interpreted with two hadronic interaction models (Antoni et al., 2005), hadrons (Hörandel et al., 1999), and a neural network analysis combining different shower components (Antoni et al., 2002), KASCADE-Grande (preliminary) (Haungs et al., 2006), MSU (Fomin et al., 1991), Mt. Norikura (Ito et al., 1997), SUGAR (Anchordoqui and Goldberg, 2004), Tibet ASγ (Amenomori et al., 2000a) and ASγ-III (Amenomori et al., 2003b), Tunka-25 (Chernov et al., 2006), and Yakutsk (Glushkov et al., 2003). The lines represent spectra for elemental groups (with nuclear charge numbers Z as indicated) according to the *poly-gonato model* (Hörandel, 2003a). The sum of all elements (galactic) and a presumably extragalactic component are shown as well. The dashed line indicates the average all-particle flux at high energies

11.6.4 Comments on Primary Energy Spectra

As a thumb rule we can say that the integral primary energy spectrum in the domain of small air showers up to about 10^{15} eV can be described by a single power law with an exponent of -1.6 and an integral intensity of $\sim 10^{-4}$ particles $m^{-2}\ s^{-1}\ sr^{-1}$ at 10^{14} eV. Well beyond the knee which occurs at $\sim (3-5)\cdot 10^{15}$ eV (3–5 PeV), where the spectral index changes, the integral spectral slope is about -2.2. At 10^{17} eV the intensity drops to $\sim 10^{-10}$ primaries $m^{-2}\ s^{-1}\ sr^{-1}$.

The revised Haverah Park primary all-particle spectrum that served for a long time as a standard for comparison with the results from other large experiments shows differences of up to 30% at a given energy with respect to the Akeno/AGASA spectrum (Nagano and Watson, 2000) and the old Haverah Park spectrum (Lawrence et al., 1991). On the other hand the re-evaluated Haverah Park spectrum (Ave et al., 2003a) is in fair agreement with the results from the HiRes-MIA experiment in the 1–10 EeV range (Abu-Zayyad et al., 2001) for which a pure iron composition was assumed, and with the results of the Monocular HiRes experiment (Sommers, 2001). The re-evaluated Haverah Park spectrum is given in tabulated form in Table 11.6. and indicated in Fig. 11.35.

The differential spectral index after the knee at $3 \cdot 10^{15}$ eV was estimated to be -3.1 ± 0.02 (Roth et al., 2001). The values obtained by Ave et al. (2003a) depend on the composition assumed and are given in Table 11.7.

The size-energy conversion factor, U [GeV/N_e)], used by Nagano et al. (1984a) to obtain the primary energy of the shower initiating particle is plotted in Fig. 10.11, Sect. 10.2. The conversion factor is shower size dependent.

Inter-Array Calibration

Inter-array calibration is an extremely important topic when it comes to the comparison of data, such as the comparison of primary spectra determined from data of different arrays. Turver suggested in the early seventies (Turver, 1973) to take a portable wide-aperture atmospheric Cherenkov detector unit consisting of a 10" photomultiplier with an autonomous absolute calibration device from array to array, implant it in each array, run it jointly with the entire array for a limited time, tabulate the array and Cherenkov data, and repeat the measurement at the next array, and so on. This would have led to a universal array calibration. Unfortunately the idea never really materialized to be applied in a global campaign.

Later efforts, mainly among the large particle detector arrays like Haverah Park, Akeno and AGASA, but also the various Fly's Eye fluorescence experiments in conjunction with particle arrays such as CASA and MIA, and the associated Cherenkov array BLANCA and the two DICE detectors made similar cross-calibration attempts. Particle detector response comparisons and calibrations are briefly discussed in Chaps. 2, 8 and 10, and likewise for the Cherenkov and fluorescence detectors in Chaps. 16 and 17.

11.6.5 Mathematical Expressions and Fits

In the following we list a number of expressions used by some experimental groups for the conversion of array specific observables measured in a shower to the energy of the shower initiating primary particle, and to describe the primary energy spectrum.

(a) Primary Energy Estimation Based on Particle Data

Here we summarize relations that link various observables to the energy of the shower initiating primary to estimate the primary energy of an event.

Bower et al. (1983) have used for the conversion of the deep water Cherenkov tank particle density, $\rho(600)$, measured in units of vertical equivalent muons ([veμ]) at 600 m from the shower axis at the Haverah Park experiment to estimate the primary energy the relation (see Chap. 8),

$$E_0 \;=\; 7.04 \cdot 10^{17}\, \rho(600)_{\mathrm{HP}}^{1.018} \;\; [\mathrm{eV}]\,, \tag{11.5}$$

and for the conversion of the densities, $S(600)$, measured with scintillation detectors

$$E_0 \;=\; 3.26 \cdot 10^{17}\, S(600)_{\mathrm{HP}}^{1.018} \;\; [\mathrm{eV}]\,, \tag{11.6}$$

where the subscripts $_{\mathrm{HP}}$ refer to the $S(600)$ and $\rho(600)$ density values as calibrated at Haverah Park.

Dai et al. (1988) at Akeno have used the relation

$$E_0 \;=\; 2.0 \cdot 10^{17}\, S(600)_{\mathrm{Akeno}}^{1.0} \;\; [\mathrm{eV}]\,, \tag{11.7}$$

and Nagano et al. (2000) to interpret the AGASA data the formula

$$E_0 \;=\; 2.15 \cdot 10^{17}\, S(600)_{\mathrm{AGASA}}^{1.015} \;\; [\mathrm{eV}]\,. \tag{11.8}$$

The corresponding expression used by Glushkov et al. (1979) at Yakutsk that includes a number of additional effects and contributions from other components reads

$$E_0 \;=\; 4.8 \cdot 10^{17}\, S(600)_{\mathrm{Yak}}^{1.0 \pm 0.02} \;\; [\mathrm{eV}]\,. \tag{11.9}$$

Aglietta et al. (1999) specify for the shower size-energy conversion for the EAS-TOP experiment the following expression which results from their simulation (cf. Fig. 11.27),

$$N_e(E_0, A) \;=\; \alpha(A) E_0^{\beta(A)} \;\;, \tag{11.10}$$

where $\alpha(A) = 197.5 A^{-0.521}$, A is the primary mass, and $\beta(A) = 1.107 A^{0.035}$.

The expression for the fluctuations is given as

$$\frac{\sigma(N_e)}{N_e} \;=\; \kappa(A) E_0^{-\xi(A)} \;\;, \tag{11.11}$$

where $\kappa(A) = 1.495 A^{-0.197}$ and $\xi(A) = 0.249 \cdot A^{-0.056}$.

(b) Primary Energy Estimation Based on Cherenkov Photon Data

For their atmospheric Cherenkov data, Dyakonov et al. (1981) give the following expression to determining the primary energy using the air Cherenkov photon density at Yakutsk at 400 m from the core,

$$E_0 \;=\; (1.29 \pm 0.37) \cdot 10^{18} \left(\frac{Q_{400}}{10^7} \right)^{1.03} \;\; [\mathrm{eV}]\,. \tag{11.12}$$

Budnev et al. (2005) specify for the determination of the primary energy from the optical photon density at a core distance of 175 m, Q_{175} [photons cm^{-2} eV^{-1}],

measured by the Tunka-25 atmospheric Cherenkov detector array the relation,

$$E_0 \;=\; 400 \cdot Q_{175}^{0.95} \;\; [\mathrm{TeV}] \,. \tag{11.13}$$

The relation is valid for the primary energy range $10^{15} \leq E_0 \leq 10^{17}$ eV.

(c) Primary Spectrum, Energy-Intensity Relations

The following expressions have been used by the respective authors to approximate the primary all-particle spectrum.

Nikolsky specified a formula, given below, which yields essentially the same result as the one proposed by Greisen (1960).

$$I(>E_0) \;=\; \frac{0.19}{E_0^{1.6}} \left(\frac{1 + (E_0/3 \cdot 10^6)}{1 + (E_0/10^3)^{0.6}} \right) \;\; [\mathrm{m^{-2}\,s^{-1}\,sr^{-1}}] \;\; , \tag{11.14}$$

where E_0 must be given in TeV.

For the limited primary energy range $3 \cdot 10^{17} \leq E \leq 10^{19}$ eV, Krasilnikov et al. (1975) find the following expression to give a good fit to the Yakutsk spectrum,

$$I(>E_0) \;=\; (3.0 \pm 0.3) \cdot 10^{-12} \left(\frac{E_0}{10^{18}} \right)^{-2.03 \pm 0.03} \;\; [\mathrm{m^{-2}\,s^{-1}\,sr^{-1}}] \;\; , \tag{11.15}$$

with the energy E_0 inserted in eV.

For the high energy portion of the spectrum around the spectral ankle, Nagano and Watson (2000) propose the following two expressions which only deviate in the exponent for the domain below and above the ankle, respectively.

$$I(E) \;=\; C \cdot \left(\frac{E_0}{6.3 \cdot 10^{18}} \right)^{-3.20 \pm 0.05} \;\; [\mathrm{m^{-2}\,s^{-1}\,sr^{-1}\,eV^{-1}}] \tag{11.16}$$

for the energy range $4 \cdot 10^{17} \leq E_0 \leq 6.3 \cdot 10^{18}$ [eV], and

$$I(E) \;=\; C \cdot \left(\frac{E_0}{6.3 \cdot 10^{18}} \right)^{-2.75 \pm 0.2} \;\; [\mathrm{m^{-2}\,s^{-1}\,sr^{-1}\,eV^{-1}}] \tag{11.17}$$

for the energy range $6.3 \cdot 10^{18} \leq E_0 \leq 4 \cdot 10^{19}$ [eV].

Fowler et al. (2001) obtain as best fit to describe the primary spectrum, measured with the CASA-BLANCA hybrid (particle and atmospheric Cherenkov data) and the BLANCA atmospheric Cherenkov detector array only, the following expression,

$$I(E) \;=\; I_k \left(\frac{E}{E_k} \right)^{\alpha} \left[1 + \left(\frac{E}{E_k} \right)^{1/w} \right]^{(\beta - \alpha)w} \tag{11.18}$$

where E_k is the energy in the center of the transition region, i.e., the *knee energy*. For $E \ll E_k$ the function is a power law with index α, while the spectral index becomes β for $E \gg E_k$. I_k is the normalization at the knee. The parameter w is the half-width, in decades, of the transition region. According to these authors, the best fit knee energy is $2.0^{+0.4}_{-0.2}$ PeV with $\alpha = -2.72 \pm 0.02$ and the width of the knee is one half decade ($w = 0.25$). They conclude from their data that the *spectral slope change is smooth*, contrary to the results from several other experiments, e.g., Allan et al. (1962).

Amenomori et al. (1996) find for the fit of the spectral data which they have acquired from measurements carried out with the densely packed Tibet particle detector array located at Yangbajing (4,300 m a.s.l.) in the primary energy range between $3 \cdot 10^{14}$ and $2 \cdot 10^{16}$ eV in the period from October 1990 to July 1993 the following expressions: in the energy range below the knee for $E_0 < 5.62 \cdot 10^{14}$ eV,

$$I(E_0) \;=\; 1.5 \cdot 10^{-20} \left(\frac{E_0}{5.62 \cdot 10^{14}} \right)^{-2.60 \pm 0.04} \quad [\mathrm{m^{-2}\,s^{-1}\,sr^{-1}\,eV^{-1}}] \qquad (11.19)$$

and above the knee, for $E_0 > 7.08 \cdot 10^{15}$ eV,

$$I(E_0) \;=\; 1.2 \cdot 10^{-23} \left(\frac{E_0}{7.08 \cdot 10^{15}} \right)^{-3.00 \pm 0.05} \quad [\mathrm{m^{-2}\,s^{-1}\,sr^{-1}\,eV^{-1}}]\,. \qquad (11.20)$$

At this nearly ideal altitude, where showers in the specified energy range are very close to the maximum development, they note that the transition from before to after the spectral knee is *gradual* (like Fowler et al., 2001) and the intensity at the knee is

$$I(E_0) \;=\; 6.7 \cdot 10^{-22} \;\; [\mathrm{m^{-2}\,s^{-1}\,sr^{-1}\,eV^{-1}}] \qquad (11.21)$$

at $E_0 = 1.78 \cdot 10^{15}$ eV.

11.7 High Energy Primary Composition

11.7.1 Introduction

Up to energies of about 10 TeV, direct measurements of the primary cosmic ray composition yield satisfactory and reliable data. However, with increasing primary energy, as the air shower domain is being approached, the accuracy of the data deteriorates rapidly because of the low counting rate. Beyond about 1 PeV, direct measurements with present-day techniques are senseless (cf. Fig. 11.2) and we must employ indirect methods to derive or rather estimate the composition, using air shower observables.

In Chap. 10 we have discussed in detail mainly the particle based methods for the extraction of parameters that are correlated with the mass of the shower

initiating primary particle from a variety of air shower observables that permit to derive mass information. Optical atmospheric Cherenkov and fluorescence methods are discussed separately, in Chaps. 16 and 17, respectively. All indirect methods hinge heavily on air shower simulations with all the intrinsic uncertainties for the interpretation.

In this section we present only a very limited selection of results from the many experiments that had been carried out through the years to estimate the primary composition in different energy regions of the air shower domain and offer no further methodical details; we only mention the method employed in each specific cases.

11.7.2 Derived Primary Mass Composition

Even relatively simple yet realistic air shower simulations using reasonable high energy hadronic interaction models reveal readily a number of shower parameters that manifest more or less distinct primary mass dependent properties and significant differences with respect to gamma ray initiated showers. These include observables that yield directly accessible shower parameters, such as the electron, muon and hadron number of a given energy class of showers and the electron to muon ratio, to mention just the most obvious, as well as experimentally partly hidden quantities such as the depth of maximum development of a shower. The latter is, of course, directly accessible with fluorescence detectors without requiring major simulation efforts. More subtle observables are the arrival time profile and the lateral distribution of the shower particles, or of particle groups. They exhibit only a weak primary mass sensitivity but are useful mainly in conjunction with other observables and may help in the event selection and discrimination process.

We must also stress once again the fact that composition and spectral features as well as high energy interaction characteristics are intimately coupled in the air shower process and cause similar observable effects, which make a clear-cut mass separation impossible. Sophisticated analyses and multi-parameter correlation studies are very fruitful, particularly when analyzing showers on an event by event basis with many observables available. However, the problems with coupled effects are the main reason why in many experiments no attempts are being made to isolate and investigate the spectra of individual masses other than protons, possibly helium, and iron nuclei, but rather specific mass groups or mean masses only. Moreover, the estimation of the mean mass as a function of primary energy bears less risks for misinterpretations than sophisticated mass separation algorithms for extracting specific masses from a given set of experimental data.

In Fig. 11.39 we show the primary proton spectrum over the energy range from 10 GeV to 1 PeV which had been constructed by Aharonian et al. (1999). Except for the HEGRA data, the compilation includes only data from direct measurements as listed in the figure caption. The former are of particular interest because the HEGRA experiment employed the atmospheric Cherenkov imaging technique. The data from the many different measurements match amazingly well which speaks for the quality of the experiments. The mathematical fit to the data is given in the plot.

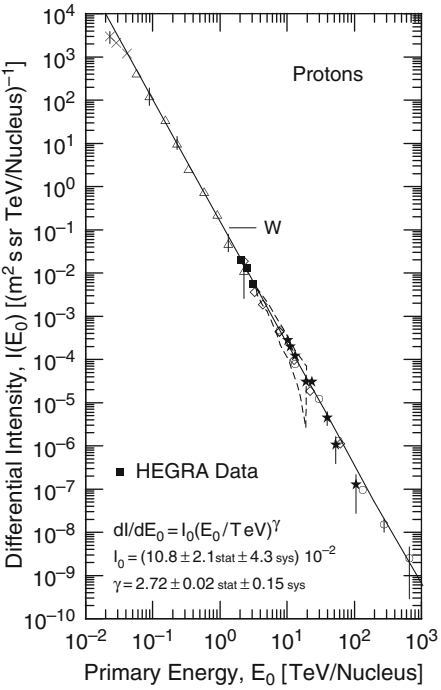

Fig. 11.39 Compilation of differential primary proton energy spectra obtained from different satellite and balloon experiments and some data points from the HEGRA air shower experiment (after Aharonian et al., 1999). W, Wiebel et al. (1998); ×, Papini et al. (1993); △, Ryan (1972); ■, HEGRA, Hemberger et al. (1999); ★, ◇, RUNJOB, Ichimura et al. (1993); Apanasenko et al. (1999a, b); ○, JACEE, Asakimori et al. (1993a, b)

The following two plots (Figs. 11.40 and 11.41) show compilations of He and CNO spectra, respectively, obtained from air shower experiments (Bertaina et al., 2005). Also shown in each figure is the low energy extension of the spectrum containing data from direct measurements for comparison, to give a broader view of the spectral trend, and to illustrate the degree of compatibility of the data from direct and indirect measurements in the overlapping energy band.

The data labeled EAS-TOP are the result of a combined experiment, using the atmospheric Cherenkov signature of the showers detected by EAS-TOP (2,005 m a.s.l.) at the surface and the high energy muon component ($E_\mu \approx 1.3$ TeV) associated with the same showers recorded by the MACRO muon detector deep underground in the Gran Sasso tunnel (the method is described in detail in Chap. 10).

At the 80 TeV energy mark in Fig. 11.40 three experimental points for He primaries from the EAS-TOP-MACRO experiment are plotted which had been obtained using three different interaction models in conjunction with CORSIKA-based simulations that had been used for the data interpretation. The three data points lie close together and at the upper boundary of the JACEE direct measurements. The interpretation of the full spectral range for He shown for this experiment

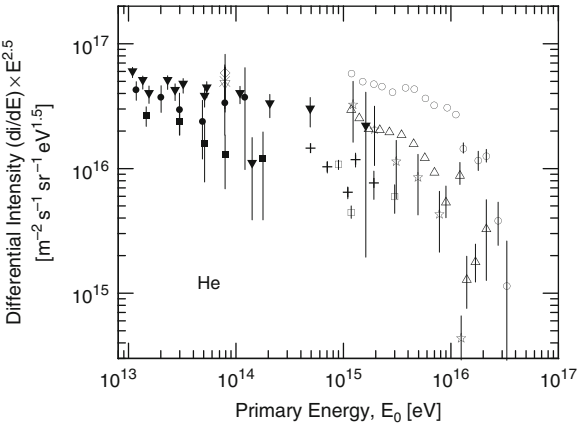

Fig. 11.40 Compilation of energy spectra of helium resulting from direct (full symbols) and indirect (open symbols) measurements (after Bertaina et al., 2005). For details see text. The data apply to the following experiments: ▼, JACEE (Takahashi, 1998); ■, RUNJOB (Furukawa et al., 2003a); ●, ATIC (Zatsepin et al., 2004); +, Tibet HD (Amenomori et al., 2003a); □, Tibet PD (Amenomori et al., 2003a); ○, $N_\mu - N_e$ QGSJET KASCADE (Antoni et al., 2005); △, $N_\mu - N_e$ SIBYLL KASCADE (Antoni et al., 2005); ⋆, EAS-TOP $N_\mu - N_e$, 50% p, 50% He (Bertaina et al., 2005); ◇, EAS-TOP TeV muons QGSJET (Bertaina et al., 2005); ×, EAS-TOP TeV muons SIBYLL (Bertaina et al., 2005); ▽, EAS-TOP TeV muons DPMJET (Bertaina et al., 2005)

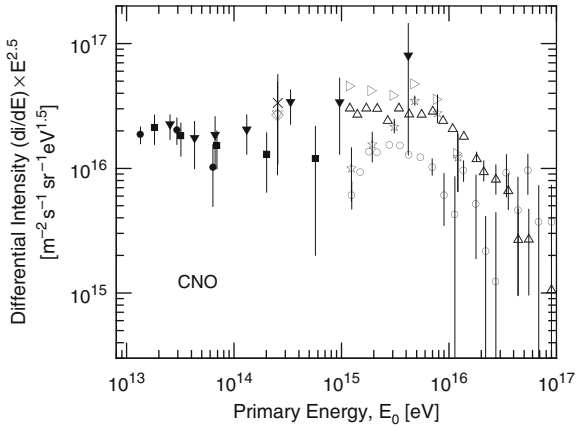

Fig. 11.41 Compilation of energy spectra of the CNO-group resulting from direct (full symbols) and indirect (open symbols) measurements (after Bertaina et al., 2005). For details see text. The data apply to the following experiments: ▼, JACEE (Takahashi, 1998); ■, RUNJOB (Furukawa et al., 2003b); ●, ATIC (Zatsepin et al., 2004); ○, $N_\mu - N_e$ QGSJET KASCADE (Antoni et al., 2005); △, $N_\mu - N_e$ SIBYLL KASCADE (Antoni et al., 2005); ⋆, EAS-TOP $N_\mu - N_e$, 50% p, 50% He (Aglietta et al., 2003b, 2004b); ▷, EAS-TOP $N_\mu - N_e$, 100% p (Aglietta et al., 2003b, 2004b); ◇, EAS-TOP TeV muons QGSJET (Bertaina et al., 2005); ×, EAS-TOP TeV muons SIBYLL (Bertaina et al., 2005); ▽, EAS-TOP TeV muons DPMJET (Bertaina et al., 2005)

is based on the assumption of a light composition (50% protons and 50% He nuclei). Also shown are the spectra obtained by the KASCADE experiment using the electromagnetic and muon components, and the Tibet array using the electromagnetic component only. For the interpretation of the data both experiments have used two different models each, as listed in the caption. The Tibet points labeled HD and PD refer to the *heavy dominance* and *proton dominance* assumptions for the interpretation.

Referring to Fig. 11.40 and the air shower experiments, we note that the data of the individual experiments show a certain consistency in the low to mid energy ranges, however, the spread of the results of the different experiments is rather alarming. We should also note that the different experiments are located at quite different altitudes; KASCADE is at 110 m a.s.l., EAS-TOP at 2,005 m and the Tibet array at Yangbajing at 4,300 m (for the array layouts see Figs. A.22, A.17 and A.31, respectively, in Appendix A, Sect. A.1). Yet, the results represent the primary spectrum and should in principle not deviate. The disagreements may be due to a calibration problem.

A problematic fact which is symptomatic for this work in general is that, depending on the simulation model employed for the data interpretation of a particular experiment, the resulting spectra show significant differences. This is particularly evident here for the KASCADE data. The same general comments made for Fig. 11.40 apply to the CNO-data of Fig. 11.41 as well, except that the spread of the data appears to be less. Note that in this case the model effect studies of the simulations had been made for the CNO-component at 250 TeV.

Another set of data on detailed mass composition studies that we have chosen to present is from the GRAPES experiment at Ootacamund in India (2,200 m a.s.l.) (Gupta et al., 2007). This experiment consists of a tightly packed shower detector array and has the presently largest muon detector coverage (for layout see Fig. A.19, Appendix A, Sect. A.1). The event analysis is based on data of the electromagnetic and muonic components (Tanaka et al., 2007b). Details of the method are outlined in Chap. 10. Figure 11.42a–e shows the derived primary spectra of protons, helium, the CNO group, aluminum for the mid-mass range, and iron, and in Fig. 11.42f the all-particle spectrum (Tanaka et al., 2007a). We note the generally good match of the low energy side of the GRAPES spectra to the high energy region of the direct measurements. The authors also note that they get better fits for their data with the SIBYLL event generator than with QGSJET.

The analysis of the data obtained with the CASA-BLANCA experiment had been carried out with different event generators in the simulations used for the data extraction and interpretation of the primary composition (Fowler et al., 2001). The results are presented in tabulated form in Table 11.8.

The separate plot of the iron spectrum displayed in Fig. 11.43 shows among data from direct measurements of the JACEE and RUNJOB experiments the amazing and very unique data obtained using the *imaging atmospheric Cherenkov telescope technique* with the High Energy Stereoscopic System, H.E.S.S., in Namibia (Bühler et al., 2007). This detector system is able to record the direct Cherenkov light which is emitted by a heavy primary, such as iron, at very high altitude in a very narrow

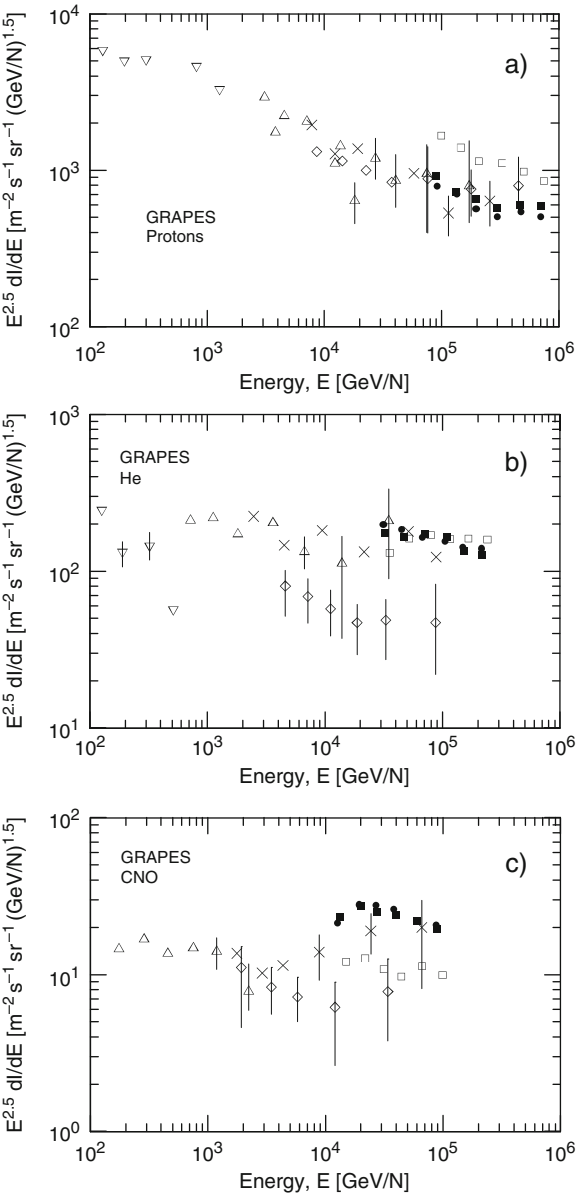

Fig. 11.42 Primary spectra of protons, He and CNO, obtained from GRAPES data using muon multiplicity distributions as outlined in Chap. 10 (Fig. 10.22) and CORSIKA with SIBYLL2.1 (●), QGSJET-II (■) and QGSJET01 (□) for the interpretation. The following data from direct measurements illustrate the good fit to the GRAPES data: Ryan (1972) ▽; Ivanenko et al. (1993) △; Asakimori et al. (1998) ×; Derbina et al. (2005) ◇ (after Tanaka et al., 2007a) (*continued on next page*)

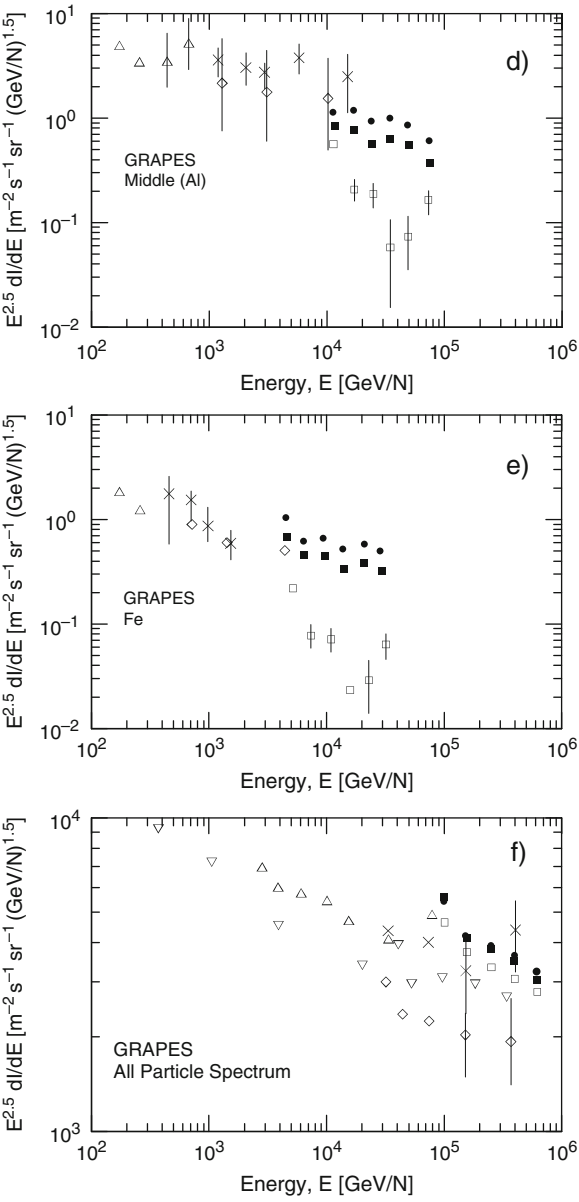

Fig. 11.42 (continued). Primary spectra of the mass groups, medium (Al) and Fe, and of the all-particle spectrum obtained from GRAPES data using muon multiplicities as outlined in Chap. 10 (Fig. 10.22) and CORSIKA with SIBYLL2.1 (●), QGSJET-II (■) and QGSJET01 (□) for the interpretation. Data from direct measurements illustrate the good fit to the GRAPES data: Ivanenko et al. (1993) △; Asakimori et al. (1998) ×; Derbina et al. (2005) ◇ (after Tanaka et al., 2007a)

Table 11.8 Results of multi-species fits to the CASA-BLANCA data (Fowler et al., 2001)

Energy range lg(E_0 [eV])	Abundance (%)				$\overline{\chi}^2$ of fit
	p	He	N	Fe	
QGSJET					
14.5–14.9	21.8 ± 0.4	40.1 ± 0.7	23.4 ± 0.7	14.6 ± 0.3	38.1
14.9–15.3	42 ± 1	21 ± 2	19 ± 1	18 ± 1	4.5
15.3–15.7	51 ± 3	33 ± 4	3 ± 3	13 ± 1	1.9
15.7–16.1	53 ± 8	14 ± 10	23 ± 6	10 ± 3	0.7
16.1–16.5	31 ± 12	12 ± 18	35 ± 17	22 ± 8	1.9
VENUS					
14.5–14.9	23.9 ± 0.4	27.6 ± 0.7	31.8 ± 0.5	16.7 ± 0.3	47.8
14.9–15.3	29 ± 1	29 ± 2	19 ± 1	23 ± 1	5.9
15.3–15.7	46 ± 2	23 ± 4	15 ± 3	16 ± 1	1.7
15.7–16.1	46 ± 6	6 ± 9	33 ± 7	15 ± 3	0.8
16.1–16.5	16 ± 9	33 ± 14	23 ± 13	29 ± 8	1.8
SIBYLL					
14.5–14.9	16.8 ± 0.4	20.9 ± 0.7	24.8 ± 0.7	37.4 ± 0.3	49.4
14.9–15.3	35 ± 1	-7 ± 2	39 ± 1	33 ± 1	21.6
15.3–15.7	37 ± 3	21 ± 5	9 ± 4	33 ± 2	4.8
15.7–16.1	31 ± 6	19 ± 10	9 ± 8	41 ± 4	1.2
16.1–16.5	9 ± 9	31 ± 17	8 ± 19	53 ± 11	2.6
HDPM					
14.5–14.9	19.9 ± 0.3	17.9 ± 0.5	31.4 ± 0.5	30.7 ± 0.2	90.0
14.9–15.3	19 ± 1	23 ± 1	24 ± 1	34 ± 1	11.5
15.3–15.7	32 ± 2	16 ± 3	26 ± 2	26 ± 1	3.2
15.7–16.1	37 ± 4	-3 ± 6	43 ± 6	23 ± 3	1.2
16.1–16.5	12 ± 6	21 ± 12	18 ± 12	49 ± 8	1.5

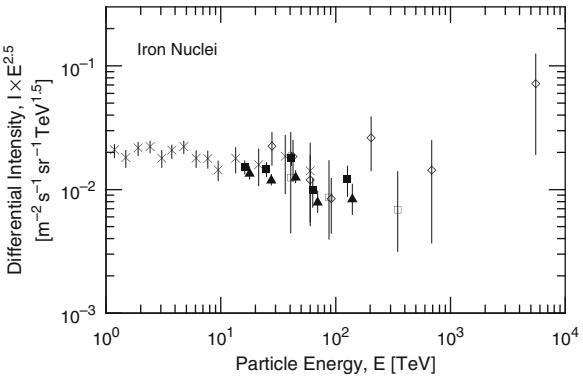

Fig. 11.43 Differential primary iron spectrum measured with the H.E.S.S. atmospheric Cherenkov telescopes in Namibia (Bühler et al., 2007). The data points ■ and ▲ apply to the QGSJET and SIBYLL event generators, respectively, used for the interpretation and spectrum reconstruction. Also shown for comparison are data from direct measurements with balloon experiments (◇ JACEE, Asakimori et al., 1995; □ RUNJOB, Derbina et al., 2005; × Ichimura et al., 1993)

light cone before it interacts in the atmosphere, causing a common air shower. The application of this method is quite restricted by the many boundary conditions that the event must fulfill for being detected. The direction of the incident particle trajectory and thus of the very narrow direct light cone emitted by the particle before interaction in the atmosphere must aim at the detector. Moreover, the energy and the minimum electric charge must be large enough to exceed the Cherenkov threshold and to produce an optical Cherenkov signal level above the system threshold.

The old Haverah Park data which had been re-interpreted by Ave et al. (2003a) that we have briefly discussed in connection with the primary spectrum in Sect. 11.6.3 (see Fig. 11.24) had also been analyzed to estimate the energy dependence of the proton fraction (Aver et al., 2003b). The analysis is based on the data extracted from the water Cherenkov tanks (lateral distributions and timing information at different zenith angles, yielding attenuation length), that had been used in this experiment. The result is plotted in Fig. 11.44. The rapid rise of the proton fraction in the shaded area below 0.2 EeV is an array effect and should be ignored.

The plot also shows simulation results using two different QGSJET event generators in conjunction with the CORSIKA program, as listed in the caption, which illustrate the discrepancies between the two generators. The method employed is not sophisticated but the only one that can be used with such an array. Its relevance, however, is that the Auger Observatory ground array uses the same kind of detectors and principle of measurement, of course complemented by the fluorescence data when available. Thus, a limited comparison of data can be made between the two experiments.

The next two figures are reproductions from the vast and excellent composition analysis of Hörandel (2003a, b, 2008), which show a wealth of very refined data from many experiments. Apart from the experimental data points a number of spectra for the different masses and mass groups obtained by several authors are also shown. The plots are extensively commented directly following the figures.

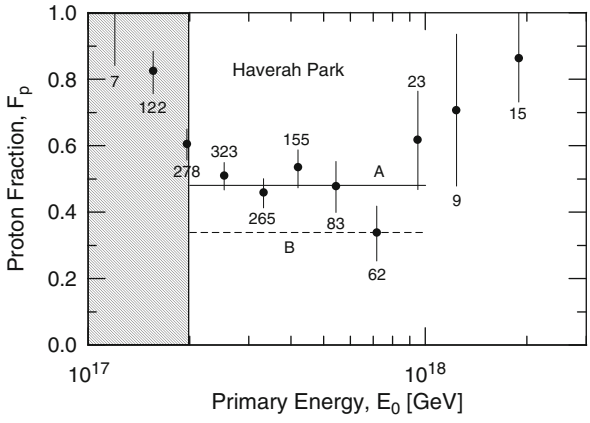

Fig. 11.44 Predicted value of the proton fraction, F_p, in the primary radiation as a function of energy derived from data obtained with the Haverah Park array. The *lines A and B* are fits to a constant composition in the indicated energy range. *Line A* applies to CORSIKA with QGSJET-01, *line B* to the older QGSJET-98 generator. The numbers indicate the number of events (after Ave et al., 2003b)

Comments and References to Figure 11.45

Cosmic ray energy spectra for four groups of elements, from top to bottom: protons, helium, CNO group, and iron group. *Protons:* Results from direct measurements above the atmosphere by AMS (Alcaraz et al., 2000b), ATIC (Wefel et al., 2005), BESS (Sanuki et al., 2000), CAPRICE (Boezio et al., 2003), HEAT (Vernois et al., 2001; Ichimura et al., 1993), IMAX (Menn et al., 2000), JACEE (Asakimori et al., 1998) MASS (Bellotti et al., 1999; Papini et al., 1993), RUNJOB (Derbina et al., 2005), RICH-II (Diehl et al., 2003; Ryan et al., 1972; Smith et al., 1973), SOKOL (Ivanenko et al., 1993; Zatsepin et al., 1993), and fluxes obtained from indirect measurements by KASCADE electrons and muons for two hadronic interaction models (Antoni et al., 2005) and single hadrons (Antoni et al., 2004b), EAS-TOP (electrons and muons) (Navarra et al., 2003) and single hadrons (Aglietta et al., 2003a), GRAPES-3 interpreted with two hadronic interaction models (Hayashi et al., 2005), HEGRA (Aharonian et al., 1999), Mt. Chacaltaya (Inoue et al., 1997), Mts. Fuji and Kanbala (Huangs et al., 2003), Tibet burst detector (HD) (Amenomori et al., 2000b) and ASγ (HD) (Amenomori et al., 2004). *Helium:* Results from direct measurements above the atmosphere by ATIC (Wefel et al., 2005), BESS (Sanuki et al., 2000), CAPRICE (Boezio et al., 2003), HEAT (Vernois et al., 2001; Ichimura et al., 1993), IMAX (Menn et al., 2000), JACEE (Asakimori et al., 1998), MASS (Bellotti et al., 1999; Papini et al., 1993), RICH-II (Diehl et al., 2003), RUNJOB (Derbina et al., 2005; Smith et al., 1973), SOKOL (Ivanenko et al., 1993; Webber et al., 1987), and fluxes obtained from indirect measurements by KASCADE electrons and muons for two hadronic interaction models (Antoni et al., 2005), GRAPES-3 interpreted with two hadronic interaction models (Hayashi et al., 2005), Mts. Fuji and Kanbala (Huangs et al., 2003), and Tibet burst detector (HD) (Amenomori et al., 2000b). *CNO group:* Results from direct measurements above the atmosphere by ATIC (C+O) (Cherry, 2006), CRN (C+O) (Müller et al., 1991), TRACER (O) (Müller et al., 2005), JACEE (CNO) (JACEE collaboration, 1999), RUNJOB (CNO) (Derbina et al., 2005), SOKOL (CNO) (Ivanenko et al., 1993), and fluxes obtained from indirect measurements by KASCADE electrons and muons (Antoni et al., 2005), GRAPES-3 (Hayashi et al., 2005), the latter two give results for two hadronic interaction models, and EAS-TOP (Navarra et al., 2003). *Iron:* Results from direct measurements above the atmosphere by ATIC (Cherry, 2006), CRN (Müller et al., 1991), HEAO-3 (Engelmann et al., 1985; Juliusson, 1974; Minagawa, 1981), TRACER (Müller et al., 2005, single element resolution, and Hareyama et al., 1999; Ichimura et al., 1993), JACEE (Asakimori et al., 1995), RUNJOB (Derbina et al., 2005), SOKOL (Ivanenko et al., 1993) (iron group), as well as fluxes from indirect measurements (iron group) by EAS-TOP (Navarra et al., 2003), KASCADE electrons and muons (Antoni et al., 2005), GRAPES-3 (Hayashi et al., 2005), and HESS direct Cherenkov light (Aharonian et al., 2007). The latter three experiments give results according to interpretations with two hadronic interaction models. *Models:* The grey solid lines indicate spectra according to the poly-gonato model (Hörandel, 2003a). The black lines indicate spectra for models explaining the knee due to the maximum energy attained during

the acceleration process according to Sveshnikova (2003) (solid curve), Berezhko and Ksenofotov (1999) (dashed curve) Stanev et al. (1993) (dotted curve) and Kobayakawa et al. (2002) (chain curve).

Comments and References to Figure 11.46

Cosmic ray energy spectra for four groups of elements. From top to bottom: protons, helium, CNO group, and iron group (for detailed information refer to the note of Fig. 11.45). The grey solid lines indicate spectra according to the poly-gonato model (Hörandel, 2003a). The black lines indicate spectra for models explaining the knee as an effect of leakage from the Galaxy during the propagation process, according to Hörandel et al. (2007) (solid curve), Ogio and Kakimoto (2003) (dashed curve), Roulet (2004) (dotted curve), as well as Völk and Zirakashvili (2003) (chain curve).

11.7.3 Mean Logarithmic Mass, $\langle \ln(A) \rangle$

In view of all the difficulties to isolate spectra of specific masses or even mass groups at high energies with their large uncertainties, the estimation of the mean mass of the shower initiating primary of a set of showers of a particular energy window and as a function of primary energy is more reliable. The values of the mean logarithmic mass a function of primary energy determined using a specific method within the frame of a particular experiment manifest in general more continuity, but as we show in the following figures, the data points obtained with the different experiments begin to deviate significantly with increasing energy.

Again, as in the previous section and subsections, we do not elaborate on the different methods to extract the data from observables since these are discussed exhaustively in Chap. 10, and present here only the results from a selection of experiments.

In Fig. 11.47 we present a compilation of mainly KASCADE data assembled by Kampert et al. (1999). The increasing spread of the data points extracted from different observables with increasing energy is rather alarming and shows clearly that we are far from having a satisfactory data interpretation. Also included are the usual data from direct measurements for comparison in the overlap zone, and data from the air shower experiments HEGRA, Chacaltaya, DICE, the Moscow array, and some points from earlier data summaries, as listed in the figure caption. We also note the rapid drop of the atmospheric Cherenkov data acquired with the DICE experiment.

Another compilation of mean logarithmic mass that covers a wide energy range was made by Ogio et al. (2004), showing data from more recent air shower measurements at Chacaltaya that were obtained using the so-called Minimum Air Shower array (MAS) and equal intensity distributions. The result is illustrated in Fig. 11.48. Also included are data from the combined experiments CASA-BLANCA and CASA-MIA, from DICE, HEGRA-CRT and KASCADE. The latter were obtained from different observables, as listed in the caption. Some Chacaltaya points resulting

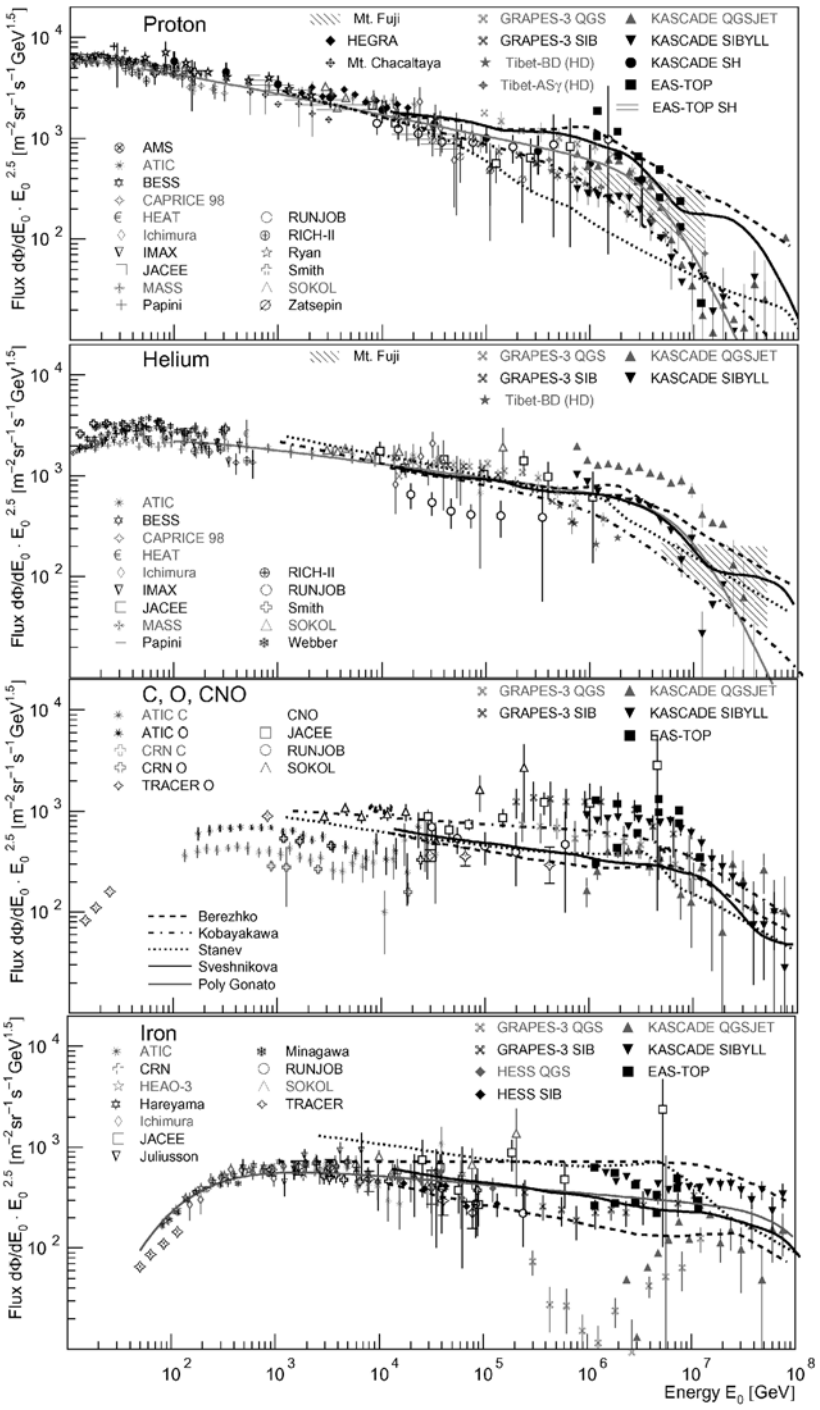

Fig. 11.45 Experimental primary spectra of major mass groups and predicted spectra (*curves*, set 1). For details see Comments and References to Fig. 11.45, page 537, and Hörandel, 2003a, b, 2008 (courtesy of J.R. Hörandel)

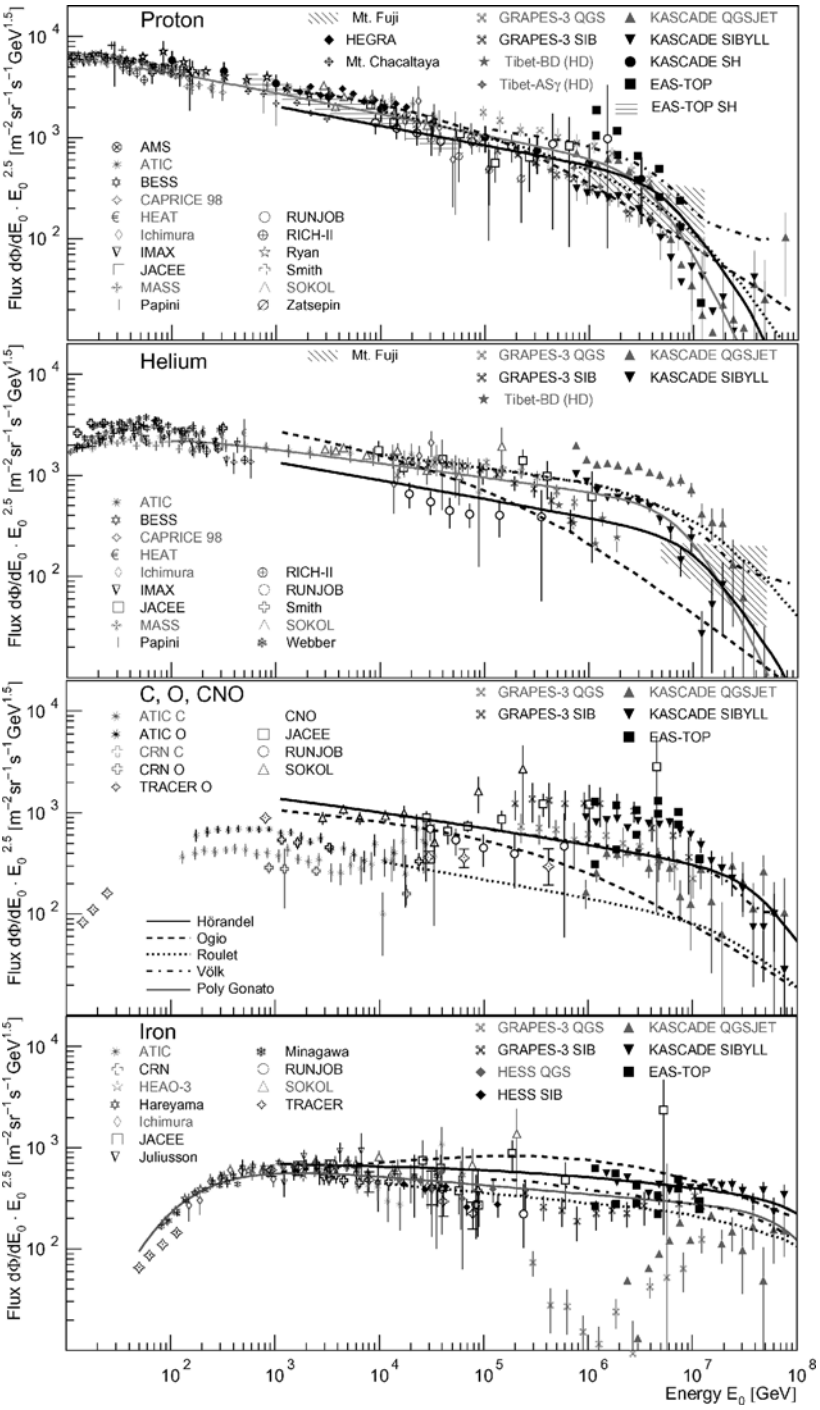

Fig. 11.46 Experimental primary spectra of major mass groups and predicted spectra (*curves*, set 2). For details see Comments and References to Figs. 11.45 and 11.46, pages 537 and 538, and Hörandel, 2003a, b, 2008 (courtesy of J.R. Hörandel)

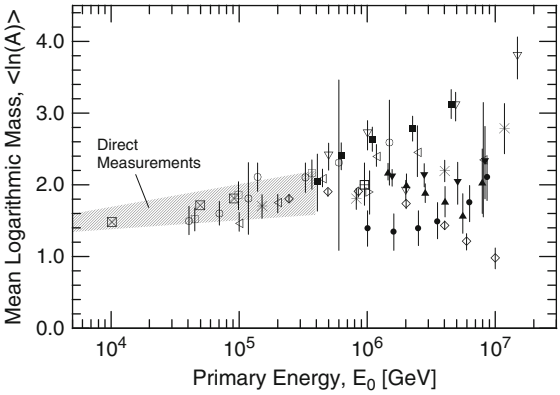

Fig. 11.47 Compilation of data of the mean logarithmic mass, $\langle \ln(A) \rangle$ from several experiments, including direct measurements, after Kampert et al. (1999). KASCADE data: ■, hadrons (Engler et al., 1999); ●, electrons (Weber et al., 1999); ▲ central granularity (Haungs et al., 1999); ▼ Bayes classification (Roth et al., 1999), all preliminary. ⋇ Moscow (Fomin et al., 1991); ◇ DICE (Boothby et al., 1998); ◁ HEGRA; ▽ Chacaltaya; ▷ Watson (1997). *Direct measurements:* ⊞ Shibata (1999); □ Asakimori et al. (1995); ○ Apanasenko et al. (1999a, b); ⊠, Wiebel-Sooth (1998)

from atmospheric Cherenkov measurements are also displayed. Whereas the new Chacaltaya data deviate little from the earlier data shown in Fig. 11.47 and follow a continuously rising trend, we note that the CASA-BLANCA mean mass points are quite low and show a very wide spread. It is also striking that the mean mass derived from particle measurements show a different behavior from that of atmospheric Cherenkov observation based results, except for the Chacaltaya Cherenkov data. The mean mass values at the very high energies are from the Fly's Eye experiment, given in Fig. 11.48.

A recent compilation which contains quite new data from direct measurements made with the ATIC experiment (Ahn et al., 2007) is plotted in Fig. 11.49. Shown, too, are the results from the air shower experiments CASA-BLANCA (Fowler et al., 2001), DICE (Swordy and Kieda, 2000) and from KASCADE. The latter data are based on electron and muon measurements (Antoni et al., 2005). A very recent compilation due to Tokuno et al. (2008) which includes data derived from new Chacaltaya atmospheric Cherenkov measurements are shown in Fig. 11.50 together with results from the EAS-TOP experiment. Some older data plotted in previous figures are included for comparison.

One of the most serious problems that we face when deriving the primary composition from air shower data is beautifully illustrated in Fig. 11.51, namely that different interaction models (event generators) used in a given simulation program frame, e.g., CORSIKA, yield different results for the interpretation of the same set of observables. The figure is from the work of Fowler et al. (2001) and applies to the CASA-BLANCA experiment.

We close this subsection with two figures from the very comprehensive compilation and analysis of the mean primary mass of Hörandel (2003a, b) (Figs. 11.52 and 11.53). Most of the relevant details are given in the captions.

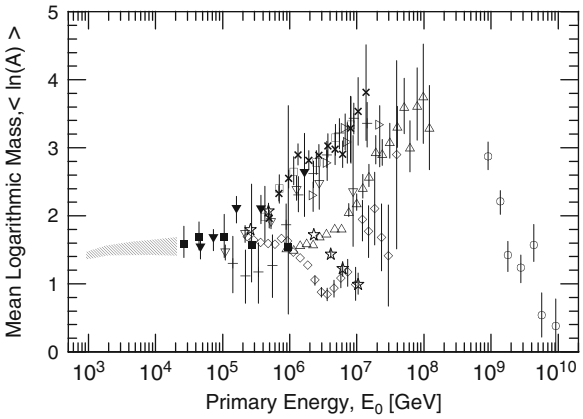

Fig. 11.48 Mean logarithmic mass, $\langle \ln(A) \rangle$, measured by the BASJE-MAS array as a function of primary energy, × (Ogio et al., 2004), compared with the results of other experiments. Balloon-borne detectors: ▼ JACEE (Asakimori et al., 1995, 1998); ■ RUNJOB (Apanasenko et al., 2001). Ground based detector systems: + CASA-MIA (Glasmacher et al., 1999b, d); □ KASCADE (hadrons) (Engler et al., 1999); ▽ HEGRA-CRT (Bernlöhr et al., 1998); △ KASCADE (electrons) (Ulrich et al., 2001); ◇ CASA-BLANCA (Fowler et al., 2001); ⋆ DICE (Swordy and Kieda, 2000); ○ Fly's Eye (Bird et al., 1993); ▷ Chacaltaya Cherenkov detector (Shirasaki et al., 2001). The hatched region represents the results of other direct observations compiled by Linsley (1983) (after Ogio et al., 2004)

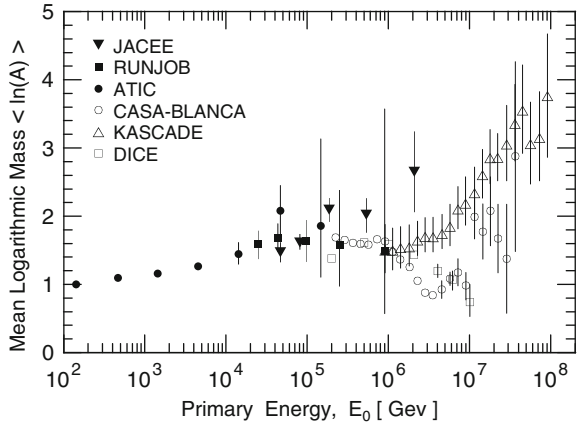

Fig. 11.49 Compilation of the mean logarithmic mass, $\langle \ln(A) \rangle$, of the primary hadronic cosmic radiation as a function of energy. Plotted is the natural logarithm of the mass number A obtained from the following experiments (after Ahn et al., 2007). Full symbols: ▼ JACEE (Takahashi, 1998); ■ RUNJOB (Apanasenko et al., 2001); ● ATIC (Ahn et al., 2005, 2006); all from balloon borne direct measurements. Open symbols: ○ CASA-BLANCA (Fowler et al., 2001); △ KASCADE (Antoni et al., 2005); □ DICE (Swordy and Kieda, 2000), all from indirect measurements based on air shower experiments

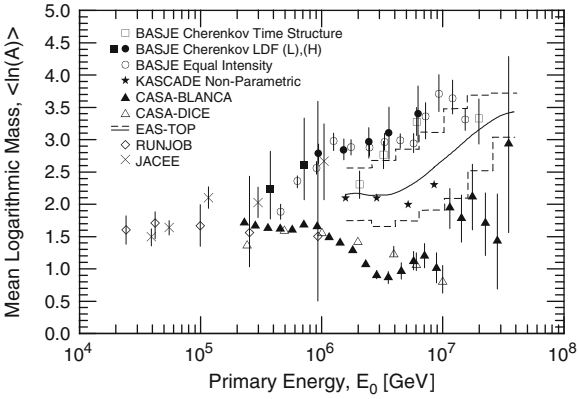

Fig. 11.50 Comparison of mean logarithmic masses, $\langle \ln(A) \rangle$, obtained by different air shower experiments and some direct measurements, as listed (after Tokuno et al., 2008)

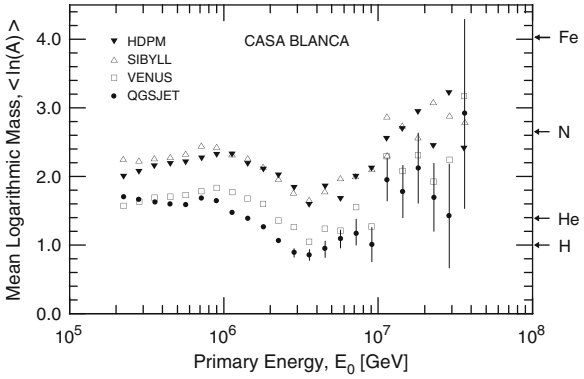

Fig. 11.51 Mean logarithmic mass, $\ln(A)$, measured by CASA-BLANCA as a function of primary energy. The four sets of symbols show the BLANCA data interpreted using CORSIKA with the respective hadronic event generators as listed in the figure. The error bars are statistical and shown for QGSJET only. They are similar for the other event generators (after Fowler et al., 2001)

11.8 Gamma Ray Initiated Showers

11.8.1 Introduction

We have summarized the situation of the low to moderately energetic diffuse primary gamma radiation and discussed gamma ray point and extended sources in view of gamma ray astronomy in Sect. 11.4. Here we want to review very briefly the situation of the primary gamma radiation at high and ultrahigh energies. The fraction of gamma rays in this energy region of the cosmic ray spectrum is intimately linked with the origin and nature of the cosmic radiation, which is still unknown, and its propagation in space.

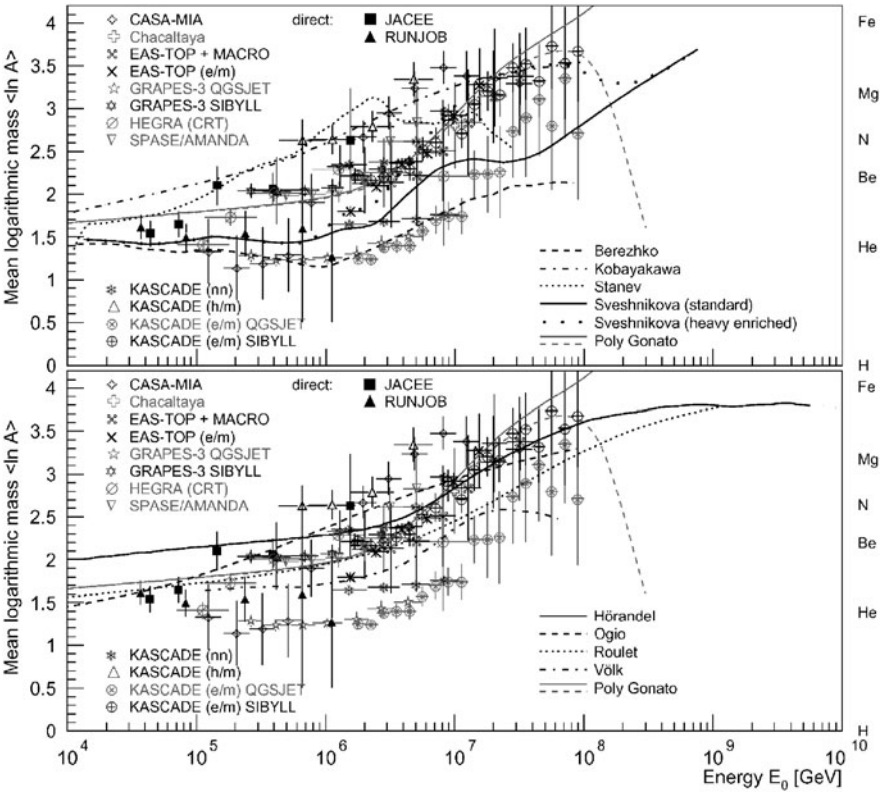

Fig. 11.52 Mean logarithmic mass of cosmic rays derived from electron, muon, and hadron data at ground level. Results are shown from CASA-MIA (Glasmacher et al., 1999a), Chacaltaya (Aguirre et al., 2000), EAS-TOP electrons and GeV muons (Aglietta et al., 2004b), EAS-TOP/MACRO TeV muons (Aglietta et al., 2004a), GRAPES-3 interpreted with two hadronic interaction models (Hayashi et al., 2005), HEGRA-CRT (Bernlöhr et al., 1998), KASCADE electrons and muons interpreted with two hadronic interaction models (Antoni et al., 2005), hadrons and muons (Hörandel, 1998), an analysis combining different observables with a neural network (Antoni et al., 2002), and SPASE/AMANDA (Rawlins et al., 2003). Data from direct measurements by JACEE (JACEE collaboration, 1999) and RUNJOB (Derbina et al., 2005) are shown for comparison. *Grey solid and dashed lines* identify spectra due to the poly-gonato model (Hörandel, 2003a). *Upper plot: lines* identify spectra from models generating the knee because of acceleration limits (Sveshnikova 2003), Berezhko and Ksenofotov (1999), Stanev et al. (1993), Kobayakawa et al. (2002). *Lower plot: lines* identify spectra for models generating the knee by leakage from the Galaxy during propagation (Hörandel et al., 2007; Ogio and Kakimoto, 2003; Roulet, 2004; Völk and Zirakashvili, 2003)

It is clear from the discussion of the all-particle spectrum in Sect. 11.6 that the question whether there is a break in the energy spectrum at the Greisen-Zatsepin-Kuzmin (GZK) cutoff (Greisen, 1966; Zatsepin and Kuzmin, 1966), located around $E_{\mathrm{GZK}} \sim 6 \cdot 10^{19}$ eV (60 EeV), or not, is now coming to an end since very recently the HiRes Fly's Eye group has announced that they have made the first observation of the GZK cutoff (Abbasi et al., 2008a). Similarly, the Auger group showed evidence

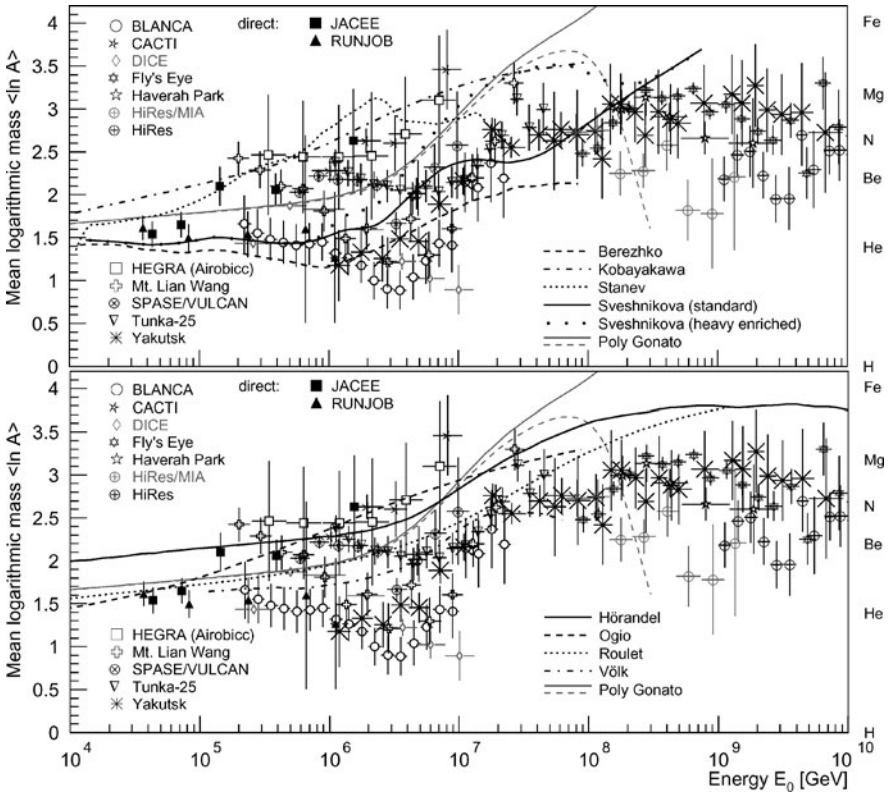

Fig. 11.53 Mean logarithmic mass of cosmic rays derived from the average depth of the shower maximum (cf. Fig. 7.28). The hadronic interaction model used to interpret the measurements was a modified version of QGSJET 01 with lower cross sections and a slightly increased elasticity (model 3a, Hörandel, 2003b). For the references of the experiments, see the caption of Fig. 7.28. For comparison, results from direct measurements from the JACEE (JACEE collaboration, 1999) and RUNJOB (Derbina et al., 2005) experiments had been included. *Models:* The *grey solid and dashed lines* indicate spectra according to the *poly-gonato model* (Hörandel, 2003a). *Upper figure*: The *curves* show spectra for models explaining the knee due to the maximum energy attained during the acceleration process according to Sveshnikova (2003) (*thick solid and dashed curves*), Berezhko and Ksenofotov (1999) (*dashed curve*), Stanev et al. (1993) (*dotted curve*), Kobayakawa et al. (2002) (*chain curve*). *Lower figure*: The *curves* indicate spectra for models explaining the knee as effect of leakage from the Galaxy during the propagation process according to Hörandel et al. (2007) (*thick solid curve*), Ogio and Kakimoto (2003) (*dashed curve*), Roulet (2004) (*dotted curve*), as well as Völk and Zirakashvili (2003) (*chain curve*) (courtesy J. Hörandel)

that they, too, observe the cutoff. Nevertheless, the question of the composition at these energies remains very uncertain.

The steepening of the energy spectrum is expected to occur if ultrahigh energy cosmic rays come from sources at cosmological distances, as is suggested by their overall isotropy, because they should be subject to the (GZK) cutoff, as discussed in Sect. 11.11. Should the sources be closer, we would expect distinctanisotropies.

There have been claims for a clustering of events on small angular scales, and correlations with possible classes of sources had been suggested, however, these claims require confirmation. Topics related to propagation and origin are discussed in Sect. 11.9 and 11.11.

High energy gamma ray initiated showers manifest similar properties as hadron initiated showers, however, they are less subject to fluctuations in the longitudinal as well as the lateral development and lack the hadron and muon components, except for occasional contributions via rare photonuclear processes (Suga et al., 1963). Large longitudinal fluctuations occur at extremely high energies where the Landau-Pomeranchuk-Migdal effect becomes relevant (Landau and Pomeranchuk 1953a, b; Migdal 1956) (see Sect. 4.5). The energy dependence of the depth of maximum development of gamma ray (photon) initiated showers is shown in Fig. 7.29.

Disregarding low energy gamma ray showers that die out before reaching the ground and can only be detected by means of the associated atmospheric Cherenkov light, high and ultrahigh energy gamma ray showers can also be detected with conventional air shower particle detector arrays and fluorescence detectors. Since it is difficult to distinguish high energy gamma ray showers from the more frequent hadron initiated showers only by their lateral structure, it is necessary to measure the muon fraction in the showers, too. Since muons are only produced via photonuclear processes in photon initiated showers, a low muon content (fraction) is a good signature of a photon shower.

11.8.2 Gamma Ray to Hadron Ratio

The photon fraction in the cosmic radiation at ultrahigh energies (UHE) is of great interest because it may reveal the origin of the most energetic cosmic rays. In particular, photons are expected to dominate over nucleon primaries in *non-acceleration models* of UHE cosmic-ray origin, i.e., in so-called *top-down* models (Bhattacharjee and Sigl, 2000; Sarkar, 2004; Gelmini et al., 2005). These have been invoked to account for the continuation of the flux of cosmic rays above the GZK cutoff without a spectral feature such as a drop-off, as is indicated by the AGASA data (Hayashida et al., 1999; Takeda et al., 2003), and because of difficulties with conventional acceleration mechanisms to produce particles with energies on the order of 10^{18} eV and higher. These topics are discussed in Sect. 11.11. Top-down models avoid these problems but create new ones. Thus, the determination of the photon contribution is a crucial probe to answer the question of the origin of the cosmic radiation and to select the correct source model.

A characteristic feature of most top-down models is that a significant fraction of the UHE cosmic rays they produce are predicted to be photons (Sarkar, 2004; Gelmini et al., 2005). UHE photons may be produced uniformly in the universe by the decay or annihilation of *relic topological defects (TD)* (Hill, 1983; Hindmarsh et al., 1995). During propagation towards the Earth, they interact with Background radiation fields and most of them cascade down to GeV energies where the extragalactic photon flux is constrained by the EGRET measurements. The remaining

UHE photons contribute to the cosmic ray flux above 10 EeV. By contrast in the *Super Heavy Dark Matter model (SHDM)* (Berezinsky et al., 1997; Michael and Sarkar, 1998), the UHE photons are generated in the decay of relic meta-stable particles, such as *cryptons* (Ellis et al., 2005) which in this model are clustered as *cold dark matter (CDM)* in our Galaxy.

Since the halo is believed to be partially transparent to UHE photons, they could be observed at Earth directly. In the *Z-Burst (ZB)* scenario (Weiler, 1982, 1999; Fargion et al., 1999), photons are generated from the resonant production of Z bosons by UHE cosmic neutrinos annihilating on the relic neutrino background. A distinctive feature of all these models is the prediction of a large photon flux at high energies, as is expected from considerations of QCD fragmentation (Fodor and Katz, 2001; Sarkar and Toldra, 2002; Barbot and Drees, 2003; Aloisio et al., 2004).

Conventional acceleration scenario produce photons via neutral pion production in collision processes. However, the corresponding photon fluxes are relatively small. Based on the primary spectrum obtained by the HiRes experiment (Abbasi et al., 2005a), the expected photon fraction is only of the order of 1% or less (Gelmini et al., 2005).

Separating photon-induced showers from events initiated by primary nuclei is experimentally easier than distinguishing light from heavy primary nuclei. As an example, simulations show that the average depths of shower maxima at 10 EeV primary energy are predicted to be about 1,000 g cm^{-2} for photons, 800 g cm^{-2} for protons, and 700 g cm^{-2} for iron nuclei (Abraham et al., 2007). Figure 11.54 shows the longitudinal development of simulated photon initiated showers and experimental points from measurements of the highest energy Fly's Eye event (320 EeV). In comparison to air showers initiated by protons and nuclei, photon initiated showers are in general expected to have a larger depth of shower maximum at energies in excess of $\sim$ 10 EeV and contain few secondary muons (cf. Fig. 7.29, Chap. 7). The latter phenomenon is due to the fact that the mean free paths for photo-nuclear interactions and direct muon pair production are more than two orders of magnitude larger than the radiation length. Therefore, only

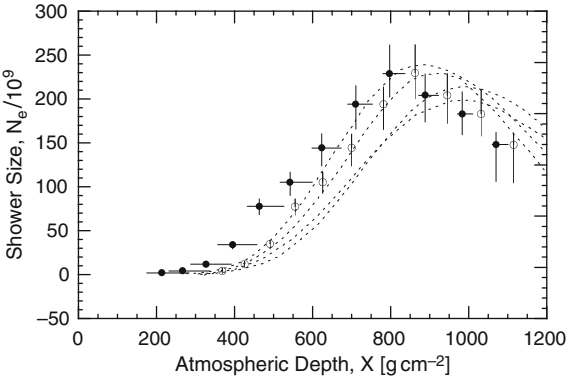

Fig. 11.54 Samples of random subset of simulated longitudinal profiles of photon initiated showers compared with Fly's Eye data of the highest energy event ($3.2 \cdot 10^{20}$ eV) (•), and the same data shifted by 1.5 σ toward greater atmospheric depth (○) (after Homola et al., 2004, 2005, 2006; Risse et al., 2004, 2006)

a small fraction of the primary energy in photon showers goes into hadronic channels.

Moreover, analyzing and interpreting the primary mass composition harbors serious uncertainties because of our inadequate knowledge of hadronic interactions at very high energies. On the other hand, photon initiated showers follow essentially the rules of electromagnetic interactions and are not subject to theoretical uncertainties. They can be simulated which much confidence in the results.

11.8.3 Experimental Situation and Gamma Ray-Hadron Ratio Data

Until recently limits on the UHE photon fraction in the primary cosmic radiation had been determined mainly by ground arrays. In this approach one can for example compare the rates of near-vertical showers to inclined ones. This method had been used at the Haverah Park experiment, yielding an upper limits (95% c.l.) of 48% above 10 EeV and 50% above 40 EeV (Ave et al., 2000, 2002). Based on an analysis of muons in air showers observed by the AGASA array, which is a rather sensitive method, the upper limits (95% c.l.) of the photon fraction had been estimated to be 28% above 10 EeV and 67% above 32 EeV (Shinozaki et al., 2002). An upper limit of 67% (95% c.l.) above 125 EeV was derived in a special analysis of the highest energy events recorded at AGASA by Risse et al., 2005.

In Fig. 11.55 we show a compilation of data of the photon fraction in the primary cosmic radiation in the low to medium energy range ($\sim 50 \leq E \leq 10^5$ GeV). Shown is a block (hatched area) containing data from several early measurements (pre 1985) and more recent data which had been obtained with the installations at Yakutsk (Glushkov et al., 1985), Tien Shan (Nikolsky et al., 1987), the Utah-Michigan experiment (Matthews et al., 1991), HEGRA (Karle et al., 1995), EAS-TOP (Aglietta et al., 1996a), and the CASA-MIA arrays at Utah (Chantell et al., 1997). The five latter data sets all use the muon contents as a criterion to select the gamma showers. Yakutsk and HEGRA use in addition optical Cherenkov data.

In a very recent study carried out by the Auger group, using some of the first data recorded by the Auger Observatory which consists of four fluorescence telescopes and a huge particle detector ground array of 1,600 units, they obtained a photon limit from the direct observation of the shower profile with the fluorescence telescopes, using the depth of the shower maximum as the discriminating observable. To avoid the uncertainties from modeling hadronic interactions, they have adopted an analysis method that does not require the simulation of hadronic cascades, but simply compares the experimental data with simulated photon initiated showers (Abraham et al., 2007).

To achieve a high accuracy in the reconstruction of the shower geometry, the authors have also used the *hybrid* detection technique, i.e. they have selected events

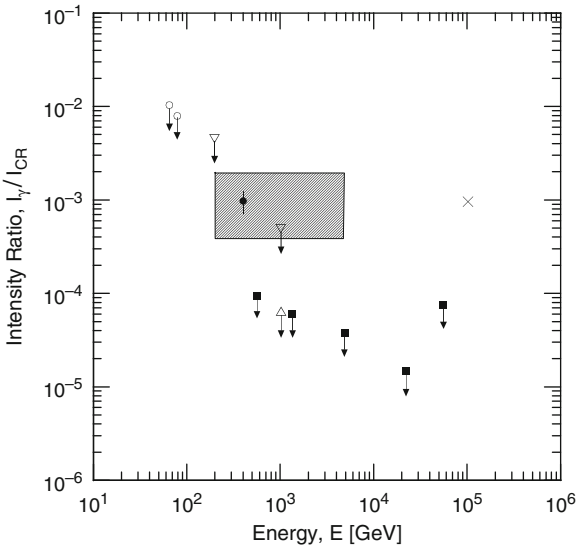

Fig. 11.55 Fraction of high energy gamma rays relative to hadronic cosmic rays. The hatched region indicates the range of gamma ray detections as published prior to 1985 (Gawin et al., 1963, 1968; Kamata et al., 1968; Suga et al., 1988). Results from Tien Shan by Nikolsky et al. (1987) and from Yakutsk by Glushkov et al. (1985) are indicated by the symbols • and ×, respectively. The symbols with the *downward arrows*, ○, ▽, △ and ■, are the data from the HEGRA (Karle et al., 1995), Utah-Michigan (Matthews et al., 1991), EAS-TOP (Aglietta et al., 1996a) and CASA-MIA (Chantell et al., 1997) experiments, respectively (after Chantell et al., 1997)

that had been observed by both the ground array and the fluorescence telescopes (Mostafá et al., 2005). In this way they were able to collect data from additional observables, such as the signal rise time that could be used for additional event classification. The result of the Auger measurement that is based on the observation of the depth of shower maximum yields and upper limit for the photon fraction at a primary energy of 10^{19} eV of 16% at 95% c.l. A plot showing the situation in the ultrahigh energy domain using data from several large experiments, including the data from the Auger hybrid detector, had been assembled by Abraham et al. (2007) and is presented in Fig. 11.56.

It should be noted that the photon flux arriving at Earth for a specific source model is subject to uncertainties arising from photon propagation. The latter is discussed in Sect. 11.11. Assumptions concerning the very low frequency (MHz) radio background and intergalactic magnetic fields must be made and are rather uncertain (Wdowczyk et al., 1972; Halzen, 1995; Sarkar, 2004; Gelmini et al., 2005). The typical range of energy loss lengths usually adopted for photons are 7–15 Mpc at 10 and 5–30 Mpc at 100 EeV.

Since photons are expected to dominate over nucleon primaries in the top-down (non-acceleration) models of the origin of ultrahigh energy cosmic rays, the gamma ray to hadron ratio is an important key to check the validity of such models.

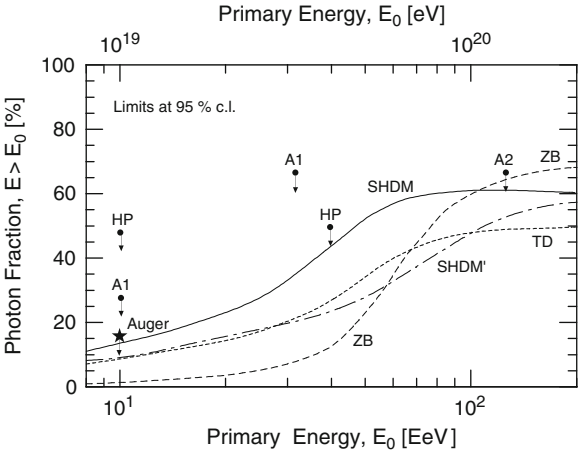

Fig. 11.56 *Upper limits* (95% c.l.) of the primary cosmic ray photon fraction at very high energies derived from data of the Auger Observatory (⋆) and earlier experiments: AGASA, A1, Shinozaki et al. (2002), A2, Risse et al. (2005); Haverah Park, HP, Ave et al. (2000, 2002). The *curves* show expectations according to the non acceleration models ZB, SHDM and TD, after Gelmini et al. (2005), and SHDM' after Ellis et al. (2005) (Abraham et al., 2007, 2008a)

11.8.4 Pre-Showering of Gamma Rays

The interpretation of gamma ray initiated showers of very high energy that are subject to *pre-showering* well outside the atmosphere in the weak geomagnetic field is more delicate. Except for the lack of muons these showers can imitate under particular conditions heavy primary initiated showers. The theory of magnetic pair production of photons (gamma rays) of ultrahigh energy in weak magnetic fields and the subsequent magnetic bremsstrahlung (curvature radiation) is discussed in detail in Sect. 4.5. The longitudinal development of such showers and the energy dependence of the height of maximum development are briefly discussed in Chap. 7 and is illustrated in Fig. 7.29.

11.8.5 Gamma Rays from Cygnus X-3

Scanning the sky for ultrahigh energy gamma ray sources has been going on since 1960, when Cocconi suggested that these may reveal likely sources of cosmic rays. However, it was not until much later when high energy gamma ray point sources were discovered. As a particular example of an intriguing gamma ray source we will briefly summarize the history of Cygnus X-3, a binary system at the fringes of our Galaxy (distance $\sim$ 37 kly or $\sim$ 11 kpc).

The search for gamma rays from the direction of Cygnus X-3, a region of known X-ray activity with a periodicity of 4.8 h, had been carried out for several years by different research groups. A wide variety of techniques, ranging from balloon and satellite born instruments to ground based atmospheric Cherenkov and air shower

particle detectors had been employed, depending on the energy range ($\sim 4 \cdot 10^7 \leq E_\gamma \leq 10^{16}$ eV) under investigation.

Samorski and Stamm (1983a, b) have re-analyzed earlier data from the Kiel air shower array which had an angular resolution of $\sim 1^\circ$ (Bagge et al., 1979). They observed a significant excess of air showers from the direction of Cygnus X-3 having a strong correlation with the 4.8 h period of the X-ray source. The energy of the detected showers was in the range from $2 \cdot 10^{15}$ to $2 \cdot 10^{16}$ eV. Since charged primary hadrons in this energy range would be deflected by the galactic magnetic fields (~ 3 μG) it appeared evident that to correlate with the Cygnus source the showers must be initiated by photons, or possibly neutrons (Jones, 1989a, b, 1990; see Fig. 11.59).

Among the many criteria which Samorski and Stamm applied to select gamma ray initiated showers with a high probability, they required a relatively flat lateral distribution of the shower particles, corresponding to a rather old shower with large age parameter, as had to be expected for photon showers of this energy at sea level. Flat distributions are atypical for hadronic showers of the selected energy range. In addition they selected events within the zenith angular range $0^\circ \leq \theta \leq 30^\circ$ to improve the accuracy of the energy determination.

The shower sample which had been used contained a total of 3,838 events. The sample was split into two groups, so-called *steep showers* with age parameter $s < 1.1$ and *flat showers* with age parameter $s > 1.1$. The group of flat showers showed an excess of 16.6 showers ($4.4\,\sigma$) above the average off-source background of 14.4 ± 0.4 showers per bin in the total declination band. According to Poissonian statistics they found a chance probability for a random excess of this magnitude of 10^{-4}.

In Fig. 11.57 we show the gamma ray spectrum of Cygnus X-3 as it had been constructed from data recorded by many experiments over a very wide spectral range and time, using different techniques (Weekes, 1988, 1996). This object is particularly puzzling because of its seemingly highly irregular activity. Another puzzling situation is that Samorski and Stamm (1983c) noticed, that the apparent gamma ray showers contained a large number of muons, about 80% of the muon content of normal hadronic showers. This led to various speculations concerning charm production cross sections and new particles (Stanev et al., 1985; Halzen et al., 1986; Cudell et al., 1987; Drees et al., 1989). The fact that the very high energy portion of the spectrum is no longer observed leaves doubts whether the events were real and quenched speculations that the events were caused by some hitherto unknown neutral particle (Lawrence et al., 1989).

11.9 Arrival Direction and Anisotropy

11.9.1 Introduction

One of the first questions which had been asked after it was realized that extensive air showers must be initiated by ultrahigh energy particles was, what is the nature of these particles or quanta and where do they come from. Partial answers to the

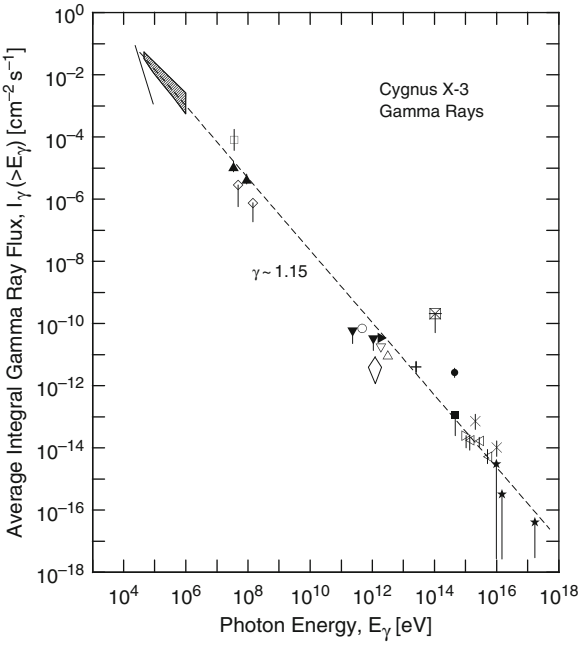

Fig. 11.57 The wide spectral range of gamma ray fluxes claimed of having been detected from Cygnus X-3 between 1972 and 1985, using many different techniques, ranging from comparatively low energy satellite experiments to high energy air Cherenkov telescope and air shower particle detector array investigations. The two symbols × identify the high energy data points of Samorski and Stamm (1983a, b) which they have observed with the air shower array at Kiel. Their measurements that showed allegedly a high muon content, atypical of gamma ray showers, triggered an intense investigation of Cygnus in the eighties of the last century, partly in search of a hitherto unknown new neutral particle. The high energy air shower data are contested since they could not be reproduced by later experiments (after Weekes, 1988; for references see Bhat et al., 1986)

question concerning the nature of the primary radiation are presented and discussed in Sect. 11.7. To answer the second question we have to study the arrival direction of the air shower initiating particles by projecting the shower axis back into space, to determine the celestial coordinates of each event, to construct the distribution in right ascension and declination. Figure 11.58 shows a typical distribution of a sample of air showers in right ascension, α. One then uses a harmonic analysis to determine the amplitude and phase of possible anisotropies in the arrival direction, in the hope to find locations of enhanced emission and hopefully identify astronomical objects as likely sources of the cosmic radiation. Deflection of the shower particle trajectories by geomagnetic fields must be accounted for when determining the arrival direction of the shower initiating particles.

Apart from the search for the sources of the primary cosmic radiation, anisotropies also reflect the general pattern of cosmic ray propagation in the Galaxy (Ptuskin, 2005). Model calculations show that the diffusion of the cosmic radiation in the galactic magnetic fields may cause anisotropies on the order of 10^{-4}–10^{-2},

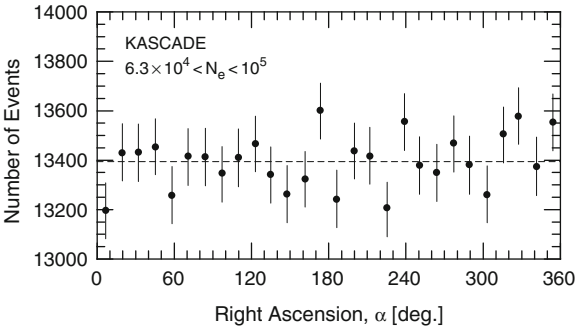

Fig. 11.58 Example of a right ascension distribution after correction for barometric pressure and temperature in the specified shower size range. The *dashed line* represents the mean number of events (after Antoni et al., 2004a)

depending on the particle energy and the strength and configuration of the magnetic fields. The diffusion of the cosmic rays is rigidity dependent and may cause anisotropies that can be as much as a factor of 5–10 larger for protons than for iron nuclei according to some models (Candia et al., 2003).

Rigidity dependent diffusion can be just one of several causes for the steepening of the spectrum around 3–5 PeV that manifests itself in the *spectral knee*. Other models suggest that he knee is due to a change in the acceleration efficiency and do not produce anisotropies (Hillas, 1979; Lagage and Cesarsky, 1983). Thus, anisotropy measurements yield important information for testing the validity of acceleration and propagation models.

11.9.2 Magnetic Deflection

Galactic and, in the case of ultrahigh energy cosmic rays, extragalactic magnetic fields, too, must be considered in the search of cosmic ray sources since they deflect charged particles in motion. The *radius of curvature*, r_c[m], of a particle of momentum p [GeV/c] and electric charge, Ze, in a magnetic field of strength B [T] (1 T (Tesla) = 10, 000 G (Gauss)) is

$$r_c \;=\; \frac{p\,\cos\phi}{0.3\,Z\,B}\;, \tag{11.22}$$

where $\cos\phi$ is the *pitch angle* with respect to the magnetic field direction. The angular deflection, δ, of a charged particle in a coherent homogeneous magnetic field after having traveled a distance $L_{\rm coh}$ is

$$\delta \;=\; L_{\rm coh}/r_c\;. \tag{11.23}$$

The galactic field which has a strength on the order of a few μG and a coherence length of ∼ 1 kPc excludes essentially charged hadron astronomy except for the energy domain well above 10^{18} eV (Jansson et al., 2007; Kachelriess et al., 2007; Han, 2008). At this energy the gyroradius of a proton is about 300 pc in a magnetic

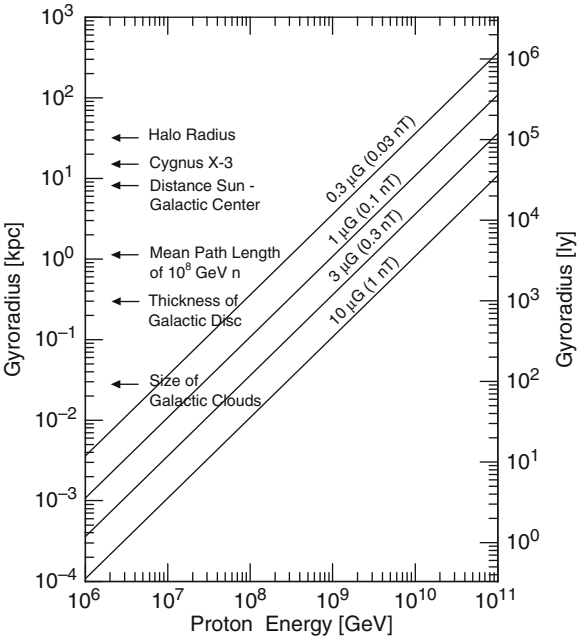

Fig. 11.59 Gyroradius in kilo parsec [kpc] and light years [ly] of a proton versus proton energy in magnetic fields of 0.3 μG (0.03 nT), 1 μG (0.1 nT), 3 μG (0.3 nT), and 10 μG (1 nT). Indicated, too, are the sizes of some astrophysical objects and regions, the approximate distance to Cygnus X-3, and the mean path length traveled by a 10^8 GeV neutron before decay

field of 3μG (cf. Fig. 11.59), which corresponds approximately to the thickness of the galactic disc. The angular deflection with respect to this dimension is on the order of degrees, thus, particles begin to escape into meta-galactic space, and vice versa.

For ultrahigh energy particles that are presumed to be of extragalactic origin, one must consider extragalactic magnetic fields as well. However, little is known about extragalactic magnetic fields. According to Kronberg (1994) it is estimated that the field strength is on the order of ∼1 nG (10^{-9} G) and is structured in cells having dimensions L_{coh} of approximately 1 Mpc within which the field orientation changes (see also Kang et al., 2007).[3] Following Hooper et al. (2007), a particle having an energy E, carrying charge Z, traversing a distance L through a series of L/L_{coh} randomly oriented uniform magnetic field regions of strength B and coherence length L_{coh} suffers an overall deflection, θ [deg], of

$$\begin{aligned}\theta(E,Z) &\approx \left(\frac{L}{L_{\mathrm{coh}}}\right)^{0.5}\delta \\ &\approx 0.8\left(\frac{10^{20}eV}{E}\right)\left(\frac{L}{10Mpc}\right)^{0.5}\left(\frac{L_{\mathrm{coh}}}{1Mpc}\right)^{0.5}\left(\frac{B}{1nG}\right)Z\ .\end{aligned} \tag{11.24}$$

[3] Gelmini et al. (2007) consider in their work extragalactic magnetic field strength as low as 10^{-11}–10^{-9} G.

Such a configuration would deflect a proton of 10^{20} eV about 3° from a straight line over a distance of 30 Mpc and would increase the effective distance to the cosmic ray source. The celestial coordinates of the ultrahigh energy cosmic radiation can be determined to better than 3° and one might therefore expect correlations between the arrival direction of the most energetic events with possible sources, such as active radio galaxies (Watson, 2000). In a very recent paper the Auger collaboration claims to have found such a correlation of ultrahigh energy events with nearby AGNs (Abraham et al., 2008b). This topic is discussed in more details in Sect. 11.11.

11.9.3 Harmonic Analysis of Data

Numerous authors have carried out anisotropy analyses of the arrival direction of showers. Some have used very sophisticated methods. In the following we outline the simple approach used by Edge et al. (1978) for their investigation using the Haverah Park data (see also Blake et al., 1978; Hayashida et al., 1999).

The harmonic amplitude, r, and the phase of the maximum, θ, are defined for a sample of n right ascensions or times $\phi_1, \phi_2, \ldots, \phi_n$, where $0 \leq \phi_i \leq 2\pi$ in terms of the components

$$a = \frac{2}{n} \sum_{i=1}^{n} \cos m\phi_i \tag{11.25}$$

and

$$b = \frac{2}{n} \sum_{i=1}^{n} \sin m\phi_i \ , \tag{11.26}$$

n being 1 and 2 for the first and second harmonics, respectively. The fractional amplitude is then

$$r = (a^2 + b^2)^{1/2} \tag{11.27}$$

and the phase is given by

$$\theta = \theta_1 \quad \text{for} \quad a, b > 0 \tag{11.28}$$

$$\theta = \theta_1 + \pi \quad \text{for} \quad a < 0 \tag{11.29}$$

$$\theta = \theta_1 + 2\pi \quad \text{for} \quad a > 0; b < 0 \tag{11.30}$$

where $\theta_1 = \tan^{-1}(b/a)$ and $-(\pi/2) \leq \theta_1 \leq (\pi/2)$.

If the samples $\phi_1 \ldots \phi_n$ are distributed randomly between 0 and 2π, then, as $n \to \infty$, the probability, P, of obtaining an amplitude greater than or equal to r is

$$P(\geq r) = \exp(-k_0) \ , \tag{11.31}$$

where $k_0 = (nr^2)/4$. This is a good approximation for $n > 10$. All phases are equally likely.

If the sample has been drawn from a parent population with harmonic amplitude s and phase ϕ, Linsley has shown how confidence limits can be placed on s and ϕ from the estimates r and θ derived from the data (Linsley 1975a, b, c). The RMS-amplitude expected from samples of n randomly distributed points is

$$r_{\mathrm{RMS}} = \frac{2}{\sqrt{n}} \tag{11.32}$$

and worthwhile confidence limits can be set when $k_0 = (r^2/r^2_{\mathrm{RMS}}) > 1$. This simply means that good estimates can only be made with sufficient data to throw the random noise level below s. k_0 is therefore an important and useful parameter and should be quoted with r and θ in all results.

If one has a sample of m k_0's, then the sum

$$K = \sum_{j=1}^{m} k_{0,j} \tag{11.33}$$

is distributed as

$$P(K)\,\mathrm{d}K = \frac{K^{m-1}}{(m-1)!} e^{-K}\,\mathrm{d}K \tag{11.34}$$

and the probability of getting K greater than some value s from a random distribution of points is

$$\int_s^{\infty} \frac{K^{m-1}}{(m-1)!} e^{-K}\,\mathrm{d}K. \tag{11.35}$$

This is identical to the χ^2 distribution with $\chi^2 = 2K$ and $2m$ degrees of freedom. All this analysis presupposes uniformity of exposure in the interval 0–2π.

When this is not so, such as in *solar diurnal time*, one should use the rate of showers in 24 equal time intervals to evaluate a and b, where

$$a = \frac{2}{24} \sum_{i=1}^{24} \frac{n_i}{t_i} \cos \overline{\phi}_i \tag{11.36}$$

$$b = \frac{2}{24} \sum_{i=1}^{24} \frac{n_i}{t_i} \sin \overline{\phi}_i \tag{11.37}$$

and n is the number of showers detected in time t_i in the i-th interval associated with $\overline{\theta}_i$. The fractional amplitude is then

$$r = \left\langle \frac{n_i}{t_i} \right\rangle^{-1} (a^2 + b^2)^{1/2} \ , \tag{11.38}$$

the phase is evaluated as before and

$$k_0 = \frac{n(a^2 + b^2)}{4\langle n_i^2 / t_i^2 \rangle} \ , \tag{11.39}$$

where $n = \sum_i n_i$ is again the total number of showers detected. In this situation the probability of obtaining an amplitude greater or equal to r is *not circularly symmetric*. The loci of constant probability become ellipses. However, even in the worst case, the probability estimated using the k_0 defined in the usual way is in error by less than about 5%.

Linsley (unpublished) has given a useful example of the behavior of amplitude and phase estimates in different experiments. If the number of events available in an experiment is such that the rms-value of r, $(2/\sqrt{n})$, is equal to the true amplitude, s, then in a sequence of experiments r will only be *significant* (say $P < 0.01$) in one experiment out of ten whereas the phase will be within 50° of the true phase in two experiments out of three. In addition, if there is a real anisotropy the distribution of k_0 from the series of experiments will converge to that with a mean given by $\langle k_0 \rangle = 1 + k$, where $k = (s^2 n)/4$.

Another method of analysis to search for directional anisotropies, called the *Rayleigh method*, had been developed to account for right ascension dependent exposure times, i.e., it is trimmed to overcome problems caused by non-uniform celestial scans, varying array efficiencies, and irregular exposures. The interested reader is referred to Mardia and Jupp (1999) and the recent paper by Mollerach and Roulet (2005).

11.9.4 Data on Arrival Direction and Anisotropy

Major experimental and theoretical efforts had been made during the past decades to solve the problem of the origin and acceleration of the cosmic radiation and its propagation in space, including many anisotropy analyses, but so far with rather modest success (Ginzburg and Ptuskin, 1976; Cesarsky, 1980; Clay, 1984; Clay et al., 1984; Kifune et al., 1986; Noda et al., 2008). New data on key parameters such as the primary energy spectrum and composition, the mean column density traversed and the magnetic fields in our Galaxy have helped to refine the models of the origin, acceleration and propagation mechanisms of the cosmic radiation.

For decades many authors have studied the amplitude of harmonic analyses and the phase of the maximum intensity. The general result of this work is that the arrival direction of the charged cosmic radiation in the energy range between 100 TeV and 10 PeV is surprisingly isotropic. An early summary is given by Sakakibara (1965)

specifying amplitudes smaller than 0.1% at energies $< 10^{14}$ eV with a possible increase of the amplitude as a function of primary energy above 10^{14} eV as $E_0^{1/2}$.

Recent evaluation of data from measurements carried out by the Torino group with the EAS-TOP experiment (Aglietta et al., 2007, see also Aglietta et al., 1996a) confirm the small anisotropies at 100 TeV in *solar time* with an amplitude of the first harmonic of $A_{\mathrm{sol}} = (2.8 \pm 0.8) \cdot 10^{-4}$ and phase $\phi_{\mathrm{sol}} = (6.0 \pm 0.1)$ h. These values are in excellent agreement and expected from the *Compton -Getting effect* (Compton and Getting, 1935) due to the revolution of the Earth around the Sun at the latitude of the experiment, i.e., $A_{\mathrm{sol},C-G} = 3.4 \cdot 10^{-4}$ and phase $\phi_{\mathrm{sol},C-G} = 6.0$ h. The same authors also specify amplitude, phase and the *Rayleigh imitation parameter*, P [%], of the first and second harmonics in *sidereal* and *anti-sidereal time*.

As the data on very high energy events began to accumulate more and more, anisotropy studies were extended to higher and higher energies, where anisotropies were expected to manifest themselves stronger (Linsley and Watson, 1977, 1981; Linsley, 1983; Hillas, 1981, 1984; Watson, 1992). The Haverah Park group (Lloyd-Evans, 1982; Lloyd-Evans et al., 1983) disclosed a statistically significant amplitude of (1.7 ± 0.4) at an energy of about 10^{17} eV. Considering an average galactic magnetic field of strength 3μG (0.3 nT) a proton of this energy has a gyroradius of about 30 pc which is about one tenth of the galactic disc thickness (cf. Fig. 11.59). Implications of such an anisotropy with respect to cosmic ray propagation and the structure of our Galaxy had been discussed by Silberberg et al. (1983), Ormes (1983) and Streitmatter et al. (1985).

Kifune et al. (1986) have carried out primary mass specific anisotropy measurements on the basis of the muon contents of the showers and present amplitude and phase plots in their paper for the primary energy range $10^{15} \leq E_0 \leq 10^{17}$ eV, analyzing approximately 300,000 showers from Akeno. Their work yields an anisotropy of $\sim 2 \cdot 10^{-3}$ at 3–5 PeV. For the second harmonic they get (1.1 ± 0.4)% in the energy range $10^{16} \leq E_0 \leq 10^{17}$ eV with a phase of $109^\circ \pm 10^\circ$ in right ascension. They observed *muon-rich showers* to come preferentially from a direction of about 230° in right ascension but point out that no statistically meaningful anisotropy was found for *muon-poor showers*.

A similar analysis using about 10^8 showers was carried out by Antoni et al. (2004a) using the Rayleigh formalism. These authors find no indication of an anisotropy in the energy range 0.7–6 PeV. A data summary of anisotropies in tabulated form covering the energy range from a few times 10^{14} eV to almost $8 \cdot 10^{17}$ eV is given by Clay et al. (1997). Very recently Over et al. (2007) have analyzed data from the KASCADE-Grande experiment in search of anisotropies and point sources using the Rayleigh method. The result of their work together with data from many experiments is displayed in Fig. 11.60.

Studies of the AGASA group led to the discovery of an anisotropy with an amplitude of the first harmonic of 4% around an energy of 10^{18} eV (Hayashida et al., 1996, 1999; Takeda et al., 2003). On a two-dimensional map they have identified an event excess of 4σ and 3σ near the galactic center and the Cygnus region, respectively, and they conclude that the anisotropy seems to be correlated with the galactic structure. In a reanalysis of the data from the SUGAR experiment in Australia (Winn

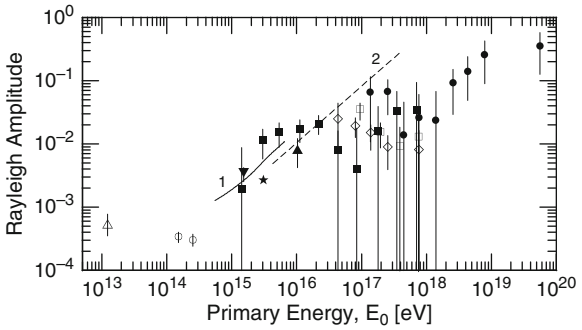

Fig. 11.60 Upper limits of the Rayleigh amplitude as obtained by harmonic analysis of the distribution of the right ascension of the arrival directions of showers compared with the results from other experiments (after Over et al., 2007). ●, AGASA; ■, Akeno; ▲, Bucklandpark (Gerhardy et al., 1983); ▼, Buckland Park (Bird et al., 1989); ○, EAS-TOP; □, Haverah Park; △, Kamiokande; ◇, Yakutsk; 1, KASCADE 95% c.l.; 2, KASCADE-Grande; ⋆, KASCADE-Grande East-West 95% c.l.

et al., 1986), Bellido et al. (2001) confirm the existence of an excess of 10^{18} eV cosmic rays from the direction of the galactic center, first reported by the AGASA group.

In Table 11.9 we show a combined list of 14 showers that had been detected by the five large experiments as listed in the table (Nagano and Watson, 2000). The events had all been classified to have a primary energy in excess of 10^{20} eV. Each shower is identified with a unique event number, the date of detection, the zenith angle of incidence, θ, the right ascension, RA, and declination, $Decl.$, and the galactic longitude, l, and latitude, b,.

Figure 11.61, assembled by Hillas (1998), shows the arrival distribution of showers of energy $\geq 4 \cdot 10^{19}$ eV that were recorded by air shower arrays only, for which the exposure in right ascension is essentially uniform. This allows a radial scale to be chosen so that an area in any part of the plot has the same exposure as an equal area in any other part of the plot. Events with energies above 10^{20} eV are shown with larger circles. No correlations are found with galactic or extra-galactic features. Thus, the distribution of the events is *isotropic*.

A cosmic ray observatory with a full sky coverage can exploit standard analysis methods to study the anisotropy of the radiation that do not work if part of the celestial sphere is never seen. Sommers (2001) has carried out an interesting analysis considering an observatory with a full-sky coverage. He concludes that the true cosmic ray anisotropy can be measured despite non-uniformity in celestial exposure, provided that the detector system is not blind to any region of the sky.

A rather detailed search for broad-scale anisotropy using Monocular and Stereo Fly's Eye data had been carried out by Dai et al. (1999). These authors arrive at the conclusion that the galactic plane enhancement factor is nonzero at the 3.2 σ level for energies less than 3.2 EeV. They note that the galactic latitude gradient is only significant in the energy range 0.4–1 EeV, where the galactic plane enhancement is strongest.

Table 11.9 Arrival direction of candidate events with energy $> 10^{20}$ eV (Nagano and Watson, 2000)

Experiment	Date	Energy 10^{20} eV	θ Degrees	RA Degrees	$Decl.$ Degrees	l Degrees	b Degrees	Ref. No.
Volcano Ranch	22.04.62	1.4	11.7	306.7	46.8	84.3	4.8	4472
Haverah Park	31.12.70	1.02 ± 0.03	35	353	19	99	−40	8185175
	05.12.71	1.05 ± 0.3	30	199	44	107	73	9160073
	18.04.75	1.2 ± 0.1	29	179	27	212	78	12701723
	12.01.80	1.05 ± 0.05	37	201	71	119	46	17684312
Yakutsk	07.05.89	1.1 ± 0.4	58.9	75.2	45.5	162.2	2.6	
Fly's Eye	15.10.91	$3.2^{0.36}_{-0.54}$	43.9	85.2	48.0	163.4	9.6	
AGASA	12.01.93	1.01 ± 0.3	33.2	124.3	16.8	206.7	26.4	20957–0382
	03.12.93	2.10 ± 0.5	22.9	18.9	21.1	130.5	−41.4	25400–0296
	06.07.94	1.06 ± 0.32	35.4	281.3	48.3	77.6	20.9	25790–0886
	11.01.96	1.44 ± 0.43	14.1	241.7	23.0	38.9	45.8	00123–3997
	22.10.96	1.05 ± 0.32	33.2	298.5	18.7	56.8	−4.8	00120–4976
	30.03.97	1.50 ± 0.45	44.2	294.6	−5.8	33.1	−13.1	01606–0578
	12.06.98	1.20 ± 0.36	27.3	349.0	12.3	89.5	−44.3	03876–9311

Note: θ is the zenith angle, RA the right ascension, $Decl.$ the declination, l the galactic longitude and b the galactic latitude. Ref. No. is the number assigned by the experimental group to the event.

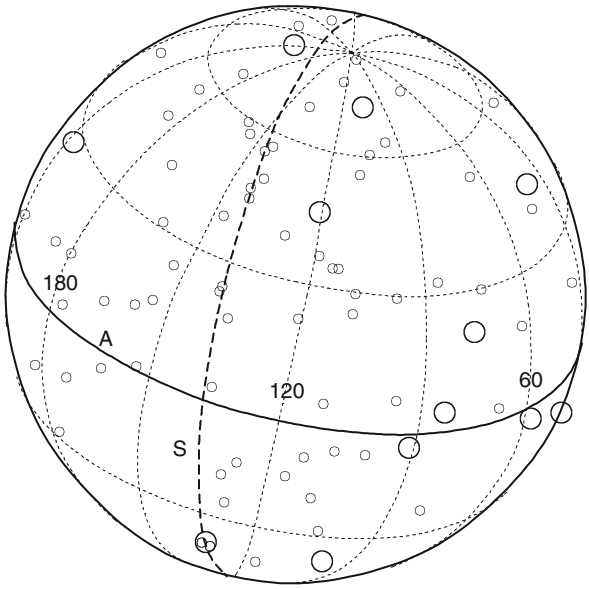

Fig. 11.61 Arrival directions of events with primary energy $\geq 4 \cdot 10^{19}$ eV. The events are from the ground arrays for which the exposure in right ascension is uniform. The *larger circles* mark the directions of the events with energy $> 10^{20}$. The super-galactic plane is represented by the heavy *dashed curve* and is labeled *S* and the *solid curve* labeled *A* is the galactic plane (after Hillas, 1998; see also Auger Collaboration, 2007)

Very recently Noda et al. (2008) evaluated the data from the LAAS (Large Area Air Shower) experiment where at present 11 compact air shower arrays located at different institutions in Japan participate, that are synchronized with an accuracy of 1 μs (Wada et al., 1999; Ochi et al., 2003; Iyono et al., 2006). The longest baseline between any two arrays measures 1,000 km. They focused their interest on the primary energy range between 10^{14} and 10^{15} eV. They have analyzed $1.2 \cdot 10^7$ showers and obtained for the amplitude and phase of the first harmonic the values of $(0.23 \pm 0.04)\%$ and (0.4 ± 0.7) h, respectively and for the second harmonic $(0.06 \pm 0.04)\%$ and (7.5 ± 2.6) h. Their results are reproduced in Fig. 11.62 which contains a compilation of results from many other analyses. The lines 1 and 2 apply to the model of Shibata (2004) and a value of the rigidity dependent diffusion coefficient of (0.339 ± 0.014).

Another recent preliminary search for anisotropies carried out with data from the new giant Auger Observatory found no significant cosmic ray flux excess in the direction of the galactic center in the two energy ranges $0.1 \leq E_0 \leq 1$ and $1 \leq E_0 \leq 10$ EeV, whereby the galactic center was treated both as an extended and a point like source (Santos, 2007; see also Li and Ma, 1983). Likewise, the search for large-scale anisotropies with data from the same experiment carried out by Armengaud (2007) came to the conclusion that at EeV energies the right ascension distribution is remarkably compatible with an isotropic sky, and an upper limit on the first harmonic modulation of 1.4% in the energy range $1 \leq E_0 \leq 3$ EeV is set. Thus these authors do not confirm the 4% *RA* modulation found by the AGASA group (Hayashida et al., 1999), however, one must note that the sky regions covered by the two experiments are not the same. The anisotropy search program of the Pierre Auger Observatory had been outlined by Clay (2003).

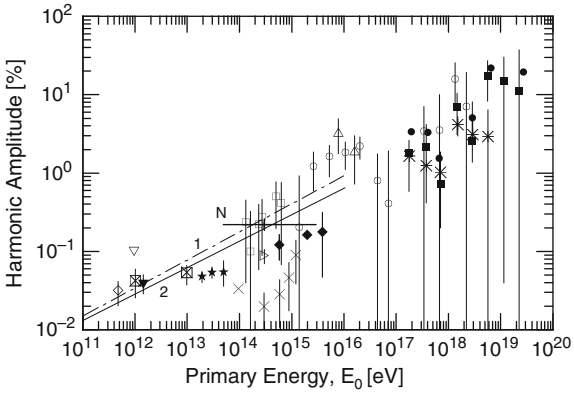

Fig. 11.62 Energy dependence of the amplitude of the first harmonic obtained by many different experiments (Noda et al., 2008)

+, N	Noda et al. (2008)	▽	Bercovitch and Agraval (1981)
×	Aglietta et al. (2003b)	▼	Bergeson et al. (1979)
✳	Hayashida et al. (1999)	◇	Davis et al. (1979)
□	Clay and Smith (1997)	♦	Daudin et al. (1956)
■	Cassiday et al. (1990a,b)	⋆	Sakakibara et al. (1979)
○	Kifune et al. (1986)	⊠	Fenton and Fenton (1976)
●	Efimov et al. (1983)	1	Noda et al. (2008), model-
△	Gerhardy and Clay (1983)	2	Noda et al. (2008), prediction
▶	Alexeenko et al. (1981)		

Most recent development concerning event and source correlations are summarized in Sect. 11.11.4.

11.10 Time Variation of Shower Intensity

11.10.1 Introduction

The question whether the intensity of the cosmic radiation varies with time arose soon after its discovery and many of the early workers have searched for temporal effects. The search was intensified after Compton and Getting (1935) published their paper on the effect that carries now their name. This effect which is latitude dependent is expected to be due to the motion of the Earth along its orbit relative to the sources of the cosmic radiation. It predicts a *sidereal* time variation of the intensity of the cosmic radiation, causing an apparent anisotropy in the arrival direction. The effect is discussed in Sect. 11.10.3.

But it was not until the fifties, after the introduction of neutron monitors mainly by J.A. Simpson and collaborator, when the systematic surveillance of the intensity of the cosmic radiation was introduced and the geomagnetic field was continuously monitored, that it was observed that the low energy component ($E \leq 1$ TeV) of

the cosmic radiation is subject to time variation. The latter is due to the solar magnetic field, to solar activity and to variations of the geomagnetic field. In addition, diurnal modulation effects (day and night) were discovered that are partly due to atmospheric and meteorological changes.

Temporal variations of the cosmic radiation can be studied in *solar* or in *sidereal time*. At high energies where solar and geomagnetic effects become negligible sidereal time which relates to the stars is the relevant time. The concepts of solar and sidereal time are defined in Sect. 11.10.2.

For a long time it was uncertain whether high energy cosmic rays that cause extensive air showers manifest time variation too. Variation of the incident radiation due to solar perturbation decreases with increasing energy and becomes negligible in the multi-TeV range, but atmospheric effects remain as the major factor of disturbance. At higher energies one faces the additional problem of the low event rate, resulting in poor statistics.

Farley and Storey (1954a, b), Cranshaw and Galbraith (1954), Cranshaw and Elliot (1956) were among the pioneers to study time variation of extensive air showers (see also references listed in these papers). Since the early investigations data from many air shower experiments have been analyzed to determine the amplitude and phase of the intensity variation due to the Compton-Getting effect. As an example we show in Fig. 11.63 the Compton-Getting effect in differential form as measured with the Tibet array by Amenomori et al. (2008b). The latitude of the array is N 20.102°. The amplitude is $a = 1.12 \pm 0.12 \cdot 10^{-4}$ and the Earth's orbital velocity is $v = 2.978 \cdot 10^4$ km s^{-1}.

Similar measurements had been carried out with other arrays. As an example we mentioned the more detailed analysis carried out with the EAS-TOP installation. There, data from events having energies between 100 and 1,000 TeV had been analyzed in *solar, sidereal* and *anti-sidereal time* using the *east-west* effect (Aglietta et al., 2007). From the shape of the solar curve of the $\geq$ 100 TeV events the Compton-Getting effect is clearly seen, while no significant structure was observed in anti-sidereal time. In sidereal time the distribution shows a structure similar to that observed in an earlier experiment by the same group using $\geq$ 10 TeV underground muon data from the Gran Sasso Laboratory MACRO (Aglietta et al., 1996b).

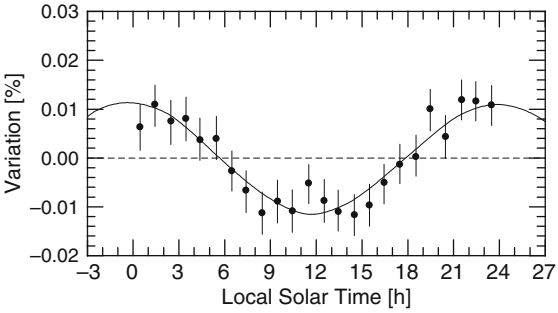

Fig. 11.63 Average solar daily variation in percent, in differential form, of the cosmic radiation around 10 TeV. The sinusoidal curve is a fit to the experimental data. The figure illustrates the anisotropy caused by the Compton-Getting effect (Amenomori et al., 2008b)

11.10.2 Solar Time and Sidereal Time

(a) General Comments

Solar time is measured by the apparent diurnal motion of the Sun, and local noon in solar time is defined as the moment when the Sun is at its highest point in the sky (exactly due south or north depending on the observer's latitude and the season). The average time taken for the Sun to return to its highest point is 24 h.

During the time needed by the Earth to complete a rotation around its axis, called a *sidereal day*, the Earth moves a short distance (∼1°) along its orbit around the Sun. Therefore, after a sidereal day, the Earth still needs to rotate a small extra angular distance before the Sun reaches its highest point. A solar day is, therefore, around 4 min longer than a sidereal day.

The stars, however, are so far away that the Earth's movement along its orbit makes a generally negligible difference to their apparent direction (except for *parallax effects*), and so they return to their highest point in a sidereal day. A sidereal day is around 4 min shorter than a mean solar day.

In other words, sidereal time relates to a measurement of time relative to the position of the stars. It is a measure of the position of the Earth in its rotation around its axis, or time measured by the apparent diurnal motion of the *vernal equinox*, which is very close to, but not identical to, the motion of stars. They differ by the *precession* of the vernal equinox in *right ascension* relative to the stars. The vernal equinox is the instant of time when the Sun's center crosses the equator and day and night are everywhere of equal length. It is the instant when the *celestial equator intersects the ecliptic* This occurs ∼March 21 or ∼September 23.

The Earth's sidereal day also differs from its rotation period relative to the background stars by the amount of *precession in right ascension* during 1 day (∼ 8.4 ms). Its mean value is 23 h 56 m 4.090530833 s (for details see Aoki et al., 1982; Seidelmann, 1992; Simon et al., 1994).

(b) Definition of Sidereal Time

Sidereal time is defined as the hour angle of the vernal equinox. When the meridian of the vernal equinox is directly overhead, local sidereal time is 00:00. Greenwich Sidereal Time is the hour angle of the vernal equinox at the prime meridian at Greenwich, England; local values differ according to longitude. When one moves eastward 15° in longitude, sidereal time is larger by one hour (note that it wraps around at 24 h). Unlike local solar time zones, sidereal time must be computed accurately according to the longitude of the location.

Greenwich Sidereal Time and Universal Time UT1 differ from each other by a constant rate (GST = 1.00273790935· UT1). Sidereal time is used at astronomical observatories to locate astronomical objects. Objects are located in the night sky using *right ascension* and *declination* relative to the celestial equator, analogous to longitude and latitude on Earth. When sidereal time is equal to an object's right ascension, the object will be overhead, at its highest point in the sky (Seidelmann, 1992).

(c) Terrestrial Precession and Its Effects

Terrestrial precession effects occur because the Earth's rotation is not only a simple rotation around an axis that would always remain parallel to itself. The Earth's rotational axis precesses about an axis which is orthogonal to the Earth's orbit around the Sun. It takes about 25,800 years to perform a complete precessional rotation. This phenomenon is called the *precession of the equinoxes*. Because of this precession, the stars appear to move around the Earth in a manner more complicated than a simple constant rotation.

For this reason, to simplify the description of the Earth's orientation in astronomy and geodesy, it is conventional to describe the Earth's rotation relative to a frame which is itself precessing slowly. In this reference frame, the Earth's rotation is close to constant, but the stars appear to rotate slowly with a period of about 25,800 years. It is also in this reference frame that the tropical year, the year related to the Earth's seasons, represents one orbit of the Earth around the Sun. The precise definition of a sidereal day is the time taken for one rotation of the Earth in this precessing reference frame. For further details the reader is referred to Simon (1994).

11.10.3 Compton-Getting Effect

It occurred to Compton and Getting on a suggestion by Lowry that the motion of the Earth through space may appreciably affect the intensity of cosmic rays (Compton and Getting, 1935). If the cosmic rays approach the Earth from a source external to the Galaxy, the effect due to our motion with the rotation of the Galaxy should be perceptible. Comparison with existing cosmic ray data at that time showed a *sidereal diurnal variation* of just the anticipated type. Compton and Getting further argue that if further experiments show this variation to be really due to the galactic rotation we would have direct evidence of the very remote origin of cosmic rays, and a new method of determining the state of the Earth's motion relative to the rest of the Universe. On the basis of data by Oort (1931), the rotational motion of our region of the Galaxy in the galactic plane is directed toward 20 h 55 min. right ascension and 47°N declination, with a probable error of a few degrees.

The most precise estimate of the speed at that time had been made from the Doppler shifts of 18 globular clusters, giving $275 \pm 50\,\mathrm{km\,s^{-1}}$ (Strömberg, 1925). Observations of the Doppler effect of extragalactic systems have given a velocity of $380 \pm 110\,\mathrm{km\,s^{-1}}$ in about the same direction (Hubble, 1929). Other methods give nearly the same result. In addition, the Sun has a small individual motion of about $20\,\mathrm{km\,s^{-1}}$. The resultant velocity should be approximately toward right ascension $\alpha = 20\,\mathrm{h}\,40\,\mathrm{min}$. and declination $\delta = +47^\circ$ at about $300\,\mathrm{km\,s^{-1}}$. It would appear from the analysis by Oort (1931) of the motions of the remote galaxies, that the peculiar velocities of these systems are probably smaller than $80\,\mathrm{km\,s^{-1}}$. This means that if the cosmic rays come uniformly from all parts of the remote Cosmos, our speed relative to their source is probably about that of the galactic rotation.

This motion with a speed of about 0.1% of that of light affects the intensity of the incoming cosmic rays by changing both their energy and the number received

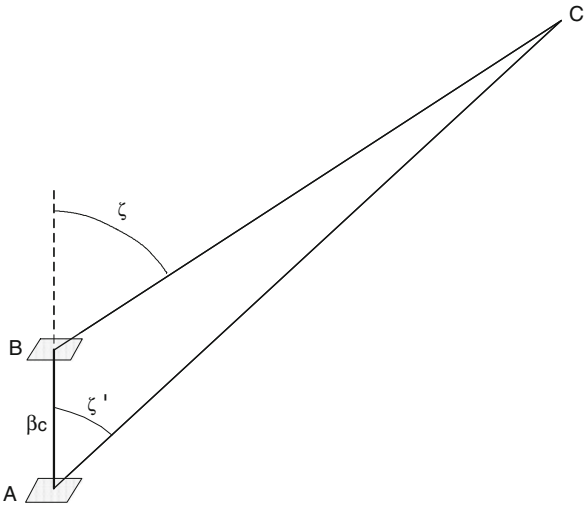

Fig. 11.64 Universal reference showing the Earth's motion with respect to the cosmic ray flux in space. The Earth moves along the *line AB*, representing an infinitesimal element of its orbit. The *lines AC and BC* represent cosmic ray trajectories

per unit of time. Referring to Fig. 11.64 and assuming the Earth to move along the line AB with a speed βc, where $\beta \ll 1$, and considering cosmic ray particles with a velocity, γc, almost equal to that of light, moving in the direction of the line CB, at an angle ζ with respect to the direction of the Earth's motion, the following relations hold:

Following the rules for the addition of velocities and kinetic energy, it can be shown that the energy of each particle relative to the moving Earth is, to the first order,

$$E' = E\left(\frac{(1+\alpha\beta(\sqrt{2}-1)\cos\zeta)}{(1-\beta\cos\zeta)}\right) , \tag{11.40}$$

where E is the particle's energy relative to an observer at rest, and $\alpha \equiv (1-\gamma)$. If $\alpha \ll 1$, we may write without sensible error,

$$E' = \frac{E}{1-\beta\cos\zeta} . \tag{11.41}$$

If E is equated to $h\nu$ this becomes the usual expression for the Doppler effect with light. To calculate the increase in the rate at which the cosmic ray particles impinging on a unit surface normal to the direction of motion AB, let $AC = \gamma c$ be the distance traveled by a particle per unit time. Then, to the first order of β, the time required for a particle from C to reach B is

$$\tau = \frac{\gamma c - \beta c\,\cos\zeta}{\gamma c} = 1 - \left(\frac{\beta}{\gamma}\right)\cos\zeta , \tag{11.42}$$

or, again by neglecting $(1-\gamma)$ when multiplied by β,

$$\tau = 1 - \beta \cos\zeta \quad . \tag{11.43}$$

Assume for convenience a constant number of particles per unit path. The number striking a stationary unit surface at B within a range of directions $\mathrm{d}\zeta$ and in the time interval τ is then proportional to

$$n = (1 - \beta \cos\zeta) \cdot \cos\zeta \cdot 2\pi \sin\zeta \, \mathrm{d}\zeta \quad , \tag{11.44}$$

while during the same interval the number striking the surface moving from A to B is

$$n' = 1 \cdot \cos\zeta' \cdot 2\pi \sin\zeta \, \mathrm{d}\zeta \quad . \tag{11.45}$$

From Fig. 11.64, however, to the first order of β,

$$\sin\zeta = \frac{\sin\zeta'}{1 - \beta \cos\zeta'} \tag{11.46}$$

and

$$\mathrm{d}\zeta = \frac{\mathrm{d}\zeta'}{1 - \beta \cos\zeta'} \quad . \tag{11.47}$$

Thus by Eq. (11.45),

$$n' = \frac{\cos\zeta' \cdot 2\pi \sin\zeta' \, \mathrm{d}\zeta'}{(1 - \beta \cos\zeta')^2} \quad , \tag{11.48}$$

where the primed angles are those observed from the moving surface. Within the same observed range of angles, therefore, the rate of receiving particles is thus increased by the motion in the ratio

$$\frac{n'}{n} = \frac{1}{(1 - \beta \cos\zeta)^3} \quad . \tag{11.49}$$

Since the intensity, I, is the energy of the particles received per unit time, per unit area, on combining Eqs. (11.49) and (11.41) we have, for the cosmic rays incident at an angle ζ with the direction of motion,

$$\frac{I'}{I} = \frac{1}{(1 - \beta \cos\zeta)^4} \quad . \tag{11.50}$$

This is the counterpart of the fact previously shown by Compton (1923) that the Doppler change in intensity of light from a moving source is equal to the 4th power of its change in frequency. With a coincidence detector telescope, arranged to record the radiation from a narrow range of directions, and disregarding atmospheric absorption, Eq. (11.49) is relevant.

With an ionization chamber it is the average effect from all angles that must be considered. We note for the interested reader that Compton and Getting (1935) in their original paper work out the details for this case, too.

11.11 Origin and Propagation

11.11.1 Origin of Primary Radiation

The topics of the origin, acceleration and propagation of the cosmic radiation are vast fields of research that are beyond the scope of this book. Nevertheless, we make a few comments on the present situation.

Many efforts had been made up to date to search for cosmic ray sources, however, so far with modest success. In the ultrahigh energy domain there are now some indications for a possible association of events with distinct likely astrophysical source objects, briefly outlined below, but they need solid confirmation (Abraham et al., 2008b). The particular spectral features such as the knee and the ankle that are being observed in the size as well as the energy spectrum of air showers are very intriguing and have stimulated speculations concerning the mechanisms that could generate these phenomena. There is no lack of candidate astronomical objects and astrophysical processes that had been proposed as likely sources and accelerators of energetic cosmic rays, e.g., binary systems or supernovas in our own Galaxy, or extragalactic objects for the highest energy cosmic rays, such as active galactic nuclei, blazars, etc (O'Halloran et al., 1998). The cause for both, the knee and the ankle, could be due to source or propagation properties, most likely to both combined.

11.11.2 Conventional Acceleration Mechanisms

Today there is strong evidence partly from direct measurements and partly from air shower studies at higher energies that the first knee which is the dominating spectral feature in the 1–10 PeV primary energy range is linked to compositional changes (see Sect. 11.7). Referring to the hadronic component, observations reveal that different primary masses or mass groups manifest different spectra, in particular, it is observed that with increasing energy the intensity of the proton spectrum begins to drop before the spectra of heavier nuclei. This suggests that the spectra are subject to rigidity dependent cutoffs. These cutoffs could be the consequence of rigidity dependent leakage of magnetically confined charged particles from our Galaxy, where protons are lost first, followed by higher and higher-Z nuclei, or to rigidity dependent acceleration.

On the theoretical side the situation is very speculative and only for the lower energy regions, below about 10^{16}–10^{17} eV do we have a viable theory that resides on conceivable observational information that appears to be able to account for the spectral knee phenomenon. In particular, supernova remnants with their magnetic fields in conjunction with the Fermi shock acceleration mechanism are today a likely and accepted model in one form or another for the acceleration of galactic cosmic rays to these energies (Völk and Biermann, 1988). Massive supernova progenitors may possibly accelerate particles to even higher energies (Biermann et al., 1995; Pelletier, 2001).

We should point out here the work of Berezhko and Völk (2004, 2006, 2007a) who developed the *nonlinear kinetic theory of diffusive shock acceleration* in supernova further and show that the accelerating nuclear cosmic ray component causes a significant amplification of the magnetic field. These authors show that their predicted galactic cosmic ray (GCR) spectrum produced in supernova remnants fits the observed GCR spectrum up to 10^{17} eV and can reproduce synchrotron emission from radio to X-ray frequencies together with gamma ray spectra observed by the H.E.S.S. telescopes (Berezhko and Völk, 2007b).

Figure 11.65 shows the energy dependence across the knee region of the mean logarithmic mass predicted by four models that are based on rigidity dependent supernova remnant shock acceleration and propagation (Biermann, 1993; Swordy, 1995; Berezhko and Ksenofotov, 1999; Erlykin and Wolfendale, 1999). Also shown in this figure is the mean logarithmic mass obtained from a detailed analysis of data from the KASCADE experiment, using different methods of analysis as listed in the figure caption (Haungs et al., 2003). The disagreement between the predicted and the experimentally derived energy dependence of the mean mass is evident. Hörandel has extensively analyzed a variety of models. A summary of his work is presented in Sect. 11.6.2, and in Sect. 11.7.2.

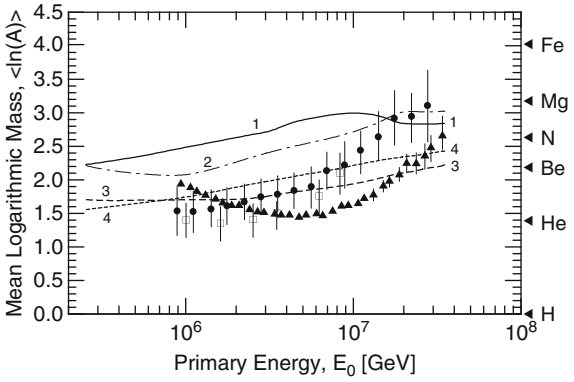

Fig. 11.65 Mean logarithmic mass distribution resulting from different analyses of the KASCADE experimental data (▲ Antoni et al., 2002; • Ulrich et al., 2001; □ Weber et al., 1999) compared with predictions of astrophysical models for the origin of the knee (Biermann, 1993; Swordy, 1995; Berezhko and Ksenofotov, 1999; Erlykin and Wolfendale, 1999; after Haungs et al., 2003)

Because of the magnetic fields in the Galaxy that deflect charged particles the projection of the shower axis backward into space cannot reveal the source location, thus, *proton astronomy* is not the road to success except possibly for the highest energy particles. From the diagram plotted in Fig. 11.59 one can readily find the radius of gyration of a proton of given energy in magnetic fields of various strength as they may exist in our Galaxy.

Above the energy regime of about 10^{17}–10^{18} eV we have to look beyond our own Galaxy, and certainly for the energy region above 10^{19} eV where conventional acceleration mechanisms (*bottom-up models*) begin to break down. Many models had been developed and are currently being studied but they all are highly speculative (Waxman, 1995). The crucial parameters are the magnetic field, B, and the dimension of the acceleration region, L. They must be large enough to keep the particle confined to the magnetic field region for the duration of the acceleration.

Hillas (1984) constructed the very instructive plot shown in Fig. 11.66 that illustrates the problem. Shown are likely ultrahigh energy astrophysical acceleration sites and objects, and their magnetic-field-size ($B - L$) correlation. The gyroradius depends also on the velocity parameter, β, of the shock wave in supernova remnants, which is of the order of $\beta \approx 0.01$. The plot is based on the following expression for the maximum estimated particle energy,

$$E_{\max} \propto Z(BL)\beta \ , \tag{11.51}$$

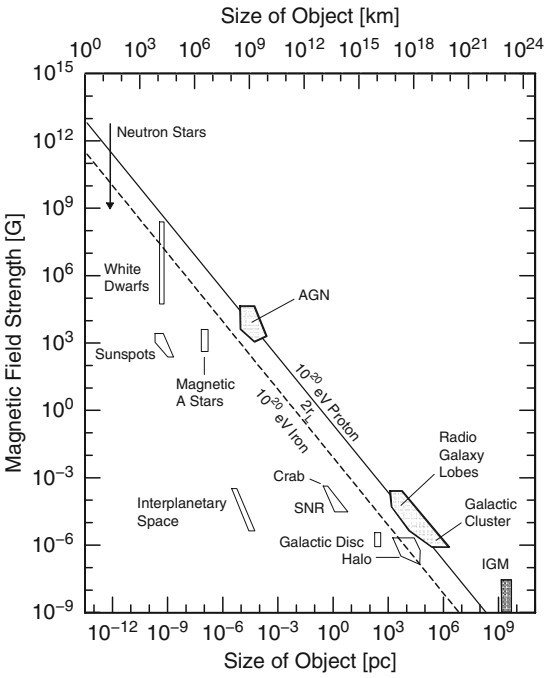

Fig. 11.66 Size and magnetic field strength of likely objects and sites of ultrahigh energy cosmic ray acceleration (Hillas, 1984, modified). The *solid and dashed lines* represent the loci of twice the gyroradii, $2r_L$, of 10^{20} eV protons and iron nuclei, respectively, in the magnetic fields considered here. Only some neutron stars, active galactic nuclei (AGN), radio galaxies, galactic clusters and the intergalactic medium (IGM) are likely scenarios to accelerate cosmic rays to the highest energies observed

where Z is the electric charge of the particle to be accelerated, disregarding radiative energy losses and interactions with the CMBR.

11.11.3 Top-Down Models

In view of the problems encountered by acceleration processes and in anticipation of the Greisen-Zatsepin-Kuzmin (GZK) cutoff, the *top-down models* offer an alternative to acceleration. This kind of model is based on the assumption that super-heavy X particles with masses in the Grand Unified Theory (GUT) domain (10^{25} eV) exist that were produced by *topological defects* in the very early universe, whose decay products constitute the ultrahigh energy cosmic rays (Michael and Sarkar, 1998 and references listed therein; for a review see Bhattacharjee and Sigl, 2000). This picture would extend the horizon for cosmic ray sources that contribute to the most energetic radiation in our part of the Universe well beyond the estimated 50 Mpc imposed by the GZK cutoff of conventional models.

However, top-down models do not really solve the problem, as the problem is simply pushed back into an even more difficult era, and likewise for the so-called Z-burst process (Weiler, 1999), where neutrinos in the ZeV (10^{21} eV) domain would interact with low energy cosmic background neutrinos and produce ultrahigh energy Z-bosons. A test in support of top-down models would be to measure the high energy photon to hadrons ratio, as top-down models would create preferentially photons (Semikoz, 2007) (see also Sect. 11.8.2).

11.11.4 Correlation of Ultrahigh Energy Events with Likely Astrophysical Source Objects

There are a number of reports that present evidence for anisotropies observed in the ultrahigh energy domain, such as the one extracted from data of the old SUGAR array and the much more recent AGASA experiment, that claim an excess from near the direction of the galactic center (Bellido et al., 2001; Takeda et al., 1999, respectively). However, the Auger experiment could not confirm these observations (Santos et al., 2007). At that time the Auger Collaboration reported no significant excess in any part of the southern hemisphere sky (Mollerach et al., 2007). In addition, AGASA recorded an event triplet in the northern sky which is correlated with a HiRes event (Abbasi et al., 2005b). A recent search in the northern hemisphere for correlations between HiRes stereo Fly's Eye events and active galactic nuclei remained fruitless (Abbasi et al., 2008b).

On the other hand, two observations of an anisotropy in the northern hemisphere sky had been reported by the AGASA and HiRes experiments, namely a *dip* in the intensity of cosmic rays in the direction of the *galactic anti-center*. Yet the significance is too low to be labeled an observation (Ivanov et al., 2007). The reports on

anisotropies in the northern hemisphere require all confirmation by the Telescope Array which will soon be in full operation (Fukushima et al., 2007).

An interesting observation worth mentioning was made by the L3 + C collaboration who used the L3 spectrometer at the LEP e^+e^- collider at CERN to study cosmic ray muons (Le Coultre et al., 2005). They recorded a 3-days lasting enhancement of the cosmic ray muon intensity originating from a fixed position in the northern sky. The "flare" as they call it was detected in a 2° by 2° sized sky cell with a chance probability for being a background fluctuation of $2.6 \cdot 10^{-3}$. The signal exhibited a clear time evolution, persisted up to muon energies above 50 GeV, thus suggesting a *neutral primary*. The event was recorded within opening angles from 2.5° down to less than 1°. It occurred between 51773.489 and 51776.333 MJD (17–20 August 2000).

The origin had been located at a galactic longitude of $(265.02 \pm 0.42)^\circ$ and a latitude of $(55.58 \pm 0.24)^\circ$. The authors conclude that the characteristics of the signal, the duration, the evolution in time, the energy spectrum, the muon charge ratio and the angular distribution suggest a Blazer-like flare. They could not attribute the event to a known source. Within a radius of 2° there is the gamma source (3EGJ $1133 + 0033$) as well as several QSO's and unidentified objects. Their estimation of the differential gamma ray flux from the large detected muon signal leads to a very steep gamma spectrum and fluxes of $3.5 \cdot 10^2$, $4.6 \cdot 10^0$, and $5.9 \cdot 10^{-1}$ Crab flux units at energies of 1, 10 and 30 TeV, respectively.

Very recent data collected by the Auger Observatory appear to have established an anisotropy with more than 99% confidence level in the arrival directions of events with energy above 60 EeV (Abraham et al., 2008b). These events correlate over angular scales of less than 6° with the directions towards nearby ($D < 100$ Mpc) AGNs. The observed correlation demonstrates the extragalactic origin of the highest energy cosmic rays. It is consistent with the hypothesis that cosmic rays with energies above 60 EeV are predominantly protons that come from AGNs within our GZK *horizon*. This provides evidence that the observed steepening of the cosmic ray spectrum at the highest energies is due to the GZK effect, and *not to acceleration limits* at the sources.

The authors conclude further that it is possible that the sources are other than AGNs, as long as their local distribution is sufficiently correlated with them. Unequivocal identification of the sources requires a larger data set, such as the Auger Observatory will gather in a few years. In particular, one could use the fact that angular departures of the events from an individual source due to magnetic deflections should decrease in inverse proportion to the energy of the cosmic rays. The observation of such an *angle-energy correlation* in clusters of events could be exploited to locate the source position unambiguously with high accuracy. This could also provide at the same time valuable and unique information about the magnetic fields along the line of sight.

The Auger results show that astronomy of charged particles is indeed feasible at the highest energies. Moreover, it can be expected that in the next few years the Auger experiment can identify sources of ultrahigh energy cosmic rays unambiguously.

11.11.5 Greisen-Zatsepin-Kuzmin (GZK) Cutoff and Propagation of Hadrons in Space

Shortly after the discovery of the universal Cosmic Microwave Background Radiation (CMBR) by Penzias and Wilson (1965), Greisen (1966) and Zatsepin and Kuzmin (1966) realized simultaneously but independently that this discovery is of great concern for the cosmic radiation, in particular for the very high energy hadronic component, but also for energetic gamma rays.

This isotropic thermal radiation has a Planck distribution with a temperature $T \simeq 2.7\,K$. Its intensity ($N_\gamma \approx 550$ photons cm^{-3}, $kT \approx 2.5 \cdot 10^{-4}$ eV) is such that unique effects arise when cosmic rays of superhigh energy pass through it, that lead eventually to a cutoff of the cosmic ray spectrum in the vicinity of 10^{20} eV.

Following Zatsepin and Kuzmin we consider as an example a proton of energy

$$E_p \sim M_p c^2 (m_\pi c^2 / E_{\mathrm{ph},\,eff}) \ . \tag{11.52}$$

M_p and m_π are the rest mass of the proton and pion, respectively, c is the velocity of light and $E_{\mathrm{ph},\,eff}$ the effective photon energy. Pion photo-production processes will occur when the protons interact with the photon gas (Zatsepin, 1951) and, as a result, the protons lose energy on the order of ($\langle \Delta E_p \rangle \sim 20\%$) (Hayakawa and Yamamoto, 1963).

If the characteristic time for proton-photon collision becomes sufficiently small compared to the lifetime of the cosmic rays of these energies in the Metagalaxy as determined by other processes (for example, the expansion of the Universe), an effective cutoff of the cosmic ray spectrum will take place. The exact analysis gives for the characteristic time $\tau_{p,\gamma}$ of a collision between a proton of energy $E_p \gg M_p c^2$ and a photon at the photon gas equilibrium temperature T,

$$\tau_{p,\gamma} = \frac{2\pi^2 c^2 \hbar^3 \gamma^2}{kT\varphi} \ [\mathrm{s}] \tag{11.53}$$

with

$$\gamma = \frac{E_p}{M_p c^2} \qquad \text{and} \tag{11.54}$$

$$\varphi = \int_{E_{\mathrm{thr}} \kappa m_\pi c^2}^{\infty} \mathrm{d}E \, E \sigma_{p,\gamma}(E) \sum_{n=1}^{\infty} \frac{1}{n} \exp\left(-\frac{nE}{2\gamma kT}\right)\left(1 + \frac{2\gamma kT}{nE}\right) . \tag{11.55}$$

Here, $\sigma(E)$ is the total cross section for the absorption of a photon of energy E by interaction with a proton. This is in fact the cross section for the photo-production of π^0 and π^+ mesons at $E \leq 1$ GeV. At higher energies, up to the highest ones, one can assume that $\sigma_{p,\gamma} = \mathrm{const} = 10^{-28}\ cm^2$.

The values of $\tau_{p,\gamma}$ calculated with Eq. (11.53) for different proton energies lead to curves as shown in Fig. 11.67a for photon gas temperatures as listed there.

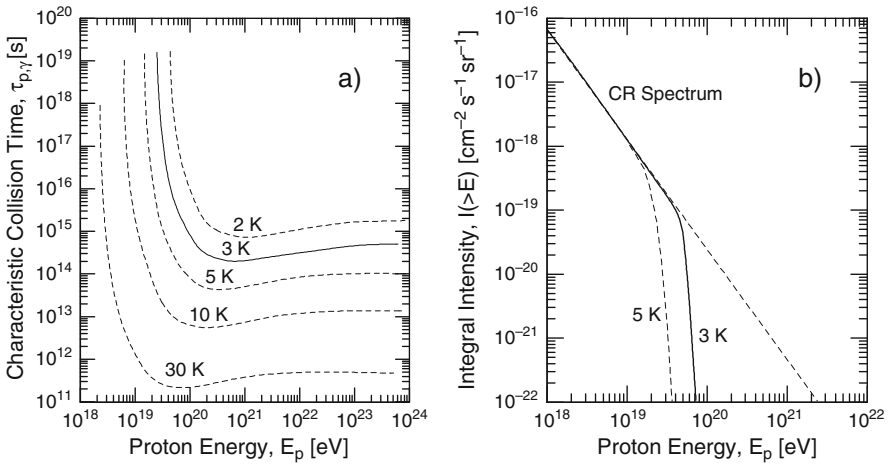

Fig. 11.67 (**a**) Values of $\tau_{p.\gamma}$ calculated with Eq. (11.53) for different proton energies and different photon gas temperatures as indicated. The figure illustrates that proton-photon interactions become rather frequent at energies $\geq 10^{20}$ eV (Zatsepin and Kuzmin, 1966). (**b**) Effect of proton-photon interactions on the intensity of the primary cosmic radiation and the shape of the cutoff of the primary energy spectrum for an assumed cosmic ray age of 10^9 years. The influence of the photon gas temperature on the onset of the cutoff is evident (after Zatsepin and Kuzmin, 1966)

Consequently, at proton energies of $E_p \geq 10^{20}$ eV, proton interactions with the photons become rather frequent, $\tau_{p,\gamma} \approx 10^7$ y. This implies that at an age of $t \geq 10^8$ y the initial proton spectrum is expected to get cutoff in the high energy domain. We show in Fig. 11.67b the original plot of Zatsepin and Kuzmin (1966) for two CMBR temperatures. Many new developments concerning the GZK cutoff can be found in the proceedings of the seminar entitled "GZK Surroundings" (Aramo et al., 2004). When considering the distance traveled by the cosmic radiation in space, the situation as shown in Fig. 11.68a arises for the proton component of given initial energy at the source. The distance to the Virgo cluster to whose location the axis of several ultrahigh energy showers are pointing is also indicated.

The situation for the propagation of ultrahigh energy nuclei of mass A, charge Z and energy E is quite different. Upon interaction with the cosmic background radiation nuclei undergo photodisintegration (photo dissociation). The rate of disintegration, R_{A,Z,i_p,i_n}, is given by Hooper et al. (2007) as

$$R_{A,Z,i_p,i_n} = \frac{A^2 m_p^2 c^2}{2E^2} \int_0^\infty \frac{\mathrm{d}\epsilon n(\epsilon)}{\epsilon^2} \int_0^{2E\epsilon/Am_pc} \mathrm{d}\epsilon' \epsilon' \sigma_{A,Z,i_p,i_n}(\epsilon') \ , \qquad (11.56)$$

where m_p is the proton mass, i_p and i_n are the numbers of protons and neutrons broken off from the nucleus in the interaction, $n(\epsilon)$ is the density of background photons of energy ϵ in the laboratory frame (in this equation), and $\sigma_{A,Z,i_p,i_n}(\epsilon')$ is the appropriate cross section. Figure 11.68b shows the energy of the heaviest fragment of oxygen and iron primaries as a function of distance (Cronin, 1992).

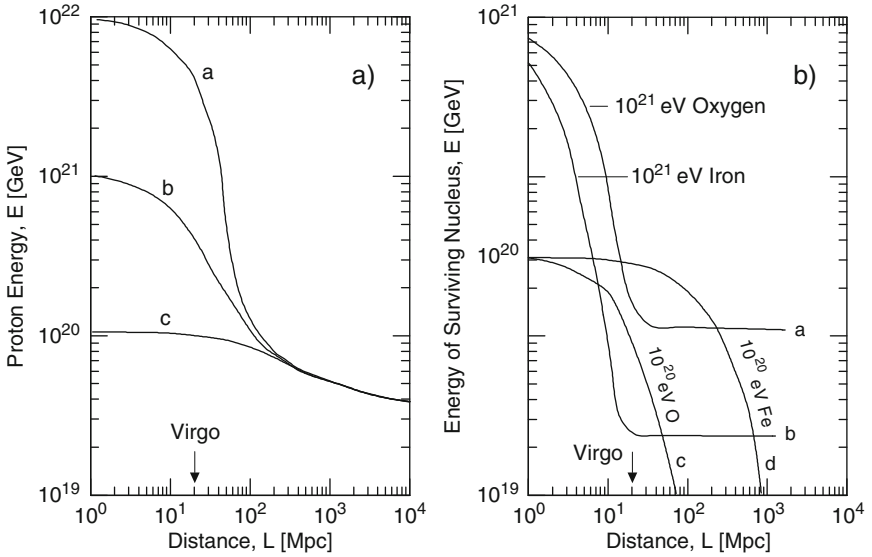

Fig. 11.68 (**a**) Mean energy of protons due to the interaction with the 2.7 K radiation as a function of distance from the source, L [Mpc], for various initial energies. (**b**) Energy of heaviest fragment of initial iron and oxygen nuclei as a function of distance from the source due to photodisintegration by the 2,7°K cosmic microwave background radiation. The *curves* are plotted for initial total primary energies at the source of 10^{20} and 10^{21} eV, respectively (after Cronin, 1992)

11.11.6 Propagation of Gamma Rays in Space

The situation for gamma ray propagation in space is similar to that for hadrons, except that electromagnetic interactions are the prime cause for their attenuation. Inspired by the discovery of the CMBR (Penzias and Wilson, 1965), Wdowczyk et al. (1972) considered the effects caused by the interaction of the high energy gamma ray component of the cosmic radiation with the background radiation field and the implication for gamma ray astronomy (Weekes, 1988, 2003; Ramana-Murthy and Wolfendale, 1993).

For a head on collision of a photon of energy E_γ with a photon of energy E_{ph} the cross section for the production of a pair of particles each of mass m is given by:

$$\sigma_1 = \pi r_e^2 \left(\frac{m}{\omega}\right)^2 \left[2\ln\left(\frac{2\omega}{m}\right) - 1\right] \tag{11.57}$$

for $\omega \gg m$, i.e., in the extreme relativistic case, and

$$\sigma_2 = \pi r_e^2 \left(1 - \left(\frac{m}{\omega}\right)^2\right)^{0.5} \tag{11.58}$$

for ω close to m, i.e., in the classical region.

In these equations we have (see Jauch and Röhrlich, 1955)

$$\omega = \sqrt{E_\gamma E_{ph}} \quad \text{and} \quad r_e = \frac{e^2}{mc^2} \ . \tag{11.59}$$

The most important process to consider is electron pair production, however, at higher energies muon pair production must also be accounted for. Using these equations, Wdowczyk et al. (1972) obtained the interaction length as a function of photon energy for the collision of energetic photons with the different components, such as starlight, the radio background and the CMBR of the electromagnetic background radiation field as shown in Fig. 11.69.

Photon–photon interactions play an important role for the propagation of gamma rays in the Universe. They are the processes that limit the range of gamma rays in space by causing them to lose energy and being scattered. Wdowczyk et al. (1972) have investigated the problem and arrived at the conclusion that the Universe is

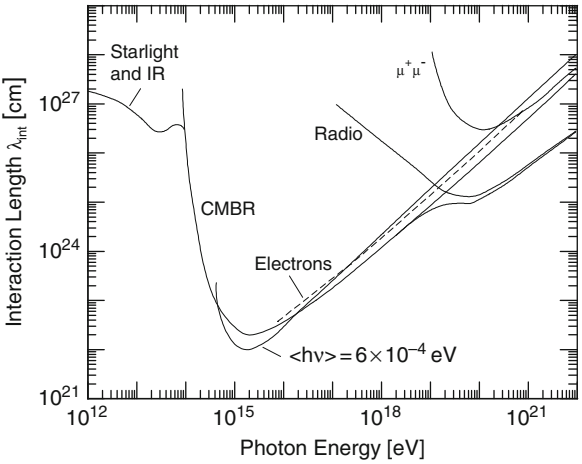

Fig. 11.69 Interaction length, λ_{int}, against photon energy for collisions of energetic photons (gamma rays) with photons of the various radiation fields in space. Unless stated otherwise the process concerned is electron pair production (e^+e^-). Also shown is the interaction length for electrons by way of inverse Compton scattering with *black body photons*, and for muon pair production (after Wdowczyk et al., 1972)

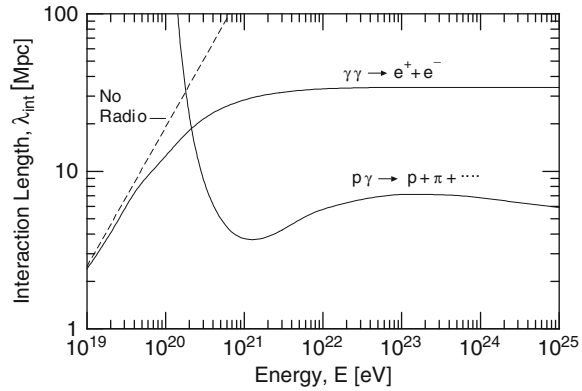

Fig. 11.70 Energy dependence of the mean free path for interactions of ultrahigh energy protons and gamma rays with the isotropic photon background of 2.7 K. The background includes the cosmic microwave and radio background radiations. The *dashed line* indicates the gamma ray interaction length in the absence of the radio background (after Halzen et al., 1995)

essentially opaque to photons between 10^{14} eV and at least 10^{18} eV because of the interaction with the 2.7 K cosmic microwave background radiation.

More recently, Halzen (1995) has carried out similar calculations as did Greisen (1966), Zatsepin and Kuzmin (1966) and Wdowczyk et al. (1972) and computed the interaction mean free path in units of [Mpc] for photon-photon ($\gamma + \gamma \rightarrow e^+e^-$) and proton-photon collisions ($p + \gamma \rightarrow p + \pi + \ldots$) with the background radiation. The results of this work are shown in Fig. 11.70.

References

Abbasi, R.U., et al.: Phys. Rev. Lett., 92, p. 151101 (2004).
Abbasi, R.U., et al.: Astropart. Phys., 23, p. 157 (2005a).
Abbasi, R.U., et al.: Astrophys. J., 623, p. 164 (2005b).
Abbasi, R.U., et al.: Phys. Rev. Lett., 100, p. 101101 (2008a).
Abbasi, R.U., et al.: Astropart. Phys., 30, p. 175 (2008b).
Abdo, A.A., Milagro Collaboration: Astrophys. J., 658. p. L33 (2007).
Abraham, J., et al., Auger Collaboration: Astropart. Phys., 27, p. 155 (2007).
Abraham, J., et al., Auger Collaboration: Astropart. Phys., 29, p. 243 (2008a).
Abraham, J., et al., Auger Collaboration: Astropart. Phys., 29, p. 188 (2008b).
Abu-Zayyad, T., et al.: Astrophys. J., 557, p. 686 (2001).
Achard, P., et al., L3 Collaboration: Astropart. Phys., 23, p. 411 (2005).
Acharya, B.S.: PICRC, 10, p. 271 (2005).
Acharya, B.S., et al.: PICRC, pre-conference edition, paper 510, Merida, Mexico (2007).
Achterberg, A., et al.: Phys. Rev. D, 75, p. 102001 (2007).
Ackermann, M., et al.: Astropart. Phys., 22, p. 339 (2005).
Afanasiev B.N., et al.: Proceedings of the Tokyo Workshop on Techniques for the Study of Extremely High Energy Cosmic Rays, M. Nagano, ed., Institute for Cosmic Ray Research, University of Tokyo, Japan p. 35 (1993).
Aglietta, M., et al.: Astropart. Phys., 6, p. 71 (1996a).
Aglietta, M., et al.: Astrophys. J., 470, p. 501 (1996b).
Aglietta, M., et al.: Astropart.Phys., 10, p. 1 (1999).
Aglietta, M., et al.: Astropart. Phys., 19, p. 329 (2003a).
Aglietta, M., et al.: PICRC, 4, p. 183 (2003b).
Aglietta, M., et al.: Astropart. Phys., 20, p. 641 (2004a).
Aglietta, M., et al.: Astropart. Phys., 21, p. 583 (2004b).
Aglietta, M., et al.: PICRC, pre-conference edition, paper 832, Merida, Mexico (2007).
Aguilar, M., et al.: Phys. Rep., 366, p. 331 (2002).
Aguirre, C., et al.: PICRC, 4, p. 2598 (1973) (Abstr).
Aguirre, C., et al.: Phys. Rev. D, 62, p. 032003 (2000).
Aharonian, F.A., et al.: Phys. Rev. D, 59, p. 092003 (1999).
Aharonian, F.A., et al.: Astron. Astrophys., 375, p. 1008 (2001).
Aharonian, F.A., et al.: Astron. Astrophys., 393, p. 89 (2002).
Aharonian, F.A.: Very High Energy Cosmic Gamma Radiation, World Scientific, Singapore (2004).
Aharonian, F.A., et al.: astro-ph/0701766 (2007).
Ahn, H.S., et al.: PICRC, 3, p. 57 (2005).
Ahn, H.S., et al.: Adv. in Space Res. 37/10, p. 1950 (2006).
Ahn, H.S., et al.: PICRC, pre-conference edition, paper 1173, Merida, Mexico (2007).
Akerlof, C.W., et al.: Proc. GRO Workshop (GSFC) 4 (1989).
Akerlof, C.W., et al.: PICRC, 2, p. 135 (1990).
Alcaraz, J., et al.: Phys. Lett. B, 484 (2000a).

Alcaraz, J., et al.: Phys. Lett. B, 490, p. 27 (2000b).
Alexeenko, V.V., et al.: PICRC, 2, p. 146 (1981).
Allan, H.R., et al.: Proc. Phys. Soc. 79, p. 1170 (1962).
Allard, D., et al.: JCAP, 9, p. 5 (2006).
Aloisio, R., et al.: Phys. Rev. D, 69, p. 094023 (2004).
Ambrosio, M., et al.: Nucl. Phys. B (Proc. Suppl.), 110, p. 519 (2002).
Ambrosio, M., et al.: Astropart. Phys., 20, p. 145 (2003).
Amenomori, M., Tibet ASγ Collaboration: Phys. Rev. D, 47, p. 2675 (1993).
Amenomori, M., Tibet ASγ Collaboration: PICRC, 3, p. 84 (1995).
Amenomori, M., Tibet ASγ Collaboration: Astrophys. J., 461, p. 408 (1996).
Amenomori, M., et al.: Phys. Rev. D, 62, p. 072007 (2000a).
Amenomori, M., et al.: Phys. Rev. D, 62, p. 112002 (2000b).
Amenomori, M., et al.: Astrophys. J., 580, p. 887 (2002).
Amenomori, M., et al.: Proceedings International Science Symposium "The Universe Viewed in Gamma Rays", University of Tokyo, Sept. 25 -28 2002, R. Enomoto, M. Mori, S. Yanagita, ed. Universal Academy Press, Inc., Japan (2003a).
Amenomori, M., et al.: PICRC, 1, p. 143 (2003b).
Amenomori, M., et al.: Phys. Rev. Lett., 93, p. 061101 (2004).
Amenomori, M., Tibet Collaboration: PICRC, 6, p. 45 (2005).
Amenomori, M., Tibet Collaboration: Adv. Space Phys., 37, p. 1932 (2006).
Amenomori, M., Tibet Collaboration: Astropart. Phys., 28, p. 137 (2007).
Amenomori, M., et al.: Nucl. Phys. B (Proc. Suppl.), 175, p. 318 (2008a).
Amenomori, M., et al.: Nucl. Phys. B (Proc. Suppl.), 175, p. 427 (2008b).
Anchordoqui, L., and H. Goldberg: Phys. Lett. B, 583, p. 213 (2004).
Anokhina, A.M., et al.: PICRC, pre-conference edition, paper 438, Merida, Mexico (2007).
Antipin, K., et al., Baikal Collaboration: PICRC, pre-conference edition, paper 1088, Merida, Mexico (2007).
Antoni, T., et al.: Astropart. Phys., 16, p. 245 (2002).
Antoni, T., et al.: Astrophys. J., 604, p. 687 (2004a).
Antoni, T., et al.: Astrophys. J., 612, p. 914 (2004b).
Antoni, T., et al.: Astropart. Phys., 24, p. 1 (2005).
Antonov, R.A., et al.: PICRC, 1, p. 313 (1999).
Antonov, R.A., et al.: Nucl. Phys. B (Proc. Suppl.), 175, p. 194 (2008).
Aoki, S., B. Guinot, G.H. Kaplan, H. Kinoshita, D.D. McCarthy, and P.K. Seidelmann: The new Definition of Universal Time. Astronomy and Astrophysics, 105 (2), p. 359 (1982).
Apanasenko, A.V., et al.: PICRC, 3, p. 163 (1999a).
Apanasenko, A.V., et al.: PICRC, 3, p. 163 (1999b).
Apanasenko, A.V., et al.: Astropart. Phys., 16, p. 13 (2001).
Aramo, C., et al., ed.: Nucl. Phys. B (Proc. Suppl.), 136, p. 1–453 (2004).
Armengaud, E., Auger Collaboration: PICRC, pre-conference edition, paper 76, Merida, Mexico (2007).
Arqueros, F., et al., HEGRA-Collaboration: Astron. Astrophys., 359, p. 682 (2000).
Asakimori, K., et al., JACEE Collaboration: PICRC, 2, p. 21 (1993a).
Asakimori, K., et al., JACEE Collaboration: PICRC, 2, p. 25 (1993b).
Asakimori, K., et al., JACEE Collaboration: PICRC, 2, p. 707 (1995).
Asakimori, K., et al., JACEE Collaboration: Astrophys. J., 502, p. 278 (1998).
Asaoka, Y., et al.: Phys. Rev. Lett., 88, p. 051101 (2002).
Atkins, R., et al.: Phys. Rev. Lett., 95, p. 251103 (2005).
Auger Collaboration: Science Magazine, 318, p. 938 (2007).
Ave, M., et al.: Phys. Rev. Lett., 85, p. 2244 (2000).
Ave, M., et al.: Phys. Rev. D, 65, p. 063007 (2002).
Ave, M., et al.: Astropart. Phys., 19, p. 47 (2003a).
Ave, M., et al.: Astropart. Phys., 19, p. 61 (2003b).

Aynutdinov, V., et al., Baikal Collaboration: Astropart. Phys., 25, p. 140 (2006).
Babson, J., et al.: Phys. Rev. D, 42, p. 3613 (1990).
Badhwar, G.D., et al.: Nature, 274, p. 137 (1978).
Bagge, E.R., M. Samorski, and W. Stamm: PICRC, 13, p. 260 (1979).
Bahcall, J.N.: Phys. Rep., 333–334, p. 47 (2000).
Barbot, C., and M. Drees: Astropart. Phys., 20, p. 5 (2003).
Barr, G.D., et al.: Phys. Rev. D, 70, p. 023006 (2004).
Barwick, S.W., et al.: Astrophys.J., 498, p. 779 (1998).
Barwick, S., et al.: Phys. Rev. Lett., 96, p. 171101 (2006).
Basini, G., et al.: PICRC, 4, p. 544 (1991).
Basini, G., et al.: PICRC, 3, p. 77 (1999).
Battistoni, G., et al.: Astropart. Phys., 19, p. 269 (2003a).
Battistoni, G., et al.: Astropart. Phys., 19, p. 291 (2003b). Erratum to Battistoni, G., et al. (2003a).
Beach, A.S., et al.: Phys. Rev Lett., 87, p. 271101 (2001).
Bell, C.J., et al.: PICRC, 3, p. 989 (1971).
Bell, C.J., et al.: PICRC, 4, p. 2519 (1973).
Bell, C.J., et al.: J. Phys. A, 7, p. 990 (1974).
Bellido, J.A., et al.: Astropart. Phys., 15, p. 167 (2001).
Bellotti, R., et al.: Phys. Rev. D, 60, p. 052002 (1999).
Bercovitch, M., and S.P. Agraval: PICRC, 10, p. 246 (1981).
Berezhko, E.G., and L.T. Ksenofotov: Soviet Phys., JETP, 89, p. 391 (1999).
Berezhko, E.G., and H.J. Völk: Astron. Astrophys., 427, p. 525 (2004).
Berezhko, E.G., and H.J. Völk: Astron. Astrophys., 451, p. 981 (2006).
Berezhko, E.G., and H.J. Völk: PICRC, pre-conference edition, paper 111, Merida, Mexico (2007a).
Berezhko, E.G., and H.J. Völk: PICRC, pre-conference edition, paper 614, Merida, Mexico (2007b).
Berezinsky, V.S., and G.T. Zatsepin: Phys. Lett. B, 28, p. 423 (1969).
Berezinsky, V.S., et al.: Astrophysics of Cosmic Rays, North Holland, Publishing Co, Amsterdam (1990).
Berezinsky, V.S., et al.: Astrop. Phys., 1, p. 281 (1993).
Berezinsky, V.S., et al.: Phys. Rev. Lett., 79, p. 4302 (1997).
Bergeson, H.E., et al.: PICRC, 4, p. 188 (1979).
Bernabei, R., et al.: arXiv:0804.2741 and Eur. Phys. J., C-DOI 10.1140/epjc/s 10052-008-0662-y (2009)
Bernabei, R., et al.: Proc. Int. Conf. New Trends in High Energy Physics, Crimea (2008).
Bernlöhr, K., et al.: Astropart. Phys., 8, p. 253 (1998).
Bertaina, M., et al.: PICRC, 6, p. 41 (2005).
Bertsch, D.L., et al.: Astrophys. J., 481, p. 295 (1993).
Bhat, P.N., et al.: Proc. Nato Workshop on V.H.E. Gamma Ray Astronomy, ed. K.E. Turver, Reidel, Dordrecht, p. 271 (1986).
Bhattacharjee, P., and G. Sigl: Phys. Rep., 327, p. 109 (2000).
Biermann, P.L.: Astron. Astrophys., 271, p. 649 (1993).
Biermann, P.L., et al.: Phys. Rev. D, 51, p. 3450 (1995).
Binns, W., et al.: Astrophys. J., 247, p. L115 (1981).
Binns, W., et al.: Astrophys. J., 346, p. 997 (1989).
Bird, J.D., et al.: Aust. J, Phys., 42, p. 465 (1989).
Bird, J.D., et al.: Phys. Rev. Lett., 71, p. 3401 (1993).
Bird, J.D., et al.: Ap. J., 424, p. 491 (1994).
Birkel, M., and S. Sarkar: Astropart. Phys., 9, p. 297 (1998).
Blake, P.R., et al.: J. Phys. G, 4, p. 1187 (1978).
Blanch-Bigas, O., et al., Auger Collaboration: PICRC, pre-conference edition, paper 603, Merida, Mexico (2007).

Bleve, C., Auger Collaboration: http://www.physics.ox.ac.uk/app2008/talks/Carla_bleve.pdf (2008).
Boezio, M., et al: Astrophys. J., 487, p. 415 (1997).
Boezio, M., et al.: Astrophys. J., 532, p. 653 (2000).
Boezio, M., et al.: Astrophys. J., 561, p. 787 (2001).
Boezio, M., et al.: Astropart. Phys., 19, p. 583 (2003).
Bogomolov, E.A., et al.: PICRC, 2, p. 72 (1987).
Boothby, K., et al.: Nucl. Phys. B (Proc. Suppl.), 60B, p. 124 (1998).
Borione, A., et al.: Astrophys. J., 493, p. 175 (1998).
Bower, A.J., et al.: J. Phys. G, 9, p. L53 (1983).
Boyle, P.J., et al.: PICRC, pre-conference edition, paper 1192, Merida, Mexico (2007).
Bradt, H., et al.: PICRC, 2, p. 715 (1965).
Brecher, K., et al.: The Observatory, 103, p. 106 (1983).
Brownlee, R.G., et al.: Acta Phys. Acad. Scie. Hung., 29, S3, p. 377 (1970).
Budnev, N.M., et al.: PICRC, 6, p. 257 (2005).
Buffington, A., et al.: Astrophys. J., 248, p. 1179 (1981).
Bühler, R., H.E.S.S. Collaboration: PICRC, pre-conference edition, paper 284, Merida, Mexico (2007).
Candia, J., et al.: J. Cosmol. Astropart. Phys. JCAP, 05, 003 (2003).
Capdevielle, J.N., et al.: The Karlsruhe Extensive Air Shower Simulation Code. Kernforschungszentrum Karlsruhe, Report KfK 4998, November (1992).
Cassiday, G.L., et al.: PICRC, 3, p. 196 (1990a).
Cassiday, G.L., et al.: Nucl. Phys. B (Proc. Suppl.), 14A, p. 291 (1990b).
Cesarsky, C.J.: Ann. Rev. Astron. Astrophys., 18, p. 289 (1980).
Chang, J., et al.: PICRC, 3, p. 1 (2005).
Chantell, M.C., et al.: Phys. Rev. Lett., 79, p. 1805 (1997).
Chernov, D. et al.: Int. J. Mod. Phys. A, 20, p. 6799 (2006).
Chernov, D. et al.: PICRC, pre-conference edition, paper 435, Merida, Mexico (2007).
Cherry, M.L.: J. Phys. Conf. Ser., 47, p. 31 (2006).
Chudakov, A.E.: Trudy conf. po cosm. lutcham, p. 69, (in Russian), Yakutsk (1972).
Clark, G.W., et al.: Phys. Rev., 122, p. 637 (1961).
Clay, R.W.: Aust. J. Phys., 37, p. 97 (1984).
Clay, R.W., et al.: Aust. J. Phys., 37, p. 91 (1984).
Clay, R.W., Auger Collaboration: PICRC, 1, p. 421 (2003).
Clay, R.W., and A.G.K. Smith: Extremely High Energy Cosmic Rays: "Astrophysics and Future Observatories", ed. M. Nagano, p. 104, ICCR, University of Tokyo, Tokyo, Japan (1997).
Clay, R.W., et al.: PICRC, 4, p. 185 (1997).
Clem, J.M., et al.: PICRC, 3, p. 5 (1995).
Cocconi, G.: PICRC, Moscow 1959, 2, p. 309 (1960).
Cocconi, G.: Texas Symposium on Relativistic Astrophysics (1967).
Compton, A.H.: Phys. Rev., 21, p. 490 (1923).
Compton, A.H., and I.A. Getting: Phys. Rev.,47, p. 817 (1935).
Corbato, D.B.S., et al.: Astrophys. J., 424, p. 491 (1994).
Cranshaw, T.E., and W. Galbraith: Phil. Mag., 45, p. 1109 (1954).
Cranshaw, J.K., and H. Elliot: Proc. Phys. Soc. A, 69, p. 102 (1956).
Cronin, J.W.: Nucl. Phys. B (Proc. Suppl.), 28B, p. 213 (1992).
Cudell, J.R., et al.: Phys. Rev. D, 36, p. 1657 (1987).
Cunningham, G., et al.: Astrophys. J., 236, p. L71 (1980a).
Cunningham, G., et al.: Catalogue od Heighest Energy Cosmic Rays, ed. M. Wada, Institute of Physical and Chemical Research, Tokyo, World Data Center C2, No 1, p. 63 (1980b).
Dai, H.Y., et al.: J. Phys., G 14, p. 793 (1988).
Dai, H.Y., et al.: Astrophys. J., 511, p. 739 (1999).
Daudin, A., et al.: Nuovo Cim., 3, p. 1017 (1956). (in French).

Daum, K., et al., Fréjus Collaboration: Zeitschr. Phys. C, 66, p. 177 (1995).
Davis, S.T., et al.: PICRC, 4, p. 210 (1979).
Derbina, V.A., et al.: Astrophys. J., 628, p. L41 (2005).
De Shong, James, A., et al.: Phys. Rev., 12, p. 3 (1964).
Diehl, E., et al.: Astropart. Phys., 18, p. 487 (2003).
Diminstein, O.S., et al.: Bulletin Naushno-technithekoj Informasli, Yakutsk 9, p. 537 (1982).
Domokos, G., et al.: J. Phys., G., 19, p. 899 (1993).
Domokos, G., and S. Kovesi-Domokos: hep-ph/0307099 (2003).
Domokos, G., and S. Kovesi-Domokos: Nucl. Phys., B (Proc. Suppl.), 151, p. 33 (2006).
Donelly, J., et al.: PICRC, 3, p. 109 (1999).
Drees, M., et al.: Phys. Rev. D, 39, p. 1310 (1989).
Drury, L.O'C.: Rep. Prog. Phys., 46, p. 973 (1983).
DuVernois, M.A., et al.: Astrphys. J., 559, p. 296 (2001).
Dyakonov, M.N., et al.: PICRC, 8, p. 168 (1979).
Dyakonov, M.N., et al.: PICRC, 6, p. 106 (1981).
Earl, J.A.: Phys. Rev. Lett., 6, p. 125 (1961).
Edge, D.M., et al.: PICRC, 4, p. 2513 (1973).
Edge, D.M.: J. Phys. G, 2, p. 433 (1976).
Edge, D.M., et al.: J. Phys. G, 4, p. 133 (1978).
Efimov, N.N., et al.: PICRC, 2, p. 149 (1983).
Egorov, T.A., et al.: PICRC, 6, p. 2059 (1971).
Ellis, J., et al.: arXiv:astro-ph/0512303 (2005).
Engel, R., et al.: Phys. Rev. D, 64, p. 093010 (2001).
Engelmann, J., et al.: Astron. Astrophys., 148, p. 12 (1985).
Engler, J., et al.: PICRC, 1, p. 349 (1999).
Erlykin, A. D., and A.W. Wolfendale: Astropart. Phys., 10, p. 69 (1999).
Evenson, P., and P. Meyer: J. Geophys. Res., 89, p. 2647 (1984).
Facal San Luis, P., Auger Collaboration: PICRC, pre-conference edition, paper 319, Merida, Mexico (2007).
Fargion, D., et al.: Astrophys. J., 517, p. 725 (1999).
Farley, F.J.M., and J.R. Storey: Nature, Lond., 173, p. 445 (1954a).
Farley, F.J.M., and J.R. Storey: Proc. Phys. Soc. A, 67, p.996 (1954b).
Fazio, G.G., et al.: Astrophys, J., 175, p. L117 (1972).
Fenton, A.G., and K.B. Fenton: Proc. Internat Cosmic Ray Symp. on High Energy Cosmic Ray Modulation, Tokyo (1976).
Fleysher, R., Milagro Collaboration: AIP Conf. Proceedings, 745, p. 269 (2005).
Fodor, Z., and S.D. Katz: Phys. Rev. Lett., 86, p. 3224 (2001).
Fomin, Yu. A., et al.: PICRC, 2, p. 85 (1991).
Fortson, L.F., et al.: PICRC, 3, p. 125 (1999).
Fowler, P., et al.: Nucl. Instr. Meth., 147, p. 195 (1977).
Fowler, P., et al.: Astrophys. J., 314, p. 739 (1987).
Fowler, J.W.: Ph. D. Thesis, University of Chicago (2000).
Fowler, J.W., et al.: Astropart. Phys., 15, p. 49 (2001).
Fukui, S., et al.: Prog. Theor. Phys. Jpn., 16, p. 1 (1960).
Fukushima, M., et al.: PICRC, pre-conference edition, paper 955, Merida, Mexico (2007).
Furukawa, M., et al.: PICRC, 4, p. 1837 (2003a).
Furukawa, M., et al.: PICRC, 4, p. 1877 (2003b).
Furukawa, M., et al.: PICRC, 4, p. 1885 (2003c).
Gaisser, T.K., T. Stanev, and G. Barr: Bartol Research Institute Preprint BA-88-1 (1988).
Gaisser, T.K.: arXiv:astro-ph/0612274v1 Dec. (2006).
Galactic Origin and Acceleration Limit Workshop, ICRC, July 26, 1993, Calgary, Canada (1993).
Gawin, J., et al.: PICRC, 4, p. 180 (1963).
Gawin, J., et al.: Can. J. Phys., 46, p. S75 (1968).

Gelmini, G., et al.: arXiv:astro-ph/0506128 (2005)
Gelmini, G., et al.: Astropart. Phys., 28, p. 390 (2007).
Gerhardy, P.R., et al.: J. Phys. G, 9, p. 1279 (1983).
Ginzburg, V.L., and V.S. Ptuskin: Rev. Mod. Phys., 48, p. 161 (1976).
Glashow, S.L.: Phys. Rev, 118, p. 316 (1960).
Glasmacher, M.A.K., et al.: Astropart. Phys., 10, p. 291 (1999a).
Glasmacher, M.A.K., et al.: Astropart. Phys., 12, p. 1 (1999b).
Glasmacher, M.A.K., et al.: PICRC, 3, p. 199 (1999c).
Glasmacher, M.A.K., et al.: PICRC, 3, p. 129 (1999d).
Glushkov, A.V., et al.: PICRC, 8, p. 158 (1979).
Glushkov, A.V., et al.: PICRC, 2, p. 186 (1985).
Glushkov, A.V., et al.: PICRC, 1, p. 389 (2003).
Golden, R.L., et al.: Astrophys. Lett. 24, p. 75 (1984a).
Golden, R.L., et al.: Astrophys. J., 287, p. 622 (1984b).
Golden, R.L., et al.: Astrophys. J., 457, p. 103 (1996).
Golden, R.L., et al.: Astrophys. J., 479, p. 992 (1997).
Goret, Ph., et al.: Astron. Astrophys., 270, p. 401 (1993).
Goret, Ph.: Towards a major atmospheric Cherenkov detector III, Tokyo, p. 359 (1994).
Gorham, P.W., et al.: Phys. Rev. Lett., 93, p. 041101 (2004).
Greisen, K.: Annual Review of Nuclear Science, Annual Reviews, Inc., Palo Alto, CA, USA, Vol 10, p. 63 (1960).
Greisen, K.: PICRC, 2, p. 609 (1965).
Greisen, K.: Phys. Rev. Lett., 16, p. 748 (1966).
Gress, O.A., et al.: Nucl. Phys. B (Proc. Suppl.), 75a, p. 299 (1999).
Grieder, P.K.F.: Proceedings of 3rd NESTOR International Workshop October 19–21 1993, Pylos, Greece, p. 168 (1993).
Grieder, P.K.F.: Cosmic Rays at Earth (Rsearcher's Reference Manual and Data Book), Elsevier Science B.V., Amsterdam, The Netherlands, ISBN 0444507108 (2001).
Grigorov, N.L., et al.: PICRC, 5, p. 1746 (1971a).
Grigorov, N.L., et al.: PICRC, 5, p. 1760 (1971b).
Grigorov, et al., (1999) after Shibara (1999).
Grimani, C.: Astrophys. Space Sci., 241, p. 295 (1996).
Grimani, C., et al.: Astron. Astrophys., 392, p. 287 (2002).
Grimani, C.: PICRC, 3, p. 9 (2005).
Guidoboni, E., et al: Vulcano Workshop 1992, Frontier Objects in Astrophysics and Particle Physics, (eds. F. Giovannelli and G, Mannocchi), Conrefence Proceedings Vol. 40, Italian Physical Society, p. 289 (1993).
Gupta, S.K., et al.: PICRC, pre-conference edition, paper 1058, Merida, Mexico (2007).
Halzen, F., et al.: Phys. Rec. D, 34, p. 2061 (1986).
Halzen, F., et al.: Astropart. Phys., 3, p. 151 (1995).
Hams, T., et al.: PICRC, pre-conference edition, paper 1119, Merida, Mexico (2007).
Han, J.L.,: Nucl. Phys. B (Proc. Suppl.), 175–176, p. 62 (2008).
Harding, A.K., and R. Ramaty: PICRC, 2, p. 92 (1987).
Hareyama, M., et al.: PICRC, 3, p. 105 (1999).
Haungs, A., et al.: PICRC, 1, p. 329 (1999).
Haungs, A., et al.: Rep. Prog. Phys., 66, p. 1145 (2003).
Haungs, A., et al.: Nucl. Phys., B (Prog. Suppl.), 151, p. 167 (2006).
Hayakawa, S., and Y. Yamamoto: Prog. Theor. Phys., Jpn., 30, p. 71 (1963).
Hayashi, Y., GRAPES Collaboration: PICRC, 10, p. 243 (2005).
Hayashida, N., et al.: Phys. Rev. Lett., 77, p. 1000 (1996).
Hayashida, N., et al.: Astropart. Phys., 10, p. 303 (1999).
Hemberger, M., et al., HEGRA Collaboration: PICRC, 3, p. 175 (1999).
Hill, C.T.: Nucl. Phys. B, 224, p. 469 (1983).

Hillas, A.M., et al.: PICRC, 3, p. 1007 (1971).
Hillas, A.M.: PICRC, 8, p. 7 (1979).
Hillas, M.: PICRC 13, p. 69 (1981).
Hillas, A.M.: Ann. Rev. Astron. Astrophys., 22, p. 425 (1984).
Hillas, A.M.: Nature, 395, p. 15 (1998).
Hindmarsh, M.B., and T.W.B Kibble: Rep. Prog. Phys., 58, p. 477 (1995).
Homola, P., et al.: Acta Phys. Polon. B, 35, p. 1893 (2004).
Homola, P., et al.: Comp. Phys. Comm., 173, p. 71 (2005).
Homola, P., et al.: Nucl. Phys. B (Proc. Suppl.), 151, p. 116 (2006).
Honda, M., et al.: Phys. Rev. D, 70, p. 043008 (2004).
Hooper, D., et al.: Astropart. Phys., 27, p. 199 (2007).
Hörandel, J.R., et al.: Proceedings of the 16-th ECRS, Alcala de Henares, 1, p. 579 (1998).
Hörandel, J.R.: PICRC, 1, p. 337 (1999).
Hörandel, J.R.: J. Phys. G, 29, p. 2439 (2003a).
Hörandel, J.R.: Astropart. Phys., 19, p. 193 (2003b).
Hörandel, J.R., et al.: Astropart. Phys., 27, p. 119 (2007).
Hörandel, J.R.: Advances in Space Research, 41, p. 442 (2008).
Huang, J., et al: Astropart. Phys., 18, p. 637 (2003).
Hubble, E.: Proc. Nat. Acad. Sci., 15, p. 270 (1929).
Hunter, S.D., et al.: Astrophys. J., 481, p. 205 (1997).
Ivanenko, I.P., et al.: PICRC, 2, p. 17 (1993).
Ichimura, M., et al.: Phys. Rev. D, 48, p. 1949 (1993).
Inoue, N., et al.: PICRC, 4, p. 113 (1997).
Ito, N., et al.: PICRC, 4, p. 117 (1997).
Ivanov, D., and G.B. Thomson: PICRC, pre-conference edition, paper 1044, Merida, Mexico (2007).
Iyono, A., et al.: Nucl. Phys. B (Proc. Suppl.), 151, p. 69 (2006).
Ishihara, A., et al., IceCube Collaboration: PICRC, pre-conference edition, paper 275, Merida, Mexico (2007).
JACEE Collaboration, 1999, after Shibata (1999).
Jansson, R., et al.: PICRC, pre-conference edition, paper 1271, Merida, Mexico (2007).
Jauch, J.M., and F. Röhrlich: The Theory of Photons and Electrons, Addison-Wesley, Cambridge, MA, USA (1955).
Jauncey, D.: Ph. D. Thesis, University of Sydney, Australia (1965).
Jones, L.W.: Vulcano Workshop 1988, Frontier Objects in Astrophysics and Particle Physics, Editrice Compositori Bologna, Italy, Italian Physical Society Conf. Proc., 19, p. 299 (1989a).
Jones, L.W.: Proceedings of the 5th International Symposium Very High Energy Cosmic Ray Interactions, Lodz. Poland 1988, University of Lodz, Poland, I, p. 358 (1989b).
Jones, L.W.: PICRC, 2, p. 75 (1990).
Juliusson, E.: Astrophys. J. 191, p. 331 (1974).
Kachelriess, M., et al.: Astropart. Phys., 26, p. 378 (2007).
Kaidalov, A.B., and K.A. Ter-Martirosyan: PICRC, 5, p. 139 (1987).
Kakimoto, F., et al.: PICRC, 6, p. 27 (1981).
Kamata, K., et al.: Can. J. Phys., 46, p. S72 (1968).
Kampert, K.-H., et al.: PICRC, 3, p. 159 (1999).
Kang, Hyesung, et al.: PICRC, pre-conference edition, paper 418, Merida, Mexico (2007).
Karle, A, et al., HEGRA Collaboration: Phys. Lett. B, 347, p. 161 (1995).
Kenrich, F.: Ph. D. Thesis, HEGRA Collaboration, M.P.I. Munich, Germany (1995).
Kieda, D.B., and S.P. Swordy: PICRC, 3, p. 191 (1999).
Kifune, T., et al.: J. Phys. G, 12, p. 129 (1986).
Kirk, J.G., and R.O. Dendy: J. Phys. G, 27, p. 1589 (2001).
Kobayakawa, K., et al.: Phys. Rev. D, 66, p. 083004 (2002).
Kobayashi, T., et al.: Astrophys. J., 601, p. 340 (2004).

Konopelko, A., et al.: Astropart. Phys., 4, p. 199 (1996).
Kopenkin, V.: PICRC, pre-conference edition, paper 343, Merida, Mexico (2007).
Koshiba, M.: Physics Reports, 220, 5 & 6, p. 229 (1992).
Krasilnikov, D.D., et al.: PICRC, 12, p. 4347 (1975).
Kraushaar, W.L., et al.: Astrophys. J., 177, p. 341 (1972).
Kravchenko, V., et al: Phys. Rev. D, 73, p. 082002 (2006).
Kronberg, P.: Rep. Prog. Phys., 57, p. 325 (1994).
Kulikov, G.V., and G.B. Khristiansen: Sov. Fiz. Zh. Eksper. Teor. Fiz., 35, p. 635 (1958) (in Russian).
Kulikov, G.V., and G.B. Khristiansen: Sov. Phys. JETP, 35 (8), p. 441 (1959).
Kwiecinski, J., et al.: Phys. Rev. D, 59, p. 093002 (1999).
Lagage, P., and C. Cesarsky: Astron. Astrophys., 118, p. 223 (1983).
Landau, L.D. and I.Ya. Pomeranchuk: Dokl. Akad. Nauk., SSSR, 92, p. 535 (1953a).
Landau, L.D. and I.Ya. Pomeranchuk: Dokl. Akad. Nauk., SSSR, 92, p. 735 (1953b).
La Pointe, M., et al.: Can. J. Phys., 46, p. S68 (1968).
Lawrence, D., et al.: Nucl. Instr. Meth. A, 420, p. 402 (1999).
Lawrence, M.A., et al.: Phys. Rev. Lett., 63, p. 1121 (1989).
Lawrence, M.A., et al.: J. Phys. G, 17, p. 733 (1991).
Le Coultre, P., et al., L3+C Collaboration: PICRC, 4, p. 399 (2005).
LeBohec, S., et al.: Astrophys. J., 539, p. 209 (2000).
Lehtinen, N.G., et al.: Phys. Rev. D, 69, p. 013008 (2004).
Lessard, R.W., et al.: PICRC, 2, p. 475 (1995).
Lewis, D., et al.: PICRC, 1, p. 279 (1993).
Li, T.-P., and Y.-Q. Ma: Astrophys. J., 272, p. 317 (1983).
Linsley, J.: PICRC, 4, p. 77 (1963).
Linsley, J.: PICRC, 5, p. 3207 (1973a).
Linsley, J.: PICRC, 4, p. 2518 (1973b).
Linsley, J.: Phys. Rev. Lett., 34, p. 1530 (1975a).
Linsley, J.: PICRC, 2, p. 592 (1975b).
Linsley, J.: PICRC, 2, p. 598 (1975c).
Linsley, J.: Catalogue of Highest Energy Cosmic Rays, M. Wada ed., Institute of Physical and Chemical Research, Tokyo, World Data Center C2, Japan (1980).
Linsley, J.: PICRC, 12, p. 135 (1983).
Linsley, J., and A.A. Watson: PICRC, 12, p. 203 (1977).
Linsley, J., and A.A. Watson: Phys. Rev. Lett., 46, p. 459 (1981).
Lloyd-Evans, J.: PhD Thesis, University of Leeds UK, (1982).
Lloyd-Evans, J., et al.: Europ. Cosmic Ray Symp., Bologna, Tecnoprint, p. 81 (1983).
Lodders, K,: Astrophys. J., 591, p. 1220 (2003).
Mannheim, K., et al.: Phys. Rev. D, 63, p. 023003 (2002).
Mardia, V., and P. Jupp: Directional Statistics, Wiley, New York (1999).
Mastichiadis, M., et al.: Proc. Astron. Soc. Aust., 9, p. 115 (1991a).
Mastichiadis, M., et al.: PICRC, 2, p. 145 (1991b).
Matthews, J., et al.: Astrophys. J., 375, p. 202 (1991).
McCusker, C.B.A., and L.S. Peak: Nuovo Cim., 31, p. 525 (1964).
McDonald, F.B.: Phys. Rev., 109, p. 1367 (1958).
Menn, M., et al.: Astrophys. J., 533, p. 281 (2000).
Meyer, P., and R. Vogt: Phys. Rev. Lett., 6, p. 193 (1961).
Migdal, A.B.: Phys. Rev., 103, p. 1811 (1956).
Minagawa, G.: Astrophys. J., 248, p. 847 (1981).
Mitchell, J.W., et al.: Phys. Rev. Lett., 76, p. 3057 (1996).
Miura, I. and H. Hasegawa: J. Phys. Soc. Jpn., 17, Suppl. A-III, p. 84 (1962).
Mollerach, S., and E. Roulet: J. Cosmol. Astropart. Phys. JCAP, 08, 004 (2005).
Mollerach, S., et al.: PICRC, pre-conference edition, paper 74, Merida, Mexico (2007).

Moskalenko, I.V., and A.W. Strong: Astrophys. J., 493, p. 694 (1998).
Mostafá, M.A.: PICRC, 7, p. 369 (2005).
Müller, D., et al.: Astrophys. J., 374, p. 356 (1991).
Müller, D., et al.: PICRC, 3, p. 89 (2005).
Müller, D., et al.: PICRC, pre-conference edition, paper 1188, Merida, Mexico (2007).
Münich, K. et al., IceCube Collaboration: PICRC, 5, p. 17 (2005).
Nagano, M.: New J. Phys., 11, 065012 (2009).
Nagano, M., et al.: J. Phys. G, 10, p. 1295 (1984a).
Nagano, M., et al.: J. Phys. Soc. Jpn., 53, p. 1667 (1984b).
Nagano, M., et al.: J. Phys. G, 18, p. 423 (1992).
Nagano, M., and A.A. Watson: Rev. Mod. Phys., 72, p. 689 (2000).
Nagano, M., et al.: Astropart. Phys., 13, p. 277 (2000).
Navarra, G., EAS-TOP Collaboration: Nucl. Phys. B (Proc. Suppl.), 60B, p. 105 (1998).
Navarra, G., et al., EAS-TOP Collaboration: PICRC, 1, p. 147 (2003).
Navarra, G.: Nucl. Phys., B (Proc. Suppl.), 151, p. 79 (2006).
Nellen, L., et al.: Phys. Rev. D, 47, p. 5270 (1993).
Nikolsky, S.I.: Proc. Fifth Interamerican Conference on Cosmic Rays, La Paz (La Paz: Lab. de Fis. Cosmica) (1962).
Nikolsky, S.I., et al.: J. Phys. G, 13, p. 883 (1987).
Nishimura, J., et al.: Astrophys. J., 238, p. 394 (1980).
Nishimura, J., et al.: PICRC, 9, p. 539 (1985).
Noda, C., et al.: Nucl. Phys., B (Proc. Suppl.), 175–176, p. 459 (2008).
Ochi, N., et al.: J. Phys. G, 29, p. 1169 (2003).
Ogio, S. and F. Kakimoto: PICRC, 1, p. 315 (2003).
Ogio, S., et al.: Astrophys. J., 612, p. 268 (2004).
O'Halloran, T., et al.: Phys. Today, 51, p. 31 (1998).
Olinto, A.V.: Phys. Rep., 333, p. 329 (2000).
Ong, R.A.: Phys. Rep., 305, p. 93 (1998).
Ong, R.A.: PICRC, 10, p. 329 (2005).
Oort, J.H.: Bull. Astron. Inst. Netherlands, 6, p. 155 (1931).
Ormes, J.F.: PICRC, 2, p. 187 (1983).
Ormes, J.F., et al.: Astrophys. J., 482, p. L-187 (1997).
Over, S., et al.: PICRC, pre-conference edition, paper 832, Merida, Mexico (2007).
Papini, P., et al.: PICRC, 1, p. 579 (1993).
Pelletier, G.: Lecture Notes in Physics, M. Lemoine ed., Springer, Berlin, 576, p. 58 (2001).
Penzias, A.A., and R.W. Wilson: Astrophys. J., 142, p. 420 (1965).
Perrone L., Auger Collaboration: PICRC, pre-conference edition, paper 316, Merida, Mexico (2007).
Peters, B.: PICRC (Moscow, 1959), 3, p. 157 (1960).
Peters, B.: Nuovo Cim., 22, p. 800 (1961).
Porter, T.A., and R.J. Protheroe: J. Phys. G, 23, p. 1765 (1997).
Prince, Thomas, A.: Astrophys. J. , 227, p. 676 (1979).
Ptuskin, V.S.: PICRC, 10, p. 317 (2005).
Ramana-Murthy, P.V., and A.W. Wolfendale: Gamma Ray Astronomy, 2nd ed., Cambridge University Press, Cambridge, New York (1993).
Ramaty, R., et al.: Proceedings of the Integral Workshop, Les Diablerets, Switzerland, (1993).
Rao, M.V.S., and B.V. Sreekantan: Curr. Sci., 62, No. 9, p. 617 (1992).
Rawlins, K., et al.: PICRC, 1, p. 173 (2003).
Risse, M., et al.: Astropart. Phys., 21, p. 479 (2004).
Risse, M., et al.: Phys. Rev. Lett., 95, p. 171102 (2005).
Risse, M., et al.: Nucl. Phys. B (Proc. Suppl.), 151, p. 96 (2006).
Röhring, A., et al., HEGRA Collaboration: PICRC, 1, p. 214 (1999).
Roth, M., et al.: PICRC, 1, p. 333 (1999).

Roth, M., et al.: PICRC, 1, p. 88 (2001).
Roulet, E.: Int. J. Mod. Phys. A, 19, p. 1133 (2004).
Ryan, M.J., J.F. Ormes, and V.K. Balasurbrahmanyan: Phys. Rev. Lett., 28, p. 985 (1972).
Saeki, T., et al.: Phys. Lett. B, 422, p. 319 (1998).
Sakaki, N., et al.: PICRC, 1, p. 329 (2001a).
Sakaki, N., et al.: PICRC, 1, p. 333 (2001b).
Sakakibara, S.: J. Geomag. Geoelectr. Jpn., 17, p. 99 (1965).
Sakakibara, S.: PICRC, 4, p. 216 (1979).
Salamon, M.H., et al.: Astrophys. J., 349, p. 78 (1990).
Samorski, M., and W. Stamm: Astrophys. J., 268, p. L17 (1983a).
Samorski, M., and W. Stamm: PICRC, 1, p. 135 (1983b).
Samorski, M., and W. Stamm: PICRC, 11, p. 244 (1983c).
Sanuki, T., et al.: Astrophys. J., 545, p. 1135 (2000).
Santos, E.M., Auger Collaboration: PICRC, pre-conference edition, paper 73, Merida, Mexico (2007).
Sarkar, S., and R. Toldra: Nucl. Phys. B, 621, p. 495 (2002).
Sarkar, S.: Acta Phys. Polonica, B, 35, p. 351 (2004).
Schönfelder, Volker, Ed.: "The Universe in Gamma Rays", Springer Verlag, Berlin, Heidelberg, New York (2001).
Schramm, D.N.: PICRC, 7, p. 55 (1987).
Seidelmann, P.K. Ed.: Explanatory supplement to the Astronomical Almanac, University Science Books Mill Valley, CA USA (1992).
Semikoz, D., Auger Collaboration: PICRC, pre-conference edition, paper 1035, Merida, Mexico (2007).
Semikoz, D., and G. Sigl: arXiv.org:hep-ph/0309328 (2003).
Seo, E.S., et al.: PICRC, pre-conference edition, paper 677, Merida, Mexico (2007).
Shibata, T.: Nucl. Phys. B (Proc. Suppl.), 75, p. 22 (1999).
Shibata, T.: Astrophys. J., 612, p. 238 (2004).
Shinozaki, K., et al.: Astrophys. J., 571, p. L117 (2002).
Shirasaki, Y., et al.: Astropart. Phys., 15, p. 357–381 (2001).
Shirk, E., and P. Price: Astrophys. J., 220, p. 719 (1978).
Sigl, Günter, et al.: Phys. Rev. D, 59, p. 043504 (1999).
Silberberg, R., et al.: PICRC, 2, p. 179 (1983).
Simon, J.L., et al.: Astron. Astrophys., 282, p. 663 (1994).
Simon, M., et al.: Astrophys. J., 499, p. 250 (1998).
Simpson, J.: Ann. Rev. Nucl. Sci., 33, p. 323 (1983).
Skibo, J.G., and R. Ramaty: PICRC, 2, p. 132 (1993).
Smialkowski, A., et al.: Astropart. Phys., 7, p. 21 (1997).
Smith, A.J., Milagro Collaboration: PICRC, 10, p. 227 (2005).
Smith, G.J., and K.E. Turver: PICRC, 4, p. 2369 (1973).
Smith, L.H., et al.: Astrophys. J., 180, p. 987 (1973).
Sommers, P.: Astropart. Phys., 14, p. 271 (2001).
Sommers, P., et al.: astro-ph/0507150 (2005).
Stamenov et al.: Trudy Fian, SSSR, 109, p. 132 (1979).
Stanev, T., et al.: Phys. Rev. D, 32, p. 1244 (1985).
Stanev, T., et al.: Astron. Astrophys., 274, p. 902 (1993).
Stecker, F.W.: Astrophys. J., 228, p. 919 (1979).
Stecker, F.W., et al.: Phys. Rev. Lett., 66, p. 2697 (1991).
Stecker, F.W., et al.: Phys. Rev. Lett., 69, p. 2738 (Errata) (1992a).
Stecker, F.W., et al.: in Proceedings of the Workshop on "High Energy Neutrino Astrophysics"; V.J. Stenger, et al. eds., World Scientific, Singapore, p. 1 (1992b).
Stecker, F.W., and M.H. Salamon: Space Sci. Rev., 75, p. 341 (1996).
Stecker, F.W., and S.T, Scully: Astropart. Phys., 23, p. 203 (2005).

Stepanian, A.A.: Nucl. Phys., B (Proc. Suppl.), 39A, p. 207 (1995).
Stephens, S.A., and R.L. Golden: Space Sci. Rev., 46, p. 31 (1987).
Streitmatter, R.E.: Astron. Astrop., 143, p. 249 (1985).
Streitmatter, R.E., et al.: PICRC, 3, p. 277 (1990).
Strömberg, C.: Astrophys. J., 61, p. 357 (1925).
Strong, A.W., et al.: Astrophys. J., 613, p. 962 (2004).
Suga, K., et al.: PICRC, 4, p. 9 (1963).
Suga, K., et al.: Astrophys. J., 326, p. 1036 (1988).
Sveshnikova. L.G.: Astron. Astrophys., 409, p. 799 (2003).
Swordy, S.: PICRC, 2, p. 697 (1995).
Swordy, S.P., and D.B. Kieda: Astropart. Phys., 13, p. 137 (2000).
Szabo, A.P., and R.J. Protheroe: Astropart. Phys., 2, p. 375 (1994).
Taira, T., et al.: PICRC, 2, p. 128 (1993).
Takahashi, Y.: Nucl. Phys. B (Proc. Suppl.), 60 B, p. 83 (1998).
Takeda, M., et al.: Phys. Rev. Lett., 81, p. 1163 (1998).
Takeda, M., et al.: Astrophys. J., 522, p. 225 (1999).
Takeda, M., et al.: Astropart. Phys., 19, p. 447 (2003).
Tanaka, H., et al.: PICRC, pre-conference edition, paper 1233, Merida, Mexico (2007a).
Tanaka, H., et al.: PICRC, pre-conference edition, paper 1235, Merida, Mexico (2007b).
Tang, K.-K.: Astrophys. J., 278, p. 881 (1984).
Tanimori, T., et al.: Astrophys. J., 429, p. L61 (1994).
Tateyama, N., and J. Nishimura: PICRC, 4, p. 2285 (2003).
Tokuno, H., et al.: Astropart. Phys., 29, p. 453 (2008).
Torii, S., et al.: Astrophys. J., 559, p. 973 (2001).
Tueller, J., and M. Israel: after Binns et al. (1981).
Turver, K.E.: In "Cosmic Rays at Ground Level", The Institute of Physics, London and Bristol, p. 159, A.W. Wolfendale, ed. (1973).
Tylka, A.J.: Phys. Rev. Lett., 63, p. 840 (1989).
Ulrich, H., et al.: PICRC, 1, p. 97 (2001).
Uryson, A., V.: PICRC, 2, p. 136 (1993).
Vacanti, G., et al.: Astrophys. J., 377, p. 467 (1991).
Vernois, M.D., et al.: PICRC, 5, p. 1618 (2001).
Vildanova et al.: Izv. Acad. Nauk. SSSR, Ser. Phys., 58, 79 (1994) (in Russian).
Völk, H.J., and P.L. Biermann: Astrophys. J., 333, p. L65 (1988).
Völk, H., and V. Zirakashvili: PICRC, 4, p. 2031 (2003).
Volkova, L.V.: Yad. Fiz., 31, p. 1510 (1980).
Volkova, L.V.: Sov. J. Nucl. Phys., 31, p. 784 (1980).
Volkova, L.V., and G.T. Zatsepin: Phys. Lett. B, 462, p. 211 (1999).
Wada, T., et al.: Nucl. Phys. B (Proc. Suppl), 75A, p. 330 (1999).
Watson, A.A.: PICRC, 11, p. 4019 (1975).
Watson, A.A.: Nucl. Phys. B (Proc. Suppl), 28B, p. 3 (1992).
Watson, A.A.: PICRC, 8, p. 257 (1997).
Watson, A.A.: Phys. Rep., 333–334, p. 309 (2000).
Waxman, E.W.: Phys. Rev. Lett., 75, p. 386 (1995).
Waxman, E., and J. Bahcall: Phys. Rev. Lett., 78, p. 2292 (1997).
Waxman, E., and J. Bahcall: Phys. Rev. D. 59, p. 023002 (1999).
Wdowczyk, J., et al.: J. Phys. A, 5, p. 1419 (1972).
Weaver, B., and A. Westphal: PICRC, 5, p. 1720 (2001).
Webber, W., et al.: PICRC, 1, p. 325 (1987).
Weber, J.H., KASCADE Collaboration: PICRC, 1, p. 341 (1999).
Weekes, T.C.: Phys. Rep., 160, p. 1 (1988).
Weekes, T.C.: Space Sci. Rev., 75, p. 1 (1996).
Weekes, T.C., et al.: Universal Academic Press, inc., Tokyo (Japan), PICRC, 8, p. 3 (2003).

Wefel, J.P., et al.: PICRC, 3, p. 105 (2005).
Wefel, J.P.: Paper presented at the XV. ISVHECRI, Paris (2008).
Weiler, T.J.: Phys. Rev. Lett., 49, p. 234 (1982).
Weiler, T.J.: Astropart. Phys., 11, p. 303 (1999).
Wiebel-Sooth, B.: Ph.D. Thesis, University of Wuppertal, Germany (1998).
Wiebel-Sooth, B., et al.: Astron. Astrophys., 330, p. 389 (1998).
Winn, M.M., et al.: J. Phys. G. 12, p. 653 (1986).
Yadav, K.K., et al.: Astropart. Phys., 27, p. 447 (2007).
Yamamoto, T., Auger Collaboration: PICRC, pre-conference edition, paper 318, Merida, Mexico (2007).
Yoshida, S., and H. Dai: J. Phys. G, 24, p. 905 (1998).
Yoshida, S., et al.: Phys. Rev. Lett., 81, p. 5505 (1998).
Yoshida, T., et al.: PICRC, 3, p. 33 (2005).
Yoshida, K., et al.: PICRC, pre-conference edition, paper 892, Merida, Mexico (2007).
Zatsepin, G.T.: Dokl. Akad. Nauk, SSSR, 80, p. 577 (1951).
Zatsepin, G.T. and V.A. Kuzmin: JETP Lett. 4, p. 78 (1966).
Zatsepin, V.I., et al: PICRC, 2, p. 13 (1993).
Zatsepin, V.I., et al., ATIC Collaboration: Proc. 28th Russian Cosmic Ray Conf., Vol. 68/11, p. 1593 (2004).
Zeilik, M.G. and A. Stephen: Introductory Astronomy and Astrophysics, Saunders College Division (1998).

Chapter 12
Common Shower Properties, Observables and Data

Overview In this chapter we discuss the most frequently recorded common shower observables, such as shower size (electron or total charged particle size) and muon size spectra, shower density spectra, density spectra at fixed core distance and shower energy loss spectra. The various concepts are defined and the experimental methods of measurement are outlined. We present a wealth of data and spectra of these observables from a selection of experiments from all epochs and a series of compilations that permit to compare the results from the different experiments. The role of the data for the interpretation of air showers is briefly outlined, however, the comprehensive evaluation of the data and implications are treated in separate chapters as referred to in the text.

12.1 General Comments

There are a number of common, purely phenomenological observables that can be detected and interpreted in a simple way without the need for having deeper insight into the complex physics of extensive air showers. These comprise besides the arrival direction, the shower size, in particular the *charged particle or electron size*, the *muon size* and the *density spectra*, as well as the calorimetric *energy loss spectra* of the shower particles at a specified observation level. These topics are discussed separately in the following sections, yet they are in fact intimately related and should be discussed as an entity together with the topics of Chaps. 2, 4, 6, 7 and 8. It is therefore recommended to consult related topics, too, when focusing on a specific problem.

In this chapter we have frequently compiled data from several experiments in one figure for reasons of comparison. In Sects. 12.2.3 and 12.2.4 the data are in general grouped according to altitude of observation and presented in ascending order, beginning with the measurements carried out at sea level and ending with high altitude observations, except for the most recent data which have been included at the end. In some cases, however, a more comprehensive compilation may precede a group of figures that contains data from different observation levels, to give a better overview or to emphasize particular problems. Whenever possible data of the

P.K.F. Grieder, *Extensive Air Showers,* DOI 10.1007/978-3-540-76941-5_12,

same kind are displayed on graphs with identical scales for easy comparison by superposition.

Note that the atmospheric depths listed for certain installations may not always be the same throughout this book. This is because some authors use sometimes for the analysis of their data an atmospheric column density which corresponds to a specific zenith angle which is different from zero. This situation arises if for statistical reasons one averages data which had been recorded over a particular zenith angular interval in place of just vertical events of which there are few. In this case one uses the *slant depth* or atmospheric overburden corresponding to the average of the particular zenith angular range, and not the mean vertical column density that corresponds to the altitude of the experimental site.

The data summary presented in this chapter is not an all-inclusive collection. In view of the very large number of experiments that were carried out through the years it was necessary to make a selection for the presentation here. Emphasis was therefore given to the historically as well as the contemporary scientifically relevant data. The fast evolving and vast field of *high energy gamma ray astronomy*, which employs air shower detection techniques, is only touched on the side, mostly in connection with particle or Cherenkov detector arrays using wide-angle apertures. It is today a field of its own that is, however, closely interlinked with air shower research, particularly what concerns astrophysical aspects such as the search for cosmic ray sources and related topics.

12.2 Shower Size or Number Spectrum

12.2.1 Introduction

The shower size is the total number of charged particles in a shower at a given level in the atmosphere. About 90% of all charged particles in a fully developed shower are electrons, i.e., positrons and negatrons. Of the remaining 10% about 90% are muons and the rest consists of hadrons. Photons constitute the largest single population in a shower and neutrinos are abundant, too, but the latter escape detection with standard air shower recording equipment. However, they represent a certain energy leakage for a shower that cannot be ignored in some cases. The photon number can exceed the electron population by as much as a factor of three to five, or even more, depending on the low energy cutoff imposed on the photon count.

In many papers, particularly of older date, authors frequently ignored the existence of shower constituents other than electrons (positrons and electrons) and simply speak of the number of electrons in a shower when discussing shower size. Some authors therefore designate shower size by $N_e(X)$, where the subscript e refers to electrons ($e^{\pm}$) and X to the atmospheric depth [$\mathrm{g\,cm^{-2}}$] to which the size applies. This is actually a leftover from the old days when it was believed that showers were initiated by photons or electrons and the existence of other particles in the cosmic ray beam was either partly unknown or ignored.

Today it is customary to use simply the symbol N to designate the common shower size as determined with scintillation or other kinds of detectors that record all charged particles in a shower, keeping N_e reserved explicitly for the electron size and, analogously, N_μ to identify the muon size of a shower (Sect. 12.3). Unfortunately, even in the recent literature the symbols N_e and N (or $N_{\rm ch}$ for all charged particles) are frequently being used in a non-discriminating manner and the reader must extract the actual meaning from the text. The situation is similar for the slope parameters of the spectra, γ, where subscripts such as γ_e and γ_μ are sometimes attached to distinguish between electron and muon spectra.

The *integral number* or *size spectrum* of air showers, $I(\geq N)$, sometimes also referred to as the *frequency-number spectrum*, is defined as the frequency of showers containing more than N charged particles, with axis crossing unit area at a given atmospheric depth, X. The general form of the integral shower size spectrum can be described approximately by a power law of the form

$$I(\geq N) \;=\; K_N N^{-\gamma} \;\; [\mathrm{m}^{-2}\,\mathrm{s}^{-1}\,\mathrm{sr}^{-1}], \tag{12.1}$$

where γ is the exponent of the spectrum and K_N a proportionality constant.

The *differential size spectrum*, $I(N)$, follows through differentiation of Eq. (12.1) and leads to

$$I(N)\mathrm{d}N \;=\; A_N N^{-(\gamma+1)}\mathrm{d}N \;\; [\mathrm{m}^{-2}\,\mathrm{s}^{-1}\,\mathrm{sr}^{-1}\,\Delta N], \tag{12.2}$$

with A_N being the proportionality constant.

Over wide portions of the spectrum γ is essentially constant. However, close inspection reveals that the entire size spectrum can be divided into three, possibly even into four different regions which require slightly different values of γ.

Accurate measurements have shown that at a size between a few times 10^5 and 10^6 particles the rather featureless shower size spectrum exhibits a slight increase of slope and gets somewhat steeper (Kulikov and Khristiansen, 1958, 1959; Kulikov et al., 1960). This spectral change is called the *knee* and now fairly well located at a primary energy of $\sim 4 \cdot 10^{15}$ eV (e.g., Antoni et al., 2003a). The knee is also seen in the muon size spectrum (Stamenov et al., 1979) and in the density spectrum (Cherenkov photon density and particle density spectra). At significantly larger sizes, around a few times 10^8 particles, corresponding to a primary energy of $\sim 10^{19}$ eV, the spectrum manifests a slight decrease of slope and gets somewhat flatter (Krasilnikov et al., 1975). This change of slope is called the *ankle*.

In recent years it became clear that what appeared to be an *additional knee*, originally discovered by the Akeno group (Nagano et al., 1992; Yoshida and Dai, 1998), is in fact a second though less pronounced increase of the spectral slope. It is located between the well established (first) knee and the ankle, positioned somewhat closer to the ankle, at an energy of about $6 \cdot 10^{17}$ eV (Matthews, 2005; Yoshida, 2005) and is called the *second knee*. The experimentally determined shower sizes where the three changes of slope occur differ somewhat from experiment to experiment and may also depend on the method of measurement. Likewise, the deduced primary

energies that are specified for the location of the spectral slope changes deviate somewhat from work group to work group, however, the existence of these spectral features is established beyond a shadow of doubt.

Thus, for an accurate description of the shower size (or energy) spectrum over the entire explored range to a size of $\sim 10^{10}$, corresponding to a primary energy of $\sim 300\,\mathrm{EeV}$ ($3 \cdot 10^{20}$ eV), four slightly different values of the exponent γ (γ_1–γ_4) are required. The published gamma-values, too, vary from experiment to experiment. They are often specified with an amazing accuracy by some authors, yet the spread of the published values deviate significantly from author to author such that the narrow error bands attached to the center values hardly ever overlap. These topics together with questions related to the nature of the primary are discussed in detail in Sects. 11.6 and 11.7. For general orientation we specify in Table 12.1 the spectral slope values found by Nagano et al. (1992). Mathematical expressions which had been fitted carefully by various authors to their experimental data are given in Sect. 12.2.5.

The concept of shower size is a basic observable of an air shower. In the lower portions of the atmosphere, near shower maximum, the shower size is almost linearly related to the total energy of the primary initiating the event. It is much less dependent on the nature of the primary. Size measurements are therefore in fact indirect measurements of the energy of the primary particle and the size or number spectrum is closely related to the primary energy spectrum.

For a given primary energy the average size of a shower changes with altitude and zenith angle; it also manifests a barometric and temperature dependence (Sects. 6.4 and 6.5). In order to link shower size with primary energy, air shower *simulations* are essential. It is extremely important for the interpretation of all experimental air shower data that the mathematical shower model that is used for the simulations is based on realistic hadronic and electromagnetic interactions that include all known processes and phenomena. Whenever highly simplified models are being used for exploratory work at ultra-high energies, the investigator must fully realize the limitations of the prediction and interpretation of such calculations.

Size spectrum measurements are at present the backbone of the very few ground based methods that allow to explore and determine the energy spectrum of the primary cosmic radiation into energy regions far beyond the range covered by direct measurements carried out with balloon or space craft borne equipment at the fringes of the atmosphere or in outer space. Other methods, discussed later on, are based on muon size spectra (Sect. 12.3), density spectra (Sects. 12.4 and 12.5), atmospheric Cherenkov (Chap. 16) and fluorescence measurements (Chap. 17). The shower size

Table 12.1 Slope parameters of differential energy spectrum (Nagano et al., 1992)

Primary energy [eV]	Spectral slope
$< 5 \cdot 10^{15}$	$\gamma_1 = 2.62 \pm 0.12$
$5 \cdot 10^{15} \leq E_0 < 6.3 \cdot 10^{17}$	$\gamma_2 = 3.02 \pm 0.03$
$6.3 \cdot 10^{17} \leq E_0 < 6.3 \cdot 10^{18}$	$\gamma_3 = 3.16 \pm 0.08$
$>6.3 \cdot 10^{18}$	$\gamma_4 = 2.8 \pm 0.3$

itself is no key to determine the nature of the primary particle that initiates the shower, it is only a coarse measure of the primary energy.

12.2.2 Problems with Size Measurements

Over the years a wide range of size spectra had been measured with the different ground based arrays, located at altitudes ranging from sea level to over 5,000 m, and beyond to heights of 12,000 m with small arrays installed in large aircraft, or mounted on a frame and flown by a balloon. For a partial list of past and current arrays and of their layouts the reader is referred to Appendix A.

In the past the results of the various arrays did not agree very well, even if one accounted properly for the differences in altitude of observation, or when comparing spectra from arrays located at about the same atmospheric depths. Fortunately the situation has improved in recent years but relevant differences between the modern large arrays and fluorescence detectors remain.

The general situation as it was about one quarter of a century ago is illustrated in Fig. 12.1, which shows a compilation of integral size spectra due to Hara et al. (1979c). The figure includes size spectra from different sea level arrays forvertically incident events, from Akeno located at 900 m a.s.l. for vertical

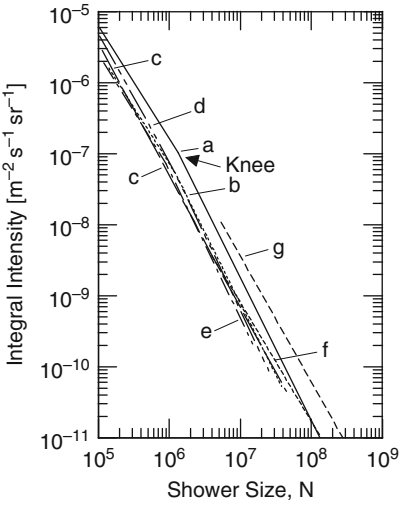

Fig. 12.1 Comparison of the integral shower size spectra obtained by various groups at or near sea level, from a compilation of Hara et al. (1979c). The Chacaltaya (5,230 m a.s.l.) spectrum of inclined showers is also shown for comparison. The location of the spectral knee, discovered by Kulikov and Khristiansen (1958, 1959) is also indicated. *a*, Akeno, 900 m a.s.l., 930 g cm^{-2}; *b*, Akeno, 1,023 g cm^{-2} (inclined); *c*, Tokyo (I.N.S.), 59 m a.s.l.; *d*, Kiel, s.l. (Büscher, 1971); *e*, Moscow, 192 m a.s.l., 1,020 g cm^{-2} (Khristiansen et al., 1965); *f*, Yakutsk, 105 m a.s.l., 1,020 g cm^{-2} (size $\times$1.78) (Diminstein et al., 1977); *g*, Chacaltaya, 5,230 m a.s.l., at 930 g cm^{-2} (inclined, size $\times$0.72), (Hatano et al., 1979; Aguirre et al., 1979)

(atmospheric column density 930 g cm^{-2}) and inclined (1,023 g cm^{-2}) showers, and from Chacaltaya, located at 5,230 m a.s.l. (550 g cm^{-2}). The latter spectrum was recorded under an inclination corresponding to an atmospheric column density (slant depth) of 930 g cm^{-2} (sec $\theta = 1.9$), which is the same as for vertical incidence at Akeno.

Inspection of this figure reveals clearly the degree of disagreement between the different spectra. The difference between the sea level measurements taken at Tokyo (I.N.S.) and Kiel are comparatively small, but the near sea level spectra from Moscow and Yakutsk shown in this figure had to be multiplied by a factor of 1.26 and 1.78, respectively, to reach partial agreement, and the spectrum from Chacaltaya required a factor of 0.72 to bring it within the range of the other spectra. The Akeno data recorded at a zenith angle corresponding to a slant depth of 1,023 g cm^{-2} (curve b) represent essentially sea level measurements. It is evident from Fig. 12.1 that the disagreement concerns mainly the absolute rates, the slopes of the different spectra appear quite similar. But the steepness of the spectra compresses the deviations of the slopes.

The differences in slope and absolute rates of the size spectra of the experiments displayed in Fig. 12.1 are emphasized in Fig. 12.2 where the ordinate of the plot is now multiplied by the square of the shower size. Such displays are useful to enhance spectral differences. In this figure the Chacaltaya spectrum is omitted but we have

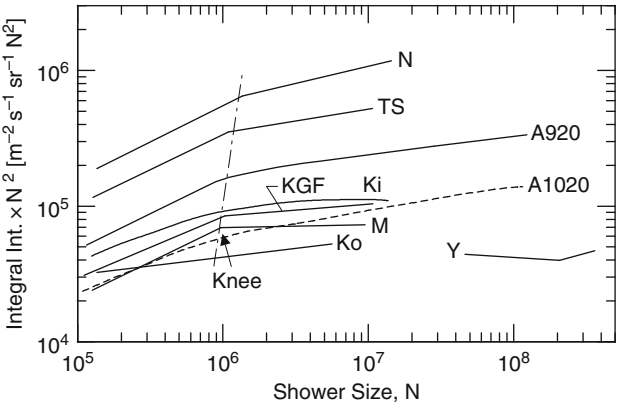

Fig. 12.2 Comparison of integral vertical shower size spectra obtained from different experiments at different altitudes, as listed below. The data are not normalized to any specific altitude (after Nagano et al., 1984). The location of the spectral knee, discovered by Kulikov and Khristiansen (1958, 1959) is marked by the *chain line*. The knee position moves to larger shower sizes with increasing altitude, as is expected, because the observations approach the shower maximum. (Note that the ordinate is multiplied by the square of the shower size.) N, Mt. Norikura, Japan (740 g cm^{-2}) (Kawakami et al., 1983, Private Communication); TS, Tien Shan, Kazakhstan (3,340 m a.s.l., 690 g cm^{-2}) (Kirov et al., 1981); A920, Akeno, Japan (930 g cm^{-2}) (Nagano et al., 1984); A1020, Akeno inclined, secθ = 1.1, (1,020 g cm^{-2}) (Nagano et al., 1984); Ki, Kiel University (s.l.) (Bagge et al., 1977); KGF, Kolar Gold Fields, India (920 g cm^{-2}) (Acharya et al., 1981); M, Moscow State University (s.l.) (Vernov et al., 1968); Ko, Kobe University, Japan (s.l.) (Asakimori et al., 1982); Y, Yakutsk, Russia (s.l.) (Diminstein et al., 1977)

added the results from the Tien Shan installation which is located at an altitude of 3,340 m (690 g cm^{-2}).

Possible causes for the deviations of the various measurements could be the different instrumentation, inadequate array size, saturation of the detectors, insufficient sampling of the showers, i.e., the detector separation is too large and the density fluctuations cannot be accounted for properly, problems with the array calibration, or a combination of all. All of these factors can lead to shower size underestimations. But the problem can also be due to core position errors or to transition effects of electrons and gamma rays in the detectors near the core, particularly if thick scintillators are being used (Sect. 2.11). This can lead to size overestimation. But also the size dependence of the age parameter introduces significant errors. The average age of the showers decreases monotonically from size 10^4 to a few times 10^7 (Sect. 10.4).

Finally, one must also keep in mind that vertical showers initiated by primaries of a given mass and energy observed at sea level are not identical to showers initiated by the same primaries observed at Chacaltaya under a zenith angle such that the slant depth is the same as for vertical trajectories at sea level. The reason is that the trajectory lengths and density profiles are different, which affects the shower development because the competition between interaction and decay of unstable particles changes in favor of decay with increasing zenith angle.

Moreover, problems can be caused by the lateral distribution function of the shower particles that is being used and the apparent variation of the age parameter versus core distance. Frequently an increase of the shower age is observed with increasing core distance at a fixed atmospheric depth in a given shower. This requires a modified NKG function with a variable age parameter to describe the lateral distribution more accurately (Greisen, 1968) (Sects. 8.7 and 10.4).

For the standard NKG function with constant age parameter (Sects. 4.6 and 4.7) the estimated error after integration due to the flattening of the distribution at larger distances, particularly beyond 1 Molière unit (Molière, 1953a, 1953b; see Sect. 4.3.3), leads to an *underestimation* of the shower size by about 20%. Last but not least different computational approaches, errors or inaccuracies in the computer programs used to convert the density measurements to shower size as well as errors in the efficiency determination of an array can lead to deviating results.

Hara et al. (1979b, c) and Böhm and Steinmann (1979) have addressed these problems. The former authors made some of the most detailed studies in this field, conducting extensive measurements at the Akeno site in Japan (900 m a.s.l.). They have used arrays of different configurations, superimposed on each other, with a densely packed array at the center, 156 detectors distributed over 1 km^2, and scintillators of very different size and thickness, in an attempt to resolve the discrepancies (Hatano et al., 1979). Their analysis included density measurements over a range of core distances from 0.01 to 6 Molière units (1 Molière unit = 91.6 m at the Akeno level). A summary of their work is given in the compilation of Fig. 12.1.

Böhm and Steinmann approached the problem from a different side. They had the size spectrum from their measurements in Kiel at sea level and carried out comparative measurements at mountain altitude (Pic du Midi 2,860 m a.s.l., 729 g cm^{-2}).

There, they accepted showers from vertical incidence to a zenith angle of 48°, thus covering a range of atmospheric thickness from 729 to 1,010 g cm^{-2}. Disregarding the different track-length-density profile through the atmosphere of inclined showers as compared to vertical showers, which does affect the showers because of the *enhanced decay* of pions and kaons at larger zenith angles, the showers inclined at 48° correspond approximately to vertical showers at Kiel.

In their analysis Böhm and Steinmann (1979) carefully evaluated the detection efficiency of their array at Kiel (see Sect. 2.10). They have used the same analysis procedure and program for the Pic du Midi data as for the Kiel measurements (van Staa et al., 1974; Böhm, 1977). The results of this investigation are shown in Fig. 12.3. The slopes of the spectra from Kiel and Pic du Midi agree quite well but there remains a difference in the absolute intensity which may be due to calibration errors. These authors have also compared their results with those from Chacaltaya and conclude that there is a systematic difference in the shower size spectra. It is largest for small showers and decreases monotonically with increasing shower size.

In conclusion we must point out that the absolute calibration of the many different air shower arrays remains a major problem. This is evident when comparing the data summary presented below. Recent size spectra determined with modern contemporary arrays agree better but there remain differences in spectral slope and absolute intensities, particularly when comparing data from particle arrays and fluorescence detectors at the highest energies (Yoshida, 2005, and references listed therein).

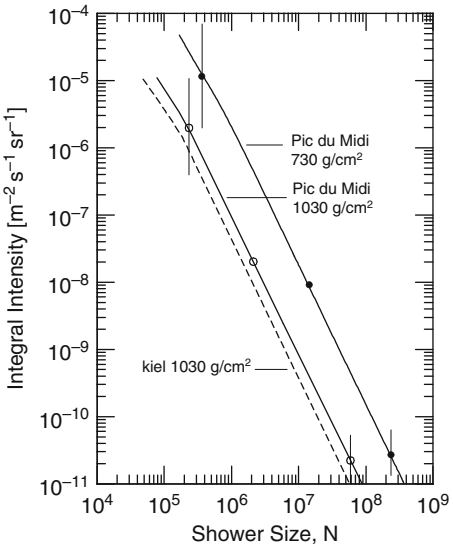

Fig. 12.3 Integral shower size spectra obtained at Pic du Midi, France (2,860 m a.s.l.) for vertical and inclined showers, corresponding to an overlaying atmospheric thickness of 730 g cm^{-2} vertical (•) and 1,030 g cm^{-2} slant depth (○), respectively, together with a spectrum for vertical showers recorded at Kiel, 1,030 g cm^{-2} (*dashed curve*) (Böhm, 1977). Systematic differences in size determination are evident

12.2.3 Shower Size Spectra, Early Epoch

Besides the compilation illustrated in Figs. 12.1, 12.2 and 12.3 we have summarized the bulk of earlier size spectra (pre mid 1980s) obtained with the different arrays, from sea level to Mount Chacaltaya (5,230 m a.s.l.) and the air plane data in Figs. 12.4–12.17. Frequently several sets of data from different sites are compiled and displayed in one graph for reasons of comparison. In some cases the compilations include different data from the same array which had been acquired at different epochs with more or less modified array layouts. Compilations of this kind reveal to some extent the degree of reliability of the measurements.

The sea level or near sea level data are summarized in Figs. 12.4, 12.5, 12.6, 12.7 and 12.8. In Fig. 12.4 we show an early compilation of measurements carried out with the array at the Institute for Nuclear Studies (I.N.S.) of the University of Tokyo (Fukui et al., 1960; Miura and Hasegawa, 1962) and with the array located at Kobe (Asakimori et al., 1979). Analogous sets of data from Moscow (Vernov et al., 1962a, b) and Verrieres (Catz et al., 1975), obtained chiefly with Geiger tube trays, are shown in Fig. 12.5.

The results of measurements carried out on very large showers with the array at Yakutsk (Kerschenholz et al., 1973; Diminstein et al., 1975; Efimov and Sokurov, 1983) showing differential and integral spectra, and the very old data from the Agassiz installation (Clark et al., 1958, 1961) showing only the differential spectrum,

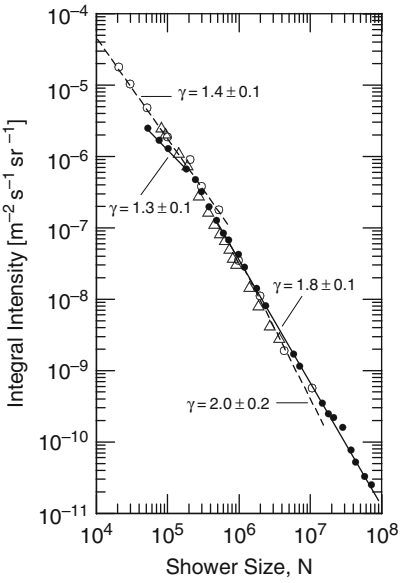

Fig. 12.4 Integral shower size spectra recorded with the arrays located at Kobe, △, (Asakimori et al., 1979) and Tokyo, ○, (Fukui et al., 1960), • (Miura and Hasegawa, 1962), at sea level. The γ give the slope of the lines that connect the different sets of points

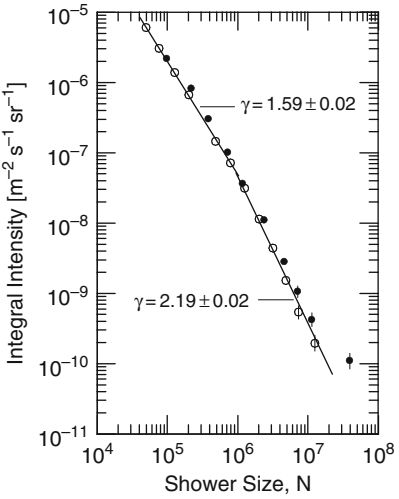

Fig. 12.5 Integral shower size spectra recorded at Verriéres, France (100 m a.s.l.) ○ (Catz et al., 1975) and Moscow (190 m a.s.l.) ● (Vernov et al., 1962a, b). The γ give the slope of the respective portions of the spectrum. The data cover the zenith angle intervals $0^\circ \leq \theta \leq 33^\circ$ and $0^\circ \leq \theta \leq 30^\circ$, respectively

are given in Figs. 12.6 and 12.7, respectively. Another set of data from Moscow (Vernov et al., 1968) and a set from Durham (Ashton and Parvaresh, 1975) and Adelaide (Buckland Park) (Gerhardy et al., 1981) are presented in Fig. 12.8. Note that there the intensity is multiplied by the shower size to the power of 1.5, to compress the display and emphasize the change of slope, known as the knee. (The most recent data from the Moscow array are given in the compilation of Fig. 12.18.)

Data from moderate altitudes, showing the results from Akeno (900 m) (Hara et al., 1979c) and the Kolar Gold Fields (KGF) (930 m) (Acharya et al., 1981) are shown in Figs. 12.9 and 12.10, respectively. It should be mentioned that for the different shower size intervals of the Akeno measurements, different trigger conditions had been used, as indicated in Fig. 12.9. For trigger A the small shower trigger was used, requiring the core to fall within the densely packed array of 8 m by 8 m (in some cases 10 m by 10 m). For triggers B and C the core had to fall within an area of 20 m by 20 m and for trigger D within 90 m by 90 m of the reference point. Additional differences in the selection criteria were imposed. For details see Hara et al. (1979a, b, c). The zenith angle dependence is also indicated in terms of spectra at different sec(θ).

The KGF size spectra, Figs. 12.10a, b, are displayed in differential and integral form. Note that the intensities of the two spectra are multiplied by the shower size to the power of 2.55 and 1.56, respectively. The differential spectrum obtained for very large showers at Volcano Ranch (1,768 m a.s.l.) is shown in Fig. 12.11 (Linsley, 1973).

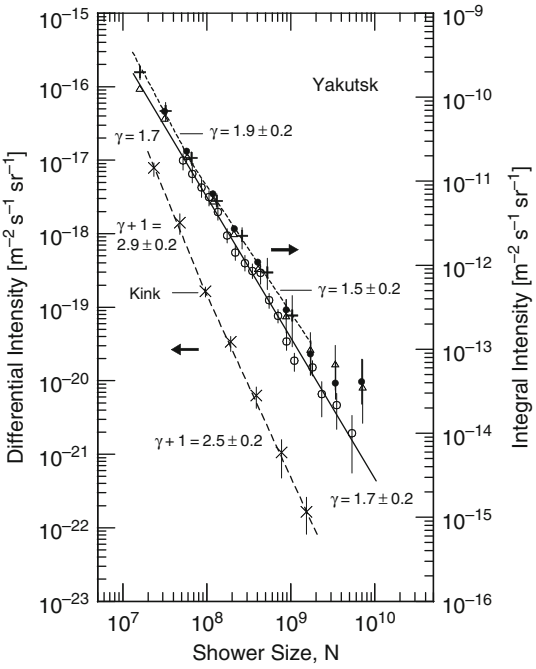

Fig. 12.6 Differential and integral shower size spectra obtained with the large array at Yakutsk (105 m a.s.l.). The graph shows data from different epochs. The symbols × and + identify the differential and integral spectra, respectively, of Egorov et al. (1971a), and ○ the integral spectrum of Diminstein et al. (1975). △ and • are spectra after Kerschenholz et al. (1973); △ applies when fluctuations are disregarded, • when accounted for. The γ values give the slope of the *straight line* fits. Note that the atmosphere at Yakutsk deviates from the standard atmosphere

At higher altitudes we have the data from Mount Norikura (altitude 2,770 m) (Miyake et al., 1979) and Pic du Midi (2,860 m) (Böhm and Steinmann, 1979), shown in Figs. 12.12 and 12.13, respectively. Note that very different array layouts had been used at Mount Norikura at different epochs. For details see Appendix A. Several measurements from Tien Shan (3,340 m) are compiled in Fig. 12.14 (Aseikin et al., 1971; Danilova et al., 1977; Machavariani et al., 1979; Stamenov, 1981, Private communication).

These data are of particular interest because the Tien Shan array had been one of the best equipped arrays for a long time (until about 1990), recording simultaneously most of the relevant observables of each detected shower, including electrons, muons ($E_\mu \geq 5$ GeV), high energy hadrons and air Cherenkov emission. For earlier Tien Shan data see Hlavac et al. (1970). Data from the first (old) Pamir site (3,860 m) are also included in Fig. 12.14 for comparison (Aseikin et al., 1971).[1]

[1] Note that at the new Pamir site (4,380 m a.s.l.) only emulsion chamber experiments are being carried out.

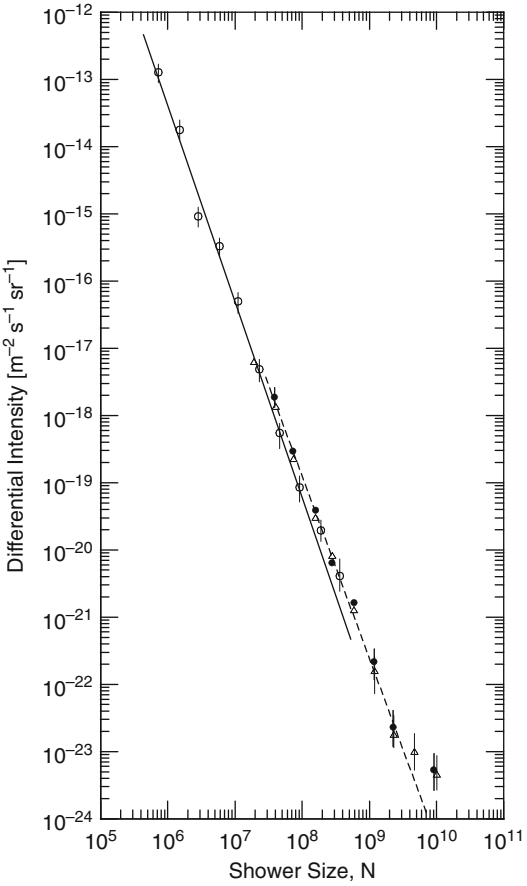

Fig. 12.7 Differential shower size spectra recorded at Agassiz, USA. (183 m a.s.l.), ○ (Clark et al., 1961) and Yakutsk, Russia (105 m a.s.l.), ●, △ (Kerschenholz et al., 1973). The *full circles* show the data with fluctuations accounted for, the triangles when disregarded. The *lines* are fits to the data

The highest ground based measurements using electronic detectors were carried out at Mount Chacaltaya (5,230 m). The installation is still in operation. The data of Bradt et al. (1965) are presented in Fig. 12.15, jointly with the earlier data from the El Alto site (4,200 m) on the foot of Mount Chacaltaya, acquired by the same authors.

The very unique air plane data taken by Antonov et al. (1973, 1974) at an altitude of 5,280 m are displayed in Fig. 12.16 together with the data from Chacaltaya shown in Fig. 12.15 (Bradt et al., 1965; La Point et al., 1968) and more recent Chacaltaya results from the work of Ohta et al. (1979). These data can be compared directly since the altitudes are essentially the same. Antonov's detectors were mounted in the wings and fuselage of a large aircraft. The separations between the most distant

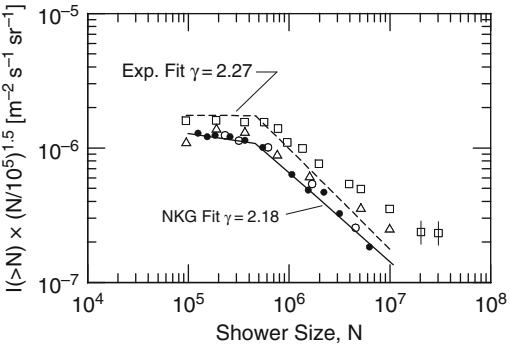

Fig. 12.8 Integral size spectra recorded at Moscow (190 m a.s.l.) △, □ (Vernov et al., 1968), Durham (60 m) ○ (Ashton and Parvaresh, 1975), and Adelaide (s.l.) • (Gerhardy et al., 1981). For the Moscow data the shower sizes were computed in two different ways, taking into account the age parameter of the showers, △, and the mean electron lateral distribution, □. The analysis includes events with zenith angles $0^\circ \leq \theta \leq 30^\circ$. The Adelaide data are corrected for vertical showers, using a median zenith angle of 13°. The data points had been fitted to a NKG-function (*solid line*) and agree well with the Durham data. They yield a spectrum that lies *lower* than the one indicated for an exponential fit (*dashed line*) (Gerhardy et al., 1981). The Moscow data of this figure are companions to the muon size spectra presented in Fig. 12.26. The ordinate, representing the intensity of events, is multiplied by the factor $(N/10^5)^{1.5}$, where N is the shower size, to compress the graph and emphasize the change in spectral slope

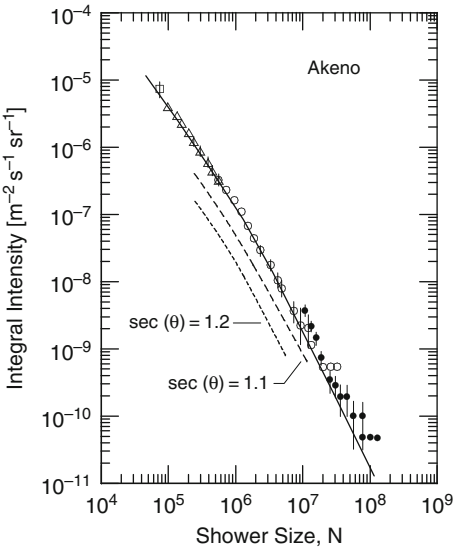

Fig. 12.9 Integral shower size spectrum obtained at Akeno (900 m a.s.l.) for vertically incident events (Hara et al., 1979c). Different trigger conditions had been used for different size intervals (□ trigger A, △ B, • C, ○ D), as outlined in the text. The two *dashed lines* show spectra of showers belonging to different zenith angle intervals, expressed in terms of sec(θ)

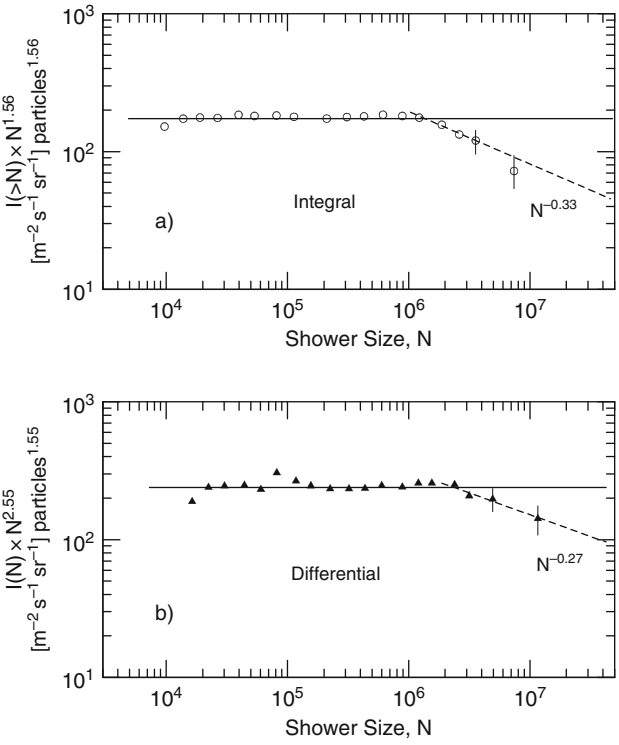

Fig. 12.10 Integral and differential shower size spectra obtained by Acharya et al. (1981) at the Kolar Gold Fields site (930 m a.s.l., 920 g cm^{-2}.). The ordinates of the two spectra representing event rates, are multiplied by the factors $N^{1.56}$ and $N^{2.55}$, respectively, where N is the shower size, showing that the two spectra can be described by a single power law up to a size of about 10^6. The three highest size points manifest a somewhat steeper slope

detectors along the longitudinal and lateral axes were 44 and 34 m, respectively (Antonov et al., 1960, 1964a, 1973, 1974).

Measurements in the upper half of the atmosphere at altitudes of 10,000 and 12,000 m were carried out by Antonov et al. (1971, 1973, 1974, 1977). These authors used the array mentioned above that was installed in an aircraft (Antonov et al., 1973, 1974) and another array, measuring 30 m by 30 m, mounted on a special frame and flown by a balloon (Antonov et al., 1977). These data are presented in Fig. 12.17.

12.2.4 Shower Size Spectra, Recent Epoch

A selection of newer data which cover the epoch from the mid 1980s to the present (2008) that are summarized here are all from rather elaborate arrays with large numbers of detectors. These arrays include besides the usual shower detectors also

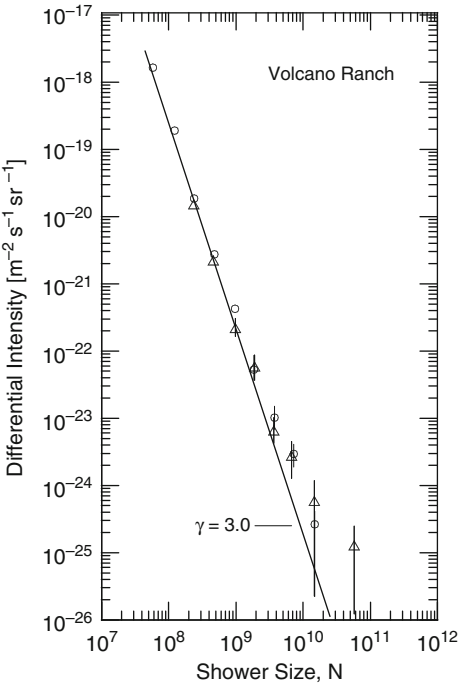

Fig. 12.11 Differential shower size spectra recorded with the Volcano Ranch array (1,768 m a.s.l.). Included are data covering a zenith angle range corresponding to an atmospheric thickness of 820 g cm^{-2} for vertical incidence and to 900 g cm^{-2} for the most inclined events. The symbols ○ refer to the originally published data (Linsley, 1963a) and the △ are the re-evaluated data (Linsley, 1973)

muon detectors, and some are equipped with hadron calorimeters, high energy muon detectors and wide-angle optical air Cherenkov detectors. Some of these arrays existed before 1984 but had been subject to major upgrades since, such as Akeno, which later on had been extended to the array called AGASA (Akeno Giant Air Shower Array) (Chiba et al., 1991, 1992).

In addition, more simple but large arrays and detectors of rather short-lived duration that were located at moderate altitudes but are no longer in operation were the interlaced arrays at Dugway, Utah (USA)(1,430–1,550 m a.s.l.), called CASA, an all-particle shower array, MIA, a muon detector array (Borione et al., 1994), and the non-imaging Cherenkov array BLANCA (Cassidy et al., 1997; Fowler et al., 2001). In addition the Dual Imaging Cherenkov Experiment, DICE, a twin Cherenkov telescope, was also located at the same site (Boothby et al., 1995, 1997; Swordy and Kieda, 2000). At times these experiments were operated jointly and together with the Fly's Eye. Note that wide-aperture atmospheric Cherenkov arrays, narrow-angle Cherenkov telescopes and fluorescence detectors such as the Fly's Eye or the HiRes detectors (Abu-Zayyad et al., 1999) do not yield directly shower size spectra, they determine primarily the optical photon flux.

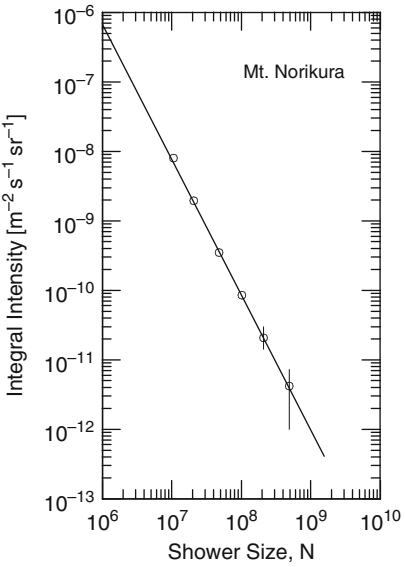

Fig. 12.12 Integral shower size spectrum at Mt. Norikura, 750 g cm^{-2} (2,770 m a.s.l.), for large showers (Miyake et al., 1979). The *line* connecting the data points corresponds to an exponent of $\gamma = 1.92$ for a power law approximation, $I(E) \propto E^{-\gamma}$

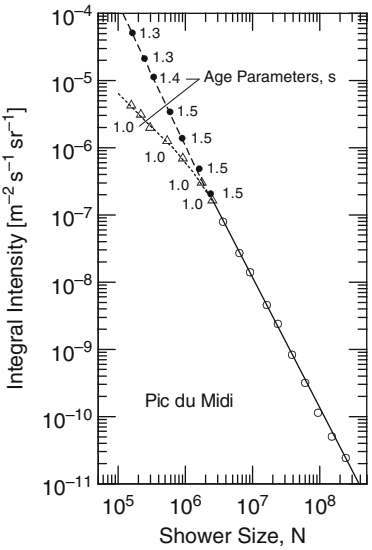

Fig. 12.13 Integral shower size spectrum obtained at Pic du Midi, 730 g cm^{-2} (2,860 m a.s.l.) (Böhm and Steinmann, 1979). The large fluctuations in longitudinal shower age, s, of small showers pose a problem in the determination of the slope of the spectrum of small showers, as is illustrated in the figure. Systematic errors may easily occur when using the age parameter of the lateral distribution function for deriving the detection efficiency. The latter changes if the core position error is taken into account

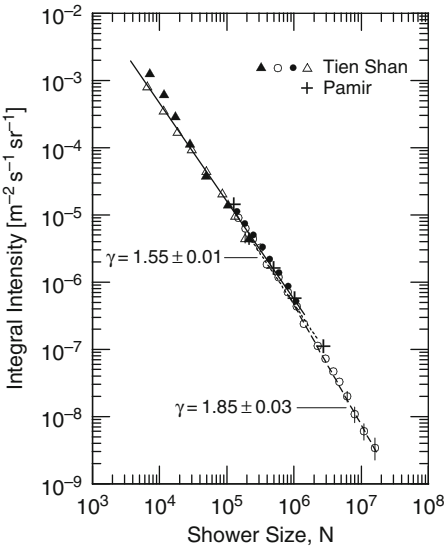

Fig. 12.14 Integral shower size spectra recorded by different authors at Tien Shan (3,340 m a.s.l., 685 g cm^{-2}) (△, Machavariani et al., 1979; ▲, Aseikin et al., 1971; •, Danilova et al., 1977; ○, Stamenov, 1981, Private communication). The γ-values give the slope and refer to the medium and large size regions of the spectrum. In addition, the data from the old Pamir experiment, +, located at 3,860 m a.s.l. (625 g cm^{-2}) are also shown (Aseikin et al., 1971)

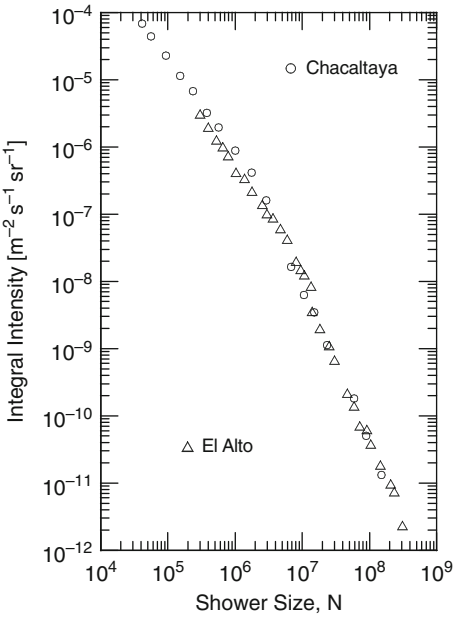

Fig. 12.15 Integral shower size spectra recorded at El Alto, 630 g cm^{-2} (4,200 m a.s.l.) for zenith angles $\leq 25^\circ$ ($1.0 \leq \sec(\theta) \leq 1.1$), and at Mt. Chacaltaya, 530 g cm^{-2} (5,230 m a.s.l.) at zenith angles $33^\circ \leq \theta \leq 40^\circ$ ($1.2 \leq \sec(\theta) \leq 1.3$) (Bradt et al., 1965)

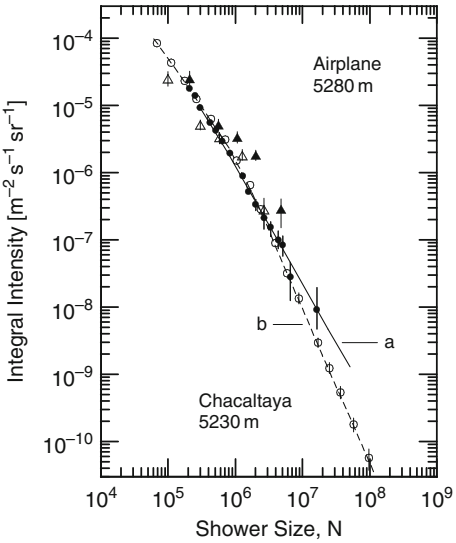

Fig. 12.16 Comparison of two integral shower size spectra obtained at Mt. Chacaltaya, 5,230 m a.s.l. ($\theta \leq 25°$) (○ Bradt et al., 1965; ● Ohta et al., 1979) and with an airplane at an altitude of 5,280 m ($\theta \leq 30°$) (▲ , △, Antonov et al., 1974) . The full triangles represent the data actually measured by Antonov et al. (1974), the open triangles are after normalization to the Chacaltaya data of Escobar et al. (1963) and Bradt et al. (1965) using the old pre-GPS altitude of 5,200 m of Chacaltaya

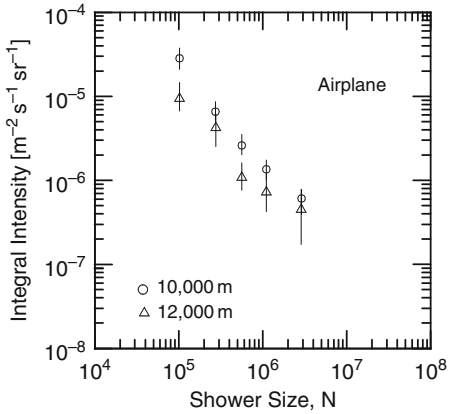

Fig. 12.17 Integral shower size spectra of Antonov et al. (1974) recorded in flight on board an aircraft at altitudes of 10,000 and 12,000 m, respectively

Other arrays, such as KASCADE at Karlsruhe (Germany) located near sea level (Antoni et al., 2003b) and the high altitude array at Yangbajing (Tibet) (Amenomori et al., 1990) are new designs and began operation in the late 1980s and early 1990s (many more arrays of past and present are listed in Table A.1 of Appendix A). More recently, the Auger experiment in Argentina which is a hybrid installation that employs an array of widely spaced Haverah Park type deep water Cherenkov and Fly's Eye type air fluorescence detectors, recently commissioned, will produce valuable data in the years to come (Blümer, 2003; Dawson, 2007), and likewise the Telescope Array in Utah (USA) (Fukushima et al., 2007; Tsunesada et al., 2007).

The size spectrum obtained with the KASCADE array (110 m a.s.l.), which was at that time the most extensively instrumented and best equipped array, is plotted in Fig. 12.18 together with spectra of relatively recent date from five other experiments, including MSU (Moscow, 190 m), EAS-TOP (Gran Sasso, Italy, 2,005 m), MAKET-ANI (Mt. Aragatz, Armenia, 3,250 m), Tien Shan (Kazakhstan, 3,340 m) and Mt. Chacaltaya (Bolivia, 5,230 m), to present a general overview of the current

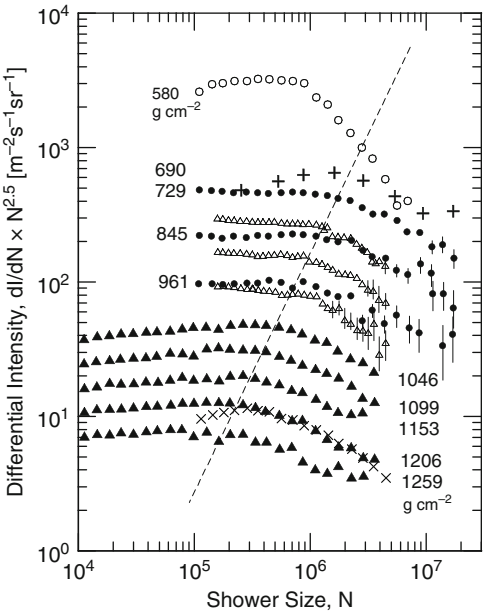

Fig. 12.18 Electron shower size (N_e) spectra of the KASCADE experiment at Karlsruhe (Germany) located at an altitude of 110 m a.s.l. (▲) recorded at different zenith angles, corresponding to different atmospheric column densities, as indicated (Glasstetter et al., 1997, 1999). The charged particle size (N) spectra of five other experiments, located at different altitudes, some of which had been recorded at different zenith angles, are also shown for comparison. They comprise Chacaltaya (○) (Honda et al., 2001), Tien Shan (+) (Nesterova et al., 1995), MAKET-ANI in Armenia (●) (Chilingarian et al., 1999), EAS-TOP (△) (Aglietta et al., 1999), and Moscow (×) (Fomin et al., 1991). The *dashed line* indicates the approximate location of the *knee* in the spectrum (disregarding the Chacaltaya data). Note that the ordinate is multiplied by $N^{2.5}$ (after Haungs et al., 2003)

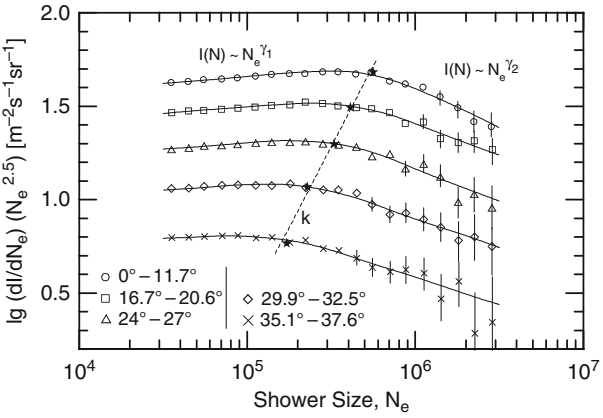

Fig. 12.19 Differential electron shower size spectra measured by the KASCADE experiment. The knee position is indicated by ⋆. Its shift with increasing zenith angle is evident and indicated by the *dashed line*, k (Antoni et al., 2003a)

situation (Haungs et al., 2003). Additional details are given in the figure caption. The KASCADE array had been extended later on to KASCADE-Grande with equipment from the dismantled EAS-TOP array, to be able to analyze higher energy events (Bertaina et al., 2001; Navarra et al., 2004).

In Fig. 12.19 we show the differential shower size spectra obtained with the KASCADE array, plotted in the compilation of Fig. 12.18, separately and with error bars (Antoni et al., 2003a). These distributions had been used to determine the shower rate attenuation length, $\Lambda_{\rm att}$, and the shower particle absorption length, $\lambda_{\rm abs}$, discussed in Chap. 6. The knee location is marked with the dashed line, labeled *k*. If one assumes that the knee is of astrophysical origin and therefore at a fixed rigidity, it can be used as an energy mark as had been done in the work of Antoni et al. (2003a) (see Chap. 6). The plot shown in Fig. 12.20 displays the shower size at the knee location as a function of $\sec\theta$, θ being the zenith angle, as obtained from Fig. 12.19.

An interesting set of data is displayed in Fig. 12.21, which shows differential size spectra for different zenith angle intervals recorded at Akeno (900 m a.s.l.) by Nagano et al. (1984). This kind of data, frequently shown in integral form, are used to construct equal intensity distributions, discussed in Sect. 6.7. Excellent statistics are required for this purpose.

At higher altitude was the EAS-TOP array, briefly mentioned before (now shut down), that was located at Gran Sasso (2,005 m) (Aglietta et al., 1986). This well equipped experiment included besides a shower particle detector array and wide aperture air Cherenkov detectors a large hadron calorimeter combined with a muon detector (two separate units with a total area of 144 m^2). Operated in combination with the huge muon detector of the MACRO experiment ($\simeq$900 m^2, also shut down), that was installed deep underneath the EAS-TOP array in the Gran Sasso tunnel with a minimum overburden of 3,100 hg cm^{-2}, the two installations yielded a unique

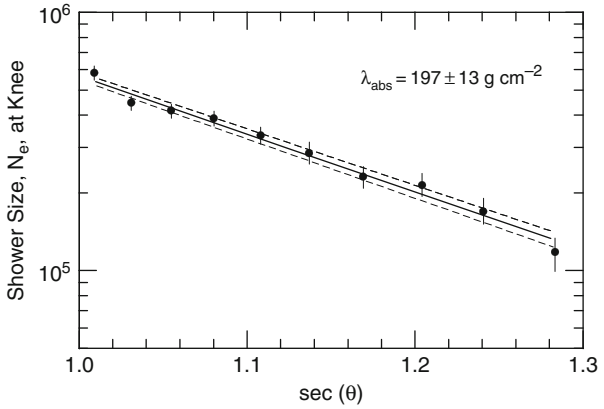

Fig. 12.20 Knee position in the differential electron shower size spectra for different angular bins measured by KASCADE. The *solid line* shows an exponential fit, the *dashed lines* the error region of the fit (Antoni et al., 2003a)

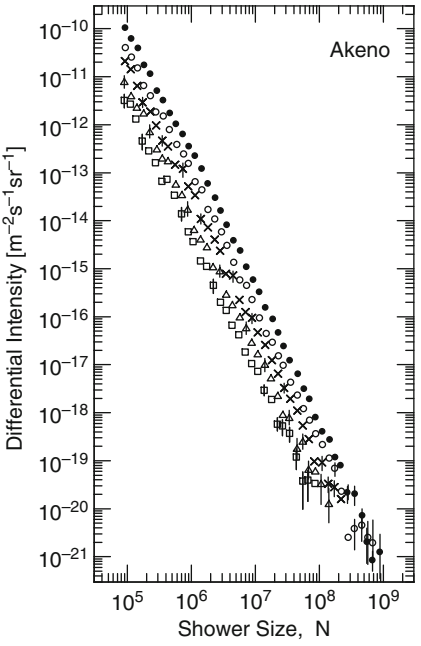

Fig. 12.21 Differential electron size spectra at five different zenith angles, θ, expressed in sec(θ), recorded at Akeno (900 m a.s.l.) (Nagano et al., 1984). •, sec(θ) = 1.0; ○, sec(θ) = 1.1; ×. sec(θ) = 1.2; △, sec(θ) = 1.3; □, sec(θ) = 1.4 (see also Nagano et al., 1992)

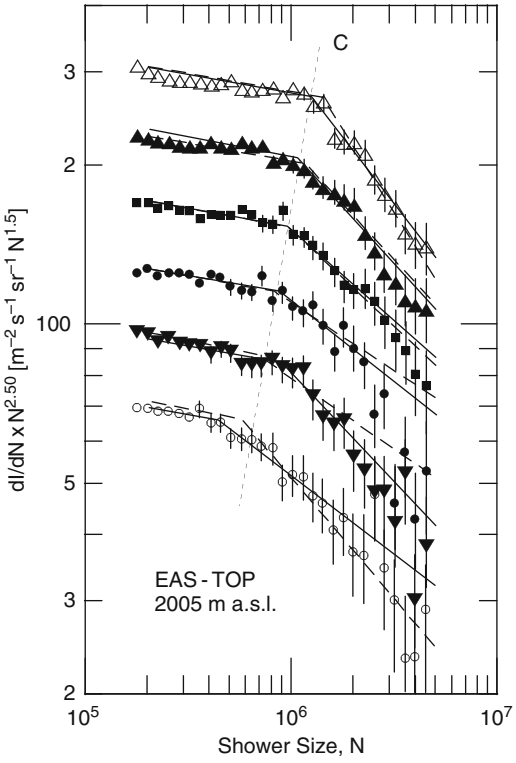

Fig. 12.22 Differential shower size spectra at six different zenith angles, θ, expressed in terms of $\sec(\theta)$, listed below, corresponding to six different atmospheric depths recorded with the EAS-TOP installation (2,005 m a.s.l.) (Aglietta et al., 1999; Navarra, 2006). *Line C* indicates the approximate location of the spectral knee. △, $1.00 < \sec(\theta) < 1.05$; ▲, $1.05 < \sec(\theta) < 1.10$; ■, $1.10 < \sec(\theta) < 1.15$; ●, $1.15 < \sec(\theta) < 1.20$; ▼, $1.20 < \sec(\theta) = 1.25$; ○, $1.25 < \sec(\theta) < 1.30$

combination of surface data of all kinds and correlated ultra-high energy muon[2] data from MACRO of individual showers.

An additional set of differential shower size spectra, complementary to those shown in Fig. 12.18 obtained with the EAS-TOP array for different zenith angles intervals, specified in terms of $\sec(\theta)$, is plotted in Fig. 12.22 (Aglietta et al., 1999; Navarra, 1998, 2006). The location of the spectral knee and its dependence on zenith angle is evident.

A very compact and densely instrumented array of rather recent date is the GRAPES-3 installation located at Ootacamund (2,200 m a.s.l., 800 g cm^{-2}) in India (Gupta et al., 2005). This array is also equipped with one of the largest muon tracking detectors (560 m^2) (Hayashi et al., 2005). The layout of the array is shown in Fig. A.19 of Appendix A.1. The differential size spectrum measured with this array

[2] The threshold energy of muons to reach MACRO was $E_\mu \geq 1.3$ TeV.

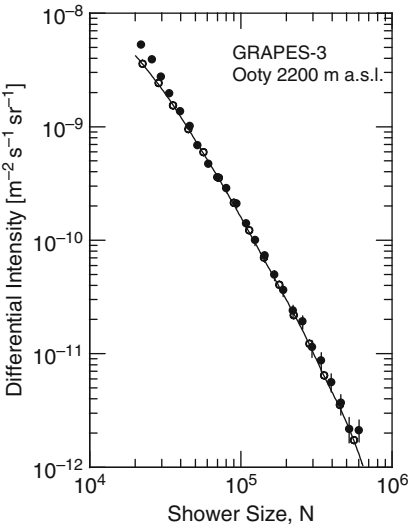

Fig. 12.23 Differential shower size spectrum for showers having a zenith angle $\theta \leq 25^{\circ}$ measured with the GRAPES-3 array at Ootacamund (2,200 m a.s.l.) in India (•). Shown, too, is a simulated spectrum (○) and a fit to the experimental data (after Hayashi et al., 1999)

is plotted in Fig. 12.23 (Hayashi et al., 1999). Finally, in Fig. 12.24 we show a rather recent series of integral shower size spectra obtained for ten different zenith angle intervals at Mt. Chacaltaya by Ogio et al. (2004). The array layout of this rather new experiment is shown in Fig. A.12 of Appendix A.

The original HEGRA array on the Canary Island of La Palma, located at an altitude of 2,200 m a.s.l. (800 g cm^{-2}) was initially installed by the University of Kiel to investigate extensive air showers and in particular to verify the observations made at Kiel on the object called Cygnus X-3. These observations suggested the existence of ultrahigh energy gamma ray initiated showers with a high muon content. The principal aim of the experiment was to detect high energy gamma ray showers under favorable conditions, in an attempt to locate possible high energy gamma ray sources such as Cygnus X-3 appeared to be (Samorski and Stamm, 1983a, b). In the course of time the installation was modified several times and operated as an instrument for gamma ray astronomy, adding several generations of atmospheric Cherenkov detectors and later on Cherenkov imaging telescopes that culminated at present with the MAGIC instrument (Mirzoyan et al., 2005). However, during its early stages of operation the HEGRA experiment has made significant contributions to air shower research, adding mainly to our knowledge of the primary energy spectrum and primary composition (Arqueros et al., 2000) (see Chap. 11).

The relatively new high altitude array at Yangbajing in Tibet, mentioned before and located at 4,370 m a.s.l. (606 g cm^{-2}) (Amenomori et al., 1990, 1997, 2005) is primarily dedicated to gamma ray work. The second and more recent experiment at Yangbajing is ARGO, a giant (100 m by 100 m) resistive plate detector carpet of

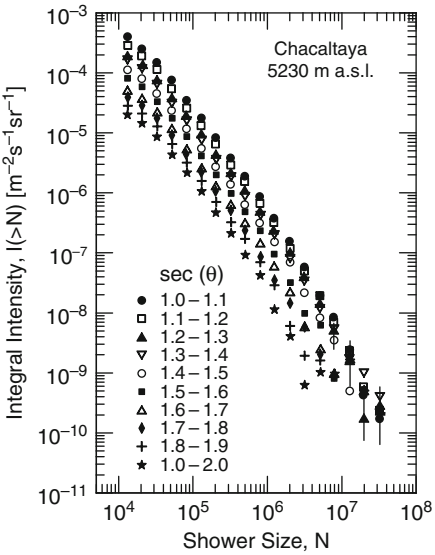

Fig. 12.24 Integral shower size spectra for different zenith angles in terms of sec(θ) covering the range $0^\circ \leq \theta \leq 60^\circ$ recorded at Mt. Chacaltaya in Bolivia (5,230 m a.s.l.) (Ogio et al., 2004)

high spatial resolution (Bacci et al., 2000; D'Ettorre-Piazzoli, 1999; Cao, 2005). ARGO has recently been taken into operation. This experiments, too, is mainly aimed at gamma ray astronomy.

12.2.5 Mathematical Expressions and Fits

Below we give some mathematical expressions that represent fits to experimental charged particle size spectra. Most authors use simple power laws.

For *vertical* showers at sea level Greisen (1960) proposed for the *integral size spectrum* the expression

$$I_v(>N) \;=\; 5.5 \cdot 10^{-8} (10^6/N)^{[1.52+0.055\,\lg(N/10^6)]} \;\; [\mathrm{m}^{-2}\,\mathrm{s}^{-1}\,\mathrm{sr}^{-1}]. \qquad (12.3)$$

For vertical showers at an elevation of 3,260 m Greisen obtained a somewhat modified fit[3]

$$I_v(>N, 3, 260\mathrm{m}) \;=\; 6 \cdot 10^{-7} (10^6/N)^{[1.48+0.065\,\lg(N/10^6)]} \;\; [\mathrm{m}^{-2}\,\mathrm{s}^{-1}\,\mathrm{sr}^{-1}]. \quad (12.4)$$

Aseikin et al. (1971) found the following function, given below, to describe their integral size spectrum recorded at Tien Shan (3,340 m a.s.l., 690 g cm^{-2}) quitewell.

[3] At that time the existence of the knee in the spectrum, discovered by Kulikov and Khristiansen (1959), was widely unknown.

However, different exponents γ were needed for different size ranges to describe the spectral range which they have explored, one valid below the knee, the other above it.

$$I(\geq N) \;=\; (2.7 \pm 0.3) \cdot 10^{-3} \left(\frac{N}{7.5 \cdot 10^5} \right)^{-\gamma_e} \quad [\mathrm{m^{-2}\,h^{-1}\,sr^{-1}}], \tag{12.5}$$

where

$$\gamma_e \;=\; (1.54 \pm 0.08) \quad \text{for } 1.8 \cdot 10^5 < N < 7.5 \cdot 10^5$$

and

$$\gamma_e \;=\; (2.11 \pm 0.30) \quad \text{for } 7.5 \cdot 10^5 < N < 3.0 \cdot 10^6.$$

The corresponding muon size data are given in Sect. 12.3 (see Fig. 12.27).

Rada et al. (1977) found for the narrow size region ($7{\cdot}10^5 \leq \mathrm{N} \leq 3{\cdot}10^6$) which they explored at Durham (GB) (60 m a.s.l.) the expression

$$I(> N) \;=\; (2.62 \pm 0.55) \cdot 10^{-8} \left(\frac{N}{10^6} \right)^{-(1.87 \pm 0.22)} \quad [\mathrm{m^{-2}\,s^{-1}\,sr^{-1}}] \tag{12.6}$$

to fit their data well. Hara et al. (1979c), using Akeno data, proposed the following relationship for the size range between 10^6 and a few times 10^7.

$$I(\geq N) \;=\; (1.4 \pm 0.1) \cdot 10^{-7} \left(\frac{N}{10^6} \right)^{-(1.90 \pm 0.13)} \quad [\mathrm{m^{-2}\,s^{-1}\,sr^{-1}}]. \tag{12.7}$$

Miyake et al. (1979) could describe their vertical shower size spectrum at Mt. Norikura with the following expression,

$$I_v(> N) \;=\; (0.83 \pm 0.03) \left(\frac{N}{10^7} \right)^{-(1.92 \pm 0.03)} \cdot 10^{-8} \;\; [\mathrm{m^{-2}\,s^{-1}\,sr^{-1}}]. \tag{12.8}$$

A somewhat different expression was used by Makhmudov and Sharibdzhanov (1977) for the *differential size spectrum*, which includes the altitude dependence. It has the form

$$I(N)\mathrm{d}N \;=\; A \cdot \exp\left(-\frac{\gamma X}{\Lambda_{\mathrm{att}}} (\sec(\theta) - 1) \right) N^{-(\gamma+1)} \cdot \mathrm{d}N \tag{12.9}$$

where X is the atmospheric depth of the observation level, Λ_{att} the relative rate attenuation length of showers of size N, θ is the zenith angle of the shower axis and dN is the size interval. The constant has the value $A = 1.7 \cdot 10^{-2.5}\,\mathrm{cm^{-2}\,s^{-1}\,sr^{-1}}$ at $N \leq 3 \cdot 10^5$. The spectral index which these authors have used is $\gamma = 1.5$ for $N \leq 3 \cdot 10^5$, $\gamma = 2.0$ for $3 \cdot 10^5 \leq N \leq 10^7$ and $\gamma = 1.6$ for $N > 10^7$.

A simple theoretical relation for the rate of vertical showers of size $\geq N$ at depth X, $I(\geq N, X)$, can be derived from the primary energy spectrum if one makes the following assumptions (Ashton et al., 1975):

(a) Assume that the integral primary energy spectrum has the form

$$I(\geq E_0) = AE_0^{-\gamma_\circ} \tag{12.10}$$

where A is a constant scale factor, E_0 the primary energy and $\gamma_\circ$ the slope of the primary spectrum.

(b) Assume that the primary energy-size relation at depth X in the atmosphere can be expressed as

$$N(E_0, X) = BE_0^{\alpha_m} e^{-X/\lambda_{\text{abs}}} \tag{12.11}$$

where B and α_m are constants. The subscript $_m$ refers to the primary mass since the spectral slopes are different for different masses, and λ_{abs} is the shower particle absorption length. Assuming the same slope for all primaries and replacing α_m by α ($\alpha \simeq 1$), it then follows that

$$I(\geq N, X) = AB^{\gamma_\circ/\alpha} N^{-\gamma_\circ/\alpha} \exp\left(-\frac{(X/\lambda_{\text{abs}})}{(\gamma_\circ/\alpha)}\right) = CN^{-\gamma} e^{-(X/\gamma_\circ)}. \tag{12.12}$$

Here $\gamma = \gamma_\circ/\alpha$, $\gamma_\circ = \lambda_{\text{abs}}/\gamma$, and C is a constant.

12.3 Muon Size or Number Spectra

12.3.1 Introduction

In analogy to the normal shower size, the muon size of an air shower is defined as the total number of muons in a shower at a particular level in the atmosphere. In a given shower muons extend to larger distances from the shower axis than electrons but exhibit lower densities. Thus, muon size measurements require in general significantly *larger* detectors than are required for general charged particle (electron) size measurements. But the detectors can be more widely spaced and should be distributed over a larger area.

Muon size measurements in place of common shower size measurements as a shower selection criterion or to estimate the primary energy are applicable only to larger showers. However, muon size and truncated muon size measurements have the advantage that they are less subject to large fluctuations, particularly when using the large Haverah Park type deep water Cherenkov detectors (Hollows et al., 1969 and references listed therein; Ave et al., 2003), if one excludes measurements in the immediate vicinity of the shower core. In this context the density at a fixed

core distance can be used as a good primary energy estimator, a topic addressed in Sect. 12.5 and 10.2.

The problems one faces when attempting to determine the muon size spectrum are similar to those encountered when determining the charged particle (or electron) size spectrum. The foremost problem for the experimentalist is the low muons density, particularly at moderate and large distances from the shower core, which requires very large detectors, on the order of ten and more square meters of area. The other problem of similar importance is the accurate knowledge of the form of the lateral distribution or structure function (LDF) of the muons. Without this information it is difficult to carry out a reliable integration and muon size determination.

12.3.2 Muon Size Spectra, Early Epoch

Among the first to explore the muon size of showers and to correlate muon size with common shower size were Fukui et al. (1960) and Miura and Hasegawa (1962). These authors show evolution or development curves of the muon-electron ratio in showers as they grow, reach their maximum and decline. They suggest that the muon number may not change dramatically in a shower beyond the shower maximum, a fact later on confirmed by detailed shower simulations (Grieder, 1977).

In addition Miura and Hasegawa (1962) found that the muon size (or number) spectrum exhibits a change in slope from -1.4 ± 0.2 to -1.9 ± 0.2 within a decade of the energy corresponding to a size of 10^5. Hence, the muon size spectrum manifests a similar feature, i.e., a *knee*, like the all-particle (electron) size spectrum. Because their muon sampling measurements did not extend beyond 200 m from the shower axis and the muon lateral distribution function was not adequately well known at the time to justify integration of the muon density over the entire shower, these authors obtained only a qualitative muon size spectrum, not reproduced here.

Muon size spectra of rather large showers had been determined by different authors during the early stages of air shower investigations. In Fig. 12.25 we show the integral muon size spectrum obtained by the Sydney group (Bell, 1976) with the Sydney University Giant Air shower Recorder, SUGAR (Brownlee et al., 1968), outlined in Appendix A, Fig. A.29. The muon threshold energy was $\simeq 0.75 \cdot \sec(\theta)$ GeV. The procedure to calculate the muon size spectrum from the experimental data is described by Bell et al. (1974).

This spectrum, which reaches toward the upper end of the explored primary cosmic ray energy spectrum at that time, is the result of a re-assessment of earlier data obtained with this array and analyzed previously (Brownlee et al., 1970; Bell, 1974) that had been troubled by photomultiplier after-pulsing. The authors claim to have overcome this problem and properly accounted for it in their paper (Bell, 1976). The lateral distribution function which these authors have used to carry out the integration is given by Eq. (12.14) (Sect. 12.3.4). They have also derived a primary

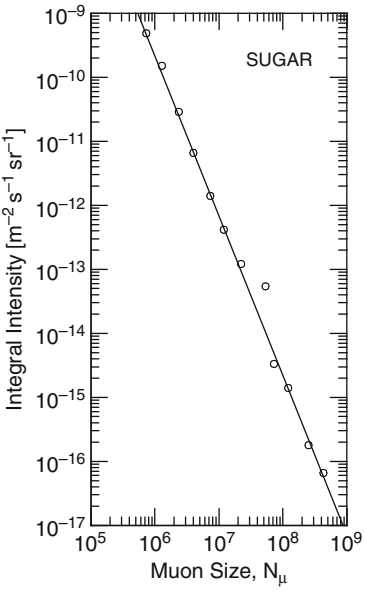

Fig. 12.25 Integral muon size spectrum near sea level obtained with the SUGAR (Sydney University Giant Air shower Recorder) array for muons of energy $\geq$0.75 GeV$\cdot$ sec(θ) and a zenith angle range of $0^\circ \leq \theta \leq 27^\circ$ ($\circ$). It is the result of a re-analysis by Bell (1976). The early interpretation of their data is shown in form of a differential spectrum (Bell et al., 1971) in Fig. 12.28

energy spectrum from the data shown in Fig. 12.25 which is presented in Chap. 11. Another re-evaluation of the SUGAR data (Horton et al., 1983) reduced the muon size spectrum presented here by another 20%.

In Fig. 12.26a we show an older muon size spectrum obtained by Vernov et al. (1968) with the installation at Moscow. Note that the ordinate is multiplied by the muon size to the power of 1.9 that yields a roughly flat spectrum below the change of slope in this representation. The spectrum shown in Fig. 12.26b is from the work of Ivanov et al. (1974) and Khristiansen (1975) for muons of energy $\geq$10 GeV, obtained at the same site.

Another set of data recorded at Tien Shan (Danilova et al., 1977; Stamenov, 1981, Private communication) at an altitude of 3,340 m (690 g cm^{-2}) is illustrated in Fig. 12.27. There, too, the rather sudden change in slope is indicated. We have added to the same figure the high altitude muon size spectrum measured at Chacaltaya, 5,230 m (530 g cm^{-2}) for muons of energy $\geq$600 MeV (Aguirre et al., 1977, 1979). The atmospheric depth of 644 g cm^{-2} that was used for this work corresponds to a zenith angle of approximately 34° which is representative for the bulk of the showers used in this analysis.

The differential muon size spectrum obtained by Edge et al. (1973a, b) at Haverah Park is shown in Fig. 12.28 together with the earlier mentioned spectrum of Bell et al. (1971), also in differential form, which had been subject to re-analysis by Bell

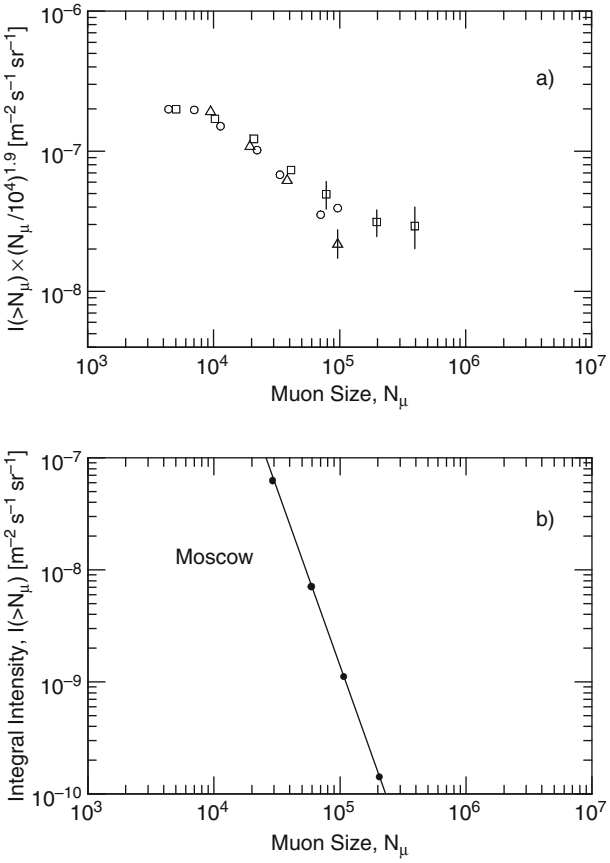

Fig. 12.26 (**a**) Integral muon size spectra obtained by the Moscow group (Vernov et al., 1968) for muons of energy ≥10 GeV. The different sets of data apply to: △, size determination taking into account the age parameter of individual showers; □, size determination taking into account the mean electron lateral distribution, and ○, derivation of the muon number from the electron size spectrum. Note that the ordinate is multiplied by the factor $(N_\mu/10^4)^{1.9}$. This figure is the companion to the electron size spectra shown in Fig. 12.8. (**b**) Integral muon size spectrum obtained by Ivanov et al. (1974) and Khristiansen (1975) for muons of energy ≥10 GeV recorded at Moscow (see also Ivanov et al., 1979). This is the companion figure to Fig. 12.8

et al. (1976) (see Fig. 12.25). The shower parameter $\rho(600)$, in units of *vertical equivalent muons per square meter* (veμ m^{-2}) is discussed in Sect. 12.5.3.

12.3.3 Muon Size Spectra, Recent Epoch

The spectrum constructed by Nagano et al. (1984) from measurements at Akeno is shown in Fig. 12.29. Also indicated in this figure is the final spectrum of the SUGAR array, mentioned above, for comparison (Horton et al., 1983). Very

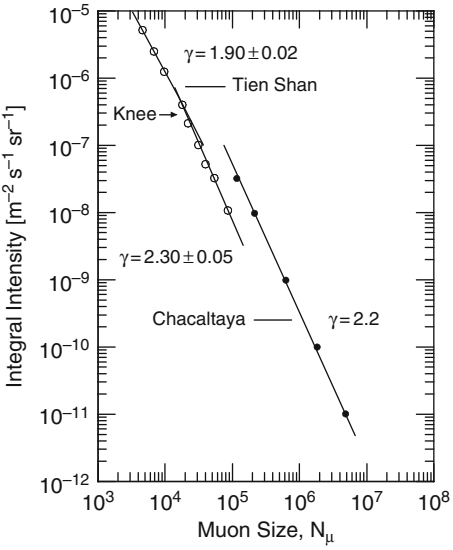

Fig. 12.27 Integral muon size spectrum of muons of energy $\geq$5 GeV at Tien Shan, 690 g cm^{-2} (3,340 m a.s.l.), ○ (Danilova et al., 1977; Stamenov, 1981, Private communication). This spectrum is the companion to the electron size spectrum recorded at Tien Shan, which is presented in Fig. 12.14. Note the knee in the Tien Shan muon spectrum. Also shown is the integral muon size spectrum in inclined showers of size $10^7 \leq N \leq 10^9$ recorded at Mt. Chacaltaya (5,230 m a.s.l.) under 644 g cm^{-2} ($\sec\theta = 1.17$) and a muon threshold energy of 600 MeV$\cdot\sec(\theta)$, • (Aguirre et al., 1977, 1979). The corresponding muon lateral density distributions are shown in Fig. 14.29

recently the KASCADE group has determined the muon size spectrum with both, the KASCADE and KASCADE-Grande arrays for the two zenith angle intervals $0^\circ \leq \theta \leq 18^\circ$ and $18^\circ < \theta \leq 25^\circ$, and muons of energy $\geq$ 230 MeV. It is plotted in Fig. 12.30 in differential form (van Buren et al., 2005).

In Fig. 12.31 we show the differential muon size spectrum measured with the EAS-TOP array at Gran Sasso (2,005 m a.s.l.) for muons of energy $\geq$ 1 GeV (Navarra, 1998). Since the two data sets are displayed differently the author has re-plotted the two spectra in the more conventional simple double-logarithmic form, shown in Fig. 12.32, to simplify comparison between these two data sets and with the results of other experiments.

12.3.4 Mathematical Expressions and Fits

Bell (1976) found that for the *differential muon size spectrum* the following expression fits the data obtained with the SUGAR array over the zenith angle range $0^\circ \leq \theta \leq 75^\circ$ quite well.

$$I(N_\mu, \theta)\mathrm{d}N_\mu \;=\; k_{N_\mu}(\theta) N_\mu^{-\gamma'_{N_\mu}(\theta)} \mathrm{d}N_\mu \;\; [\mathrm{m}^{-2}\,\mathrm{s}^{-1}\,\mathrm{sr}^{-1}], \tag{12.13}$$

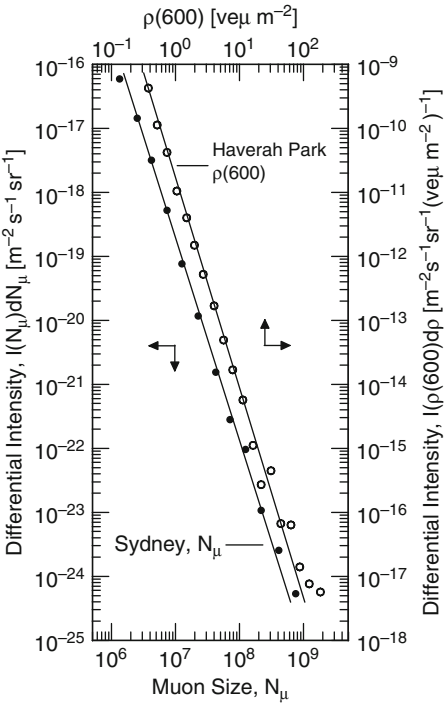

Fig. 12.28 Comparison of the early differential muon size spectrum obtained with the Sydney SUGAR array, • (Bell et al., 1971) with the spectrum derived from the Haverah Park ground parameter $\rho(600)$, ○ (Edge et al., 1973a, b). The results of a re-analysis of the Sydney data (Bell, 1976) is presented in integral form in Fig. 12.25. A summary of $\rho(600)$ and equivalent data is given in Sect. 12.5

where N_μ is the number of muons and $k_{N_\mu}(\theta)$ and γ'_{N_μ} are constants for fixed zenith angle ranges, as specified in Table 12.2. The normalizing constant $k_{N_\mu}(\theta)$ refers to a muon size of 10^7. Best fit slopes and errors based on a χ^2 method are also given by Bell (1976).

The lateral muon distribution function used by the Sydney group was of the form (Bell et al., 1971)

$$\rho(r) \;=\; K \cdot N_\mu \cdot r^{-0.75} \left(1 \,+\, \frac{r}{320}\right)^{-[1.50\,+\,1.86\cos(\theta)]} \quad [\mathrm{m}^{-2}] \qquad (12.14)$$

where K is a normalization constant.

From the measurements carried out by the Yakutsk group, Diminstein et al. (1975) obtained the following relationship for the *integral muon size spectrum* (not shown here), that is applicable for a shower (charged particle) size range $5{\cdot}10^7 \le N_e \le 10^9$ and muons of energy ≥ 0.7 GeV.

$$I(>N_\mu) \;=\; 4.94 \cdot 10^{-11} \cdot (N_\mu/10^6)^{-1.85} \;\; [\mathrm{m}^{-2}\,\mathrm{s}^{-1}\,\mathrm{sr}^{-1}] \qquad (12.15)$$

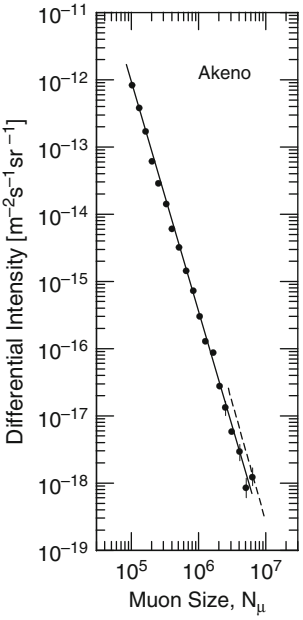

Fig. 12.29 Differential muon size spectrum recorded at Akeno within a zenith angle interval corresponding to $1.0 \leq \sec(\theta) \leq 1.1$, • (Nagano et al., 1984). The latest re-analyzed version of the SUGAR array spectrum is also indicated by the *dashed line*. (Horton et al., 1983)

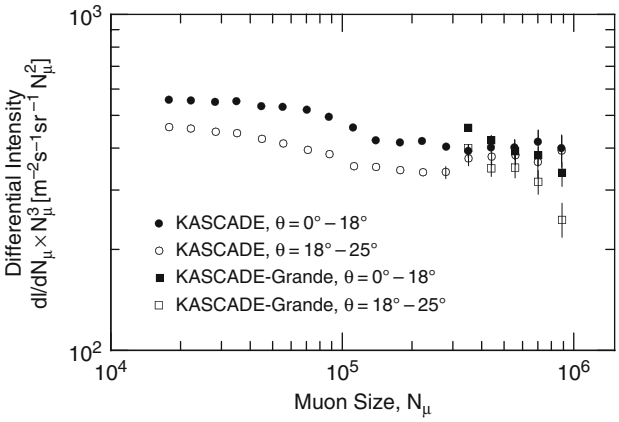

Fig. 12.30 Differential muon size spectra for $E_\mu \geq 230$ MeV recorded with the KASCADE and KASCADE-Grande arrays at Karlsruhe (110 m a.s.l.) for the two zenith angle intervals as listed in the plot (van Buren et al., 2005). Note that the intensity is multiplied by the muon size to the third power, N_μ^3

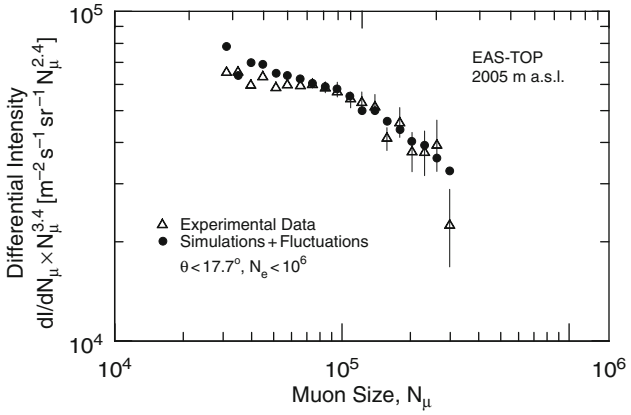

Fig. 12.31 Differential muon size spectra for $E_\mu \geq 1$ GeV recorded with the EAS-TOP array at Gran Sasso (2,005 m a.s.l.) for the zenith angle interval $0^\circ \leq \theta \leq 17.7^\circ$ and showers of size $\leq 10^6$ (Navarra, 1998). Note that the intensity is multiplied by the muon size to the power of 3.4, $N_\mu^{3.4}$

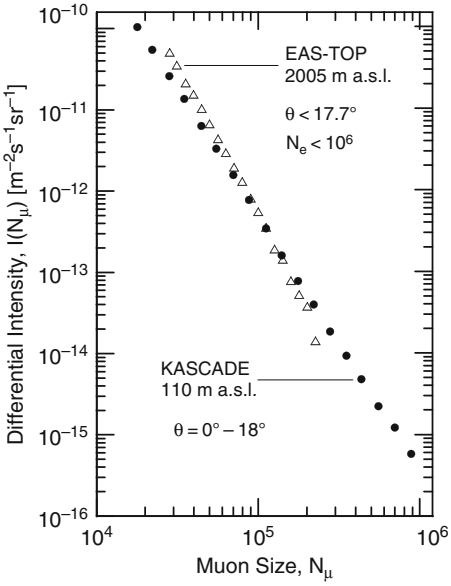

Fig. 12.32 The data points • of Fig. 12.30 (van Buren et al., 2005) and △ of Fig. 12.31 (Navarra et al., 1998) are re-plotted by the author in normal double-logarithmic mode, for comparison among themselves and with the results of other experiments

Table 12.2 Spectral constants of differential muon size spectrum (Bell, 1976)

Zenith angle range	$\gamma'_{N_\mu}(\theta)$	$\lg\left(k_{N_\mu}(\theta)\right)$
0°–27°	3.53 ± 0.07	-19.25 ± 0.08
27°–36°	3.55 ± 0.08	-19.29 ± 0.08
36°–45°	3.47 ± 0.08	-19.56 ± 0.06
45°–60°	3.50 ± 0.06	-19.91 ± 0.06
60°–75°	3.3 ± 0.3	-20.33 ± 0.22

A more recent expression given by the same group (Diminstein et al., 1979) which also applies to a muon threshold of 0.7 GeV and a muon size range $2 \cdot 10^6 \leq N_\mu \leq 2 \cdot 10^7$ is

$$I(> N_\mu) \;=\; (4.0 \pm 1.0) \cdot 10^{-13} (N_\mu/10^7)^{-2.2 \pm 0.3} \;\; [\mathrm{m^{-2}\,s^{-1}\,sr^{-1}}] \qquad (12.16)$$

Aseikin et al. (1971) obtained the following expression to describe the integral muon size spectrum derived from their data recorded at Tien Shan (3,340 m, 690 g cm^{-2}) for a muon threshold of 5 GeV.

$$I(\geq N_\mu) \;=\; (1.3 \pm 0.2) \cdot 10^{-3} \left(\frac{N_\mu}{1.8 \cdot 10^4}\right)^{-\gamma_\mu} \;\; [\mathrm{m^{-2}\,h^{-1}\,sr^{-1}}], \qquad (12.17)$$

where

$$\gamma_\mu \;=\; 1.92 \pm 0.07 \;\; \text{for} \; 6 \cdot 10^3 < N_\mu < 1.8 \cdot 10^4$$

and

$$\gamma_\mu \;=\; 2.65 \pm 0.23 \;\; \text{for} \; 1.8 \cdot 10^4 < N_\mu < 7.5 \cdot 10^4$$

are the spectral slope parameters (See also the corresponding electron size data in Sect. 12.2).

12.4 Shower Density Spectra

12.4.1 Introduction

Under the term density spectrum of air showers is generally understood the *density frequency spectrum* of charged particles in extensive air showers. The *differential density spectrum* of air showers, $G(\rho)\mathrm{d}\rho$, is the frequency of occurrence of showers having a particle density between ρ and $\rho + \mathrm{d}\rho$ at a particular location, irrespective of shower size and location of the shower axis. It is generally assumed in this context that all showers have the same structure. Therefore, the particle density, ρ, at a given

distance r from the axis is proportional to the total number of particles in a shower, i.e., $\rho(r) = f(r) \cdot N$, where $f(r)$ is the lateral structure function and N the shower size.

The *integral density spectrum* of air showers, $G(\geq \rho)$, is defined as the rate at which the charged particle density (or the mean particle density of the shower) at a fixed depth of observation in the atmosphere exceeds the value ρ. It is found empirically that the integral density spectrum follows approximately a power law of the form (Cocconi et al., 1943, 1944; Daudin, 1943, 1944)

$$G(\geq \rho) \; = \; K_\rho \rho^{-\gamma} \;\; [\mathrm{s}^{-1}], \tag{12.18}$$

where K_ρ is not strictly a constant. The exponent of the spectrum, γ, is determined experimentally by taking the logarithmic derivative

$$\gamma \; = \; -\frac{\partial \ln (G(\geq \rho))}{\partial \ln(\rho)}. \tag{12.19}$$

γ varies very slowly over a wide range of densities.[4] To a first approximation the density spectrum of air showers has a simple relationship to the size spectrum and both are closely related to the primary energy spectrum (Greisen, 1956, 1960; Cocconi and Cocconi Tongiorgi, 1949; Cocconi, 1961).

If the integral size spectrum, $I(> N)$, is assumed to follow a power law of the form of Eq. (12.1), Sect. 12.2, with an exponent γ', and if we assume in addition that the *lateral distribution function* $f(r/r_M)$, r_M being the Molière radius, remains independent of shower size, the frequency of showers having a density $\geq \rho$ is given by

$$G(\geq \rho) \; = \; 2\pi \int_0^\infty I\left(r_M^2 \rho / f(r/r_M)\right) r \mathrm{d}r \tag{12.20}$$

or

$$G(\geq \rho) \; = \; 2\pi r_M^{-2(\gamma'-1)} \rho^{-\gamma'} K_N \int_0^\infty (f(r/r_M))^{\gamma'} \left(\frac{r}{r_M}\right) \mathrm{d}\left(\frac{r}{r_M}\right) . \tag{12.21}$$

From Eq. (12.21) it follows that $G(\geq \rho) \propto \rho^{-\gamma'}$, which indicates that this relation follows from Eq. (12.1), and vice versa, and that $\gamma' = \gamma$. Thus, the density spectrum is closely linked to the size spectrum and the lateral distribution function.

Analogously, one can also define the density spectrum of muons (Sect. 12.4.4) and of optical atmospheric Cherenkov photons (Sect. 12.4.5) of showers, and some researchers have determined these spectra, too (see Figs. 12.42, 12.43 and 12.44, respectively).

More recent and refined measurements show that the density spectrum has a rather strong dependence on *shower age*, s (see Sect. 12.4.3), and exhibits a *knee*

[4] At that time the knee in the primary spectrum was unknown.

similar to the size spectrum (see Sect. 12.2). Many workers in the field agree that a change of slope occurs at a density between 400 and 1,000 particles m^{-2}, measured at or near sea level, where the spectral slope appears to get steeper. Furthermore a similar consensus exists with respect to the altitude dependence of the spectrum, in particular, that the change of slope moves to higher densities at higher altitudes.

However, the opinions differ on the behavior of the spectrum at very low densities; some authors claim that it gets flatter, others disagree. There remains also some uncertainty at very high densities, because of poor statistics. These and other effects may well decrease the sensitivity of the density spectrum with respect to spectral features of the size or primary energy spectrum.

12.4.2 Phenomenological – Theoretical Aspects

In the following we summarize the phenomenological-theoretical analysis of Cocconi and Cocconi Tongiorgi (1949) of the shower density spectrum. In this work these authors have assumed that K_ρ and γ of Eq. (12.18) are constant over a large density range and vary with altitude above sea level (and zenith angle of incidence). The determination of the value of γ can then be achieved through different methods, as follows:

(a) A number n of detectors, all with the same effective area S, are placed at proper distances from each other on a horizontal plane and the coincidence rates $M_{n-1}(S)$ and $M_n(S)$ are recorded. Under the assumption that the density of showers is the same at all detector locations, then, following Cocconi and Cocconi Tongiorgi (1949), one can deduce γ from the ratio $M_n(S)/M_{n-1}(S)$ by using the expression

$$\frac{M_n(S)}{M_{n-1}(S)} = \frac{\left[\binom{n}{1} - \binom{n}{2}2^\gamma + \binom{n}{3}3^\gamma - \ldots..\right]}{\left[\binom{n-1}{1} - \binom{n-1}{2}2^\gamma + \binom{n-1}{3}3^\gamma - \ldots..\right]}. \quad (12.22)$$

By varying the area S of the detectors, γ can be evaluated for sets of showers of different densities since showers recorded by detectors of surface S have mean density $\simeq 1/S$. When γ is known, the constant K_ρ of the integral density spectrum can be deduced with the help of the equation

$$K_\rho = \frac{M_n(S)}{I_{(n,\gamma)} S^\gamma \cdot \gamma}, \quad (12.23)$$

where

$$I_{(n,\gamma)} = \int_0^\infty x^{-(\gamma+1)}(1 - e^{-x})^n \mathrm{d}x. \quad (12.24)$$

This expression can be rewritten as (see also Daudin, 1947)

$$I_{(n,\gamma)} = -\frac{\Gamma_{(2-\gamma)}}{\gamma(\gamma-1)}\left[\binom{n}{1} - \binom{n}{2}2^{\gamma} + \binom{n}{3}3^{\gamma} - \ldots..\right], \tag{12.25}$$

(b) When $M_n(S)$ is measured for different values of the detector area S, γ may be deduced from the equation

$$\gamma = \frac{\mathrm{d}\ln(M_n(S))}{\mathrm{d}\ln(S)}, \tag{12.26}$$

From this equation γ can be evaluated for different densities if S is varied.

The above mentioned authors pointed out that if the lateral distribution function is the same for all showers, it can easily be shown that the previous requirement for uniform shower density over all detectors can be dropped.

(c) By plotting the frequency versus the number of particles crossing a detector (cloud chamber, etc.) γ can be determined.

(d) Finally γ can be deduced theoretically provided that the primary parameters, including spectral features, and the physics of shower development are known.

Suppose that the sea level integral shower size spectrum, $I(>N)$, as defined in Sect. 12.2, obeys Eq. (12.1), and if we assume that the lateral distribution function $f(r)$ of charged particles (electrons) in a shower can be described by $\rho(r) = N \cdot f(r)$, then the total number of particles in a shower, N, is given by

$$N = 2\pi \int_0^{\infty} N f(r) r \mathrm{d}r \tag{12.27}$$

or

$$2\pi \int_0^{\infty} f(r) r \mathrm{d}r = 1. \tag{12.28}$$

For showers falling at a distance r from a detector, the minimum shower size necessary to produce a density ρ in the detector is $N_{\min} = \rho/f(r)$. If γ and $f(r)$ are independent of N, the rate of recording showers of density $> \rho$ is given by (Ashton et al., 1973)

$$G(>\rho) = 2\pi K_N \int_0^{\infty} \left(\frac{\rho}{f(r)}\right)^{-\gamma} r \mathrm{d}r, \qquad \text{or}$$

$$G(>\rho) = 2\pi K_N \rho^{-\gamma} \int_0^{\infty} \frac{r}{f(r)^{-\gamma}} \mathrm{d}r = K_\rho \rho^{-\gamma} \ [\mathrm{s}^{-1}]. \tag{12.29}$$

Under the approximations made above the slope of the density spectrum should be the same as that of the size spectrum. In other words, if there is a change in the

slope of the size spectrum from γ_1 to γ_2 at a particular shower size N_c, then a similar change in slope must be expected in the density spectrum at that density ρ_c which is generated by showers of size N_c whose axes make a direct hit on the detector. Similarly, all showers which fall at some distance r from the detector and produce a density $\rho > \rho_c$ at the detector have sizes $> N_c$.

12.4.3 Charged Particle Density Spectra

(a) Density Measurements, Spectra and Decoherence

Density measurements were some of the first investigations carried out after the discovery of the phenomenon of air showers (Auger, 1938). Over the years a large number of density spectra had been measured with a wide variety of detector arrangements, ranging from just a few detectors on a small lot to large modern arrays. A correspondingly large number of references can therefore be found in the literature. Initially it was believed that the density spectrum could be described by a single power law.

Early work consisted of simple density rate measurements with just a few detectors (Geiger counters) in coincidence. The counting rate was then explored as a function of discriminator level, detector area, separation between the detectors or any combination of these parameters. This work was carried out at different altitudes with shielded and unshielded detectors. In some cases mobile equipment was moved to different locations (Hillberry, 1941).

At an early stage *decoherence* and density measurements with ground based equipment covered the full range of altitudes from sea level to high mountains (over 4,000 m), and after 1945 to levels as high as 12,000 m with detectors on board of airplanes (Antonov et al., 1964a, b, c; Hodson, 1953; Kraybill, 1949, 1952, 1954a; Maze et al., 1948). A cloud chamber experiment was carried out by Brown and McKay (1949) at Echo Lake, Colorado (3,260 m). Table 12.3 below summarizes the early data that were interpreted on the basis of a single power law spectrum with exponent γ and scale factor K_ρ. More recent decoherence measurements were carried out by Andrews et al. (1970a).

Around about 1960 it was generally believed that the slope of the density spectrum varies very slowly with increasing density (see Sect. 12.4.6). Most of these measurements were made relatively close to the shower core. Later on more and more evidence was presented that indicated the presence of a relatively *sharp knee* in the spectrum (Kulikov and Khristiansen, 1958).

A compilation of integral density spectra due to Hara et al. (1979c, 1981) is presented in Fig. 12.33. The measurements carried out by these authors at the Akeno site (900 m) do not show any abrupt change in slope as other authors claim. Hara et al. (1979c) point out that they took great care to avoid transition effects in the detectors by using very thin scintillators (see Sects. 2.11, 12.1 and 12.2) and that no tendency for saturation was observed in the core region of showers. Other integral

Table 12.3 Early experimental values of γ and K_ρ (Cocconi and Cocconi Tongiorgi, 1949)

Author	Altitude [m.a.s.l.]	Density range	γ [m^{-2}]	K_ρ [a]
Cocconi et al. (1944, 1946)	110	10–1,000	1.46	0.124
	2,200	10–1,000	1.55	1.0
Auger and Daudin (1945)	50	≃70	1.66	
	2,060	≃70	1.50	
	2,860	≃70	1.46	
Maze et al. (1948)	0	≃100	1.67	
	6,700	≃100	1.41	
Treat and Greisen (1948)	3,260–4,300	30–200	1.55	
	3,260–4,300	30–200	1.40	
Loverdo and Daudin (1948)	2,900	4–800	1.52–1.65	
	2,900	4–800	1.30	
Williams (1948)	3,050	300–2,000	1.50–1.90	2.70

[a] The constant K_ρ is adjusted for ρ expressed in units of [m^{-2}] and time in [s].

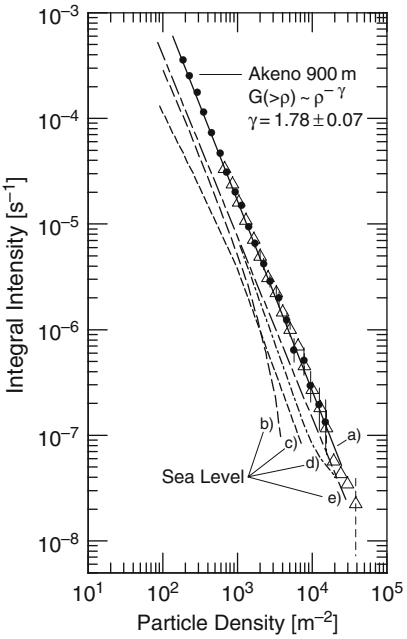

Fig. 12.33 Compilation of integral density spectra of charged particles. The symbols • and △ represent data recorded at Akeno with 3 mm thick plastic scintillators at different epochs (Hara et al., 1979c, 1981, respectively). The *solid line (a)* is a hand-drawn fit to the data points of Hara et al. (1979c). The *broken lines* are data from sea level measurements compiled by Hara et al. (1979c): (*b*) Sydney (McCaughan et al., 1965a, b; see also Prescott, 1956), (*c*) Durham (GB) (Ashton and Parvaresh, 1975), (*d*) Kiel (Germany) (Büscher, 1971) and (*e*) Tokyo (Nagano, 1976), respectively

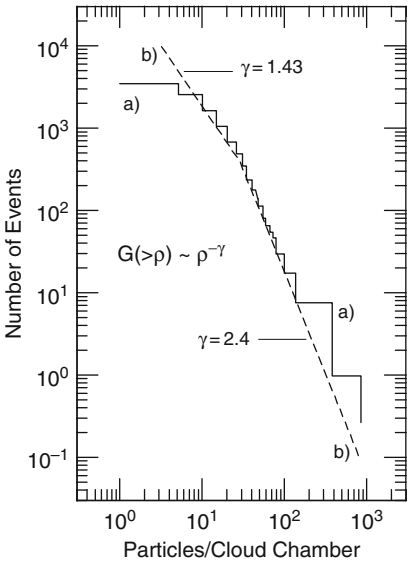

Fig. 12.34 Integral density spectrum obtained with a Wilson cloud chamber at Sydney during a 2-year run (histogram, *line (a)*). A single event from a second cloud chamber, 1 m away, with an estimated density $>$ 2000 particles per cloud chamber ($\simeq 18,000\,\mathrm{m}^{-2}$, see text) had been added conservatively by the authors at a density $>$900 particles per cloud chamber. The *broken dashed line (b)* represents two power laws of slope -1.43 and -2.4, joining at 28 particles per cloud chamber. The apparent cutoff at very low densities is due to trigger criteria (McCusker and Winn, 1979)

spectra, all from sea level measurements, included in Fig. 12.33, are those from the arrays at Kiel (Büscher, 1971), Durham (Ashton and Parvaresh, 1975), Sydney (McCaughan et al., 1965a, b) and Tokyo (Nagano, 1976).

In Fig. 12.34 we show the more recent integral event distribution of particle densities recorded with two *cloud chambers* at Sydney (Australia) in a 2-year run (McCusker and Winn, 1979). The cloud chambers measured 30 cm in diameter and had a depth of 20 cm. The mid-plane illuminated area of the chambers measured 505 cm^2. These data suggest a change of slope at about 400 particles m^{-2}, in fair agreement with the earlier work of McCaughan et al. (1965a, b) and other authors.

Another set of data from the same epoch obtained with Geiger counters at the Moscow array are shown in Fig. 12.35 (Khristiansen et al., 1979b). The authors have used a method of successive approximation to compute the density spectrum. The data are presented in a compressed form where the ordinate showing the frequency of events is multiplied with the density to the power of 1.5. The solid curves are theoretical results from an earlier simulation of Makhmudov et al. (1975) and Makhmudov and Sharibdzhanov (1977), showing integral density spectra for showers of different age.

These authors also derive an analytic expression for the differential electron density spectrum and include the altitude dependence. The expression is given in

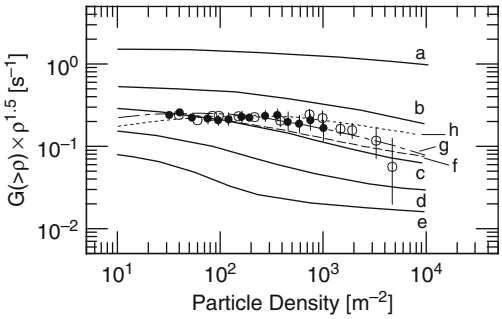

Fig. 12.35 Integral density spectrum of charged particles, $G(>\rho)$, multiplied by $\rho^{1.5}$, obtained with Geiger counters at Moscow (○, Khristiansen et al., 1979b) compared with the results from Durham (●, Ashton and Parvaresh, 1975). *Curves (a)–(e)* show theoretical results of Makhmudov and Sharibdzhanov (1977) for lateral distribution functions that are independent of shower size, corresponding to age parameters of $s = 0.8$, 1.0, 1.2, 1.4, and 1.6, respectively. *Curve (f)* uses an age distribution function with $\langle s \rangle = 1.18$. *Curves (g) and (h)* are for size dependent age parameters as discussed in the text

Sect. 12.4.6, Eq. (12.36). Also shown in their work is the spectral index of the density spectrum versus density for different age parameters. They point out that because of the rapid attenuation of showers with increasing zenith angle, θ, which goes as

$$\exp\left(-\frac{\gamma X}{\Lambda_{\text{att}}}(sec(\theta)-1)\right) \simeq \cos^{8.5}(\theta)\,, \tag{12.30}$$

where γ is the spectral exponent, X the atmospheric depth of the observation level and Λ_{att} the shower rate attenuation length, one may ignore the contribution from inclined showers when computing the density spectrum.

Makhmudov and Sharibdzhanov (1977) conclude from their work that the density spectra cannot be described by a single power law. For young showers ($0.8 \leq s \leq 1.0$) they found the power law exponent to vary very slowly (by about 0.1–0.2) over a density range of approximately four orders of magnitude, whereas for older showers ($1.4 \leq s \leq 1.6$) that are well below maximum development the density spectrum is more sensitive to the shower size, as one would expect.

Since the lateral distribution of real showers fluctuates from shower to shower, and therefore the age parameter s, too, the latter must be included in any reliable analysis. Simulated differential density spectra by Makhmudov and Sharibdzhanov (1977), not reproduced here, support this argument. These authors also emphasize the importance of accurate knowledge of the lateral distribution function at small and large distances from the shower axis. For comparison the results of Ashton and Parvaresh (1975) had been added to Fig. 12.35.

Figure. 12.36 shows the work of Ashton and Parvaresh (1975) which find a change in slope from $\gamma = 1.5$ at low densities to $\gamma = 2.0$ at high densities with the joining point for the two power laws being at a density of approximately 1,000

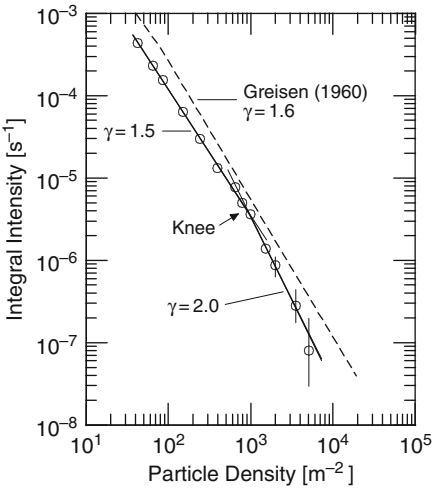

Fig. 12.36 Integral density spectrum of air showers at sea level recorded with proportional counters by Ashton and Parvaresh (1975) at Durham, ○, compared with an early spectrum given by Greisen (1960), *dashed curve* (see also Ashton et al., 1973). The spectral indices, γ, of power law fits of the form $G(> \rho) \propto \rho^{-\gamma}$ are also indicated. Note the existence of a knee in the Astron and Parvaresh spectrum

particles m^{-2}. Thus, the density spectrum, too, exhibits a *knee*. For comparison the summary spectrum of Greisen (1960) had been added.

Swinson and Prescott (1965) have carried out extensive investigations of the density spectrum. Their results obtained at Sulfur Mountain (Canada, 2,285 m a.s.l.) and Echo Lake (CO, 3,260 m a.s.l.) are presented in Fig. 12.37 together with sea level data of Prescott (1956). The more recent results from measurements at Mt. Evans (CO, 4,300 m a.s.l.) and Albuquerque (NM, 1,575 m a.s.l.) are shown in Fig. 12.38 (Swinson and Prescott, 1968). The data are given as integral counts.

The same apparatus had been used in the two experiments carried out by Swinson and Prescott (1965, 1968), jointly. Moreover, their counters which consisted of three proportional counters and associated Geiger counters, arranged in triangular configuration, had their separations adjusted proportional to the lateral scattering length of air showers in the atmosphere that depends on the barometric pressure. Since the density at any particular altitude depends on the lateral spread of the particles in the shower, and thus on the lateral scattering length, these authors consider it more appropriate to express densities in units of square scattering length at each altitude. The density scale-change for densities expressed in these units is 1:7:13.5:47 for sea level, 1,575, 2,285 and 3,260 m a.s.l., respectively.

In Fig. 12.38 we also show the density spectrum of McCaughan et al. (1965a, b) obtained at sea level and Sulfur Mountain with a cloud chamber. These authors as well as Swinson and Prescott (1965, 1968) conclude that the exponent of the density spectrum is about -1.5 and very nearly constant up to densities of about

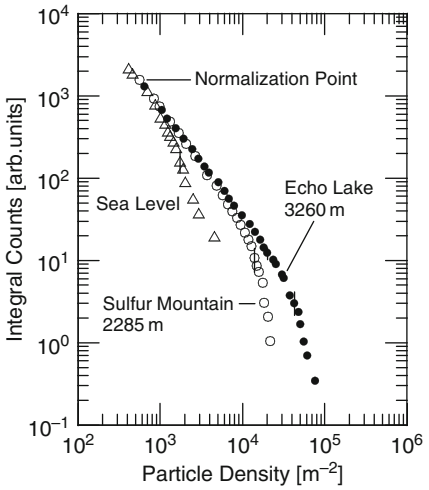

Fig. 12.37 Integral density spectra measured at different altitudes with proportional counters. For ease of comparison the spectra are normalized at the point corresponding to >600 particles m^{-2}, irrespective of the absolute counting rate. The sea level data, △, are from the work of Prescott (1956), the Sulfur Mountain (Alberta, Canada), ○, and Echo Lake (Colorado, USA) data, ●, after Swinson and Prescott (1965)

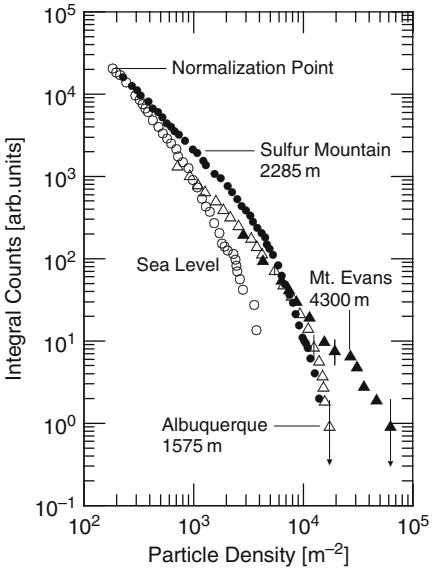

Fig. 12.38 Integral density spectra measured with proportional counters at Albuquerque (NM) (1,575 m), △, and Mt. Evans (CO) (4,300 m), ▲, (Swinson and Prescott, 1968). Also shown are density spectra measured with a cloud chamber at sea level, ○, and on *top* of Sulfur Mountain (Canada) (2,285 m), ●, (McCaughan et al., 1965a, b)

500 particles m^{-2}. However, sea level observations seem to indicate that there is a rapid steepening for densities >500 particles m^{-2}.

A similar steepening is found at higher altitudes but it occurs at considerably higher densities. In addition it was found that the ratio of densities between sea level and mountain altitudes measured with proportional counters or ionization chambers are in good agreement with cloud chamber measurements. This is illustrated in Fig. 12.39 which shows the relative values of densities for different altitudes, plotted as a function of atmospheric pressure and normalized to sea level. The straight line in Fig. 12.39 represents the relative energy retained by a primary particle as a function of altitude, assuming an inelasticity of 0.58 per collision and an energy independent interaction length of 78 g cm^{-2}. It should be pointed out that neither of these two parameters are critical, a choice of combinations yield lines of similar slope.

More recent measurements made by Clay and Gerhardy (1980) with four counters arranged in a square with sides measuring $30\sqrt{2}$ m yield a spectral index of $\gamma = 1.85 \pm 0.02$ for densities between about 15 and 400 particles m^{-2}. This corresponds to a shower size range from $4 \cdot 10^5$ to 10^7. For lower densities or smaller shower sizes they find an appreciably flatter spectrum.

A specific set of differential density spectra obtained by Antonov et al. (1964a) at high altitude is shown in Fig. 12.40. These data were obtained from a complete set of showers, using the *Gross transformation* (see Appendix B, Sect. B.5) (Gross, 1933).

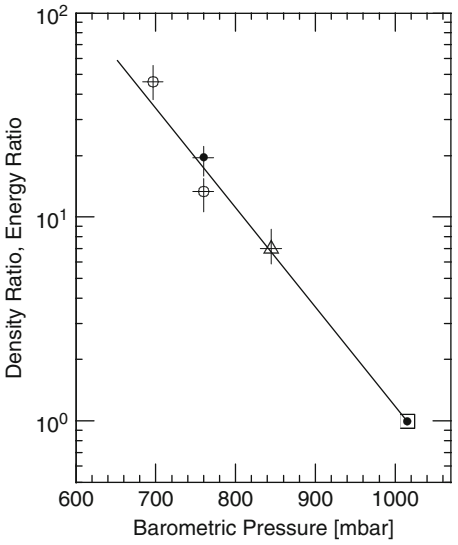

Fig. 12.39 Relative values of the density of charged particles observed at different altitudes. The different symbols identify the work of the following authors: □, Prescott (1956); •, McCaughan et al. (1965a, b); ○ and △, Swinson and Prescott (1965, 1968), respectively. The *straight line* shows the relative energy retained by a primary proton as a function of altitude expressed in terms of atmospheric (barometric) pressure, assuming a constant inelasticity of 0.58 and a constant mean nuclear interaction length of 78 g cm^{-2} (after Swinson and Prescott, 1965, 1968)

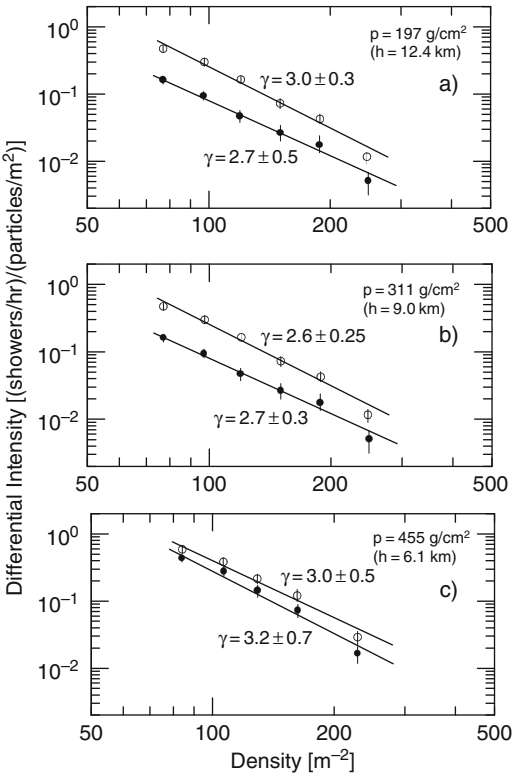

Fig. 12.40 Differential particle density spectra of vertical showers at different altitudes (**a**, **b**, **c**), as indicated by the pressure p and corresponding approximate altitude h in parentheses (Antonov et al., 1964a). The *upper spectra* in each figure, ○, include all showers, the *lower spectra*, •, only those where the ratio of the peripheral density to the central density is ≥0.3. The spectra can be described by power laws with exponents γ as indicated. The systematic drop of the points at density near 250 is believed to be due to an increase in the slope of the spectrum. The *lines* are fits to the data

The data fit a power law with average exponent $\gamma = 2.75 \pm 0.20$ for the levels corresponding to pressures of 197 g cm^{-2} ($h \simeq 12.4$ km) and 311 g cm^{-2} ($h \simeq 9$ km) if all data points are included. However, it is evident that all the points of highest density (near 250 particles m^{-2}), including those at the pressure of 455 g cm^{-2} ($h \simeq 6.1$ km), are systematically low. The authors suggest that this may be due to a change in the slope of the spectrum. If these points are disregarded, the slopes of the two higher altitude measurements (197 and 311 g cm^{-2}) fit a power law with exponent $\gamma = 2.6 \pm 0.20$.

(b) Exponents of Density Spectra

As discussed above the exponent of the power law describing the density spectrum is a much debated parameter. Greisen (1956) has summarized the data that were

available at the time for different altitude ranges. His data compilation is reproduced in Fig. 12.41, frames a, b and c. In addition we have updated the compilation by adding some results of more recent measurements. Inspection of Fig. 12.41c, which covers the data from sea level to an altitude of 750 m, reveals that apart from the early data by Lapp (1943, 1946) and the comparatively recent results of Clay and Gerhardy (1980), the data show the same general trend of a slow rise with increasing density.

At mountain level, Fig. 12.41b, the agreement is inferior and large errors add to the uncertainty. It is not excluded that the general trend of an accelerated increase of the exponent with increasing density could be due to saturation effects. Little can be concluded from the very difficult high altitude measurements (Fig. 12.41a) except that the few scattered data point do not deviate much from those obtained at lower levels in the same density range.

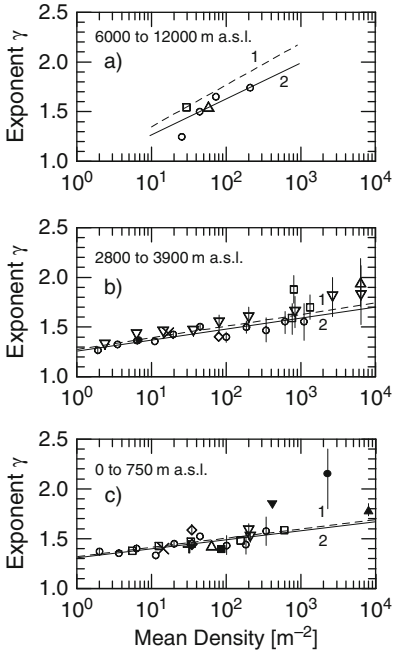

Fig. 12.41 Compilation of measured values of the exponent of the density spectrum of extensive air showers for different altitude ranges after a compilation by Greisen (1956). (**a**): High altitude data. ○ Kraybill (1949, 1954b), △ Hodson (1953) and □ Biehl and Neher (1951). (**b**): Mid altitude data. △ Hudson (1950), □ Williams (1948), ○ Cocconi and Cocconi (1949), × Ise and Fretter (1949), ◇ Treat and Greisen (1948), ▽ Zatsepin et al. (1947, 1953), ● Daudin and Daudin (1953a, b). (**c**): Sea level to 750 m a.s.l. ● Lapp (1943, 1946), ○ Cocconi and Cocconi (1949), × Milone (1952), △ Hodson (1953), □ Zatsepin et al. (1947, 1953), ◇ Keck and Greisen (1949), + Broadbent et al. (1950), □ Singer (1951), ▽ Kraybill (1949). We have also added the more recent date of Hara et al. (1981) ▲ and those of Clay and Gerhardy (1980) ▼

For additional very early data on the altitude variation of the exponent of the density spectrum see also Sect. 6.6 and Fig. 6.25.

12.4.4 Muon Density Spectra

Only few researchers have approached the problem of the muon density spectrum. Several obvious reasons have discouraged major efforts to determine the pure muon density spectrum, above all the relatively low particle density, the difficulty to separate muons from the dominating electromagnetic (and hadronic) component, and occasional so-called punch-throughs, i.e., very energetic electrons that can penetrate thick shields because of the LPM (Landau - Pomeranchuk - Migdal) effect (Landau and Pomeranchuck, 1953a, b; Migdal, 1956; see also Misaki, 1993). Moreover, many common density spectra include of course the usual fraction of muons as well. In addition there is a relationship between electrons and muons.

However, an interesting theoretical analysis had been presented by Makhmudov and Sharibdzhanov (1977) which is mentioned in the previous subsection. Besides their computation of the density spectrum of electrons (Fig. 12.35) they have also computed the muon density spectrum of air showers. Starting from their expression for the size spectrum, given in Sect. 12.2.5, Eq. (12.9), which includes the altitude dependence, but inserting for γ the exponent

$$\gamma_\mu \;=\; \frac{\gamma_e}{0.78}, \tag{12.31}$$

they obtain for the muon size the simple relation

$$\langle N_\mu \rangle \;=\; (3.24 \pm 0.22) \cdot 10^3 \left(\frac{N_e}{10^5} \right)^{0.78 \pm 0.01} . \tag{12.32}$$

Using the expression

$$f_\mu(k, r) \;=\; C(k) \cdot r^{-k} \cdot e^{-(r/80)} \tag{12.33}$$

for the lateral density distribution function of muons of energy $\geq$10 GeV, where $k \;=\; 0.5 \pm 0.07$ and r is in meters, Makhmudov and Sharibdzhanov obtain the functional form of the integral density spectrum for muons, shown in Fig. 12.42. The dependence of the spectral index versus muon density for different values of k is shown in Fig. 12.43.

Firkowski et al. (1965, 1973) have measured the exponent γ of the density spectrum of the so-called *penetrating component* in showers (chiefly muons) and obtained $\gamma = 2.10 \pm 0.05$ for a muon energy threshold of $\geq$5 GeV. They have also

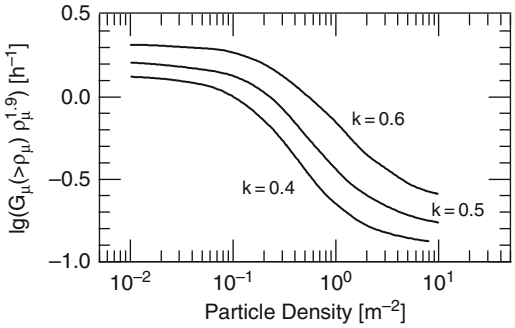

Fig. 12.42 Integral muon density spectra, $G_\mu(>\rho)$ [hr^{-1}], for different muon distribution function exponents, k (Eq. 12.33), after Makhmudov and Sharibdzhanov (1977). For details see text

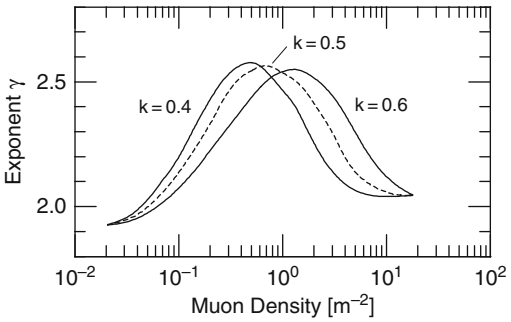

Fig. 12.43 Spectral index, γ, of muon density spectra, $G_\mu(>\rho)$, shown in the previous figure versus muon density for different muon distribution function exponents, k (Eq. 12.33), after Makhmudov and Sharibdzhanov (1977). For details see text

determined the barometric coefficient for the same trigger conditions which is given in Sect. 6.6.

12.4.5 Cherenkov Photon Density Spectra

Some authors have also determined the Cherenkov density spectrum of showers (Gerdes et al., 1973, 1975; Hartman et al., 1977, 1979; Bhat et al., 1977; Dyakonov et al., 1979; Efimov and Sokurov, 1979, 1983). The primary aim of this work was to study the cosmic ray spectrum in the region of the knee, between 10^{14} and 10^{16} eV, and to search for correlations with other observables. We present here in Fig. 12.44 the data obtained from measurements carried out by Hartman et al. (1977) at Mt. Hopkins and by Efimov and Sokurov (1979) at Yakutsk. Experimental Cherenkov density spectra were interpreted by Glushkov et al. (1978, 1979) and Khristiansen et al. (1979a), using the results of their calculations. A more extensive analysis based on simulations was carried out by Protheroe and Patterson (1984).

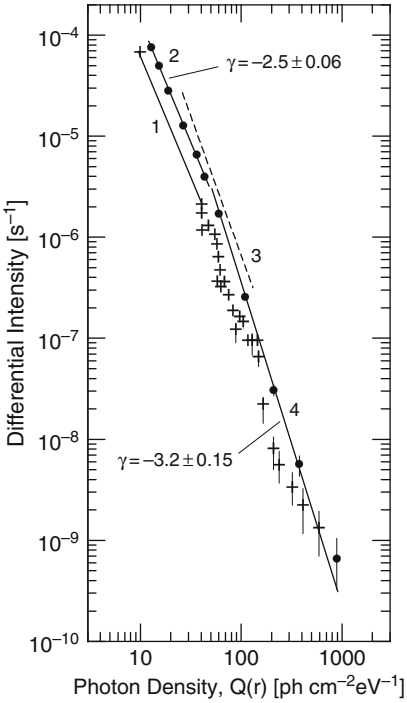

Fig. 12.44 Differential optical Cherenkov photon density spectra observed at Yakutsk (105 m a.s.l.), • (Efimov and Sokurov, 1979, 1983), and Mt. Hopkins, +, 2,300 m a.s.l. (Hartman et al., 1977). The *solid lines* are fits to the data and the slopes for simple power law fits are indicated. The Yakutsk data show definitely a change of slope at a density of about 70–80 photons $\mathrm{cm}^{-2}\,\mathrm{eV}^{-1}$

12.4.6 Mathematical Expressions and Fits

Greisen (1956) found that a more accurate description of the sea level particle density spectrum of air showers in the density range $1 \leq \rho \leq 1000\,\mathrm{m}^{-2}$ could be obtained by replacing the exponent of Eq. (12.18) by γ' as follows,

$$G(>\rho) = K_\rho \rho^{-\gamma'}, \tag{12.34}$$

where

$$\gamma' = \gamma_0 + \alpha \cdot \ln\left(\frac{\rho}{\rho_0}\right). \tag{12.35}$$

The numerical values of the parameters are $\alpha = 0.038$, $\rho_0 = 1\ \mathrm{m}^{-2}$, $K_\rho = 0.167\ \mathrm{s}^{-1}$ and $\gamma_0 = 1.32$.

Makhmudov and Sharibdzhanov (1977) derived the following expression for the differential electron density spectrum.

$$G(\rho)\mathrm{d}\rho \;=\; \sum_{i=1}^{3} B_i(\rho,\gamma_i)\cdot\rho^{-(\gamma_i+1)}\mathrm{d}\rho \;\; [\mathrm{s}^{-1}]\,, \tag{12.36}$$

where

$$B_i(\rho,\gamma_i) \;=\; 2\pi A_i \int_0^{\theta_{\max}} \sin(\theta)\exp\left(-\frac{\gamma_i h}{\Lambda_{\mathrm{att}}}(\sec(\theta)-1)\right)\cos^{\gamma_i}(\theta)\mathrm{d}\theta \cdot \int_{r_{i-1}}^{r_i} r f^{\gamma_i}(r)\cdot \mathrm{d}r. \tag{12.37}$$

Here ρ is the particle density, γ_i the spectral index of the i-th portion of the size spectrum, A_i the corresponding scale factor, h the level of observation, Λ_{att} the rate attenuation length of showers of size N and θ is the zenith angle of the shower. The expression for the size spectrum is given in Sect. 12.2 and for the lateral density distribution a Nishimura Kamata function is inserted (see Chap. 4 and Sect. 8.4).

Based on their analysis presented above Hara et al. (1979c) (Fig. 12.33) find the following expression to give a good fit to the particle density spectrum of showers over the density range $3\cdot 10^2$–10^4,

$$G(>\rho) \;=\; (6.3\pm 0.6)\cdot 10^{-2}\left(\frac{\rho}{10^3}\right)^{-(1.78\pm 0.07)} \;\; [\mathrm{h}^{-1}]\,. \tag{12.38}$$

Today density spectra play a rather insignificant role.

12.5 Density Spectra at Fixed Core Distance, Energy Loss Spectra of Showers

12.5.1 Introduction

One of the objectives of air shower research is the determination of the energy spectrum of the primary radiation that initiates the showers. A widely used approach towards this goal is to determine the shower size, because it is related to the primary energy. As outlined in Sect. 12.2, the size of a shower is determined experimentally by sampling the particle flux in a shower at a given atmospheric depth over a limited area. This is usually done with thin detectors to avoid transition effects near the shower core, as discussed in Sect. 2.11. Subsequent integration of the local densities using an appropriate lateral distribution function yields the shower size.

To explore the regions of the primary energy spectrum at 10^{17} eV and beyond, a shower array must cover a very large area to have an adequate counting rate. To fulfill this demand the standard method requires a very large number of conventional shower detectors in order to measure the particle densities close enough to the shower core which strikes randomly, to insure adequate accuracy of the size determination and core location. If one relaxes on the requirement of detector

coverage of a given area for an array the problem of shower fluctuations gets very serious.

Monte Carlo simulations show that fluctuations manifest themselves very severely in the vicinity of the shower core and in detectors responding strongly to the electromagnetic component of a shower. This phenomenon is even more pronounced in proton initiated showers where fluctuations are extreme as compared to heavy primary initiated showers. Consequently, conventional arrays having poor detector coverage, particularly in the shower core area, falsify the basic measurements from which the shower size is computed.

To avoid these problems another approach had been developed, chiefly by the Leeds group in conjunction with the Haverah Park air shower array (212 m a.s.l.), to assess showers in a different manner. This approach is based on a particular feature of the detectors which had been used at Haverah Park for some time to explore the primary energy spectrum, without considering the structure of the showers in detail (Lillicrap et al., 1963; Tennent, 1967, 1968; Hollows et al., 1969).

In contrast to smaller arrays having a large number of relatively small scintillation detectors, the Haverah Park array had rather poor detector coverage, using comparatively few but very large deep water Cherenkov detectors. The likelihood for such an array of having a shower core strike close to a detector is therefore relatively small and the recorded data are less subject to large fluctuations.

12.5.2 Concept of Energy Loss Density

Air shower simulations carried out with a very simple but not unreasonable shower model in combination with detector response simulations have shown that at distances of several hundred meters from the shower axis, the fluctuations of the response of a large deep-water Cherenkov detector to the unshielded flux of particles in large showers reach a minimum (Hillas et al., 1970, 1971a, b). In addition the signal produced by such a detector is proportional to an *energy loss surface density* in the detector, expressed in MeV m^{-2}. The latter is defined as the energy lost by a shower in 120 cm of water, measured in the direction of the shower axis, per unit area normal to the shower axis. It is usually referred to as the *energy loss density* of a shower.

Another significant result of these calculations is that to a first approximation the constant of proportionality relating energy loss density to detector signal (amplitude) is the same for both the muon and the electron-photon component of big showers at large core distances. The relationship is nearly independent of inclination of the shower axis for zenith angles from 0° to about 40°. Under certain conditions the energy loss density of a shower is proportional to the number density [m^{-2}] of the muon component and the energy density [MeV m^{-2}] of the electron-photon component (Hollows, 1968; Hollows et al., 1969).

In addition, it was found that the response of a deep water Cherenkov detector within the core distance range of a few 100 m is almost directly proportional

to the energy of the primary over the energy range explored; more specifically, at about 400 m from the core for a primary energy of $\simeq 10^{17}$ eV, and at slightly larger distances for more energetic events. This implies that under the assumption that high energy nucleus-nucleus interactions can be described by a simple superposition model,[5] the response of such a detector is insensitive to primary mass (Hillas et al., 1970). This is an enormous advantage for exploring the primary energy spectrum, at least in an approximate manner, irrespective of the nature of the primaries initiating the showers, and it can be done with relatively cheap detectors.

The initial standard water Cherenkov detector consisted of a cluster of closely packed modules of area 2.3 m^2, adding up to a total area of 34 m^2 per cluster, with a depth of 120 cm (Lillicrap et al., 1963; Tennent, 1967, 1968). The large detector area was chosen to avoid fluctuations due to low particle densities at large core distances. In the later stages of the array smaller detectors and a variety of other equipment had been added to extend the capabilities of the array.

The response of the detector (for details see Chaps. 2 and 8) is a measure of the energy deposited by the particles of the shower at the particular location. The particle composition at core distances of several 100 m from the shower axis is a mixture of relatively low energy muons, electrons and photons. At moderate core distances the relative weight of the contributions from the muon and electromagnetic components to the energy loss density are roughly in the ratio of two to one.

The great thickness of the Cherenkov medium causes the detector to respond to some extent as a water Cherenkov calorimeter. The bulk of the muons penetrate the water whereas the electromagnetic component is almost completely absorbed. It is the relative insensitivity of the densities of the different shower constituents at large core distances and their energy spectra to the general cascade development in combination with the array geometry that generate this favorable overall response of the detector to the showers.

This simple technique which is best suited for large air showers is also being employed as backbone for the new Auger Observatory in Argentina (Cronin, 2001a, b; Suomijärvi et al., 2007).

12.5.3 Calibration and Units of Energy Loss Density

A standard measure for the response of a deep water Cherenkov detector is the energy deposited by a relativistic muon penetrating the detector vertically. It also serves as a means of calibration. The response of the detector per unit area, i.e., the unit signal amplitude thus produced in 120 cm of water, is expressed in

[5] In a simple superposition model it is assumed that a nucleus-nucleus collision in air can be described by A proton-nitrogen or A proton-oxygen interactions, where A is the mass number of the incident projectile nucleus. However, for computing the location of the first interaction of each shower the interaction mean free path of a nucleus of mass A in air must be taken. This model implies total fragmentation of the primary, which is not realistic.

vertical equivalent muons per square meter , [veμ m^{-2}]. 1 veμ corresponds in such a detector to an energy deposit of about 220 MeV. The same measure is used for electromagnetic radiation, irrespective of the degree of penetration into the water column (for details see Sect. 2.11.3).

The energy loss density is a shower property measured by thick detectors, in particular by deep water Cherenkov detectors. It can be regarded as a shower observable analogous to the charged particle density recorded by thin scintillation detectors, spark chambers, Geiger counters or flash tubes, or the optical atmospheric (air) Cherenkov photon density recorded with phototube arrangements. Energy-loss density can be related to the more familiar quantity of showers size and to primary energy.

Extensive studies of the properties of the deep water Cherenkov detector type used at Haverah Park were made by Blake and coworkers (Blake et al., 1978a, b; Blake and Saltmarsh, 1979). These authors have also compared the response of the detector to those of a variety of other kinds of detectors. Their work was of theoretical and experimental nature and included a careful analysis of the dependence of the detector responses as a function of core distance. This is of particular interest because the average energy of the particles in a shower depends on the distance from the shower axis and affects possible transition effects in the detectors. Details of this work are given in Sect. 2.11.

12.5.4 Energy Loss of Showers and Energy Loss Spectra

The parameter obtained by integrating the *energy loss density* of a shower over a specified range of core distances is termed the *energy loss of a shower*. For near vertical showers of large size, corresponding to primary energies in the range from 10^{17} to 10^{18} eV, the integrated energy loss over a core distance range from 100 to 1000 m at sea level amounts to about 1% of the total energy of the primary initiating the shower (Suri, 1965, 1968).

According to Hollows et al. (1969) the lateral distribution of the energy loss density of a shower over the lateral distance range from about 100 to over 1,000 m can be represented by a power law of the form

$$\rho(r) \;=\; k(r)e^{-n} \quad [m^{-2}]. \tag{12.39}$$

An *energy loss parameter* $E_{100}(k, n)$, defined as

$$E_{100}(k, n) \;=\; 2\pi \int_{r=100}^{r=1000} r\rho(r)\mathrm{d}r \;\propto\; N, \tag{12.40}$$

where N is the shower size, had been introduced to classify the showers thus recorded, and to compare them with showers recorded in the conventional manner.

For showers of given intervals of energy loss and zenith angles, the exponent n shows a wide distribution. In addition its mean value, m, manifests a zenith angle

dependence, $m(\theta)$, that can be represented over the zenith angle range $0^\circ \leq \theta \leq 55^\circ$ by the expression (Hollows et al., 1969)

$$m(\theta) \;=\; 6.37 - 4.56\sec(\theta) + 1.45\sec^2(\theta) - 0.15\sec^3(\theta). \tag{12.41}$$

Furthermore, $m(\theta)$ exhibits a slight energy dependence. The energy dependence of the lateral distribution had been studied by England et al. (1979). For near vertical showers ($0^\circ \leq \theta \leq 20^\circ$) it can be expressed by

$$m(E_{100}) \;=\; (3.05 \pm 0.02) + (0.5 \pm 0.03)\log\left(\frac{E_{100}}{10^{15}}\right). \tag{12.42}$$

In analogy to the shower size spectrum the differential or integral *energy loss spectrum* of air showers is another readily available observable and can be used in place of the former. It can also be used to infer the primary energy spectrum with the help of air shower simulations (Andrews et al., 1970b).

Frequently energy loss spectra presented do not show intensity as a function of energy loss of the showers, but as a function of the energy loss density $\rho(xxx)$ [veμ m^{-2}] at a particular core distance (xxx), the so-called *ground parameter* $\rho(xxx)$. The optimized core distance (xxx) depends weakly on shower size. $\rho(500)$ and $\rho(600)$ are frequently used parameters for showers in the primary energy range 10^{17}–10^{20} eV. Such spectra are referred to as the $\rho(500)$, $\rho(600)$, etc. -spectra, depending on the particular core distance which had been chosen for the measurements (for the Auger surface array $\rho(1000)$ is being used).

Since within reasonable limits the energy flow in large showers at core distances of several hundred meters does not depend critically on a number of cascade parameters, but chiefly on primary energy, the ground parameter $\rho(xxx)$, as discussed above, is a very useful quantity to classify showers and at the same time represents a directly accessible and fairly reliable observable to establish a link to the energy spectrum of the primaries.

In a recent paper Risse and Heck (2004) have analyzed the energy release or energy deposit of showers in the atmosphere. Their results concerning the longitudinal energy release, i.e., the energy deposit as a function of atmospheric depth and the energy spectrum of the associated electrons are summarized in Chap. 6. The lateral distribution of the energy dissipation is discussed in Sect. 8.4.

12.5.5 Absorption Coefficient and Energy Loss Spectra

Some papers that deal with this subject are sometimes confusing because different authors use different terminologies and symbols when discussing energy loss spectra of showers. Frequently the term *shower absorption length* and the symbol Λ^* are being used in the context of energy loss spectra. It is important to note that a direct comparison of Λ^* with the conventional shower rate attenuation length $\Lambda_{\rm att}$ and the

shower particle absorption length λ_{abs}, defined and discussed in detail in Sect. 6.3, would be misleading because the quantity Λ^* is defined differently.

$$\Lambda^* = -\frac{\partial \ln\{I(> E_{100}, X)\}}{\partial X} \quad [\mathrm{g\,cm^{-2}}], \tag{12.43}$$

where $I(>E_{100}, X)$ is the integral energy loss spectrum at atmospheric depth X and $E_{100} = F \cdot E$. The fraction F of the total energy loss E that falls in the range of core distances $100 < r < 1000$ m varies itself with depth X, and Λ^* may possibly depend on E_{100} (Hollows et al., 1969).

12.5.6 Air Cherenkov Photon Density and Energy Loss

On the basis of their simulations, Egorov et al. (1971b) and Dyakonov et al. (1973, 1974) have shown that the *air Cherenkov photon density*, $Q(xxx)$, at a particular core distance (xxx) in large showers manifests properties similar to those of the $\rho(xxx)$ ground parameter. It is also subject to comparatively small fluctuations because of the large photon density compared to the typical particle density (Krasilnikov et al., 1977; Dixon and Turver, 1974; Dixon et al., 1974a, b, c).

Because of the small opening angle of the Cherenkov light produced by the shower particles in the atmosphere, convoluted with the lateral distribution function of the particles and optical photon absorption in the atmosphere, the optimized distances for $Q(xxx)$ measurements are closer to the shower axis than for Haverah Park ground parameter $\rho(xxx)$ measurements. *Air Cherenkov photon density spectra* showing the intensity of events as a function of the $Q(xxx)$ parameter can be constructed and interpreted in an analogous manner as $\rho(xxx)$ or shower size spectra. Further details concerning air Cherenkov data are given in Chap. 16.

Shower size, energy loss density, air Cherenkov density and the respective spectra can be converted mutually for comparison and related to the primary energy spectrum (Dyakonov et al., 1979). Phenomenological mathematical expressions to describe the spectra and relationships between the different observables are given in Sect. 12.5.8. The determination of the primary energy spectrum from the data discussed in this section are discussed in Chap. 10, Sects. 11.6, and Chap. 16.

12.5.7 Measurements and Data of $\rho(xxx)$, $Q(xxx)$ and Shower Energy Loss Spectra

Since the deep water Cherenkov detectors had been used in the past exclusively at Haverah Park,[6] genuinely measured energy loss spectra of air showers are presently

[6] A Haverah Park type deep water Cherenkov detector had been used at Akeno/AGASA for comparison with scintillation detectors.

available only from this installation.[7] However, several authors have converted standard shower size spectra obtained by other large arrays to energy loss spectra for reasons of comparison and for cross checking the properties of derived primary energy spectra, and likewise using the Cherenkov photon densities of the large air Cherenkov installation at Yakutsk.

Typical energy loss spectra for different zenith angle intervals are shown in Fig. 12.45 (Hollows et al., 1969). They can all be fitted by a simple power law of the form

$$I(>E_{100}, \overline{X}) \;=\; I_{15}(\overline{X}) \left(\frac{E_{100}}{10^{15}} \right)^{-\gamma} \quad [\mathrm{m}^{-2}\,\mathrm{s}^{-1}\,\mathrm{sr}^{-1}], \tag{12.44}$$

where $\overline{X}$ is the mean atmospheric depth corresponding to a particular zenith angle interval, $I_{15}(\overline{X})$ is the intensity of showers with $E_{100} > 10^{15}$ eV, valid for the energy range indicated in Fig. 12.45, and γ is the slope of the integral energy loss spectrum. Figure 12.46 shows an analogous spectrum for near vertically incident showers by the same authors and in addition the corresponding spectra from Chacaltaya and Vlocano Ranch (Bradt et al., 1965; Linsley, 1963b).

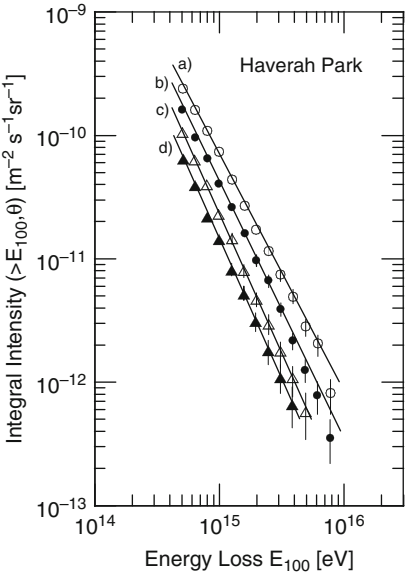

Fig. 12.45 Integral intensity E_{100} energy loss spectra for zenith angle intervals (*a*) $0^\circ \le \theta \le 20^\circ$, (*b*) $20^\circ \le \theta \le 30^\circ$, (*c*) $30^\circ \le \theta \le 35^\circ$, and (*d*) $35^\circ \le \theta \le 40^\circ$ (Hollows et al., 1969)

[7] The Auger experiment employs 1,600 deep water Cherenkov detectors and is expected to publish similar shower data.

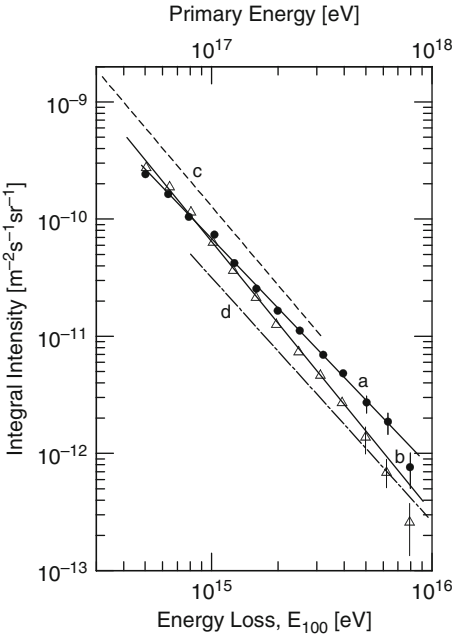

Fig. 12.46 Integral intensity E_{100} energy loss spectra for near vertical showers obtained by using a median exponent with and without energy loss dependence of the exponent γ, • (*line a*) and △ (*line b*), respectively (Hollows, 1968; Hollows et al., 1969). The figure also shows the Chacaltaya (*line c*, Bradt et al., 1965) and Volcano Ranch (*line d*, Linsley, 1963b) primary energy spectra. (See also Suri, 1965)

Figure 12.47 shows zenith angle distributions for energy loss intervals as specified in the caption and Fig. 12.48 the variation of the median exponent $m(E_{100}, \theta)$ as a function of energy loss E_{100} for different zenith angle intervals (Hollows et al., 1969).

In Fig. 12.49 we present the results obtained by Brooke et al. (1979). Note that the ordinate is multiplied by the density to the third power to compress the plot and to emphasize the change of slope of the spectrum (a slight decrease) beyond the density $\rho(600) \geq 13.6\,\mathrm{m}^{-2}$, showing as a rise in this representation. Thus, two different exponents are required to describe this spectrum.

In addition the authors also show separate spectra for two different zenith angle intervals, as indicated. The ground parameter $\rho(600)$ had been used for this work, i.e., the energy loss density at a core distance of 600 m. Various problems inherent to the method are discussed by Brooke et al. (1979) and in earlier papers of the Leeds and Nottingham groups.

Earlier results showing the differential ground parameter $\rho(600)$ spectrum of showers recorded with the Haverah Park installation by Edge et al. (1973a) are reproduced in Fig. 12.50. An approximate energy spectrum is indicated at the top

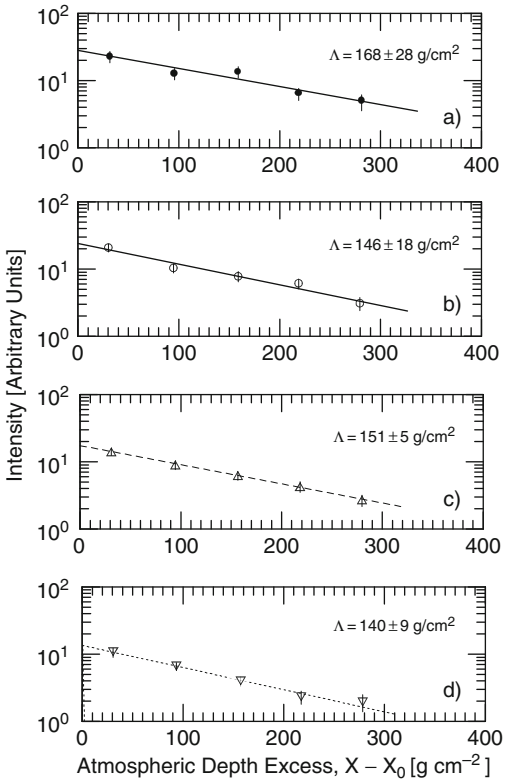

Fig. 12.47 Zenith angle distributions in the form of atmospheric depth excess for E_{100} energy loss intervals (**a**) $8 \cdot 10^{14}$–10^{15} eV, (**b**) 10^{15}–$1.3 \cdot 10^{15}$ eV, (**c**) $1.3 \cdot 10^{15}$–$2 \cdot 10^{15}$ eV and (**d**) $> 2 \cdot 10^{15}$ eV. The depth excess is defined as $X - X_0$, where $X = X_0 \sec(\theta)$ and $X_0 = 1016\,\mathrm{g\,cm^{-2}}$ (Hollows et al., 1969)

of the figure. The flattening of this spectrum is also evident beyond $\rho(600) \simeq 50$, yet not so apparent because of the different representation. Two integral $\rho(600)$ spectra are shown in Fig. 12.51 for different zenith angle intervals, after Andrews et al. (1971). Again the flattening of the spectrum is evident, yet statistics is poor beyond an estimated primary energy of 10^{19} eV.

Similar data from the large array at Yakutsk, taken at core distances of 300, 400 and 500 m, are presented in Fig. 12.52 (Dyakonov et al., 1979). However, the particle densities are determined with scintillation detectors in place of deep water Cherenkov detectors but also expressed in terms of vertical equivalent muons per square meter. A $\rho(600)$ integral spectrum obtained by the same authors and plotted in the same manner as the one in Fig. 12.49, except that the ordinate is multiplied by the density to the power of two, is shown in Fig. 12.53. These two graphs can be compared directly.

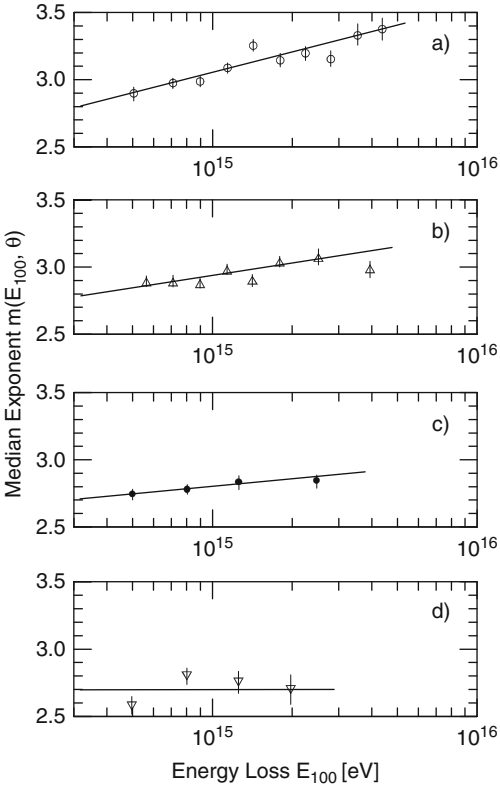

Fig. 12.48 Variation of the median exponent $m(E_{100}, \theta)$ with energy loss E_{100} for zenith angle intervals (**a**) $0^\circ \leq \theta \leq 20^\circ$, (**b**) $20^\circ \leq \theta \leq 30^\circ$, (**c**) $30^\circ \leq \theta \leq 35^\circ$ and (**d**) $35^\circ \leq \theta \leq 40^\circ$ (Hollows et al., 1969)

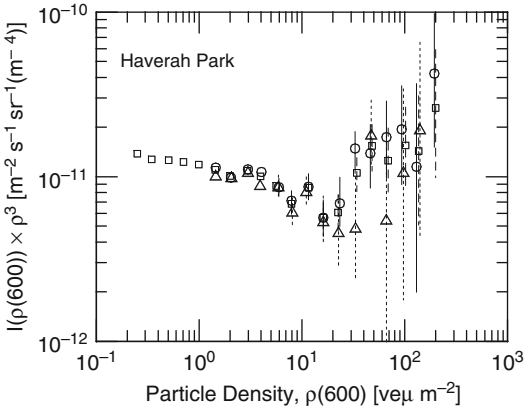

Fig. 12.49 Differential energy loss spectra in terms of $\rho(600)$ density spectra at fixed core distance of 600 m, derived from a total of 3,345 showers recorded at Haverah Park (Brooke et al., 1979). The three different symbols represent spectra obtained for three different zenith angle ranges: △, $\theta > 45^\circ$; ○, $\theta < 45^\circ$; □, $\theta < 60^\circ$. The so-called ground parameter $\rho(600)$, defined in the text, is expressed in vertical equivalent muons per square meter (veμ m^{-2}). (For earlier Haverah Park spectra see Cunningham et al., 1977). Note that the ordinate is multiplied by the density to the 3rd power, ρ^3

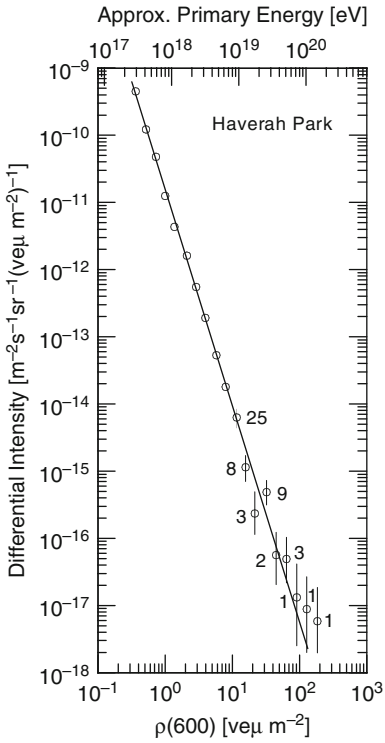

Fig. 12.50 Differential density spectrum, $\rho(600)$ [veμ m^{-2}], normalized to a zenith angle of 13°, recorded at Haverah Park (Edge et al., 1973a, b). The actual measurements include zenith angles θ up to 60°. The numbers attached to the *lower data points* indicate the number of showers upon which each point is based. A comparison of this spectrum with the corresponding muon size spectrum obtained by the Sydney group is presented in Fig. 12.28 of Sect. 12.3 of this chapter

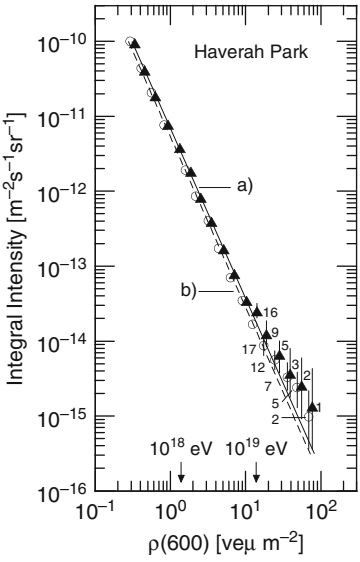

Fig. 12.51 Integral density spectra at a fixed core distance of 600 m, $\rho(600)$, recorded at Haverah Park for two zenith angle ranges; ▲, $\theta < 30°$ (2,371 events); ○, $\theta < 60°$ (1,323 events). (Andrews et al., 1971). *Lines* (*a*) and (*b*) indicate two power law spectra with exponents $\gamma = 2.30 \pm 0.04$ and $\gamma = 2.28 \pm 0.04$, respectively. The numbers attached to the *lower data points* refer to the integral number of showers recorded

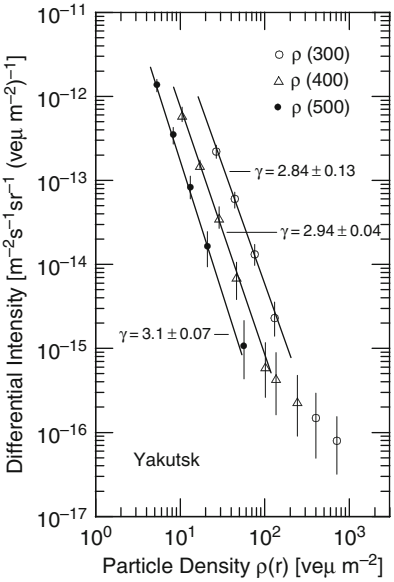

Fig. 12.52 Differential density spectra at fixed core distances, $\rho(r)$, with $r = 300$, 400 and 500 m of 137 showers with $N \geq 10^8$ particles and zenith angles $\theta \leq 30^\circ$, obtained with the Yakutsk array during the period from 1970 to 1971 (Dyakonov et al., 1979)

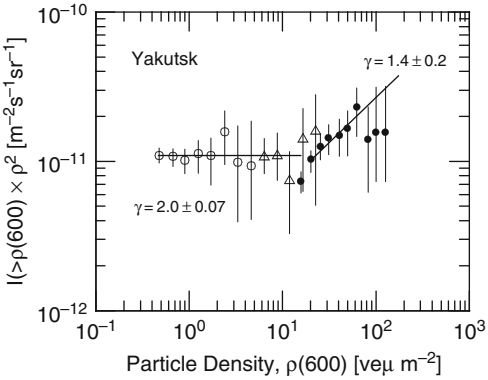

Fig. 12.53 Integral density spectrum, $\rho(600)$, for showers with zenith angles $\theta \leq 30^\circ$ (○, △) and $\theta \leq 60^\circ$ (•), recorded at Yakutsk from November 1976 to January 1977. The spectrum is reduced to vertical incidence, using a shower absorption length $\Lambda^*_{600} = 400$ g cm^{-2} in equation 12.46 (Dyakonov et al., 1976, 1979; Krasilnikov et al., 1977). Note that the ordinate is multiplied by the density squared

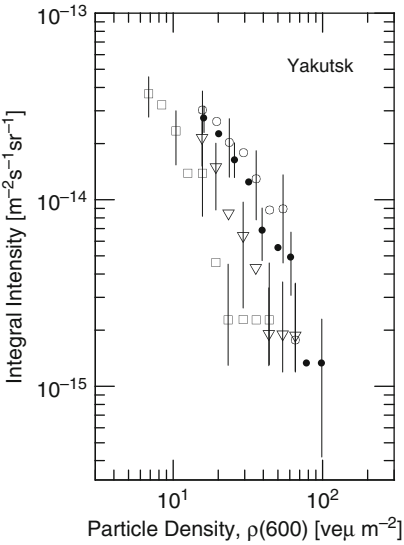

Fig. 12.54 Integral density spectrum, $\rho(600)$, obtained at Yakutsk for three different zenith angle ranges: •, $0° \div 30°$; ○, $30° \div 45°$; △, $45° \div 60°$. The fourth set of data points, □, represent the reduction of the data to an atmospheric depth of 1,020 g cm^{-2}, using the expression given in the text (Sect. 12.5.8, Eq. 12.51) (Krasilnikov et al., 1977)

Figure 12.54 shows a compilation of integral $\rho(600)$ distributions recorded at Yakutsk with scintillation detectors at three different zenith angle intervals, and the reduced data for a vertical atmospheric depth of $X_0 = 1020\,\mathrm{g\,cm^{-2}}$.

Differential and integral Cherenkov photon density spectra obtained at Yakutsk for a core distance of 400 m are shown in Figs. 12.55a, b, respectively. Displayed is the intensity of events as a function of $Q(400)$. The ordinates are displayed in compressed form and emphasize the rising trend beyond $Q(400) \geq 10^8$ photons m^{-2}, as stated in the caption (Dyakonov et al., 1979; see also Krasilnikov et al., 1977).

12.5.8 Mathematical Expressions and Fits

(a) Absorption Length of $\rho(600)$ and Zenith Angle Relationship

Assuming an exponential absorption of showers in the atmosphere over the depth range corresponding to the extremes of inclination, the values of $\rho(600)$ observed at Haverah Park by Edge et al. (1973a) for showers generated by primaries of the same energy but incident at different zenith angles θ are related by the expression

$$\rho(600)(\theta)\exp\left(\frac{1018}{\Lambda^*}\sec(\theta)\right) = \text{constant}, \tag{12.45}$$

where Λ^* is the absorption length as defined above (Eq. 12.43). A value of 1,018 g cm^{-2} was inserted for the atmospheric depth of Haverah Park.

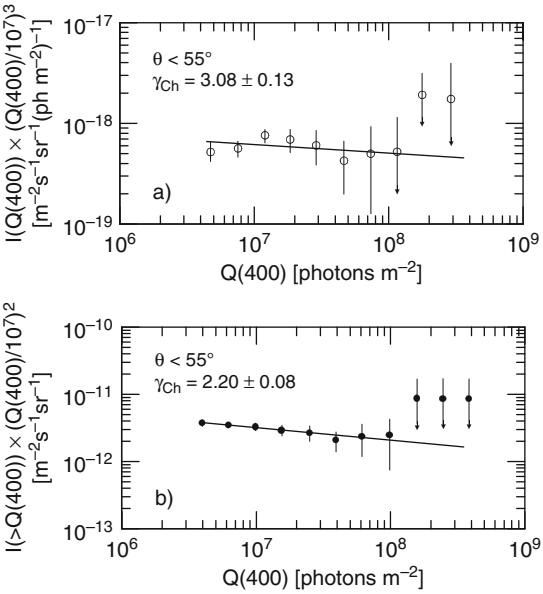

Fig. 12.55 Differential, ○, and integral, ●, Cherenkov light density spectra at fixed core distance of 400 m, recorded at Yakutsk in the period from December 1973 to March 1977 (Dyakonov et al., 1979). γ_{Ch} represents the slope of the respective spectrum

To reduce the shower integral density spectrum for a given atmospheric depth $\rho(600)(X)$ to the depth X_0, the following expression is given by Krasilnikov et al. (1977).

$$\rho(600)(X_0) \;=\; \rho(600)(X)\exp\left(\frac{X - X_0}{\Lambda^*(600)}\right), \tag{12.46}$$

where $\Lambda^*(600) = 400\,\mathrm{g\,cm^{-2}}$ for zenith angles $\theta \le 45^\circ$ and $650\,\mathrm{g\,cm^{-2}}$ for $45^\circ \le \theta \le 60^\circ$.

(b) Cherenkov Density Spectra $Q(400)$

For the Cherenkov density spectrum the Yakutsk group gives the following relation that fits their experimental data (Dyakonov et al., 1979).

$$I(>Q(400)) \;=\; (3.2 \pm 0.2)10^{-12}\left(\frac{Q(400)}{10^7}\right)^{-(2.20\pm0.08)} \quad [\mathrm{m^{-2}\,s^{-1}\,sr^{-1}}]. \tag{12.47}$$

This expression is valid for the following range of $Q(400)$,

$$4 \cdot 10^6 \;\le\; Q(400) \;\le\; 10^8 \;\; [\mathrm{photons\,m^{-2}}]. \tag{12.48}$$

(c) Energy Loss Spectra $\rho(600)$

One of the first energy loss density spectra was presented by Andrews et al. (1970b). In a later publication these authors give a slightly modified expression (Andrews et al., 1971). It is for the zenith angle range $0^\circ \leq \theta \leq 30^\circ$ and has the form

$$I(>\rho(600)) \;=\; (5.7 \pm 0.1)10^{-12}(\rho(600))^{-(2.30 \pm 0.04)} \;\; [\mathrm{m}^{-2}\,\mathrm{s}^{-1}\,\mathrm{sr}^{-1}]. \qquad (12.49)$$

A slightly different and somewhat more recent relation for showers subtending zenith angles $\theta \leq 60^\circ$ is given by Edge et al. (1973a), who claim to get a good fit to the integral energy loss spectrum at 600 m from the shower axis,

$$I(>\rho(600)) \;=\; (6.1 \pm 0.1)10^{-12}(\rho(600))^{-(2.22 \pm 0.02)} \;\; [\mathrm{m}^{-2}\,\mathrm{s}^{-1}\,\mathrm{sr}^{-1}]. \qquad (12.50)$$

This function also describes the spectrum of Edge et al. (1973a), shown in Fig. 12.50.

The Yakutsk group obtained the following expression as best fit to represent their vertical integral density spectrum at 600 m (Krasilnikov et al., 1977).

$$I(>\rho(600)(X_0)) = (2.25 \pm 0.45)10^{-14}\left(\frac{\rho(600)X_0}{20}\right)^{-(1.44 \pm 0.20)} \;\; [\mathrm{m}^{-2}\,\mathrm{s}^{-1}\,\mathrm{sr}^{-1}]\,. \qquad (12.51)$$

(d) Lateral Distribution Functions

For the integration of the density distribution a lateral distribution function is required. It can be written as

$$\rho(r) \;=\; kf(r) \qquad (12.52)$$

where $\rho(r)$ is the observed energy loss density (energy absorption signal per unit area), usually expressed in vertical equivalent muons per square meter [veμ m^{-2}], as defined in Sect. 12.5.3, k is a constant determined by the shower size parameter, and $f(r)$ is the lateral distribution function.

Some authors have used purely empirical expressions, others functions predicted by model calculations. Andrews et al. (1971) have used the following function which can be fitted over a wide range of distances,

$$f(r) \;=\; \left(\frac{1}{r}\right)\left(1 - \frac{r}{r_0'}\right)^{-(\eta'-1)}. \qquad (12.53)$$

Here η' and r_0' depend on the zenith angle and must be fitted. A value of $r_0' = 243$ m, independent of zenith angle, and $\eta' = 4.51$ give a good fit for vertical showers.[8]

[8] r_0' is a Molière-like unit for Haverah Park deep water Cherenkov detectors.

On the other hand, Edge et al. (1973a) have used a function of the form

$$f(r) \;=\; r^{-[\eta+(r/r_0)]} \tag{12.54}$$

to describe the lateral distribution. With suitable values for η and r_0 this function fits the empirical data well in the distance range $50\,\mathrm{m} \leq r \leq 1500\,\mathrm{m}$ from the shower axis. η is again a function of the zenith angle and can be well represented by (see Sect. 8.10 and Sect. 10.2.2)

$$\eta \;=\; 3.78 - 1.44\sec(\theta). \tag{12.55}$$

Values for $r_0 = 4000\,\mathrm{m}$ and $\eta = 2.3$ yield good density distributions for vertical showers over the range of primary energies explored by these authors from $5 \cdot 10^{17}$ to $5 \cdot 10^{19}$ eV.

(e) Relation between Energy Loss Density and Cherenkov Density

Krasilnikov et al. (1977) give the following expression for the relationship between the energy loss density at a core distance of 600 m, $\rho(600)$ [veμ m^{-2}], and the Cherenkov photon density at core distance of 400 m, $Q(400)$ [ph m^{-2}], for vertically incident showers at Yakutsk at atmospheric depth $X_0 = 1020\,\mathrm{g\,cm}^{-2}$,

$$\rho(600)(\theta = 0^\circ) \;=\; (3.2 \pm 1.0)\left(\frac{Q(400)}{10^7}\right)^{0.85\,\pm\,0.05} \quad [\mathrm{m}^{-2}]. \tag{12.56}$$

The relations of $\rho(xxx)$ and $Q(xxx)$ to primary energy are discussed in Sect. 10.2 and 16.2, respectively.

f) Concept of Air Shower Universality

The concept of *air shower universality* emerged initially from cascade theory, expressing the similarity of all showers in a broad sense, and allowed to describe showers in terms of the primary energy and the shower age. In the early seventies of the last century the idea was extended by Hillas (1970), who noticed on the basis of air shower simulations that in hadron induced showers of fixed total primary energy the response of deep water Cherenkov detectors located at moderate core distance exhibits only a weak primary mass dependence, and could therefore be used as a measure of the primary energy.

More recently, Chou et al. (2005) and Schmidt et al. (2007) revisited the topic and investigated the concept further theoretically, considering correlations of various shower observables. They arrived at the conclusion that universality appears to establish a model independent converter of ground level detector signal to primary energy.

References

Abu-Zayyad, T., et al.: PICRC, 5, p. 349 (1999).
Acharya, B.S., et al.: PICRC, 9, p. 162 (1981).
Aglietta, M., et al.: Nuovo Cim. C, 9, p. 262 (1986).
Aglietta, M., et al.: Astropart.Phys., 10, p. 1 (1999).
Aguirre, C., et al.: PICRC, 8, p. 213 (1977).
Aguirre, C., et al.: J. Phys. G, 5, p. 151 (1979).
Amenomori, M., et al.: Nucl. Instr. Meth. A, 288, p. 619 (1990).
Amenomori, M., et al.: PICRC, 5, p. 249 (1997).
Amenomori, M., et al., Tibet Collaboration: PICRC, 4, p. 211 (2005).
Andrews, D., et al.: Acta Phys. Acad. Sci. Hung., 29, S3, p. 337 (1970a).
Andrews, D., et al.: Acta Phys. Acad. Sci. Hung., 29, S3, p. 343 (1970b).
Andrews, D., et al.: PICRC, 3, p. 995 (1971).
Antoni, T., et al.: Astropart. Phys., 19, p. 703 (2003a).
Antoni, T., et al.: Nucl. Instr. Meth. A, 513, p. 490 (2003b).
Antonov, R.A., et al.: PICRC, 2, p. 96 (1960).
Antonov, R.A., et al.: Sov. Phys. JETP, 18, p. 1279 (1964a).
Antonov, R.A., et al.: Sov. Phys. JETP, 19, p. 20 (1964b).
Antonov, R.A., et al.: Trudi FIAN, 26, p. 142 (1964c) (in Russian).
Antonov, R.A., et al.: PICRC, 6, p. 2194 (1971).
Antonov, R.A., et al.: Yadernaya Fiz. 18, p. 554 (1973) (in Russian).
Antonov, R.A., et al.: Sov. J. Nucl. Phys., 18, p. 285 (1974).
Antonov, R.A., et al.: PICRC, 8, p. 137 (1977).
Arqueros, F., et al., HEGRA-Collaboration: Astron. Astrophys., 359, p. 682 (2000).
Asakimori, K., et al.: PICRC, 8, p. 247 (1979).
Asakimori, K., et al.: J. Phys. Soc. Jpn., 51, p. 2059 (1982).
Aseikin, V.S., et al.: PICRC, 6, p. 2152 (1971).
Ashton, F., et al.: PICRC, 4, p. 2489 (1973).
Ashton, F., and A. Parvaresh: PICRC, 8, p. 2719 (1975).
Ashton, F., et al.: PICRC, 8, p. 2831 (1975).
Auger, P.: Comptes Rendus Acad. Sci. Paris, 207, p. 907 (1938). (in French).
Auger, P., and J. Daudin: J. de Phys. et Radium, 6, p. 233 (1945). (in French).
Ave, M., et al.: Astropart. Phys., 19, p. 47 (2003).
Bacci, C., et al., ARGO-YBJ Collaboration: Nucl. Instr. Meth. A, 443, p. 342 (2000).
Bagge, E.R., et al.: PICRC, 12, p. 24 (1977).
Bell, C.J., et al.: PICRC, 3, p. 989 (1971).
Bell, C.J.: Ph. D. Thesis University of Sydney, Australia (1974).
Bell, C.J., et al.: J. Phys. A, 7, p. 990 (1974).
Bell, C.J.: J. Phys. G, 2, p. 867 (1976).
Bertaina, M., et al.: PICRC, 2, p. 792 (2001).
Bhat, C.L., et al.: PICRC, 8, p. 508 (1977).
Biehl, A. T., and H. V. Neher: Phys. Rev., 83, p. 1169 (1951).
Blake, P.R., et al.: J. Phys. G, 4, p. 617 (1978a).
Blake, P.R., et al.: J. Phys. G, 4, p. 597 (1978b).
Blake, P.R., and C.G. Saltmarsh: PICRC, 8, p. 76 (1979).
Blümer, J.: The Pierre Auger Collaboration. Frontiers of Cosmic Ray Science, Universal Academic Press, Inc., Tokyo (Japan), PICRC, 8, p.361 (2003).
Böhm, E.: PICRC, 8, p. 29 (1977).
Böhm, E. and E. Steinmann: PICRC, 8, p. 294 (1979).
Boothby, K., et al.: PICRC, 3, p. 444 (1995).
Boothby, K., et al.: Nucl. Phys. B (Proc. Suppl.), 52 B, p. 166 (1997).
Borione, A., et al.: N.I.M. A, 346, p. 329 (1994).

Bradt, H., et al.: PICRC, 2, p. 715 (1965).
Broadbent, D., et al.: Proc. Phys. Soc. A, 63, p. 864 (1950).
Brooke, G., et al.: PICRC, 8, p. 13 (1979).
Brown, W.W., and A.S. McKay: Phys. Rev., 76, p. 1034 (1949).
Brownlee, R.G., et al.: Can. J. Phys., 46, p. 259 (1968).
Brownlee, R.G., et al.: Acta Phys. Acad. Scie. Hung., 29, S3, p. 651 (1970).
Büscher, W.D.: Thesis, University of Kiel, Germany (1971).
Cao, Z., ARGO Collaboration: PICRC, 5, p. 299 (2005).
Cassidy, M., et al.: PICRC, 5, p. 189 (1997).
Catz, Ph., et al.: PICRC, 12, p. 4329 (1975).
Chiba, N., et al.: ICRR Report 249-91-18 (July 1991).
Chiba, N., et al.: Nucl. Instr. Meth. A, 311, p. 338 (1992).
Chilingarian, A., et al.: PICRC, 1, p. 240 (1999).
Chou, A.S., et al.: PICRC, 7, p. 319 (2005).
Clark, G., et al.: Nuovo Cim., Suppl. 8, p. 623 (1958).
Clark, G.W., et al.: Phys. Rev., 122, p. 637 (1961).
Clay, R.W., and P.R. Gerhardy: J. Phys. G, 6, p. 909 (1980).
Cocconi, G., et al.: Nuovo Cim. 1, p. 314 (1943).
Cocconi, G., et al.: Nuovo Cim. 2, p. 14 (1944).
Cocconi, G., et al.: Phys. Rev., 70, p. 841 (1946).
Cocconi, G., and V. Cocconi Tongiorgi: Phys. Rev., 75, p. 1058 (1949).
Cocconi, G.: Handbuch der Physik, S. Flügge, ed., Kosmische Strahlung, XLVI/I, Extensive Air Showers, p. 215, Springer Verlag, Berlin (1961).
Cronin, J.W.: Nucl. Phys. B (Proc. Suppl.), 97, p. 3 (2001a).
Cronin, J.W.: Highlight Lecture, 27th. International Cosmic Ray Conference, Hamburg, Germany, Rapporteur and Highlight Papers, p. 234 (2001b).
Cunningham, G., et al.: PICRC, 2, p. 303 (1977).
Danilova, T.V., et al.: PICRC, 8, p. 129 (1977).
Daudin, J.: Comptes Rendus Acad. Sci. Paris, 216, p. 483 (1943). (in French).
Daudin, J.: Comptes Rendus Acad. Sci. Paris, 218, p. 882 (1944). (in French).
Daudin, J.: J. de Phys. et Radium, 8, p. 301 (1947). (in French).
Daudin, A., and J. Daudin: J. Atmos. Terr. Phys., 3, p. 245 (1953a). (in French).
Daudin, A., and J. Daudin: Bagneres-de-Bigorre Conf. J. Phys. Radium 14 ,p. 169 (1953b). (in French).
Dawson, B.R., Telescope Array Collaboration: PICRC, pre-conference edition, paper 0976, Merida, Mexico (2007).
D'Ettorre-Piazzoli, B., ARGO Collaboration: PICRC, 2, p. 373 (1999).
Diminstein, O.S., et al.: PICRC, 12, p. 4325 (1975).
Diminstein, O.S., et al.: PICRC, 8, p. 154 (1977).
Diminstein, O.S., et al.: PICRC, 8, p. 122 (1979).
Dixon, H.E., and K.E. Turver: Proc. R. Soc. A, 339, p. 171 (1974).
Dixon, H.E., et al.: Proc, R. Soc. A, 339, p. 133 (1974a).
Dixon, H.E., et al.: Proc. R. Soc. A, 339, p. 157 (1974b).
Dixon, H.E., et al.: J. Phys. A, 7, p. 1010 (1974c).
Dyakonov, M.N., et al.: PICRC, 4, p. 2384 (1973).
Dyakonov, M.N., et al.: Izv. AN SSSR, ser. fiz., 38, p 999 (1974).
Dyakonov, M.N., et al.: V sbornike "Kharakteristiki ShAL kosmicheskikh luchei sverhvysokikih energii", Yakutsk, 87 (1976).
Dyakonov, M.N., et al.: PICRC, 8, p. 168 (1979).
Edge, D.M., et al.: J. Phys. A, 6, p. 1612 (1973a).
Edge, D.M., et al.: PICRC, 4, p. 2513 (1973b).
Efimov, N.N., and V.F. Sokurov: PICRC, 8. p. 152 (1979).
Efimov, N.N., and V.F. Sokurov: PICRC, 2. p. 123 (1983).

Egorov, T.A., et al.: PICRC, 6, p. 2059 (1971a).
Egorov, T.A., et al.: PICRC, 6, p. 2164 (1971b).
England, C.D., et al.: PICRC, 8, p. 88 (1979).
Escobar, I., et al.: PICRC, 4, p. 168 (1963).
Firkowski, R., et al.: PICRC, 2, p. 694 (1965).
Firkowski, R., et al.: PICRC, 4, p. 2605 (1973).
Fomin, Y.A., et al.: PICRC, 2, p. 85 (1991).
Fowler, J.W., et al.: Astropart. Phys., 15, p. 49 (2001).
Fukui, S., et al.: Progr. Theor. Phys. Jpn., 16, p. 1 (1960).
Fukushima, M., et al.: PICRC, pre-conference edition, paper 0955, Merida, Mexico (2007).
Gerdes, C., et al.: PICRC, 1, p. 219 (1973).
Gerdes, C., et al.: PICRC, 8, p. 3040 (1975).
Gerhardy, P.R., et al.: PICRC, 11, p. 305 (1981).
Glasstetter, R., KASCADE Collaboration: PICRC, 6, p. 157 (1997).
Glasstetter, R., et al.: PICRC, 1, p. 222 (1999).
Glushkov, A.V., et al.: Preprint YaFAN, Yakutsk (1978).
Glushkov, A.V., et al.: PICRC, 8, p. 158 (1979).
Greisen, K.: Progress in Cosmic Ray Physics, North-Holland Publishing Co, Amsterdam, Vol. 3, p. 1 (1956).
Greisen, K.: Annual Review of Nuclear Science, Annual Reviews, Inc., Palo Alto, CA, USA, Vol 10, p. 63 (1960).
Greisen, K.: Ann. Rev. Nucl. Sci., 10, p. 63 (1968).
Grieder, P.K.F.: Rivista del Nuovo Cim., 7, p. 1 (1977).
Gross, B: Zeitschr. f. Physik, 83, p. 214 (1933).
Gupta, S., et al.: Nucl. Instr. Meth., A 540, p. 311 (2005).
Hara, T., et al.: PICRC, 8, p. 135 (1979a).
Hara, T., et al.: PICRC, 13, p. 148 (1979b).
Hara, T., et al.: PICRC, 13, p. 154 (1979c).
Hara, T., et al.: PICRC, 11, p. 250 (1981).
Hartman, D.H., et al.: PICRC, 8, p. 233 (1977).
Hartman, D.H., et al.: Nuovo Cim., 51 A, p. 131 (1979).
Hatano, Y., et al.: PICRC, 11, p. 161 (1979).
Haungs, A., et al.: Rep. Prog. Phys., 66, p. 1145 (2003).
Hayashi, Y., et al.: PICRC, 1, p. 236 (1999).
Hayashi, Y., et al.: Nucl. Instr. Meth., A 545, p. 643 (2005).
Hillas, A.M., et al.: Acta Phys. Acad. Scie. Hung., 29, S3, p. 533 (1970).
Hillas, A.M., et al.: PICRC, 3, p. 1001 (1971a).
Hillas, A.M., et al.: PICRC, 3, p. 1007 (1971b).
Hillberry, N.: Phys. Rev., 60, p. 1 (1941).
Hlavac, T., et al.: Acta Phys. Acad. Scie. Hung., 29, S1, p. 521 (1970).
Hodson, A. L.: Proc. Phys. Soc. A, 66, p. 49 (1953).
Hollows, J.D.: Ph.D. Thesis, University of Leeds, England, UK (1968).
Hollows, J.D., et al.: J. Phys. A, 2, p. 591 (1969).
Honda, K., et al.: PICRC, 1, p. 141 (2001).
Horton, L., et al.: PICRC, 6, p. 124 (1983).
Hudson, D.E.: Thesis, Cornell University, Ithaca, NY, USA (1950).
Ise, J., Jr., and W.B. Fretter: Phys. Rev., 76, p. 933 (1949).
Ivanov, A.A., et al.: Paper presented at the IV. European Symposium on Cosmic Rays, Lodz, Poland (1974).
Ivanov, A.A., et al.: PICRC, 9, p. 132 (1979).
Keck, J.C. and K. Greisen: Proc. Echo Lake Cosmic Ray Conf. (1949).
Kerschenholz, I.M., et al.: PICRC, 4, p. 2507 (1973).
Khristiansen, G.B., et al.: PICRC, 2, p. 799 (1965).

Khristiansen, G.B.: i dr. Kosmicheskoe izluchenie sverhvysokoi energii. M., Atomizdat, p. 256 (1975).
Khristiansen, G.B., et al.: PICRC, 9, p. 67 (1979a).
Khristiansen, G.B., et al.: PICRC, 8, p. 365 (1979b).
Kirov, I.N., et al.: PICRC, 2, p. 109 (1981).
Krasilnikov, D.D., et al.: PICRC, 12, p. 4347 (1975).
Krasilnikov, D.D., et al.: PICRC, 8, p. 159 (1977).
Kraybill, H.L.: Phys. Rev., 76, p. 1092 (1949).
Kraybill, H.L.: Phys. Rev., 86, p. 590 (1952).
Kraybill, H.L.: Phys. Rev., 93, p. 1360 (1954a).
Kraybill, H.L.: Phys. Rev., 93, p. 1362 (1954b).
Kulikov, G.V., and G.B. Khristiansen: Zh. Eksper. Teor. Fiz., 35, p. 635 (1958) (in Russian).
Kulikov, G.V., and G.B. Khristiansen: Sov. Phys. JETP, 35(8), p. 441 (1959).
Kulikov, G.V., et al.: PICRC (Moscow 1959), 2, p. 85 (1960).
La Pointe, M., et al.: Can. J. Phys., 46, p. 68 (1968).
Landau, L.D., and I.Ya. Pomeranchuck: Doklady Akad. Nauk., SSSR, 92, p. 535 (1953a).
Landau, L.D., and I.Ya. Pomeranchuck: Doklady Akad. Nauk., SSSR, 92, p. 735 (1953b).
Lapp, R. E.: Phys. Rev., 64, p. 129 (1943).
Lapp, R. E.: Phys. Rev., 69, p. 321 (1946).
Lillicrap, S.C., et al.: Proc. Phys. Soc., 82, p. 95 (1963).
Linsley, J.: PICRC, 4, p. 295 (1963a).
Linsley, J.: PICRC, 4, p. 77 (1963b).
Linsley, J.: PICRC, 5, p. 3207 (1973).
Loverdo, A., and J. Daudin: J. de Phys. et Radium, 9, p. 134 (1948).
Machavariani, S.K., et al.: PICRC, 8, p. 240 (1979).
Makhmudov, B.M., et al.: Izv. Akad. Nauk SSSR, Ser. Fiz., 40, p. 1001 (1975).
Makhmudov, B.M., and R.I. Sharibdzhanov: PICRC, 8, p. 496 (1977).
Matthews, J.: Rapporteur Paper, PICRC, 10, p. 281 (2005).
Maze, R., et al.: Phys. Rev., 73, p. 418 (1948).
McCaughan, J.B.T., et al.: PICRC, 2, p. 720 (1965a).
McCaughan, J.B.T., et al.: Nuovo Cim., 38, p. 697 (1965b).
McCusker, C.B.A., and M.M. Winn: J. Phys. G, 5, p. 159 (1979).
Migdal, A.B.: Phys. Rev., 103, p. 1811 (1956).
Milone, C.: Nuovo Cim., 9, p. 549 (1952).
Mirzoyan, R., MAGIC Collaboration: PICRC, 4, p. 23 (2005).
Miura, I., and H. Hasegawa: J. Phys. Soc. Jpn., 17, Suppl. A-III, p. 84 (1962).
Misaki, A.: Nucl. Phys. B (Proc. Suppl), 33AB, p. 192 (1993).
Miyake, S., et al.: PICRC, 13, p. 171 (1979).
Molière, G.: Vorträge über Kosmische Strahlung, 2. Auflage (in German), W. Heisenberg, ed., Springer, Berlin, p. 446 (1953a).
Molière, G.: Cosmic Radiation, by W. Heisenberg, ed., 2nd ed., Springer, Berlin (1953b).
Nagano, M.: CRL-Hokoku 20-76-4, p. 57 (1976) (in Japanese).
Nagano, M., et al.: J. Phys. G, 10, p. 1295 (1984).
Nagano, M., et al.: J. Phys. G, 18, p. 423 (1992).
Navarra, G., EAS-TOP Collaboration: Nucl. Phys. B (Proc. Suppl.), 60B, p. 105 (1998).
Navarra, G., et al.: Nucl. Instr. Meth. A, 518, p. 207 (2004).
Navarra, G.: Nucl. Phys., B (Proc. Suppl.), 151, p. 79 (2006).
Nesterova, N.M., et al.: PICRC, 2, p. 748 (1995).
Ogio, S., et al.: Astrophys. J., 612, p. 268 (2004).
Ohta, K., et al.: PICRC, 13, p. 177 (1979).
Prescott, J.R.: Proc. Phys. Soc. London, A, 69, p. 870 (1956).
Protheroe, R.J., and J.R. Patterson: J. Phys. G, 10, p. 841 (1984).
Rada, W.S., et al.: PICRC, 8, p. 13 (1977).

Risse, M., and D. Heck: Astropart. Phys., 20, p. 661 (2004).
Samorski, M., and W. Stamm: Astrophys. J., 268, p. L17 (1983a).
Samorski, M., and W. Stamm: PICRC, 1, p. 135 (1983b).
Schmidt, F., et al.: PICRC, pre-conference edition, paper 752, Merida, Mexico (2007).
Singer, S.F.: Phys. Rev., 81, p. 579 (1951).
Stamenov, J.N., et al.: Trudy Fian, SSSR, 109, p. 132 (1979).
Suomijärvi, T., et al., Auger Collaboration: PICRC, pre-conference edition, paper 0299, Merida, Mexico (2007).
Suri, A.N.: PICRC, 2, p. 751 (1965).
Suri, A.: Can. J. Phys., 46, p. 13 (1968).
Swinson, D.B., and J.R. Prescott: PICRC, 2, p. 721 (1965).
Swinson, D.B., and J.R. Prescott: Can. J. Phys., 46, p. 292 (1968).
Swordy, S.P., and D.B. Kieda: Astropart. Phys., 13, p. 137 (2000).
Tennent, R.M.: Proc. Phys. Soc., 92, p. 622 (1967).
Tennent, R.M.: Can. J. Phys., 46, p. 1 (1968).
Treat, J.E., and K.I. Greisen: Phys. Rev., 74, p. 414 (1948).
Tsunesada, Y., et al.: PICRC, pre-conference edition, paper 0820, Merida, Mexico (2007).
van Buren, J., et al.: PICRC, 6, p. 301 (2005).
van Staa, R., et al.: J. Phys. A, 7, p. 135 (1974).
Vernov, S.N., et al.: Sov. Phys., JETP, 15, p. 528 (1962a).
Vernov, S.N., et al.: J. Phys. Soc. Jpn., 17, Suppl. A III, p. 118 (1962b).
Vernov, S.N., et al.: Can. J. Phys., 46, p. 197 (1968).
Williams, R.W.: Phys. Rev., 74, p. 1689 (1948).
Yoshida, S., and H. Dai: J. Phys. G, 24, p. 905 (1998).
Yoshida, S.: Rapporteur Papaer, PICRC, 10, p. 297 (2005).
Zatsepin, G. T., et al.: J. Exp. Theor. Phys., 17, p. 1125 (1947).
Zatsepin, G. T., et al.: Izv. Akad. Nauk. SSSR, Ser. Fiz., 17, p. 39 (1953).

Chapter 13
Hadrons

Overview After the introduction we give a brief historic account of the early work on hadrons in air showers, followed by comments on recent work. We outline the relevance and contributions of the experimental work using nuclear emulsion and emulsion chambers as stand-alone experiments and in conjunction with air shower arrays that have vastly increased our knowledge on ultrahigh energy hadronic interactions. Subsequently, we discuss the general properties of the hadronic component of air showers, their lateral distribution, the energy spectrum, temporal properties, and present experimental data from the large modern calorimeters and theoretical results from simulations. These basic subjects are followed by more specific topics, like the charge-to-neutral ratio, the hadron contents and composition in showers, such as antinucleons, pions, kaons and charmed particles, and some miscellaneous topics like multi-core showers, large transverse momentum phenomena and the production height of hadrons. We do not discuss spectra and properties of so-called unaccompanied hadrons, i.e., hadrons that are not directly associated with local air showers.

13.1 Introduction

The first fruitful attempts to demonstrate the presence of hadrons in air showers were made by Brown and McKay (1949), Cocconi (1949), Cocconi et al. (1949), Cocconi-Tongiorgi (1949), Greisen (1949), and Ise and Fretter (1949). These authors investigated the so-called *penetrating* or *hard component* of showers as compared to the *soft* or *electromagnetic component*.[1] Since the hard component contains muons as well, the term *nuclear active particles* (NAP) was introduced to distinguish the strongly interacting particles, the nature of which could not be resolved in these experiments, from the muons. The term hadrons was introduced at a later time. For an early review of this subject the interested reader is referred to the reviews of Greisen (1956, 1960) and the references listed therein.

[1] To separate the soft from the hard component a lead absorber of 20 cm thickness was generally used at that time.

P.K.F. Grieder, *Extensive Air Showers,* DOI 10.1007/978-3-540-76941-5_13,

Hadron measurements in extensive air showers are extremely difficult and require large and costly detectors, nowadays sophisticated calorimeters, in order to obtain reliable and reproducible data. There are at least four major problems one is confronted with when carrying out hadron investigations, namely (a) the particle identification, i.e., to ascertain that the particle under investigation is in fact a hadron,[2] (b) the determination of the hadron energy or momentum, (c) the spatial resolution of the hadron detector, and (d) the specific limitations of the shower array. These problems and associated inadequacies in the determination of relevant observables manifest themselves in the large spread of the early data acquired under comparative conditions from showers of similar size groups in different experiments, as will be evident from the compilations presented below.

13.1.1 Early Work

A large number of experiments had been carried out since the early fifties of the last century to gather basic information on the hadron content in shower cores, on hadron spectra and their properties. Rather remarkable pioneering contributions to the field had been made by the following authors who operated a variety of dedicated hadron detectors, most of them at a different altitude:

In their initial work Heinemann and Hazen (1953) used multi-channel ionization chambers at 280 m a.s.l. and Hazen et al. (1954) a multiplate cloud chamber in combination with thin-walled ionization chambers at Echo Lake, Colorado (3,200 m a.s.l.). At an installation in Moscow (192 m a.s.l.) Goryunov et al. (1960) have used separate common ionization chambers to study the shower phenomenon. Kameda et al. (1960, 1962a, b, 1965) and Matano et al. (1965) had used a multi-plate Wilson cloud chamber at Tokyo (s.l.). Neon hodoscope matrices, initially developed at Tokyo, had been used by Oda and Tanaka (1962) at Tokyo, by Bagge et al. (1965) and Samorski et al. (1965) at Kiel (s.l.), and by van Staa et al. (1974) at Pic du Midi, France (2,860 m). Later on the Tokyo group used spark chambers in place of neon hodoscopes (Matano et al., 1968). Large and tightly packed scintillator arrays measuring 16 and 12 m^2 were used as burst detectors at Sydney (s.l.) (Bray et al., 1964) and Mount Norikura (2,770 m a.s.l., Miyake et al., 1970), respectively.

A 60 m^2 burst detector consisting of a scintillator matrix covered with target material and lead underneath as converter was used by Suga et al. (1962) and Hasegawa et al. (1965) at Mt. Chacaltaya (5,230 m a.s.l.). Chatterjee et al. (1965a, b) used a total absorption scintillation spectrometer (TASS) at Ootacamund (2,200 m a.s.l.), Miyake et al. (1963, 1968, 1970) employed a large multi-plate cloud chamber measuring 2.0 × 0.7 × 1.3 (height) m^3 with 21 Pb plates of thickness 1 cm, and in some cases an up to 2 m thick water target and scintillator combination at

[2] The majority of hadron measurements made in air showers cannot distinguish between the different kinds of hadrons, i.e., nucleons, pions, etc., they usually include all hadrons unless stated otherwise.

Mt. Norikura. Babaian et al. (1965) operated a 10 m^2 ionization calorimeter at Mt. Aragatz (Armenia) at an altitude of 3,250 m a.s.l. and Aseikin et al. (1975) acquired a great wealth of hadron data over a very long period with an ionization calorimeter at Tien Shan (3,340 m a.s.l.) in Kazakhstan. Finally, we should also mention the remarkable combination of scintillators, ionization calorimeter and X-ray film emulsion chamber used by Nikolsky (1969) at Tien Shan.

A very remarkable experiment that should be mentioned even though it was not primarily aimed at air shower investigations but at the analysis of very high energy cosmic ray initiated hadronic interactions, primarily at proton-proton interactions, was carried out at Echo Lake (altitude 3,260 m a.s.l.) by Jones and collaborators (Jones et al., 1967, 1970a, b). This experiment, that was specifically designed to avoid the usual uncertainties that are typical for most cosmic ray experiments, i.e., that the target nucleus is unknown, used mainly a large liquid hydrogen target, and at times a carbon target. The detector was triggered on so-called unaccompanied hadrons (Jones et al., 1972; Vishwanath et al., 1975).

In another experiment, Hook et al. (1970) operated a magnet spectrometer in combination with a neutron monitor at Durham, GB (s.l.) and attempted to determine the pion fraction of the total of nuclear active particles detected on the basis of the negatively charged particle population.

13.1.2 Emulsion Chambers

A separate category of hadron measurements are those made with emulsion chambers (EC). These consist of sandwiches of lead and photographic emulsion sheets,[3] interlaced with layers of X-ray films and have usually a lead or carbon target on top or in between. They enable the study of interactions of high energy hadrons and the cascades which they initiate as well as electromagnetic cascades in great detail and permit the determination of relevant interaction parameters (Haungs et al., 2003a; Haungs, 2006). EC experiments are usually stand-alone experiments.[4]

Unfortunately, the application of ECs in air shower experiments is subject to severe limitations. This is chiefly because events detected with ECs lack the time stamp that would allow their association weeks later, after development of the emulsion, with the showers that caused them and with the data that had been acquired of the particular shower with the array.

However, ingenious methods pioneered chiefly by the Tokyo group (Shibata et al., 1965; Matano et al., 1968, 1970, 1971) that were incorporated into the Tokyo and Mt. Norikura arrays, and later on into the BASJE installation at Mt. Chacaltaya (5,230 m a.s.l.) (Shibata et al., 1968; Matano et al., 1979) have overcome this problem and allow the EC events to be associated with the showers that caused them

[3] frequently referred to as *nuclear emulsion*

[4] For a comprehensive review on emulsion chambers, the interested reader is referred to the article of Lattes et al. (1971, 1980).

anytime after the event had been recorded. This permits at once to carry out far more refined studies of shower cores and to extract extremely detailed information on the most energetic shower constituents and their interactions, and to evaluate the specific emulsion data in conjunction with the regular shower parameters.

Two different methods were developed that establish the link between a shower and an EC event. In the first an emulsion chamber is operated in conjunction with a large spark chamber located above it and a scintillator matrix underneath it. The latter serves as so-called burst detector. The instrument package is placed in the center of an air shower array. The burst detector below the EC detects major *particle bursts* produced in combined hadronic and electromagnetic cascades initiated by high energy hadronic shower constituents in the lead or carbon target, or in the air above, and triggers the spark chamber. From the scintillator matrix elements the time stamp, the approximate burst locations and sizes are obtained while the spark chamber yields the accurate coordinates of the incident hadrons in the EC. These data are stored together with an event signature to associate the EC events with the shower that caused it and complementary array data for subsequent analysis (Matano et al., 1968).

The second and more refined method yields similar but improved results. It consists of a thin scintillator sheet that is spread out across the full area underneath the EC and serves as particle burst detector. It reveals the passage of particle bursts and their locations by producing local light flashes or light spots. The scintillator sheet is located inside a dark enclosure and viewed by a first image intensifier that is optically coupled to a second. Thus, the two intensifiers work in series, the second intensifying the screen image of the first (Machida et al., 1970). The first intensifier is operated continuously and its screen serves with its persistence as image storage device for whatever light patterns may occur across the scintillator sheet. The second intensifier is operated in gated mode and is continuously viewed by a camera with open shutter. In addition, the scintillator sheet is also viewed separately by a fast high-gain photomultiplier.[5]

If now the target or the EC below it is hit by one or several high energy hadrons, one or several hadronic cascades may be produced within the target or the EC. The accompanying photon-electron cascades resulting from neutral pion decay in the hadron initiated cascades penetrate the EC and generate simultaneous local light flashes in the scintillator sheet that are approximately proportional in intensity to the size of the photon-electron cascades. These are displayed after intensity amplification on the screen of the first image intensifier.

Simultaneously, the cascade initiated light flashes across the scintillator sheet are also detected by the fast photomultiplier. If the brightness of the light flashes exceeds a prefixed threshold the photomultiplier output pulse will gate the second image intensifier which then displays on its screen the intensified image produced

[5] A similar system using only one image intensifier, called the *luminescent chamber*, was developed independently in the late fifties and early sixties by Jones and Perl (Perl and Jones, 1959, 1960; Jones and Perl, 1961).

by the first intensifier. This second image is photographically recorded together with the shower event number. Thus, the EC event and the shower that caused it are unambiguously identified for subsequent analysis. In more recent years the image intensifier had been replaced by a multi-channel plate (Tsushima et al., 1979).

From the photograph of the light spots the coordinates of the cascades and thus the location of the hadrons in the EC that are associated with a particular shower can now be determined and a joint event analysis can be performed. Similar patterns can also be produced by electromagnetic cascades that are initiated by high energy gamma rays in the EC. Additional detectors above the EC help to distinguish gamma rays from hadrons.

The Chacaltaya experiment has employed this method extensively over a long period, focusing predominantly on the detailed analysis of very high energy hadronic interactions in well defined showers (Matano et al., 1981, 1985; Kawasumi et al., 1997).

13.1.3 Recent Work

It was not until the late eighties of the last century that the statistical situation of the available hadron data has markedly improved and the first relevant and reliable distributions and spectra became available. However, it is only very recently that exhaustive measurements with high statistics, good energy and spatial resolutions, using very large and sophisticated calorimeters, had been carried out that have removed many, but not all, of the lingering uncertainties and have extended the energy range of the investigated hadron spectra significantly (Aglietta et al., 1990; Engler et al., 1990).

The size and layout, in particular the detector element type and the granularity of a calorimeter are of great importance. The proper choice of the relevant parameters and quality marks insures sufficient spatial and energy resolution. Large size calorimeters help to prevent the possible loss of particles through outward scattering and leakage and, vice versa, help to identify contributions of particles scattered from the outside into the calorimeter. Such deficiencies led to misinterpretation of the measured energy deposits in some of the early calorimeters and to false spectra.

13.1.4 Comments on Data Presentation

It must be noted that the different constituents of the hadronic component in showers can in general not be identified and analyzed separately with common detector arrangements. To distinguish pions (or kaons) from the nucleonic component more sophisticated techniques and methods are required. However, in some installations using more refined calorimeters the neutron component can be identified from the rest of the hadrons and, in exceptional experiments, low energy antiprotons in magnet cloud chambers or in calorimeters with high time resolution. Thus, in general the data presented in this chapter comprise all hadrons, unless specified otherwise.

13.2 Lateral Distribution and Structure Function

13.2.1 Experimental Results, Early Work

The determination of the lateral density distribution of hadrons in showers is of interest when studying propagation, interaction and energy flow of the hadronic component. The lateral distribution is intimately linked to the transverse momentum acquired by secondaries in the interactions from which they emerge. Transverse momenta of secondaries are important properties of hadronic interactions and represent a key parameter of interaction dynamics. The transverse momentum distribution is a characteristic ingredient of interaction models. It plays an important role in energy and momentum conservation aspects, affects the secondary particle multiplicity, and has far reaching consequences for the development and propagation of showers both laterally and longitudinally.

Essentially the same kind of instruments and measurements are required to determine the lateral density distribution of hadrons as are needed to measure hadron energy spectra; as a matter of fact, lateral density distributions and energy (or momentum) spectra are usually co-products of the same experiment. In the following we present a selection of lateral density distributions of hadrons of different energy groups, measured at different observation levels in the atmosphere, during widely different epochs in showers belonging to different size groups.

In Fig. 13.1 the lateral density distributions, $\rho_h(r)$, of very low energy hadrons ($\langle E_h \rangle \sim 1\,\mathrm{GeV}$) obtained from two different sea level experiments are illustrated. Presented are older results from the work of Böhm et al. (1970) carried out at Kiel and of Kozlov et al. (1979, 1981) using the installations at Yakutsk. These two experiments did not employ calorimetric methods but used NM-64 neutron monitors, operated at widely varying distances from the shower axis, to detect the occurrence of hadronic interactions and, thus, to identify the presence of hadrons.

Since the measurement is based on the detection of thermalized evaporation neutrons from low energy hadronic interactions in the lead target of the monitor, the average energy of the interaction initiating hadrons is very low, on average about 1 GeV or less. Closer to the shower core the average energy is somewhat higher but it decreases with increasing core distance. It must be realized that this method does not yield the full integral flux of hadrons. Further details concerning neutron monitor applications for hadron measurements in showers are described in connection with the determination of the total hadron content of showers in Sect. 13.6.

Also shown in Fig. 13.1 are two lateral density distributions of low energy hadrons that were obtained by Ashton and Nejabat (1981) at Durham (GB) (60 m a.s.l.), using a neon flash tube calorimeter. The measurements apply to hadrons of energy $E_h \geq 13\,\mathrm{GeV}$ and cover the shower size range from 10^4 to over 10^8.

A twin set of lateral density distributions of very high energy hadrons recorded by Fritze et al. (1970) in small to medium size showers in the near core area is shown in Figs. 13.2a, b. These measurements were carried out at Kiel with a shielded $14\,\mathrm{m}^2$ neon hodoscope that was used as core detector and analyzer underneath an $800\,\mathrm{g\,cm}^{-2}$ concrete target, in combination with a $32\,\mathrm{m}^2$ neon hodoscope

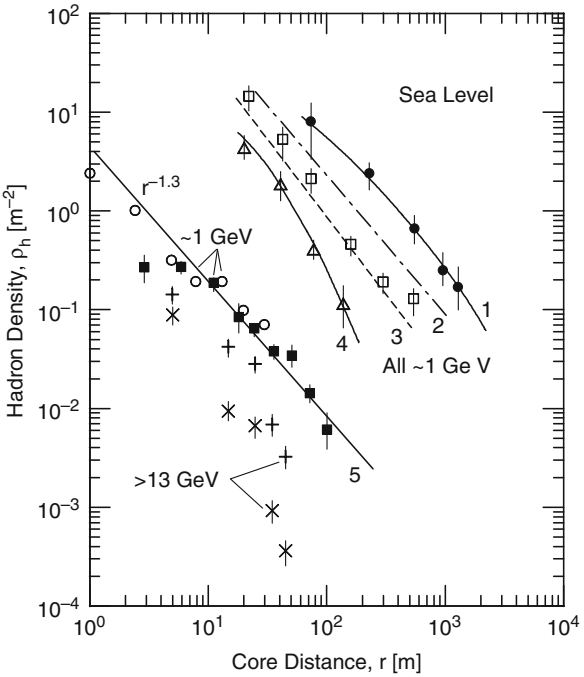

Fig. 13.1 Lateral density distribution of low energy hadrons ($\langle E_h \rangle \simeq 1$ GeV) in air showers. The data points •, □ and △ are from the work of Kozlov et al. (1979, 1981) at Yakutsk (105 m a.s.l.) and apply to showers of size $N_e = 2 \cdot 10^8$, $N_e = 1.8 \cdot 10^7$ and $N_e = 3 \cdot 10^6$, respectively. *Lines 1 and 4* connect the experimental points • and △; *lines 2 and 3* connect corresponding points from the same experiment, not shown individually in this figure, that are for sizes $N_e = 5.1 \cdot 10^7$ and $N_e = 7.4 \cdot 10^6$, respectively. Points ■ are from the work of Böhm et al., (1970) at Kiel (s.l.), normalized to an average size of $\langle N_e \rangle = 10^5$, *line 5* is a fit to these data and ○ are data from Ootacamund (2,200 m) (Sreekantan, 1963). All these experiments used neutron monitors for the hadron identification. Points × and + are for hadrons ≥ 13 GeV in showers of size $10^4 \leq N_e \leq 2.3 \cdot 10^5$ ($\langle N_e \rangle = 10^5$) and $2.3 \cdot 10^5 \leq N_e \leq 4 \cdot 10^6$ ($\langle N_e \rangle = 6 \cdot 10^5$), respectively, recorded at Durham (GB) (60 m a.s.l.) using a flash tube chamber (Ashton and Nejabat, 1981)

consisting of 180,000 tubes (area 1 cm^2 each) above the target (Bagge et al., 1965; Böhm et al., 1968). The arrangement was located at the center of the shower array. Another set of comparative data acquired at Tokyo for showers belonging to similar size groups using spark chambers as burst detectors and emulsion is displayed in Fig. 13.3a (Matano et al., 1970, 1971). A compilation of distributions from several other experiments at sea level is shown in Fig. 13.3b.

Turning to moderate mountain altitudes (2,200 m a.s.l.) where the conditions for hadron studies are significantly more favorable than at sea level because of reduced atmospheric attenuation, we present in Fig. 13.4 a compilation of data of the extensive work at Ootacamund in southern India (Vatcha and Sreekantan, 1973a). This work was carried out on mid-size showers as listed in the caption and produced distributions of low to moderate energy hadrons (> 1, > 50 and > 200 GeV). The

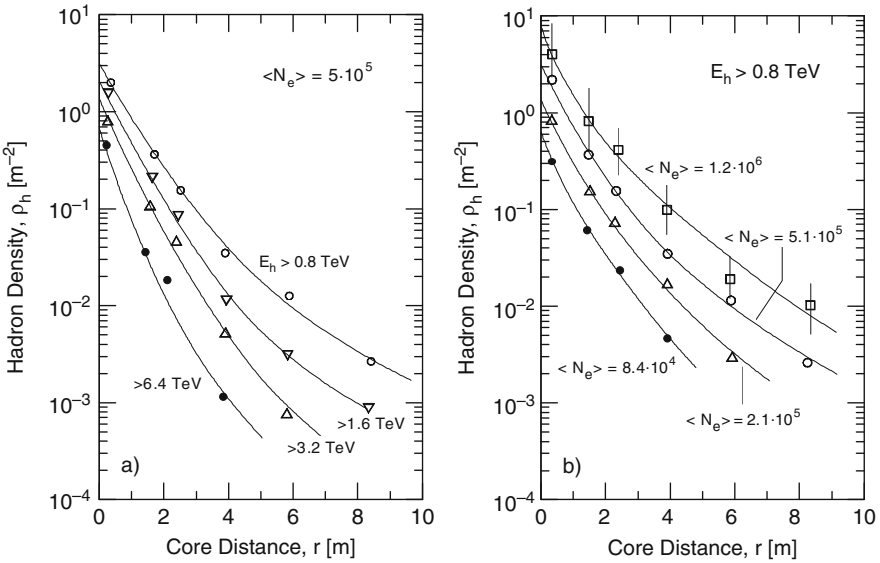

Fig. 13.2 (**a**) Average lateral density distribution of hadrons of different energy groups, as indicated, near the core in showers of average size $\langle N_e \rangle = 5.1 \cdot 10^5$ measured at Kiel (sea level) (Fritze et al., 1970). (**b**) Lateral density distribution of hadrons of energy $E_h \geq 0.8$ TeV in showers of different average sizes, as indicated. The data are from measurements made at Kiel (sea level) (Fritze et al., 1970)

various distributions cover different lateral distance ranges from the shower axis and were obtained with the TASS instrument. Also shown in the same figure are low energy distributions of van Staa et al. (1973) obtained at Pic du Midi, France (2,860 m a.s.l.).

Data of lateral distributions of hadrons in larger showers from the work of Miyake et al. (1970, 1979) acquired at Mt. Norikura (2,770 m a.s.l.) in Japan covering the energy range from 20 to 2000 GeV, using different detectors techniques, such as cloud chambers and calorimetric methods, are plotted in Figs. 13.5 and 13.6.

A similar set of data of energetic hadrons resulting from the work of van Staa et al. (1974) using the Kiel neon hodoscope at Pic du Midi and another set obtained with the relatively small calorimeter at Tien Shan (3,340 m a.s.l.) by Romakhin et al. (1977) are illustrated in Figs. 13.7 and 13.8a, b), respectively. A compilation of hadron lateral distributions in showers of moderate size recorded at mountain levels ranging from 2200 to 3340 m a.s.l. that cover a hadron energy range from >70 to >400 GeV is presented in Fig. 13.9. More recent data from measurements with the Tien Shan calorimeter carried out by Danilova et al. (1985) are summarized in Fig. 13.10 a, b together with results from their simulations. The relatively large spread of the energetic hadrons which they observe as compared to the simulations is interpreted as a consequence or the rising transverse momenta.

Lateral distributions of hadron initiated bursts of different size groups detected in showers of size $3 \cdot 10^6 \leq N_e \leq 9 \cdot 10^6$ with a tightly packed 60 m^2 scintillation burst detector at Mt. Chacaltaya (5,230 m a.s.l.) are shown in Fig. 13.11. The hadron target

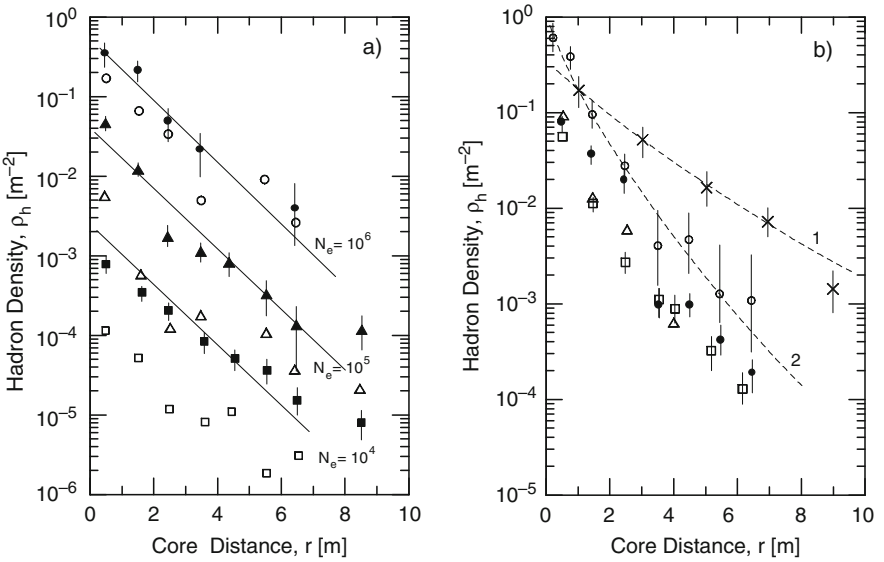

Fig. 13.3 (**a**) Lateral density distribution of high energy hadrons recorded at Tokyo (sea level) in showers of different size groups. The full symbols (●, ▲, ■) are for hadrons with energy $E_h \geq 1.7$ TeV, the open symbols (○, △, □) for $E_h \geq 5$ TeV (Matano et al., 1970, 1971). The distributions can be described with an exponential of the form $\rho_h e^{(-r/r_0)}$, with $r_0 = 1.1$ m. (**b**) Lateral density distribution of high energy hadrons near the shower core. The compilation includes data from the following authors for hadron energy thresholds E_h and size groups N_e as specified below, measured at sea level. The expression $\rho_h(r) = 0.3 \cdot e^{(-r/r_0)}$ m^{-2}, where $r_0 = 1.8$ m, describes the data adequately

×	$E_h \geq 0.3$ TeV	$5{\cdot}10^4 \leq N_e \leq 10^6$	(Ashton and Nasri, 1979)
●	$E_h \geq 0.5$ TeV	$N_e = 10^5$	(Kellermann and Hillas, 1981)
○	$E_h \geq 0.5$ TeV	$5{\cdot}10^4 \leq N_e \leq 10^6$	(Baruch et al., 1977)
□	$E_h \geq 1.7$ TeV	$N_e = 10^5$	(Matano et al., 1971)
△	$E_h \geq 6.4$ TeV	$\langle N_e \rangle = 5.1 \cdot 10^5$	(Fritze et al., 1970)

consisted of a layer of 165 g cm^{-2} of galena (lead ore) placed above 132 g cm^{-2} of concrete. The former served at the same time as shield against the electromagnetic component. A layer of 23 g cm^{-2} of lead underneath the concrete was used as converter for the gamma rays from neutral pions to determine the hadron energy (Suga et al., 1962; Hasegawa et al., 1965).

13.2.2 Experimental Results, Recent Work

As briefly mentioned earlier, in the late eighties of the last century two large hadron calorimeters came into operation. The first was incorporated into the EAS-TOP array on Gran Sasso, Italy, at an altitude of 2,005 m a.s.l. (810 g cm^{-2}), the other at the KASCADE site near Karlsruhe, Germany, at an altitude of 110 m a.s.l. (1,022 g cm^{-2}).

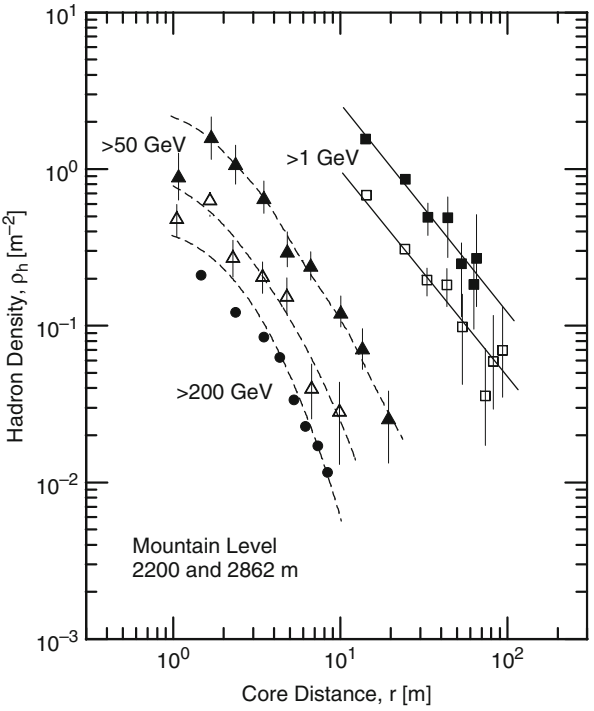

Fig. 13.4 Compilation of data on the lateral density distribution of hadrons of different energy groups recorded at mountain level. Data ■ and □ are low energy distributions ($E_h \geq 1$ GeV) recorded at Pic du Midi (2,860 m) for showers of size $N_e = 7 \cdot 10^5$ and $N_e = 2.2 \cdot 10^5$, respectively (van Staa et al., 1973). ▲ and △ are data from measurements at Ootacamund (2,200 m) for hadrons of energy ≥ 50 GeV and apply to the shower size groups $10^6 \leq N_e \leq 1.8 \cdot 10^6$ and $1.8 \cdot 10^5 \leq N_e \leq 3.2 \cdot 10^5$ particles, respectively (Vatcha and Sreekantan, 1973a). The symbols • apply to hadrons of energy $E_h \geq 200$ GeV, recorded at Pic du Midi in showers of size $N_e = 1.25 \cdot 10^5$ (van Staa et al., 1973)

The EAS-TOP calorimeter was actually a combined muon-hadron detector because it was also equipped to track muons. It consisted of two units, arranged side by side, and had a combined area of 144 m^2 (Aglietta et al., 1989, 1990, 1999). The calorimeter consisted of 10 so-called active layers that were separated each by 13 cm thick iron absorbers, corresponding to a total of 7 interaction lengths. Each active layer had two orthogonally oriented planes of streamer tubes for muon tracking and one layer of proportional tubes for hadron calorimetry.

The spatial resolution of the detector was 1 cm for muons, whereas for hadrons it depended on the dimensions of the pads, arranged in a grid of 30×30 (40×39) cm^2, that were used to read out the proportional tubes. The energy resolution was 15% for 1 TeV hadrons. The calorimeter thickness allowed to determine the location of the maximum of hadron initiated cascades having energies as high as 100 TeV. The muon energy threshold was 2 GeV.

This combined detector system was mainly used to measure the muon component in showers. Unfortunately no data are available from measurements of the lateral density distribution nor of the energy spectrum of the hadron component in showers.

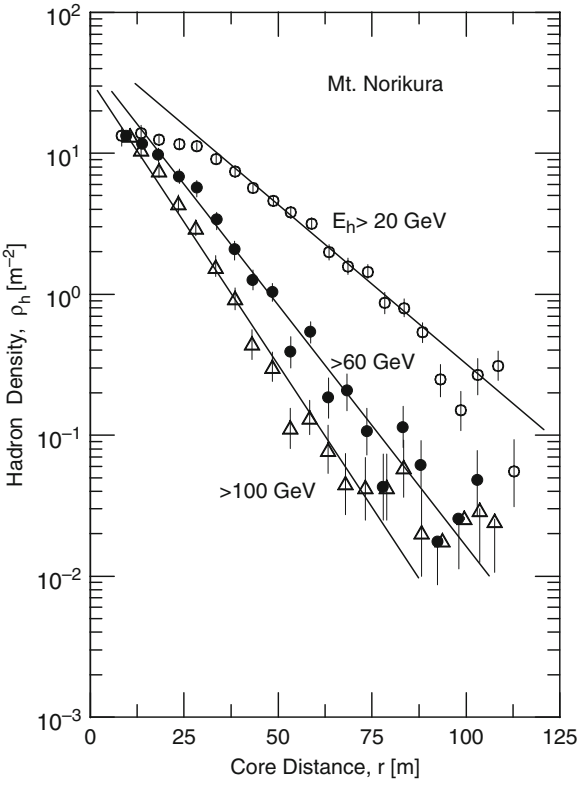

Fig. 13.5 Lateral density distribution of hadrons recorded at Mt. Norikura (2,770 m) in showers of size $10^7 \leq N_e \leq 2 \cdot 10^7$ (Miyake et al., 1979)

The Karlsruhe calorimeter, shut-down since 2007, was a highly sophisticated device. It measured $16 \times 20 \times 4.5\,\mathrm{m}^3$, thus having an area of $320\,\mathrm{m}^2$. The absorber consisted of eight layers, starting with iron slabs of 10 cm thickness on top and ending with layers of concrete of different thicknesses. It was equipped with 7 layers of liquid ionization chambers and one layer of scintillators for trigger purposes (Engler et al., 1990, 1999). Its total vertical thickness amounted to 11.5 nucleon interaction mean free paths (i.m.f.p.), λ_{int}, which implies that hadrons of energy up to 25 TeV are absorbed. The energy leakage was less than 2.5% and the horizontal granularity measured $25 \times 25\,\mathrm{cm}^2$ (Antoni et al., 2003).

The calorimeter was designed to identify hadrons and to measure their energy over the range from 10 GeV to $>$ 10 TeV with sufficient accuracy. The prototype had scintillation counters above the calorimeter which allowed to measure local particle (electron) densities but these were abandoned at a later time. Muon detectors underneath the calorimeter recorded muons of energy >2 GeV, the threshold needed to penetrate the calorimeter.

The original KASCADE array was laid out to study showers having primary energies in the range from $3 \cdot 10^5$ to 10^8 GeV (Antoni et al., 2003). The extended array, called KASCADE-Grande (Haungs et al., 2003b), had the 39 shower detectors of the former EAS-TOP array added and could handle primary energy events of up to $\sim 10^9$ GeV (Bertaina et al., 2001; Chiavassa et al., 2003; Navarra et al., 2004).

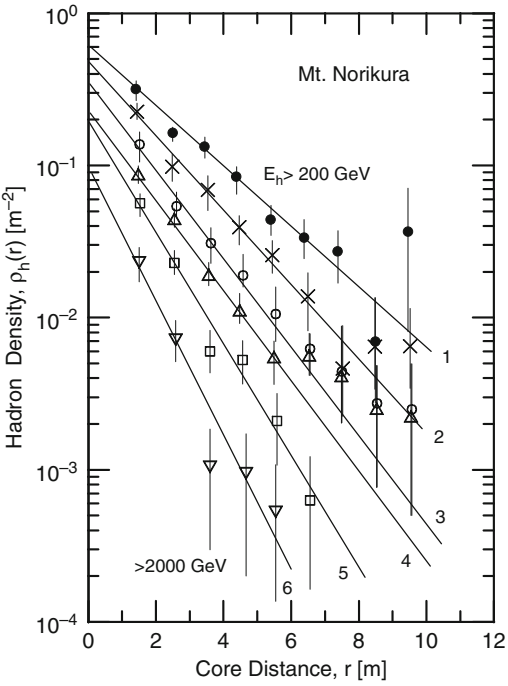

Fig. 13.6 Lateral distribution of high energy events recorded at Mt. Norikura for the shower size group $3 \cdot 10^5 \leq N_e \leq 5 \cdot 10^5$. The *lines 1–6* are fits to the distributions and obey the empirical relation (Eq. 13.4) $\rho_h(E_h, r) = A \exp(-r/r_0)$, where $r_0 \propto E_h^{-0.33}$ for hadron energies $E_h \geq 500\,\text{GeV}$, with r_0 and the event energies given in the table (Miyake et al., 1970)

Symbol	E_h [GeV]	r_0 [m]	Symbol	E_h [GeV]	r_0 [m]
•	≥ 200	2.2 ± 0.1	×	≥ 400	1.7 ± 0.1
○	≥ 600	1.6 ± 0.1	△	≥ 800	1.4 ± 0.1
□	≥ 1200	1.2 ± 0.1	▽	≥ 2000	1.0 ± 0.2

Because of great difficulties with the identification of individual high energy hadrons in the center of the core of air showers the wealth of data from this highly sophisticated and unique detector on the lateral distribution of very energetic hadrons is relatively limited. Figure 13.12, taken from the work of Antoni et al. (2001), shows in the lower portion (open symbols, left hand ordinate) the lateral density distribution of hadrons having threshold energies $E_{\text{th}} = 50\,\text{GeV}$, $E_{\text{th}} = 150\,\text{GeV}$, $E_{\text{th}} = 300\,\text{GeV}$ and $E_{\text{th}} = 500\,\text{GeV}$. The data apply to showers subtending zenith angles $\theta < 18^\circ$ and having a so-called *truncated muon number (size)* in the range $2.5 \cdot 10^3 < N_\mu^{\text{tr}} < 5 \cdot 10^3$. The truncated muon size refers to the muon size that is obtained from measurements that are radially confined by the size of the detector array and do not cover the full extent of the shower, i.e., the measurement is *truncated*. In the upper portion of Fig. 13.12 (full symbols, right hand ordinate) is shown the hadronic energy density carried by these particles.

The plots presented in Fig. 13.13 are from the same authors and show in the lower portion (open symbols, left ordinate) the lateral density distribution of hadrons of fixed threshold energy $E_{\text{th}} = 50$ GeV but belonging to showers of different

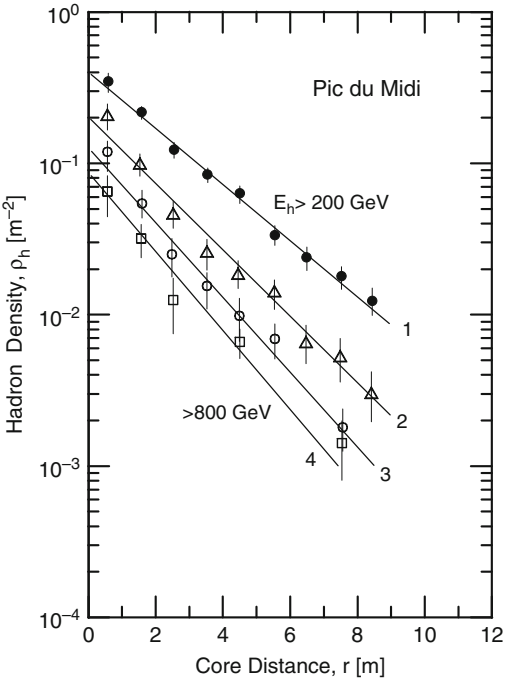

Fig. 13.7 Lateral density distribution of hadrons of different energy groups in showers of size range $1.25 \cdot 10^5 \leq N_e \leq 3.15 \cdot 10^6$ measured at Pic du Midi (France). The *lines 1–4* are fits to guide the eye (van Staa et al., 1974)

Symbol	Hadron energy	Symbol	Hadron energy
•	$E_h > 200$ GeV	△	$E_h > 400$ GeV
○	$E_h > 600$ GeV	□	$E_h > 800$ GeV

truncated muon size ranges, as indicated in the figure. The upper set of curves with the filled symbols (right hand ordinate) represent the hadronic energy density, analogous to the previous figure.

Finally, in Fig. 13.14 we show the lateral density distribution of low energy (>50 GeV) hadrons recorded with the KASCADE calorimeter near sea level (110 m a.s.l.) and the TASS calorimeter at Ootacamund (2,200 m a.s.l.) in Fig. 13.14a, and the distribution of high energy hadrons (>1 TeV) in the KASCADE and the Tien Shan (3,340 m a.s.l.) calorimeters in showers of size $1.8 \cdot 10^5 \leq N_e \leq 3.2 \cdot 10^5$ in Fig. 13.14b (Antoni et al., 1999).

13.2.3 Mathematical Expressions and Fits

Many authors worked out empirical mathematical expressions to describe the lateral density distributions of hadrons in showers and to fit the data. The distributions depend on hadron energy, E_h, and shower size, N_e. They are usually valid only over a restricted range of core distances, r. Kameda et al. (1965) who began systematic

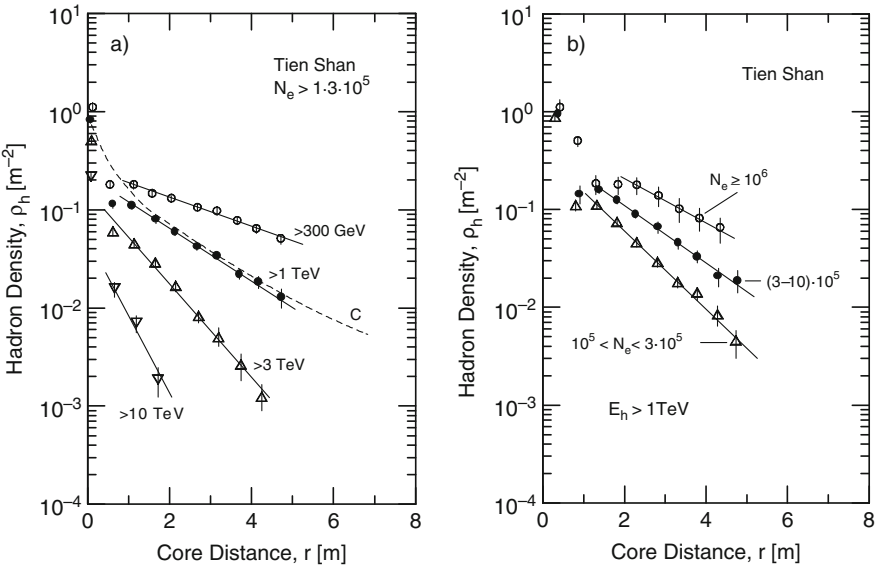

Fig. 13.8 (**a**) Lateral density distribution of hadrons of different energy groups as indicated in showers of size $N_e \geq 1.3 \cdot 10^5$ at Tien Shan (3,340 m a.s.l.) (Romakhin et al., 1977). The *dashed line, c*, shows an approximated fit. (**b**) Lateral density distribution of hadrons of energy $E_h > 1$ TeV at Tien Shan (3,340 m a.s.l.) in showers of different size groups: $\triangle$ $N_e = 10^5 \leq N_e \leq 3 \cdot 10^5$; • $3 \cdot 10^5 \leq N_e \leq 10^6$ and ○ $N_e \geq 10^6$ (Romakhin et al., 1977)

studies of hadrons in air showers as early as 1960 obtained an excellent fit to their data using the following expression.

$$\rho_h(E_h, r, N_e)\mathrm{d}E_h\mathrm{d}r \;=\; 0.35\left(\frac{N_e}{10^5}\right)^{0.35}\left(\frac{E_h}{100}\right)^{-1.2}\exp\left(-\frac{r}{r_0}\right)\mathrm{d}\left(\frac{E_h}{100}\right)\mathrm{d}r\;, \tag{13.1}$$

where

$$r_0 \;=\; A\left(\frac{N_e}{10^5}\right)^{0.32}\left(\frac{E_h}{100}\right)^{-0.25}\quad. \tag{13.2}$$

E_h is in units of [GeV], r in [m], $A = 2.4 \pm 0.3$ for the shower size group $4 \cdot 10^4 \leq N_e \leq 10^6$ and $E_h \geq 100$ GeV.

Bradt and Rappoport (1967) proposed the following expression to describe the lateral density distribution of hadrons in air showers,

$$\rho_h(E_h, r) \;\propto\; \exp(-\sqrt{r/r_0})\;, \tag{13.3}$$

where r_0 was found to vary with hadron energy as $r_0 \propto E_h^{0.6}$ and appears to be independent of primary energy, E_0.

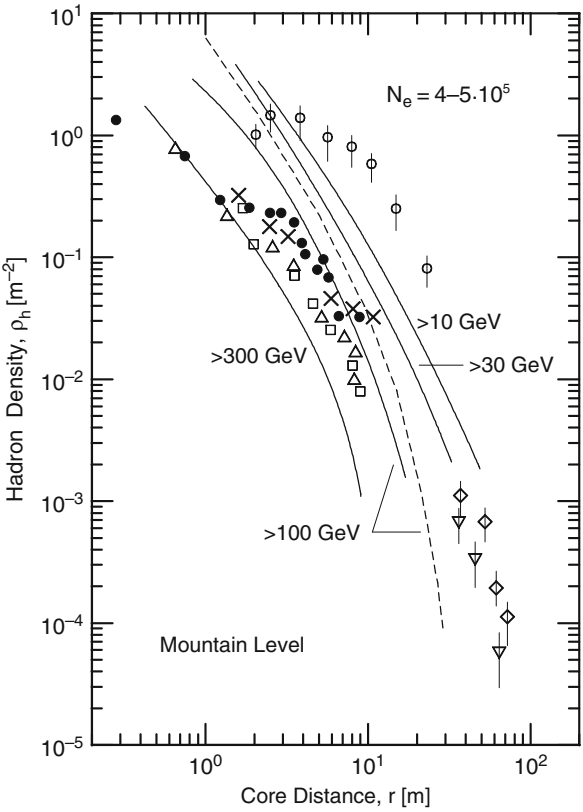

Fig. 13.9 Compilation of lateral density distributions of hadrons from different experiments and comparison with theoretical data (Nesterova and Chubenko, 1979). The theoretical distributions are for proton primaries having an energy of 10^6 GeV. The *solid curves* are from the work of Grieder (1977c), the *dashed curve* is after Fomin (1972). The experimental data are as follows:

Symbol	E_h [GeV]	Reference	Altitude [m]
◇	> 70	Nesterova and Chubenko (1979)	3,340
▽	>150	Nesterova and Chubenko (1979)	3,340
•	>400	Dubovy et al. (1978)	3,340
△	>200	van Staa et al. (1974)	2,860
×	>200	Miyake et al. (1970)	2,770
□	>400	Miyake et al. (1970)	2,770
○	>50	Chatterjee et al. (1968)	2,200

However, most authors use simple exponential expressions to fit their data (e.g., Fritze et al., 1970; Miyake et al., 1970; Baruch et al., 1977; and others), such as

$$\rho_h(E_h, r) \;=\; A \exp(-r/r_0) \;\;, \tag{13.4}$$

where $A \propto E_h^{-1.0}$ for $E_h \geq 500\,\text{GeV}$ and $r_0 \propto E_h^k$ with $k = -0.33$. Both, r_0 and A depend on showers size as $r_0 \propto N_e^{0.16}$ and $A \propto N_e^{0.40}$, according to Miyake et al. (1970). The distribution gets flatter for hadron energies $\leq$500 GeV.

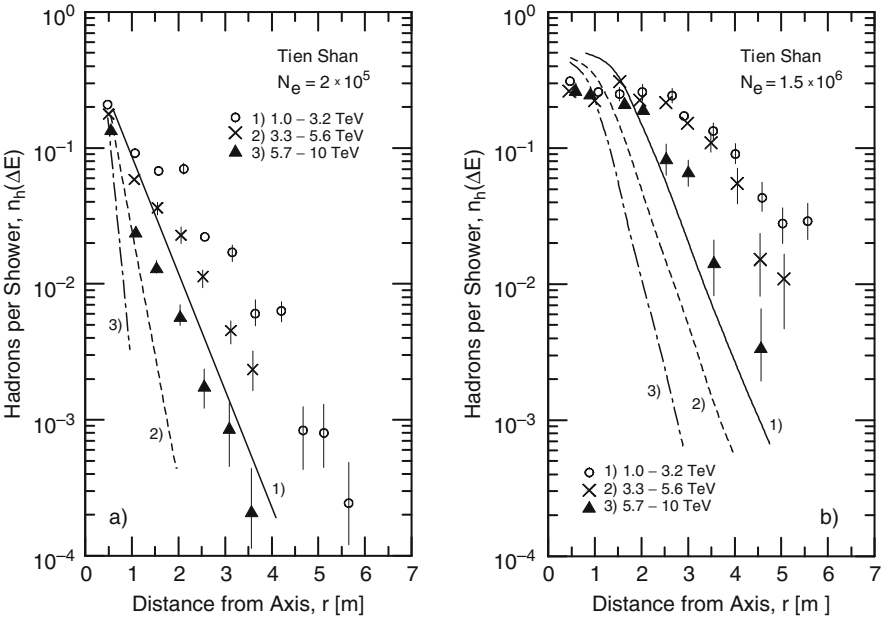

Fig. 13.10 Lateral density distribution of three energy groups of hadrons in showers of two different size groups (Figs. (**a**) and (**b**), respectively), as indicated, detected with the Tien Shan calorimeter (3,340 m a.s.l., 690 g cm^{-2}). The *curves* labeled (1), (2) and (3) refer to distributions obtained from simulations using a normal transverse momentum distribution (after Danilova et al., 1985)

After extensively studying the subject, Kempa (1976a, b) concludes that the best expression to describe the lateral density distribution of hadrons in air showers is given by

$$\rho_h(E_h, r) \;=\; N_h(>E_T)\, f_h(r) \;\;, \tag{13.5}$$

where $N_h(>E_T)$ is the total number of hadrons with energy $>E_T$, and $f_h(r)$ is the characteristic function of the lateral distribution of the hadrons and is given by

$$f_h(r) \;=\; \frac{1}{8!\pi r_0^2} \exp[(-r/r_0)^{0.25}] \;\;. \tag{13.6}$$

More recently, Antoni et al. (2001) found that an NKG function as is used to describe the electron distribution, properly adapted, with $r_0 = 10$ m, gives a good fit to the hadron distribution. In this case the latter shows a similar trend as the electron distribution. For fixed r_0 the age parameter thus obtained yields similar values as are obtained from electrons and muons.

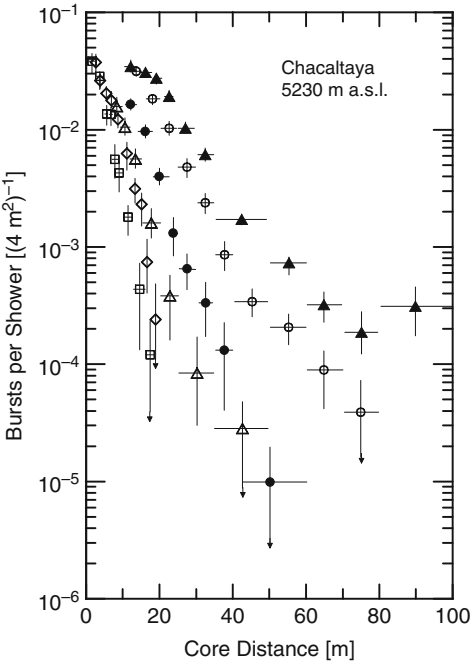

Fig. 13.11 Lateral distribution of bursts observed in the 4 m^2 element of the 60 m^2 scintillation burst detector matrix in showers of size $3 \cdot 10^6 \leq N_e \leq 9 \cdot 10^6$ recorded at Mt. Chacaltaya (5,230 m a.s.l.) (Hasegawa et al., 1965). The burst size groups are listed below

Symbol	Burst Size	Symbol	Burst Size
▲	100–200	○	200–500
●	500–1000	△	1000–2000
◇	2000–5000	□	5000–10000

13.3 Energy Spectra and Related Data

Today energy spectra of hadrons in air showers are usually measured with ionization calorimeters. The standard technique is to determine the ionization density distribution across each of the detector planes within the calorimeter target block that sample the longitudinal development of the hadron initiated combined nuclear and electromagnetic cascades, from which the hadron energy can be computed.

Since the beginning of cosmic ray research Wilson cloud chambers had been used for decades for track detection, interaction and event analysis. Often cloud chambers were placed in strong magnetic fields for charge sign and momentum determination. They reveal a lot of details on interactions, have good spatial resolution but are tricky to operate and have a long dead time. Consequently, their yield of data is not very rich. In some experiments magnet spectrometers in combination with spark or discharge chambers, or neutron monitors had been used, too. Today, cloud chambers are no longer used, except for demonstration purposes.

In the past major problems with such measurements were the limited size of the detectors, poor spatial and energy resolutions. However, during the past decade and

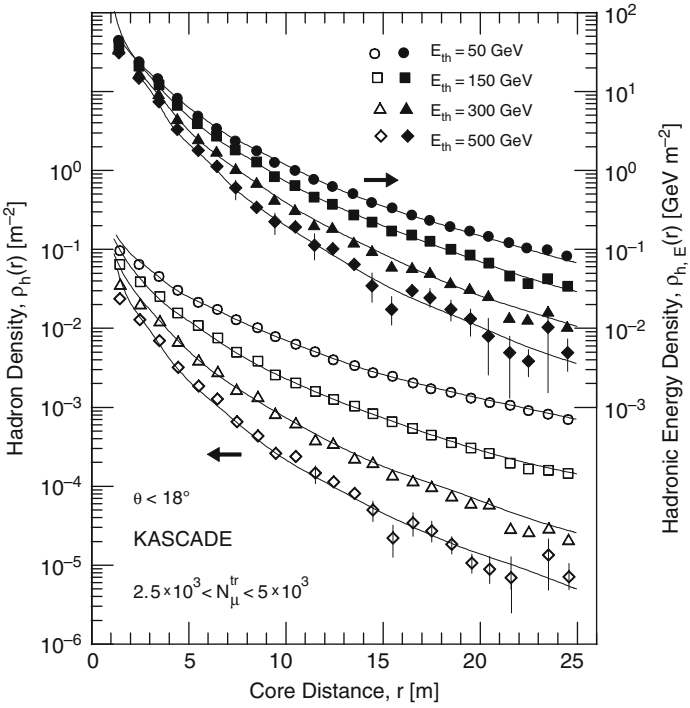

Fig. 13.12 Density distribution of hadrons (open symbols, *left ordinate*) and of hadronic energy carried by the same groups of particles (full symbols, *right hand ordinate*) having different threshold energies E_{th} as indicated, as a function of core distance in showers belonging to the truncated muon size range $2.5 \cdot 10^3 < N_\mu^{\text{tr}} < 5 \cdot 10^3$, measured by the KASCADE experiment. The curves are fits of the data points to an NKG function (Antoni et al., 2001)

a half significant improvements have been achieved in air shower hadron calorimetry with the availability of two very large instruments, one at the KASCADE array near Karlsruhe, Germany (110 m a.s.l.) (Engler et al., 1990; Antoni et al., 2003), the other at EAS-TOP, on top of Gran Sasso, Italy (2,005 m a.s.l.) (Aglietta et al., 1986, 1990). Both instruments had a relatively good spatial and energy resolution.[6]

13.3.1 Experimental Results, Early Work

In Figs. 13.15, 13.16, 13.17, 13.18, 13.19 and 13.20 we summarize the results of the most relevant hadron energy spectrum measurements, including very early results. Figures 13.15 and 13.16 show compilations of data obtained with different kinds of installations at sea level. Details concerning shower size selection criteria are

[6] The EAS-TOP experiment had been shut down in 2000 and KASCADE in 2009.

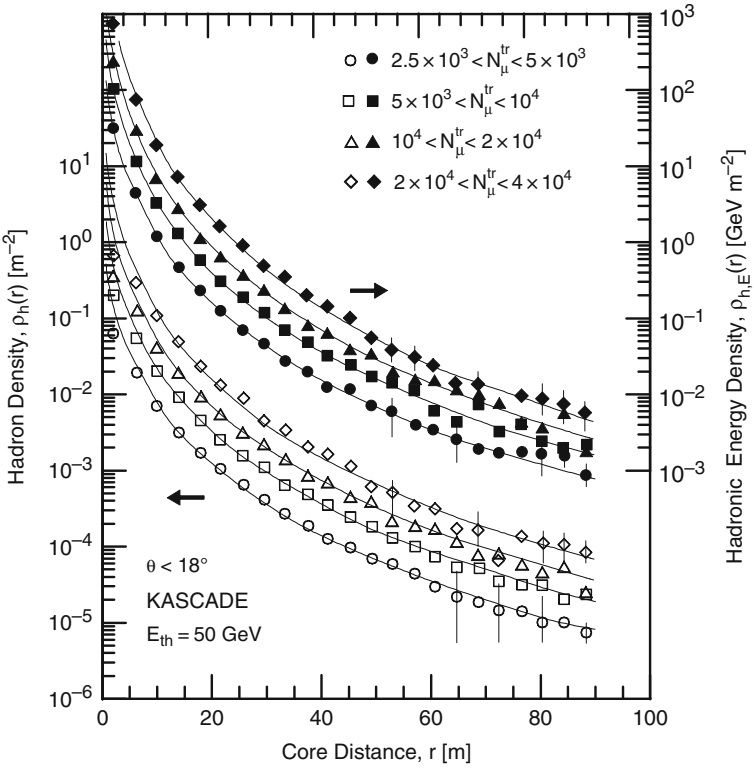

Fig. 13.13 Density distribution of hadrons (open symbols, *left ordinate*) and of hadronic energy carried by the same groups of particles (full symbols, *right hand ordinate*) having a threshold energy $E_{\text{th}} = 50\,\text{GeV}$ as a function of core distance in showers belonging to different truncated muon size ranges, as indicated, measured by the KASCADE experiment. The *curves* are fits of the data points to an NKG function (Antoni et al., 2001)

given in the figure captions. When comparing these data, it is important to keep in mind that data that are based on a rather wide shower size range are dominated by the overwhelming contribution from the smaller size showers. Considering the different instrumentation used and selection criteria applied, the spread of the data can be understood.

Inspection of Fig. 13.15 reveals that the spectrum of Kameda et al. (1965) for large showers that was obtained with a cloud chamber measuring $1.2 \times 1.0 \times 0.5\,\text{m}^3$ is relatively low lying as compared to the spectra from other experiments for smaller showers, shown in this figure. This could be due to an intrinsic problem of the rather delicate technique that had been used in this experiment that may lead to an underestimation of the hadron energy, or possibly to transition effects in the shower detectors that can result in shower size overestimation. On the other hand, the neon hodoscope data obtained by the Kiel group tend to yield rather flat spectra at high energies and seem to overestimate the true hadron flux and/or energy. The

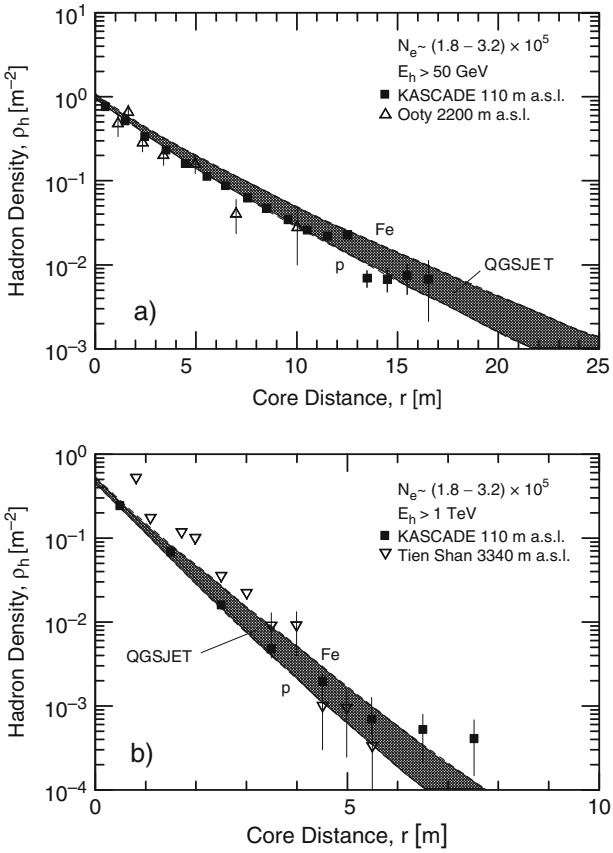

Fig. 13.14 Lateral density distribution of hadrons in showers of electron size $1.8 \cdot 10^5 \leq N_e \leq 3.2 \cdot 10^5$. The experimental data are from the following experiments: (**a**), ■ KASCADE (Karlsruhe, Germany) located at 110 m a.s.l. (Antoni et al., 1999), △, Ootacamund (India) 2,200 m a.s.l. (Vatcha and Sreekantan, 1973a) and apply to hadrons of energy $E_h \geq 50$ GeV. (**b**), ■ KASCADE, ▽ Tien Shan (Kazakhstan) 3,340 m a.s.l. (Romakhin et al., 1977) and include hadrons of energy $E_h \geq 1$ TeV. The hashed ribbon in either figure indicates the range covered by predictions from CORSIKA simulations with the QGSJET event generator for proton (*lower boundary*) to iron (*upper boundary*) primaries (after Antoni et al., 1999)

measurements of Baruch et al. (1977) and Ashton and Nejabat (1981) employed calorimeters whereas Matano et al. (1970, 1971) used an emulsion chamber.

Results from spectral measurements made at moderate to higher mountain altitudes, such as those carried out at Ootacamund (2,200 m), Mt. Norikura (2,770 m), Pic du Midi (2,860 m), Tien Shan (3,340 m) and the old Pamir station (3,860 m) are presented in Figs. 13.17, 13.18 and 13.19. In all of these experiments calorimetric methods of some form had been used. In addition, a magnet cloud chamber was occasionally employed at Mt. Norikura. Referring to Fig. 13.17, it is evident that the early Ootacamund data (Chatterjee et al., 1968) yield a hadron spectrum that lies

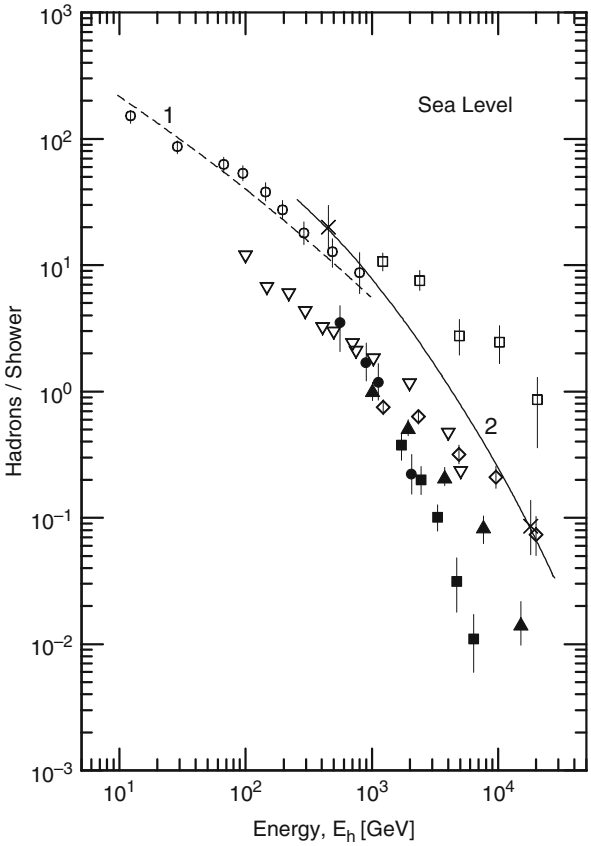

Fig. 13.15 Compilation of integral energy spectra of hadrons in showers at sea level. *Curve 1* is from calculations of Grieder (1971) for 10^7 GeV proton initiated showers, *curve 2* is a fit to the two experimental data points of Aschenbach (1974), listed below. The experimental data apply to the following size groups

•	$5 \cdot 10^4 \leq N_e \leq 10^6$	Baruch et al. (1977)
◇	$N_e = 8 \cdot 10^4$	Fritze et al. (1970)
■	$N_e = 10^5$	Matano et al. (1970)
▲	$\langle N_e \rangle = 10^5$	Böhm et al. (1968)
○	$N_e = 5 \cdot 10^5$	Ashton and Nejabat (1981)
×	$\langle N_e \rangle = 10^6$	Aschenbach (1974)
□	$N_e = 1.2 \cdot 10^6$	Fritze et al. (1970)
▽	$\langle N_e \rangle = 5.7 \cdot 10^6$	Kameda et al. (1965)

about one order of magnitude higher than the rest of the data from other experiments at comparative altitudes and shower sizes. The latter are in good agreement with each other. In a later publication the Tata group presents a more acceptable spectrum (Vatcha and Sreekantan, 1973a). The discrepancy of the earlier data appears to be due to leakage into the calorimeter.

The Pamir spectrum (Fig. 13.17) (Dovzenko et al., 1960) that was collected at a significantly higher altitude is expected to lay above the spectra recorded at lower altitudes for showers of comparable primary energy because of lesser absorption.

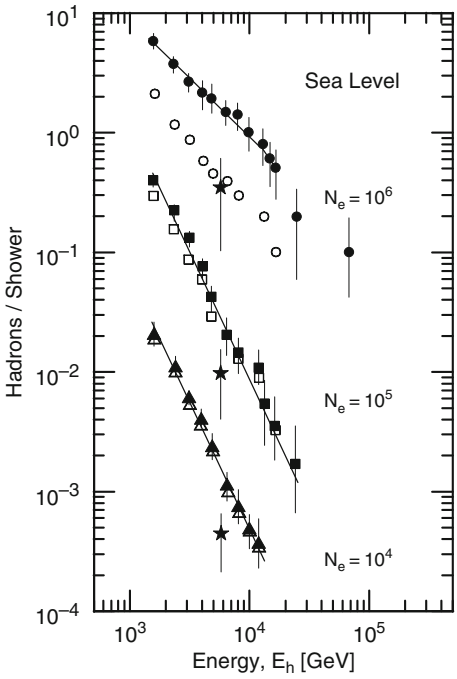

Fig. 13.16 Integral energy spectra of hadrons in showers of different size groups recorded at Tokyo (sea level) (Tanahashi, 1965; Matano et al., 1970, 1971). The full symbols (●, ■, ▲) include all events of the given shower size groups, the open symbols (○, □, △) are for single bursts and ★ applies to events in which the hadrons have been identified in the emulsion chamber (for details see text)

The theoretical spectra predicted by the calculation of Grieder (1977a) apply to vertical showers at an altitude of 3,000 m. The slope of either of the two spectra agrees well with the measured spectra. As a matter of fact the theoretical proton spectrum is in excellent agreement with the actually measured Pamir spectrum if one considers that the bulk of the detected showers have on average zenith angles around 30°. The traversed atmospheric overburden to reach the Pamir level is therefore about equal to that traversed by vertical showers to reach an altitude of 3,000 m. The spectrum predicted by Ouldridge and Hillas (1978) is much too steep and therefore unacceptable.

Inspection of Fig. 13.18 reveals again that extracting reliable information from the calorimeter at Ootacamund is very difficult, mostly because of its small size and poor spatial resolution. The Mt. Norikura data plotted in this figure show a remarkable consistency and have small errors. Likewise, of excellent quality and remarkable consistency, too, are the data resulting from the Tien Shan experiment illustrated in Fig. 13.19. The Pamir data are also plotted in this figure for comparison and an overall summary of mountain level data is given in Fig. 13.20. Inspection of the Norikura data plotted in this figure (+, lines 1, 2 and 3) reveal an apparent discrepancy, namely that line 2 ($s = 0.9$) is located above line 1 ($s = 1.0$).[7] However, the discrepancy is so small that this may well be explained by the facts that the

[7] Young showers ($s < 1.0$) manifest a steeper lateral distribution than old showers ($s > 1.0$).

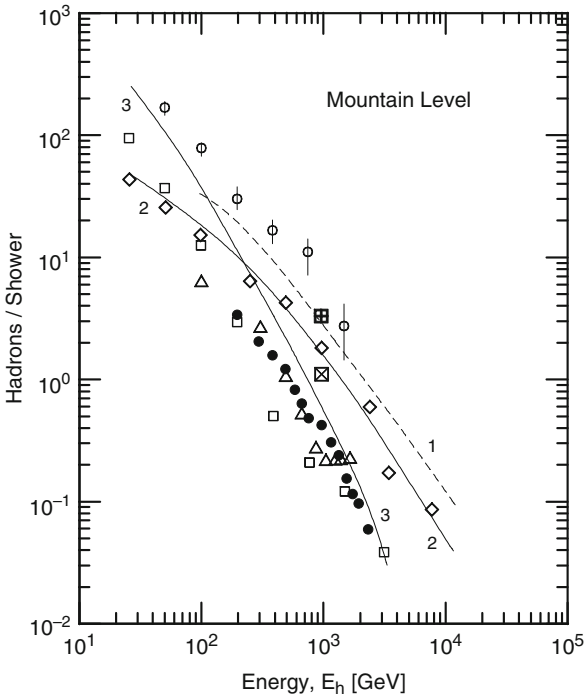

Fig. 13.17 Compilation of integral energy spectra of hadrons in showers of average size $\langle N_e \rangle = 10^5$ at mountain level (Sreekantan and Tonwar, 1979). The curves are simulation results. *1 and 2* are from calculations of Grieder (1977a) for iron and proton initiated showers, respectively, *curve 3* is from the work of Ouldridge and Hillas (1978) for proton showers. ⊞ and ⊠ are two predictions for proton and iron initiated showers, respectively, at mountain level after Vernov et al. (1977). The rest of the data are from the experiments listed below

Symbol	Location	Reference
○	Ootacamund, 800 g cm^{-2}	Chatterjee et al. (1968)
●	Mt. Norikura, 750 g cm^{-2}	Miyake et al. (1970)
□	Ootacamund, 800 g cm^{-2}	Vatcha and Sreekantan (1973a)
◇	Pamir, 650 g cm^{-2}	Dovzenko et al. (1960)
△	Pic du Midi 730 g cm^{-2}	van Staa et al. (1974)

showers concerned cover a spread in size, that the measurements involve inaccuracies in core location and that it is often difficult to fit the lateral density distribution of the shower particles with an NKG function with a single age parameter, s (for details see Chap. 4, 8, and 10, Sect. 10.4).

13.3.2 Experimental Results, Recent Work

The two major detector systems capable of measuring the energy of hadrons in showers that had been used in recent years were the calorimeters at EAS-TOP and at the KASCADE site, which had been shut-down in 2000 and 2009, respectively. Both are briefly discussed in Sect. 13.2.2.

At certain periods during the operation of the EAS-TOP experiment the installed calorimeter had been used to measure the energy spectrum of the so-called

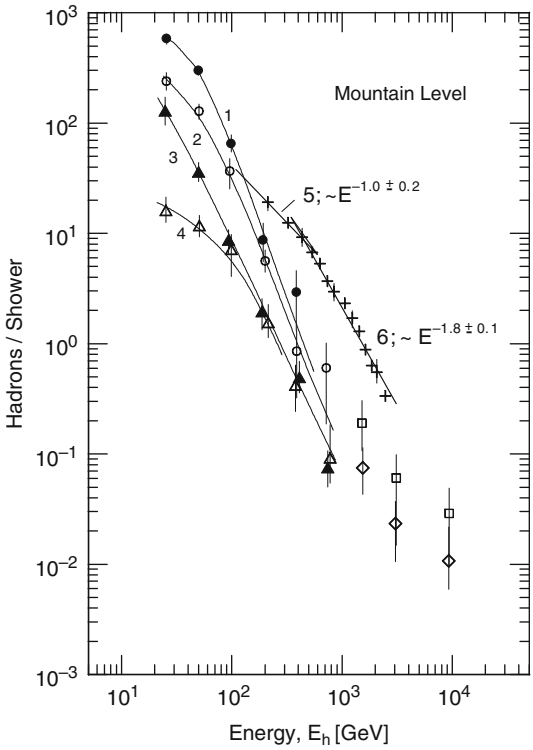

△	$4.0 \cdot 10^4 < N_e \leq 7.1 \cdot 10^4$	
▲	$1.8 \cdot 10^5 < N_e \leq 3.2 \cdot 10^5$	All Ootacamund
○	$5.6 \cdot 10^5 < N_e \leq 10^6$	
●	$1.8 \cdot 10^6 < N_e \leq 3.2 \cdot 10^6$	
◇	$4.0 \cdot 10^4 < N_e \leq 3.2 \cdot 10^5$	($E_0 \simeq 3 \cdot 10^5$ GeV)
□	$3.2 \cdot 10^5 < N_e \leq 3.2 \cdot 10^6$	($E_0 \simeq 2 \cdot 10^6$ GeV)
+	$3.0 \cdot 10^5 < N_e \leq 10^6$	Mt. Norikura

Fig. 13.18 Compilation of integral energy spectra of hadrons from measurements carried out at Ootacamund (2,200 m a.s.l.) (Vatcha and Sreekantan, 1973a) and Mt. Norikura (2,770 m) (Miyake, 1970) for the size groups and locations listed below. E_0 is the primary energy estimate made by Vatcha and Sreekantan (1973a) for the larger size groups (□, ◇). The *curves 1 to 4* help to guide the eye, *lines 5 and 6* indicate the slope of the spectrum

unaccompanied hadrons (Aglietta et al., 1997, 2003). Note that there is a difference between hadron spectra measured in showers, where the entire event is well defined, and unaccompanied hadron spectra. In the latter case one only accepts *isolated events* in the calorimeter without accompanying shower particles or hadrons in the vicinity. Caution is required when comparing data of unaccompanied hadrons from different experiments because in each case the restriction or term *unaccompanied* is defined differently. Such measurements do not contribute directly to our knowledge of hadrons in air showers. Unfortunately no data on hadrons associated with air showers are available from this experiment.

From the lateral density distribution of hadrons of different energy groups measured with the KASCADE calorimeter that are displayed in Figs. 13.12 and 13.13 one can plot energy spectra for different core positions in the near core area, but they

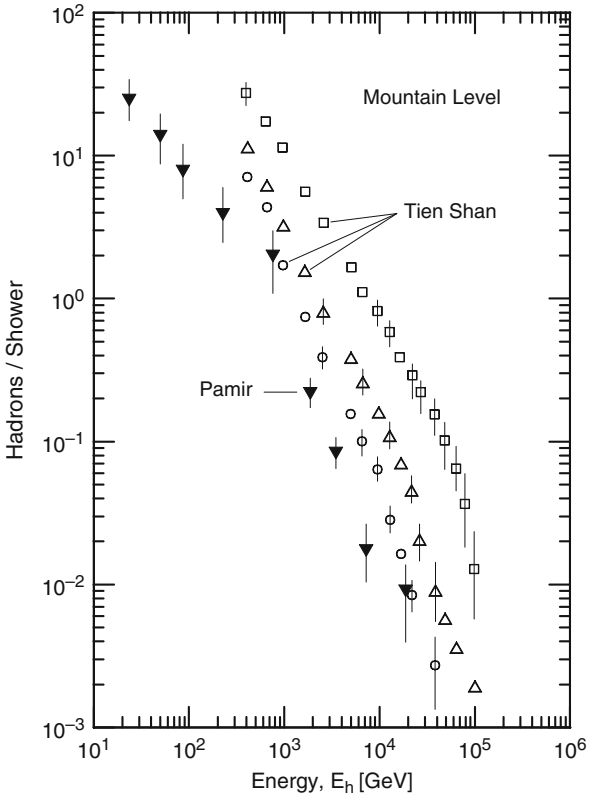

Fig. 13.19 Integral energy spectra of hadrons in showers of different size groups observed at Tien Shan (3,340 m, 750 g cm^{-2}): □, $\langle N_e \rangle = 9 \cdot 10^5$; △, $\langle N_e \rangle = 3 \cdot 10^5$ and ○, $\langle N_e \rangle = 1.5 \cdot 10^5$ (Nesterova and Chubenko, 1979). The results of measurements made at Pamir (3,860 m, 650 g cm^{-2}) in showers of size $4 \cdot 10^4$ is also shown ▼ (Dovzhenko et al., 1960)

include only hadrons of energy up to 500 GeV. General hadron spectra in showers covering the range $100 \leq E_h \leq 8 \cdot 10^4$ GeV had been constructed from data acquired with the KASCADE calorimeter (Antoni et al., 1999) and from measurements carried out with the MAKET-ANI experiment (Ter-Antonian et al., 1995). These are plotted in Fig. 13.21.

13.4 Temporal Properties

13.4.1 General Comments

Temporal properties of hadrons in air showers contain a significant amount of information and can be regarded as a distinct signature of particular processes, events or particle types. The time tag of a particle with respect to the shower front or tangent plane is a very useful parameter that can serve as a means of selection criterion or for discrimination purposes.

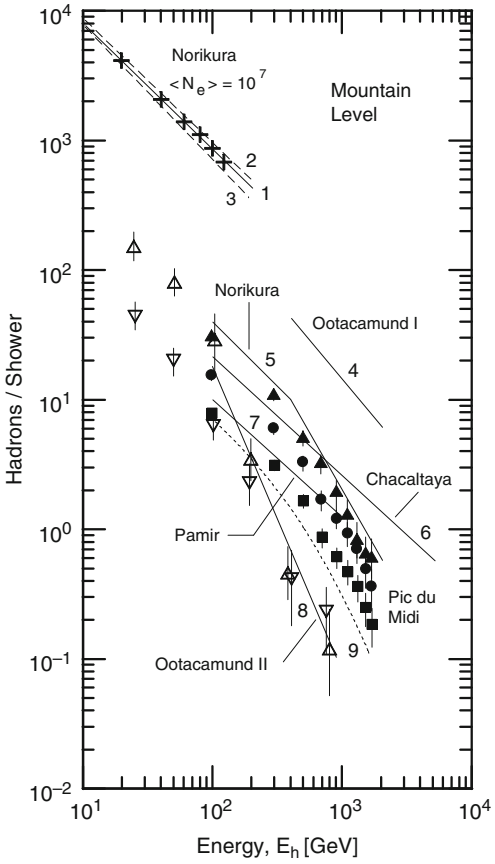

Fig. 13.20 Compilation and comparison of integral energy spectra of hadrons from different experiments at mountain level. +, Mt. Norikura (2,770 m) for large showers ($\langle N_e \rangle = 10^7$) of age $s = 1.0$ (*line 1*). *Lines 2 and 3* are for $s = 0.9$ and $s = 0.8$, respectively, not shown by data points (Miyake et al., 1979). The full symbols are from measurements at Pic du Midi (2,860 m) for showers of size groups $5 \cdot 10^5 \leq N_e \leq 8 \cdot 10^5$ (▲), $2.5 \cdot 10^5 \leq N_e \leq 4 \cdot 10^5$ (●) and $1.25 \cdot 10^5 \leq N_e \leq 2 \cdot 10^5$ (■) (van Staa et al., 1974; Aschenbach 1974). The open symbols are from Ootacamund (2,200 m) for showers of sizes $3.2 \cdot 10^5 \leq N_e \leq 5.6 \cdot 10^5$ (△) and $7.1 \cdot 10^4 \leq N_e \leq 1.3 \cdot 10^5$ (▽) (Vatcha and Sreekantan, 1973a). *Curves 3–8* represent previous hadron spectra from other experiments that apply to similar shower size groups: 4, Ootacamund I, $3 \cdot 10^5 \leq N_e \leq 6 \cdot 10^5$ (Chatterjee et al., 1968); 5, Norikura $3 \cdot 10^5 \leq N_e \leq 10^6$ (Miyake et al., 1970); 6, Chacaltaya (5,300 m) $3 \cdot 10^5 \leq N_e \leq 9 \cdot 10^5$ (Hasegawa et al., 1965). 7, Pamir (3,860 m) for $N_e = 10^5$, (Dovzenko et al., 1960); 8, Ootacamund II, $3.2 \cdot 10^5 \leq N_e \leq 6 \cdot 10^5$ (Sreekantan, 1971). *Curve 9*, prediction IDFB model (Grieder 1970a, b, 1977a) (for details see text)

In some of the first quark hunt experiments using air showers the concept of time lag of stable massive particles with respect to the shower front was used as a selection criterion. These experiments were based on the assumption that quarks exist as free, stable massive particles that are produced copiously abovethe kinematic

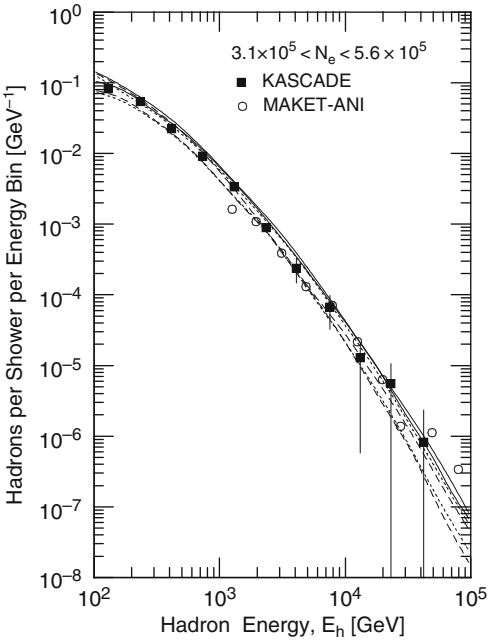

Fig. 13.21 Hadron differential energy spectra for a fixed shower size range as indicated, corresponding to a primary energy of approximately $6\cdot10^{15}$ eV. The data points are from the KASCADE (■) (Antoni et al., 1999) and MAKET-ANI (○) (Ter-Antonian et al., 1995) experiments. The three sets of *curves* are from simulations using the VENUS (*solid curves*) QGSJET (*dashed curves*) and SIBYLL (*dotted curves*) event generators; the *upper curves* apply to proton, the *lower curves* of the same kind to iron primaries (after Antoni et al., 1999)

threshold in shower cores where numerous ultra energetic hadronic interactions occur (Damgaard et al., 1965a, b; Chatterjee et al., 1965c; Pal and Tandon, 1965; Bjornboe et al., 1968), an assumption which, as we know today, is incorrect.

Nevertheless, quarks thus produced would be most abundant near the kinematic threshold because of the rapidly falling spectrum and number of projectile particles, and therefore emerge almost at rest in the center of mass. Consequently they would also be slow in the laboratory frame and accumulate large delays with respect to the shower front, which is part of the signature of slow stable massive particles. Similar studies were also carried out by other authors in later years (Goodman et al., 1979).

13.4.2 Simulation Results

Monte Carlo simulations using refined shower and interaction models have shown that for example charged pions cannot be significantly delayed with respect to the shower front except for occasionally very locally produced low energy pions. The bulk of charged pions in a shower that have energies $\geq$10 GeV are hardly

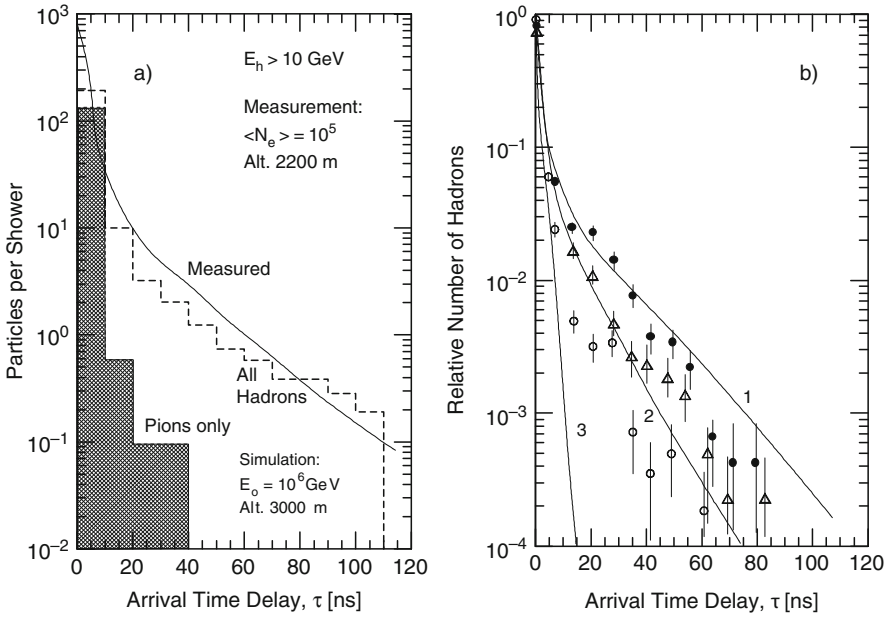

Fig. 13.22 (**a**) Predicted arrival time distributions of all hadrons and of pions only in showers initiated by primary protons of energy 10^6 GeV, observed at 3,000 m a.s.l. (*dashed histograms*) (Grieder, 1977a). Also shown is a measured distribution (*solid curve*, Tonwar and Sreekantan, 1971a, b). (**b**) Arrival time distributions of hadrons of different energy groups in showers recorded at Ootacamund (2,200 m a.s.l.) and predicted distributions (•, curve 1, 5–10 GeV; △, curve 2, 10–20 GeV; ○, > 20 GeV). The experimental errors are statistical (Tonwar and Sreekantan, 1971a, b; Tonwar et al., 1971a, b, 1972)

ever delayed by more than about 10 ns because they are subject to decay (Grieder, 1970b, 1977a). This is illustrated in Fig. 13.22a).

On the other hand, baryons and antibaryons are massive stable particles which can accumulate significant delays with respect to the shower front unless they are highly relativistic or, in the case of antibaryons, removed from the particle population through occasional annihilation (Fig. 13.22a). Part of their delay may also be accumulated by parent particles that are subject to scattering and elongated trajectories while propagating through the atmosphere (Pal and Tandon, 1965; Murthy et al., 1968; Grieder 1970b, c, 1977a).

13.4.3 Experimental Exploitation and Data

The above mentioned temporal properties of the different particle types had been used in an interesting experiment carried out by the Tata group at Ootacamund (India), using their relatively small (1.4 m^2) total absorption scintillation spectrometer (TASS) in an attempt to search for and deliver proof of the existence

of low energy antinucleons in air showers (Chatterjee et al. 1965b, c; Tonwar et al., 1971a, b; Tonwar and Sreekantan, 1971a, b). They operated the TASS at the center of an air shower array and recorded the time delay, up to 300 ns, with respect to the shower front, of strongly interacting particles of energy $\geq$ 5 GeV. The resulting distribution is illustrated in Fig. 13.22b.

These data have shown that the peak of the delay distribution of interacting particles is centered around 20 ns, that the average delay is a function of particle energy, as expected, that 30% of the particles of energy $\geq$5 GeV are delayed by more than 50 ns and only 0.4% are delayed more than 100 ns, with a tail ending at 250 ns. Simulations rule out the possibility that strongly interacting particles of energy $\geq$5 GeV having delays $\geq$50 ns are charged pions or kaons, only nucleons and antinucleons can fulfill the above requirements. Consequently, the conclusion from this work was that $N\overline{N}$ production must occur at a significant rate in air showers. This implied a major increase of the $N\overline{N}$ production cross section from 30 GeV, the maximum energy where the $N\overline{N}$ cross section hand been explored at that time in fixed target experiments at accelerators, up to the multi-TeV energy range of air showers (see Chap. 3).

Experimental and simulation results of this analysis are shown in Fig. 13.22b. The conclusions drawn from this work were confirmed by the results of subsequent experiments at the CERN *Intersecting Storage Ring* (ISR) which revealed a significant increase of the production cross section of nucleon-antinucleon pairs in proton-proton collisions over its operating range from 22 to 62 GeV total energy in the center of mass, corresponding to a range from about 250 to 2000 GeV in the laboratory frame (Albrow et al., 1972; Banner et al., 1972; Alper et al., 1972, 1973a, b).[8]

13.5 Charge to Neutral Ratio

In order to extract information on high energy hadronic interactions and the primary composition, many authors have studied the charge to neutral ratio, C/N, or vice versa, the neutral to charge ratio, N/C, as well as the proton to neutron ratio, p/n, and vice versa, in the unaccompanied cosmic radiation as well as in air showers. The charge to neutral ratio is related to the primary composition but also to particle production properties (Peters, 1952; Pal and Peters, 1964). The usual instruments for this kind of investigation are calorimeters, multi-plate cloud chambers with or without magnetic fields and, in some cases, emulsion chambers that are operated in conjunction with air shower arrays.

To determine these ratios in air showers has the advantage that in each individual event in spite of the fact that the parameters of the collisions from which the particles originate are unknown, the overall event is defined by the shower size. Kameda

[8] A recent review on multiparticle production based on QCD and the comparison with experimental data from many experiments, including the ratios of produced particles can be found in the paper by Kabana and Minkowski (2001).

Table 13.1 Charge to neutral ratio, C/N, versus hadron energy, E_h (Kameda et al., 1965)

E_h [GeV]	<500	≥500	≥1000	All energies
C/N	6 ± 1	$2.5^{+1.5}_{-0.5}$	1.5 ± 0.5	4.5 ± 0.5

et al. (1965) were among the first to study systematically the charge to neutral ratio of hadrons in extensive air showers as a function of shower size as well as hadron energy, using a multi-plate cloud chamber. They have noticed that the charge ratio does not depend on shower size but on hadron energy and tends to unity at very high energies. Their results are given in Table 13.1.

In conjunction with Monte Carlo simulations, valuable information can thus be extracted. However, an additional problem encountered when measuring the C/N ratio in showers is that the high density of energetic particles near the shower core, where the most energetic particles are to be found, sets limits to the minimum distance from the core where measurements can be made. The closest approach depends on the spatial resolution of the hadron detector. Moreover, *punch-throughs* in the near core region can lead to misinterpretations and falsify the C/N ratio.[9] On the other hand, with increasing distances from the shower axis the hadron number and their energy decrease rapidly and set practical limits, too. In the following we summarize the results of relevant C/N measurements.

In Fig. 13.23 we show a compilation of the C/N ratio as a function of hadron energy in showers of various average primary energies or size groups, obtained by different authors at sea level (Ashton et al., 1975; Asakimori et al., 1979; Dobrzynski et al., 1981) and at Ootacamund, 2,200 m a.s.l. (Sreekantan, 1971; Vatcha and Sreekantan, 1973b), as indicated.

The charge to neutral ratio, C/N, as a function of shower size obtained in different experiments measured at sea level and at moderate mountain altitude are shown in Fig. 13.24. Included in this study are hadrons of moderate energy (≥25 and ≥50 GeV). Some studies indicate a decreasing C/N ratio with increasing distance from the shower axis which appears to be independent of shower size (Dobrzynski et al., 1981). This finding can be explained on the grounds that generally speaking at a given observation level the density of energetic hadrons decreases with increasing core distance for kinematic reasons, and because of scattering. On the other hand, contrary to charged hadrons, neutrons are not subject to ionization losses and scattered neutrons are likely to enrich the hadron population further away from the shower core, thus affecting the C/N ratio in their favor.

A compilation of mostly very early experimental and theoretical results of the ratio of neutral to charged hadrons, N/C, and of the neutron to proton ratio, n/p, as a function of atmospheric depth is presented in Fig. 13.25. Details concerning the different studies are given in the caption of the figure. Because of the charge symmetry among the secondary particles resulting from high energy nuclear interactions

[9] Punch-throughs are energetic particles, frequently $e^{\pm}$, that may occasionally penetrate an absorber beyond the expected range and lead to misinterpretations, a problem well known in measurements near or inside the shower core and in muon experiments.

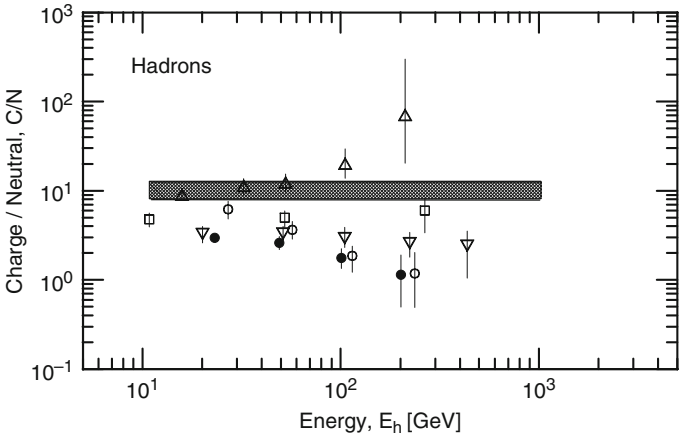

Fig. 13.23 Charge to neutral ratio (C/N) of hadrons in showers versus hadron energy, E_h, from various experiments and for primary energies, E_0, or shower sizes, N_e, as follows: △, $E_0 \simeq 1.4 \cdot 10^5$ GeV (Ashton et al., 1975); □, $E_0 \simeq 2.0 \cdot 10^5$ GeV (Asakimori et al., 1979); ▽, $E_0 \simeq 10^6$ GeV (Dobrzynski et al., 1981); ○, $N_e < 3.2 \cdot 10^5$ (Vatcha and Sreekantan, 1973b); ●, $N_e > 3.2 \cdot 10^5$ (Vatcha and Sreekantan, 1973b). The shaded area is from a calculation of Gaisser and Rudolf (1976)

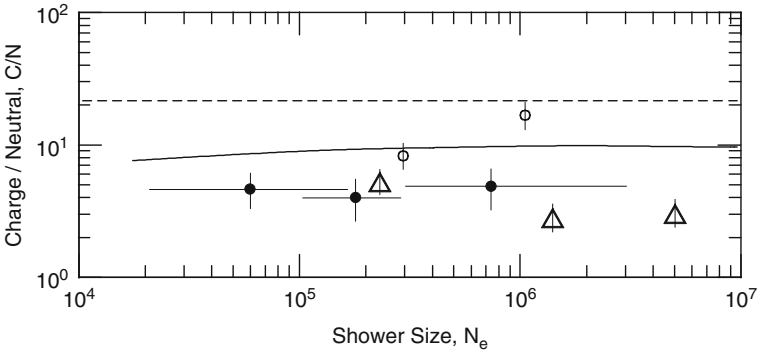

Fig. 13.24 Charge to neutral ratio, (C/N), of hadrons in showers as a function of shower size, N_e. ○, Ashton et al. (1977), recorded at Durham (GB) (s.l.); △, Vatcha and Sreekantan (1973b), recorded at Ootacamund (India) (2,200 m a.s.l.). Both sets of data include all hadrons of energy ≥25 GeV. ●, Asakimori et al. (1979) for hadrons of energy ≥50 GeV recorded at Tokyo (I.N.S.) (s.l.). The *dashed and solid curves* show predictions from calculations that include the production of K_0 and $\overline{K}_0$ only, and of K_0, $\overline{K}_0$, N (nucleons) and $\overline{N}$ (antinucleons) (Gaisser and Rudolf, 1976)

it is expected that the charge to neutral ratio tends asymptotically toward unity at very high energies. In addition, heavy primaries add to the population of neutral particles, too.

As Hazen et al. (1976) have pointed out, it is important for these experiments not to be too restrictive with the event selection criteria with respect to the particle density above the hadron detector. Selecting data samples where a very low particle density is required above the event analyzer leads to a strong bias in favor of low energy events, i.e., one focuses in this case mostly on the C/N ratio of unaccompanied particles and not on the C/N ratio of hadrons in air showers.

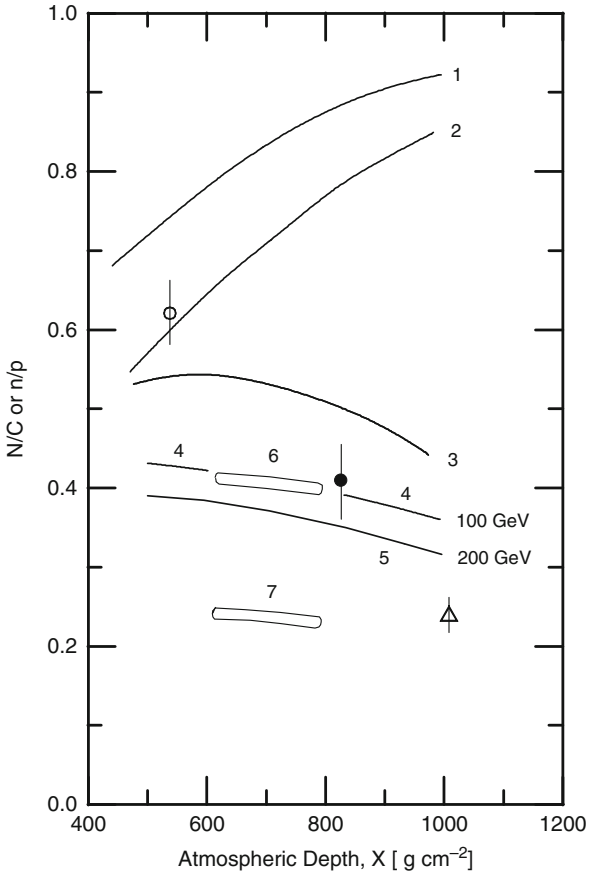

Fig. 13.25 Compilation of early data on the atmospheric depth dependence of the ratio of neutral to charged hadrons, (N/C), and of neutrons to protons (n/p). *Curves 1 and 2* are predictions for the ratio (n/p) according to Pal and Peters (1964) and Garraffo et al. (1973), respectively, and *curve 3* is the (N/C) ratio after Pal and Peters (1964). The symbol ○ shows an experimental result obtained at Chacaltaya (5,230 m) for the ratio (N/C) (Hazen et al., 1976). The two *curves 4 and 5* show the (N/C) ratio obtained by Hazen et al. (1976) at 100 and 200 GeV, using the (n/p) and (π/p) ratios of Garraffo et al. (1973). △ is the (N/C) ratio obtained by Cowan and Matthews (1971). Region 6 is the (n/p) ratio calculated by Adair (1974) for atmospheric depths of 600–800 g cm^{-2} and • is the (N/C) ratio at 2,000 m after Alakoz et al. (1968). Region 7 shows the (N/C) ratio calculated by Hazen et al. (1976) using the (π/p) ratio of Garraffo et al. (1973)

Apshev et al. (1977) have determined the energy spectra of low energy charged and neutral hadrons in small showers at the Elbrus laboratory, located at an altitude of 1,850 m a.s.l. These authors have used a Wilson cloud chamber with two independently operating volumes of $23 \times 15 \times 11\,\text{cm}^3$ each, that were separated by a $40\,\text{g cm}^{-2}$ copper plate ($\lambda_{\text{int}} \approx 0.3$) and placed in a magnetic field of strength 4300 G inside a hodoscope arrangement. The effective area was $0.02\,\text{m}^2$. The maximum detectable momentum for charged particles was 6 GeV/c. An air shower detection

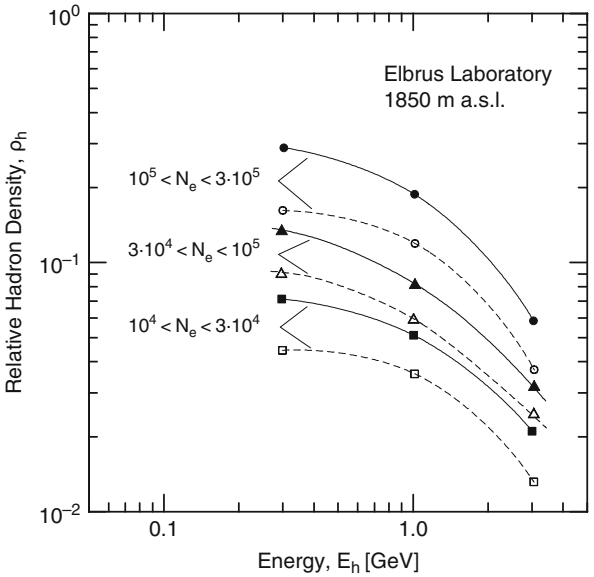

Fig. 13.26 Integral energy spectra of low energy charged and neutral hadrons measured with a Wilson cloud chamber in a magnetic field of 4,300 G at the Elbrus laboratory (1,850 m a.s.l.) for three different shower size groups, as indicated. The data show relative intensities and apply to an average core distance of 15 m. The full symbols include all hadrons, the open symbols neutral hadrons only (Apshev et al., 1977)

Table 13.2 Ratio $R = N/(N + C^{\pm})$ of low energy hadrons in showers of size N_e (Apshev et al., 1977)

N_e	$10^4 - 3 \cdot 10^4$	$3 \cdot 10^4 - 10^5$	$10^5 - 3 \cdot 10^5$
R	0.70 ± 0.021	0.72 ± 0.019	0.70 ± 0.07

array was placed around the cloud chamber. The accepted showers were divided into three size groups, $10^4 \leq N_e \leq 3 \cdot 10^4$, $3 \cdot 10^4 < N_e \leq 10^5$ and $10^5 < N_e \leq 3 \cdot 10^5$. The accuracy of the shower axis determination was only ± 5 m. The results of this work are plotted in Fig. 13.26. From these measurements the ratio $R = N/(N+C^{\pm})$ of low energy hadrons within a radius of about 15 m from the shower axis was extracted. The data are summarized in Table 13.2.

13.6 Hadron Content and Composition

Hadrons constitute the least abundant particle group in air showers. They contribute about 1% to the total particle flux but are chiefly responsible for the energy transport and supply in the shower process. With the exception of the most energetic events most showers reach their maximum development at altitudes well above sea level. It is therefore more favorable to study hadrons in air showers at elevated altitudes.

13.6.1 Low Energy Hadrons

Cocconi and Cocconi (1950) were among the first to investigate systematically the hadron content in showers at mountain altitude. In their experiment at Echo Lake, Colorado (3,260 m a.s.l.) they have used neutron detectors that were in fact an early form of neutron monitors, to identify hadronic interactions in air showers. A similar attempt was made by Chatterjee et al. (1963) who followed the same basic procedure, using neutron monitors, in a more elaborate shower array at Ootacamund (2,200 m a.s.l.) to estimate the flux of low energy hadrons associated with showers. It is important to realize that hadron measurements using neutron detectors are sensitive mainly to very low energy hadrons that cause so-called nuclear evaporation reactions.[10]

The interpretation of the neutron multiplicity, m, in a neutron monitor that is operated within an air shower array and its correlation with the density and energy of the shower hadrons that initiate the evaporation reactions in the lead target of the monitors which then produce the neutrons that are thermalized eventually and detected by the BF_3 counters, is not a trivial matter.

A rather detailed theoretical analysis, partly based on earlier work of other authors (Cocconi et al., 1950; Hughes et al., 1964) was carried out by Böhm et al. (1970) to interpret their measurements, using standard NM-64 type neutron monitors within the array at Kiel to measure the lateral density distribution of low energy hadrons and to determine the total number of hadrons, N_h, in showers (Clem, 1999; Clem and Dorman, 2000; see Hatton, 1971 for a review). In this work contributions from electromagnetic processes, mostly via the ∼15 MeV giant resonance, are disregarded.

One of the key observables for the analysis of neutron monitor data is the neutron multiplicity-frequency distribution over the core distance range that is of interest. The corresponding Kiel data are illustrated in Fig. 13.27a and the derived mean energy of the detected hadrons in the showers as a function of core distance in Fig. 13.27b. The resulting low energy hadron content in showers versus shower size is shown in Fig. 13.28a. A large fraction of the detected low energy hadrons that produced the registered neutrons consisted most likely of nucleons. The pion content must have been small for reasons discussed earlier in this chapter.

Also shown in the same figure are low energy hadron data of the same kind obtained in a similar experiment, using neutron monitors within the giant Yakutsk array, recorded in very large showers (Kozlov et al., 1979, 1981). These data follow along the extrapolated line that connects the Kiel data, thus confirming that the same power law relationship between shower size and low energy hadron content holds over a wide range of sizes.

[10] The bulk of these hadrons have energies $\leq$1 GeV at core distances $\geq$10 m. Modern simulations to study neutron monitor responses are usually cut off at $\leq$100 GeV where the probability for evaporation reactions becomes negligible.

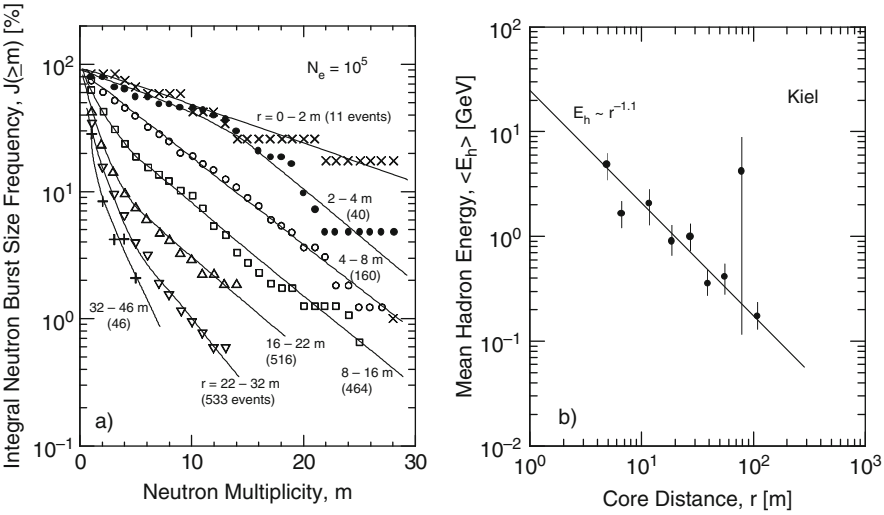

Fig. 13.27 (**a**) Integral neutron burst size spectra of multiplicity $\geq m$ in showers of size 10^5 in different core distance intervals, r [m], as indicated, measured with three 7 m^2 NM 18–64 neutron monitors at Kiel. The number of events for each interval is given in *parenthesis*; the neutron counting gate width was 2 ms (Böhm et al., 1970). (**b**) Lateral distribution of the mean energy of the hadrons in showers, $E_h(r)$, that are responsible for the neutron production in the neutron monitors at the Kiel array (Böhm et al., 1970)

Inspection of the neutron multiplicity-frequency relation of the Yakutsk measurements, displayed in Fig. 13.28b, reveals a kink in the distribution of the large shower size group. The authors ascribe this kink, which does not seem to affect the hadron-number/shower-size ($N_h - N_e$) correlation, to the change in the shower selection method which they have applied to part of the data, to cope with the large range of core distances, out to 1,000 m from the core, over which the data were collected.

It should be noted that the irregular behavior of the $N_h - N_e$ correlation for low energy hadrons observed in the size range $10^4 \leq N_e \leq 10^6$ in the early experiment of Danilova and Nikolsky (1963) and Danilova (1964, 1965), not discussed here, using neutron detectors, that was carried out at 3,340 m a.s.l., has not been confirmed by other investigators. Likewise, the small slope of the $N_h - N_e$ correlation with an index of $\alpha \leq 0.4$ (see Eq. 13.7 below) which these authors have found around $N_e \sim 10^5$.

Other discrepancies between the results of the contemporary experiments of Chatterjee et al. (1963) and Danilova appear to be due to the different kind of shower detectors that had been used; scintillators in the former and Geiger counter trays in the latter. Transition effects in the scintillators could have led to shower size overestimation. Recently, Jedrzejczak et al. (2006) have revisited the topic of neutron measurements in air showers, using neutron monitors as a tool, to estimate the low energy hadron contents of showers.

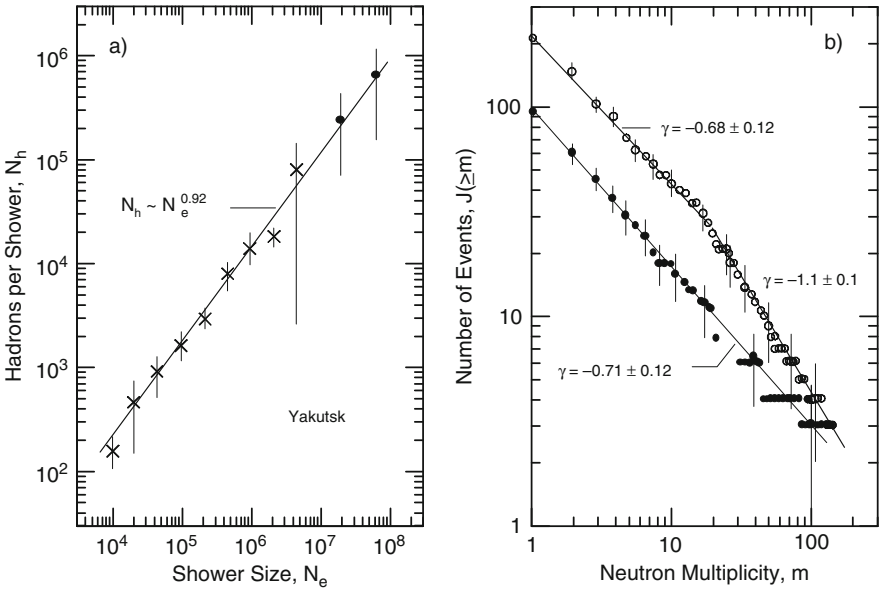

Fig. 13.28 (**a**) Average number of very low energy charged and neutral hadrons combined as a function of shower size recorded at Kiel, × (Böhm et al., 1970) and Yakutsk, • (Kozlov et al., 1979) (both s.l.), using neutron monitors. (**b**) Integral neutron multiplicity spectrum in showers of different average sizes at large core distances (≤1000 m) at Yakutsk: •, $\langle N_e \rangle = 1.7 \cdot 10^7$; ○, $\langle N_e \rangle = 5.1 \cdot 10^7$. The *lines* are fits to the data and the γ-values indicate the slope of the spectral sections. The knee in the upper distribution is due to a change in the shower selection method. The neutron collection time window was 360 μs (Kozlov et al., 1979)

13.6.2 Medium and High Energy Hadrons

In an early experiment at Tokyo, Kameda et al. (1965) have used a multi-plate Wilson cloud chamber to extracted the hadron content in showers at sea level and likewise Apshev et al. (1977) with the previously mentioned experiment at 1,850 m a.s.l. at the Elbrus laboratory. The Apshev data include mostly low energy hadrons ($E_h \geq 10$ GeV) whereas the data of Kameda cover higher energies ($E_h \geq 100$ GeV). These data are plotted in Fig, 13.29 together with the results from the work of Fritze et al. (1970) at Kiel that were obtained with the neon hodoscope burst detector described earlier and involve hadrons of energy $E_h \geq 800$ GeV.

Rather recent data of measurements made by Antoni et al. (2002) of the content of hadrons of different energy groups in showers as a function of the electron shower size, made with the KASCADE installation (110 m a.s.l.), are plotted in Fig. 13.30, together with predictions from simulations for proton and iron primary initiated showers. Also shown in the same plot are old data from an experiment at Kiel (s.l.) by Fritze et al. (1970) and from the high altitude installation at Mt. Chacaltaya (5,230 m a.s.l.) of Matano et al. (1970), for comparison.

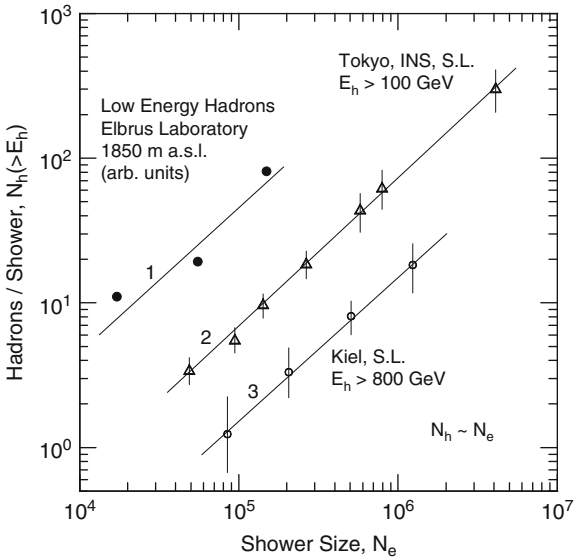

Fig. 13.29 Average number of hadrons, charged and neutral combined, of different threshold energies, $> E_h$, in showers as a function of shower size at sea level: △, Kameda et al. (1965); ○, Fritze et al. (1970); •, Apshev et al. (1977) (the latter are based on the average over 15 m from the core). Kameda and Apshev used a cloud chamber, Fritze the 14 m^2 neon hodoscope

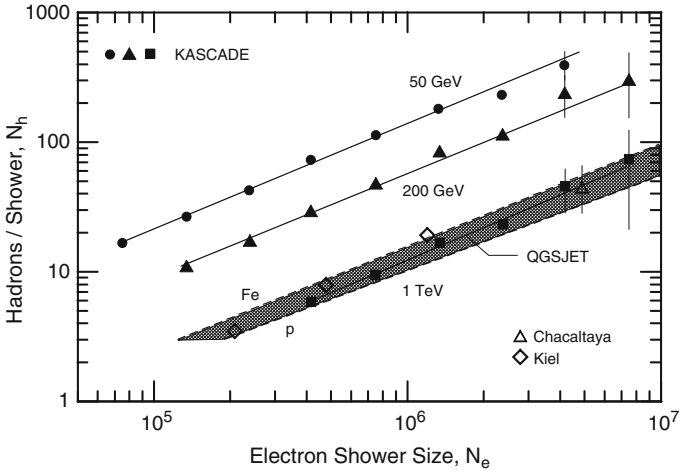

Fig. 13.30 Hadron number per shower, N_h, versus electron shower size, N_e correlation for three different hadron energy groups (• $E_h \geq 50$ GeV, ▲ $E_h \geq 200$ GeV and ■ $E_h \geq 1$ TeV), as indicated, obtained with the KASCADE experiment. Also shown are data from the Kiel experiment ◇ (Fritze et al., 1970) and from Mt. Chacaltaya △ (Matano et al., 1970). The hashed ribbon indicates the range covered by predictions from CORSIKA simulations with the QGSJET event generator for proton (*lower boundary*) to iron (*upper boundary*) primaries (after Antoni et al., 1999)

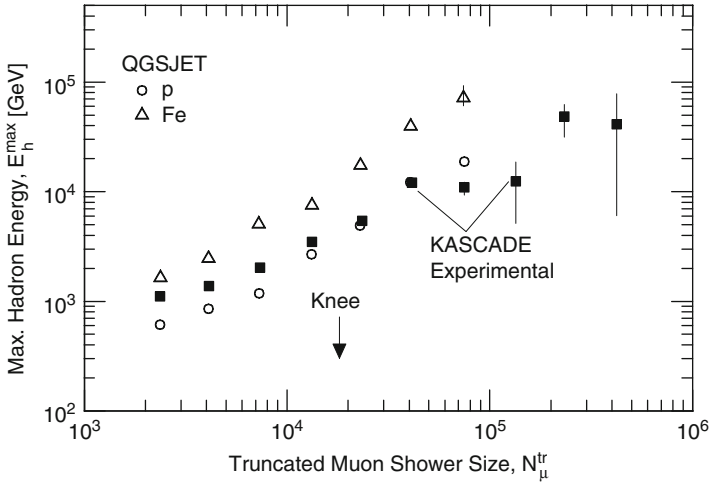

Fig. 13.31 Maximum hadron energy in a shower as a function of the truncated muon shower size, N_μ^{tr}. The data points (■) are from the KASCADE experiment the open symbols from simulations with the CORSIKA program using the VENUS and QGSJET event generators for primary protons and iron nuclei, as indicated. The location of the spectral knee is also indicated (after Antoni et al., 1999)

An instructive set of data which illuminates the leading particle effect and other properties of hadrons and hadron production in showers is displayed in Fig. 13.31. There the maximum hadron energy in showers is plotted as a function of the truncated muon size. This plot suggests a possible flattening of the distribution at high primary energies, implying a slight increase of the inelasticity.

Another interesting trend, discussed in Chap. 19 (see Figs. 19.16 and 19.17) which deals with correlations among shower observables, that is not evident from Fig. 13.30 but worth mentioning here is that the measured total number of hadrons per shower as a function of electron or truncated muon shower size appears to increase more slowly with increasing shower size for large showers than is predicted by current interaction models. This implies an increasing deficit of hadronic energy in the showers. This statement, however, requires confirmation.

The primary mass dependence of the number of hadrons of energy $E_h \geq 100\,\text{GeV}$ as a function of the truncated muon size had been investigated by Antoni et al. (2002). The results are summarized in Fig. 13.32 where data from measurements made with the KASCADE calorimeter and predictions using different event generators are plotted.

A compilation of data on the correlation between the very high energy hadron content in showers ($E_h > 1\,\text{TeV}$) and shower size at higher altitudes is presented in Fig. 13.33. Most of these data were acquired with calorimeters. Details and references are given in the figure caption.

All these experiments, including the low energy measurements with neutron detectors, confirm that the number of hadrons in a shower is almost proportional to the shower size and therefore to the energy of the primary initiating the shower,

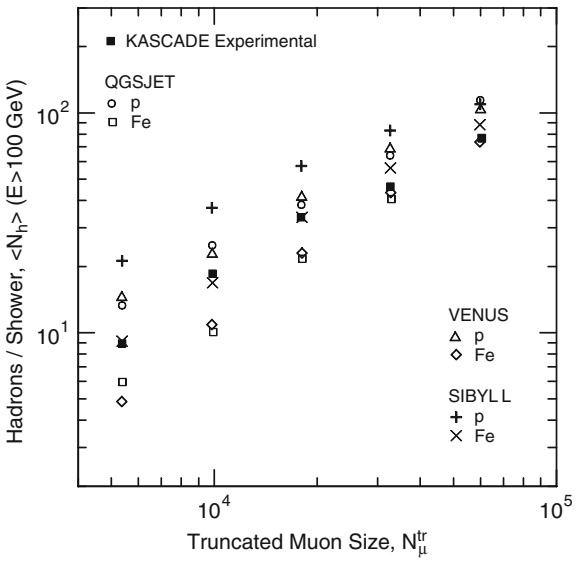

Fig. 13.32 Mean number of hadrons $\langle N_h \rangle$ of energy $\geq$ 100 GeV versus truncated muon shower size, N_μ^{tr}. The full symbols (■) are from measurements with the KASCADE calorimeter, the other symbols are predictions from simulations for primary protons and iron nuclei initiated showers using CORSIKA and the event generators as indicated in the figure (after Antoni et al., 2002)

a fact that is confirmed by air shower simulations with current event generators. Thus,

$$N_h \propto N_e^{\alpha} \tag{13.7}$$

where α varies from author to author between 0.9 and 1.0.

13.6.3 Antinucleons

It is evident today that based on accelerator data and on theoretical grounds antinucleons must be present in extensive air showers (see Sect. 13.4.1). However, before 1970 little was known about the energy dependence of their production cross section and the significance of nucleon-antinucleon ($N\overline{N}$) production in a nuclear cascade for the energy transport within it and in a shower (Danilova et al., 1962; Peters, 1966). Serious investigations to shed light on this question began in 1965 as a sideline, when the delayed particle experiment at the Niels Bohr Institute in Copenhagen, discussed in Sect. 13.4, was initiated to search for quarks (for a review see Jones, 1976).

This work was followed by a major simulation effort which revealed that the production of a significant number of nucleons and antinucleons in showers is a necessity for showers of hadronic origin to propagate through the atmosphere and to manifest themselves at sea level as they do (Murthy et al., 1968; Grieder, 1970a, b, 1973; Tonwar et al., 1972).

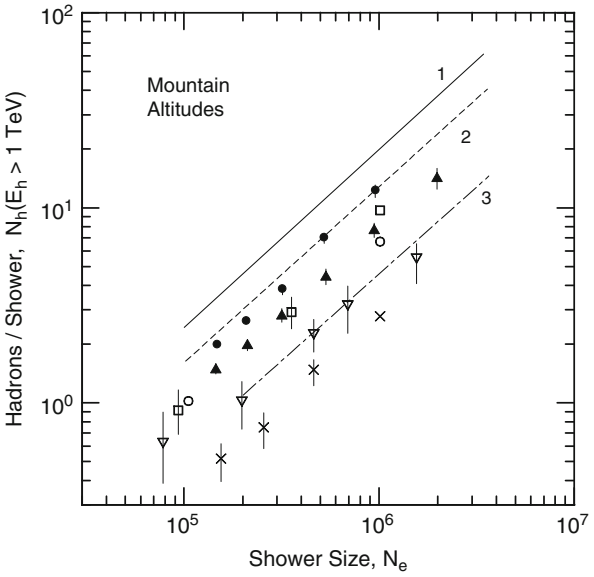

Fig. 13.33 Average number of hadrons, charged and neutral combined, of energy $E_h \geq 1$ TeV detected in air showers as a function of shower size. The data were recorded by different experiments and under different atmospheric overburdens, as listed below. *Lines 1, 2 and 3* are predictions of Vernov et al. (1978) using a particular scaling model and different model parameters

Symbol	Location	Altitude m	Overburden g cm^{-2}	Reference
●	Tien Shan	3,340	715 [a]	1
▲	Tien Shan	3,340	840 [b]	1
□	Aragatz	3,250	695	2
○	Pamir	3,860	650	3
▽	Norikura	2,770	750	4
×	Pic du Midi	2,860	730	5

[a] average zenith angle $\langle\theta\rangle = 15°$, [b] average zenith angle $\langle\theta\rangle = 35°$
References: (1) Nesterova and Chubenko (1979); (2) Nymmik (1970); (3) Vavilov et al. (1964); (4) Miyake (1970); (5) Böhm (1977), Aschenbach et al. (1974).

These calculations which are discussed in more detail in Chap. 20 were based on a variety of very detailed and realistic hadronic interaction models (for a review see Grieder, 1977a, 1979). More specific, the results of this work showed clearly that disregarding nucleon and antinucleon production and considering only pion production causes showers to develop more rapidly in the upper atmosphere, followed by an equally rapid attenuation of the very energetic hadronic components, leaving essentially only muons, a relatively small number of electrons, the leading particle[11] with few pions and recoil nucleons in the lower atmosphere, near sea level. This

[11] The leading particle is the most energetic hadron emerging from a high energy hadronic interaction. In nucleon-nucleon collisions it is usually a nucleon, rarely a pion (see Sect. 3.8).

phenomenon is primarily the consequence of the higher inelasticity of pion initiated interactions as compared to nucleon initiated interactions.

Apart from the experiments discussed in Sect. 13.4, very few attempts have been made to verify the existence of antinucleons in air showers, as it is an extremely difficult task. Some searches for antiprotons were also made in early experiments using cloud chambers (Kameda et al., 1960) but apart from a few candidate events no data on antinucleons in air showers exist other than those of the Tata group acquired at Ootacamund (Tonwar et al., 1972 and references listed therein).

13.6.4 Pions, Kaons and Charmed Particles

Hook et al. (1970) who operated a magnet spectrometer at Durham in conjunction with a neutron monitor surrounded by a small air shower array carried out measurements on hadrons in showers. They made the first attempt to resolve the fraction of pions among the hadrons in air showers, however, without much success.

Estimates of the kaon and charmed particle content in showers were obtained from underground experiments, operated in conjunction with surface detectors. The measurements were based on the angular distribution of high energy muons underground, analogous to similar measurements in the general unaccompanied cosmic ray flux, with the exception that the size of the initiating event at the surface and thus the primary energy were known (Elbert et al., 1983; Castellina et al., 1985; Andreyev et al., 1987).

For the shower development kaons play a very minor role and charmed particles an even lesser. Their production cross sections are small, even at very high energies and they are subject to rapid decay, particularly the charmed particles. However, kaons and even more so charmed particles are responsible for part of the most energetic muons in showers. Kinematically, kaons are similar to pions and, unlike nucleons, they are irrelevant for the energy transport in a shower.

13.7 Miscellaneous Topics

13.7.1 Single-Core Showers and Leading Particles

Single-core showers are events that manifest a rapidly and monotonic falling particle density with increasing radial distance from the axis. At great atmospheric depth they are a characteristic result of the *leading particle effect* observed in high energy hadronic interactions. This effect is described in detail in Sect. 3.8, together with the elasticity (inelasticity) of high energy hadronic collisions, the interaction mean free path ($\lambda_{\rm int}^{p,{\rm air}}$, $\lambda_{\rm int}^{\pi,{\rm air}}$, etc.), the cross sections of pp, p-air and π-air interactions ($\sigma_{\rm int}^{\rm pp}$, $\sigma_{\rm int}^{p,{\rm air}}$, $\sigma_{\rm int}^{\pi,{\rm air}}$, etc.), and related topics. Without the phenomenon of the leading particle effect the longitudinal development of the showers would be very different.

The majority of all showers up to moderate primary energies are single-core events that are most likely proton initiated. However, energetic showers with high hadron densities in the central core region may sometimes consist of superimposed and interlaced multiple hadron cascades that cannot be resolved spatially. These may be due to a small group of energetic secondaries emerging from a single interaction at moderate distance above the detector, or originate from fragments of heavy primary nuclei which had been subject to small transverse momenta and exceptionally little scattering. The latter kind of events are normally expected to yield flat central particle density distributions or multi-core showers.

Carrying out elasticity (inelasticity) studies of high energy hadronic interactions in air showers is a difficult task and requires an adequately resolving calorimeter of sufficient size incorporated in an array.

The elasticity and the leading particle effect are of prime importance for the development of nuclear cascades and the longitudinal shower development. Simulations have shown that air shower build-up and decay proceeds much faster without a high elasticity, i.e., without the leading particle effect, leaving mainly the muon, electron and neutrino components as survivors in the deeper regions of the atmosphere, down to sea level. This phenomenon leads therefore irrevocably to the necessity of nucleon-antinucleon production at high energies, which then enables the hadron cascade to be an efficient energy transport mechanism in the atmosphere, since only massive particles (nucleons and antinucleons) are efficient energy transport agents and not pions because of the lower elasticity of pion initiated collisions. (see Sect. 13.6.3 and Chap. 3).

Since the announcement made by Grigorov et al. (1965) that the inelastic proton-air cross section, $\sigma_{\text{inel}}^{p,\text{air}}$, appears to increases with energy, the investigation of the energy dependence of *key observables* such as the shower rate attenuation length, Λ_{atten}, and shower particle absorption length, λ_{abs}, the interaction mean free path, λ_{int}, the inelasticity, K, and the hadronic interaction cross sections, σ_{int}, was pursued in several experiments using unaccompanied cosmic rays (Jones et al., 1972; Yodh et al., 1972), and in many air shower experiments to the highest energies.

These efforts were intensified after the confirmation by Yodh et al. (1972) that the total pp cross section, $\sigma_{\text{total}}^{\text{pp}}$, is indeed increasing with energy in the range from 1 to 30 TeV in the laboratory frame. These authors specify a cross section as large as 60 mb at the highest energies investigated. Accounting for the large experimental errors a value of $\sigma_{\text{total}}^{\text{pp}} \geq 48$ mb is specified around 30 TeV with a confidence level of 95%. Almost at the same time the cosmic ray results were confirmed by one of the first experiments at the CERN Intersecting Storage Ring (I.S.R.) (Amaldi et al., 1973a, b; Amendolia et al., 1973).[12]

In a particular experiment, Böhm et al. (1975) have studied the energy spectrum of the surviving *leading particle* (hadron) in the core of showers of different size groups and constructed their spectra. For comparison the work was carried out at Pic du Midi and at Kiel. In either case the hadron detection was based on calorimetric

[12] For a more detailed discussion of this topic see Chap. 3

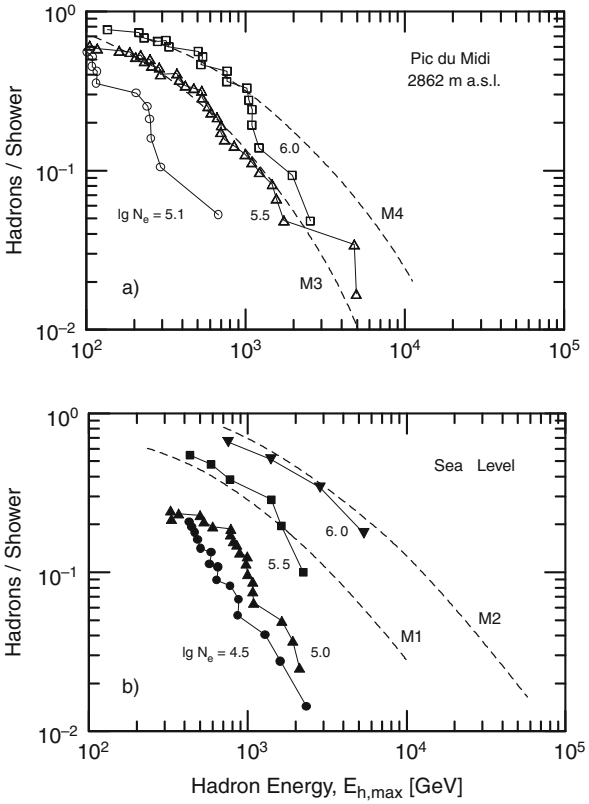

Fig. 13.34 Integral energy spectra of the most energetic hadrons (leading particles) in shower cores, normalized to the total number of cores in the detector for fixed shower size. Each point represents one event; points belonging to the same size group, N_e, are linked together with *solid lines*. (**a**) Shows the results obtained with the array at Pic du Midi (2,860 m) and (**b**) those from Kiel (sea level) (Böhm et al. 1975). The *dashed curves* M1–M4 are from model calculations by the same authors

measurements using a neon hodoscope as burst detector (Bagge et al., 1965). The results of the two experiments are shown in Fig. 13.34. Also shown are predicted distributions from simulations.

In conjunction with a theoretical analysis based on shower simulations Böhm et al. (1975) attempted to extract information on the primary composition. However, because of uncertainties in the cross sections and the elasticity of the interactions, no unambiguous solution could be extracted.

13.7.2 Multi-Core Showers

As pointed out in the introduction (Sect. 1.1 and Fig. 1.4), some showers exhibit single cores with rapidly falling central electron densities (Fig. 1.4a), others have

multiple cores (Fig. 1.4b), i.e., their central electron density distributions show two or more separate peaks or, in some cases, a very flat distribution. The discovery of multi-core showers goes back to the early fifties of the last century (Heinemann and Hazen, 1953; Hazen et al., 1954). In the late fifties and early sixties, when the existence of heavy primaries up to iron nuclei was established (Bradt and Peters, 1950), it was suggested that showers that have multiple cores could be due to heavy primaries (Peters, 1960). However, it was pointed out that multi-core showers could also be the result of *large transverse momenta*, imparted on energetic secondary particles, or of the decay products from massive clusters (fireballs) emerging from ultrahigh energy interactions.

Proof for the existence of so-called high transverse momentum events in ultrahigh energy cosmic ray initiated hadronic interactions was delivered in the early sixties in emulsion experiments (Akashi et al., 1965a, b). It was then evident that these processes are likely to obscure the mass information that was believed to be contained in the structure of multi-core events. On the other hand it was obvious that multi-core showers as well as showers that have a dominating main core and one or several so-called *sub-cores*, i.e., smaller cores that cluster around the main core, may prove to be useful for studying transverse momenta, p_t, at very high energies. This subject is discussed in more detail in Sect. 13.7.3 (see also Sect. 3.6 and 3.7).

Monte Carlo simulations of hadronic cascades and showers helped to illuminate the multi-core puzzle somewhat (Bradt and Rappoport, 1967). The calculations showed clearly that due to fluctuations and scattering processes multiple cores could not be associated reliably with primary mass five and more interaction mean free paths deep in the atmosphere. The different nuclear sub-cascades that are initiated by nucleons of dissociated heavy primaries and nuclear fragments are strongly intermixed in most cases and do not show a unique pattern that is distinguishable from density patterns resulting from sub-cascades of energetic secondaries in proton showers.

Nevertheless, numerous experiments were carried out by many groups using different techniques and detection methods to study multi-core showers in an effort to resolve the problem (Goryunov et al., 1960; Grieder, 1962; Oda and Tanaka, 1962; Miyake et al., 1963; Bray et al., 1964; Bagge et al., 1965; Matano et al., 1968; Nikolsky, 1969).

13.7.3 Transverse Momenta and $(E_h \cdot r)$ Product

For a long time it appeared that the mean transverse momentum, $\langle p_t \rangle$, acquired by secondary particles in high energy hadronic collisions was on the order of $\approx$250 MeV/c and independent of incident energy. This belief was based partly on the results from many experiments with cosmic rays over a wide energy range but with very limited statistics and partly on high statistics accelerator experiments with particle beams up to 30 GeV, the maximum energy available in the sixties. On the theoretical side the then popular thermodynamic model of Hagedorn (Hagedorn, 1965;

Hagedorn and Ranft, 1968) and the multi-peripheral model (Amati et al., 1962) suggested a transverse momentum distribution that follows a *power law* of the form (see Fig. 3.15)

$$f(p_t) \propto \exp(-6p_t) \ . \tag{13.8}$$

This expression fits the data well for $p_t \leq 1\,\text{GeV}$. However, occasionally puzzling events were observed in the core of air showers, in particular multi-core events, that could only be explained by invoking the presence of unusually large transverse momenta.

Proof that very large transverse momenta, on the order of 5 GeV/c, do in fact occur beyond a shadow of doubt in ultrahigh energy nuclear interactions ($E \geq 100\,\text{TeV}$) was first delivered by emulsion experiments. The first observations were reported by the joint Japanese and Brazilian Emulsion Group who operated emulsion chambers at Mt. Norikura (2,770 m) in Japan and Mt. Chacaltaya (5,230 m) in Bolivia (Japanese and Brazilian Emulsion Groups, Akashi et al., 1965a, b, reported by Nishimura at the London Conference; for a review see Lattes et al., 1980). Somewhat later, Matano et al. (1968) reconstructed from their analysis of *multi-core showers* detected with the $20\,\text{m}^2$ high resolution spark chamber of the air shower array at the Institute for Nuclear Studies (I.N.S.) of the University of Tokyo events with transverse momenta up to tens of GeV/c.

These discoveries and the belief that the transverse momentum could possibly depend on energy motivated many air shower researchers to carry out experiments to look for corresponding effects in the cores of air showers. The confirmation from accelerator experiments that large transverse momentum events really exist came from some of the first experiments with the Intersecting Storage Rings (ISR) at CERN in Geneva, Switzerland (Banner et al., 1973; Büsser et al., 1973; Sivers et al., 1976; Jacob and Landshoff, 1978).

As discussed in Sect. 13.7.2, multi-core showers may not only be caused by heavy primaries that are fragmented in the first and subsequent interactions into lighter nuclei and nucleons that lead to the superposition of several hadronic *subcascades* in showers, but also by high energy secondary particles emerging from ultra energetic nucleon initiated interactions in the upper atmosphere with a high transverse momentum. Multi-core showers are therefore also of interest to explore the transverse momentum, p_t, its energy dependence, $p_t(E)$, and the height of origin or production, h, of high energy hadrons that are detected at ground level.

To determine the transverse momentum of high energy particles that may be responsible for multi-core showers, i.e., for showers with several separated peaks in the central electron density distribution, the following procedure was adopted: Assume that the peaks are due to the gamma rays of decayed neutral pions resulting from the same interaction.[13] In this case we can calculate the minimum value of the

[13] The two electromagnetic cascades initiated by the two gamma rays from a decayed neutral pion are intermixed and cannot be resolved.

transverse momentum from the relation

$$p_t = \frac{p_l \cdot r}{h} \approx \frac{E_h \cdot r}{h} , \tag{13.9}$$

where r is the separation of a given core from the centroid of the distribution of peaks (or from the shower axis if there is a main core and sub-cores), p_l the longitudinal momentum of the pion in the laboratory frame, and h the height of production of the pion. To get the latter value one takes the electron density of the peak and uses the well known electromagnetic cascade theory (Kamata and Nishimura, 1958; Nishimura, 1967). On the right hand side of Eq. (13.9), E_h stands for the energy of the event initiating hadron which can in general be used in this kind of analysis in place of p_l since E_h is usually very large and therefore, $E_h \approx p_l$.

However, in general the pions will not have come from the same interaction and often not even from consecutive interactions of the same parent hadron. Usually the spread of peaks of similar size can be due to nucleons from fragmented heavy primaries having undergone scattering and interaction processes or, likewise, to very energetic secondaries, mostly nucleons, originating from the first or first few interactions of primary protons. In either case the transverse momenta resulting from Eq. (13.9) still yield an estimate of the mean transverse momentum, $\langle p_t \rangle$, of the various interactions through the atmosphere.

Early attempts to relate multi-core showers with large transverse momenta were made by Oda and Tanaka (1962) and Oda (1963) at Tokyo, Samorski et al. (1965) at Kiel, and by the Sydney air shower group (Bakich et al., 1968, 1970a, b). The latter claimed the observation of transverse momenta as high as 100 GeV/c. Parallel to the experimental work the Sydney group explored the multi-core shower problem theoretically, using extensively Monte Carlo simulations (McCusker et al., 1969; see also McCusker, 1975). Some of their data are shown in Fig. 13.35. However, in view of the fact that these values were more than one order of magnitude larger than those found in emulsion, and on the grounds of a number of other arguments, such as Poissonian and detection fluctuations, the Sydney results were seriously contested (Trümper and Samorski, 1971).

Another, more general approach to estimate p_t of high energy hadrons that are identified as such in a shower with a core analyzer at ground level is based on the assumption that the height of production of these particles lies one interaction mean free path above the observation level. But h is obviously subject to large fluctuations and very difficult to measure, and p_t emerges from a distribution. The determination of $\langle p_t \rangle$ and its energy dependence based on this method is more speculative than the previous one and subject to larger uncertainties.

Analyses based on the methods discussed above were carried out by Matano et al. (1968) and Samorski et al., (1970a, b) at sea level. Similar studies at elevated altitudes were made by Miyake et al. (1970) and Vatcha and Sreekantan (1973b) with their installations at Mt. Norikura and Ootacamund, respectively. The results from Ootacamund are plotted in Fig. 13.36 together with theoretical estimates. Similar studies were made by Machavariani et al. (1979) and Romakhin

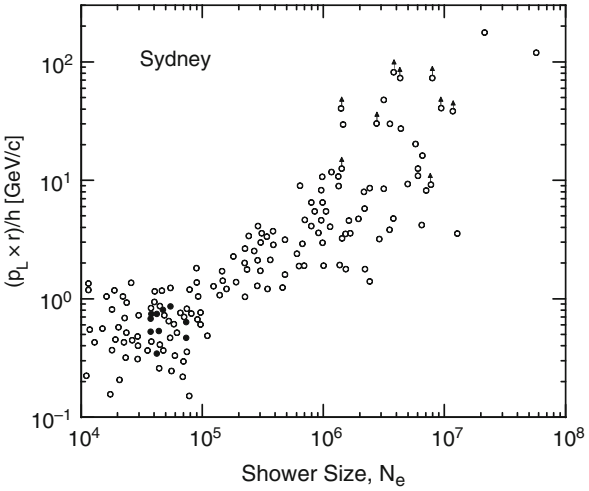

Fig. 13.35 Experimentally determined $(p_l \cdot r)/h$ values, expressed in units of GeV/c, obtained for some events with the Sydney 64 scintillator array plotted against shower size, N_e (○), interpreted as large transverse momentum events. The *full dots* (●) are simulated events for primary copper nuclei and mean transverse momentum of 0.5 GeV/c (after Bakich et al., 1970b)

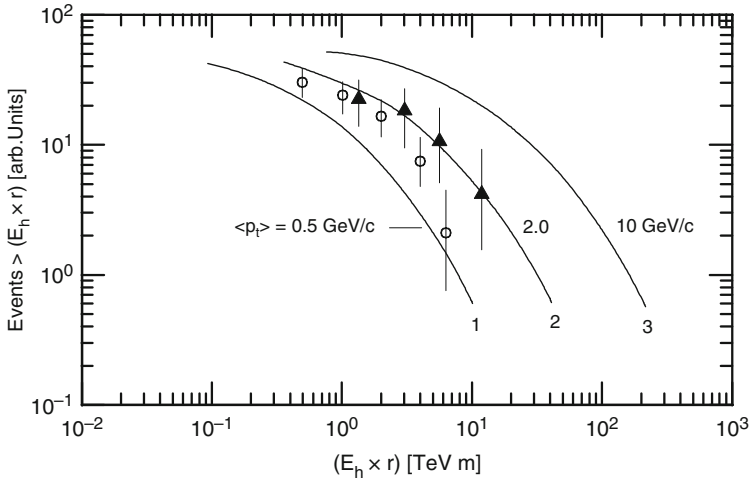

Fig. 13.36 Lateral distribution of cascades of energy >1 TeV initiated by hadrons associated with air showers. Plotted is the product of the cascade energy [TeV], initiated by hadrons, versus distance from the shower axis [m]. *Curves 1, 2*, and *3* are from model calculations and were obtained for average transverse momenta of 0.5, 2.0 and 10 GeV/c, respectively (Vatcha and Sreekantan, 1973b). The measurements were made at Ootacamund (2,200 m) and apply to showers corresponding to a primary energy $\geq 10^6$ GeV

and Nesterova (1979) at Tien Shan who analyzed the dependence of the $(E_h \cdot r)$ product on shower size and by Aseikin et al. (1975) who measured its dependence on the hadron energy, E_h. The data are presented in Figs. 13.37 and 13.38, respectively. Theoretical work concerning these topics were carried out by Fomin (1972), Grieder (1977b) and other authors.

In a more recent experiment at Baksan (North Caucasus, 1,700 m a.s.l.) Chudakov et al. (1981, 1983) have studied multi-core events with a tightly packed 400

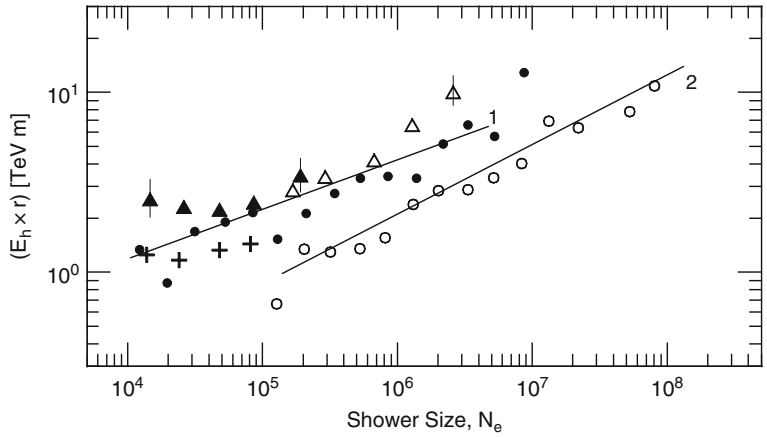

Fig. 13.37 The product $(E_h \cdot r)$ in units of [TeV m] as a function of shower size. The data points are from the following experiments: ▲, Machavariani et al. (1981); △, Nesterova and Romakhin (1977) and Romakhin and Nesterova (1979), Tien Shan for $E_h > 1$ TeV; +, Danilova et al. (1981), Tien Shan for $E_h > 0.6$ TeV; ○ and ●, Böhm et al. (1977), Pic du Midi and Kiel, respectively, *lines 1* and *2* are approximate fits to the data

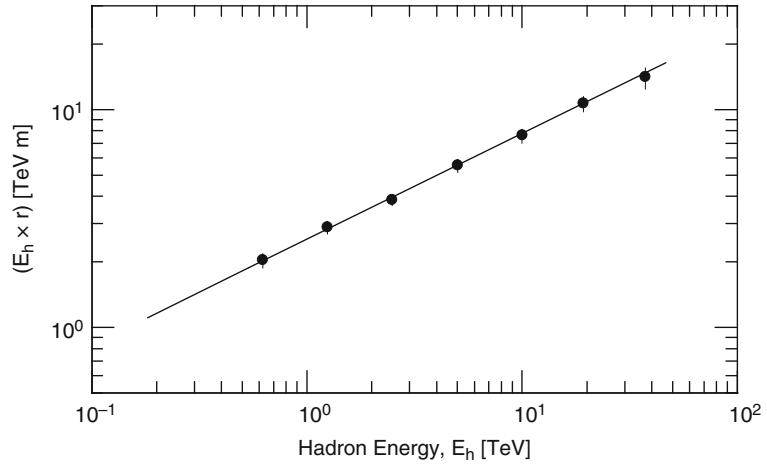

Fig. 13.38 Dependence of the product $(E_h \cdot r)$ in units of [TeV m] on hadron energy, E_h, determined with the ionization calorimeter at Tien Shan in showers of size $N_e \geq 10^5$, ● (Aseikin et al., 1975)

unit liquid scintillator carpet measuring $14 \times 14\,\mathrm{m}^2$, that was placed at the center of the air shower array to extract information on the transverse momentum distribution. This experiment is described by Aglietta et al. (1995) and follows the same basic procedure that was used in a later experiment at EAS-TOP (Aglietta et al., 1999), discussed in greater detail below. The event selection and analysis was very similar to the more recent experiment, however, with far inferior statistics. In Fig. 13.39 we show the data summary of this experiment together with collider data from CERN experiments (Aglietta et al., 1995).

In a new study Aglietta et al. (1999) have explored the structure of multi-core air showers in the size range $10^{5.26} \leq N_e \leq 10^{5.60}$ ($1.8 \cdot 10^5 \leq N_e \leq 3.98 \cdot 10^5$) with the large hadron calorimeter of the EAS-TOP installation at Gran Sasso (2,005 m a.s.l. or $810\,\mathrm{g\,cm}^{-2}$). Their aim was to extract the transverse momentum distribution of hadron-air (nucleon-air-nucleus) interactions at center of mass energies around

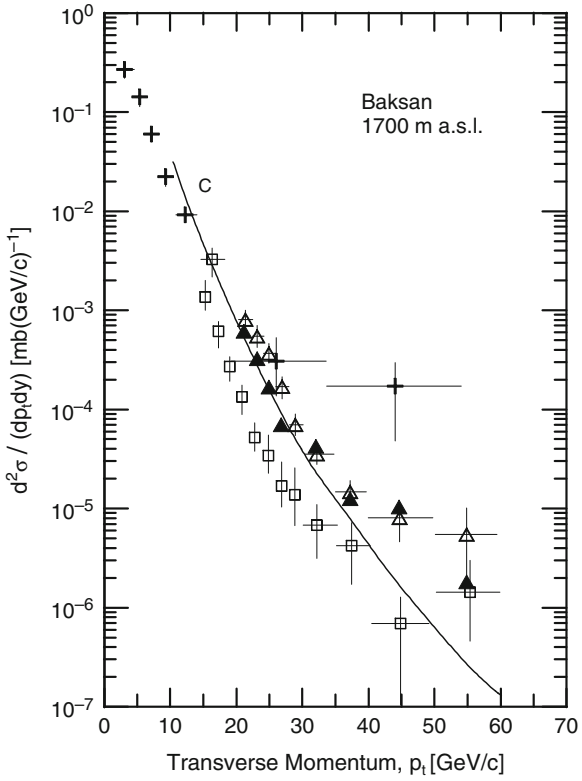

Fig. 13.39 Cross section ($d^2\sigma/dp_t dy$) for high p_t events obtained at Baksan, 1,700 (m a.s.l.) (+, Chudakov et al., 1983; Lidvansky, 1984). The energy of the interactions analyzed in this work is approximately 500 GeV in the center of mass and the mean primary energy of the showers involved $6.9 \cdot 10^4$ GeV. Also shown are inclusive cross sections from the collider experiments UA1 (▲ window algorithm, △ cluster algorithm) and UA2 (□) (Banner et al., 1983, 1985), and predictions for QCD jets (*curve C*, Horgan and Jacob, 1981) (after Aglietta et al., 1995)

500 GeV and to compare these with *jet production* data and resulting p_t distributions of proton-proton interactions obtained at accelerators and colliders at comparable energies. Of particular interest was the question whether the distributions of p-p and p-A interactions are different or not.

The selected energy of 500 GeV in the center of mass implies that the required multi-core events must originate from interactions of leading particles in the specified shower size group that occur at atmospheric depths between 250 and 480 g cm^{-2}. The analysis relied heavily on computer simulations carried out with the CORSIKA-HDPM code (Capdevielle et al., 1992) for the shower simulation, reconstruction and interpretation, including the standard NKG shower particle distribution function to compute shower size and core location (Kamata and Nishimura, 1958), and on the GEANT code (CERN W-5013, 1994) for the energy deposit determination in the calorimeter.

The cross section for inclusive particle production in hadron-nucleus interactions has been found to grow as a power of the mass number, A, of the nucleus, i.e.,

$$\frac{\mathrm{d}^3\sigma}{\mathrm{d}p^3} \propto A^{\alpha} \quad . \tag{13.10}$$

The exponent α depends on the flavor and momentum of the produced particle, in particular on the transverse momentum, p_t, of the particle. For particles emitted around 90° in the center of mass with respect to the direction of motion of the colliding particles, α was observed to increase from about 0.8 at low transverse momenta to ≥ 1 at $p_t \geq 2$ GeV/c, an effect called *anomalous nuclear enhancement* (Brown et al., 1983). This also applies to jet production.

The important result of the experiment of Aglietta et al. (1999) is illustrated in Fig. 13.40a. Shown is the rate of events per shower of transverse momenta in the range $10 \leq p_t \leq 20$ GeV/c determined for the selected shower size group exhibiting multi-core events that satisfy the imposed selection criteria, after accounting for the known uncertainties. Also plotted is the predicted event rate for the same p_t window obtained from a calculation based on $p\overline{p}$ collider data for the same rapidity interval and average center of mass energy.

For the specific case under consideration we can rewrite Eq. (13.10) as follows,

$$\left(\frac{\mathrm{d}\sigma}{\mathrm{d}p_t}\right)^{\mathrm{jet}}_{pA} = \left(\frac{\mathrm{d}\sigma}{\mathrm{d}p_t}\right)^{\mathrm{jet}}_{p\overline{p}} \cdot A^{\alpha} \quad , \tag{13.11}$$

where A is the mass number. Inspection of Fig. 13.40a reveals at once that the two p_t distributions run nearly parallel and can be represented by a power law of the form

$$f(p_t) \propto p_t^{-\delta} \quad . \tag{13.12}$$

The resulting exponents are $\delta = 6.04 \pm 0.56$ for the measured p-air interactions and $\delta = 6.16 \pm 0.09$ for the distribution calculated on the basis of $p\overline{p}$ data for the

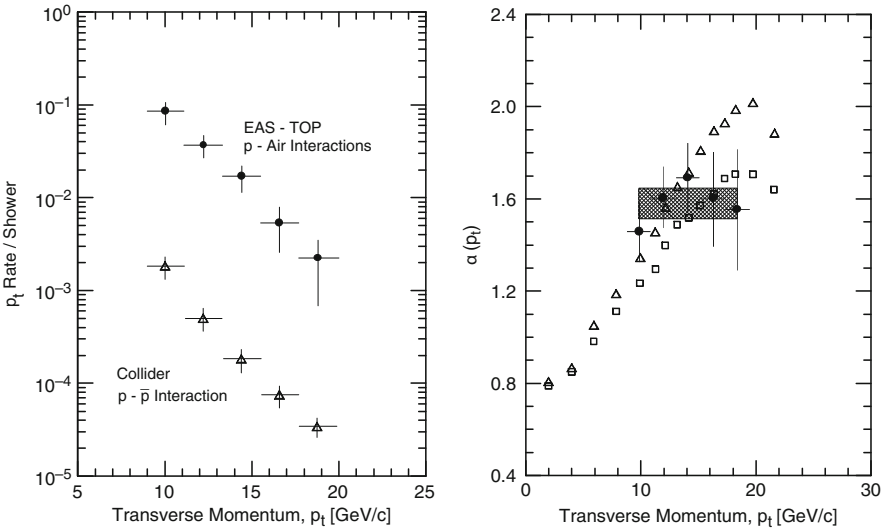

Fig. 13.40 (**a**) Distribution of the rate of large transverse momentum events measured in air showers for nucleon-air interactions in the pseudo rapidity interval $1.6 \leq \eta \leq 2.6$, •, and the rate per shower calculated from collider cross section data for the same rapidity interval, △ (after Aglietta et al., 1999). The slopes of the two p_t-distributions ($F(p_t \propto p_t^{-\delta})$ are $\delta = 6.04 \pm 0.56$ for the measured and $\delta = 6.16 \pm 0.09$ for the calculated. The shower size range used in this experiment was $1.8 \cdot 10^5 \leq N_e \leq 4 \cdot 10^5$. Statistical and systematic errors are included (for details see text). (**b**) Dependence of the exponent α of Eq. (13.11) versus p_t determined with the EAS-TOP experiment at Gran Sasso (•) and corresponding results obtained at FNAL from fixed target experiments shown for comparison (△ Al target, □ Pb target, both at $\sqrt{s} = 27.4$ GeV; Brown et al., 1983; Rice et al., 1984; Miettinen et al., 1988). The shaded area shows the mean value of α with its uncertainties (after Aglietta et al., 1999)

same rapidity interval. Thus, the p_t dependencies of $p\overline{p}$ and p-air jet production cross sections are compatible. Moreover, the cross section ratio, R, is essentially constant,

$$R = \frac{\left(\frac{d\sigma}{dp_t}\right)^{\text{jet}}_{p,\text{air}}}{\left(\frac{d\sigma}{dp_t}\right)^{\text{jet}}_{p\overline{p}}} \quad . \tag{13.13}$$

The average value of R resulting from this work is $\langle R \rangle = 60.4 \pm 12.9$ and the value for the exponent α of Eq. (13.11) with air as target ($\langle A \rangle = 14.7$ for standard air) is $\alpha = 1.56 \pm 0.07$. The difference in the absolute rates of the two distributions is a measure for the differences between the $p\overline{p}$ and p-air cross sections.

The p_t dependence of α resulting from the EAS-TOP experiment for an average center of mass energy of 500 GeV is shown in Fig. 13.40b together with data obtained from fixed target accelerator experiments at CM-energies of 27.4 GeV for p-Al and p-Pb collisions for comparison (Aglietta et al., 1999; Brown et al., 1983).

The cosmic ray deduced data are in good agreement with the fixed target results at much lower energy and prove that no change in α occurs over the center of mass energy range from 30 to 500 GeV. This work is an excellent example for what high quality cosmic ray experiments can achieve.

13.7.4 Production Height of High Energy Hadrons

The production height, h_h, of high energy hadrons is of considerable interest to learn more about the longitudinal development of showers. The methods of estimating the production height had been outlined briefly in the previous section in connection with the determination of the transverse momentum. Only few attempts had been made in the past to tackle this problem. In the following we discuss briefly one of them.

In their effort Böhm et al. (1975, 1977) have analyzed hadron data obtained in two similar experiments, one carried out at Kiel (s.l.), the other one at Pic du Midi (2,860 m a.s.l., 730 g cm^{-2} vertical overburden). In either case they have used concrete targets but of different thickness, 880 g cm^{-2} at Kiel and 400 g cm^{-2} at Pic du Midi, and neon hodoscopes as burst detectors to determine the hadron energy. To check the data and method they have measured the Pic du Midi spectrum at a zenith angle such that the slant depth of the atmosphere corresponded to that for vertical showers at Kiel (1,030 g cm^{-2}). The two spectra run parallel but are slightly displaced, the Kiel spectrum laying lower. The cause for the difference is due partly to the different atmospheric density profiles that affect mainly the ratio of the pion decay to interaction probabilities.

Taking constant intensity cuts from the two size spectra, the authors converted the size spectra to spectra of fixed primary energy. From these the absorption length

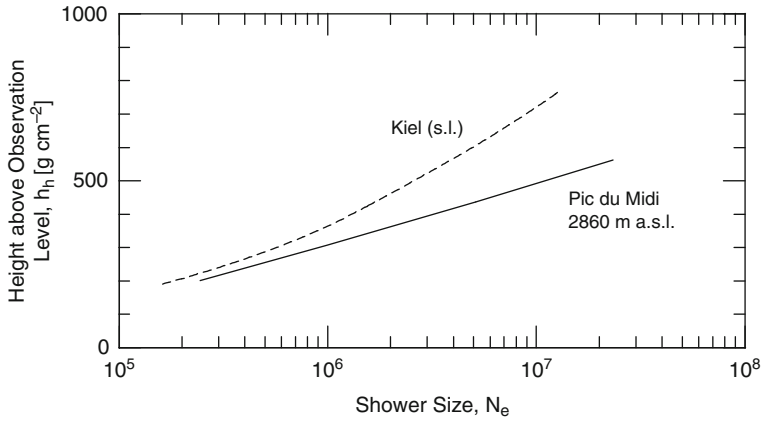

Fig. 13.41 Average production height, h_h, of energetic hadrons ($E_h \geq 300$ GeV) above the observation level as derived from measurements at Pic du Midi (2,860 m a.s.l., 730 g cm^{-2}) and Kiel (s.l., 1,030 g cm^{-2}) as a function of shower size (Böhm 1977)

of shower particles, λ_{abs}, was determined. The analysis shows that the absorption length for electrons is larger than that for hadrons. Thus the electron component is not in *equilibrium* with the hadron component.

The rather elaborate method of analysis was based on the difference of the hadron spectra at the two observation levels for fixed primary energy under consideration of the particle absorption length and elasticity thus obtained, as well as the difference of the steepness of the respective lateral hadron distributions. The latter can be related to the production height. Assuming a value for the average transverse momentum of the produced particles ($\langle p_t \rangle = 0.5\,\text{GeV/c}$), Böhm et al. (1977) used Eq. (13.9) to estimate the production height of the hadrons in showers. Data from this work are shown in Fig. 13.41.

The authors argue that this behavior can be understood if the starting point in the atmosphere of small showers is lower and vice versa for larger showers. This behavior is a consequence of the rising hadronic cross section with energy. Moreover, the decrease of the probability for a low starting point is canceled by the rapid increase of the primary intensity with decreasing energy and the presence of large fluctuations. The complex argumentation presented here illuminates the degree of difficulty involved when treating this problem.

References

Adair, R.K.: Phys. Rev. Lett., 33, p. 115 (1974).
Aglietta, M., et al.: Nuovo Cim. C, 9, p. 141 (1986).
Aglietta, M., et al.: Nucl. Instr. Meth. A, 277, p. 23 (1989).
Aglietta, M., et al.: PICRC, 10, p. 316 (1990).
Aglietta, M., et al.: Nuovo Cim., 18 C, p. 663 (1995).
Aglietta, M., et al.: PICRC, 6, p. 81 (1997).
Aglietta, M., et al.: Phys. Lett. B, 460, p. 474 (1999).
Aglietta, M., et al.: Astropart. Phys., 19, p. 329 (2003).
Akashi, M., et al.: PICRC, 2, p. 835 (1965a).
Akashi, M., et al.: Prog. Theor. Phys. (Suppl.), 32, p. 1 (1965b).
Alakoz, A.V., et al.: Can. J. Phys., 46, p. S694 (1968).
Albrow, M.G., et al.: Phys. Lett., 40 B, p. 136 (1972).
Alper, B., et al.: Proc. XVI. Internat. Conf. on High Energy Physics, Batavia, IL, USA (1972).
Alper, B., et al.: Phys. Lett., 44 B, p. 527 (1973a).
Alper, B., et al.: Phys. Lett., 47 B, p. 275 (1973b).
Amaldi, U., et al.: Phys. Lett., 43 B, p. 231 (1973a).
Amaldi, U., et al.: Phys. Lett., 44B, p. 112 (1973b).
Amati, D., et al.: Nuovo Cim., 26, p. 896 (1962).
Amendolia, S.R., et al.: Phys. Lett., 44B, p. 119 (1973).
Andreyev, Y.M., et al.: PICRC, 6, p. 200 (1987).
Antoni, T., et al.: J. Phys. G, 25, p. 2161 (1999).
Antoni, T., et al.: Astropart. Phys., 14, p. 245 (2001).
Antoni, T., et al.: Astropart. Phys., 16, p. 245 (2002).
Antoni, T., et al.: Nucl. Instr. Meth. A, 513, p. 490 (2003).
Apshev, S.Zh., et al.: PICRC, 8, p. 62 (1977).
Asakimori, K., et al.: PICRC, 13, p. 229 (1979).
Aschenbach, B.: Thesis, University of Kiel, Germany (1974).

Aseikin, V.S., et al.: PICRC, 8, p. 2960 (1975).
Ashton, F., et al.: PICRC, 8, p. 2980 (1975).
Ashton, F., et al.: PICRC, 12, p. 18 (1977).
Ashton, F., and A. Nasri: PICRC, 13, p. 251 (1979).
Ashton, F., and H. Nejabat: PICRC, 6, p. 203 (1981).
Babaian, Kh., et al.: PICRC, 2, p. 646 (1965).
Bagge, E., et al.: PICRC, 2, p. 738 (1965).
Bakich, A.M., et al.: Can. J. Phys., 46, p. S30 (1968).
Bakich, A.M., et al.: Acta Phys. Acad. Scie. Hung., 29, S3, p. 501 (1970a).
Bakich, A.M., et al.: J. Phys. A, 3, p. 662 (1970b).
Banner, M., et al.: Phys. Lett., 41B, p. 547 (1972).
Banner, M., et al.: Phys. Lett., 44B, p. 537 (1973).
Banner, M., et al., UA2 Collaboration: Phys. Lett. B, 122, p. 322 (1983).
Banner, M., et al., UA2 Collaboration: Z. Phys. C, 27, p. 329 (1985).
Baruch, J.E.F., et al.: PICRC, 8, p. 184 (1977).
Bertaina, M., et al.: PICRC, 2, p. 792 (2001).
Bjornboe, J., et al.: Nuovo Cim., 53B, p. 241 (1968).
Böhm, E., et al.: Can. J. Phys. 46, p. 50 (1968).
Böhm, E., et al.: Acta Phys. Acad. Scie. Hung. 29, S3, p. 487 (1970).
Böhm, E., et al.: PICRC, 8, p. 2974 (1975).
Böhm, E.: PICRC, 8, p. 29 (1977).
Bradt, H.L., and B. Peters: Phys. Rev., 77, p. 54 (1950).
Bradt, H.V., and S.A. Rappoport: Phys. Rev., 164, p. 1567 (1967).
Bray, A.D., et al.: Nuovo Cim., Ser., 10, 32, p. 827 (1964).
Brown, W.W., and A.S. McKay: Phys. Rev., 76, p. 1034 (1949).
Brown, B., et al.: Phys. Rev. Lett., 50, p. 11 (1983).
Büsser, F.W., et al.: Phys. Lett., 46B, p. 471 (1973).
Capdevielle, J.N., et al.: The Karlsruhe EAS simulation code CORSIKA, KFK Report 4998 (1992).
Castellina, A., et al.: Nuovo Cim., 8 C, p. 93 (1985).
CERN W-5013: Application Software Group and Network Division. Detector Description and Simulation Tool GEANT 3.21 (1994).
Chatterjee, B.K., et al.: PICRC, 4, p. 227 (1963).
Chatterjee, B.K., et al.: PICRC, 2, p. 734 (1965a).
Chatterjee, B.K., et al.: PICRC, 2, p. 802 (1965b).
Chatterjee, B.K., et al.: PICRC: 2, p. 805 (1965c).
Chatterjee, B.K., et al.: Can. J. Phys., 46, p. S136 (1968).
Chiavassa, A., et al.: PICRC, 2, p. 989 (2003).
Chudakov, A.E., et al.: PICRC, 6, p. 183 (1981).
Chudakov, A.E., et al.: PICRC, 6, p. 29 (1983).
Clem, J.M.: PICRC, 7, p. 317 (1999).
Clem, J.M., and L.I. Dorman: Space Sci. Rev., 93, p. 335 (2000).
Cocconi, G.: Phys. Rev., 76, p. 984 (1949).
Cocconi-Tongiorgi, V.: Phys. Rev., 76, p. 192 (1949).
Cocconi, G., et al.: Phys. Rev., 75, p. 1063 (1949).
Cocconi, G., and V. Cocconi Tongiorgi: Phys. Rev., 79, p. 730 (1950).
Cocconi, G., et al.: Phys. Rev., 79, p. 768 (1950).
Cowan, E.W., and K. Matthews: Phys. Rev., D 4, p. 37 (1971).
Damgaard, G., et al.: PICRC, 2, p. 808 (1965a).
Damgaard, G., et al.: Phys. Lett., 17, p. 152 (1965b).
Danilova, T.V., et al.: J. Phys. Soc. Jpn., 17, Suppl. A III, p. 205 (1962).
Danilova, T.V., and S.I. Nikolsky: PICRC, 4, p. 221 (1963).
Danilova, T.V.: ZhETF, 46/5, p. 1561 (1964).
Danilova, T.V.: PICRC, 2, p. 660 (1965).

Danilova, T.V., et al.: PICRC, 6, p. 146 (1981).
Danilova, T.V., et al.: PICRC, 7, p. 40 (1985).
Dobrzynski, K., et al.: PICRC, 6, p. 206 (1981).
Dovzenko, O.J., et al.: PICRC, 2, p. 134 (1960).
Dubovy, A.G., et al.: Kratkie soob., FIAN No 10, p. 8 (1978).
Elbert, J.W., et al.: Phys. Rev. D, 27, p. 1448 (1983).
Engler, J., et al.: PICRC, 10, p. 273 (1990).
Engler, J., et al.: Nucl. Instr. Meth. A, 427, p. 528 (1999).
Fomin, Y.A.: Thesis MSU (1972).
Fritze, R., et al.: Acta Phys. Acad. Scie. Hung., 29, S3, p. 439 (1970).
Gaisser, T.K., and P. Rudolf: J. Phys. G, 2, p. 781 (1976).
Garraffo, Z., et al.: Nucl. Phys. B, 53, p. 419 (1973).
Goodman, J.A., et al.: Phys. Rev. D, 19, p. 2572 (1979).
Goryunov, N.N., et al.: PICRC (Moscow, 1959), 2, p. 70 (1960).
Greisen, K.: Phys. Rev., 75, p. 1071 (1949).
Greisen, K.: Progress in Cosmic Ray Physics, North Holland Publishing Co, Amsterdam Vol. 3, p. 1 (1956).
Greisen, K.: Annual Review of Nuclear Science, Annual Reviews, Inc., Palo Alto, CA, USA, 10, p. 63 (1960).
Grieder, P.K.F.: Nuovo Cim., 26, N. 2, p. 271 (1962).
Grieder, P.K.F.: Acta Phys. Acad. Sci. Hung., 29, S3, p. 563 (1970a).
Grieder, P.K.F.: Acta Phys. Acad. Sci. Hung., 29, S3, p. 569 (1970b).
Grieder, P.K.F.: Institute for Nuclear Study, University of Tokyo, Tokyo, Japan. Report Nr. I.N.S. J 125 (1970c).
Grieder, P.K.F.: PICRC, 3, p. 976 (1971).
Grieder, P.K.F.: PICRC, 4, p. 2467 (1973).
Grieder, P.K.F.: Rivista del Nuovo Cim., 7, p. 1 (1977a).
Grieder, P.K.F.: PICRC, 8, p. 376 (1977b).
Grieder, P.K.F.: PICRC, 8, p. 387 (1977c).
Grieder, P.K.F.: PICRC, 9, p. 161 (1979).
Grigorov, N.L., et al.: PICRC, 2, p. 860 (1965).
Hagedorn, R.: Nuovo Cim., Suppl., 3, p. 147 (1965).
Hagedorn, R., and J. Ranft: Nuovo Cim., 6, Suppl., N. 2, Ser. I, p. 169 (1968).
Hasegawa, H., et al.: PICRC, 2, p. 642 (1965).
Hatton, C.J.: Progr. Elementary Particle and Cosmic Ray Phys., 10, p. 1 (1971).
Haungs, A., et al.: Rep. Prog. Phys., 66, p. 1145 (2003a).
Haungs, A., et al.: PICRC, 2, p. 985 (2003b).
Haungs, A.: Nucl. Phys. B (Proc. Suppl.), 151, p. 215 (2006).
Hazen, W.E., et al.: Phys. Rev., 93, p. 578 (1954).
Hazen, W.E., et al.: J. Phys. G, 2, p. L61 (1976).
Heinemann, R.E., and W.E. Hazen: Phys. Rev., 90, p.496 (1953).
Hook, J.R., et al.: Acta Phys. Acad. Scie. Hung., 29, S3, p. 474 (1970).
Horgan, R., and M. Jacob: Nucl. Phys. B, 179, p. 441 (1981).
Hughes, E.B., et al.: Proc. Phys. Soc., 83, p. 239 (1964).
Ise, J., Jr., and W.B. Fretter: Phys. Rev., 76, p. 933 (1949).
Jacob, M., and P.V. Landshoff: Phys. Reports, 48, p. 285 (1978).
Jedrzejczak, K., et al.: Nucl. Phys., B (Proc. Suppl.), 151, p. 329 (2006).
Jones, L.W., and M.L. Perl: Nucl. Instr. Meth., 10, p. 348 (1961).
Jones, L.W., et al.: Phys. Rev., 164, p. 1584 (1967).
Jones, L.W., et al.: Acta Phys. Acad. Sci. Hung. 29, S3, p. 205 (1970a).
Jones, L.W., et al.: Phys. Rev. Lett., 25, p. 1679 (1970b).
Jones, L.W., et al.: Nucl. Phys. B, 43, p. 477 (1972).
Jones, L.W.: Rev. Mod. Phys.: 49, p. 717 (1976).

Kabana, S., and P. Minkowski: New J. Phys., 3, p. 4 (2001).
Kamata, K., and J. Nishimura: Prog. Theor. Phys. Jpn., 6, Suppl., p. 93 (1958).
Kameda, T., et al.: J. Phys. Soc. Jpn., 15, p. 1565 (1960).
Kameda, T., et al.: J. Phys. Soc. Jpn., 17, p. 270 (1962a).
Kameda, T., et al.: J. Phys. Soc. Jpn., 17, (Suppl. A-III), p. 270–274 (1962b).
Kameda, T., et al.: PICRC, 2, p. 681(1965).
Kawasumi, N., et al.: PICRC, 6, p. 73 (1997).
Kellermann, E.W., and A.M. Hillas: PICRC, 6, p. 223 (1981).
Kempa, J.: Nuovo Cim., 31 A, p. 568 (1976a).
Kempa, J.: Nuovo Cim., 31 A, p. 581 (1976b).
Kozlov, V.G., et al.: PICRC, 8, p. 356 (1979).
Kozlov, V.G., et al.: PICRC, 6, p. 210 (1981).
Lattes, C., et al., The CHACALTAYA Emulsion Chamber Experiment, Brazil-Japan Group: Supplement, Progress of Theoretical Physics, No.47 , 1, (1971).
Lattes, C.M.G., et al.: Phys. Reports, 65, p.152–229 (1980).
Lidvansky, A.S.: Thesis, Institute for Nuclear Research, Moscow (1984).
Machavariani, S.K., et al.: PICRC, 8, p. 240 (1979).
Machavariani, S.K., et al.: PICRC, 6, p. 193 (1981).
Machida, M., et al.: Acta Phys. Acad. Sci. Hung., 29, S4, p. 427 (1970).
Matano, T., et al.: PICRC, 2, p. 1045 (1965).
Matano, T., et al.: Can. J. Phys., 46, p. S56 (1968).
Matano, T., et al.: Acta Phys. Acad. Sci. Hung., 29, S3, p. 451 (1970).
Matano, T., et al.: PICRC, 7, p. 2724 (1971).
Matano, T., et al.: PICRC, 13, p. 185 (1979).
Matano, T., et al.: PICRC, 11, p. 318 (1981).
Matano, T., et al.: PICRC, 6, p. 296 (1985).
McCusker, C.B.A., et al.: Phys. Rev., 177, p. 1902 (1969).
McCusker, C.B.A.: Phys. Reports, 20, p. 229 (1975).
Miettinen, H.E., et al.: Phys. Lett. B, 207, p. 222 (1988).
Miyake, S., et al.: J. Phys. Soc. Jpn., 18, p. 592 (1963).
Miyake, S., et al.: Can. J. Phys., 46, p. S25 (1968).
Miyake, S., et al.: Acta Phys. Acad. Sci. Hung., 29, S3, p. 463 (1970).
Miyake, S., et al.: PICRC, 13, p. 165 (1979).
Murthy, G.T., et al.: Can. J. Phys., 46, p. S159 (1968).
Navarra, G., et al.: Nucl. Instr. Meth. A, 518, p. 207-209 (2004).
Nesterova, N.M., and V.A. Romakhin: PICRC, 8, p. 113 (1977).
Nesterova, N.M., and A.P. Chubenko: PICRC, 8, p. 340 (1979).
Nesterova, N.M., and A.G. Dubovy: PICRC, 8, p. 345 (1979).
Nikolsky, S.I.: Izv. Acad. Sci. U.S.S.R., 33, p. 1501 (1969).
Nishimura, J.: Handbuch der Physik, 46/2, p. 1, Springer Verlag, Berlin (1967).
Nymmik, R.A.: Thesis, University of Moscow, Russia (1970).
Oda,M., and Y. Tanaka: J. Phys. Soc. Jpn., 17, Suppl. A-III, p. 282 (1962).
Oda, M.: PICRC, 4, p. 60 (1963).
Ouldridge, M., and A.M. Hillas: J. Phys. G, 4, p. L35 (1978).
Pal, Y.A., and B. Peters: Dansk. Vidensk. Selsk., Mat. Fys. Medd., 33 (15) (1964).
Pal, Y., and S.N. Tandon: PICRC, 2, p. 802 (1965).
Perl, M.L., and L.W. Jones: Phys. Rev. Lett., 2, p. 116 (1959).
Perl, M.L., and L.W. Jones: Nucleonics, 18, 5, p. 92 (1960).
Peters, B.: Progr. in Cosmic Ray Phys., Vol. 1, Chapter 4, North-Holland, Amsterdam (1952).
Peters, B.: PICRC (Moscow, 1959), 3, p. 157 (1960).
Peters, B.: CERN Yellow Report 66-22 (1966).
Rice, J.A., et al.: Nucl. Phys. A, 418, p. 315 (1984).
Romakhin, V.A., et al.: PICRC, 8, p. 107 (1977).

Romakhin, V.A., and N.M. Nesterova: Trudy, FIAN, 109, p. 77 (1979).
Samorski, M., et al.: PICRC, 2, p. 676 (1965).
Samorski, M., et al.: Z. Phys. 230, p. 1 (1970a).
Samorski, M., et al.: Acta Phys. Acad. Scie. Hung., 29, S3, p. 417 (1970b).
Shibata, S., et al.: PICRC, 2, p. 672 (1965).
Shibata, S., et al.: Can. J. Phys., 46, p. S60 (1968).
Sivers, D., et al.: Phys. Reports, 23, p. 1 (1976).
Sreekantan, B.V.: PICRC, 4, p. 143 (1963).
Sreekantan, B.V.: PICRC, 7, p. 2706 (1971).
Sreekantan, B.V., and S.C. Tonwar: PICRC, 8, p. 287 (1979).
Suga, K., et al.: J. Phys. Soc. Jpn., 17, Suppl. A-III, p. 128 (1962).
Tanahashi, G.: J. Phys. Soc. Jpn., 20, p. 883 (1965).
Ter-Antonian, S.V., et al.: PICRC, 1, p. 369 (1995).
Tonwar, S.C., and B.V. Sreekantan: J. Phys. A, 4, p. 868 (1971a).
Tonwar, S.C., and B.V. Sreekantan: PICRC, 3, p. 1177 (1971b).
Tonwar, S.C., et al.: Lett. Nuovo Cim., 1, p. 531 (1971a).
Tonwar, S.C., et al.: PICRC, 3, p. 1171 (1971b).
Tonwar, S.C., et al.: J. Phys. A, 5, p. 569 (1972).
Trümper, J., and M. Samorski: J. Phys. A, 4, p. L45 (1971).
Tsushima, I., et al.: PICRC, 13, p. 189 (1979).
van Staa, R., et al.: PICRC, 4, p. 2676 (1973).
van Staa, R., et al.: J. Phys. A 7, p. 135 (1974).
Vatcha, R.H., and B.V. Sreekantan: J. Phys. A, 6, p. 1050 (1973a).
Vatcha, R.H., and B.V. Sreekantan: J. Phys. A, 6, p. 1078 (1973b).
Vavilov, Y.N., et al.: Trudi FIAN, 26, p. 17 (1964).
Vernov, S.N., et al.: PICRC, 8, p. 320 (1977).
Vernov, S.N., et al.: Izv. Akad. Nauk. SSSR, Ser. Fiz., 42, p. 1376 (1978).
Vishwanath, P.R., et al.: Phys. Lett., 53B, p. 479 (1975).
Yodh, G.B., et al.: Phys. Rev. Lett., 28, p. 1005 (1972).

Chapter 14
Muons

Overview In this chapter we discuss exclusively muons in air showers. After outlining the role and the general properties of muons in showers we give a brief account of the different mathematical structure functions that are used to describe the lateral density distribution of muons in hadron initiated events. These comprise the classical Greisen function as well as some semi-empirical functions which had been adopted by various work groups to describe and fit their experimental data. We then touch briefly the subject of simulated data. Subsequently we present a summary of experimental data from different sites acquired at different epochs. These include lateral distributions and parameters, energy and momentum spectra, charge ratio and geomagnetic charge separation, temporal properties, core angle distributions, height of origin and the $(E \cdot r)$ product, muon genetics, multi-muon data, and fluctuations.

14.1 Introduction

Muons and neutrinos are weakly interacting particles and have correspondingly small interaction cross sections. Muons, though much less abundant than photons and electrons, play a very important role in air shower research. Since they are mainly subject to ionization losses only, energetic muons travel long distances in the atmosphere. The most energetic muons originate in general from parent particles that are produced mainly in the forward region of the center of mass of the first few interactions and are potential messengers, carrying relevant information on the early history of the showers to the observer at ground level. They can therefore be considered as a sort of test or sample particles that may provide insight into the first few interactions of the primaries and their fragments with nuclear targets of air constituents, occurring at the fringes of the atmosphere. Moreover, simulations show that high energy muons carry in fact partly hidden signatures of the nature of the primary, of its mass and of the location of their origin in the atmosphere.

However, there are relatively few very energetic muons. They are difficult to detect and it is almost impossible to determine the relevant parameters. Fortunately, low energy muons, too, carry relevant primary mass information. This information is contained in their number relative to the electron (or charged particle) size and

P.K.F. Grieder, *Extensive Air Showers,* DOI 10.1007/978-3-540-76941-5_14,

requires large area detectors to extract reliable data. The method to estimate the primary mass from low energy muon data is discussed in Chap. 10.

As mentioned before, muons are charged leptons and subject to electromagnetic interactions, analogous to electrons, however, their much larger mass must be properly accounted for. The main energy loss of muons up to high energies is through ionization and excitation. As a thumb rule the typical energy loss of a moderately energetic muon ($E_\mu \simeq 10\,\mathrm{GeV}$) in air is about $2\,\mathrm{MeV}\ [\mathrm{g}^{-1}\,\mathrm{cm}^2]$. This implies that relativistic muons produced near the top of the atmosphere lose about 2 GeV along a vertical trajectory down to sea level. At high energies ($E_\mu \geq 100\,\mathrm{GeV}$) muon bremsstrahlung, discussed in Sect. 5.2.5, becomes important since muons can lose a major fraction of their energy in a single, so-called catastrophic collision.

Muons in extensive air showers are extremely important messengers of the shower process. Their number and properties such as the energy spectrum, the lateral distribution, the arrival time and direction, the charge ratio, etc., reveal a rich palette of information on the development, propagation and history of the showers. In comparison to hadrons they are relatively easy to detect and to identify among the bulk of other shower constituents. This can be achieved by shielding charged particle detectors or spectrometers above ground, or by installing the detectors underground to remove the electromagnetic component. Because of the low density, large spread and comparatively small number, which amounts to only about 10% of all charged particles in a shower, muon measurements require comparatively large detectors. On the other hand, many of their properties are more readily accessible to measurement than those of the other shower constituents, in particular of hadrons.

Apart from the fact that they are subject to geomagnetic deflection, an effect which is rapidly decreasing with increasing energy, muons are only exposed to ionization losses, occasional bremsstrahlung and to photonuclear reactions while propagating through the atmosphere. This allows the experimenter to use them as a pointing tool for triangulation, to reconstruct the shower axis, to study the longitudinal as well as the lateral shower development and even to estimate the height of origin of their hadronic parents.

Having essentially only hadrons as parents, muons serve as first hand probes to investigate directly the hadronic component and interactions. They reveal the angular distribution and energy spectrum of their parent particles, i.e., of the secondaries produced in high energy hadronic interactions. Strongly inclined and horizontal showers allow to investigate muon bremsstrahlung, photo-nuclear processes and, in conjunction with vertical shower, to estimate the kaon contents and the production of charmed particles at very high energies.

Muon timing information with respect to the shower front offers another though more restricted direct observable to explore the shower development, the front curvature and the arrival direction. The arrival time of muons is sometimes used in combination with other observables, such as the *fractional muon content* of a shower and other observables, in event by event multi-parameter analyses to estimate the primary mass.

At ground level the muon energy spectrum, the lateral density and temporal distributions are to some extent a superimposed projected image of the numerous hadronic processes that occur along the shower trajectory above the ground impact area. These observables are intimately linked to the energy and the transverse momentum of the muon parent particles, and to their location of creation and decay in the atmosphere.

The energy spectrum and the lateral distribution of the muons do not change significantly in larger showers ($10^6 \leq E \leq 10^8$ GeV) across the deeper portion of the atmosphere. However, simulations have shown that the low energy population is continuously being exchanged in these regions of the atmosphere (Grieder, 1977a). This process becomes evident when exploring the genetics of muons in showers with simulations, as is discussed in Sect. 14.9. The reason for this phenomenon is that some of the muons decay while others get degraded in energy through ionization losses and replace the lost population together with contributions from continuously occurring pion decays.

Very high energy muons whose parents may originate from the first or first few generations of interactions of the primary, from its fragments if the primary is a nucleus, or from ultra-energetic secondaries of the first interaction in the atmosphere carry information that is important for the understanding of these processes that are at present inaccessible for accelerator experiments, for energetic reasons.

In the following sections we discuss the relevant observables and summarize important results. For correlations of muons with other shower observables and constituents the reader is referred to Chap. 19.

14.2 Lateral Structure Functions and Density Distributions

14.2.1 Mathematical Lateral Structure Functions

A large number of experiments had been carried out since the early days of air shower research to study the lateral structure of air showers, in particular since the discovery of the muon, which then allowed to resolve the problem of the so-called penetrating component of the showers into the hadronic (initially called the *nuclear active*) and muonic components.

Muon measurements like all other shower studies require that each event is well defined, i.e., the basics such as the shower size, the zenith angle and the core location with respect to the detector array must be known to estimate the primary energy, the energy flux in a shower, the degree of shower development, the shower age, and to account for the atmospheric absorption in order to interpret a shower on the basis of simulation data.

Significant pioneering work on the exploration of the muon component in showers was carried out by groups in France, India, Japan, Russia, and the US, as listed below (Greisen, 1956, 1960). Lacking a viable theory to describe hadron initiated showers, several groups have proposed empirical mathematical expressions to

describe the lateral (radial) distribution of the muons with respect to the shower axis, in analogy to the *lateral distribution functions* (LDF) for electrons that were constructed empirically or borrowed from the electromagnetic cascade theory.

Of the many parameterizations that had been worked out to describe the muon lateral density distribution in air showers, the empirical formula first introduced by Greisen (1960) and valid for muons of energy ≥1 GeV in mid-size showers, given below, is still widely used today.

$$\rho_\mu(r) = N_\mu(t) f_{G,\mu}(r) \tag{14.1}$$

where

$$f_{\mu,G}(r,s) \propto \left(\frac{r}{r_G}\right)^{-0.75} \left(1+\frac{r}{r_G}\right)^{-2.5} , \tag{14.2}$$

and s is the shower age parameter. Thus,

$$\rho_\mu(r,N_\mu) \;=\; k_G N_\mu \left(\frac{r}{r_G}\right)^{-a} \left(1+\frac{r}{r_G}\right)^{-b} \;[\mathrm{m}^{-2}]\,. \tag{14.3}$$

Here, N_μ is the muon size at distance t [rl] along the shower axis, k_G a proportionality constant, r is the core distance in meters, $a = 0.75$, $b = 2.5$, and $r_G = 320$ m is the Greisen radius, a Moliére unit equivalent for muons. The relatively high threshold energy of 1 GeV chosen for recording muons was simply to get rid experimentally of the bulk of the electromagnetic component. The above equation is known as the *Greisen formula for muons*.

As discussed in Chap. 8 and 10 for the common lateral distribution of all shower particles, many work groups have developed their own empirical LDF to describe the results of their muon measurements. Bennett et al. (1962) obtained the following fit for the lateral density distribution of muons with threshold energy between 1 and 10 GeV in showers of size $2 \cdot 10^7$,

$$\rho_\mu(r) \;=\; \frac{14.4 r^{-0.75}}{(1+r/320)^{2.5}} \left(\frac{N}{10^6}\right)^{0.75} \left(\frac{51}{E_{\mathrm{th}}+50}\right) \left(\frac{3}{E_{\mathrm{th}}+2}\right)^{(0.14\cdot r^{0.37})} \;[\mathrm{m}^{-2}]\;, \tag{14.4}$$

where r is in meters and the threshold energy E_{th} in GeV. At distances closer than 20 m the above distribution is steeper than the actually measured ones. The apparent flattening of the experimental distribution which is observed for 1 and 10 GeV muons could be due to core location errors.

Another semi-analytic structure function to describe the muon distribution was proposed and had been used by Vernov et al. (1968a). It has the form

$$f_{\mu,V}(r) \propto C \left(\frac{r}{r_V}\right)^{-a} \exp\left(-\frac{r}{r_V}\right) \tag{14.5}$$

with $a = 0.4$ and $r_V = 80\,\mathrm{m}$.

Equations (14.2) and (14.5) describe the experimental data very well at intermediate radial distances from the shower axis but not so at the extreme locations. The slopes predicted by both functions give similar values for $r < r_G$ and $r < r_V$, respectively, and yield flatter distributions close to the shower core than observed, however, the Vernov formula yields a distribution that drops off faster at larger distances. The cause for the disagreement with respect to the actually measured distributions is almost certainly the fact that neither of the two expressions (Eqs. 14.2 and 14.5) accounts for the shower development correctly.

To interpret the data recorded with the giant SUGAR muon array at Narrabri (Aus.) (260 m a.s.l.), the Sydney group used the following zenith angle dependent structure function to describe the muon density distribution,

$$\rho_\mu(r) \;=\; N_\mu k(\theta) r^{-0.75} \left(1 + \left(\frac{r}{320}\right)\right)^{-\alpha} \;\; [\mathrm{m}^{-2}]\,. \tag{14.6}$$

Here, $\alpha = (1.50 + 1.86 \cdot \cos\theta)$ is the structure function index, $k(\theta)$ is a normalizing constant and r is in units of meters. This function which had been developed by Fisher (1970) (see also Brownlee et al., 1970a; Bell et al., 1974) was derived from the study of showers of muon sizes between 10^6 and 10^7.

At Haverah Park, Armitage et al. (1973) have found that the following expression originally proposed by Linsley (1963) describes the data obtained with the water Cherenkov detectors quite well,

$$\rho_\mu \;\propto\; \frac{1}{r}\left(1 + \frac{r}{r_0}\right)^{-(\eta-1)}\,, \tag{14.7}$$

where $r_0 = 600 \sec\theta - 400$ and $\eta = 4.0 - 0.5 \sec\theta$.

Another empirical array specific expression developed by the Tien Shan group (Stamenov et al., 1979) for the interpretation of their high altitude muon data reads

$$\rho_\mu(r) \;=\; 5.95 \cdot 10^{-4} r^{-0.7} \exp\left(-\frac{r}{80}\right) \;\; [\mathrm{m}^{-2}]\,. \tag{14.8}$$

More recently, Hara et al. (1983a) have used Eq. (14.3) with the slightly modified parameter $r_G = 280\,\mathrm{m}$ to describe the density distribution of muons of energy > 0.5

and >1 GeV in the core distance range from 200 to 1,000 m at Akeno, and in a later paper, Nagano et al. (1984) have used the expression

$$\rho_\mu(r, N_\mu) \;=\; \left(\frac{\Gamma(2.5)}{2\pi\,\Gamma(1.25)\Gamma(1.25)}\right) r_0^{-1.25}\; N_\mu\, r^{-0.75} \left(1+\frac{r}{r_0}\right)^{-2.5} \qquad (14.9)$$

where Γ is the usual gamma function and $r_0 = 280$ m. This expression is claimed to be valid for core distances $r \geq 50$ m.

A more recent empirical muon distribution function that had been used by the AGASA group for muons of energy >0.25 GeV, which describes the data very well over a wide lateral range is given below (Nagano et al., 2000),

$$\rho_\mu(r) \;=\; N_\mu \left(\frac{C_\mu}{R_0^2}\right) R^{0.75}(1+R)^{-2.52} \left(1.0+\left(\frac{r}{800}\right)^3\right)^{-0.6} \quad . \qquad (14.10)$$

Here, N_μ is the total number of muons, C_μ a normalization factor, $R = r/R_0$, and R_0 is the characteristic distance, given by the following relation, which is a function of the zenith angle, θ,

$$\lg(R_0) \;=\; (0.58 \pm 0.04)(\sec\theta - 1) + (2.39 \pm 0.05) \quad . \qquad (14.11)$$

This formula is claimed to be valid out to a core distance of 3,000 m for showers of energy $E_0 > 3 \cdot 10^{19}$ eV (Doi et al., 1995).

The lateral density distribution function used to interpret the data of the KASCADE and KASCADE-Grande experiments for muons of energy ≥230 MeV in showers belonging to different muon size groups is similar to the one proposed by Lagutin and Raikin (2001) and reads (Antoni et al., 2001; van Buren et al., 2005),

$$\rho_\mu(r) = N_\mu \frac{0.28}{r_0^2} \left(\frac{r}{r_0}\right)^{p1} \left(1+\frac{r}{r_0}\right)^{p2} \left(1+\left(\frac{r}{10r_0}\right)^2\right)^{p3} \quad . \qquad (14.12)$$

The parameters $p1$, $p2$ and $p3$ have the values of -0.69, -2.39 and -1.0, respectively, and were obtained by fitting the function to 10^{16} and 10^{17} eV proton and iron initiated showers, using the CORSIKA code (Heck et al., 1998) with the QGSJET event generator (Kalmykov et al., 1997). A value of $r_0 = 320$ m was used for the reference radius.

14.2.2 Simulated Lateral Distributions

Numerous authors have presented lateral density distributions of muons of different energy thresholds in simulated showers initiated by primaries of different energies and masses. We display in Fig. 14.1a, b as examples two sets of lateral distributions of low energy muons from relatively recent simulations of near

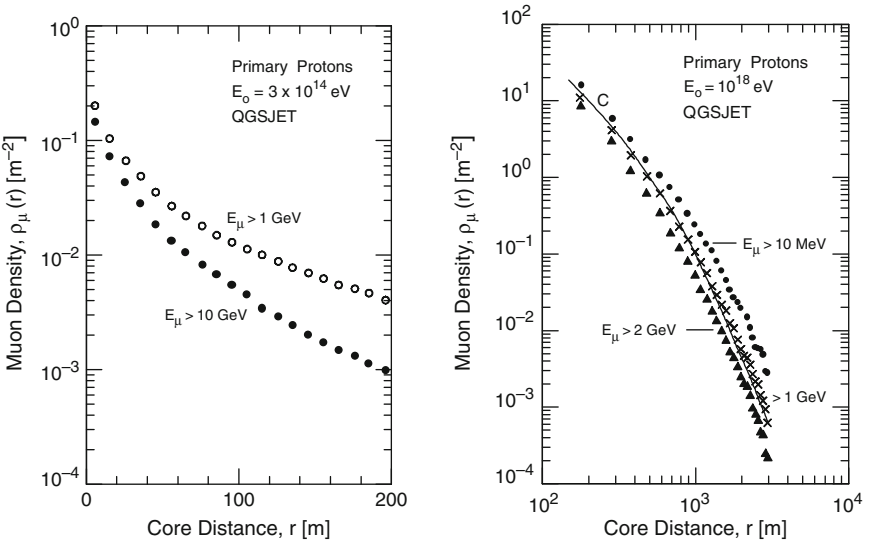

Fig. 14.1 (**a**) Average lateral density distribution of muons of different threshold energies, as indicated, in showers initiated by primary protons of energy $3 \cdot 10^{14}$ eV from a simulation of Gupta et al. (2005) using CORSIKA with QGSJET. (**b**) Lateral density distribution of muons of different threshold energies, as indicated, resulting from simulations of vertically incident 10^{18} eV proton initiated showers using the QGSJET event generator in a hybrid calculation with a thinning factor of 10^{-6}, after Nagano et al. (2000). The *curve C*, shows the distribution described by the AGASA empirical distribution function given by Eq. (14.10)

vertical ($0^\circ \leq \theta \leq 18^\circ$) and vertical $3 \cdot 10^{14}$ and 10^{18} eV proton initiated showers from the work of Gupta et al. (2005) and Nagano et al. (2000), respectively, both using the QGSJET event generator but different program packages. Predictions from other calculations are shown together with experimental distributions in the next subsection.

14.2.3 Experimental Lateral Distributions

Besides the lateral density distribution of the bulk of the shower particles, the density distribution of the muons is one of the most intensively studied observables in air showers. The reason for this particular interest is that in the first place muons are important information carriers and, secondly, muon measurements are relatively easy to carry out.[1]

A variety of detector types are suitable for muon measurements. The detectors are usually of relatively large area because of the low density of the muons. Many

[1] One must be aware of electromagnetic punch-throughs under thin shielding near the shower core that can falsify muon measurements.

of the larger detection systems that are located near an array center are frequently placed underground, usually in relatively shallow tunnels with the desired overburden (Abdrashitov et al., 1981; Zabierowski et al., 2001, 2003; Doll et al., 2002; Büttner et al., 2003), or at ground level, either inside thick-walled concrete structures with massive roofs (bunkers) (Bagge et al., 1965; Hara et al., 1979; Chiba et al., 1992), or under massive hadron calorimeters that serve at the same time as a shield against the unwanted shower components (Klages et al., 1997; Navarra et al., 2004), to achieve the desired muon threshold energy of at least 0.5 GeV or more.

The bunker principle, for example, had been used at the Akeno/AGASA experiment, where several such structures were installed within the array (Hayashida et al., 1979; Nagano et al., 2000). Other installations where the muon size of showers is being recorded, or both the muon and electron size, require a large number of shielded detectors that must be distributed over a large area, or, as in the latter case, detector sandwiches that consist of an electron detector placed on top of a muon detector with a thick lead shielding ($\sim$10 cm) in between, to prevent the electromagnetic component from reaching the muon detector. Such an arrangement had also been used at the KASCADE/KASCADE-Grande site (Antoni et al., 2003b).

Only very few of the muon detectors that were installed at great depth underground were located underneath or in the immediate vicinity of an air shower array, that permitted the simultaneous recording of the showers at the surface that were associated with the high or ultrahigh energy muons detected underground. These included the detectors at Baksan (Alexeyev et al., 1979, 1993), MACRO (Aglietta et al., 2004) and LVD (Aglietta et al., 1998) at Gran Sasso, Ohya in Japan (Mitsui et al., 1987) and several detectors at the Kolar Gold Fields (KGF) in India (Acharya et al., 1981), all briefly mentioned in Sect. 2.8.3.

In the following we present a selection of data on the lateral density distribution of muons from a variety of experiments. The presentation is in ascending order of the altitude of the sites where the measurements were made. The data cover a wide span in time and include results from early work to the present.

In Figs. 14.2, 14.3 and 14.4 we present three compilations of early data on the lateral density distribution of low energy muons ($0.3 \leq E_\mu \leq 2$ GeV) in showers of different sizes from measurements made at various sites at or near sea level. The details are given in the captions. Another compilation, showing distributions of higher energy muons ($E_\mu \geq 40$ and $E_\mu \geq 200$ GeV) is given in Fig. 14.5 together with a series of theoretical distributions obtained from simulations of different authors, as listed in the caption.

Two excellent sets of measurements of near vertical ($0 \leq \theta \leq 18^\circ$) showers of small and medium size are presented in Figs. 14.6 and 14.7 that were obtained with the KASCADE installation at Karlsruhe (110 m a.s.l.) (Glasstetter et al., 1999; Zabierowski et al., 2001; van Buren et al., 2005). The originally published data shown in Fig. 14.7 were displayed in a semi-logarithmic plot as given in the insert (van Buren et al., 2005). I have re-plotted these data in double-log representation for easier comparison with many other data of comparable range that are frequently presented in this manner.

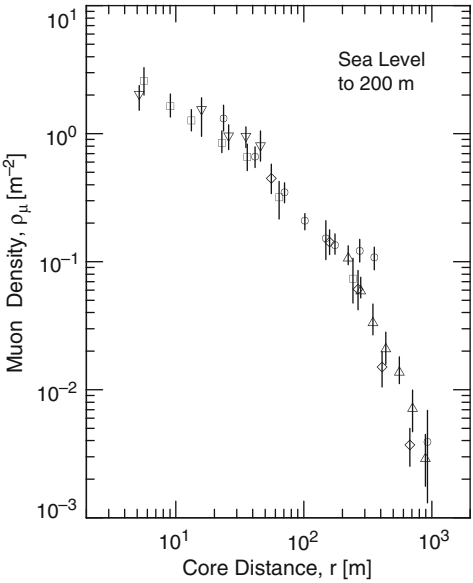

Fig. 14.2 Compilation of data on the lateral density distribution of low energy muons at and near sea level (De Beer et al., 1966). The data apply to an average zenith angle of $\theta = 30^\circ$ and are normalized to a size of $N_e \simeq 10^6$. The figure shows data from the following authors: □ Abrosimov et al. (1958), $E_\mu \geq 0.5$ GeV, $N_e = 5 \cdot 10^5$; △ Abrosimov et al. (1960), $E_\mu \geq 0.5$ GeV, $N_e = 2 \cdot 10^7$, Moscow (192 m a.s.l.); ○ Earl (1959), Agassiz, US (183 m a.s.l.), $E_\mu \geq 1$ GeV, $N_e = 10^6$ to $3 \cdot 10^7$; ◇ Porter et al. (1957), Harwell, England (∼50 m a.s.l.), $E_\mu \geq 0.4$ GeV, $N_e = 6 \cdot 10^6$; ▽ Lehane et al. (1958), Sydney, Aus. (30 m a.s.l.), $E_\mu \geq 0.38$ GeV, $N_e = 2 \cdot 10^5$–$2 \cdot 10^6$

A similar set of lateral density distributions of near vertical ($0 \leq \theta \leq 18^\circ$) showers of very high primary energy ($2.0 \cdot 10^{17} \leq E_0 \leq 1.86 \cdot 10^{19}$ eV) recorded with the installation at Yakutsk (105 m a.s.l.) from the work of Glushkov et al. (1995) is presented in Fig. 14.8.

Of particular interest are the distributions shown in Fig. 14.9 from the work of Sarkar et al. (1993). Shown is a series of lateral density distributions of muons of different threshold energy, ranging from $E_\mu \geq 2.5$; ≥ 11.3; ≥ 25.5 to ≥ 53.7 GeV in relatively small showers ($N_e \simeq 1.5 \cdot 10^4$). The data were acquired with two solid iron magnet spectrometers that are part of the North Bengal University's (NBU) air shower array, located near Siliguri (India) at an altitude of 130 m a.s.l.

A next series of data on low energy muons, still from measurements made at low altitude, resulting mainly from the work of the Nottingham group at Haverah Park using shielded scintillators, is presented in Fig. 14.10 (Blake, 1977; Blake et al., 1979a; Armitage et al., 1973, 1974, 1979). Details of the measurements are given in the figure caption. In this work the shower energy is estimated from the parameters $\rho(500)$ and $\rho(600)$, expressed in vertical equivalent muons per square meter [veμm^{-2}], that can be converted to primary energy (see Chap. 8 and 10).

Figures 14.11, 14.12, 14.13 and 14.14 show a set of distributions that were obtained with the underground detector installation that was part of the Moscow

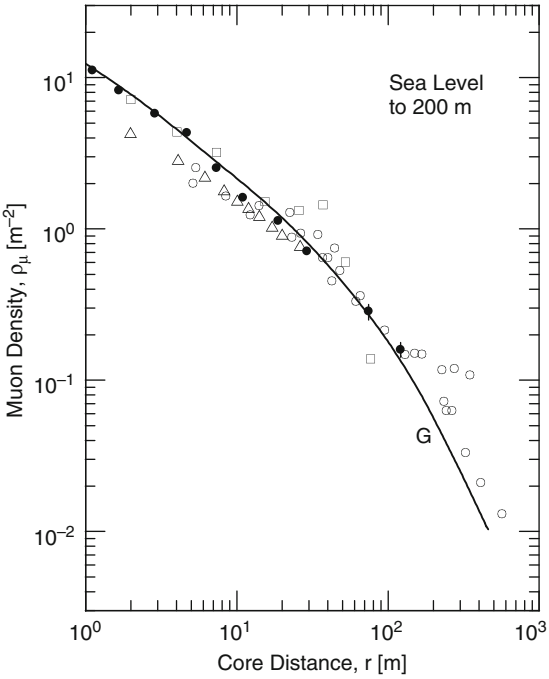

Fig. 14.3 Compilation of data on the lateral density distribution of low energy muons near sea level (Staubert et al., 1970). The data are normalized to a shower size of 10^6 and include results from the following groups: • Kiel, Germany (s.l.), $E_\mu \geq 2$ GeV (Staubert et al., 1970); ○ Durham, England (60 m a.s.l.) compilation, $E_\mu \geq 1$ GeV (De Beer et al., 1966); □ Tokyo I.N.S. (s.l.), $E_\mu \geq 1$ GeV (Fukui et al., 1960); △ Lodz, Poland (230 m a.s.l.), $E_\mu \geq 0.6$ GeV (Bonczak et al., 1968, 1969). The *solid curve, G*, represents the Greisen distribution described by the mathematical expression of Greisen (1960) and Bennett and Greisen (1961) for $E_\mu > 2$ GeV

State University array which included a solid iron magnet spectrometer. The data include showers of different size groups and muons of higher energy, as listed in the figures. The compilation of Fig. 14.15 shows results from measurements made with the underground installations at Lodz, Poland (230 m a.s.l.), which had a muon threshold of 5 GeV (for installation layout see Bonczak et al., 1969; Dzikowski et al., 1979). We have added data from the work at Haverah Park for muons of energy ≥1 GeV and the Greisen (1960) distribution to these data for comparison.

Data of rather low energy muons from the large array at Yakutsk in Siberia, the SUGAR array at Narrabri in Australia and from Haverah Park are plotted in Fig. 14.16. The distribution of 13 very large showers recorded with the SUGAR array are displayed in Fig. 14.17. Average distributions from measurements with the SUGAR array only, obtained for different zenith angles are given in Fig. 14.18, and the zenith angle dependence of the lateral structure function index, α (Eq. 14.6), in terms of the slant depth resulting from this analysis is given in Fig. 14.19 (Brownlee et al., 1970a; Bell et al., 1974).

A set of distributions for showers of different sizes obtained from the Akeno experiment which is at somewhat higher altitude (900 m a.s.l.) is presented in Fig. 14.20 (Hara et al., 1981). Also shown in the following figure (Fig. 14.21) is the size and zenith angle dependence of the characteristic radius of the Greisen muon distribution functions, given in the caption.

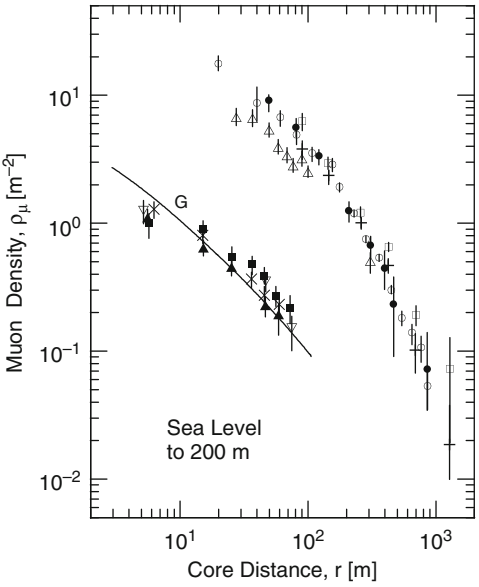

Fig. 14.4 Compilation of lateral density distributions of low energy muons near sea level. Symbols □ and + are after Gibson et al. (1979) for $E_\mu \geq 0.3$ and ≥ 1 GeV, respectively, in showers of $\rho(500) = 0.5$ veμ m^{-2}; △, Dixon et al. (1973a) for $E_\mu \geq 1$ GeV, zenith angles $\theta \leq 30^\circ$ and $\rho(500) = 0.33$ ($E_0 \simeq 1.5 \cdot 10^{17}$ to $2 \cdot 10^{17}$ eV); ○, Earnshaw et al. (1967, 1968) for $E_\mu \geq 1$ GeV and shower size $2 \cdot 10^7$, all measured at Haverah Park, England (212 m a.s.l.). Data points • were obtained at Agassiz, USA (183 m a.s.l.) (Clark et al., 1958). These data are for $E_\mu \geq 1$ GeV, mean zenith angle $\langle\theta\rangle = 22^\circ$ and size $N_e = 2 \cdot 10^7$ particles. For earlier data see also Allan et al. (1968). The *lower left* set of data is for muons of energy $E_\mu \geq 0.5$ GeV recorded at Durham, England (60 m a.s.l.) (Ashton et al., 1979). ▲ and × include the size range $1.5 \cdot 10^4 \leq N \leq 3 \cdot 10^5$ and the zenith angle intervals $\theta < 25^\circ$ (1,617 events) and $\theta \geq 25^\circ$ (731 events), respectively; ▽ and ■ cover the size range $3 \cdot 10^5 \leq N \leq 4 \cdot 10^6$ and the same zenith angle intervals with 1,275 and 860 events, respectively. The *smooth curve, G*, is the distribution according to Greisen (1960). These measurements had been normalized to a shower size of $N = 3 \cdot 10^5$

Particularly interesting are the rather unique data from the Kolar Gold Fields, where several muon detectors were installed at different depth in the rock underground, underneath the surface shower array (see Fig. A.40). Figure 14.22 shows two distributions of muons of energy ≥220 GeV recorded at the 270 m level underground in rather small showers. The selection of the shower size was restricted because of the very small aperture (area-solid-angle product) (Acharya et al., 1979, 1981).

The EAS-TOP installation which had been dismantled several years ago was an excellently instrumented experiment that measured practically all shower components. In addition it was located in the vicinity of the Gran Sasso underground laboratories MACRO (discontinued) and LVD (still operating), and was therefore one of the very few installations that could simultaneously access high energy muon data of the showers that were detected at the surface. The low energy muon data

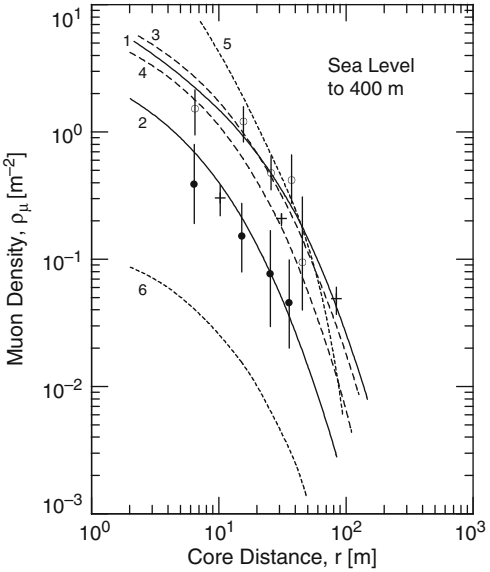

Fig. 14.5 Lateral density distributions of energetic muons in showers of size $N_e \simeq 10^6$. The experimental data ○ and ● are from the work of Rada et al. (1979) for near vertical muons of energy ≥40 and ≥200 GeV, respectively, in near vertical showers recorded at Durham, England (60 m a.s.l., 1,025 g cm^{-2}), using the solid iron magnet spectrometer MARS (Ayre et al., 1972a, b). The data points + are from the work of Barnaveli et al. (1963, 1964) for $E_\mu \geq 40$ GeV in somewhat larger showers ($N_e \simeq 6 \cdot 10^6$) and average zenith angle of 15°, recorded with an underground installation at Tbilisi, Georgia (former USSR), located at 400 m a.s.l. *Curves 1–6* are a comparison made by Rada et al. (1979) with predictions made by other authors for muons of energy ≥50 GeV. *Curves 1, 3* and *5* are the results of simulations for proton initiated showers using the SMFB model within the frame of the ASICO program (Grieder, 1975, 1977a, b), the CKP model (Olejniczak, 1975) and the scaling model (Grieder, 1977a, b), respectively. *Curves 2, 4 and 6* are from corresponding simulations of the same author for showers initiated by iron primaries

($E_\mu \geq 1$ GeV) were obtained from the combined hadron–muon detector that served as hadron calorimeter. In Fig. 14.23 we show their muon lateral distribution for two different shower size groups (Aglietta et al., 1997).

A relatively new and very densely packed air shower array (GRAPES) is located at Ootacamund (2,200 m a.s.l.) in southern India. It is equipped with the presently largest muon tracking detector which has a total area of 560 m^2 and a threshold of 1 GeV (Gupta et al., 2005; Hayashi et al., 2005). In Fig. 14.24 we present the lateral density distributions obtained with this installation for five different shower size groups (Hayashi et al., 1999).

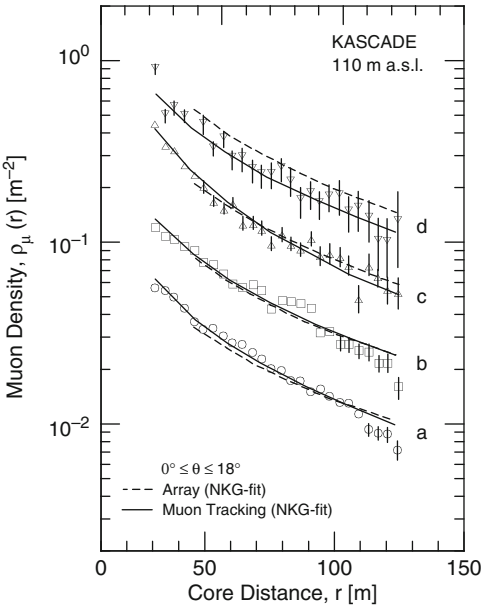

Fig. 14.6 Muon lateral density distribution of four different shower size groups as listed below, for the zenith angle range $0° \le \theta \le 18°$ recorded with the KASCADE detector system. The symbols show the data points as measured with the muon tracking detector and the *solid curves* are corresponding NKG fits. The *dashed lines* are fits to the data from the shielded scintillator array, corrected for the threshold difference, for the same shower sample. The size groups are as follows: *a*, $0.8 \cdot 10^3 \le N_\mu^{tr} \le 2 \cdot 10^3$; *b*, $2 \cdot 10^3 < N_\mu^{tr} \le 5 \cdot 10^3$; *c*, $5 \cdot 10^3 < N_\mu^{tr} \le 1.25 \cdot 10^4$; *d*, $1.25 \cdot 10^4 < N_\mu^{tr} \le 3.16 \cdot 10^4$ (Glasstetter et al., 1999; Zabierowski et al., 2001)

Several sets of distributions recorded at Mt. Norikura in Japan (2,770 m a.s.l.) are plotted in Figs. 14.25 and 14.26a, b, c). The latter plots show the age dependence of the distribution (Miyake et al., 1968, 1977).

Excellent data were obtained for muons of energy ≥5 GeV with the well equipped installation at Tien Shan, in Kazakhstan (3,340 m a.s.l.) that are reproduced in Fig. 14.27 (Aseikin et al., 1977). In Fig. 14.28 the shower age dependence of the muon lateral distribution is illustrated (Stamenov et al., 1977). To close this subsection, Fig. 14.29 shows average distributions of muons of energy ≥0.6 GeV from measurements of older date made at the high altitude laboratory at Mt. Chacaltaya (5,230 m a.s.l.) in Bolivia (Aguirre et al., 1973, 1977, 1979).

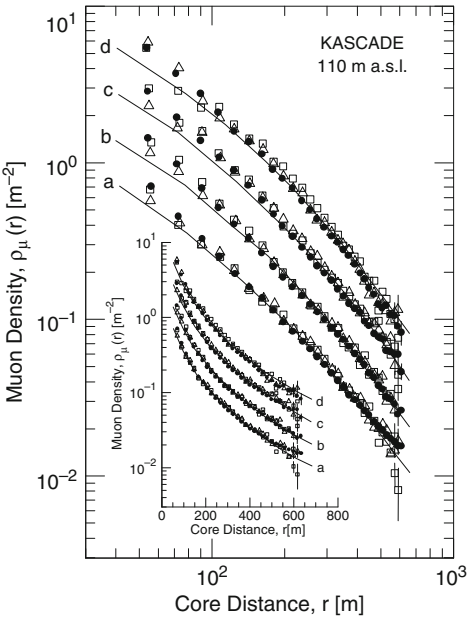

Fig. 14.7 Lateral density distribution of muons of energy $E_\mu \geq 230\,\text{MeV}$ recorded with the KASCADE-Grande array at Karlsruhe (Germany) (110 m a.s.l.) (•), and simulated distributions for pure proton (□) and pure iron (△) primaries for four different muon shower sizes and zenith angles $0 \leq \theta \leq 18^\circ$. The small inserted figure shows same data as the main figure with the exception that the core distance is plotted on a linear scale, as in the original publication, whereas in the large figure we have used the more common logarithmic scale for reasons of better comparison with data from other experiments that are frequently displayed in double-logarithmic plots. The *curves* are described by Eq. (14.12) given in the text. The muon size range of the showers to which the four distributions apply are as follows: *a*, $8 \cdot 10^4 \leq N_\mu \leq 1.6 \cdot 10^5$; *b*, $1.6 \cdot 10^5 < N_\mu \leq 3.1 \cdot 10^5$; *c*, $3.1 \cdot 10^5 < N_\mu \leq 6.3 \cdot 10^5$; *d*, $6.3 \cdot 10^5 < N_\mu \leq 1.25 \cdot 10^6$ (van Buren et al., 2005)

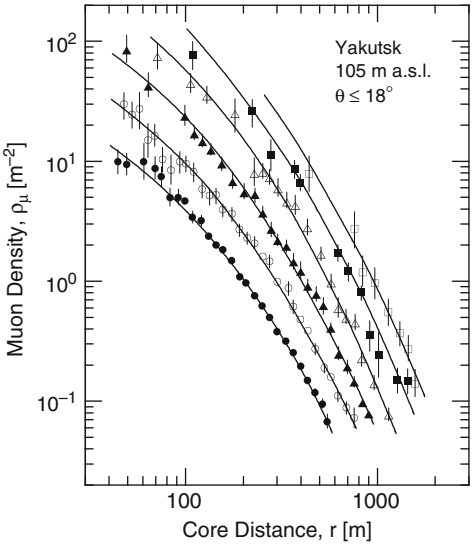

Fig. 14.8 Mean lateral density distribution of muons of energy $\geq 1 \cdot \sec\theta$ GeV recorded at Yakutsk during the period from January 1974 to May 1992 (Glushkov et al., 1995). The symbols apply to showers belonging to primary energy groups as listed below. The *curves* represent density distributions described by a modified Greisen muon distribution function.
● $2.0 \cdot 10^{17}$ eV
○ $5.0 \cdot 10^{17}$ eV
▲ $1.26 \cdot 10^{18}$ eV
△ $3.16 \cdot 10^{18}$ eV
■ $8.0 \cdot 10^{18}$ eV
□ $1.86 \cdot 10^{19}$ eV

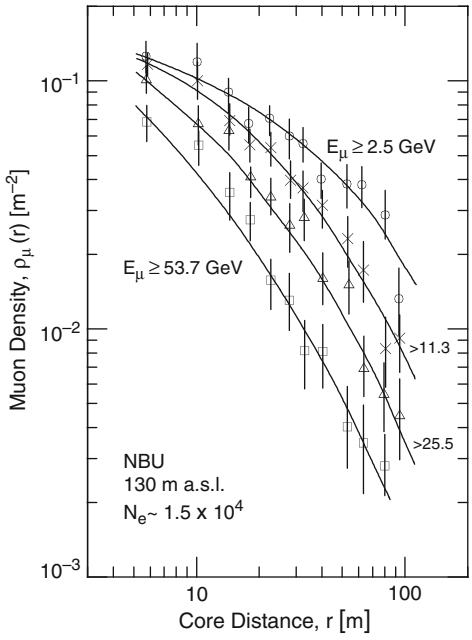

Fig. 14.9 Lateral density distribution of muons of different threshold energies, measured with the two magnet spectrometers of the air shower array of the North Bengal University (NBU), located near Siliguri, India (Sarkar et al., 1993)

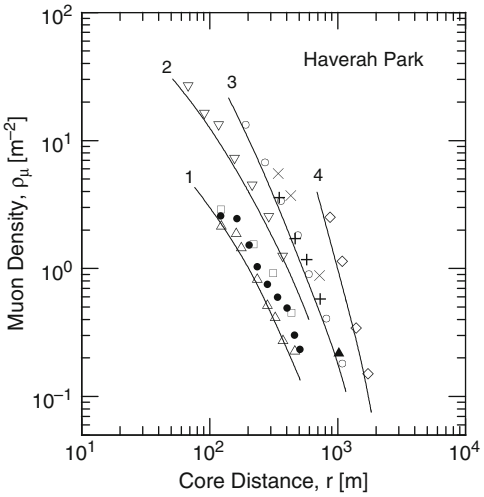

Fig. 14.10 Compilation of lateral density distributions of low energy muons ($E_\mu \geq 0.41\,\mathrm{GeV}$) in showers of different sizes, defined by $\rho(500)$ and $\rho(600)$, and different zenith angles, at large core distances, recorded at Haverah Park, England. △, • and □ Blake (1977), normalized to a shower size parameter of $\rho(600) = 0.178$ veμ m^{-2} ($E_0 \simeq 1.2 \cdot 10^{17}$ eV). The zenith angles are △ $\theta < 25°$, • $35° \leq \theta \leq 45°$ and □ $45° < \theta \leq 55°$. ▽ is for $0.46 \leq \rho(500) \leq 2.15$ veμ m^{-2} with $\langle\rho(500)\rangle = 0.88$ veμ m^{-2} (10^{17} eV $\leq E_0 \leq 10^{18}$ eV), $\theta \leq 25°$ and the lateral distribution parameter (Eq. 14.7) is $\eta = (2.175 - 2.425)$ (Armitage et al., 1979). ○ is for $\langle\rho(600)\rangle = 2.0$ veμm^{-2} ($\langle\rho(500)\rangle \simeq 3.6$ veμ m^{-2}) and $\theta < 25°$ (Armitage et al., 1973 and 1974). Note that for these data the muon threshold energy was 300 MeV. +, ×, ◇ and ▲, Blake et al. (1979a). + is for $1.46 \leq \rho(600) \leq 3.15$, with $\langle\rho(600)\rangle = 2.0$ veμ m^{-2} ($E_0 \simeq 1.4 \cdot 10^{18}$ eV) and $\theta < 25°$. × is for $1.46 \leq \rho(600) \leq 3.15$, $\theta > 25°$, normalized to $\langle\rho(600)\rangle = 2.0$ veμ m^{-2}. ⋄ average data from large showers with $\rho(600) = 13.7$ veμ m^{-2} and $\theta \leq 35°$. ▲ average data for $1.46 \leq \rho(600) \leq 3.15$ with $\langle\rho(600)\rangle = 2.0$ veμ m^{-2} ($E_0 \simeq 1.4 \cdot 10^{18}$ eV). The curves are fits to the experimental data; 1, 2 and 4 after Blake et al. (1979a), 3 after Armitage et al. (1973), based on a function (Eq. 14.7) proposed by Linsley (1963)

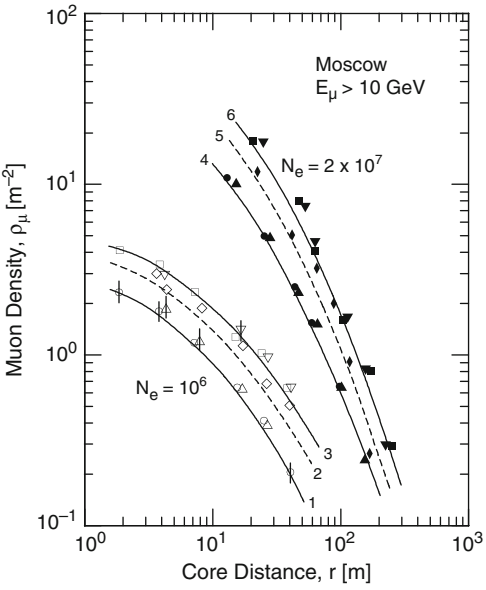

Fig. 14.11 Lateral density distributions of muons of energy $\geq$10 GeV in showers of different size, N_e, and age, s, recorded with the Moscow installation (192 m a.s.l.): $\circ$ $s \leq 1.0$, $\square$ $s \geq 1.3$, both for $N_e = 10^6$ (Khristiansen et al., 1975). $\triangle$ $s < 1.0$, $\diamond$ $1.0 \leq s \leq 1.3$, $\triangledown$ $s > 1.3$, $N_e = 10^6$; $\blacktriangle$ $s < 1.2$, $\blacklozenge$ $1.2 \leq s \leq 1.4$, $\blacktriangledown$ $s > 1.4$, $N_e = 2 \cdot 10^7$ (Khristiansen et al., 1977). $\bullet$ $s \leq 1.2$, $\blacksquare$ $s \geq 1.4$, $N_e = 2 \cdot 10^7$ (Khristiansen et al., 1975). (For earlier data see Vernov et al., 1964b, 1965a, b.) The *curves* are simple fits to the experimental data

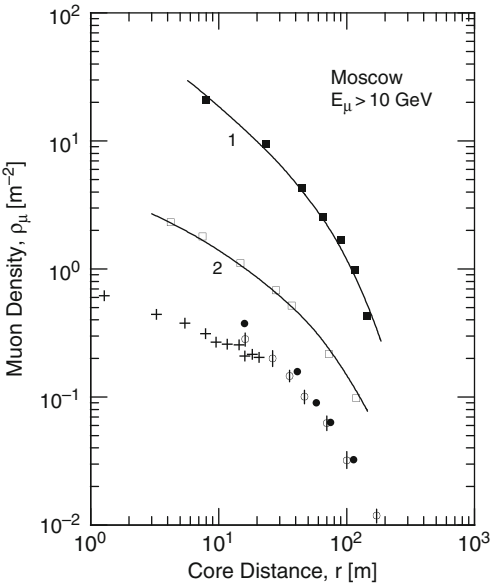

Fig. 14.12 Lateral density distributions of muons of energy $E_\mu \geq 10$ GeV, obtained with the Moscow air shower installation (192 m a.s.l.). Points $\circ$ and $\bullet$ apply to showers of size $N_e = 2 \cdot 10^5$ and $2 \cdot 10^7$, respectively, normalized to $N_e = 2 \cdot 10^5$, using the relationship $\rho_\mu \propto N_e^{0.78}$, and $\rho_\mu(r) = N_\mu \cdot f_\mu(r)$, with $f_\mu(r) = A \cdot r^{-n} \cdot e^{(r/80)}$. $A = 2.5 \cdot 10^4$, $n = 0.5$ for $\langle N_e \rangle = 2 \cdot 10^5$; and $A = 6.0 \cdot 10^4$, $n = 0.7$ for $\langle N_e \rangle = 2 \cdot 10^7$) (Khristiansen et al., 1971). Data points + are from a report of Ilyina et al. (1971); $\square$ and $\blacksquare$ which are connected by *curves 1 and 2* represent the shower size groups $2 \cdot 10^5 \leq N_e \leq 10^6$ and $10^7 \leq N_e \leq 5 \cdot 10^7$, respectively (Khristiansen et al., 1977)

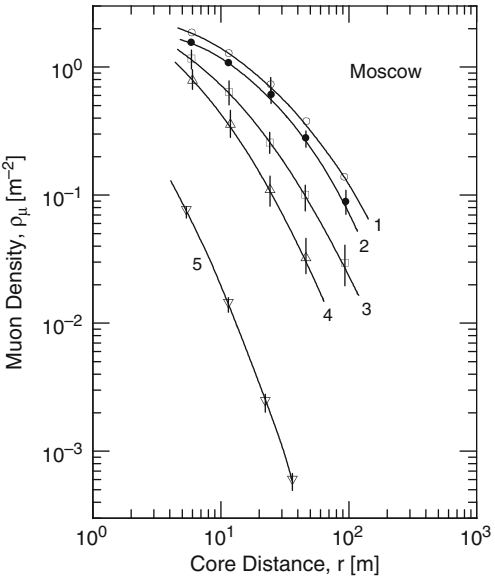

Fig. 14.13 Lateral density distribution of muons of different energy groups in showers of size $3 \cdot 10^4 \leq N_e \leq 10^6$. The data were taken with the magnet underground muon spectrograph at the Moscow State University, located at a depth of 40 m.w.e.;
○ $E_\mu \geq 10$ GeV
• $E_\mu \geq 20$ GeV
□ $E_\mu \geq 50$ GeV
△ $E_\mu \geq 90$ GeV
(Rozhdestvensky et al., 1975)
▽ $E_\mu \geq 235$ GeV
(Khrenov et al., 1979)

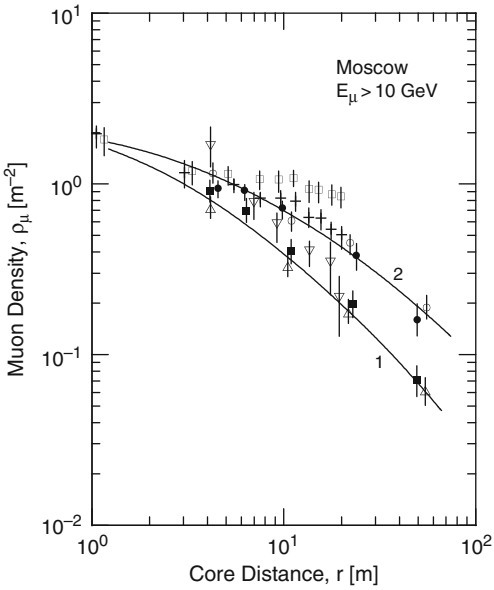

Fig. 14.14 Age dependence of lateral density distribution of ≥10 GeV muons near sea level. The data were obtained with the Moscow installation (192 m a.s.l.). □, + and ▽ are for showers of size $1.2 \cdot 10^6$ and age parameters $s \geq 1.2$, $1.0 < s < 1.2$ and $s \leq 1.0$, respectively (Ilyina et al., 1971); Data △, ■, ○ and • are from the more recent work of Grishina et al. (1981) and apply to similar size showers ($3 \cdot 10^4 \leq N_e \leq 10^6$, $\langle N_e \rangle = 2 \cdot 10^5$); (△) and (■) are for young showers with $s = 0.9$ (*curve 1*); (○) and (•) for old showers with $s = 1.37$ (*curve 2*)

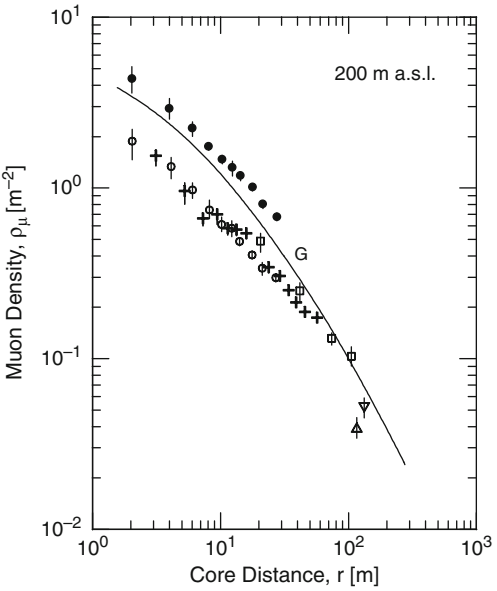

Fig. 14.15 Compilation of lateral density distributions of low energy muons recorded with the installation at Lodz, Poland (230 m a.s.l.). + Grochalska et al. (1972, Unpublished), $E_\mu \geq 5$ GeV, ○ Bonczak et al. (1968, 1969), $E_\mu \geq 0.6$ GeV; both for $N_e = 3.4 \cdot 10^5$. • Bonczak et al. (1968), $E_\mu \geq 0.6$ GeV, $N_e = 10^6$. ▽ and △ are from the work of Dzikowski et al. (1975) for muons of energy $E_\mu \geq 1$ GeV and $E_\mu \geq 5$ GeV, respectively, in showers of size $3.4 \cdot 10^5$. For comparison we have added the Greisen *curve, G* (Greisen, 1960), for a shower age $s = 1.2$, and the Haverah Park, England (212 m a.s.l.) data, □, from the work of Earnshaw et al. (1967) for $E_\mu \geq 5$ GeV and size $5 \cdot 10^5$ (compare also with Fig. 14.4)

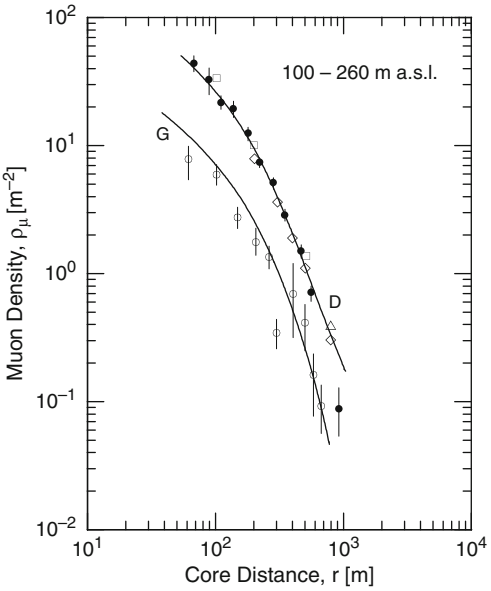

Fig. 14.16 Lateral density distribution of low energy muons in very large showers. Points • are for muon energies $E_\mu \geq 0.7$ GeV, average zenith angle $\langle\theta\rangle = 21^\circ$ and $\langle\rho(600)\rangle = 2.34$ veμ m^{-2}, recorded at Yakutsk, Russia (105 m a.s.l.) (Diminstein et al., 1979; see also Diminstein et al., 1975a, b); □ scintillator data, △ flash tube data, both for $E_\mu \geq 0.3$ GeV, measured at Haverah Park, England (212 m a.s.l.) (Blake, 1977). ◇ was obtained with the SUGAR array in Narrabri, Australia (260 m a.s.l.) for $E_\mu \geq 0.7$ GeV (Bell et al., 1973). Data points •, □, △ and ◇ apply to showers having an estimated primary energy $E_0 > 10^{18}$ eV and an average zenith angle of 21°. The data points ○ are from the SUGAR array (Bell et al., 1973) for $E_\mu \geq 0.7$ GeV and showers having a muon size $N_\mu > 2 \cdot 10^6$. *Curve D* is a fit to the Diminstein data and *G* is the Greisen curve for data set ○. Data □, △, ◇ and ○ had been normalized by Diminstein to a core distance of 200 m

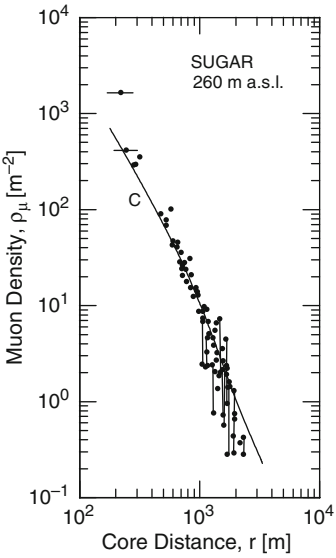

Fig. 14.17 Muon lateral density distribution of 13 very large showers with muon size $10^8 \leq N_\mu \leq 10^9$ and zenith angles $0^\circ \leq \theta \leq 45^\circ$ detected with the SUGAR array at Narrabri (Aus) (Bell et al., 1974). The densities are normalized to a muon size of $4.5 \cdot 10^8$. The *vertical lines* connecting two data points are interpolated densities for detectors that did not trigger. The high point is an exceptional event. *Curve C* is the Fisher function (Fisher, 1970)

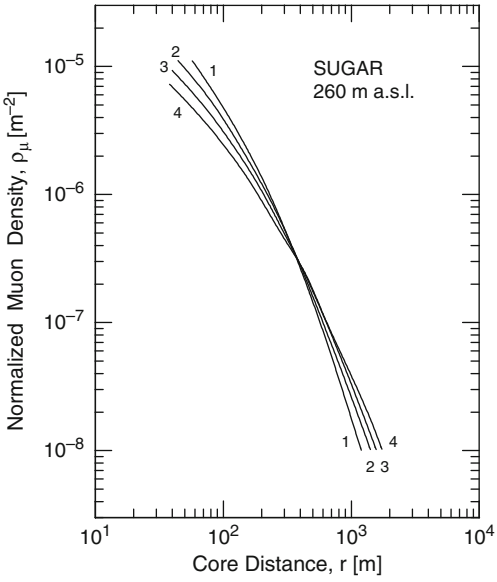

Fig. 14.18 Normalized muon structure functions for the lateral density distribution of large showers obtained by Bell et al. (1974) with the SUGAR array at Narrabri (Aus.) (260 m a.s.l.). *Curves 1–4* apply to shower zenith angles of 0°, 45°, 60° and 75°, respectively. The analytic expression which describes the curves is given by Eq. (14.8)

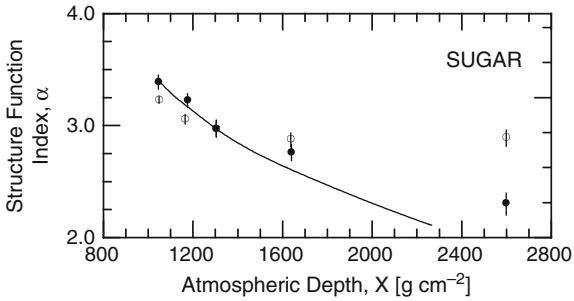

Fig. 14.19 Structure function index α of Eq. (14.6) as a function of atmospheric (slant) depth X for two values of muon shower size, N_μ (Bell et al., 1974). The *open circles*, ○, are for showers of muon sizes $10^6 < N_\mu < 10^7$, the *full circles*, ●, for $10^7 < N_\mu < 10^8$, detected with the SUGAR array. The *curve* indicates the expected behavior based on purely geometrical considerations (Brownlee et al., 1970a). For details see text

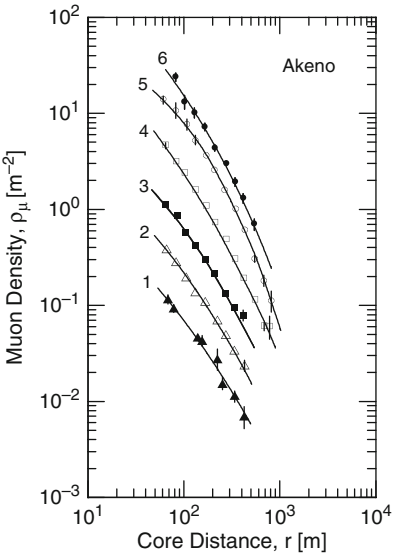

Fig. 14.20 Lateral density distributions of muons of energy $E_\mu \geq 1$ GeV and zenith angle interval $1.0 < \sec(\theta) < 1.1$, recorded at Akeno, Japan (900 m a.s.l.), (Hara et al., 1981). The data points belong to different average shower size groups:
▲ $\langle N_e \rangle = 4 \cdot 10^5$
△ $\langle N_e \rangle = 1.6 \cdot 10^6$
■ $\langle N_e \rangle = 6.3 \cdot 10^6$
□ $\langle N_e \rangle = 2.5 \cdot 10^7$
○ $\langle N_e \rangle = 10^8$
● $\langle N_e \rangle = 2.5 \cdot 10^8$.
The *curves 1–6* connect the data points

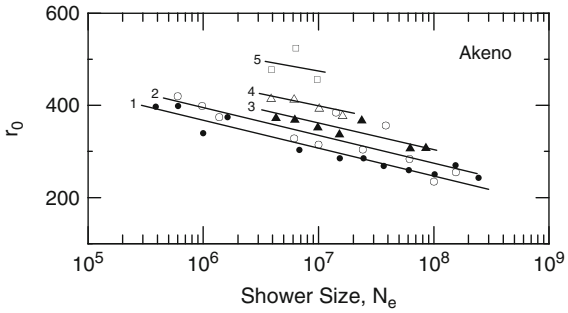

Fig. 14.21 Variation of the variable r_0 of the slightly modified Greisen formula (Eq. 14.3), $\rho_\mu(r) \propto r^{-0.75}(1 + r/r_0)^{-2.5}$, as a function of shower size, N_e (Greisen, 1960). The different data sets are from measurements made at Akeno, Japan (900 m a.s.l.), and apply to different zenith angles of the shower axes, expressed in sec(θ). • $1.0 \leq \sec(\theta) < 1.1$; ○ $1.1 \leq \sec(\theta) < 1.2$; △ $1.2 \leq \sec(\theta) < 1.3$; ▲ $1.3 \leq \sec(\theta) < 1.4$; □ $1.4 \leq \sec(\theta) \leq 1.5$. The *curves 1 to 5* outline the data points (Hara et al., 1981)

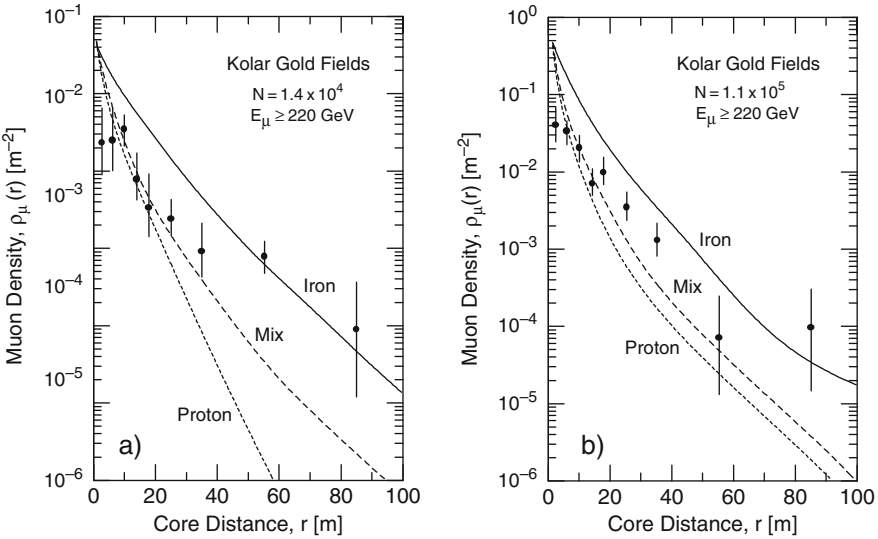

Fig. 14.22 Lateral density distribution of high energy muons ($E_\mu \geq 220$ GeV) in showers of average size $\langle N \rangle = 1.4 \cdot 10^4$, (**a**), and $\langle N \rangle = 1.1 \cdot 10^5$, (**b**), respectively, recorded at the 270 m underground level at the Kolar Gold Fields in India (920 m a.s.l.). The *curves* show the expected distributions for proton and iron primaries and the "normal mix", as indicated (Sivaprasad, 1970, Unpublished; Acharya et al., 1979, 1981)

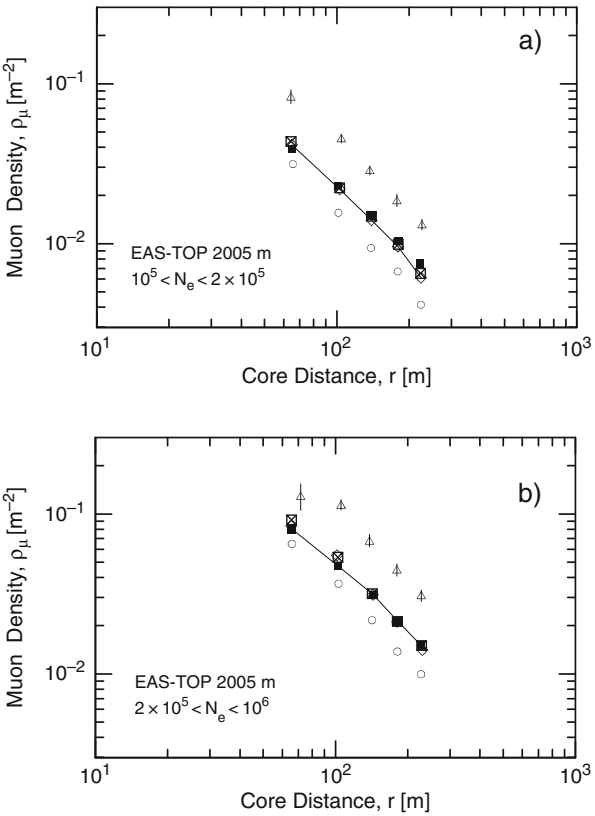

Fig. 14.23 Comparison of lateral density distributions of muons of energy $\geq$1 GeV in air showers of two different size groups, as indicated, measured with the EAS-TOP installation at Gran Sasso (2,005 m a.s.l.) (■) and simulated showers. The simulations were carried out for different primary mass groups as follows: ○ protons, ◇ He, △ Fe, ☒ mixed (Aglietta et al., 1997)

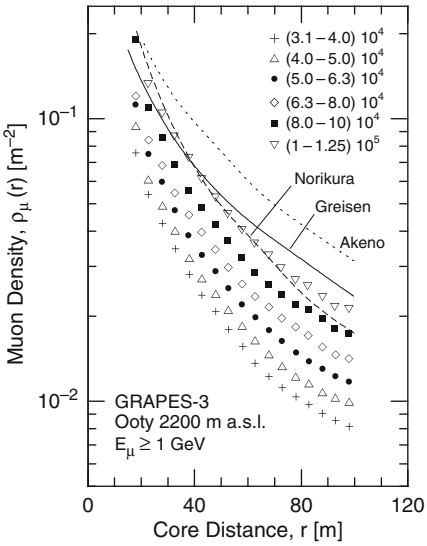

Fig. 14.24 Lateral density distributions of muons of energy ≥ 1 GeV recorded with the air shower array GRAPES-3 at Ootacamund (2,200 m a.s.l.) in India, in showers of a range of size groups as indicated (Hayashi et al., 1999). The *curves* show distributions obtained by other experiments for comparison (Mt. Norikura, Sakuyama, 1972; Akeno and Hayashida, 1995; Greisen, 1960)

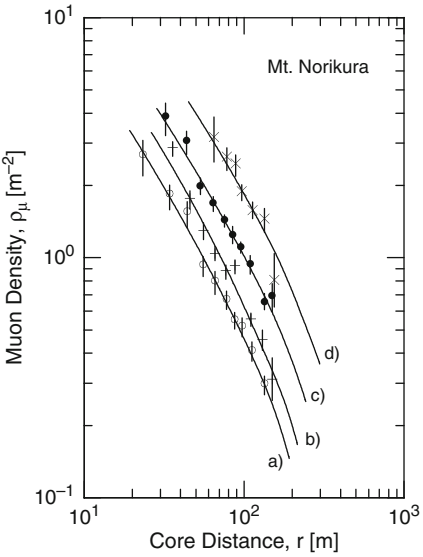

Fig. 14.25 Lateral density distributions of muons of energy $E_\mu \geq 0.7$ GeV, measured at Mount Norikura, Japan (2,770 m a.s.l.) (Miyake et al., 1977). The *lines* connect sets of data points belonging to the same shower size group: $\circ$ (*a*) $5 \cdot 10^6 \leq N_e < 7 \cdot 10^6$, + (*b*) $7 \cdot 10^6 \leq N_e < 10^7$, $\bullet$ (*c*) $10^7 \leq N_e < 2 \cdot 10^7$, and $\times$ (*d*) $2 \cdot 10^7 \leq N_e \leq 5 \cdot 10^7$. The empirically found structure function is given by $\rho_\mu(r) \propto r^{-\alpha} e^{-(r/250)}$, where r is the core distance in meters. The parameter α depends on shower size: $\alpha = 1.02 \pm 0.06$ for data group (*a*), $\alpha = 1.04 \pm 0.10$ for (*b*), $\alpha = 0.84 \pm 0.07$ for (*c*) and $\alpha = 0.84 \pm 0.17$ for (*d*)

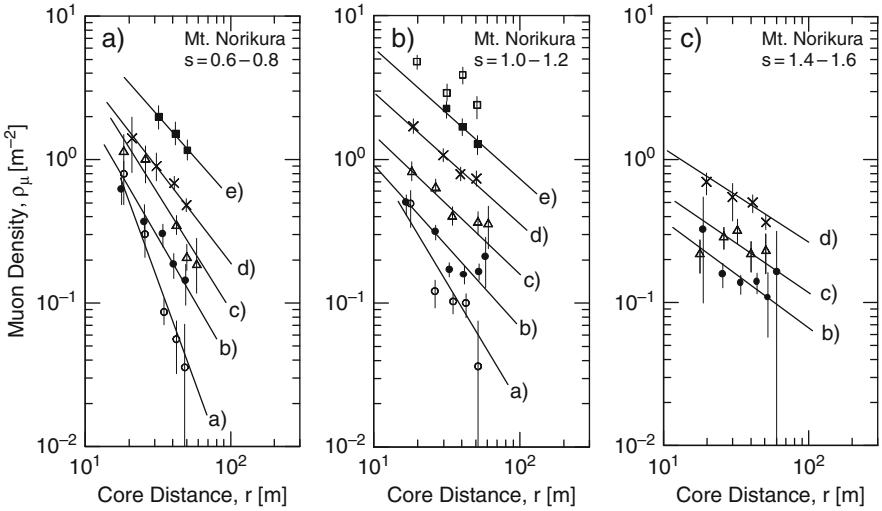

Fig. 14.26 Lateral density distributions of muons of energy ≥ 0.3 GeV observed at Mount Norikura, Japan (2,770 m a.s.l.) (Miyake et al., 1968). The showers are grouped according to age, as indicated. The different shower size groups are identified by symbols and letters attached to the fitted straight lines: ○ (*a*) $2 \cdot 10^5 \leq N_e < 5 \cdot 10^5$, ● (*b*) $5 \cdot 10^5 \leq N_e < 10^6$, △ (*c*) $10^6 \leq N_e < 2 \cdot 10^6$, × (*d*) $2 \cdot 10^6 \leq N_e < 5 \cdot 10^6$, ■ (*e*) $5 \cdot 10^6 \leq N_e < 10^7$, and □ $10^7 \leq N_e < 2 \cdot 10^7$

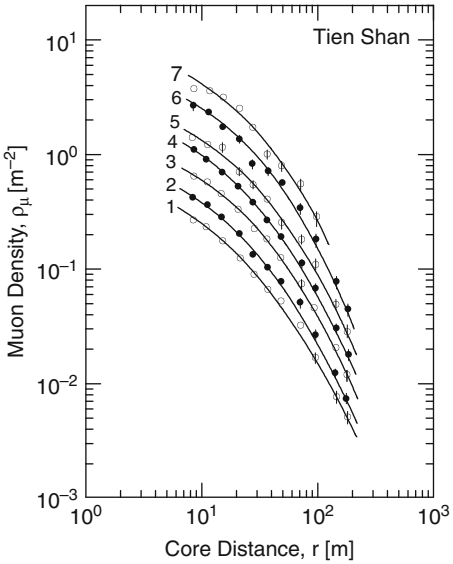

Fig. 14.27 Lateral density distributions of muons of energy $E_\mu \geq 5$ GeV in showers of different size groups, recorded at the Tien Shan station in Kazakhstan (3,340 m a.s.l., 690 g cm^{-2}) (Aseikin et al., 1977) for zenith angles $\theta \leq 30^\circ$. *Curves 1–7* are *smooth curves* drawn through the data points to guide the eye. They apply to the following average shower size groups: (*1*) $\langle N \rangle = 1.79 \cdot 10^5$, (*2*) $\langle N \rangle = 3.04 \cdot 10^5$, (*3*) $\langle N \rangle = 5.15 \cdot 10^5$, (*4*) $\langle N \rangle = 8.9 \cdot 10^5$, (*5*) $\langle N \rangle = 1.44 \cdot 10^6$, (*6*) $\langle N \rangle = 2.20 \cdot 10^6$, and (*7*) $\langle N \rangle = 4.21 \cdot 10^6$

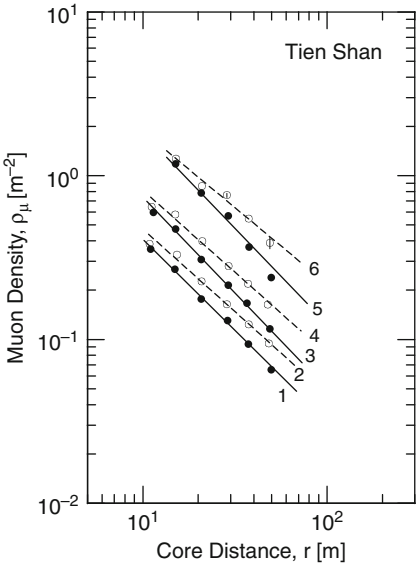

Fig. 14.28 Age dependence of the lateral density distribution of muons of energy $E_\mu > 5$ GeV as determined at Tien Shan, Kazakhstan (3,340 m a.s.l.) (Stamenov et al., 1977; see also Kabanova et al., 1973). The *solid and dashed lines* connect the *full and open circle* data points which identify the two shower age groups with $s < 0.8$ (•) and $s > 0.8$ (○), respectively. The data labeled *1* and *2* cover the average size group $\langle N \rangle = 3.04 \cdot 10^5$, *3* and *4* $\langle N \rangle = 5.15 \cdot 10^5$, *5* and *6* $\langle N \rangle = 1.44 \cdot 10^6$

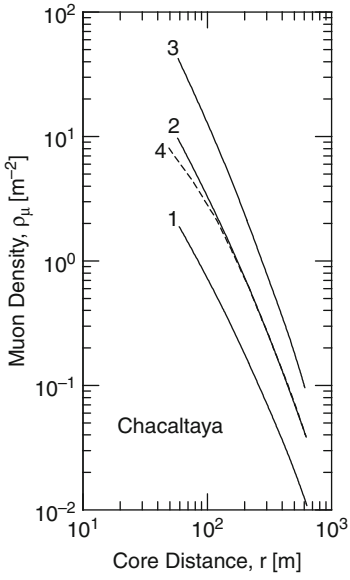

Fig. 14.29 Summary of average lateral density distributions for muons of energy $E_\mu \geq 0.6$ GeV, detected at Mount Chacaltaya, Bolivia (5,230 m a.s.l.) under an overburden of 644 g cm^{-2} (Aguirre et al., 1977, 1979; see also Aguirre et al., 1973). *Curves 1–3* are for shower sizes of $N = 1.6 \cdot 10^7$, $N = 10^8$ and $N = 6.3 \cdot 10^8$, respectively. The *dashed curve, 4*, shows a fit, normalized to $N = 10^8$, after Kaneko et al. (1975), using the expression $\rho_\mu(r) \propto r^{-0.75}(1 + r/r_G)^{-2.5}$. The parameter $r_G = 140$ m for $N = 10^7$ and $r_G = 90$ m for $N = 10^9$

14.3 Energy and Momentum Spectra

Relatively few energy and momentum spectra of muons in air showers had been measured. For energy measurements one uses common absorption spectrometers (absorption telescopes) or underground installations. Because of the high penetrating power of muons surface laboratory installations consist usually of sandwiches of

steel plates, interlaced with scintillators. Such measurements are generally limited to a few GeV. For higher energy thresholds, measurements are usually made with underground installations that have a sufficient overburden (Vernov et al., 1965c, 1968b), and to record ultrahigh energy (TeV) muons with detectors located at great depth, underneath air shower arrays (Acharya et al., 1977; Aglietta et al., 2004). As mentioned before, only very few deep underground installations had air shower arrays overhead, at the surface, with the capability to define the events that produced the TeV muons.

Only few air shower experiments had magnet spectrometers. Very few installations had magnets with an air gap (Brooke et al., 1962; Brooke and Wolfendale, 1964; Hook et al., 1970; Atanelishvili et al., 1977) and some had magnets in combination with a Wilson Cloud Chamber (Apshev et al., 1977) that allowed, in principle, to study a variety of particles. In some experiments simple solid iron magnets had been used that are suitable for muon studies only (Rochester et al., 1965; Earnshaw et al., 1968, 1971a; Machin et al., 1970; Vernov et al., 1979; Grishina et al., 1981; Bhadra et al., 1998). These instruments were placed either at the surface, or at

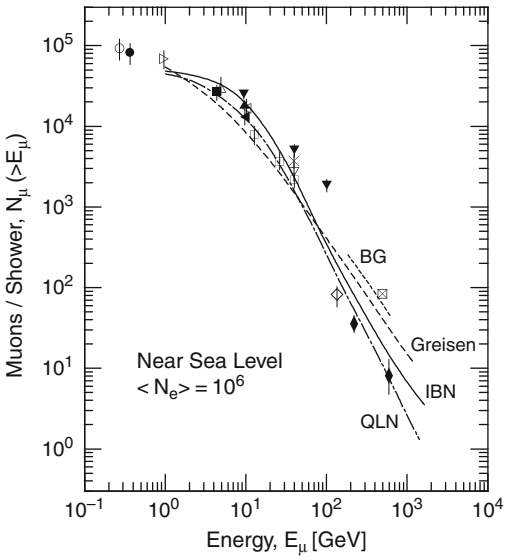

Fig. 14.30 Compilation of early data on integral energy spectra of muons measured in air showers at or near sea level, normalized to a shower size of 10^6 particles. The references of the data are listed below. The *dashed curve* is the Greisen spectrum (Greisen, 1960). Shown, too, are the results of early theoretical work. The *solid curve* labeled QLN and the *chain curve* labeled IBN are simulation data from the work of Murthy et al. (1968) and refer to the quarter-law and isobar model, respectively, that include nucleon-antinucleon production (see also Sreekantan, 1971). ⊠, Barrett et al. (1952); ●, Porter et al. (1957); ○, Abrosimov et al. (1958, 1960); △, Khrenov (1961); □, Andronikashvili and Kazarov (1960); ■, Hasegawa et al. (1962); ×, Barnaveli et al. (1964); ▽, Barnaveli et al. (1964); ◁, Vernov et al. (1964a); ◀, Vernov et al. (1965b); ◇, Chatterjee et al. (1968); ▼, Earnshaw et al. (1968); ▲, Vernov et al. (1968b); ♦, Sreekantan (1971); ▷, Earl (1959) for core distances ≤ 900 m; BG, (short *dashed line*) Bennett and Greisen (1961)

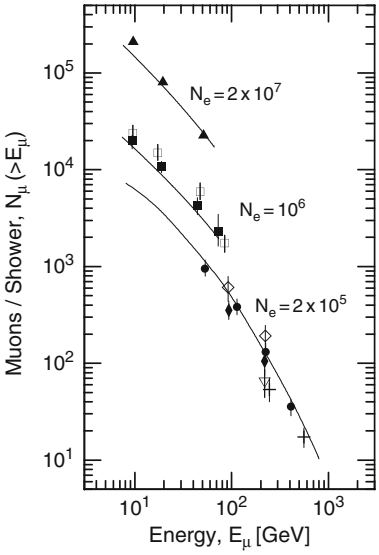

Fig. 14.31 Compilation of data on energy spectra of muons in showers belonging to different average size groups, as indicated. The data of Grishina et al. (1981) ($\langle N_e \rangle = 2 \cdot 10^5$) are grouped according to age parameter, s, as determined from measurement (see below). The Moscow shower data apply essentially to sea level whereas those from the Kolar Gold Fields (KGF) were recorded at ≈1,000 m a.s.l.. Included are data from the following authors: •, Moscow (Khrenov et al., 1979); +, KGF (Acharya et al., 1977); □, Moscow (Vernov et al., 1977); ■, ▲, Moscow (Rozdhestvensky et al., 1975); ▽, Moscow (Grishina et al., 1981), $s = 1.08$; ♦, Moscow (Grishina et al., 1981), $s = 1.18$; ◇, Moscow (Grishina et al., 1981), $s = 1.30$

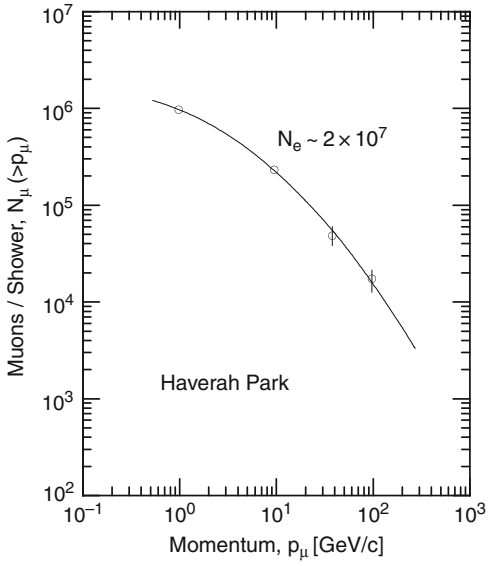

Fig. 14.32 Integral momentum spectrum of muons in showers of size $2 \cdot 10^7$ GeV, recorded at Haverah Park, England with a solid iron magnet spectrometer (Earnshaw et al., 1968)

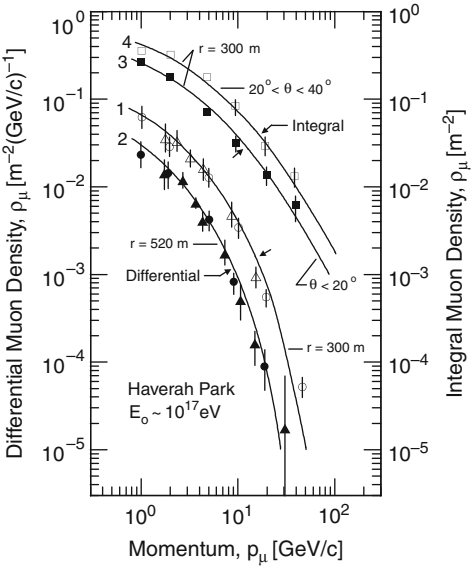

Fig. 14.33 Differential momentum spectra of muons in showers of primary energy around 10^{17} eV recorded at Haverah Park, England at core distances of 300 and 520 m, respectively (*left hand ordinate*). ○ and ● are re-analyzed data from the Mark I spectrograph (Machin et al., 1970), △ and ▲ are more recent data from Mark II (Dixon et al., 1973a). The experimental data are for showers having zenith angles $\leq 40°$. *Curves 1 and 2* are predictions from model calculations of Dixon et al. (1973b) for core distances as indicated and a zenith angle of 30°. The integral momentum spectra of muons of a similar set of showers falling into zenith angular bins $\theta < 20°$ (■) and $20° \leq \theta \leq 40°$ (□), recorded at Haverah Park at a core distance of 300 m are also illustrated (*upper data sets and right hand ordinate*). The two *curves 3 and 4*, are hand fitted to guide the eye (Earnshaw et al., 1971a)

relatively shallow depth underground, within the boundaries of an air shower array, and could be used to measure momentum spectra of muons in air showers. In the following we present a summary of energy and momentum spectra from a variety of experiments at different altitudes.

Figure 14.30 shows data points from very early measurements carried out with many different installations that cover a very wide energy range. The spectrum applies to showers of average size $\langle N \rangle = 10^6$. In Fig. 14.31 we present a compilation of muon spectra in showers of three different size groups that are mainly from measurements made at different periods by different authors with the solid iron magnet spectrometer at the University of Moscow. The instrument was located underground at a depth of 40 m w.e. in the center of the shower array. We have added to this figure two points from underground absorption measurements at the Kolar Gold Fields. The references of the data and additional details are given in the figure captions.

The following three figures (Figs. 14.32, 14.33 and 14.34) show differential and integral muon momentum spectra in large showers, at different radial distances from

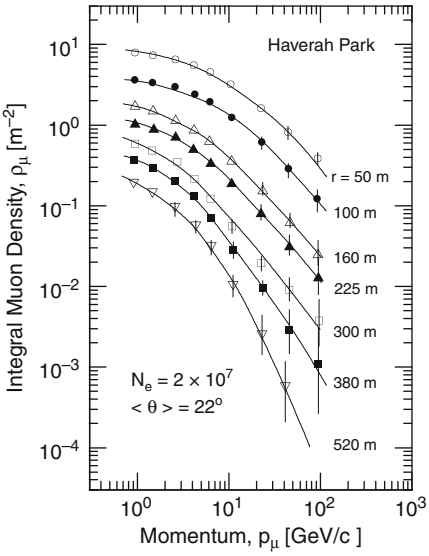

Fig. 14.34 Integral momentum spectra of muons in showers of size $2 \cdot 10^7$ obtained at Haverah Park, England for different core distances, as indicated (Earnshaw et al., 1968). The median zenith angle is 22°. The *curves* are rough fits to the data and help to guide the eye

the shower axis, recorded at Haverah Park by the Durham (GB) group (Earnshaw et al., 1968, 1971a; Machin et al., 1970; Dixon et al., 1973a, b), using a solid iron magnet spectrometer. Further details are given in the captions. Measurements made with a similar kind of spectrometer at Kiel (Bürger et al., 1975) in smaller showers ($N_e = 5 \cdot 10^5$) are plotted in Fig. 14.35 together with some data points of Earnshaw et al. (1967) for comparison.

More recent data are shown in Fig. 14.36 from the measurements of Sarkar et al. (1993), using the two solid iron magnet spectrometers that are part of the

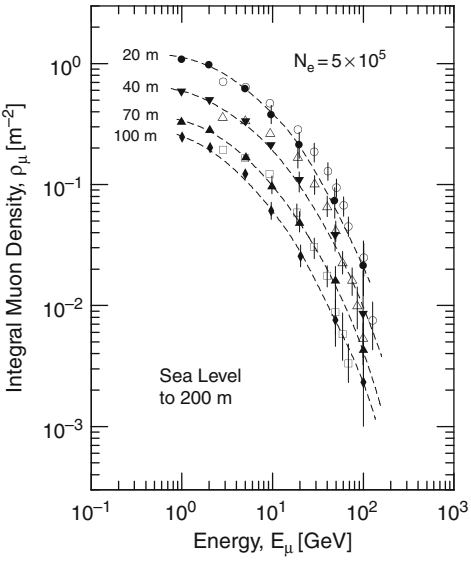

Fig. 14.35 Integral energy spectra of muons in showers of size 10^5 measured at three different core distances with the installation at Kiel, Germany (open symbols): ○, $r \leq 25$ m; △, $25 < r \leq 50$ m; □, $50 < r \leq 80$ m (Bürger et al., 1975). For comparison we have added the data of Earnshaw et al. (1967), recorded at Haverah Park, England at four comparative core distances (full symbols). These data had been acquired from larger showers but had been normalized to a shower size of 10^5: ●, 20 m; ▼, 40 m; ▲, 70 m; and ◆, 100 m

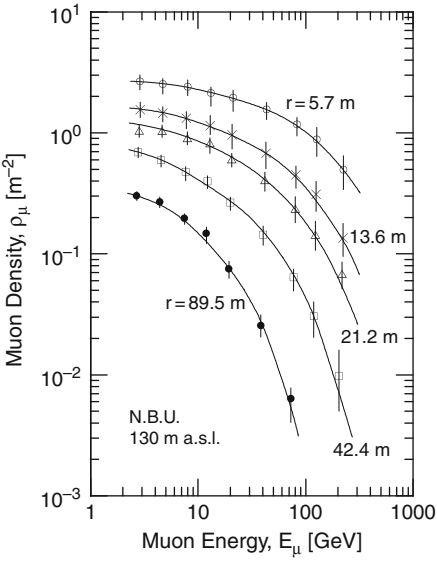

Fig. 14.36 Energy spectra of muons at different radial distances from the shower core, measured with the two magnet spectrometers of the air shower array of the North Bengal University (NBU), located near Siliguri, India (Sarkar et al., 1993)

North Bengal University air shower array near Siliguri (130 m a.s.l.). The data apply to particular radial distances from the shower axis, ranging from 5.7 to 89.5 m, as indicated.

Two data points from absorption measurements made at the high altitude installation of Tien Shan (3,340 m a.s.l.) by Aseikin et al. (1971) that fix the muon energy spectrum in small showers ($N_e = 3 \cdot 10^4$) are given in Figs. 14.37 and 14.38 shows the ratio of 0.5–1 GeV muons at a core distance of 700 m in showers of sizes $3 \cdot 10^7 \leq N_e \leq 10^9$ determined by Hara et al. (1983c) at Akeno (900 m a.s.l.).

Spectral information on ultrahigh energy muons in showers is extremely difficult to obtain. Most explorations of this group of muons were made with solid iron magnets in horizontally oriented spectrometers on unaccompanied muons, i.e., these data are not associated with detected showers. On the other hand, the few installations that were suited to carry out simultaneously measurements at the surface and deep underground have a small aperture and therefore poor statistics. This was particularly the case for some of the Kolar Gold Field experiments.

The situation was much improved at Gran Sasso, where a very large detector was available at great depth underground (MACRO, Ambrosio et al., 2002), near the EAS-TOP array at the surface. One aspect of a combined surface and underground experiment carried out with these two detectors is discussed in Sect. 10.3.4, in the context of primary mass determination, using very high energy muons. There we discuss the combined EAS-TOP and MACRO data and present results from simulations of the lateral distribution and energy spectrum of ultrahigh energy muons.

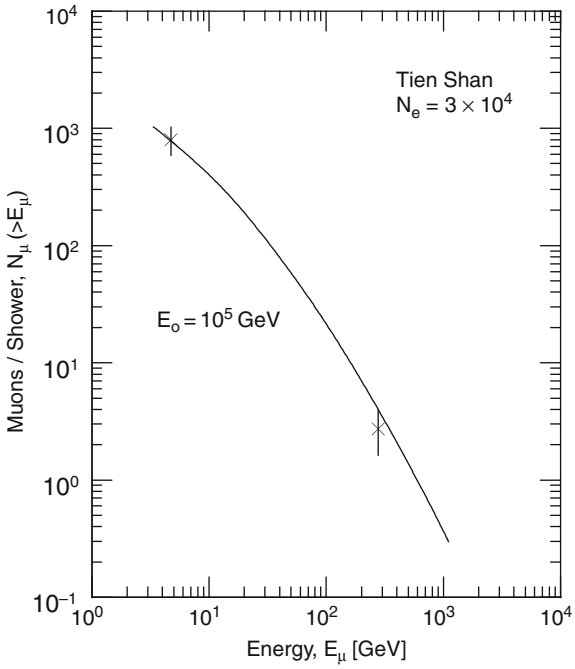

Fig. 14.37 Integral energy spectra of muons in small showers of $\langle N_e \rangle = 3 \cdot 10^4$, recorded at Tien Shan (Kazakhstan) (3,340 m a.s.l.) (Aseikin et al., 1971). The *curve* shows a theoretical spectrum obtained with the CKP model

Another similar experiment was conducted using the EAS-TOP array and the deep underground LVD (Large Volume Detector) detector at Gran Sasso. The energy of muons which had been recorded in LVD that had been time correlated with air showers registered at the surface, could be estimated from the *energy deposit per*

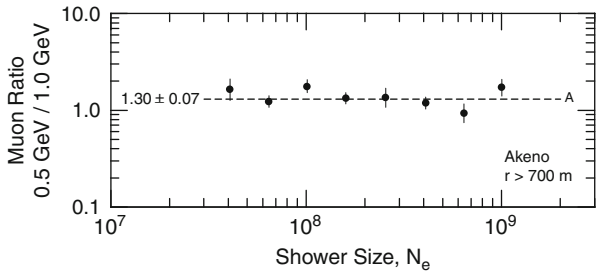

Fig. 14.38 Ratio of the density of muons of energy $\geq$0.5 GeV to muons of energy $\geq$1.0 GeV as a function of shower size, N_e, measured at a distance $\geq$700 m from the shower axis at Akeno (900 m a.s.l.). The *dashed line, A*, indicates the average of the ratio (1.30 $\pm$ 0.07) over the full size range (Hara et al., 1983c)

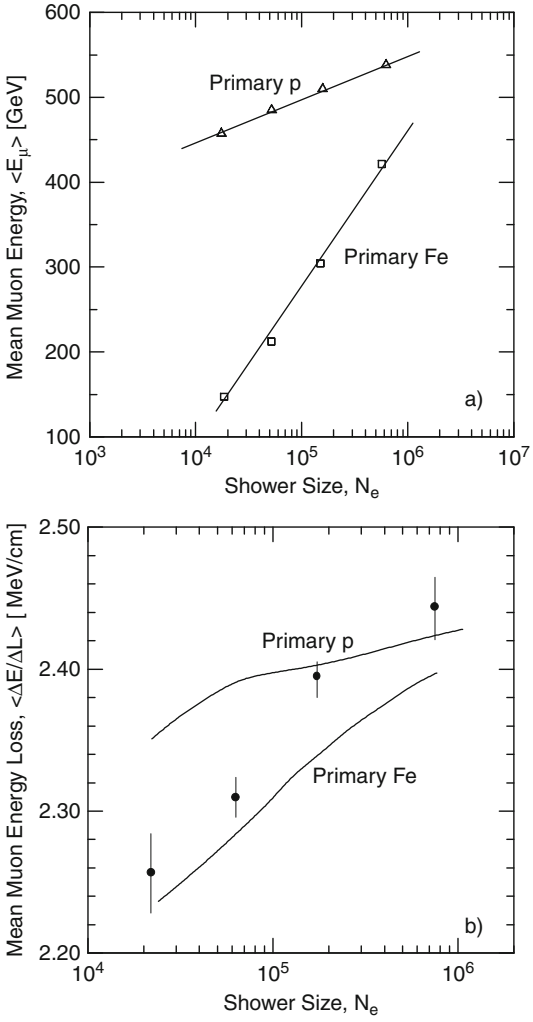

Fig. 14.39 (**a**) Expected mean muon energy at the LVD level underground (3,000 m w.e.) as a function of shower size N_e at the EAS-TOP level (2,005 m a.s.l.) for showers initiated by primary protons and iron nuclei. (**b**) Mean energy deposit per unit track length of high energy muons resulting from radiative energy losses, mainly direct pair production and also transition radiation processes, in the detector medium of the LVD detector that are time correlated with showers recorded by the EAS-TOP array at the surface as a function of shower size (Aglietta et al., 1998)

unit path length in the LVD medium. The energy loss is mainly due to radiative losses. Figure 14.39a shows a plot of the predicted mean energy of muons in simulated primary proton and iron initiated showers of different sizes, and Fig. 14.39b the expected energy loss of the muons per unit path length in the detector. Also indicated in this second figure are the measured energy deposits in the detector medium of muons belonging to showers of four different size groups (Aglietta et al., 1998).

14.4 Temporal Properties and Muon Front Curvature

In this section we discuss temporal topics that concern only the muon component in showers. General temporal properties of air shower particles are discussed in Chap. 9. Over the past 50 years many authors have studied the arrival time

distribution of muons, both experimentally (Linsley and Scarsi, 1962; Blake and Harris, 1970; Aguirre et al., 1979; Kakimoto et al., 1986; Rebel et al., 1995; Haeusler et al., 2002) and with simulations (Grieder, 1970a, b, 1977a; Brancus et al., 1997; Antoni et al., 2001, 2003a).

Of particular interest are the rise and fall time of the muon burst arriving at a detector at a particular core distances, the full width of the burst at half amplitude, and the curvature of the muon front, in an attempt to extract useful information on the shower development and the nature of the primary.

From these observables, in particular from the full width at half height of the muon detector pulse, one can estimate the height (or depth) of maximum development of an individual shower in the atmosphere. The methods to achieve this goal are discussed in detail in Chap. 7. In the following we present data samples of the typical temporal observables.

Figure 14.40 shows the result of a set of rise time measurements of the muon component as a function of core distance in large showers for different zenith angles of incidence, covering the range from 13° to 58°, made at Haverah Park (Blake

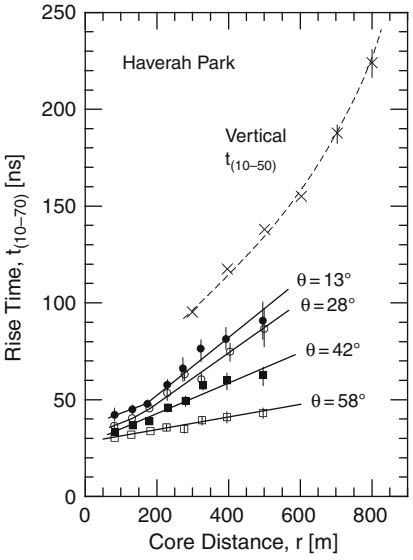

Fig. 14.40 Mean muon detector pulse rise time as a function of core distance observed with a 10 m^2 shielded scintillation counter in showers of primary energies between 10^{17} and 10^{18} eV recorded at Haverah Park. The figure shows the rise time, $t_{(10-70)}$, defined as the time between the 10 and 70% levels of the leading edge of the photomultiplier pulse versus core distance for different zenith angles, θ, as indicated (●, ○, ■, □). The detector threshold for these measurements was 318 MeV (Blake et al., 1981). The symbols × show measured average values of the pulse rise time, $t_{(10-50)}$, defined to be the time between the 10 and 50% levels of the leading edge of the Haverah Park deep water Cherenkov detector pulse as a function of core distance (Barrett et al., 1975b; see also Watson and Wilson, 1974). These data apply to showers of approximately 10^{18} eV primary energy and vertical incidence. The *solid and dashed lines* are hand drawn fits to the experimental points made by the author to guide the eye

et al., 1981). The rise time was measured from the 10 to the 70% level, $t_{(10-70)}$, of the amplitude of the leading edge of the signal pulses of shielded scintillation detectors that served as muon detectors. The threshold energies of the three detectors that had been used were E_μ >318, >420 and >489 MeV (shown are the results for >318 MeV).

Also shown in the same figure is the result from an analogous measurement made with a standard Haverah Park deep water Cherenkov detector. In this case the rise time was measured over the reduced amplitude range, from 10 to 50%, $t_{(10-50)}$. It is evident from this figure that in spite of the narrower amplitude window chosen here the rise time is significantly larger. This is related to the very different particle mix and geometry of the detector.

Blake et al. (1981) confirm the results of earlier measurements that the $t_{(10-70)}$ parameter depends on core distance and zenith angle. Moreover, they observe a muon threshold energy dependence of the delay parameter and conclude that for muons of energy less than 500 MeV *velocity delays* ($\beta = v/c$) become important. In addition, they note that for core distances in excess of 200 m delay fluctuations get large.

A similar plot with analogous data from measurements of $t_{(20-70)}$ with scintillation detectors at Akeno (900 m a.s.l.) by Tamura et al. (1981) is displayed in

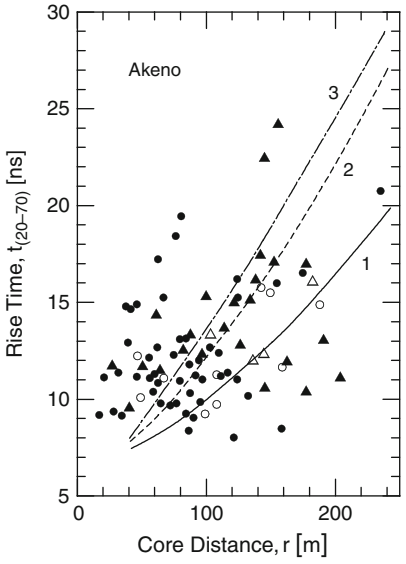

Fig. 14.41 Scatter plot of the muon detector pulse rise time, $t_{(20-70)}$, as defined in the text, versus core distance in showers of different size groups and sec(θ) cuts, obtained at Akeno, Japan (900 m a.s.l.): • and ▲ are for $1.0 \leq \sec(\theta) \leq 1.2$, ○ and △ for $1.2 \leq \sec(\theta) \leq 1.4$. • and ○ cover the shower size group $10^7 \leq N_e < 3.16 \cdot 10^7$, ▲ and △ apply to $3.16 \cdot 10^7 \leq N_e \leq 10^8$. *Curves 1–3* were obtained from simulations using a quarter-, half- and enhanced half-law multiplicity model, respectively, and primary protons of energy 10^{17} eV (Tamura et al., 1981)

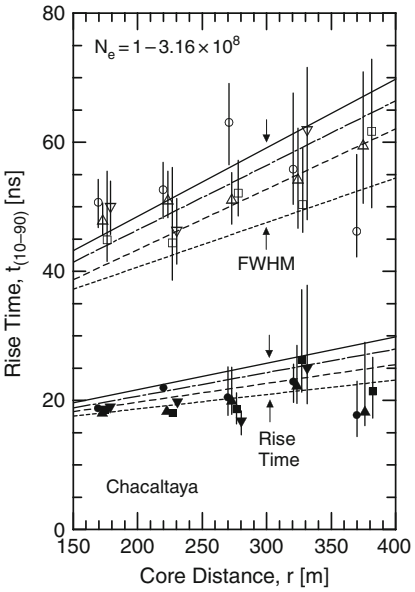

Fig. 14.42 Rise time, $t_{(10-90)}$ (full symbols), and full width at half maximum, FWHM (open symbols), of the muon detector pulses in showers of size $10^8 \leq N_e \leq 3.16 \cdot 10^8$ as a function of core distance, determined at Chacaltaya, Bolivia (5,230 m a.s.l.) for different zenith angles, θ, expressed in sec(θ) (slant depth with respect to vertical incidence). The *different lines* represent corresponding predictions from simulations for 10^{17} eV proton initiated showers: ○, ● and *solid lines*, sec(θ) = 1.1; △, ▲ and *dot-dash lines*, sec(θ) = 1.3; □, ■ and *dashed lines*, sec(θ) = 1.5, ▽, ▼ and *dotted lines*, sec(θ) = 1.7 (Suga et al., 1979; see also Kakimoto et al., 1981)

Fig. 14.41 (see also Kakimoto et al., 1986), and data of $t_{(10-90)}$ from work carried out at Mt. Chacaltaya (5,230 m a.s.l.) in Fig. 14.42 (Suga et al., 1979; Kakimoto et al., 1981). In the same figure is also shown the full width at half maximum ($FWHM$) of the same sets of pulses. The experimental arrival time distribution as measured at Mt. Chacaltaya is plotted in Fig. 14.43 together with theoretical distributions from simulations using different interaction models (Suga et al., 1979).

The *curvature* of the muon front in large air showers had been investigated by Brownlee et al. (1970b) with their special muon shower array SUGAR at Narrabri, Australia (260 m a.s.l.). They calculated the radius of curvature from arrival delay measurements with respect to the tangent plane of the shower. The result is displayed in Fig. 14.44.

Data on the *fluctuations* of the rise time parameter $t_{(10-50)}$, $\sigma_f(t_{(10-50)})$, obtained by Barrett et al. (1975a, b) and Watson and Wilson (1974) from measurements with deep water Cherenkov detectors at Haverah Park are reproduced in Fig. 14.45. For comparison the authors have added the predicted dependence of the delay fluctuations on core distance from simulations for proton and alpha particle initiated showers, using model E of Hillas et al. (1971a). It is noted that the experimentally

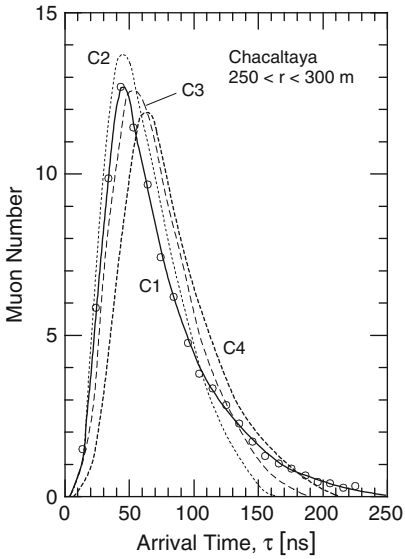

Fig. 14.43 Arrival time distribution of muons in showers of average primary energy $7.3 \cdot 10^{17}$ eV at core distances between 250 and 300 m, recorded at Chacaltaya (5,230 m a.s.l.). *Curve C1* is a fit to the experimental data, ○. *Curves C2–C4* are predictions from simulations using different shower models (Suga et al., 1979)

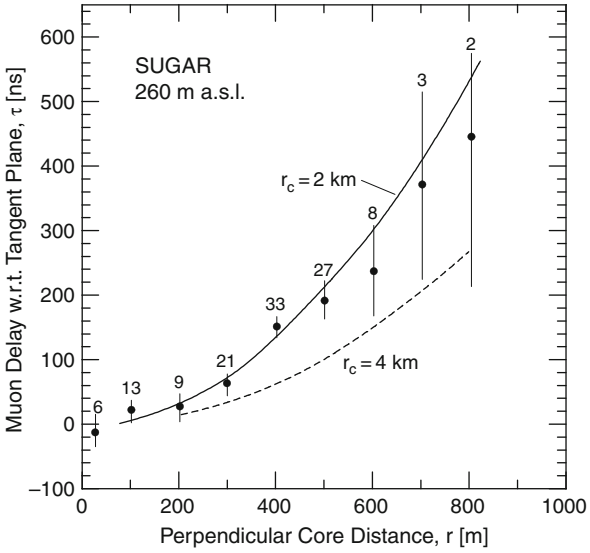

Fig. 14.44 Arrival delay of muons with respect to the tangent plane against perpendicular distance from the shower core of 28 showers of muon size $4 \cdot 10^6 < N_\mu < 8 \cdot 10^6$ and zenith angle range $0^\circ < \theta < 30^\circ$. The numbers identify the number of detector stations that recorded an event at the respective core distance. The *solid and dashed curves* give the location of the radius of curvature, r_c, of 2 and 4 km, respectively (after Brownlee et al., 1970b)

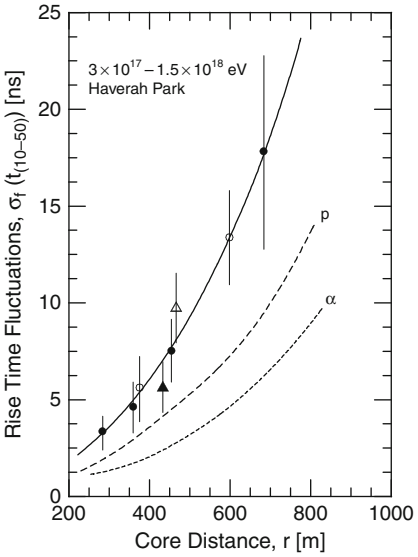

Fig. 14.45 Fluctuations, $\sigma_f(t_{(10-50)}$, of the rise time measurements, $t_{(10-50)}$, of the shower front as defined in the text, obtained with the Haverah Park installation versus core distance in showers of an estimated primary energy range from $3 \cdot 10^{17}$ to $1.5 \cdot 10^{18}$ eV. ●, ○, Barrett et al. (1975a, b); ▲, △, Watson and Wilson (1974). The *full symbols* were obtained in showers where only two individual measurements of $t_{(10-50)}$ met the required shower selection criteria, for the *open symbols* three measurements met the criteria. *Curves p and α* show results of simulations for primary protons and alpha particles, respectively (Lapikens, 1975; Hillas et al., 1971a). The *solid line* is an approximate fit to the experimental points, drawn by the author

determined rise times and the fluctuations are systematically larger than those predicted.

Relatively recent studies of the temporal features of muons had also been carried out by the KASCADE group (Antoni et al., 2003a; see Chap. 9).

14.5 Charge Ratio and Geomagnetic Charge Separation

Very few measurements had been carried out to determine the muon charge ratio in air showers. Such measurements require magnet spectrometers that usually have a very limited aperture. Air gap magnets allow to investigate low energy muons but have in general a rather low maximum detectable momentum. On the other hand, solid iron magnets can handle higher momentum muons but have a fairly high lower cutoff energy because to the absorption in the magnet itself.

In Fig. 14.46 we show a compilation of data of the muon charge ratio in air showers from three experiments which had been carried out at Durham (GB), Kiel and Haverah Park, covering the energy range from 1 GeV to almost 1,000 GeV. Similar data of much more recent date that were acquired by the Darjeeling group of the

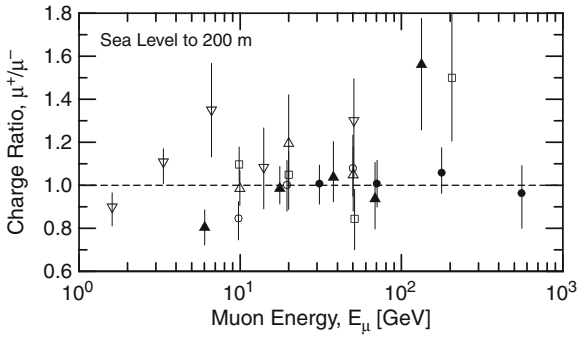

Fig. 14.46 Compilation of data on the muon charge ratio in different shower groups as a function of muon energy measured near sea level as follows: • $5 \cdot 10^3 < N_e < 10^7$, $r \leq 100$ m (Hawkes et al., 1977) at Durham, England. ▲ $5 \cdot 10^4 \leq N_e \leq 5 \cdot 10^6$, $r \leq 50$ m, $\langle r \rangle = 32$ m, $\langle E_\mu \rangle = 23$ GeV (Bürger et al., 1975) at Kiel. ▽ $E_0 \simeq 10^{17}$ eV, $r \simeq 300$ m (Earnshaw et al., 1971b); ○ $10^5 \leq N_e \leq 10^6$, △ $10^6 \leq N_e \leq 10^7$, □ $N_e > 10^7$, 10 m $\leq r \leq$ 600 m (Orford et al., 1968), both at Haverah Park

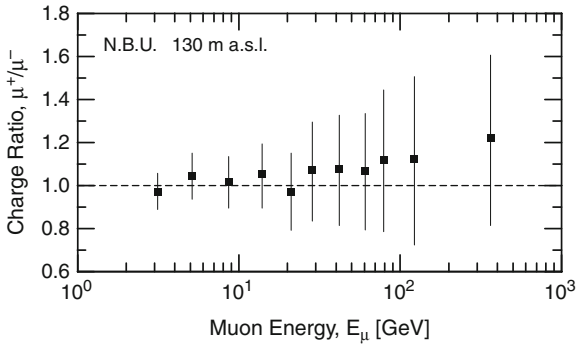

Fig. 14.47 Recent data set on the muon charge ratio as a function of the muon energy in showers of size $10^4 \leq N_e \leq 10^6$, recorded with the two solid iron magnet spectrometers of the N.B.U. array near Siliguri, India (Sarkar et al., 1993)

North Bengal University (NBU), using the two solid iron magnet spectrometers that are part of their air shower array located near Siligury at an altitude of 130 m a.s.l. are given in Fig. 14.47 (Sarkar et al., 1993).

Some very approximate and coarse muon charge information can in principle be obtained from the geomagnetic deflection of the muons in sufficiently inclined showers that are incident perpendicular to the geomagnetic field direction. As an example we show in Fig. 14.48 the azimuthal dependence of the charge ratio of muons of energy $\geq$1 GeV which is due to geomagnetic deflection (Earnshaw et al., 1971b).

Under optimized conditions with respect to the geomagnetic field, the particle density distribution may take the form of two lobes, symmetrically located about the shower axis in the transverse shower plane (see Fig. 8.17, Sect. 8.8). In Fig. 14.49

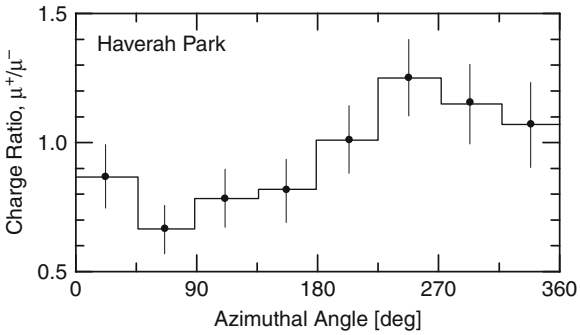

Fig. 14.48 Charge ratio of muons of momentum ≥ 1 GeV/c as a function of the azimuthal angle of incidence of the showers (Earnshaw et al., 1971b). The data apply to a core distance of approximately 300 m in showers with $E_0 \simeq 10^{17}$ eV, measured at Haverah Park

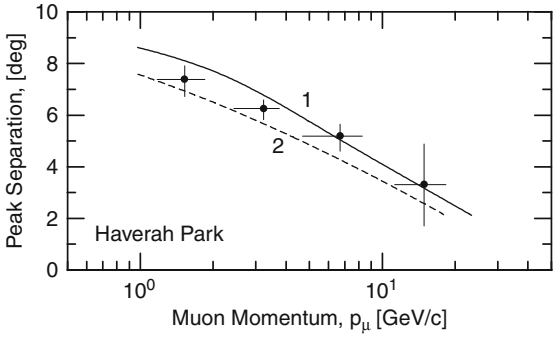

Fig. 14.49 Geomagnetic separation of the peaks of the angular distributions of positively and negatively charged muons as a function of their momentum measured at Haverah Park (Earnshaw et al., 1971b). *Curves 1 and 2* are results of model calculations and are for primary protons and iron initiated showers, respectively

we show the separation of the two peaks of the lobes that had been observed by Earnshaw et al. (1971b) as a function of muon momentum. Also plotted in the same figure are predicted separations from simulations that are in good agreement with the observations.

This phenomenon had been studied by many authors and is discussed in Sect. 8.8 in general terms since it affects the lateral density distribution not only of muons but of all charged particles, and the size and energy determination of showers. Xue and Ma (2007) revisited this problem recently and carried out an interesting analytic calculation, using a revised Heitler model (Matthews, 2005).

Very recently, Rebel et al. (2007a, b) carried out refined Monte Carlo studies of the geomagnetic effect on the lateral density distribution of muons in mid-size showers. In particular they studied the azimuthal density distribution of positively and negatively charged muons, the muon charge ratio as a function of azimuthal

angle at different radial distances from the shower axis of different muon energy groups, and in showers having different zenith angles. In the simulation the authors of this work have considered and properly accounted for the additional azimuthal asymmetries that are caused by the differences in the trajectory lengths of the particles in inclined showers, that lead to an azimuthal angle dependent absorption and shower age, as discussed in more detail in Chap. 8. The results of this work are summarized in Fig. 14.50a–d).

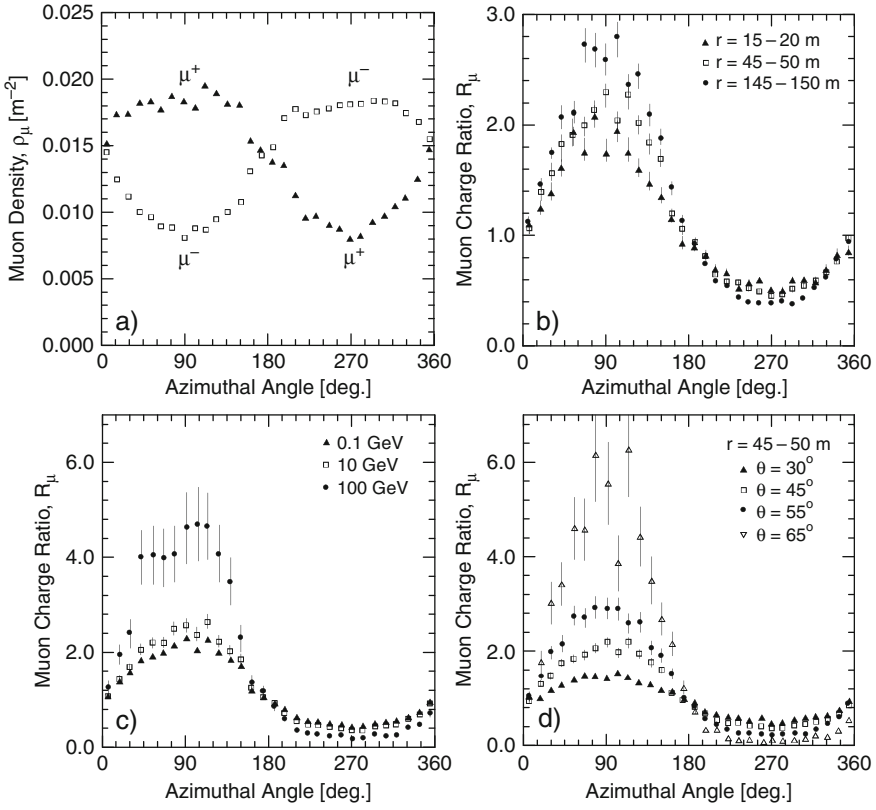

Fig. 14.50 (**a**) Mean azimuthal positive and negative muon density distributions in simulated 10^{15} eV primary proton initiated showers, incident from the North under a zenith angle of 45°, at a core distance between 45 and 50 m. (**b**) Azimuthal variation of the muon charge ratio, $R_\mu(r, \varphi) = N_{\mu+}/N_{\mu-}$, of the mean muon density distribution in the same showers at different core distance ranges, r, as specified. (**c**) Azimuthal variation of the muon charge ratio, $R_\mu(r, \varphi) = N_{\mu+}/N_{\mu-}$ of the muon density distributions of the same showers, at a core distance between 45 and 50 m, for different muon threshold energies, as listed. (**d**) Azimuthal variation of the muon charge ratio, $R_\mu(r, \varphi) = N_{\mu+}/N_{\mu-}$, of the muon density distribution at a core distance between 45 and 50 m, in the same showers, incident under different zenith angles, θ, as listed in the figure (Rebel et al., 2007a, b)

14.6 Height of Origin, Core Angle Distribution and ($E_\mu \cdot r_\mu$) Product

14.6.1 General Comments on Experimental Methods

Since muons are highly penetrating particles whose trajectories are almost undisturbed between the points of creation and detection, they yield information on the longitudinal development of the showers and thus are likely to help identify the nature of the primary. Consequently the determination of the height of origin of muons is of considerable interest.

The most energetic muons in a shower are likely to originate from the first (or first few) interactions of the primary in the atmosphere and represent first hand signatures of the initial phase of each event. However, because of the relatively small number and low density of very energetic muons, most of which are clustered within the shower core and are untraceable, an event by event analysis of individual showers cannot be realized using this group of muons, leaving only the possibility of establishing distributions and mean values of the production height of lower energy muons.

Nevertheless, the variation of the mean value of the production height of a specific category of muons or of the entire muon population in showers as a function of primary energy is a relevant observable, as it reveals changes of the primary mass composition with energy and yields information on high energy hadronic interactions. Quantities such as the muon pseudo-rapidity can be defined and had been used to explore interaction properties in conjunction with muon tracking data (Pentchev and Doll, 2001; Zabierowski et al., 2005, 2007).

In the course of time the subject of the height of origin of muons had been approached by many investigators theoretically and experimentally. The basic concept is simple and is based on *triangulation* and/or *timing*. A muon tracking device or telescope in an air shower array determines the spatial location of the muon track with respect to that of the shower axis, or the arrival delay of the muon with respect to the shower front, from which the height of origin, h_μ^{orig}, is determined. Frequently for such analyses it is assumed that muons are produced along the shower axis, to simplify the problem for a first approximation (e.g., Ambrosio et al., 1999; Zabierowski et al., 2001; Doll et al., 2002). Details of the track reconstruction procedure are discussed in the next subsection.

The first attempt to locate the height of origin of particles was made by Linsley and Scarsi (1962) who employed the *timing method*. Later on, Earnshaw et al. (1971b, 1973a, b), Dixon et al. (1973a) and Gibson et al. (1979, 1981) carried out so-called *core angle measurements*, using the muon tracking technique and their magnet spectrometer at Haverah Park to select particular energy groups of muons. Figure 14.51 shows the results of the core angle measurements of Gibson et al. (1981).

These studies are closely linked to efforts made to determine the transverse momenta, p_t, of secondaries emerging from high energy hadronic interactions. Böhm et al. (1977) have investigated this topic and studied the correlation between

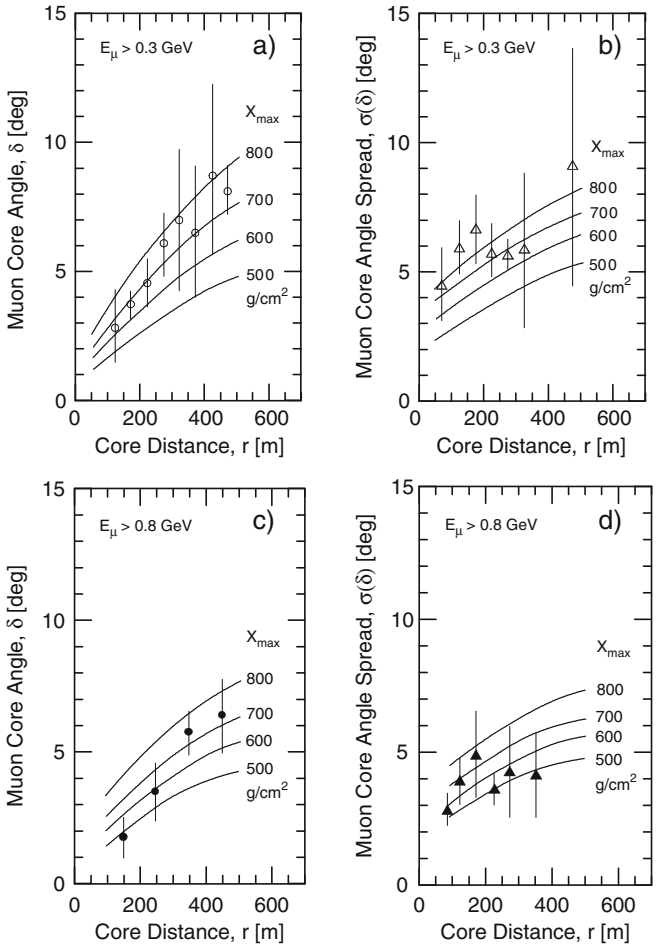

Fig. 14.51 Average angle between shower axis and muon trajectories (muon core angle δ) and spread ($\sigma(\delta)$), of muons of energy $E_\mu > 0.3$ GeV (**a**), and (**b**), and $E_\mu > 0.8$ GeV (**c**), (**d**), respectively, in showers of primary energy between 10^{17} and 10^{18} eV versus core distance, recorded at Haverah Park (Gibson et al., 1981). The *curves* represent predictions from simulations by the same authors for showers of specific depth of maximum, X_{max}, as indicated. A scaling model had been used for the simulations

the transverse momentum of muons and their parent particles (pions and kaons), using the arrival delay at ground level with respect to the first arriving particle, and the muon production height. The result is illustrated in Fig. 14.52.

Bürger et al. (1975) have carried out similar work in conjunction with spectrometric measurements. The results of this work are plotted in Fig. 14.53. Assuming that the muons are produced along the shower axis, these authors have analyzed the *energy-core-distance product* of the muons, $(E_\mu \cdot r_\mu)$, where E_μ is the muon energy and r_μ the distance from the axis, which relates to the height of origin, h_μ^{orig}, as

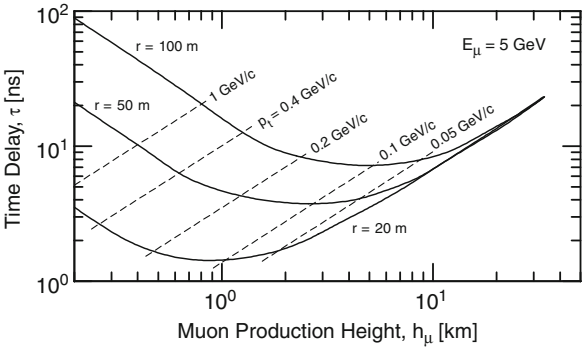

Fig. 14.52 Predictions of the arrival time delay of 5 GeV muons in showers with respect to the shower front as a function of the height of production, using a purely geometrical model (Böhm et al., 1977). The *curves* are for constant core distances, r, the *dashed diagonal lines* connect loci of fixed transverse momentum, p_t, as indicated

$$E_\mu \, r_\mu \;=\; (p_t \, c) \, h_\mu^{\text{orig}} \, . \tag{14.13}$$

A detailed theoretical-analytical treatment of the problem based on fundamental concepts to get the $E_\mu \cdot r_\mu$ distribution of the first generation of muons had been carried out by Murzin and Sarycheva (1968) who solved the diffusion equation. The relevant results of this work are discussed by Danilova et al. (1989) in connection with muon families. Analogous studies are conducted to investigate the apparent transverse momentum of high energy hadrons (see Chap. 3).

A compilation of early data of the production height of muons as a function of core distance, based on different methods is displayed in Fig. 14.54, and as a

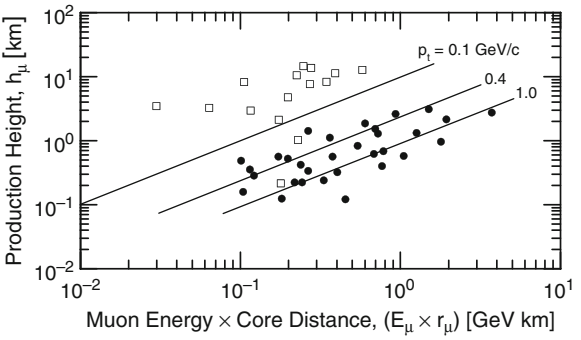

Fig. 14.53 Production height of individual muons of average energy $< E_\mu \geq 23$ GeV in showers of size range $5 \cdot 10^4 \leq N_e \leq 5 \cdot 10^5$, recorded at Kiel, using different methods of determination, • and □ (Bürger et al., 1975). The *solid lines* indicate loci for muons of constant transverse momenta, p_t, as indicated, taking into account purely geometric relations (for details see text)

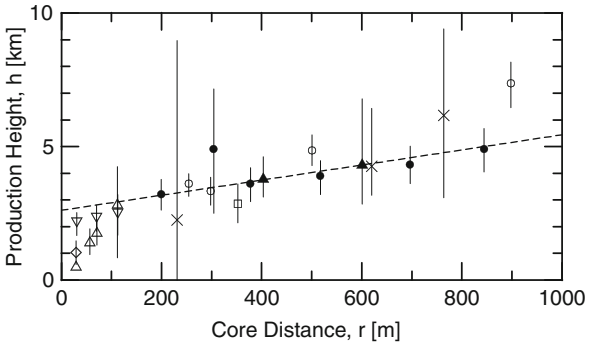

Fig. 14.54 Mean production height of muons of different energy as a function of core distance. The results were obtained using different methods. • Dixon et al. (1973a) and Earnshaw et al. (1973a, b), ○ Suri (1966), ▲ Baxter (1967), × Linsley and Scarsi (1962), □ De Beer et al. (1960), all for $E_\mu \leq 0.3\,\text{GeV}$ in showers of primary energy around $10^{17}\,\text{eV}$. △ Böhm et al. (1977), arrival time method for $\langle E_\mu \rangle = 3\,\text{GeV}$ in showers of average size $1.6 \cdot 10^5$. ◇ and ▽ are from the work of Bürger et al. (1975), using the time delay and energy methods, respectively. The dashed line shows the approximate trend

function of muon energy from the work of Dixon et al. (1973a) with the magnet spectrometer at Haverah Park in Fig. 14.55.

We have outlined the methods to determine the production height of the muons and their parent particles in air showers with the aim to identify the primary mass in general terms in Sect. 10.3.5, and will therefore limit the subsequent discussion to specific details.

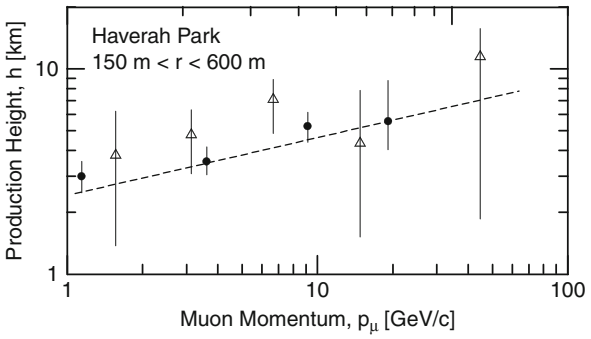

Fig. 14.55 Mean production height of muons in the lateral interval $150\,\text{m} \leq r \leq 600\,\text{m}$ derived from data obtained at Haverah Park (Dixon et al., 1973a; see also Orford et al., 1968). The symbols • show the results using the trigonometric (triangulation) method, the points △ identify data using the geomagnetic method

14.6.2 Reconstruction Procedure

The reconstruction of the apparent height of production can be made by measuring the *muon core angle*, i.e., the angle between the shower axis and the muon track, and the distance of the muon track from the shower axis at ground impact. The slant height of the origin of the muon (which includes the slant height of the parent particle when neglecting scattering in the parent particle-muon decay) is given by

$$h_\mu = \frac{x_\mu \cos\varphi_\mu + y_\mu \sin\varphi_\mu}{\tan\theta_\mu} = \frac{r_\mu}{\tan\theta_\mu}\,, \tag{14.14}$$

where r_μ, x_μ, φ_μ and y_μ are the coordinates of the muon at detection in a cartesian frame of reference, with the shower axis taken as the z-axis, and θ_μ is the angle between the muon trajectory and the shower axis.

The more general expression in terms of a perpendicular cartesian coordinate system in which the shower axis, impacting at X_0, Y_0 with zenith angle θ_0 and azimuthal angle φ_0 at time τ_0, can have any direction and the muon (plus parent) production height is assumed to be at the minimum distance between two straight lines, i.e., the shower axis and the muon trajectory, the slant height for $X_0 = 0$ and $Y_0 = 0$ is given by the expression (Danilova et al., 1994),

$$h_\mu^{\text{track}} = \frac{(a_0^2 + b_0^2 + 1)(a_\mu X_\mu + b_\mu Y_\mu) - (a_0 a_\mu + b_0 b_\mu + 1)(a_0 X_\mu + b_0 Y_\mu)}{(a_0 a_\mu + b_0 b_\mu + 1)^2 - (a_\mu^2 + b_\mu^2 + 1)(a_0^2 + b_0^2 + 1)}\,. \tag{14.15}$$

Here, $a_0 = \tan\theta_0 \cos\varphi_0$, $b_0 = \tan\theta_0 \sin\varphi_0$, $a_\mu = \tan\theta_\mu \cos\varphi_\mu$, and $b_\mu = \tan\theta_\mu \sin\varphi_\mu$. Because the definition of the closest approach of the muon trajectory and the shower axis as postulated above is not unique, Linsley (1992, Unpublished) has introduced a more refined definition that we will not elaborate on.

Since one deals here often with relatively small angles, usually $\leq 5^\circ$, this simple picture requires of course proper accounting of the geomagnetic deflection and of multiple Coulomb scattering of the muons to avoid large errors.

Ambrosio et al. (1997, 1999) carried out some measurements with a muon tracker having a threshold of 200–300 MeV (Aramo, 2008, private communication) on showers in the primary energy range $2.5 \cdot 10^{11} \leq E_0 \leq 10^{16}$ eV at Haverah Park. Figure 14.56 shows the core angle distribution, i.e., the distribution of the angle between the shower axis and the muon trajectory (Fig. 14.56a), and the azimuthal angular distribution (Fig. 14.56b) of the recorded muons. The average core angle is approximately 3°. The azimuthal asymmetry is mainly due to geomagnetic effects.

The reconstructed height of production of the recorded muons as a function of radial distance from the shower axis is displayed in Fig. 14.57. There two sets of experimental data are plotted, one which shows all reconstructed events, the other for selected muons where the geomagnetic effects are not effective. In the same figure is also shown the result from simulations for proton and iron initiated showers, incident under a zenith angle of 25°, using assumed spectral conditions, as stated in the figure caption.

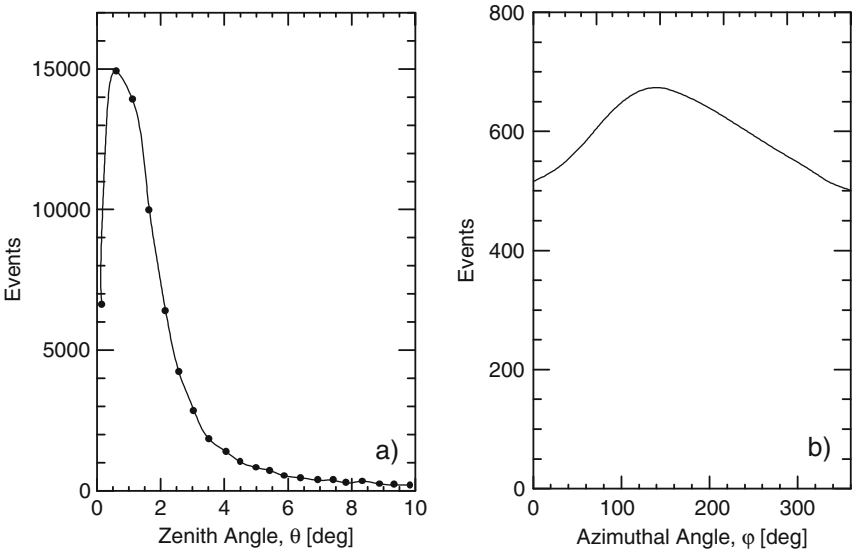

Fig. 14.56 Distribution of the zenith angle, θ_μ (**a**), and the azimuthal angle, φ_μ (**b**), of muons of energy greater than about 200–300 MeV (Aramo, 2008, private communication) in air showers of primary energy $2.5 \cdot 10^{11} \leq E_0 \leq 10^{16}$ eV recorded at Haverah Park (Ambrosio et al., 1999). The azimuthal non-uniformity is mainly due to geomagnetic effects

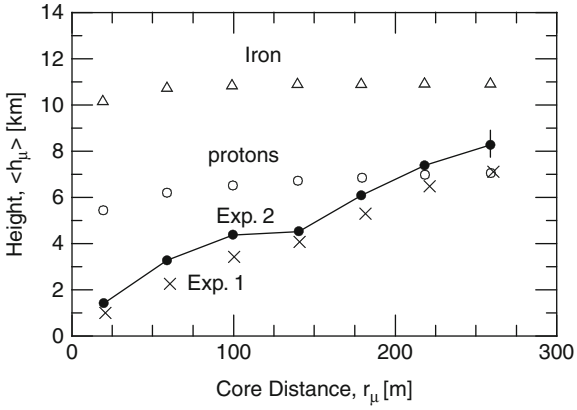

Fig. 14.57 Correlation between the average height of production, $\langle h_\mu \rangle$ and the distance from the shower axis, r_μ, of all reconstructed muons (Exp. 1, $\times$) and of selected muons (Exp. 2, $\bullet$) only. Also shown are simulation results of proton ($\circ$) and iron ($\triangle$) initiated showers incident at a zenith angle of $\theta = 25^\circ$ covering the primary energy spectral range $2.5 \cdot 10^{11} \leq E_0 \leq 4 \cdot 10^{15}$ eV. The assumed spectral slopes were -2.6 below and -3.05 above $2.5 \cdot 10^{15}$ eV (after Ambrosio et al., 1999)

The conclusion from this work when comparing the experimental and predicted data is that the arrival direction alone is *not sufficient* to reproduce the longitudinal shower development. Complementary information, such as timing is needed to get a more realistic picture.

The *timing* approach to estimate the height of production of the muons, which had been chosen by some authors, is based on the *arrival delay* of the muons with respect to the shower front (e.g., Rebel et al., 1995). The method is briefly outlined in Chap. 10. The basic assumption here is again that the muons are produced in the shower axis. Referring to Fig. 10.24, one can write for the generalized case of a non-vertical shower the following relation to get the production height of the muons,

$$h_\mu^{\text{time}} = \frac{[(X\mu - X_0)^2 + (Y_\mu - Y_0)^2 - (c\Delta\tau)^2]\cos\theta_0}{2(c\Delta\tau + \sin\theta_0[(X_\mu - X_0)\cos\varphi_0 + (Y_\mu - Y_0)\sin\varphi_0])}\,, \tag{14.16}$$

where $\Delta\tau = \tau_\mu - \tau_0$, τ_0 being the arrival time of the leading edge of the shower front at the shower axis (or the hypothetical spherical light front), usually taken as zero, and τ_μ is the arrival time of the muon under investigation.

The combination of the two methods, timing and core angle measurements, had been studied by Danilova et al. (1994) and led to the concept of *time-track complementarity* (TTC). We will not elaborate on it and refer the interested reader to the original paper.[2] However, we want to mention that the authors of the TTC method point out that the method works best in the interesting atmospheric depth range of $<250\,\mathrm{g\,cm^{-2}}$, where high energy hadron cascades begin to grow rapidly. The accuracy of the method when applied to muons of energy $\geq$5 GeV at core distances of 200–250 m is claimed to be about 35 $\mathrm{g\,cm^{-2}}$, which is about 10 $\mathrm{g\,cm^{-2}}$ less than for each of the other two methods separately.

A recent investigation using muon *triangulation* had been carried out by Doll et al. (2007) with the Karlsruhe muon tracking installation. This work was aimed at the study of high energy hadronic interactions and the determination of the primary mass composition. The authors use arguments borrowed from the energy dependent electron and muon depth of maximum development relation and the muon maximum yield elongation rate, and obtain a primary mass dependent expression for the height of origin, $h_\mu(A)$, of muons which is the difference between the measured height, h_μ and the energy dependent penetration depth of the primary cosmic ray. In Fig. 14.58 we show the height of origin distribution of muons in showers of truncated muon size $10^4 \leq N_\mu^{\text{tr}} \leq 1.8 \cdot 10^4$ and three zenith angle intervals as stated in the figure obtained from this work.

[2] Time-track Complementarity (TTC) is briefly discussed in Chap. 9.

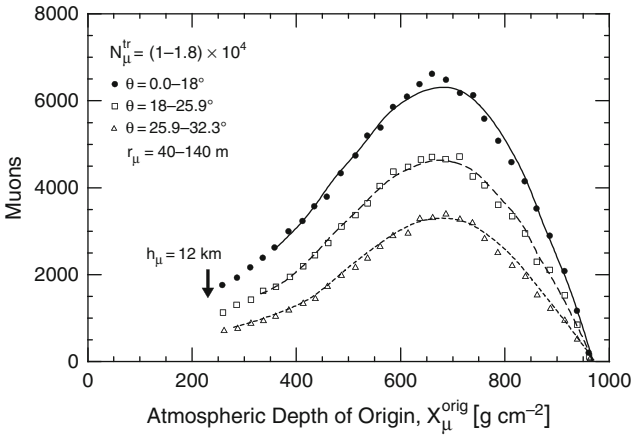

Fig. 14.58 Distribution of depth of origin, X_μ^{orig} [g cm^{-2}] of muons of energy $E_\mu \geq 0.8$ GeV in the atmosphere in showers having a truncated muon size of $4.0 \leq \lg(N_\mu^{\text{tr}}) \leq 4.25$, recorded with the muon tracker of the KASCADE experiment at Karlsruhe, Germany (110 m a.s.l.) (after Doll et al., 2007)

14.7 Multi-Muon Events and Muon Families

The terms multiple muons, multi-muon events and muon groups are frequently used to describe di-muon events, so-called muon tridents, or closely packed bundles of muons, usually of high energy that appear to originate from parents created in the same or from closely related high energy interactions. The term muon family is used in analogy to gamma and hadron families. Such events are more stringently defined (Danilova et al., 1989). Whereas for multi-muon events one usually knows the coordinates and only an experimental threshold energy of the particles, for muon families the actual energy of each family member is known.

Multi-muon events are used to explore the properties of very high energy hadronic interactions, of specific interaction details, or to study the longitudinal development of showers. This latter aspect is a link to the mass of the shower initiating primary.

An early analysis had been carried out by Khrenov et al. (1979) on muon pairs. These authors have measured the pair density at different radial distances from the shower axis as a function of muon energy to energies as high as 1,000 GeV in smaller showers ($N_e \simeq 2 \cdot 10^5$). This work was carried out using the solid iron magnet that was part of the Moscow air shower array. The data are presented in Fig. 14.59 together with predicted distributions from simulations using different interaction models, as stated in the caption, and a mixed primary composition.

We have briefly discussed primary mass and interaction signatures in the frame of kinematic properties of shower particles and the (primary) energy dependence of mass specific interaction properties in Chap. 10 (Grieder, 1977a, 1986; Forti et al., 1990). Danilova et al. (1989) have studied these aspects in more detail, focusing their interest on the energy dependence of high energy muon families and on the

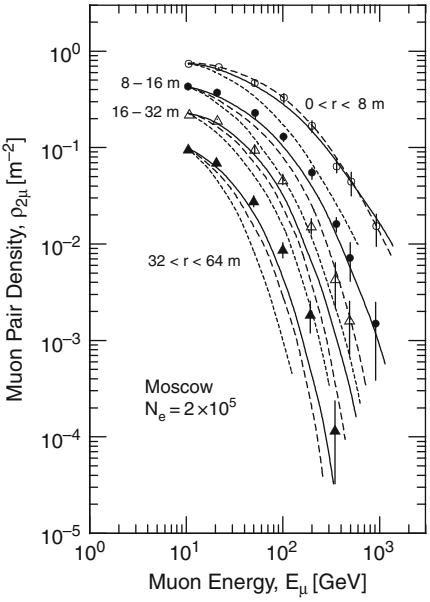

Fig. 14.59 Muon pair density, $\rho_{2\mu}$, as a function of muon energy for different core distance intervals in showers of size $2 \cdot 10^5$ (Khrenov et al., 1979). Shown are four sets of experimental data, ○, ●, △ and ▲, and four sets of predicted distributions using different models and primary compositions. The *solid* and *dotted curves* are simulation results using a mixed primary composition. The former applies to a half-law secondary particle multiplicity model, the latter to a scaling model with a logarithmic multiplicity dependence. The *dashed curves* were obtained using a scaling model and pure iron primaries

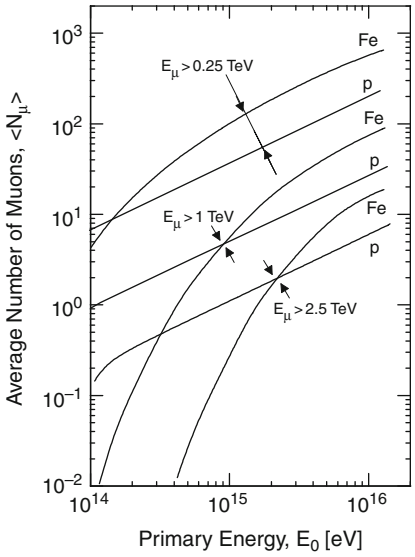

Fig. 14.60 Energy dependence of the mean multiplicity of muon families having different muon threshold energies as indicated, in simulated primary proton and iron initiated showers (after Danilova et al., 1989)

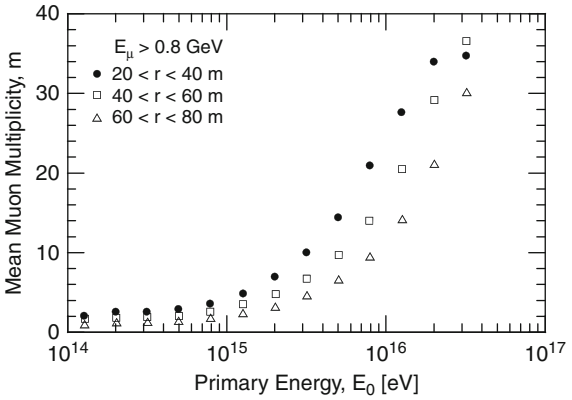

Fig. 14.61 Primary energy dependence of the mean muon multiplicity, m, of muons of energy $\geq$0.8 GeV, recorded with the muon tracking detector of the KASCADE experiment at different radial intervals from the shower axis, as listed in the figure (after Doll et al., 2002)

muon multiplicity as a function of collision energy. The results of their theoretical studies are shown in Fig. 14.60. It is obvious that the possibilities to exploit these signatures experimentally are very marginal.

Of similar interest is the low energy muon number and the *muon multiplicity*, m, at specific core locations in well defined showers, since this observable also manifests some primary mass sensitivity. To acquire reliable data large muon tracking detectors are best suited. The analysis and interpretation are rather subtle and require major computational efforts. The method is discussed in Chap. 10 and results are presented in Chap. 11.

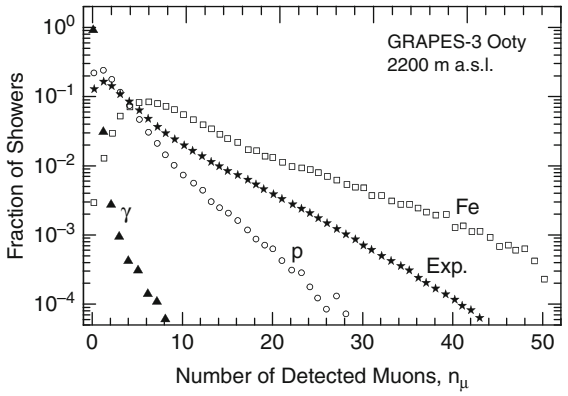

Fig. 14.62 Muon multiplicity distribution observed by the GRAPES-3 detector array at Ootacamund (2,200 m a.s.l.) in India (⋆) and expected muon multiplicities obtained from simulations for gamma ray (▲), proton (○) and iron nuclei (□) initiated showers and zenith angles $\theta \leq 25^\circ$. The plot applies to particular shower selection criteria, using reasonable cuts on the number of detected shower particles. In addition the same power law of the differential primary spectrum ($E^{-2.7}$) was assumed for all primary components (after Hayashi et al., 2005)

The multiplicity of low energy muons had been studied by the GRAPES (Tanaka et al., 2007a, b) and the KASCADE groups (Doll et al., 2002) with their large muon tracking facilities having threshold energies of 1.0 and 0.8 GeV, respectively.

The primary energy dependence of the multiplicity of muons of energy ≥ 0.8 GeV in showers of different primary energy as measured by KASCADE is displayed in Fig. 14.61. The results from a similar analysis carried out with data from measurements with the GRAPES-3 detector is shown in Fig. 14.62. This plot shows the fraction of showers from a large sample as a function of the muon multiplicity recorded by the detector. Upper and lower cuts of the shower size had been used to have a clean sample. Also shown in this figure are expected muon multiplicities from simulations obtained for showers initiated by primary gamma rays, protons and iron nuclei only, using the same power law spectrum of the form $E^{-2.7}$ for all components (Hayashi et al., 2005).

14.8 Muon Fluctuations

Fluctuations are a typical phenomenon of all air shower observables and represent a major problem. On the other hand fluctuations also yield information on specific processes and may help to identify the magnitude of some hidden parameters. As an example we should mention the primary mass. The largest fluctuations in the shower process are caused by the location and properties of the first interaction. The former is strongly dependent on the primary mass, i.e., on the inelastic cross section of the collision partners, and on the secondary particle multiplicity of the interaction.

Since muons are the decay products of pions which account for the bulk of the secondaries emerging from hadronic interactions, muons stand essentially in a one-to-one relationship with the pions and thus with the fluctuations occurring in the parent interactions. Moreover, since muons are much less abundant than electrons in showers and are spread much more apart, their detection is automatically subject to large (Poissonian) fluctuations. Such a situation does not exist when recording optical photons from the air Cherenkov light flash of showers, since the Cherenkov photon density is six to seven orders of magnitude higher than that of muons.

Many workers have studied and analyzed fluctuations of shower observables, mainly with the aim to extract information on the primary mass (Linsley, 1967; Hillas et al., 1971b; Dzikowski et al., 1977; Blake et al., 1979b; Ulrich et al., 2007). In this context muons play an important role. Fluctuations are also discussed in Chap. 6 and 7 in the context of the longitudinal development, equal intensity distributions, the height of maximum development and the elongation rate of showers, and in Sect. 11.7.

An interesting study had been carried out by Hara et al. (1983b) at Akeno. These authors have measured the muon size-frequency distribution of large showers for constant electron size in order to analyze the fluctuations of the muon size. The study was made for two different fixed electron shower sizes and the result is plotted in Fig. 14.63. An attempt had been made to interpreted the result in terms of the energy dependence of the primary mass composition. Correlation studies based on

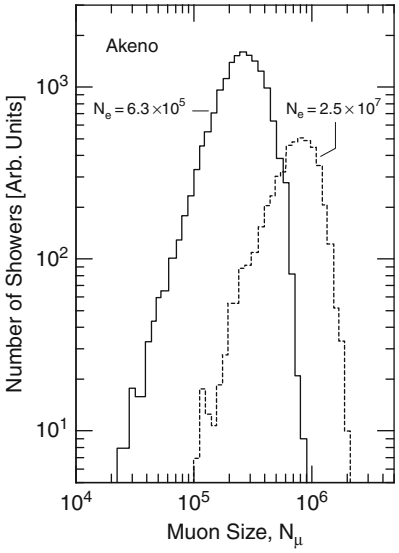

Fig. 14.63 Frequency histogram of the muon size distribution in showers of fixed electron size, illustrating the large fluctuations of the muon size of the showers and shower development. The histogram applies to showers of size $N_e = 6.3 \cdot 10^5$ and $N_e = 2.5 \cdot 10^7$ (after Hara et al., 1983b)

these data with other shower observables are discussed in Chap. 19. Similar work had been carried out very recently by Doll et al. (2007) for showers of truncated muon size $10^4 \leq N_\mu^{\text{tr}} \leq 1.8 \cdot 10^4$ and different zenith angle intervals.

14.9 Genetics of Muons

To gain better insight into the cascade process that takes place in an air shower and to learn more about the information carried by the muons of the longitudinal development process, Grieder (1977a, b) expanded his ASICO air shower simulation program system and introduced what he called *genetic parameters* (for details see Chap. 20). This required the introduction of four additional parameters to the already existing eight parameters that specify all relevant particle parameters in space and time.

These new parameters comprised (a) the generation of interaction from which the particle originated, (b) the height where this particular interaction took place in the atmosphere, (c) the generation of last scattering or, in case of a pion-muon decay, signaled the decay, and (d) the height where the last scattering or pion muon decay occurred.[3]

[3] This feature which applies to all particles in ASICO is also included in CORSIKA.

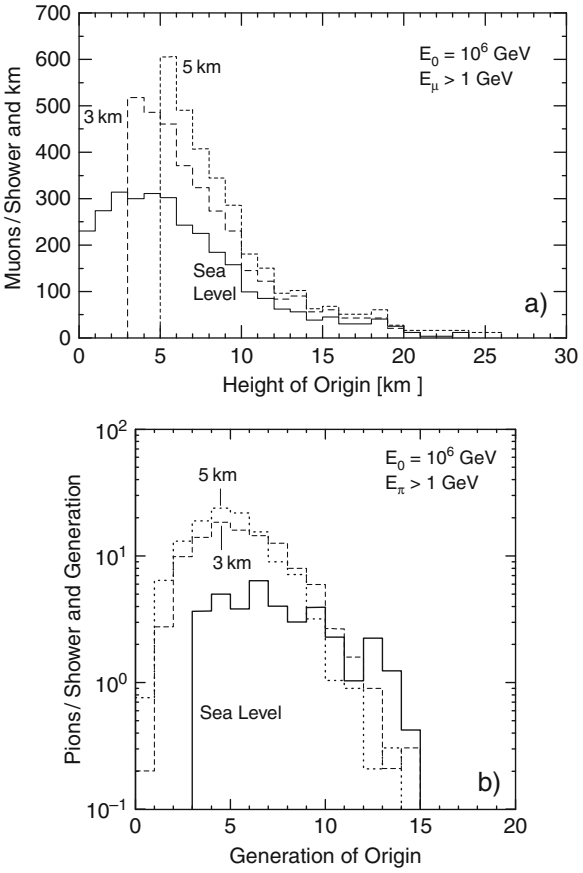

Fig. 14.64 (**a**) Shows the height of origin distribution of muons of energy ≥ 1 GeV arriving at three different observation levels, as indicated, in vertical 10^{15} eV proton initiated showers simulated with the ASICO program, using the so-called SMFB hadronic interaction model. (**b**) Shows the distribution of the generation of interaction from where the parent pions of the muons shown in (**a**) originate (after Grieder, 1977a, b)

In conjunction with a special program that allows to construct target diagrams of the ground impacts of any specifically selected muon group (or any other particle), the full *genetic* information, i.e., the history of the chosen muon (or particle) group is available. Figures 14.64, 14.65, 14.66 and 14.67 show some examples of this powerful tool for the analysis of simulated events that allows to perform a very detailed exploration on individual showers or of shower groups on average at any altitude.

In Fig. 14.64a the distribution of the height of origin of muons (pion decay) of energy ≥ 1 GeV in 10^6 GeV proton initiated vertical showers is plotted for three different observation levels, as indicated in the figure, and in Fig. 14.64b the corresponding generation of interaction from which the parent pions of the muons under consideration originate. Figure 14.65 illustrates in frames (a) and (b) the height and

generation of origin, respectively, of muons of the same group of showers at sea level but for different muon threshold energies, and in frames (c) and (d) for the selected group arriving in the radial interval from the shower axis between 400 and 600 m.

In Fig. 14.66a we show the distribution of the height of creation of three energy groups of parent pions of genetic origin as specified in the particle pixels in the figure, whose distribution of the height of decay to muons is displayed in Fig. 14.66b, together with the same complementary energy and genetic information of the muons. The previously mentioned target diagram of high energy muons of a particular shower as specified in the figure, with listed height of first interaction, is plotted in Fig. 14.67. The points of ground impact are labeled with the relevant genetic parameters and the muon energy.

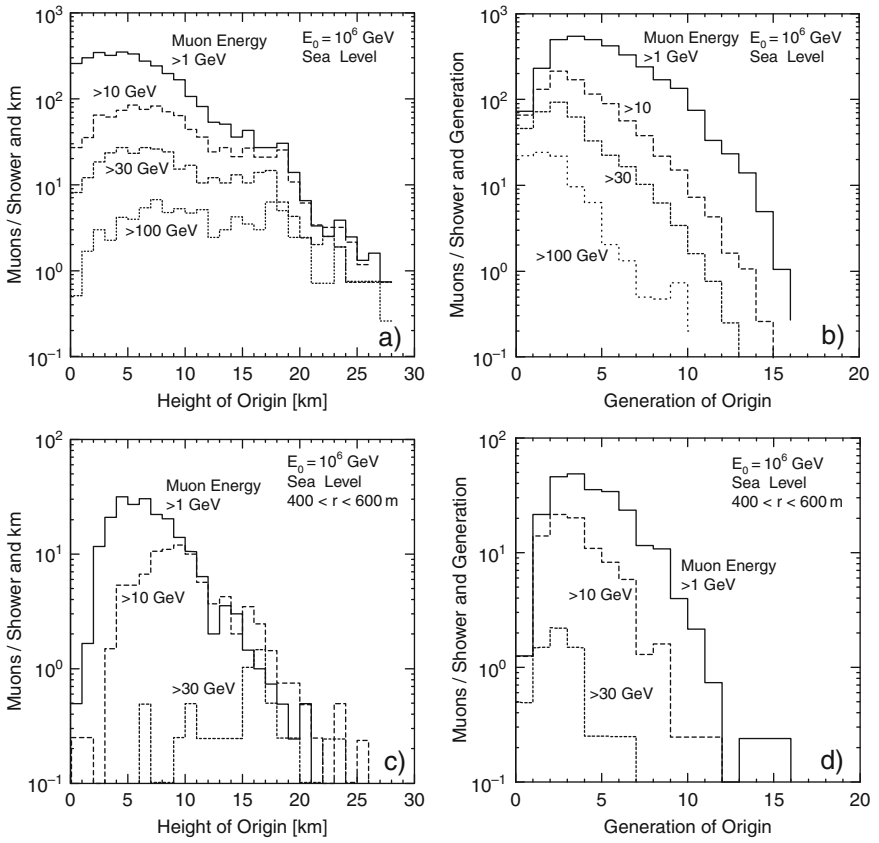

Fig. 14.65 (**a**) Distribution of the height of origin of muons (height of decay of parent pions) arriving at sea level, resulting from the same simulation as had been used for Fig. 14.64, grouped according to energy; (**b**) distribution of the generation of origin of the parent pions of the same groups of muons; (**c**), and (**d**) are analogous plots, restricted to include only muons falling in the annular ring measuring $400 \leq r \leq 600$ m from the shower axis (after Grieder, 1977a, b)

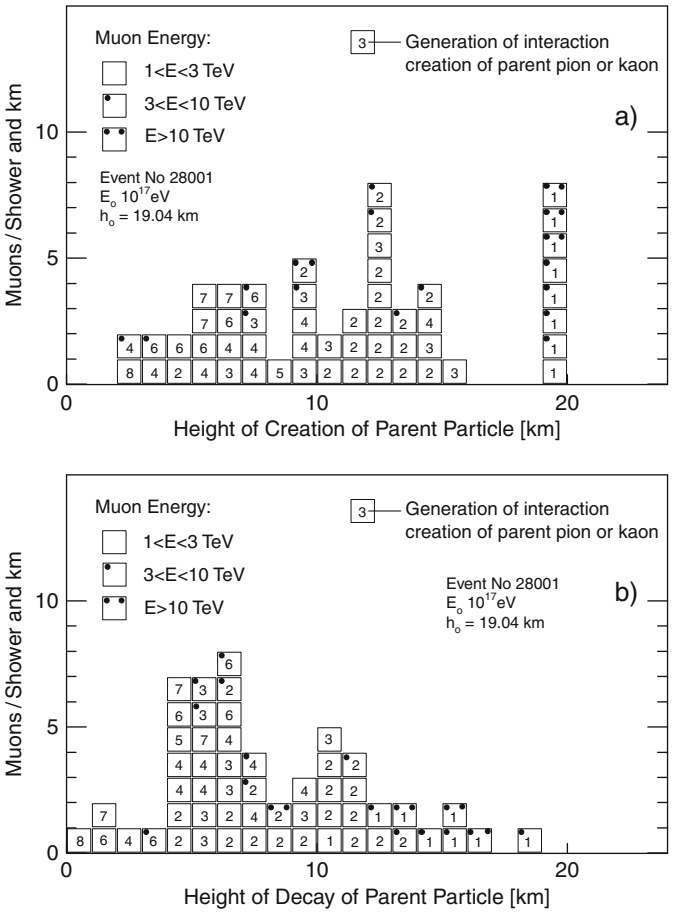

Fig. 14.66 Histogram of the very high energy muonic component ($E_\mu \geq 1\,\text{TeV}$) in a vertical 10^{17} eV proton initiated shower at sea level, showing the so-called *genetic parameters* which the ASICO program supplies. These include the height of creation of the parent pions and the generation of interaction in which they had been produced (**a**), identified by the number in each box representing a muon. The energy group to which each muon belongs is also indicated. (**b**) Shows the height of decay of the parent pions of the same muon population as in (**a**). The height of the first interaction is $h_1 = 19.04\,\text{km}$ (Grieder, 1986)

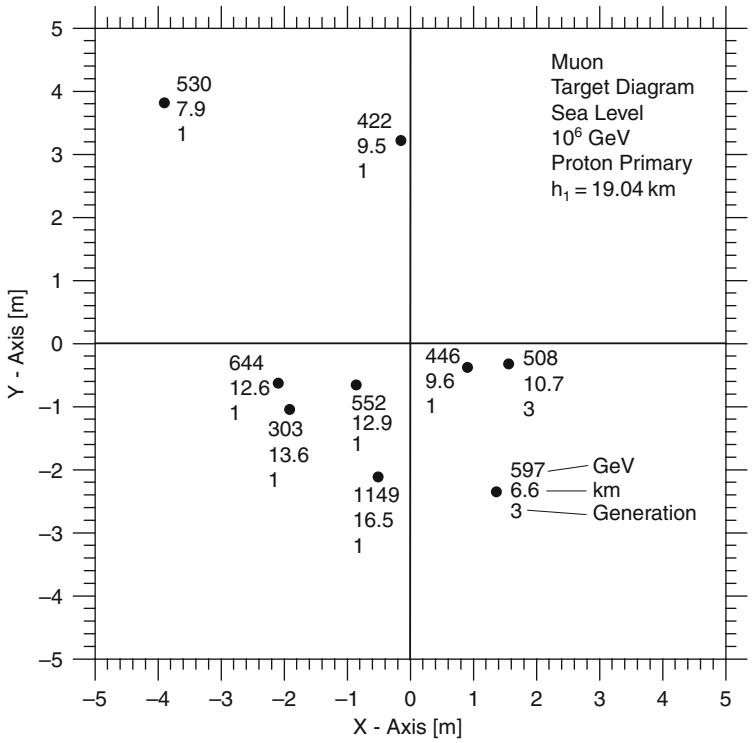

Fig. 14.67 Example of a target diagram of high energy muons at sea level of a 10^6 GeV primary proton initiated shower with the height of the first interaction at $h_1 = 19.04$ km (Grieder, 1977a). The parameters listed are the muon energy at ground level [GeV], the height of decay of the parent pion [km] above sea level, and the generation of interaction from which the parent pion originates

References

Abdrashitov, S.F., et al.: PICRC, 6, p. 156 (1981).
Abrosimov, A.T. et al.: Zh. Eksp. Teor. Fiz., 28, p. 1782 (1958).
Abrosimov, A.T., et al.: J. Exp. Theor. Phys., U.S.S.R., 38, p. 100 (1960) (in Russian); Sov. Phys. JETP, 11, 1, p. 74 (1960).
Acharya, B.S., et al.: PICRC, 8, p. 36 (1977).
Acharya, B.S., et al.: PICRC, 8, p. 304 (1979).
Acharya, B.S., et al.: PICRC, 11, p. 385 (1981).
Aglietta, M., et al.: Nuovo Cimento, B 112B, p. 139 (1997).
Aglietta, M., et al.: Astropart. Phys., 9, p. 185 (1998).
Aglietta, M., et al.: Astropart. Phys., 21, p. 223 (2004).
Aguirre, C., et al.: PICRC, 4, p. 2598 (1973) (Abstract).
Aguirre, C., et al.: PICRC, 8, p. 213 (1977).
Aguirre, C., et al.: J. Phys. G, 5, p. 151 (1979).
Alexeyev, E.N., et al.: PICRC, 10, p. 276 (1979).

Alexeyev, E.N., et al.: PICRC, 2, p. 474 (1993).
Allan, H.R., et al.: Can. J. Phys., 46, p. S98 (1968).
Ambrosio, M., et al.: J. Phys. G., 23, p. 219 (1997).
Ambrosio, M., et al.: Nucl. Phys. B (Proc. Suppl.), 75A, p. 312 (1999).
Ambrosio, M., et al.: Nucl. Instr. Meth. A, 486, p. 663 (2002).
Andronikashvili, E.L., and R.E. Kazarov: J. Exp. Theor. Phys. (U.S.S.R.), 38, p. 703 (1960) (in Russian); Sov. Phys. JETP, 11, 3, p. 507 (1960).
Antoni, T., et al.: Astropart. Phys., 14, p. 245 (2001).
Antoni, T., et al.: Astropart. Phys., 18, p. 319 (2003a).
Antoni, T., et al.: Nucl. Instr. Meth. A, 513, p. 490 (2003b).
Apshev, S.Zh., et al.: PICRC, 8, p. 62 (1977).
Armitage, M.L., et al.: PICRC, 4, p. 2539 (1973).
Armitage, M.L., et al.: J. Phys. A, 7, p. 2041 (1974).
Armitage, R., et al.: PICRC, 8, p. 72 (1979).
Aseikin, V.S., et al.: PICRC, 6, p. 2132 (1971).
Aseikin, V.S., et al.: PICRC, 8, p. 98 (1977).
Ashton, F., et al.: PICRC, 13, p. 243 (1979).
Atanelishvili, M.I., et al.: PICRC, 7, p. 66 (1977).
Ayre, C.A., et al.: Nucl. Instr. Meth., 102, p. 19 (1972a).
Ayre, C.A., et al.: Nucl. Instr. Meth., 102, p. 29 (1972b).
Bagge, E., et al.: PICRC, 2, p. 738 (1965).
Barnaveli, T.T., et al.: PICRC, 4, p. 273 (1963).
Barnaveli, T.T., et al.: Izv. Akad. Nauk SSSR, Ser. Fiz. 28, p. 1894 (1964).
Barrett, P.H., et al.: Rev. Mod. Phys., 24, p. 133 (1952).
Barrett, M.L., et al.: PICRC, 8, p. 2753 (1975a).
Barrett, M.L., et al.: PICRC, 8, p. 2758 (1975b).
Baxter, A.J.: Ph.D. Thesis, University of Leeds, England, UK (1967).
Bell, C.J., et al.: PICRC, 4, p. 2569 (1973).
Bell, C.J., et al.: J. Phys. A, 7, p. 990 (1974).
Bennett, S., and K. Greisen: Phys. Rev., 124, p. 1982 (1961).
Bennett, S., et al.: J. Phys. Soc. Jpn., 17, Suppl. A III, p. 196 (1962).
Bhadra, A., et al.: Nucl. Instr. Meth. A, 414, p. 233 (1998).
Blake, P.R., and D.M. Harris: Acta Phys. Acad. Sci. Hung., 29, S3, p. 633 (1970).
Blake, P.R.: PICRC, 8, p. 189 (1977).
Blake, P.R., et al.: PICRC, 8, p. 67 (1979a).
Blake, P.R., et al.: PICRC, 8, p. 82 (1979b).
Blake, P.R., et al.: PICRC, 6, p. 20 (1981).
Böhm, E., et al.: PICRC, 8, p. 25 (1977).
Bonczak, B., et al.: Can. J. Phys., 46, p. 102 (1968).
Bonczak, B., et al.: J. Phys. A, 2, p. 334 (1969).
Brancus, I.M., et al.: Astropart. Phys., 7, p. 343 (1997).
Brooke, G., et al.: Proc. Phys. Soc., 80, p. 674 (1962).
Brooke, G., and A.W. Wolfendale: Proc. Phys. Soc., 83, p. 843 (1964).
Brownlee, R.G., et al.: Acta Phys. Acad. Sci. Hung., 29, S3, p. 651 (1970a).
Brownlee, R.G., et al.: Acta Phys. Acad. Sci. Hung., 29, S3, p. 645 (1970b).
Bürger, J., et al.: PICRC, 8, p. 2784 (1975).
Büttner, C., et al.: Nucl. Phys. B (Proc. Suppl.), 122, p. 289 (2003).
Chatterjee, B.K., et al.: Can. J. Phys., 46, p. S13 (1968).
Chiba, N., et al.: Nucl. Instr. Meth. A, 311, p. 338 (1992).
Clark, G., et al.: Nuovo Cimento, Suppl. 8, p. 623 (1958).
Danilova, T.V., et al.: J. Phys. G., 15, p. 509 (1989).
Danilova, T.V., et al.: J. Phys. G., 20, p. 961 (1994).
De Beer, J.F.: Ph.D. Thesis, University of Potchefstroom, South Africa (1960).

De Beer, J.F., et al.: Proc. Phys. Soc., 89, p. 567 (1966).
Diminstein, O.S., et al.: PICRC, 12, p. 4325 (1975a).
Diminstein, O.S., et al.: PICRC, 12, p. 4318 (1975b).
Diminstein, O.S., et al.: PICRC, 8, p. 122 (1979).
Dixon, H.E., et al.: PICRC, 4, p. 2556 (1973a).
Dixon, H.E., et al.: PICRC, 4, p. 2473 (1973b).
Doi, T., et al.: PICRC, 2, p. 764 (1995).
Doll, P., et al.: Nulc. Instr. Meth. A, 488, p. 517 (2002).
Doll, P., et al.: PICRC, pre-conference edition, paper 0514, Merida, Mexico (2007).
Dzikowski, T., et al.: PICRC, 8, p. 2795 (1975).
Dzikowski, T., et al.: J. Phys. G, 3, p. 1591 (1977).
Dzikowski, T., et al.: PICRC, 8, p. 276 (1979).
Earl, J.: M.I.T. Tech. Rep., No 70 (1959).
Earnshaw, J.C., et al.: Proc. Phys. Soc., 90, p. 91 (1967).
Earnshaw, J.C., et al.: Can. J. Phys., 46, p. S122 (1968).
Earnshaw, J.C., et al.: PICRC, 3, p. 1086 (1971a).
Earnshaw, J.C., et al.: PICRC, 3, p. 1081 (1971b).
Earnshaw, J.C., et al.: Department of Physics Report, University of Durham, Durham, UK (1973a).
Earnshaw, J.C., et al.: J. Phys. A, 6, p. 1244 (1973b).
Fisher, A.J.: PhD Thesis, University of Sydney, Australia (1970).
Forti, C., et al.: Phys. Rev., D 42, p. 3668 (1990).
Fukui, S., et al.: Prog. Theor. Phys. Jpn., 16, p. 1 (1960).
Gibson, A.I., et al.: PICRC, 8, p. 101 (1979).
Gibson, A.I., et al.: PICRC, 6, p. 16 (1981).
Glasstetter, R., et al.: PICRC, 1, p. 222 (1999).
Glushkov, A.V., et al.: Astropart. Phys., 4, p. 15 (1995).
Greisen, K.: Progress in Cosmic Ray Physics, North-Holland Publishing Co., Amsterdam, Vol. 3, p. 1 (1956).
Greisen, K.: Annual Review of Nuclear Science, Annual Reviews, Inc., Palo Alto, CA, USA, Vol 10, p. 63 (1960).
Grieder, P.K.F.: Acta Phys. Acad. Sci. Hung., 29, S3, p. 563 (1970a).
Grieder, P.K.F.: Acta Phys. Acad. Sci. Hung., 29, S3, p. 569 (1970b).
Grieder, P.K.F.: PICRC, 8, p. 2889 (1975).
Grieder, P.K.F.: Rivista del Nuovo Cimento, 7, p. 1 (1977a).
Grieder, P.K.F.: PICRC, 8, p. 326 (1977b).
Grieder, P.K.F.: Proceedings of the Japan-U.S. Seminar on Cosmic Ray Muon and Neutrino Physics/Astrophysics using Deep Underground/Underwater Detectors, Tokyo, Japan June 1986, p. 183 (1986).
Grishina, N.V., et al.: PICRC, 6, p. 3 (1981).
Grochalska, B., et al.: Paper presented at the European Cosmic Ray Symposium, Paris (1972) (unpublished).
Gupta, S., et al.: Nucl. Instr. Meth. A, 540, p. 311 (2005).
Haeusler, R., et al.: Astropart. Phys., 17, p. 421 (2002).
Hara, T., et al.: PICRC, 8, p. 135 (1979).
Hara, T., et al.: PICRC, 11, p. 227 (1981).
Hara, T., et al.: PICRC, 11, p. 281 (1983a).
Hara, T., et al.: PICRC, 11, p. 285 (1983b).
Hara, T., et al.: PICRC, 11, p. 276 (1983c).
Hasegawa, H., et al.: J. Phys. Soc. Jpn., 17, Suppl. A-III, p. 189 (1962).
Hawkes, R.C., et al.: PICRC, 8, p. 514 (1977).
Hayashi, Y., et al.: PICRC, 1, p. 276 (1999).
Hayashi, Y., et al.: Nucl. Instr. Meth. A, 545, p. 643 (2005).
Hayashida, N., et al.: PICRC, 8, p. 143 (1979).

Hayashida, N., et al.: J. Phys. G, 21, p. 1101 (1995).
Heck, D., et al.: Report FZKA 6097, Forschungszentrum Karlsruhe (1998).
Hillas, A.M., et al.: PICRC, 3, p. 1007 (1971a).
Hillas, A.M., et al.: PICRC, 3, p. 1001 (1971b).
Hook, J.R., et al.: Acta Phys. Acad. Sci. Hung., 29, S3, p. 474 (1970).
Ilyina, N.P., et al.: PICRC, 6, p. 2109 (1971).
Kabanova, N.V., et al.: PICRC, 4, p. 2534 (1973).
Kakimoto, F., et al.: PICRC, 6, p. 27 (1981).
Kakimoto, F., et al.: J. Phys. G, 12, p. 151 (1986).
Kalmykov, N.N., et al.: Nucl. Phys., B (Proc. Suppl.), 52, p. 17 (1997).
Kaneko, T., et al.: PICRC, 12, p. 4343 (1975).
Khrenov, B.A.: Zh. Eksp. Teor. Fiz., 41, p. 1402 (1961).
Khrenov, B.A., et al.: PICRC, 8, p. 351 (1979).
Khristiansen, G.B., et al.: PICRC, 6, p. 2097 (1971).
Khristiansen, G.B., et al.: PICRC, 8, p. 2801 (1975).
Khristiansen, G.B., et al.: PICRC, 8, p. 148 (1977).
Klages, H.O., et al.: Nucl. Phys. B (Proc. Suppl.), 52, p. 92 (1997).
Lagutin, A.A., and R.I. Raikin: Nucl. Phys. B (Proc. Suppl.), 97, p. 274 (2001).
Lapikens, J.L.: J. Phys. A, 8, p. 838 (1975).
Lehane, J.A., et al.: Nature, 182, p. 1699 (1958).
Linsley, J., and L. Scarsi: Phys. Rev., 128, p. 2384 (1962).
Linsley, J.: PICRC, 4, p. 77 (1963).
Linsley, J.: Rev. Sci. Instr., 38, p. 1268 (1967).
Linsley, J.: IFCAI Palermo technical report (1992) (unpublished).
Machin, A.C., et al.: Acta Phys. Acad. Sci. Hung., 29, S3, p. 579 (1970).
Matthews, J.: Astropart. Phys., 22, p. 387 (2005).
Mitsui, K., et al.: PICRC, 6, p. 204 (1987).
Miyake, S., et al.: Can. J. Phys., 46, p. 107 (1968).
Miyake, S., et al.: PICRC, 12, p. 36 (1977).
Murthy, G.T., et al.: Can. J. Phys., 46, p. S153 (1968).
Murzin, V.S., and L.I. Sarycheva: Cosmic Rays and Their Interaction, Atomizd, Moscow, (in Russian) (1968).
Nagano, M., et al.: J. Phys. G, 10, p. 1295 (1984).
Nagano, M., et al.: Astropart. Phys., 13, p. 277 (2000).
Navarra, G., et al.: Nucl. Instr. Meth. A, 518, p. 207 (2004).
Olejniczak, J.: Ph. D. Thesis, University of Lodz, Poland (1975).
Orford, K.J., et al.: Can. J. Phys., 46, p. 119 (1968).
Pentchev, L., and P. Doll: J. Phys., G, 27, p. 1459 (2001).
Porter, N.A., et al.: Phil. Mag., 2, p. 900 (1957).
Rada, W.S., et al.: Nuovo Cimento, 54 A, p. 208 (1979).
Rebel, H., et al.: J. Phys. G, 21, p. 451 (1995).
Rebel, H., et al.: Forschungszentrum Karlsruhe, Germany, Report FZKA 7294 (2007a).
Rebel, H., et al.: PICRC, pre-conference edition, paper 0861, Merida, Mexico (2007b).
Rochester, G.D., et al.: PICRC, 2, p. 765 (1965).
Rozhdestvensky, S.M., et al.: PICRC, 8, p. 2790 (1975).
Sakuyama, H., et al.: J. Phys. Soc. Jpn., 32, p. 3 (1972).
Sarkar, S.K., et al.: PICRC, 4, p. 339 (1993).
Sivaprasad, K.: Ph.D. Thesis, Bombay University, Bombay, India unpublished (1970).
Sreekantan, B.V.: PICRC, 7, p. 2706 (1971).
Stamenov, J.N., et al.: PICRC, 8, p. 102 (1977).
Stamenov, J.N., et al.: Trudy Fian SSSR, 109, p. 132 (1979).
Staubert, R., et al.: Acta Phys. Acad. Sci. Hung., 29, S3, p. 661 (1970).
Suga, K., et al.: PICRC, 13, p. 142 (1979).

Suri, A.: Ph.D. Thesis, University of Leeds, England, UK (1966).
Tamura, T., et al.: PICRC, 6, p. 24 (1981).
Tanaka, H., et al.: PICRC, 6, p. 209 (2005).
Tanaka, H., et al.: PICRC, pre-conference edition, paper 1233, Merida, Mexico (2007a).
Tanaka, H., et al.: PICRC, pre-conference edition, paper 1235, Merida, Mexico (2007b).
Ulrich, R., et al.: PICRC, pre-conference edition, paper 1027, Merida, Mexico (2007).
van Buren, J., et al.: PICRC, 6, p. 301 (2005).
Vernov, S.N., et al.: Izv. Akad. Nauk SSSR Ser. Fiz. 28, p. 1886 (1964a).
Vernov, S.N., et al.: Izw. Akad. Nauk SSSR Ser. Fiz., 28, p. 1774 (1964b).
Vernov, S.N., et al.: Izv. AN SSSR Ser. Fiz., 29, p. 1876 (1965), transl.; Bull. Acad. Sci. USSR Phys. Ser., p. 1708 (1965a).
Vernov, S.N., et al.: PICRC, 2, p. 769 (1965b).
Vernov, S.N., et al.: PICRC, 2, p. 624 (1965c).
Vernov, S.N., et al.: Can. J. Phys., 46, p. S197 (1968a).
Vernov, S.N., et al.: Can. J. Phys., 46, p. 110 (1968b).
Vernov, S.N., et al.: PICRC, 8, p. 320 (1977).
Vernov, S.N., et al.: PICRC, 8, p. 129 (1979).
Watson, A.A. and J.G. Wilson: J. Phys. A, 7, p. 1199 (1974).
Xue, B.K., and B.-Q. Ma: Astropart. Phys., 27, p. 286 (2007)
Zabierowski, J., et al.: PICRC, 2, p. 810 (2001).
Zabierowski, J., et al.: Nucl. Phys. B (Proc. Suppl.), 122, p. 275 (2003).
Zabierowski, J., et al.: PICRC, 6, p. 357 (2005).
Zabierowski, J., et al.: PICRC, 6, p. 357 (2007).

Chapter 15
Electrons and Photons

Overview In this chapter we focus our attention first on the purely electromagnetic (EM) component (electrons, i.e., negatrons and positrons, and photons). We discuss the lateral density distribution of the EM component as derived in Chap. 4, including the classical NKG lateral distribution functions and a variety of other theoretical and empirically modified functions that are also applicable to the bulk of shower particles. We subsequently expand the scope to include all charged shower particles, most of which consist of electrons with some percentage of muon contamination and converted photons, as they are recorded by thin charged particle shower detectors. A variety of experimental data of the different EM components are discussed and presented that include energy spectra, energy flow, mean energy, the photon–electron ratio, and the charge ratio of the electronic component as well as some temporal characteristics.

15.1 Introduction

The electromagnetic (EM) component, i.e., electrons (negatrons and positrons) and photons, constitute the bulk of all the particles in an extensive air shower over a major portion of its development through the atmosphere and has given the phenomenon its name. Giant showers initiated by ultrahigh energy primaries reach their maximum development near sea level and can spread laterally over tens of square kilometers, whereas very low energy showers may die out before reaching ground level, except for part of their muon component and the neutrinos. The density of the shower particles and photons drops rapidly with increasing radial distance from the core region outward and likewise the average energy of the particles. Both of these characteristics manifest some primary mass dependence, as outlined in Chap. 10. Similarly, the particle composition of a shower, i.e., the ratio of photons to electrons to muons to hadrons, also changes with radial distance from the shower axis and depends weakly on primary mass. These topics are discussed globally in Chap. 8. Specific distributions are presented in the chapters that are dedicated exclusively to individual components.

The overwhelming part of the EM component originates from photons resulting from neutral pion decay, but also from the decay of a variety of other particles and

P.K.F. Grieder, *Extensive Air Showers,* DOI 10.1007/978-3-540-76941-5_15,

decay channels. Neutral pions are produced copiously in high energy hadronic interactions within the hadron cascade as it propagates through the atmosphere, together with charged pions that outnumber the former on average by about a factor of two. A much smaller contribution to the EM component comes from electrons (negatrons and positrons) that result from the decay of muons, but also from the decay of kaons and other particles.

Photons and electrons initiate EM cascades as discussed in Chap. 4. These are produced throughout a shower, are spatially partly overlapping and account for the bulk of all the particles in a shower. The EM cascades are interlaced with the parent hadron cascade and the accompanying muon shower. The most energetic EM sub-cascades[1] are those that are associated with the first interaction. EM parent particles emerging from the second and higher order generations of interactions are less and less energetic and produce EM sub-cascades of smaller and smaller sizes.

In the lower half of the atmosphere the photon number is significantly larger than the number of electrons. The ratio of photons to electrons depends critically on the low energy cutoff considered. At altitudes where showers are near their maximum development, there exists an approximately linear relationship between the primary energy and the shower size.

The pure electromagnetic component in air showers is rather difficult to investigate because there is always contamination from other components such as muons and, in the near core region, from energetic hadrons. At some distance from the core where the hadronic component becomes insignificant one can remove the ever present muon component by subtraction. This implies having shielded detectors below the electron detectors to record the muons and to subtract the muon count from the total particle count in each EM detector to get the electron count. Only few experiments are equipped to separate the two components reliably (Nagano et al., 2000; Antoni et al., 2003). EM punch-through events must be accounted for in the muon detectors in stacked detector arrangements for accurate measurements.

Some minor degree of hadron contamination is almost unavoidable and can usually be accounted for in the data analysis. Beyond the shower core, out to radial distances of a few hundred meters, the muon density amounts to about 5–10% of the total particle density. It is increasing with increasing radial distance from the axis. The muon contamination is often disregarded in more rudimentary shower size measurements, particularly when thin scintillators are being used for this purpose instead of deep water Cherenkov detectors. The latter respond preferentially to muons (for details see Chaps. 8 and 10).

Frequently when discussing the shower size many authors refer to the electron size, N_e, but are in fact dealing with the charged particle size, N_{ch} (or N). For many aspects the distinction is irrelevant, particularly when the data were obtained with scintillators. However, when discussing exclusively the *electromagnetic component* or for precision experiments one must distinguish between bulk and refined

[1] We call EM cascades initiated by individual photons or electrons in an air shower that contribute to the total shower *sub-cascades* or *sub-showers*.

measurements. The distinction is also very important when studying the detector response to shower particles and transition effects. These topics are carefully illuminated in Sect. 2.11.2 and in Chaps. 8 and 10.

Because of the difficulties outlined above and the relative insignificance of specific data on the pure EM component in showers, comparatively few dedicated investigations were carried out over the last decades, and rarely to study the EM component in the shower core. Most of the work that had been focused on the very energetic EM component was carried out with emulsion experiments at high altitude, using so-called unaccompanied events that were not knowingly associated with air showers.

During the early era of air shower research a number of careful studies of the EM component were conducted. These experiments employed special detector arrangements within air shower arrays, where measurements were made under stacks of lead converters, using spark and ionization chambers, and neon flashtube hodoscopes to determine the density and energy of the photons and electrons (Fukui et al., 1960). Wilson cloud chambers were rarely used (Toyoda et al., 1962a, b). In the late seventies a few rather sophisticated experiments were carried out to study the EM component and its energy flux in shower cores (Tsushima et al., 1979).

More recently the interest had been focused on the response of deep water Cherenkov detectors and scintillators to the particle mix to which they are exposed in large air showers. This work was undertaken mainly to resolve disagreements concerning the primary spectrum when deducing it from measurements using different kinds of detector in air shower arrays, or fluorescence detectors. This activity triggered a number of simulation projects to investigate the electromagnetic as well as the muonic components down to very low energies across the entire impact area of large showers, to get accurate density distributions and energy spectra of these components and their ratio (Honda et al., 1997; Nagano et al., 2000; Risse and Heck, 2004). Some of this work is discussed in Chap. 8.

The most widely used detector type to record the EM component today is the plastic scintillator. Liquid scintillators, ionization chambers, proportional or Geiger counters are now rather seldom used for this purpose. They were frequently employed in older experiments. The fast response and easy handling of modern plastic scintillators, having rise times on the order of ≤ 3 ns, makes them an ideal tool for fast timing applications, such as arrival time measurements of the shower front to determine the arrival direction of showers, to measure the thickness of the shower particle disc (shower profile), or for delayed particle experiments. They also permit quick and easy reconfiguration of an array.

Scintillation detectors measure ionization and respond even to very low energy particles. In comparison to gas filled detectors scintillators have the disadvantage that they are subject to transition effects (e.g., gamma conversion), that can falsify particle density measurements significantly. Transition effects increase with detector thickness and are more pronounced near the shower core at distances $r \leq 30$ m, where the particle energy is high (Nagano et al., 2000). This topic is discussed in Sect. 2.11.

Some large experiments have used deep water Cherenkov detectors as shower detectors in the past, such as Haverah Park (Andrews et al., 1970) and presently the Auger array (Bertou, 2005). This kind of detector is not suitable for investigating the EM component because the contribution from the muons to the total signal may be as much as 50% and can even outweigh that of the former at large distances as is shown in Figs. 8.7 and 10.3a, b.

15.2 Lateral Distribution Functions

15.2.1 Classical Theoretical Distribution Functions

As explained in Chap. 2, it is customary to use for the description of the lateral density distribution of *all shower particles combined* distribution (or structure) functions that have their roots in the electromagnetic cascade theory. Frequently a simple or modified Nishimura-Kamata-Greisen (NKG) function (Eq. 4.162) is used. This is partly justified because the EM component is so dominating in well developed air showers and represents the bulk of all particles.

Moreover, for many applications this approach is fully adequate as long as the observations are carried out in the radial mid range from the shower axis. However, near the core, where the particle densities are so large, the particles so energetic, transition effects in the detectors important and significant hadronic and muonic components are present, conventional density measurements become impractical and the distribution functions invalid. Similarly, at large core distances where the density gets very low and muons and very low energy photons are the dominating components, observations show that the particle distribution appears to deviate from predictions.[2]

From the electromagnetic cascade theory developed by Rossi and Greisen (1941) and Kamata and Nishimura (1958), Greisen (1956, 1960) formulated the approximate expression, given below (cf. Eq. (4.162), Chap. 4), that is valid for an age parameter range $0.5 < s < 1.5$ and is known as the Nishimura-Kamata-Greisen (NKG) *lateral distribution function* (LDF) for the particle density in a pure electromagnetic shower,

$$\rho_e(r, s, N_e) = \left(\frac{N_e}{r_{\mathrm{M}}^2}\right) \frac{\Gamma(4.5 - s_N)}{2\pi\,\Gamma(s_N)\Gamma(4.5 - 2s_N)} \left(\frac{r}{r_{\mathrm{M}}}\right)^{s_N - 2} \left(1 + \frac{r}{r_{\mathrm{M}}}\right)^{s_N - 4.5}, \tag{15.1}$$

where

$$s_N = \frac{3}{(1 + [2\ln(E_0/E_{\mathrm{crit}})/t])} \tag{15.2}$$

[2] Some authors claim that the measured distributions drop off faster than predicted, others claim an opposite behavior.

and

$$t = \int_z^\infty \rho_{\text{atm}}(z)\mathrm{d}z/\chi_0 \,. \tag{15.3}$$

N_e is the total number of electrons, E_{crit} the critical energy, E_0 the primary energy, χ_0 the radiation length of the medium (air for air showers), s_N the NKG age parameter, t is the particle track length in units of radiation length, $\rho_{\text{atm}}(z)$ the atmospheric density at depth z, and r_{M} the Molière radius, all as defined in Chap. 4.

The lateral spread of the electrons is dominated by Coulomb scattering which determines the characteristic dimension of the shower. Moreover, the Molière radius characterizes the spread of the low energy electrons by multiple scattering.

The lateral development of an EM cascade in different materials scales with the Molière radius,

$$r_{\text{M}} = E_{\text{scatt}} \left(\frac{\chi_0}{E_{\text{crit}}} \right) \tag{15.4}$$

where E_{scatt} is the scattering energy (cf. Sect. 4.2.4, Eq. (4.19)),

$$E_{\text{scatt}} = mc^2 \sqrt{\frac{4\pi}{\alpha}} \,. \tag{15.5}$$

The Molière radius varies inversely proportional to the density of the medium, thus, Eq. (15.4) can be parameterized (Dova et al., 2003) as follows,

$$r_{\text{M}} = r_{\text{M}}(h_0) \left(\frac{\rho_{\text{atm}}(h_0)}{\rho_{\text{atm}}(h)} \right) = \frac{9.6\,\text{g}\,\text{cm}^{-2}}{\rho_{\text{atm}}(h)} \,. \tag{15.6}$$

The NKG function gives also a good description of bulk (all-particle) measurements of the particle distribution of a common air shower outside the immediate core region, mainly because the EM component is so dominating. However, many investigators have noticed discrepancies between theory and experiment, mainly at large radii. In particular, it was observed that even in pure electromagnetic (photon or electron initiated) showers the lateral spread of the electrons is less than predicted by the NKG theory (Allan et al., 1975). This fact was also confirmed by Monte Carlo simulations (Hillas and Lapikens, 1977). Additional problems arise when we deal with extremely energetic and strongly inclined showers, where marked azimuthal asymmetries in the particle distribution at ground level occur. This topic is addressed in Sect. 8.7.

The deficiency of the NKG function to describe the observed particle distribution over the entire lateral range has occupied many authors through the years (Linsley, 1973; Aguirre et al., 1973; Porter, 1973; Kawaguchi et al., 1975; Nagano et al., 1984a), and even in recent times (Yoshida et al., 1994; Glushkov et al., 1997; Coy et al., 1997; Nagano et al., 2000; Sakaki et al., 2001a, b; Takeda et al., 2003).

The roots of the discrepancies are partly due to the fact that the parent hadron cascade is ignored. Many authors have proposed modified forms of the distribution function and different mathematical approaches to solve the cascade problem analytically (Bourdeau et al., 1980; Lagutin et al., 1979, 1997a, b; Plyasheshnikov et al., 1979; Uchaikin, 1979).

Others have developed array and detector specific empirical distributions to fit their data for subsequent analysis. The most relevant are discussed in Sects. 8.10 and 10.2.

At this point we should recall that for accurate shower size computations the molecular nature of air must be considered because the radiation length is slightly different for air consisting of N_2 and O_2 molecules as compared to simply N and O atoms (see Sects. 4.2 and 6.2).

15.2.2 Lagutin Distribution Function

Since the so-called Lagutin lateral distribution function is encountered from time to time in the literature (Lagutin et al., 1997a, b, 1998, 1999) we list it below for reference. These authors proposed a distribution function and scaling relation that is based on Monte Carlo simulations and valid for *pure electromagnetic cascades*. They suggested a normalized distribution function, $f(x)$, of the form

$$x\, f(x) \;=\; \exp\left(-3.63 - 1.89\ln(x) - 0.370\ln^2(x) - 0.0168\ln^3(x)\right) \qquad (15.7)$$

where $(x = r/r_s)$, r being the distance from the shower axis to the location of observation and r_s is the scale radius analogous to the Molière radius of the NKG function; it is the r.m.s. radius of the shower at ground level ($r_s = r_{\rm rms} = \sqrt{\langle r^2\rangle}$). Equation (15.7) is claimed to be practically independent of primary energy, E_0, for $0.5 \le x \le 25$, and of shower age, s.

A more specific form given by Lagutin and Raikin (2001) reads

$$\begin{aligned}\rho_e(r, N_e) \;=\; & \left(\frac{C_e N_e}{r_{\rm rms}^2}\right)\left(\frac{r}{r_{\rm rms}}\right)^{-\alpha}\left(1+\frac{r}{r_{\rm rms}}\right)^{\alpha-\beta} \\ & \cdot\left(1+\left(\frac{r}{10r_{\rm rms}}\right)^2\right)^{-\delta} \quad [\mathrm{m}^{-2}]\,,\end{aligned} \qquad (15.8)$$

where $C_e = 0.28$ is the normalizing factor, N_e the total number of electrons at the observation depth, $X_{\rm obs}$ [g cm^{-2}], $\alpha = 1.2$, $\beta = 4.53$, and $\delta = 0.6$. The root mean square radius, $r_{\rm rms}$, is given by the approximation,

$$r_{\rm rms}(E_0, X_{\rm obs}) = \left(\frac{\rho_0}{\rho_{\rm obs}^{\rm air}}\right) A(X_{\rm obs}) \exp\left(\frac{B(X_{\rm obs})}{\ln(E_0[\mathrm{eV}]/10^9)}\right) \;\; [\mathrm{m}]. \qquad (15.9)$$

Here,

$$A = 6.69 \cdot 10^{-2} X_{\text{obs}} - 5.25 \ , \tag{15.10}$$

$$B = 13.37 \left(1 - 581.3 \cdot \exp[-1.44 \cdot^{-2} X_{\text{obs}}]\right) \ , \tag{15.11}$$

$\rho_{\text{obs}}^{\text{air}}$ is the air density at the observation level, X_{obs}, and $\rho_0 = 1.255 \cdot 10^{-3}\,\text{g cm}^{-2}$.

15.2.3 Simulated Lateral Distributions

Of the many theoretical studies and simulations that had been carried out through the years to investigate electromagnetic cascades either separately or in air showers, frequently the EGS program package had been used in one form or another and, recently, in combination with the CORSIKA or a similar program system, or by using hybrid (thinning) methods at very high energies (see Chap. 20 for details). In Fig. 15.1 we show as an example the lateral density distribution of electrons (positrons and negatrons combined) in a 10^{19} eV iron nucleus initiated shower from the work of Risse and Heck (2004). Shown are two curves that illustrate the distribution at two stages of development, one for an age parameter of $s = 0.7$, i.e., a young shower, the other at shower maximum ($s = 1.0$).

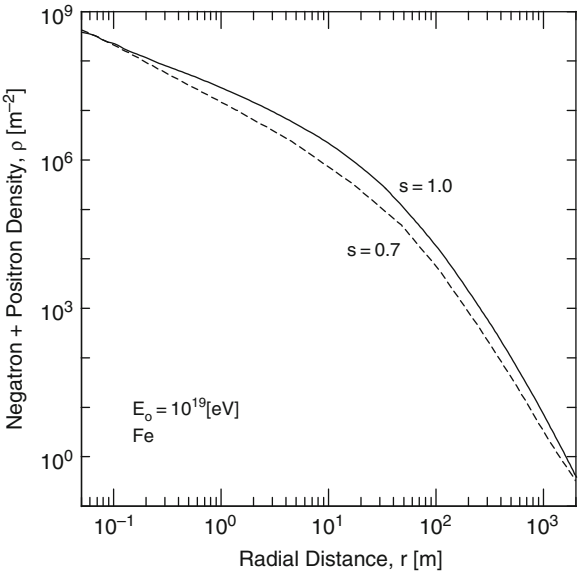

Fig. 15.1 Lateral density distribution of positrons and electrons combined in a simulated 10^{19} eV iron nucleus initiated shower at two stages of its development, identified by the age parameters $s = 0.7$, *dashed curve*, and $s = 1.0$, *solid curve* (after Risse and Heck, 2004) (simulation based on CORSIKA)

Additional simulation data concerning the electromagnetic component in showers are given in Chap. 8 where a plot of the distribution of the different shower constituents is displayed (Fig. 8.1).

15.2.4 Experimental Lateral Distributions

a) Results of Measurements

Only few experiments were designed to record exclusively the electron–photon component in showers. These employed usually lead absorbers and converters in combination with scintillation detectors or ionization chambers. Some of these experiments were rather sophisticated and allowed to study the lateral distribution of the EM component even in the shower core of smaller showers (Tsushima et al., 1979). Occasionally penetrating muons do not affect the results of these particular measurements significantly.

However, the majority of the lateral density distribution measurements are so-called bulk measurements made with relatively thin scintillation detectors (≤ 5 cm) where all charged particles are recorded. In these detectors transition effects are small outside the shower core and muons contribute essentially the signal of a minimum ionizing particle. Because of the overwhelming presence of electrons (and photons) such bulk measurements give fairly accurate information on the lateral distribution of the EM component if one avoids the immediate core area and the very distant regions of a shower where muons are likely to make the larger contribution to the detector signal.

Of the large number of data that is available on the lateral distribution of the shower particles we present a selection from different epochs and atmospheric depths, ranging from sea level to airplane altitudes (12 km). It is important, however, to keep in mind that many of these data that had been classified by the respective workers as electron data are in fact charged particle data, i.e., they are more or less contaminated by muons and possibly some hadrons. Irrespective of this inaccuracy we are using in the following summary of experimental data the original labeling which the authors of the papers had used in their data presentation. The data are presented in ascending order of altitude where they had been acquired and within this order in approximately chronological sequence.

In Fig. 15.2 we present the results of a very early and very carefully conducted experiment which had been carried out by Fukui et al. (1960) at Tokyo. Shown is the average distribution of many showers having sizes around 10^6, normalized to a size of 10^6. The spread of the densities of this group of showers as recorded by the many detectors is also indicated. Also shown are the particle distributions of two smaller individual showers ($N = 10^5$) where the shower axis hit the central detector which consisted of a neon hodoscope, to avoid saturation effects in the vicinity of the shower axis.

Distributions from a later epoch obtained from measurements carried out at Kiel, Germany (sea level) by Bagge et al. (1979) and at Verrières, France (100 m a.s.l.)

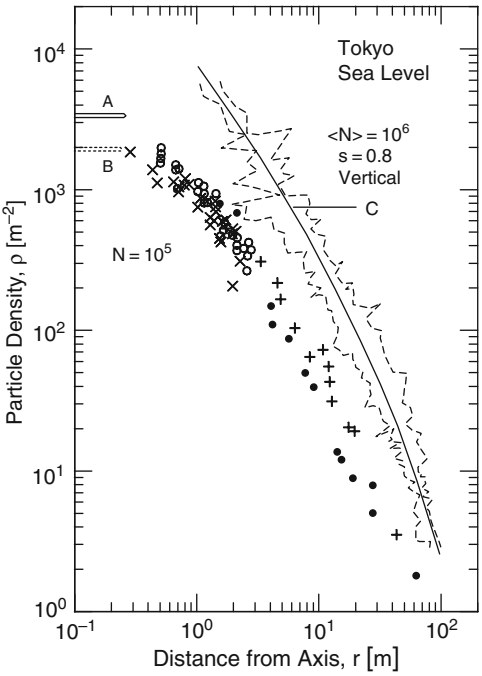

Fig. 15.2 Lateral density distributions of particles, chiefly electrons, in showers recorded at Tokyo (57 m a.s.l.). The *solid curve, C*, is the average NKG distribution for age $s = 0.8$ of many showers of sizes around 10^6 particles, normalized to a size of 10^6 at sea level. The region outlined by the irregular *dashed curves* above and below *C* shows the spread of the recorded densities of the different detectors at the indicated locations with respect to the shower axis of a selected set of showers. Two individual showers of size $N = 10^5$ and $\theta = 20^\circ$ are also shown. The densities with symbols ○, A, × and B were obtained with the neon hodoscope, the data points • and + with scintillators; A, ○ and • belong to the shower with the steeper distribution, B, × and + to the flatter (after Fukui et al., 1960)

by Catz et al. (1975) are displayed in Figs. 15.3 and 15.4, respectively. The authors claim that the data contain mainly electrons.

The results of an excellent series of measurements of recent date carried out by the KASCADE team at Karlsruhe, Germany (Antoni et al., 2001) are presented in Fig. 15.5. In this experiment the EM detectors have well shielded muon detectors underneath that were used to record and subtract the muon count in the EM detectors. In addition a variety of other corrections were applied to the data to get the true electromagnetic particle density essentially free of contamination by other shower constituents. The corrections include also accounting for EM punch-throughs that reach the muon detectors and falsify the muon count.

The next set of distributions that we have included in our summary are still from very low altitudes. They comprise data from the Moscow array (200 m a.s.l.) by Khristiansen et al. (1981a) acquired mainly with Geiger Counter trays (Fig. 15.6) and from Haverah Park (212 m a.s.l.), exceptionally recorded with a liquid paraffin

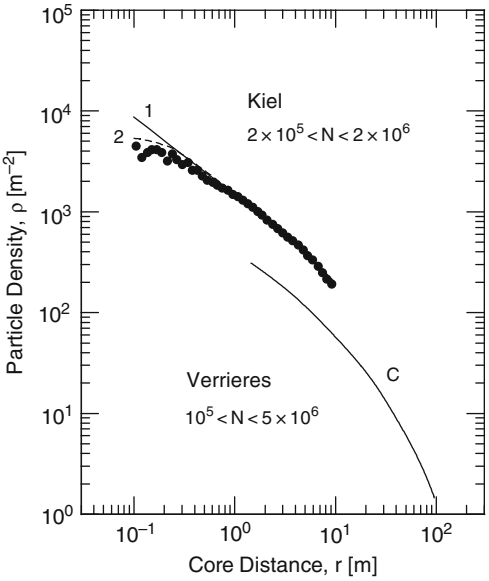

Fig. 15.3 Mean lateral density distribution of mainly electrons in showers covering the size range $2 \cdot 10^5$–$2 \cdot 10^6$ (average size 10^6) at sea level. The experimental data points, •, are from the neon hodoscope experiment at Kiel. *Curve 1* represents the usual NKG function fitted at $1 < r < 10$ m and *curve 2* includes core location error corrections in x and y of ± 0.15 m (Bagge et al., 1979). The *lower curve* labeled *C* shows the summarized sea level results of Catz et al. (1975) measured at Verrières (France) (100 m a.s.l.), presented in Fig. 15.4, for comparison

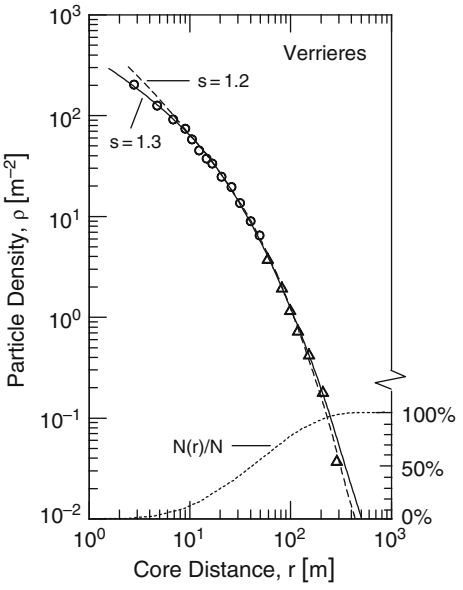

Fig. 15.4 Lateral density distribution of all charged particles in showers recorded with Geiger counter trays at Verrières (near Paris, France) (100 m a.s.l.) (Catz et al., 1975). The data points ○ are actual measurements whereas points △ are extrapolations, both for $10^5 \leq N_e \leq 5 \cdot 10^6$. The two curves labeled with the age parameters $s = 1.2$ and $s = 1.3$ are theoretical fits. The *lower curve* labeled $N(r)/N$ shows the percentage of all shower particles laying within radius r for the assumed lateral distribution

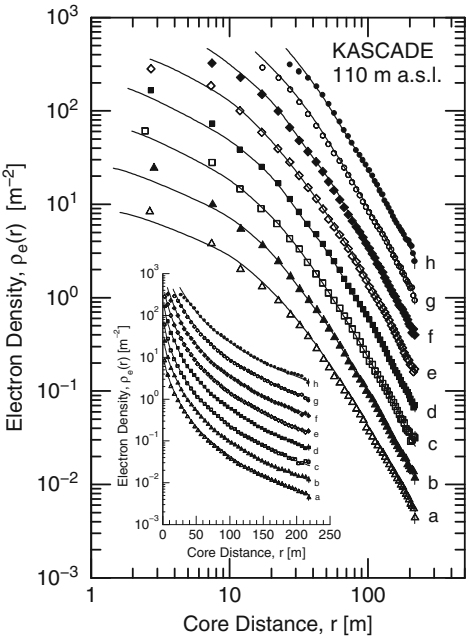

Fig. 15.5 Lateral density distribution of electrons of kinetic energy ≥ 5 MeV in showers of zenith angle $\theta \leq 18^\circ$ recorded at Karlsruhe, Germany (110 m a.s.l.) (Antoni et al., 2001). Shown is the originally published semi-logarithmic plot (insert) and the more common double-logarithmic display re-plotted by the author. The different distributions apply to the shower size groups as listed in the table and the *curves* are NKG functions for a fixed age parameter $s = 1.65$ but varying characteristic radii called r_e, where $r_e \neq r_M$, the Moliére radius. *a*, $7.9 \cdot 10^3 \leq N_e \leq 2.0 \cdot 10^4$; *b*, $2.0 \cdot 10^4 \leq N_e \leq 5.0 \cdot 10^4$; *c*, $5.0 \cdot 10^4 \leq N_e \leq 1.26 \cdot 10^5$; *d*, $1.26 \cdot 10^5 \leq N_e \leq 3.16 \cdot 10^5$; *e*, $3.16 \cdot 10^5 \leq N_e \leq 7.9 \cdot 10^5$; *f*, $7.9 \cdot 10^5 \leq N_e \leq 2.0 \cdot 10^6$; *g*, $2.0 \cdot 10^6 \leq N_e \leq 5.0 \cdot 10^6$; *h*, $5.0 \cdot 10^6 \leq N_e \leq 1.25 \cdot 10^7$

based scintillation detector of thickness $8\,\mathrm{g\,cm^{-2}}$, by Towers (1971) and Blake et al. (1975) (Fig. 15.7). Thus, both sets of data represent essentially electron distributions. The Russian data include showers of different size and age groups, as listed in the figure caption, that are normalized to a size of 10^6 and displayed in a particular way (density multiplied by the distance from the axis).

The four Haverah Park distributions apply to showers belonging to four different primary energy groups. They are classified according to the vertical equivalent muon density per square meter at a core distance of 500 m, recorded with 1.2 m deep water Cherenkov detectors. The lateral distribution function used by Blake et al. (1975) and Armitage et al. (1973b) to fit the data shown in Fig. 15.7 is of the form

$$\rho(r) \;=\; \frac{A}{r}\left(1+\frac{r}{r_0}\right)^{-(\eta-1)} \quad [\mathrm{ve\mu\ cm^{-2}}]\ , \tag{15.12}$$

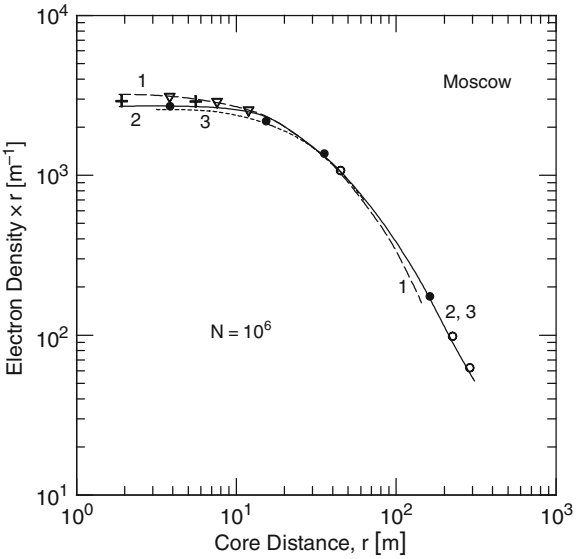

Fig. 15.6 Average lateral density distribution of electrons in showers recorded at Moscow (192 m a.s.l.) multiplied by the core distance, r (Khristiansen et al., 1981a). The data are normalized to a size of $N_e = 10^6$. The different symbols identify the following shower size groups: $+$ $N_e = 6.8 \cdot 10^4$, $\triangledown$ $N_e = 1.3 \cdot 10^5$, $\bullet$ $10^6 \leq N_e \leq 2 \cdot 10^6$, and $\circ$ $10^7 \leq N \leq 2 \cdot 10^7$. The *dashed curve 1* is for an age parameter of $s = 1.13$, *curve 2* for $s = 1.18$, and *curve 3* for $s = 1.33$

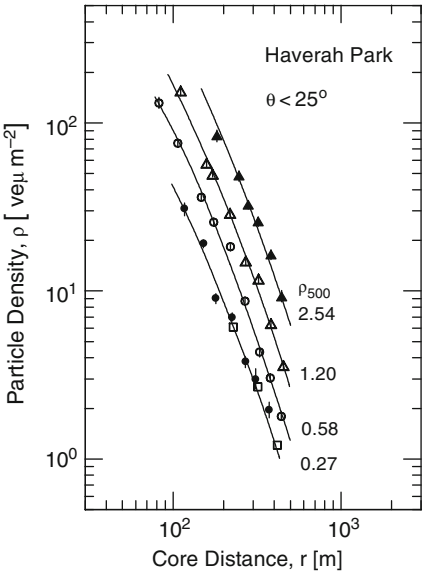

Fig. 15.7 Total charged particle density distributions resulting from measurements with unshielded 8 g cm^{-2} scintillators at Haverah Park (212 m). Points ▲, △, ○ and ● are from the work of Blake et al. (1975), □ is from Towers (1971). For further details see text. The density is expressed by the authors of this work in units of vertical equivalent muons per square meter (veμ m^{-2}), which implies simply minimum ionizing particles in the scintillators. The *curves* represent showers of different size groups. They are labeled according to the density ρ at a core distance of 500 m, (ρ(500)), as measured with deep water Cherenkov detectors, which is a measure of primary energy

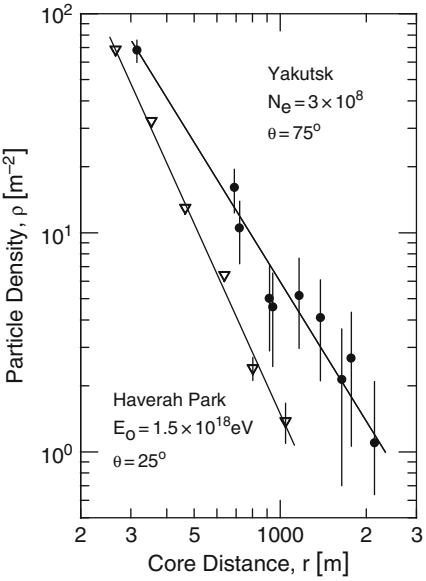

Fig. 15.8 Lateral density distribution of all charged particles in large showers incident at zenith angles $\theta \leq 25^\circ$ recorded with the few but large deep water Cherenkov detectors at Haverah Park (212 m a.s.l.), ∇ ($\rho(600) = 2.0$ veμ; $E_0 \simeq 1.8 \cdot 10^{18}$ eV) (Armitage et al., 1973b). For comparison we have plotted the distribution of an individual shower of somewhat higher energy ($N_e = 3 \cdot 10^8$; estimated $E_0 \sim 10^{19}$ eV), incident at a zenith angle of 75° at Yakutsk (105 m a.s.l.), •, recorded with scintillation detectors. The curvature of the shower front of this event is plotted in Fig. 9.2a of Chap. 9 (Kozlov et al., 1973)

where A is the proportionality constant, r the distance from the shower axis, $\eta = 3.79 \pm 0.05$ the slope parameter, and the parameter $r_0 = 160$ m.

In Fig. 15.8 we present data of two individual showers of similar primary energy (about a factor of two different) that were recorded under very different zenith angles and with very different detector systems that do not allow to make a real comparison for reasons discussed in Chaps. 2 and 8. At the Haverah Park array in England (212 m a.s.l.), deep water Cherenkov detectors had been used (Armitage et al., 1973b), whereas at Yakutsk in Siberia (105 m a.s.l.) the measurements were made with a scintillator array (Kozlov et al., 1973).

Of particular interest is the work of Tsushima et al. (1979), carried out at Yamanashi (310 m a.s.l.), who used a very elaborate experimental setup in conjunction with an air shower array, to investigate the electromagnetic component in showers. They have used scintillators under a lead absorber-converter in combination with two channeltron image intensifiers, operated in series, that were optically coupled with glass fibers.

The first channeltron was operated continuously and viewed the scintillators. It served as image storage device of the scintillation flashes that are a measure of the EM cascade size. The second channeltron was gated by a separate photomultiplier

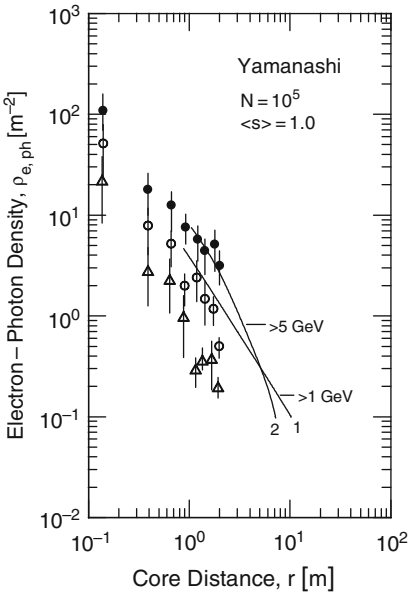

Fig. 15.9 Lateral density distribution of the electron–photon component recorded at Yamanashi (310 m a.s.l.) for showers of average size 10^5 ($E_0 \simeq 10^6$ GeV), age parameter $s = 1$ and three different electron energy thresholds: • > 4 GeV, ○ > 18 GeV, △ > 43 GeV (Tsushima et al., 1979). For comparison *curve 1* shows the theoretical lateral density distribution of hadrons of energy $E_h \geq 1$ GeV, obtained by Grieder (1977) for 10^6 GeV proton initiated showers using the SMFB model. *Curve 2* represents earlier electron–photon data from cloud chamber measurements of Toyoda (1962a, b)

whenever the light flashes of the scintillators which it viewed directly exceeded the predetermined threshold. A photographic camera recorded the light spots that were subsequently densitometrically evaluated to determine the electron–photon density distribution and the local EM cascade size, which revealed the energy of the cascade initiating photon or electron. The data could then be associated with the air shower that caused the event. The results of this work are shown in Figs. 15.9 and 15.10. The detector system permitted to investigate the EM component even in the core of small showers.

The following figures show lateral density distributions of showers of different ages and size groups recorded at Akeno, Japan (900 m a.s.l.) (Figs. 15.11 and 15.12) (Hara et al., 1979), at Baksan, Russia (2,060 m a.s.l.) (Fig. 15.13) (Alexeyev et al., 1975 and 1977) and, in Fig. 15.14, a set of electron distributions of simulated proton showers of different primary energies at the altitude of the EAS-TOP experiment (2,005 m a.s.l.) (Aglietta et al., 1986) (the actually measured data are shown in Chap. 8, Fig. 8.13a). Data from Mt. Norikura in Japan (2,770 m a.s.l.) are presented in Fig. 15.15 and two extensive sets from measurements at Tien Shan, Kazakhstan (3,340 m a.s.l.) in Figs. 15.16 and 15.17.

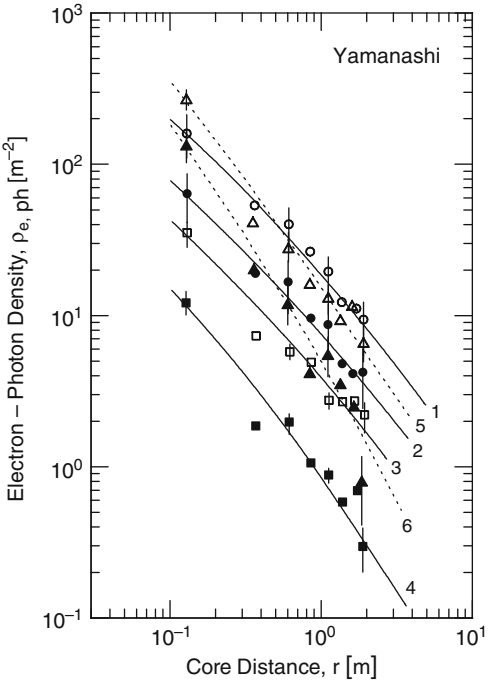

Fig. 15.10 Lateral density distribution of the electron–photon component recorded at Yamanashi (310 m a.s.l.) (Tsushima et al., 1979). The symbols identify the data according to the electron energy groups as follows: ○ $E > 4$ GeV, ● $E > 18$ GeV, both for the shower size group $5 \cdot 10^5 < N_e < 5 \cdot 10^6$ and $s \leq 1.0$, normalized to $N_e = 10^6$. △ $E > 4$ GeV, ▲ $E > 18$ GeV, both for the size group $3 \cdot 10^4 < N_e < 5 \cdot 10^5$ and $s \leq 0.8$, normalized to $N_e = 10^5$. □ $E > 4$ GeV, ■ $E > 18$ GeV, both for the size group $5 \cdot 10^4 < N_e < 5 \cdot 10^5$ and $s \geq 1.0$, normalized to $N_e = 10^5$. The *curves 1–6* are hand-drawn fits to guide the eye

In their studies of the lateral distribution of the electrons in showers carried out by Hara et al. (1979) at Akeno, these authors have used the following modified NKG function to describe the lateral particle density distributions shown in Figs. 15.11 and 15.12,

$$f\left(\frac{r}{r_{\mathrm{M}}}\right) = C_1 \left(\frac{r}{M}\right)^{s-2} \left(1 + \frac{r}{r_{\mathrm{M}}}\right)^{s-4.5} \left[1 + C_2 \left(\frac{r}{r_{\mathrm{M}}}\right)^{d}\right] , \qquad (15.13)$$

where r is again the core distance, r_{M} the Molière radius and C_1 the normalizing factor given in terms of a *Beta function* by

$$C_1 = \left(\frac{N}{2\pi r_{\mathrm{M}}^2}\right) [B(s, 4.5 - 2s) + C_2\, B(s + d, 4.5 - d - 2s)]^{-1} \qquad (15.14)$$

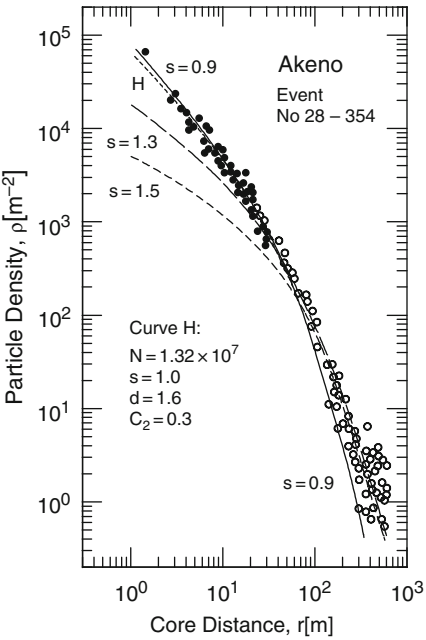

Fig. 15.11 Example of a shower of size $N_e = 1.32 \cdot 10^7$, recorded at Akeno (900 m a.s.l.). Points • were determined with scintillators of area 0.25 m^2, ○ with such of area 1 m^2 (Hara et al., 1979). It is evident from this figure that the distribution does not fit an NKG function with a single age parameter, s, over the entire lateral range (*solid curve* $s = 0.9$; *dashed curves* $s = 1.3$ and $s = 1.5$). Hara et al. (1979) have used a modified NKG function, given in the text (Eq. 15.13), with parameters as indicated in the *lower left corner* of the figure, that generates *curve H* (*short dashes*), which gives a good fit at all distances

According to the authors, the last factor of Eq. (15.13) had been added to the NKG function to account for the *flattening of the distribution observed beyond one Molière unit*.[3] For the parameter d fixed at 1.6, C_2 is slightly size dependent, varying between zero for a shower size of $N = 10^5$ to about 0.2–0.3 for $N = 10^7$. This correction increases the shower size at 10^7 by about 20% with respect to the prediction using a pure NKG function (Hara et al., 1979). In this context the transition effects in the scintillators had also been investigated. The results of this work are summarized in Sect. 2.11. In later years slightly modified distribution functions had been used (Nagano et al., 1984b; Sakaki et al., 2001a, b; see Chaps. 8 and 10).

Data from Mt Chacaltaya in Bolivia (5,230 m a.s.l.), the highest ground based array, are illustrated in Fig. 15.18 (Kaneko et al., 1975) and the very unique results from measurements of a balloon bound array that was operated at an altitude between 11.2 and 11.8 km in Fig. 15.19 (Antonov et al., 1979a, b, 1981). To

[3] This observation is in contradiction to a later statement made by Nagano et al. (2000) (see Sect. 8.10) where a more rapid drop of the particle density was noticed.

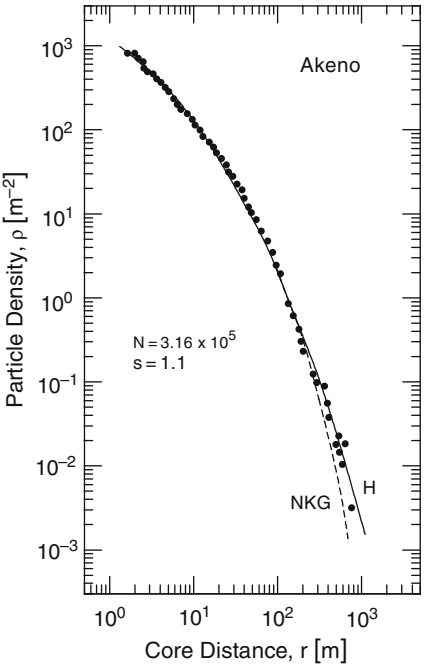

Fig. 15.12 Average lateral density distribution of particles in smaller showers of age $s = 1.1$ recorded at Akeno (900 m a.s.l.). The *curve labeled NKG* is the normal Nishimura-Kamata-Greisen function (Kamata and Nishimura, 1958; Nishimura, 1967) for $s = 1.1$, the other, H, is described by a different function, given in the text, with parameter values $C_2 = 0.1$ and $d = 1.6$ (Hara et al., 1979). A more recent series of lateral electron distributions measured at Akeno in showers of different sizes are given by Nagano et al. (1984b) (see Chap. 8)

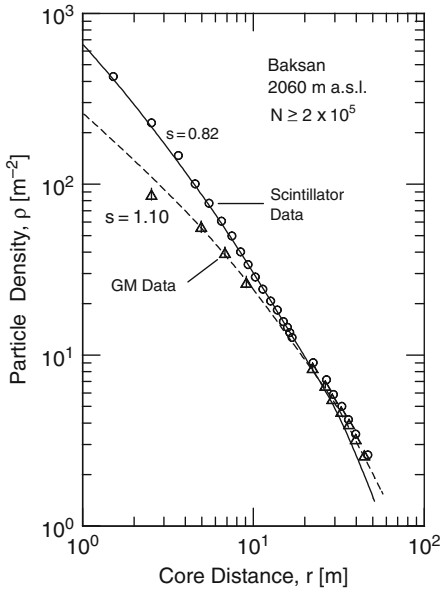

Fig. 15.13 Lateral density distribution of shower particles recorded at Baksan, (2060 m) in showers of size $N_e \simeq 6 \cdot 10^5$–$7 \cdot 10^5$. Points ○ were obtained with 30 cm thick liquid scintillators, △ with Geiger-Müller counters (Alexeyev et al., 1975, 1977). The *curves* are NKG functions with age parameters as indicated. Transition effects due to the great thickness of the liquid scintillators and their consequences for the age parameter are evident (see also Sect. 2.11)

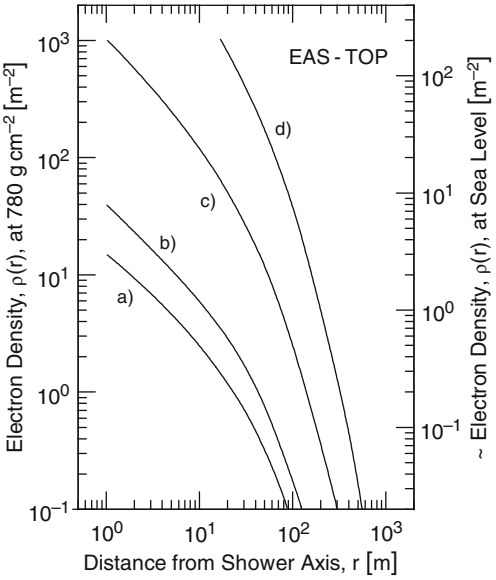

Fig. 15.14 Electron density as a function of distance from the shower axis of simulated vertically incident showers of different primary energy at the location of the EAS-TOP array (altitude 2,005 m a.s.l.; 810 g cm^{-2}) at Gran Sasso (*left* ordinate). The *curves* apply to the following primary energies: (a) $E_0 = 5 \cdot 10^{13}$ eV, (b) $E_0 = 10^{14}$ eV, (c) $E_0 = 10^{15}$ eV, (d) $E_0 = 10^{16}$ eV. The right ordinate gives the approximate densities at sea level (after Aglietta et al., 1986). The actually measured all-charged particle density distribution at this site is plotted in Fig. 8.13

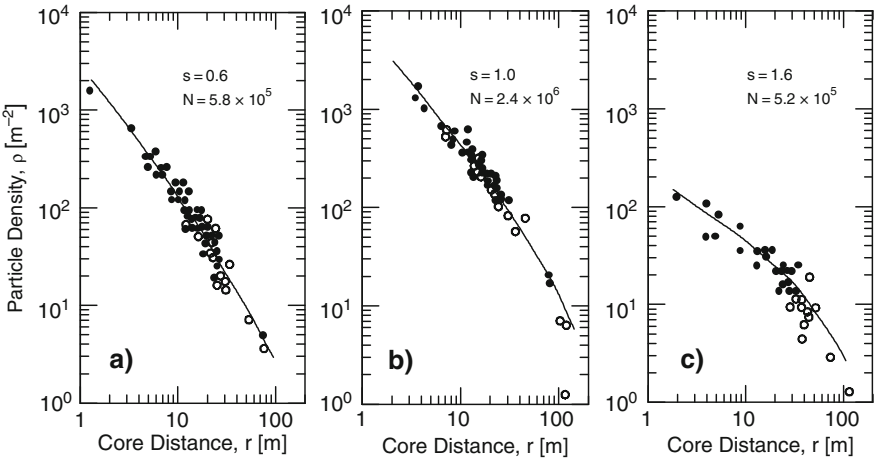

Fig. 15.15 Examples of lateral density distributions of shower particles in showers of different size and age groups recorded at Mt. Norikura (2770 m a.s.l.), in Japan, with an array configuration as shown in Fig. A.25 (Miyake et al., 1968)

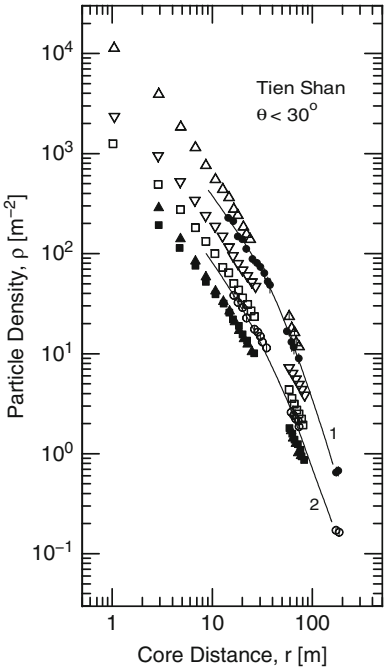

Fig. 15.16 Compilation of data from the Tien Shan installation (3,340 m a.s.l., 700 g cm^{-2}) of the lateral density distribution of *charged particles* in showers of different size groups, acquired with different detectors, as follows (Sc, scintillators; GM, Geiger counters) (Aseikin et al., 1975): △ (Sc), $10^6 \leq N_e \leq 1.8 \cdot 10^6$, $\theta \leq 30°$; • (GM), $10^6 \leq N_e \leq 1.8 \cdot 10^6$, $\theta \leq 30°$; *curve 1*, NKG function, $s = 0.8$; ▽ (Sc), $3.2 \cdot 10^5 < N_e \leq 5.6 \cdot 10^5$, $\theta > 0°$; □ (Sc), $1.8 \cdot 10^5 \leq N_e \leq 3.2 \cdot 10^5$, $\theta \leq 30°$; ○ (GM)$1.8 \cdot 10^5 \leq N_e \leq 3.2 \cdot 10^5$, $\theta \leq 30°$; *curve 2*, NKG function, $s = 0.8$; ▲ (Sc) $10^5 \leq N_e \leq 1.8 \cdot 10^5$; and ■ (Sc) $1.8 \cdot 10^5 \leq N_e \leq 3.2 \cdot 10^5$, all from the work of Aseikin et al. (1977b). The central densities, ρ_c, of the distributions shown here are as follows △ 316 − 178, • 177 − 100, ▽ 99 − 56, □ 55 − 32, ○ 31 − 18, ▲ 17 − 10, and ■ 9–5 particles m^{-2} (Machavariani et al., 1979)

complete the data on the lateral distribution of electrons and electron dominated shower particles we have included with Figs. 15.20 and 15.21 two old compilations that summarize and allow to compare many of the previously presented data in two common plots, to inspect the extent of agreement.

b) Comments on Measured Data

Many of the measurements made with scintillators at close proximity of the shower axis seem to yield distributions that cannot be fitted with a single age parameter (see Sect. 10.4). Apart from core position errors that may lead occasionally to density underestimations, it is mostly transition effects in the detectors, discussed in Sect. 2.11, that frequently lead to higher particle densities than theory predicts near the shower core. This is beautifully illustrated in Fig. 15.13 from the work of

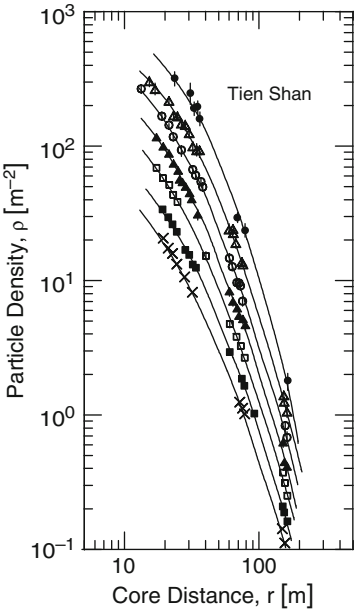

Fig. 15.17 Compilation of data from the Tien Shan installation (3,340 m, 700 g cm^{-2}), on the lateral density distribution of *electrons* in showers of different size groups, as indicated below. The data were acquired with scintillation detectors that were calibrated with Geiger counters. The *curves* are fits to the data. The errors are the size of the symbols unless indicated (Aseikin et al., 1977b). • $\langle N_e \rangle = (4.21 \pm 0.02) \cdot 10^6$; ○ $\langle N_e \rangle = (1.44 \pm 0.03) \cdot 10^6$; □ $\langle N_e \rangle = (5.15 \pm 0.05) \cdot 10^5$; × $\langle N_e \rangle = (1.79 \pm 0.01) \cdot 10^5$; △ $\langle N_e \rangle = (2.20 \pm 0.06) \cdot 10^6$; ▲ $\langle N_e \rangle = (8.90 \pm 0.11) \cdot 10^5$; ■ $\langle N_e \rangle = (3.04 \pm 0.02) \cdot 10^5$

Alexeyev et al. (1977), where two sets of measurements are plotted that were made in the same showers, using trays of Geiger counters in one case and scintillators in the other. Thin-walled Geiger counters have negligible transition effects because of the low density of the detector medium (gas).

15.3 Energy Spectra, Energy Flow and Related Data

15.3.1 Simulated Photon–Electron Spectra

Only few experiments were carried out to investigate the energy spectrum of the electromagnetic component in showers. The energy of the bulk of the electrons and photons at ground level is relatively low except in the immediate core region. Recent theoretical studies and simulations were carried out mainly in the context of the earlier mentioned calibration of shower detectors (Honda et al., 1997; Nagano et al., 2000; Risse and Heck, 2004).

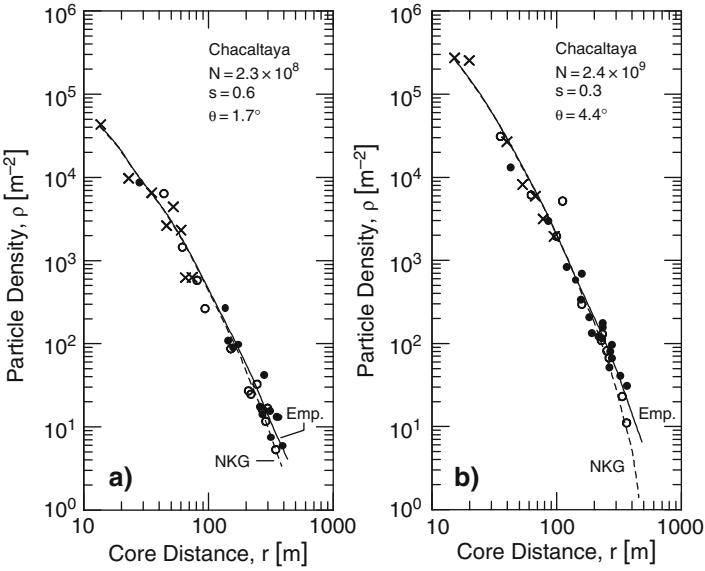

Fig. 15.18 Examples of the lateral density distribution of two different showers at Mt. Chacaltaya (5,230 m a.s.l.). Shown are the experimentally determined densities obtained from three different sets of scintillation counters (○ 0.87 m^2 fast timing and density, × 1/16 m^2 and ● 0.83 m^2 for density measurements only). The *solid curves* represent fits of the experimental data with the empirical mathematical expression of Kaneko et al. (1975), the *dashed curve* to the NKG function (Kaneko et al., 1975)

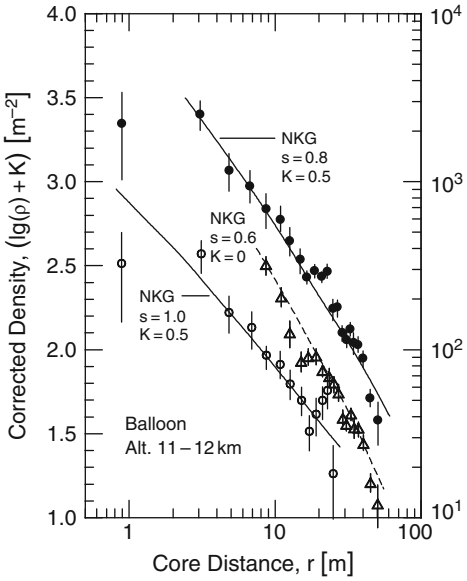

Fig. 15.19 Lateral density distributions of charged particles in showers at an altitude between 11.2 and 11.8 km from a balloon experiment by Antonov et al. (1979a, b, 1981). The data are normalized to a size of $1.5 \cdot 10^6$ and include zenith angles from $0^\circ \leq \theta \leq 60^\circ$. K is a correction coefficient that depends on the distance r between installation center and shower axis. ○ applies to events with $0 < r < 15$ m and $K = 0.0$; △ is for $15 < r < 50$ m and $K = 0.0$; and ● for $0 < r < 50$ m and $K = 0.5$

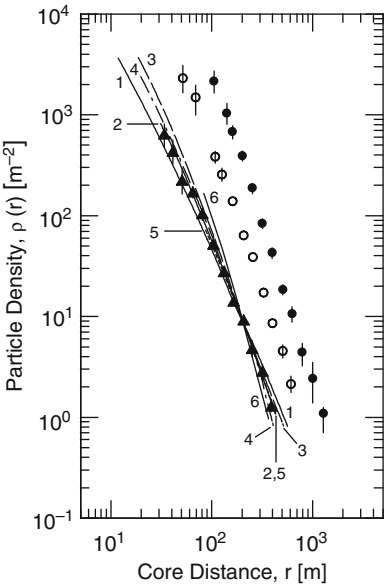

Fig. 15.20 Compilation of average lateral density distributions of air shower particles from several experiments at different altitudes, normalized to an atmospheric depth of 1,060 g cm^{-2}. The *curves* show approximations of distributions that are normalized to a shower size of $\langle N \rangle \approx 2 \cdot 10^7$ which corresponds to a density of 9.1 m^{-2} at 200 m at Yakutsk. This calibration point was used by different experimental groups for comparison: *1*, Tokyo (s.l.) (Kawaguchi et al., 1975); *2*, Moscow (200 m) (Atrashkevich et al., 1977); *3*, Chacaltaya (5,230 m) (Kaneko et al., 1975); *4*, Volcano Ranch (1,768 m) (Linsley 1977a, b); *5*, Haverah Park (212 m) (Blake et al., 1975); and *6*, Sydney (s.l.) (Bray et al., 1975). The three sets of data points, ▲, ○ and • are from measurements with the Yakutsk installation (105 m a.s.l.) (Diminstein et al., 1981) and apply to showers having densities at 200 m of 9.1 , 72.4 and 363 particles m^{-2}, corresponding to a size of $N_e = 1.5 \cdot 10^7$, $N_e = 1.5 \cdot 10^8$ and $N_e = 6.8 \cdot 10^8$ particles, respectively

In Fig. 15.22 we show as an example of a photon and an electron energy spectrum the results of a simulation of Sakaki (2003) that applies to a 10^{19} eV proton initiated shower at a core distance of 600 m for the altitude of the Akeno/AGASA site (900 m a.s.l.) (for details see Honda et al., 1997). Similar results at larger core distances from the work of the same authors are displayed in Sect. 8.3. The muon spectrum at the same location is also shown for comparison.

15.3.2 Measured Photon–Electron Spectra

Note that in many experimental setups where the energy of photons and/or electrons are being measured the distinction between photons and electrons cannot be made. This is particularly the case when EM cascade sizes are being used to determine the energy, and in regions of high radiation fields. This is why in the following the energy is specified for photons and electrons combined.

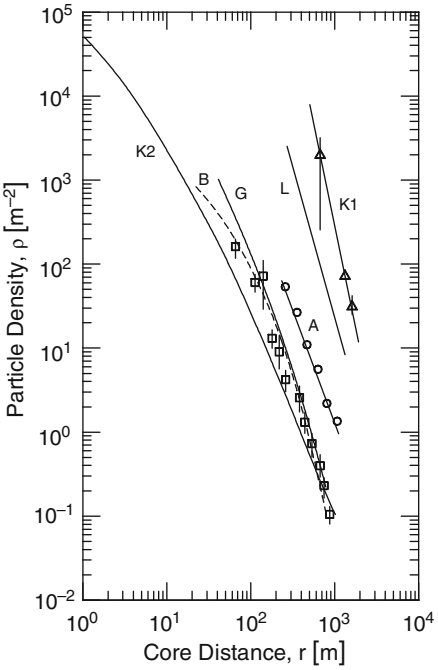

Fig. 15.21 Compilation of experimental lateral density distributions of charged particles in large and very large showers. Points ○ and *curve A* are after Armitage et al. (1973a, b, c) for showers with a density of $2.0\,\mathrm{m}^{-2}$ at a core distance of 600 m, recorded at Haverah Park (212 m a.s.l.). Points □ and *curve B* are from the work of Bell et al. (1973) for showers with a muon number of $2 \cdot 10^6$ observed with the SUGAR array at Narrabrai (Australia) (260 m). *G* represents the Greisen formula for size $N_e = 3.1 \cdot 10^7$ (Greisen, 1960). Points △ and *curve K1* represent a unique event recorded at Tokyo (s.l.). It is the largest shower that had been observed to that date and had a size of $2 \cdot 10^{12}$ (Kawaguchi et al., 1971). It was later on somewhat downgraded. *L* is the largest shower recorded at Volcano Ranch (1,768 m) with $N_e = 5 \cdot 10^{10}$ (Linsley, 1963). *K2* is normalized to $N_e = 10^7$ particles and includes the size range $10^7 \leq N_e \leq 5 \cdot 10^7$, observed at Tokyo (Kawaguchi et al., 1975)

Figure 15.23 shows measured combined integral electron and photon energy spectra, $N_{e,\mathrm{ph}}(> E)$, in showers within four radial intervals from the shower axis, as specified in the caption, from the previously mentioned work of Tsushima et al. (1979), using a rather sophisticated experimental arrangement. The measurement was made at Yamanashi, Japan (310 m a.s.l.) in showers of smaller sizes, normalized to $N_e = 10^5$, and average age $\langle s \rangle = 1.0$. An additional requirement for these measurements was that the core detector indicated a particle density of $\geq 10^4$.

In Fig. 15.24 we display a plot showing the measured energy flow density as a function of distance from the shower axis of showers of different ages and sizes, as indicated in the caption. These data are from the same work as those of Fig. 15.23. A similar set of data is displayed in Fig. 15.25 from measurements at the high

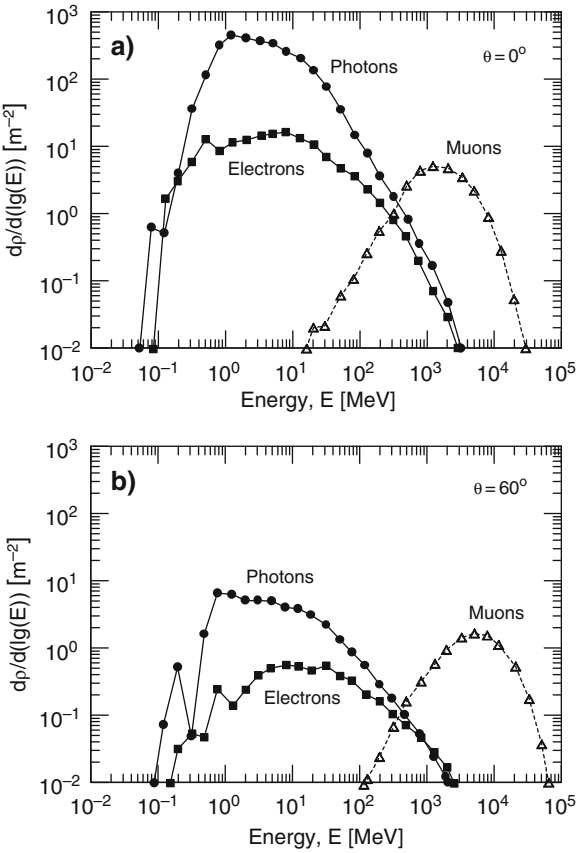

Fig. 15.22 An example of energy spectra of photons, electrons and muons at a core distance of 600 m in a 10^{19} eV proton initiated shower from a simulation of Sakaki for the AGASA site (Honda et al., 1997; Sakaki, 2003)

altitude station of Tien Shan, Kazakhstan (3,340 m a.s.l.) carried out by Aseikin et al. (1977a) and Machavariani et al. (1979).

A compilation of data from measurements of the mean energy of the electron–photon component as a function of core distance acquired at different altitudes, ranging from Mt. Chacaltaya to sea level is shown in Fig. 15.26. It is interesting to note that all data shown there fit nicely into a rather narrow energy band, from the near core area out to about 1,000 m. This suggests a rather rapid energy degradation of the bulk of the EM component in the atmosphere and a continuous rejuvenation of it by the hadron cascade. Finally, Fig. 15.27 shows the average electron–photon energy per detected electron in showers of sizes ranging from less than 10^4–10^6 at Tien Shan (Aseikin et al., 1977a). The practical independence of the mean energy from the shower size is in support of the previous statement.

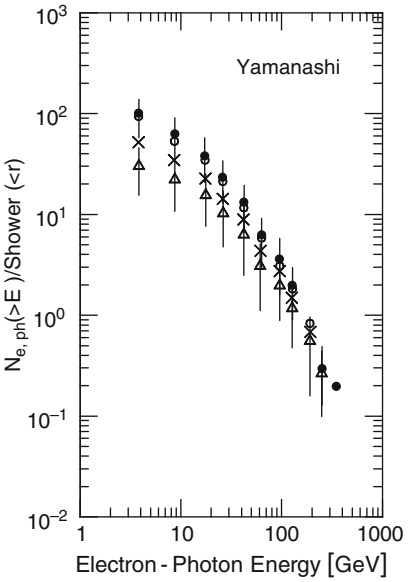

Fig. 15.23 Integral energy spectrum of the electron–photon component in air showers recorded at Yamanashi (310 m a.s.l.) (Tsushima et al., 1979). The showers are normalized to a size of $N_e = 10^5$ and $\langle s \rangle = 1.0$. The different symbols identify the radial distance range from the shower axis: •, $r \leq 2$ m; ○, $r \leq 1.5$ m; ×, $r \leq 1$ m; △, $r \leq 0.5$ m. Corresponding lateral density distributions obtained with the same experiment are given in Figs. 15.9 and 15.10, and energy flow distributions in Fig. 15.24

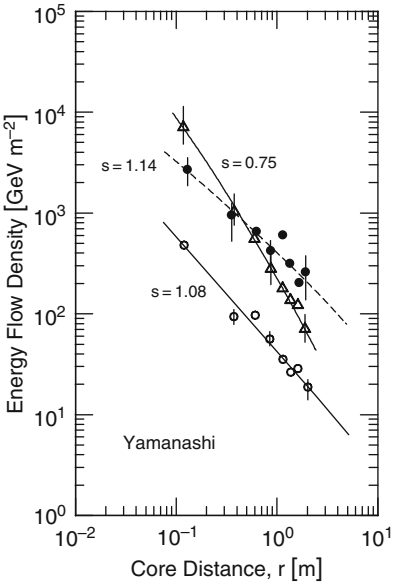

Fig. 15.24 Lateral distribution of energy flow of the electron–photon component in the shower core, under 2.5 cm of lead, measured at Yamanashi (310 m a.s.l.). The energy threshold is 4 GeV. The data groups belong to events with $N_e = 10^6$, $\langle s \rangle = 1.14$ (•); $N_e = 10^5$, $\langle s \rangle = 0.75$ (△) and $N_e = 10^5$, $\langle s \rangle = 1.08$ (○), respectively, after Tsushima et al. (1979). The corresponding exponents of the distributions are –0.94, –1.7 and –1.1

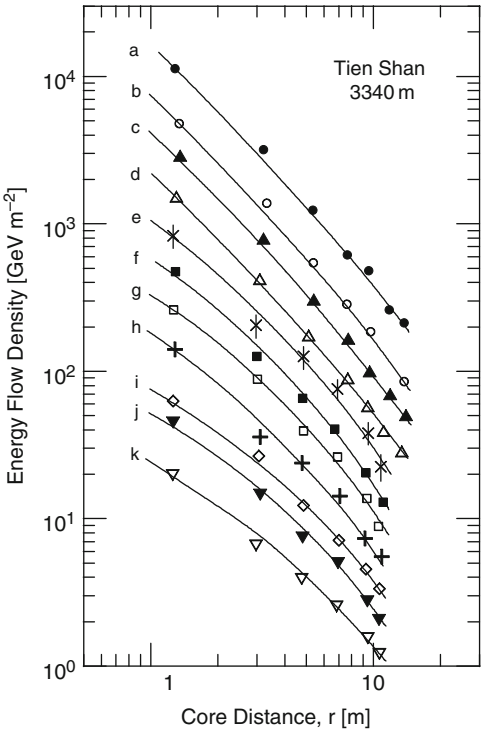

Fig. 15.25 Compilation of energy flux data of the electron–photon component recorded with the ionization calorimeters at Tien Shan. *Curves* (*a*), (*b*), (*c*), (*d*) and the corresponding data points are from the work of Aseikin et al. (1977a) for $\langle N_e \rangle = 2 \cdot 10^6$ (uncorrected), $2 \cdot 10^6$, $4.7 \cdot 10^5$, and $2.6 \cdot 10^5$, respectively. Data (*e*)–(*k*) are for the size groups $\langle N_e \rangle = 1.4 \cdot 10^5$, $8.6 \cdot 10^4$, $5.6 \cdot 10^4$, $3.3 \cdot 10^4$, $2.3 \cdot 10^4$, $1.35 \cdot 10^4$, and $\langle N_e \rangle = 8.3 \cdot 10^3$, respectively, after Machavariani et al. (1979). All data include events with zenith angles $\theta \leq 30^\circ$

15.4 Photon–Electron and Charge Ratio, Geomagnetic Effects

Data from two of the very few measurements of the energy ratio of electrons (positrons and negatrons) to photons in showers made a long time ago near the shower core are displayed in Fig. 15.28. They are from the work of Green and Bracus (1962) obtained from an experiment at Abluquerque (NM), and from Lillicrap (1963) at Haverah Park. The prediction of the theory of Kamata and Nishimura (1958) is also indicated for comparison.

The density ratio of photons to electrons in showers as a function of core distance from the near core region out to 100 m was determined by Khristiansen et al. (1981b) at the Moscow site and is plotted in Fig. 15.29. Two sets of measurements are shown, one where the threshold energy was chosen at 50 keV, the other at 1.2 GeV.

Of some interest is the electrical charge ratio, i.e., the ratio of negatrons to positrons, e^-/e^+, in air showers as a function of particle energy. Experimental data

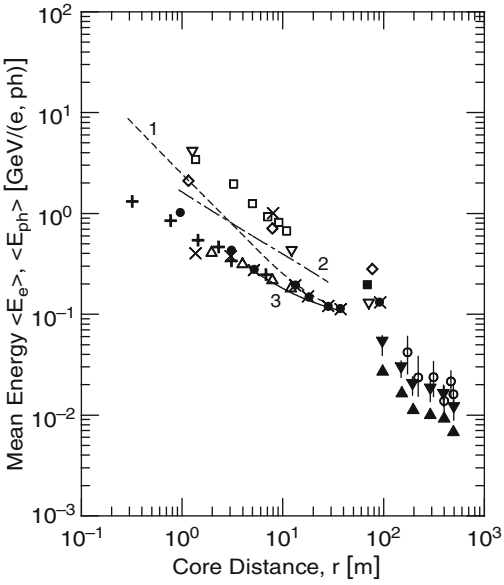

Fig. 15.26 Compilation of data on the mean energy carried by the electron-photon component per electron as a function of core distance, for showers of different size groups, N_e, or primary energies, E_0, at different altitudes. The symbols represent the following data: ▼ photons, ▲ electrons, in showers at Haverah Park with particle density $\rho(600)$ of $0.67\,\mathrm{m}^{-2}$ at a core distance of 600 m ($E_0 \simeq 4.7 \cdot 10^{17}$ eV) (Blake et al., 1978). □ electrons, $\langle N_e \rangle = 2.6 \cdot 10^6$; ■ electrons, $N_e > 10^7$; and ▽ photons (theoretical) at Tien Shan for an overburden of $680\,\mathrm{g\,cm}^{-2}$ (Aseikin et al., 1977a). ○ photons, $N_e = 2{\cdot}10^7$, at Haverah Park (Kellermann and Towers, 1970). ◇ electrons, $N_e = 2{\cdot}10^9$, at Chacaltaya (Escobar et al., 1963). △, +, ×, and • are for electrons at sea level, after Lillicrap et al. (1963), Fukui et al. (1960 and 1961), Dimitriev et al. (1959a, b), and Vernov et al. (1959), respectively. *Curve* (*1*) is the NKG function for $s = 1.0$ and $N_e = 10^5$, *curve* (*2*) shows the results from Mt. Norikura, Kaneko et al. (1962) and the Pamir mountains, Vavilov et al. (1964). These data are practically overlapping. *Curve* (*3*) is a fit to Vernov's data

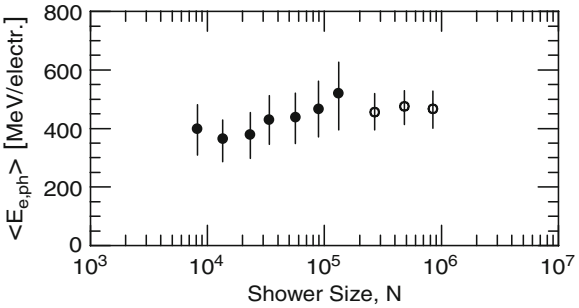

Fig. 15.27 Shower size dependence of the mean energy of the electron–photon component per electron at Tien Shan (3,340 m). Data points • are from the work of Machavariani et al. (1979), ○ from Aseikin et al. (1977a)

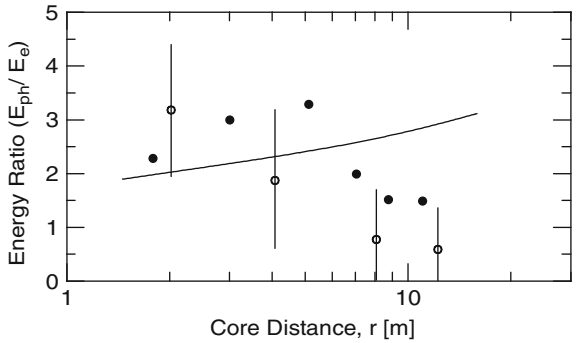

Fig. 15.28 Ratio of the energy carried by photons to that carried by electrons (positrons + negatrons) versus core distance. The symbols ○ identify the work of Lillicrap (1963) at Haverah Park, ● are after Green and Bracus (1962) at Albuquerque (NM). The *full curve* is based on the theory of Kamata and Nishimura (1958). The discrepancy between theory and experiment is probably due to the assumptions made for the interpretation of the data

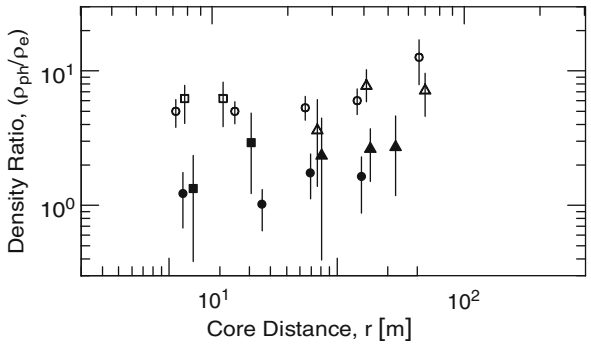

Fig. 15.29 Ratio of the detected photon to electron density recorded at Moscow (Khristiansen et al., 1981b). Open symbols (○, △, □) apply to an energy threshold of 50 keV, filled symbols (●, ■, ▲) to 1.2 GeV. In either set the squares are for showers with an average size of $\langle N_e \rangle = 7 \cdot 10^4$, the circles for $\langle N_e \rangle = 2.8 \cdot 10^5$ and the triangles for $\langle N_e \rangle = 2 \cdot 10^6$

of this ratio from measurements at Hongkong by Fong and Ng (1977) are illustrated in Fig. 15.30. Shown, too, in this figure are predicted integral ratios from calculations of Fujii and Nishimura (1970), and Guzhavin et al. (1968).

Geomagnetic effects on the bulk of the charged particles in showers are discussed in detail in connection with the lateral density distribution and azimuthal asymmetry of shower particles in Chap. 8. The same topic is of relevance for muons and is discussed in Chap. 14. For electrons, however, Coulomb scattering is more dominant than geomagnetic effects because of their shorter trajectories.

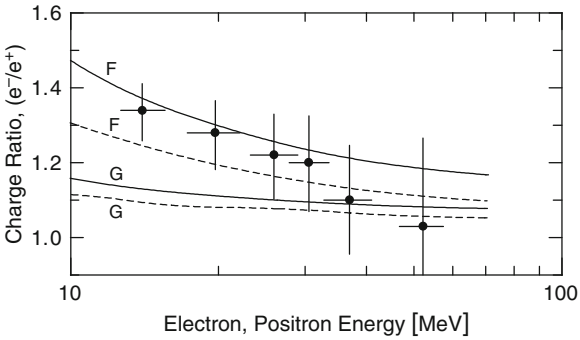

Fig. 15.30 Charge ratio of negatrons to positrons in small showers as a function of energy, determined with a magnetic spectrograph by Fong and Ng (1977) at Hong Kong. The energy represents the lower limit of the measured value. *F* and *G* refer to calculations by Fujii and Nishimura (1970) and Guzhavin et al. (1968), respectively. *Dashed curves* represent integral charge ratios. *Solid curves* are integral ratios with an upper energy limit of 80 MeV

15.5 Temporal Properties

Temporal properties of the bulk of shower particles are discussed in detail in Chap. 9, and of specific shower constituents, such as hadrons, muons and Cherenkov photons, in the respective chapters (Chaps. 13, 14 and 16). The usefulness of temporal properties of shower constituents with respect to mass composition is discussed in Chap. 10. We therefore present here only a small selection of some basic temporal features of the electronic component.

Some early but instructive data on the temporal distribution of the predominantly electronic component in showers are displayed in Fig. 15.31. This figure shows the distribution (dispersion) of the arrival time of electrons in the near core region of showers with respect to the arrival of the first muon from the work of Woidneck et al. (1971) at Kiel. The data sample includes showers from a wide range of sizes and confirms the presence of late particles, even close to the shower axis.

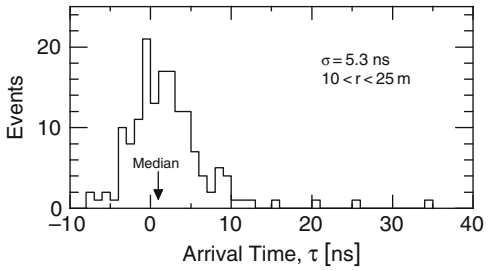

Fig. 15.31 Arrival time distribution of single electrons with respect to single muons in the lateral interval between 10 and 25 m from the core, in showers of size $10^4 \leq N_e \leq 10^7$ at sea level (Woidneck et al., 1971). The standard deviation of the distribution is 5.3 ns

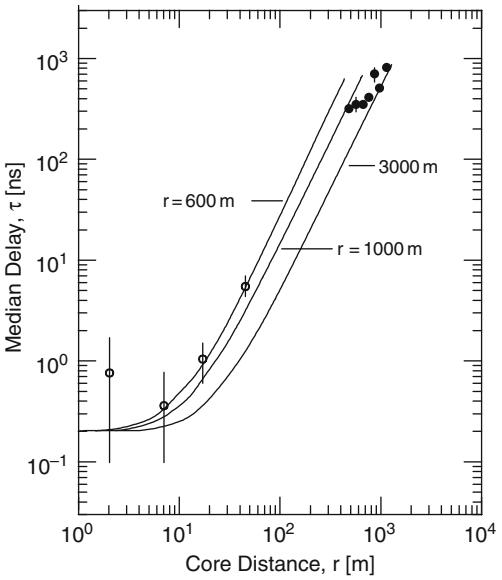

Fig. 15.32 Curvature of the electron disk of a shower. The data points ○ are from the work of Woidneck et al. (1971) at Kiel (s.l.) for showers with $10^4 \leq N_e \leq 10^7$ at sea level (cf. Fig. 15.31) and the symbols • identify the data from the Volcano Ranch (1,768 m a.s.l.) measurements of Linsley and Scarsi (1962) for large showers. The *solid lines* represent spheres of constant curvature. (See also Chap. 9)

The median delay of shower particles (predominantly electrons) as a function of core distance is illustrated in Fig. 15.32. Two set of experimental points are given, one from the work at Kiel for showers covering the size range $10^4 \leq N \leq 10^7$ (Woidneck et al., 1971) and from the pioneering work at Volcano Ranch for large showers (Linsley and Scarsi, 1962). The curvature of the shower front is evident from this figure and the radii of curvature for different shower sizes are indicated.

References

Aglietta, C., et al.: Nuovo Cimento C, 9, p. 262 (1986).
Aguirre, C., et al.: PICRC, 4, p. 2592 (1973).
Alexeyev, E.N., et al.: PICRC, 8, p. 2996 (1975).
Alexeyev, E.N., et al.: PICRC, 8, p. 52 (1977).
Allan, H.R., et al.: PICRC, 8, p. 3071 (1975).
Andrews, D., et al.: Acta Phys. Acad. Sci. Hung., 29, S3, p. 337 (1970).
Antoni, T., et al.: Astropart. Phys., 14, p. 245 (2001).
Antoni, T., et al: Nucl. Instr. Meth. A, 513, p. 490 (2003).
Antonov, R.A., et al.: PICRC, 9, p. 258 (1979a).
Antonov, R.A., et al.: PICRC, 9, p. 263 (1979b).
Antonov, R.A., et al.: PICRC, 6, p. 229 (1981).
Armitage, M.L., et al.: J. Phys. A, 6, p. 878 (1973a).

Armitage, M.L., et al.: J. Phys. A, 6, p. 886 (1973b).
Armitage, M.L., et al.: PICRC, 4, p. 2539 (1973c).
Aseikin, V.S., et al.: PICRC, 8, p. 2807 (1975).
Aseikin, V.S., et al.: PICRC, 8, p. 118 (1977a).
Aseikin, V.S., et al.: PICRC, 8, p. 98 (1977b).
Atrashkevich, V.B., et al.: PICRC, 8, p. 142 (1977).
Bagge, E.R., et al.: PICRC, 13, p. 260 (1979).
Bell, C.J., et al.: PICRC, 4, p. 2569 (1973).
Bertou, X. (Pierre Auger Collaboration): PICRC, 7, p. 1 (2005).
Blake, P.R., et al.: PICRC, 8, p. 2773 (1975).
Blake, P.R., et al.: J. Phys. G, 4, p. 617 (1978).
Bourdeau, M.F., et al.: J. Phys. G, 6, p. 901 (1980).
Bray, A.D., et al.: PICRC, 8, p. 2762 (1975).
Catz, Ph., et al.: PICRC, 12, p. 4329 (1975).
Coy, R.N., et al.: Astropart. Phys., 6, p. 263 (1997).
Diminstein, O.S., et al.: PICRC, 6, p. 47 (1981).
Dimitriev, V.A., et al.: Zh. Eksp. Teor. Fiz., 36, p. 992 (1959a).
Dimitriev, V.A., et al.: Sov. Phys. JETP, 9, p. 702 (1959b).
Dova, M.T., et al.: Astropart. Phys., 18, p. 351 (2003).
Escobar, I., et al.: PICRC, 4, p. 168 (1963).
Fong, S.W., and L.K. Ng: PICRC, 12, p. 120 (1977).
Fujii, M., and J. Nishimura: Acta Phys. Acad. Sci. Hung., 29, S3, p. 709 (1970).
Fukui, S., et al.: Prog. Theor. Phys. Jpn., 16, p. 1 (1960).
Fukui, S.: J. Phys. Soc. Jpn., 16, p. 604 (1961).
Glushkov, A.V., et al.: PICRC, 6, p. 233 (1997).
Green, J.R., and J.R. Bracus: Nuovo Cimento, 23, p. 708 (1962).
Greisen, K.: Progress in Cosmic Ray Physics, North Holland, Amsterdam, Vol. 3, p. 1 (1956).
Greisen, K.: Annual Review of Nuclear Science, Annual Reviews, Inc., Palo Alto, CA, Vol. 10, p. 63 (1960).
Grieder, P.K.F.: PICRC, 8, p. 326 (1977).
Guzhavin, V.V., et al.: Can. J. Phys., 46, p. S209 (1968).
Hara, T., et al.: PICRC, 13, p. 148 (1979).
Hillas, A.M., and J. Lapikens: PICRC, 8, p. 460 (1977).
Honda, K., et al.: Phys. Rev. D, 56, p. 3833 (1997).
Kamata, K., and J. Nishimura: Prog. Theor. Phys. Jpn., 6, Suppl., p. 93 (1958).
Kaneko, T., et al.: J. Phys. Soc Jpn., 17, Suppl. A-IV, p. 317 (1962).
Kaneko, T., et al.: PICRC, 8, p. 2747 (1975).
Kawaguchi, S., et al.: PICRC, 7, p. 2736 (1971).
Kawaguchi, S., et al.: PICRC, 8, p. 2826 (1975).
Kellermann, E.W., and L. Towers: J. Phys. A, 3, p. 284 (1970).
Khristiansen, G.B., et al.: PICRC, 6, p. 39 (1981a).
Khristiansen, G.B., et al.: PICRC, 6, p. 142 (1981b).
Kozlov, V.I., et al.: PICRC, 4, p. 2588 (1973).
Lagutin, A.A., et al.: PICRC, 7, p. 18 (1979).
Lagutin, A.A., et al.: PICRC, 6, p. 285 (1997a).
Lagutin, A.A., et al.: PICRC, 6, p. 289 (1997b).
Lagutin, A.A., et al.: Nucl. Phys. B (Proc. Suppl.), 60B, p. 161 (1998).
Lagutin, A.A., et al.: Nucl. Phys. B (Proc. Suppl.), 75A, p. 290 (1999).
Lagutin, A.A., and R.I. Raikin: Nucl. Phys. B (Proc. Suppl.), 97, p. 274 (2001).
Lillicrap, S.C., et al.: Proc. Phys. Soc., 82, p. 95 (1963).
Linsley, J., and L. Scarsi: Phys. Rev., 128, p. 2384 (1962).
Linsley, J.: PICRC, 4, p. 77 (1963).
Linsley, J.: PICRC, 5, p. 3212 (1973).

Linsley, J.: PICRC, 12, p. 56 (1977a).
Linsley, J.: PICRC, 12, p. 89 (1977b).
Machavariani, S.K., et al.: PICRC, 8, p. 240 (1979).
Miyake, S., et al.: Can. J. Phys., 46, p. S17 (1968).
Nagano, M., et al.: J. Phys. Soc. Jpn., 53, p. 1667 (1984a).
Nagano, M., et al.: J. Phys. G, 10, p. 1295 (1984b).
Nagano, M., et al.: Astropart. Phys., 13, p. 277 (2000).
Nishimura, J.: Handbuch der Physik, S. Flügge, ed., Springer Verlag, Berlin, Vol. 46/2, p. 1 (1967).
Plyasheshnikov, A.V., et al.: PICRC, 7, p. 1 (1979).
Porter, N.A.: PICRC, 5, p. 3657 (1973).
Risse, M., and D. Heck: Astropart. Phys., 20, p. 661 (2004).
Rossi, B., and K. Greisen: Rev. Mod. Phys., 13, p. 240 (1941).
Sakaki, N., et al.: PICRC, 1, p. 329 (2001a).
Sakaki, N., et al.: PICRC, 1, p. 333 (2001b).
Sakaki, N.: Ph.D. Thesis, Department of Physics, University of Yamanashi, Kofu, 400-8511, Japan (2003).
Takeda, M., et al.: Astropart. Phys., 19, p. 447 (2003).
Towers, L.: Ph.D. Thesis, University of Leeds (1971).
Toyoda, Y.: J. Phys. Soc. Jpn., 17, p. 3 (1962a).
Toyoda, Y.: J. Phys. Soc. Jpn., 17, p. 415 (1962b).
Tsushima, I., et al.: PICRC, 13, p. 189 (1979).
Uchaikin, V.V.: PICRC, 7, p. 24 (1979).
Vavilov, Yu.N., et al.: Trudi FIAN, 26, p. 17 (1964).
Vernov, S.N., et al.: Zh. Eksp. Teor. Fiz., 37, p. 1481 (1959) (in Russian).
Woidneck, C.P., et al.: PICRC, 3, p. 1038 (1971).
Yoshida, S., et al.: J. Phys. G, 20, p. 651 (1994).

Chapter 16
Atmospheric Cherenkov Radiation

Overview After a brief historic review the basic phenomenology and the fundamental physical process that are responsible for producing Cherenkov radiation in refractive media are explained, followed by the elementary theory of single particle Cherenkov radiation that covers the radiation yield and spectral features. Subsequently the phenomenology and theory of Cherenkov radiation in air showers are discussed, including characteristic features such as the lateral, temporal and spectral distribution of the photons, polarization aspects, the curvature of the light front and distribution substructures. The relation between the energy of the shower initiating primary and the optical observables at ground level are analyzed and the procedure to estimate the primary energy is outlined. The effects of the nature of the primary on the Cherenkov pattern, in particular of the mass if the primary is a hadron, are outlined and correlations between Cherenkov and particle observables are illuminated. Gamma ray astronomy is briefly touched and the technique of Cherenkov imaging is presented. These topics are followed by a discussion of the optical background, atmospheric light scattering, absorption and attenuation. The chapter ends with a compilation of data that cover the entire scope of experimental work, from the early stages to the present.

16.1 Introduction

In this chapter only general aspects and data of the optical Cherenkov signature of showers in the atmosphere are discussed. For more specific data concerning temporal features of the shower particles the reader is referred to Chap. 9, for topics related to the longitudinal development to Chap. 6, and for the determination of the depth (or height) of maximum development of showers and the elongation rate to Chap. 7, respectively.

Many of the early explorers of radioactivity noticed the bluish-white glow from transparent substances when placed in the neighborhood of strong radioactive sources (Curie, 1941). The first attempt to study the phenomenon was made by Mallet (1926, 1928, 1929). However, it was not until 1934 when Cherenkov began with systematic studies of the production of coherent radiation by the passage of relativistic particles through refractive media that the effect began to arouse the interest

P.K.F. Grieder, *Extensive Air Showers,* DOI 10.1007/978-3-540-76941-5_16,

of a broader scientific community (Cherenkov, 1934, 1936, 1937a, b, c, d, 1938a, b, c). (A brief historical review is given by Jelley, 1958a.)

A classical explanation of this effect was given by Frank and Tamm (1937) in terms of coherent emission from regions in which the passage of a particle with a velocity in excess of the phase velocity of light in the medium has caused transient polarization of the refractive medium. A more general treatment of the problem was carried out by Tamm (1939). Ginsburg (1940a, b) developed the quantum theory of the phenomenon, henceforth known as Cherenkov (Čerenkov) radiation, that is known to occur over certain regions of the electromagnetic spectrum, between the far ultraviolet and the radio frequency domain.

Blackett (1948) suggested that Cherenkov radiation at optical wavelengths must be produced by energetic cosmic ray particles in the atmosphere. First measurements with single particles in dense gases and later on in air at STP were made by Ascoli and Balzanelli (1953). Jelley and Gailbraith pursued Blackett's idea and suggested that the Cherenkov radiation produced by air showers of size $\geq 10^5$ particles might be detectable above the night sky optical background. In a subsequent experiment this radiation was discovered (Jelley and Galbraith, 1953; Galbraith and Jelley, 1953). Polarization measurements delivered proof beyond a shadow of doubt that it was in fact Cherenkov radiation.

After these pioneering efforts many more exploratory experiments followed by Jelley and co-workers at the Harwell site in England (Galbraith and Jelley, 1955; Jelley and Galbraith, 1955; Jelley, 1958b), by Russian workers at their Pamir station (3,860 m a.s.l.) (Nesterova and Chudakov, 1955; Chudakov and Nesterova, 1958; Chudakov et al., 1960), in the United States at Kitt Peak, Arizona (2,070 m a.s.l.) (Boley et al. 1961), in Australia (Brennan et al., 1958; Malos et al., 1962), and at many other sites. In the late sixties and early seventies more and more Cherenkov detection systems were integrated in air shower arrays for systematic studies, e.g., at Mt. Chacaltaya in Bolivia (5,230 m a.s.l.) (Krieger and Bradt, 1968, 1969) and Yakutsk, Siberia, near sea level (105 m) (Egorov et al., 1971a).

The initial work was aimed chiefly at the exploration of the lateral density distribution of the Cherenkov photons, i.e., at the photon lateral structure function (Zatsepin and Chudakov, 1962). Boley et al. (1962) studied the altitude dependence of the longitudinal distribution of atmospheric Cherenkov radiation by analyzing the temporal properties of the light pulse and carried out measurements in the Death Valley, CA (−46 m) and on White Mountain, CA. (3,801 m a.s.l.).

It was soon realized that the Cherenkov signal must contain much more information than had initially been anticipated (Malos et al., 1962; Sitte, 1962). Boley (1964) was one of the first to point out that the Cherenkov pulse time profile must image the longitudinal development of an air shower, making it a direct probe to explore the early history of the showers in the upper atmosphere and to investigate the longitudinal development of individual showers. It became evident that the integral of the Cherenkov light flash produced by a shower is in fact representative for the integral of the entire electron cascade through the atmosphere and a measure of the primary energy. Thus, it can be used for a particular kind of *calorimetry* to determine the

primary energy of a shower. For a summary of the early work the reader is referred to the review of Jelley (1967).

Today highly dedicated Cherenkov arrays and very sophisticated Cherenkov imaging systems are the backbone of high energy gamma ray astronomy. Many of the large new air shower laboratories employ Cherenkov arrays combined with particle detectors. Such installations record a multitude of simultaneous yet different observables of each individual shower that are recorded and permit to carry out extensive correlation studies that yield hitherto unrevealed information of the air shower process.

16.2 Phenomenology and Theory of Single Particle Cherenkov Radiation

16.2.1 Fundamental Physical Process

Whenever a charged particle moves at high velocity in a dielectric medium it causes a polarization that is symmetrical in the azimuthal plane but not along the axis of motion. There a dipole field results that extends to relatively large distances from the particle track. The wavelets of electromagnetic radiation emitted by the dipole transitions spread over a band of frequencies corresponding to the Fourier components of the polarization pulse. Normally the radiated wavelets from all parts of the track interfere destructively such that at a distant point the resulting field is zero.

However, if the velocity of the charged particle exceeds the phase velocity of light in the medium, the wavelets from all points of the particle track will be in phase with one another under a particular emission angle, θ, measured with respect to the direction of motion of the charge and combine to form a plane wave beyond a certain distance from their origin. According to Huygen's principle the coherent radiation from each element of track can only be observed at the particular angle θ with respect to the particle track. Because of the azimuthal symmetry the emission from an element of track propagates along the mantle of a cone whose semi-opening angle is θ and whose apex lies on the track (Fig. 16.1).

If $\beta = v/c$, where v is the velocity of the charged particle and c that of light in vacuum, and if n is the index of refraction of the medium in which the particle travels, the coherence condition, also known as the *Cherenkov relation*, can be written as

$$\cos(\theta) = \frac{1}{\beta n} \quad . \tag{16.1}$$

Considering the photon recoil action on the moving charged particle that causes a tiny deflection of the latter, Eq. (16.1) gets slightly modified and reads

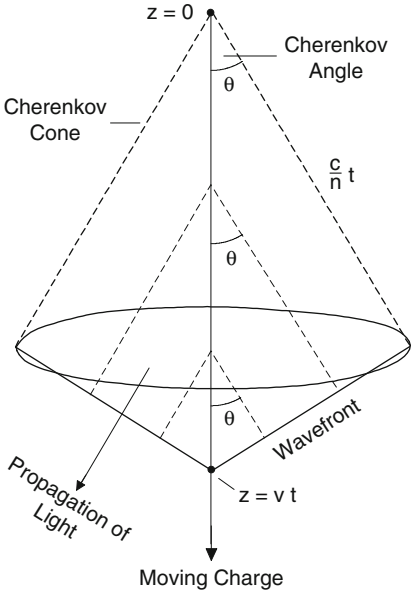

Fig. 16.1 Basic geometry of Cherenkov radiation phenomenon. Shown are the Cherenkov emission angle, θ, of a charged relativistic particle moving along the z-axis, the instantaneous position of the wavefront and the direction of propagation of the Cherenkov photons

$$\cos(\theta) \;=\; \frac{1}{\beta n} + \frac{\hbar k}{2p}\left(1 - \frac{1}{n^2}\right) \;. \tag{16.2}$$

Here, $\hbar k$ and p are the momenta of the photon and the moving charged particle, respectively, $k = 2\pi/\lambda$ and λ is the wavelength of the photon. θ is again the angle between the direction of the incident particle and the emitted photon. Since this correction is minute we will disregard it in the subsequent discussion.
From Eq. (16.1) the following important conclusions follow:

- For a given index of refraction n there is a *threshold velocity*

$$\beta_{\text{th}} \;=\; (1/n) \tag{16.3}$$

  below which no radiation is produced. At threshold the emission occurs in the direction of motion of the particle, i.e., the angle of emission, θ, is zero.
- For each medium there exists a distinct *maximum angle of emission*, $\theta_{\max}$, also called *Cherenkov angle*, that is reached at $\beta = 1$, i.e., in the ultra relativistic limit. Thus

$$\theta_{\max} \;=\; arc\cos(1/n) \;. \tag{16.4}$$

The energy dependence of the Cherenkov emission angle, θ, of electrons in air at different altitudes is plotted in Fig. 16.2.

- Since $|\cos(\theta)| \leq 1$, it follows from Eq. (16.1) that $1/\beta n \leq 1$. Rewritten one obtains $n \geq 1/\beta$. This expression is also valid for $\beta = 1$. Therefore the condition

$$n > 1 \tag{16.5}$$

must be fulfilled for the Cherenkov process to take place.

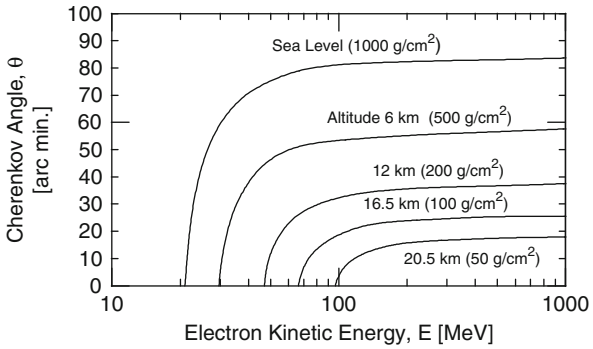

Fig. 16.2 Relation between Cherenkov emission angle θ in arc minutes and the kinetic energy of an electron at different altitudes in the atmosphere. The corresponding column density in $\mathrm{g\,cm^{-2}}$ is also indicated (after Jelley, 1958a)

Hence, Cherenkov radiation is produced only in media and at frequencies ω where $n(\omega) > 1$. This implies that it is predominantly produced in the visible and near visible part of the spectrum and only a small fraction of the radiated energy lies in the radio frequency region. Consequently *clear transparent dielectric media* are required to maximize the effect. X-ray emission via the Cherenkov mechanism is not possible because in these parts of the spectrum the condition $n < 1$ prevails (for details see Jenkins and White, 1937).

The emitted radiation is highly polarized with the electric vector everywhere perpendicular to the mantle of the cone, and the magnetic vector tangential. The distribution in θ is δ-function-like provided that the track length, l, of the particle in the medium is large compared to the emitted wavelength, λ. If this condition is not satisfied diffraction effects will distribute the radiation over an angle $\delta\theta \sim \lambda/l \cdot \sin(\theta)$. In addition, to achieve coherence the velocity of the particle must remain constant while passing through the medium.

In other words the differences in the times for a particle to traverse successive distances must be small compared with (λ/c). Moreover, the medium must be homogeneous and have a constant index of refraction. Dispersion, diffraction, Coulomb scattering, radiation reaction and the finite length of the medium contribute to broaden the width of the conical shape of light emerging from the track.

These effects are also responsible that there is no sharp cut-off of the light intensity at the threshold when $\beta n = 1$.

16.2.2 Radiation Yield and Spectral Distribution

The energy loss of a fast charged particle due to Cherenkov radiation when traversing a medium can be derived classically (Frank and Tamm, 1937) or quantum-mechanically (Ginsburg, 1940a; Sokolov, 1940; Beck, 1948; Schiff, 1955; Taniuti, 1951; Neamtan, 1953; Tidman, 1956a, b). Either method yields essentially the same result, the differences are extremely small (Cox, 1944). Effects due to the spin of the moving particle were considered by Sokolov and Loskutov (1957). For the classical derivation that is fully adequate for most applications of the Cherenkov effect one gets for the energy $\mathrm{d}E$ radiated per unit path element $\mathrm{d}l$ the expression

$$\left(\frac{\mathrm{d}E}{\mathrm{d}l}\right)_{\mathrm{Ch}} = 4\pi \left(\frac{ze}{c}\right)^2 \int_{\beta n>1} \left(1 - \frac{1}{\beta^2 n^2}\right) \cdot \omega \mathrm{d}\omega \ \ [\mathrm{eV/cm}] \tag{16.6}$$

where ze is the charge of the particle, and ω the angular frequency of the emitted radiation. Without a frequency cut-off the integral diverges. However, limits on the range of integration are imposed by the finite size of the electron and the fact that the integral is valid only for frequencies where $\beta n \geq 1$, which keep it from diverging.

To get an order of magnitude of the Cherenkov radiation yield we approximate $n^2(\omega)$ according to Sommerfeld (1954) by

$$n^2(\omega) = 1 + \left(\frac{A}{\omega_0^2 - \omega^2}\right) \tag{16.7}$$

$$n^2(0) = \epsilon = 1 + \left(\frac{A}{\omega_0^2}\right) \ , \tag{16.8}$$

where ω_0 is the frequency of the first resonance in the spectrum. Substituting Eqs. (16.7) and (16.8) into Eq. (16.6) we obtain the following approximate expression for the energy loss per unit path length of a highly relativistic particle

$$\left(\frac{\mathrm{d}E}{\mathrm{d}l}\right)_{\mathrm{Ch}} = \frac{1}{2}\left(\frac{e\omega}{c}\right)^2 (\epsilon - 1) \ln\left(\frac{\epsilon}{\epsilon - 1}\right) \ . \tag{16.9}$$

Typically $\omega_0 = 6 \cdot 10^{15}\ \mathrm{s}^{-1}$, so that $\mathrm{d}E/\mathrm{d}l$ is of the order of a few keV/cm. In comparison to the energy losses by ionization and excitation, the energy loss through Cherenkov radiation is almost negligible and amounts to only about 0.1% of the energy loss by ionization for a relativistic particle.

Equation (16.6) can readily be converted to yield the number of photons, N_{ph}, radiated along a path of length l. We then obtain

$$N_{\mathrm{ph}} \;=\; 2\pi z^2 \alpha l \left(\frac{1}{\lambda_1} - \frac{1}{\lambda_2}\right) \cdot \left(1 - \frac{1}{\beta^2 n^2}\right) \quad , \tag{16.10}$$

where z is the charge of the particle, α is the fine-structure constant ($\alpha = e^2/\hbar c = 1/137$) and n the average index of refraction of the Cherenkov medium. With the help of Eq. (16.1) we can rewrite Eq. (16.10) which then takes the form

$$N_{\mathrm{ph}} \;=\; 2\pi z^2 \alpha l \left(\frac{1}{\lambda_1} - \frac{1}{\lambda_2}\right) \cdot \sin^2(\theta) \quad . \tag{16.11}$$

As an example a relativistic electron in a slab of glass with refractive index $n = 1.5$ produces about 200 photons/cm in the visible portion of the spectrum (∼400–750 nm). In air it is about $8.2 \cdot 10^3$ photons/radiation length or 30 ph/m at sea level between 350 and 500 nm. Since $\mathrm{d}E/\mathrm{d}l$ is proportional to $1/\lambda$, the energy loss per unit wavelength is proportional to $1/\lambda^2$. This explains why Cherenkov radiation is emitted predominantly at short wavelength, giving it a bluish hue.

In air at sea level, the refractive index is $n = 1.00029$. From this one obtains for the Cherenkov threshold energy of an electron $E_{\mathrm{th}} = 21$ MeV and a maximum Cherenkov emission angle of $\theta_{\mathrm{max}} = 1.3^\circ$. The rate of Cherenkov photon production of an electron of energy well above threshold is per unit path length, $\mathrm{d}N/\mathrm{d}l$, in this medium approximately 0.3 photons/cm in the wavelength interval between 400 and 500 nm. The comparative figures in water are $n = 1.33$, $E_{\mathrm{th}} = 260$ keV, $\theta_{\mathrm{max}} = 41^\circ$ and $\mathrm{d}N/\mathrm{d}l = 250$ photons/cm.

For Cherenkov applications in connection with air showers we are dealing with a variable index of refraction, depending on the atmospheric depth and the local air density where the process takes place. To compute the index of refraction as a function of atmospheric depth, X [g cm^{-2}], and temperature T [K], the following expression can be used

$$n(X,T) \;=\; 1.0 + 0.00029 \left(\frac{X}{1030}\right) \left(\frac{273.2}{T}\right) \quad , \tag{16.12}$$

and for T one can write $T = 204 + 0.091X$ (Hillas, 1982).

The spectral distribution of the Cherenkov radiation can be expressed in various ways as summarized below (Jelley, 1958a).

$$\frac{\mathrm{d}^2 E}{\mathrm{d}l \; \mathrm{d}\omega} \;\propto\; \omega \tag{16.13}$$

Energy per unit path per unit frequency interval.

$$\frac{\mathrm{d}^2 E}{\mathrm{d}l \; \mathrm{d}\lambda} \;\propto\; \lambda^{-3} \tag{16.14}$$

Energy per unit path per unit wavelength interval.

$$\frac{\mathrm{d}^2 N_{\mathrm{ph}}}{\mathrm{d}l\ \mathrm{d}\omega} \ \text{const.} \tag{16.15}$$

Number of photons per unit path per unit frequency interval.

$$\frac{\mathrm{d}^2 N_{\mathrm{ph}}}{\mathrm{d}l\ \mathrm{d}\lambda} \propto \lambda^{-2} \tag{16.16}$$

Number of photons per unit path per unit wavelength interval.

16.3 Phenomenology and Theory of Cherenkov Radiation in Air Showers

16.3.1 Comments on Theoretical Studies

In this section we consider the superposition and resulting effects of the Cherenkov radiation produced by the large number of electrons and positrons of the electromagnetic cascade of a shower along its trajectory through the atmosphere. These particles which are the chief contributors to the Cherenkov light produced in a shower are laterally scattered and distributed over a large volume in the atmosphere, around the shower axis.

Early calculations to explore Cherenkov radiation in air showers were based on analytical methods that were superseded in the sixties by computer simulations. The first major theoretical treatment of the Cherenkov phenomenon in air showers that included the lateral distribution of Cherenkov light was carried out by Gol'danskii and Zdanov (1954), after a previous one-dimensional attempt by Jelley and Galbraith (1953). Subsequently extensive three-dimensional studies using analytical and simulation methods were made by Chudakov and Nesterova (1958), Sitte (1962), Zatsepin and Chudakov (1962), Zatsepin (1964, 1965), and others.

Fomin and Khristiansen (1971) were among the first to explore systematically the temporal behavior of the Cherenkov light pulse produced by showers in the atmosphere with the help of simulation calculations. This work was followed by numerous contributions of experimental and theoretical nature from other groups. Table 16.1 taken from a paper of Protheroe and Turver (1979) and extended by the author gives an overview of the major theoretical efforts made by many individuals and groups working in this field during the exploratory phase of this technique.

An important step forward in the development of the air Cherenkov method was made by Orford and Turver (1976) who carried out an analysis that was based primarily on rigorous four-dimensional computer simulations, followed up by a series of experiments, that went beyond the usual technique. Previously, Cherenkov light measurements of extensive air showers were aimed at recording the gross features of the light flux on the ground, using an approach similar to the classical array-based particle detection. Orford and Turver have gone further and used precise measurements of the detailed shape of the Cherenkov light pulse recorded by several well

Table 16.1 Overview of early air Cherenkov calculations

Reference	Primary		θ Zenith deg.	Obs. level km	Opt. atten.	Lat. dis.	Ang. dis.	Temp. Str.
	Mass[a]	Energy eV						
Gol'danskii et al. (1954)	–	–	0	–	–	√	–	–
Jelley and Galbraith (1955)	0; 1	10^{12}–10^{16}	0	0; 2.9	–	√	–	–
Sitte (1962)	–	–	2.5–20	–	–	√	√	–
Zatsepin and Chudakov (1962)	0; 1	10^{11}–$4.5 \cdot 10^{15}$	0	0; 3.9	–	√	–	–
Zatsepin (1964, 1965)	0; 1	10^{12}–$4.5 \cdot 10^{15}$	0	0; 3.9	–	√	√	–
Castagnoli et al. (1967)	0	10^{12}–10^{14}	0	0; 3.5; 6.5	–	√	–	√
Krieger and Bradt (1969)	1	10^{15}–10^{17}	0	5.2	–	√	–	–
Sitte (1970)	–	–	–	–	–	–	–	√
Rieke (1970)	0	10^{11}	0–60	2.3	–	√	√	√
Fomin and Khristiansen (1971)	1–50	10^{17}	0	0	–	–	–	√
Bosia et al. (1972)	0	10^{11}–10^{14}	10	0; 3.5	–	–	√	√
Castagnoli et al. (1972)	0	10^{11}–10^{12}	0	2.3	–	√	√	√
Smith and Turver (1973a)	1	10^{15}–10^{18}	0	0	√	√	–	–
Dyakonov et al. (1973b)	0	10^{16}–10^{18}	0	0	√	–	–	–
Efimov et al. (1973)	1	10^{17}	0	0	–	–	–	√
Grindlay (1974)	≥ 1	$\geq 10^{12}$	0	2.3	–	√	√	–
Guzhavin et al. (1975b)	1	10^{12}–10^{16}	0	0; 3.9	–	√	–	√
Kalmykov et al. (1975)	1–52	10^{17}	0	0	–	–	√	–
Protheroe et al. (1975)	1	10^{17}	0	0	√	√	√	√
Ivanenko et al. (1976)	0	10^{12}–10^{17}	0	0	–	√	–	√
Browning and Turver (1977)	0	10^{10}–$3 \cdot 10^{11}$	0	2.4	√	√	√	√
Hara et al. (1977)	0; 1	10^{15}–10^{18}	0	0	√	√	√	√
Hammond et al. (1978)	1; 4; 56	10^{16}–10^{18}	0	0; 1.8	√	√	√	√
Protheroe and Turver (1979)	1; 4; 56	10^{16}–10^{18}	0	0; 1.8	√	√	√	√
Ivanenko et al. (1979a, b)	1	10^{17}–10^{18}	16	0	–	√	–	√
Makarov et al. (1981)	1	10^{15}–10^{16}	0	0	–	√	–	√
McComb and Turver (1981)	56	10^{15}–10^{18}	0–60	0; 1.8	√	√	√	√
McComb and Turver (1982)	56	10^{15}–10^{17}	0–60	0; 1.45	√	√	√	√
Patterson and Hillas (1983a, b)	1	10^{15}–10^{17}	0–40	0	√	√	–	√
Bernlöhr (2000)	0	10^{11}	0–80	0–20	√	√	√	√
Aglietta et al. (2004)	1; 4; CNO	$4 \cdot 10^{13}$–$3 \cdot 10^{14}$	0; 35	2	√	√	√	√

[a] Mass 0 stands for γ rays.

spread simple optical detectors to reconstruct accurately an image of the Cherenkov light, thus introducing the important new field of *Cherenkov imaging of air showers*.

The experimental work was focused on showers of primary energy $\geq 10^{17}$ eV and required signals from at least six detectors located at distances between 100 and 600 m from the shower axis. No particle density measurements were used to define the events. The measurements included the exact timing within ± 2 to ± 3 ns of the occurrence of the light levels of 10, 50 and 90% of the full pulse height on the rising and falling edges. The correlation between the height of origin of the observed light and the time of the various signal levels of the rising and falling edges of the pulse was obtained from computer simulations.

In an attempt to illuminate the basic sensitivity of the Cherenkov light pulse of an air shower with respect to the longitudinal shower development, Hillas (1982) has used a highly simplified shower model. He first considered one-dimensional showers in which the charged particles propagate along the axis and studied the lateral and temporal photon distributions. The concept is illustrated in Fig. 16.3a for a vertical shower and the resulting pulse shape as observed by a detector at some distance, r, from the shower axis is plotted in Fig. 16.3b. The locations of the light contributions thus obtained from the different altitude regions, h_n, along the shower track in the overall light pulse profile observed at the detector are identified in this figure.

The lateral density distribution resulting from this simplified analysis is shown in Fig. 16.4a. The Cherenkov ring effect is evident. It is due to the fact that the Cherenkov angle varies with altitude because of the changing air density and index of refraction. At high altitude when the index of refraction is very close to unity the angle of emission is small. It then grows with increasing air density and so does the emission angle. This is shown in Fig. 16.3a. When scattering of the particles about the shower axis is included the Cherenkov ring effect is much less pronounced, which is illustrated in Fig. 16.4b.

The Cherenkov light yield per charged particle per g cm^{-2} in an average 10^{16} eV proton initiated shower as a function of vertical atmospheric depth (or altitude) at different radial distances from the shower axis, including particle scattering, is illustrated in Fig. 16.5. The distributions are typical and vary little with primary energy for large showers.

This work eventually lead to the full understanding of the power and insight which optical Cherenkov radiation associated with air showers offers to carry out three- and four-dimensional investigations on individual showers, and to study the hitherto inaccessible longitudinal development as well. The latter is intimately linked to the energy and nature of the primary particle and identifies the depth (or height) of maximum development of a shower. Moreover, the initial portion of the longitudinal profile of a shower is linked to the height of the first interaction of the primary in the atmosphere and holds information on the interaction cross section; it may even reveal its energy dependence at ultrahigh energies.

The ultimate aim of this work is to extract the mass composition of the primary cosmic radiation in the energy region that is inaccessible to direct measurements (see Sect. 11.7). The key observable to obtain the needed information from a shower

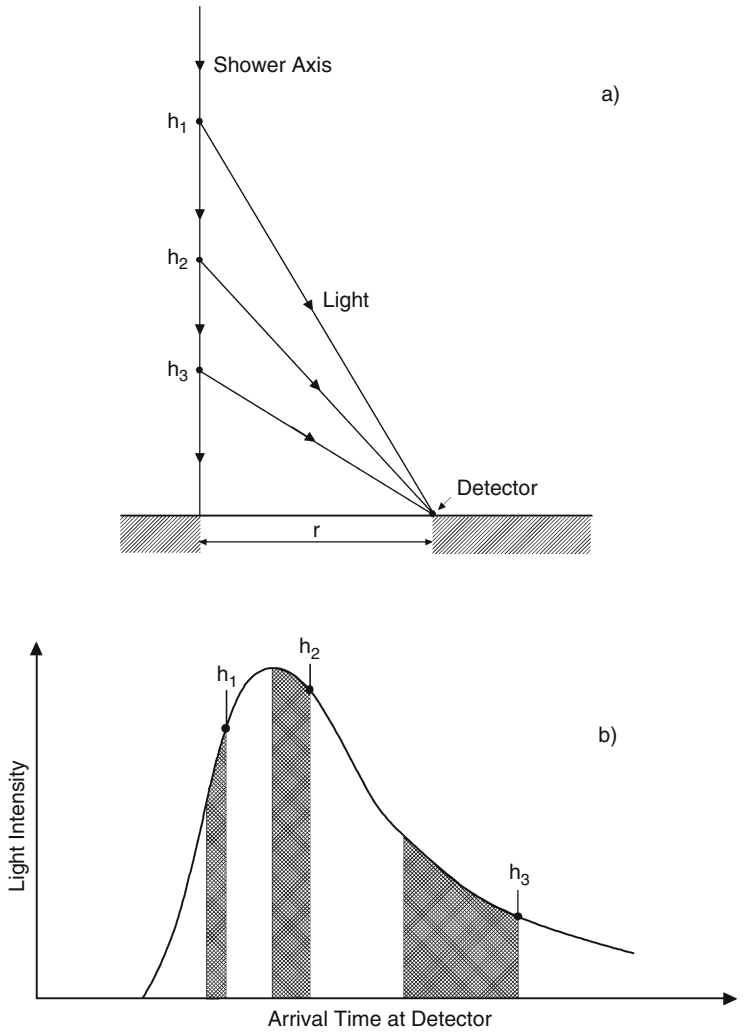

Fig. 16.3 (**a**) Simplified model of Cherenkov light emission in a hypothetical one-dimensional air shower where the particles propagate along the axis, neglecting any lateral spread. The Cherenkov emission angles are grossly exaggerated in this figure. (**b**) Overall Cherenkov light pulse received at the detector and contributions from regions of definite altitudes along the shower trajectory as indicated in (**a**) (after Hillas, 1982)

is the depth of maximum development of a shower, $X_{\max}$, discussed in Chap. 7. It is evident that this goal can only be achieved in conjunction with detailed computer simulations for the interpretation of the experimental data.

In the following sections of this chapter we only discuss general aspects of optical Cherenkov bursts associated with extensive air showers. Details concerning the determination of $X_{\max}$ are treated in Chap. 7, and Sect. 11.7 deals with the primary mass composition.

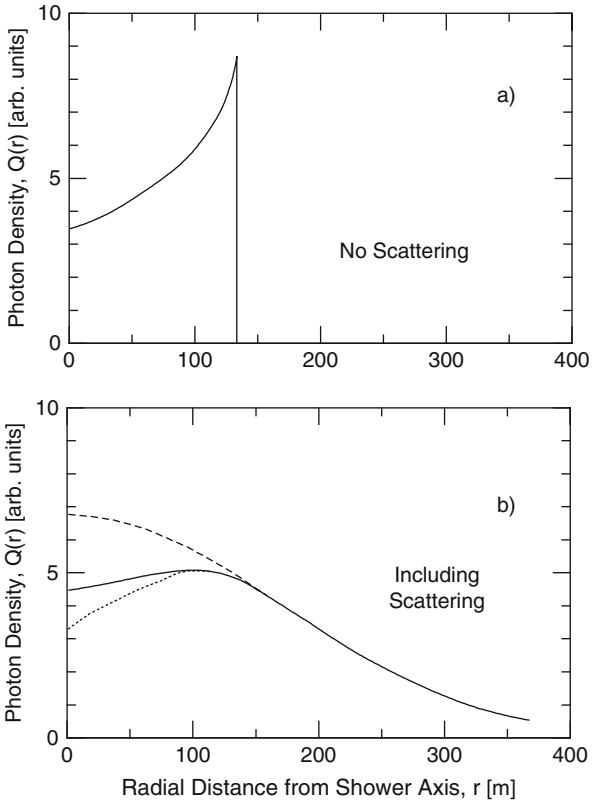

Fig. 16.4 (**a**) Lateral photon density distribution of Cherenkov radiation resulting from charged particles that propagate along the shower axis with scattering disregarded. The Cherenkov ring effect is evident. (**b**) Lateral distribution when the particles are subject to scattering about the axis. The ring effect is dramatically reduced (*solid curve*). For low developing showers the ring effect essentially disappears (*dashed curve*) and vice versa (*dotted curve*) (after Hillas, 1982)

16.3.2 Lateral and Angular Distribution

Parallel to the pioneering work discussed above, early systematic studies of the optical Cherenkov radiation of very large showers were carried out by Krieger and Bradt (1969) at Mt. Chacaltaya and subsequently mostly by the Yakutsk (Egorov et al., 1971b; Efimov et al., 1973; Dyakonov et al., 1973a, b; Glushkov et al., 1979), and Durham (GB) groups (Smith and Turver, 1973a, b; Orford and Turver, 1976). Initially the interest was focused mainly on the lateral (radial) density distribution of the photons with respect to the showers axis.

This work was chiefly motivated by the results of refined computer simulations of air showers which indicated that Cherenkov photons that are generated everywhere in a shower by relativistic electrons, from the first interaction of the primary high in the atmosphere to the observer on the ground, may carry valuable information of the entire shower development and its history, in space and time. It was realized that the

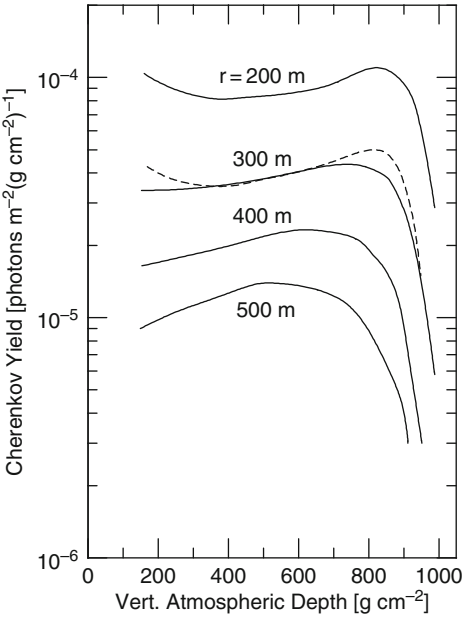

Fig. 16.5 Cherenkov light yield, $(\mathrm{d}Q/\mathrm{d}X)/N_e(X)$ per charged particle per g cm^{-2} as a function of vertical depths in an average 10^{16} eV proton initiated vertical shower at a detector at different radial distances from the shower axis. The *dashed curve* is for a zenith angle of 30° (after Hillas, 1982)

photons hold the key to access the information needed to reconstruct the longitudinal development of individual showers that would allow eventually to reveal the mass (or mass group) of the primary initiating the shower and, hopefully, may also shed some light on the energy dependence of the inelastic nucleon-nucleus and nucleus–nucleus cross sections. These speculations have proved to be correct.

It was found that the lateral distribution of the intensity of optical Cherenkov emission in a shower is sensitive primarily to the distance between the location of the maximum development of a shower and the observer, measured along the shower axis, and also to the shape of the shower profile for marked deviations from normal. These properties make this observable one of the prime candidates for investigating the longitudinal development of showers and to determine the location of the depth of shower maximum in the atmosphere, a topic discussed in detail in Chap. 7.

Near the axis in smaller showers ($\leq 10^{15}$ eV) the information is contained in the slope of the lateral distribution expressed by the ratio of the intensities at 50 and 150 m, i.e., by $Q(50)/Q(150)$, in the shower plane. In view of the fact that there is an increased sensitivity to late development fluctuations and changes of the aerosol contents in the atmosphere, measurements should be made preferably on near vertical showers for low energy events.

In their initial work the Durham group (Hammond et al., 1978; Protheroe and Turver, 1979) found that the lateral density distribution of photons in the Cherenkov light pulse of showers could be adequately described by the following simple power law

$$Q(r) \sim r^{\gamma} \quad . \tag{16.17}$$

In later papers, after it was established that the slope of the distribution increases with increasing primary energy and decreases with increasing zenith angle, confirming that the distribution depends on the distance between the detector and the shower maximum, the following slightly modified form had been introduced by McComb and Turver (1982) to account for the leveling off of the distribution near the shower axis ($\simeq$100 m) and to allow for larger front curvature

$$Q(r) \propto (r + r_0)^{\eta} \quad . \tag{16.18}$$

On the other hand, some authors found that for the lateral distribution function an exponential expression of the form given below gave a satisfactory fit (Kuhlmann et al., 1977; Kuhlmann and Clay, 1981; Andam et al., 1979; Tornabene, 1979)

$$Q(r) \propto \exp(-br) \quad . \tag{16.19}$$

The parameter b shows the same general behavior as γ and η of Eqs. (16.17) and (16.18) above.

In Fig. 16.6a, b we show the lateral density distribution of Cherenkov photons in simulated showers of primary energy 10^{15}, 10^{16} and 10^{17} eV for different

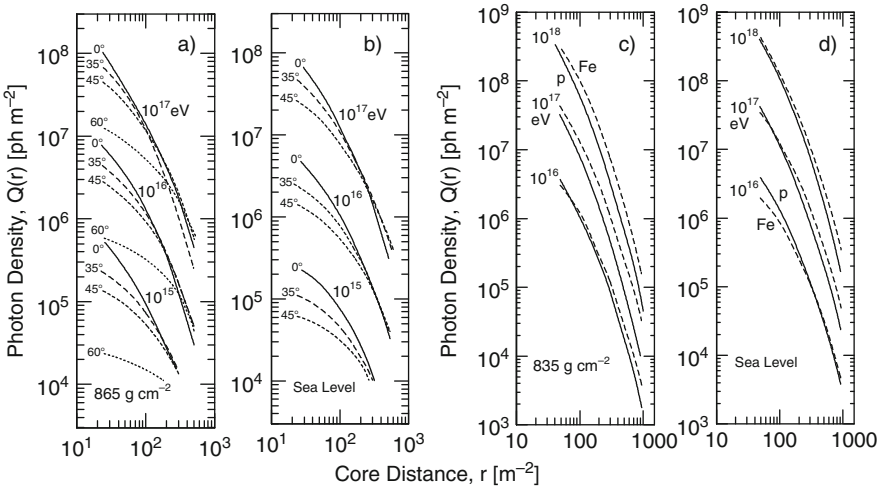

Fig. 16.6 Optical Cherenkov photon density as a function of core distance in simulated 10^{15}, 10^{16} and 10^{17} eV proton initiated air showers at an atmospheric depth of 865 g cm^{-2} (Dugway site, (**a**)) and at sea level (**b**), for different zenith angles (McComb and Turver, 1982). Lateral distribution of atmospheric Cherenkov photons in simulated air showers initiated by 10^{16}–10^{18} eV primary protons (*solid curves*) and iron nuclei (*dashed curves*) at observation levels of 835 g cm^{-2}, (**c**), and sea level, (**d**), after Hammond et al. (1978)

zenith angles, and two observation levels (865 g cm^{-2} and sea level) from a calculation of McComb and Turver (1982). The primary mass dependence of the lateral distribution was calculated by Hammond et al. (1978) and is illustrated in Fig. 16.6c, d.

16.3.3 Temporal Properties and Pulse Shape

(a) General Comments

After an initial attempt by Boley et al. (1961) to extract details of the longitudinal development of showers from the Cherenkov pulse, Fomin and Khristiansen (1971), Kalmykov et al. (1971) and Efimov et al. (1973) were among the first to explore systematically the temporal features of the atmospheric Cherenkov light pulse theoretically as well as experimentally. Subsequent theoretical studies (see Table 16.1) revealed that the temporal properties of the Cherenkov pulse represents a *less ambiguous* signature of the history of a shower than the lateral structure function (see Chap. 7).

The theoretical work was followed up by countless experimental efforts that finally established the air Cherenkov method as an invaluable tool for detailed air shower studies and, above all, high energy gamma ray astronomy ($E_\gamma \geq 10^{11}$ eV) (Weekes, 1988; Ong, 1998; Catanese and Weekes, 1999; Weekes, 2003).

(b) Arrival Time Distribution

Hammond et al. (1978) derived the following expression for the propagation time $t(h, r)$ [s] of a photon emitted from the core region of a vertical shower at altitude h [m] to reach ground level at a distance r [m] from the shower axis, considering the changing index of refraction of the atmosphere with altitude.

$$t(h, r) \simeq \frac{\sqrt{h^2 + r^2}}{c} \left\{ 1 + \frac{h_s}{h}(n_\circ - 1)(1 - \exp[-h/h_s]) \right\} \text{ [s]} , \qquad (16.20)$$

where h_s is the atmospheric scale height [m] and $n_\circ$ the index of refraction of air at sea level.

Figure 16.7, taken from the work of Hammond et al. (1978), illustrates the temporal relation of the photons in a shower using a simple geometrical model which, however, includes refractive index effects. Shown is the arrival time delay at different radial distances from the shower axis of photons originating from different altitudes with respect to photons originating at an altitude of 1 km.

Ascribing a thickness to the photon disk and using a similar shower geometry, one can also compute the Cherenkov pulse width for a particular detector location

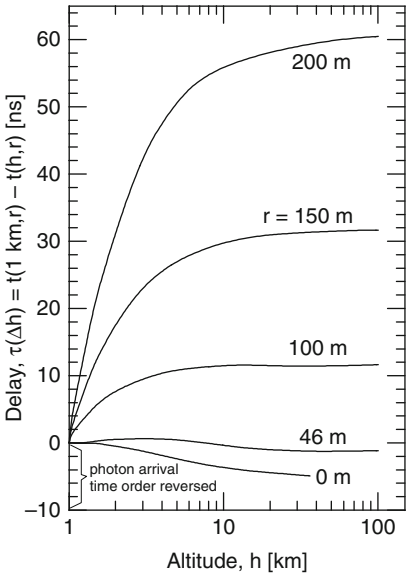

Fig. 16.7 Time delay, $\tau(\Delta h)$, of light originating at an altitude of 1 km with respect to that originating from a height of h km, as a function of h for different radial distances from the shower axis. The calculation is based on a simple geometrical model and allows for refractive index effects and path length differences (after Hammond et al., 1978)

and the Cherenkov light front curvature (for details see Guzhavin et al., 1975a; Khristiansen, 1980).

(c) Light Pulse Shape and Cherenkov Substructures

A typical example of the shape of the Cherenkov light pulse of a simulated average 10^{17} eV proton initiated shower, as seen by a detector located at 300 m from the axis, is shown in Fig. 16.8a, curve 1. The corresponding longitudinal development of its parent electron cascade in the atmosphere from which the Cherenkov pulse was computed is shown in Fig. 16.8b, curve 1. Illustrated, too, are the major electron sub-cascades in this shower, numbered 2–9, resulting from high energy gamma rays, chiefly from neutral pion decays. The corresponding optical sub-pulses that add up to form the overall Cherenkov light pulse are identified in Fig. 16.8a (Hammond et al., 1978).

It is evident from these figures that the earliest light arriving at the detector originates high in the atmosphere and the pulse shape is clearly a direct measure of the cascade development. Further steps of the analysis are based on the assumption that the light at a certain point in each pulse originates from a particular location in the atmosphere and generates a spherical light front.

Large fluctuations in the hadron cascade cause fluctuations in the neutral pion production and thus in the distribution of the electron sub-cascades and Cherenkov

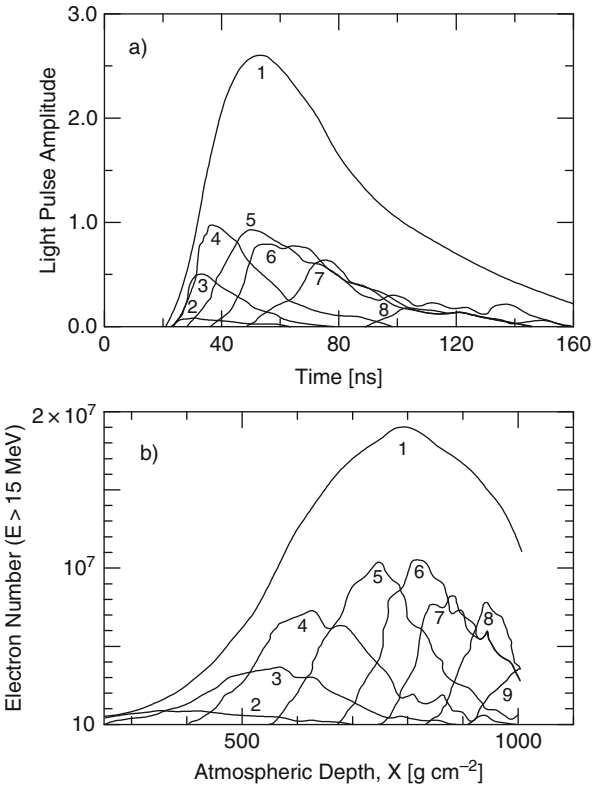

Fig. 16.8 (**a**) Atmospheric Cherenkov light pulse shape at 300 m from the axis of this shower (*curve 1*). The light sub-pulses arising from the electron sub-cascades shown in (**b**) are also plotted in (**a**) and correspondingly numbered. They reveal their origin in time in the electron cascade. The pulse widths are much narrower near the shower axis and arrive early, whereas they broaden rapidly with increasing core distance and arrive delayed (Orford and Turver, 1976). (**b**) Longitudinal development of the electron component ($\geq$ 15 MeV) in an average simulated 10^{17} eV proton initiated air shower (*curve 1*). Also shown are the eight major electron sub-cascades, numbered *2–9*, in this shower that are the chief contributors which sum up to make the overall shower

bursts along the shower trajectory that may manifest themselves at the detectors in the form of substructures in the overall Cherenkov light pulse.

Studies of theoretical and experimental nature on the substructures of atmospheric Cherenkov light pulses of air showers were carried out by many authors (e.g., Bosia et al., 1980). Böhm et al. (1977) cautioned that using narrow angle focusing mirrors on larger showers may cause problems for the data interpretation because at larger distances from the shower axis such detectors may sample the lateral structure of showers rather than their longitudinal profile, particularly when the showers are inclined. A detailed discussion of the temporal features and shape variations of the Cherenkov pulse in connection with the longitudinal development of the showers and the resulting implications is given in Chap. 7.

16.3.4 Light Front Curvature

Light front curvature studies had been carried out by several authors (Orford et al., 1975a, b; Protheroe et al., 1975; Andam et al., 1979). The Cherenkov technique allows to measure accurately the time of arrival of the first photons in the shower front. After properly correcting for time delays in the detector system, it is possible to fit a front of spherical curvature to the arrival time distribution of the first light. By simultaneously optimizing the radius of curvature of this spherical shell and the zenith and azimuthal angles which specify the shower arrival direction, a best fit may be obtained.

Radii resulting from this procedure are rather small, around 3 km. This is partly because at larger core distances the main contribution to the Cherenkov light pulse comes from scattered particles away from the axis, whose trajectory subtends an angle with respect to the shower axis that exceeds by far the Cherenkov angle in air. Further details concerning the Cherenkov light front curvature are given in Chap. 7, in conjunction with the determination of the depth of maximum development of the showers and in Chap. 9.

Generally speaking it is difficult to define a definite radius of curvature for the Cherenkov light disk over a larger radial distance from the shower axis for the reason just mentioned. From arrival delay measurements of the light with respect to the tangent plane of the shower it is found that the light front has rather a parabolic than a spherical shape, reflecting the fact that the photons arriving at different radial distances from the shower axis originate from different locations in the shower both, longitudinally and laterally.

16.3.5 Spectrum and Polarization of Cherenkov Light

The spectrum of the optical and near ultraviolet components of the Cherenkov emission in air showers ($250 \leq \lambda \leq 600$ nm) had been investigated by Protheroe and Turver (1979). The spectral distributions of the light in an average proton shower of primary energy 10^{17} eV had been computed by these authors for locations in the shower axis and at radial distances of 100 and 900 m from the axis at sea level, including absorption. The latter was computed on the basis of the data of Elterman and Toolin (1965) and Elterman (1968). The results are shown in Fig. 16.9.

The polarization of the Cherenkov light in air showers was studied theoretically, using simulations, and experimentally, on large showers (10^{17} eV) by McComb et al. (1979). These authors find good agreement between theory and measurements. They find that the maximum polarization of up to about 35% occurs at core distances around 125 m and is in the plane containing the shower axis and the detector. Light at large distances from the core (~ 600 m) is not polarized. They did also study the dependence of the polarization as a function of depth of shower maximum and note that a difference in the depth of maximum of 100 g cm^{-2} affects the polarization by only $\sim 5\%$. Some of the results of this work are illustrated in Fig. 16.10.

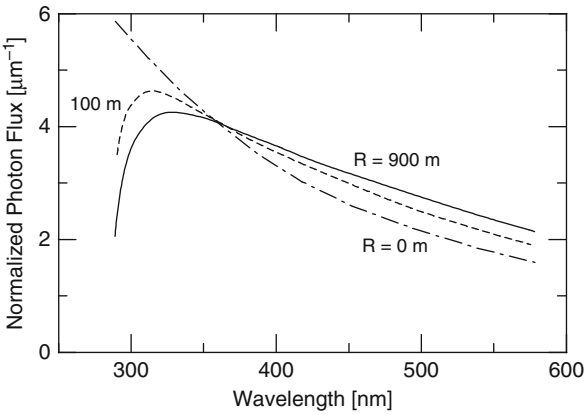

Fig. 16.9 The wavelength spectrum of Cherenkov light in an average 10^{17} eV proton initiated shower at sea level for different radial distances from the axis, as indicated (after Protheroe and Turver, 1979)

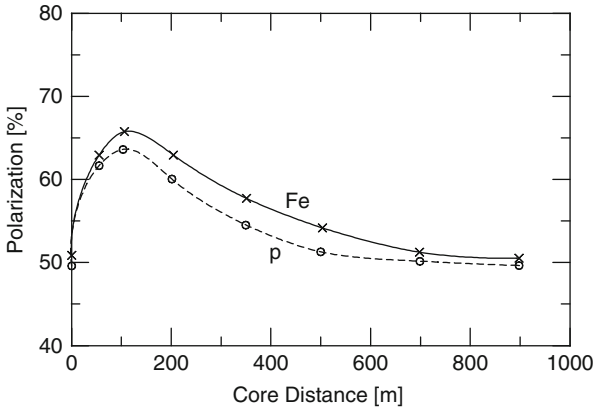

Fig. 16.10 Calculated percentage of the total signal recorded by the North–South sensitive element of a polarimeter as a function of core distance due North of the shower core for a 10^{17} eV proton (p) and iron nucleus (Fe) initiated shower (McComb et al., 1979)

16.3.6 Basic Primary Energy Estimation Using Optical Cherenkov Photons

It became evident at an early stage of atmospheric Cherenkov studies that there must be a nearly linear relationship between the total flux of the Cherenkov photons in a shower and the primary energy. This is obvious if we consider that the shower size, too, is an approximately linear function of the primary energy over several decades of energy in the lower atmosphere, at the shower maximum, which is rather broad, and that the total Cherenkov photon flux is about proportional to the total number of electrons in a shower. Modern computer simulations confirm that the total flux of

Cherenkov photons in a shower scales about linearly with primary energy to within a few percent. Thus, air Cherenkov measurements represent a sort of *Cherenkov calorimetry*.

Consequently, we can write for the total number of Cherenkov photons, Q, produced by an air shower through the atmosphere down to sea level, neglecting absorption, the following expression,

$$Q = \int_{E_{\rm th}(t)}^{E_0} \int_0^{t_0} N_e(t, E, E_0) \frac{{\rm d}q(t)}{{\rm d}l} \frac{{\rm d}l}{{\rm d}t} {\rm d}t {\rm d}E \ . \tag{16.21}$$

Here, $N_e(t, E, E_0)$ is the number of electrons of energy E at atmospheric depth t [radiation units], E_0 the energy of the primary initiating the shower, t_0 the atmospheric depth at sea level, $E_{\rm th}(t)$ the Cherenkov threshold energy at depth t, $({\rm d}q(t)/{\rm d}l)$ is the number of produced optical photons per unit path length at t, and $({\rm d}l/{\rm d}t) = X_0(t)$ is the radiation unit expressed in meters.

Assuming that the energy spectrum of the electrons in a shower varies little with N_e, then the number of electrons capable of producing Cherenkov photons is proportional to the total number of electrons at a given level. Thus we get for the total number of Cherenkov photons

$$Q = f(t') \frac{{\rm d}n(t')}{{\rm d}l} X_0(t') \int_0^{t_0} N_e(t) {\rm d}t \ . \tag{16.22}$$

$f(t')$ is the fraction of shower electrons with energy $\geq E_{\rm th}$ and ${\rm d}n(t')/{\rm d}l$ the number of optical photons per unit path length at some mean depth, t'.

To get a rough estimate of the Cherenkov photon number in a shower we use the following approximate numerical values for the different terms. Since the quantity $({\rm d}n/{\rm d}l)X_0 \approx constant$ we may insert for ${\rm d}n(t)/{\rm d}l$ the sea level value which is about $0.3\,{\rm cm}^{-1}$ and for $X_0 = 3.1 \cdot 10^4$ cm. For an equilibrium electron spectrum $f(t') \simeq 0.4$ and taking $t' = 500\,{\rm g\,cm}^{-2}$ we obtain (Khristiansen, 1980)

$$Q \simeq 3500 \int_0^{t_0} N_e(t) {\rm d}t \ \ \text{photons} \, . \tag{16.23}$$

Further studies showed that in large showers the photon lateral density distribution, $Q(r)$, manifests similar properties over a particular region of core distances with respect to the primary energy as does the particle density distribution, $\rho(r)$, over a different radial range, namely that it is a good estimator of the primary energy, irrespective of the mass of the primary or the details of the hadronic interaction (Dyakonov et al., 1973a; Dixon et al., 1973; Orford et al., 1975a) (see Sect. 12.5).

In an analysis the Haverah Park group shows that the quantities $Q(200)$, i.e., the Cherenkov photon density at 200 m from the axis, and $\rho(500)$, the vertical equivalent muon density at 500 m, are strongly correlated, both mutually and with the primary energy (Turver, 1992). Moreover, $Q(200)$ scales linearly with the primary energy. In an earlier investigation Dixon et al. (1973) noticed that for large showers

the photon density is a good energy estimator out to lateral distances from the axis of about 300 m. They specify the following expression for the relation between the photon density at 300 m and the primary energy in large showers,

$$Q(300) \;=\; 10^6 \left(\frac{E_0}{10^{17}} \right)^{1.0} \text{[photons/m}^2\text{]} \;. \tag{16.24}$$

It should be noted that the application of this method is limited to a primary energy range from about 10^{16}–10^{18} eV. The small radial distance from the shower core where the independent energy estimator, $Q(200)$ or $Q(300)$, can be used disfavors large showers ($\geq 10^{19}$ eV) because of the low event rate.

Hartman et al. (1979) have extensively explored the primary cosmic ray energy spectrum between 10^{12} and 10^{15} eV using the air Cherenkov method. They conclude that due to the large fluctuations in the shower development the technique is relatively insensitive to hadron initiated showers in the primary energy range between 10^{11} and 10^{13} eV. They note that the importance of fluctuations decreases with increasing primary energy.

Further details concerning primary energy estimation are discussed in Sect. 11.6.

16.3.7 Modern Refined Energy Estimation and Primary Mass Effects

Optical atmospheric Cherenkov emission manifests on average a particular lateral photon density distribution pattern and the photon number is directly related to the primary energy. In particular, at specific distances from the shower axis, which vary slightly with primary energy for optimized conditions, the *photon density is a direct measure of the primary energy*.

Note that the lateral density distribution function (l.d.f.) depends on the zenith angle. It must therefore be taken into account and care must be taken when comparing simulation and/or experimental data which are frequently given for vertical incidence. In Fig. 16.11a we show a typical average l.d.f. for vertical and 35° inclined showers of $8 \cdot 10^{13}$ eV proton initiated showers from the work of Aglietta et al. (2004).

In the core region the photon density is subject to large fluctuations that reflect mainly the large fluctuations of the *height of the first interaction*. This is illustrated in Fig. 16.11b. Another important fact is that the characteristic shape of the l.d.f. for different primary masses and identical total primary energy (not energy per nucleon) are very similar. They differ only in the absolute photon flux and the photon density at a given core distance, which is lower for larger primary masses, as is shown in Fig. 16.12a. The photon density at the fixed distance of $r = 130$ m from the shower axis, which is an optimum distance for the primary energy range under consideration, is plotted as a function of primary energy in Fig. 16.12b for different primary masses.

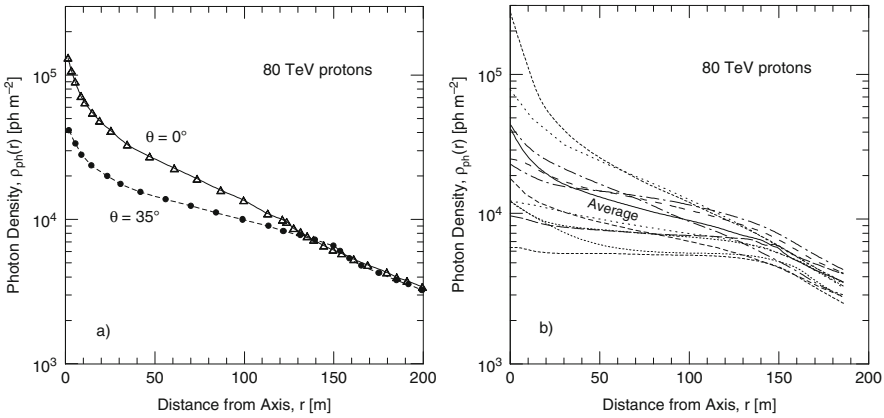

Fig. 16.11 (**a**) Typical shape of the average lateral density distribution of optical Cherenkov photons in simulated 80 TeV ($8 \cdot 10^{13}$ eV) proton initiated showers incident at zenith angles of $\theta = 0^\circ$ and $\theta = 35^\circ$, respectively, at EAS-TOP (altitude 2,005 m a.s.l., 820 g cm^{-2}). (**b**) Shapes of individual lateral density distributions of Cherenkov photons in simulated 80 TeV proton initiated showers incident at a zenith angle of $\theta = 0^\circ$ at EAS-TOP. The *solid curve* shows the average of 100 events. The large fluctuations in the near-core region are mainly due to the fluctuations of the height of the first interaction (after Aglietta et al., 2004)

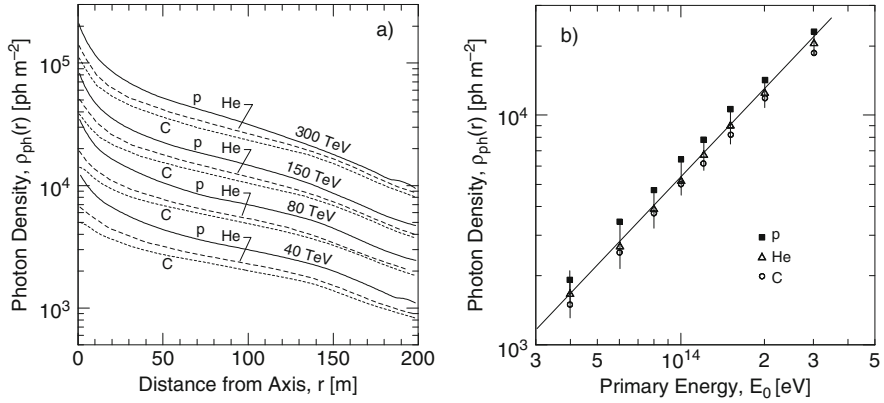

Fig. 16.12 (**a**) Typical shapes of average lateral density distributions of optical Cherenkov photons in simulated vertically incident showers initiated by primary protons, helium and carbon nuclei of total energy 40, 80, 150 and 300 TeV, respectively, at EAS-TOP (altitude 2,005 m a.s.l., 820 g cm^{-2}). (**b**) Predicted Cherenkov photon densities at a distance of 130 m from the shower axis as a function of the total energy for primary protons, helium and carbon nuclei at EAS-TOP (after Aglietta et al., 2004)

Contrary to the shower particles, these shower agents yield information on the longitudinal development of a shower that particles detected at ground level cannot supply, or at most in a very diluted form. These topics are discussed in the previous subsections.

16.3.8 Correlations Between Cherenkov Observables

Many authors have investigated correlations between the various Cherenkov observables discussed in this section to extract valuable information on shower development and other shower properties (Orford et al., 1975a, b). The most significant are those that are linked to the depth of maximum development of the showers because there are only very few observables that yield direct information on the longitudinal development of individual showers. This topic is discussed in detail in Chap. 7.

The other relevant correlation is the one mentioned in the previous subsection concerning the quantity $Q(200)$ which is a good estimator for the primary energy, applicable to medium size showers. Further details on primary energy estimation are discussed in Sect. 11.6.

16.4 Gamma Ray Initiated Showers and High Energy Gamma Ray Astronomy

16.4.1 General Comments

Of particular interest are showers produced by high energy primary gamma rays. Cocconi (1960) was one of the first who suggested to look for gamma ray initiated showers in an attempt to search for possible galactic sources of the cosmic radiation.[1] Unlike protons and nuclei, gamma rays are not deflected by magnetic fields in the Galaxy nor by the geomagnetic field when approaching the Earth. Thus, retracing the trajectory of a gamma ray points directly to its source. In addition, since high energy gamma rays are most likely the byproduct of high energy hadronic processes, originating from neutral pion decay and not from electromagnetic processes like bremsstrahlung, a high energy gamma ray source is also a likely source of high energy hadrons.

Since gamma ray showers have a very low muon content, the initial search was focused on so-called muon-poor showers, using standard air shower arrays that had muon detection capability (Chudakov et al., 1963; Firkowski et al., 1962, 1963; Gawin et al., 1963, 1965; Matano and Narasimham, 1963; Suga et al., 1963; Toyoda et al., 1965; Kamata et al., 1968). However, this method proved to be very difficult and the results were not conclusive.

[1] For a historic account see Weekes (1996).

One of the major problems encountered when searching for gamma ray initiated showers with standard arrays is the high flux of hadronic showers that represent an enormous background. The early experiments listed above yielded upper limits for the intensity of the *diffuse flux* of TeV gamma rays that were more than four orders of magnitude lower than the flux of charged particles at comparative energies.[2] Moreover, the limited angular resolution of common arrays which is of the order of one to a few degrees did not allow to resolve point sources that would have been easier to detect because of a better signal to noise ratio. Therefore, theoretical studies were the only possible approach to search for specific differences between hadron and gamma ray showers that could reveal experimentally distinguishable signatures to be applied in dedicated gamma ray search experiments.

With the development of the air Cherenkov technique that was heavily guided by simulations and initially aimed at the study of the longitudinal development of common hadron initiated showers, as discussed above, it was discovered that the Cherenkov image of hadronic showers observed at ground level is significantly different from that of a gamma ray shower. The latter is much more compact because of its more rapid development in the atmosphere. Moreover, it does not contain a penetrating component and the electrons are not subject to large scattering as is the case for hadron initiated showers (Browning and Turver, 1977; Turver and Weekes, 1978; Protheroe and Turver, 1979; Weekes, 1981; Cawley et al., 1983; MacKeown et al., 1983). The longitudinal development of a 10 GeV gamma ray initiated shower and the associated Cherenkov photon flux through the atmosphere is illustrated in Fig. 16.13 (Konopelko, 1997).

This discovery prompted numerous individuals and groups to explore the peculiarities of gamma ray initiated showers further. Because of the background situation the initial exploratory work was confined to purely theoretical studies. These efforts eventually lead to the development of the *air Cherenkov imaging technique* (Hillas, 1985; Cawley et al., 1985; Lewis et al., 1987; Weekes, 1989; for brief reviews see Weekes, 1996; Hillas, 1996; Fegan, 1996).[3]

Today the air Cherenkov imaging technique is the backbone of ground based high energy gamma ray astronomy ($E \geq 10^{11}$ eV). Numerous highly specialized instruments are presently in operation worldwide and new generations are under construction and on the drawing boards. In the following we will briefly outline the most important aspects of this technique.

Gamma ray astronomy is a relatively new and rapidly expanding field that will not be treated in this book. The interested reader is referred to the specialized literature (see for example the books of Ramana-Murthy and Wolfendale, 1993; Schönfelder, 2001; Weekes, 2003a; as well as conference proceedings and reviews,

[2] The integral rate of hadron induced showers producing a $\geq$1 TeV equivalent gamma ray shower signal is $\sim 5 \cdot 10^{-8}\,\mathrm{cm}^{-2}\mathrm{s}^{-1}$, masking completely the general Galactic disk emission expected at a rate of approximately $10^{-12}\,\mathrm{cm}^{-2}\mathrm{s}^{-1}$ within an acceptance angle of 1° (Drury, 1996).

[3] The first to use the air Cherenkov imaging technique on common air showers were Hill and Porter (1961) who used an opto-electronic image intensifier.

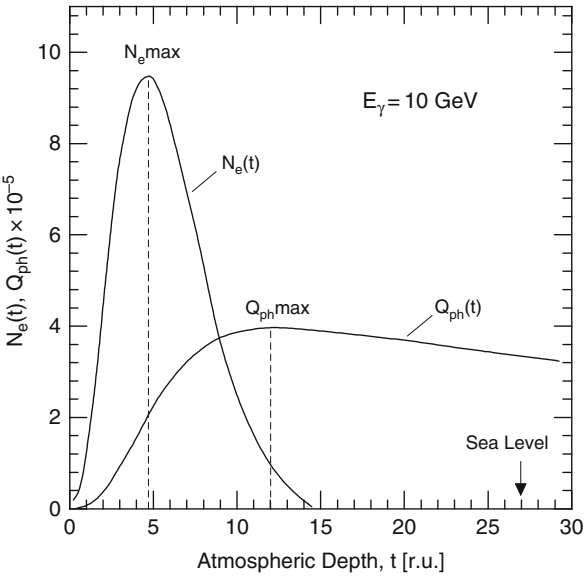

Fig. 16.13 Longitudinal development of a 10 GeV gamma ray initiated shower in the atmosphere. Shown is the rapid rise and fall of the number of electrons, $N_{e^{\pm}(t)}$, in the classical photon-electron cascade and the corresponding photon flux, $Q_{\mathrm{ph}}(t)$, as a function of atmospheric depth, t, expressed in radiation units [r.u.]. $Q_{\mathrm{ph}}(t)$ is essentially the integral of the generated Cherenkov photons, including absorption along their path. Since absorption removes more Cherenkov photons than are produces as the electron cascade dies out, $Q_{\mathrm{ph}}(t)$ reaches its maximum before the latter ends. Moderate absorption then continues as the Cherenkov component propagates through the atmosphere to ground level (figures adopted from Konopelko, 1997)

e.g., Weekes, 1988; Trümper, 1993; Ong, 1998; Catanese and Weekes, 1999; Buckley, 2000; Weekes, 2003b). A short but very interesting account of the early history of gamma ray astronomy is given by Pinkau (1996).

16.4.2 Cherenkov Imaging Technique

Gamma ray initiated showers show light patterns on an imaging detector that are much more compact than proton showers, exhibiting frequently an elongated elliptic shape. On the other hand, proton showers show often isolated light patches away from the relatively broad more or less elliptic region over which the bulk of the light spots are distributed in irregular patches. It is these differences that are being used in a rationalized way to identify gamma initiated showers with a high degree of efficiency and confidence, and to discriminate against hadron initiated showers.

The typical *pixel pattern* of an air Cherenkov image of a gamma ray shower has an approximately elliptic or asymmetric elliptic, in some cases an almost comet like shape. An example of such a shower with an impact parameter of some 10 m with respect to the center of the mirror of an imaging detector and a direction slightly

off-axis with respect to the telescope axis is illustrated in Fig. 16.14.[4] The solid ellipse in the upper right of this figure represents the contour of the resulting pixel pattern and the parameters characterizing the Cherenkov light image in terms of shape and orientation are identified.

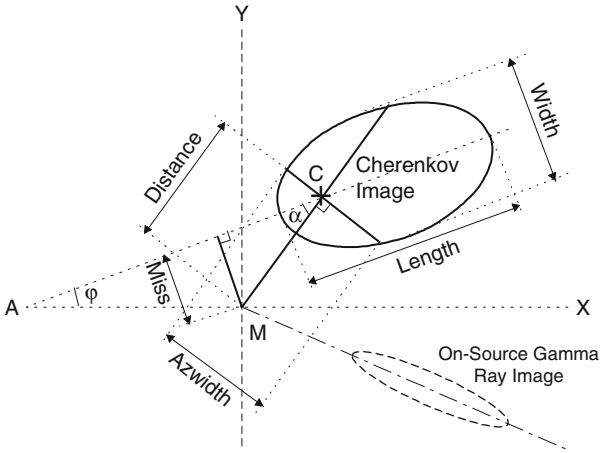

Fig. 16.14 Principle and basic parameters of air Cherenkov image analysis to select gamma ray initiated showers and discriminate against proton showers. The *solid ellipse* indicates the pixel image contour, *C* is the *centroid* of the image (location of highest brightness) and *M* the center of the field of view. The relevant parameters are the major and minor axis of the ellipse, labeled *Length* and *Width* in the plot, the angle α between the major axis and the line connecting the centroid *C* with the center of the field of view *M*, the *Distance* between *C* and *M*, and the two new quantities called *Miss* and *Azwidth*. Miss is the offset or the perpendicular distance between the extension of the major axis of the ellipse and *M*, and Azwidth is the azimuthal width of the image as indicated; it is the r.m.s. spread of light perpendicular to the line connecting *C* with *M*. Except for the clean regular elliptic shape this image is also representative for hadronic showers. The *dashed ellipse* at the lower right with the extension of the major axis intercepting the *center M* of the mirror, labeled *On-Source Gamma Ray Image*, shows the typical narrow elliptic contour of a gamma ray shower when the mirror axis is pointing at the source and the impact parameter is non-zero (for details see Fegan, 1996)

C is the *centroid* of the image, i.e., the center of brightness, and M is the center of the field of view. The relevant parameters are the major and minor axis of the ellipse, labeled *Length* and *Width* in the plot, which mark the r.m.s. spread of the light and represent the development of the cascade, the angle α between the major axis and the line connecting the centroid C with the center of the field of view M, the *Distance* between C and M, and the two quantities called *Miss* and *Azwidth*. Miss is the offset or perpendicular distance between the extension of the major axis of the ellipse and M. It is a measure of the shower orientation. Azwidth is the r.m.s. spread of light perpendicular to the line connecting the centroid of the image to the center of the field of view, M. The angle φ is the major axis orientation angle with

[4] Modern large imaging systems are operated over an impact parameter range from 0 to 500 m.

respect to the X-Y-coordinate system as indicated in Fig. 16.14. Today, in place of the parameter *miss* the angle α is being used.

The shape and orientation of the contour of the pixel pattern depends on the angle between the shower axis and the optical axis of the telescope, and on the location of the telescope with respect to the ground impact of the shower axis. If the two axes coincide the pixel pattern is circular and located at the center, if the axes are parallel but laterally displaced an ellipse results whose major axis intercepts the center of the mirror, M, (dashed ellipse in the lower right of Fig. 16.14) and if the two axes are not parallel and displaced the major axis of the ellipse does not intercept M. These statements apply in general to gamma ray and hadronic showers. However, as pointed out before, the pixel distributions are quite different, usually much more irregular for hadronic events and frequently with substructures.

To reduce the background caused by hadronic showers a high angular resolution is required. The latter should be matched to the angular size of the Cherenkov flash. Angular resolution is a key parameter to lower the threshold energy, $E_{\gamma,\mathrm{th}}$, for the detection of gamma ray showers since $E_{\gamma,\mathrm{th}} \propto A^{-2}$, where A is the light collection area. On the other hand the background is proportional to $A\theta$, where θ is the angle of acceptance. Proper choice of the relevant parameters can result in an up to 99.7% suppression of hadronic showers. Obviously, the narrow-angle telescope technique does not permit an all-sky survey, it is aimed at point source detection. The *ultimate background* that will be indistinguishable from gamma ray initiated showers are showers initiated by *primary electrons*.

Hillas (1985) in his initial analysis compared the different parameters of simulated gamma, proton and oxygen initiated showers recorded in *different zones* of a particular imaging telescope at the Whipple Observatory on Mt. Hopkins (2,380 m a.s.l.) to find the most reliable and efficient identification of gamma ray events. He also introduced signal threshold conditions for accepting or discarding pixels and various methods to fix the centroid.

In general air Cherenkov image analyses must be tailor-made for each detector. It is not only the detector geometry (size, pixel number, etc.,) that plays a role but also the altitude of its location because of the spread and the attenuation of the photons. The actual selection criteria which are based on the detection parameters listed above (see Fig. 16.14) and the instrumental parameters are then optimized for the given detector configuration in conjunction with simulations, using author specific approaches to optimize the detection efficiency for gamma showers. It usually boils down to fix particular cuts on image sensitive quantities like α, *width, length* and others.

As an example for a procedure, one can fix for each of the 6 image parameters a boundary, marking off the gamma ray domain which contains most gamma images, but only few proton events. Following Hillas' recipe (Hillas, 1985), requiring that 4 out of the 6 parameters lie in the gamma domain, one may expect in the case of simulated images to accept 60–70% of the gamma showers and only 1–2% of the proton background showers. For further details concerning these topics the reader is referred to the specialized literature (Weekes, 1996; Hillas, 1996; Fegan, 1996; Konopelko, 1997; Aharonian, 2004).

In recent years the *stereo imaging technique* has been developed and is being used quite successfully (for a review see Chadwick et al., 1996).

16.5 Optical Background, Atmospheric Light Scattering, Absorption and Attenuation

16.5.1 Optical Background

The optical background of the night sky is discussed in detail in Sects. 17.2.2 and 17.3 in connection with air fluorescence and Fly's Eye type detector experiments. Optical Cherenkov observations of air showers are troubled by the same sources and levels of background and face the same problems.

Disregarding man made background, the background of the night sky due to airglow, starlight and the general galactic background amounts to $\leq 10^8$ [ph cm^{-2}s^{-1} sr^{-1}] (Jelley, 1959). The Cherenkov background from the general cosmic radiation in the atmosphere was estimated by Blackett (1948) to amount to about a factor of 10^{-4} of the night sky luminosity. Gol'danskii and Zdanov (1954) carried out a calculation and arrived at a figure of $\sim 6 \cdot 10^3$ [ph cm^{-2}s^{-1}sr^{-1}]. Polikarov (1954) shows that a single particle in traversing the atmosphere produces about a total of 10^5 photons. From this result one obtains a contribution of $\sim 1.6 \cdot 10^3$ [ph cm^{-2}s^{-1}sr^{-1}] from the unaccompanied cosmic radiation.

Considering a photocathode with an efficiency of 10% the night sky background light yields several orders of magnitude more photoelectrons than the dark current of an average phototube.

16.5.2 Atmospheric Light Scattering, Absorption and Attenuation

In principle two types of scattering must be considered, *Rayleigh scattering* and *Mie scattering*. The former handles scattering on air molecules, the latter on aerosols. In clean air it is chiefly Rayleigh scattering that is relevant for air Cherenkov detection. In addition absorption with or without re-emission may have to be considered. Most relevant is absorption on ozone. Optical scattering, absorption and attenuation of light are discussed in detail in Sect. 17.3. Here we only mention briefly some specific work and present data that concern exclusively air Cherenkov applications.

Browning and Turver (1975) and Protheroe and Turver (1979) have studied the attenuation of Cherenkov light in the atmosphere. The former have carried out calculations of the propagation of the light of showers produced by 10–300 GeV gamma rays, the latter of 10^{17} eV proton and iron nuclei initiated showers. In either case absorption of the Cherenkov light in the atmosphere was included in the calculations using the data of Elterman and Toolin (1965) and Elterman (1968). In Fig. 16.15 we show the percentage of surviving Cherenkov photons at sea level emitted by an electron in the atmosphere as a function of atmospheric depth of emission (Protheroe and Turver, 1979).

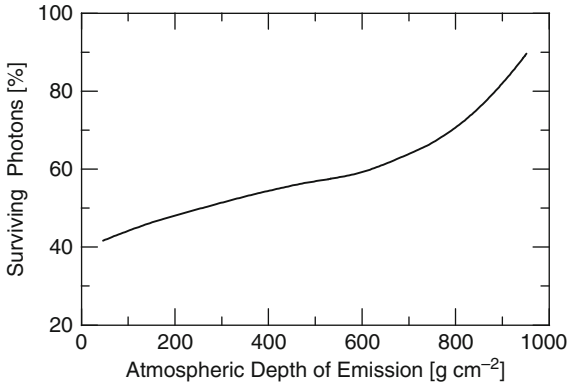

Fig. 16.15 Percentage of Cherenkov light emitted by an electron in the atmosphere surviving down to sea level as a function of depth of emission (Protheroe and Turver, 1979)

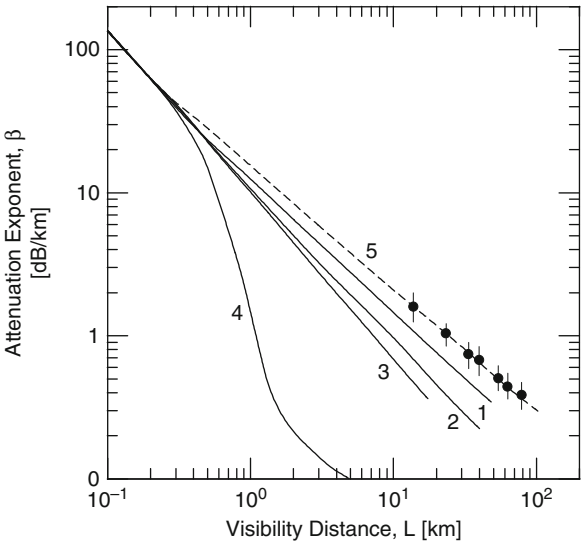

Fig. 16.16 Dependence of the exponent of light attenuation in the atmosphere, β, on the distance of visibility, L, for different wavelengths. The experimental points, •, and *line 5* are from the work of Efimov and Sokurov (1979), *curves 1* to *4* after Smirnov (1973) and apply to the following wavelengths: (*1*) $\lambda = 0.63\mu$m, (*2*) $\lambda = 0.91\mu$m, (*3*) $\lambda = 1.05\mu$m, (*4*) $\lambda = 10.5\mu$m

Efimov and Sokurov (1979) have investigated the attenuation of atmospheric Cherenkov light employing a rather elaborate method using air showers incident at different zenith angles at the Yakutsk array and various atmospheric visibility conditions. Their results giving the coefficient of exponential attenuation, β, as a function of the distance of visibility, L, are shown in Fig. 16.16 together with data from a study of Smirnov (1973) that cover much longer wavelengths. They conclude

that approximately 25% of the optical photon flux produced in showers are lost in the atmosphere.

Relatively recent measurements of the optical background night sky photon intensity at high altitude were carried out by Shirasaki et al. (2001) at Mount Chacaltaya (5,230 m a.s.l.) in Bolivia. The data are displayed in Fig. 16.17. Also shown are predictions from a simulation.

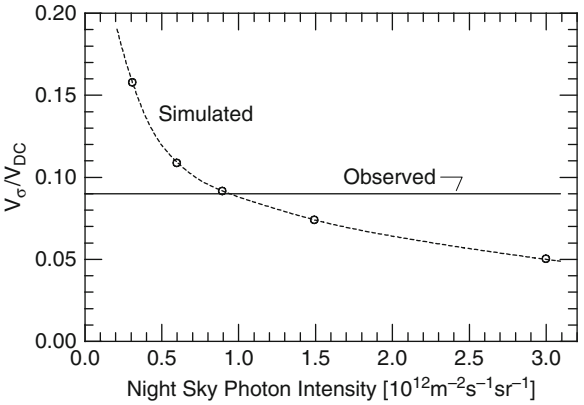

Fig. 16.17 Estimated night-sky optical background photon intensity at Mt. Chacaltaya, Bolivia (5,230 m a.s.l.). V_σ is the r.m.s. fluctuation of the base line optical noise level, V_{DC}. The figure shows the actually measured ration V_σ / V_{DC} (*straight line*) and the prediction from a simulation (Shirasaki et al., 2001)

16.6 Experimental Data and Interpretation

16.6.1 Environmental and Instrumental Aspects and Detectability

Air Cherenkov detector sites require careful investigation of the environmental conditions, in particular of the atmosphere and the night sky, and permanent monitoring. On the instrumental side calibration and noise in the photonic devices used are important issues and numerous papers had been written which, however, are frequently site or instrument specific. Clay and Gregory (1977) and Chantler et al. (1979) have extensively studied the dark current problem of photomultipliers. Likewise Patterson and Hillas (1983a, b) have analyzed the effects of phototube properties and aerosols in the atmosphere on air Cherenkov measurements.

The detectability of the Cherenkov light pulse of a shower depends on the signal to noise ratio, ($R = S/N$), and fluctuations, σ_f. As pointed out before, the night sky represents usually the dominating background. Considering an optical window between 350 and 550 nm, the background is approximately $6.5 \cdot 10^7$ [ph cm^{-2}s^{-1}].[5]

[5] Optical filters were frequently used in the past to reduce contributions from longer wavelengths to the background; today photomultipliers with appropriate photocathode sensitivities are being used.

For a given photon detector with a geometric factor of $A\Omega$ [cm^{2}sr] and a quantum efficiency of η the number of photoelectrons (pe) per unit time is $6.5 \cdot 10^7\, A\Omega\eta$ [ph cm^{-2}s^{-1}sr^{-1}]. For a time resolution of the system of τ [s], the fluctuations within the time interval τ are

$$\sigma_f \;=\; \sqrt{6.5 \cdot 10^7 A\Omega\eta\tau}\;\; . \tag{16.25}$$

It is the value of σ_f that determines the effective amplitude of the noise. On the other hand, the signal amplitude is given by $q\,A\Omega\eta$, where q is the number of Cherenkov photons per unit area-solid-angle product and depends on the shower size, core distance and zenith angle.Thus, we require that

$$q\,A\Omega\eta \;\geq\; R\sigma_f\;\; . \tag{16.26}$$

For a given signal to noise ratio, R, and the stated night sky brightness we obtain for the minimum detectable signal level the required number of photons per unit geometric factor,

$$q \;=\; R\sqrt{\frac{6.5 \cdot 10^7\tau}{A\Omega\eta}}\;\; . \tag{16.27}$$

The above considerations must be extended to include the wavelength dependence of the different parameters to get specific numbers.

A back of the envelope calculation yields for a 2-in photomultiplier with a conversion efficiency of $\eta = 0.1$ for a signal to noise ratio of $R \geq 3$ a required photon signal intensity of approximately 20 [ph cm^{-2}sr^{-1}] for a system with a 1 μs resolution; it is obviously better for higher resolution systems. However, the sampling time should not be shorter than the signal burst.

16.6.2 Lateral and Angular Distribution, Structure Functions

Egorov et al. (1971a) have carried out some of the first systematic measurements of the lateral density distribution of the Cherenkov light in giant showers to large core distances while recording simultaneously the density distribution of the particle component and derived lateral structure functions for the two quantities (for details see Chap. 8). They also established in conjunction with simulation calculations the relationship to the primary energy and the differential and integral primary energy spectra from their data. Details of this work are discussed in Sect. 11.6.

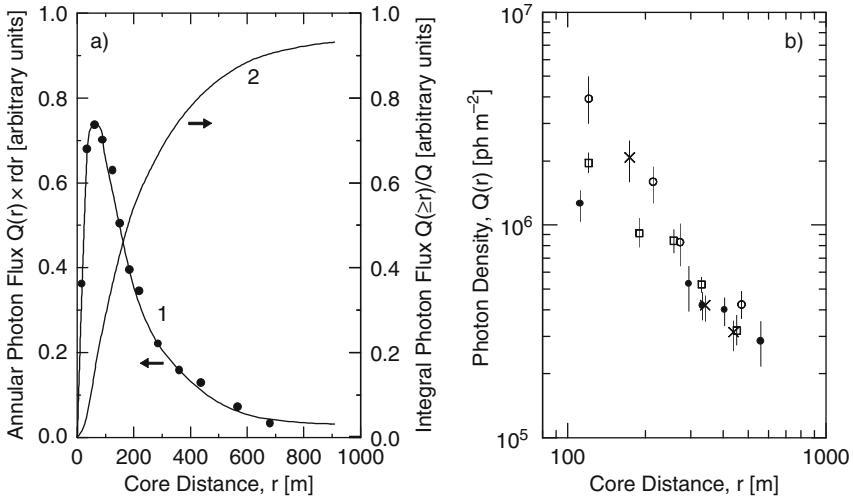

Fig. 16.18 (**a**) Normalized measured Cherenkov light flux within an annular ring of area $2\pi r\mathrm{d}r$ versus distance from the axis (•, *curve 1*), and integrated flux (*curve 2*) in showers of average size $N_e = 5.5 \cdot 10^7$ ($\rho(600) \simeq 0.1$ veμ m^{-2}; $E_0 \simeq 3.65 \cdot 10^{17}$ eV) near sea level, incident under an average zenith angle of $\langle\theta\rangle = 16.5^\circ$ (Glushkov et al., 1979). The *curves* are fits to the experimental data. The total photon fluxes for different shower size groups obtained by integration of Eq. (16.29) are given in Table 16.2. (**b**) Experimentally determined lateral density distribution of air Cherenkov photons in showers having a primary energy of $\sim 3 \cdot 10^{17}$ eV observed at Haverah Park under different zenith angles (Hammond et al., 1978). × $0 \le \theta \le 25^\circ$; □ $35^\circ \le \theta \le 45^\circ$; ○ $25^\circ \le \theta \le 35^\circ$; • $45^\circ \le \theta \le 65^\circ$

The measured annular and radially integrated photon fluxes in showers of size $5.5 \cdot 10^7$, corresponding to a primary energy of about $3.65 \cdot 10^{17}$ eV, observed at Yakutsk are illustrated in Fig. 16.18a (Glushkov et al., 1979).

The experimentally determined dependence of the lateral density distribution of optical Cherenkov photons on zenith angle in showers of primary energy $\sim 3 \cdot 10^{17}$ eV resulting from measurements made at Haverah Park by Hammond et al. (1978) is plotted in Fig. 16.18b. The primary energy dependence of the lateral Cherenkov photon density distribution for moderately inclined showers resulting from the same experiment is illustrated in Fig. 16.19a. The primary energy is specified in terms of $\rho(500)$, the Haverah Park energy estimator, expressed in vertical equivalent muons per square meter [veμ m^{-2}], described in Sect. 12.5.3.

Two similar data sets from the Haverah Park experiment for two different shower size groups are shown in Fig. 16.19b together with two corresponding data sets from Yakutsk (Diminstein et al., 1972). The results from the two experiments agree very well.

A rich set of data of experimentally determined lateral photon density distributions in large showers from the work at Yakutsk is shown in Figs. 16.20, 16.21, 16.22, 16.23 and 16.24b, covering a range of primary energies from $3 \cdot 10^{17}$ to 10^{19}

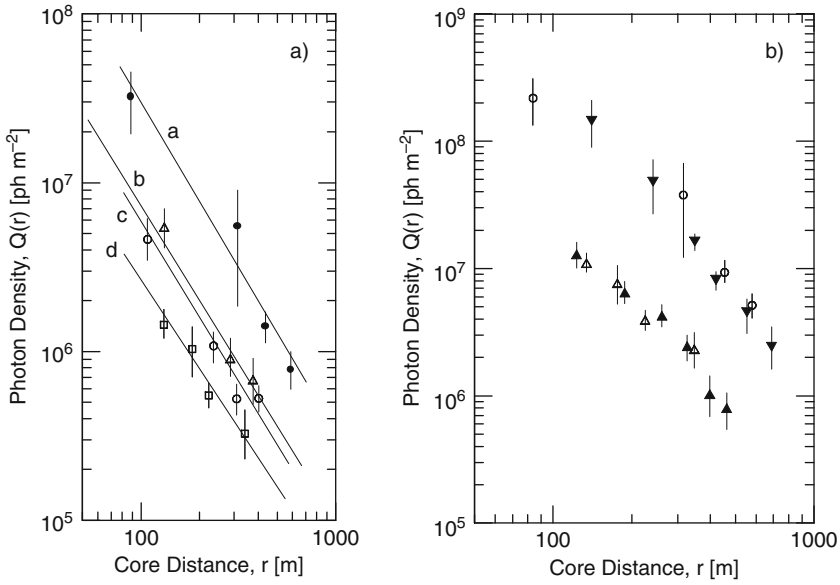

Fig. 16.19 (**a**) Lateral density distribution of Cherenkov photons in showers of different primary energy, characterized by the vertical equivalent muon density, $\rho(500)$, incident at 25°–35° to the zenith, recorded at Haverah Park (Hammond et al., 1978). •, $\rho(500) = 1.915$ veμ m^{-2}, $\gamma = 1.93$; △, $\rho(500) = 0.735$ veμ m^{-2}, $\gamma = 1.89$; ○, $\rho(500) = 0.422$ veμ m^{-2}, $\gamma = 1.85$; □, $\rho(500) = 0.194$ veμ m^{-2}, $\gamma = 1.67$, where γ is the slope of the distribution. (**b**) Comparison of the lateral density distribution of Cherenkov photons recorded at Haverah Park, △ and ○ (Hammond et al., 1978), with the results of the Yakutsk array, ▲ and ▼ (Diminstein et al., 1972). The plot includes two sets of showers from each experiment that differ in their $\rho(500)$ veμ densities by a factor of 10, corresponding to showers of mean sea level size $N_e = 1.4 \cdot 10^7$ and $N_e = 1.7 \cdot 10^8$ particles, respectively

eV subdivided into five groups, and a range of zenith angles of $0° \leq \theta \leq 55°$ (Diminstein et al., 1975; Dyakonov et al., 1979; Glushkov et al., 1979). The lateral density distributions follow approximately the power law representation

$$Q(r) \propto r^{-n_Q} \quad , \tag{16.28}$$

where the exponent n must be adapted to the shower size group and is given in Table 16.2. For the class II showers listed in the table it was found that approximately 50% of all the Cherenkov light falls within a radius of ∼170 m. The quantity $\overline{\rho}(600)$ in the table is the usual particle based primary energy estimator for large showers.

The curves shown in Fig. 16.24a that follow the experimental points very closely are generated from an analytic *lateral structure function* derived by Glushkov et al. (1979) that reads

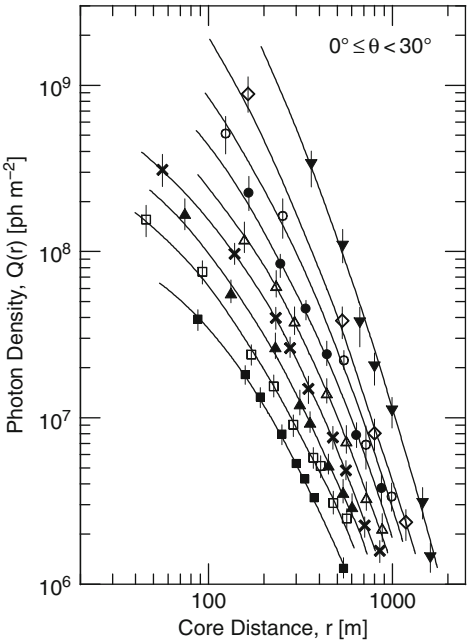

Fig. 16.20 Measured Cherenkov photon density distributions versus distance from the shower axis for the zenith angle interval $0^\circ \leq \theta \leq 30^\circ$, recorded at Yakutsk (Dyakonov et al., 1979). The data include showers with photon densities in the range $3 \cdot 10^6 \leq Q(400) \leq 2.5 \cdot 10^8$ photons m^{-2} in the wavelength window $0.3\,\mu\mathrm{m} \leq \lambda \leq 0.8\,\mu\mathrm{m}$. The corresponding primary energy range is $3 \cdot 10^{17} < E_0 \leq 10^{19}$ eV

$$f(x) = \frac{CQ}{2\pi r_0^2}\left(\frac{1}{k+x}\right)\frac{1}{(1+x)^b} \quad . \tag{16.29}$$

Q is the total flux of photons, $x = (r/r_0)$, C is the normalization factor[6] and k, r_0 and b are parameters that depend on the shower size, as specified in Table 16.2. In this work the authors included a 23% loss of photons as a result of atmospheric absorption and scattering, a value that is based on a special analysis.

Air Cherenkov measurements on smaller showers with sizes around $4 \cdot 10^5$–10^6 particles were carried out at Adelaide (sea level) (Aus.) and Samarkand (~900 m a.s.l.) (Uzbekistan) with small arrays. The lateral photon density distributions were normalized to the shower size and are plotted in Fig. 16.24b together with a predicted distribution for the Samarkand installation.

[6] Glushkov et al. (1979) specify in their paper a very weak size dependence of C, $C = C(b, k)$; in other work of the same group the size dependence is disregarded.

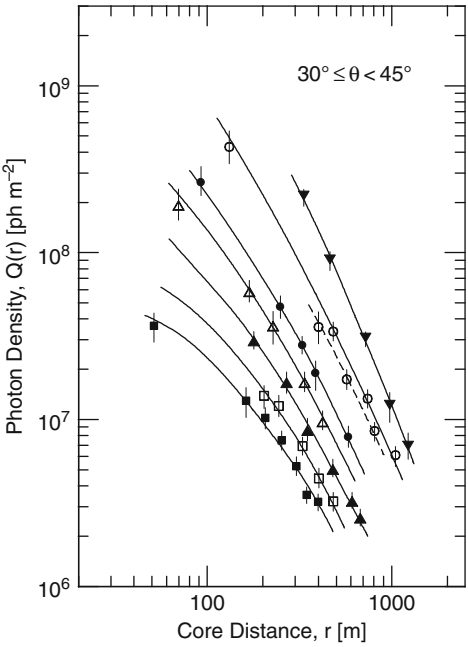

Fig. 16.21 Measured Cherenkov photon density distributions versus distance from the shower axis for the zenith angle interval $30^\circ \leq \theta \leq 45^\circ$, recorded at Yakutsk (Dyakonov et al., 1979). The data include showers with photon densities in the range $3 \cdot 10^6 \leq Q(400) \leq 2.5 \cdot 10^8$ photons/m^2 in the wavelength range $0.3\,\mu\text{m} \leq \lambda \leq 0.8\,\mu\text{m}$. The corresponding primary energy range is $3 \cdot 10^{17} < E_0 \leq 10^{19}$ eV

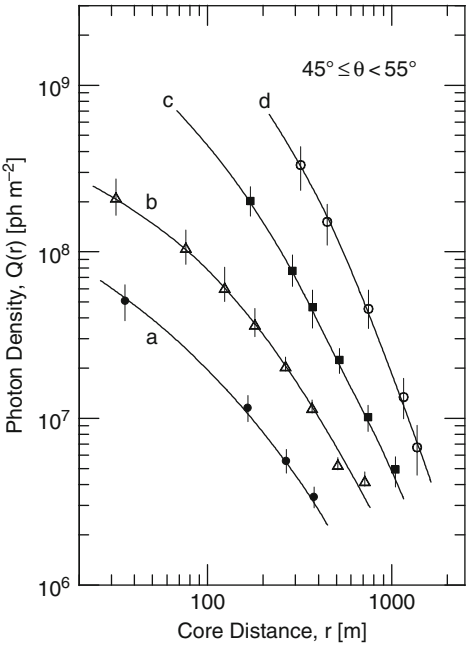

Fig. 16.22 Measured Cherenkov photon density distributions versus distance from the shower axis for the zenith angle interval $45^\circ \leq \theta \leq 55^\circ$, recorded at Yakutsk (Dyakonov et al., 1979). The data include showers with photon densities in the range $3 \cdot 10^6 \leq Q(400) \leq 2.5 \cdot 10^8$ photons m^{-2} in the wavelength range $0.3\,\mu\text{m} \leq \lambda \leq 0.8\,\mu\text{m}$. The corresponding primary energy range is $3 \cdot 10^{17} < E_0 \leq 10^{19}$ eV

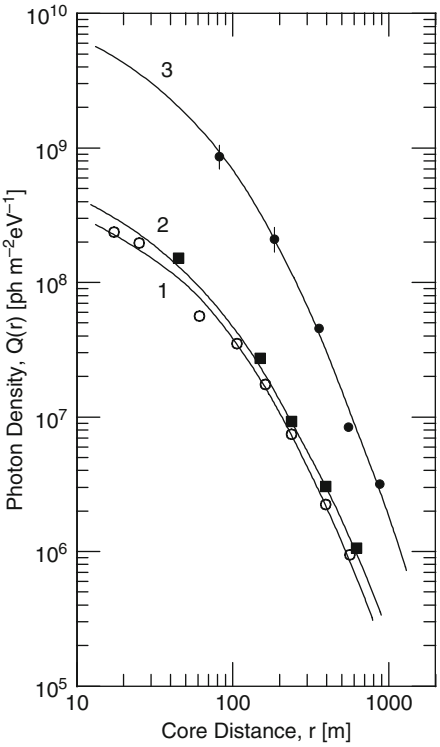

Fig. 16.23 Photon density per m^2 and eV of energy lost by the electron component versus distance from the shower axis, for three groups of showers observed at Yakutsk with the following parameters (Diminstein et al., 1975):

○	$\langle\theta\rangle = 19^\circ$, $\langle N\rangle = 6.1 \cdot 10^7$
curve 1	$B = 2.87$, $\lambda = 0.07$, $R_0 = 300$ m, $Q = 9.3 \cdot 10^{12}$ ph/eV
■	$\langle\theta\rangle = 37^\circ$, $\langle N\rangle = 5 \cdot 10^7$
curve 2	$B = 2.9$, $\lambda = 0.02$, $R_0 = 400$ m, $Q = 1.4 \cdot 10^{13}$ ph/eV
•	$\langle\theta\rangle = 21^\circ$, $\langle N\rangle = 1.3 \cdot 10^9$
curve 3	$B = 2.9$, $\lambda = 0.10$, $R_0 = 230$ m, $Q = 1.44 \cdot 10^{14}$ ph/eV

In their early work Zatsepin and Chudakov (1962) noted that the ratio of the flux of Cherenkov photons, Q, to the shower size, N_e, i.e., Q/N_e, seems to manifest only a weak dependence on N_e over the size range $10^6 \leq N_e \leq 10^8$. Dyakonov et al. (1973b) conclude from their work at Yakutsk that there seems to be no dependence of Q/N_e on shower size over the range $10^7 \leq N_e \leq 3 \cdot 10^8$ from measurements made over the lateral distance interval $150 \leq r \leq 700$ m from the shower axis.

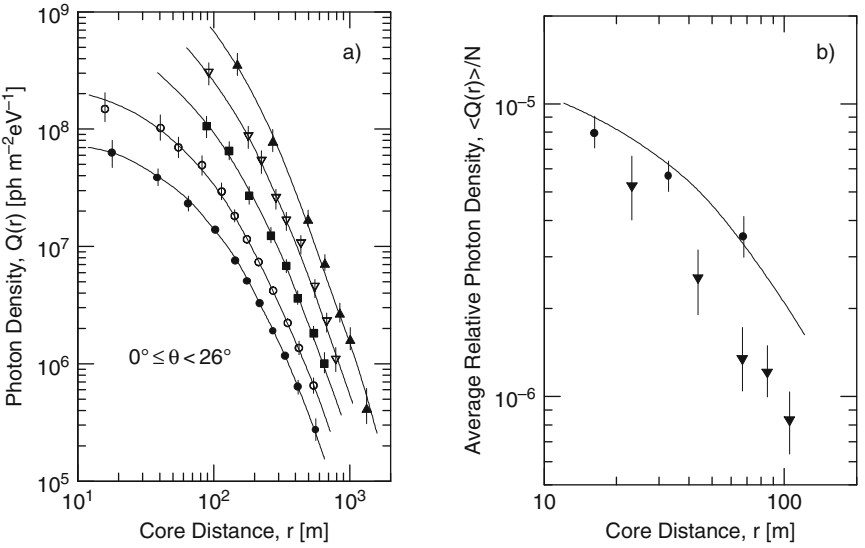

Fig. 16.24 (**a**) Mean lateral density distribution of air Cherenkov photons per m^2 and eV of energy lost by the electron component versus core distance in showers of different average sizes, observed at Yakutsk: • $N_e = 2.2 \cdot 10^7$, ○ $N_e = 5.5 \cdot 10^7$, ■ $N_e = 1.9 \cdot 10^8$, ▽ $N_e = 5.0 \cdot 10^8$, and ▲ $N_e = 1.9 \cdot 10^9$. The data cover a zenith angular range from 0° to 26°. The *curves* were obtained from an analytical approximation of the lateral distribution function (Eq. (16.29), Glushkov et al., 1979). (**b**) Comparison of normalized averaged lateral density distribution of Cherenkov photons in showers of size 10^6. The data points • were obtained at Samarkand by Makhmudov et al. (1979), points ▼ are from the work of Kuhlmann et al. (1977) at Adelaide (Aus.) and cover the size range $4{\cdot}10^5 \le N_e \le 10^6$. The solid curve is an approximation due to Glushkov et al. (1978)

Table 16.2 Parameters for Eq. (16.29)

Group	lg $\overline{N_e}$	lg $\overline{\rho}(600)$ [veμ]	$\overline{\theta}$ [deg]	n_Q	b	k	r_0 [m]	lg ϕ [ph/eV]	E_0 [$\cdot 10^{17}$eV]
I	7.34	−0.48	16.0	2.58	3.3	0.35	265	12.55	1.62
II	7.74	−0.10	16.5	2.64	3.3	0.32	245	12.90	3.65
III	8.28	+0.41	17.5	2.70	3.3	0.29	268	13.36	10.90
IV	8.70	+0.82	20.0	2.74	3.3	0.23	273	13.79	29.60
V	9.27	+1.36	17.0	2.76	3.3	0.18	270	14.26	89.30

16.6.3 Temporal Properties, Pulse Shape and Light Front Curvature

Much of the systematic early work on atmospheric Cherenkov bursts associated with air showers was focused mainly on the exploration of the photon lateral density distribution and to relate it to the particle distribution. This work was followed by studies of the temporal features of the Cherenkov light pulse as a function of core distance and zenith angle.

It was, of course, soon realized that there must be an intimate correlation between the shower development and the Cherenkov light burst, but it was not until the pioneering efforts of Castagnoli et al. (1967) and others, and the theoretical work of Fomin and Khristiansen (1971) which illuminated the new possibilities that promised the ground based observer to gain direct access to the longitudinal development of individual showers, that the field began to evolve rapidly.

It was above all the fact that the longitudinal development of the shower is mapped directly into the Cherenkov component and manifests itself most clearly in the pulse shape. Moreover, the temporal properties of the Cherenkov pulse hold the richest information and reveal the depth of maximum development, as discussed briefly in Sect. 16.3.3. However, the experimental work thus initiated depends heavily on computer simulations for exploratory work as well as for the analysis and interpretation of the measurements.

In view of the relevance of this topic we have devoted a separate chapter to it (Chap. 7). There we discuss not only the very successful Cherenkov techniques to determine the depth of maximum development of showers but also all other methods. For this reason we present here only some very rudimentary results of the early temporal exploration of the Cherenkov light pulse.

In Fig. 16.25a we show the typical dependence of the full width at half maximum (FWHM) of the Cherenkov light pulse as a function of distance from the shower axis. The three sets of data taken over a period of several years with the installation at Yakutsk on large showers ($10^7 \leq N_e \leq 5 \cdot 10^8$) show the consistency and reliability of the method. No correction for the system bandwidth that was not very broad in this experiment had been used. In other experiments where corrections for the system bandwidth were made the pulse widths are in general somewhat shorter. The effect of bandwidth limitation was analyzed by Protheroe et al. (1975).

For comparison we have added in Fig. 16.25a the data obtained by Thornton and Clay (1978b) for smaller showers at closer range to the axis with their array at Adelaide. These authors have accounted for the system bandwidth and give net pulse widths. The scatter and zenith angle dependence of the FWHM of a small sample of individual showers from the work at Yakutsk is shown in Fig. 16.25b. Numerous similar measurements were carried out at other experiments, including the high altitude array at Chacaltaya (Inoue et al., 1981a, b).

16.6.4 Correlations Between Cherenkov and Particle Observables

As must be expected there exist numerous Cherenkov observables that are correlated with particle observables in a shower or manifest other characteristic dependencies. However, the relevant question is how significant and experimentally accessible these quantities are. Unfortunately many observables show only week correlations and are insignificant. Others, though very subtle, have unique features but require delicate measurements and often extensive computer assisted evaluations

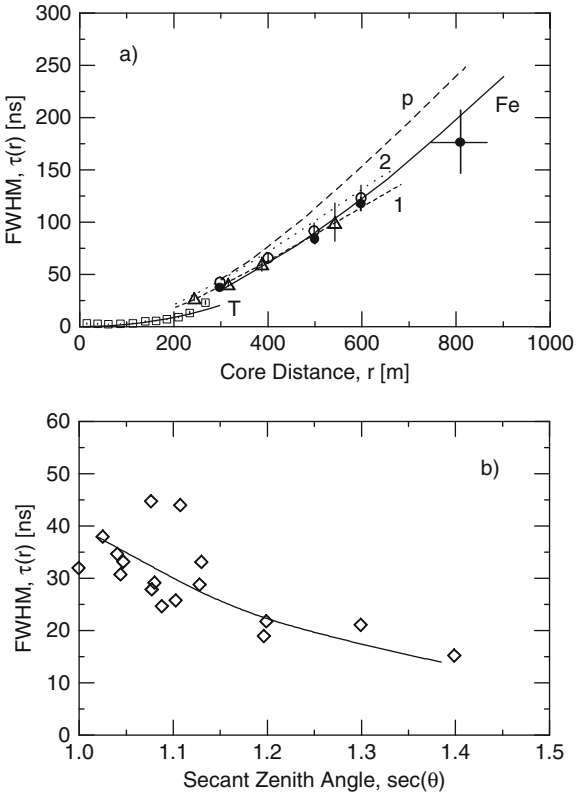

Fig. 16.25 (**a**) Cherenkov pulse full width at half maximum (FWHM), $\tau(r)$, as a function of core distance, r, in large showers ($10^7 \leq N_e \leq 5 \cdot 10^8$) from different experimental epochs measured at Yakutsk. △, Efimov et al. (1973); ○, Kalmykov et al. (1975); •, Kalmykov et al. (1977). The *curves* labeled *Fe* and *p* show the predicted dependence based on a scaling model calculation for iron and proton primaries, *curves 1* and *2* are for primary protons and the high multiplicity and CKP models, respectively, for showers of size $\sim 10^7$. The data points at small core distances, □, are bandwidth corrected data from measurements at Adelaide in small showers, $6{\cdot}10^5 \leq N_e \leq 7.8{\cdot}10^6$, $\langle N_e \rangle = 7.7 \cdot 10^5$. The errors are smaller than the symbols (Thornton and Clay, 1978a). (**b**) Pulse width dependence at 300 m from the shower axis as a function of zenith angle θ (same experiment) (Kalmykov et al., 1975)

and interpretations. Only few of the correlations are unambiguously interpretable with reasonable effort.

The most significant and valuable correlations are observations that relate photon density measurements to shower size and primary energy, and temporal properties of the Cherenkov pulse to the longitudinal shower development. As mentioned in the two previous sections, in view of the relevance of these topics separate sections are devoted to them.

An example of one of the many correlations that had been explored we show in Fig. 16.26 the weak dependence of the Cherenkov pulse width at fixed core distance on shower size.

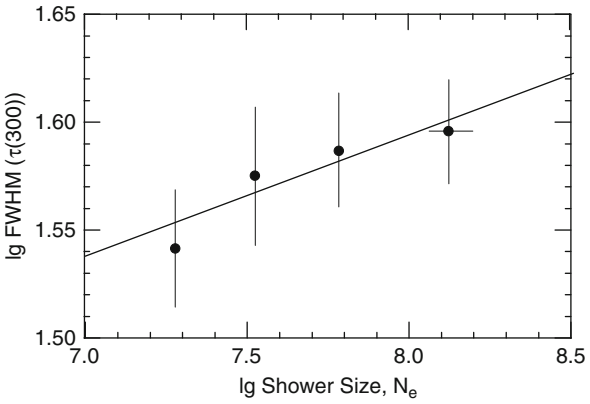

Fig. 16.26 Cherenkov pulse full width at half maximum (FWHM) measured at Yakutsk at a distance of 300 m from the shower axis, ($\tau(300)$), as a function of shower size, N_e, in large showers. The *line* is a fit to the data by the method of least squares (Kalmykov et al., 1977)

16.6.5 Cherenkov Density Spectra

For a brief discussion and some data on optical Cherenkov density spectra of showers the reader is referred to Sect. 12.4.

16.6.6 Miscellaneous Data

Specific calculations for the production of Cherenkov radiation in nuclear emulsion and gases, including the density effect were made by Sternheimer (1953).

References

Aglietta, M., et al.: Astropart. Phys., 21, p. 223 (2004).
Aharonian, F.A.: Very High Energy Cosmic Gamma Radiation, World Scientific, Singapore (2004).
Andam, A., et al.: PICRC, 9, p. 48 (1979).
Ascoli, R., and A. Balzanelli: Nuovo Cimento, 10, p. 1345 (1953).
Beck, G.: Phys. Rev., 74, p. 795 (1948).
Bernlöhr, K.: Astropart. Phys., 12, p. 255 (2000).
Blackett, P.M.S.: Phys. Soc. London, Gassiot Committee Report, p. 34 (1948).
Böhm, E., et al.: J. Phys. A, 10, p. 441 (1977).
Boley, F.I., et al.: Phys. Rev., 124, p. 1205 (1961).

Boley, F.I., et al.: Phys. Rev., 126, p. 734 (1962).
Boley, F.I.: Rev. Mod. Phys., 36, p. 792 (1964).
Bosia, G., et al.: Nuovo Cimento, 9 B, p. 201 (1972).
Bosia, G., et al.: Nuovo Cimento, 3 C, p. 215 (1980).
Brennan, M.H., et al.: Nuovo Cimento, Suppl. 8, p. 662 (1958).
Browning, R., and K.E. Turver: PICRC, 8, p. 3002 (1975).
Browning, R., and K.E. Turver: Nuovo Cimento, 38 A, p. 223 (1977).
Buckley, J.H.: Rapporteur Paper XXVI International Cosmic Ray Conference (1999), AIP Conference Proceedings, 516, p. 195 (2000).
Castagnoli, C., et al.: Nucl. Phys. B, 2, p. 369 (1967).
Castagnoli, C., et al.: Nuovo Cimento, 9 B, p. 213 (1972).
Catanese, M., and T.C. Weekes: Publication Astron Soc Pacific, 111, p. 1193 (1999).
Cawley, M.F., et al.: PICRC, 1, p. 118 (1983).
Cawley, M.F., et al.: PICRC, 3, p. 453 (1985).
Chadwick, P.M., et al.: Space Sci. Rev., 75, p. 153 (1996).
Chantler, M., et al.: PICRC, 9, p. 42 (1979).
Clay, R.W., and A.G. Gregory: J. Phys. A, 10, p. 135 (1977).
Cherenkov, P.A.: Dokl. Akad. Nauk SSSR, 2, p. 451 (1934).
Cherenkov, P.A.: Dokl. Akad. Nauk SSSR, 3, p. 413 (1936).
Cherenkov, P.A.: Dokl. Akad. Nauk SSSR, 14, p. 101 (1937a).
Cherenkov, P.A.: Dokl. Akad. Nauk SSSR, 14, p. 105 (1937b).
Cherenkov, P.A.: Phys. Rev., 52, p. 378 (1937c).
Cherenkov, P.A.: Byull. Akad. Nauk SSSR, 4–5, pp. 455 and 492 (1937d).
Cherenkov, P.A.: Dokl. Akad. Nauk SSSR, 20, p. 651 (1938a).
Cherenkov, P.A.: Dokl. Akad. Nauk SSSR, 21, p. 116 (1938b).
Cherenkov, P.A.: Dokl. Akad. Nauk SSSR, 21, p. 319 (1938c).
Chudakov, A.E., and N.M. Nesterova: Nuovo Cimento, Suppl. 8, p. 606 (1958).
Chudakov, A.E., et al.: PICRC, 2, p. 50 (1960).
Chudakov, A.E., et al.: PICRC, 4, p. 199 (1963).
Cocconi, G.: PICRC, Moscow 1959, 2, p. 309 (1960).
Cox, R.T.: Phys. Rev., 66, p. 106 (1944).
Curie, E.: Madame Curie, Heinemann, London (1941).
Diminstein, O.S., et al.: Paper presented at the 3rd. European Symposium on Air Showers, Paris (1972).
Diminstein, O.S., et al.: PICRC, 12, p. 4318 (1975).
Dixon, H.E., et al.: PICRC, 4, p. 2473 (1973).
Drury, L.O'C.: Space Sci. Rev., 75, p. 269 (1996).
Dyakonov, M.N., et al.: PICRC, 4, p. 2384 (1973a).
Dyakonov, M.N., et al.: PICRC, 4, p. 2389 (1973b).
Dyakonov, M.N., et al.: PICRC, 8, p. 174 (1979).
Efimov, N.N., et al.: PICRC, 4, p. 2378 (1973).
Efimov, N.N., and V.F. Sokurov: PICRC, 8, p. 152 (1979).
Egorov, T.A., et al.: PICRC, 6, p. 2059 (1971a).
Egorov, T.A., et al.: PICRC, 6, p. 2164 (1971b).
Elterman, L., and R.B. Toolin: Handbook of Geophysics and Space Environments, Chap. 7, Air Force Cambridge Research Laboratory, Office of Aerospace Research, USAF (1965).
Elterman, L.: Air Force Cambridge Research Laboratory, Ref. AFC RL-68-0153 (1968).
Fegan, D.J.: Space Sci. Rev., 75, p. 137 (1996).
Firkowski, R., et al.: Nuovo Cimento, 26, p. 1422 (1962).
Firkowski, R., et al.: Nuovo Cimento, 29, p. 19 (1963).
Fomin, Yu.A., and G. Khristiansen: Yad. Fiz., 14, S3, p. 654 (1971).
Frank, I.M., and I.G. Tamm: Dokl. Akad. Nauk SSSR, 14, p. 109 (1937).
Galbraith, W., and J.V. Jelley: Nature, 171, p. 349 (1953).

Galbraith, W., and J.V. Jelley: J. Atmos. Terr. Phys., 6, p. 250 (1955).
Gawin, J., et al.: PICRC, 4, p. 180 (1963).
Gawin, J., et al.: PICRC, 2, p. 639 (1965).
Ginsburg, V.L.: Zh. fiz. SSSR, 2, p. 441 (1940a).
Ginsburg, V.L.: Zh. Eksp. Teor. Fiz., 10, p. 589 (1940b).
Glushkov, A.V., et al.: Preprint YaFAN, Yakutsk (1978).
Glushkov, A.V., et al.: PICRC, 8, p. 158 (1979).
Gol'danskii, V.I., and G.B. Zhdanov: Zh. Eksp. Teor. Fiz., 26, p. 405 (1954). [Engl. transl.: Sov. Phys. JETP, 26, p. 405 (1954)].
Grindlay, J.E.: Harvard College Obs. and Smithsonian Astrophys. Obs., Center for Astrophysics, preprint Series No. 150 (1974).
Guzhavin, V.V., et al.: PICRC, 8, p. 3029 (1975a).
Guzhavin, V.V., et al.: PICRC, 8, p. 3024 (1975b).
Hammond, R.T., et al.: Nuovo Cimento, 1 C, p. 315 (1978).
Hara, T., et al.: PICRC, 8, p. 308 (1977).
Hartman, D.H., et al.: Nuovo Cimento, 51A, p. 131 (1979).
Hill, D.A., and N.A. Porter: Nature, 191, p. 690 (1961).
Hillas, A.M.: J. Phys. G, 8, p. 1475 (1982).
Hillas, A.M.: PICRC, 3, p. 445 (1985).
Hillas, A.M.: Space Sci. Rev., 75, p. 17 (1996).
Inoue, N., et al.: PICRC, 11, p. 270 (1981a).
Inoue, N., et al.: PICRC, 11, p. 274 (1981b).
Ivanenko, I.P., et al.: Acad. of Sci. of U.S.S.R., P.N. Lebedev Phys. Inst., preprint ref. 98 (1976).
Ivanenko, I.P., et al.: PICRC, 9, p. 83 (1979a).
Ivanenko, I.P., et al.: PICRC, 9, p. 88 (1979b).
Jelley, J.V., and W. Galbraith: Phil. Mag., 44, p. 619 (1953).
Jelley, J.V., and W. Galbraith: J. Atmos. Terr. Phys., 6, p. 304 (1955).
Jelley, J.V.: Cherenkov Radiation and its Applications, Pergamon Press, London (1958a).
Jelley, J.V.: Nuovo Cimento, Suppl. VIII, p. 578 (1958b).
Jelley, J.V.: Planetary and Space Science, Pergamon Press, Oxford, Vol. 1, p. 105 (1959).
Jelley, J.V.: Prog. Cosmic Ray Phys., IX, p. 41 (1967).
Jenkins, F.A., and H.E. White: Fundamentals of Physical Optics, 1st ed., McGraw-Hill Co., New York (1937).
Kalmykov, N.N., et al.: PICRC, 6, p. 2074 (1971).
Kalmykov, N.N., et al.: PICRC, 8, p. 3034 (1975).
Kalmykov, N.N., et al.: PICRC, 8, p. 244 (1977).
Kamata, K., et al.: Can. J. Phys., 46, p. 72 (1968).
Khristiansen, G.B.: Cosmic Rays of Superhigh Energies, Karl Thiemig Verlag, München (1980).
Konopelko, A.K.: Towards a Major Atmospheric Cherenkov Detector – V. Kruger National Park Workshop on TeV Gamma Ray Astrophysics, 8–11 August 1997, Kruger National Park, South Africa, O.C. de Jager Ed.,Potchefstroom University, p. 208 (1997).
Krieger, A.S., and H.V. Bradt: Can. J. Phys., 46, p. 87 (1968).
Krieger, A.S., and H.V. Bradt: Phys. Rev., 185, p. 1629 (1969).
Kuhlmann, J.D., et al.: PICRC, 8, p. 239 (1977).
Kuhlmann, J.D., and R.W. Clay: J. Phys. G, 7, p. L183 (1981).
Lewis, D.A., et al.: PICRC, 2, p. 338 (1987).
MacKeown, P.K., et al.: PICRC, 9, p. 175 (1983).
Makarov, V.V., et al.: PICRC, 11, p. 289 (1981).
Makhmudov, B.M., et al.: PICRC, 9, p. 61 (1979).
Mallet, L.: Comptes Rendus Acad. Sci. Paris, 183, p. 274 (1926).
Mallet, L.: Comptes Rendus Acad. Sci. Paris 187, p. 222 (1928).
Mallet, L.: Comptes Rendus Acad. Sci. Paris 188, p. 445 (1929).
Malos, J., et al.: J. Phys. Soc. Jpn, 17, p. 114 (1962).

Matano, T., and V.S. Narasimham: PICRC, 4, p. 290 (1963).
McComb, T.J.L., et al.: PICRC, 9, p. 53 (1979).
McComb, T.J.L., and K.E. Turver: PICRC, 6, p. 130 (1981).
McComb, T.J.L., and K.E. Turver: Nuovo Cimento C, 5, p. 131 (1982).
Neamtan, S.M.: Phys. Rev., 92, p. 1362 (1953).
Nesterova, N.M., and A.E. Chudakov: Zh. Eksp. Teor. Fiz., 28, p. 384 (1955). Sov. Phys. JETP, 1, p. 388 (1955).
Ong, R.A.: Phys. Rep., 305, p. 93 (1998).
Orford, K.J., et al.: PICRC, 8, p. 3014 (1975a).
Orford, K.J., et al.: PICRC, 8, p. 3019 (1975b).
Orford, K.J., and K.E. Turver: Nature, 264, p. 727 (1976).
Patterson, J.R., and A.M. Hillas: J. Phys. G, 9, p. 323 (1983a).
Patterson, J.R., and A.M. Hillas: J. Phys. G, 9, p. 1433 (1983b).
Pinkau, K.: Astron. Astrophys., Suppl. Ser., 120, p. 43 (1996).
Polikarov, A.: C.R. Acad. Bulg. Sci., 7, 2, p. 29 (1954).
Protheroe, R.J., et al.: PICRC, 8, p. 3008 (1975).
Protheroe, R.J., and K.E. Turver: Nuovo Cimento, 51 A, p. 277 (1979).
Ramana-Murthy, P.V., and A.W. Wolfendale: Gamma Ray Astronomy, 2nd ed., Cambridge University Press, Cambridge (1993).
Rieke, G.H.: Acta Phys. Acad. Sci. Hung., 29, S3, p. 601 (1970).
Schiff, L.I.: Quantum Mechanics, McGraw-Hill, New York, p. 267 (1955).
Schönfelder, V., ed.: "The Universe in Gamma Rays", Springer Verlag, Berlin, Heidelberg, New York (2001).
Shirasaki, Y., et al.: Astropart. Phys., 15, p. 357 (2001).
Sitte, K.: Nuovo Cimento, 25, p. 86 (1962).
Sitte, K.: Acta Phys. Acad. Sci. Hung., 29, S3, p. 389 (1970).
Smirnov, V.A.: Vvedenie v opticheskuyu radioelektroniku. Moskwa, izd. Sov. radio, 208 s (1973).
Smith, G.J., and K.E. Turver: J. Phys. A, 6, p. L121 (1973a).
Smith, G.J., and K.E. Turver: PICRC, 4, p. 2369 (1973b).
Sokolov, A.: Dokl. Akad. Nauk SSSR, 28, p. 415 (1940).
Sokolov, A.A., and Yu.M. Loskutov: Zh. Eksp. Theor. Fiz., 32, p. 630 (1957).
Sommerfeld, A.: Optics, Academic Press, New York, p. 328 (1954).
Sternheimer, R.: Phys. Rev., 91, p. 256 (1953).
Suga, K., et al.: PICRC, 4, p. 9 (1963).
Tamm, I.G.: Zh. fis., SSSR, 1, p. 439 (1939).
Taniuti, T.: Prog. Theor. Phys. Jpn, 6, p. 207 (1951).
Thornton, G.J., and R.W. Clay: J. Phys. G, 4, p. L193 (1978a).
Thornton, G.J., and R.W. Clay: J. Phys. G, 4, p. L251 (1978b).
Tidman, D.A.: Nuovo Cimento, 3, Ser. 10, p. 503 (1956a).
Tidman, D.A.: Nuclear Phys., 2, p. 289 (1956b).
Tornabene, H.: PICRC, 9, p. 94 (1979).
Toyoda, Y., et al.: PICRC, 2, p. 708 (1965).
Trümper, J.: Cosmic Rays 92 – Astrophysical, High Energy and Heliospheric Processes. Proceedings of the 13th European Cosmic Ray Symposium, Geneva, 1992, P.K.F. Grieder, ed., Nucl. Phys. B (Proc. Suppl.), 33A/B, p. 126 (1993).
Turver, K.E., and T.C. Weekes: Nuovo Cimento, 45B, p. 99 (1978).
Turver, K.E.: Nucl. Phys. B (Proc. Suppl.), 28 B, p. 16 (1992).
Weekes, T.C.: PICRC, 8, p. 34 (1981).
Weekes, T.C.: Phys. Rep., 160, p. 1 (1988).
Weekes, T.C.: Harvard-Smithsonian Center for Astrophysics, Cambridge, MA 02138, Preprint Series No. 2802 (1989).
Weekes, T.C.: Space Sci. Rev., 75, p. 1 (1996).

Weekes, T.C.: Very High Energy Gamma-Ray Astronomy, Institute of Physics Publishing, Bristol, Vol. XV, p. 221 (2003a).
Weekes, T.C.: Invited paper presented at the 28th. ICRC, Tsukuba, Japan, July 31 – August 7, 2003. Frontiers of Cosmic Ray Science, Universal Academic Press, inc., Tokyo (Japan), PICRC, 8, p. 3 (2003b).
Zatsepin, V.I., and A.E. Chudakov: Zh. Eksp. Teor. Fiz., 42, p. 1622 (1962). JETP, 15, p. 1126 (1962).
Zatsepin, V.I.: Zh. Eksperim. i. Theor. Fiz., 47, p. 689 (1964) (in Russian)
Zatsepin, V.I.: Sov. Phys. JETP, 20, p. 459 (1965).

Chapter 17
Atmospheric Fluorescence

Overview This chapter deals exclusively with atmospheric fluorescence caused by air showers, its production, detection and interpretation. After discussing the basic mechanisms of gas fluorescence, in particular of air and nitrogen fluorescence, including associated quenching effects, we illuminate its role in air shower research. We outline the unique features of atmospheric fluorescence and discuss the detection principle, describe the atmospheric effects of dust and aerosols, scattering processes such as Rayleigh and Mie scattering, and the influence of seasonal pressure changes that cause varying absorption and attenuation of the fluorescence light. The evaluation of the data to determine the energy and composition of the primary radiation is summarized together with specific data. The resulting primary spectrum and conclusions on the primary mass and its energy dependence are presented in Chap. 11.

17.1 Introduction

The detection of air showers by means of *air fluorescence emission* (air scintillation) caused by air shower particles in the atmosphere along their track has long been considered by a number of scientists as a mean for exploring the most energetic region of the primary cosmic ray spectrum. To our knowledge Suga and Oda were among the first to discuss this possibility as early as the mid fifties. Following these ideas Ozaki and collaborators in Osaka, Japan, attempted viewing large showers side-on from a distance with an image intensifier, using the isotropically emitted fluorescence light, however, without success. In the sixties more concrete ideas began to evolve and tangible solutions were discussed by several authors (Chudakov, 1962; Suga, 1962; Suga et al., 1962; Greisen, 1965). Subsequently, a variety of exploratory experiments were carried out (Bunner, 1967; Hara et al., 1970; Porter et al., 1970; Tanahashi et al., 1975).

The basic concept that eventually evolved is shown in Figs. 17.1 and 17.2. It consists of a large hemispherically sensitive optical detector of modular design with good angular and high time resolution. With adequate sensitivity such a system can track large showers across its field of view under favorable atmospheric and optical background conditions. For constructional, operational and economic reasons the single large hemispherical detector structure of the pioneering days (Bunner, 1967;

P.K.F. Grieder, *Extensive Air Showers,* DOI 10.1007/978-3-540-76941-5_17,

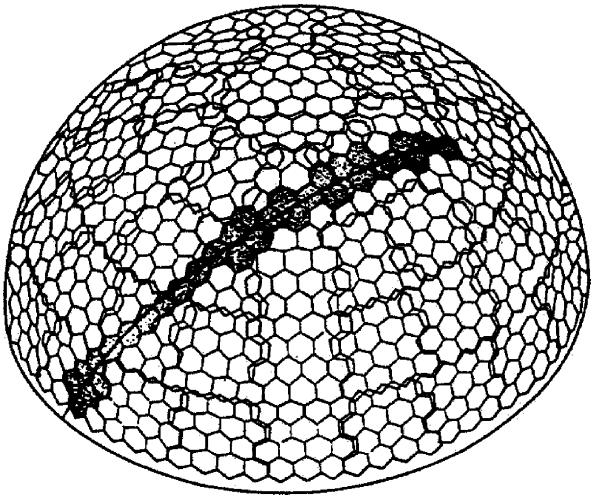

Fig. 17.1 Principle of a Fly's Eye type atmospheric fluorescence detector. Shown are the hexagonal elements that define the field of view of the optical detector units that view a well defined section of solid angle of the sky, each. A perfect geometrical fit of the individual elements would be very restricted in number (compare a championship football) and is not required, as long as full coverage is achieved. The figure also shows the image of a light patter of an inclined shower that strikes at some distance, as is seen by the "Eye"

Hara et al., 1970) was abandoned in later years in favor of many smaller separate modules, each containing a cluster of individual sensor elements, that are grouped around the site's center such that combined they have the same full hemispherical sky coverage. This constructional change does not affect the principle of operation and event reconstruction.

The air fluorescence method offers several important advantages when compared with common particle detector type shower arrays:

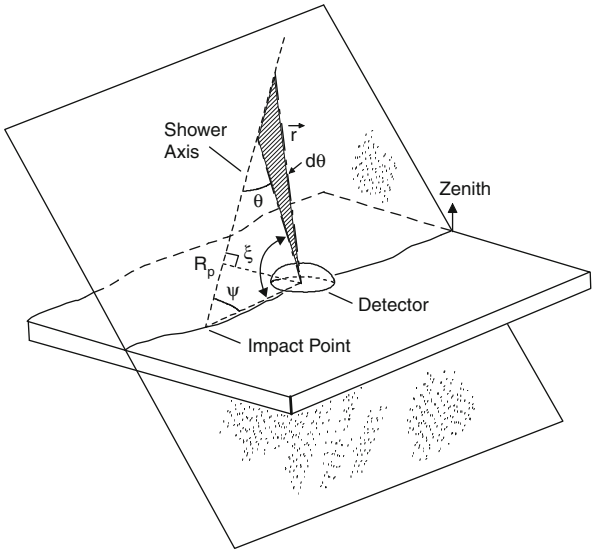

Fig. 17.2 Geometry of an air shower trajectory as seen by a hemispherical Fly's Eye type detector. The shower-detector plane contains both the shower axis and the *center* of the detector. It is specified by fits to the spatial pattern of "hit" photomultipliers which must lie along a great *circle* on the celestial sphere. The angle ψ and impact parameter R_p are obtained by fits to the observation angles, ξ, versus time of observation (after Baltrusaitis et al., 1985)

- Instead of sampling the showers only at a few points in a loose pattern of an array on the ground at a particular stage of development and requiring that the shower axis be within the detector array for reliable data interpretation, the atmospheric fluorescence method allows to observe the shower so to say from the outside, at some distance and angle, side-on with a relatively compact detector system.
- It is capable of revealing almost the entire history of each of the recorded events since, unlike particle detector arrays, it records the longitudinal profile of the showers as well.
- It provides a direct measure of the number of particles above about 20 eV in a shower because the fluorescence is assumed to be proportional to the energy dissipated in the air by ionization.
- It uses the atmosphere as a calorimeter and permits to determine the total energy of a shower directly without requiring uncertain interaction models, theories and simulations.
- It is not subject to large observational fluctuations because of the abundant number of photons that are detected, even from distant events, as compared to the small number of particles that are usually recorded by the detectors of an array per shower.
- The radiation that is detected is emitted isotropically from the shower, and hence diminishes more slowly with distance from the axis than the other detectable effects of a shower, such as Cherenkov radiation or radio emission.
- The effective radial distance for event recognition increases with primary energy.
- Like particle detector arrays, it is capable to determine the direction of incidence of the primary and the point of impact of the axis on the ground.
- Two or more locally separated fluorescence detector systems permit stereo view of the events, which enriches the information contents and reduce ambiguities in the data interpretation.

There are, however, severe disadvantages and limitations to this method that restrict its application:

- A fluorescence detector site must be in a climatically and meteorologically suitable region with little cloud coverage and low precipitation.
- The atmosphere must be stable and should have a low aerosol and dust content to reduce light scattering and attenuation.
- The detector must be in an area of low optical background, away from urban settlements.
- It can only be operated on clear, moonless nights.
- Fluctuations in the background caused by starlight and light from the night sky set a threshold and obscure fluorescence radiation from small showers.
- The atmosphere (a large shower may utilize well over 10^{12} m^3 of air) is neither a very efficient scintillator nor an ideal transmitter of emitted radiation.

In spite of these drawbacks the fluorescence method is now being used very successfully.

17.2 Fluorescence and Its Detection in E.A.S.

17.2.1 Basics and Early Work

First measurements of the spectrum of the light produced by fast particles in air, excluding Cherenkov light, had been carried out by Davidson and O'Neil, (1964) using 50 keV electrons at a pressure of 600 mmHg, and by Bunner using 4 MeV α-particles and deuterons in air (Bunner, 1964, unpublished). The results of Bunner are shown in Fig. 17.3. According to these authors, the usable light is almost entirely in the $2P$ and $1N$ band systems of molecular nitrogen (N_2) (Nicholls et al., 1959; Hughes et al., 1961).[1] The photon yield, Y, is inversely proportional to the density $(\rho + \rho_k)$ per unit of ionization energy loss,

$$Y \propto (\rho + \rho_k)^{-1} \text{ [ph/MeV]} . \tag{17.1}$$

The density ρ_k corresponds to a pressure of 13 mbar for the $2P$ system and 8 mbar for the $1N$ system. Figure 17.4 shows the altitude dependence of the photon yield at 360 nm. Since showers do not develop significantly until $\rho \gg \rho_k$ and the ionization loss per unit path length, $\mathrm{d}E/\mathrm{d}x$, is proportional to ρ, the light yield per unit of path length is almost independent (within $\simeq 10\%$) of pressure (or altitude) and temperature because of radiationless molecular collision de-excitation (*quenching*) that is in competition with fluorescence (Greisen, 1965; Landecker, 1967, unpublished). The decay time of air fluorescence is typically less than 10 ns.

The total measured yield per MeV of energy loss in air at one atmosphere is about 15 photons in the spectral region between 300 and 430 nm. This represents a

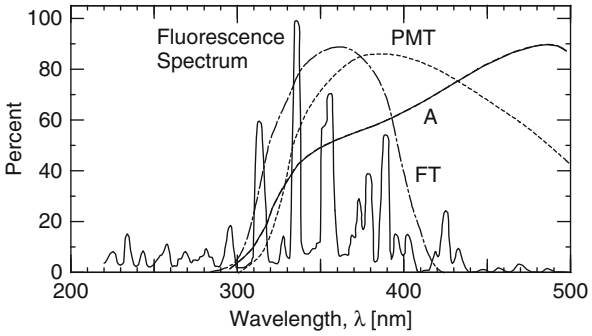

Fig. 17.3 Atmospheric fluorescence light spectrum (*solid curve* with the many peaks) (Bunner, 1964, unpublished; Bunner, 1966). Also shown are the atmospheric transmission (*curve A*), the combined phototube-lens sensitivity (PMT) and the filter transmission (FT) to remove longer wavelength background light (Porter et al., 1970)

[1] The typically used wavelength region is 300–400 nm and for this range the contribution of $1N$ is only about 10%.

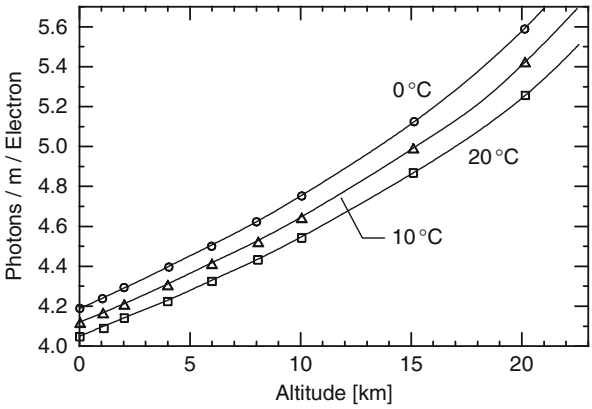

Fig. 17.4 Atmospheric fluorescence yield as a function of altitude (equivalent 360 nm ph (e^{-1} m^{-1})) (Baltrusaitis et al., 1985)

conversion efficiency of $\simeq$0.005% and yields 4.4 photons in this wavelength range per meter of track length per minimum ionizing particle at sea level (4.4 ph m^{-1} e^{-1}).

According to Bunner (1964, unpublished), 25% of the emission occurs at short wavelength that is very poorly transmitted by the atmosphere. Hardly any of the light is found at wavelengths longer than 428 nm, hence, the signal-to-noise ratio can be improved by using a filter that transmits only in the deep blue and ultraviolet. Taking into account the transmission of a normal atmosphere as well as the energy loss of fast electrons in air, the *effective yield at the detector* is approximately one to two photons per meter of track length for a large shower that strikes at a distance of about 10 km. *Rayleigh scattering* (Rayleigh, 1881; Gans, 1925), discussed in Sect. 17.3.3, reduces the light from great distances by a factor of about two for each additional 10 km. The *background light* from the dark (moonless) night sky is at best about 10^5 ph m^{-2} μs^{-1} sr^{-1}.

The fundamental problem is the optimization of the signal-to-noise ratio. The key to success lies to a great part in the detection and signal processing systems. Pioneering work was carried out chiefly at Cornell University (Greisen, 1965; Bunner, 1967; Bunner et al., 1968) and in Tokyo (Hara et al., 1970), where the *Fly's Eye* concept was born. It was further developed and realized later on, on a large scale in the US at Dugway, Utah (Bergeson et al., 1975a, b, 1977; Cassiday, 1985).

The detection concept is illustrated in Fig. 17.2. It consists of an optical recording system with a field of view of 2π [sr] that covers the sky from horizon to horizon, all around, therefore the name "Fly's Eye". The entire detector is subdivided into many individual detector modules. Each module views a well defined small element of solid angle, and has a high time resolution, in order to track a shower geometrically and in time. The latter represents the *third dimension* in the trajectory image.

Neglecting absorption and possible contributions from direct and scattered Cherenkov light, the basic criteria for such a detector and the steps that are required for event reconstruction can be formulated as follows (Greisen, 1965).

Let the solid angle element $\Delta\Omega = (\pi/4)(\Delta\phi)^2$, where $\Delta\phi$ is the full width of the angular resolution or pixel width, and Δt the integration time of the signal. Assume $\Delta\phi$ and the distance $|\vec{r}|$ of the receiver from the shower to be such that the source of light can be treated as a point moving across the sky at the speed of light, c. Let θ be the angle between the radius vector $\vec{r}$ and the shower axis, so that the impact parameter of the shower with respect to the receiver is $R_p = |\vec{r}| \cdot \sin(\theta)$.

Furthermore, let N_e be the number of electrons in the shower, Y the light yield in photons per electron per meter of path length, A the optical light collecting area, ϵ_{pe} the photon conversion efficiency of the photocathode, and B the background light in photons per unit area, solid angle and time. The light received in the time interval Δt comes from the path length element Δl of the shower, where

$$\Delta l \;=\; \Delta(R_p/\tan(\theta)) \;=\; c\;\Delta t\left(\frac{1+\cos(\theta)}{\sin^2(\theta)}\right)\;\;[\mathrm{m}]\;, \tag{17.2}$$

and amounts to a photon number, N_{ph}, of

$$N_{\mathrm{ph}} \;=\; \frac{N_e Y \Delta A}{4\pi r^2}\;\;[\mathrm{ph}]\;. \tag{17.3}$$

Excluding absorption, the signal, S, expressed by the number of *photoelectrons* [pe] produced in the detector due to *fluorescent light only* from the source in this time interval is

$$S \;=\; \left(\frac{1\;+\;\cos(\theta)}{4\pi R_p^2}\right)\epsilon_{\mathrm{pe}} A N_e Y c \Delta t\;\;[\mathrm{pe}]\;. \tag{17.4}$$

It should be noted that S depends on R_p rather than on $|\vec{r}|$, so the observability of a shower depends on the impact parameter rather than the instantaneous distance.

Similarly, the noise, N, expressed by the number of photoelectrons due to the background light received in the same time interval is

$$N \;=\; \sqrt{\epsilon_{\mathrm{pe}} A B \Delta t \Delta\Omega}\;\;[\mathrm{pe}]\;. \tag{17.5}$$

Hence the signal-to-noise ratio, κ, is

$$\kappa \;=\; \frac{S}{N} \;= N_e Y c\left(\frac{1\;+\;\cos(\theta)}{4\pi R^2}\right)\sqrt{\frac{A\epsilon_{\mathrm{pe}}\Delta t}{B\Delta\Omega}}\;\;. \tag{17.6}$$

If this ratio must exceed κ for detectability and measurability of an event, the requirement is that

$$N_e\left(\frac{1\;+\;\cos(\theta)}{R^2}\right) > \frac{4\pi\kappa}{Yc}\sqrt{\frac{B\Delta\Omega}{A\epsilon_{\mathrm{pe}}\Delta t}}\;\;. \tag{17.7}$$

Note that κ need not be very large, because in the selection of the event one may use the fact that numerous phototubes at neighboring angles will display successive signals. As an example, with $\kappa = 5$, $Y = 1\ \mathrm{ph\,m^{-1}(e^{\pm})^{-1}}$, $B = 10^5\ \mathrm{ph\,m^{-2}\mu s^{-1}\,sr^{-1}}$, $\Delta\Omega = 10^{-2}$ sr, $A = 10^{-1}\ \mathrm{m^2}$, $\epsilon_{\mathrm{pe}} = 0.1$ and $\Delta t = 1\,\mu\mathrm{s}$, one finds that the shower size N_e must exceed $1.3 \cdot 10^{10}$ for an impact parameter of $R_p = 20\,\mathrm{km}$.

Even taking into account Rayleigh scattering, a shower of 10^{11} particles should be observable out to about 30 km, i.e., over a sensitive area $\geq 2,500\,\mathrm{km^2}$. It is also possible to have several such detectors, enlarging the total area of surveillance to 10^4 km and more. Most of the showers will occur at larger zenith angles, where the atmosphere is thick enough to contain almost the entire life history of each event.

As briefly mentioned earlier, a modern Fly's Eye type all-sky detector system does not have the hemispherical geometry as shown in Fig. 17.1 for explaining the basic principle, but may count several dozen separate sub-units that are placed at close proximity of each other at the detector site. The units consist of a large spherical mirror with a cluster of tightly packed photomultipliers tubes (PMT) or CCD units mounted in the focal zone, viewing the mirror through a set of optical filters. The optical detectors (PMTs or CCDs) are placed in cone shaped blinds (Winston Funnels) (Winston, 1970) to accurately define the field of view of each detector element. Each of the sub-units points in a particular direction of the sky, covering a certain solid angle. Combined the units cover the full sky or that part that is of interest for the particular experiment or site.

The orientation of the plane containing the shower axis, the radius vectors $\vec{r}$ and impact parameter R_p are fixed by the identity of the sequence of tubes which register the light pulses. The angle θ between the shower axis and $\vec{r}$ in this plane and the distance R_p are determined by the pulse duration and the time intervals between them. Having their coordinates and disregarding perturbing effects, the particle number as a function of time, $N_e(t)$, is obtained from the pulse heights and the relations given above.

Fluorescence light only is a direct measure of the total energy deposited by a shower in the atmosphere. However, direct as well as scattered Cherenkov light entering the detector's field of view disrupt that relationship and must be accounted for. Likewise scattering and attenuation of the fluorescence component must be considered, too, when interpreting an event. For more accurate calculations Eqs. (17.4), (17.6) and (17.7) must be refined, to include absorption and scattering of light as well as other effects. These topics are discussed in Sects. 17.3.5 and 17.3.6.

17.2.2 Recent Fluorescence Studies, Yield

Recently with the coming of a new generation of Fly's Eye type detectors, such as the *High Resolution Fly's Eye* (HiRes) in Utah (Corbato et al., 1992; Abu-Zayyad et al., 2000),[2] the *Japanese Telescope Array* (Teshima et al., 1992; Kawai

[2] HiRes had been shut-down in 2006.

et al., 2005), the directionally confined air fluorescence detectors at the Auger site in Argentina (Guérard, 1999),[3] or the proposed EUSO (Scarsi, 1999, 2001) and OWL-AIRWATCH (Catalano, 1999) satellite based instruments, where far better optics will permit more precise measurements, it became necessary to study the air fluorescence phenomenon more thoroughly and fix the relevant parameters more accurately.

Kakimoto et al. (1995a, b, 1996) have carried out detailed measurements of the fluorescence caused by electrons of energy 1.4, 300, 650, and 1,000 MeV, the range relevant for air showers, using dry air at different temperatures over a pressure range from 40 to 760 mmHg, and 99.998% pure nitrogen whose yield is about a factor of 5.6 higher than that of air. The reduced yield of air is due to the presence of oxygen molecules with their many low lying energy states that reduce the fluorescence yield by collision de-excitation (Bunner, 1964, unpublished). Care was taken to eliminate any contribution from direct Cherenkov light. The contribution from scattered Cherenkov light was calculated to be negligible in their set-up.

These authors have made precision measurements in the near ultraviolet and the visible regions, covering the 337.1, 357.7, and 391.4 nm bands of nitrogen separately with narrow band filters, and confirm that the yield is strongest in the 300–400 nm range. They note that in this spectral range the fluorescence yield, Y, in photons per meter per electron [ph $\mathrm{m}^{-1}(\mathrm{e}^{\pm})^{-1}$] of air is proportional to the energy loss of an electron per unit path length, $(\mathrm{d}E/\mathrm{d}x)$, that the 337 and 357 nm bands have the same pressure dependence, and that the 391 nm band does not show much dependence over the pressure range from 760 down to 40 mmHg.

The above mentioned results had been parametrized by Kakimoto et al. (1995a, b, 1996) who specify the following equation to compute the fluorescence yield,

$$Y = \left(\frac{\left(\frac{\mathrm{d}E}{\mathrm{d}x}\right)}{\left(\frac{\mathrm{d}E}{\mathrm{d}x}\right)_{1.4\,\mathrm{MeV}}} \right) \rho \left\{ \frac{A_1}{1+\rho B_1 \sqrt{T}} + \frac{A_2}{1+\rho B_2 \sqrt{T}} \right\} \quad [\mathrm{ph\,m^{-1}(e^{-})^{-1}}] \quad (17.8)$$

where $(\mathrm{d}E/\mathrm{d}x)$ is the energy loss [MeV m^{-1}], ρ the density of the medium [kg m^{-3}], T is the temperature [K], and $(\mathrm{d}E/\mathrm{d}x)_{1.4\ \mathrm{MeV}}$ is the energy loss evaluated at 1.4 MeV. The constants A_1, A_2, B_1, and B_2 are given in Table 17.1. Both, relativistic rise and density effects are accounted for in the energy loss calculations. In order to compare their results with those of Davidson and O'Neil (1964) and Bunner (1964, unpublished), Kakimoto et al. (1996) calculated the fluorescence efficiencies, defined as the radiated energy divided by the energy loss in the observed medium, for the three emission lines. The results are shown in Table 17.2. The authors specify for their work a systematic error of 10% and statistical error of 3%.

In a similar study Nagano et al. (2003, 2004), using beta particles from a ^{90}Sr source ($E_{\max} = 2.28$ MeV) and a threshold of 0.3 MeV (mean energy 0.85 MeV) investigated the photon yield in nitrogen and dry air in the wavelength range from 300 to 406 nm. Some of the results of this experiment and of the work of

[3] For an extensive description of the Auger Project that is in partial operation since 2006, see reference Abraham et al. (2004), listed in Chap. 1.

Table 17.1 Constants of Eq. (17.8) (Kakimoto et al., 1996)

A_1	89.0 ± 1.7 m^2 kg^{-1}	B_1	1.85 ± 0.04 m^3 kg^{-1} K$^{-1/2}$
A_2	55.0 ± 2.2 m^2 kg^{-1}	B_2	6.50 ± 0.33 m^3 kg^{-1} K$^{-1/2}$

Table 17.2 Comparison of fluorescence efficiencies for 3 different wavelengths and particle beams (Kakimoto et al., 1996)

		Davidson and O'Neil (1964)	Kakimoto et al. (1995a, b)	Bunner (1964)
	Beam	50 keV e$^-$	1.4 MeV e$^-$	4 MeV α
	Pressure (nm)	600 mmHg	600 mmHg	760 mmHg
Wavelength	337	$2.1 \cdot 10^{-5}$	$2.1 \cdot 10^{-5}$	$1.5 \cdot 10^{-5}$
	357	$1.5 \cdot 10^{-5}$	$2.2 \cdot 10^{-5}$	$1.2 \cdot 10^{-5}$
	391	$0.70 \cdot 10^{-5}$	$0.84 \cdot 10^{-5}$	$0.43 \cdot 10^{-5}$

Kakimoto et al. (1996) and the more recent work of Arciprete et al. (2005) (AIRFLY experiment) are summarized in Fig. 17.5 (see also Bérat et al., 2003).

In a new major effort, partly in connection with the development of air fluorescence detectors for the Auger project in Argentina and their operation, several groups have undertaken very systematic studies to settle open questions and lingering uncertainties concerning air fluorescence production and its dependence on a variety of parameters (pressure, temperature, humidity and particle energy). Apart from studying the fundamental process experimentally, using electron beams of different energies in several experiments such as FLASH (Hüntemeyer, 2005; Reil and Hüntemeyer, 2005), AIRFLY (Arciprete et al., 2005), and AirLight (Waldenmaier et al., 2005), several groups have also investigated theoretically and experimentally air fluorescence in the atmosphere, and the effects of environmental parameters on the atmospheric profile and the fluorescence yield (Arqueros et al., 2006; Keilhauer et al., 2004, 2005, 2006).

This latter topic is, of course, of relevance for all other air shower investigations, but above all for those that are aimed at the determination of the height of maximum development, as the conclusions drawn from these data affect subsequently derived observables, such as the primary composition. General and specific atmospheric properties are discussed in Sect. B.3, and related topics concerning the longitudinal development of the showers in Chaps. 6 and 7.

As mentioned in Sect. 17.2.1, nitrogen molecules (N_2) that are excited mostly by the copiously present electrons ($e^{\pm}$) in a shower are the principal contributors to air fluorescence and non-radiative molecular collision de-excitation which acts as a fluorescence quencher plays an important role, too. In addition, electron affine constituents such as O_2, H_2O and other agents can reduce the low energy electron population by electron attachment and therefore fluorescence production.

The quantum efficiency for fluorescence, ϵ, is given by the ratio of the rates of radiative de-excitation to the total de-excitation, where the rates of de-excitation are inversely proportional to the mean life of the states. Thus,

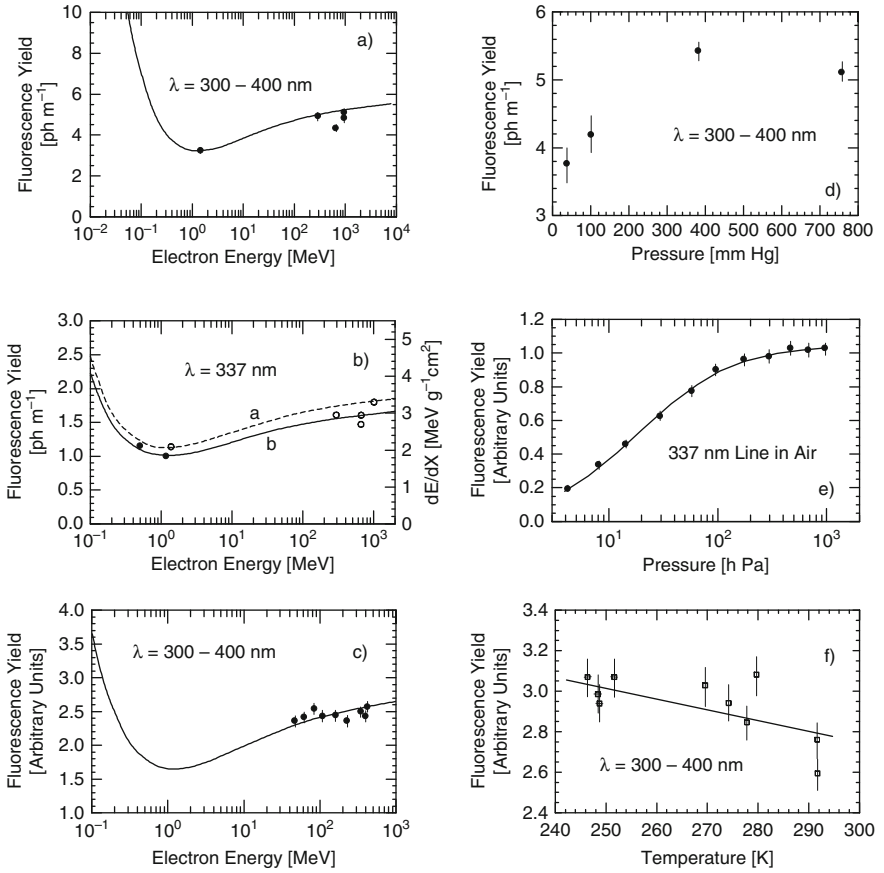

Fig. 17.5 Compilation of data showing the predicted (*curves*) and measured (*symbols*) dependence of the fluorescence yield as a function of different parameters. (**a**) (Kakimoto et al., 1996) at 760 mmHg total for the wavelength band 300–400 nm, (**b**) (Nagano et al., 2003, 2004; Ueno, 1996) at 1,000 hPa for the 337 nm line, and (**c**) (Arciprete et al., 2005) for the band from 300 to 400 nm in arbitrary units, all in dry air. The pressure dependence is shown in (**d**) (Kakimoto et al., 1996) for the band 300–400 nm, and (**e**) (Arciprete et al., 2005) the relative dependence for the 337 nm line (the *curve* is a fit to the data). The relative temperature dependence is shown for the band 300–400 nm in (**f**) (Arciprete et al., 2005)

$$\epsilon = \frac{\tau_q}{\tau_0 + \tau_q} \ , \tag{17.9}$$

where τ_q and τ_0 are the mean lives for collision quenching and radiative transitions to any lower state, respectively.

Collision quenching is a function of the collision rate, which is a function of the mean velocity of the molecules,

$$\overline{v} \;=\; \sqrt{\frac{8kT}{\pi M}} \;, \tag{17.10}$$

and depends also on the density and the collision cross section. Hence,

$$\tau_q \;=\; \sqrt{2}\rho_n \sigma_{N,N} \overline{v} = \left(\frac{1}{4\rho_n \sigma_{N,N}}\right) \sqrt{\frac{\pi M}{kT}} \;. \tag{17.11}$$

Here, ρ_n is the particle number density, $\sigma_{N,N}$ the molecular collision cross section for nitrogen (N_2), T the temperature in [K], k the Boltzmann constant, and M the molecular mass.

The fluorescence efficiency at the wavelength λ is defined as (Keilhauer et al., 2005, 2006)

$$\epsilon_\lambda(P,T) \;=\; \frac{\epsilon_\lambda(P \to 0)}{1 + (P/P'_\nu(T))} \;=\; \frac{n\, E_\gamma}{E_{\text{dep}}} \;. \tag{17.12}$$

Here, $\epsilon_\lambda(P \to 0)$ is the fluorescence efficiency at wavelength λ without collisional quenching, n is the number of photons, $P/P'_\nu = \tau_{0,\nu}/\tau_{q,\nu}$, P is the pressure of the medium (N_2, air), and P'_ν is a reference pressure (Greisen, 1965). The parameters $\tau_{0,\nu}$ and $\tau_{q,\nu}$ are the mean life times of the excitation levels ν.

Following Keilhauer et al. (2005, 2006), one gets for the pressure ratio p/p'_ν in a simple two-component atmosphere consisting of nitrogen and oxygen the following expression:

$$\begin{aligned} \frac{P}{P'_\nu} \;&=\; \tau_{0,\nu}\left(\frac{1}{\tau_{NN,\nu}(\sigma_{NN,\nu})} + \frac{1}{\tau_{NO,\nu}(\sigma_{NO,\nu})}\right) = \frac{\tau_{0,\nu} P_{\text{air}} \cdot N_A}{RT}\sqrt{\frac{kTN_A}{\pi}} \\ &\times \left(4 \cdot \text{vol}\%(N_2) \cdot \sigma_{NN,\nu}\sqrt{\frac{1}{M_{m,N}}}\right. \\ &+\; \left. 2 \cdot \text{vol}\%(O_2) \cdot \sigma_{NO,\nu}\sqrt{2\left(\frac{1}{M_{m,N}} + \frac{1}{M_{m,O}}\right)}\right), \end{aligned} \tag{17.13}$$

where N_A is Avogadro's number, $M_{m,N}$ and $M_{m,O}$ are the masses per mole of nitrogen and oxygen, respectively, and $\sigma_{NN,\nu}$ and $\sigma_{NO,\nu}$ the corresponding collision cross sections.

The equations listed above had been used by Keilhauer et al. (2005, 2006) in their theoretical study of atmospheric fluorescence. These authors have calculated the fluorescence yield using a variety of input parameters obtained partly by different authors. In Table 17.3 we reproduce data of the deactivation constant, τ_0, in the lower atmosphere and molecular collision cross sections, $\sigma_{N,O}$ and $\sigma_{N,N}$, according to Bunner (1967) and Morozov et al. (2005), and likewise, in Table 17.4 the fluorescence yields, Y, at sea level obtained by different authors (after Keilhauer et al., 2005).

Table 17.3 Deactivation constants for air in the lower atmosphere (Keilhauer et al., 2005)

	Bunner (1967)			Morozov et al. (2005)		
	$\sigma_{N,O}$ [cm^2]	$\sigma_{N,N}$ [cm^2]	τ_0 [ns]	$\sigma_{N,N}$ [cm^2]	$\sigma_{N,\mathrm{Vapor}}$ [cm^2]	τ_0 [ns]
$1N\ v=0$	$13 \cdot 10^{-15}$	$4.37 \cdot 10^{-15}$	65.8	–	–	–
$2P\ v=0$	$2.1 \cdot 10^{-15}$	$1.0 \cdot 10^{-16}$	44.5	$1.82 \cdot 10^{-16}$	$8.53 \cdot 10^{-15}$	41.7
$v=1$	$5.0 \cdot 10^{-15}$	$3.5 \cdot 10^{-16}$	49.3	$3.77 \cdot 10^{-16}$	$8.04 \cdot 10^{-15}$	41.7
$v=2$	$7.0 \cdot 10^{-15}$	$8.0 \cdot 10^{-16}$	44.5	–	–	–
$v=3$	$8.0 \cdot 10^{-15}$	$1.2 \cdot 10^{-15}$	66.5	–	–	–

Taking for granted that the fluorescence yield in air is proportional to the energy deposited, the following relation can be used to compute the fluorescence yield at a given wavelength,

$$Y_\lambda = \epsilon_\lambda(P,T)\,\frac{\lambda}{hc}\,\frac{dE}{dX}\,\rho_{\mathrm{air}}\ \ [\mathrm{ph\,m^{-1}}]\ , \tag{17.14}$$

Table 17.4 Fluorescence yields at sea level in the US standard atmosphere (Keilhauer et al., 2005)

Wavelength [nm]	Band	ϵ_λ $(P \rightarrow 0)$ %	Fluorescence yield [ph m^{-1}] at sea level				
			Bunner (1967)	Davidson and O'Neil (1964)	Keilhauer et al. (2005)		Nagano et al. (2004)
					Table 17.3, Bunner (1967)	Table 17.3, Morozov et al. (2005)	
311.7	$2P$ (3–2)	0.005	0.008	–	0.009	0.009	–
313.6	$2P$ (2–1)	0.029	0.090	–	0.094	0.094	–
315.9	$2P$ (1–0)	0.050	0.224	–	0.240	0.279	0.549
328.5	$2P$ (3–3)	0.0154	0.027	0.035	0.029	0.029	0.180
330.9	$2P$ (2–2)	0.002	0.007	–	0.007	0.007	–
333.9	$2P$ (1–1)	0.0041	0.019	–	0.021	0.024	–
337.1	$2P$ (0–0)	0.082	0.887	1.173	1.169	1.109	1.021
346.9	$2P$ (3–4)	0.0063	0.012	0.015	0.013	0.013	–
350.0	$2P$ (2–3)	0.004	0.014	0.013	0.014	0.014	–
353.7	$2P$ (1–2)	0.029	0.146	0.188	0.156	0.181	0.130
357.7	$2P$ (0–1)	0.0615	0.707	0.889	0.930	0.882	0.799
367.2	$2P$ (3–5)	0.0046	0.009	0.012	0.010	0.010	–
371.1	$2P$ (2–4)	0.010	0.037	0.047	0.038	0.038	–
375.6	$2P$ (1–3)	0.0271	0.150	0.187	0.155	0.180	0.238
380.5	$2P$ (0–2)	0.0213	0.261	0.328	0.343	0.325	0.287
389.4	$2P$ (3–6)	0.003	0.006	–	0.007	0.007	–
391.4	$1N$ (0–0)	0.33	0.281	0.454	0.315	0.315	0.302
394.3	$2P$ (2–5)	0.0064	0.025	0.032	0.026	0.026	0.063
399.8	$2P$ (1–4)	0.016	0.090	0.119	0.097	0.113	0.129
Sum of $\lambda = 300$–400 nm			3.001	3.490[a]	3.672	3.653	3.698
Sum of all Nagano-wavelengths			2.798	3.404[a]	3.460	3.438	3.698

[a] Includes only data >328 nm.

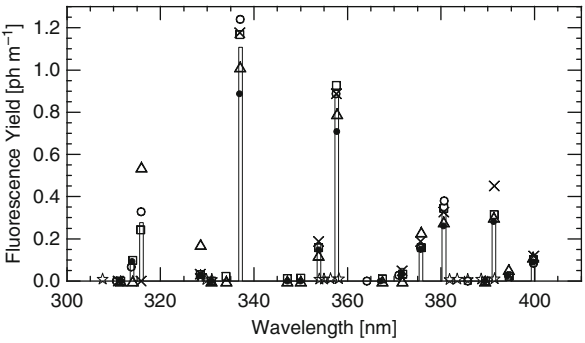

Fig. 17.6 Fluorescence yield spectra obtained by different calculations and experiments. The bars represent the model preferred and used by Keilhauer et al. (2006). The different symbols represent results obtained by Keilhauer for input data supplied by different authors (for details see original paper)

where $\epsilon_\lambda(P, T)$ is the fluorescence efficiency in percent at pressure P and temperature T for wavelength λ [nm], hc is the conversion constant (0.00123984 [MeV nm]), $\mathrm{d}E/\mathrm{d}X$ is the energy deposit [MeV kg^{-1} m^2] and ρ_{air} is the air density [kg m^3].

Figure 17.6, taken from Keilhauer et al. (2006), shows theoretical and measured fluorescence yields and Fig. 17.7, taken from Reil and Hüntemeyer (2005), shows essentially the same data with the original Bunner (1967) emission spectrum superimposed for comparison. The same authors have also studied the effect of humidity in the atmosphere.

Applying the data thus obtained, Keilhauer et al. (2006) did also calculate the fluorescence efficiency profiles for different wavelengths across the US Standard Atmosphere, that are shown in Fig. 17.8. Of particular interest for direct applications are the seasonal variations of the fluorescence yield efficiency of the real atmosphere at particular experimental sites, such as the Auger detector site in Argentina. This is sown in Fig. 17.9 where four local seasonal averages of the real situation are compared with the yield calculated for the US Standard Atmosphere (after Keilhauer et al., 2006). The corresponding atmospheric density profiles, in particular their deviation from the Standard US Atmosphere, are shown in Fig. B.5.

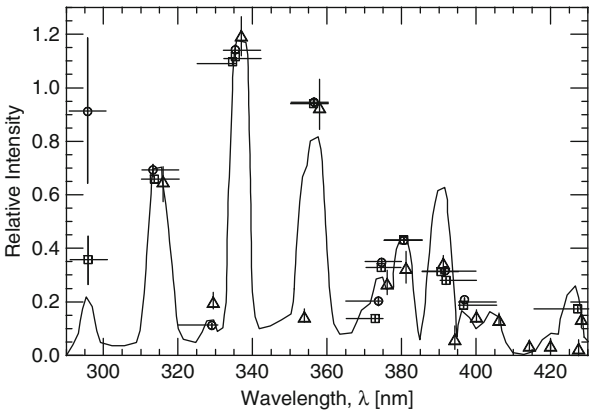

Fig. 17.7 Optical emission spectrum measured in dry air. The *continuous curve* is the spectrum measured by Bunner (1967). Shown, too, are the data obtained by Nagano et al. (2004), △, and those from the FLASH thin target experiment, ○, □, using 28.5 GeV electrons (Reil and Hüntemeyer, 2005)

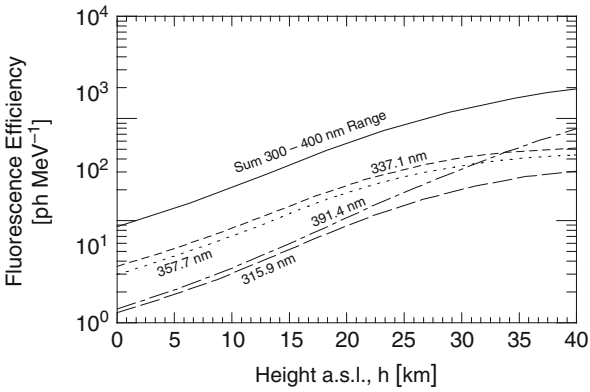

Fig. 17.8 Fluorescence efficiency profiles at different wavelengths as indicated in the US Standard Atmosphere (NASA, 1976; Keilhauer et al., 2006)

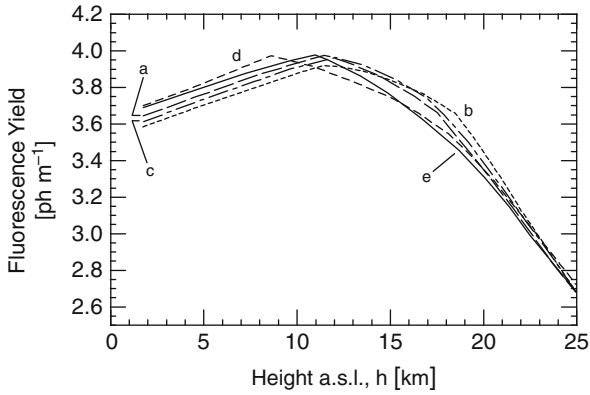

Fig. 17.9 Calculated fluorescence yield profiles of an 0.85 MeV electron in the standard US atmosphere (*curve e*) and in four seasonally different measured Argentine atmospheres: (*a*) spring, (*b*) summer, (*c*) autumn and (*d*) winter (Keilhauer et al., 2006). The corresponding atmospheric profiles are shown in Fig. B.5

The latest results from fluorescence studies with accelerator beams and electron sources as well as theoretical studies can be found in the Proceedings of the 5th Fluorescence Workshop, El Escorial, Spain, 2007 (Arqueros et al., 2008).

17.3 Optical Background, Atmospheric Scattering and Absorption

17.3.1 General Background

The optical background which significantly affects the threshold sensitivity of a fluorescence detector is the same kind of natural and man-made background that affects the air Cherenkov observations briefly mentioned in Chapter 16.

The list of natural light sources includes starlight of distinctly resolved stars, the general night sky background of faint and unresolved stars and galaxies, light emitted by or scattered off intergalactic or interstellar matter (gas, dust), but also sunlight and scattered moonlight that get backscattered on dust particles in interplanetary

space into the night sky, photochemical processes in the ionosphere, aurora phenomena, air glow, light flashes due to micro meteorites, Cherenkov background from cosmic radiation pointing at the detector and distant lightning (Baum, 1962; Chamberlain, 1961).

Man-made background is due to scattered or even direct light from neighboring urban settlements, distant cities, or from aircraft passing occasionally across the field of view of the detector.

Limiting the wavelength window of the detector to the blue and ultraviolet regions by placing filters in front of the photomultiplier tubes (PMT) or light sensors, or by choosing appropriate photocathodes can improve the signal-to-noise ratio of the detector significantly.

17.3.2 Night Sky Luminosity

The average *night sky background luminosity* yields a photon intensity between 10^5 and 10^6 ph m^{-2} μs^{-1} sr^{-1} in the relevant spectral region ($330 \leq \lambda \leq 450$ nm). With an ultraviolet filter reduction of the background to about 40 ph m^{-2} deg^{-2} μs^{-1} can be achieved (Sommers, 1995). At the Fly's Eye site at Dugway it is about $5 \cdot 10^5$ ph m^{-2} μs^{-1} sr^{-1}. This background level averages about a fourth magnitude per square degree (Baltrusaitis et al., 1985; Allen, 1976; Roach, 1963; Jelley, 1958).

Earlier measurements of the optical brightness of the night sky were made by Babcock and Johnson (1941) and Chuveyev (1952). Their results are summarized in Tables 17.5 and 17.6. Moonlight at a quarter phase doubles the background, at full phase it raises the level by a factor 10–20, inhibiting detector operation. Certain passing stars and planets, and the milky way may cause additional problems and increase background temporarily in the sensors concerned, resulting in an average night sky brightness seen by a photomultiplier of about a first magnitude star.

Table 17.5 Optical brightness of night sky (Babcock and Johnson, 1941)

Wavelength [nm]	Intensity
400–425	$130 \cdot 10^{-8}$ [erg (cm^2 s sr nm)$^{-1}$]
425–550	$200 \cdot 10^{-8}$ [erg (cm^2 s sr nm)$^{-1}$]
400–550	$23 \cdot 10^{-5}$ [erg (cm^2 s sr)$^{-1}$]

Table 17.6 Optical brightness of night sky (Chuveyev, 1952)

Source	Wavelength [nm]	Intensity
Atmosphere	472–558	$6.77 \cdot 10^{-8}$ [erg (cm^2 s deg^2)$^{-1}$][a]
Oxygen Line, O_1	557.7	$1.38 \cdot 10^{-8}$ [erg (cm^2 s deg^2)$^{-1}$][a]
Star + Zodiacal Light	472–558	$3.6 \cdot 10^{-8}$ [erg (cm^2 s deg^2)$^{-1}$][b]
Total	472–558	$8.4 \cdot 10^{-8}$ [erg (cm^2 s deg^2)$^{-1}$][b]
Total	472–558	$2.8 \cdot 10^{-4}$ [erg (cm^2 s sr)$^{-1}$][b]

[a] Maximum value.
[b] Mean value.

17.3.3 Light Scattering in the Atmosphere

The same basic optical scattering processes that are relevant for atmospheric Cherenkov radiation, briefly discussed in Sect. 16.5, apply to air fluorescence phenomena as well. Thus, light produced by an air shower that propagates in the atmosphere is subject to Rayleigh[4] as well as Mie scattering.[5] The light may be scattered into or out of the field of view of the detector, thus enhancing or reducing the signal (Pekala et al., 2005). The specific conditions are, however, different for fluorescence detection than standard air Cherenkov detection applications.

(a) Rayleigh Scattering

Rayleigh scattering (Rayleigh, 1881, 1914, 1918; Gans, 1925) plays a significant role for Fly's Eye type detectors. At a wavelength of $\lambda = 400$ nm the Rayleigh scattering length at sea level is $L_R = 23{,}000$ m (Flowers et al., 1969), which corresponds to a column density of X_R 2,974 g cm^{-2}. The number of photons that are subject to Rayleigh scattering in a beam containing $N_{\rm ph}$ photons along an optical path l is

$$\frac{{\rm d}N_{\rm ph}}{{\rm d}l} = -\rho \frac{N_{\rm ph}}{X_R} \left(\frac{400}{\lambda}\right)^4 \quad [{\rm ph\,m^{-1}}] \tag{17.15}$$

where ρ is the local air density.

For an isothermal atmosphere (Eq. 21.73) the following expression can be used to estimate the amount of Cherenkov light scattered out of the Cherenkov beam of a shower toward the detector at an angle θ within a solid angle element dΩ (Baltrusaitis et al., 1985).

$$\frac{{\rm d}^2 N_{\rm ph}}{{\rm d}/{\rm d}\Omega} = \frac{3}{16\pi} \left(1 + \cos^2(\theta)\right) \frac{{\rm d}N_{\rm ph}}{{\rm d}l} \quad [{\rm ph\,m^{-1}}] \ . \tag{17.16}$$

(b) Mie Scattering

Because of its characteristic properties, Mie scattering (Mie, 1908) constitutes only a minor correction to the total light balance of a fluorescence detector.[6] At Dugway the relevance of Mie scattering is further reduced by the low local aerosol and dust content in the atmosphere (Flowers et al., 1969). Under the assumption of the validity of a simplified model (Elterman and Toolin, 1965), where Mie scattering falls

[4] Scattering on air molecules.

[5] Scattering on aerosols.

[6] Typically Mie scattering is less important because the experimental sites are a priori chosen accordingly, however in dusty areas it plays an important role.

off exponentially with altitude, Baltrusaitis et al. (1985) give for the amount of light Mie scattered from a beam of N_{ph} photons along an optical path l the approximate expression,

$$\frac{\mathrm{d}N_{\mathrm{ph}}}{\mathrm{d}l} = -\left(\frac{N_{\mathrm{ph}}}{L_M}\right) e^{-h/h_M} \ [\mathrm{ph\,m^{-1}}] \ , \tag{17.17}$$

where $h_M = 1,200$ m is the scale height and $L_M = 14,000$ m the mean free path at 360 nm for Mie scattering. The angular distribution is strongly peaked in the forward direction but not as much as that of the direct Cherenkov light. For the angular distribution the following approximate expression that is valid over the angular range $5^\circ \leq \theta \leq 60^\circ$ gives an adequate description.

$$\frac{\mathrm{d}^2 N_{\mathrm{ph}}}{\mathrm{d}/\mathrm{d}\Omega} = 0.80 \left(\frac{\mathrm{d}N_{\mathrm{ph}}}{\mathrm{d}l}\right) e^{-\theta/\theta_M}, \ \ [\mathrm{ph\,m^{-1}}] \tag{17.18}$$

where $\theta_M = 26.7^\circ$ is the Mie angle.

17.3.4 Light Absorption and Attenuation in the Atmosphere

(a) Light Absorption

The loss of light in the range between 250 and 600 nm through absorption is mostly due to ozone (O_3) and oxygen molecules (O_2). For ozone, the most relevant agent in the clean dry atmosphere, the absorption cross section rises rapidly from about 10^{-23} cm^2 at 370 nm to 10^{-17} cm^2 at 250 nm and, on the other side of the absorption dip, toward the long wavelength side it rises slowly to reach a flat peak of approximately $5 \cdot 10^{-21}$ cm^2 at 600 nm (Andrews et al., 1987). Recently, the role of ozone in this context had been extensively studied by Keilhauer (2003, 2004; for ozone absorption cross sections the reader is referred to the work of Molina and Molina, 1986). It is evident from inspection of the fluorescence emission spectrum, Fig. 17.3, that absorption mechanisms in pure air are not very relevant for fluorescence detection. It is more significant for Cherenkov light detection.

The absorbed light is essentially lost since re-emission, if any, is isotropic and in the cases of de-excitation by collision no contribution to the light flux results. For further details the reader is referred to the special literature (Goody, 1995; Salby, 1996; and references listed therein).

(b) Light Attenuation

The scattering processes discussed above result in a reduction of the number of photons that reach a detector and thus attenuate the signal. Based on the previous equations, one can readily write the expressions for the *transmission factors* for Rayleigh and Mie scattering, T_R and T_M, respectively, that specify the fraction of

photons emitted from a source that reaches a distant detector unaffected by either process.

Consider a light source at location X_1 in the atmosphere and a detector at location X_2, given in atmospheric *slant depth* as defined by Eq. (21.7). The *slant angle*, θ_s, is given by the inclination of the line of sight that connects the two locations in the atmosphere with respect to the zenith. Using then Eq. (17.15) one obtains for the Rayleigh transmission factor T_R at wavelength λ [nm] the expression

$$T_R \;=\; \exp\left\{-\left(\frac{|X_1 - X_2|}{X_R}\right)\left(\frac{400}{\lambda}\right)^4\right\} \quad . \tag{17.19}$$

A corresponding expression can be derived for Mie scattering. Using the altitudes h_1 and h_2, expressed in [m], for the light source and detector locations, respectively, and Eq. (17.17), one obtains for the Mie transmission factor T_M the relation

$$T_M \;=\; \exp\left\{\left(\exp\left(-\frac{h_1}{h_M}\right) - \exp\left(-\frac{h_2}{h_M}\right)\right)\frac{h_M \sec(\theta)}{L_M}\right\} \quad . \tag{17.20}$$

The resulting overall transmission factor T is the product of the two expressions,

$$T \;=\; T_R \cdot T_M \quad . \tag{17.21}$$

17.3.5 Cherenkov Background

Besides the omnidirectionally emitted fluorescence light whose integral is a measure of the calorimetric energy of a shower (Pierog et al., 2005), direct as well as scattered Cherenkov light that accompanies the shower can contribute to the signal received by a fluorescence detector if beamed in its direction. Depending on the direction of propagation of a shower with respect to the location of the detector the Cherenkov contribution may constitute a large fraction of the signal received by the detector and can disrupt the energy relationship if not properly accounted for. These effects must be carefully considered to interpret an event correctly.

According to studies carried out by Bunner et al. (1968), the directly-beamed Cherenkov light dominates the signal received by the detector at emission angles, θ, relative to the shower axis of less than 25° (Fig. 17.2), which makes the inference of shower size difficult for early stages of shower development. Moreover, the Cherenkov component accumulates as the shower front propagates. As a result, at lower altitudes where the showers are dying out rapidly and likewise local fluorescence production, *scattered* Cherenkov light may contribute as much as 30% to the total optical signal received by the detector. Most affected are those showers that strike close to the detector, within about 1 km or so, since a large portion of these events can only be observed at emission angles $\theta \leq 25°$. At small angles directly

beamed Cherenkov light may exceed the fluorescence contribution by as much as a factor of one hundred. The Cherenkov contamination is obviously strongly geometry dependent (see Nerling et al., 2005).

Based on a number of assumptions and simplifications that are applicable to the Utah Fly's Eye detector, including its limited optical bandwidth of about 250 nm, Baltrusaitis et al. (1985) obtained the following expression for the approximate number of Cherenkov photons per meter, $\mathrm{d}N_{\mathrm{ph}}/\mathrm{d}l$, produced along the shower track (accuracy $\simeq \pm 10\%$).

$$\frac{\mathrm{d}N_{\mathrm{ph}}}{\mathrm{d}l} \simeq 33 \cdot N_e F(1.57 \cdot E_{\mathrm{th}}) e^{-(h/h_0)} \ [\mathrm{ph\,m^{-1}}] \ . \tag{17.22}$$

N_e is the number of electrons in the shower, $F(1.57 \cdot E_{\mathrm{th}})$ the fraction of electrons above the Cherenkov photon production threshold energy, E_{th}, which depends slightly on shower age, s, the vertical height in the atmosphere, h, and the atmospheric scale height, h_s (see Chap. 16, and Hillas, 1982).

The angular spread of the Cherenkov light with respect to the narrow theoretical Cherenkov cone centered about the shower axis that one might expect is primarily due to the spread, i.e., the *scattering* of the electrons in the shower, including geomagnetic deflection (Elbert et al., 1983). For the relevant angular region, in this case $\theta < 30^\circ$, where direct Cherenkov light could hit the detector, the distribution $\mathrm{d}N_{\mathrm{ph}}/\mathrm{d}\theta$ is an exponential with a characteristic angle θ_0 that depends on the Cherenkov threshold energy, E_{th}, approximately as

$$\theta_0 \approx 0.83 E_{\mathrm{th}}^{-0.67} \ . \tag{17.23}$$

The resulting Cherenkov contribution per solid angle interval can then be written as (Baltrusaitis et al., 1985)

$$\frac{\mathrm{d}^2 N_{\mathrm{ph}}}{\mathrm{d}/\mathrm{d}\Omega} = \frac{\mathrm{d}N_{\mathrm{ph}}}{\mathrm{d}l} \left(\frac{e^{-(\theta/\theta_0)}}{2\pi \sin(\theta)} \right) \ [\mathrm{ph\,m^{-1}}] \ . \tag{17.24}$$

17.3.6 Relative Contributions of Fluorescence and Cherenkov Light to Detector Signal

Generally speaking, fluorescence photons from a shower that are initially propagating toward the detector are attenuated chiefly by the loss of photons due to scattering. On the other hand the light intensity at the detector is also enhanced by photons that are originally directed away from the detector and subsequently scattered towards it. At the same time the recorded signal may be enhanced by

Cherenkov light that is scattered out of the direct Cherenkov region toward the detector.[7]

The relative yields of the different mechanisms that contribute to the total signal recorded by a detector from a shower can be computed with the help of the theories and formulas that are presented above for any particular case. In Fig. 17.10 we show the results obtained by Baltrusaitis et al. (1985) and Cassiday (1985) for a simulated shower having a primary energy of 10^{18} eV (1 EeV) and an impact parameter of $R_p = 4.0$ km.

Shown are the fractions of photoelectron yields at the detector produced by fluorescence light, direct Cherenkov light, and Rayleigh and Mie scattered Cherenkov light versus altitude and corresponding emission angle θ. The figure also shows the longitudinal shower profile, i.e., the shower size, N_e, versus altitude, h. An earlier study to estimate the relative contributions of Cherenkov and fluorescence light to an optical detector from distant air showers had been carried out by Protheroe (1982).

In a recent study using Monte Carlo simulations, Pekala et al. (2005) have computed the contributions of Cherenkov and fluorescence photons that were originally not directed at the detector but subsequently scattered towards it, to the direct photon component. Considering the resulting signal enhancement, they have analyzed

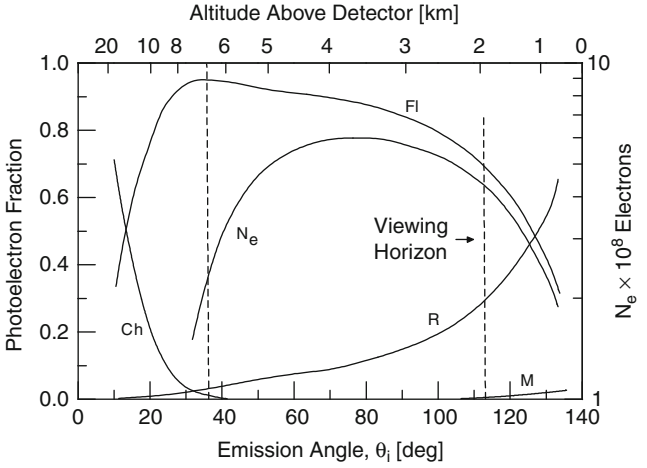

Fig. 17.10 Relative photoelectron fraction produced by all light generating mechanisms as a function of altitude above the Fly's Eye detector (*upper scale* in km) and emission angle subtended between the shower axis and direction to the detector, θ_i (*lower scale* in degrees), for a shower of primary energy 10^{18} eV with impact parameter, R_p, as defined in Figs. 17.2 and 17.13 of 4 km. Fl is for fluorescence light, Ch for the Cherenkov component, R and M identify the Rayleigh and Mie scattered fractions of the Cherenkov light component. The *curve* labeled N_e is the actual shower profile along the shower trajectory (*right hand ordinate*). Also indicated are the viewing horizon (*dashed vertical lines*) (after Baltrusaitis et al., 1985)

[7] It is assumed that the shower trajectory points away from the detector, such that no direct Cherenkov light can reach it.

the consequences that follow for the interpretation of fluorescence data (see also Sect. 17.3.3).

These authors conclude from a preliminary analysis that the scattered components from both sources, Cherenkov and fluorescence, must be considered in the data evaluation to obtain correct results. Moreover, they point out that the contributions depend on the instantaneous altitude of the particle disk above ground, and that they can amount to as much a ∼5% of the total shower signal. The enhancement affects the shower profile and with it the height of maximum development with all its consequences for subsequent data interpretation. Figure 17.11 shows the altitude dependence of the full longitudinal shower profile of a one-dimensional simulated shower in terms of photoelectrons and the contributions from the two scattered components (Pekala et al., 2005).

A refined method for the deduction of the air Cherenkov component[8] from the total signal to get the pure fluorescence component had been developed by

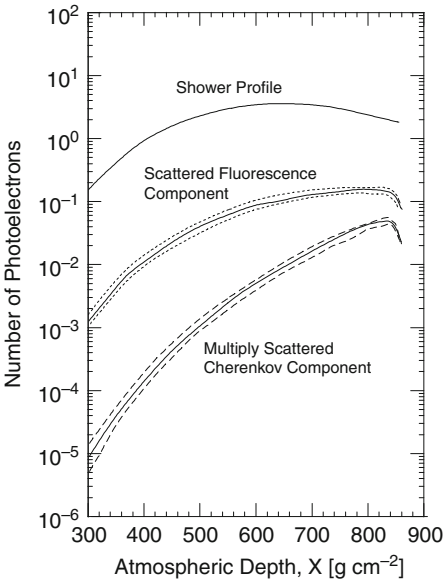

Fig. 17.11 Simulation results obtained for a vertically incident one-dimensional 10^{19} eV shower impacting 15 km from the fluorescence detector. Shown is the full longitudinal shower profile in photoelectrons at the detector (Pekala et al., 2005). The shower *curve*, (*a*) includes the contribution from direct fluorescence and direct and singly scattered Cherenkov photons. The *solid curves* (*b*) and (*c*) show the *center lines* of bands of separate data points from contributions of scattered fluorescence and multiply scattered Cherenkov photons, respectively. The *dotted* and *dashed curves* surrounding curves (*b*) and (*c*) indicate the approximate width of the data bands. Widely scattered data points shown in the original paper are not plotted here (the author)

[8] Mainly the scattered part since the direct contribution had been strongly reduced by appropriate cuts.

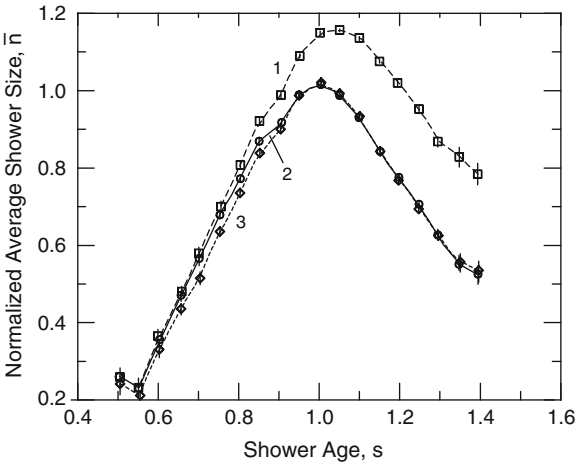

Fig. 17.12 Normalized average shower transition curves obtained with the HiRes/MIA hybrid experiment. *Curve 1* (□) shows the raw signal, including the Cherenkov component, *curve 2* (○) refers to the so-called bin signal based recurrent Cherenkov light subtracting method, and *curve 3* (◇) corresponds to a different Cherenkov subtraction method (Abu-Zayyad et al., 2001)

Abu-Zayyad et al. (2001) for the HiRes/MIA hybrid experiment. These authors point out that the Cherenkov contribution varies along the track. Deeper positions in the atmosphere tend to have more scattered Cherenkov light because the Cherenkov beam accumulates with increasing shower development and the molecular and aerosol scattering gets stronger in the deeper atmospheric regions. The relevance of properly accounting for the Cherenkov component is evident when inspecting Fig. 17.12.

17.4 Shower Detection and Event Reconstruction

One of the principal purposes of a Fly's Eye type detector is to determine the size of a shower as a function of its trajectory, i.e., the longitudinal shower profile. Therefrom a number of shower parameters can be derived directly, such as the primary energy, E_0, and the depth of maximum development, $X_{\max}$. From the latter one can infer the mass of the primary, M_0 and other parameters.

However, in order to compute the shower size the trajectory must be known accurately. The latter is also of interest for astronomical and astrophysical reasons, to determine the arrival direction, study questions related to anisotropy and the origin of ultra energetic cosmic ray primaries. The detector observables used to achieve this goal are the geometrical pattern of the phototubes that are triggered by the shower, their sequentially timing and amplitudes.

Many of the specific data that are given and discussed in the following sections refer to the Fly's Eye at Dugway. However, apart from the site and instrument specific data, most statements and relations are of general validity and applicable to any air shower fluorescence detector. A new improved technique of shower reconstruction developed for handling the HiRes monocular data is described by Abu-Zayyad et al. (1999).

17.4.1 Signal Level at Detector and Time Structure

(a) Signal Level

To compute the actual signal level, S, at a photomultiplier of the detector expressed in photoelectrons resulting from fluorescence only, including photon loss due to Rayleigh scattering, we must modify Eq. (17.4) accordingly and obtain

$$S = \epsilon_{\mathrm{pe}} A N_e Y c \Delta t \left(\frac{1 + \cos(\theta)}{4\pi R_p^2} \right) e^{-(r/L_R)} \ [\mathrm{pe}] \ , \tag{17.25}$$

where Δt is an integration time which is event dependent. It is the time interval during which the track is in view of that particular photomultiplier. In practice Δt ranges from 50 ns to 10 µs. L_R is the Rayleigh scattering length, as defined earlier. For rough back of the envelope estimates we can insert for the fluorescence yield, Y, a value of ≈ 4 ph m^{-1}(e$^{\pm}$)$^{-1}$ within the useful optical window from about 300 to 430 nm; for accurate values the reader is referred to Table 17.4.

To obtain a conservative figure for the noise several authors multiply the average local night sky background level due to starlight, B, Eq. (17.5), by a factor of 4 to account for other contributing effects (see Sect. 17.2.1). Considering this correction and Eqs. (17.25) and (17.6), the following expression is obtained for the signal-to-noise ratio.

$$\kappa = N_e N_{\mathrm{ph}} c \left(\frac{1 + \cos(\theta)}{4\pi R_p^2} \right) e^{-(r/L_R)} \sqrt{\frac{\epsilon_{\mathrm{pe}} A \Delta t}{4 B \Delta \Omega}} \ . \tag{17.26}$$

(b) Time Structure

In a time interval dt the source as seen by the observer moves a distance

$$\mathrm{d}\left(\frac{R_p}{\tan(\theta)} \right) = -R \ \mathrm{cosec}^2(\theta) \, \mathrm{d}\theta \ , \tag{17.27}$$

and, in the absence of absorption, the light flux reaching the observer as a function of θ is

$$F(\theta) = cY \left(\frac{1 + \cos(\theta)}{4\pi R_p^2} \right) \ [\mathrm{ph\,cm^{-2}\,s^{-1}}] \ . \tag{17.28}$$

The duration of the entire light pulse, τ, depends on the distance of the shower from the detector, its track length and direction of propagation. Under the assumption that the first photons arrive simultaneously with the passage of the shower front plane through the detector, the pulse width is given by

$$\tau \;=\; \frac{R_p}{c}\,\cot\left(\frac{\psi}{2}\right)\,, \tag{17.29}$$

where ψ is the ground impact angle in the shower-detector plane (Fig. 17.2). Typically, showers produce light pulses in the range $4\,\mu\text{s} \leq \tau \leq 40\,\mu\text{s}$.

17.4.2 Trajectory Reconstruction

The geometrical pattern of hit photomultiplier tubes resulting from an air shower describes part of a great circle over the hemispherical detector or when projected upon the celestial sphere. It locates the shower-detector plane in space and is a direct measure of the shower's vertically projected zenith angle.

Determination of the shower trajectory requires four parameters. Two are needed to locate the shower-detector plane in space, i.e., the plane which contains the shower axis and detector location. They are the azimuthal and zenith angles of the unit vector, $\vec{n}$, normal to the shower-detector plane (Fig. 17.2). This vector is found by minimizing the quantity

$$\Sigma \;=\; \vec{r}_i \cdot \vec{n}, \tag{17.30}$$

where $\vec{r}_i$ is the i-th observation direction vector pointing toward the i-th light source on the shower trajectory.

Orientation and distance of the shower trajectory with respect to the detector can be determined from timing information. From Fig. 17.13 it is evident that the light that reaches the detector from a point P on the shower trajectory is delayed with respect to the arrival time of the shower front tangent plane by a time interval

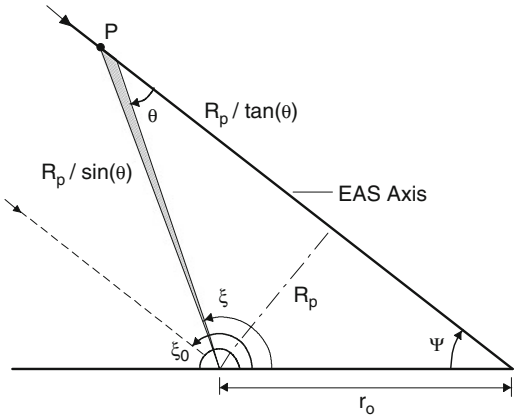

Fig. 17.13 Geometry of shower event reconstruction. Light received from the Fly's Eye from a point P along the shower trajectory lags behind the time of passage of the shower front by an interval $\Delta t(\theta) = R_p/(c \cdot \sin(\theta)) - R_p/(c \cdot \tan(\theta)) = (R_p/c)\tan(\theta/2)$

$\Delta t(\theta)$, given by the expression

$$\Delta t(\theta) \;=\; \frac{R_p}{c\ \sin(\theta)} - \frac{R_p}{c\ \tan(\theta)} \;=\; \frac{R_p}{c}\ \tan\left(\frac{\theta}{2}\right) \;, \tag{17.31}$$

where θ is the light emission angle measured from the shower axis. It follows further from Fig. 17.13 that

$$\xi_0 \;=\; \xi_i \;+\; \theta \quad , \tag{17.32}$$

where ξ_i is the observation angle in the shower-detector plane of the i-th phototube and ξ_0 the direction of the approaching shower. Consequently

$$\xi_i(t_i) \;=\; \xi_0 \;-\; 2\tan^{-1}\left(\frac{c(t_i - t_0)}{R_p}\right) \quad . \tag{17.33}$$

A best fit of the observed $\xi_i(t_i)$ to this function yields the parameters R_p and ξ_0, which fixes the shower trajectory.

Accurate reconstruction is possible for tracks whose lengths exceed a total subtended angle of $\geq 50^\circ$. For tracks covering arc lengths in the range from 30° to 50° fitting of ξ_0 becomes very inaccurate. However, the accuracy of R_p remains quite good down to 30°, typically better than $\pm 30\%$ (Baltrusaitis et al., 1985).

Combined operation of Fly's Eye I with 880 PMTs and the smaller Fly's Eye II with 120 PMTs in a synchronized mode (± 100 ns), recording the same events in coincidence, can improve results significantly.

17.4.3 Shower Profile, Primary Energy and Mass Determination

(a) Shower Profile Reconstruction

After the determination of the shower trajectory, the energy determination involves two additional steps (Cassiday, 1985). First the longitudinal shower size distribution is calculated using an iterating process to remove the contributions due to direct and scattered Cherenkov light. Secondly, each resultant longitudinal profile is fitted with two functions in order to obtain best estimates of (a) the shower size at maximum development, $N_{\max}$, (b) the location of maximum development, $X_{\max}$, and (c) the integral of the longitudinal development profile,

$$\int N_e(X)\mathrm{d}X \;, \tag{17.34}$$

where $N_e(X)$ is the shower size as a function of trajectory position, X.[9]

One of the two functions that are being used to describe the shower development $N_e(X)$ is the function of Gaisser and Hillas (1977) (Gaisser, 1990) which is of the form

$$N_e(X_{\text{obs}}) \;=\; N_{e,\max}\left(\frac{X_{\text{obs}}-X_0}{X_{\max}-X_0}\right)^{(X_{\max}-X_0)/\lambda_i} e^{(X_{\max}-X_{\text{obs}})/\lambda_i}\,, \qquad (17.35)$$

where X_{obs} is the atmospheric depth at observation, X_0 the depth of the first interaction [g cm^{-2}], and λ_i is the interaction mean free path ($\lambda_i \approx 70\,\text{g cm}^{-2}$ for protons).[10] The other function that is being used is a Gaussian. An example of the two fits is given in Fig. 17.14.

Knowing the local atmospheric parameters, the shower trajectory and the efficiency-gain product, the actual longitudinal shower profile can be computed from the recorded data. On the other hand, with the help of computer simulations the longitudinal profile can be calculated for a variety of primary masses and energies. Comparison of the two sets of data permits to convert the experimentally observed

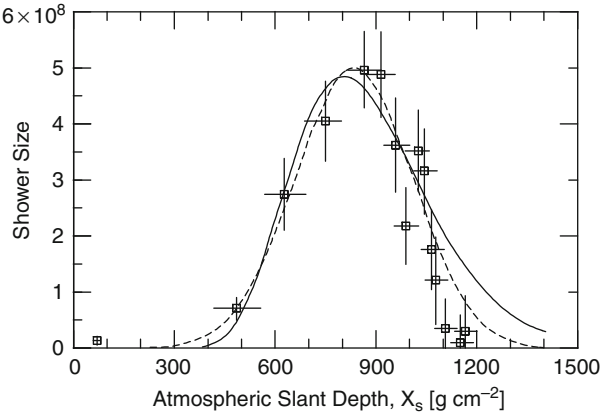

Fig. 17.14 Shower development *curve* showing the shower size versus atmospheric slant depth of a $(5.5 \pm 0.04) \cdot 10^{17}$ eV shower detected with the Fly's Eye I on November 12, 1982. Also shown are a Gaussian fit (*dashed curve*) and a fit according to Gaisser and Hillas (1977) (*solid curve*) that yield a maximum shower size of $N_e = (5.0 \pm 0.28) \cdot 10^8$ and $(4.9 \pm 0.33) \cdot 10^8$, a height of maximum development of $X_{\max} = 830 \pm 46$ and 800 ± 47 g cm^{-2} with a width of 180 ± 34 and 190 ± 33 g cm^{-2}, respectively (Baltrusaitis et al., 1985)

[9] Today it is recommended to reconstruct the energy loss ($\text{d}E/\text{d}X$) profile from the fluorescence measurements instead of the shower size $N_e(X)$, and to integrate it over the entire trajectory to get the total *calorimetric energy* of the shower, since $\text{d}E/\text{d}X$ is more directly related to the fluorescence (Keilhauer, 2006, private communication).

[10] In CORSIKA a refined expression is now being used (Keilhauer, 2006, private communication).

depth of maximum development and the estimated height of the first interaction to primary mass and inelastic cross section, respectively.

A more sophisticated method of event reconstruction had been developed for the processing of the HiRes Monocular data (e.g., Abu-Zayyad et al., 1999, 2000). A significant improvement of the accuracy in the determination of the shower parameters and consequently of the results can be achieved with hybrid experiments, such as the combined HiRes/MIA installations (Abu-Zayyad et al., 2001), the Auger experiment (Bellido, 2005) and the Telescope Array (Kawai et al., 2005).

(b) Primary Energy Determination

The electromagnetic energy deposited by the primary, $E_{\rm em}$, is estimated from the integral of either fit to the experimental data.

$$E_{\rm em} = \frac{E_{\rm crit}}{\chi_0} \int N_e(X) {\rm d}X \ , \tag{17.36}$$

where $E_{\rm crit}/\chi_0$ is the ratio of the critical energy of an electron ($E_{\rm crit} = 84\,{\rm MeV}$)[11] to the radiation length in air ($\chi_0 = 37.1\ {\rm g\,cm^{-2}}$) (Dovzenko and Pomanski, 1964). This gives an energy loss rate of $2.18\,{\rm MeV\,e^{-1}\,g\,cm^{-2}}$.

To determine the total primary energy of a shower, E_0, corrections must be introduced to account for *energy lost due to long-lived neutral particles* that escape detection. As a thumb rule 10% of the electromagnetic energy as determined by Eq. (17.36) are added to get E_0.

More recently, the primary energy estimation is based on the local energy deposit as discussed by Song et al. (2000), and by Risse and Heck (2004).

(c) Primary Mass Determination

The estimation of the primary mass on the basis of air fluorescence measurements hinges on the height of initiation and mostly on the depth of maximum development of the shower, $X_{\rm max}$ (or slant depth, $X_{s,{\rm max}}$). The former, in particular the height of the first interaction, h_1, cannot be detected directly as the light level of the initial phases of a shower is too low. Relevant is therefore the height of the first visible appearance of the shower, viewed side-on at some angle and the height of maximum development, $h_{\rm max}$.

The latter is experimentally a relatively easy accessible signature. However, the problems is that the particle number and their lateral spread, and consequently the fluorescence intensity near maximum development vary slowly with track length along the shower axis. This makes it difficult to determine the location of the shower maximum accurately. Nevertheless, the air fluorescence method is the most direct,

[11] Note that some authors use for $E_{\rm crit} = 81\,{\rm MeV}$.

accurate and least ambiguous way to determine this observable. Further details concerning the primary mass spectrum and its determination are presented in Sect. 11.7.

17.4.4 Trigger Criteria, Aperture and Counting Rates

(a) Trigger Criteria

Proper choice of the trigger criteria is important to optimize the reconstructable event rate and avoid processing of useless noise. Thus, a minimum number of standard deviations, σ, above the noise level for the amplitudes of the photomultiplier signals and a minimum number of sequential hits, K, defining the arc length as seen by the detector must be imposed.

Varying these quantities, however, affects the energy dependent aperture of the detector system. The more stringent the requirements are the more the detector sensitivity is reduced. In particular, increasing the threshold amplitude increases not only the lower limit of the primary energy window for detecting showers but also reduces at the same time the range of impact parameters for a given shower class. On the other hand, increasing the number of sequentially hit detector elements discriminates more and more against the shorter projected trajectories.

(b) Aperture Considerations

The detector aperture is energy dependent in a rather complicated way. Extensive Monte Carlo simulations are needed to determine it. The method is described by Cassiday (1985) and Baltrusaitis et al. (1985). We will only very briefly outline the general procedure.

An isotropic cosmic ray flux having a standard primary energy spectrum is assumed to be incident on a standard atmosphere. From this flux random shower trajectories originating at randomly distributed depths in the atmosphere are generated. A simple expression is used to describe the shower development along the trajectory and the expression for fluorescence production as discussed in Sect. 17.2 is applied to calculate the photon flux reaching the detector. The detector response is simulated and trigger conditions applied. The resulting data are analyzed using the same procedure as applied to the real experimental data.

This method has proven to be most sensitive to energy spectra and leads to an estimate of the energy dependence of the aperture of the detector. The aperture is calculated by summing up the area-solid angle bins in which an event of energy between E and $E + \Delta E$ will produce a trigger. The differential rate for these events is

$$\frac{\mathrm{d}N}{\mathrm{d}E} = \int_{A_\Omega(E)} j(E)\mathrm{d}(A_\Omega(E)) \tag{17.37}$$

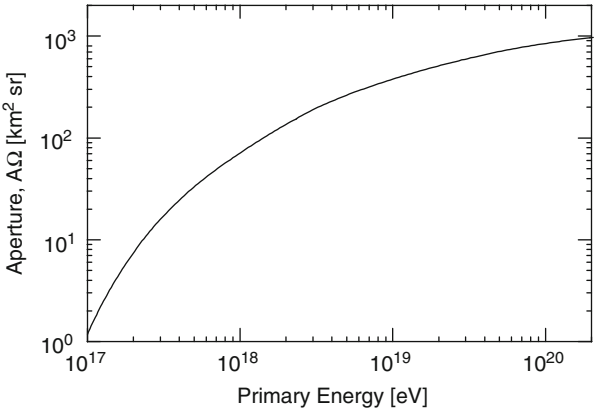

Fig. 17.15 Calculated aperture of the Fly's Eye I detector for air showers as a function of primary energy for a 50° track length cut (Baltrusaitis et al., 1985)

where $j(E)$ is the differential primary cosmic ray energy spectrum and $A_\Omega(E)$ is the acceptance in units of [m^2 sr] for events falling within the specified energy interval. The results of the study of Baltrusaitis et al. (1985) for the Fly's Eye at Dugway and events that have an angular track length $\leq 50^\circ$ is shown in Fig. 17.15. As mentioned above, the aperture is highly sensitive to trigger criteria, particularly in the lower energy region.

(c) Counting Rates

The counting rate is intimately related to the trigger criteria imposed and the resulting detector aperture. This problem has been treated extensively by Cassiday et al. (1977b, 1979) for the Fly's Eye at Dugway. These authors have used the generally accepted primary cosmic ray spectrum and simulations, and normalized the theoretical rates to the experimental data which they have obtained with prototype detectors that were operated jointly with the shower array at Volcano Ranch, as discussed in Sect. 17.4.5. Their results for the expected event rates for what was considered to be a reasonable trigger criterion ($K = 4$ for the number of phototubes and $\sigma = 5$ standard deviations for the signal level above noise) are shown in Fig. 17.16.

These results show that the detector system is capable of recording showers over an impact parameter range $0.2 \leq R_p \leq 50$ km. The corresponding range of pulse width is $0.7\ \mu s \leq \Delta t \leq 17\ \mu s$. The size requirement ranges from $N_e \simeq 10^7$ ($E_0 \simeq 2 \cdot 10^{16}$ eV) for showers impacting at several hundred meters to $N_e \simeq 4 \cdot 10^{11}$ ($E_0 \simeq 10^{21}$ eV) at 50 km. The corresponding event counting rates are $10^6\ y^{-1}$ and $1\ y^{-1}$, respectively.

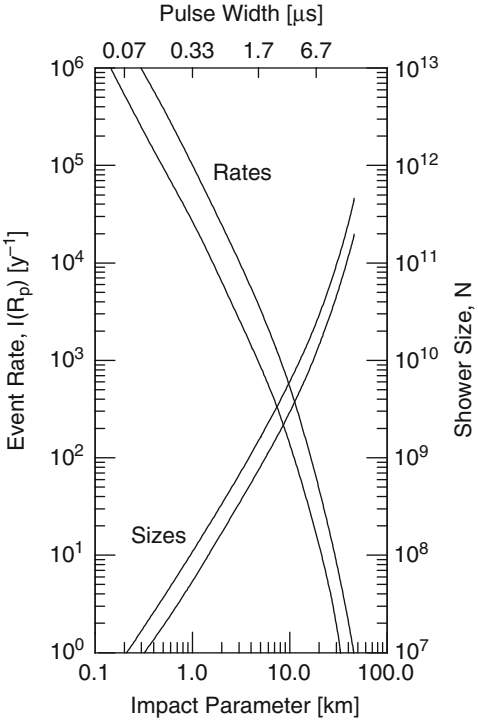

Fig. 17.16 Event rates per year (*left hand scale*) and observed shower sizes N (*right hand scale*) of the Fly's Eye detector as a function of shower impact parameter, R_p, (*lower scale*) and corresponding pulse widths (*upper scale*). The *curves* delimit the error bands (Cassiday et al., 1979)

17.4.5 Detector Calibration and Optimization

(a) Optical Calibration and Timing

The optical calibration of the detector determines the conversion factor, or efficiency-gain product, $\epsilon_{\text{tot}}G$, that relates the photoelectron yield of a multiplier to the number of photons incident upon the detector module. ϵ_{tot} is the overall efficiency, i.e., the product of the efficiencies of the photocathode, mirror, Winston cone, and filter, if applicable, and G is the overall electronic gain. Calibration is effectuated with a calibrated light source and must be repeated from time to time because of aging of the components.

Similarly, timing is checked with short upward going collimated light pulses originating from an array of permanently installed sources on the ground (xenon flashers and lasers) that simulated upward going showers and provide fiducial tracks for geometric reconstruction calibration. An r.m.s. reconstruction error of 1.7° for the zenith angle θ and of 100 m for the impact parameter R_p are specified for the flashers out to distances of 2 km.

In addition, the transmission of the atmosphere and the effects that influence it must be checked periodically. A detailed account of the procedures is given by Baltrusaitis et al. (1985) and Cassiday (1985) for the Fly's Eye, and by Cester et al. (2005) for the Auger detector. Sadowski et al. (2002) proposed to use catalogued

stars whose positions are very accurately known to perform geometrical and optical checks of the HiRes Fly's Eye. This method is of course applicable to all fluorescence and air Cherenkov detectors and can also be used to cross check atmospheric parameters obtained by other methods (see Sect. 17.3.4).

(b) Cross-Calibration with Detector Arrays

Simultaneous operation of 3 Fly's Eye detector modules and an air shower array at the same site to observe the same showers for purposes of cross-calibration was conducted during the early phase of the Dugway Fly's Eye project at Volcano Ranch (Bergeson et al., 1977; Cassiday et al., 1977a, b, 1979; Elbert et al., 1977; Mason et al., 1977). During the operation of the CASA-MIA array, calibration was locally possible for showers that strike the array (Borione et al., 1994).

However, arrays can only give the shower size at ground level. Nevertheless, initially the agreement between the two methods appeared to be fair at that time, but a recent comparison of measurements from the AGASA surface array and HiRes suggest a difference of $\sim$20%. Hopefully the Auger experiment which uses both methods simultaneously can resolve this problem. The accuracy of other important shower observables, such as the ground impact location of the shower axis and its arrival direction, i.e., the zenith and azimuthal angles, can be determined and improved when using a classical detector array together with a Fly's Eye type detector.

The advantages of a giant hybrid air shower detector consisting of one or several Fly's Eye detectors in combination with a detector array are discussed by Sommers (1995) in view of the Auger Project in Argentina (Guérard, 1999), which is presently in partial operation and is approaching completion (Mostafá, 2005).

(c) Detector Optimization

Light gathering power and angular resolution are important design parameters of a Fly's Eye type detector. However, economic aspects require that an optimum compromise be found. An interesting discussion on detector optimization is given by Baltrusaitis et al. (1985).

17.4.6 Atmospheric Monitoring Techniques

Accurate and continuous monitoring of the atmosphere is a necessity to interpret the measurements correctly. Incorrect or inaccurate atmospheric parameters lead to wrong or inaccurate energy assignments for the detected showers.

Different techniques are being used to monitor the properties of the atmosphere. LIDAR (LIght Detection And Ranging) systems are being used to measure the backscattered photons as a function of time in various directions, i.e., the photon

intensity versus distance to the scatterer, using short light pulses. These measurements yield vertical and inclined aerosol profiles (the aerosol extinction coefficient) and reveal scattering and scattering inhomogeneities, also along a shower track if aimed accordingly.

Other measurements include the horizontal attenuation length at several wavelengths using unpulsed light sources, the taking of meteorological data such as temperature and pressure profiles with balloon borne radiosounds, and survey of the cloud coverage (for details see Mostafá, 2003; Mussa et al., 2004; Abbasi et al., 2006a, b).

An interesting alternative possibility to check the attenuation through the atmosphere in any direction pointing away from an optical detector was explored by Sadowski et al. (2002). These authors have used catalogues stars and recorded their intensity as a function of elevation.

17.5 Measurements and Data

The principal goals of the measurements carried out with the original Fly's Eye detector and the subsequent High Resolution (HIRES) and STEREO combination of Fly's Eye detectors as well as the hybrid experiments (e.g., HiRes/MIA, Abu-Zayyad et al., 2001) were aimed at the exploration of the properties of the highest energy region of the primary cosmic ray spectrum.

Of particular interest is the shape of the energy spectrum and the question whether the spectrum exhibits the predicted Greisen-Zatsepin-Kuzmin (GZK) cutoff (Zatsepin, 1951; Greisen, 1966; Zatsepin and Kuzmin, 1966; Kuzmin and Zatsepin, 1968). However, questions concerning the primary composition, the inelastic hadronic cross section and the arrival directions of the most energetic cosmic rays are of similar significance. With adequate statistics the data will eventually reveal whether the most energetic components manifest an anisotropy, which may be the key in our search to locate likely source objects. Moreover, Fly's Eye type detectors can distinguish between downward and upward going showers. The observation of upward going showers would be an indication of neutrino induced events, confirming the presence of ultrahigh energy neutrinos in the cosmic radiation.

The results obtained with the Fly's Eye detectors that are related to the primary radiation are summarized in the appropriate sections of Chap. 11, i.e., the primary energy spectrum in Sect. 11.6, mass composition in Sect. 11.7, arrival direction and anisotropy in Sect. 11.9. Data on hadronic cross sections are presented in Chap. 3. However, cross section related topics are also discussed in Sect. 11.7 in connection with primary composition.

References

Abbasi, R.U., et al.: Astropart. Phys., 25, p. 74 (2006a).
Abbasi, R.U., et al.: Astropart. Phys., 25, p. 93 (2006b).
Abraham, J., et al.: Nucl. Instr. Meth., A 523, p. 50 (2004).

Abu-Zayyad, T., et al.: PICRC, 3, p. 264 (1999).
Abu-Zayyad, T., et al.: Nucl. Instr. Meth. A, 450, p. 253 (2000).
Abu-Zayyad, T., et al.: Astropart. Phys., 16, p. 1 (2001).
Allen, C.W.: Astrophysical Quantities, Athlone Press, University of London, London (GB), (1976).
Andrews, D., et al.: Middle Atmosphere Dynamics, Academic Press, San Diego (1987).
Arciprete, F., et al.: PICRC, 7, p. 55 (2005).
Arqueros, F., et al.: Astropart. Phys., 26, pp. 231–242 (2006).
Arqueros, F., et al.: Proceedings of the 5th Fluorescence Workshop, El Escorial, Madrid, Spain, September 16–20 (2007). Nucl. Instr. Meth. A, 597, pp. 1–120 (2008).
Babcock, H.W., and J.J. Johnson: Astrophys. J., 94, p. 271 (1941).
Baltrusaitis, R.M., et al.: Nucl. Instr. Meth. A, 240, p. 410 (1985).
Baum, N.A.: Stars and Stellar Systems, Astronomical Techniques, The Detection and Measurement of Faint Astronomical Sources, University of Chicago Press, Chicago, London, Vol. 2, p. 1 (1962).
Bellido, J.A., et al.: PICRC, 8, p. 113 (2005).
Bérat, C., et al., (EUSO Collaboration): PICRC, 2, p. 883 (2003).
Bergeson, H.E., et al.: PICRC, 8, p. 3059 (1975a).
Bergeson, H.E., et al.: PICRC, 8, p. 3064 (1975b).
Bergeson, H.E., et al.: Phys. Rev. Lett., 39, p. 847 (1977).
Borione, A., et al.: Nucl. Instr. Meth. A, 346, p. 329 (1994).
Bunner, A.N.: Cornell-Sydney University Astronomy Center Report 62 (1966).
Bunner, A.N.: Sky Telescope, p. 204, October (1967).
Bunner, A.N., et al.: Can. J. Phys., 46, p. 266 (1968).
Cassiday, G.L., et al.: PICRC, 8, p. 258 (1977a).
Cassiday, G.L., et al.: PICRC, 8, p. 270 (1977b).
Cassiday, G.L., et al.: Cosmic Rays and Particle Physics – 1978 (Bartol Conference). American Institute of Physics, AIP Conference Proceedings No. 49, T.K. Gaisser, ed., Particles and Fields Subseries No. 16, p. 417 (1979).
Cassiday, G., L.: Annu. Rev. Nucl. Part. Sci., 35, p. 321 (1985).
Catalano, O.: PICRC, 2, p. 411 (1999).
Cester, R., et al., Auger Collaboration: PICRC, 8, p. 347 (2005).
Chamberlain, J.W.: Physics of the Aurora and Air Glow, Academic Press, New York (1961).
Chudakov, A.E.: Proceedings of the 5th Inter-American Seminar on Cosmic Rays, Bolivia, 2, XLIX-1 (1962).
Chuveyev, K.: Dokl. Akad. Nauk SSSR, 87, 4, p. 551 (1952).
Corbato, S.C., et al.: Nucl. Phys. B (Proc. Suppl.), 28B, p. 36 (1992).
Davidson, G., and R. O'Neil: J. Chem. Phys., 41, p. 3946 (1964).
Dovzenko, O.J., and A.A. Pomanski: Sov. Phys. JETP, 18, p. 187 (1964).
Elbert, J.W., et al.: PICRC, 8, p. 264 (1977).
Elbert, J.W., et al.: PICRC, 6, p. 227 (1983).
Elterman, L., and R.B. Toolin: Handbook of Geophysics and Space Environments, Chap. 7, Air Force Cambridge Research Laboratory, Office of Aerospace Research, USAF (1965).
Flowers, E.C., et al.: J. Appl. Metereol., 8, p. 955 (1969).
Gaisser, T.K., and A.M. Hillas: PICRC, 8, p. 353 (1977).
Gaisser, T.K.: Cosmic Ray and Particle Physics, Cambridge University Press, Cambridge (1990).
Gans, R.: Ann. Physik, 76, p. 29 (1925).
Goody, R.: Principles of Atmospheric Physics and Chemistry, Oxford University Press, Oxford, ISBN 0-19-509362-3 (1995).
Greisen, K.: PICRC, 2, p. 609 (1965).
Greisen, K.: Phys. Rev. Lett., 16, p. 748 (1966).
Guérard, C.K.: Nucl. Phys. B (Proc. Suppl.), 75A, p. 380 (1999).
Hara, T., et al.: Acta Phys. Acad. Sci. Hung., 29, S3, p. 369 (1970).
Hillas, A.M.: J. Phys. G, 8, p. 1461 (1982).
Hughes, R.H., et al.: Phys. Rev., 123, p. 2084 (1961).
Hüntemeyer, P., FLASH Collaboration: PICRC, 8, pp. 319–322 (2005)

Jelley, J.V.: Cherenkov Radiation and Its Applications Pergamon, London (1958).
Kakimoto, F., et al.: University of Tokyo, ICRC Report 346-95-12, November (1995a).
Kakimoto, F., et al.: PICRC, 1, p. 1047 (1995b).
Kakimoto, F., et al.: Nucl. Instr. Meth. A, 372, p. 527 (1996).
Kawai, H., et al., Telescope Array (TA) Collaboration: PICRC, 8, p. 141 (2005).
Keilhauer, B.: Dissertation Universität Karlsruhe (2003) and Wissenschadtliche Berichte, FZKA 6958, Forschungszentrum Karlsruhe, Germany (2004).
Keilhauer, B., et al.: Astropart. Phys., 22, p. 249 (2004).
Keilhauer, B., et al.: PICRC, 7, p. 119 (2005).
Keilhauer, B., et al.: Astropart. Phys., 25, p. 259 (2006).
Kuzmin, V.A., and G.T. Zatsepin: Can. J. Phys., 46, p. S617 (1968).
Mason, G.W., et al.: PICRC, 8, p. 252 (1977).
Mie, G.: Ann. Physik, 25, p. 377 (1908).
Molina, L.T., and M.J. Molina: J. Geophys. Res., 91, D13, p. 14501 (1986).
Morozov, A., et al.: Eur. Phys. J. D, 33, p. 207 (2005).
Mostafá, M.A., Pierre Auger Collaboration: PICRC, 1, p. 465 (2003).
Mostafá, M.A., Pierre Auger Collaboration: PICRC, 7, p. 369 (2005).
Mussa, R., et al.: Nucl. Instr. Meth. A, 518, p. 183 (2004).
Nagano, M., et al.: Astropart. Phys., 20, p. 293 (2003).
Nagano, M., et al.: Astropart. Phys., 22, p. 235 (2004).
NASA: National Aeronautics and Space Administration, US Standard Atmosphere 1976, NASA-TM-X-74335 (1976).
Nerling, F., et al., Auger Collaboration: PICRC, 7, p. 131 (2005).
Nicholls, R.W., et al.: Proc. Phys. Soc., 74, p. 87 (1959).
Pekala, J., et al.: PICRC, 7, p. 207 (2005).
Pierog, T., et al.: PICRC, 7., p. 103 (2005).
Porter, L.G., et al.: Nucl. Instr. Meth., 87, p. 87 (1970).
Protheroe, R.J.: J. Phys. G, 8, p. L165 (1982).
Rayleigh, L.: Phil. Mag., 12, p. 81 (1881) (Sci. Papers 74).
Rayleigh, L.: Proc. Roy. Soc., A90, p. 219 (1914) (Sci. Papers 381).
Rayleigh, L.: Proc. Roy. Soc., A94, p. 296 (1918) (Sci. Papers 427).
Reil, K., and P. Hüntemeyer, FLASH Collaboration: PICRC, 8, pp. 323–326 (2005).
Risse, M., and D. Heck: Astropart. Phys., 20, p. 661 (2004).
Roach, F.E.: Adv. Electron. Electron Phys., 18, p. 1 (1963).
Sadowski, P.A., et al., High Resolution Fly's Eye Collaboration: Astropart. Phys., 18, pp. 237–248 (2002).
Salby, M., L.: Fundamentals of Atmospheric Physics, Academic Press, Inc., San Diego, ISBN 0-12-615160-1 (1996).
Scarsi, L.: PICRC, 2, p. 384 (1999).
Scarsi, L.: Nuovo Cimento, 24 C, p. 471 (2001).
Sommers, P.: Astropart. Phys., 3, p. 349 (1995).
Song, C., et al.: Astropart. Phys., 14, p. 7 (2000).
Suga, K.: 5th Inter-American Seminar on Cosmic Rays, Bolivia, 2, XLIX-1 (1962).
Suga, K., et al.: J. Phys. Soc. Jpn., 17, Suppl. A III, p. 128 (1962).
Tanahashi, G., et al.: PICRC, 12, p. 4385 (1975).
Teshima, M., et al.: Nucl. Phys. B (Proc. Suppl.), 28B, p. 169 (1992).
Ueno, S.: Master Thesis (in Japanese), Tokyo Institute of Technology, Tokyo (1996).
Waldenmaier, T., et al.: PICRC, 8, p. 53 (2005).
Winston, R.: J. Opt. Soc. Am., 60, p. 245 (1970).
Zatsepin, G.T.: Dokl. Akad. Nauk SSSR, 80, p. 577 (1951).
Zatsepin, G.T., and V.A. Kuzmin: JETP Lett., 4, p. 78 (1966).

Chapter 18
Radio Emission and Detection

Overview In this chapter we treat radio emission and detection in air showers. We offer in the introduction a historic review of the subject, from the early attempts in the fifties to the present activities. We then present the different mechanisms that are believed to be responsible for radio emission in showers and the accompanying theories, we discuss coherence and polarization, the relevance of the various mechanisms and their relative contribution to the total radio burst generated by a shower. This is followed by a summary of experimental and simulation data.

18.1 Introduction

Giant air showers are rare events that require very large and costly surface arrays to be detected at a reasonable rate to construct reliable shower size and primary energy spectra. As an alternative to the methods discussed in the previous chapters the detection of radio pulses from air showers, briefly mentioned in Chap. 2, appears to be an interesting option, provided that air showers actually emit radio waves, that these are detectable out to some distance from the shower axis, and that the measured data can be properly interpreted.[1] This method would have the great advantage over the atmospheric fluorescence technique, which allows to detect distant showers, that it could be operated round the clock and would have a 100% duty factor, which is not the case for optical detection in general, e.g., atmospheric fluorescence or Cherenkov detection.

The idea to explore the radio detection method found broad interest at an early stage of air shower investigations, when it was first proposed by Jelley (1958), and awakened high hopes for being the key to extend the observable primary energy spectrum well beyond the contemporary experimental limits. In addition, radio burst data may possibly even reveal information on the longitudinal shower development and therefore on the mass of the primary particles. Unfortunately no viable theory was available at that time to make predictions of the field strength to be expected and

[1] The method of RADAR echo ranging to investigate air showers proposed originally by Blackett and Lovell (1941), which had been explored by Matano et al. (1968) and surfaced recently again in theoretical studies, is briefly discussed in Sect. 2.6.

P.K.F. Grieder, *Extensive Air Showers,* DOI 10.1007/978-3-540-76941-5_18,

the effective frequency bands which such transient effects would occupy. Moreover, it was uncertain what kind of mechanism would play a major role, though it was evident from the beginning that different processes entered into consideration.

In view of the fact that the field had been explored rather intensely in the 1960s and early 1970s by a few research teams, followed by a long period of only sporadic contributions until it had been revived only recently with remarkable activity, we group the material of this chapter accordingly. We first present a list of likely radio burst (or pulse) generation processes, give an account of the early investigative work which led to the discovery of radio bursts associated with air showers, discuss theoretical considerations and theories of radio emission and present a selection of experimental data from that epoch. This is followed by a summary of the new experimental and theoretical initiatives that are currently under way and the presentation of some results from recent theoretical studies.

18.2 Radio Burst Generation Processes

In the course of time a variety of processes had been proposed that occur in an air shower as it grows, propagates and declines in the atmosphere, that are expected to generate radio frequency (RF) bursts. Essentially three primary causes are of importance from which different radiation processes can be derived. These are:

1. The differences in the nature of the interactions of the positrons, negatrons and photons of a shower with the atmospheric constituents.
2. The interaction of the charged particles of a shower with the geomagnetic field.
3. The interaction of the charged particles of a shower with the geoelectric field, i.e., with the electrostatic field of the atmosphere.

The actually contributing mechanisms comprise the following:

Item 1 listed above leads to charge asymmetry among the particle population of a shower, in particular to an increasing negative charge excess as the shower develops in the atmosphere, that results in the emission of coherent radio frequency Cherenkov radiation (Askar'yan, 1962a, b, 1965a, b; Jelley, 1965; Fujii and Nishimura, 1970).

Item 2 is the basis for several mechanisms. It causes geomagnetically induced acceleration and deflection of charged particles, and charge separation. As a further consequence of the latter a moving electric dipole moment, a transverse current and a magnetic shock are produced. The acceleration generates synchrotron radiation whereas the dipole and current cause a Cherenkov-like radio emission (Kahn and Lerche, 1966; Lerche, 1967; Colgate, 1967). These processes occur even if there is no net charge excess. Similar effects take place under the influence of an atmospheric electrostatic field mentioned under item 3 above (Wilson, 1957; Charman, 1967, 1968; Charman and Jelley, 1968).

Additional processes can occur that may contribute to radio emission by showers, such as *transition radiation*. This process may play a certain role for giant

air showers, that reach their maximum near ground, and is caused by the particle disk as it passes the interface between the atmosphere and the ground (Frank and Ginzburg, 1945; see also Sect. 4.4.4). Small radio signal contributions can also be expected from the low energy tail end of the *bremsstrahlung* spectrum, from *molecular transitions*, or from *reflections* of continuous waves from transmitters by the particle disk, which is a RADAR-like effect (see Sect. 2.6). However, it was shown at an early stage that these processes are insignificant (Rozental and Filchenkov, 1966; Jelley, 1965, b; Charman and Jelley, 1968).

18.3 Early Work

18.3.1 Initial Search for Radio Bursts and Production Mechanisms

The first to investigate the question whether air showers emit radio frequency bursts or pulses was Jelley, shortly after he discovered the emission of optical Cherenkov radiation by atmospheric showers, in the mid 1950s (Jelley and Galbraith, 1953; Galbraith and Jelley, 1953; Jelley, 1958, 1967a) and Suga (1962). Of all the mechanisms that were considered at that time to be likely sources of radio burst generation in showers, the Cherenkov effect appeared to be a very probable contributor, given the successful experience with its optical domain, and Jelley and collaborators began to explore the radio frequency band of the Cherenkov emission spectrum.[2]

The very fundamental question that had to be answered first was whether the process which leads to the production of the visible radiation yields also detectable intensities of radiation at radio frequencies. The conclusion which Jelley has reached in his studies was discouraging. The power radiated per unit bandwidth, $\mathrm{d}P/\mathrm{d}\nu$, by a particle with charge ze traveling a path length l in a medium of refractive index n with velocity β, expressed in units of the velocity of light, c, ($\beta = v/c$), is given by the expression (Frank and Tamm, 1937)

$$\frac{\mathrm{d}P}{\mathrm{d}\nu} = \alpha \left(\frac{4\pi^2\hbar}{c}\right) z^2 \nu \left(1 - \frac{1}{\beta^2 n^2}\right) l \ , \tag{18.1}$$

where ν is the frequency, α the fine-structure constant ($\alpha = 1/137$) and $\hbar$ the reduced Planck constant ($\hbar = h/2\pi = 1.054571 \cdot 10^{-34}\ Js = 6.582122 \cdot 10^{-18}$ eV s).

Equation (18.1) shows that the frequency spectrum of the Cherenkov radiation has the form $\nu \mathrm{d}\nu$. Therefore, a jump from the optical to the radio frequency range means that ν is reduced by a factor of the order of 10^7, and likewise the radiated power, while the bandwidth, $\mathrm{d}\nu$, must be reduced even more in the radio domain for practical reasons. Consequently, to use the microwave portion of the spectrum

[2] For a historic review concerning the discovery of radio bursts from air showers see Jelley et al., (1966).

as proposed by Jelley (1958) to circumnavigate the poor duty factor of optical Cherenkov detection, and to exploit the (at that time) relatively quiet millimeter and centimeter wave bands for air shower studies, did not appear to be feasible.

On the other hand, for the emission of radio waves where the wavelength is large compared to the distance between individual radiating particles (or the physical dimensions of a shower), or, where the electric transient generated by the particles is short compared to the period of the produced waves, the particles cannot be considered as radiating independently because the radiation becomes *coherent*. In this case one must *add amplitudes instead of intensities*. For the coherent radiation of N contributing charges the radiated power is proportional to $N^2\langle l\rangle$ and not $N\langle l\rangle$ as would be the case for *incoherent* emission, thus leading to an enhancement of the radiation which is important for the detection (for details see Askar'yan, 1962a, b, 1965a, b; Fujii and Nishimura, 1970).

Of concern was that positive and negative charges give wave amplitudes of opposite phase, so that their effects tend to cancel out. Should the number of positive and negative charges in a shower be equal, then there will be essentially no Cherenkov radiation at all at wavelengths longer than a few centimeters. Thus, the crucial point here is whether we have *charge symmetry*, i.e., equal numbers of positrons and negatrons, or not.

Obviously, at the early stage of shower development, where the particles have a very high energy, one expects to have charge symmetry because of the dominating pair production mechanism. However, as the shower develops and the average energy of the particles decreases, one would expect a growing negative charge excess because Compton scattering of electrons, positron annihilation, knock-on electrons and delta rays begin to affect the charge ratio in favor of negative charges. Hence, the conditions for Cherenkov radio emission are given. Charge excess is further discussed in Sect. 18.4.

18.3.2 Discovery of Radio Bursts

In spite of the discouraging early predictions, experimental work was initiated. Some of this work was carried out as joint venture with radio astronomers, whereby some of the existing large astronomical radio telescopes had been used in conjunction with air shower arrays. An exploratory experiment was carried out in 1964 by a team from Harwell, Jodrell Bank, and the University College Dublin in which radio pulses were indeed observed that were in coincidence with some of the air showers that were recorded with a conventional array of Geiger counters (Jelley et al., 1965, 1966; Porter et al., 1965a, b; Smith et al., 1965, 1968). The experimental arrangement consisted of a receiver tuned to a frequency of 44 MHz with a bandwidth of 2.75 MHz. The antenna system was a broad-side array of 72 horizontal dipoles directed towards the zenith. The receiver frequency was chosen to be fairly high, to take advantage of the $\nu \mathrm{d}\nu$ factor in the Cherenkov radiation formula, Eq. (18.1), mentioned before.

From the array characteristics, the collected data, and from the event rate recorded, the air shower energies responsible for the observed pulses were estimated as being

greater than $5 \cdot 10^{16}$ eV. The radio pulses themselves were small and barely distinguishable from the background noise. The energy actually picked up by the Jodrell Bank receiver in this particular experiment was $\sim$ 1 eV, and it was estimated that the total radio emission was less than 1 part in 10^8 of the shower energy (Allan et al., 1968). The poor and partly ambiguous results obtained by the various groups active at that time in this field of research quickly dimmed the initially rather euphoric hopes and made it clear that it will be a difficult task to extract useful information by this method.

In conclusion we can say that the experimental work discussed so far has established beyond doubt that air showers can emit detectable pulses of electromagnetic radiation. However, irrespective of the arguments discussed above, it does not follow necessarily that the origin of the detected radiation is due to the *phase-coherent* Cherenkov process.

Besides field strength measurements at different frequencies as a function of the distance from the ground impact of the shower axis and the zenith angle, the early work did also include *polarization measurements* of the radio waves, and correlation studies between the amplitude and polarization of the burst components with respect to the angle between the shower axis and the direction of the geomagnetic field (Hazen et al., 1969; Prescott et al., 1968, 1970; Vernov et al., 1968, 1970).

The results of this work revealed a dependence of the observables on the geomagnetic field, which suggested that at least part of the radio burst must be linked in one way or another to a production mechanism that involves geomagnetic interactions of the shower constituents. This discovery gave strong support to the theories of radio emission developed by Kahn and Lerche (1966) and Colgate (1967), briefly outlined in Sect. 18.4 (see also Lerche, 1967).

For decades this theory served as the standard to estimate radio frequency field strengths in air showers and to interpret experimental data, though other theories that considered the interaction of the shower particles with the *electrostatic field of the atmosphere*[3] were proposed in the years before and after the work of Kahn and Lerche (Wilson, 1957; Charman, 1967).

18.4 Theoretical Considerations and Theories of Radio Emission

18.4.1 Negative Charge Excess and Cherenkov Radio Emission

Consider a pure electromagnetic cascade initiated by a high energy electron or photon. The processes of pair production and bremsstrahlung dominate the shower development at high energy. These processes are symmetrical with respect to positive and negative charges. However, as the shower develops the average energy of the particles decreases because of energy repartition and the different energy losses mechanisms that take place. The bulk of the particles in a shower near

[3] Apart from the fact that there is an electrostatic field in the atmosphere, it was noticed that in some cases during approaching thunderstorms the radio bursts of showers appeared to be enhanced.

maximum development have energies on the order of 30 MeV or less. As a result, a considerable *negative charge excess* must be expected due to Compton scattering, delta-ray production, knock-on electrons and positron annihilation that become important at low energies. Hence, the condition for the production of a radio Cherenkov component is fulfilled.

The process originally suggested as the source of negative charge excess was annihilation of the positrons in flight with atmospheric electrons (Askar'yan, 1962a, b) as the cross section for this process rises rapidly with decreasing energy below 30 MeV. But according to calculations by Fujii and Nishimura (1970, 1971, 1973) annihilation in flight is responsible for only about one tenth of the total charge excess, the greater part is due to Compton recoils.[4] The negative charge excess depends on the particle energy considered and the approximations used in the calculation. The results of the work of Fujii and Nishimura (1970) are shown in Fig. 18.1. According to a calculation by Allan (1971a) the charge excess, κ, varies at shower maximum from $\kappa =\sim 20\%$ for a threshold energy of $E_{\rm th} = 2\,\text{MeV}$ to $\kappa =\sim 1\%$ at $E_{\rm th} \geq 100\,\text{MeV}$.

In the frame of a new initiative undertaken by several research groups to explore radio burst generation by air showers and their information contents with modern

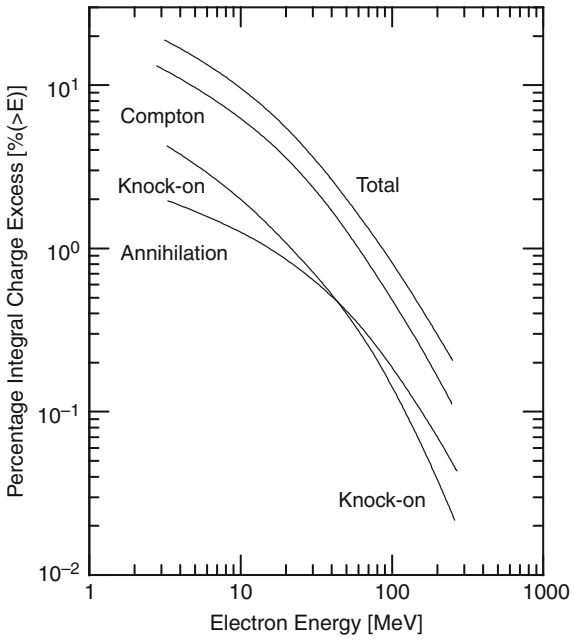

Fig. 18.1 Dependence of the integral negative charge excess on shower particle energy in percent, due to different processes, as indicated, at shower maximum (after Fujii and Nishimura, 1970)

[4] Earlier calculations by Guzhavin et al. (1968) which gave smaller values appear to be in error.

methods, briefly discussed in Sect. 18.6, Kalmykov et al. (2006) have carried out a detailed Monte Carlo simulation of 1 TeV photon initiated vertical electromagnetic cascades in the atmosphere and the associated radio emission. The simulation accounts for the different mechanisms that affect the charge ratio. All showers were started at an altitude of 30 km. Figure 18.15, taken from their work, shows the longitudinal development curves, averaged over five showers, of the positrons and negatrons separately, and of the sum of both. The low energy cutoff for the particles was set to 1 MeV. The figure illustrates beautifully the negative charge excess as a function of shower development. It amounts to a value of $\kappa = \sim 23\%$ for a cutoff at $E_{\rm th} = 1$ MeV at shower maximum, which is at approximately 8.5 km on average in this case. The charge excess increases to $\kappa = \sim 27\%$ for a cutoff at $E_{\rm th} = 0.1$ MeV.

In order to compute the Cherenkov radiation yield the atmospheric pressure dependent threshold energy for the production of Cherenkov radiation ($\sim$21 MeV at sea level) must be considered, which depends on the altitude dependent index of refraction, n. This implies that in the above example with a cutoff energy of 1 MeV only about 1/3 of the particles of the charge excess of 23% contributes to Cherenkov radiation.[5]

18.4.2 Geomagnetic Charge Separation

Askar'yan (1962a, b, 1965b) in his articles drew attention to the alternative mechanism of *charge separation* that occurs in the Earth's magnetic field, but it was left to Kahn and Lerche (1966) to show in a paper of fundamental importance that this process could well be the dominant, one accounting for air shower generated radio bursts in the 30–100 MHz frequency range (see also Lerche, 1967).

As a shower propagates through the atmosphere, the Lorentz force, i.e., $\boldsymbol{F} = e(\boldsymbol{v} \times \boldsymbol{B})$, deflects the positively charged particles to one side, and the negatively charged particles to the other. The total transverse deflection is limited by the finite range of individual particles. With each generation of particles in the shower, the separation of charge must begin all over again, since the new particles are created as electron pairs, with the positive and negative charge appearing simultaneously at one point. On averaging over many particles and overlapping generations, one obtains a quasi-steady state in which the centroids of the positive and negative charges carried by the shower move parallel to one another but with a definite lateral separation. In effect, the shower acquires a *transverse electric dipole moment*. Since this polarization is being sustained by repeated charge separation, there is also a continuous flow of *transverse current* throughout the lifetime of the shower.

[5] Note that because of the large index of refraction of ice ($n_{\rm ice} \approx 1.78$) the bulk of the charge excess is subject to Cherenkov radiation (Zas et al., 1992). Studies of the RF yield in solids (aluminum foils and silica sand targets) using accelerator beams were made by Gorham et al. (2000) and Saltzberg et al. (2001).

(a) Effects of the Electric Dipole Field

The movement of the *electric dipole* through the atmosphere produces a *Cherenkov-like radiation* even in the *absence* of a negative charge excess. The radiation fields produced by the positive and negative charges, considered separately, no longer cancel out completely as they do when the charge separation is zero. Instead of the phase difference between them being exactly π, an additional phase shift appears which is a function of the ratio Δ/λ, where Δ is the lateral separation of the charges and λ the wavelength of the radiation considered. Now Δ/λ is proportional to the frequency ν, so the cancelation becomes progressively less complete as the frequency increases. Thus, while the energy radiated by a moving charge as normal Cherenkov radiation is proportional to $\nu d\nu$, the energy radiated by the dipole field increases more rapidly, in fact, as $\nu^2 d\nu$.

In a shower which radiates both from negative charge excess and from dipole polarization, the dipole contribution becomes relatively more important as the frequency increases. However, the requirement that there must be near coherence between the radiation from different parts of the shower as outlined earlier, in particular, that the disk thickness or the *longitudinal dispersion* of the particles in the direction of the shower axis must be small compared with λ, leads to an *upper frequency limit* for the validity of both, the $\nu d\nu$ and $\nu^2 d\nu$ formulae. Above this limit, the amount of energy radiated falls rapidly; there is left only the *incoherent* radiation produced by each of the shower particles acting independently. The lateral extent of the shower particle disk and its curvature as well as the changing index of refraction of the atmosphere affect the degree of coherence, too (Fujii and Nishimura, 1970).

(b) Effects of the Transverse Current

There is a *second radiation mechanism* associated with the geomagnetic charge separation which arises from the *transverse current* flow. As discussed above, the shower carries with it along its track a short element of current of length Δ, moving perpendicularly to its axis, with the speed of the shower. This current element acts as a source of magnetic field, and plays a role corresponding to that of the charge excess in normal Cherenkov radiation. When the shower velocity is greater than the velocity of light in the atmosphere, an electromagnetic shock wave is produced just as it is with Cherenkov radiation. The frequency dependence of the energy radiated is the same as for Cherenkov radiation, $\nu d\nu$, with the same upper limit due to the onset of decoherence.

In their theory Kahn and Lerche (1966) disregarded the changing index of refraction across the atmosphere, assumed that the shower propagates indefinitely without abrupt changes in size, and that the particle disk was of infinitesimal thickness. More specifically, in their model they substituted the particle disk by two rings of opposite charge having diameters a each and being displaced by a distance Δ. Castagnoli et al. (1969) and Allan (1970) have used more realistic models, accounting for the changing shower size, the finite thickness of the particle disk, the time and energy dispersion of the particles, and a changing index of refraction. They conclude that

these changes as well as the lateral distribution of the particles affect the degree of coherence across the frequency spectrum, but the effects are not very dramatic.

(c) Predicted Field Strength

The essential result of the theory of Kahn and Lerche (1966) is the following equation that yields the *radial electric field strength*, $\mathcal{E}(r)$, of the Fourier components that result from the effects caused by the charge separation in the geomagnetic field *and* the charge excess,

$$\begin{aligned}\mathcal{E}(r) \;=\; -\frac{1}{2}\,kq\,J_0(k\alpha a)\Bigg\{\Delta\cos\theta\left(\frac{1}{cr}+ik\alpha^2\right)H_0^{(1)}(k\alpha r)\\ +\,i\alpha\left(\epsilon+\frac{\Delta\cos\theta}{r}\right)H_0^{(1)'}(k\alpha r)\Bigg\}\;.\end{aligned} \tag{18.2}$$

Here, a is the radius of the charge carrying rings representing the shower front, Δ their displacement, q the line charge of the rings, i.e., $q = \kappa Ne$ with κ the charge excess, N the shower size and e the electronic charge, k is the wave number, α the Cherenkov angle, r the distance to the observer, θ the angle with respect to the shower axis, ϵ the dielectric constant, and J_0 and H_0 are the Bessel and Hankel functions, respectively,

The successive terms on the right hand side of this equation are due to the *transverse current, dipole, excess charge and dipole*, respectively. The relative significance of the different terms for the *near* and *far zones* are discussed in detail by Kahn and Lerche (1966). Shortcomings of this theory are discussed by Lerche (1967) and other authors.

Several authors have carried out calculations to compute the radio emission from air showers due to geomagnetic charge separation. Of interest was the radio frequency spectrum, the field strength as a function of radial distance from the point of impact of the shower axis on the ground and of the axis orientation with respect to the geomagnetic field direction for different primary energies, and the polarization (e.g., Fujii and Nishimura, 1970; Hough and Prescott, 1970; and Hough, 1973; Allan et al., 1975a).

Fujii and Nishimura (1970) carried out a more detailed calculation than Kahn and Lerche (1966), considering the actual shower evolution instead of a shower of constant size and three-dimensional shower development. Their results are displayed in Fig. 18.2a, b that show the frequency dependence of the RF field intensity and the percentage of polarization, respectively. Included in the calculation of either authors are the contributions due to the dipole current, E_J, the dipole moment, E_M, and the negative charge excess, E_C. The ratio of the relative field intensities at 100 m from the shower axis for vertical showers are

$$E_J \;:\; E_M \;:\; E_C \;=\; 3.4 \;:\; 0.21 \;:\; 1.3$$

according to Fujii and Nishimura, and

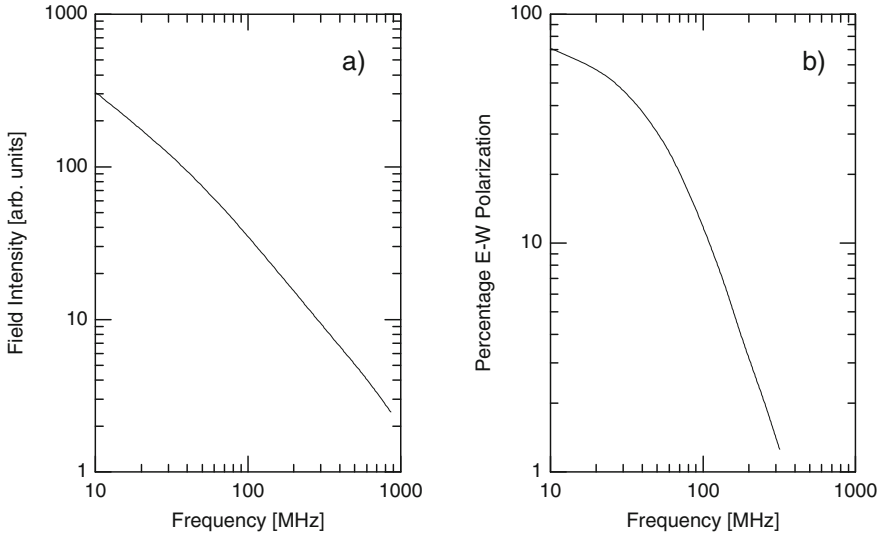

Fig. 18.2 (**a**) Frequency dependence of the field intensity of the radio waves in extensive air showers and (**b**) frequency dependence of the degree of the East–West polarization (after Fujii and Nishimura, 1970)

$$E_J : E_M : E_C = 16 : 3 : 1$$

according to Kahn and Lerche. The differences between the two sets of results are due to the more refined handling of both, the processes causing the charge excess and the lateral distribution of the charge by Fujii and Nishimura (1970). These authors point out the strong sensitivity of the RF field intensity and phase on the electrical charge distribution and the consequence it has on the coherence.[6]

18.4.3 Geoelectric Charge Separation

A vertical electrostatic field gradient of ∼100 V/m exists at the surface of the Earth under normal conditions. This field extends upward into the atmosphere with diminishing strength, reaching a few volts per meter at an altitude between 10 and 20 km. These values vary significantly with locality, time, season and weather. In areas of thunderstorms the field gradient can reach field strength of as much as ∼50 kV/m (Schonland, 1953) and up to 200 kV/m inside thunderclouds (Buitink et al., 2005). Field direction reversals can also occur with varying altitude and there may also be a significant horizontal component.

[6] The clear separation and independence of the different processes as assumed here is questioned by some authors (Haungs, 2006, Private communication).

Wilson (1957) was among the first to carry out a theoretical study, attempting to answer the question whether air showers could generate detectable radio pulses in the atmosphere. He investigated the interaction of moving electrons and ions produced by the shower with the *electrostatic field* of the atmosphere. Wilson's conclusion from his very rudimentary analysis was that the interaction of the moving electrons with the Earth's electric field would nullify the latter momentarily, thus producing a fast electrical transient that should be detectable as a fast electric field pulse, and likewise for the ions that would generate a slow pulse.

The interaction of air shower particles with the geoelectric field was revisited by Charman (1967). He considered the fact that the field component which is perpendicular to the direction of the trajectory of an air shower causes a transverse separation of the charged particles as the shower propagates. The consequence is the formation of an *electric dipole* and a *transverse current*, analogous to the previously discussed case of the geomagnetic charge separation. The resulting separation, Δ_{TE}, of a newly created electron pair due to the transverse component of the geoelectric field, E_T, after a time, t_s, is given by

$$\Delta_{\mathrm{TE}} = \frac{eE_T}{2\gamma m_e} t_s^2 \ , \tag{18.3}$$

where γ and m_e are the Lorentz factor and the rest mass of an electron, respectively, and t_s is the lifetime of the particles. For the latter one usually considers the time it takes to traverse one radiation length in air, χ_0, near sea level at the speed of light, c, i.e., $\chi_0/c \sim 1\,\mu\mathrm{s}$. This can be compared with the transverse displacement due to the geomagnetic effect,

$$\Delta_{\mathrm{TM}} = \frac{ecB_T}{2\gamma m_e} t_s^2 \ , \tag{18.4}$$

where B_T stands for the transverse geomagnetic field component.

To produce a displacement comparable to that caused by a transverse geomagnetic field component of $\sim$0.2 G, a transverse geoelectric field strength of $E_T \sim 6\,\mathrm{kV/m}$ ($6 \cdot 10^9$ e.m.u. cm^{-1}) is required. This comparison shows that under normal conditions contributions from electrostatic charge separation can be neglected as compared to the geomagnetic. However, a strong enhancement must be expected when high static field strength exist, as is the case in the vicinity of thunderstorms.

Charman (1967) has carried out a similar analysis for the geoelectric field component along the shower axis,[7] taking a parallel electric field strength of $E_P = 100\,\mathrm{V/m}$ and assuming an average Lorentz factor of the electrons of $\gamma = 40$. The resulting longitudinal charge displacement of a positron-negatron pair amounts to

$$\Delta_{\mathrm{PE}} = \frac{eE_P}{\gamma^3 m_e} t^2 = 3 \cdot 10^{-4}\ \mathrm{m}. \tag{18.5}$$

[7] There is no geomagnetic analogue to this case.

Considering dipole Cherenkov emission in the meter-band range and the participation of all N shower particles, the radiation yield at $\lambda = 3\,\mathrm{m}$ is $\sim 10^{-7}N$ as compared to a contribution of $\sim 10^{-1}N$ for the normal charge excess Cherenkov radiation (assuming $\kappa = 0.3$ and an electron energy of 20 MeV). Note that analogous to geomagnetic charge separation, radiation processes due to electrostatic charge separation effects do not depend on charge excess.

The conclusion from the work of Charman (1967) is that the geoelectric charge separation is relevant only under unusual meteorological conditions and contributions are only due to the transverse field component. However, under such conditions random atmospheric discharges are likely to mask radio bursts caused by air showers.

Recently, Buitink et al. (2005) have revisited the topic of electric field effects on the radio pulse of air showers. In particular, these authors have studied the effect of thunderstorm conditions on the RF field intensity. They compared showers of similar electron and muon sizes and found that the RF signal can be enhanced by more than a factor of three during thunderstorms, depending on the direction of the electric field with respect to the direction of motion of the electrons and positrons.

This study made clear that under extreme thunderstorm conditions the electric force can even exceed the Lorentz force resulting from the geomagnetic field which is responsible for the geo-synchrotron component. Large fluctuations of the RF signal observed under such conditions are believed to be due to variations of the electric field strength and field orientation and it became evident that RF data obtained during thunderstorms must be analyzed separately from data recorded during fair weather.

18.4.4 Transition Radiation

Radio emission by transition radiation is expected from very large showers that have the shower maximum near ground level. Since for wavelengths of the order of meters the surface of the ground is smooth, the soil conductivity high and the boundary between the ground and the poorly conducting atmosphere sharp, transition radiation will be produced as the particle disk passes the interface between the two media. The radiation is emitted in the forward and backward directions, and only the negative charge excess will contribute.

According to the work of Frank and Ginzburg (1945), the relativistic far-field intensity radiated by an electron per frequency interval is given by

$$\frac{\mathrm{d}P}{\mathrm{d}\nu} = \frac{8}{3}\frac{e^2}{c}\left[\frac{3}{8}\left(\frac{\beta^2+1}{\beta^3}\right)\ln\left(\frac{1+\beta}{1-\beta}\right) - \frac{3}{4\beta^2}\right] \quad [\mathrm{erg\,Hz^{-1}}]\ , \tag{18.6}$$

where e is the charge of the electron and β its velocity in units of c, the velocity of light. Since the wavelengths under consideration are much smaller than the dimension of the shower at impact there will be no enhancement by coherence. In

addition the detectable radiation will be emitted upwards, into a cone of half angle $\theta \sim (m_e c^2/E_e)$, where $m_e c^2$ and E_e stand for the rest mass energy and total energy of the electron, respectively.

As an example, for a shower containing $N \sim 10^6$ particles at ground impact, corresponding to a primary energy of approximately 10^{16} eV, with electrons of average energy $E_e = 100$ MeV and a receiver bandwidth of 2.75 MHz, the total energy emitted is $4.7 \cdot 10^{-16}$ erg ($\sim 3 \cdot 10^{-4}$ eV). This is a factor of 10^{-3} to 10^{-4} times less than the measured values (Jelley, 1965; Smith et al., 1965). So far the mechanism of transition radiation has obtained little attention in the context of air shower physics (Kalpana and Pranayee, 2001; Baishya and Datta, 2005).

18.4.5 Geo-Synchrotron Radiation

In recent years synchrotron radiation produced by the charged particles of an air shower when interacting with the geomagnetic field while propagating in the atmosphere, briefly discussed by Jelley (1965) and Allan (1968), has surfaced again under the new label of *geo-synchrotron radiation*, in particular *coherent* geo-synchrotron radiation. In view of the observed correlation between the amplitude and polarization of the RF signal and the angle between the direction of the shower axis and that of the geomagnetic field, geo-synchrotron radiation appears to be a likely and basically simple model for explaining radio emission by air showers (Falcke and Gorham, 2003). Coherent geo-synchrotron emission from highly relativistic positron-negatron pairs gyrating in the Earth's magnetic field is a mechanism similar to the transverse current proposed by Kahn and Lerche (1966).

Several authors began to tackle the problem theoretically at different levels of complexity. Some chose the analytic approach (Aloisio and Blasi, 2002; Huege and Falcke, 2003), others Monte Carlo (MC) simulations (Suprun et al., 2003; Huege and Falcke, 2005a; Engel et al., 2005; Kalmykov et al., 2006), and Huege and Falcke 2005b c) worked out a parametrization. This work was driven partly by new experimental initiatives such as LOPES and LOFAR (Haungs et al., 2003; Horneffer et al., 2003; Nehls et al., 2005), mentioned earlier, by CODALEMA (Ravel et al., 2004), the balloon based detector project ANITA (Du Vernois et al., 2005a), other space bound detector projects, and possibly an antenna array at the Auger detector in Argentina.

For the treatment of the problem, one usually starts from the classical formula for synchrotron radiation of a single particle.[8] If the trajectory of the particle is known analytically, the radiation an observer at location $\boldsymbol{x}$ will measure at time t is given by Jackson (1975) as

[8] Charge excess and the Cherenkov emission process are usually disregarded in this context as well as the altitude dependent index of refraction of air, setting $n = 1.0$.

$$\boldsymbol{E}(\boldsymbol{x}, t_a) = \frac{e\mu}{4\pi\epsilon_0}\left[\frac{\boldsymbol{n} - n\boldsymbol{\beta}}{\gamma^2(1 - n\boldsymbol{\beta}\cdot\boldsymbol{n})^3 R^2}\right]_{\text{ret}} + \frac{e\mu}{4\pi\epsilon_0 c}\left[\frac{\boldsymbol{n}\times[(\boldsymbol{n} - n\boldsymbol{\beta})\times\dot{\boldsymbol{\beta}}]}{(1 - n\boldsymbol{\beta}\cdot\boldsymbol{n})^3 R}\right]_{\text{ret}} . \tag{18.7}$$

Here, $\boldsymbol{E}(\boldsymbol{x}, t_a)$ is the electric field in space and time, e the electronic charge, n the index of refraction of the atmosphere, μ and ϵ_0 the magnetic permeability and dielectric constant, respectively, $\boldsymbol{\beta}(t) = \boldsymbol{v}(t)/c$ is the particle velocity vector $\boldsymbol{v}(t)$ in units of c, $\dot{\boldsymbol{\beta}} = \mathrm{d}\boldsymbol{\beta}/\mathrm{d}t$, $R(t) = |\boldsymbol{R}(t)|$, refers to the distance between the radiating particle and the observer, and $\boldsymbol{n}(t) = \boldsymbol{R}(t)/R(t)$ is the unit vector pointing along $\boldsymbol{R}(t)|$. The subscript $_{\text{ret}}$ implies that the expressions in brackets must be taken at the *retarded time*, where

$$t_{\text{ret}} = t - \frac{R(t_{\text{ret}})}{c} . \tag{18.8}$$

The first term of Eq. (18.7) represents the *static field* and is usually disregarded as it decreases proportional to $1/R^2$ whereas the second represents the *radiation field* and goes as $1/R$. The denominator in the second term, $(1 - \boldsymbol{\beta}\cdot\boldsymbol{n})^3$, causes the strong beaming effect known for highly relativistic particles that bundles the normal dipole radiation pattern into a narrow cone of semi-opening angle of order $1/\gamma$, where γ is the Lorentz factor of the moving charge. This phenomenon produces for the observer a short but intense pulse of radiation which contains frequencies that are much higher than the particle's gyro frequency.

The pure full-fledged Monte Carlo approach to compute the RF signal of a shower and its properties is relatively trivial. A good program generates a realistic charge and energy distribution of the particles in the shower disk, including the front and tail curvatures of the disk, that should yield reliable results. In this case one is only faced with the problem of diverging computing time when considering ultrahigh energy showers. This can be overcome in a variety of ways such as using simplified MC codes, or the so-called thinning method, or a hybrid computation. However, the different approximations and simplifications can quickly introduce significant errors and can drastically change radiation patterns. Thus, one has to be very cautions when introducing approximations.

On the other hand, the analytic treatment of the problem is mathematically far more difficult but highly instructive. An outstanding example for this approach is the paper of Huege and Falcke (2003), which exposes the problem in a most illuminating way and is highly recommend for the interested student.

As pointed out before, when executing simplified calculations or simulations, a major difficulty is the proper incorporation of the time dependent spatial distribution of the charged particles of the shower front, i.e., in the particle disk as it propagates through the atmosphere, into the calculation. There is a wide variety of approximations that had been used by the different authors. The most simple approach is to

contract the entire charge of the particle disk into just one large point charge, q, where $q = Ne$, N being the shower size and e the unit electronic charge.

Some authors have used a pencil-like line charge using different particle distributions within the "pencil", others have used a pancake-like package of charge and different charge distributions within it, and again others consider also curvature aspects of the shower disk. In some simplified calculations (MC, analytic or semi analytic) the shower evolution, i.e., the build-up and decay of the shower, is disregard and only the emission from the shower maximum is considered (e.g., Suprun et al., 2003). We discuss some of these calculations in Sect. 18.6.

18.4.6 Comments on Coherence

As briefly mentioned before, irrespective of the mechanism of radio pulse emission, it follows immediately that *phase coherence* of the radiation from the different parts of the shower that will take place at the longer wavelengths will lead to a substantial increase in the intensity of the emitted radiation. Taking as an example common Cherenkov radio emission, and assuming that in a shower of N particles there are κN excess negatrons, then, ignoring coherence, we would expect an intensity N times that given by a single particle. With coherence the intensity will be $(\kappa N)^2$ times that from a single particle. The enhancement due to coherence is therefore a factor $\kappa^2 N$, or roughly 10^5 if we put as an example $\kappa = 0.03$ and $N = 10^8$ (Allan, 1971a). That such enhancement must take place under suitable conditions was first pointed out by Askar'yan (1962a, b, 1965b). It was his work which motivated experimentalists to re-examine the possibility of detecting radio-frequency emission from air showers.

In order to preserve coherence during propagation, the radiating particles must be at all time at equal distances from the antenna to an accuracy of a fraction of a wavelength (Allan, 1967). Therefore, if one considers the longitudinal dispersion of the bulk of the particles in a shower (the so-called *disk thickness*) to be 2–3 m (Bassi et al., 1953a, b; Linsley, 1986; Agnetta et al., 1997), then it follows that the radiation to be explored should have a wavelength longer than about ~ 7 m, which means an upper frequency limit of 40–50 MHz.

18.4.7 Polarization of the Radiation

Polarization of the radiation is an important observable because it is the only quantity that can be measured and interpreted quite easily without the need of having detailed knowledge of the structure of the shower available. For a given volume element in the particle disk of a shower with given electrical charge distribution one can compute the relative importance of the radiation from the charge excess, the electric dipole and the displacement current.

The radiation resulting from the negative charge excess is *radially polarized*, whereas the dipole and the displacement current produce a radiation that is *polarized perpendicular to the direction of the geomagnetic field*. The polarization is therefore an important key to determine the relative weight of the contribution to the radio emission by the different processes (Allan et al., 1968).

More specifically, on the ground the polarization due to the electric dipole and the displacement current is in the direction of the vector product of the direction of the shower and that of the geomagnetic field (Smith et al., 1968; Fujii and Nishimura, 1970; Allan, 1971a). For near vertical showers this is nearly east-west. Furthermore the vector product is smaller for showers propagating nearly along the field than for those propagating almost perpendicular to it. These two effects are the basis for polarization measurements. Experimental aspects of polarization are discussed in Sect. 18.5.

18.5 Experimental Data and Phenomenology

18.5.1 Background

Lightning and less dramatic discharges or simply sudden changes of atmospheric electricity that occur at random intervals at a rate depending on local weather conditions and ionospheric reflections will be detected and are expected to interfere with measurements. Likewise, man-made radio frequency sources such as radio (AM, FM) and television transmitters, communication services, broad-band sources like automobile ignitions, and welding machines. Of particular concern are relatively weak sources that are located within the experimental area (Green et al., 2003). The propagation of noise from distant sources depends strongly on frequency, the height of reflecting ionospheric layers and on solar activity.

Galactic noise can be the dominant signal in exceptionally radio-quiet environments for frequencies in the 30–80 MHz range, possibly to 100 MHz (Allan, 1971a). For higher frequencies in such environments, thermal receiver noise becomes the dominant effect. The so-called *Johnson noise* across the equivalent input resistor, R of a receiver is give by the expression

$$U_{\text{noise}} = 2\sqrt{RkT\,\mathrm{d}\nu}\ [V]\ , \tag{18.9}$$

where k is the Boltzmann constant $8.617343(15) \cdot 10^{-5}$ [eV/K] and T the absolute temperature in [K]. Figure 18.3 shows the antenna sky-noise temperature as a function of frequency of the major contributing sources. A similar graph is shown in Fig. 18.4 which also contains data points from actual radio burst measurements ascribed to showers that were recorded simultaneously by a detector array for confirmation (Allan, 1971a).

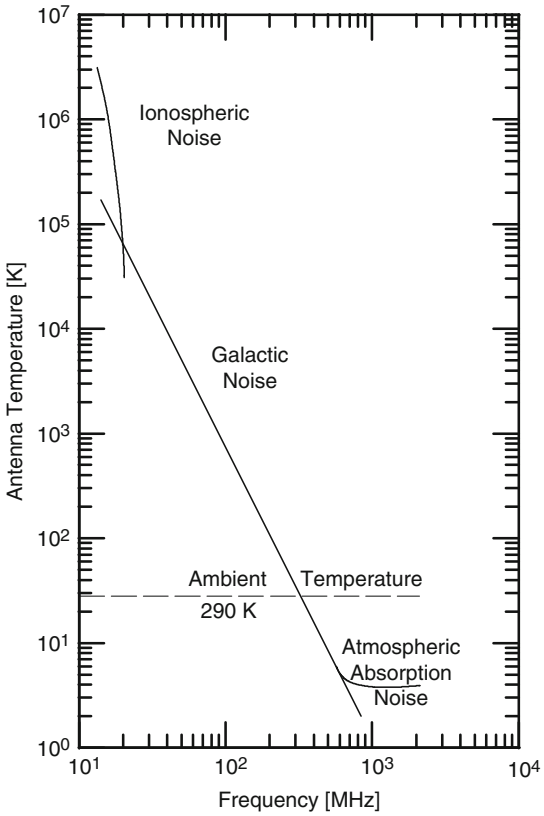

Fig. 18.3 Antenna sky-noise temperature as a function of frequency. The major contributing sources are indicated. The fast rising ionospheric contribution at low frequencies appears to be due to the increasing reflectivity of the ionospheric layer with decreasing frequency. Low frequency noise contributions are from many different sources, including very distant thunderstorms (after Allan, 1971a; see also Minnis and Horner, 1964)

18.5.2 Measurements and Empirical Relations

(a) Radial Distribution of RF Burst and Energy Dependence

The work of Jelley and collaborators stimulated several other groups to explore radio emission by air showers. In particular, the groups working at Haverah Park (GB) (Allan 1967; Allan et al., 1975b), Tokyo (Suga, 1962); Kharkov (former USSR) (Borzhkovsky et al., 1966), Moscow (Vernov et al., 1967, 1968, 1970; Khristiansen et al., 1971), Mt. Chacaltaya (Bolivia) (Barker et al., 1967, 1968; Hazen et al., 1969, 1970a, b), Dublin (IRL) and Jodrell Banks (GB) (Porter et al., 1965a, b; Fegan et al., 1968), Calgary and Penticton (CND) (Prescott et al., 1968, 1970), and at Bologna (Italy) (Galli et al., 1970; Mandolesi and Palumbo, 1970; Mandolesi et al., 1970) were among the most active and made important contri-

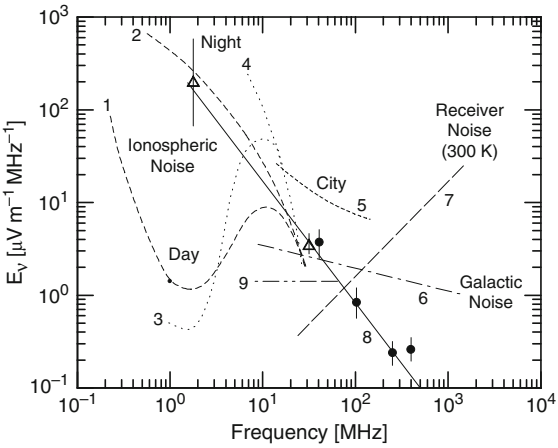

Fig. 18.4 Radio pulse spectra from different sources as indicated. *Curves 1* to *4* show ionospheric noise; *1* and *2* apply to daytime and nighttime, respectively, and likewise *3* and *4*, but the two sets refer to different conditions. *Curve 5* indicates the level of urban noise that can vary significantly, *curve 6* is the galactic noise. The receiver noise, *curve 7*, corresponds to the Johnson noise across the input terminals. *Line 8* is an approximate fit to radio pulses associated with air showers and *line 9* indicates a possible flattening of the air shower radio pulse amplitude below about 100 MHz (Sun, 1975). The figure gives an indication of the minimum detectable field strength for a half-wave dipole antenna versus frequency (Allan, 1971a)

butions to the field. A very comprehensive review of the exploratory phase of the study of radio emission by air showers including radio burst generation, detection, theory and interpretation is given by Allan (1971a). The article discusses numerous associated topics that are of practical relevance.

In the pioneering experiments of Jelley and collaborators, narrow-band techniques at 44 and 70 MHz were used (Jelley et al., 1965, 1966; Porter et al., 1965a, b). On the other hand, the Moscow group investigated radio frequency signals at 30 MHz (Vernov et al., 1967, 1968), while the University of Michigan team working at the BASJE[9] Cosmic Ray Station on Mt. Chacaltaya (Bolivia) studied pulses in the 40–90 MHz range (Barker et al., 1967; Hazen et al., 1969, 1970a, b).

The group working at Haverah Park (England) carried out very systematic studies of the dependence of the RF signals on primary energy, E_0, as well as on the radial distance, r, between the shower core and the antenna, on the zenith angle, θ, and the angle between the shower axis and the geomagnetic field vector, α (Allan et al., 1971a, b). Their results indicated that the electric field strength per unit of frequency, $\mathcal{E}_\nu$, could be expressed as

$$\mathcal{E}_\nu = a \left(\frac{E_0}{10^{17}} \right) (\sin\alpha \, \cos\theta) \exp\left(-\frac{r}{r_f(\nu, \theta)} \right) \quad [\mu\mathrm{V\,m^{-1}\,MHz^{-1}}] \ , \qquad (18.10)$$

[9] Brazilian Air Shower Joint Experiment.

where r_f is an increasing function of θ; it is $110 \pm 10\,\mathrm{m}$ for $\nu = 55\,\mathrm{MHz}$ and $\theta < 35^\circ$. The constant a which is a scale factor was readjusted several times after re-calibration with respect to the particle detector array. Originally fixed at a value of 25 for $10^{17}\,\mathrm{eV}$ showers (Allan et al., 1970a, b), it was changed to 20 (Allan, 1971a) and later on to $a = 1.6$. This low value yields an RF field strength of only $0.6\,\mu\mathrm{V\,m^{-1}\,MHz^{-1}}$ for a $10^{17}\,\mathrm{eV}$ shower at $r = 100\,\mathrm{m}$ from the axis. On the other hand, measurements carried out by the Moscow group yielded $a = 9.2$ which gives a field strength of $3.4\,\mu\mathrm{V\,m^{-1}\,MHz^{-1}}$ at $r = 100\,\mathrm{m}$ for the same shower (Atrashkevich et al., 1977). The reasons for these uncertainties are probably due to errors in the energy estimation, shower core location and the calibration of the RF system.

Note that the measured quantity $\mathcal{E}_\nu$ of Eq. (18.10) and the electrical field strength $\boldsymbol{E}(\boldsymbol{x}, t_a)$ of Eq. (18.7) (or $\boldsymbol{E}(\boldsymbol{R}, \omega)$ used in other derivations to compute geosynchrotron radiation) are linked by the relation

$$\frac{E(t)_{\max}}{\delta\nu} = \mathcal{E}_\nu = \sqrt{\frac{128}{\pi}}\,|\boldsymbol{E}(\boldsymbol{R}, \omega = 2\pi\nu)| \ . \tag{18.11}$$

This relation is obtained after time averaging of the reconstructed field pulse $\boldsymbol{E}(t)$, for an ideal bandpass of width $\Delta\nu$ (Huege and Falcke, 2003).[10]

In another study it was found that the signal power for showers of average primary energy $E_0 = 5 \cdot 10^{16}\,\mathrm{eV}$ was about 4 times that of the *galactic noise*, for which Allan (1971a) specified a field strength of $\mathcal{E}_\nu^{\mathrm{Gal}} \simeq 1 - 2\,\mu\mathrm{V\,m^{-1}\,MHz^{-1}}$. Thus, for $10^{17}\,\mathrm{eV}$ showers one expects $\mathcal{E}_\nu \simeq 2 - 4\,\mu\mathrm{Vm^{-1}\,MHz^{-1}}$ at $r \sim 100\,\mathrm{m}$. For a given field strength and antenna one can compute the voltage across the input termination resistor of an amplifier using the engineering formula (Allan, 1971a)

$$V_{\mathrm{peak}} = \frac{c}{2\sqrt{Z}} \left(\frac{G\,R}{\pi}\right)^{1/2} \left(\frac{\delta\nu}{\nu}\right) \mathcal{E}_\nu \quad [\mathrm{V}]\,, \tag{18.12}$$

where Z is the impedance of free space ($120\pi\,\Omega$), G is the antenna gain, R the receiver input termination resistance, and $\delta\nu$ the bandwidth centered at frequency ν.

For an assumed gain of $G = 5$ ($\sim$7 dB) and $\delta\nu/\nu = 2.75/44$ one gets a value of $\mathcal{E}_\nu \simeq 2.4\,\mu\mathrm{V\,m^{-1}\,MHz^{-1}}$ at a primary energy of $5 \cdot 10^{16}\,\mathrm{eV}$, or about $5\,\mu\mathrm{V\,m^{-1}\,MHz^{-1}}$ at $10^{17}\,\mathrm{eV}$ at $r \sim 100\,\mathrm{m}$ if $\mathcal{E}_\nu$ scales linearly with primary energy (Allan, 1971a; see also Weekes, 2001). For $G = 5$ the data of Jelley et al. (1965, 1966) and Porter et al. (1965b) are therefore in favor of the higher field-strength parameter a as proposed by Atrashkevich et al. (1977). Figures 18.5 and 18.6 show as an example of the extensive experimental work which had been done during the pioneering years several sets of data on the lateral distribution of the RF field strength (Allan et al., 1970b; Allan, 1971a, b).

[10] This relation is based on certain assumptions and is not generally applicable to all data (Haungs, 2006, Private communication).

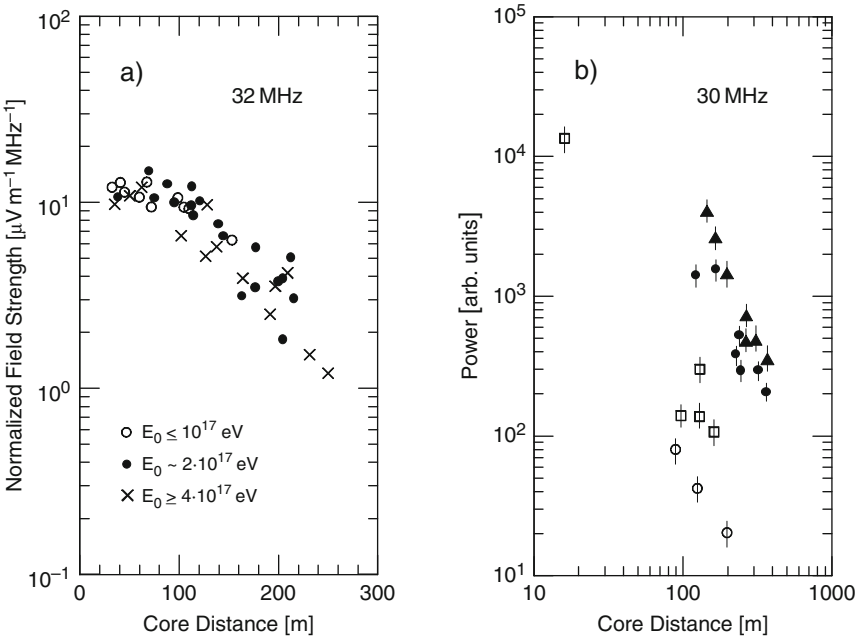

Fig. 18.5 (**a**) Lateral distribution of the radio signal at 32 MHz in large showers. The field strength $\mathcal{E}_\nu^N$ is normalized with respect to shower size in terms of the so-called ground parameter, ρ_{500} (see Sect. 12.5), and the angle between the shower axis and the geomagnetic field, α (after Allan et al., 1971a). (**b**) Lateral distribution of the radio power flux recorded in four showers at a wavelength of 10 m (30 MHz) (bandwidth 3–4.5 MHz) with the Moscow installation (Vernov et al., 1968). The parameters of the four showers are listed below; θ and ψ are the zenith and azimuthal angles, respectively, and P the spectral density of the power flux received by the antenna

Symbol	Size	θ	ψ	P at ($R = 150$ m)
▲	$3.2 \cdot 10^8$	35°	239°	$3.3 \cdot 10^{-17}$ W m^{-2} Hz^{-1}
□	$1.4 \cdot 10^8$	25°	142°	$1.2 \cdot 10^{-18}$ W m^{-2} Hz^{-1}
●	$7.1 \cdot 10^7$	–	–	$1.5 \cdot 10^{-17}$ W m^{-2} Hz^{-1}
○	$1.0 \cdot 10^7$	38°	162°	$3.5 \cdot 10^{-19}$ W m^{-2} Hz^{-1}

The period of intense work on radio bursts associated with air showers ceased early in the seventies of the last century as it appeared to be hopeless to extract useful information on the development of air showers. However, some sporadic work was continued through the years by some groups whereby the interest was focused more on the exploration of the very low, low and medium frequency (VLF, LF and MF) domains of the RF spectrum (Clay et al., 1973, 1975; Suga et al., 1985; Suga and Nishi, 1987; Artamonov et al., 1990, 1991; Kadota et al., 1993; Castagnoli et al., 1993; Golubnichii et al., 1994), and likewise some theoretical work (Kaneko et al., 1983; Nishimura, 1985; Aleksandrov et al., 1987). Little attention was given to the very high frequency (VHF) region, except for a re-analysis of 110 MHz data by Baishya et al. (1993). A review of these and more recent activities can be found in the proceedings of the RADHEP-(2000) workshop.

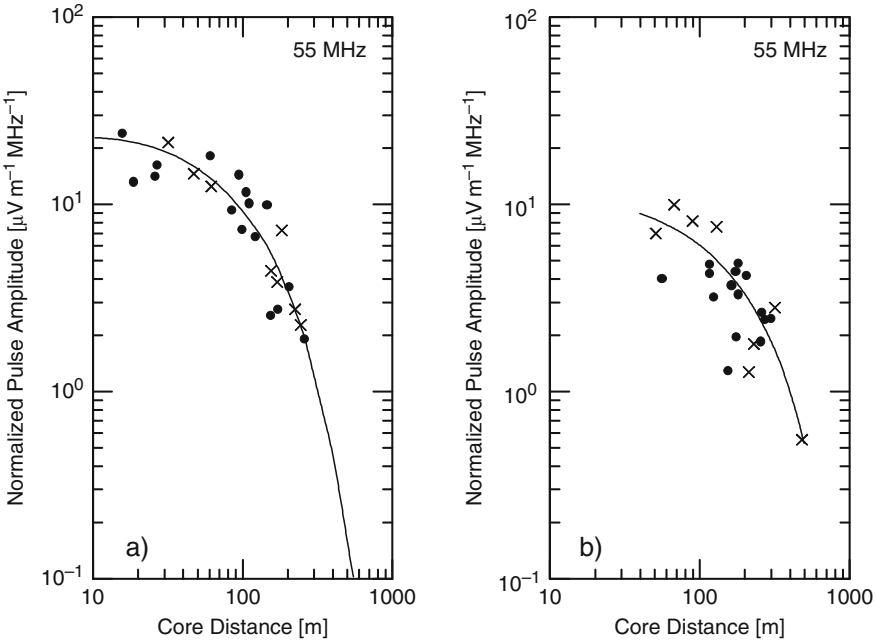

Fig. 18.6 Normalized radio pulse amplitude at 55 MHz as a function of core distance. The normalization is carried out assuming the amplitude is proportional to the total shower energy, E_0, and to the sine of the angle between the shower axis and the direction of the geomagnetic field. Both figures are for showers propagating perpendicularly to the Earth's magnetic field; the symbols • apply to an energy range $10^{17} \leq E_0 \leq 3 \cdot 10^{17}$ eV, × to $3 \cdot 10^{17} \leq E_0 \leq 10^{18}$ eV. The zenith angle range is $\theta < 35^\circ$ for all showers of (**a**). In (**b**) it is $35^\circ \leq \theta < 42^\circ$ for × and $42^\circ \leq \theta < 50^\circ$ for • (after Allan et al., 1970b)

Several authors have investigated the correlation between the muon number in a shower and the field strength of the radio signal at different frequencies and core distances, including polarization effects (Barker et al., 1967; Smith et al., 1968; Atrashkevich et al., 1973). Atrashkevich et al., (1975) found a linear relation between the muon number and the field strength normalized to $\sin(\boldsymbol{v}, \boldsymbol{H})$, where $\boldsymbol{v}$ is the direction of the shower axis and $\boldsymbol{H}$ that of the geomagnetic field, at 32 MHz and a distance of 100 m from the shower axis. Very recently a similar analysis had been carried out by Falcke et al. (2005) that is discussed in Sect. 18.6.

(b) Polarization Measurements

In a number of experiments *polarization measurements* of the radio pulse had been carried out (Abrosimov et al., 1970; Prescott et al., 1970; Vernov et al., 1970; Allan, 1971a; Atrashkevich et al., 1975) and some authors have conducted theoretical studies (Fujii and Nishimura, 1970; Castagnoli et al., 1969). This work indicated that the geomagnetic mechanism appears to dominate over all other emission mechanisms (Cherenkov and electrostatic). The results of the work of Prescott et al. (1970) are shown in Fig. 18.7.

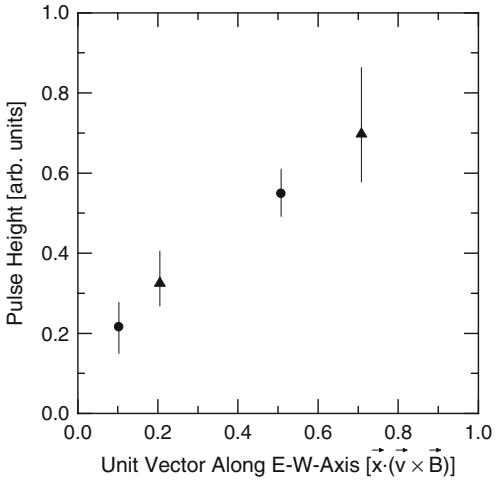

Fig. 18.7 Radio signals at 22 MHz, showing their dependence on the relative orientation of the shower axis and the geomagnetic field. The symbols ▲ are for a zenith angle of 30°, ● for 14.5° (after Prescott et al., 1970)

Atrashkevich and collaborators (1975) have measured the amplitudes of the voltage pulses of the east–west (V_{E-W}) and north–south (V_{N-S}) components with crossed antennae at 32 and 58 MHz. They come to the conclusion that their polarization data are more consistent with geomagnetic polarization than with any other polarization effect. Likewise, in the analysis of Vernov et al. (1970) the ratio D as defined below between the experimentally measured ratio of the east–west and north–south polarizations, $(P_{E-W}/P_{N-S})_{\text{exper.}}$, and the theoretically expected polarization ratio, $(P_{E-W}/P_{N-S})_{\text{theor.}}$, of the geomagnetic and geoelectric charge separation, and the negative charge excess (Cherenkov) radio emission mechanisms was determined,

$$D = \lg\left(\frac{(P_{E-W}/P_{N-S})_{\text{exper.}}}{(P_{E-W}/P_{N-S})_{\text{theor.}}}\right) . \tag{18.13}$$

The average lower limits of the absolute deviations of D from zero for the three mechanisms of two sets of shower measurements are given in Table 18.1. Details of the data are plotted in Fig. 18.8. Again, the experimental data agree best with the prediction of the geomagnetic process.

Table 18.1 Values of the ratio D of Eq. (18.13) for the three processes (Vernov et al., 1970)

Year of measurements	Number of events	D		
		Geomagnetic	Geoelectric	Cherenkov
1969	9	0.3 ± 0.15	1.4 ± 0.2	0.7 ± 0.2
1967 and 1969	18	0.36 ± 0.12	1.4 ± 0.2	0.7 ± 0.15

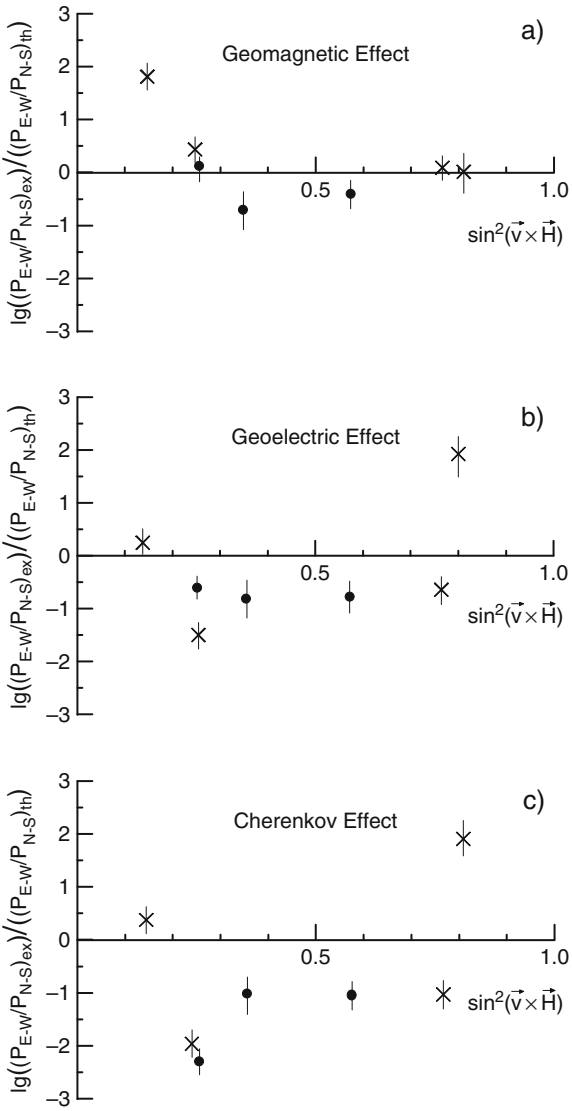

Fig. 18.8 Polarization analysis of radio bursts detected with the antenna system at the Moscow air shower array site with respect to the three different radio burst generation mechanisms: (**a**) geomagnetic, (**b**) geoelectric (atmospheric electrostatic) charge separation, and (**c**) negative charge excess induced Cherenkov radiation. The plot shows the logarithm of the ratio of the experimentally measured to the theoretically predicted ratios of the east-west (P_{E-W}) to the north–south polarizations (P_{N-S}), i.e., the value D of Eq. (18.13) (Vernov et al., 1968)

18.5.3 Pulse Characteristics and Frequency Spectrum

Allan (1971a) summarizes his findings with respect to the RF pulse properties as follows. The Haverah Park observations are consistent with a model in which the RF pulse's onset is generated by the start of the shower at an elevation of about 10 km above sea level, while its end is linked to the greater total path length (shower + signal propagation distance) associated with the shower's absorption about 5 km above sea level (Allan, 1968, 1971a). If a vertical shower is observed at a distance of 100 m from its core, the pulse should rise and fall back to zero within about 10 ns, with a subsequent longer-lasting negative component. High frequencies should be less visible far from the shower axis. Heavy primaries should lead to showers originating higher in the atmosphere, with consequent higher-frequency radio components as a result of the geometric aspect ratio with which they are viewed by the antenna, and possibly a greater $\mathcal{E}_\nu$ for a given primary energy (Allan, 1971a; Allan et al., 1971a, b). The polarization of the pulse should be dictated by the mechanism of pulse generation, e.g., perpendicular to the line of sight with a component along $(\boldsymbol{v} \times \boldsymbol{B})$ for the charge separation mechanism.

18.6 Recent Work

In the many years that followed the pioneering days, occasional experiments and theoretical studies had been carried out by different groups, covering the spectral range from 10 kHz to over 1 GHz (Fegan and Slevin, 1968; Fegan and Jennings, 1969; Spencer, 1969; Clay et al., 1973, 1975; Kaneko et al., 1983; Artamonov et al., 1990, 1991; Zas et al., 1992; Allen et al., 1997; Alvarez-Muñiz et al., 2001; Kalpana and Pranayee, 2001),[11] however, so far without bringing a major breakthrough. As a matter of fact, it is still impossible today to detect showers reliably using only the radio detection technique, not to mention to specify the relevant shower parameters from radio burst measurements (Lafebre et al., 2005). Moreover, many basic questions about the origin of the radio component are still not properly answered.

In this context, a prototype experiment was set up at the Dugway site in Utah (US), on the side of the CASA/MIA array (Borione et al., 1994) to further explore radio emission by air showers and to develop suitable equipment that could possibly be used in conjunction with the Auger project in Argentina. Unfortunately no useful radio pulses could be detected during the operating period (Green et al., 2003).

In recent years the field has been reactivated with significant efforts, both, experimental and theoretical. Hopes are currently high that dedicated modern antenna systems in combination with fast digital data handling and advanced information technology, as will be incorporated in the giant LOFAR antenna array (Nigl et al., 2005) and in other projects will finally bring the break-through and success. The new

[11] Some of the work listed here deals with the detection of neutrinos as well as air showers in ice.

methods are presently being tested with the LOPES array, a prototype of LOFAR (Falcke and Gorham, 2003; Badea et al., 2005; Horneffer et al., 2003, 2005; Nehls et al., 2005), and with the CODALEMA experiment (Ravel et al., 2004). They are expected to vastly refine the quality of the data and analysis, and should also improve background rejection.

The new theoretical initiatives consider mainly the *geo-synchrotron radiation mechanism*, briefly outlined in Sect. 18.4.5. This work seems to verify that this process may be the main contributor to radio burst emission from relativistic charged particles in low density media, such as air, though negative charge excess Cherenkov radiation will certainly contribute its part. Nevertheless, recent simulations applying the geo-synchrotron mechanism to air showers appear to yield results that are in support of existing experimental data.

It is evident from the above discussion that the problem is highly complex and no single process can fully account for the radio phenomenon associated with air showers. The deviations among the different simulations, particularly when comparing the results of older simulations with more recent ones, are most likely due to the approximations chosen by the different workers.

In the following we briefly summarize some of the relevant new theoretical studies, most of which are closely related to the new projects mentioned above, and we present some of the results that have emerged from this work.

In the paper of Huege and Falcke (2003), mentioned in Sect. 18.4.5, these authors carry out a very detailed study of the RF emission by air showers due to geo-synchrotron radiation. In this work where the problem is treated mainly analytically, the authors analyze chiefly the effects of the charged particle distribution in the shower disk, discussing the effects of the longitudinal, lateral and energy distribution of the particles separately and in various combinations. Of the great wealth of data presented in this chapter, we reproduce some particularly instructive results (Figs. 18.9, 18.10, 18.11 and 18.12) that illustrate how subtle the charge distribution is.

The data shown in the four figures apply to vertically incident 10^{17} eV showers with size $N = 10^8$ at shower maximum, which is located at a height[12] of $R_0 = 4$ km. For simplicity a horizontally oriented geomagnetic field of 0.3 G was assumed and what the authors call a "reasonable" lateral particle distribution function that agrees with experimental data had been used for the calculation.

Figure 18.9 shows the resulting electrical field strength as a function of frequency for different particle distributions within the shower disk, as specified in the caption, including a case without lateral distribution, for comparison. Similarly, Fig. 18.10 displays the field strength as a function of radial distance from the shower axis for the specified parameters at three frequencies.

The effect of the integration of the contributions of all shower particles over the entire shower evolution to the RF signal is illustrated in Figs. 18.11 and

[12] We use here the same notation as in the original paper, to simplify matters for the student when consulting the paper.

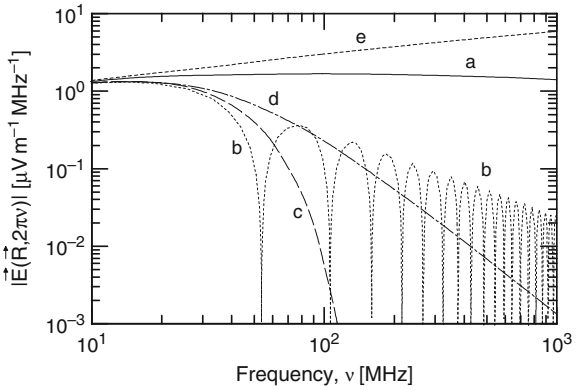

Fig. 18.9 Frequency spectrum of the electric field strength $|\boldsymbol{E}(\boldsymbol{R}, 2\pi\nu)|$ in the *center* of the surface illuminated by a vertical 10^{17} eV shower at its maximum, using a "realistic" lateral particle distribution, a broken power-law energy spectrum with $\gamma = 5$–1,000 for the electrons in the disk, at a minimum distance between shower front and observer of $R_0 = 4$ km. *Curve* (*a*) applies to *full longitudinal coherence*, *curves* (*b*) to (*d*) to different longitudinal distributions within the disk: (*b*) uniform 5.6 m long; (*c*) Gaussian with $\sigma = 1.61$ m; (*d*) Γ-distribution defined by $f(t) = At^B \exp(-Ct)$ with $t = x/c$ and $c\sigma_t = 1.61$ m. *Curve* (*e*) shows the result for full coherence without lateral distribution (Huege and Falcke, 2003)

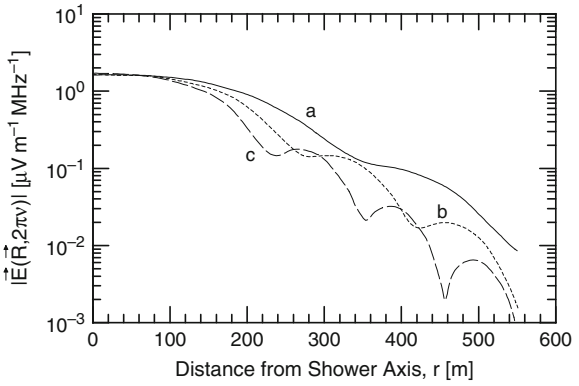

Fig. 18.10 Radial distribution of the electric field strength $|\boldsymbol{E}(\boldsymbol{R}, 2\pi\nu)|$ of the RF burst due to geo-synchrotron radiation of a vertical 10^{17} eV shower at maximum development and for *full longitudinal coherence*. The data were obtained for $R_0 = 4$ km, a "realistic" lateral distribution and a broken power-law energy spectrum with Lorentz factor $\gamma = 5$–1, 000 for the electrons in the disk. The *curves* apply to frequencies of (*a*) 50 MHz, (*b*) 75 MHz and (*c*) 100 MHz (after Huege and Falcke, 2003)

18.12, whereby the so-called *flaring particle disk* had been considered (Agnetta et al., 1997), i.e., a particle disk where the thickness varies with distance from the shower axis. The figures contain a few experimental data points from old measurements of Spencer (1969) and Prah (1971) that had been re-scaled.

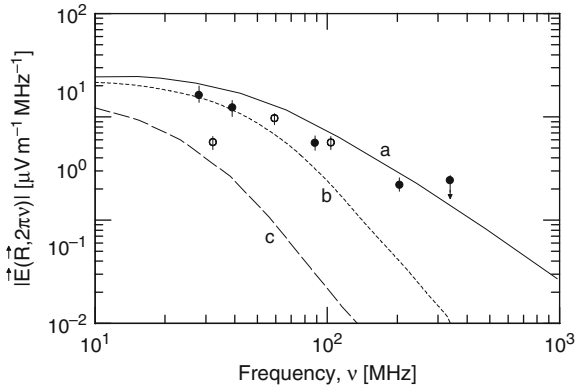

Fig. 18.11 Frequency spectrum of the electric field strength $|\boldsymbol{E}(\boldsymbol{R}, 2\pi\nu)|$ of the RF burst due to geo-synchrotron radiation at different locations on the ground generated by a vertical 10^{17} eV shower as in Fig. 18.9 but for a flaring particle disk *Curve (a)* applies to shower axis impact on the ground, (*b*) to 100 m and (*c*) to 250 m from the axis. The experimental points are re-scaled data of Spencer (1969) after Allan (1971a) (·), and Prah (1971) (after Huege and Falcke, 2003)

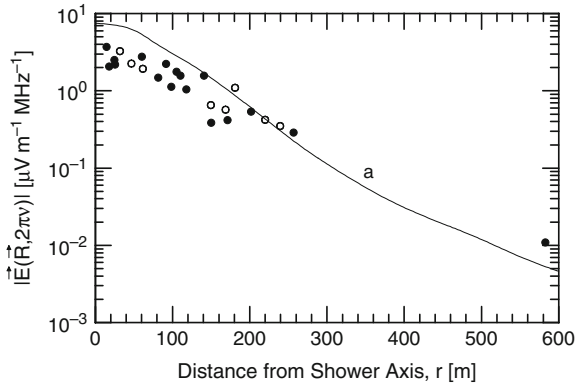

Fig. 18.12 Radial distribution of the electric field strength $|\boldsymbol{E}(\boldsymbol{R}, 2\pi\nu)|$ of the RF burst due to geo-synchrotron radiation of a vertical 10^{17} eV shower using the flaring disk model. The remaining assumptions are the same as for Figs. 18.10, 18.11 and 18.12. The data are from Allan et al. (1970b) (after Huege and Falcke, 2003)

Results from additional studies of the effect of the charge distribution in the shower disk (or pancake) and other aspects influencing the RF radiation field on the ground, based on Monte Carlo simulations, are presented in Huege and Falcke (2005a, c), where radiation patterns are also displayed (see also Suprun et al., 2003, who carried out a similar calculation, and Du Vernois et al., 2005b). The parametrization of the problem is discussed in Huege and Falcke (2005b, c).

Within the frame of the CODALEMA experiment Ravel et al. (2004) carried out a calculation using a very simple model to compute the electric field pulse, $\boldsymbol{E}(t)$. These authors considered only the charge excess component and used a

one-dimensional charge distribution propagating along the shower axis to compute the radio frequency emission. They calculated the pulse for a vertical 10^{20} eV (100 EeV) shower, taking $(7 \cdot 10^9)$ negatrons at shower maximum and have used the following equation,

$$\boldsymbol{E}(t) = \frac{1}{4\pi\epsilon} \sum_{t'} \frac{e(t')(1-\beta^2)(\boldsymbol{n}-\boldsymbol{\beta})}{R^2|1-\boldsymbol{n}\cdot\boldsymbol{\beta}|^3} + \frac{1}{4\pi\epsilon c} \sum_{t'} \frac{e'(t')(\boldsymbol{n}-\boldsymbol{\beta})}{R(1-\boldsymbol{n}\cdot\boldsymbol{\beta})|1-\boldsymbol{n}\cdot\boldsymbol{\beta}|} \quad , \tag{18.14}$$

where $\boldsymbol{\beta} = \boldsymbol{v}/c$ is the velocity vector of the charge in units of c, $\boldsymbol{n} = \boldsymbol{R}/R$ is the direction and $c(t - t') = R$ the distance of the line connecting the moving charge with the observer, and $e(t')$ describes the charge excess distribution along the shower axis.

The results of this computation are illustrated in Figs. 18.13 and 18.14. Figure 18.13 shows the pulse height of the electric field as a function of time for three different impact parameters, i.e., distances between axis ground impact and observer location, and Fig. 18.14 shows the frequency spectrum at 500 m.

In a similar calculation Gousset et al. (2004) analyzed the prospects for detecting very inclined (near horizontal) showers by means of radio bursts. The conclusion is that the signal strength is significantly enhanced as compared to vertical showers and that the RF detection method may be useful for recording neutrino induced showers.

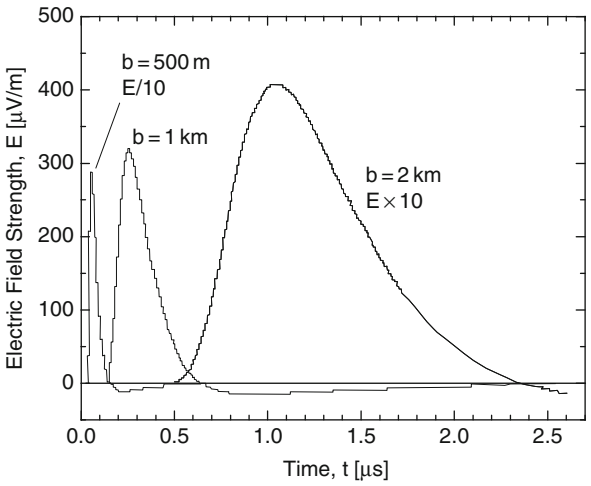

Fig. 18.13 Pulse shapes of the electric field of an one-dimensional simulated shower of primary energy 100 EeV due only to charge excess assumed to amount to $7{\cdot}10^9$ negatrons, for three different impact parameters as indicated (after Ravel et al., 2004)

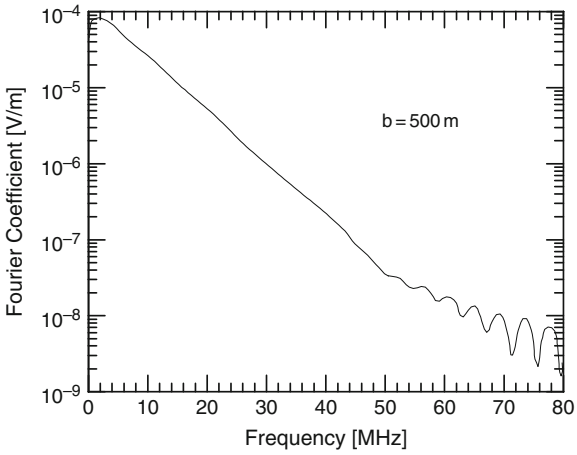

Fig. 18.14 Fourier spectrum of the radio frequency burst at an impact parameter of $b = 500$ m of a simulated one-dimensional shower of primary energy 100 EeV having an assumed charge excess of $7 \cdot 10^9$ at its maximum development (after Ravel et al., 2004)

Kalmykov et al. (2006) have carried out Monte Carlo simulations of 1 TeV photon initiated showers, briefly mentioned in Sect. 18.4.1 where they have considered both, Cherenkov and geo-synchrotron radio frequency emission. In Fig. 18.15, briefly mentioned in Sect. 18.4, the longitudinal shower development is shown

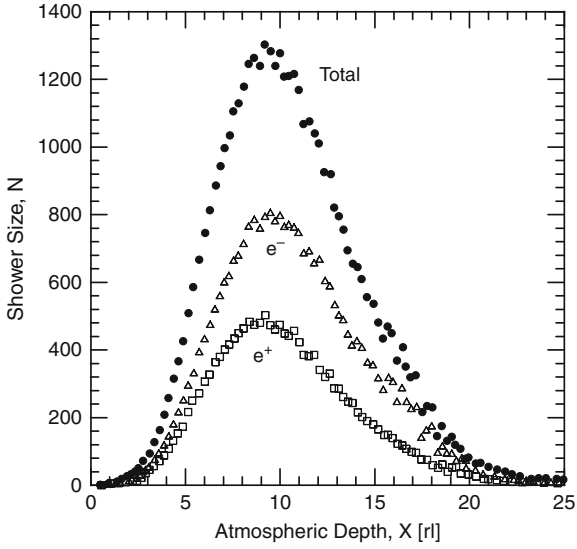

Fig. 18.15 Shower development curves averaged over five 1 TeV photon initiated showers with a low energy cutoff of 1 MeV. The symbols represent the following: • the sum of negatrons and positrons, △ negatrons only, □ positrons only (after Kalmykov et al., 2006). The calculation uses an EGSnrc-based program code (www.sao.nrc.ca/inms/irs/EGSnrc/)

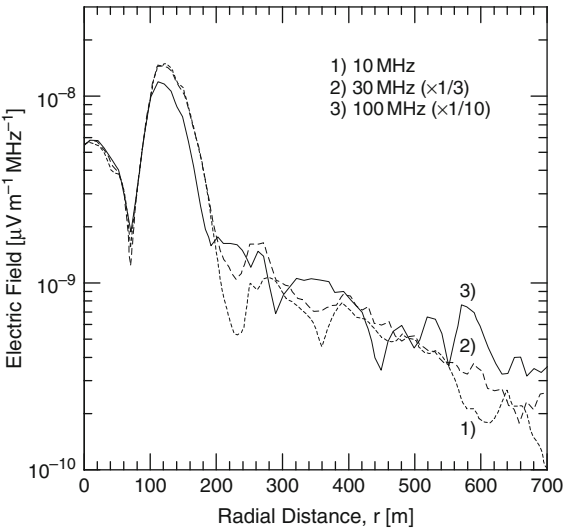

Fig. 18.16 Lateral distribution of the Fourier components of the electric field due to Cherenkov radio emission, averaged over the same set of five showers as specified for Fig. 18.15, valid for the Karlsruhe location (106 m a.s.l.). Note the multiplication factors for the *different curves* and the drop of the coherent contribution at 120 m from the shower axis at 100 MHz (after Kalmykov et al., 2006)

whereby the development of the positrons and negatrons is plotted separately as well as the sum of both, thus illustrating very clearly the negative charge excess. The lateral field strength distribution for all Cherenkov RF components combined is displayed in Fig. 18.16 for different frequencies, and in Figs. 18.17 and 18.18 the contributions of the geo-synchrotron and the total radio emission at 50 and 200 MHz, respectively. A similar calculation was performed by Engel et al. (2005) for 1 and 10 TeV photon initiated showers considering only the geo-synchrotron component.

Very recently Falcke et al. (2005) have carried out a correlation analysis between the electrical field strength produced by showers, measured with the LOPES antennae located at the KASCADE experimental site, and the muon number determined with the KASCADE muon detectors.[13] They find the strongest correlation between the absolute value of the electrical field strength $\mathcal{E}$ and the muon number, N_μ, and between $\mathcal{E}$ and the angle between the shower axis and the geomagnetic field vector, α. This situation is illustrated in Fig. 18.19. A similar analysis, briefly mentioned in Sect. 18.5.2b, had been carried out by Atrashkevich et al. (1975).

[13] The muon number used is the so-called truncated muon number as determined by the KASCADE experiment and not the total muon number of the showers.

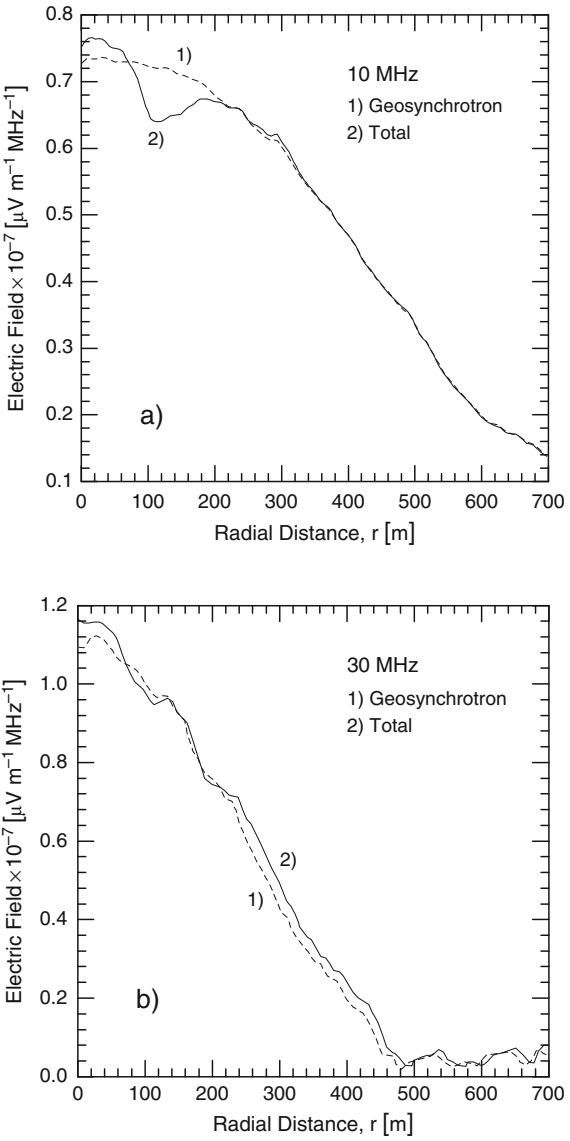

Fig. 18.17 Lateral distribution of the Fourier components of the electric field due to geosynchrotron and total radio emission, averaged over the same set of five showers as specified for Fig. 18.15 valid for the Karlsruhe location (106 m a.s.l.) (after Kalmykov et al., 2006)

18.7 Concluding Comments and Outlook

The problem of fluctuations of the radio signal had been investigated by Huege et al. (2005). In a very recent paper these authors conclude from their work that at a characteristic core distance the amplitude of the bandpass-filtered radio signal

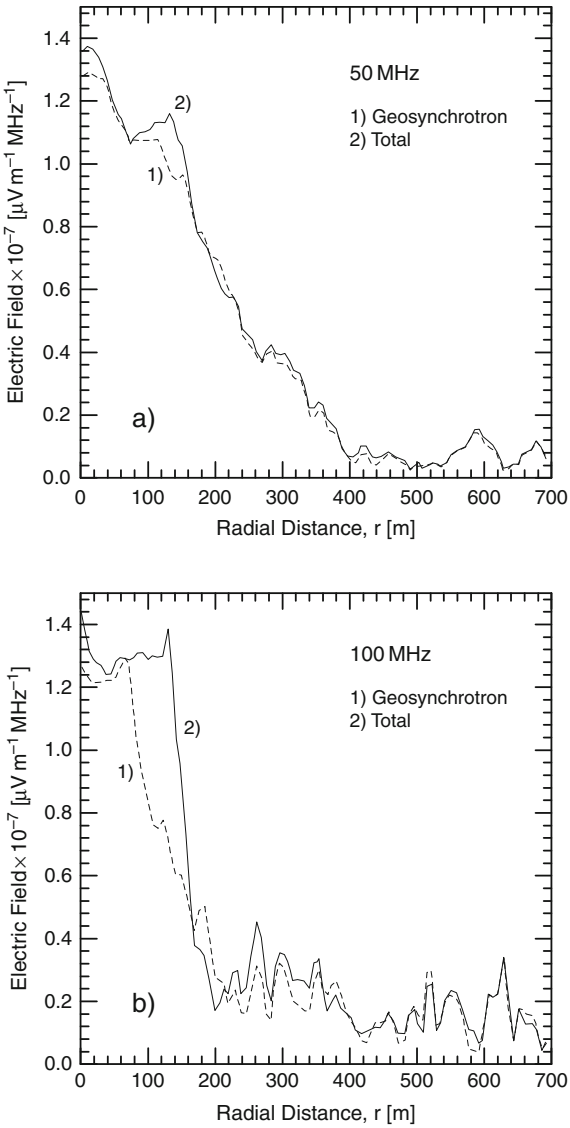

Fig. 18.18 Lateral distribution of the Fourier components of the electric field due to geosynchrotron and total radio emission, averaged over the same set of five showers as specified for Fig. 18.15 valid for the Karlsruhe location (106 m a.s.l.) (after Kalmykov et al., 2006)

is directly proportional to the energy deposited in the atmosphere by the electromagnetic cascade with an r.m.s. uncertainty due to shower to shower fluctuations of ∼3%. Furthermore, the ratio of this signal amplitude and that at a larger distance is directly related to the depth of shower maximum with an r.m.s. uncertainty

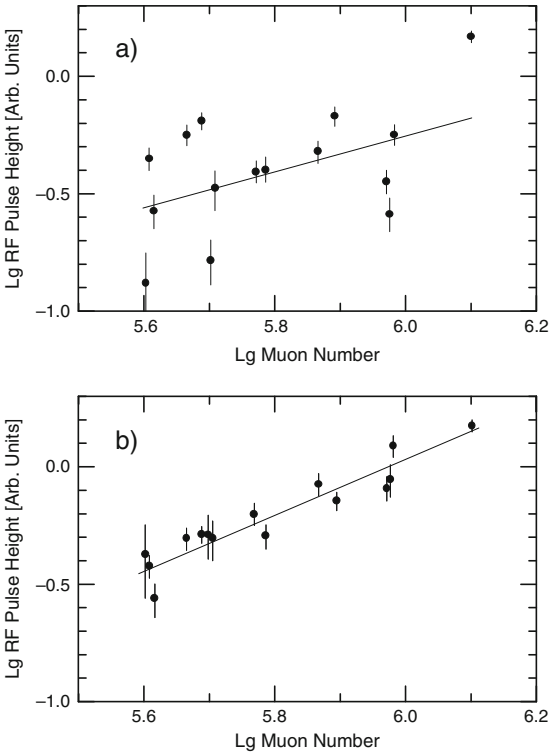

Fig. 18.19 Correlation between the radio emission pulse height and the muon number of showers. The RF signal was recorded with the LOPES antenna system located at the KASCADE experimental site in Karlsruhe, Germany. The RF bursts are associated with showers recorded by the KASCADE array whose core fell within 70 m of the center of LOPES, that contained a truncated muon number $N_{\mu,tr} \geq 4 \cdot 10^5$, corresponding to a primary energy of $E_0 \geq 10^{17}$ eV and subtended a zenith angle of $\theta \leq 45^\circ$. In (**a**) the dependence of the RF signal on the angle between the shower axis and the direction of the geomagnetic field, α, is ignored, whereas in (**b**) it is accounted for (Falcke et al., 2005)

of $\sim$15–20 g cm^{-2} (Huege et al., 2008). Consequently, these observables permit to determine the primary energy and the depth of shower maximum on a shower-to-shower basis.

References

Abrosimov, A.T., et al.: Acta Phys. Acad. Sci. Hung., 29, S3, p. 705 (1970).
Agnetta, G., et al.: Astropart. Phys., 6, p. 301 (1997).
Aleksandrov, A.V., et al.: PICRC, 6, p. 132 (1987).
Allan, H.R.: J. Atmos. Terr. Phys., 29, p. 1103 (1967).
Allan, H.R.: Can. J. Phys., 46, p. S234 (1968).
Allan, H.R., et al.: Can. J. Phys., 46, p. S238 (1968).

Allan, H.R.: Acta Phys. Acad. Sci. Hung., 29, S3, p. 699 (1970).
Allan, H.R., et al.: Nature Lond., 225, p. 253 (1970a).
Allan, H.R., et al.: Nature Lond., 227, p. 1116 (1970b).
Allan, H.R.: Progress in Elementary Particle and Cosmic Ray Physics, North-Holland, Amsterdam, X, pp. 169–302 (1971a).
Allan, H.R.: PICRC, 3, p. 1108 (1971b).
Allan, H.R., et al.: PICRC, 3, p. 1097 (1971a).
Allan, H.R., et al.: PICRC, 3, p. 1102 (1971b).
Allan, H.R., et al.: PICRC, 8, p. 3077 (1975a).
Allan, H.R., et al.: PICRC, 8, p. 3082 (1975b).
Allen, C., et al.: PICRC, 7, p. 85 (1997).
Aloisio, R., and P. Blasi: Astropart. Phys., 18, p. 183 (2002).
Alvarez-Muñiz, J., et al.: PICRC, 3, p. 1305 (2001).
Artamonov, V.A., et al.: PICRC, 9, p. 210 (1990).
Artamonov, V.P., et al.: PICRC, 4, p. 375 (1991).
Askar'yan, G.A.: Sov. Phys. JETP, 14, p. 441 (1962a).
Askar'yan, G.A.: J. Phys. Soc. Jpn, 17, Suppl. A-III, p. 257 (1962b).
Askar'yan, G.A.: Sov. Phys. JETP, 48, p. 988 (1965a) (in Russian).
Askar'yan, G.A.: JETP, 21, p. 658 (1965b).
Atrashkevich, V.B., et al.: PICRC, 4, p. 2399 (1973).
Atrashkevich, V.B., et al.: PICRC, 8, p. 3086 (1975).
Atrashkevich, V.B., et al.: PICRC, 8, p. 142 (1977).
Badea, F., et al.: PICRC, 6, p. 273 (2005).
Baishya, R., et al.: ICRC, 4, p. 266 (1993).
Baishya, R., and P. Datta: PICRC, 9, p. 111 (2005).
Barker, P.R., et al.: Phys. Rev. Lett., 18, p. 51 (1967).
Barker, P.R., et al.: Can. J. Phys., 46, p. 243 (1968).
Bassi, P., et al.: Phys. Rev., 91, p. 432 (1953a). (Abstract A.P.S. Spring meeting.)
Bassi, P., et al.: Phys. Rev., 92, p. 441 (1953b).
Blackett, P.M.S., and A.C.B. Lovell: Proc. R. Soc. (Lond.), 177 A, p. 183 (1941).
Borione, A., et al.: Nucl. Instr. Meth., A 346, p. 329 (1994).
Borzhkovsky, I.A., et al.: Zh. E.T.F., Pis. Red., 3, p. 118 (1966) (in Russian), and JETP Lett., 3, p. 118 (1966).
Buitink, S., et al.: PICRC, 6, p. 333 (2005).
Castagnoli, C., et al.: Nuovo Cimento, 63 B, p. 373 (1969).
Castagnoli, C., et al.: PICRC, 4, p. 258 (1993).
Charman, W.N.: Nature, 215, p. 497 (1967).
Charman, W.N.: J. Atmos. Terr. Phys., 30, p. 195 (1968).
Charman, W.N., and J.V. Jelley: Can. J. Phys., 46, p. S216 (1968).
Clay, R.W., et al.: PICRC, 4, p. 2420 (1973).
Clay, R.W., et al.: PICRC, 8, p. 3093 (1975).
Colgate, S.A.: J. Geophys. Res., 72, p. 4869 (1967).
Du Vernois, M.A., et al.: PICRC, 5, p. 107 (2005a).
Du Vernois, M.A., et al.: PICRC, 8, p. 311 (2005b).
Engel, R., et al.: PICRC, 6, p. 9 (2005).
Falcke, H., and P. Gorham: Astropart. Phys., 19, p. 477 (2003).
Falcke, H., et al.: Nat. Lett., 435, p. 313 (2005).
Fegan, D.J., and P.J. Slevin: Nature Lond., 217, p. 440 (1968).
Fegan, D.J., et al.: Can. J. Phys., 46, p. S250 (1968).
Fegan, D.J., and D.M. Jennings: Nature Lond., 223, p. 722 (1969).
Frank, I.M., and I.G. Tamm: Dokl. Akad. Nauk SSSR, 14, p. 109 (1937).
Frank, I.M., and V.L. Ginzburg: J. Phys. Moscow, 9, p. 353 (1945).
Fujii, M., and J. Nishimura: Acta Phys. Acad. Sci. Hung., 29, S3, p. 709 (1970).

Fujii, M., and J. Nishimura: PICRC, 7, p. 2753 (1971)
Fujii, M., and J. Nishimura: PICRC, 5, p. 3196 (1973).
Galbraith, W., and J.V. Jelley: Nature Lond., 171, p. 349 (1953).
Galli, M., et al.: Acta Phys. Acad. Sci. Hung., 29, S3, p. 737 (1970).
Golubnichii, P.I., et al.: Izv. Akad. Nauk, 58, p. 45 (1994).
Gorham, P.W., et al.: Phys. Rev. E, 62, p. 8590 (2000).
Gousset, T., et al.: Astropart. Phys., 22, p. 103 (2004).
Green, K., et al.: Nucl. Instr. Meth. A, 498, pp. 256–288 (2003).
Guzhavin, V.V., et al.: Can. J. Phys., 46, p. S209 (1968).
Haungs, A., et al.: PICRC, 2, p. 985 (2003).
Hazen, W.E., et al.: Phys. Rev. Lett., 22, p. 35 (1969).
Hazen, W.E., et al.: Phys. Rev. Lett., 24, p. 476 (1970a).
Hazen, W.F., et al.: Acta Phys. Acad. Sci. Hung., 29, S3, p. 743 (1970b).
Horneffer, A., et al.: PICRC, 2, p. 969 (2003).
Horneffer, A., et al.: PICRC, 6, p. 285 (2005).
Hough, J.H., and J.R. Prescott: Proceedings of the VI. Interamerican Seminar on Cosmic Rays, 2, p. 527, (1970).
Hough, J.H.: J. Phys., A, 6, p. 892 (1973).
Huege, T., and H. Falcke: Astron. Astrophys., 412, p. 19 (2003).
Huege, T., and H. Falcke: Astron. Astrophys., 430, p. 779 (2005a).
Huege, T., and H. Falcke: Astropart. Phys., 24, p. 116 (2005b).
Huege, T., and H. Falcke: PICRC, 6, p. 289 (2005c).
Huege, T., et al.: PICRC, 7, p. 107 (2005).
Huege, T., et al.: Astropart. Phys., 30, p. 96 (2008).
Jackson, J.D.: Classical Electrodynamics, John Wiley and Sons, New York, 2nd ed. (1975).
Jelley, J.V., and W. Galbraith: Phil. Mag., 44, p. 619 (1953).
Jelley, J.V.: Nuovo Cimento, VIII, Suppl. 2, p. 578 (1958).
Jelley, J.V.: PICRC, 2, 698 (1965).
Jelley, J., et al.: Nature London, 205, p. 327 (1965).
Jelley, J.V., et al.: Nuovo Cimento, 46, p. 649 (1966).
Jelley, J.V.: Progress Elementary Particle and Cosmic Ray Phys. IX, p. 41 (1967a).
Jelley, J.V.: Phys. Lett., 25 A, p. 346 (1967b).
Kadota, K., et al.: PICRC, 4, p. 262 (1993).
Kahn, F.D., and I. Lerche: Proc. R. Soc. A, 289, p. 206 (1966).
Kalmykov, N.N., et al.: Nucl. Phys. B (Proc. Suppl.), 151, p. 347 (2006).
Kalpana, R.S., and D. Pranayee: PICRC, 3, p. 1309 (2001).
Kaneko, T., et al.: PICRC, 8, p. 118 (1983).
Khristiansen, G.B., et al.: PICRC, 6, p. 2181 (1971).
Lafebre, S., et al.: PICRC, 8, p. 245 (2005).
Lerche, I.: Nature London, 215, p. 268 (1967).
Linsley, J.: J. Phys. G, 12, p. 51 (1986).
Mandolesi, N., and G.G.C. Palumbo: Nuovo Cimento Lett., 3, p. 40 (1970).
Mandolesi, N., et al.: Nuovo Cimento, 67 B, p. 153 (1970).
Matano, T., et al.: Can. J. Phys., 46, p. S255 (1968).
Minnis, C.M., and F. Horner: Advances in Radio Research, J.A. Saxton, ed., Vol. 2, Academic Press, New York (1964).
Nehls, S., et al.: PICRC, 8, p. 45 (2005).
Nigl, A., et al.: PICRC, A-abs1-he13 (2005).
Nishimura, J.: PICRC, 7, p. 308 (1985).
Porter, N.A., et al.: PICRC, 2, p. 706 (1965a).
Porter, N.A., et al.: Phys. Lett., 19, p. 415 (1965b).
Prah, J.H.: Thesis University of London (1971).
Prescott, J.R., et al.: Can. J. Phys., 46, p. S246 (1968).

Prescott, J.R., et al.: Acta Phys. Acad. Sci. Hung., 29, S3, p. 717 (1970).
RADHEP-2000: Proceedings of the First International Workshop on Radio Detection of High Energy Particles (RADHEP) 2000; D. Saltzberg and P. Gorham, eds., A.I.P. Conference Proceedings, Vol. 579 (2001).
Ravel, O., et al.: Nucl. Instr. Meth. A, 518, p. 213 (2004).
Rozental, I.L., and M.L. Filchenkov: Izv. Akad. Nauk. Ser. Fiz., 30, p. 1703 (1966) (transl. Bull. Acad. Sci. USSR Phys. Ser., 30, p. 1773 (1966).
Saltzberg, D.P., et al.: Phys. Rev. Lett., 86, p. 2802 (2001).
Schonland, B.F.J.: Atmospheric Electricity, Methuen, London, 2nd ed. (1953).
Smith, F.G., et al.: PICRC, 2, p. 701 (1965).
Smith, F.G., et al.: Can. J. Phys., 46, p. S 230 (1968).
Spencer, R.E.: Nature London, 222, p. 460 (1969).
Suga, K.: 5th Inter-American Seminar on Cosmic Rays, Bolivia, 2, XLIX-1 (1962).
Suga, K., et al.: PICRC, 7, p. 268 (1985).
Suga, K., and K. Nishi: PICRC, 6, p. 125 (1987).
Sun, M.P.: Radio Emission from Extensive Air Showers, Ph.D. Thesis, University of London (1975).
Suprun, D.A., et al.: Astropart. Phys., 20, p. 157 (2003).
Vernov, S.N., et al.: JETP Lett., 5, p. 157 (1967).
Vernov, S.N., et al.: Can. J. Phys., 46, p. 241 (1968).
Vernov, S.N., et al.: Acta Phys. Acad. Sci. Hung., 29, S3, p. 731 (1970).
Weekes, T.C.: Proceedings of the First International Workshop on Radio Detection of High Energy Particles (RADHEP) 2000; D. Saltzberg and P. Gorham, eds., A.I.P. Conference Proceedings, Vol. 579, p. 3 (2001).
Wilson, R.R.: Phys. Rev., 108, p. 155 (1957).
Zas, E., et al.: Phys. Rev. D, 45, p. 362 (1992).

Chapter 19
Correlations and Miscellaneous Topics

Overview In this chapter we summarize the relevance of correlations among the different shower observables, interlinked with air shower simulations, to analyze and interpret experimental air shower data. Since we have discussed correlations in many places in this book, in particular in those chapters that are dedicated to specific observables, we present here only a very limited number of representative examples from all epochs of air shower studies, many of which are of early date but contain valuable data that have not been extracted from measurements in more recent times.

19.1 Introduction

In view of the enormous complexity of the air shower process and in view of the fact that the information that can be gathered with a ground based particle detector array represents only a very limited number of samples across the event at a particular time and stage of its development at a given location in the atmosphere, a unique description and interpretation of the event is not possible on the grounds of a single kind of observable, e.g., a number of charged particle density samples. A large number of shower simulation models and a wide selection of shower initiating primaries yield similar particle density distributions at a given total primary energy. This had been proven decades ago by the first and second generation of the more elaborate air shower simulations that were based on distinct hadronic interaction models (Grieder, 1970a, b). Obviously no observable in a shower is really independent, all particles and quanta that can be recorded are more or less interrelated. It is therefore absolutely essential to collect from each individual event as many separate, "quasi independent" observables as possible, and to correlate as many observables as possible to obtain unique answers (Grieder, 1977).

Correlations are of extreme importance to extract relevant information and dependencies of shower observables, cascade parameters, properties of the primary and the primary spectrum. It is particularly the primary mass composition but also the interaction properties at the highest energies that are extremely difficult to determine from measurements and observables acquired at ground level. The deeper the observation level is located in the atmosphere the more generations of interactions have occurred along the shower trajectory and the stronger first and second generation

P.K.F. Grieder, *Extensive Air Showers,* DOI 10.1007/978-3-540-76941-5_19,

interaction features are masked. Moreover, the bulk of the particles are secondaries of relatively low energy interactions.

In the preceding chapters where the properties of the different observables, particles and quanta as well as their detection are discussed, we have presented numerous important cross connections and correlations. In the following sections we want to illuminate once more the relevance of correlations and the importance of reliable simulations that are essential for a unique interpretation of experimental results. We show a limited selection of examples and results from various epochs to the present in the form of a summary.

Major advances will soon be made when the Large Hadron Collider (LHC) at CERN in Geneva (Switzerland) will produce its first data, since these will enable us to fix key parameters and distributions of ultrahigh energy (UHE) hadronic interactions in our models, that play such a decisive role for the interpretation of cosmic ray air shower data. With 14 TeV center of mass energy for proton-proton collisions an important step into the ultrahigh energy cosmic ray physics (astro-particle physics) domain is made that brings accelerator (collider) and air shower physics to overlap, that will help to supply unique answers to many of the burning questions. These answers are expected to yield valuable guidance to tackle the open questions concerning the origin of the cosmic radiation.

19.2 Electron-Muon Correlations

19.2.1 General Comments

Disregarding atmospheric Cherenkov and fluorescence detection methods and focusing our attention here strictly on particle detection, the electron-muon correlation is, apart from difficultly tangible particular features of the hadronic component, the most primary mass sensitive air shower observable. It is experimentally relatively easily accessible and had been studied by most air shower research groups that had muon detection facilities. However, it is only in conjunction with air shower simulations that the interpretation of the experimental data becomes possible. This statement is generally valid for all observables and correlations. Details of the analysis method are discussed in Chap. 10.

19.2.2 Experimental Data and Simulation Results

Figure 19.1 shows a set of event by event measured electron-truncated-muon number ratios, i.e., an N_e versus N_μ^{tr} plot, obtained with the KASCADE experiment. One observes that the spread is very large, particularly at low energies where the event rate is large and the fluctuations from shower to shower are enhanced. From such a plot one can determine the average N_μ^{tr}/N_e ratio as a function of N_e and draw the corresponding correlation curve. It is found that this curve is nearly a straight line

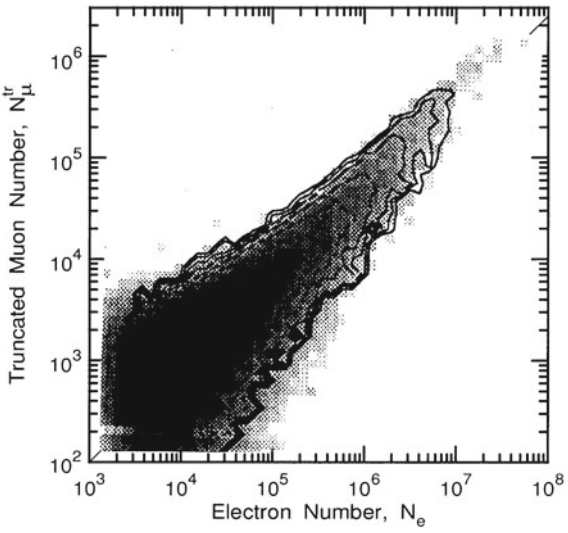

Fig. 19.1 Truncated muon number, N_μ^{tr}, as a function of electron number (shower size), measured with the KASCADE experiment (Haungs et al., 2003). The correlation between the two observables is well demonstrated, however, the wide spread at low shower size (low primary energy) where the event number is very large is a major problem for the data evaluation and interpretation

in a double logarithmic representation with a slope of about 0.8. Thus, we can write the relation,

$$N_\mu \propto N_e^\alpha \,, \tag{19.1}$$

with $\alpha \simeq 0.8$. Different experiments yield slightly different slope values that may depend on the muon threshold energy chosen.

The distribution shown in Fig. 19.1 is the result of a certain period of data acquisition by the KASCADE array. Included are all showers that fulfilled the trigger criteria, i.e., showers that had been initiated by any kind of primary, from protons to iron and possibly beyond, covering an energy range from a few times 10^{13} eV to a few times 10^{17} eV total energy. In order to extract information on the primary mass these data must now be compared with sets of like distributions of simulated showers of different primary mass or mass groups and for different primary energies. Such simulations are usually carried out for proton and iron primaries to enhance the differences. The result of such a set of simulations is shown in Fig. 19.2.

The average correlation between the muon and electron number as a function of electron shower size obtained from the KASCADE experiment (110 m a.s.l.) for the two different muon threshold energies of >400 MeV and >2 GeV is shown in Fig. 19.3. The displacement of the two data sets is as expected, since there are fewer muons having energies >2 GeV in a shower than muons having energies >400 MeV. Also shown in the same plot are the data for >1 GeV muons recorded with the Akeno array (920 m a.s.l.). As can be seen from this figure the >2 GeV KASCADE and the >1 GeV Akeno data lay almost exactly on the same straight line in this correlation plot that can be described by the following empirical equation,

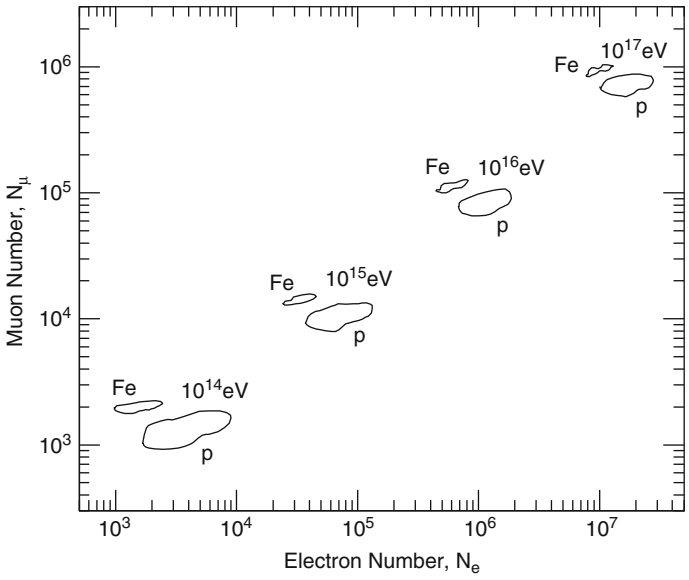

Fig. 19.2 Example of $N_\mu - N_e$-correlation obtained from a simulation of proton and iron nuclei initiated showers of fixed primary energies, as indicated in the figure. The plot shows beautifully the power of correlation analyses to extract relevant information. The contours represent half-width maxima of the distributions (Haungs et al., 2003, after Heck, KASCADE Collaboration)

$$N_\mu = (2.94 \pm 0.14) \cdot 10^5 \left(\frac{N_e}{10^7} \right)^{(0.76 \pm 0.02)} \quad . \tag{19.2}$$

Average muon-electron correlation lines of simulated proton and iron nuclei initiated showers covering a shower size range from 10^4 to 10^8 are presented in Fig. 19.4. The primary energy for each event was selected from a spectrum. Shown in the plot are the results for two altitudes, 3,000 and 1,000 m a.s.l. and muon threshold energies $\geq$5 GeV and $\geq$220 GeV, respectively. These levels correspond approximately to the altitudes of the Tien Shan and KGF experimental sites, and likewise to the respective detector thresholds. Data from these two experiments are also included in the plot. Muon-electron data from measurements carried out at the same two sites during the similar epoch but made by other work groups are displayed in Fig. 19.5.

The data presented in Fig. 19.6 are of older data but quite instructive. Figure 19.6a shows the muon-electron size correlation for muons of energy $>$10 GeV recorded with the installations of the Moscow State University (MSU) located near sea level (192 m a.s.l.). Data from two measurements are displayed that were taken at different epochs (Khristiansen et al., 1971, 1977; Vernov et al., 1977). The results are very consistent. Also indicated for comparison is the spread of the N_μ/N_e distribution at three shower sizes of muons having an energy $>$1 GeV, and a prediction for $>$10 GeV muons from a simulation using a naive Feynman scaling model, showing the well known muon deficit.

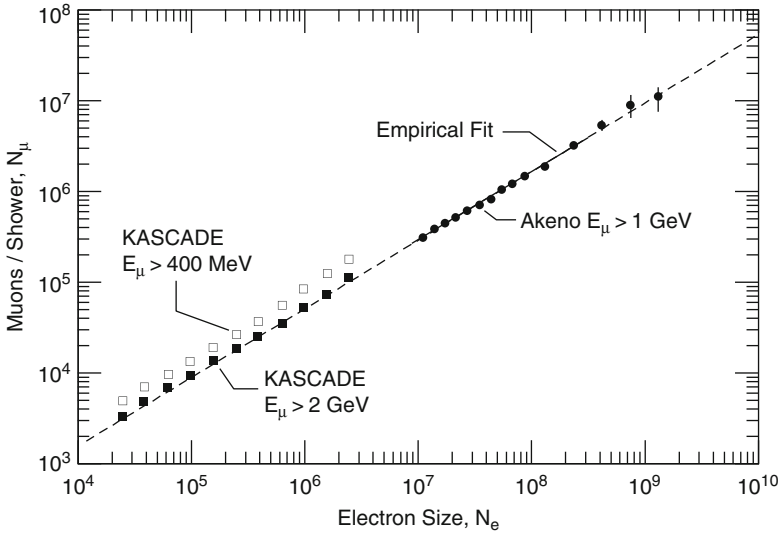

Fig. 19.3 Correlation between the muon and electron number (muon size versus electron size) of showers over a very large size range. Shown are data obtained from the KASCADE experiment (110 m a.s.l.; 1,020 g cm^{-2}) for muons of energy $\geq$400 MeV (□) and $\geq$2 GeV ■, and the Akeno experiment (900 m a.s.l.; 920 g cm^{-2}) for muons of energy $\geq$1 GeV (•). The solid line is a fit with the empirical formula, Eq. (19.2), given in the text (after Nagano et al., 2000)

In Fig. 19.6b the correlation between the relative standard deviation of the number of muons of energy >10 GeV is plotted as a function of shower size. Note that the abscissa of the two figures refers in fact to the charged particle and not the electron shower size. Shown, too, is the theoretically expected spread for low energy muons according to a simulation of Elbert et al. (1976b).

The relative width of the fluctuations of the muon to electron ratio in showers as a function of shower size is given in Fig. 19.7. The plot includes data from measurements carried out with the large underground muon detector at Lodz (Poland) (Dzikowski et al., 1977) and the installations at Moscow (Vernov et al., 1965a, b, 1970).

The zenith angle dependence of the muon to electron ratio had been investigated by the group at Verrières (France, 50 m a.s.l.) where an identical underground muon detector had been operated as in Lodz (Hochart et al., 1975). The results are plotted in Fig. 19.8. To account for the zenith angle dependence of the muon absorption, the authors have used a muon absorption length of 690 g cm^{-2} (Firkowski et al., 1967).

The shower size dependence of the muon *density at fixed core distance* had been investigated by the Tokyo group at Tokyo (I.N.S., sea level) and Akeno (900 m a.s.l.), and at Mt. Chacaltaya (5,230 m a.s.l.) (Matano et al., 1962; Hara et al., 1970, 1981). The results are plotted in Fig. 19.9. At Akeno the core distance where the measurements were made was 70 m and the muon threshold energy $E_\mu \geq 1$ GeV; at Tokyo the corresponding figures were 200 m and $E_\mu \geq 5$ GeV, and

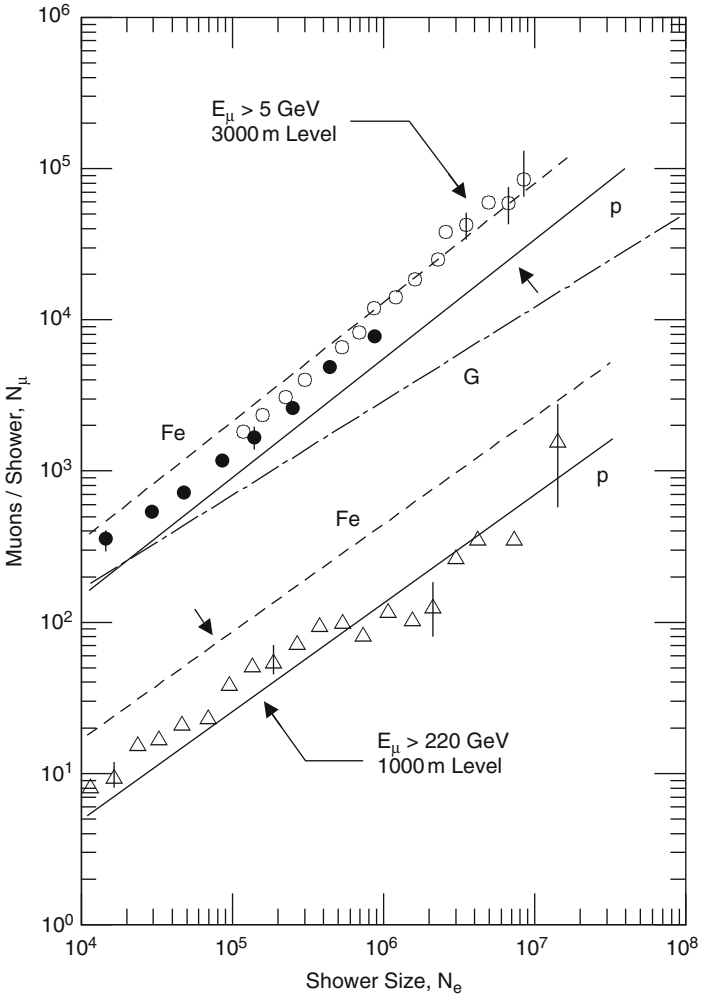

Fig. 19.4 Muon-electron correlations in proton and iron nuclei initiated showers at two altitudes, 1,000 and 3,000 m a.s.l. The *dashed* and *solid lines* are from a simulation of Grieder (1980), using ASICO. The experimental data for $E_\mu \geq 5$ GeV (• and ○) are from the Tien Shan experiment, altitude 3,340 m a.s.l. (Kabanova et al., 1973; Machavariani et al., 1979), those for $E_\mu \geq 220$ GeV (△) from the KGF experiment in India, altitude 1,000 m a.s.l. (Acharya et al., 1983). The *dot-dash line* labeled *G* is from the work of Gaisser et al. (1978) and applies to muons of energy $E_\mu \geq 10$ GeV at sea level, for proton showers using the scaling model (after Grieder, 1984)

at Mt. Chacaltaya 200 m and $E_\mu \geq 400$ MeV. These data reveal that the densities of the different muon groups recorded at sea level, at 900 m and at 5,230 m lie over the wide range of shower sizes, from about 10^6 to 10^9, on straight lines, i.e., no change of slope occurs. This suggests that no change of composition takes place over this range of shower sizes, which is in contradiction with more recent measurements (see Chap. 11).

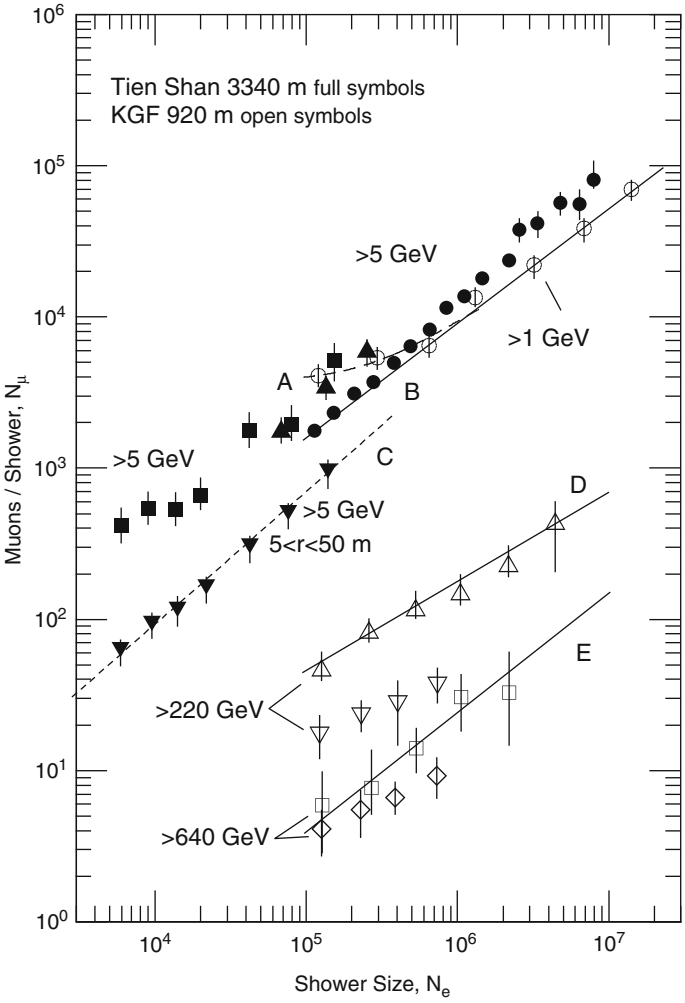

Fig. 19.5 Correlation between muon number and shower size for muons of different energy groups recorded at different locations. The full symbols are for muons of energy $\geq$5 GeV, recorded at Tien Shan (3,340 m a.s.l.). Data points ●, ▲ and ■ are from the work of Kabanova et al. (1973), Kalmykov et al. (1971) and Aseikin et al. (1973), respectively; ▼ includes only muons in the annular ring $5 < r < 50$ m (Aseikin et al., 1973). The open symbols are from measurements made at the Kolar Gold Fields (920 m a.s.l.). Data points ○, △ and □ are from the work of Chatterjee et al. (1968a), points ▽ and ◇ from Vatcha and Sreekantan (1973b). Points ○ apply to muons of energy $\geq$1 GeV, △ and ▽ to muons of energy $\geq$220 GeV, □ and ◇ to $\geq$640 GeV. (See also Cowsik, 1968). *Lines A* to *E* are approximate fits to the data

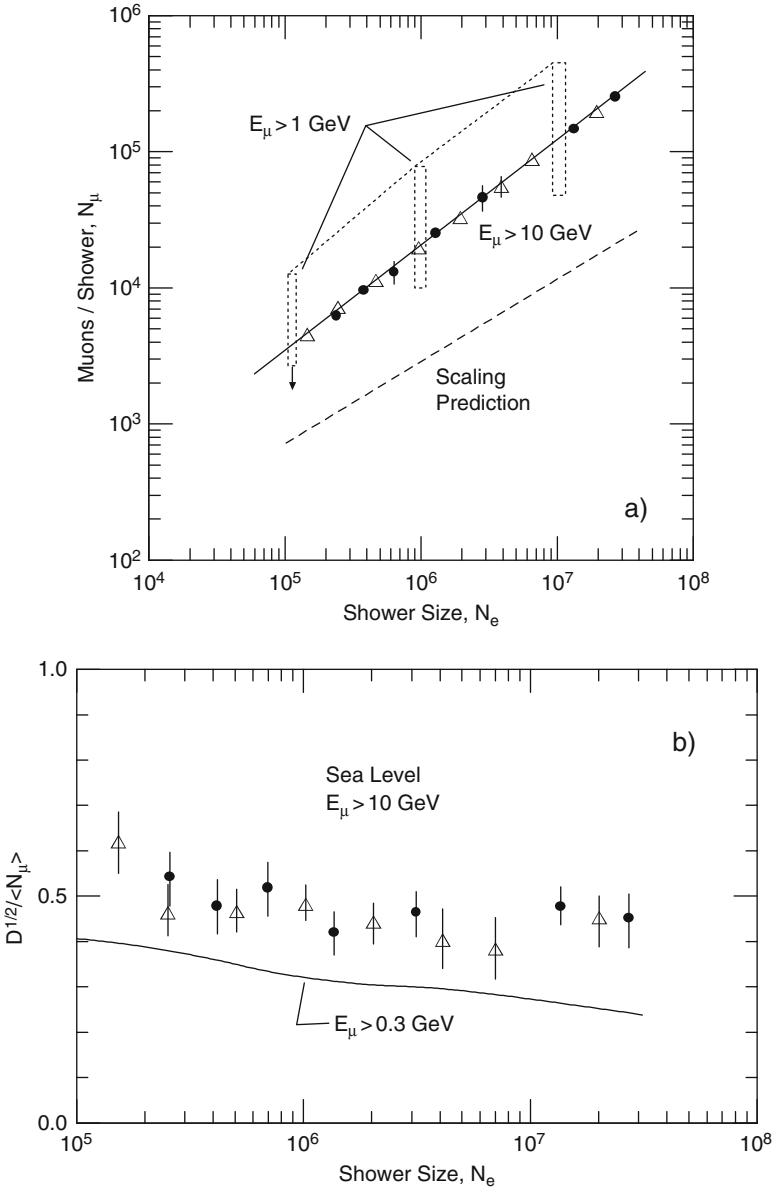

Fig. 19.6 (**a**) Correlation between muon number and shower size at sea level. Points • and △ are for muons of energy >10 GeV recorded at Moscow (Khristiansen et al., 1971, 1977; Vernov et al., 1977). The *solid line* is a fit to the data. The *dashed boxes* show the approximate spread in the number of muons of energy ≥1 GeV for a fixed shower size, as observed by the Tokyo group (Hara et al., 1979). The *dashed line* indicates the average correlation according to a simulation using a scaling model. (**b**) Correlation between the relative standard deviation, $D^{1/2}$, of the muon number for $E_\mu \geq 10$ GeV and the shower size for the data of Khristiansen et al. (1977), •, and Vernov et al. (1970), △, plotted in Fig. 19.6a. The *curve* shows the theoretically expected dependence for muons of energy ≥0.3 GeV, according to a calculation of Elbert et al. (1976a) for proton primaries; the disagreement is even worse for muons ≥10 GeV

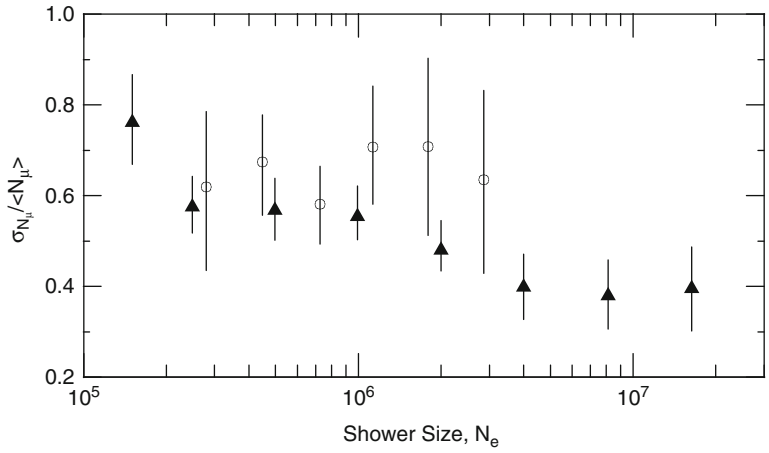

Fig. 19.7 Relative width of the fluctuations of the ratio of the muon to electron number, $\sigma_{N,\mu}$ as a function of shower size. Data points ▲ are from the work of Dzikowski et al. (1977) obtained with the installation at Lodz ($E_\mu \geq 5.6\,\text{GeV}$). The data points ○ are from Vernov et al. (1965a, b, 1970) at Moscow

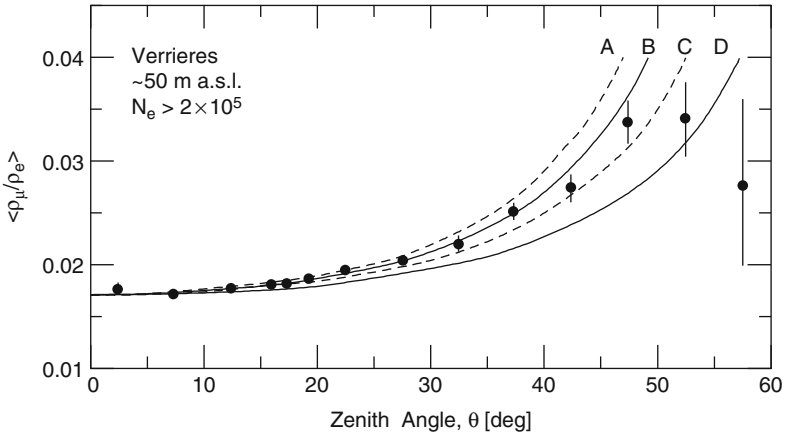

Fig. 19.8 Dependence of the muon to electron density ratio on the shower zenith angle for showers of size $N_e \simeq 5\cdot10^5$ measured with the installation at Verrières, France. The muon absorption length used is $\lambda_\mu = 690\,\text{g cm}^{-2}$ and was taken from the work of Firkowski et al. (1967) (after Hochart et al., 1975)

19.3 Electron-Hadron and Muon-Hadron Correlations

Since there had been only very few hadron calorimeters incorporated in the numerous air shower experiments, correspondingly few hadron data and correlation studies had been carried out and are available today. The majority of hadron related correlation studies concern the hadron number-shower size relationship and had been acquired at altitudes ranging from sea level to Mt. Chacaltaya (5,230 m). We

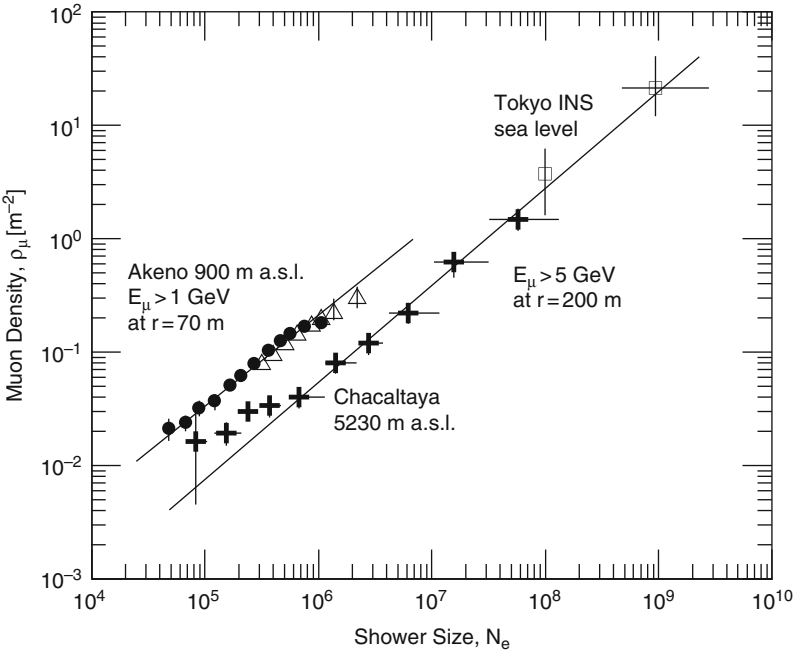

Fig. 19.9 Compilation of data on the size dependence of the muon density at different core distances and altitudes. Points • and △ are from Akeno (900 m a.s.l.) for muons of energy >1 GeV and zenith angles $1.0 \leq \sec(\theta) \leq 1.1$ recorded at a core distance of 70 m (Hara et al., 1981); △ are older data. Points + are data from measurements at Chacaltaya (5,230 m a.s.l.) (Matano, 1962), and □ are from Tokyo, I.N.S. (s.l.), both sets are for muons of energy ≥5 GeV at a core distance of 200 m (Hara et al., 1970). The *lines* are fits to the data

disregard here the results of isolated Emulsion chamber experiments since these do not have the relevant information of the showers associated with the events that would allow proper interpretation of the data. Note that many details concerning the data that are presented here can be found in Chap. 13.

In Figs. 19.10, 19.11, 19.12, 19.13, 19.14, 19.15 and 19.16 we present a collection of hadron-charged particle number (shower size) correlations from the early days of hadron studies to the present that give a representative overview of the available results, and in Fig. 19.17 an analogous set of data relating the truncated muon number with the hadron number.

Turning to older data, we present a compilation of sea level and near sea level hadron numbers per shower as a function of shower size from measurements carried out at Kiel (Böhm et al., 1970), Yakutsk (Kozlov et al., 1979, 1981), Tokyo (Fukui et al., 1960; Kameda et al., 1965) and Durham (Ashton et al., 1977) for hadron threshold energies of 1, 100 and 200 Gev in Fig. 19.10. The three sets of low energy (1 GeV) data were obtained from neutron monitor measurements and follow very well a single straight line of slope slightly less than one.

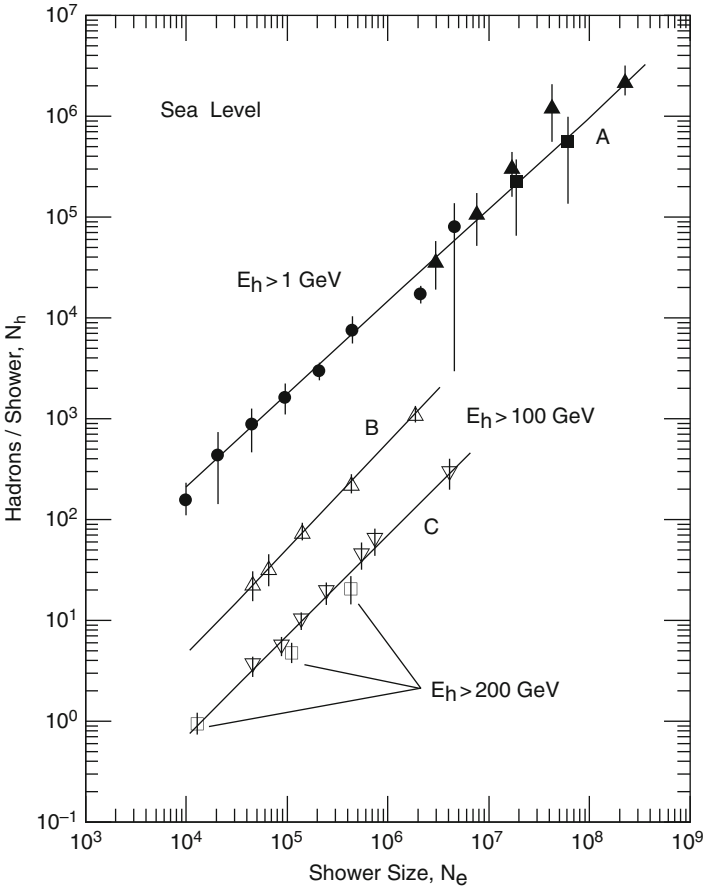

Fig. 19.10 Correlation between hadron number and shower size for hadrons of different energy groups. The low energy data points ($E_h > 1$ GeV) • are from the experiment at Kiel (Böhm et al., 1970) using neutron monitor bursts, ▲ and ■ are from Yakutsk (Kozlov et al., 1979, 1981). Points △ (Fukui et al., 1960) and ▽ (Kameda et al., 1965) represent hadrons of energy $E_h >$ 100 GeV recorded at Tokyo. The Kameda measurements were made with a cloud chamber. The disagreement between the Fukui and Kameda data is evident and could be due to misses in the cloud chamber. The results from the work of Ashton et al. (1977) at Durham (GB), □, are for $E_h > 200$ GeV. All installations are located essentially at sea level. *Lines A, B* and *C* are fits to the data

The situation is different for the 100 GeV data. The two measurements show the same slope for the line of correlation but the cloud chamber measurements of Kameda et al. (1965) yield almost a factor of ten less hadrons per shower of the given size than those of Fukui et al. (1960). We assume that the difference is probably due to misses of the cloud chamber. The higher energy data of Ashton et al. (1977) are as expected.

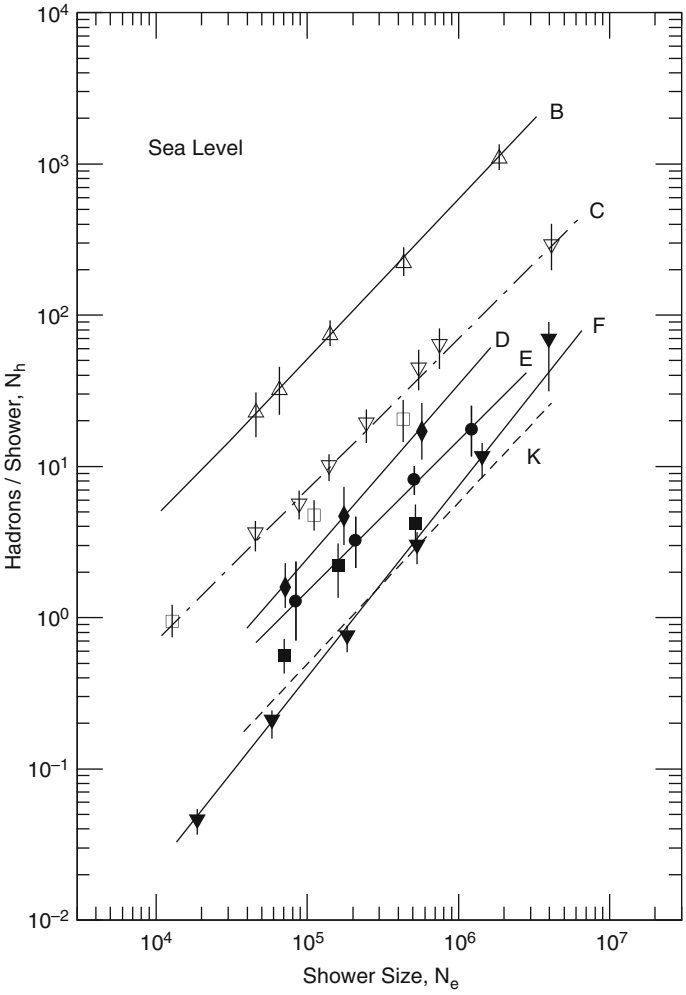

Fig. 19.11 Hadron number versus shower size for high energy hadrons at sea level. The compilation includes the following data: ♦ $E_h > 500$ GeV (Baruch et al., 1977), • $E_h > 800$ GeV (Fritze et al., 1970), ■ $E_h > 1$ TeV (Baruch et al., 1977), and ▼ $E_h > 1.7$ TeV (Matano et al., 1970). In addition we have added the 100 and 200 GeV data from the previous figure (same symbols, too) for comparison, i.e., △ (Fukui et al., 1960), ▽ Kameda et al. (1965) and □ (Ashton et al., 1977). The *lines* are fits to the data. The *thin dashed line K* indicates an estimate for 1.7 TeV hadrons based on energy spectra measurements with the cloud chamber of Kameda et al. (1965) at 60 GeV

Another compilation of high energy hadron-electron correlation data recorded at sea level is shown in Fig. 19.11. The data comprise the results from the work of Baruch et al. (1977) for hadrons of energy $E_h \geq 500$ GeV and $E_h \geq 1{,}000$ GeV recorded at Haverah Park, Fritze et al. (1970) for $E_h \geq 800$ GeV recorded at Kiel, and Matano et al. (1970) for $E_h \geq 1{,}700$ GeV recorded at Tokyo. The lines are

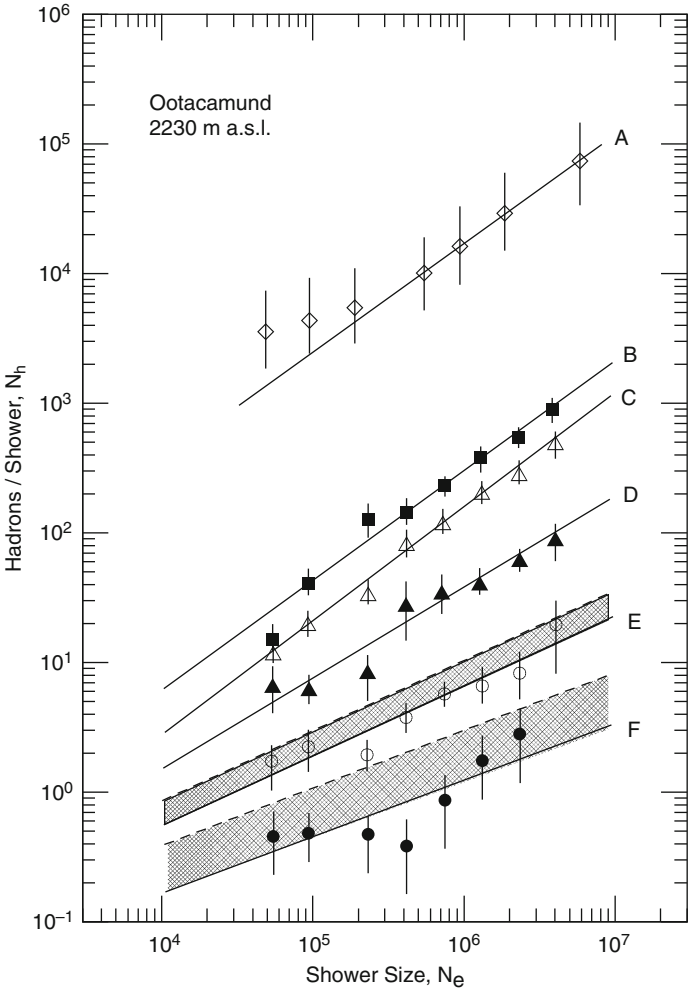

Fig. 19.12 Hadron number versus shower size measured at Ootacamund, altitude 2,200 m. The compilation includes particles of the following energy groups: ◇ low energy hadrons ($E_h \simeq 1$ GeV) (Sreekantan, 1971), ■ $E_h > 25$ GeV, △ $E_h > 50$ GeV, ▲ $E_h > 100$ GeV, ○ $E_h > 200$ GeV, and • $E_h > 400$ GeV (Sreekantan, 1971; Vatcha and Sreekantan, 1973a). The *lines* labeled A–F are least square fits to the data. The hatched regions pertaining to hadrons of energy >200 GeV (*line E*) and >400 GeV (*line F*) indicate the effects of a maximum probable underestimation of the energy of such hadrons

hand-drawn fits to the data to guide the eye. Also included for comparison are the >100 GeV data from the work of Fukui et al. (1960), Kameda et al. (1965), and the >200 GeV data of Ashton et al. (1977) of the previous figure.

A series of results from measurements carried out at higher altitude which is more favorable for hadron studies are displayed in Fig. 19.12. Shown are the data

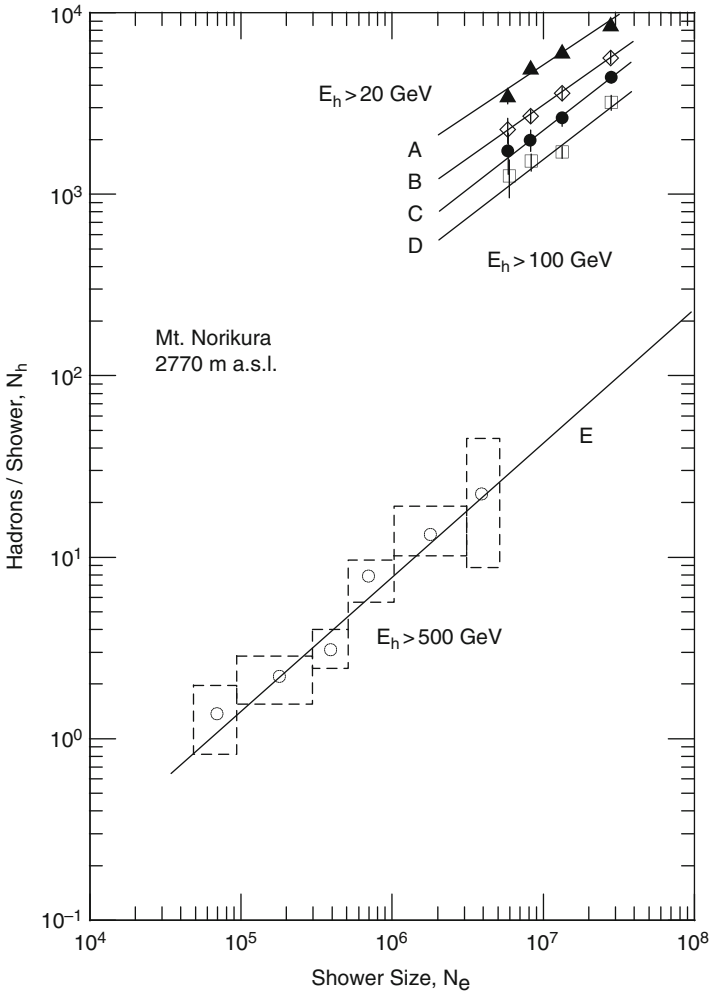

Fig. 19.13 Correlation between hadron number and shower size at Mt. Norikura, altitude 2,770 m. The data points connected by the *lines* marked 1, 2, 3, and 4 with symbols +, ◇, • and △ are for hadrons of energy >20 GeV, >40 GeV, >60 GeV, and >100 GeV, respectively (Miyake et al., 1979). The 500 GeV data (○) connected by *line E* are earlier data (Miyake et al., 1970). The *dashed boxes* surrounding the *open circles* represent the errors

obtained with the total absorption scintillation spectrometer (TASS) that was part of the air shower array located at Ootacamund (2,200 m a.s.l.) in southern India (Sreekantan, 1971; Vatcha and Sreekantan, 1973a). The results from this experiment are presented in different energy groups having hadron thresholds of $E_h \geq 25$ GeV, $E_h \geq 50$ GeV, $E_h \geq 100$ GeV, $E_h \geq 200$ GeV, and $E_h \geq 400$ GeV. Since the TASS was a relatively small detector, having an effective area of only 1.4 m^2 it suffered

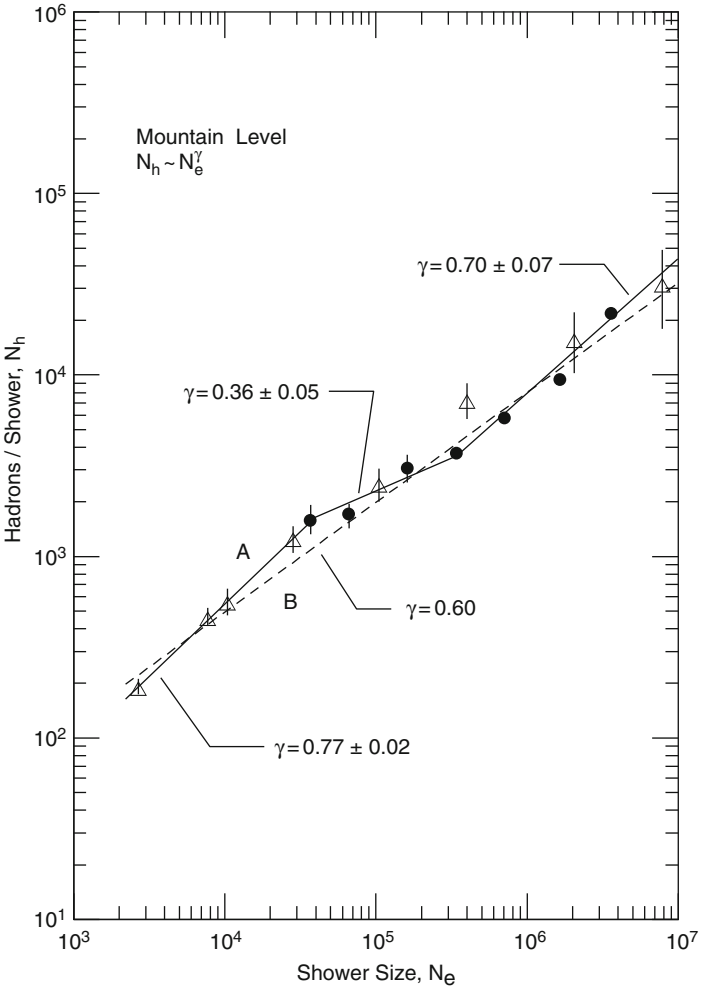

Fig. 19.14 Correlation between hadron number and shower size for low energy hadrons (E_h >1 GeV) at mountain level. Data set △ is from the work at Tien Shan, 3,340 m (Danilova and Nikolsky, 1963; Danilova, 1965; Erlykin et al., 1965). For comparison we have added the low energy data ($E_h \geq 1$ GeV) from the Ootacamund experiment at 2,230 m, •, (Sreekantan, 1971), shown previously in Fig. 19.12. The slopes, γ, of the three *solid line* sections that connect the data points are also indicated. The *dashed line* is a hand-drawn average through all the points

of particle leakage in both directions, into and out of the instrument, thus causing errors in the energy determination.

Analogous data, with hadron thresholds between 20 and 60 GeV mainly in rather large showers and one data set spanning over a very large shower size range with hadron threshold of 500 GeV, acquired with different instrumentation at

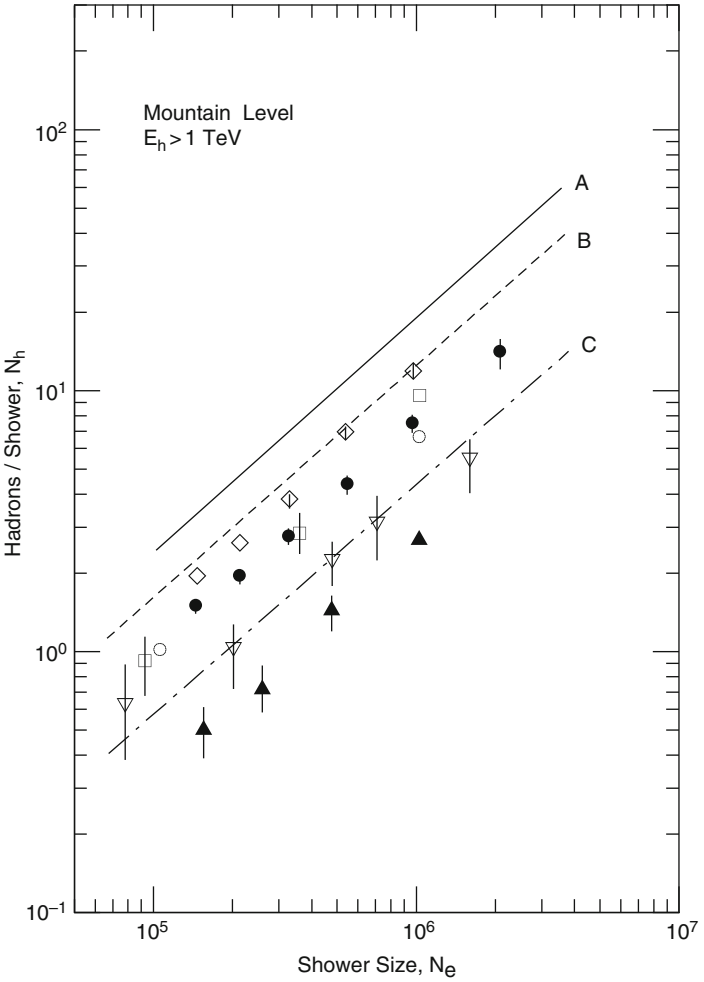

Fig. 19.15 Correlation between hadron number and shower size at various mountain levels. The data labeled >1 TeV are from the following measurements: ◇ and ● Tien Shan, altitude 3,340 m, for zenith angles corresponding to atmospheric depths of 715 and 840 g cm^{-2}, respectively (Nesterova and Dubovy, 1979); □ is from Aragatz, 3,250 m (Nymmik, 1970); ○ Pamir, 3,860 m (Vavilov et al., 1964); ▽ are estimates derived by Nesterova and Dubovy (1979) from early Mt. Norikura data, 2,770 m, obtained by Miyake et al. (1970) and ▲ is from Pic du Midi, 2,862 m (Van Staa et al., 1974; Böhm, 1977). *Lines A, B* and *C* are predictions from calculations of Vernov et al. (1978)

Mt. Norikura (2,770 m a.s.l.), Japan, are displayed in Fig. 19.13 (Miyake et al., 1970, 1979). An additional $N_h - N_e$ correlation plot based on measurements carried out with the well equipped experiment at Tien Shan (3,340 m a.s.l.) for low energy hadrons ($E_h \geq 1$ GeV) is illustrated in Fig. 19.14. The low energy data from the Ooty site are also plotted for comparison. It is seen that the data match quite well.

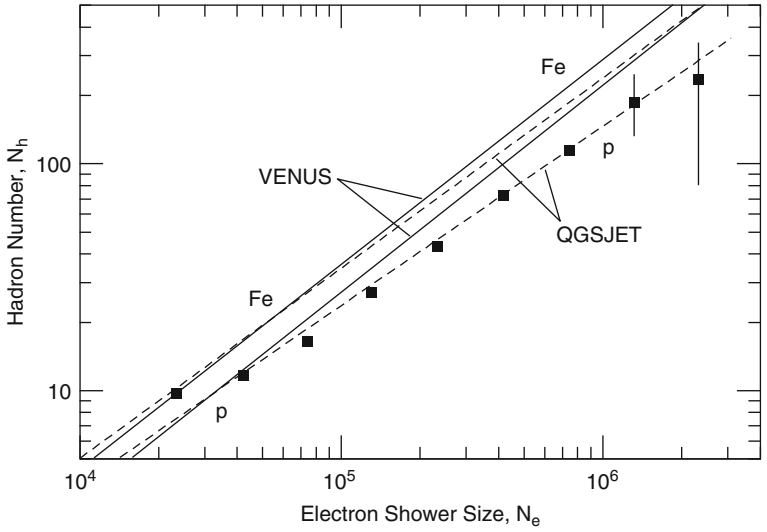

Fig. 19.16 Hadron number per shower, N_h, as a function of electron shower size, N_e, for hadrons of energy $\geq$50 GeV. The data points ■ are from the KASCADE experiment that can determine the electron size. The *curves* are from simulations with the CORSIKA program using the VENUS and QGSJET event generators for primary protons and iron nuclei (after Antoni et al., 1999)

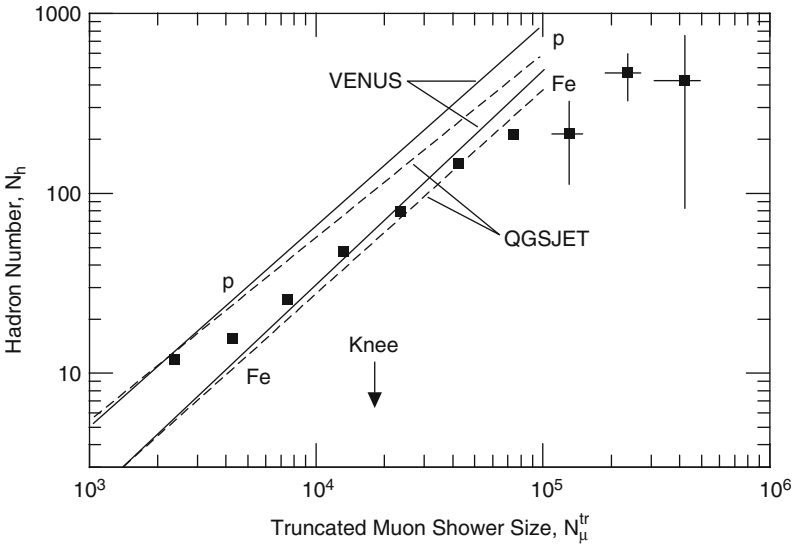

Fig. 19.17 Hadron number per shower, N_h, as a function of the truncated muon shower size, N_μ^{tr}, for hadrons of energy $\geq$50 GeV. The data points are from the KASCADE experiment. The *lines* are from simulations with the CORSIKA program using the VENUS and QGSJET event generators, as indicated, for primary protons and iron nuclei (after Antoni et al., 1999)

Figure 19.15 shows a compilation of hadron-shower-size correlations of very high energy hadrons (>1 TeV) from different high altitude experiments, ranging from 2,770 to 3,860 m a.s.l. The highest location is the old Pamir site that had an air shower array operating for some time. Included are three theoretical correlation lines from a prediction of Vernov et al. (1978). The slopes of all data points are very similar and the $N_h - N_e$ ratios reflect the expected differences due to the different altitudes.

In Figs. 19.16 and 19.17 we display some of the most recent data from the large KASCADE hadron calorimeter, showing the electron shower size-hadron number, and the truncated muon shower size-hadron number correlations, respectively. The threshold energy of the recorded hadrons is 50 GeV in either case (Antoni et al., 1999). The experimental data are compared with the predictions from simulations carried out with the CORSIKA program for proton and iron primaries, using the QGSJET and VENUS event generators. Note that the predicted correlation curves for iron primaries lie above the proton curves for both event generators in the N_h/N_e plot (Fig. 19.16), whereas for the N_h/N_μ^{tr} plot (Fig. 19.17) the situation is reversed.

These properties are intimately linked with kinematic and interaction details that are primary particle specific. They are typical for showers initiated by protons and heavy primaries of the same total energy and have their roots in the energy per nucleon and the different spectra of the secondaries in the two hadron cascades. These problems are discussed in more detail in Chaps. 10 and 13.

Referring to Fig. 19.16, comparison of the predictions with the experimental data reveals that if we exclude showers of very small size the experimental data are in good agreement with the QGSJET prediction for proton primaries. For the highest shower size bin, however, the measured hadron number seems to be slightly low but still well within the error limits. Figure 19.17 suggests a change in composition from a light to a heavy with increasing energy, however, for very large showers the experimental data deviate significantly from predictions.

19.4 Miscellaneous Correlations

In this section we present a summary of a variety of less common correlation data. Nevertheless, they offer useful additional details of shower properties.

19.4.1 Hadron Related Correlations

The dependence of the mean energy of hadrons as a function of core distance in small size showers recorded with the installation at Kiel (Germany) is plotted in Fig. 19.18 (Böhm et al., 1970). This work illustrates very well how compact the hadron component is concentrated even at great atmospheric depth near the shower

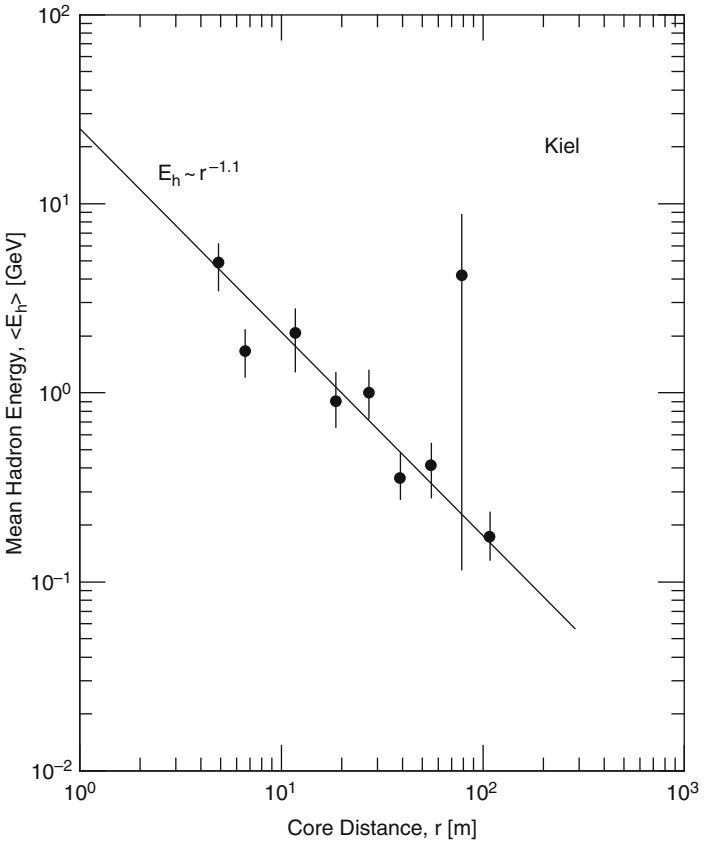

Fig. 19.18 Dependence of the mean hadron energy on core distance in normalized showers of size 10^5 measured at Kiel (s. l.) (Böhm et al., 1970)

axis, which makes a detailed analysis of the very high energy component extremely difficult. Hadron calorimeters require in fact a large size to avoid energy leakage into and out of the calorimeter, high spatial as well as good energy resolution, and above all a large dynamic range with an adequate depth in terms of interaction mean free paths.

The lateral distribution of the hadronic component had been studied by several groups. Similar to the lateral distribution function of the electromagnetic component one can obtain a characteristic radius, a sort of Molière radius, for hadrons, r_h. In Fig. 19.19 we show a compilation of results of analyses of data from four different experiments, located at altitudes ranging from sea level to 3,340 m. Included are results from measurements at Tokyo (I.N.S.), Ootacamund, Mt. Norikura and Tien Shan. A similar study was made much more recently by Antoni et al. (1999) (see Chap. 13).

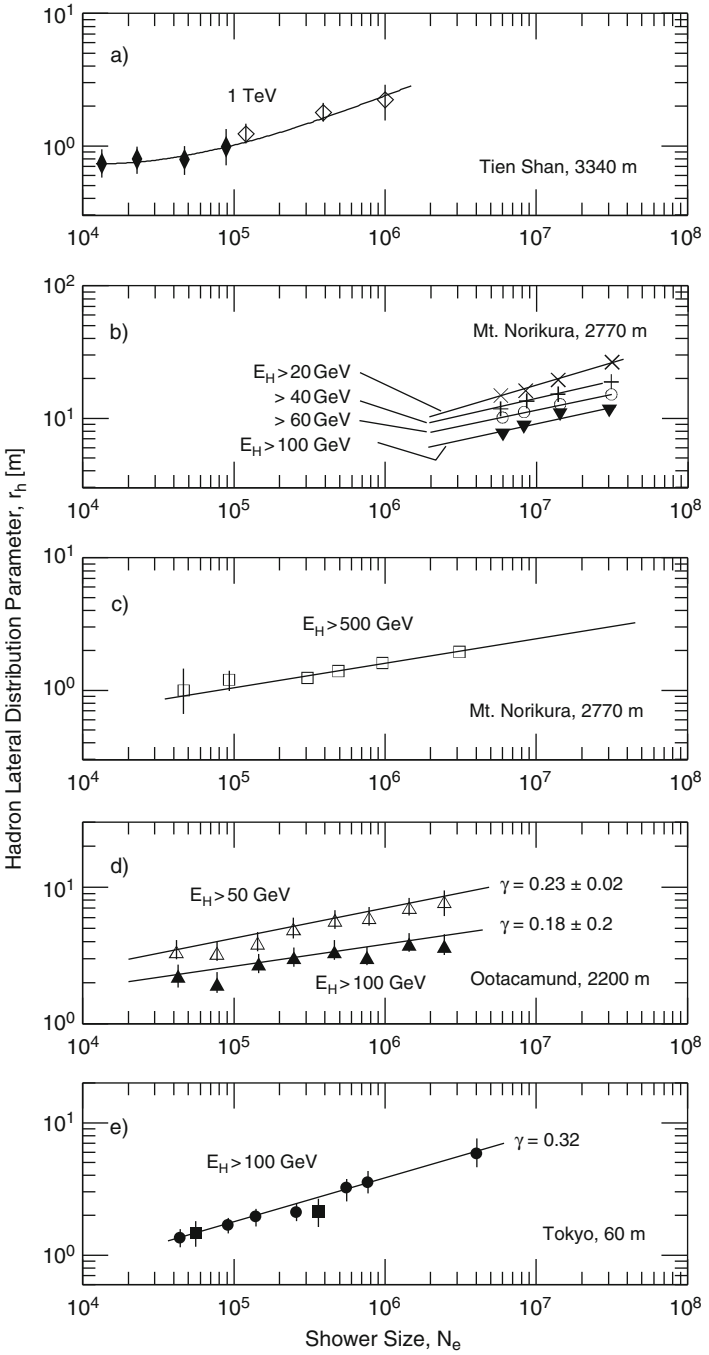
a)
1 TeV
Tien Shan, 3340 m
b)
Mt. Norikura, 2770 m
E_H > 20 GeV
> 40 GeV
> 60 GeV
E_H > 100 GeV
c)
E_H > 500 GeV
Mt. Norikura, 2770 m
d)
E_H > 50 GeV
γ = 0.23 ± 0.02
γ = 0.18 ± 0.2
E_H > 100 GeV
Ootacamund, 2200 m
e)
E_H > 100 GeV
γ = 0.32
Tokyo, 60 m
Hadron Lateral Distribution Parameter, r_h [m]
Shower Size, N_e

19.4.2 Muon Energy – Core Distance Correlations

A similar correlation plot as shown in Fig. 19.18 for hadrons is illustrated in Fig. 19.20 for the dependence of the mean momentum of muons on core distance. The data were collected at Haverah Park and apply to large showers of size $\sim 2 \cdot 10^7$ (Earnshaw et al., 1967). A magnetic spectrograph had been used for the measurements.

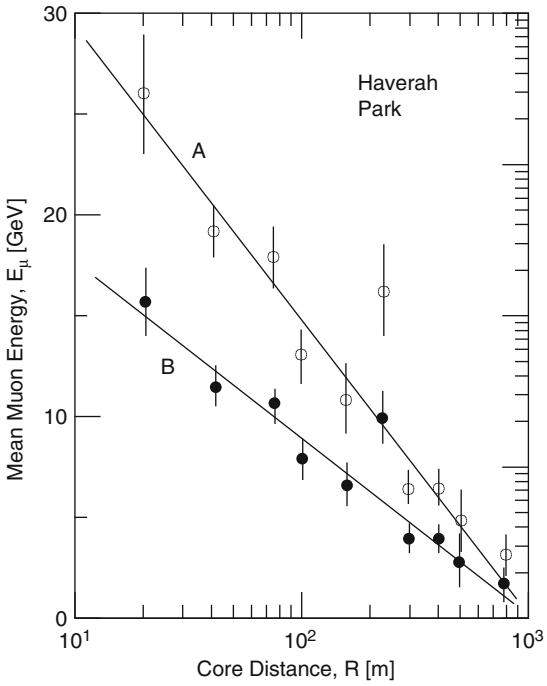

Fig. 19.20 Mean momenta carried by muons at various distances from the core of a shower of size $2 \cdot 10^7$ recorded at Haverah Park (212 m a.s.l.) (Earnshaw et al., 1967). The symbols ○ apply to muons with momenta $p_\mu \geq 1$ GeV/c, • includes all muons, assuming that 40% have $E_\mu < 1$ GeV/c

19.4.3 Muon/Electron – Core Distance Correlations

As we have shown mainly in Chap. 8, the lateral density distribution of the different shower constituents are different, yet they can be described by similar functions,

Fig. 19.19 Correlation between the characteristic lateral distribution parameter, r_h, of hadrons for different energy groups and shower size, N_e, obtained from different experiments. (**a**), ♦ and ◇, are from the Tien Shan experiment (Machavariani et al., 1981; Romakhin et al., 1977, 1979), (**b**) and (**c**) are from Mt. Norikura (Miyake et al., 1979), (**d**) is from Ootacamund (Chatterjee et al., 1968b), and (**e**) from Tokyo (Kameda et al., 1965). The symbols ■ in (**e**) represent data derived from high energy electron measurements

however, with different characteristic radii. Consequently, the ratio of the different particle types is a function of distance from the shower axis. This characteristic property of air showers is relevant for their detection and interpretation. At distances larger than about a few 10 m from the showers axis one can essentially disregard the hadronic component and needs to consider only the electron–photon and muon components. Nevertheless, the type of detector and the ratio of the electromagnetic to the muonic components are of great significance for the correct interpretation of the recorded events.

The following figures show some examples of the dependence of the muon to charged particle ratio, and vice versa, of the charged particle to muon ratio as a function of core distance, determined in rather large showers.

The results from an analysis of measurements made by Blake et al. (1970) and Armitage et al. (1973) at Haverah Park for the ratio ρ_{ch}/ρ_{μ} of low energy muons ($\geq$300 MeV) are plotted in Fig. 19.21a. They show the expected trend but deviate somewhat from the very early results of Greisen (1960). On the other hand, analogous data showing the opposite ratio (ρ_{μ}/ρ_{ch}) taken at Tokyo for muons of energy >5 GeV and at Mt. Chacaltaya for less energetic muons (>400 MeV) give a rather chaotic picture as is evident from Fig. 19.21b.

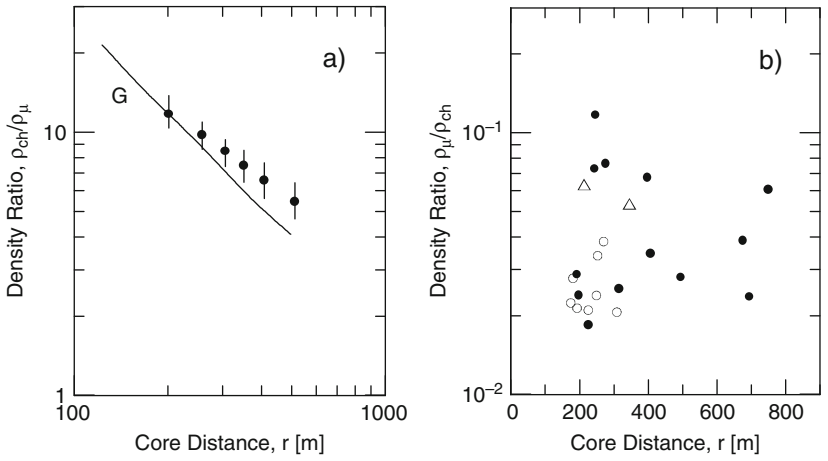

Fig. 19.21 (**a**) Ratio of charged particle density to muon density measured at Haverah Park as a function of core distance in showers having a primary energy $>10^{18}$ eV. The threshold energy for the muons is 300 MeV (Armitage et al., 1973; Blake et al., 1970). The corresponding density distributions for the charged particles and the muons from which the above ratios had been derived are shown in Fig. 15.8, and Fig. 14.10, respectively. *Curve G* is the Greisen distribution (Greisen, 1960). (**b**) Muon to charged particle density ratio versus core distance obtained by two different experiments. ○ and △ are from Chacaltaya for muons of energy ≥400 MeV in showers of size $\geq 5 \cdot 10^8$, recorded at zenith angle inclinations corresponding to an atmospheric slant depth of 820 and 1,060 g cm^{-2}, respectively (Matano, 1962). The symbols • represent sea level data from Tokyo (I.N.S.) for muons of energy >5 GeV in showers of the same size group, recorded at zenith angles corresponding to an atmospheric depth between 1,030 and 1,460 g cm^{-2} (Hara et al., 1970)

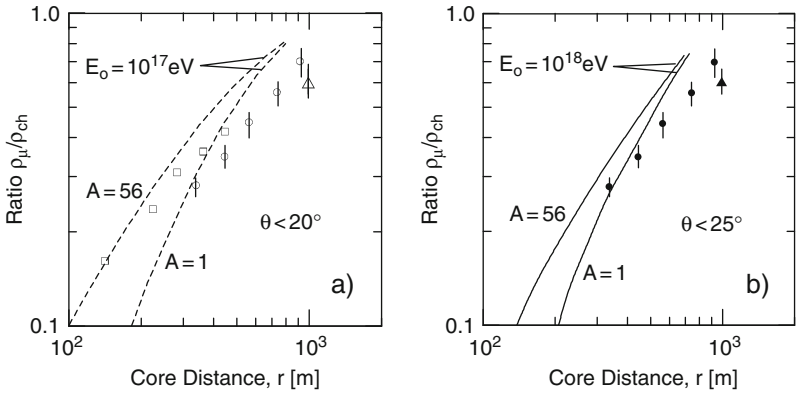

Fig. 19.22 Ratio of muon density, ρ_μ, to charged particle density, ρ_{ch} in water Cherenkov detectors, as a function of core distance. The muon energy is $\geq$420 MeV and the experimental data are from Haverah Park (Blake et al., 1979). □, • and △ are for showers having a primary energy of approximately 10^{17}, 10^{18} and 10^{19} eV, respectively. The two sets of *curves*, each for proton and iron initiated showers, are from model calculations of Gaisser et al. (1978)

More recent data from Haverah Park acquired by Blake et al. (1979) of showers belonging to two different primary energy groups show a clear trend of the ratio ρ_μ/ρ_{ch} for muons of energy >420 MeV, as expected, but do not follow the prediction from an early simulation of Gaisser et al. (1978) for proton and iron initiated showers (Fig. 19.22).

19.4.4 Age Parameter Related Correlations

A detailed discussion of the properties of the age parameter is given in Chaps. 4 and 10. Here we show in Fig. 19.23 the results of some studies made by Hara et al. (1983) of the relationship of the mean local age parameter, $\langle s \rangle$, in a N_e–N_μ correlation diagram for near vertical showers at Akeno that include muons of energy >1 GeV· sec(θ). Also indicated is the correlation with equal intensity distributions.

The dependence of the mean shower age on shower size at the Akeno level for near vertical showers of constant muon size groups is displayed in Fig. 19.24. An instructive plot is given in Fig. 19.25 which shows the dependence of the average shower age as a function of the muon to charged particle ratio worked out by Catz et al. (1973).

19.4.5 Long-Distance Correlated Events and Astrophysical Implications

The search for long-distance temporal and angular correlated air showers is of interest from an astrophysical point of view (Carrel and Martin, 1994; Kitamura

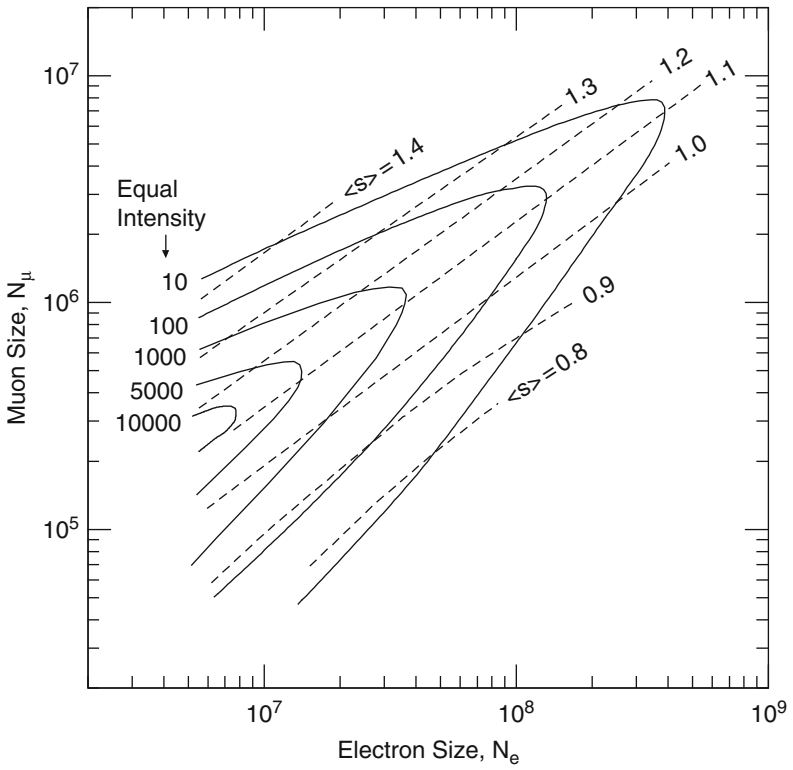

Fig. 19.23 Average local age distribution, $\langle s \rangle$, in a N_e–N_μ correlation diagram for showers incident in the zenith angle range corresponding to $1 \leq \sec(\theta) \leq 1.1$. The *dashed lines* represent constant age as labeled. The *curved* contours are equal intensity curves and the numbers attached are relative rates that apply to the Akeno array. The muon threshold energy is 1 GeV$\cdot \sec(\theta)$ (Hara et al., 1983)

et al., 1997; Ochi et al., 2005). The quasi-simultaneous arrival of air showers at widely separated locations on Earth, say of the order of 100–1,000 km apart, whose axes are parallel and point in the same direction are likely to come from the same source. They may signal the occurrence of an intense burst of activities at the source. On the other hand such events could be the result of an interaction of an ultrahigh energy cosmic ray with a target nucleus in space or with the background radiation.

Another possibility is that if the direction of arrival of the events points toward the vicinity of the Sun, it could be due to a heavy nucleus which dissociates in the intense radiation field of the Sun. This effect was first proposed by Zatsepin (1951) and Gerasimova and Zatsepin (1960) and had been revisited by different authors through the years, most recently by Medina-Tanco and Watson (1999). The nuclear fragments could trigger simultaneous multiple air shower if they hit theatmosphere

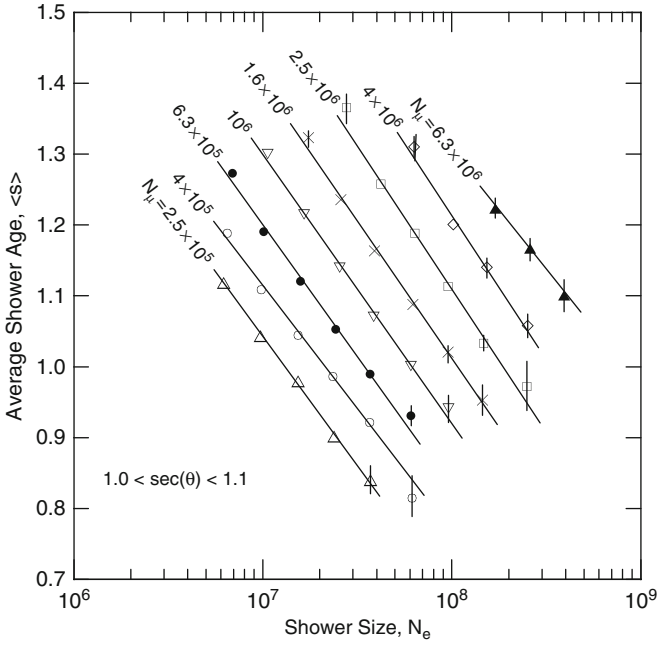

Fig. 19.24 Correlation plot of the average age $\langle s \rangle$ versus shower size, N_e, for fixed muon sizes, N_μ, as indicated, resulting from the same experiment as the data of Fig. 19.23 (Hara et al., 1983)

in the exposed region of the Earth. Time of flight corrections imposed by the geometry of the event must of course be properly accounted for.

One of the first experiments to search for the occurrence of such events was performed by Carrel and Martin (1994) using an arrangement that consisted of four scintillation detectors that were located at Geneva, Bern, Basel and Le Locle in Switzerland, covering a region measuring approximately 60 km by 200 km. These authors found time correlations with a typical spread of 0.3 ms with a significance of 4.2σ during a specific period. The very rudimentary equipped experiment could not determine the direction of arrival nor the energy of the events.

A much larger and far more sophisticated experiment of the same kind using GPS timing information was designed by several Japanese university groups and is now operating (Ochi et al., 2003, 2005; Iyono et al., 2006). This experiment that was initiated in 1996 is called the *Large Area Air Shower (LAAS)* experiment or network. It includes today 10 sites that are spread across the island of Honshu, spanning over roughly 1,000 km. Figure 19.26 shows the locations of the different sites on the map of Japan, identifying the different institutions that are associated with the project.

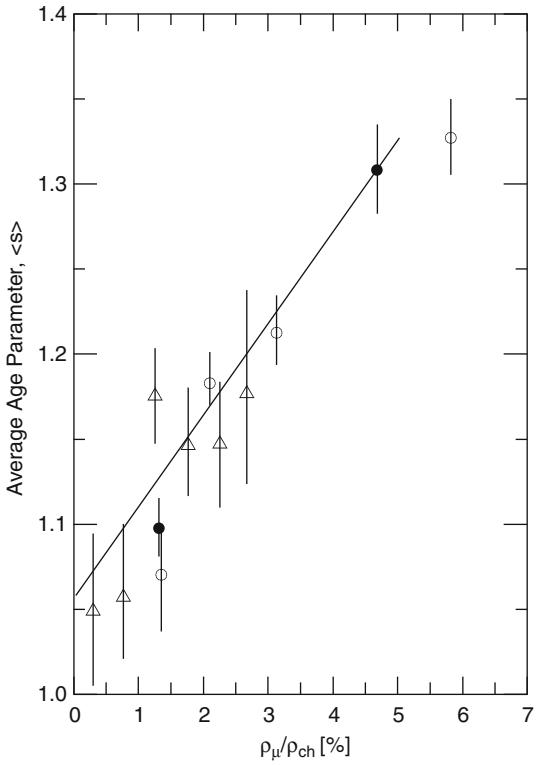

Fig. 19.25 Correlation between the average shower age parameter $\langle s \rangle$ and the muon to electron density ratio, in percent. Points △ are from the Lodz experiment, • and ○ from Verrieres (Catz et al., 1973). The core distance is not specified but must be approximately 20 m, as can be concluded from an earlier publication (Catz et al., 1971) where the age parameter calculation is discussed. The *solid line*, A, is from a measurement of Seller, after Catz et al. (1973)

The measurements carried out so far with the LAAS network, using 7 stations, yielded an anisotropy amplitude and phase for the galactic cosmic ray intensity derived from the arrival direction analysis of $(2.04 \pm 0.05) \cdot 10^{-3}$ and (-0.1 ± 1.6) h in the primary energy range from 10 TeV to 10 PeV. They also observe a small region of event deficit around $(\alpha, \delta = 150^\circ,\ 10^\circ)$ which is considered to be insignificant (Iyono et al., 2007; Noda et al., 2008).

A similar experiment had been carried out jointly by the Baksan and EAS-TOP groups, using their air shower arrays to search for temporally and spatially correlated gamma ray transients of energy $\geq 5 \cdot 10^{13}$ eV (Aglietta et al., 2000). Baksan is located in the North Caucasus, near Mt. Elbrus (Russia) at 1,700 m a.s.l., above the Baksan Neutrino Observatory (latitude 43.3° N, longitude 42.7° E), the EAS-TOP experiment (now shut down) was at Campo Imperatore, Gran Sasso (Italy), at an altitude of 2,005 m a.s.l., above various underground installations (latitude 42.5° N, longitude 13.5° E). The two experimental sites are separated in longitude by $\Delta\lambda \approx 33.7^\circ$. The combined search conducted by these two experiments for correlated events did not yield a significant excess. For the three point sources Crab Nebula, Markarian 421 and Markarian 501 they obtained upper limits.

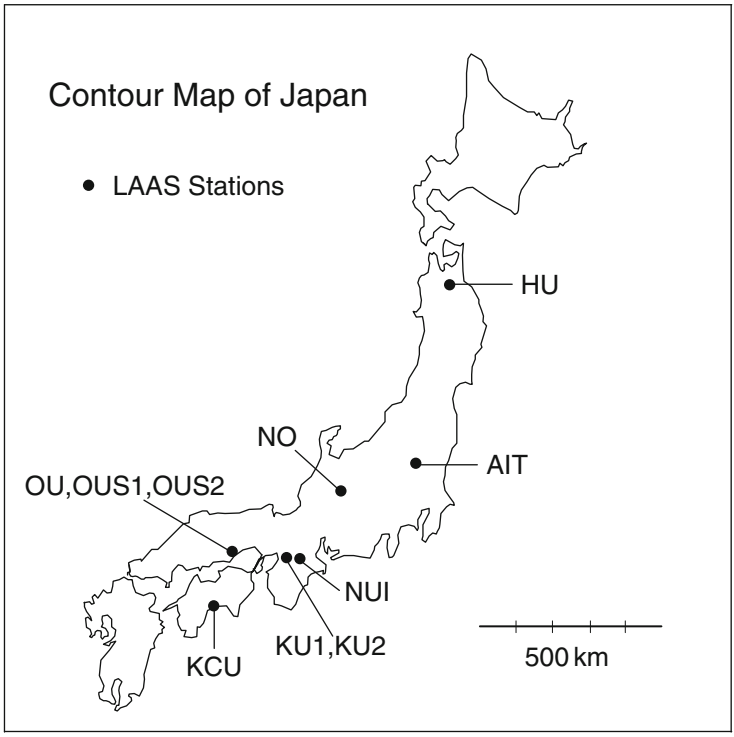

Fig. 19.26 Map of Japan showing the locations of the 10 LAAS stations (Ochi et al., 1999, 2003)

Code	Institution	Altitude [m]
AIT	Ashikaga Institute of Technology	49
HU	Hirosaki University	64
KU1	Kinki University 1	50
KU2	Kinki University 2	30
KCU	Kochi University	34
NUI	Nara University of Industry	130
NO	Norikura Observatory	2,770
OU	Okayama University	30
OUS1	Okayama University of Science 1	63
OUS2	Okayama University of Science 2	81

19.5 Miscellaneous Topics

19.5.1 General Comments

In this section we present a selection of special topics that do not necessarily follow the mainstream of present-day air shower research but are of some relevance, be it historically or because of contemporary interest. Some of the topics briefly discussed here had remained more or less dormant for a long time, however, in

particular the topic of *horizontal air showers (HAS)*, began to arouse a broader interest in recent years among many researchers in the field, as they harbor a certain potential for yielding hitherto unexploited information. In addition HAS allow to study neutrino fluxes, neutrino reactions and the properties of muons in giant showers.

Other items, such as *muon poor* and *muon rich showers*, *lost energy*, and strange phenomena such as *Centauro* and *coplanar events*, but also the *long flying component* are issues that surface from time to time. These unusual events are documented in the literature but confirmation is vague or non-existent and the situation remains unclear whether they are the result of unique fluctuations or rare physical processes. Up to date accelerator and collider experiments were unable to reproduce any of these unusual phenomena. We will not elaborate on them but will simply list them for reason of completeness and include some references.

19.5.2 Horizontal and Upward Directed Air Showers

Air showers observed at large zenith angles ($\theta \geq 60^\circ$) are referred to as *horizontal air showers* (HAS). Most strongly inclined events contain only the surviving muon component. Very high energy muons originating from the first or first few interactions of highly inclined hadron initiated showers have a high probability to survive to great depth in the atmosphere long after the initial shower is extinct because of their large Lorentz factor. However, they are subject to major energy losses by bremsstrahlung along their trajectories in the deeper atmosphere, usually after the common shower constituents are absorbed.

The resulting photons initiate electromagnetic showers that may be observed at ground level, and possibly rare photonuclear processes may yield occasionally a new generation of hadrons. On the other hand, highly inclined showers can also be initiated by neutrinos of all flavors. Common to both, muon and neutrino initiated showers, is that they manifest themselves very differently from regular showers. In particular, if initiated in the deep atmosphere they have the characteristics of young showers.

This kind of showers was first observed with the Tokyo (I.N.S.) air shower array in conjunction with a large spark chamber and a cloud chamber (Matano et al., 1965a, c). The particular event had a zenith angle of $86^{+1}_{-2}{}^\circ$ and traversed an atmospheric thickness of $\approx 12,000\,\mathrm{g\,cm^{-2}}$. Its lateral density distribution was extremely narrow as is illustrated in Fig. 19.27. The event could be well described by a Nishimura-Kamata function with age parameter $s = 0.6$. Thus it was a very young shower that must have been initiated very deep in the atmosphere. The detailed analysis showed that its starting point must have been at a slant depth of about $400\,\mathrm{g\,cm^{-2}}$ above the detectors. The particle count in the shielded detector proved the presence of muons and the cloud chamber analysis showed that a nuclear interaction having an energy between 30 and 50 GeV occurred in a lead plate. It was

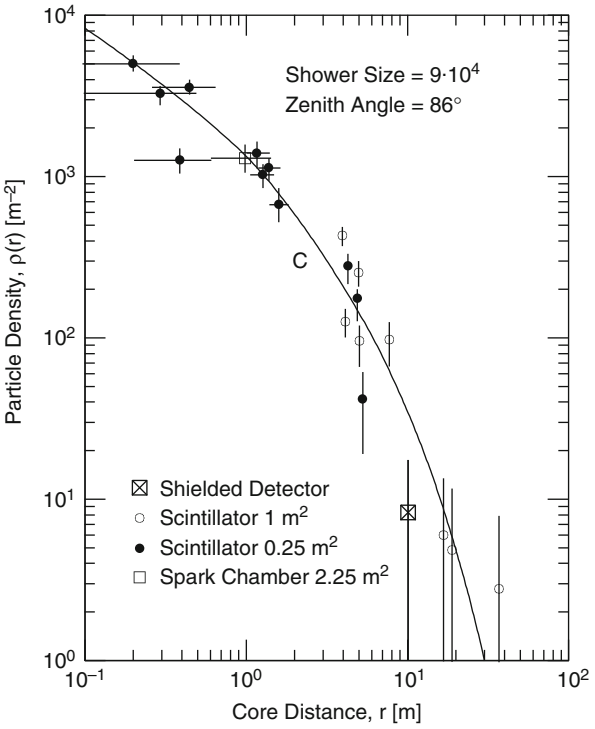

Fig. 19.27 Lateral density distribution of charged particles in a very inclined shower (so-called horizontal air shower) having a zenith angle of $86^{+1}_{-2}{}^{\circ}$, detected with the Tokyo (I.N.S.) air shower array (Matano et al., 1965a, c). The shielded detector was buried under 10 m of earth ($\approx$ 20 m w.e.)

therefore concluded that this shower was produced by a nuclear interaction of a muon or a neutrino at the specified depth.

Events like the one described above proved to be most suitable for studying the flux and properties of high energy muons ($E_\mu \geq 50$ TeV) and neutrinos (Matano et al., 1968b; Böhm et al., 1971; Kiraly et al., 1971; Nagano et al., 1971; Mikamo et al., 1971, 1982; Böhm and Nagano, 1973). Spectral measurements in this energy region are also of interest because of the relation of these muons to the primary proton flux and permit to study prompt muon production via charmed particles, and possibly other processes, too[1] (Mikamo et al. (1982).

Gamma ray family measurements with nuclear emulsion carried out by the Mount Fuji group (Akashi et al., 1981) indicate a steepening of the primary proton spectrum above ~100 TeV. This implies that the slope of the muon spectrum, too,

[1] The strongly inclined muon energy spectrum had been measured up to ~20 TeV with an independent experiment using the MUTRON detector at ground level in Tokyo (Matsuno et al., 1984), and by the KGF group underground in southern India to 50 TeV (Krishnaswami et al., 1979)

must get steeper at a few tens of TeV, and likewise the slope of the size spectrum of HAS around a size of a few times 10^4.

However, the muon spectrum is also affected by contributions from the direct processes, thus enriching the muon spectrum and causing a change of slope, making it flatter. Evidence for such a behavior was first presented by Mikamo et al. (1982).

Today, inclined and even upward directed showers are of interest mainly to study ultra high energy neutrinos from astrophysical sources, their interactions in the deep atmosphere, inside rock, in large bodies of water or ice, and to search for tau neutrinos (Fargion et al., 1999; Fargion, 2001; Sinitsyna et al., 2003) (see also Sect. 1.3). Many theoretical studies and simulations had been carried out to get deeper insight and to estimate background problems (Tascau et al., 2007).

Other work is directed to analyze and interpret the unaccompanied muon flux (Nagano et al., 1986). Another aspect of muon investigations in large inclined showers is to study the muon pattern as a function of the azimuthal angle and the charge separation due to the geomagnetic field, using surface detectors.[2] Theoretical studies in this respect and studies related to neutrinos had been carried out by several authors for surface arrays (Ave et al., 2000; Liu and Huang, 2007; Xue and Ma, 2007), and fluorescence detectors (Boyer, 1991; Boyer et al., 1995; Cooper et al., 1991; Nellen et al., 2005; Miele et al., 2006).

Experimental work of relatively recent date on inclined and horizontal air showers had been carried out by Aglietta et al. (1993, 1995), using the EAS-TOP installation. This work yielded an excess of events at zenith angles $\theta > 70^\circ$ above the rate of air showers expected from their attenuation length in the atmosphere. The integral muon intensity obtained by these authors amounts to

$$I_\mu(E_\mu > 20\ \mathrm{TeV}) = (2.9 \pm 0.8) \cdot 10^{-11}\ \ [\mathrm{cm}^{-2}\,\mathrm{s}^{-1}\,\mathrm{sr}^{-1}]\ , \tag{19.3}$$

and the upper limit for the integral neutrino intensity

$$I_\nu(E_\nu > 10^5\ \mathrm{GeV}) < 8.5 \cdot 10^{-9}\ \ [\mathrm{cm}^{-2}\,\mathrm{s}^{-1}\,\mathrm{sr}^{-1}]\ . \tag{19.4}$$

A very recent limit on the diffuse tau neutrino (ν_τ) flux had been given by the Auger collaboration, using very inclined showers detected with the deep water Cherenkov surface detectors (Blanch-Bigas et al., 2007). For an E^{-2} incident spectrum of diffuse ν_τ, they got for the 90% C.L. limit,

$$E_\nu^2 \cdot \frac{\mathrm{d}N_{\nu_\tau}}{\mathrm{d}E_\nu} < 1.5^{+0.5}_{-0.8} \cdot 10^{-7}\ \ [\mathrm{GeV}\,\mathrm{cm}^{-2}\,\mathrm{s}^{-1}\,\mathrm{sr}^{-1}]\ . \tag{19.5}$$

Their data are plotted in Fig. 11.16, Sect. 11.5.

[2] Geomagnetic effects are discussed in greater detail in Chap. 8.

19.5.3 Muon Poor and Muon Rich Showers

Muon poor showers are presumably initiated by gamma rays, protons or light nuclei (He, etc.) whose muon content amounts to a comparatively small fraction of all charged particles. They have been investigated for a long time by many authors with the aim to distinguish gamma ray initiated showers from common hadron initiated showers, and also proton from iron showers, though there are more reliable methods for the latter purpose, as is described in Chap. 10.

The muon signature is being used today particularly in connection with dedicated gamma ray experiments, mainly wide-aperture atmospheric Cherenkov arrays. This kind of experiments is troubled by an almost crushing number of proton initiated showers that represent a large background. Many of these events can fake gamma ray showers unless the muon count is recorded and used as a veto against accepting an event if it exceeds a certain critical fraction of the charged particles.

On the other hand, muon rich showers are generally ascribed to be due to heavy primary (iron) initiated showers. Consequently, the muon fraction of a shower had been used and is still being used in some primary mass studies as a discriminating factor against proton initiated events to get an apparently heavy primary enriched set of showers to apply further mass sensitive criteria.

Matano et al. (1965b) have carried out a rather unique study, searching for arrival direction anisotropies of muon rich showers. They confirmed a decrease in the arrival rate of muon rich showers of size $\sim 10^6$ between 15 and 21 h in right ascension, thus confirming earlier results from similar studies which these authors have carried out (Matano et al., 1963a, b) and likewise Hasegawa et al. (1962).

19.5.4 Decoherence Measurements

This kind of measurement was used during the early epoch of air shower exploration and is linked to shower size measurements (see Sects. 12.2 and 12.4). Matano et al. (1968a) carried out decoherence measurements on big air showers at large distances from the axis. One of the aims of this experiment was to search for changes in the slope of the primary energy spectrum. The decoherence rate R [s^{-1}] of showers recorded at two stations a distance d [m] apart is approximately given by the following expression,

$$R \propto \rho^{-\gamma} d^{2-\alpha\gamma} \quad , \tag{19.6}$$

where ρ is the particle threshold density [m^{-2}] measured by the detectors, α the exponent of the lateral distribution when expressed as a power law, and γ is the exponent of the integral size spectrum.

The value of γ obtained at fixed detector separation, d, is equated with the slope of the integral size spectrum, while measurements of $(2-\alpha\gamma)$ at fixed density ρ are used to establish the size range to which the slope refers.

The measurements of Matano et al. (1968a) were made with two sets of scintillation detector pairs of area 2 m^2 each, placed 50 m apart, and the separation of the two pairs was 115, 500 and 1,300 m for different runs. The exponents of the density spectra thus obtained were 1.6 ± 0.05, 2.0 ± 0.1 and 2.4 ± 0.4, respectively, for the density ranges (1–30) m^{-2}, (1–10) m^{-2} and (1–4) m^{-2}. The results are plotted in Fig. 19.28 together with those from other authors.

Andrews et al. (1970) carried out similar measurements at Haverah Park. Their results are also plotted in Fig. 19.28. They have used a slightly different expression for the decoherence relation, including the exponent α also in the exponent of ρ. Their expression reads

$$R \propto \rho^{2/\alpha-\gamma} d^{2-\alpha\gamma} \quad . \tag{19.7}$$

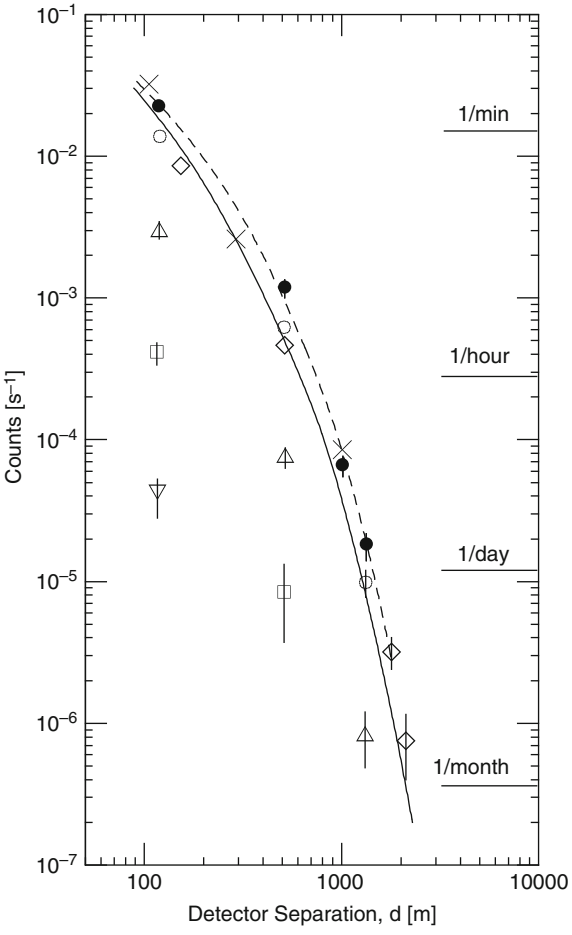

Fig. 19.28 Decoherence *curve* of air showers for various particle densities (Matano et al., 1968a). The *symbols* represent the threshold densities of the detectors for the different runs: ○ ≥1 particle per 2 m^2, △ ≥3 particles per 2 m^2, □ ≥10 particles per 2 m^2, ▽ ≥30 particles per 2 m^2, and • stands for the total of all events. The *dashed curve* is the best fit to these data. The *symbols* × show the rate expected for the total of all events according to Skobeltzyn et al. (1947). The *symbols* ◇ are comparative data from Haverah Park for a particle density ≥0.5/m^2 (Andrews et al., 1970). The *solid curve* represents the expected frequency obtained from the size spectrum and the lateral distribution of air showers by Linsley (1963)

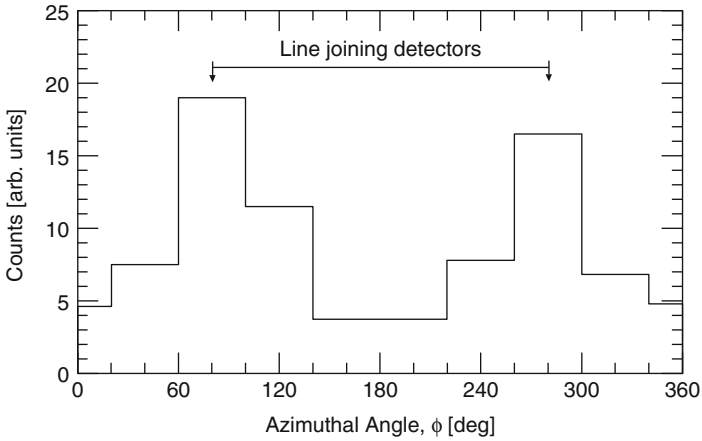

Fig. 19.29 Azimuthal distribution of showers for a detector separation of 1,640 m (Andrews et al., 1970). The majority of showers which trigger the detectors at this separation arrive in those azimuthal directions which reduce the separation of the detectors in the plane of the shower front. The results show that 75% of the showers thus observed have zenith angles $\theta \geq 40^\circ$ and 30% have $\theta \geq 60^\circ$, whereas at detector separations of only 150 and 500 m more than 80% of the showers have zenith angles $\theta \geq 40^\circ$

These authors point out that at detector separations of 150 and 500 m more than 80% of the showers have zenith angles $\theta < 40^\circ$, at separations of 1,640 and 2,140 m 75% have zenith angles $\theta > 40^\circ$ and 30% have $\theta > 60^\circ$. The azimuthal distribution for a separation of 1,640 m which is plotted in Fig. 19.29 shows that the majority of showers which trigger the detectors at this separation arrive in those azimuthal directions which reduce the separation of the detectors in the plane of the shower front. As the exponent of the lateral distribution varies from a value of ≈ 3 for $\theta < 40^\circ$ to ≈ 2 for $\theta > 60^\circ$, the inclusion of high zenith angle data will have a marked and misleading effect on the inferred exponent of the primary energy spectrum.

19.5.5 Unusual Phenomena

(a) Introductory Comments

In Chap. 3 we have briefly mentioned some unusual phenomena which had been observed occasionally in cosmic ray experiments during the past several decades. Their interpretation was often based on highly speculative hypothetical processes or have led the observers to suggest the existence of new particles. In the following we will just outline the most common of these phenomena and give some references for the interested reader.

(b) Centauro and Anti-Centauro Events

The origin of so-called *Centauro events* goes back to the observation of a very energetic event in a nuclear emulsion chamber which had been exposed to the

cosmic radiation at the Mt. Chacaltaya laboratory (5,230 m a.s.l., 540 g cm^{-2}) (Lattes et al., 1973). In this emulsion chamber a rather unusual very high energy event, called a *"cosmic ray family"* (a collimated group of particles) ($\Sigma E \sim 230$ TeV) had been observed which consisted of only one high energy gamma ray and 49 hadrons. The event pattern (shape) was very particular which led to the name Centauro (Lattes et al., 1980). Later on similar events were discovered by other work groups at the Pamir Laboratory (4,360 m a.s.l.) (Borisov et al., 1987).

Ever since, events that consist almost exclusively of hadrons are called Centauro (or mini Centauro) events (Ohsawa et al., 2004). Conversely, gamma family dominated events are sometimes referred to as *anti-Centauro events* (Yakovlev, 2003a). Accelerator investigations have never delivered proof of the existence of Centauro-like events (Alner et al., 1987). The question whether new physics would be required to explain the occurrence of Centauro events remained unanswered for a long time (Bellandi et al., 1979) until new detailed re-analyses had been undertaken some years ago that showed a flaw in the analysis of the original Centauro event (Kopenkin et al., 2003; Kopenkin and Fujimoto, 2006).

(c) Aligned, Coplanar Events

Another long-standing puzzling kind of events detected so far in emulsion chambers only are the so-called *coplanar events*, where members of a cosmic ray super family consisting of a number $n > 3$ clusters of particles are aligned along a straight line in the plane of the target diagram, i.e., they lie in a plane (Baradzei et al., 1984). The analysis of Borisov et al. (1991) has shown that the occurrence of such events is experimentally much more frequent than in simulations and rises with energy. They state that approximately 20–30% of all investigated events are *aligned events*.

For a particular analysis these authors use 9 super families defined as gamma-hadron families with gamma ray energy $\Sigma E_\gamma > 400$ TeV. They find that for $n \geq 3$ the ratio of events with and without alignment is 6:3. Many attempts had been undertaken to explain the phenomenon but so far without satisfactory success (Halzen and Morris, 1990; Royzen, 1994; Mukhamedshin, 2007).

(d) Halo Events

At energies >10 PeV so-called *halo events* are observed in emulsion chambers. These events manifest themselves as a blob or a large diffuse dark spot in the center of "families". The spot looks like a poorly focused beam of accelerated particles and is produced by narrow bundles of relativistic particles with densities in excess of 10^4 particles per square centimeter. Besides single core halos there exist halos with 2, 3, 4 and more cores. The centers of many halos lie on a straight line and form coplanar events as discussed above (Slavatinski, 2003).

(e) Long Flying Components

The so-called *long-flying component* of the core of air showers (or the C-particle as it was called by its discoverers) that appeared to yield elongated cascades is another

phenomenon that has been known for a long time (Aseikin et al., 1975; Yakovlev et al., 1977, 1979, 2003b; Bazarov et al., 1981). It was first observed at the Tien Shan laboratory (3,340 m a.s.l.) in the calorimeter under lead absorbers having a thickness of 450 g cm^{-2} and 1,440 g cm^{-2} and appears to emerge from hadronic interactions in showers of energy $\geq$100 TeV. It is also known as the *Tien Shan effect*. The particle appeared to have a long attenuation length and a smaller cross section than ordinary nucleons.

Many theoretical and experimental papers had been devoted to this phenomenon, mainly by the Tien Shan group, however, without ever being able to give an acceptable answer. Recently, several paper have been published that offer explanations for the phenomenon. These are linked to charm production in air showers and to the properties of charmed particles. We will not further elaborate on this topic but refer the interested reader to the papers of Yakovlev (2004, 2005) and Dremin and Yakovlev (2006).

19.5.6 Missing Energy in Air Showers

Several methods are employed to estimate the primary energy of air showers (see Chaps. 2, 10, 16 and 17). The choice of the method depends on the kind of experiment that is used for this purpose. Particle detector arrays make use of the shower size which is determined at a particular atmospheric depth where the equipment is located. Obviously such energy estimates are not very reliable as they are based on a single assessment of a shower at the particular atmospheric depth that includes mainly particles from the last generation of production.

The situation is similar for air Cherenkov arrays where the photon size of the shower is measured at a well defined depth in the atmosphere. Here, however, the situation is somewhat different as the photon count includes a large fraction of all the photons that are produced along the entire shower, since the atmospheric absorption is relatively modest in the visible portion of the spectrum. In either case the actual primary energy is estimated with the help air shower simulations.

On the other hand, shower energy estimates based on the fluorescence method have the advantage that a certain fraction of the fluorescence photons are collected from along the entire shower trajectory. Thus, it is actually a calorimetric method.

Nevertheless, in either case an observer cannot determine the actual primary energy on the basis of the methods mentioned above since a certain fraction of the energy of a shower is converted to neutrinos and is therefore in the form of invisible (unseen) energy that escapes detection. Air shower simulations permit to estimate this fraction so that for a given experimental set-up one can estimate the missing energy. However, one must be careful with errors introduced by cutoff and/or threshold energies that are usually incorporated in air shower simulations to keep interaction processes, particle propagation and the entire computation in bounds.

Frequently, authors have ignored the missing energy when estimating the primary energy of recorded air showers. Attempts to account for it had been made

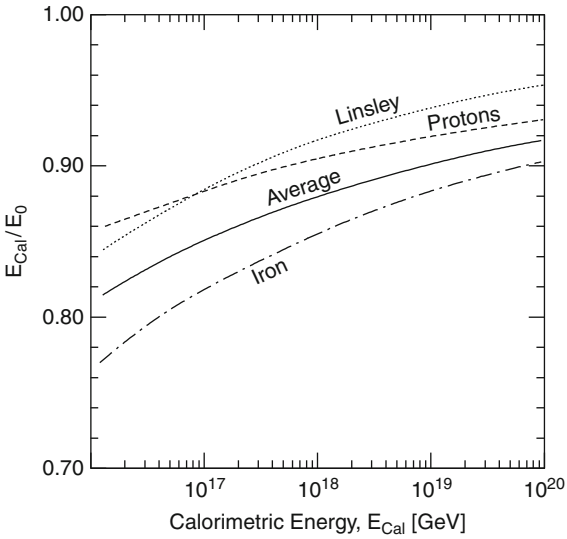

Fig. 19.30 Function for correcting the calorimetric energy to obtain the primary energy as a function of calorimetric energy. The *curves* represent the correction needed for primary proton and iron nuclei initiated showers, for an average mass as well as the original Linsley correction curve (Linsley, 1983) (after Song et al., 2000)

by Linsley (1983) and Baltrusaitis et al. (1985). Some time ago Song et al. (2000) have revisited the problem of missing or lost energy in air showers. Their work is specifically aimed to estimate the energy loss for the fluorescence (calorimetric) method and is based on simulations using CORSIKA with the QGSJET event generator (Heck et al., 1998) and the EGS4 code for the electromagnetic cascade part (Bielajew, 1993; Bielajew and Rogers, 1993). Figure 19.30 shows the results of the calculations of Song et al. (2000) for hadronic showers. Since the primary mass is a-priori unknown one is forced to use the corrections for an average primary mass, as given in the figure.

References

Acharya, B.S., et al.: PICRC, 9, p. 191 (1983).
Aglietta, et al.: PICRC, 4, p. 255 (1993).
Aglietta, M., et al.: PICRC, 1, p. 638 (1995).
Aglietta, et al.: Astropart. Phys., 14, p. 189 (2000).
Akashi, M., et al. (Mt. Fuji Collaboration): PICRC, 5, p. 247 (1981).
Alner, G.J., et al., UA5 Collaboration: Phys. Rep., 154, p. 247 (1987).
Andrews, D., et al.: Acta Phys. Acad. Sci. Hung., 29, S3, p. 337 (1970).
Antoni, T., et al.: J. Phys. G, 25, p. 2161 (1999).
Armitage, M.L., et al.: PICRC, 4, p. 2539 (1973).
Aseikin, V.S., et al.: PICRC, 4, p. 2599 (1973).
Aseikin, V.S., et al.: PICRC, 7, p. 2462 (1975).
Ashton, F., et al.: PICRC, 12, p. 18 (1977).
Ave, M., et al.: Astropart. Phys., 14, p. 91 (2000).
Baltrusaitis, R.M., et al.: PICRC, 7, p. 159 (1985).
Baradzei, L.T., et al.: Proceedings of the International Symposium on Cosmic Ray and Particle Physics, Tokyo 1984, University of Tokyo, p. 136 (1984).

Baruch, J.E.F., et al.: PICRC, 8, p. 184 (1977).
Bazarov, E.V., et al.: PICRC, 5, p. 32 (1981).
Bellandi Filho, J., et al.: In Cosmic Rays and Particle Physics-1978 (Bartol Conference) T.K. Gaisser, ed., American Institute of Physics, A.I.P. Conference Proceedings No. 49, Particles and Fields Subseries No 16, p. 317 (1979).
Bielajew, A.F.: Report PIRS-0393, National Research Council of Canada (1993). (http://ehssun.lbl.gov/egs/epub.html).
Bielajew, A.F., and D.W.O. Rogers: Report PIRS-0394, National Research Council of Canada (1993). (http://ehssun.lbl.gov/egs/epub.html).
Blake, P.R., et al.: Acta Phys. Acad. Sci. Hung., 29, S3, p. 639 (1970).
Blake, P.R., et al.: PICRC, 8, p. 67 (1979).
Blanch-Bigas, O., et al.: PICRC, pre-conference edition, paper 603, Merida, Mexico (2007).
Böhm, E., et al.: Acta Phys. Acad. Sci. Hung., 29, S3, p. 487 (1970).
Böhm, E., et al.: PICRC, 4, p. 1438 (1971).
Böhm, E., and M. Nagano: J. Phys. A, 6, p. 1262 (1973).
Böhm, E.: PICRC, 8, p. 29 (1977).
Borisov, A.S., et al. (Pamir Collaboration): Phys. Lett. B, 190, p. 226 (1987).
Borisov, A.S., et al.: PICRC, 4, p. 125 (1991).
Boyer, J.: PICRC, 4, p. 634 (1991).
Boyer, J., et al.: PICRC, 1, p. 750 (1995).
Carrel, O., and M. Martin: Phys. Lett. B, 325, p. 526 (1994).
Catz, Ph., et al.: PICRC, 3, p. 1035 (1971).
Catz, Ph., et al.: PICRC, 4, p. 2495 (1973).
Chatterjee, B.K., et al.: Can. J. Phys., 46, p. S13 (1968a).
Chatterjee, B.K., et al.: Can. J. Phys., 46, p. S136 (1968b).
Cooper, R., et al.: PICRC, 4, p. 623 (1991).
Cowsik, R.: Can. J. Phys., 46, p. S144 (1968).
Danilova, T.V., and S.I. Nikolsky: PICRC, 4, p. 221 (1963).
Danilova, T.V.: PICRC, 2, p. 660 (1965).
Dremin, I.M., and V.I. Yakovlev: Astropart. Phys., 26, p. 1 (2006).
Dzikowski, T., et al.: J. Phys. G, 3, p. 1591 (1977).
Earnshaw, J.C., et al.: Proc. Phys. Soc., 90, p. 91 (1967).
Elbert, J.W., et al.: J. Phys. G, 2, p. 971 (1976a).
Elbert, J.W., et al.: J. Phys. G, 2, p. 971 (1976b).
Erlykin, A.D., et al.: PICRC, 2, p. 731 (1965).
Fargion, D., et al.: PICRC, 2, p. 396 (1999).
Fargion, D.: PICRC, 3, p. 1297 (2001).
Firkowski, R., et al.: Institute of Nuclear Research, Warsaw, Poland, Report No. 803/VI-PH (1967).
Fritze, R., et al.: Acta Phys. Acad. Sci. Hung., 29, S3, p. 439 (1970).
Fukui, S., et al.: Prog. Theor. Phys. Jpn., 16, p. 1 (1960).
Gaisser, T.K., et al.: Rev. Mod. Phys., 50, p. 859 (1978).
Gerasimova, N.M., and G.T. Zatsepin: Sov. Phys. JETP, 11, p. 899 (1960).
Greisen, K.: Annual Review of Nuclear Science, Annual Reviews, inc., Palo Alto, California, USA, Vol. 10, p. 63 (1960).
Grieder, P.K.F.: Acta Phys. Acad. Sci. Hung., 29, S3, p. 563 (1970a).
Grieder, P.K.F.: Acta Phys. Acad. Sci. Hung., 29, S3, p. 569 (1970b).
Grieder, P.K.F.: Rivista del Nuovo Cim., 7, p. 1 (1977).
Grieder, P.K.F.: Proceedings of the 1980 European Cosmic Ray Symposium, Leningrad, Academy of Sciences USSR, p. 325 (1980).
Grieder, P.K.F.: Nuovo Cim., 84 A, p. 285 (1984).
Halzen, F., and D.A. Morris: Phys. Rev. D, 42, p. 1435 (1990).
Hara, T., et al.: Acta Phys. Acad. Sci. Hung., 29, S3, p. 361 (1970).
Hara, T., et al.: PICRC, 13, p. 159 (1979).
Hara, T., et al.: PICRC, 6, p. 52 (1981).

Hara, T., et al.: PICRC, 11, p. 281 (1983).
Hasegawa, H., et al.: J. Phys. Soc. Jpn., 17, Suppl. A-III, p. 86 (1962).
Haungs, A., et al.: Rep. Prog. Phys., 66, p. 1145 (2003).
Heck, D., et al.: Report FZKA 6019, Forschungszentrum Karlsruhe (1998).
Hochart, J.P., et al.: PICRC, 8, p. 2736 (1975).
Iyono, A., et al.: Nucl. Phys. B (Proc. Suppl.), 151, p. 69 (2006).
Iyono, A., et al.: PICRC, pre-conference edition, paper 114, Merida, Mexico (2007).
Kabanova, N.V., et al.: PICRC, 4, p. 2534 (1973).
Kalmykov, N.N., et al.: PICRC, 6, p. 2074 (1971).
Kameda, T., et al.: PICRC, 2, p. 681 (1965).
Khristiansen, G.B., et al.: Izv. Akad. Nauk SSSR, Ser. Fiz., 35, p. 2107 (1971).
Khristiansen, G.B., et al.: PICRC, 8, p. 148 (1977).
Kiraly, P., et al.: J. Phys. A, 4, p. 367 (1971).
Kitamura, T., et al.: Astropart. Phys., 6, p. 279 (1997).
Kopenkin, V., et al.: Phys. Rev. D, 68, p. 052007 (2003).
Kopenkin, V., and Y. Fujimoto: Phys. Rev. D, 73, p. 082001 (2006).
Kozlov, V.G., et al.: PICRC, 8, p. 356 (1979).
Kozlov, V.G., et al.: PICRC, 6, p. 210 (1981).
Krishnaswami, M.R., et al: PICRC, 13, p. 383 (1979).
Lattes, C.M.G., et al.: PICRC, 4, p. 2671 (1973).
Lattes, C.M.G., et al.: Phys. Rep., 65, p. 152 (1980).
Linsley, J.: PICRC, 4, p. 77 (1963).
Linsley, J.: PICRC, 12, p. 135 (1983).
Liu, T.C., and M.A. Huang: PICRC, pre-conference edition, paper 832, Merida, Mexico (2007).
Machavariani, S.K., et al.: PICRC, 8, p. 240 (1979).
Machavariani, S.K., et al.: PICRC, 6, p. 193 (1981).
Matano, T.: J. Phys. Soc. Jpn., 17, p. 745 (1962).
Matano, T., et al.: PICRC, 4, p. 129 (1963a).
Matano, T., et al.: PICRC, 4, p. 248 (1963b).
Matano, T., et al.: Phys. Rev. Lett., 15, p. 594 (1965a).
Matano, T., et al.: PICRC, 2, p. 637 (1965b).
Matano, T., et al.: PICRC, 2, p. 1045 (1965c).
Matano, T., et al.: Can. J. Phys., 46, p. S255 (1968a).
Matano, T., et al.: Can. J. Phys., 46, p. S369 (1968b).
Matano, T., et al.: Acta Phys. Acad. Sci. Hung., 29, S3, p. 451 (1970).
Matsuno, S., et al.: Phys. Rev. D, 29, p. 1 (1984).
Medina-Tanco, G.A., and A.A. Watson: Astropart. Phys., 10, p. 157 (1999).
Miele, G., et al.: Phys. Lett. B, 634, p. 137 (2006).
Mikamo, S., et al.: PICRC, 7, p. 2836 (1971).
Mikamo, S., et al.: Lett. Nuovo Cim., 34, p. 237 (1982).
Miyake, S., et al.: Acta Phys. Acad. Sci. Hung., 29, S3, p. 463 (1970).
Miyake, S., et al.: PICRC, 13, p. 165 (1979).
Mukhamedshin, R.: PICRC, pre-conference edition, paper 158, Merida, Mexico (2007).
Nagano, M., et al.: J. Phys. Soc. Jpn., 30, p. 33 (1971).
Nagano, M., et al.: J. Phys. G, 12, p. 69 (1986).
Nagano, M., et al.: Astropart. Phys., 13, p. 277 (2000).
Nellen, L., et al.: PICRC, 7, p. 183 (2005).
Nesterova, N.M., and A.G. Dubovy: PICRC, 8, p. 345 (1979).
Noda, C., et al.: Nucl. Phys. B, (Proc. Suppl.), 175–176, p. 459 (2008).
Nymmik, R.A.: Thesis University of Moscow (1970).
Ochi, N., et al. (LAAS group): PICRC, 2, p. 419 (1999).
Ochi, N., et al.: J. Phys. G, 29, p. 1169 (2003).
Ochi, N., et al.: PICRC, 6, p. 201 (2005).
Ohsawa, A., et al.: Phys. Rev. D, 70, p. 074028 (2004).

Romakhin, V.A., et al.: PICRC, 8, p. 107 (1977).
Romakhin, V.A., and N.M. Nesterova: Trudy, FIAN, 109, p. 77 (1979).
Royzen, I.I.: Mod. Phys. Lett. A, 9, p. 3517 (1994).
Sinitsyna, V.G., et al.: PICRC, 3, p. 1517 (2003).
Skobeltzyn, D.V., et al.: Phys. Rev., 71, p. 315 (1947).
Slavatinski, S.A.: Nucl. Phys. B (Proc. Suppl.), 122, p. 3 (2003).
Song, C., et al.: Astropart. Phys., 14, p. 7 (2000).
Sreekantan, B.V.: PICRC, 7, p. 2706 (1971).
Tascau, O., et al.: PICRC, pre-conference edition, paper 183, Merida, Mexico (2007).
Van Staa, R., et al.: J. Phys. A, 7, p. 135 (1974).
Vatcha, R.H., and B.V. Sreekantan: J. Phys. A, 6, p. 1050 (1973a).
Vatcha, R.H., and B.V. Sreekantan: J. Phys. A, 6, p. 1078 (1973b).
Vavilov, Yu.N., et al.: Trudi FIAN, 26, p. 17 (1964).
Vernov, S.N., et al.: Izv. AN SSSR, ser fiz., 29, p. 1876 (1965), transl.: Bull. Acad. Sci. USSR Phys. Ser., p. 1708 (1965a).
Vernov, S.N., et al.: PICRC, 2, p. 769 (1965b).
Vernov, S.N., et al.: Acta Phys. Acad. Sci. Hung., 29, S3, p. 429 (1970).
Vernov, S.N., et al.: PICRC, 8, p. 320 (1977).
Vernov, S.N., et al.: Izv. Akad. Nauk. SSSR, Ser. Fiz., 42, p. 1367 (1978).
Xue, B.K., and B.-Q. Ma: Astropart. Phys., 27, p. 286 (2007).
Yakovlev, V.I., et al.: PICRC, 7, p. 115 (1977).
Yakovlev, V.I., et al.: PICRC, 6, p. 59 (1979).
Yakovlev, V.I.: Nucl. Phys. B (Proc. Suppl.), 122, p. 201 (2003a).
Yakovlev, V.I.: Nucl. Phys. B (Proc. Suppl.), 122, p. 417 (2003b).
Yakovlev, V.I.: Nucl. Phys. B (Proc. Suppl.), 136, p. 350 (2004).
Yakovlev, V.I.: PICRC, 9, p. 251 (2005).
Zatsepin, G.T.: Dokl. Acad. Nauk SSSR, 80, p. 577 (1951).

Chapter 20
Air Shower Simulations

Overview This chapter discusses very briefly the essentials of the *architecture* of a highly structured full fledged complex air shower simulation program that includes all basically relevant processes such as particle propagation, interaction and/or decay needed to simulate complete air showers in space and time, to extract all significant observables at any location in the atmosphere. We do not discuss interaction models or subsidiary program systems such as the standard EGS package, analysis or correlation programs; we only outline their implementation in the program flow and outline useful auxiliary service programs for tests and simulation supervision. Interaction model aspects are discussed in Chap. 3. As an example we have taken the essential elements of the ASICO program system which is the forerunner of the currently widely used successful CORSIKA program. The concepts of energy splitting, hybrid and thinning approaches for ultrahigh energy applications are briefly mentioned.

20.1 Introduction

An air shower is one of the most complex physical processes in the field of particle and nuclear physics. An emulation of the process to get at the roots of the interactions from which the numerous particles emanate to seek insight into the relevant fundamental interactions is not possible. The only approach to gain access to this information is with the help of computer simulations of extensive air showers on the basis of hypothetical, phenomenological mathematical models, since we lack a general theory of hadronic interactions, which are the primary processes responsible for the development of the predominantly hadron initiated showers.

Air shower simulations are of paramount importance for the evaluation and interpretation of experimental air shower data. The technique is simply a trial and error method, i.e., one builds and inserts a shower model that corresponds to the best of our knowledge to the reality, simulates showers, compares the results with the experimental data, modifies the model and/or its parameters, tries again, fine-tunes the model, and so on, until the best agreement between prediction and experiment is obtained.

P.K.F. Grieder, *Extensive Air Showers,* DOI 10.1007/978-3-540-76941-5_20,

Basically a primary hadron initiated air shower consists of the superposition of two fundamental cascade processes, one a hadronic, the other an electromagnetic (EM) cascade. In the rare case of a primary gamma ray or electron initiated shower an EM cascade only is produced if we disregard photonuclear and other relatively rare processes that occur occasionally. The EM cascade is well understood (for details see Chap. 4) and poses only practical problems, mainly because of the very large number of participating particles, if we deal with very high energies. However, a major problem exists with the hadronic cascade, as briefly mentioned above, because we still do not have an all-inclusive and self consistent theory of hadronic interactions to describe the collision and particle production processes.

Associated with the hadron cascade are its decay products. Some of these are again hadrons that remain in the hadronic channels of the simulation, others are leptons, mainly muons and neutrinos, and particles that enter electromagnetic channels, the bulk of which are the photons from neutral pion decays. But also decay products of kaons, charmed particles and muons, such as electrons and photons, and matter-antimatter annihilation products contribute to the EM channel. All the so-called EM source products trigger EM sub-cascades that are superimposed and interlaced with the hadron cascade and make up the bulk of all the particles in a well developed shower.

On the other hand, once created the muons propagate through the atmosphere and are little affected, suffering only ionization losses, unless they are extremely energetic or of very low energy. In the former case they may be subject to bremsstrahlung whereas in the latter to decay before reaching ground level.[1] In most cases the neutrino components are disregarded unless a specific interest is pursued, such as in the study of horizontal or upward going air showers (see Chap. 1, Sects. 1.3 and 19.5.2).

Through the years a wide scope of models describing hadronic interactions had been developed and were used, ranging from the very naive pictorial collision and particle production descriptions of the early days, where pions were the only secondary particles considered, to today's contemporary formulations that are based on modern *quantum chromodynamics* (QCD) and the *Gribov-Regge* theory (for details see Chap. 3 and references listed therein).

At the beginning of Monte Carlo (MC) based air shower simulations in the late fifties and early sixties of the last century, the hadronic cascade models were built on knowledge which had been acquired mainly from the study of individual very high energy hadronic interactions in photographic (nuclear) emulsion exposed to the cosmic radiation on mountain tops or during balloon flights, and by Wilson Cloud Chambers at ground level (Bradt et al., 1965; Tanahashi, 1965; Murthy et al., 1968a, b, 1968c; Fomin and Khristiansen, 1970; Grieder, 1970a, b, c). The statistics of these data are poor but many of the fundamental properties of ultrahigh energy hadronic interactions could be established that are still valid today. The knowledge that resulted from accelerators experiments was extremely modest as at that time the energy of the machines was limited to the order of 1 GeV.

[1] In air at high energies these processes have comparable cross sections.

It was only with the coming into operation of the 30 GeV proton synchrotron at CERN in Geneva (Switzerland) in 1959 that significant new knowledge became available, causing a major evolution of the models and, above all, after the Intersecting Storage Ring (ISR) at CERN began operating. This storage ring collider produced proton–proton collisions at fixed target (laboratory frame) equivalent energies of up to 1.8 TeV by 1972, revealing a lot of new phenomena and set bench marks or *anchor points* for simulation models in the TeV energy range. However, the picture that evolved from the ISR had to be extrapolated enormously, by at least 6 orders of magnitude, to handle the first few generations of interactions, even of moderately energetic showers, what made the predictions rather unreliable.

Moreover, considering nuclear projectiles colliding with the light nuclei of the atmospheric constituents at 10^{18} eV and not just pp-collisions reduced the credibility of the models even more. Subsequent heavy ion fixed-target experiments at CERN and Fermi National Accelerator Laboratory (FNAL) in the US yielded valuable insight into the collisions of nuclei with nuclear targets and served as guideline to formulate interaction models.

Other important steps forward that helped to orient the model makers could be made when the $p\overline{p}$ collider at CERN, the Tevatron at FNAL and more recently the Relativistic Heavy Ion Collider (RHIC) at Brookhaven, NY (USA) became operational. However, the ultimate step forward is expected to take place when the Large Hadron Collider (LHC) at CERN in Geneva will produce its data at (7+7) TeV (pp-collisions) in the center of mass, which corresponds to $\sim$100 PeV (10^{17} eV) in the laboratory frame. This energy is well within the air shower domain.

The LHC results are expected to answer most of the relevant questions concerning hadronic interactions and particle production in pp-collisions in this energy domain. Hopefully it will also deliver data of heavy ion collisions at comparable energies per nucleon in the not too distant future. The LHC data will allow us to check and adapt our simulation models. They will also be the base to build new mathematical models that can accurately reproduce accelerator results up to this energy. The degree of extrapolation needed to simulate interactions at the highest cosmic ray energies (at present $\sim 3 \cdot 10^{20}$ eV) will then be reduced drastically, thus improving the reliability of air shower simulations.

In the following sections we will outline the general strategy and architecture of air shower simulation programs rather than discuss the advantages and disadvantages of specific models. Results of some of the presently popular models and program packages are presented in Sects. 11.6 and 11.7.

20.2 Monte Carlo Methods

20.2.1 Simulation Strategy

Comprehensive computer programs to simulate high energy hadronic or electromagnetic cascades, or entire air showers, are highly complex unless gross approximations

are being made. Basically two different cascades, the hadronic and the electromagnetic, must be included in a complete air shower simulation. All relevant processes must be considered, most of which are of stochastic nature and many are in competition with each other, requiring the folding of distributions and appropriate random selection of the individual competing interaction or decay processes. Moreover, in place of the standard atmosphere specific local and seasonally dependent atmospheric profiles as outlines in Sects. 7.7 and B.3 (Keilhauer et al., 2004) must be considered for accurate simulations, as well as molecular effects of the atmospheric constituents on the radiation length and geomagnetic effects (Cillis and Sciutto, 2000; Hansen et al., 2005). In addition, a large number of Lorentz and angular transformations are required since most processes must be handled in the center of mass or in the respective rest frame of the particular interaction or decay, and the calculations must be carried out in space and time.

Furthermore, cascade simulations must include a variety of crucial observables for the subsequent analysis, for the comparison with experimental data, to carry out correlation studies, and for the interpretation of the data. This implies that each particle must carry a number of parameters that specify its state, i.e., the particle type (mass, charge, etc.), its energy, E, or momentum, p, the location of its creation in space and time, x, y, z, t, and the angular orientation of the trajectory with respect to a reference frame, θ and ϕ. The running time, t, is taken with respect to a reference clock. The latter is usually set to zero at the instant of the first interaction. Many of these parameters are also required to handle the propagation in the atmosphere and the interaction or decay processes during the simulation.

Additional and very useful parameters for getting deeper insight into the cascade process are the so-called *genetic parameters*. These reveal the generation and height of the interaction where a particle was created, the height of decay if the particle is unstable, such as a pion, kaon, hyperon or a charmed particle, or if it is subject to annihilation, such as an antinucleon, in order to know the height of origin of the resulting muon and neutrino, and possibly additional data. All of these parameters, including those mentioned before, are assigned at the point of creation of the particle. They require updating after each process to which the particle is subjected and at the end of the particular trajectory, after propagation to the next point of interaction or decay, and when passing an observation level. There the particle and its parameters are recorded (stored) for subsequent analysis and evaluation of the simulated shower data with an analysis program.

Consequently, the execution of cascade simulation programs requires very long computing times, even on fast machines, particularly for energetic cascades where the number of particles involved becomes very large. The vast amount of data that are being produced in air shower simulations require also unusually large mass storage capabilities. Additional complexity is introduced if the atmospheric Cherenkov or fluorescence components must be included. In this case the amount of data runs the risk to diverge and more sophisticated computational methods must be employed, so called *hybrid* methods.

A variety of *hybrid* approaches and simplifications had been proposed by many authors and are currently being used, including the so-called thinning method and

transitions to analytical methods once the particle number is very large and the fluctuations become small. However, these methods bear the danger of being inaccurate or even unreliable. Hybrid methods are briefly discussed in Sect. 20.3.

In general the development and propagation of a cascade from the point of initiation (first interaction) downstream to the level of observation is far more time consuming than the subsequent analysis of the produced data, i.e., the sorting of the particle parameters at the required observation levels, to form spectra and distributions. This situation may provoke a programmer to merge the analysis with the simulation to simplify the operation and avoid mass storage of data. This, however, is a great disadvantage since the vast amount of data resulting from the costly and time consuming simulation is lost for future analysis.

It is therefore highly recommended to separate the cascade and/or shower simulation program from the analysis program to maintain the utmost flexibility and the ability to carry out later analyses of the data, to study other aspects of a particular set of simulations. In addition, from the previous discussion it is evident that the hadron cascade and the resulting decay products that are led into the leptonic (muon and neutrino) channel can be separated easily and in a very natural way from those that must be treatment subsequently by the EM cascade simulation routines. The proper separation of the hadron-muon and the EM cascade, and the separate treatment, will prove to be most useful and guarantees the highest degree of flexibility, as will become evident below.

A variety of data that emerge in general automatically during the hadronic cascade simulation process, subsequently called *Step 1*, some of which are most useful not only for on-line internal statistics, housekeeping and the surveillance of the simulation process, but are also of scientific significance, such as, e.g., the elasticity and secondary particle multiplicity distributions of the hadronic interactions in the different energy bins, and many more, can and should be stored directly during simulation for later use. The same applies for the EM cascade simulation, subsequently called *Step 2*. The merger of the results of the two simulations that form the complete air shower is referred to as *Step 3*. Figures 20.1a, and b and 20.2 show the three steps schematically.

In the following we will briefly discuss some more details of the simulation strategy and outline a program architecture on the basis of the very successful ASICO program system as an example. ASICO was the first highly structured and very detailed air shower simulation program that contained all the essential hadronic physics that was known from the 30 and 60 GeV machines at CERN and Serpukhov (former U.S.S.R.), and from emulsion experiments, even in its initial version, and treated all processes kinematically correct without using dubious approximations or short-cuts. Its size and complexity was such that at that time it could only be run on very large and powerful main frame computers, the reason why in the late sixties and early seventies of the last century the initial calculations with ASICO by this author were carried out at CERN in Geneva with a CDC6600 machine, and later on IBM and CRAY computers.

ASICO contained initially nucleon resonances, cluster formation, the essentials of the thermodynamic (statistical) model, and ideas that were borrowed from

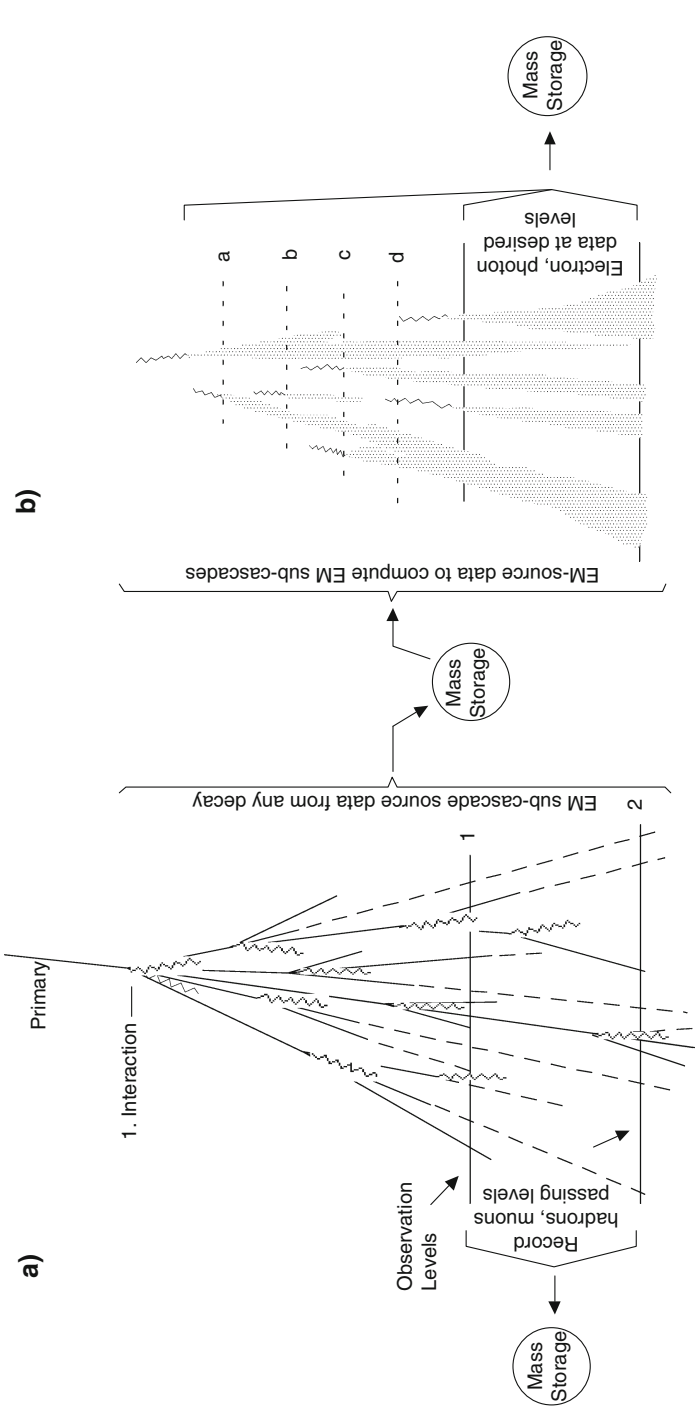

Fig. 20.1 Schematic representation of air shower (cascade) simulation procedure. (**a**) shows *Step 1* which generates and handles the parent hadron cascade (*solid lines*) and the muon decay products (*dashed lines*) together with the electromagnetic decay channels (*wavy lines*). (**b**) shows *Step 2*, the electromagnetic cascade simulation, using the EM sub-cascade parent particles produced in step 1 (Grieder, 1981, 1987)

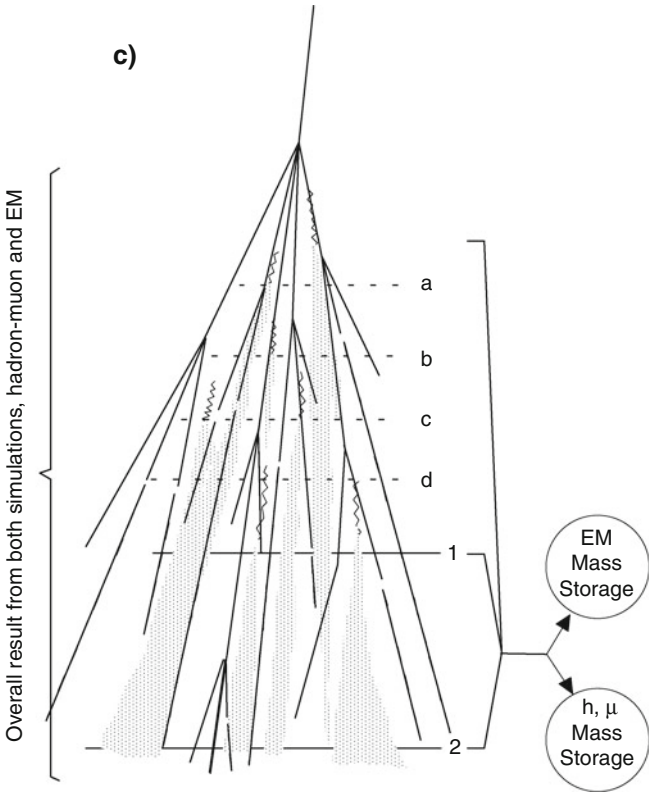

Fig. 20.2 *Step 3* which is the merger of steps 1 and 2, i.e., the sum of Fig. 20.1a, b (Grieder, 1981 and 1987)

ultrahigh energy cosmic ray studies with emulsion. Pion interactions were treated differently from nucleon interactions, including different elasticity distributions for the two processes and, as a novelty at that time, it considered nucleon-antinucleon production.[2]

One of the outstanding results that emerged from the work with this program was the prediction of the rapid rise of the nucleon-antinucleon ($N\overline{N}$) production cross section beyond several 100 GeV. The simulations with ASICO have shown that in order to generate air showers as they are observed at ground level, $N\overline{N}$ production is essential (Grieder, 1970a, b, 1971a, b) (see Sect. 13.6). Without $N\overline{N}$ neither the electron-muon nor the hadron-muon ratios in air showers could be correctly predicted. This prediction was confirmed in 1972 by the first ISR experiments (Albrow et al., 1972; Alper et al., 1972, 1973a, b; Banner et al., 1972). ASICO

[2] Murthy et al. (1968a, b, c) pursued a similar idea in their calculation but the simulation was not carried out in a self-consistent manner.

had also demonstrated that naive Feynman scaling could not generate air showers correctly (Grieder, 1973, 1977). ASICO had been continuously updated, expanded and adapted as new knowledge became available. This can only be done efficiently with a highly structured program architecture, such as ASICO that guarantees a very high degree of flexibility, the reason why we take ASICO as an example.

ASICO stands for "Air shower SImulation and COrrelation" and is in fact an entire program system. It includes the hadron cascade generator[3] with the associated muon shower, the electromagnetic cascade generator,[4] a universal analysis program to produce spectra and three-dimensional distributions using any combination of the set of 12 parameters which ASICO uses to define the particle (including 4 genetic parameters), a target diagram extractor, and a three-dimensional EM density matrix program to compute the distribution of the EM component, the shower size and the array efficiency, both with plotting options for two and three dimensional displays. In addition a general correlation study program was originally available, too. Part of the ASICO program system is the parent of the currently popular CORSIKA program, maintained and continuously updated and expanded by the Karlsruhe KASCADE simulation team and its associates (Knapp and Heck, 1993; Heck, 1997; Heck and Knapp, 1998; Heck et al., 1998a, b; Heck and Schröder, 1999; Heck, 2004a, b, 2006a, b; see also http://www-ik.fzk.de/corsika/). The structure of CORSIKA is essentially the same as that of ASICO.

The essential difference between ASICO as it was when it was given to the KASCADE group in 1988 by this author and the present-day CORSIKA is that the old interaction models, the so-called event generators, had been exchanged by contemporary ones, most of which are listed in Sect. 3.11. Some of these, too, are by now obsolete but are listed for historic and reference reasons. A detailed description of CORSIKA and operating instructions are available from the Karlsruhe group (e.g., Heck and Pierog, 2006). ASICO is no longer available.

20.2.2 Program Architecture

In general it is necessary to analyze or re-analyze the results of a set of cascade simulations at a given level for a variety of theoretical reasons or for different experimental configurations several times. Appropriate storage of the data is therefore both necessary and economical. There may also be operational reasons for interrupting a long computational procedure, thus requiring it to be broken up into convenient steps with intermediate data storage.

Data storage is a major problem, particularly if their number is large, as is the case for most cascade simulations. It is important that the kind of data that have to be stored preserve a maximum of relevant information of the simulation process and of its results, while maintaining at the same time the utmost flexibility. Experience

[3] Any kind of external interaction model (event generator) can be plugged in.

[4] Any kind of external EM cascade generator can be inserted.

has shown that the raw data are usually of prime interest to most subsequent users of cascade simulation data, particularly to experimental groups. By raw data we mean the list of all the particles and parameters that end users may want to have for future analysis, either for directly producing spectra and distributions, or for folding with experimental configurations and trigger conditions, to compute detector or array responses, or to propagate and analyze the shower constituents at a particular observation level in a specific detector, such as a calorimeter.

These data include essentially all particles that reach (or penetrate) one or several *predetermined observation levels*, i.e., the altitude of the experimental site(s) under consideration. In case of hadrons and muons the number of particles involved is large but not too large to be stored together with 12 relevant parameters per particle, even for very energetic showers ($E_0 \geq 10^{18}$ eV). Data resulting from electromagnetic cascades, or from Cherenkov or fluorescence yield calculations involve too many particles and quanta that cannot be stored in a practical manner individually, but in the form of density matrices. Variable matrix resolution can be used in this case to retain structural details in the core area for later investigations.

In addition, to study for example the longitudinal development of the electromagnetic cascade of a shower, one requires in general many observation levels, say one every 10 g cm^{-2}, to generate the development (or transition) curves, whereas lateral distributions of the different particle types are usually needed just for the level of the experimental site. This situation together with the fact that the hadron-muon cascade (Step 1), which is the parent of the electromagnetic cascade that generates all the source particles that produce the numerous electromagnetic sub-cascades in a second generation cascade process (Step 2), both adding up to form eventually the complete photon-electron shower, suggest to separate the simulation of the electromagnetic component from that of the hadron-muon component, as proposed in Sect. 20.2.1 (Figs. 20.1 and 20.2). The block diagram of Fig. 20.3 illustrate this concept.

The hadron cascade products together with the resulting muons (and neutrinos) are propagated in the usual way. The parameters of all the particles reaching one or several of the predetermined observation levels are fully updated and recorded on a separate mass storage device for later analysis. On the other hand, cascade products that enter electromagnetic channels are at once recorded on a second storage device with all their parameters updated at the point of creation, including the information of the location of their creation in space and time (c.f. Fig. 20.3). These data are processed later on with an electromagnetic cascade simulation program that creates analogous but electromagnetic raw data, usually in the form of density matrices at the desired observation level(s), or directly as longitudinal shower curves (see Figs. 6.1 and 6.2). It is evident that the vital genetic relationship among the different particles is fully preserved and the computational procedure becomes much more universal.

The two sets of raw data thus produced are now in a most general and highly flexible form. They can be used by third parties for an almost arbitrary variety of analyses, for correlation studies or as input data for simulating particular experimental configurations such as calorimeter or entire array responses. With the exception

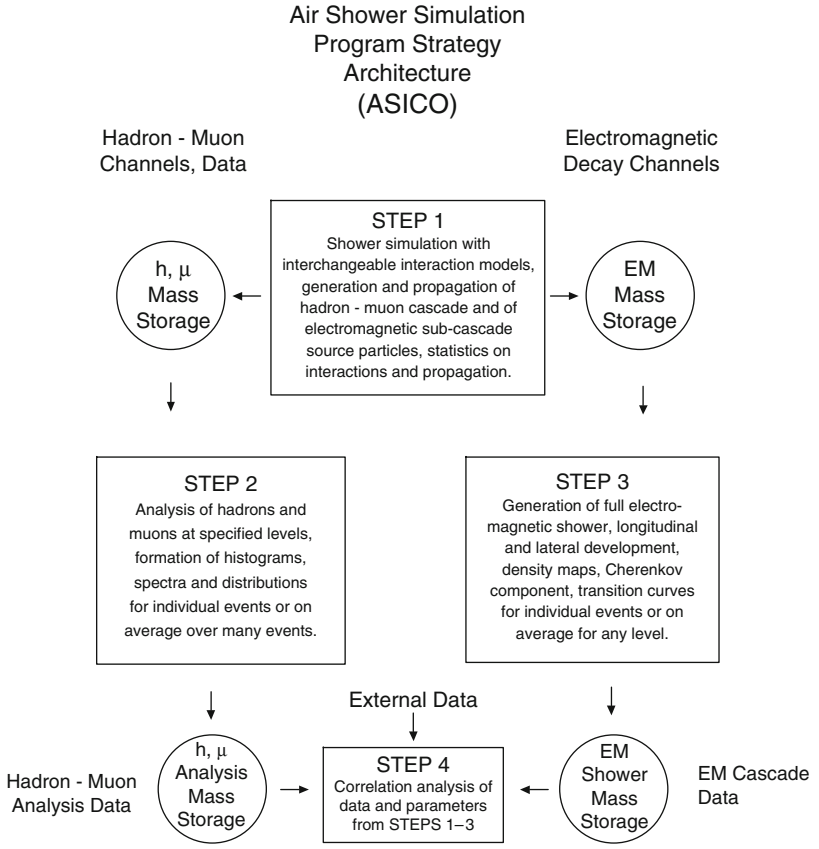

Fig. 20.3 Coarse block diagram of the general strategy behind the ASICO air shower simulation program system (Grieder, 1979)

of calorimeter response simulations, the demands on the computing facilities for analyzing the raw data are by far more modest than in the previous steps for the simulation. The block diagram shown in Fig. 20.3 illustrates some of the possibilities offered by the program architecture as outlined above. A more detailed description of this approach and of its merits is given elsewhere (Grieder, 1979).

A coarse flow diagram of the ASICO hadron-muon and EM source particle generator part is shown in Fig. 20.4a, b as an example. Without going into details, the program principle is to pick either from a spectrum or a set of prefixed primary particles (INPRIM in part (a) of the flow diagram)[5] the next in line and propagates the particle. A random generator routine (FIRST INTERACTION) selects the particle type-dependent location of the first interaction in the atmosphere unless it is prefixed, which may be desirable for certain studies.

[5] Capitalized names refer to specific boxes in the flow diagram.

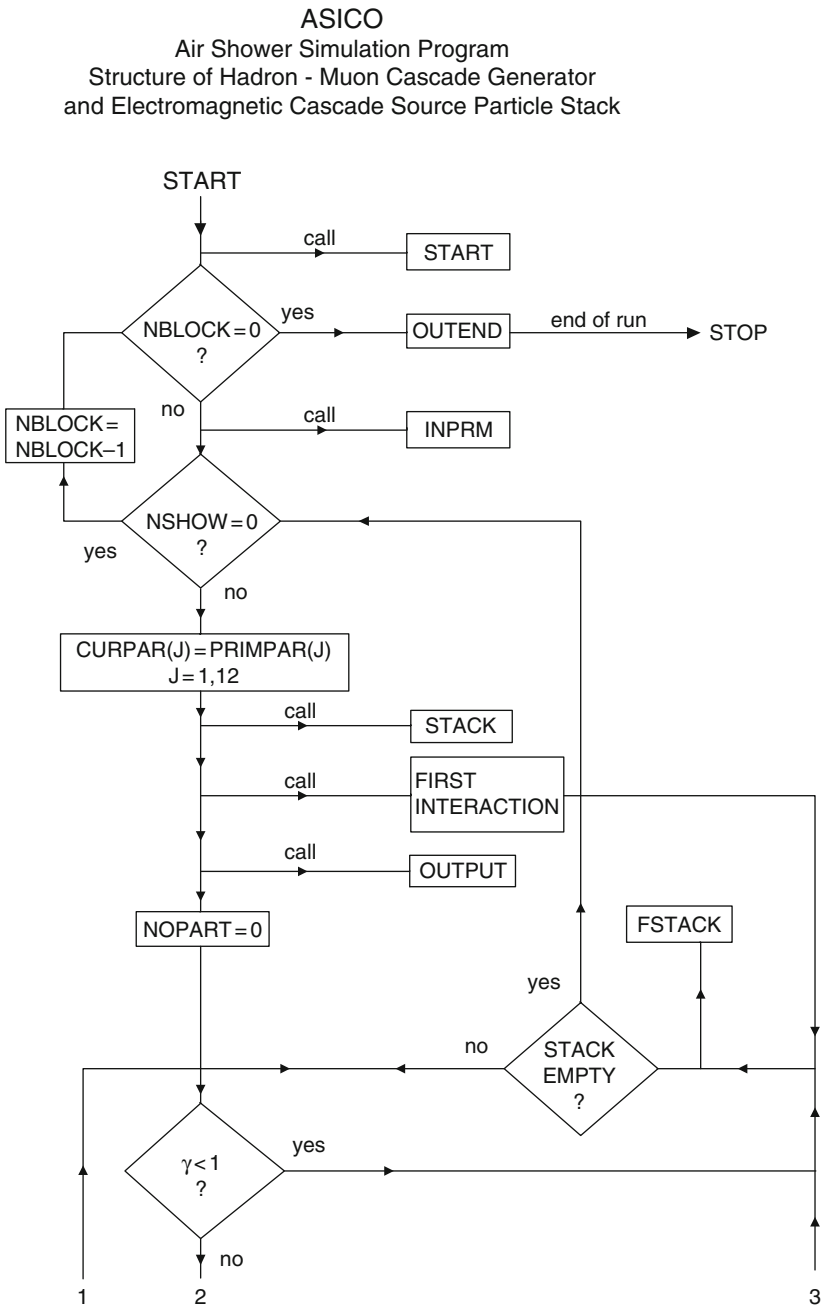

Fig. 20.4 (**a**) Part 1 of the flow diagram of the hadron-muon cascade simulation part of the highly structured ASICO air shower simulation program, the parent of the presently widely used CORSIKA program which has become a standard (Grieder, 1987)

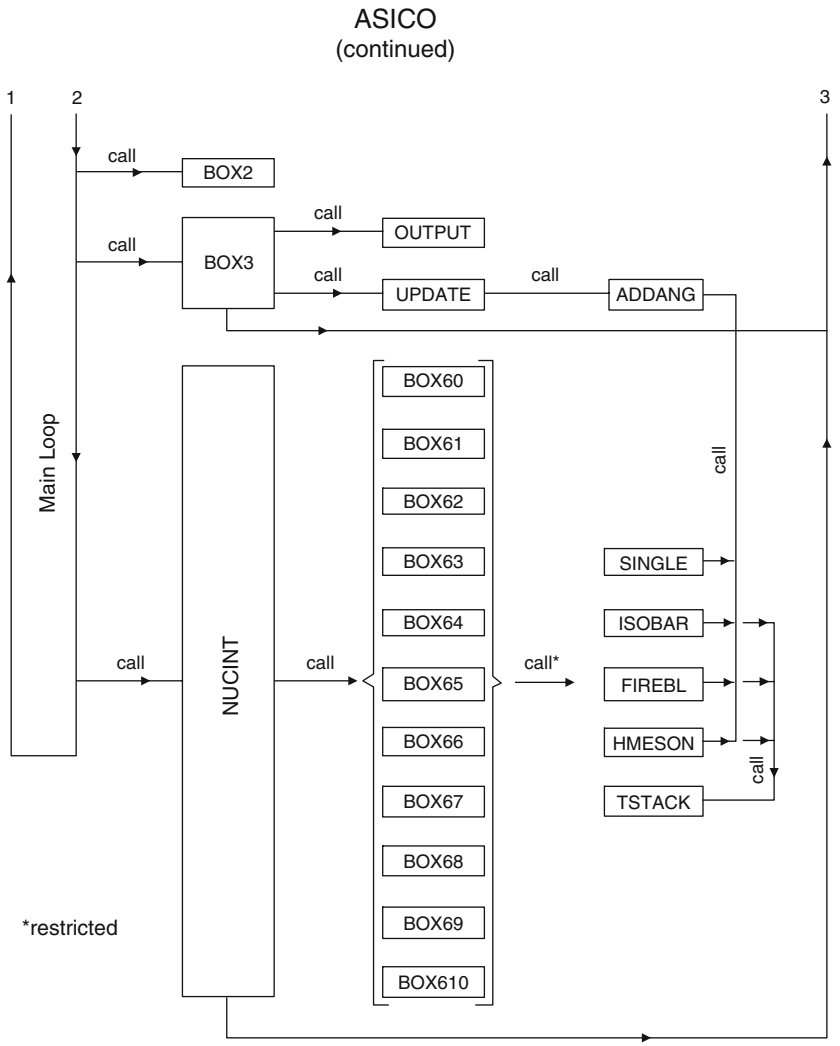

Fig. 20.4 (continued) (**b**) Part 2 of the flow diagram of the hadron-muon cascade simulation part of the ASICO air shower simulation program (Grieder, 1987)

The details of the interaction are decided in part (b) of the flow diagram and are controlled by the routine called NUCINT. In the example shown which is taken from one of the early versions of ASICO, the many boxes labeled from BOX60 to BOX610 contain energy dependent hadronic interaction processes that may call on individual sub-processes of particle production or resonance formation. These boxes, labeled from SINGLE to HMESON, are the subroutine packages that handle the sub-processes. They are fully interchangeable and can be replaced by modern event generators such as QGSJET (Kalmykov and Motova, 1986; Kalmykov and

Ostapchenko, 1993a, b; Kalmykov et al., 1997; Ostapchenko, 2006a, b) and others to handle the interactions of the different energy regimes.

All particles that emerge from an interaction are fully updated in space and time and all other parameters (genetic, etc.), and put into temporary storage (TSTACK). The last of these newly created particles continues propagation in the atmosphere along the momentum vector as determined by the interaction process from its point of creation. Depending on the nature of the particle a MC routine (BOX2) will either determine the location in the atmosphere where the next interaction will take place or initiate the energy and particle type dependent competition between interaction and decay.[6] Upon decision of that location the particle parameters are fully updated (x, y, z, t in BOX3 and θ, ϕ in ADDANG) before being submitted to the next step.

After each step of propagation BOX3 checks whether the trajectory has intersected an observation level or not. If so the particle parameters are fully updated to this level and recorded by the OUTPUT routine on the hadron-muon mass storage device. If the particle is a neutral pion or a decaying muon its parameters at decay are recorded only on the EM cascade source-particle mass storage device. If the particle is a hadron it enters again the interaction decision routine NUCINT and the cycle continues. If decay leads to a muon it is propagated in BOX2 and checked for observation level passage. If so the usual updating and recording routine is initiated. All particles that pass the lowest observation level are discarded.

As mentioned before, the last of the produced particles of the first interaction is propagated, will undergo the first of a series of second generation interactions of the particular shower. The procedure is now repeated, and so on, until the n-th generation particle runs into ground. The program then retraces backward, takes the second last particle of the n-th generation and the process is repeated. When all particles of the first n-th generation interaction are consumed the program moves upward and the sequence begins now with the first of the (n-1st) interactions, taking particle after particle, and so on until the unit called FSTACK which is the main intermediate storage stack during the cascade simulation is empty. This procedure is repeated until all the requested hadron cascades are simulated.

The procedure is now very similar for simulating the numerous EM sub-cascades initiated by the decay products that enter the EM channel. For this any kind of EM cascade program can in principle be used to get the photon and electron distributions at the requested observation levels, or to compute the longitudinal shower profile. Likewise a Cherenkov or fluorescence photon generation routine can be linked with or inserted into the EM cascade simulation routine to obtain the Cherenkov or fluorescence light pattern. Similarly, radio emission programs can be implemented to get RF field intensities. A large choice of such programs is available, where the particle number and not the physics involved are the problem. A widely used EM cascade program is the well known EGS4 code (Nelson et al., 1985).

[6] Originally, ASICO handled about one dozen kaon decay branches and about the same number of $N\overline{N}$ annihilations modes.

20.2.3 Program Reliability, Overall Tests and Simulation Supervision Routines

A major problem with large simulation programs is the uncertainty about their reliability. Doubts are frequently raised by third parties whether a particular program actually does what it is supposed to do. Besides the fact that there may be logical errors, there is a certain probability that mathematical expressions may be wrong or contain errors. These may be programming errors or simply wrongly copied formulae. Another source of errors are approximations that are unknowingly inadequate. Since no compiler can trace or find such errors, extensive testing and checking must be done before the program is used for production runs and conclusions about the physics involved can be drawn.

However, reliable testing of large programs that simulate complex physical processes is in general not a trivial affair. In the following we suggest ways and means to test cascade simulation programs that we have used successfully even for the most complex hadronic interaction models. There are obviously different approaches one can choose. The applicability of a particular method and the time and effort needed to work out a test procedure depends to some extent on the detailed architecture of the simulation program. In the following we assume a well designed, not too much interlaced program, where the various functions are clearly divided into appropriate subroutines, such as is the case for ASICO. In particular we assume that the treatment of hadronic interactions and particle production processes is handled apart from other physical processes, including propagation, by separate subroutine packages. In this case it is easy to assemble another program version, whose aim it is, to simulate with exactly the same hadronic interaction and particle production routine a common high energy accelerator experiment.

For this we do not need all the other physical processes that are included in the cascade program, nor the propagation part that can easily be checked separately. Only the Lorentz transformations together with some new sorting routines and momentum or rapidity transformations will be needed. These are used to compute histograms and distributions for longitudinal and transverse momenta and rapidity in the center of mass and laboratory frames of reference. Multiplicity and elasticity distributions, statistics on the different kinds of particles and, above all, on the energy and momentum balance, in particular accounting of energy and momentum conservation errors, should also be included. The addition of sorting and histogram routines does not require any basic modification of the strict model part of a simulation program.

Thus, with such a program an objective test can be made, even for the most complex interaction model. By simply interchanging the model routine, any kind of particle production model can be extensively tested, for all kinds of incident particles and at all energies. Apart from these partly qualitative, partly quantitative tests, the book keeping on energy and momentum balance in the center of mass and laboratory frames are valuable quantitative checks. It is well worth to incorporate some of these, that are not very time consuming, into the standard working versions

of simulation programs. It may be adequate to simply check the incident energy against the total outgoing energy of every interaction to discover significant and/or accumulating errors.

A simple, not necessarily physical model for particle production, that could be plugged into anyone's shower simulation program to check, so to say, the infrastructure of a program, i.e., to check all standard routines that handle particle propagation, the Lorentz transformation, reconstruction in space and time, and all common physical processes, such as ionization losses, Coulomb scattering, etc., excluding the particle production routine. The latter will have to be checked separately, using a method as suggested and described above.

The ultimate test of an air shower simulation program is of course the comparison of its predictions with actual experimental data (Nagano et al., 2000). From the previous discussion it is clear that it is particularly the hadronic interactions and the resulting cascade, the spectra and distributions, that require our special attention. Beyond accelerator energies this can only be done with cosmic rays under the well known very difficult conditions. One option is to use modern emulsion chambers with X-ray films and/or thermoluminescent layers as stand alone experiments or as an integral part of an air shower array with various electronic aids integrated, as discussed in Chap. 13 and used at Mt. Chacaltaya for many years. The other is the use an electronic hadron calorimeter, usually operated as part of an air shower experiment with a well equipped array for sufficient event definition.

In the past a number of calorimeters had been constructed and were operated, mainly in conjunction with high altitude installations such as those at Ootacamund (India), Gran Sasso (Italy) and at Tien Shan (Kyrgyzstan) where the conditions are more favorable because the intensity of high energy hadrons is much higher. Unfortunately, progress with these instruments was very slow and many of the data were contested. The major drawback was that the calorimeters were much too small and suffered from leakage into and out of the sensitive volume.

Much progress could be made in recent years with the giant and relatively new calorimeter that is part of the KASCADE experiment at Karlsruhe (Germany). This 320 m^2 large, deep and spatially as well as energetically highly resolving instrument has delivered valuable and reliable data that could remove some of the uncertainties. However, the altitude of only 110 m a.s.l. is disadvantageous and there are still no data available on very high energy hadrons.

The comparison made by Antoni et al. (1999) between the experimentally determined hadron distributions obtained with the Karlsruhe calorimeter and simulations carried out with CORSIKA using different interaction models (QGSJET, VENUS and SIBYLL) revealed good agreement at large core distances with different models (Engel et al., 1999, 2001; Engel, 2001, 2003; Ostapchenko, 2006b). At close proximity to the shower core large differences were found for the lateral distributions among the different interaction models. It was also found that the QGSJET model reproduced the hadronic distributions best, but when showers were classified according to muon size instead of the electron size the investigation showed that the hadron number was generally too large.

In conclusion we can say that the program architecture outlined in Sect. 20.2.2 above on the basis of ASICO as an example of a highly structured program offers ultimate flexibility to construct, modify and expand complex air shower simulation programs for generating shower raw data, i.e., experimental observables, that can be used for a wide scope of applications. These may include not only the formation of an almost arbitrary variety of histograms, spectra and distributions, but also allow correlation studies and analyses of particular experimental configurations. Moreover, raw data of the form described above are best suited for subsequent target diagram or detector and system response simulations. The tests suggested to check the reliability of cascade and entire air shower simulation programs are essentially fail-safe and should be used in conjunction with complex model calculations.

20.3 Energy Splitting, Thinning and Hybrid Methods

In view of the diverging CPU time required to run complex Monte Carlo based air shower simulations at very high energy, several methods had been suggested and were developed through the years to avoid at least in part the lengthy step-by-step treatment of the classical MC method. Two different methods had been suggested by Hillas (1981), the so-called *energy splitting* and the *thin sampling* method, sometimes referred to as the *thinning algorithm*. Another approach that was proposed by Dedenko (1968) is the so-called *hybrid method*.

All of these methods are essentially more or less gross approximations of the cascade process and most ignore all physical details over a major portion of the cascade process. They yield coarse results, partly averages with self-inflicted or intentionally generated fluctuations and illuminate the general trend of a shower. Depending on the degree of refinement maintained, the results of the different methods may or may not be sensitive to specific physical processes.

The *energy splitting method* is partly based on experience collected with *Feynman scaling* (Feynman, 1969) and the principle of *radial scaling* (Yen, 1974) in the interpretation of data from ISR experiments. The calculation is a pure MC approach carried out in the *laboratory frame* only and assigns transverse momenta to the particles. The secondary particle multiplicity manifests an approximately logarithmic increase with energy, as is the case for the classical Feynman scaling model. A description of the method and the rules of the energy splitting procedure are given in the papers of Hillas (1979, 1981).

The *thin sampling method* uses the standard MC simulation to some prefixed cutoff energy, E_{cut}, which is about three to four orders of magnitude lower than the energy of the incident primary particle. All particles are followed to this energy and treated in all details that are provided for by the MC simulation. Below this threshold the particles are only retained with a certain probability, $P = E_0/E_{\mathrm{cut}}$, for further propagation and get a weight $w = 1/P$ assigned that is relevant for assembling spectra and distributions later on for the analysis. The probability and weight assignments are repeated for the subsequent generations of interactions, and so on through the rest of the simulation. The rules for this procedure are described in

the previously mentioned paper (Hillas, 1981; see also Hillas, 1997). More recently Konishi et al. (2001) have re-assessed the validity of the thinning method for EM shower simulations, including the LPM effect.

For the *hybrid method* different approaches had been suggested and were actually developed. An excellent review of the different methods had been given by Drescher (2006). A hybrid simulation consists of two or three parts. The first consists of a standard Monte Carlo simulation that handles the entire particle cascade, the hadronic as well as the electromagnetic channels, beginning with the primary particle and ending at some *prefixed cutoff energy*, as outlined in the previous paragraph. There the procedure is being changed. Frequently this first (MC) domain covers two orders of magnitude in energy, sometimes more. Below the MC cutoff energy two different approaches are currently popular.

In one, pre-simulated longitudinal shower profiles, taken from a library, are now used in place of the MC sub-cascades that would normally be continued and followed as part of the full shower simulation process down to the observation level. These one-dimensional sub-shower profiles are then combined to a full one-dimensional shower (Gaisser et al., 1997). The resulting longitudinal profile is then fitted with a Gaisser-Hillas function (see Eq. 17.35) (Gaisser and Hillas, 1977) and the resulting parameters and data are recorded for later analysis and comparison with experimental data (Alvarez-Muñiz and Zas, 1997; Alvarez-Muñiz et al., 2002).

In the other approach, the nuclear and electromagnetic sub-cascades below the cutoff energy are generated using classical cascade transport equations to compute the sub-showers down to a second energy cutoff, using the MC results obtained at the first cutoff as initial data. Both the Monte Carlo and the analytical-numerical parts use the same physics but in the numerical part the calculation is carried out one-dimensionally, in the direction of the shower axis. The low energy source function resulting from the cascade equations serves as probability distribution for the low energy particles that are now again treated by a second Monte Carlo simulation, representing the third step that re-establishes the lateral structure (Bossard et al., 2001; Drescher and Farrar, 2003; Pierog et al., 2003, 2006; Bergmann et al., 2007). This second cutoff is frequently set to about 10^4 GeV, where the lateral spread of the cascade begins to become important.

In either of the two hybrid methods discussed here, trusted event generators such as the QGSJET (Kalmykov et al., 1996, 1997), NEXUS (Drescher, 1999), or others are used in the Monte Carlo part and to pre-calculate average secondary particle spectra for shower libraries and later use in the analytical-numerical part. In some applications low energy models such as GHEISHA (Fesefeldt, 1985) and others are used to compute low energy spectra and lateral distributions. The decays of unstable particles are often handled in a simplified manner that may vary, depending on the particular simulation, and rare processes are usually disregarded in hybrid and other simplified procedures. The very recently developed hybrid program called CONEX (Alekseeva et al., 2005; Pierog et al., 2006, 2007) appears to be well tested. It can be used for the simulation of one-dimensional shower profiles, including fluctuations, initiated by primary gamma rays, protons and iron nuclei to primary energies as high as 10^{22} eV.

Comparisons of the simulation results obtained with well tuned hybrid methods that use good standard MC simulations in the first step and are carefully adapted at the interface to step 2 have shown that the deviations between basic observables, such as the lateral distribution or the height of maximum development may be kept quite small (Drescher and Farrar, 2003; Knapp et al., 2003; Pierog et al., 2006; Pryke, 2001). However, problems may surface in the merger region, at the interface between the different computational regimes, where the three-dimensional MC process passes the relevant information on to the one-dimensional analytic continuation of the cascade. The same statement applies at the second cutoff where the transition from the analytic regime back to a MC or another procedure is performed for preparing the final data for analysis and interpretation. There, at these neuralgic points the relevant parameters must be carefully adapted and tuned.

References

Albrow, M.G., et al.: Phys. Lett., 40 B, p. 136 (1972).
Alekseeva, M., et al.: PICRC, 7, p. 139 (2005).
Alper, B., et al.: Proceedings of the XVI. International Conference on High Energy Physics, Batavia, Ill. (1972).
Alper, B., et al.: Phys. Lett., 44 B, p. 527 (1973a).
Alper, B., et al.: Phys. Lett., 47 B, p. 275 (1973b).
Alvarez-Muñiz, J., and E. Zas: Phys. Lett. B, 411, p. 218 (1997).
Alvarez-Muñiz, J., et al.: Phys. Rev. D, 66, p. 033011 (2002).
Antoni, T., et al.: J. Phys. G, 25, p. 2161 (1999).
Banner, M., et al.: Phys. Lett., 41 B, p. 547 (1972).
Bergmann, T., et al.: Astropart. Phys., 26, p. 420 (2007).
Bossard, G., et al.: Phys. Rev. D, 63, p. 054030 (2001).
Bradt, H., et al.: PICRC, 2, p. 651 (1965).
Cillis, A., and S.J. Sciutto: J. Phys. G, 26, pp. 309–321 (2000).
CORSIKA: http://www-ik.fzk.de/corsika/
Dedenko, L.G.: Can. J. Phys., 46, p. s178 (1968).
Drescher, H.J.: in Bass et al. (1999); Nucl. Phys. A, 661, p. 216c (1999).
Drescher, H.J., and G. Farrar: Phys. Rev. D, 67, p. 116001 (2003).
Drescher, H.J.: Nucl. Phys. B (Proc. Suppl.), 151, p. 151 (2006).
Engel, R., et al.: PICRC, 1, p. 415 (1999).
Engel, R.: PICRC, Invited, Rapporteur, and Highlight papers, p. 181 (2001).
Engel, R., et al.: PICRC, 2, p. 431 (2001).
Engel, R.: Nucl. Phys. B (Proc. Suppl.), 122, p. 40 (2003).
Fesefeldt, H.: The Simulation of Hadronic Showers, Physics and Applications, Report PITHA 82/02, RWTH Aachen, Germany (1985).
Feynman, R.P.: Phys. Rev. Lett., 23, p. 1415 (1969).
Fomin, Yu.A., and G.B. Khristiansen: Acta Phys. Acad. Sci. Hung. 29, S3, p. 435 (1970).
Gaisser, T.K., and A.M. Hillas: PICRC, 8, p. 353 (1977).
Gaisser, T.K., et al.: PICRC, 6, p. 281 (1997).
Grieder, P.K.F.: Acta Phys. Acad. Sci. Hung., 29, S3, p. 563 (1970a). Ibid p. 569 (1970b).
Grieder, P.K.F.: Institute for Nuclear Study, University of Tokyo, Tokyo, Japan. Report Nr. INS J 125 (1970c).
Grieder, P.K.F.: PICRC, 3, p. 970 (1971a). Ibid p. 976 (1971b).
Grieder, P.K.F.: PICRC, 4, p. 2467 (1973).

Grieder, P.K.F.: Rivista del Nuovo Cim., 7, p. 1 (1977).
Grieder, P.K.F.: PICRC, 9, p. 161 (1979).
Grieder, P.K.F.: The Architecture of Large Cascade Simulation Programs and Comments on Indispensable Tests. Proceedings of the I. International Symposium on Cosmic Ray Cascades, Implications for Particle Physics and Astrophysics above 10^{15} eV, Sofia, Bulgaria (1981).
Grieder, P.K.F.: ASICO Program System Description and Operating Manual, Physikalisches Institut, University of Bern, Switzerland (1987).
Hansen, P., T.K. Gaisser, T. Stanev, and S.J. Sciutto: Phys. Rev. D, 71, p. 083012 (2005).
Heck, D., KASCADE Collaboration: PICRC, 6, p. 245 (1997).
Heck, D., and J. Knapp: Upgrade of the Monte Carlo Code CORSIKA to Simulate Extensive Air Showers with Energies $\geq 10^{20}$ eV, Report FZKA 6097, Forschungszentrum Karlsruhe, Germany (1998).
Heck, D., et al.: Report FZKA 6019, Forschungszentrum Karlsruhe (1998a).
Heck, D., et al.: Report FZKA 6097, Forschungszentrum Karlsruhe (1998b).
Heck, D., and F. Schröder, KASCADE Collaboration: PICRC, 1, p. 498 (1999).
Heck, D.: The CURVED Version of the Air Shower Simulation Program CORSIKA, Report FZKA 6954, Forschungszentrum Karlsruhe, Germany (2004a).
Heck, D.: The SLANT Option of the Air Shower Simulation Program CORSIKA, Report FZKA 7082, Forschungszentrum Karlsruhe, Germany (2004b).
Heck, D.: The Air Shower Simulation with CORSIKA at Arbitrary Direction of Incidence, Report FZKA 7254, Forschungszentrum Karlsruhe, Germany (2006a).
Heck, D.: Nucl. Phys. B (Proc. Suppl.), 151, p. 127 (2006b).
Heck, D., and T. Pierog: Extensive Air Shower Simulation with CORSIKA. A User's Guide, Forschungszentrum Karlsruhe, Germany. Version 6.500, March 6 (2006); updated versions see CORSIKA.
Hillas, A.M.: PICRC, 6, p. 13 (1979).
Hillas, A.M.: PICRC, 1, p. 193 (1981).
Hillas, A.M.: Nucl. Phys. B (Proc. Suppl.), 52B, p. 29 (1997).
Kalmykov, N.N., and M.V. Motova: Yadernaya Fizika (Rus), 43, p. 630 (1986).
Kalmykov, N.N., and S.S. Ostapchenko: Yad. Fiz., 56, p. 105 (1993a).
Kalmykov, N.N., and S.S. Ostapchenko: Phys. Atom. Nucl. (Elementary Particles and Fields, Experiment), 56, 3, p. 346 (1993b).
Kalmykov, N.N., et al.: Bull. Russ. Acad. Sci. (Physics), 58, p. 1994 (1996).
Kalmykov, N.N., et al.: Nucl. Phys. B (Proc. Suppl.), 52, p. 17 (1997).
Keilhauer, B., et al.: Astropart. Phys., 22, pp. 249–261 (2004).
Knapp, J., and D. Heck: KfK Report 5196 B (1993).
Knapp, J., et al.: Astropart. Phys., 19, p. 77 (2003).
Konishi, E., et al.: PICRC, 2, p. 508 (2001).
Murthy, G.T., et al.: Can. J. Phys., 46, p. S147 (1968a). ibid p. S153 (1968b); and ibid p. S159 (1968c).
Nagano, M., et al.: Astropart. Phys., 13, p. 277 (2000).
Nelson, W.R., et al.: The EGS4 Code System, Report No. SLAC-265, Stanford Linear Accelerator Center, Stanford, California (Dec. 1985).
Ostapchenko, S.: Nucl. Phys. B (Proc. Suppl.), 151, p. 143 (2006a).
Ostapchenko, S.: Nucl. Phys. B (Proc. Suppl.), 151, p. 147 (2006b).
Pierog, T., et al.: Nucl. Phys. A, 715, p. 895 (2003).
Pierog, T., et al.: Nucl. Phys. B (Proc. Suppl.), 151, p. 159 (2006).
Pierog, T., et al.: PICRC, pre-conference edition, paper 0899, Merida, Mexico (2007).
Pryke, C.L.: Astropart. Phys., 14, p. 319 (2001).
Tanahashi, G.: J. Phys. Soc. Jpn., 20, pp. 883–006 (1965).
Yen, E.: Phys. Rev. D, 10, p. 836 (1974).

Chapter 21
Definitions and Relations

Overview In this chapter, which is intended to serve as a quick reference, we define terms, quantities and relations that are frequently used in air shower terminology. *Italic* terms in the explanations of Sect. 21.2 below indicate that they themselves are defined in this section. The topics are listed in alphabetic order. Details of the topics listed here can be found with the help of the Subject Index in the appropriate Chapters.

21.1 General Comments

The student of high energy cosmic ray physics and air shower phenomena will find that there is not a high degree of standardization with respect to symbols in the literature. In this chapter and throughout this book the author has attempted to use the terminology and nomenclature, i.e., the characters, symbols and abbreviations that have been adopted by a majority of authors. In some exceptional cases, however, where the same symbol is used for different observables we had to deviate from this principle to avoid confusion. A list of symbols, abbreviations and acronyms is given in Appendix C.

Inconsistencies are often encountered in the literature when dealing with *shower size*. To represent shower size we use the character N (or $N_{\rm ch}$) for the total of *all charged particles* at a given level in a shower, N_e refers to the combined *electron + positron size*, N_μ to the *muon size*, $N_\mu^{\rm tr}$ to the truncated muon size, and N_h to the *hadron number*. Thus, $N = N_e + N_\mu + N_h$. Distinction between N and N_e is often ignored by many authors when determining the shower size for experimental reasons, because of the overwhelming number of electrons in normal showers, and because of the difficulties to distinguish between the different kinds of particles with simple shower detectors. Moreover, the difference between N and N_e is on the order of 10% or less, unless we deal with horizontal or very old air showers. In addition, shower size measurements may be subject to large errors if an inadequate number of detectors are being used because they are based on the sampling technique.

Within the frame of electromagnetic cascade theory the symbol t is used to specify the thickness of a target or of a track length in a medium in units of *radiation length*, χ_0. When dealing with showers in the atmosphere, path length

P.K.F. Grieder, *Extensive Air Showers,* DOI 10.1007/978-3-540-76941-5_21,

or atmospheric depth are usually expressed in units of [g cm^{-2}], also called the *column density*, and is represented by the character X. For inclined trajectories the inclined column density along a given path in the atmosphere is referred to as the *slant depth*, X_s.

Similarly, when dealing with hadronic cascades the *interaction mean free path* (i.m.f.p.), $\lambda_{\rm int}$ ($\lambda^{\pi}_{\rm int}$ for pions, $\lambda^{N}_{\rm int}$ for nucleons, etc.), expressed in [g cm^{-2}] is frequently used in place of the interaction cross section, $\sigma_{\rm int}$, given in units of [cm^2] or barn [b] (1 barn = 10^{-24} cm^2). The two quantities are inversely proportional to each other (see Eq. 21.31).

21.2 Definitions of Terms and Quantities

Absorption Coefficient of Shower Particles. The particle number or shower size absorption (or mass absorption) coefficient μ_p of a shower of fixed primary energy with atmospheric depth is defined as

$$\mu_p \;=\; -\frac{\partial \ln N(X)}{\partial X} \;\; [\mathrm{cm^2 g^{-1}}] \;\; , \tag{21.1}$$

where $N(X)$ is the total number of particles in the shower, i.e., the *shower size*, and X is the *atmospheric depth* in g cm^{-2}, measured along the shower axis for $X > X_{\rm max}$, i.e., below shower maximum. If we are dealing with electrons one usually replaces the atmospheric depth by the thickness, t, expressed in units of *radiation lengths*, χ_0 (Greisen, 1960).

Absorption Length of Shower Particles. The absorption (or mass absorption) length of shower particles, $\lambda_{\rm abs}$, in a shower of fixed primary energy with atmospheric depth, X, for $X > X_{\rm max}$, i.e., below its maximum development, is the reciprocal of the *absorption coefficient of shower particles*, μ_p, thus,

$$\lambda_{\rm abs} \;=\; \frac{1}{\mu_p} \;=\; \Lambda_{\rm att} \cdot \gamma \;\; [\mathrm{g\,cm^{-2}}] \;\; . \tag{21.2}$$

$\Lambda_{\rm att}$ is the *attenuation length of the shower rate* in the atmosphere and γ the exponent of the shower *size spectrum*, given below (Eq. 21.13) (Greisen, 1960).

Age Parameter. The age parameter s of an air shower is related to the state of its longitudinal development. In particular it is related to the energy spectrum of the photons and electrons (positrons and negatrons) in the cascade. It varies from $s = 0.0$ to $s = 2.0$. For $s < 1.0$ a shower is called young, for $s > 1.0$ it is called old. At $s = 1.0$ the shower is at its maximum development; at $s = 2.0$ it is reduced to about 1 particle. Laterally across the shower s is not necessarily a constant but may vary with distance from the axis (Kamata and Nishimura, 1958).

Depending on the approximations used, the expressions for s given in the literature are slightly different. Without including the lateral dependence one can use the expression

$$s \simeq \frac{3t}{t + 2\ln(E/E_{\text{crit}})} . \tag{21.3}$$

Including the lateral dependence, s takes the following form

$$s \simeq \frac{3t}{t + 2\ln(E/E_{\text{crit}}) + 2\ln(r/r_M)} , \tag{21.4}$$

where E is the energy of the photon initiating the shower, E_{crit} the *critical energy*, t the thickness of the column of air traversed in units of *radiation lengths*, χ_0, r the lateral distance in units of r_M, and r_M is the *scattering length* or *Molière unit*, also referred to as the *Molière radius*.

Altitude Dependence of Shower Rate. (See *attenuation coefficient of shower rate*, also *barometric coefficient*).

Angular Distribution of Air Showers. (See *azimuthal asymmetry, zenith angle distribution*).

Approximation A (in Cascade Theory). For electrons and photons of energy much larger than the *critical energy*, E_{crit}, of the material under consideration (air), ionization losses are negligible. If one considers in cascade computations only bremsstrahlung and pair creation, and assumes complete screening, neglecting Compton scattering, direct pair creation and photo – nuclear processes, the method is called approximation A. Thus, there is no energy dissipation term included. (Rossi and Greisen 1941; Rossi, 1952; Kamata and Nishimura, 1958, Nishimura, 1967).

Approximation B (in Cascade Theory). With reference to *approximation A*, if in addition ionization losses are included, the approach is referred to as approximation B. (Rossi and Greisen, 1941; Rossi, 1952; Kamata and Nishimura, 1958; Nishimura, 1967).

Approximation C (in Cascade Theory). With reference to *approximations A* and *B*, if in addition the Compton effect is included, and the more accurate formula is used to describe the radiation process and pair production instead of the asymptotic expression, the treatment is sometimes called *approximation C*. (Misaki, 1964, 1970, 1976, 1993; Belyaev et al., 1980).

Astronomical Unit. An astronomical unit, [AU], is a unit of length or distance. It is the mean distance between the Sun and the Earth and corresponds to

$$1[AU] \;=\; 1.496 \cdot 10^8 [\mathrm{km}] \;. \tag{21.5}$$

(see also *light year, parsec*).

Atmospheric Depth. The atmospheric depth X, also referred to as the *overburden*, is the amount of matter per unit area ($\mathrm{g\,cm^{-2}}$) in the vertical column of air, overlaying a particular location in the atmosphere. At sea level it is $X(h = 0) = X_0 \simeq 1,030\,\mathrm{g\,cm^{-2}}$, at any other level it is determined by the barometric equation. For the *standard isothermal atmosphere* it is given by

$$X(h) \;=\; X_0 \cdot e^{-(h/h_s)} \;\; [\mathrm{g\,cm^{-2}}] \,. \tag{21.6}$$

h is the height above sea level and h_s is the *scale height* of the atmosphere.

For inclined trajectories the atmospheric column density or *slant depth* $X_s(\theta)$ can be approximated by

$$X_s(h, \theta) \;=\; X(h, \theta = 0) \cdot \sec(\theta) \;\; [\mathrm{g\,cm^{-2}}] \,, \tag{21.7}$$

where θ is the *zenith* or *slant angle* of the trajectory, provided that the zenith angle does not exceed about 70–80°, depending on the accuracy desired.

At large zenith angles the curvature of the Earth must be considered, requiring the *Chapman function* to compute the column density of a given path in the atmosphere (Chapman, 1931) .

Attenuation Coefficient of Shower Rate. The attenuation (or mass attenuation) coefficient of the rate of air showers of particle density $\geq \rho$ with *atmospheric depth* is defined as

$$\mu_N \;=\; -\frac{\partial \ln G(\geq \rho, X)}{\partial X} \;\; [\mathrm{cm^2 g^{-1}}] \;, \tag{21.8}$$

where $G(\geq \rho, X)$ is the rate of showers of density $\geq \rho$ and X the atmospheric depth [$\mathrm{g\,cm^{-2}}$], measured along the shower axis.

Since the slope of the *density spectrum* of air showers in the lower third of the atmosphere is essentially identical to the slope of the *size spectrum* over a wide range of shower sizes, we may also write

$$\mu_N \;=\; -\frac{\partial \ln I(\geq N, X)}{\partial X} \;\; [\mathrm{cm^2 g^{-1}}] \;, \tag{21.9}$$

where $I(\geq N, X)$ is the rate of showers of size $\geq N$.

μ_N is also related to the *absorption coefficient of air shower particles*, μ_p, namely

$$\mu_N \;=\; \gamma \cdot \mu_p \;=\; -\frac{\beta_{\text{mass}}}{\sec(\theta)} \;\; [\text{cm}^2\text{g}^{-1}] \;\; , \tag{21.10}$$

where

$$\beta_{\text{mass}} \;=\; \beta - \left(\frac{T}{P}\right)\alpha \;\; . \tag{21.11}$$

β_{mass} is the pure mass dependent part of the *barometric coefficient* β, γ the exponent of the integral *size spectrum*, α the *temperature coefficient*, T the absolute temperature, P the atmospheric pressure and θ the *zenith angle* (Greisen, 1960).

Attenuation Length of Shower Rate. The attenuation (or mass attenuation) length of the rate of air showers of particle density $\geq \rho$ or size $\geq N$ with *atmospheric depth*, X, is the reciprocal of the *attenuation coefficient of the shower rate*, μ_N, thus,

$$\Lambda_{\text{att}} \;=\; \frac{1}{\mu_N} \;=\; \frac{\lambda_{\text{abs}}}{\gamma_{\text{ave}}} \;\; [\text{g cm}^{-2}] \;\; . \tag{21.12}$$

λ_{abs} is the *absorption length of shower particles* in g cm^{-2} of individual showers in the atmosphere and γ_{ave} is the average of the exponent γ of the integral *size spectrum*, often referred to as the *spectral index* or *spectral slope* (Greisen, 1960),

$$\gamma \;=\; -\frac{\partial \ln I(\geq N)}{\partial \ln N} \;\; . \tag{21.13}$$

Avogadro's Number. Avogadro's Number, N_A, is the number of molecules per mole or in a mass in grams of substance equal to its molecular weight; it is

$$N_A \;=\; 6.022142 \cdot 10^{23} \;\; [\text{mol}^{-1}] \, . \tag{21.14}$$

Azimuthal Asymmetry. Besides the lateral displacement due to scattering, D_s, the particles in a shower are also subject to the geomagnetic field which produces an additional displacement, D_m, of the particles in the East–West direction, causing an azimuthal asymmetry with respect to the shower axis (Cocconi, 1954a, b; Nikolsky and Satzevich, 1956). The ratio, K, of the total displacement, D_{m+s}, to that due to scattering only, D_s, of positrons and electrons in a shower in the East–West

direction, sometimes referred to as the *displacement factor*, can be estimated using the following expression (Cocconi, 1954b, 1961; Galbraith, 1958; Allkofer, 1975),

$$K = \frac{D_{m+s}}{D_s} \simeq \sqrt{1 + 0.05 \left(\frac{\cos(\lambda_G)}{P} \right)^2} . \tag{21.15}$$

λ_G is the geomagnetic latitude and P the pressure in atmospheres of the place of observation. For electrons at sea level at a geomagnetic latitude of $\lambda_G = 50^\circ$ the above expression yields $K = 1.01$.

Barometric Coefficient. The barometric coefficient β expresses the dependence of the rate of showers of particle density $\geq \rho$ [cm^{-2}], $G(\geq \rho)$ (or of size $\geq N$, $I(\geq N)$), on atmospheric pressure, P, usually given in [cm Hg], for a given ambient temperature, T. It is defined as

$$\beta = -\frac{\partial \ln G(\geq \rho)}{\partial P} \ [\text{cm}^{-1}\,\text{Hg}] . \tag{21.16}$$

For showers of size $10^4 \leq N \leq 10^5$, $\beta \simeq 0.10$ [cm^{-1} Hg], it increases to $\beta \simeq 0.16$ [cm^{-1} Hg] for sizes $N \simeq 10^7$. These data apply to sea level as well as mountain altitude (Cocconi, 1961; Cranshaw et al., 1958a, b; Khristiansen, 1980).

For an isothermal atmosphere the product $P \cdot V$ is proportional to the product $M \cdot T$, where M is the mass of air within a volume V at pressure P and temperature T. If $G(\geq \rho)$ is a function of P and air density, ρ_{air} [g cm^{-3}], and since the latter is a function of temperature, one can show that

$$\beta = \mu_p - \frac{\partial \ln G(\geq \rho)}{\partial T} \cdot \left(\frac{T}{P} \right) = \mu_p - \left(\frac{T}{P} \right) \alpha \ [\text{cm}^{-1}\,\text{Hg}] , \tag{21.17}$$

where μ_p is the *absorption coefficient of shower particles* and

$$\partial \ln G(\geq \rho)/\partial T = \alpha \tag{21.18}$$

is the *temperature coefficient* of showers. (Greisen, 1956, 1960; Galbraith, 1958; Cocconi, 1961; Khristiansen, 1980). The temperature coefficient amounts to a fraction of 1% per degree. The value of μ_p differs from β by a correction due to the density effect (for details see *Temperature Coefficient*).

Cascade Unit. (See *radiation length, radiation unit.*)

Chapman Function. The Chapman function permits to compute the thickness or column density of inclined trajectories in the atmosphere accurately, taking into account the curvature of the Earth, as compared to the "flat Earth" approximation (Eq. 21.7) (Chapman, 1931). It is discussed in detail in Appendix B. Depending

on the accuracy required it should be used for trajectories whose zenith angle, θ, exceeds about 70° (Fitzmaurice, 1964).

Characteristic Length of Cascade Development. (See *radiation length, radiation unit*.)

Characteristic Length of Electron Scattering. (See *Molière radius, unit.*)

Cherenkov Angle of Emission. The angle of emission, δ, of Cherenkov radiation (light) of a relativistic charged particle in a refractive medium with respect to its direction of motion is given by

$$\cos(\delta) \;=\; \frac{1}{\beta \cdot n}\,, \tag{21.19}$$

where $\beta = v/c$, v being the particle velocity and c the velocity of light, and n is the *index of refraction* of the medium. In air at normal temperature and pressure (NTP) $\delta = 1.3°$, in water it is $\delta = 41°$.

Cherenkov Intensity of Radiation. The intensity of Cherenkov radiation for a relativistic charged particle in the wavelength interval $350\,\text{nm} \le \lambda \le 550\,\text{nm}$ is equal to 0.3 photons/cm of path in air at NTP, and 250 photons/cm of path length in water.

CKP Formula. The CKP (Cocconi, Koester and Perkins) formula is a phenomenological mathematical expression describing the momentum distribution of secondary particles emerging from a high energy proton-proton collision (Cocconi, 1961; Cocconi et al., 1962; Cocconi, 1966, 1971). It has the form

$$\frac{\mathrm{d}^2\sigma}{\mathrm{d}p \cdot \mathrm{d}\omega} \;=\; \frac{A \cdot p^2}{p_0^{1/2}} \cdot e^{-\left(\frac{p}{B \cdot p_0^{3/4}}\right)} \cdot e^{-\left(\frac{p \cdot \theta}{C}\right)}\,, \tag{21.20}$$

where p_0 is the incident proton momentum, p the secondary pion momentum, θ the angle of emission in radians ($\theta \ll 1$), all in the laboratory frame. A, B and C are independent parameters; A relates to the secondary pion multiplicity, B determines the scale of the exponential decrease of the longitudinal component of the momentum spectrum of secondaries, and C sets the scale of the transverse momentum distribution ($p_t = p\theta$).

Critical Energy of Electrons. At critical energy, E_{crit}, an electron loses equal amounts of energy through bremsstrahlung and ionization per *radiation unit* of

matter traversed (Rossi, 1952; Greisen, 1956). In a medium of atomic number Z, the critical energy is given by the approximate expression

$$E_{\rm crit} \simeq 750/Z \ \ [\rm MeV] \,. \tag{21.21}$$

In air $E_{\rm crit} \approx 83$ MeV. In Tables B.1 and B.2 of Appendix B the values of $E_{\rm crit}$ of a variety of other materials are listed.

Cross Section, Geometric Nuclear. The expressions for the geometrical nuclear cross section of a nucleon projectile on a target nucleus of mass number A is

$$\sigma_g = \pi R_0^2 A^{2/3} \ \ [\rm cm^2] \,, \tag{21.22}$$

where R_0 is the radius of the nucleon. Frequently the cross section is expressed in units of *barn* [b] (1 barn $= 10^{-24}$ cm^2).

Declination. Declination, *dec* or δ, is comparable to geographic latitude projected to the sky (the celestial sphere). It is measured to the north and south of the celestial equator in units of degrees. Points to the north have a positive declination, points to the south a negative declination. An object at the celestial equator has declination 0°, at the celestial north pole $+90^\circ$, and at the celestial south pole -90°.

Decoherence. The decoherence rate is the dependence of the n-fold coincidence rate, R_n, of a set of detectors of given area as a function of distance, d, between the detectors.

If $d \gg r_M$, where r_M is one *Molière unit* (radius), and if at distance $r \gg r_M$ from the shower axis the *lateral distribution function* of the particles is of the form $1/r^n$, then

$$R_n(d) \propto \frac{1}{d^{(n\gamma-2)}} \ \ [\rm s^{-1}] \,, \tag{21.23}$$

where γ is the *spectral exponent* (Skobeltsyn, 1949; Khristiansen, 1980). The form of the *lateral distribution function* can be determined from the decoherence curve. However, at small core distances, ($r \ll r_M$), it is rather insensitive to changes in the lateral distribution function and therefore not very suitable to study the latter.

Delta-Rays. When an electron ejected from an atomic shell has sufficient energy to produce its own trail of ionization it is called a δ-ray. The ionization which is associated with it is called *secondary ionization*.

Density Spectrum. The differential density spectrum of air showers $G(\rho)d\rho$ is the frequency of occurrence of showers having a particle density between ρ and $\rho + d\rho$ at a particular location, irrespective of shower size and location of the shower axis.

It is generally assumed in this context that all showers have the same structure. Therefore, the particle density, ρ, at a given distance r from the axis is proportional to the total number of particles in a shower, i.e., $\rho(r) = f(r) \cdot N$, where $f(r)$ is the lateral structure function.

The integral density spectrum of air showers $G(\geq \rho)$ is defined as the rate at which the charged particle density (or the mean particle density of the shower) at a fixed depth of observation in the atmosphere exceeds the value ρ. It is found empirically that the integral density spectrum follows approximately a power law of the form (Cocconi et al., 1943, 1944; Cocconi and Cocconi-Tongiorgi, 1949; Daudin, 1943, 1944),

$$G(\geq \rho) \; = \; K_\rho \rho^{-\gamma} \;\; [\mathrm{s}^{-1}] \, . \tag{21.24}$$

Depth of Maximum Development of a Shower, $X_{\max}$. The depth of maximum development of a shower in the atmosphere is the location where the showers contains the maximum number of particles in a plane perpendicular to the shower axis. It depends on the energy and nature of the primary initiating the shower and is measured from the top of the atmosphere. The rate of change of its location with energy is called the *elongation rate* (Linsley, 1977).

Displacement Factor. (See *azimuthal asymmetry*.)

Distribution Function (Lateral). (See *lateral distribution function of shower particles*.)

Diurnal Variation. The solar diurnal variation is the variation of an observable per one solar day (see *Solar time*).

Elongation and Elongation Rate. The term elongation denotes the increase in atmospheric *depth of* the position of *maximum development* of a shower in the atmosphere with increasing primary energy (for showers of a given type) (Linsley, 1977). By extension this term also refers to the corresponding increase in depth at which showers attain a given age, s. Shower type refers to the nature (mass number A) of the primary initiating the shower. Elongation is expressed in $[\mathrm{g\,cm}^{-2}]$.

The elongation rate, ER, of a shower is defined as

$$ER \; = \; \frac{\mathrm{d}X_{\max}}{\mathrm{d}\lg(E_0)} \;\; [\mathrm{g\,cm}^{-2}\text{per decade}] \, , \tag{21.25}$$

where $X_{\max}$is the depth of maximum development in $[\mathrm{g\,cm}^{-2}]$ of an average shower of primary energy, E_0. It is usually expressed per decade of primary energy.

Energy Loss Spectrum of E.A.S. The energy loss spectrum of a shower can be computed from the energy loss density distribution. The energy loss density is a shower property measured with thick detectors, in particular with deep water Cherenkov detectors (Hollows, 1969) and is expressed in MeV per unit area normal to the shower axis, per unit of path length in the direction of the shower axis. It is an observable analogous to the charged particle density, recorded by thin counters, or to the photon density of air Cherenkov detectors, and can be used to infer the energy of the primary (see Sect. 12.5 for further details).

Exclusive Cross Section, Reaction. A multi-particle reaction is called exclusive when all of the n produced particles are considered. Thus, if $a + b$ is the initial state, and n_1 is the number of particles of type c_1, etc., then an exclusive reaction is represented as

$$a + b \;\rightarrow\; n_1 c_1 + n_2 c_2 + \cdots + n_l c_l \;\; . \tag{21.26}$$

Feynman Variable, x. The Feynman variable, x, is defined as

$$x \;=\; \frac{2 p_{\ell,CM}}{\sqrt{s}} \;\simeq\; \frac{p_{\ell,CM}}{p_0} \;\; , \tag{21.27}$$

where $p_{\ell,CM}$ is the longitudinal momentum of the particle in the center of mass, p_0 its maximum value, and s is the center of mass energy squared.

Fluctuations in E.A.S. Most observables in air showers are subject to very large fluctuations from event to event when comparing apparently similar events. This is due to the numerous competing stochastic processes that are superimposed within a shower. However, the chief contributors are the hadronic processes, purely electromagnetic cascades (photon or electron initiated) are much less subject to fluctuations. Some of the most significant sources of fluctuations are the randomness and broadness of the distributions of the height of the first interaction in the atmosphere and of the elasticity and secondary particle multiplicity of the first interaction. The former is a consequence of the low density and the exponential nature of the atmosphere.

Gross Transformation. The Gross transformation allows to transform the *altitude dependence* of the rate of air showers to the *zenith angle distribution* (Gross, 1933). It is discussed in detail in Sect. B.5.

Hard Component. In the early days of air shower research, the hard component was defined as that part of the particle population that could penetrate a lead absorber of 20 cm thickness. The absorbed component was called the *soft component*.

Inclusive Cross Section, Reaction. A multi-particle reaction is called inclusive when only m out of n produced particles are considered. Frequently, in inclusive experiments $m = 1$ or possibly $m = 2$. Thus, if $a + b$ is the initial state and c_1 is produced particle 1, c_2 produced particle 2, etc., and X stands for the remaining particles, then an inclusive reaction is represented as

$$a + b \;\rightarrow\; c_1 + c_2 + \cdots + c_m + X \;\; . \tag{21.28}$$

Index of Refraction of Air. The index of refraction of air, n_{air}, depends on the density of the air and therefore on altitude h (or pressure P). It can be described by the relation

$$n \;=\; 1 \;+\; \epsilon_0 e^{-(h/h_s)} \;, \tag{21.29}$$

where $\epsilon_0 = 3 \cdot 10^{-4}$, h is the altitude in m and h_s is the *scale height* of the atmosphere, $h_s \simeq 8,400$ m at sea level and varies with altitude.

Interaction Mean Free Path. The interaction mean free path (i.m.f.p.) of a particle, λ_{int} (or λ_{int}^N for nucleons, or λ_{int}^π for pions, etc.), is the mean thickness or column of matter, measured in [g cm^{-2}], that a projectile particle traverses in a given medium or target of mass number A before undergoing an interaction. It is the depth, X [g cm^{-2}] in the target where the initial projectile particle beam intensity, $I(X = 0)$ has dropped to the $(1/e)$-th value, i.e., where

$$I(X) \;=\; I(X = 0) \cdot e^{-(X/\lambda_{\text{int}})} \;=\; \frac{I(X = 0)}{e} \;\; [\text{particles cm}^{-2}\ \text{s}^{-1}] \;\; . \tag{21.30}$$

λ_{int} can easily be calculated from the *interaction cross section*, σ_{int} [cm^2], of the particular process, using the relation

$$\lambda_{\text{int}} \;=\; \frac{A}{N_A \sigma_{\text{int}}} \;\; [\text{g cm}^{-2}] \; . \tag{21.31}$$

Substituting for σ_{int} in Eq. (21.22) the expression for the nucleon–nucleus cross section we get

$$\lambda_{\text{int}} \;=\; \frac{A^{1/3}}{\pi\, R_0^2 N_A} \;\; [\text{g cm}^{-2}] \;\; , \tag{21.32}$$

Here, R_0 is the appropriate radius of the nucleon (not the geometric radius) and N_A is Avogadro's number.

The interaction mean free path can also be expressed in units of [cm] for a given material,

$$\lambda_{\text{int}} \;=\; \frac{A}{N_A \sigma_{\text{int}} \rho} \;\; [\text{cm}] \;\; , \tag{21.33}$$

where N_A is in [molecules/mole], A, the atomic weight, in [$\text{g}\,\text{mol}^{-1}$] and ρ, the density, in [$\text{g}\,\text{cm}^{-3}$].

Invariant Cross Section. The expression $d^3\sigma/(d\vec{p}^{\,3}/E)$ is called the invariant cross section because $(d\vec{p}^{\,3}/E)$ is a relativistic invariant. This can be shown in the following steps.

$$\mathrm{d}p_x \cdot \mathrm{d}p_y \cdot \mathrm{d}p_z \;=\; \frac{\partial(p_x, p_y, p_z)}{\partial(p'_x, p'_y, p'_z)} (\mathrm{d}p'_x \cdot \mathrm{d}p'_y \cdot \mathrm{d}p'_z) \, . \tag{21.34}$$

The Jacobian determinant is

$$\frac{\partial(p_x, p_y, p_z)}{\partial(p'_x, p'_y, p'_z)} \;=\; \begin{vmatrix} \frac{\partial p_x}{\partial p'_x} & 0 & 0 \\ 0 & \frac{\partial p_y}{\partial p'_y} & 0 \\ 0 & 0 & \frac{\partial p_z}{\partial p'_z} \end{vmatrix} \;\; . \tag{21.35}$$

Using the following expressions of the Lorentz transformation,

$$\begin{pmatrix} cp_x = \gamma(cp'_x + vE'/c) \\ p_y \;=\; p'_y \\ p_z \;=\; p'z \\ E \;=\; \gamma(E' + vp'_x \end{pmatrix} \tag{21.36}$$

we get

$$\frac{\partial p_y}{\partial p'_y} \;=\; \frac{\partial p_z}{\partial p'_z} \;=\; 1 \;\; , \tag{21.37}$$

$$\frac{\partial p_x}{\partial p'_x} \;=\; \gamma \left(1 + \beta \, \frac{\partial E'}{\partial p'_x} \right) \;\; , \tag{21.38}$$

and using the relation

$$E^2 \;=\; \vec{p}^{\,2} c^2 + m^2 c^4 \;\; , \tag{21.39}$$

we obtain

$$\frac{\partial E'}{\partial p'_x} = \frac{\partial}{\partial p'_x}\left(p'^2_x + p'^2_y + p'^2_z + m^2\right)^{1/2} = \frac{p'_x}{E'} \ . \tag{21.40}$$

It then follows with Eq. (21.36) that

$$\frac{\partial(p_x, p_y, p_z)}{\partial(p'_x, p'_y, p'_z)} = \gamma\left(1 + \beta\frac{p'_x}{E'}\right) = \frac{E}{E'} \ . \tag{21.41}$$

Inserted into Eq. (21.35) yields

$$\mathrm{d}^3\vec{p} = \left(\frac{E}{E'}\right)\mathrm{d}^3\vec{p'} \ . \tag{21.42}$$

Ionization Losses of a Relativistic Particle. The ionization losses of a minimum ionizing particle in air is $\sim$2.2 MeV g^{-1} cm^2.

Landau Approximation. A three-dimensional shower theory using the Fokker – Planck approximation for multiple scattering is called a treatment in Landau approximation (Kamata and Nishimura, 1958, Nishimura, 1967).

Landau Pomeranchuk Migdal (LPM) Effect. The Landau – Pomeranchuk – Migdal (LPM) effect results in a decrease of the bremsstrahlung and pair production cross sections at very high energy (Landau and Pomeranchuck, 1953a, b; Migdal, 1956). In dense media the effect begins to play an important role at much lower energies than in air. In lead it must be considered at energies >30 TeV.

The LPM effect causes showers to develop slower, to reach their maximum development at greater depth, to be subject to larger fluctuations and to have a smaller size than corresponding showers computed with the standard Bethe – Heitler theory. Energy estimates based on electron number at shower maximum can result in an underestimation by one order of magnitude at a primary energy of 10^{17} eV if the LPM effect is disregarded (Ivanenko and Kirillov, 1977; Misaki, 1989, 1993, see also references listed therein).

Lateral Distribution Function (LDF) of Shower Particles. A large number of approximations to describe the lateral (density) distribution of shower particles are offered in the literature. (Molière, 1943; Nishimura and Kamata, 1952; Greisen, 1956, 1960; Kamata and Nishimura, 1958; Nishimura, 1967). They are based on the electromagnetic cascade theory and disregard the parent nuclear cascade. Nevertheless, they prove to be very useful for analyzing and interpreting air shower measurements. There are also many purely empirical fits and expressions that are used by various

experimentalists that will not be discussed here, however, some of these are given in Sect. 8.4.

The most frequently used distribution function is the so-called Nishimura-Kamata-Greisen (NKG) function (Greisen, 1956, see also Greisen, 1960). This semi-empirical formula which is very similar to the more exact expression derived by Kamata and Nishimura (1958), is given below.

$$f\left(\frac{r}{r_M}\right) = C(s)\left(\frac{r}{r_M}\right)^{s-2}\left(1+\frac{r}{r_M}\right)^{s-4.5} . \tag{21.43}$$

$C(s)$ is computed from the normalization condition

$$2\pi \int \frac{r}{r_M} f\left(\frac{r}{r_M}\right) g\left(\frac{r}{r_M}\right) = 1 . \tag{21.44}$$

Here, r is the distance from the shower axis, r_M is the *scattering length* or *Molière radius* and s is the *age parameter* of the shower. This formula is valid for the age parameter range $0.6 \leq s \leq 1.8$ and for $0.01 \leq r/r_M \leq 10$. The values of $C(s)$ for a range of s-values are given in Table 21.1.

Table 21.1 Values for s and $C(s)$ of Eq. (21.43)

s	0.6	0.8	1.0	1.2	1.4	1.6	1.8
$C(s)$	0.22	0.31	0.40	0.44	0.43	0.36	0.25

Since the distribution does not depend strongly on s, and because the s value of showers observed at the same atmospheric depth, say at sea level, changes slowly with primary energy, it is justified to assume in a first approximation that showers covering a reasonable primary energy range manifest the same lateral distribution function for electrons.

For the particle density distribution the following expression can be used (Greisen, 1956, 1960).

$$\rho(N,r) = \frac{0.4N}{r_M^2}\left(\frac{r_M}{r}\right)^{0.75}\left(\frac{r_M}{r+r_M}\right)^{3.25}\left(1+\frac{r}{11.4r_M}\right) \ [\mathrm{m}^{-2}] . \tag{21.45}$$

A more recent distribution obtained by Lagutin et al. (1979a, b, 1981) (sometimes referred to as Uchaikin distribution) is claimed to be in better agreement with observations. In terms of the NKG distribution it is expressed as follows,

$$\rho(r) = (m\, r_M)^{-2}\rho^{\mathrm{NKG}}\left(\frac{r}{m}\right) \ [\mathrm{m}^{-2}] , \tag{21.46}$$

where $r_M = 80\,\text{m}$ and $m \simeq (0.78 - 0.21s)$ for $0.8 \leq s \leq 1.6$ and ρ^{NKG} is the density obtained with the NKG formula.

As a rough approximation one can use the expression $\rho(r) \propto r^{-n}$, where $n \simeq 0.8$ near the shower axis, $n = 1$ at 10 m, $n = 2$ at 50 m and $n = 3$ at distances $> 200\,\text{m}$ in showers of size 10^6 at sea level.

Light Year. A light year, [ly], is an *astronomical unit* of length or distance. It is the distance traveled by light in vacuum in one year.

$$1\ [\text{ly}] = 9.461 \cdot 10^{15}\ [\text{m}] = 0.307\ \text{parsec [pc]}$$
$$1\ ]\text{ly}] = 6.32 \cdot 10^4\ \text{Astronomical units [AU]}.$$

Limiting Fragmentation Hypothesis. The limiting fragmentation hypothesis (Benecke et al., 1969) postulates the existence of limiting momentum distributions of secondaries of a collision when studied in the rest frame of the interacting hadrons. The physical idea behind this statement is a picture of the interaction as independent fragmentation of the two colliding particles. The two groups of fragments are intermixed at low energy and tend to separate in the limit of very high energies. Each group then becoming independent of the energy of the other projectile. This can be expressed as

$$E\frac{\mathrm{d}^3\sigma}{\mathrm{d}p^3}(s, y_{\text{proj}}, p_t) \rightarrow f(y_{\text{proj}}, p_t) \text{ for } s \rightarrow \infty\ , \tag{21.47}$$

where $E(\mathrm{d}^3\sigma/\mathrm{d}p^3)$ is the *invariant cross section*, p_t and y_{proj} are the transverse momentum and the *rapidity* of the selected particle in the projectile rest frame, and s is the center of mass energy squared.

Note that *Feynman scaling* and the *limiting fragmentation hypothesis* are equivalent in the fragmentation cones.

Magnetic Deflection of Charged Particles. (See *radius of curvature of charged particles in a magnetic field.*)

Mass Absorption Coefficient, – Length, of Shower Particles. (See *absorption coefficient, absorption length of shower particles.*)

Mass Attenuation Coefficient, – Length, of Shower Rate. (See *attenuation coefficient, attenuation length of shower rate.*)

Mean Square Scattering Angle, Scattering Energy. The scattering energy, E_s, is a constant in the expression for the mean square scattering angle, $\langle\theta_s^2\rangle$, as given by Rossi and Greisen (1941) in their approximation for multiple Coulomb scattering

of electrons (see also Rossi, 1952). When traversing a medium of thickness δt, t being expressed in units of *radiation lengths* χ_0 (in air $\chi_0 = 37.7\,\mathrm{g\,cm^{-2}}$), the mean square scattering angle, $\langle\theta_s^2\rangle$, is given by

$$\langle\delta\theta_s^2\rangle \;=\; \left(\frac{E_s}{E}\right)^2 \delta t \;\;, \tag{21.48}$$

where E is the total energy of the electron ($E \gg m_e c^2$), and E_s the *scattering energy* defined as

$$E_s \;=\; m_e c^2 \sqrt{4\pi/\alpha} \;=\; 21.2 \;\; [\mathrm{MeV}] \;\; . \tag{21.49}$$

m_e is the rest mass of the electron, c the velocity of light and α the fine-structure constant (1/137).

Molecular Effects on Radiation Length. (See *Radiation Length.*)

Molière Distribution. The Molière distribution describes the lateral density distribution of electrons about the axis of an air shower (more precisely of a pure electron–photon cascade) for an age parameter of $s = 1.0$. It has the form

$$f(r) \;=\; 0.45 r^{-1}(1+4r)\exp(-4r^{2/3}) \;\; , \tag{21.50}$$

where r is expressed in units of r_M, the *characteristic* or *scattering length*, also called the *Molière unit* or *Molière radius* (Molière, 1953). The above expression (Eq. 21.50) is a good approximation for values of $r \leq 2r_M$.

Molière Radius, Molière Unit. The lateral distance, r_M, an electron of *critical energy*, E_{crit}, is scattered in traversing a longitudinal distance of one unit of *radiation length* is $E_{\mathrm{scatt}}/E_{\mathrm{crit}}$ [radiation units]. This distance is called the *scattering length* or *Molière unit* (Molière, 1942, 1943, 1947, 1948a, 1948b, 1949, 1950, 1952, 1953, 1954). It is approximately 1/4 radiation unit or $9.5\,\mathrm{g\,cm^{-2}}$ and is a natural or characteristic unit of length in high energy electron scattering calculations. Thus,

$$r_M \;=\; \left(\frac{E_{\mathrm{scatt}}}{E_{\mathrm{crit}}}\right)\chi_0 \;\; [\mathrm{g\,cm^{-2}}] \;\; , \tag{21.51}$$

where E_{scatt} is a constant called the *scattering energy* (21.2 MeV) and χ_0 is the *radiation length* of the medium (Rossi and Greisen, 1941; Rossi, 1952). Numerical values for E_{crit} and χ_0 are given in Tables B.1 and B.2.

In air and expressed in units of meters we get for the Molière unit,

$$r_{M,\mathrm{air}} \;=\; \left(\frac{73.5}{P}\right)\left(\frac{T}{273}\right) \;\; [\mathrm{m}] \;\; , \tag{21.52}$$

where P is the pressure in atmospheres and T the temperature in degrees K. This quantity is also referred to as the *Molière radius*. At sea level $r_{M,\mathrm{air}} \simeq 79\,\mathrm{m}$, at 3250 m $r_{M,\mathrm{air}} \simeq 120\,\mathrm{m}$ (Cocconi, 1961; Khristiansen, 1980).

Since the equilibrium between the shower and the atmosphere is not attained, the lateral distribution at a given level is influenced by that at a higher level, where the pressure P is smaller. Greisen (1956) analyzed this effect and concluded that in the lower atmosphere the lateral spread is equal to that in a uniform atmosphere, having a pressure P_2 of the level two radiation lengths higher. Thus, $P_2 = (P - 0.07)$ [atm.] and the expression for the Molière radius should be modified to read,

$$r_{M',\mathrm{air}} = \left(\frac{73.5}{P - 0.07}\right)\left(\frac{T}{273}\right) \ [\mathrm{m}]\,. \tag{21.53}$$

Because of the approximations under which the parameters involved were derived, the Molière unit characterizes the scattering length in a medium only if the scattering angles are small and only for electron energies $\gg E_{\mathrm{crit}}$ (Crannell et al., 1978).

For a mixture of n substances the Molière radius can be computed with the formula,

$$\frac{1}{r_M} = \frac{1}{E_{\mathrm{scatt}}} \sum_{i=1}^{n} \frac{f_i \cdot E_{i,\mathrm{crit}}}{\chi_i}\,, \tag{21.54}$$

where $E_{i,\mathrm{crit}}$ and χ_i are the critical energy and the radiation length of substance i, and f_i is the fraction of the i-th substance.

Multiple Coulomb Scattering Angle. See *Mean square scattering angle*.)

NKG (Nishimura-Kamata-Greisen) Function. (See *lateral distribution function; age parameter.*)

Number Spectrum. (See *size spectrum.*)

Overburden. The overburden is the vertical column or amount of matter in $\mathrm{g\,cm^{-2}}$ overlaying a particular location, detector or array. It can refer to the atmosphere, to rock or to the combined rock and air overburden of underground installations.

The matter column along an incline is referred to as the *slant depth* (see *atmospheric depth*).

Parsec. A parsec, [pc], is an astronomical unit of length or distance. It is defined as the distance from the Sun that would result in a parallax of 1 s of arc as seen from the Earth, i.e.,

$$\tan(1'') = \frac{1\mathrm{AU}}{1\mathrm{pc}}\,. \tag{21.55}$$

Penetrating Component. (See *Hard Component*.)

Peyrou Plot. The Peyrou plot is a scatter plot displaying the longitudinal versus the transverse momentum of particles in the center of mass. It is useful for studying kinematic regions in single particle inclusive measurements (Peyrou, 1961; Horn, 1972; Sivers, 1976; see Sect. 3.6).

Pitch Angle. The pitch angle, ϕ, of a charged particle is the angle between the momentum vector of the particle and the direction (vector) of the magnetic field in which it moves.

Pseudo-rapidity. The pseudo-rapidity, η, is frequently used by high energy and cosmic ray physicists as an approximation in place of the *rapidity*, y, when dealing with relativistic secondary particles where only the angles of emission with respect to the direction of the incident momentum, θ, are known, and not the masses and momenta, p.

The angle of emission of a particle in the laboratory frame, θ_L, and the corresponding angle in the center of mass, $\theta_{\rm CM}$, are linked by the relation

$$\tan(\theta_L) = \frac{p_t}{p_{\ell,L}} = \frac{p_t}{\gamma(p_{\ell,\rm CM} + \beta E_{\rm CM})} = \frac{p_{\rm CM}\sin(\theta_{\rm CM})}{\gamma(p_{\rm CM}\cos(\theta_{\rm CM}) + \beta E_{\rm CM})}\ , \quad (21.56)$$

where $p_{\ell,L}$ and $p_{\ell,\rm CM}$ are the longitudinal momenta in the laboratory and center of mass frames, respectively, $p_{\rm CM}$ and $E_{\rm CM}$ the total momentum and energy of the particle in the center of mass, p_t the transverse momentum, and $\beta = v/c$ is the velocity in terms of the velocity of light.

If the conditions $\beta E_{\rm CM}/p_{\rm CM} \approx 1$ is fulfilled, the following expression can be used,

$$\tan(\theta_L) \simeq \left(\frac{1}{\gamma}\right)\tan\left(\frac{\theta_{\rm CM}}{2}\right)\ . \quad (21.57)$$

If in addition $p_t^2 \gg m^2$ and $p_\ell \approx E$ apply, we get the approximate expression for the rapidity in the laboratory frame, y_L, which is called the pseudo-rapidity, η_L,

$$y_L \simeq \ln\left(\frac{2p_{\ell,L}}{p_t}\right) = \ln(2\cot(\theta_L)) = \eta_L\ . \quad (21.58)$$

Using Eq. (21.71) of this chapter, the relation for the pseudo-rapidity in the center of mass is obtained.

$$\eta_{\rm CM} = \eta_L - \ln(2\gamma) \simeq y_{\rm CM} \text{ or} \quad (21.59)$$

$$\eta_{\rm CM} = -\ln\left(\tan\left(\frac{\theta_{CM}}{2}\right)\right)\ . \quad (21.60)$$

Punch-through. The longitudinal leakage of particles in a (hadron) calorimeter are usually referred to as punch- through(s). Punch-through may be caused by rare extreme fluctuations of the *interaction length* (skipping of several *interaction mean free paths*) of energetic particles (or photons), or by muon and/or neutrino contamination of a particle beam. In shielded detectors such as muon detectors electromagnetic punch-throughs may be a concern.

Radiation Length, Radiation Unit. The radiation length, χ_0 (radiation unit, ru, or *cascade unit*, cu), is the characteristic length or unit used to express thickness of matter when treating electromagnetic processes. It is the scale length for the energy loss of an electron by bremsstrahlung,

$$-\frac{\mathrm{d}E}{\mathrm{d}x} = \frac{E}{\chi_0} \,. \tag{21.61}$$

In one unit of radiation length an electron loses $(1 - e^{-1})$ of its energy by radiation.

The expression for the definition of the radiation length (unit) depends on the approximation considered in the calculation. Frequently, the simplified expression

$$\frac{1}{\chi_0} = 4\alpha r_e^2 \left(\frac{N_A}{A}\right) Z^2 \cdot \ln(183 Z^{1/3}) \ \ [\mathrm{cm}^2\mathrm{g}^{-1}] \tag{21.62}$$

is used (Rossi and Greisen, 1941; Rossi, 1952; Greisen, 1956). Here $N_A = 6.022 \cdot 10^{23}$ [mol^{-1}] is Avogadro's number, Z is the atomic number, A the atomic weight of the material, α the fine-structure constant (1/137), and $r_e = 2.817 \cdot 10^{-13}$ [cm] is the classical electron radius.

The more refined expression given by Nishimura (1967) has the form

$$\frac{1}{\chi_0} = 4\alpha r_e^2 \left(\frac{N}{A}\right) Z(Z+\zeta) \cdot \left(\ln(191 Z^{-(1/3)}) - f(Z)\right) \ \ [\mathrm{cm}^2\mathrm{g}^{-1}] \ , \tag{21.63}$$

where ζ and $f(Z)$ are

$$\zeta = \frac{\ln\left(1440 Z^{-(2/3)}\right)}{\ln\left(191 Z^{-(1/3)}\right)} \ , \tag{21.64}$$

$$f(Z) = \beta^2 \sum_{n=1}^{\infty} \frac{1}{n(n^2+\alpha^2)} \tag{21.65}$$

and

$$\beta = \frac{Ze^2}{\hbar c} \ . \tag{21.66}$$

The second expression for $1/\chi_0$ (Eq. 21.63) differs from the first only by a correction for the contribution of atomic electrons and for the deviation from the Born approximation. For small Z the correction due to ζ is effective whereas for large Z that due to $f(Z)$ becomes important (Nishimura, 1967). In air with $\chi_0 = 37.7$ g cm^{-2} this corresponds to a length, l, of

$$l = 292 \left(\frac{1}{P}\right)\left(\frac{T}{273}\right) \text{ [m]}, \tag{21.67}$$

where P is the pressure in atmospheres and T the absolute temperature of the air (Cocconi, 1961). At sea level $\chi_0 \simeq 308$ m. The radiation lengths of various materials are given in Tables B.1 and B.2.

Several authors have derived expressions for the radiation length. Genannt and Pilkuhn (1973) have considered the molecular nature of the air constituents. This brought about a reduction of the commonly used value of χ_0 for air from 37.7 to 34.6 g cm^{-2}. In a later paper, Tsai (1974) specifies a value of 36.66 g cm^{-2}. More recently, Linsley (1985) carried out a detailed analysis including molecular effects and obtained 37.15 g cm^{-2}. Bourdeau et al. (1975a, b, 1976) and Procureur et al. (1975) have studied the effect of different radiation lengths, ranging from 30 to 40 g cm^{-2}, on the shower development (for details see Chaps. 4 and 6).

Radius of Curvature of Charged Particles in Magnetic Field. The radius of curvature of a relativistic charged particle in a magnetic field, r, is given by

$$r = \frac{p\,c}{300\,Z\,H} \text{ [cm]}, \tag{21.68}$$

where $pc \simeq E$. E is the energy of the particle in eV, p its momentum in eV/c, c the velocity of light in cm/s, Z the electric charge of the particle in units of the electronic charge, and H the magnetic field in Gauss.

Rapidity. The rapidity of a particle, y, is defined as (Feynman, 1969)

$$y = \sinh^{-1}\frac{p_\ell}{\sqrt{p_t^2 + m_s^2}} = \frac{1}{2}\ln\left(\frac{E + p_\ell}{E - p_\ell}\right) = \ln\left(\frac{E + p_\ell}{\sqrt{p_t^2 + m_s^2}}\right), \tag{21.69}$$

where E and p_ℓ are the total energy and the longitudinal momentum of the particle; p_t and m_s are the transverse momentum and mass of the particle when we are dealing with secondary particles. The quantity $\sqrt{p_t^2 + m_s^2}$ is called the transverse mass. Under Lorentz transformation rapidity is additive, i.e., when going fromone frame

of reference to another parallel moving frame the rapidity distributions are simply shifted along the y-axis, they maintain their shape. Thus, we get

$$y' = \ln\left(\frac{E' + p'_\ell}{\sqrt{p_t^2 + m_s^2}}\right) = \ln\left(\frac{\gamma(E + \beta p_\ell) + \gamma(p_\ell + \beta E)}{\sqrt{p_t^2 + m_s^2}}\right) \tag{21.70}$$

or,

$$y' = y + \ln(\gamma(\beta + 1)) \ . \tag{21.71}$$

Right Ascension. Right ascension, α, is the equivalent of terrestrial longitude. Both measure an east-west angle along the equator with the zero point on the equator. For longitude it is the so-called *Prime Meridian* whereas for right ascension it is the *First Point of Aries*. The latter is the location in the sky where the Sun crosses the celestial equator at the *March Equinox*. It is measured eastward from that point. Right ascension is usually measured in hours, minutes and seconds, 24 h correspond to the full circle.

Rigidity. The rigidity R of a particle of momentum p and electrical charge Ze is defined as

$$R = \frac{p\,c}{Z\,e} \ \text{[GV]} \ , \tag{21.72}$$

where p is in GeV/c, Z in units of the electronic charge e, and R in GV.

Particles of equal rigidity moving in a given magnetic field have orbits of equal radii. As an example, a proton having a rigidity of 100 GV has twice the kinetic energy per nucleon than a helium nucleus (^{4}He) of the same rigidity, but both have the same radius of curvature in the same magnetic field.

Scale Height of Atmosphere, Isothermal. In a *static isothermal atmosphere*, for which complete mixing equilibrium of all constituents is assumed, the following relation applies for the atmospheric density $\rho(h)$ at altitude h.

$$\rho(h) = \rho_0 e^{-(h/h_s)} \ [\text{g cm}^{-3}] \ , \tag{21.73}$$

where $\rho_0 = 0.00107\,\text{g cm}^{-3}$ is the density at sea level ($h = 0.0\,\text{m}$) and h_s is the mean *scale height* of the atmosphere in [m]. h_s depends on altitude. It is approximately 8,400 m at sea level (1,030 g cm^{-2}) (Swider and Gardner, 1967).

The following relation holds for altitudes $\leq$100 km,

$$h_s = \frac{kT}{Mg} = \frac{\mathcal{R}T}{\mu g} \ \text{[m]} \ , \tag{21.74}$$

$k = 1.38 \cdot 10^{-23}$ [J K^{-1}] is the Boltzman constant, T [K] the absolute temperature, M [kg] the mean molecular mass, $g = 9.81$ [m s^{-2}] the gravitational acceleration, $\mathcal{R} = 8.314$ [J K^{-1} mol^{-1}] the universal gas constant and $\mu = 28.964$ [g mol^{-1}] the mean molecular weight of air (78% N_2, 21% O_2, 1% Ar) at 239.4 K, at sea level. Note that T is in fact a function of altitude (Brasseur and Solomon, 1986).

Scaling Hypothesis, Feynman. The scaling hypothesis (Feynman, 1969) states that at infinite energy the single-particle production cross section depends on the ratio of the center of mass longitudinal component of the particle momentum, $p_{\ell,\mathrm{CM}}$, to its maximum value, $p_{0,CM}$, and not separately on these two variables. Thus,

$$E\frac{\mathrm{d}^2\sigma}{\mathrm{d}p_{\ell,\mathrm{CM}}\mathrm{d}(p_t^2)} \;\rightarrow\; f(p_t, x) \;, \tag{21.75}$$

where σ is the total inelastic cross section, p_t the transverse momentum of the particle, and x its *Feynman variable*.

Note that *Feynman scaling* and the *limiting fragmentation hypothesis* are equivalent in the fragmentation cones.

Scattering Angle, Energy. (See *mean square scattering angle, scattering energy.*)

Scattering Length. (See *Molière radius, unit.*)

Screening Energy. The screening energy, E_{scr}, is defined as

$$E_{\mathrm{scr}} \;=\; \left(\frac{m_e c^2}{\alpha\, Z^{(1/3)}}\right) \quad [\mathrm{MeV}] \;, \tag{21.76}$$

where m_e is the rest mass of the electron, c the velocity of light, α the fine-structure constant, and Z the atomic charge of the medium.

Secondary Ionization. Secondary ionization in the context of this book is the ionization caused by *delta-rays* (δ-rays).

Shower Age. (See *age parameter.*)

Sidereal Time. One sidereal day is defined as the time required for the Earth to make one complete 360° revolution about its axis with respect to a fixed star, or a distant galaxy. It is also the time that elapses between successive transits of the *vernal equinox*. The sidereal year has a length of 365.2564 solar days. Because the Earth is moving along its orbit, a solar day is a little longer than a sidereal day. After a period of one year, one additional sidereal day has transpired compared to the number of solar days.

Sidereal Variation. The sidereal variation (of the cosmic radiation, etc.) is the variation with respect to *sidereal time*. Radiation features from distant point sources appear periodically in sidereal time or manifest sidereal variations when observed from the Earth.

Size Spectrum. The integral number or size spectrum of air showers, $I(\geq N)$, sometimes also referred to as the frequency-number spectrum, is defined as the frequency of showers containing more than N charged particles, with axis crossing unit area at a given atmospheric depth. It can be approximated by a power law of the form,

$$I(\geq N) \;=\; K_N N^{-\gamma} \;\; [\mathrm{m}^{-2}\mathrm{s}^{-1}\mathrm{sr}^{-1}]\,, \tag{21.77}$$

where γ is the exponent of the spectrum and K_N is a constant. Further details are given in Sect. 12.2.

Slant Depth. (See *atmospheric depth*.)

Soft Component. The soft component of an air shower is defined as that part of the particle population that is being absorbed by 20 cm of lead. The surviving part is called the *hard* or *penetrating component*.

Solar Time. Solar time is our daily time, from noon to noon. It is the time required for one complete revolution of the Earth about its axis with respect to the Sun. Many directional variations that we observe in heliospheric coordinates are recurrent in solar time and are called *solar diurnal variations*. Astronomical features (excluding lunar and planetary phenomena), however, are recurrent in *sidereal time*. A solar day is a little longer than a sidereal day.

Spectral Index, Slope. (See *density spectrum, size spectrum, attenuation coefficient, attenuation length*.)

Structure Function. (See *lateral distribution function*.)

Temperature Coefficient. The temperature coefficient, α, expresses the dependence of the rate of showers of density $\geq \rho$, $G(\geq \rho)$ (or the rate of showers of *size* $\geq N$, $I(\geq N)$), on temperature, T. It is defined as (see also *barometric coefficient*),

$$\alpha \;=\; \frac{\partial \ln G(\geq \rho)}{\partial T} \;=\; \frac{\partial \ln N}{\partial T} \;\; [\mathrm{cm}^{-1}\mathrm{Hg}]\,. \tag{21.78}$$

The temperature effect is in fact a combination of three separate effects. Since the air density, ρ_{air} [g cm^{-3}] varies with temperature, T, a change in temperature affects the *radiation length*, χ_0 [cm^{2}g^{-1}], and with it the lateral spread. This implies

a change in the density distribution of the particles and therefore a change in the detection efficiency of showers for a given detector setup. More specifically, the three effects are as follows:

- An increase of the air density decreases the lateral spread and increases the number of shower particles per detector area. Consequently the counter area increases effectively by a factor f that is proportional to $\rho_{\rm air}^2$. But a change in area by a factor f causes a change in the rate of showers by the factor f^γ, where γ is the exponent of the integral density spectrum. Thus, a change in $\rho_{\rm air}$ results in a factor $\rho^{2\gamma}$ in the shower rate.
- To record the same rate of showers of a given size at two different altitudes, the detector separation must be modified according to the characteristic change of the particle spread with altitude. The *decoherence rate* of showers is proportional to $r^{-\delta}$, where r is the detector separation and δ varies between 0.1 and 0.5, depending on detector configuration and altitude of observation. The dependence of the decoherence on air density is proportional to $\rho_{\rm air}^{-\delta}$.
- The rate of showers whose axis falls within a certain detector configuration and satisfy the threshold condition depends on the lateral spread of the particles. Since the spread varies as ρ^{-1}, the area for detection of the showers is proportional to ρ^{-2}.

In summary we obtain for the combined effects a dependence of the shower counting rate that is proportional to $\rho^{(2\gamma-\delta-2)}$, and the dependence on temperature is $T^{-(2\gamma-\delta-2)}$, where T is measured in [K]. Thus, the temperature coefficient is

$$\alpha \;=\; \frac{\partial \ln R}{\partial T} \;=\; -\left(\frac{(2\gamma-\delta-2)}{T}\right) \;\; [(^\circ\mathrm{C})^{-1}]\,. \tag{21.79}$$

Measurements have shown that the temperature coefficient amounts to approximately $\alpha = (-0.38 \pm 0.11)\%\ [(^\circ\mathrm{C})^{-1}]$ (Hodson, 1951). For further details see Cranshaw et al., 1958a, b; Galbraith, 1958; Khristiansen, 1980.

Zenith Angle. The zenith angle, θ, of a shower is the angle which the shower axis subtends with respect to the vertical. It is zero for vertically incident showers.

Zenith Angle Distribution of Air Showers. The zenith angle distribution of the shower counting rate $I(X,\theta)$ can be represented by the following expression,

$$I(X,\theta) \;=\; I(X,0)\cos^n(\theta) \;\; [\mathrm{m}^{-2}\mathrm{s}^{-1}\mathrm{deg}^{-1}]\,, \tag{21.80}$$

where X is the vertical depth of the observation level in the atmosphere in units of *radiation lengths* and θ is the *zenith angle* of the shower axis. The exponent n is a function of altitude. It is approximately 8 at sea level and 5 at 3,500 m altitude.

References

Allkofer, O.C.: Introduction to Cosmic Radiation, Verlag Karl Thiemig, München (1975).
Belyaev, A.A., et al.: In "Electron-Photon Cascades in Cosmic Rays at Superhigh Energy", A.T. Abrosimov Ed., Nauka (1980), in Russian.
Benecke, J., et al.: Phys. Rev., 188, p. 2159 (1969).
Bourdeau, M.F., et al.: J. Phys. G, 1, p. 821 (1975a).
Bourdeau, M.F., et al.: PICRC, 8, p. 2878 (1975b).
Bourdeau, M.F., et al.: J. Phys. G, 2, p. 57 (1976).
Brasseur, G., and S. Solomon: Aeronomy of the Middle Atmosphere, D. Reidel Publishing Company, Dordrecht/Boston/Lancaster (1986).
Chapman, S.: Proc. Phys. Soc. (Lond.), 43, p. 483 (1931).
Cocconi, G., et al.: Nuovo Cim., 1, p. 314 (1943).
Cocconi, G., et al.: Nuovo Cim., 2, p. 14 (1944).
Cocconi, G., and V. Cocconi-Tongiorgi: Phys. Rev., 75, p. 1058 (1949).
Cocconi, G.: Phys. Rev., 93, p. 646 (1954a).
Cocconi, G.: Phys. Rev., 95, p. 1705 (1954b).
Cocconi, G.: Handbuch der Physik, S. Flügge, ed., Kosmische Strahlung, XLVI/I, Springer Verlag, Berlin, p. 215 (1961).
Cocconi, G., et al.: UCRL, 10022, p. 167 (1961). (LRL 28, Part 2, VCID-144, 1 (1962)).
Cocconi, G.: In 200 BeV Accelerator: Studies on Experimental Use, 1964–1965, Lawrence Radiation Laboratory Report UCRL – 16830, Vol. 1, p. 25 (1966).
Cocconi, G.: Nucl. Phys., B28, p. 341 (1971).
Crannell, C.J., et al.: Phys. Rev. D, 18, p. 216 (1978).
Cranshaw, T.E., et al.: Phil. Mag., 3, p. 811 (1958a).
Cranshaw, T.E., et al.: Nuovo Cim., Suppl. 8, p. 567 (1958b).
Daudin, J.: Comptes Rendus Acad. Sci. Paris, 216, p. 483 (1943) (in French).
Daudin, J.: Comptes Rendus Acad. Sci. Paris, 218, p. 882 (1944) (in French).
Feynman, R.P.: Phys. Rev. Lett., 23, p. 1415 (1969).
Fitzmaurice, J.A.: Appl. Opt., 3, p. 640 (1964).
Galbraith, W.: Extensive Air Showers, Butterworths Scientific Publications, London (1958).
Genannt, R., and H. Pilkuhn: PICRC, 4, p. 2434 (1973).
Greisen, K.: Progress in Cosmic Ray Physics, North Holland, Amsterdam, Vol. 3, p. 1 (1956).
Greisen, K.: Annual Review of Nuclear Science, Annual Reviews, inc., Palo Alto, California, USA, Vol. 10, p. 63 (1960).
Gross, B.: Zeitschr. f. Physik, 83, p. 214 (1933).
Hodson, A.L.: Proc. Phys. Soc. A, 64, p. 1061 (1951).
Hollows, J.D., et al.: J. Phys. A, 2, p. 591 (1969).
Horn, D.: Phys. Rep., 4, p. 1 (1972).
Ivanenko, I.P., and A.A. Kirillov: PICRC, 8, p. 432 (1977).
Kamata, K., and J. Nishimura: Prog. Theor. Phys. Jpn., 6, Suppl., p. 93 (1958).
Khristiansen, G.B.: Cosmic Rays of Superhigh Energies, Verlag Karl Thiemig, München (1980).
Lagutin, A.A., et al.: PICRC, 7, p. 18 (1979a).
Lagutin, A.A., et al.: PICRC,7, p. 18 (1979b).
Lagutin, A.A., et al.: PICRC, 6, p. 260 (1981).
Landau, L.D., and I.Ya. Pomeranchuck: Doklady Akad. Nauk. SSSR, 92, p. 535 (1953a).
Landau, L.D., and I.Ya. Pomeranchuck: Doklady Akad. Nauk. SSSR, 92, p. 735 (1953b).
Linsley, J.: PICRC, 12, p. 89 (1977).
Linsley, J.: PICRC, 7, p. 163 (1985).
Migdal, A.B.: Phys. Rev., 103, p. 1811 (1956).
Misaki, A.: Prog. Theor. Phys., Suppl. 32, p. 100 (1964).
Misaki, A.: Acta Phys. Acad. Sci. Hung., 29, S3, p. 593 (1970).
Misaki, A.: Three-dimensional Cascade Shower in Lead, Tokyo, CRL Report 36-76-3 (1976).

Misaki, A.: Phys. Rev. D, 40, p. 3086 (1989).
Misaki, A.: Nucl. Phys. B (Proc. Suppl.), 33AB, p. 192 (1993).
Molière, G.: Naturwiss, 30, p. 87 (1942).
Molière, G.: In "Kosmische Strahlung", W. Heisenberg, ed., Springer Verlag, Berlin (1943).
Molière, G.: Zeitschr. f. Naturforschung, 2a, p. 133 (1947).
Molière, G.: Zeitschr. f. Naturforschung, 3a, p. 78 (1948a).
Molière, G.: Zeitschr. f. Physik, 125, p. 250 (1948b).
Molière, G.: Nuovo Cim., 6, Suppl., p. 374 (1949).
Molière, G.: Phys. Rev., 77, p. 715 (1950).
Molière, G.: Zeitschr. f. Naturforschung, 7a, p. 280 (1952).
Molière, G.: In Cosmic Radiation, W. Heisenberg, ed., Dover Publication, New York (1953).
Molière, G.: Phys. Rev. Lett., 93, p. 636 (1954).
Nikolsky, S.I., and I.E. Satzevich: J. Exp. Theor. Phys., 31, p. 714 (1956).
Nishimura, J., and K. Kamata: Prog. Theor. Phys., 7, p. 185 (1952).
Nishimura, J.: Handbuch der Physik, Springer Verlag, Berlin, Vol. 46/2, p. 1 (1967).
Peyrou, Ch.: Proceedings of "The Aix-en-Provence International Conference on Elementary Particles", 14–20 Sept. 1961, Plenary Sessions, II, p. 103 (1961).
Procureur, J., et al.: PICRC, 8, p. 2878 (1975).
Rossi, B.: High Energy Particles, Prentice-Hall, Englewood Cliffs, NJ (1952).
Rossi, B., and K. Greisen: Rev. Mod. Phys., 13, p. 240 (1941).
Sivers, D., et al.: Phys. Rep., 23, pp. 1–121 (1976).
Skobeltsyn, D.V.: Dokl. Akad. Nauk SSSR, 67, p. 255 (1949).
Swider, W., and M.E. Gardner: Environmental Research Papers No 272, Air Force Cambridge Research, Bedford, MA (1967).
Tsai, Y.S.: Rev. Mod. Phys., 46, p. 815 (1974).

Appendix A
Experimental Installations

A.1 EAS Arrays and Cosmic Ray Ground Facilities

A.1.1 Lists of Array and Facility Sites

In the following we present a list of air shower arrays of the past and present (Table A.1). The altitudes of the arrays are listed together with the corresponding atmospheric depths. The latter are in most cases the vertical atmospheric depths, i.e., the average vertical overburden [g cm^{-2}]. In some cases, however, authors may specify different values for the overburden in different publications for the same array. The reason for these discrepancies is that in some cases authors consider the slant depth for the average near vertical shower, e.g., $\sim 15^{\circ}$, as compared to the depth for perfectly vertical showers, that are rather rare exceptions in practice. Some table entries with similar altitudes suggest contradicting altitude-overburden relations, but these are explained by differing average atmospheric and meteorological conditions (see Sect. B.3).

Figure A.1, which is a reproduction from a web page of the Yakutsk group, shows the aperture in units of square kilometer-steradian [km^2 sr] of the largest air shower arrays of the past and present, and of arrays and detector systems currently under construction or in the planing phase.

In Table A.2 we list emulsion chamber sites, and in Table A.3 the threshold energies of the muon detectors of some of the arrays listed in Table A.1. Note that for some arrays different threshold energies were used simultaneously, in others different thresholds at different times. Table A.4 is a partial list of major gamma ray air Cherenkov detectors of past and present.

P.K.F. Grieder, *Extensive Air Showers,* DOI 10.1007/978-3-540-76941-5_22,

Table A.1 EAS array sites and experiments of past and present

Name, place, country (nearest major city, region)	Approximate Altitude a.s.l. [m]	Atmospheric depth [g cm^{-2}]
AGASA, Akeno (Kofu) Japan[a]	900	935
Agassiz, (Boston) USA[a]	183	1,020
ANI/MAKET Mt. Aragats, (Yerevan), Armenia	3,200	700
ARGO, Yangbajing, (Lhasa), Tibet, China[b]	4,370	606
Auger South, (Malargüe), Argentina	1,300–1,400	875
Auger North, (Lamar) Colorado, USA[d]	∼1,500	∼865
Bagnères de Bigorre, France[a]	456	965
Baksan, Kabardian-Balkarian Rep., Russia[c]	2,060	805
Buckland Park, (Adelide), SA, Australia	s.l.	1,033
CASA/MIA, (Dugway), Utah, USA[a]	1,435	870
Chacaltaya, (La Paz), Bolivia	5,230	530
Cornell, (Ithaca), NY, USA[a]	260	998
Cygnus, (Los Alamos), New Mexico, USA[a]	2,220	800
Darjeeling, India (Exp. at Siliguri, s.l.)	2,200	802
Dugway, Utah, USA (Durham (GB) Exp.)[a]	1,450	865
Durham, England[a]	60	1,025
EAS-Top, Gran Sasso, Italy[a]	2,005	810
Echo Lake, Colorado, USA[a]	3,260	715
El Alto, (La Paz), Bolivia[a]	4,200	630
Elbrus Laboratory	1,850	820
Evans, Mt., (Denver) Colorado, USA[a]	4,300	615
Fly's Eye 1, (Dugway), Utah, USA[a]	1,585	860
Fly's Eye 2, (Dugway), Utah, USA[a]	1,435	870
GAMMA, (Yerevan), Armenia	3,200	700
GRAND, (Notre Dame), Indiana, USA	220	1,018
GRAPES, Ootacamund (Mysor), India	2,200	800
GREX, Haverah Park, (Leeds), England[a]	220	1,018
Gulmarg, (Srinagar), Kashmir, India[a]	2,743	740
Haverah Park, (Leeds), England[a]	212	1,018
HEGRA, La Palma, Canary Islands[a]	2,250	800
Homestake, South Dakota, USA[a]	1,615	843
Issyk-Kul Lake, (Almaty), Kazakhstan[b]	1,600	845
JANZOS, New Zealand[a]	1,640	840
KASCADE-Grande, Karlsruhe, Germany[a]	110	1,022
Kiel, Germany[a]	s.l.	1,033
Kobe, Japan	s.l.	1,033
KGF, Kolar Gold Fields, (Karnataka), India[a]	920	920
L3+C (CERN, Geneva) Switzerland[a]	374	1,000
Liang Wang, Mt., Yun-Nan, China[b]	2,720	735
Lodz, Poland[a]	230	1,000
MILAGRO, (Los Alamos), N.M., USA	2,630	750
Moscow, Russia	192	1,020
Musala Mountain, Bulgaria[a]	2,925	713
NASCA, see Akeno	–	–
Norikura, Mt., (Matsumoto), Japan[a]	2,770	750
Ohya, (Nikko), Japan[a]	149	1,020
Ootacamund, (Mysore), India	2,200	800
Pamir (old), Tadzhikistan[a]	3,860	650
Pamir (new), Tadzhikistan	4,380	590

Table A.1 (continued)

Name, place, country (nearest major city, region)	Approximate Altitude a.s.l. [m]	Atmospheric depth [g cm^{-2}]
Pic du Midi, Pyrenees, France[a]	2,860	729
Samarkand, Uzbekistan	750	958
SPASE[a], SPASE-II, South Pole	3,300	695
SPICA, see Akeno	–	–
SUGAR, (Narrabri), Australia[a]	260	998
Sulphur Mountain, Alberta, Canada[a]	2,285	800
Sydney, Australia[a]	30	1,016
Telescope Array, Dugway, Utah, USA	1,400	865
Tibet, Yangbajing, (Lhasa)	4,370	606
Tien Shan, (Almaty), Kazakhstan	3,340	690
Tokyo, INS, Japan[a]	59	1,020
TUNKA-133, (Baikal), Russia[b]	675	960
UMC array, see CASA/MIA/Fly's Eye[a]	–	–
Verrières (Paris), France[a]	100	1,020
Volcano Ranch, (Albuquerque), N.M., USA[a]	1,768	834
Yakutsk, Siberia, Russia	105	1,020

[a] Shut-down.
[b] Under construction or partial operation.
[c] 1,700 m a.s.l. for underground laboratory.
[d] In planning phase or proposed.
Note: Some of the atmospheric depths listed above do not correspond exactly to the vertical air column at the specified altitude, but to the effective air column of an incident trajectory subtending a mean zenith angle of about 10–15°. This zenith angular cut is frequently used to select a reasonable number of quasi vertical events for analysis.

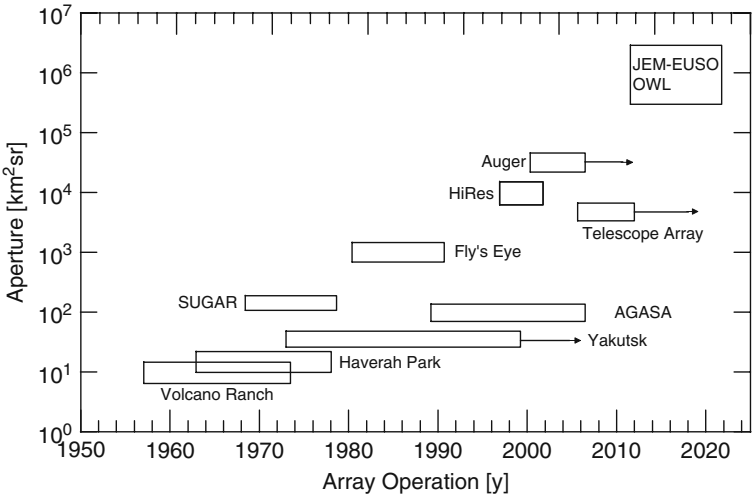

Fig. A.1 Apertures of the large arrays of the past and present, of arrays under construction or expansion, and of the proposed JEM-EUSO and OWL satellite based detector systems (curtesy of the Yakutsk Group)

Table A.2 Emulsion chamber sites

Name, place, country (nearest major city, region)	Approximate Altitude a.s.l. [m]	Atmospheric depth [g cm^{-2}]
Chacaltaya, (La Paz), Bolivia[a]	5,230	530
Fuji, Mt., Japan	3,776	650
Kanbala, Mt., Tibet, China[b]	5,500	520
Pamir Mountains, Tadzhikistan (Old Station)[b]	3,860	625
Pamir Mountains, Tadzhikistan (New Station)	4,237	600

[a] coupled with dedicated electronic detector array.
[b] shut-down.

Table A.3 Threshold energies of Muon detectors at various EAS sites

Site	Threshold energy [GeV] comments
Agassiz	$\geq$0.4, $\geq$0.5, $\geq$1.0
Akeno/AGASA	$\geq$0.5, $\geq$1.0
AMANDA	$\geq$1,000
ANI/Aragaz	$\geq$5.0
Auger	$\sim$1.0
Baksan	$\geq$230
Chacaltaya	$\geq$0.6
Cornell	$\geq$2.0
Cygnus	$\geq$1.0, $\geq$2.0
EAS-Top	$\geq$1.5, $\geq$2.0
EAS-1000	$\geq$1.0
GAMMA	$\geq$5.0
GRAPES-3	$\geq$1.0
Haverah Park	$\geq$0.3, $\geq$0.41, $\geq$0.6, $\geq$0.7, $\geq$1.0
Haverah Park/Durham	$1 \leq p \leq 1,000$ GeV/c magn. spectrometer[a]
HEGRA	$\geq$0.3
Ice Cube	$\approx$1 TeV
KASCADE	$\geq$ 0.23, $\geq$ 0.49, $\geq$ 0.8, $\geq$ 2.4
KGF	$\geq$1.0, $\geq$220, $\geq$640,$\geq$1,700, $\geq$12 TeV
Kiel	$\geq$2.0, magn. spectrometer[a]
Lodz	$\geq$0.6, $\geq$5.0
LVD	$\geq$1,300
MACRO	$\geq$1,300
MIA	$\geq$0.85
Milagro	$\geq$2, $>$500, $>$1,200
Moscow	$\geq$0.5, $\geq$10.0, magn. spectrometer[b]
Norikura, Mt.	$\geq$0.3, $\geq$0.7
North Bengal (NBU)	$\geq$2.5, 2 magn. spectrometers[a]
Nottingham	$\geq$0.41
Ohya	$\geq$14.0
SUGAR	$\geq$0.75
Tien Shan	$\geq$5.0
Tokyo (Fukui)	$\geq$2.0
Volcano Ranch	$\geq$0.22
Yakutsk	$\geq$0.3, $\geq$0.7, $\geq$1.0[c]

[a] solid iron magnet spectrometer (Earnshaw et al., 1968).
[b] maximum detectable momentum 600 GeV/c (Vernov et al., 1979).
[c] since 1979 (Diminstein et al., 1979).

Table A.4 TeV[a] gamma ray air Cherenkov detector sites and experiments of past and present (Arrays and Telescopes, partial List only)

	Approximate	
Name, place, country (nearest major city, region)	Altitude [m]	Atmospheric depth [g cm^{-2}]
AIROBIC (see HEGRA)	–	–
ANI, Aragats Mt., (Erevan), Armenia	3,200	690
ASGAT, (Targasonne) France	1,650	840
BLANCA, (Dugway, Utah) USA	1,435	865
CACTUS, (Daggett), CA, USA	610	965
Cangaroo, (Woomera), South Australia	160	1,020
Crimean AP Obs., (Nauchny), Ukraina	2,100	800
Cygnus, (Los Alamos), NM, USA	2,200	800
GAMMA, Mt. Aragats (Erevan), Armenia	3,200	700
GASP 1, South Pole	3,300	695
DICE, (Dugway, Utah) USA	1,450	865
Haleakala, (Maui, HI) USA	3,297	695
HEGRA, (La Palma), Canary Islands	2,200	800
H.E.S.S., (Windhoek), Namibia	1,800	830
JANZOS, (Wellington), New Zealand	1,640	840
MACE, (Hanle), India	4,240	600
MAGIC, (see HEGRA)	–	–
Pachmarhi, (Madhya Pradesh),India	1,100	920
Plateau Rosa, Italy	3,500	675
Potchefstrom, South Africa	1,429	880
SHALON, (Tien Shan), Kazakhstan	3,340	690
Srinagar, (Kashmir), India	1,730	835
STACEE, (Albuquerque), NM, USA	1,740	830
TACTIC,(Mt. Abu, Rajasthan) India	1,219	905
TACT, Tien Shan, Kazakhstan	3,340	690
Themistocle, (Targasonne), France	1,650	840
VERITAS (see Whipple)	–	–
Whipple Obs., Mt. Hopkins, Arizona, USA	2,380	730
Woomera, South Australia	320	1,000

[a] Some systems claim to have thresholds as low as 0.1 TeV. For a summary of early gamma ray air Cherenkov detectors, see Baillon (1991) or Lorenz (1993).

Table A.5 Locations of some old cosmic ray experimental sites

Name, location	Altitude [m a.s.l.]
Albuquerque, New Mexico (USA)	1,575
Echo Lake, CO (USA)	3,260
Ithaca, NY (USA)	260
Jungfrau-Joch (Switzerland)	3,454
Mt. Evans, CO (USA)	4,300
Sulfur Mountain Alberta (Canada)	2,285

A.1.2 Layouts of Selected Air Shower Arrays of Past and Present

On the following pages we show a selection of layouts of air shower arrays of the past and present. Some of the older arrays are historically relevant as they represent landmarks of air shower research efforts and discoveries. It should be kept in mind that layouts and configurations of most arrays are being changed in the course of time to suit new and particular scientific aims. Thus, the layouts shown here apply to particular periods. On the other hand, some array layouts had not been changed for many years. In a few cases different array configurations are shown that existed at the same site but at different times. For accurate current array configurations the reader should consult the particular research group or the proceedings of recent Cosmic Ray conferences.

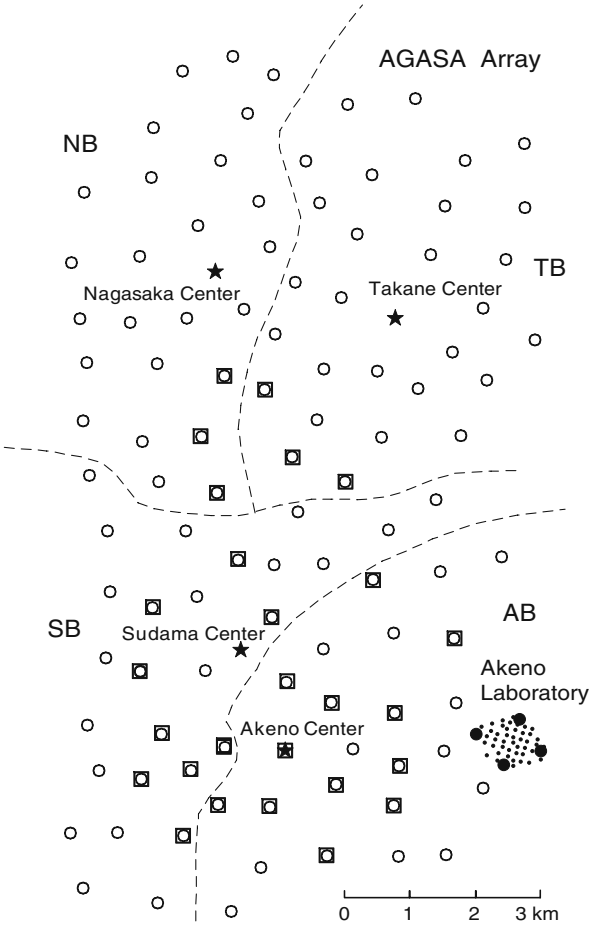

Fig. A.2 Layout of the AGASA array at Akeno (Japan), located at 900 m a.s.l. (920 g cm^{-2}). The *symbols* ○ represent scintillation detectors of area 2.2 m^2, □ muon detector of different area, · are 1 m^2 large scintillation detectors belonging to the 1 km^2 Akeno array, four of them shown as • belong to *AGASA*. The *dashed lines* identify the boundaries between the four sections, labeled as *NB, TB, SB* and *AB*, and the *symbols* ⋆ indicate the location of the branch centers (Chiba et al., 1992)

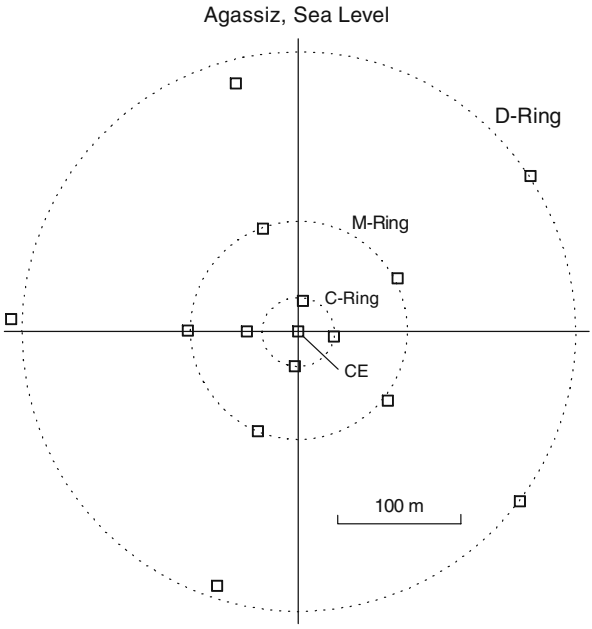

Fig. A.3 Layout of the M.I.T. detector array used by Clark et al. (1961) at Agassiz. The four detectors in the C-ring were used to record showers as small as $5 \cdot 10^4$ particles

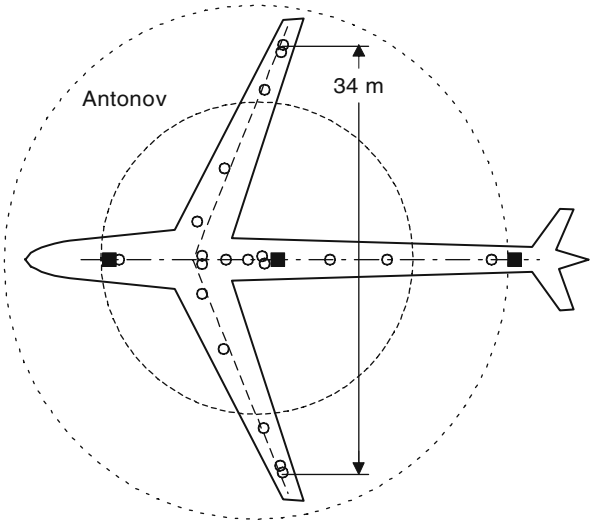

Fig. A.4 Air shower array installed on board of an air plane, used by Antonov et al. (1971, 1973) to study air showers in the stratosphere. The spark chambers (■) were used to determine the direction of incidence of the shower, the scintillation detectors (○) to determine the lateral distribution, the shower size, and to locate the position of the shower axis

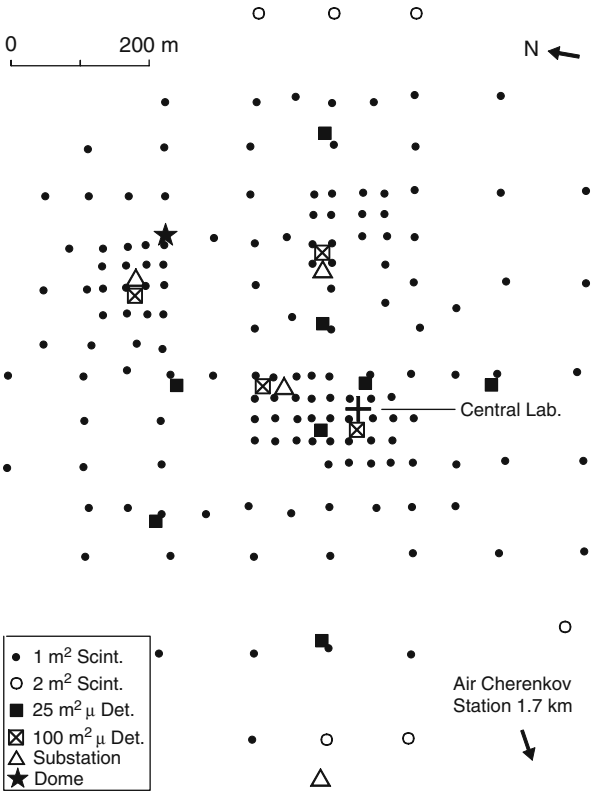

Fig. A.5 Layout of the Akeno array of the 1980s for which the detection efficiency is plotted in Fig. 2.7. This configuration covers an area of approximately 1 km^2, has a slope of 11° to the south–west and is located at 900 m a.s.l. (920 $g\,cm^{-2}$). The different detector types and dimensions are identified in the insert at the lower left. A 90 m^2 hadron calorimeter is located at the central laboratory (+). The thresholds for of the muon detectors are 1 and 0.5 GeV for the 25 and 100 m^2 detectors, respectively (for further details see Hara et al., 1979)

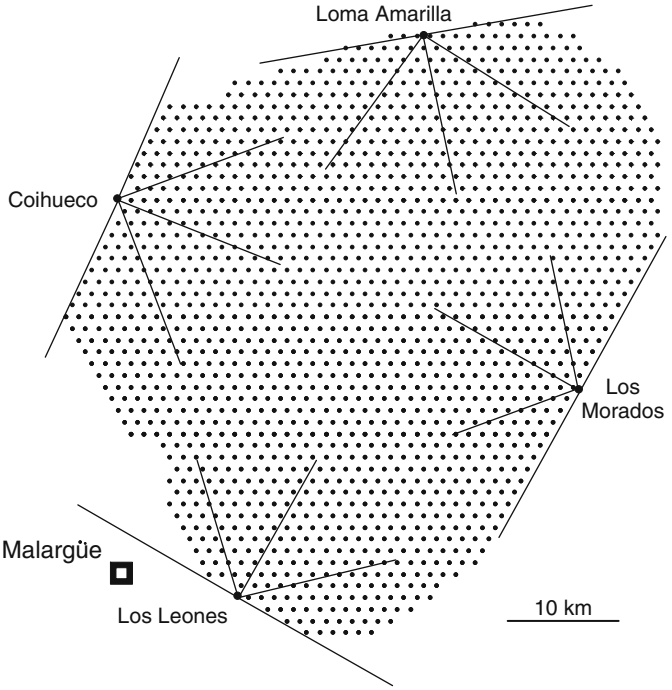

Fig. A.6 Layout of the giant Auger (South) Observatory installations in Argentina. Shown are the 1,600 deep water Cherenkov surface detectors and the four fluorescence detector telescopes that overlooking the surface array (courtesy of A. Haungs, FZ Karlsruhe, Germany and the Auger Collaboration)

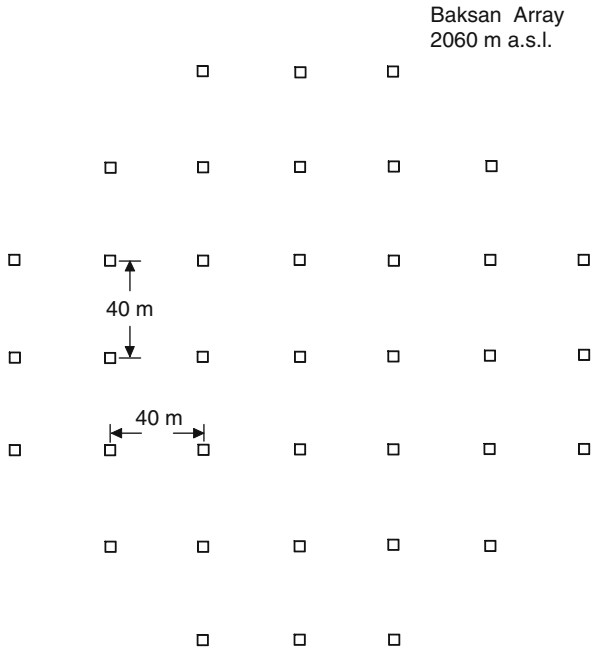

Fig. A.7 The Baksan "Andyrchy" air shower array is located above the large Baksan underground 4-level scintillation telescope. The *array* is located at an average height of 2,060 m a.s.l. and is inclined. It consists of 37 plastic scintillators of 5 cm thickness and 1 m^2 area. The detector separation as given in the figure is the approximate separation in the horizontal projection. A cutaway view of the entire installation at Baksan is drawn in Fig. A.38 of the Appendix A.2 (Alexeyev et al., 1993; Chudakov et al., 1999)

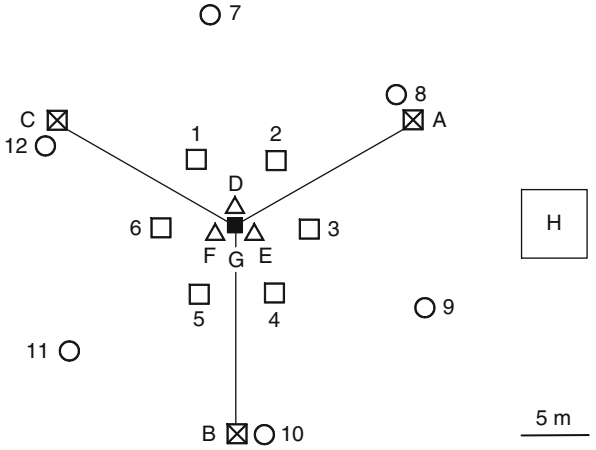

Fig. A.8 Balloon mounted air shower array layout, used by Antonov et al. (1977), to explore the altitude dependence of air shower observables up to 12 km. The symbols labeled *A*, *B* and *C* are scintillation detectors of area 0.25 m^2 each; *D*, *E* and *F* are small scintillators, each of area 0.07 m^2. The central unit labeled *G* represents an arrangement of 30 large Geiger-Mueller (GM) counters, each of area 86 cm^2, and 30 small counters, each of area 5.4 cm^2. The half filled *circles 1–6* show the location of GM trays containing 20 large and 20 small counters, the open *circles 7–12* are similar trays holding 20 large and 10 small GM counters of dimensions as specified above. The square on the right labeled *H* represents a cluster of counters consisting of 24 sub-assemblies of area 688 cm^2 each and 12 units of large GM counters (86 cm^2), mounted below the main array. Each of the sub-assemblies holds a set of 8 large GM counters

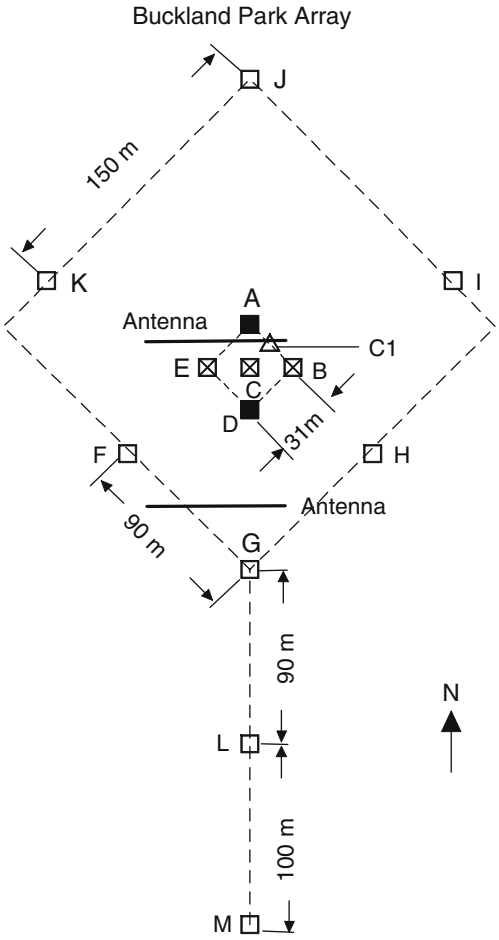

Fig. A.9 Plan of the extended Buckland Park EAS array (sea level), status 1977. The various *boxes* represent detector locations. Sites *A* to *H* have particle detectors; *A*, *D*, *I*, *J* and *K* were used for particle density measurements, *A* to *E* served also for fast timing. In addition sites *A*, *F*, *G*, *H*, *L* and *M* were equipped with Cherenkov detectors. At location *C*1 was a caravan holding a Cherenkov detector for pulse profile measurements (rise time ∼2 ns) (Kuhlmann et al., 1977). At times the array was also equipped with antennae for EAS radio burst studies (Clay et al., 1975)

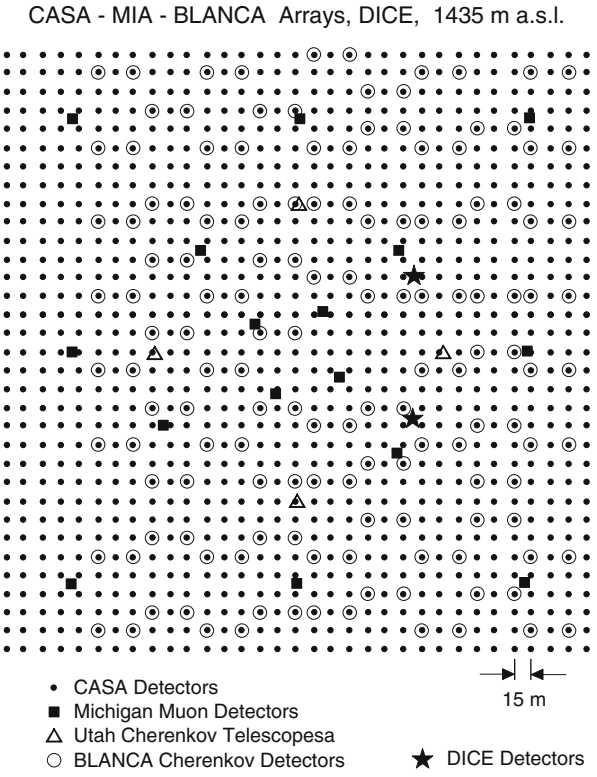

Fig. A.10 Layouts of the CASA (Chicago Air Shower Array), MIA (MIchigan muon Array), and BLANCA (Broad Lateral Non-imaging Cherenkov Array) arrays, and of the two DICE (Double Imaging Cherenkov Experiment) detectors at Dugway, Utah (USA). Also indicated are the Utah air Cherenkov telescopes (Cassidy et al., 1997; Ong et al., 2007)

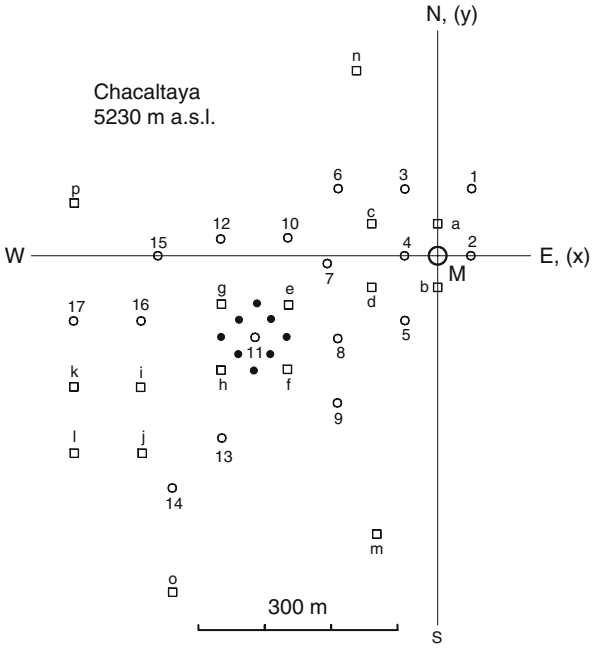

Fig. A.11 Layout of the Chacaltaya air shower array, status 1977 (Aguirre et al., 1977). The covered area measures approximately 700 m by 700 m at an altitude of 5,230 m (550 g cm^{-2}). It holds sixteen unshielded fast-timing scintillation detectors, twelve of area 0.87 m^2, 9.6 cm thick, (*a* to *l*) and four of area 1 m^2, 10 cm thick (*m* to *p*). The latter are also used to measure particle densities together with twenty 0.83 m^2 scintillators, 7.5 cm thick, indicated by *open circles* (1–20) and eight 2 cm thick scintillators of area 1/16 m^2 (*full circles*). In addition a shielded scintillator of 60 m^2 ($15 \cdot 4$ m^2) and thickness 5 cm, labeled *m* and located at the origin of the reference frame is used as muon detector with a threshold of 600 MeV

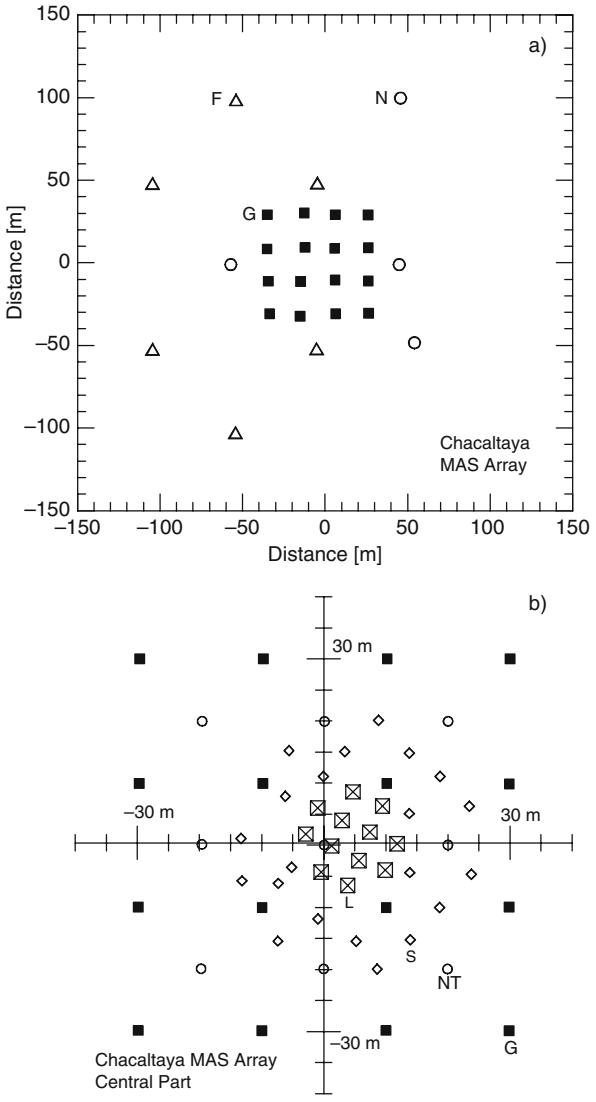

Fig. A.12 Chacaltaya (5,230 m a.s.l.) Minimum Air Shower (MAS) array, (**a**), and central part of array, (**b**). L, G, S, N, F and NT detectors are unshielded. The L detectors are $4\,m^2$ plastic scintillators with an additional $1\,m^2$ scintillator. The L, G, S and NT detectors are used as timing detectors and to measure particle density. A $60\,m^2$ muon detector with a threshold of 600 MeV is located at the array center (Shirasaki et al., 1997; Ogio et al., 2004)

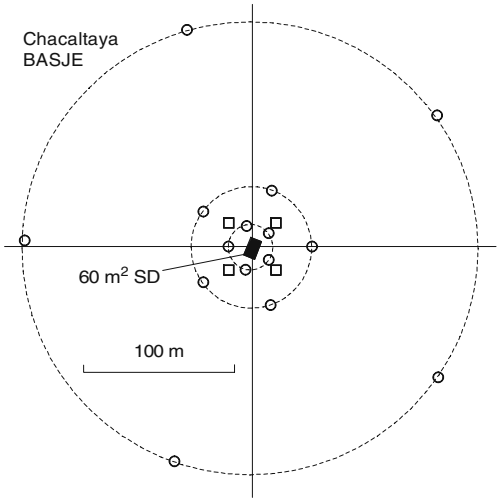

Fig. A.13 Layout of the BASJE air shower array at Chacaltaya (5,230 m a.s.l.) in 1965 (Toyoda et al., 1965)

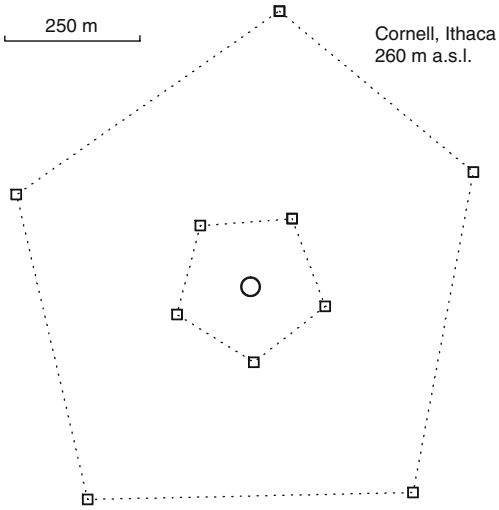

Fig. A.14 Cornell air shower array (Linsley, 1963b)

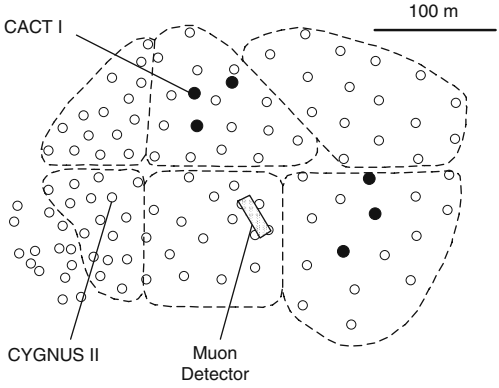

Fig. A.15 The CYGNUS II array was located near the Los Alamos National Laboratory at an altitude of 2,310 m a.s.l. (780 g cm^{-2}) and consisted of 96 scintillation detectors (○) and a 70 m^2 muon detector with a threshold of ∼2 GeV (Allen et al., 1992). The CACTI experiment consisted of 6 wide angle Cherenkov detectors (●) (Paling et al., 1997)

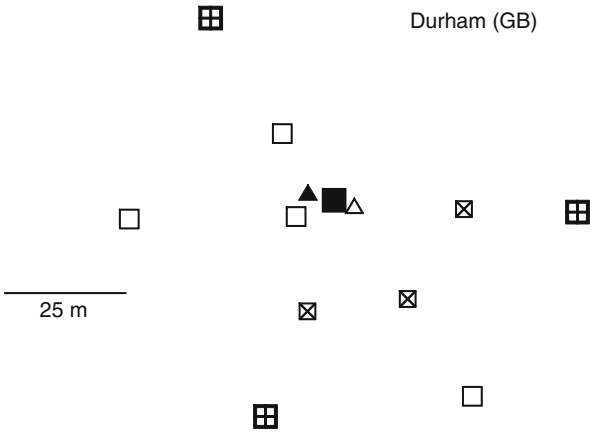

Fig. A.16 The Durham (GB) array consisted of scintillation detectors measuring 2 m^2 (⊞), 1.6 m^2 (□), 1 m^2 (⊠) and 0.75 m^2 (△). It had a solid iron magnet spectrometer (MARS) (Ayre et al., 1972a, b) (■) and a hadron chamber (▲) (Rada et al., 1977)

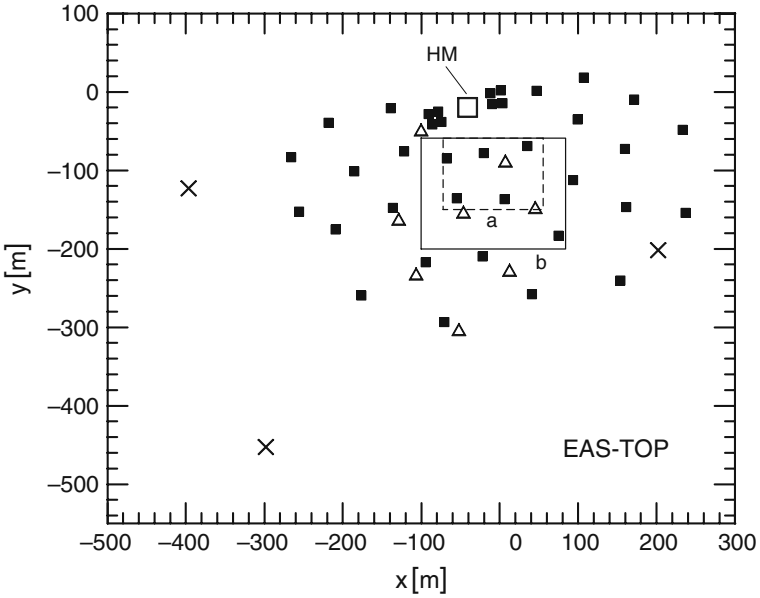

Fig. A.17 EAS-TOP air shower array (2,005 m a.s.l.) status of 1998. The symbols which indicate the location of different detector units represent the following kind of detectors: ■ scintillator module, △ wide acceptance Cherenkov telescope, × radio antennae for the detection of radio bursts associated with air showers, and □ the combined hadron calorimeter-muon detector, labeled *HM* (twin units). The two rectangular areas that are outlined with *dashed* and the *solid lines*, labeled *a* and *b*, identify the fiducial regions, i.e., the core location regions, for two sets of spectral measurements (Aglietta et al., 1989, 1999)

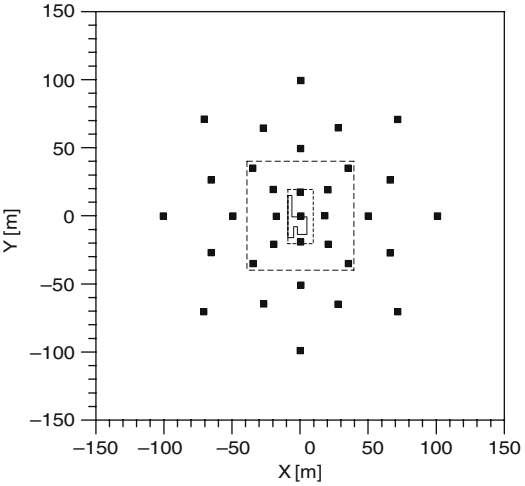

Fig. A.18 GAMMA air shower experiment at Mt. Aragats in Armenia located at an altitude of 3,200 m a.s.l. (700 g cm^{-2}). The 33 *black squares* represent scintillation detectors consisting of 3 units, each measuring 1 m^2. The *dashed contour* indicates the underground part with 150 m^2 of scintillation detectors having a muon threshold energy of $\geq$5 GeV. The *inner rectangle* is the contour of the calorimeter of the ANI project, currently under construction (Shaulov, 2007; Garyaka et al., 2007)

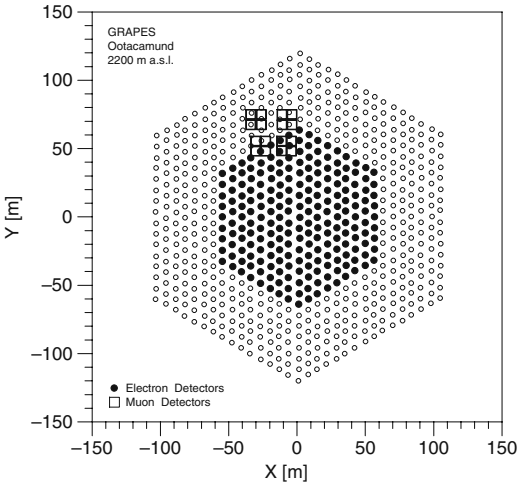

Fig. A.19 Layout of the GRAPES experiment at Ootacamund, India (2,200 m a.s.l., 800 g cm^{-2}). The muon tracking detector combination which is at present the largest of its kind has an effective area of 560 m^2 (Gupta et al., 2005). The shower detectors plotted as • are those that were used at that epoch. The muon detector which has a threshold of 1 GeV consists of 16 modules measuring 35 m^2 each (□). The modules consist of large proportional counters (Hayashi, 2005; Hayashi et al., 2005)

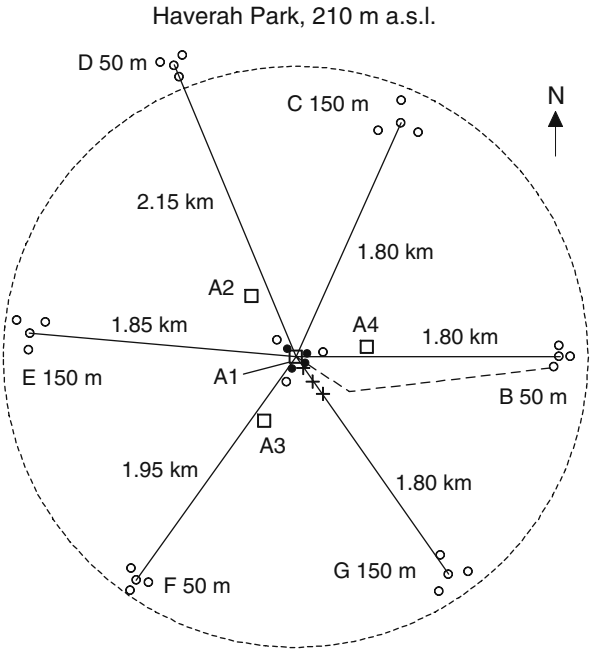

Fig. A.20 Haverah Park air shower array status of 1968 (Earnshaw et al., 1968). The *crosses* indicate the location of radio antennae for the detection of radio bursts associated with air showers (Allan, 1971)

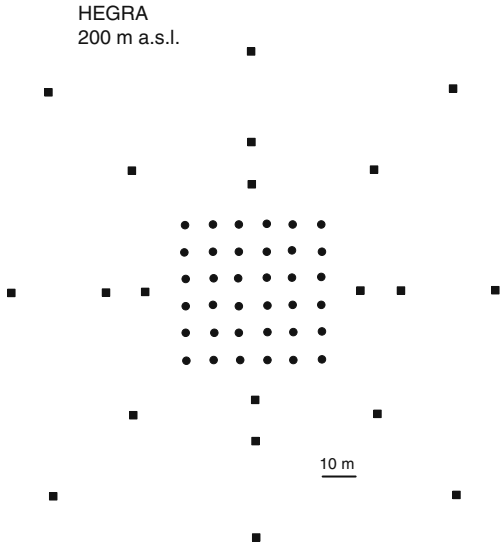

Fig. A.21 Original proposal of first HEGRA array at Roque de los Muchachos (2,250 m a.s.l.), La Palma (Canary Islands), by Allkofer (1985) who founded the project in the early 1980s, showing two kinds of 1 m^2 scintillation detectors. Up to date, the site has seem a wide variety of particle and air Cherenkov detectors and Cherenkov telescopes (for details see the HEGRA web site)

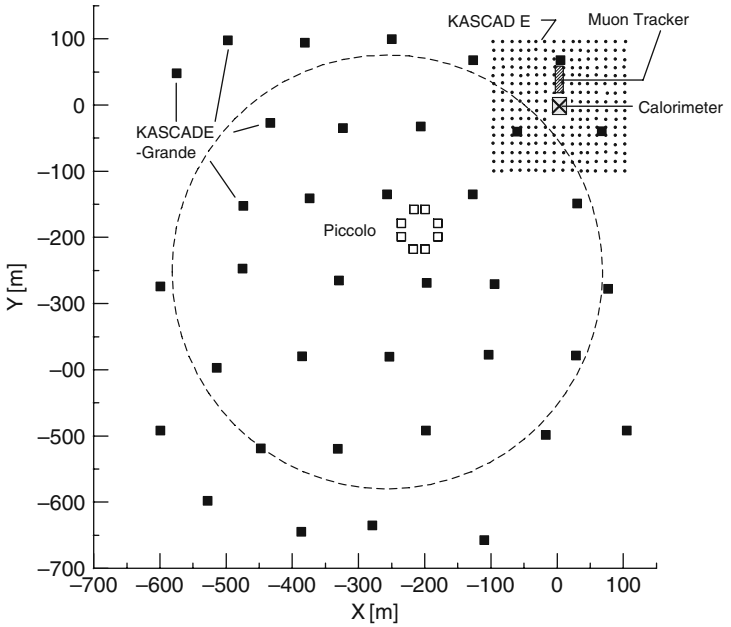

Fig. A.22 Layout of the elaborate KASCADE-Grande air shower array at the Forschungszentrum Karlsruhe (Germany) (110 m a.s.l.) (Kampert et al., 2003; Haungs et al., 2003; Navarra et al., 2004). The resolutions of the Grande array are 13 m for core location, 0.3° for arrival direction, and 15% for the shower size at a primary energy of 100 PeV (10^{17} eV). The KASCADE array has 252 stations that are distributed over an area of $200 \times 200\,\mathrm{m}^2$ (Antoni et al., 2003). Each station consists of liquid scintillators to measure the shower particle density ($E_{\mathrm{EM}} \geq 5\,\mathrm{MeV}$) and shielded (10 cm Pb + 4 cm Fe) plastic scintillators underneath to measure the muon density ($E_{\mu} > 0.23\,\mathrm{GeV}$). The central detector consists of a 9-layer hadron calorimeter with 40,000 channels of liquid ionization chambers; it has a threshold energy of 50 GeV. Additional muon facilities are located in and under the calorimeter with threshold energies of 0.49 and 2.4 GeV, and a muon tracker in a tunnel with a threshold of 0.8 GeV. The Picolo cluster sub-array serves as a trigger. The array has a 100% trigger efficiency for events with primary energy of 10 PeV over the entire Grande collecting area (*dashed circle*). A low frequency radio antenna array (40–80 MHz) called LOPES (not shown above), a prototype of LOFAR, is also integrated in the KASCADE-Grande array to detect air shower radio pulses (Horneffer et al., 2003)

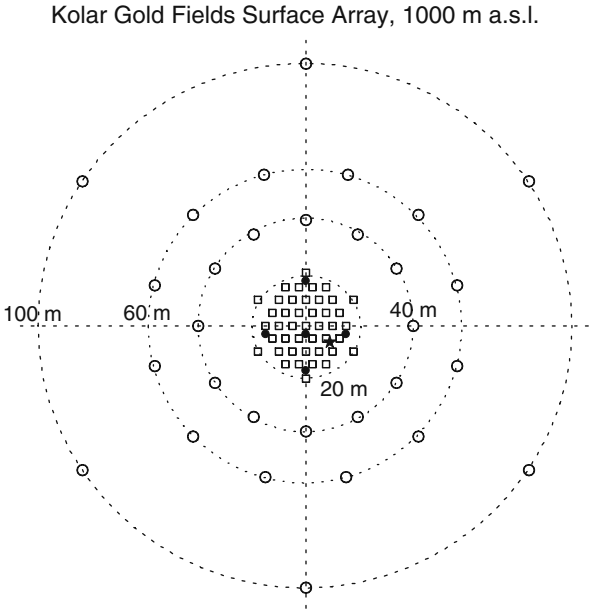

Fig. A.23 Air shower array at the Kolar Gold Fields, status 1977 (Acharya et al., 1977). The *squares* and *circles* are 2.25 and 1 m^2 plastic scintillation detectors, respectively, the *full circles* 1.15 m^2 liquid scintillation detectors used for fast timing. The symbol ⋆ marks the intersection of a perpendicular from the center of the $2 \times 1 \times 2$ m^3 neon flash tube telescope, located at a depth of 266 m underground (muon threshold $\simeq$220 GeV). A cross-sectional view of the abandoned underground installations is shown in Fig. A.40

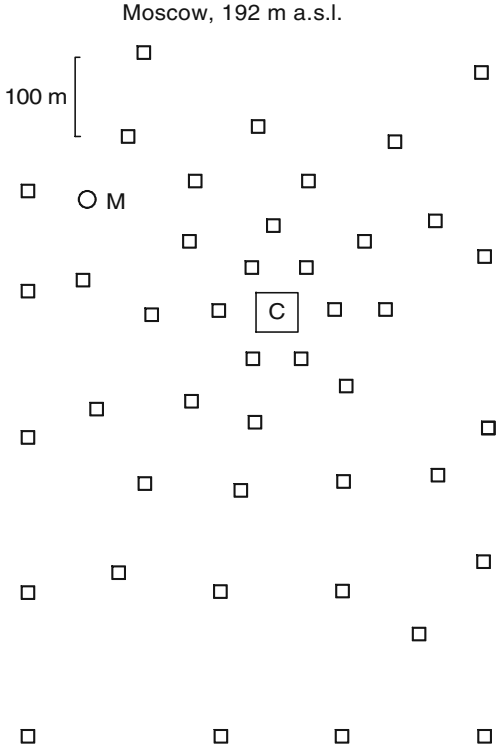

Fig. A.24 Air shower array at the Moscow State University (Vernov et al., 1979). The *open squares* are charged particle detectors, the central system (*C*) contains 3,000 hodoscope counters. A total of 8,160 Geiger counters are used. At each detector location which is 60 m or more from the center of the array a 0.5 m^2 scintillation detector is installed. Muon detectors of area 18 m^2 and threshold 10 GeV are located at 180, 250 and 280 m from the *center*. In addition a 32 m^2 muon detector and a solid iron magnetic muon spectrometer are located at the *center*, at a depth of 40 m.w.e

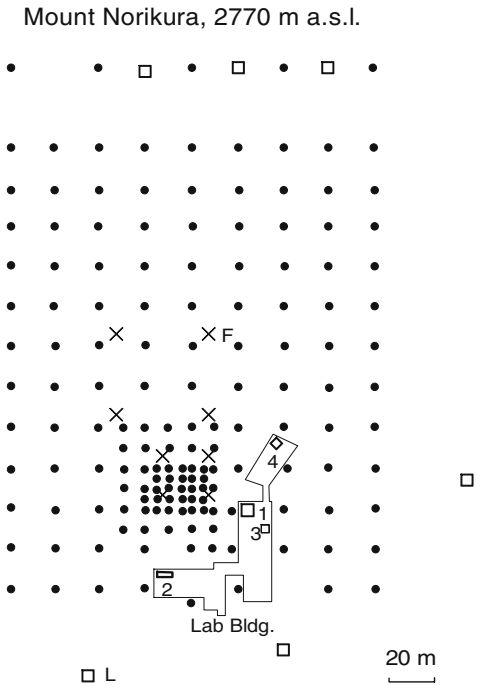

Fig. A.25 One of many air shower array configurations used at Mt. Norikura in Japan (Miyake et al., 1979). The figure shows a total of 152 scintillation detectors of area 0.25 m^2 (•) each, arranged in a lattice as shown, and 6 additional detectors of area 1 m^2 (□) in the outer area. × identifies fast timing detectors. A 25 m^2 proportional counter array shielded with 2 cm of Pb located under a 6 m by 5.5 m water tank of height 2 m (*1*) was used to observe high energy gamma rays. During a certain period the proportional counters were replaced by 48 plastic scintillators above and 48 below the tank. This arrangement served as core detector. In addition a cloud chamber (*2*) was used occasionally. Two neon hodoscopes of 6 and 4 m^2 (3 and 4) shielded by 35 cm of lead were also incorporated. For details of special apparatuses see Sasaki et al. (1979); for earlier array layouts see Miyake et al. (1968, 1973) and Kino et al. (1975)

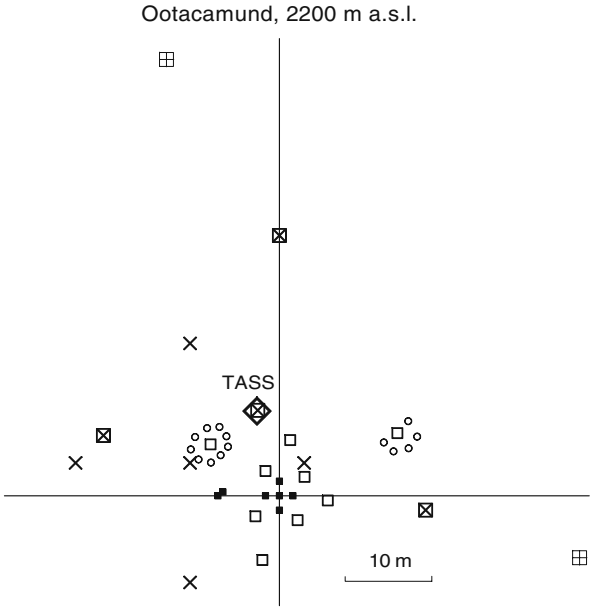

Fig. A.26 One of several arrangements used for the air shower array at Ootacamund, India (Chatterjee et al., 1965b). The different *symbols* identify the following detectors: ■, □ and ⊞ represent 0.36, 1.0 and 1.44 m^2 scintillators, respectively; ⊠ 1.0 m^2 muon detectors consisting of Pb-shielded Geiger-Mueller hodoscope arrays, × fast timing scintillators, ○ BF_3 neutron detectors, and ◇ the 1 m^2 total absorption scintillation spectrometer (TASS) to record nuclear interacting particles of energy >100 GeV, with a muon detector underneath. In addition there was a 4 m^2 combination of energy flow detectors for the soft and hadronic components

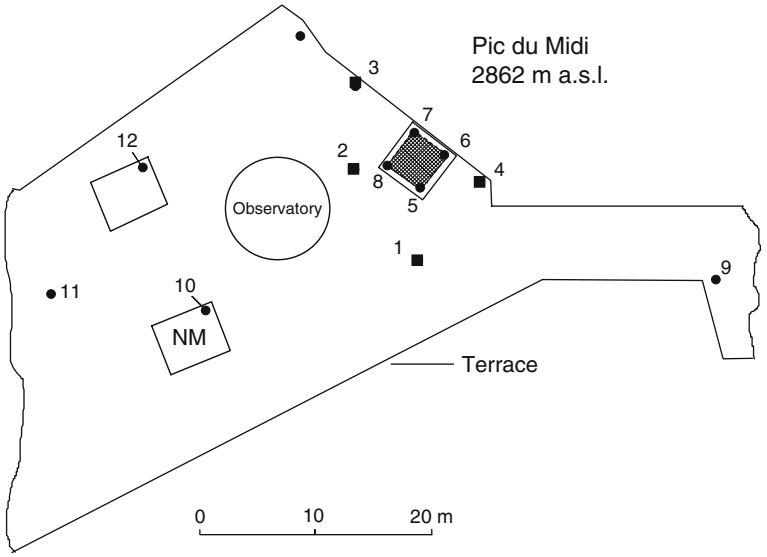

Fig. A.27 Air shower array of the University of Kiel at the terrace of Pic du Midi, France, located at an altitude of 2,862 m. (Van Staa et al., 1973, 1974). The full symbols *1–13* represent 0.25 m^2 scintillation detectors. Detectors 1–4 were equipped for fast timing, and NM indicated a neutron monitor. The *square* containing the four scintillators *5–8* that serve as trigger detectors represents the hadron detector and the hatched area within it is the 14 m^2 neon hodoscope with approximately 80,000 neon tubes that serves as burst detector. The hadron target consists of a layer of 100 cm of sand and 25 cm of concrete, topped with a 10 cm thick layer of lead to absorb the photon-electron component

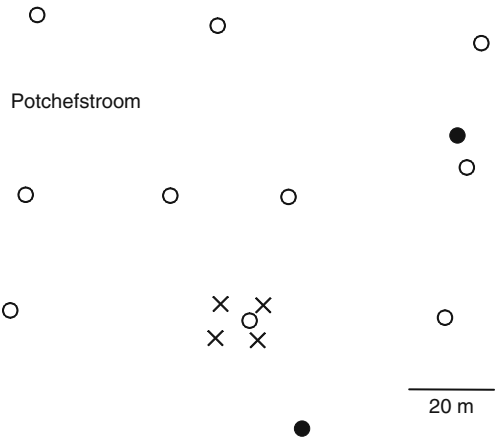

Fig. A.28 The Potchefstroom array was very small and consisted of 10 scintillation detectors and 2 muon detectors (De Villiers et al., 1979)

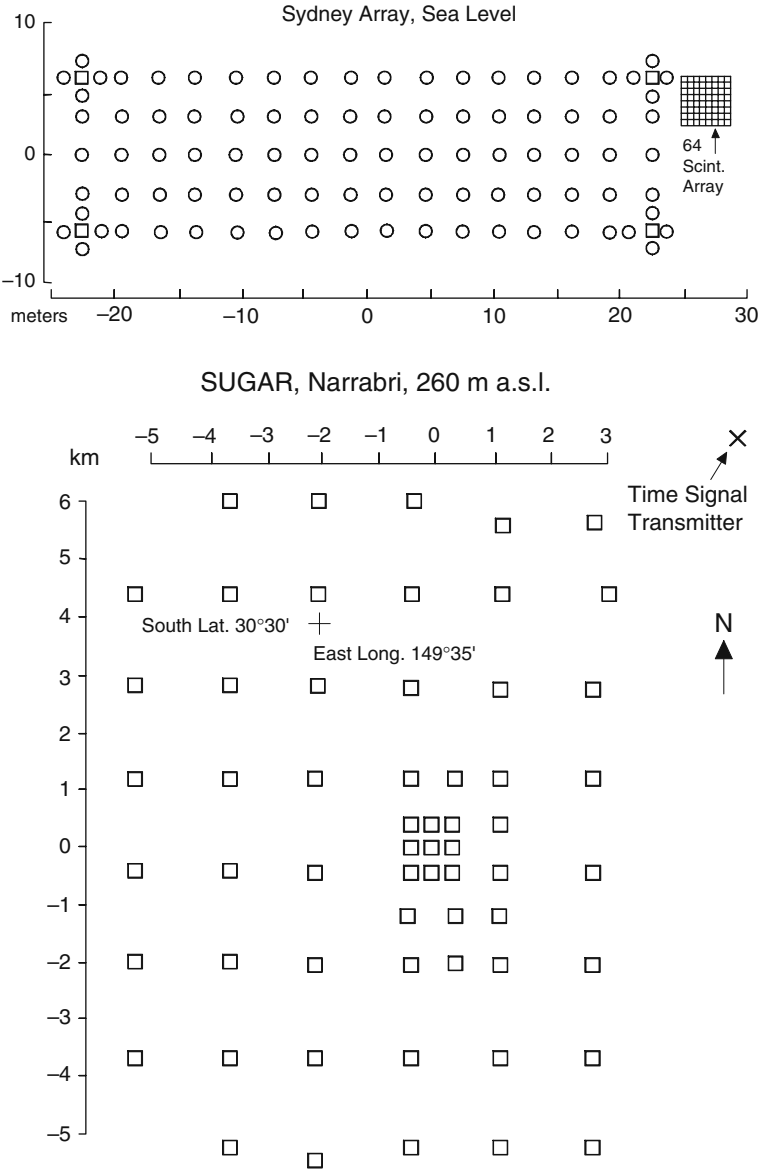

Fig. A.29 *Upper figure*: Sydney air shower array, status 1965 (Bray et al., 1965). *Circles* represent trays with 3 Geiger counters, the four *boxes* at the corners hold 48 Geiger counters each. In the *upper right corner* is the 64 scintillator array. *Lower figure*: Layout of early status of the Sydney University Giant air shower Array (SUGAR) at Narrabri (Brownlee et al., 1970). Except for the central section the counters are underground and record chiefly muons

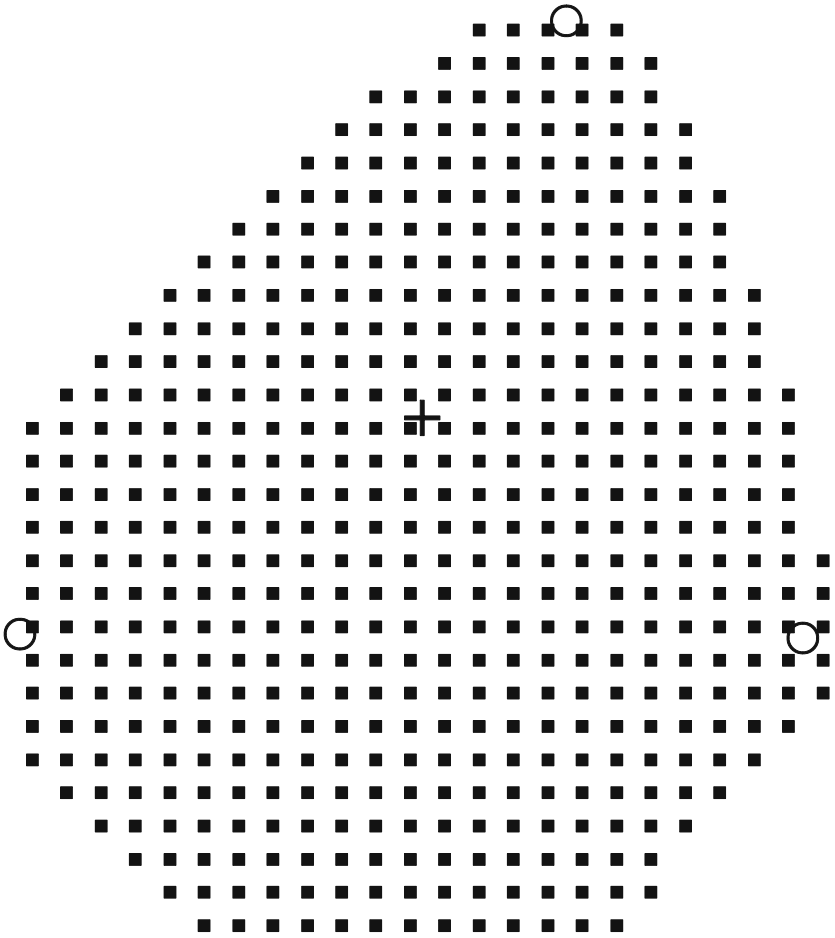

Fig. A.30 Layout of the giant Telescope Array located at Dugway, Utah (USA), 1,400 m a.s.l., 39.3° N, long. 112.9° W (Kasahara et al., 2007). It consists of 3 fluorescence stations, each having 12 identical telescopes, and 512 plastic scintillation detectors. The aperture of the surface detectors is 1,900 km^2sr and the fluorescence detectors have a stereoscopic aperture of 860 km^2sr at 10^{20} eV with a duty factor of ∼10%. Participating in this joint venture project are mainly Japanese universities and institutions, some American and a few Korean universities, and a German institution. The approximate linear dimensions of the array are 17 km by 20 km (courtesy of Ken Honda and the Telescope Array Collaboration)

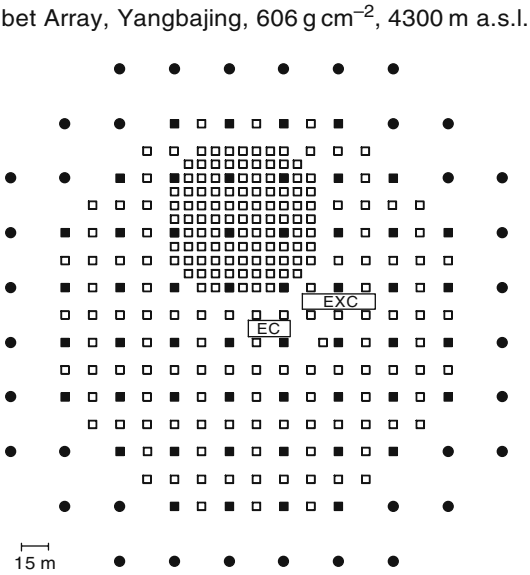

Fig. A.31 Layout of Tibet II Array located at Yangbajing (606 g cm^{-2}, 4,300 m a.s.l.). The array consists of 221 scintillation detectors that are placed 15 m apart and has a threshold for particles and gamma rays of 10 TeV. Its angular resolution is about 1° (Amenomori et al., 1997a, b). For the layout of the Tibet III array see Amenomori et al. (2003, 2006)

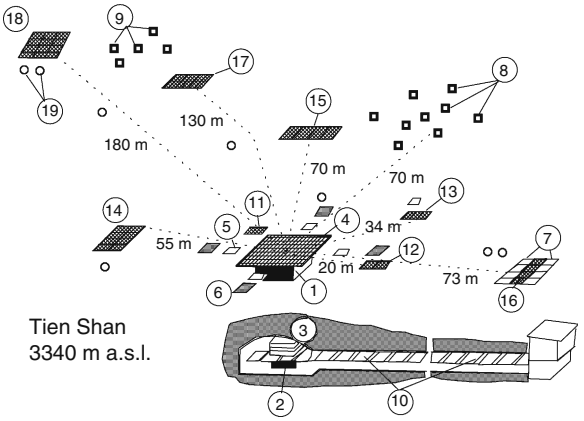

Fig. A.32 Layout of the complex air shower array at Tien Shan (Kazakhstan) (690 g cm^{-2}, 3,340 m a.s.l.) (Abdrashitov et al., 1981). This array was for many years the worldwide best equipped air shower installation. It consisted of a 6 m by 6 m (36 m^2) central ionization chamber calorimeter (*1*) that was interlaced with 15 rows of ionization chambers, each measuring $10 \times 15 \times 300$ cm^3, that were separated by layers of 2.5 cm and 5 cm of Pb, totaling 850 g cm^{-2} of Pb. The accuracy of the hadron spatial resolution was 25–30 cm, that of the energy measurement 15%. The chamber was covered with an carpet of 64 scintillation detectors of 0.25 m^2 area each that were uniformly distributed about the chamber center over an area measuring 11 m by 11 m (121 m^2). The shower detection array comprised 115 scintillation detectors, partly arranged in clusters (*4, 5, 7, 8*, and *9*) with a total effective area of 53 m^2, distributed out to 130 m from the *center* of the ionization chamber. The four detectors of type (*5*) of 1 m^2 area were used to determine the shower axis location and direction. The circular symbols (*19*) represent air Cherenkov detectors. A total of 9 Geiger-Müller hodoscope detector trays (*6, 11, 12, 13, 14, 15, 16, 17*, and *18*) with an effective area of 38.4 m^2, located at distances of 5, 10, 20, 34, 55, 70, 73, 130 and 180 m from the *center* (see labels attached to the *thin dotted lines*) permitted reliable muon measurements. In addition, a 45 m^2 muon detector hodoscope was operated in a tunnel (*10*) at a depth of 20 m w.e., having a muon energy threshold of $\geq$5 GeV. An underground calorimeter of 9 m^2 effective area (*2, 3*) below the larger surface unit with 15 trays of ionization chambers, separated by 5 cm of Pb, served to analyze the high energy muon component in the shower core. (For earlier layout versions see Erlykin et al., 1965; Aseikin et al., 1971; Betev et al., 1977.) Note that the new Tien Shan installation is at a slightly different location and consists mainly of air Cherenkov detectors for gamma ray astronomy purposes. For a recent layout see Slavatinsky (2001)

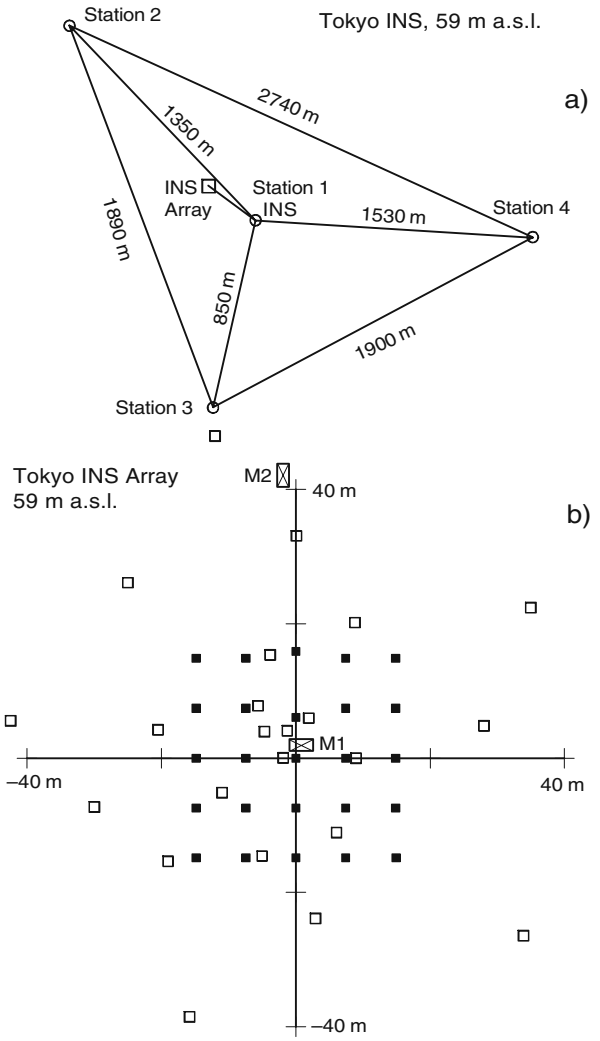

Fig. A.33 (**a**) Air shower array at the Institute for Nuclear Studies (INS) of the University of Tokyo, status 1973 (Kawaguchi et al., 1973). *Stations 1–4* have a pair of scintillation detectors of area 2 m^2 each that are 50 m apart. (See also Suga et al., 1971). (**b**) Details of local INS array. *M1* and *M2* are muon detectors having a threshold of 5 and 15 GeV, respectively. The *open squares* represent 1 m^2 scintillation detectors, the *full squares* are a later addition. For further details see Matano et al. (1971). For earlier arrangements see Hara et al. (1970)

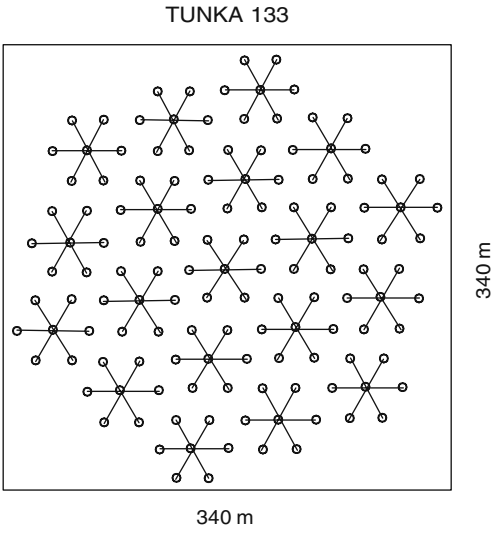

Fig. A.34 Layout of the TUNKA-133 optical Cherenkov array, located in the Tunka valley (675 m a.s.l.) in Russia, near lake Baikal (Budnev et al., 2005, 2007). The array was operated at earlier stages with much fewer detector units while it was under construction and systematically enlarged

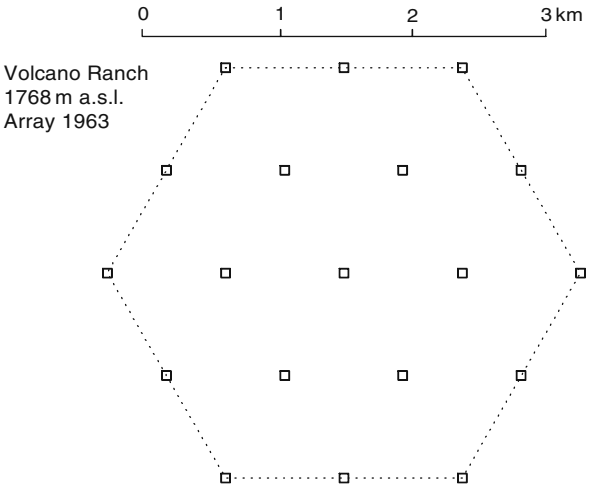

Fig. A.35 Layout of Volcano Ranch air shower array, status 1963 (Linsley, 1963a, b)

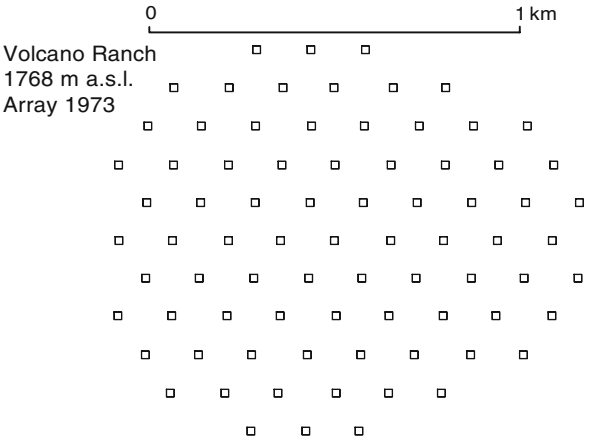

Fig. A.36 Layout of Volcano Ranch array 1973 (Linsley, 1973)

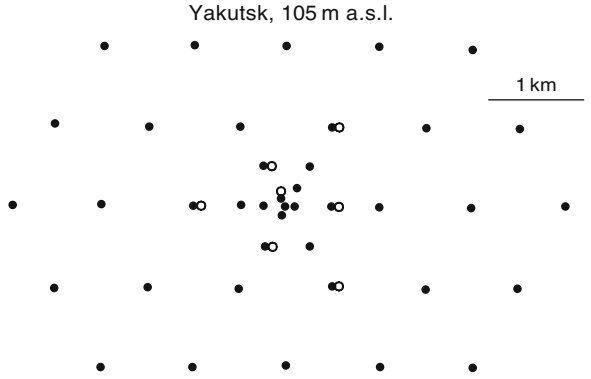

Fig. A.37 Layout of Yakutsk air shower array, status 1973 (Diminstein et al., 1973). For an earlier layout see Egorov et al. (1971); further details are also given by Kozlov et al. (1979), Diminstein et al. (1979) and Artamonov et al. (1983, 1991)

A.2 Cosmic Ray Underground Installations of Past and Present

A.2.1 Underground Muon and Neutrino Detectors

Table A.6 is a list of muon and neutrino detectors of the past and present. Most of these detectors are being operated or had been operated autonomously, but some could be used jointly with nearby air shower arrays. Those underground installations that are or were located underneath of an air shower array or in its immediate vicinity, so that components of the same shower event could be recorded simultaneous, that had been operated jointly, are marked.

Table A.6 List of major underground muon and neutrino detectors of past and present

Detector (Location)	Mass tons	Depth m.w.e.	Size m	E_μ TeV	Status
AMANDA (Antarctica)	$\sim 10^6$ m^3 IČ	$\simeq$1,000	evolving	0.4	operating
Antares (France)	WČ				constr.
Baikal (Russia)	$3{\cdot}10^7$ WČ	1,300	200·300	0.5	operating
			0.400		
Baksan (Russia) [a]	85 Sc	850	16·16	0.23	operating
C.W.I. (SA)	20 ScFt	8,200	90·0.13·1.5	$\simeq$ 10	shut-dn.
DUMAND 1 (USA)	$3{\cdot}10^5$ WČ	4,500	70ø·70	3.5	shut-dn.
DUMAND 2 (USA)	$2{\cdot}10^6$ WČ	4,500	106ø·230	3.5	discont.
Frejus (F/I)	912 Fe	4,400	6·12	3	shut-dn.
Gallex (Italy)	110 $GaCl_3$	$\sim$ 3,300	54 m^3	3	shut-dn.
Homestake (USA)	615 C_2 Cl_4	4,200	390 m^3	3	shut-dn.
Homestake (USA) [a]	300 WČ	4,200	8·24	3	shut-dn.
HPW/(USA)	1,000 WČ	1,700	10ø	0.6	discont.
Icarus (Italy)	10^4 LA	3,100	–	3	discont.
ICECUBE (Antarctica) [a]	$\sim 10^9$ IČ	$\simeq$1,200	1 km^3	0.5	operating
IMB (USA)	8,000 WČ	1,570	17·23	0.6	shut-dn.
Issyk-Kul (Kyrgyzstan)	10^6 m^3 WČ	500	$\sim$1 km^2	$\geq$ 0.15	discont.
Kamiokande (J)	2,900 WČ	2,700	16ø·16	$>$ 1	shut-dn.
KGF (India) [a]	- Sc	730	6 m^2	0.22	shut-dn.
KGF (India) [a]	- WČ	1,590	10 m^2	0.64	shut-dn.
KGF (India)	- ScFt	2,895	6·6	1.7	shut-dn.
KGF (India)	375 Fe Pc	7,500	6·6	12	shut-dn.
LSD (Italy)	200 Sc	5,200	7·8	4	shut-dn.
LVD (Italy) [a]	3,600 Sc	3,100	31·13·12	1.3	operating
MACRO (Italy) [a]	- ScStTe	3,100	72·12·10	1.3	shut-dn.
NEMO (Italy)	WČ				planning
NESTOR (Greece) [b]	$2.8{\cdot}10^5$ WČ	3,800	34ø·400	3.0	discont.
NUSEX (Italy)	150 Fe Ft	5,000	3.5·3.5	4	shut-dn.
Ohya (Japan) [a]	- Fe	31	400 m^2	0.015	shut-dn.
SAGE (Russia)	- Ga				operating
Soudan 1 (USA)	30 FeCon	2,100	3·3	0.6	shut-dn.
Soudan 2 (USA) [a]	1,000 FeCon	2,100	8·16	0.6	operating
SNO Sudburry (CND)	- D_2				operating
Super Kamiokande (J)	32,000 WČ	2,700	38ø·40	$>$ 1	operating
Utah	1,800 WČSpMag.	$>$ 150	$12 \cdot 10 \cdot 6$	0.5	shut-dn.

[a] EAS array at surface.

[b] per tower.

E_μ – muon threshold; ø – diameter; IČ – ice Cherenkov; WČ – water Cherenkov; Sc – scintillation counters; Ft – Flash tubes; Con – concrete; LA - liquid argon; St – Streamer tubes; Te – Track etching; Sp - Spark chambers; D_2 - deuterium; Mag. – magnetized iron plates.

A.2.2 Layouts of Major Underground Detectors Associated with Air Shower Arrays

(a) Comments to Layouts

The underground detector experiments shown here had been operated autonomously but also in coincidence with an air shower array at the surface above or near the underground installation. The simultaneous acquisition of data from a surface and underground installation enriches the data and improves their interpretation significantly. Underground detectors supply complementary data that are otherwise inaccessible to surface measurements, such as data on single and multiple high energy muons in showers, on delayed penetrating particles, and other phenomena. They also offer an alternative method to determine the arrival direction of showers.

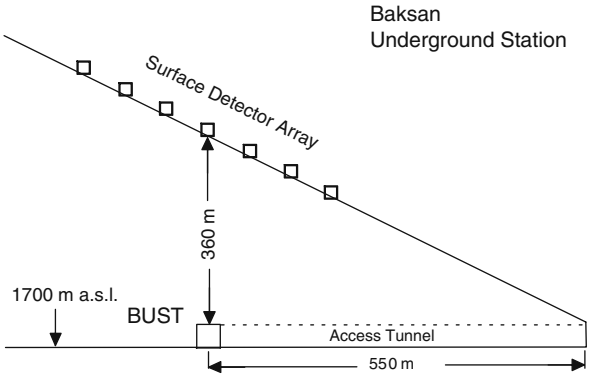

Fig. A.38 Cutaway view of the Baksan installation showing the surface array and the underground scintillation telescope BUST ($16 \times 16 \times 11\,m^3$) under an overburden of $\sim 850\,g\,cm^{-2}$. The layout of the surface array is given in Fig. A.7. (Alexeyev et al., 1979a, b, 1993; Chudakov et al., 1999)

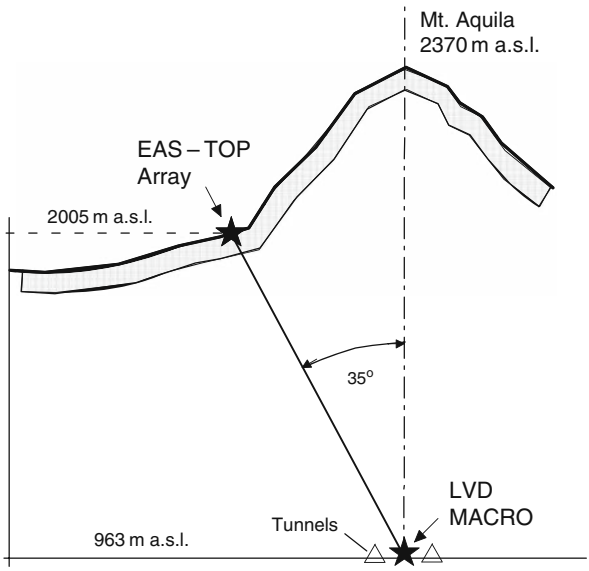

Fig. A.39 Cutaway view showing the locations of the EAS-TOP, LVD and MACRO detectors at Gran Sasso (Aglietta et al., 2004). Details of the EAS-TOP installation are shown in Fig. A.17. The minimum rock overburden in the direction of the EAS-TOP array is 3,100 m w.e. The MACRO detector measured $76.6 \times 12 \times 4.8\,m^3$ (Ahlen et al., 1992, 1993; Ambrosio et al., 2002), the LVD detector (still operating) measures $22.7 \times 13.2 \times 10\,m^3$ (Bari et al., 1989; Aglietta et al., 1992)

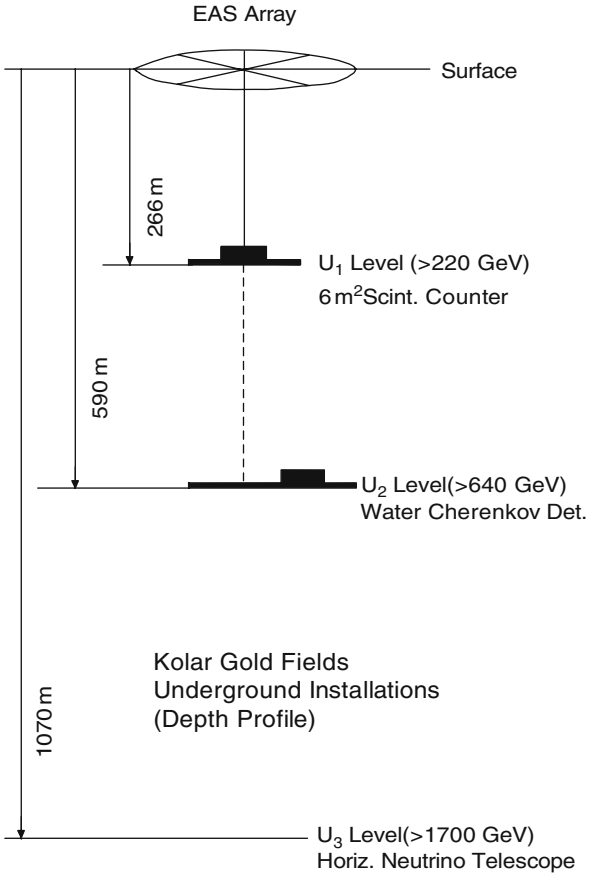

Fig. A.40 Muon and neutrino telescopes underneath the Kolar Gold Fields (KGF) air shower array, now shut-down (Chatterjee et al., 1965a). Illustrated are the experimental sites at the three different depth levels. The surface is at an altitude of 920 m a.s.l. (920 g cm^{-2}), the lowest level is 1,070 m below the surface which corresponds to a depth of approximately 7,500 m w.e. (water equivalent)

References

Abdrashitov, S.F., et al.: PICRC, 6, p. 156 (1981).
Acharya, B.S., et al.: PICRC, 8, p. 36 (1977).
Aglietta, M., et al.: Nucl. Instr. Meth., A277, p. 23 (1989).
Aglietta, M., et al.: Nuovo Cim. A, 12, p. 1793 (1992).
Aglietta, M., et al.: Astropart. Phys., 10, p. 1 (1999).
Aglietta, M., et al.: Astropart. Phys., 21, pp. 223–240 (2004).
Aguirre, C., et al.: PICRC, 8, p. 208 (1977).
Ahlen, S., et al., MACRO Collaboration: Phys. Rev. D, 46, p. 4836 (1992).
Ahlen, S., et al., MACRO Collaboration: Nucl. Instr. Meth. A, 324, p. 337 (1993).
Alexeyev, E.N., et al.: PICRC, 10, p. 276 (1979a).
Alexeyev, E.N., et al.: PICRC, 10, p. 282 (1979b).
Alexeyev, E.N., et al.: PICRC, 2, p. 474 (1993).

Allan, H.R.: Progress in Elementary Particle and Cosmic Ray Physics, North-Holland, Amsterdam, Vol. X, pp. 169–302 (1971).
Allen, R.C., et al.: Nucl. Instr. Meth. A, 311, p. 350 (1992).
Allkofer, O.C.: PICRC, 3, p. 418 (1985).
Ambrosio, M., et al.: Nucl. Instr. Meth. A, 486, p. 663 (2002).
Amenomori, M., et al.: PICRC, 5, p. 245 (1997a).
Amenomori, M., et al.: PICRC, 5, p. 249 (1997b).
Amenomori, M., et al.: Proceedings of the International Science Symposium "The Universe Viewed in Gamma Rays", University of Tokyo, Sept. 25–28, 2002, R. Enomoto, M. Mori, S. Yanagita, ed., Universal Academy Press, Inc., Japan (2003).
Amenomori, M., et al.: Adv. Space Res., 37, p. 1932 (2006).
Antoni, T., et al.: Nucl. Instr. Meth. A, 513, p. 490 (2003).
Antonov, R.A., et al.: PICRC, 6, p. 2194 (1971).
Antonov, R.A., et al.: Yadernaya Fiz. 18, p. 554 (1973) (in Russian).
Antonov, R.A., et al.: PICRC, 8, p. 137 (1977).
Artamonov, V.P., et al.: PICRC, 8, p. 196 (1983).
Artamonov, V.P., et al.: PICRC, 4, p. 375 (1991).
Aseikin, V.S., et al.: PICRC, 6, p. 2152 (1971).
Ayre, C.A., et al.: Nucl. Instr. Meth., 102, pp. 19–28 (1972a).
Ayre, C.A., et al.: Nucl. Instr. Meth., 102, pp. 29–34 (1972b).
Baillon, P.: CERN/PPE 91-12 (1991).
Bari, G., et al.: Nucl. Instr. Meth., A277, p. 11 (1989).
Betev, B., et al.: PICRC, 8, p. 123 (1977).
Bray, A.D., et al.: PICRC, 2, p. 685 (1965).
Brownlee, R.G., et al.: Acta Phys. Acad. Sci. Hung., 29, S3, p. 651 (1970).
Budnev, N.M., et al.: PICRC, 8, p. 255 (2005).
Budnev, N.M., et al.: PICRC, pre-conference edition, paper 0629, Merida, Mexico (2007).
Cassidy, M., et al.: PICRC, 5, p. 189 (1997).
Chatterjee, B.K., et al.: PICRC, 2, p. 627 (1965a).
Chatterjee, B.K., et al.: PICRC, 2, p. 734 (1965b).
Chiba, N., et al.: Nucl. Instr. Meth., A311, pp. 338–349 (1992).
Chudakov, A.E., et al.: arXiv:astro-ph/9912192v1 Dec. (1999).
Clark, G.W., et al.: Phys. Rev., 122, p. 637 (1961).
Clay, R.W., et al.: PICRC, 8, p. 3093 (1975).
De Villiers, E.J., and D.J. van der Walt: PICRC, 13, p. 277 (1979).
Diminstein, A.S., et al.: PICRC, 5, p. 3232 (1973).
Diminstein, O.S., et al.: PICRC, 8, p. 122 (1979).
Earnshaw, R.A., et al.: Can. J. Phys., 46, p. S5 (1968).
Egorov, T.A., et al.: PICRC, 6, p. 2059 (1971).
Erlykin, A.D., et al.: PICRC, 2, p. 731 (1965).
Garyaka, A.P., et al.: Astropart. Phys., 26, p. 169 (2007).
Gupta, S., et al.: Nucl. Instr. Meth. A, 540, p. 311 (2005).
Hara, T., et al.: Acta Phys. Acad. Sci. Hung., 29, S3, p. 361 (1970).
Hara, T., et al.: PICRC, 8, p. 135 (1979).
Haungs, A., et al.: PICRC, 2, p. 985 (2003).
Hayashi, Y., GRAPES Collaboration: PICRC, 10, p. 243 (2005).
Hayashi, Y., et al.: Nucl. Instr. Meth. A, 545, p. 643 (2005).
Horneffer, A., et al.: PICRC, 2, p. 696 (2003).
Kampert, K.H., et al.: Nucl. Phys. B (Proc. Suppl.), 122, p. 422 (2003).
Kasahara, K., et al.: PICRC, pre-conference edition, paper 0955, Merida, Mexico (2007).
Kawaguchi, S., et al.: PICRC, 4, p. 2562 (1973).
Kino, S., et al.: PICRC, 8, p. 2837 (1975).
Kozlov, V.G., et al.: PICRC, 8, p. 356 (1979).

Kuhlmann, J.D., et al.: PICRC, 8, p. 239 (1977).
Linsley, J.: Phys. Rev. Lett., 10, p. 146 (1963a).
Linsley, J.: PICRC, 4, p. 77 (1963b).
Linsley, J.: PICRC, 5, p. 3212 (1973).
Lorenz, E.: Nucl. Phys. B (Proc. Suppl.), 33A,B, p. 93 (1993).
Matano, T., et al.: PICRC, 7, p. 2724 (1971).
Miyake, S., et al.: Can. J. Phys., 46, p. S17 (1968).
Miyake, S., et al.: PICRC, 5, p. 3220 (1973).
Miyake, S., et al.: PICRC, 13, p. 171 (1979).
Navarra, G., et al.: Nucl. Instr. Meth. A, 518, pp. 207–209 (2004).
Ogio, S., et al.: Astrophys. J., 612, pp. 268–275 (2004).
Ong, R.A., et al., CASA-MIA Collaboration: PICRC, pre-conference edition, paper 814, Merida, Mexico (2007).
Paling, S., et al.: PICRC, 5, p. 253 (1997).
Rada, W.S., et al.: PICRC, 8, p. 13 (1977).
Sasaki, H., et al.: PICRC, 8, p. 190 (1979).
Shaulov, S., et al.: PICRC, pre-conference edition, paper 483, Merida, Mexico (2007).
Shirasaki, Y., et al.: PICRC, 4, p. 53 (1997).
Slavatinsky, S.A., Tien Shan Collaboration: Nucl. Phys. B (Proc. Suppl.), 97, p. 109 (2001).
Suga, K., et al.: PICRC, 7, p. 2742 (1971).
Toyoda, Y., et al.: PICRC, 2, p. 708 (1965).
Van Staa, R., et al.: PICRC, 4, p. 2676 (1973).
Van Staa, R., et al.: J. Phys. A, 7, p. 135 (1974).
Vernov, S.N., et al.: PICRC, 8, p. 129 (1979).

Appendix B
Miscellaneous Relations, Tables, Lists and Constants

B.1 Electromagnetic Interaction Related Constants and Parameters

Table B.1 Radiation length $\chi_\circ$, critical energy E_{crit} and density ρ of frequently used elements

Element	Z	A	$\chi_\circ$ g cm^{-2}	$\chi_\circ$ cm	E_{crit} MeV	ρ g cm^{-3}
Aluminum	13	26.98	24.1	8.9	40	2.70[a]
Carbon	6	12.01	42.7	18.8	79	2.25[b]
Copper	29	63.54	12.9	1.43	18.8	8.89[c]
Hydrogen	1	1.008	62.8	7,500 (m)	350	0.07[d]
Helium	2	4.003	93.1	5,600 (m)	250	0.15[d]
Iron	26	55.85	13.8	1.76	20.7	7.85[e]
Lead	82	207.21	6.4	0.56	7.40	11.34
Nitrogen	7	14.008	38.6	331 (m)	85	0.81[d]
Oxygen	8	16.00	34.6	258 (m)	75	1.14[d]
Silicon	14	28.09	21.8	9.36	37.5	2.35[f]

[a] drawn.
[b] graphite.
[c] hard drawn.
[d] liquid.
[e] wrought.
[f] amorphous.

Table B.2 Radiation length $\chi_\circ$ and critical energy E_{crit} of mixtures and compounds

Compound	Z	A	$\chi_\circ$ g cm^{-2}	$\chi_\circ$ cm	E_{crit} MeV
Air	7.4	14.8	37.15	304 (m)	84.4
Water	7.2	14.3	36.1	36.1	73.0
Emulsion-G5			11.4	2.98	16.4

Table B.3 Data on Ilford G-5 emulsion

Property		Composition g cm^{-3}		Z
Density	3.907 g cm^{-3}	Silver	1.85	47
Atoms cm^{-3}	$8.12 \cdot 10^{22}$	Bromine	1.36	35
Mean A	28.98	Iodine	0.024	53
Mean Z	13.17	Carbon	0.27	6
Mean Z^2	456	Hydrogen	0.056	1
Radiation Length, χ	2.93 cm	Oxygen	0.27	8
$\lambda_{\rm int}^{p,\rm Emul}$	$\sim$37 cm	Sulfur	0.010	16
		Nitrogen	0.067	7

B.2 Bethe-Bloch Ionization Loss Formula

The Bethe-Bloch equation given below includes the *density correction term* of Sternheimer et al. (1984) to account for the density effect of ionization, δ. The equation is written in the form derived by Petrukhin and Shestakov (1968) (see also Sternheimer, 1952, 1953, 1954a, b, 1956, 1959, 1961, 1971, 1984; Eidelman et al., 2004).

$$-\left(\frac{{\rm d}E}{{\rm d}x}\right) = 2\pi N_A \alpha^2 \lambda_e^2 \frac{Z m_e}{A\beta^2}\left[\ln\left(\frac{2m_e\gamma^2\beta^2 E'_m}{I^2(Z)}\right) - 2\beta^2 + \frac{E'^2_m}{4E^2} - \delta\right]. \quad \text{(B.1)}$$

The symbols stand for the following quantities:

$\alpha = 1/137.036$	fine structure constant
$N_A = 6.023 \cdot 10^{23}$	Avogadro's number
Z	atomic number of absorber
A	atomic weight of absorber
m_e	rest masses of electron
m_μ	rest masses of muon
$\beta = p/E$	
p	p muon momentum
E	E muon energy
$\gamma = E/m_\mu$	Lorentz factor of muon
$\lambda_e = 3.8616 \cdot 10^{-11}$ cm	Compton wavelength of electron
$I(Z)$	mean ionization potential of absorber and
E'_m	maximum energy transferable to electron

For E'_m we write

$$E'_m = \frac{2m_e p^2}{m_e^2 + m_\mu^2 + 2m_e\sqrt{p^2 + m_\mu^2}}, \quad \text{(B.2)}$$

and δ is the density correction term,

$$\delta(X) = 4.6052\,X + a(X_1 - X)^m + C\ , \quad \text{for } X_0 < X < X_1 \tag{B.3}$$

and

$$\delta(X) = 4.6052\,X + C\ , \quad \text{for } X > X_1\ . \tag{B.4}$$

The quantity X as used by Sternheimer et al. (1984) is expressed as

$$X = \lg\left(\frac{p}{mc}\right)\ , \tag{B.5}$$

where p is the momentum and m the rest mass of the particle, and c is the velocity of light.

Additional Physical Constants

Avogadro constant	N_A	$6.023 \cdot 10^{23}\ \text{mol}^{-1}$
Boltzman constant	k	$1.380 \cdot 10^{-23}\ \text{JK}^{-1}$
Classical electron radius	r_e	$2.817 \cdot 10^{-13}\ \text{cm}$

B.3 The Atmosphere

B.3.1 Characteristic Data and Relations

To provide a better understanding of the secondary processes which take place in the atmosphere, some of its basic features are outlined. The Earth's atmosphere is a large volume of gas with a density of almost 10^{19} particles per cm^3 at sea level. With increasing altitude the density of air decreases and with it the number of molecules and nuclei per unit volume, too. Since the real atmosphere is a complex system we frequently use an approximate representation, a simplified model, called the *standard isothermal exponential atmosphere*, where accuracy permits it.

The atmosphere consists mainly of nitrogen and oxygen, although small amounts of other constituents are present. In the *homosphere* which is the region where thermal diffusion prevails the atmospheric composition remains fairly constant. This region extends from sea level to altitudes between 85 and 115 km, depending on thermal conditions. Beyond this boundary molecular diffusion is dominating. Table B.5 gives the number of molecules, n_i, per cm^3 of each constituent, i, at standard temperature and pressure (STP), i.e., at 273.16 K and 760 mmHg, and the relative percentage, q_i, of the constituents.

Table B.4 Parameters for Eq. (4.9) and unit radiation length of atoms, χ_0 (after Tsai, 1974) Z–Atomic Number, A–Atomic Weight, f–Coulomb Corrections

Z	A	f	χ_0 [g cm^{-2}]	Z	A	f	χ_0 [g cm^{-2}]
1	1.0080	$6.4005 \cdot 10^{-5}$	63.0470	36	83.8000	$7.8323 \cdot 10^{-2}$	11.3722
2	4.0026	$2.5599 \cdot 10^{-4}$	94.3221	37	85.4700	$8.2478 \cdot 10^{-2}$	11.0272
3	6.9390	$5.7583 \cdot 10^{-4}$	82.7559	38	87.6200	$8.6719 \cdot 10^{-2}$	10.7623
4	9.0122	$1.0234 \cdot 10^{-3}$	65.1899	39	88.9050	$9.1046 \cdot 10^{-2}$	10.4101
5	10.8110	$1.5984 \cdot 10^{-3}$	52.6868	40	91.2200	$9.5456 \cdot 10^{-2}$	10.1949
6	12.0111	$2.3005 \cdot 10^{-3}$	42.6983	41	92.9060	$9.9948 \cdot 10^{-2}$	9.9225
7	14.0067	$3.1294 \cdot 10^{-3}$	37.9879	42	95.9400	$1.0452 \cdot 10^{-1}$	9.8029
8	15.9994	$4.0845 \cdot 10^{-3}$	34.2381	43	99.0000	$1.0917 \cdot 10^{-1}$	9.6881
9	18.9984	$5.1654 \cdot 10^{-3}$	32.9303	44	101.0700	$1.1389 \cdot 10^{-1}$	9.4825
10	20.1830	$6.3715 \cdot 10^{-3}$	28.9367	45	102.9050	$1.1869 \cdot 10^{-1}$	9.2654
11	22.9898	$7.7022 \cdot 10^{-3}$	27.7362	46	106.4000	$1.2356 \cdot 10^{-1}$	9.2025
12	24.3120	$9.1566 \cdot 10^{-3}$	25.0387	47	107.8700	$1.2850 \cdot 10^{-1}$	8.9701
13	26.9815	$1.0734 \cdot 10^{-2}$	24.0111	48	122.4000	$1.3351 \cdot 10^{-1}$	8.9945
14	28.0860	$1.2434 \cdot 10^{-2}$	21.8234	49	114.8200	$1.3859 \cdot 10^{-1}$	8.8491
15	30.9738	$1.4255 \cdot 10^{-2}$	21.2053	50	118.6900	$1.4373 \cdot 10^{-1}$	8.8170
16	32.0640	$1.6196 \cdot 10^{-2}$	19.4953	51	121.7500	$1.4893 \cdot 10^{-1}$	8.7244
17	35.4530	$1.8236 \cdot 10^{-2}$	19.2783	52	127.6000	$1.5419 \cdot 10^{-1}$	8.8267
18	39.9480	$2.0435 \cdot 10^{-2}$	19.5489	53	126.9040	$1.5951 \cdot 10^{-1}$	8.4803
19	39.1020	$2.2731 \cdot 10^{-2}$	17.3167	54	131.3000	$1.6489 \cdot 10^{-1}$	8.4819
20	40.0800	$2.5142 \cdot 10^{-2}$	16.1442	55	132.9050	$1.7032 \cdot 10^{-1}$	8.3052
21	44.9560	$2.7668 \cdot 10^{-2}$	16.5455	56	137.3400	$1.7581 \cdot 10^{-1}$	8.3073
22	47.9000	$3.0308 \cdot 10^{-2}$	16.1745	57	138.9100	$1.8134 \cdot 10^{-1}$	8.1381
23	50.9420	$3.3059 \cdot 10^{-2}$	15.8425	58	140.1200	$1.8693 \cdot 10^{-1}$	7.9357
24	51.9960	$3.5921 \cdot 10^{-2}$	14.9444	59	140.9070	$1.9256 \cdot 10^{-1}$	7.7379
25	54.9380	$3.8892 \cdot 10^{-2}$	14.6398	60	144.2400	$1.9824 \cdot 10^{-1}$	1.7051
26	55.8470	$4.1971 \cdot 10^{-2}$	13.8389	61	145.0000	$2.0396 \cdot 10^{-1}$	7.5193
27	58.9332	$4.5156 \cdot 10^{-2}$	13.6174	62	150.3500	$2.0972 \cdot 10^{-1}$	7.5727
28	58.7100	$4.8445 \cdot 10^{-2}$	12.6820	63	151.9600	$2.1553 \cdot 10^{-1}$	7.4377
29	63.5400	$5.1837 \cdot 10^{-2}$	12.8616	64	157.2500	$2.2137 \cdot 10^{-1}$	7.4830
30	65.3700	$5.5331 \cdot 10^{-2}$	12.4269	65	158.9240	$2.2725 \cdot 10^{-1}$	7.3563
31	69.7200	$5.8924 \cdot 10^{-2}$	12.4734	66	162.5000	$2.3317 \cdot 10^{-1}$	7.3199
32	72.5900	$6.2615 \cdot 10^{-2}$	12.2459	67	164.9300	$2.3911 \cdot 10^{-1}$	7.2332
33	74.9216	$6.6402 \cdot 10^{-2}$	11.9401	68	167.2600	$2.4509 \cdot 10^{-1}$	7.1448
34	78.9600	$7.0284 \cdot 10^{-2}$	11.9082	69	168.9340	$2.5110 \cdot 10^{-1}$	7.0318
35	79.9090	$7.4258 \cdot 10^{-2}$	11.4230	70	173.0400	$2.5714 \cdot 10^{-1}$	7.0214
71	174.9700	$2.6321 \cdot 10^{-1}$	6.9237	82	207.1900	$3.3128 \cdot 10^{-1}$	6.3688
72	178.4900	$2.6930 \cdot 10^{-1}$	6.8907	83	208.9800	$3.3756 \cdot 10^{-1}$	6.2899
73	180.9480	$2.7541 \cdot 10^{-1}$	6.8177	84	210.0000	$3.4384 \cdot 10^{-1}$	6.1907
74	183.8500	$2.8155 \cdot 10^{-1}$	6.7630	85	210.0000	$3.5013 \cdot 10^{-1}$	6.0651
75	186.2000	$2.8771 \cdot 10^{-1}$	6.6897	86	222.0000	$3.5643 \cdot 10^{-1}$	6.2833
76	190.2000	$2.9389 \cdot 10^{-1}$	6.6763	87	223.0000	$3.6273 \cdot 10^{-1}$	6.1868
77	192.2000	$3.0008 \cdot 10^{-1}$	6.5936	88	226.0000	$3.6904 \cdot 10^{-1}$	6.1477
78	195.0900	$3.0629 \cdot 10^{-1}$	6.5433	89	227.0000	$3.7535 \cdot 10^{-1}$	6.0560
79	196.9670	$3.1252 \cdot 10^{-1}$	6.4608	90	232.0380	$3.8166 \cdot 10^{-1}$	6.0726
80	200.5900	$3.1876 \cdot 10^{-1}$	6.4368	91	231.0000	$3.8797 \cdot 10^{-1}$	5.9319
81	204.3700	$3.2502 \cdot 10^{-1}$	6.4176	92	238.0300	$3.9429 \cdot 10^{-1}$	5.9990

Table B.5 Composition of the atmosphere (STP)

Molecule	n_i [cm^{-3}]	$q_i = n_i/n_{\text{air}}$[%]
air	$2.687 \cdot 10^{19}$	100
N_2	$2.098 \cdot 10^{19}$	78.1
O_2	$5.629 \cdot 10^{18}$	20.9
Ar	$2.510 \cdot 10^{17}$	0.9
CO_2	$8.87 \cdot 10^{15}$	0.03
He	$1.41 \cdot 10^{14}$	$5.0 \cdot 10^{-4}$
Ne	$4.89 \cdot 10^{14}$	$1.8 \cdot 10^{-3}$
Kr	$3.06 \cdot 10^{13}$	$1.0 \cdot 10^{-4}$
Xe	$2.34 \cdot 10^{12}$	$9.0 \cdot 10^{-6}$

Specific regions within the atmosphere are defined according to their temperature variations. These include the *troposphere* where the processes which constitute the weather take place, the *stratosphere* which generally is without clouds, where ozone is concentrated, the *mesosphere* which lies between 50 and 80 km, where the temperature decreases with increasing altitude, and the *thermosphere* where the temperature increases with altitude up to about 130 km. The *temperature profile* of the atmosphere versus altitude is shown in Fig. B.1. The layers between the different regions are called *pauses*, i.e., *tropopause, stratopause, mesopause and thermopause.*

The variation of density with altitude in the atmosphere is a function of the barometric parameters. The variation of each component can be represented by the *barometric law*,

$$n_i(X) = n_i(X_0) \left(\frac{T(h_0)}{T(h)} \right) \exp\left(- \int_{h_0}^{h} \frac{\mathrm{d}h}{h_{s,i}} \right) , \tag{B.6}$$

where

$n_i(X)$ number of molecules of i-th component at X [molecules cm^{-3}]
$n_i(X_0)$ number of molecules of i-th component at X_0 [molecules cm^{-3}]
$h_{s,i} = RT/M_i g(h)$ scale height of i-th component [cm]
R universal gas constant ($8.313 \cdot 10^7$ [erg mole^{-1} K^{-1}])
M_i atomic or molecular mass of the i-th component [g/mole]
h altitude (height) at X [cm]
X atmospheric depth at h [g cm^{-2}]
X_0 atmospheric depth at h_0 [g cm^{-2}] (usually sea level)
h_0 altitude (height) at X_0 [cm]
$T(h)$ temperature at h [K]
$T(h_0)$ temperature at h_0 [K]
$g(h)$ gravitational acceleration [cm s^{-2}]

In a *static isothermal atmosphere*, for which complete mixing equilibrium of all constituents is assumed, Eq. (B.6) reduces to

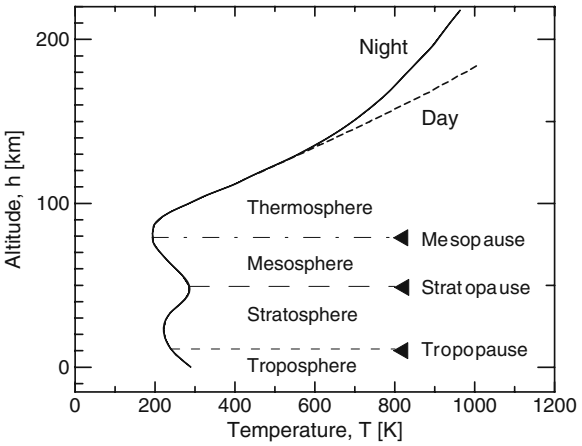

Fig. B.1 Schematic representation of the atmosphere showing its temperature profile

$$n(h) = n(h_0)\,\exp\left(-\frac{h}{h_s}\right)\,, \tag{B.7}$$

where h_s [cm] is the mean *scale height* of the mixture (see Table B.6).

Table B.6 Scale heights at different depths in the atmosphere

X [g cm^{-2}]	10	100	300	500	900
h_s [10^5cm]	6.94	6.37	6.70	7.37	8.21

For the *real atmosphere*, the same relation applies, but the scale height varies slightly with altitude. Table B.6 gives some values of h_s for different atmospheric depths. A similar relation applies to the variation of pressure with altitude.

Figure B.2 shows the relation between density and altitude in an isothermal atmosphere, in the region which is important for cosmic ray propagation and transformation processes. In an inclined direction, i.e., for non-zero zenith angles, the change of density per unit path length is less than in the vertical direction. Furthermore, for an incident particle the total thickness of atmosphere that must be traversed to reach a certain fixed altitude increases with increasing zenith angle.

For small zenith angles the *"flat Earth" approximation* can be used to compute the inclined column density (or slant depth) that follows a $\sec(\theta)$ dependence as given below,

$$X(h,\theta) = X(h,\theta=0)\cdot\sec(\theta)\ \ [\mathrm{g\,cm^{-2}}]\,. \tag{B.8}$$

However, for large zenith angles ($\theta \to 90^\circ$) this approximation diverges and the curvature of the Earth must be considered, requiring the Chapman function (Chapman, 1931), discussed in Sect. B.4, to compute the column density of a given path in the atmosphere correctly.

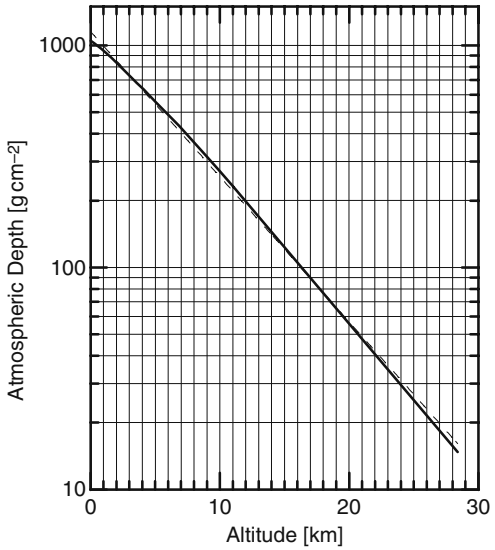

Fig. B.2 Relation between vertical depth and altitude in an isothermal atmosphere. The *dashed line* is an exponential fit to the overall data

B.3.2 Standard and Real Atmospheres

As briefly discussed before, for many applications and calculations the simple *Standard, Isothermal, Exponential Atmosphere* is adequate. However, several organizations have developed formulas to describe the density profile of the atmosphere more accurately and offer density profiles in tabulated form. One must also be aware of the fact that besides seasonal changes the atmospheric density and temperature profiles exhibit also a latitude dependence, and for special applications in-situ measurements may be required.

The relation between altitude and depth in the real atmosphere is illustrated in Fig. B.3. Frequently used tabulated density profiles are those available from COSPAR or the *Standard US Air Force Atmosphere*. In Table B.7 we present the basic data of the COSPAR International Reference Atmosphere (Barnett and Chandra,1990).

B.3.3 Special Atmospheres and Their Variations

The real average atmospheric profile manifests significant variations across the entire globe. Some of these are related to local climatic conditions, the structure of the Earth, to gravitational anomalies, and to the Earth's rotation. There is a well pronounced latitude dependence. In addition, the atmospheric profile is influenced by the ambient temperature and pressure, and is therefore subject to seasonal as

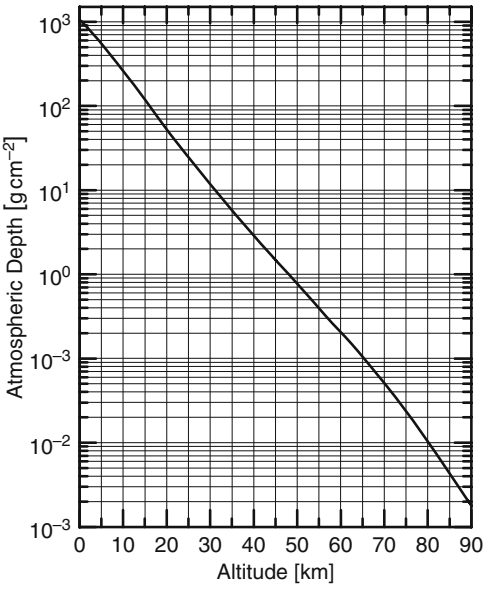

Fig. B.3 Relation between vertical depth or column density and altitude in the real atmosphere, after Cole and Kantor (1978)

Table B.7 COSPAR international reference atmosphere: 30°N annual mean (after Barnett and Chandra, 1990)

Pressure scale height[a]	Pressure [mb]	Geometric height[b] [m]	Geopotential height[c] [m]	Temperature [K]
17.50	$2.544 \cdot 10^{-5}$	119,656	11,7361	370.1
17.25	$3.266 \cdot 10^{-5}$	116,732	11,4545	324.8
17.00	$4.194 \cdot 10^{-5}$	114,192	11,2096	287.2
16.75	$5.385 \cdot 10^{-5}$	111,965	109,948	256.9
16.50	$6.914 \cdot 10^{-5}$	109,982	108,034	233.7
16.25	$8.878 \cdot 10^{-5}$	108,161	106,275	218.1
16.00	$1.140 \cdot 10^{-4}$	106,471	104,642	207.5
15.75	$1.464 \cdot 10^{-4}$	104,861	103,085	199.6
15.50	$1.880 \cdot 10^{-4}$	103,319	101,594	194.1
15.25	$2.413 \cdot 10^{-4}$	101,823	100,146	189.9
15.00	$3.099 \cdot 10^{-4}$	100,364	98,734	187.0
14.75	$3.979 \cdot 10^{-4}$	98,931	97,345	185.0
14.50	$5.109 \cdot 10^{-4}$	97,518	95,976	183.7
14.25	$6.560 \cdot 10^{-4}$	96,118	94,619	182.8
14.00	$8.423 \cdot 10^{-4}$	94,727	93,269	182.5
13.75	$1.082 \cdot 10^{-3}$	93,340	91,924	182.5
13.50	$1.389 \cdot 10^{-3}$	91,953	90,577	183.3
13.25	$1.783 \cdot 10^{-3}$	90,562	89,226	185.2
13.00	$2.290 \cdot 10^{-3}$	89,158	87,862	187.9
12.75	$2.940 \cdot 10^{-3}$	87,733	86,477	191.2
12.50	$3.775 \cdot 10^{-3}$	86,284	85,068	194.8

Table B.7 (continued)

Pressure scale height[a]	Pressure [mb]	Geometric height[b] [m]	Geopotential height[c] [m]	Temperature [K]
12.25	$4.847 \cdot 10^{-3}$	84,804	83,628	198.6
12.00	$6.224 \cdot 10^{-3}$	83,298	8,216	201.9
11.75	$7.992 \cdot 10^{-3}$	81,766	80,670	204.4
11.50	$1.026 \cdot 10^{-2}$	80,217	79,161	206.3
11.25	$1.318 \cdot 10^{-2}$	78,662	77,646	207.8
11.00	$1.692 \cdot 10^{-2}$	77,097	76,120	209.2
10.75	$2.172 \cdot 10^{-2}$	75,521	74,581	210.8
10.50	$2.789 \cdot 10^{-2}$	73,932	73,031	212.5
10.25	$3.582 \cdot 10^{-2}$	72,333	71,469	214.3
10.00	$4.599 \cdot 10^{-2}$	70,720	69,893	216.4
9.75	$5.905 \cdot 10^{-2}$	69,087	68,296	219.2
9.50	$7.582 \cdot 10^{-2}$	67,433	66,678	222.6
9.25	$9.736 \cdot 10^{-2}$	65,754	65,035	226.4
9.00	0.1250	64,048	63,364	230.4
8.75	0.1605	62,308	61,660	234.5
8.50	0.2061	60,539	59,926	238.9
8.25	0.2647	58,739	58,160	243.6
8.00	0.3398	56,905	56,361	248.5
7.75	0.4363	55,029	54,519	253.9
7.50	0.5603	53,116	52,639	259.1
7.25	0.7194	51,170	50,726	263.5
7.00	0.9237	49,198	48,786	266.5
6.75	1.1861	47,213	46,832	267.1
6.50	1.5230	45,231	44,880	266.0
6.25	1.9556	43,265	42,942	263.0
6.00	2.5110	41,325	41,030	258.8
5.75	3.2242	39,425	39,155	253.8
5.50	4.1399	37,563	37,316	248.7
5.25	5.3157	35,737	35,513	243.7
5.00	6.8255	33,948	33,744	238.9
4.75	8.7642	32,198	32,013	234.4
4.50	11.25	30,479	30,313	230.3
4.25	14.45	28,788	28,638	226.9
4.00	18.55	27,120	26,986	223.9
3.75	23.82	25,478	25,359	221.0
3.50	30.59	23,860	23,754	218.3
3.25	39.28	22,267	22,174	215.6
3.00	50.43	20,697	20,616	212.8
2.75	64.76	19,151	19,080	210.0
2.50	83.15	17,625	17,564	207.1
2.25	106.77	16,116	16,065	205.8
2.00	137.09	14,604	14,561	208.5
1.75	176.03	13,055	13,019	214.8
1.50	226.03	11,450	11,421	223.6
1.25	290.23	9,771	9,750	234.6
1.00	372.66	8,011	7,995	247.0
0.75	478.51	6,148	6,138	259.9

Table B.7 (continued)

Pressure scale height[a]	Pressure [mb]	Geometric height[b] [m]	Geopotential height[c] [m]	Temperature [K]
0.50	614.42	4,197	4,192	272.1
0.25	788.93	2,166	2,164	283.1
0.00	1013.00	57	57	295.1

[a] The pressure scale height is minus the natural logarithm of pressure relative to the surface pressure; it is dimensionless.

[b] The geometric height or altitude of an element is its distance above the reference sea level terrestrial ellipsoid, given in meters.

[c] The geopotential height above the reference sea level ellipsoid is given in meters. It can be considered to be its geometric height plus (or minus) a correction which depends upon latitude and height. The difference between geometric and geopotential height is zero at the surface at 30°N and increases with height; the difference varies with latitude.

well as daily variations. Moreover, the profile of the polar atmospheres deviates strongly from mid-latitude or equatorial profiles and there are also remarkable differences between the arctic and Antarctic atmospheric profiles for corresponding seasons.

As an example of the seasonal variations of local atmospheres we present in Figs. B.4 and B.5 the seasonal deviation of the average atmospheric profiles measured at Stuttgart, Germany, and at Pampa Amarilla, Mendoza, Argentina, respectively (Keilhauer et al., 2004; Blümer et al., 2005), from the US Standard Atmosphere (NASA, 1976). Similar studies were carried out for the Fly's Eye site at Dugway, Utah (Wilczyńska et al., 2005) and at other locations. The consequences of these variations are discussed in Sect. 7.7 and in Chap. 17 in connection with air fluorescence measurements and longitudinal shower development (see Fig. 7.24).

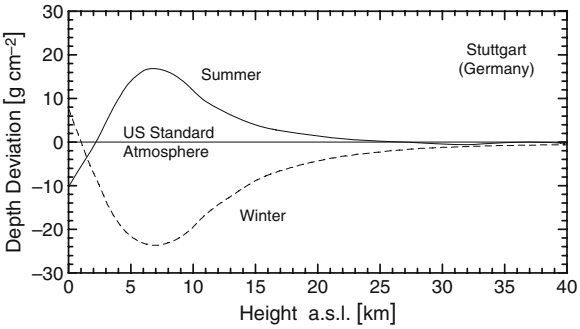

Fig. B.4 Deviation of the average seasonal atmospheric depth profiles measured at Stuttgart, Germany, from the US Standard Atmosphere (NASA, 1976; Keilhauer et al., 2004)

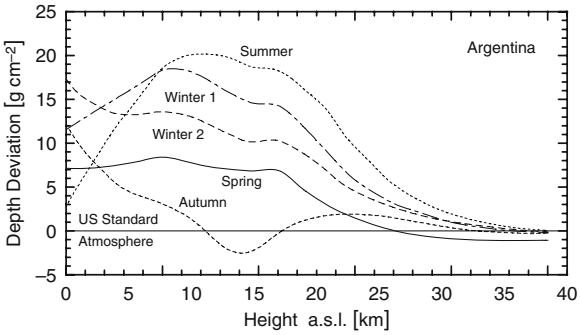

Fig. B.5 Deviation of the average seasonal atmospheric depth profiles measured at Pampa Amarilla, Argentina, from the US Standard Atmosphere (NASA, 1976). *Winter 1* and *winter 2* refer to two different atmospheric models, depending on the pressure condition (for details see Keilhauer et al., 2004)

B.4 Chapman Function

In a standard isothermal exponential atmosphere that is characterized by a constant scale height $h_s = (kT/Mg)$ [cm], where k is Boltzman's constant, T [K] the temperature in Kelvin, M [g/mole] the molecular weight and g [$\mathrm{cm^{-1}s^{-2}}$] the gravitational acceleration, the vertical column density X [$\mathrm{g\,cm^{-2}}$] of air overlaying a point P at altitude h [cm] is given by the common *barometer formula*

$$X(h) = X(h=0)e^{-(h/h_s)} \ \ [\mathrm{g\,cm^{-2}}]\,. \tag{B.9}$$

For inclined trajectories the *Chapman function* permits to compute the thickness or column density of inclined trajectories in the atmosphere accurately, taking into account the *curvature* of the Earth (Chapman, 1931). Depending on the accuracy required it should be used for trajectories whose zenith angle, θ, exceeds about 70°. Various approximate forms of the Chapman function are available (see Fitzmaurice, 1964; Swider and Gardner, 1967; Brasseur and Solomon, 1986). We give here the expression of Swider and Gardner (1967) for zenith angles $\leq (\pi/2)$ which gives the ratio of the total amount of atmosphere in the inclined direction, θ, with respect to the vertical (cf Fig. B.6).

$$Ch\left(x, \theta \leq \frac{\pi}{2}\right) = \left(\frac{\pi x}{2}\right)^{1/2} \left(1 - \mathrm{erf}\left[x^{1/2}\,\cos\,\frac{\theta}{2}\right]\right) \exp\left(x\,\cos^2\,\frac{\theta}{2}\right)\ , \tag{B.10}$$

where

$$x = \frac{R_E + h}{h_s}\ . \tag{B.11}$$

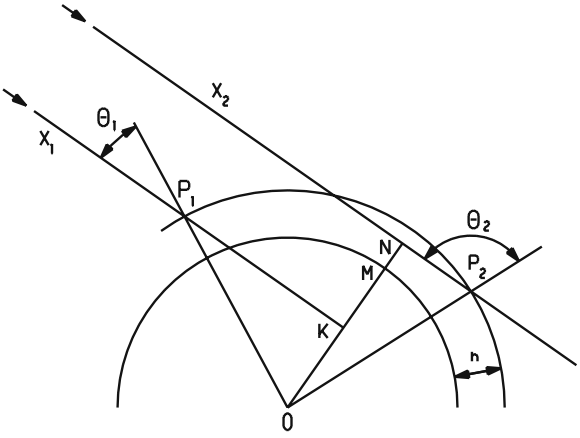

Fig. B.6 Atmospheric column density X_1 in *curved* atmosphere encountered by a cosmic ray incident under zenith angle $\theta_1 \leq \pi/2$ to reach point P_1 at altitude h. Also shown is the situation for point P_2 at $\theta > \pi/2$ and column density X_2, a situation that may arise when h is large

R_E is the radius of the Earth, h the altitude of observation in the atmosphere, and h_s is the appropriate scale height of the atmosphere.

For $\theta = \pi/2$, i.e., for horizontal direction we get

$$\mathrm{Ch}(x, \frac{\pi}{2}) = (\pi x/2)^{1/2} \quad , \tag{B.12}$$

which is about equal to 40. In other words, the column density or atmospheric thickness is approximately 40 times larger than for vertical incidence ($\theta = 0^\circ$). Figure B.7 displays the atmospheric column density as a function of zenith angle as is obtained with the Chapman function.

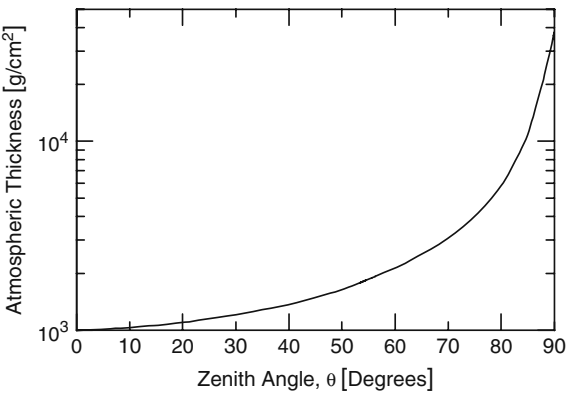

Fig. B.7 Relation between zenith angle and atmospheric thickness or column density at sea level for the "curved" Earth, as described by the Chapman function

B.5 Gross Transformation

The Gross transformation allows to transform the *altitude dependence* of the rate of air showers to the *zenith angle distribution* (Gross, 1933). Moreover, it permits to calculate the vertical intensity $R_V(X, \theta = 0)$ of air showers per unit solid angle at an atmospheric depth X in terms of the measured rate of all showers $R(X)$ at this depth. The Gross transformation can be written in different forms; it is frequently expressed as (Galbraith, 1958; Allkofer, 1975)

$$R_V(X, \theta = 0) = \frac{1}{2\pi}\left((n+1)R(X) - X\frac{\partial R(X)}{\partial X}\right) \quad [\mathrm{m}^{-2}\mathrm{s}^{-1}] \tag{B.13}$$

where

$$n = 2(\gamma - 1) + (k\gamma) - \kappa \quad .$$

γ is the exponent of the *density spectrum*, κ is the exponent of the *decoherence* rate, R, i.e., $R \propto d^{-\kappa}$, determined empirically, k is related to the counter geometry and response, and d is the counter separation (Galbraith, 1958; Allkofer, 1975, Khristiansen, 1980).

B.6 Energy, Particle, Photon and Magnetic Field Densities in Space

Energy and field densities in space are of great importance for the propagation of cosmic rays, irrespective whether they are of galactic or extragalactic origin. Magnetic fields in space deflect the charged particles and thus mask their origin for the observer on Earth. On the other hand radiation in space provokes interactions that degrade the original primary energy of all particles, charged and neutral.

In Table B.8 we have listed the energy and/or number densities of particles and photons in the different regions of space, i.e., in the heliosphere, the Galaxy, extragalactic (metagalactic) space and the Universe. Some of the data are rather speculative.

The anisotropy of the cosmic microwave background radiation CMBR is discussed in the article of Smoot (2000). The spectral distributions of the CMBR and of the radiation from other contributing sources are plotted in Fig. B.8. The plot shows the distribution of the power per unit frequency bandwidth per unit area and solid angle.

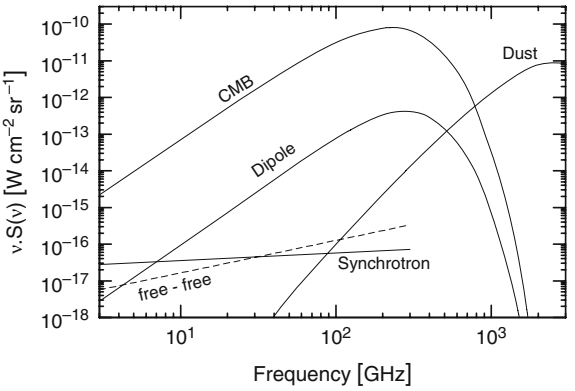

Fig. B.8 Intensity of the microwave sky from 3 to 3,000 GHz near a Galactic latitude of $b = 20^\circ$. The ordinate is the brightness of the sky, $S(\nu)$, multiplied by the frequency, ν (Smoot, 2000)

Table B.8 Energy and number density of particles and photons

Type of particle or photon	Energy density [eV cm^{-3}]	Number density [cm^{-3}]
Cosmic rays in Galaxy, all[a,b]	0.9	–
Cosmic rays in Galaxy, p only[a]	0.65	–
Cosmic rays near Earth, solar min.[d]	0.60	–
Cosmic rays at 1 pc from Sun[e]	0.80–1.0	–
2.7 K CMBR $< E >= 6.4 \cdot 10^{-4}$ eV [f,g]	0.24	$\simeq 410$
Starlight, $< E >= 1$ eV[h]	0.6	0.25
EG Starlight, $< E >= 2$ eV[f]	10^{-2}	$5 \cdot 10^{-3}$
Neutrinos, $E \simeq 0.03$ eV[b,c]	–	$\simeq 10^8$
Galactic magnetic field[h]	0.2	–
Local Galactic magnetic field strength $B \simeq 4 - 9\mu$G[i]		
Galactic magnetic field strength at few pc $B \simeq 1.6\mu$G[i]		
Extragalactic magnetic field strength $B \simeq 1$nG[j,k]		

[a] Ginzburg (1958).
[b] Khristiansen (1980).
[c] Fermi energy.
[d] Ginzburg and Syrovatskii (1969).
[e] Bloemen (1987).
[f] Ramana Murthy and Wolfendale (1993).
[g] Bergstrom and Goober (2004).
[h] Longair (1981).
[i] Beck (2009a, b).
[j] Kotera and Lemoine (2008).
[k] Kronberg (1994).

B.7 Data on Cherenkov Radiation

B.7.1 Cherenkov Radiation in the Atmosphere

Figure B.9 is a quick reference diagram for practical applications to extract the relevant parameters of Cherenkov radiation in the atmosphere, and in Table B.9 we list the Cherenkov threshold energies in water and air (at NTP) for electrons, muons, pions and protons.

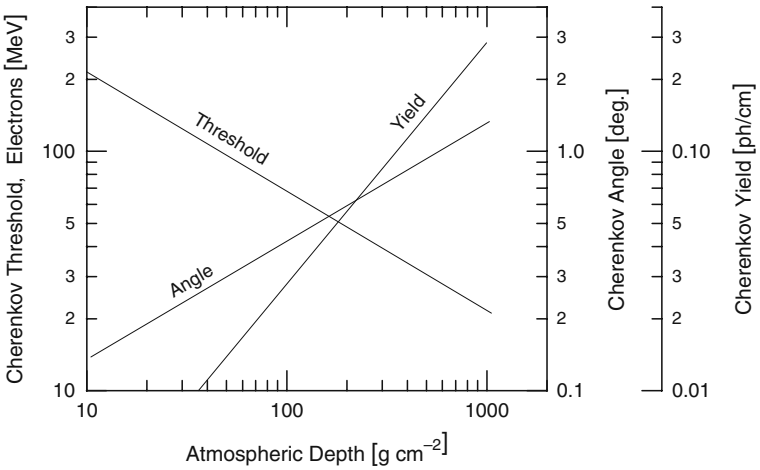

Fig. B.9 Characteristic properties of the Cherenkov radiation of electrons in the Earth's atmosphere. Shown is the threshold energy for the production of Cherenkov photons, the opening angle of the Cherenkov cone of emission with respect to the velocity vector of the electrons and the photon yield per centimeter as a function of atmospheric depth

Table B.9 Cherenkov threshold energies of particles in water and air

	Kinetic energy in	
Particle	Water	Air (NTP)
Electron	257 keV	21 MeV
Muon	53 MeV	4.4 GeV
Pion	70 MeV	5.8 GeV
Proton	475 MeV	39 GeV

References

Allkofer, O.C.: Introduction to Cosmic Radiation, Verlag Karl Thiemig, Munchen (1975).
Barnett, J.J., and S. Chandra: COSPAR International Reference Atmosphere. Adv. Space Res., 10, 12, p. 7 (1990).
Beck, R.: arXiv:0810.2923v4 [astro-ph] 12 Jan (2009a).
Beck, R.: Astrophys. Space Sci. Trans., 5, p. 43 (2009b)
Bergström, L., and A. Goobar: Cosmology and Particle Astrophysics, Springer, Berlin, 2nd ed. (2004).
Bloemen, H.: Proc. Symp. Interstellar Processes, Hollenbach, D.J., and H.A. Thronson, Jr., eds., Astrophysics and Space Science Library, D. Reidel Publ. Co. Dordrecht (1987).
Blümer, J., et al., Pierre Auger Collaboration: PICRC, 7, p. 123 (2005).
Brasseur, G., and S. Solomon: Aeronomy of the Moddle Atmosphere, D. Reidel Publishing Company, Dordrecht/Boston/Lancaster (1986).
Chapman, S.: Proc. Phys. Soc. (Lond.), 43, p. 483 (1931).
Cole, A.E., and A.J. Kantor: Air Force Reference Atmosphere, AFGL-TR-78-0051 (1978).

Eidelman, S., et al.: Particle Physics Booklet, Particle Data Group, Springer, Berlin (available from LBNL and CERN) (2004), and Phys. Lett. B, 592, p. 1 (2004).
Fitzmaurice, J.A.: Appl. Opt., 3, p. 640 (1964).
Galbraith, W.: Extensive Air Showers, Butterworths Scientific Publishers, London (1958).
Ginzburg, V.L.: Progress in Elementary and Cosmic Ray Physics, North Holland Publishing Co., Amsterdam, Vol. 4 (1958).
Ginzburg, V.L., and S.I. Syrovatskii: The Origin of Cosmic Rays, Gordon and Breach, New York (1969).
Gross, B: Zeitschr. f. Physik, 83, p. 214 (1933).
Keilhauer, B., et al.: Astropart. Phys., 22, p. 249 (2004).
Khristiansen, G.B.: Cosmic Rays of Superhigh Energies, Verlag Karl Thiemig, Munchen (1980).
Kotera, K., and M. Lemoine: arXiv:0706.1891v2 [astro-ph] 4 Jan (2008).
Kronberg, P.P.: Rep. Prog. Phys., 57, p. 325 (1994).
Longair, M.S.: High Energy Astrophysics, Cambridge University Press, Cambridge, MA (1981).
NASA, National Aeronautics and Space Administration, US Standard Atmosphere 1976, NASA-TM-X-74335 (1976).
Petrukhin, A.A., and V.V. Shestakov: Can. J. Phys., 46, part 1, p. S377 (1968).
Ramana-Murthy, P., V., and A. W. Wolfendale: Gamma Ray Astronomy, Cambridge University Press, Cambridge, MA, 2nd ed. (1993).
Smoot, G.F.: Phys. Rep., 333–334, pp. 269–308 (2000).
Sternheimer, R.M.: Phys. Rev., 88, p. 851 (1952).
Sternheimer, R.M.: Phys. Rev., 89, p. 1309 (1953), Erratum.
Sternheimer, R.M.: Phys. Rev., 93, p. 351 (1954a).
Sternheimer, R.: Phys. Rev., 93, p. 1434 (1954b), Erratum.
Sternheimer, R.: Phys. Rev., 103, p. 511 (1956).
Sternheimer, R.: Phys. Rev., 115, p. 137 (1959).
Sternheimer, R.: Phys. Rev., 124, p. 2051 (1961).
Sternheimer, R.M., and R.F. Peierls: Phys. Rev. B, 3, p. 3681 (1971).
Sternheimer, R.M., et al.: "The Density Effect for the Ionization Loss of Charged Particles in Various Substances", Atomic and Nuclear Data Tables, 30, p. 261 (1984). See also Groom, D.E., et al., ibid 78, pp. 183–356 (2001) and Ivanov, D.Yu., et al.,: Phys. Lett. B, 442, p. 453 (1998) for corrections.
Swider, W., and M.E. Gardner: Environmental Research Papers No 272, Air Force Cambridge Research, Bedford, MA (1967).
Tsai, Y.S.: Rev. Mod. Phys., 46, p. 815 (1974).
Wilczyńska, B., et al.: PICRC, 7, p. 203 (2005).

Appendix C
List of Symbols

Table C.1 Roman symbols used in this book

a	Length, distance
	Parameter
A	Area
	Atomic weight or mass
	Mass number
	Parameter
b	Length, distance
	Parameter
B	Magnetic induction
	Parameter, general constant, background
c	Velocity of light in vacuum
C	Constant, parameter
D	Distance, separation
e	Electric charge of the electron
e^-	Electron
E_0	Initial or primary energy of a particle
E_s	Scattering energy
ER	Elongation rate
$f(dN)$	Differential shower size spectrum
$F(N)$	Integral number or size spectrum
$FWHM$	Full width at half maximum of pulse
$G(\rho)$	Shower density spectrum
h	Height (vertical) or altitude in atmosphere
h_s	Scale height of atmosphere
H	Magnetic field strength
$\mathcal{H}$	Humidity
I	Intensity
$I(N)$	Differential spectrum
$I(> N)$	Integral spectrum
J	Flux, integral spectrum,
k	Constant, scale factor
K	Inelasticity
	Azimuthal asymmetry ratio (geomagnetic)
	Constant, normalizing -, scale factor
l	Length, element of
L	Distance, scattering length

Table C.1 (continued)

m_e	Rest mass of electron
M	Coincidence fold
M_0	Azimuthal asymmetry factor
	Primary mass
n	Index of refraction
	Exponent, secondary particle multiplicity
N	All-particle shower size
N_A	Avogadro's number
N_{ch}	Charged particle shower size
N_e	Electron shower size
N_μ	Muon shower size
p	Momentum
p_l	Longitudinal momentum
p_t	Transverse momentum
P	Pressure
Q	Cherenkov photon density (visible)
r	Radius, radial distance
r_e	Classical electron radius
R	Rate of events
	Radius, radius of nucleon, radial distance
	Radial distribution function (of Cherenkov photons)
s	Age parameter of air showers
	Center of mass energy squared
S	Magnetic rigidity
	Path length
	Sensitivity
t	Time
	Thickness (of target, air, etc.) in radiation units
t_d	Delay time
t_f	Fall time of a pulse
t_r	Rise time of a pulse
t_t	Top time of a pulse
T	Temperature of atmosphere, etc.
$\mathrm{ve}\mu/\mathrm{m}^2$	Vertical equivalent muons per square meter
	(for definition see Blake et al., ICRC 8, p. 189, 1977)
x	Distance, path length
X	Column density, atmospheric, underground, etc.
X_s	Slant depth, atmospheric, underground
X_{max}	Depth of shower maximum in atmosphere
X_0	Vertical atmosperic column density at sea level
y	Rapidity
Y	Yield
Z	Atomic number, atomic charge

Table C.2 Greek symbols used in this book

α	Fine structure constant
	Barometric coefficient of air showers
	Decoherence exponent
β	Temperature coefficient of air showers
	Velocity divided by velocity of light, v/c
χ_0	Radiation length, cascade unit
χ_a	Radiation length in air
δ	Angle
Δ	Increment
ϵ_c	Critical energy (of electrons)
η	Elasticity
ϕ	Azimuthal angle
γ	Exponent of spectra (size, number, density, etc.)
Γ	Exponent of integral primary spectrum
κ	Ratio, signal-to-noise
λ	Geomagnetic latitude
	Optical wavelength
$\lambda_{\rm abs}$	Absorption length of shower particles
$\lambda_{\rm abs}^{\mu}$	Absorption length of muons in showers
$\lambda_{\rm int}$	Interaction mean free path (i.m.f.p.)
$\lambda_{\rm int}^{N}$	Interaction mean free path of nucleons
$\lambda_{\rm int}^{\pi}$	Interaction mean free path of pions
$\Lambda_{\rm att}$	Attenuation length of air shower rate
μ_N	Attenuation coefficient of air shower rate
μ_p	Absorption coefficient of shower particles
ρ	Particle or photon density
	Radius of curvature of charged particle
	In magnetic field
σ	Cross section
	Standard deviation
σ_0	Total $e^{\pm}$ pair production probability
$\sigma_{\rm inel}$	Inelastic cross section
$\sigma_{\rm inel}^{p,{\rm air}}$	Inelastic proton-air cross section
$\sigma_{\rm int}$	Interaction cross section
θ	Zenith angle
	Angle of emission
ξ	Angle
	Function
ζ	Constant related to the cascade unit

Appendix D
Abbreviations and Acronyms

The following table contains a partial list of frequently used abbreviations and acronyms of experimental sites, installations, experiments and instruments.

Table D.1 List of abbreviations and acronyms

AGASA	Akeno Giant Air Shower Array (Japan)
AIRES	AIR shower Extended Simulation
AMANDA	Antarctic Muon and Neutrino Detector Array
ANITA	Antarctic Impulsive Transient Antenna experiment
ASICO	Air shower SImulation and COrrelation
BLANCA	Broad Lateral Non-imaging Cherenkov Array
CASA	Chicago Air Shower Array (Dugway, Utah, USA)
CERN	European Center for Particle Physics (Geneva, CH)
CMBR	Cosmic Microwave Background Radiation
CORSIKA	COsmic Ray SImulation for KAscade
CREAM	Cosmic Ray Energy And Mass experiment
DICE	Dual Imaging Cherenkov Experiment (Dugawy, USA)
DPM	Dual Parton Model
EM	Electro-Magnetic
EPOS	Energy Parton Off-shell Splitting (MC simulation)
FNAL	Fermi National Accelerator Laboratory (Chicago, USA)
FORTE	Fast On-orbit Recording of Transient Events
FWHM	Full Width at Half Maximum
GLUE	Goldstone Lunar Ultrahigh energy neutrino Experiment
GRAPES	Gamma Ray Astronomy at PeV EnergieS (Ooty, India)
GZK	Greisen-Zatsepin-Kuzmin cutoff
HAS	Horizontal Air Shower
HEGRA	High Energy Gamma Ray Astronomy (Canary Islands)
HESS	High Energy Stereoscopic System (Namibia)
HSA	Hillas Splitting Algorithm
IC	Inverse Compton scattering
ISR	Intersecting Storage Ring (CERN, Geneva, Switzerland)
KASCADE	KArlsruhe Shower Core and Array DEtector (Germany)
KNO	Koba-Nielsen-Olesen scaling
LAAS	Large Area Air Shower experiment (Japan)
LANL	Los Alamos National Laboratory (NM, USA)
LAP	Local Age Parameter, Lateral Age Parameter
LDF	Lateral Distribution Function

Table D.1 (continued)

LEP	Large Electron Positron collider (CERN, Geneva, CH)
LHC	Large Hadron Collider (CERN, Geneva, Switzerland)
LPM	Landau – Pomeranchuk – Migdal effect
LVD	Large Volume Detector (Gran Sasso, Italy)
MACRO	Monopole Astrophysics Cosmic Ray Observatory (Italy)
MC	Monte Carlo method
MIA	MIchigan Array (Dugway, Utah, USA)
MOCCA	MOnte Carlo CAscade simulation program
NKG	Nishimura – Kamata – Greisen – function
NTP	Normal Temperature and Pressure
OWL	Orbiting Wide-angle Light collector
QGS	Quark Gluon String
RHIC	Relativistic Heavy Ion Collider (Brookhaven, USA)
RICE	Radio Ice Cherenkov Experiment (Antarctica)
SHALON	Russian abbr. for "EAS from Neutrinos" (Tien Shan)
SIBYLL	MC event generator
SPS	300 GeV Super Proton Synchrotron (CERN, Switzerland)
TACTIC	TeV Atmospheric Cherenkov Telescope with Imaging Camera
TRACER	Transition Radiation Array for Cosmic Energetic Radiation
TTC	Time-Track-Complementarity
VERITAS	Very Energetic Radiation Imaging Telescope Array System (Whipple Observatory, Arizona, USA)

Appendix E
List of Cosmic Ray Conferences

1.	Cracow, Poland	1947	17.	Paris, France	1981
2.	Como, Italy	1949	18.	Bangalore, India	1983
3.	Bagneres de Bigorre, F	1953	19.	La Jolla, Ca., USA	1985
4.	Guanjuato, Mexico	1955	20.	Moscow, U.S.S.R.	1987
5.	Varenna, Italy	1957	21.	Adelaide, Australia	1990
6.	Moscow, U.S.S.R.	1959	22.	Dublin, Ireland	1991
7.	Kyoto, Japan	1961	23.	Calgary, Canada	1993
8.	Jaipur, India	1963	24.	Rome, Italy	1995
9.	London, England	1965	25.	Durban, South Africa	1997
10.	Calgary, Canada	1967	26.	Salt Lake City, USA	1999
11.	Budapest, Hungary	1969	27.	Hamburg, Germany	2001
12.	Hobart, Tasmania, Aus.	1971	28.	Tsukuba, Japan	2003
13.	Denver, Co., USA	1973	29.	Pune, India	2005
14.	Munich, Germany	1975	30.	Merida, Mexico	2007
15.	Plovdiv, Bulgaria	1977	31.	Lodz, Poland	2009
16.	Kyoto, Japan	1979	32.	Beijing, China	2011

Appendix A
Experimental Installations

A.1 EAS Arrays and Cosmic Ray Ground Facilities

A.1.1 Lists of Array and Facility Sites

In the following we present a list of air shower arrays of the past and present (Table A.1). The altitudes of the arrays are listed together with the corresponding atmospheric depths. The latter are in most cases the vertical atmospheric depths, i.e., the average vertical overburden [g cm^{-2}]. In some cases, however, authors may specify different values for the overburden in different publications for the same array. The reason for these discrepancies is that in some cases authors consider the slant depth for the average near vertical shower, e.g., $\sim 15^{\circ}$, as compared to the depth for perfectly vertical showers, that are rather rare exceptions in practice. Some table entries with similar altitudes suggest contradicting altitude-overburden relations, but these are explained by differing average atmospheric and meteorological conditions (see Sect. B.3).

Figure A.1, which is a reproduction from a web page of the Yakutsk group, shows the aperture in units of square kilometer-steradian [km^2 sr] of the largest air shower arrays of the past and present, and of arrays and detector systems currently under construction or in the planing phase.

In Table A.2 we list emulsion chamber sites, and in Table A.3 the threshold energies of the muon detectors of some of the arrays listed in Table A.1. Note that for some arrays different threshold energies were used simultaneously, in others different thresholds at different times. Table A.4 is a partial list of major gamma ray air Cherenkov detectors of past and present.

P.K.F. Grieder, *Extensive Air Showers,* DOI 10.1007/978-3-540-76941-5_22,

Table A.1 EAS array sites and experiments of past and present

Name, place, country (nearest major city, region)	Approximate	
	Altitude a.s.l. [m]	Atmospheric depth [g cm^{-2}]
AGASA, Akeno (Kofu) Japan[a]	900	935
Agassiz, (Boston) USA[a]	183	1,020
ANI/MAKET Mt. Aragats, (Yerevan), Armenia	3,200	700
ARGO, Yangbajing, (Lhasa), Tibet, China[b]	4,370	606
Auger South, (Malargüe), Argentina	1,300–1,400	875
Auger North, (Lamar) Colorado, USA[d]	∼1,500	∼865
Bagnères de Bigorre, France[a]	456	965
Baksan, Kabardian-Balkarian Rep., Russia[c]	2,060	805
Buckland Park, (Adelide), SA, Australia	s.l.	1,033
CASA/MIA, (Dugway), Utah, USA[a]	1,435	870
Chacaltaya, (La Paz), Bolivia	5,230	530
Cornell, (Ithaca), NY, USA[a]	260	998
Cygnus, (Los Alamos), New Mexico, USA[a]	2,220	800
Darjeeling, India (Exp. at Siliguri, s.l.)	2,200	802
Dugway, Utah, USA (Durham (GB) Exp.)[a]	1,450	865
Durham, England[a]	60	1,025
EAS-Top, Gran Sasso, Italy[a]	2,005	810
Echo Lake, Colorado, USA[a]	3,260	715
El Alto, (La Paz), Bolivia[a]	4,200	630
Elbrus Laboratory	1,850	820
Evans, Mt., (Denver) Colorado, USA[a]	4,300	615
Fly's Eye 1, (Dugway), Utah, USA[a]	1,585	860
Fly's Eye 2, (Dugway), Utah, USA[a]	1,435	870
GAMMA, (Yerevan), Armenia	3,200	700
GRAND, (Notre Dame), Indiana, USA	220	1,018
GRAPES, Ootacamund (Mysor), India	2,200	800
GREX, Haverah Park, (Leeds), England[a]	220	1,018
Gulmarg, (Srinagar), Kashmir, India[a]	2,743	740
Haverah Park, (Leeds), England[a]	212	1,018
HEGRA, La Palma, Canary Islands[a]	2,250	800
Homestake, South Dakota, USA[a]	1,615	843
Issyk-Kul Lake, (Almaty), Kazakhstan[b]	1,600	845
JANZOS, New Zealand[a]	1,640	840
KASCADE-Grande, Karlsruhe, Germany[a]	110	1,022
Kiel, Germany[a]	s.l.	1,033
Kobe, Japan	s.l.	1,033
KGF, Kolar Gold Fields, (Karnataka), India[a]	920	920
L3+C (CERN, Geneva) Switzerland[a]	374	1,000
Liang Wang, Mt., Yun-Nan, China[b]	2,720	735
Lodz, Poland[a]	230	1,000
MILAGRO, (Los Alamos), N.M., USA	2,630	750
Moscow, Russia	192	1,020
Musala Mountain, Bulgaria[a]	2,925	713
NASCA, see Akeno	–	–
Norikura, Mt., (Matsumoto), Japan[a]	2,770	750
Ohya, (Nikko), Japan[a]	149	1,020
Ootacamund, (Mysore), India	2,200	800
Pamir (old), Tadzhikistan[a]	3,860	650
Pamir (new), Tadzhikistan	4,380	590

Table A.1 (continued)

Name, place, country (nearest major city, region)	Approximate	
	Altitude a.s.l. [m]	Atmospheric depth [g cm^{-2}]
Pic du Midi, Pyrenees, France[a]	2,860	729
Samarkand, Uzbekistan	750	958
SPASE[a], SPASE-II, South Pole	3,300	695
SPICA, see Akeno	–	–
SUGAR, (Narrabri), Australia[a]	260	998
Sulphur Mountain, Alberta, Canada[a]	2,285	800
Sydney, Australia[a]	30	1,016
Telescope Array, Dugway, Utah, USA	1,400	865
Tibet, Yangbajing, (Lhasa)	4,370	606
Tien Shan, (Almaty), Kazakhstan	3,340	690
Tokyo, INS, Japan[a]	59	1,020
TUNKA-133, (Baikal), Russia[b]	675	960
UMC array, see CASA/MIA/Fly's Eye[a]	–	–
Verrières (Paris), France[a]	100	1,020
Volcano Ranch, (Albuquerque), N.M., USA[a]	1,768	834
Yakutsk, Siberia, Russia	105	1,020

[a] Shut-down.
[b] Under construction or partial operation.
[c] 1,700 m a.s.l. for underground laboratory.
[d] In planning phase or proposed.
Note: Some of the atmospheric depths listed above do not correspond exactly to the vertical air column at the specified altitude, but to the effective air column of an incident trajectory subtending a mean zenith angle of about 10–15°. This zenith angular cut is frequently used to select a reasonable number of quasi vertical events for analysis.

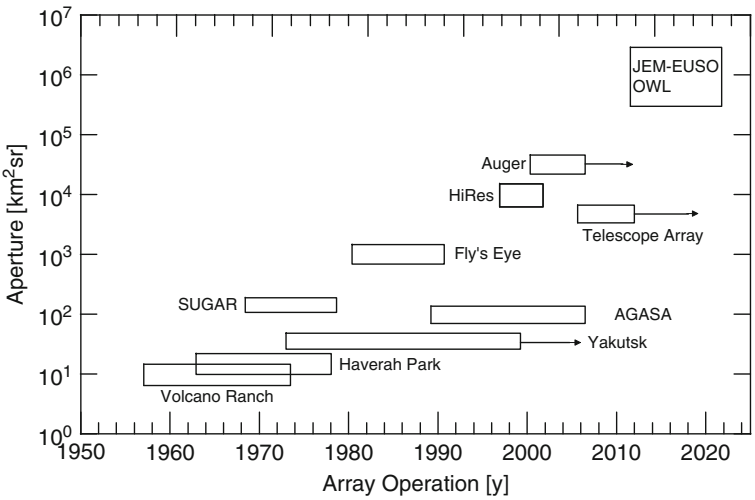

Fig. A.1 Apertures of the large arrays of the past and present, of arrays under construction or expansion, and of the proposed JEM-EUSO and OWL satellite based detector systems (curtesy of the Yakutsk Group)

Table A.2 Emulsion chamber sites

Name, place, country (nearest major city, region)	Approximate	
	Altitude a.s.l. [m]	Atmospheric depth [g cm^{-2}]
Chacaltaya, (La Paz), Bolivia[a]	5,230	530
Fuji, Mt., Japan	3,776	650
Kanbala, Mt., Tibet, China[b]	5,500	520
Pamir Mountains, Tadzhikistan (Old Station)[b]	3,860	625
Pamir Mountains, Tadzhikistan (New Station)	4,237	600

[a] coupled with dedicated electronic detector array.
[b] shut-down.

Table A.3 Threshold energies of Muon detectors at various EAS sites

Site	Threshold energy [GeV] comments
Agassiz	$\geq$0.4, $\geq$0.5, $\geq$1.0
Akeno/AGASA	$\geq$0.5, $\geq$1.0
AMANDA	$\geq$1,000
ANI/Aragaz	$\geq$5.0
Auger	$\sim$1.0
Baksan	$\geq$230
Chacaltaya	$\geq$0.6
Cornell	$\geq$2.0
Cygnus	$\geq$1.0, $\geq$2.0
EAS-Top	$\geq$1.5, $\geq$2.0
EAS-1000	$\geq$1.0
GAMMA	$\geq$5.0
GRAPES-3	$\geq$1.0
Haverah Park	$\geq$0.3, $\geq$0.41, $\geq$0.6, $\geq$0.7, $\geq$1.0
Haverah Park/Durham	$1 \leq p \leq 1,000$ GeV/c magn. spectrometer[a]
HEGRA	$\geq$0.3
Ice Cube	$\approx$1 TeV
KASCADE	$\geq$ 0.23, $\geq$ 0.49, $\geq$ 0.8, $\geq$ 2.4
KGF	$\geq$1.0, $\geq$220, $\geq$640,$\geq$1,700, $\geq$12 TeV
Kiel	$\geq$2.0, magn. spectrometer[a]
Lodz	$\geq$0.6, $\geq$5.0
LVD	$\geq$1,300
MACRO	$\geq$1,300
MIA	$\geq$0.85
Milagro	$\geq$2, $>$500, $>$1,200
Moscow	$\geq$0.5, $\geq$10.0, magn. spectrometer[b]
Norikura, Mt.	$\geq$0.3, $\geq$0.7
North Bengal (NBU)	$\geq$2.5, 2 magn. spectrometers[a]
Nottingham	$\geq$0.41
Ohya	$\geq$14.0
SUGAR	$\geq$0.75
Tien Shan	$\geq$5.0
Tokyo (Fukui)	$\geq$2.0
Volcano Ranch	$\geq$0.22
Yakutsk	$\geq$0.3, $\geq$0.7, $\geq$1.0[c]

[a] solid iron magnet spectrometer (Earnshaw et al., 1968).
[b] maximum detectable momentum 600 GeV/c (Vernov et al., 1979).
[c] since 1979 (Diminstein et al., 1979).

Table A.4 TeV[a] gamma ray air Cherenkov detector sites and experiments of past and present (Arrays and Telescopes, partial List only)

Name, place, country (nearest major city, region)	Approximate	
	Altitude [m]	Atmospheric depth [g cm^{-2}]
AIROBIC (see HEGRA)	–	–
ANI, Aragats Mt., (Erevan), Armenia	3,200	690
ASGAT, (Targasonne) France	1,650	840
BLANCA, (Dugway, Utah) USA	1,435	865
CACTUS, (Daggett), CA, USA	610	965
Cangaroo, (Woomera), South Australia	160	1,020
Crimean AP Obs., (Nauchny), Ukraina	2,100	800
Cygnus, (Los Alamos), NM, USA	2,200	800
GAMMA, Mt. Aragats (Erevan), Armenia	3,200	700
GASP 1, South Pole	3,300	695
DICE, (Dugway, Utah) USA	1,450	865
Haleakala, (Maui, HI) USA	3,297	695
HEGRA, (La Palma), Canary Islands	2,200	800
H.E.S.S., (Windhoek), Namibia	1,800	830
JANZOS, (Wellington), New Zealand	1,640	840
MACE, (Hanle), India	4,240	600
MAGIC, (see HEGRA)	–	–
Pachmarhi, (Madhya Pradesh),India	1,100	920
Plateau Rosa, Italy	3,500	675
Potchefstrom, South Africa	1,429	880
SHALON, (Tien Shan), Kazakhstan	3,340	690
Srinagar, (Kashmir), India	1,730	835
STACEE, (Albuquerque), NM, USA	1,740	830
TACTIC,(Mt. Abu, Rajasthan) India	1,219	905
TACT, Tien Shan, Kazakhstan	3,340	690
Themistocle, (Targasonne), France	1,650	840
VERITAS (see Whipple)	–	–
Whipple Obs., Mt. Hopkins, Arizona, USA	2,380	730
Woomera, South Australia	320	1,000

[a] Some systems claim to have thresholds as low as 0.1 TeV. For a summary of early gamma ray air Cherenkov detectors, see Baillon (1991) or Lorenz (1993).

Table A.5 Locations of some old cosmic ray experimental sites

Name, location	Altitude [m a.s.l.]
Albuquerque, New Mexico (USA)	1,575
Echo Lake, CO (USA)	3,260
Ithaca, NY (USA)	260
Jungfrau-Joch (Switzerland)	3,454
Mt. Evans, CO (USA)	4,300
Sulfur Mountain Alberta (Canada)	2,285

A.1.2 Layouts of Selected Air Shower Arrays of Past and Present

On the following pages we show a selection of layouts of air shower arrays of the past and present. Some of the older arrays are historically relevant as they represent landmarks of air shower research efforts and discoveries. It should be kept in mind that layouts and configurations of most arrays are being changed in the course of time to suit new and particular scientific aims. Thus, the layouts shown here apply to particular periods. On the other hand, some array layouts had not been changed for many years. In a few cases different array configurations are shown that existed at the same site but at different times. For accurate current array configurations the reader should consult the particular research group or the proceedings of recent Cosmic Ray conferences.

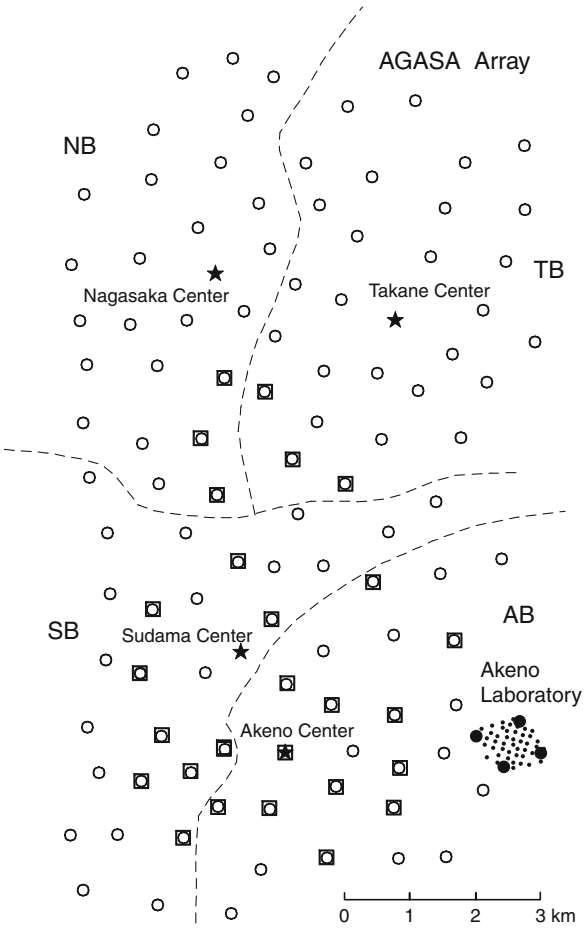

Fig. A.2 Layout of the AGASA array at Akeno (Japan), located at 900 m a.s.l. (920 g cm^{-2}). The *symbols* ○ represent scintillation detectors of area 2.2 m^2, □ muon detector of different area, · are 1 m^2 large scintillation detectors belonging to the 1 km^2 Akeno array, four of them shown as • belong to *AGASA*. The *dashed lines* identify the boundaries between the four sections, labeled as *NB, TB, SB* and *AB*, and the *symbols* ⋆ indicate the location of the branch centers (Chiba et al., 1992)

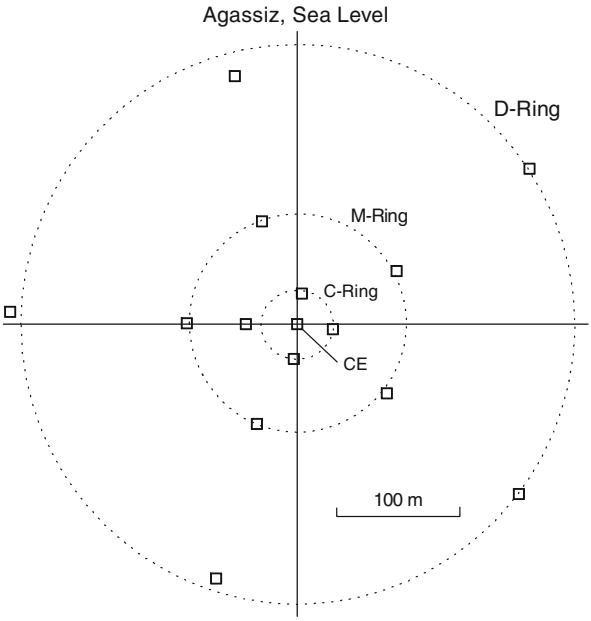

Fig. A.3 Layout of the M.I.T. detector array used by Clark et al. (1961) at Agassiz. The four detectors in the C-ring were used to record showers as small as $5 \cdot 10^4$ particles

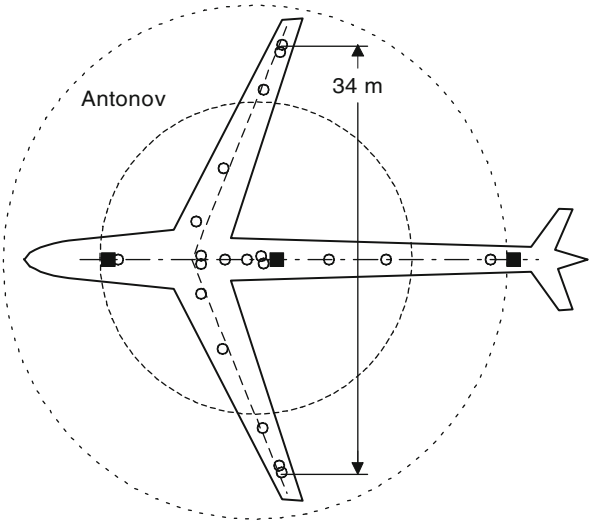

Fig. A.4 Air shower array installed on board of an air plane, used by Antonov et al. (1971, 1973) to study air showers in the stratosphere. The spark chambers (■) were used to determine the direction of incidence of the shower, the scintillation detectors (○) to determine the lateral distribution, the shower size, and to locate the position of the shower axis

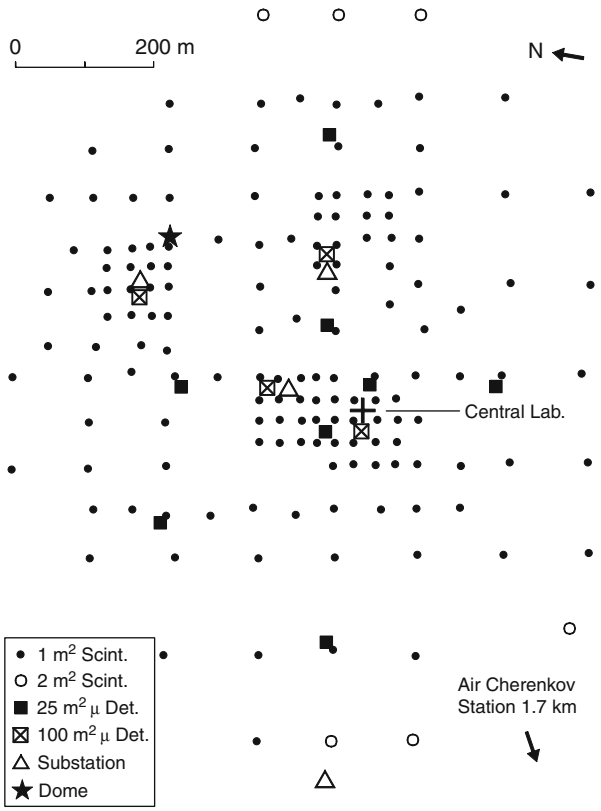

Fig. A.5 Layout of the Akeno array of the 1980s for which the detection efficiency is plotted in Fig. 2.7. This configuration covers an area of approximately 1 km^2, has a slope of 11° to the south–west and is located at 900 m a.s.l. (920 g cm^{-2}). The different detector types and dimensions are identified in the insert at the lower left. A 90 m^2 hadron calorimeter is located at the central laboratory (+). The thresholds for of the muon detectors are 1 and 0.5 GeV for the 25 and 100 m^2 detectors, respectively (for further details see Hara et al., 1979)

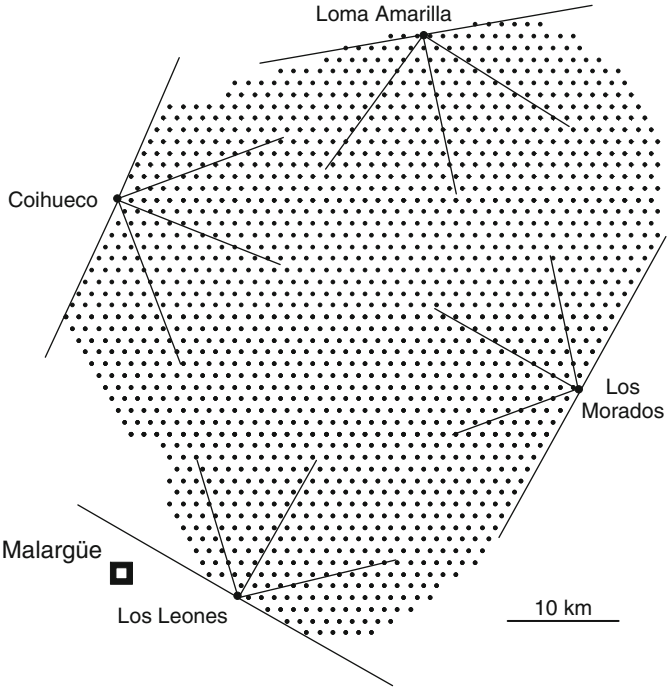

Fig. A.6 Layout of the giant Auger (South) Observatory installations in Argentina. Shown are the 1,600 deep water Cherenkov surface detectors and the four fluorescence detector telescopes that overlooking the surface array (courtesy of A. Haungs, FZ Karlsruhe, Germany and the Auger Collaboration)

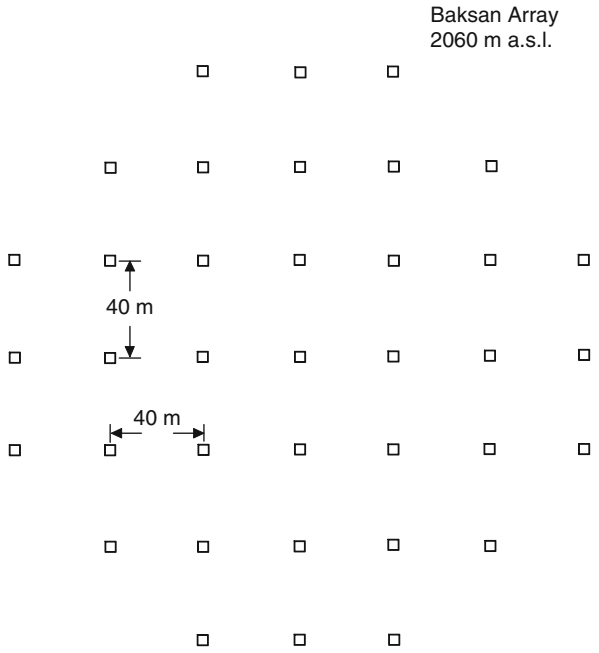

Fig. A.7 The Baksan "Andyrchy" air shower array is located above the large Baksan underground 4-level scintillation telescope. The *array* is located at an average height of 2,060 m a.s.l. and is inclined. It consists of 37 plastic scintillators of 5 cm thickness and 1 m^2 area. The detector separation as given in the figure is the approximate separation in the horizontal projection. A cutaway view of the entire installation at Baksan is drawn in Fig. A.38 of the Appendix A.2 (Alexeyev et al., 1993; Chudakov et al., 1999)

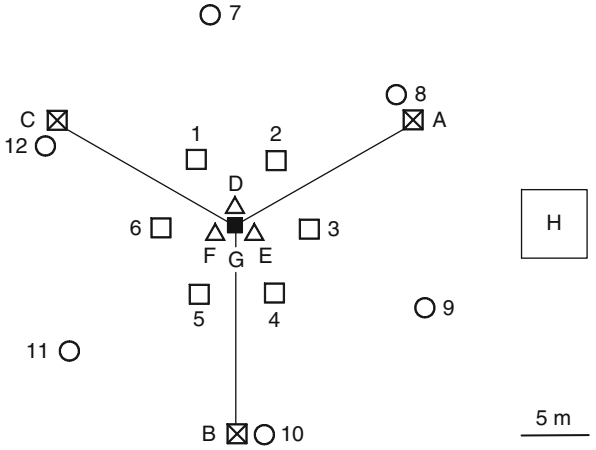

Fig. A.8 Balloon mounted air shower array layout, used by Antonov et al. (1977), to explore the altitude dependence of air shower observables up to 12 km. The symbols labeled *A*, *B* and *C* are scintillation detectors of area 0.25 m^2 each; *D*, *E* and *F* are small scintillators, each of area 0.07 m^2. The central unit labeled *G* represents an arrangement of 30 large Geiger-Mueller (GM) counters, each of area 86 cm^2, and 30 small counters, each of area 5.4 cm^2. The open *squares 1–6* show the location of GM trays containing 20 large and 20 small counters, the open *circles 7–12* are similar trays holding 20 large and 10 small GM counters of dimensions as specified above. The square on the right labeled *H* represents a cluster of counters consisting of 24 sub-assemblies of area 688 cm^2 each and 12 units of large GM counters (86 cm^2), mounted below the main array. Each of the sub-assemblies holds a set of 8 large GM counters

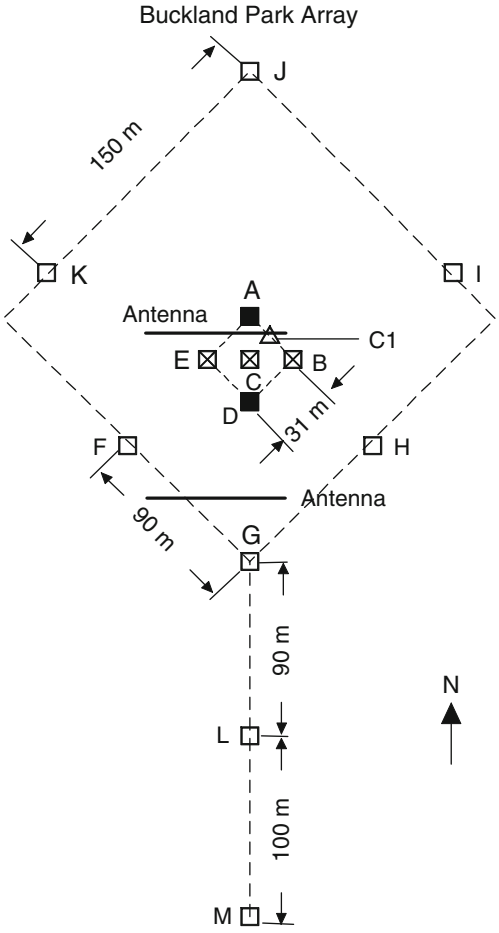

Fig. A.9 Plan of the extended Buckland Park EAS array (sea level), status 1977. The various *boxes* represent detector locations. Sites A to H have particle detectors; A, D, I, J and K were used for particle density measurements, A to E served also for fast timing. In addition sites A, F, G, H, L and M were equipped with Cherenkov detectors. At location $C1$ was a caravan holding a Cherenkov detector for pulse profile measurements (rise time ∼2 ns) (Kuhlmann et al., 1977). At times the array was also equipped with antennae for EAS radio burst studies (Clay et al., 1975)

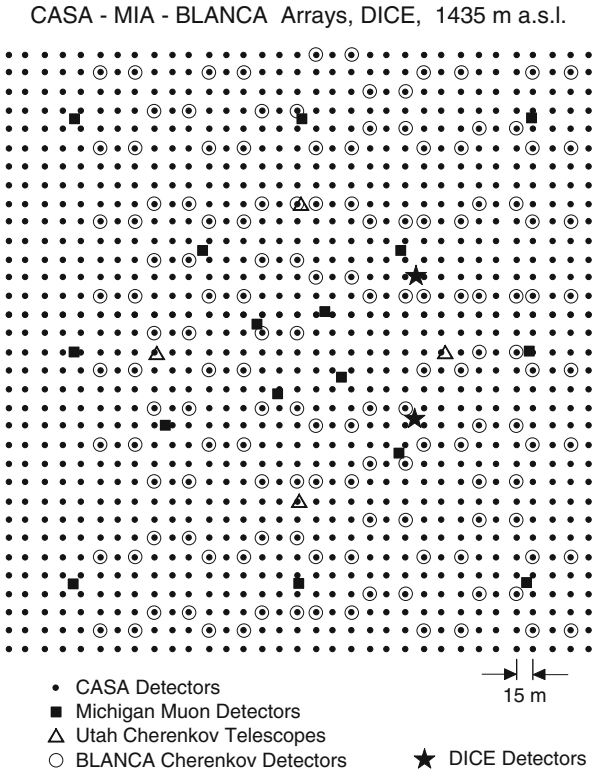

Fig. A.10 Layouts of the CASA (Chicago Air Shower Array), MIA (MIchigan muon Array), and BLANCA (Broad Lateral Non-imaging Cherenkov Array) arrays, and of the two DICE (Double Imaging Cherenkov Experiment) detectors at Dugway, Utah (USA). Also indicated are the Utah air Cherenkov telescopes (Cassidy et al., 1997; Ong et al., 2007)

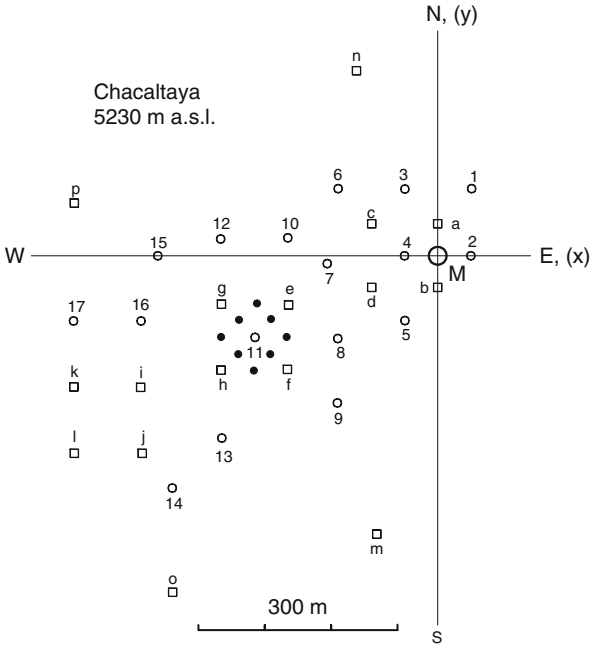

Fig. A.11 Layout of the Chacaltaya air shower array, status 1977 (Aguirre et al., 1977). The covered area measures approximately 700 m by 700 m at an altitude of 5,230 m (550 g cm^{-2}). It holds sixteen unshielded fast-timing scintillation detectors, twelve of area 0.87 m^2, 9.6 cm thick, (*a* to *l*) and four of area 1 m^2, 10 cm thick (*m* to *p*). The latter are also used to measure particle densities together with twenty 0.83 m^2 scintillators, 7.5 cm thick, indicated by *open circles* (1–20) and eight 2 cm thick scintillators of area 1/16 m^2 (*full circles*). In addition a shielded scintillator of 60 m^2 ($15 \cdot 4$ m^2) and thickness 5 cm, labeled *m* and located at the origin of the reference frame is used as muon detector with a threshold of 600 MeV

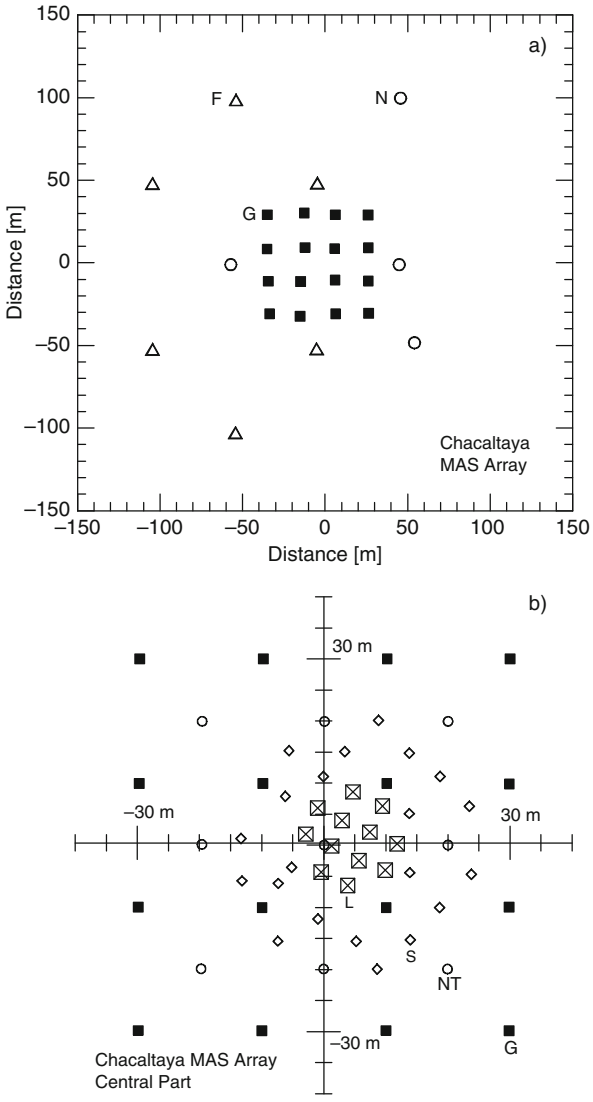

Fig. A.12 Chacaltaya (5,230 m a.s.l.) Minimum Air Shower (MAS) array, (**a**), and central part of array, (**b**). L, G, S, N, F and NT detectors are unshielded. The L detectors are 4 m^2 plastic scintillators with an additional 1 m^2 scintillator. The L, G, S and NT detectors are used as timing detectors and to measure particle density. A 60 m^2 muon detector with a threshold of 600 MeV is located at the array center (Shirasaki et al., 1997; Ogio et al., 2004)

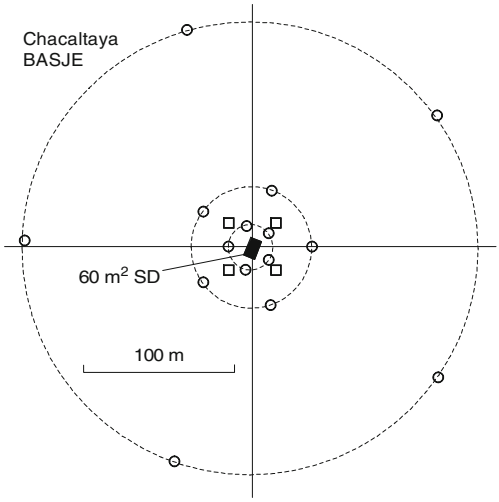

Fig. A.13 Layout of the BASJE air shower array at Chacaltaya (5,230 m a.s.l.) in 1965 (Toyoda et al., 1965)

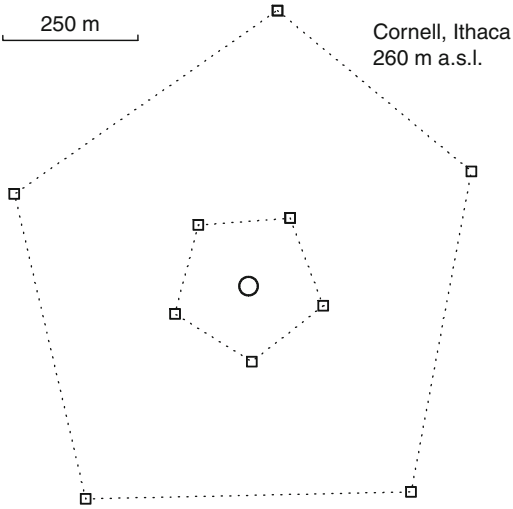

Fig. A.14 Cornell air shower array (Linsley, 1963b)

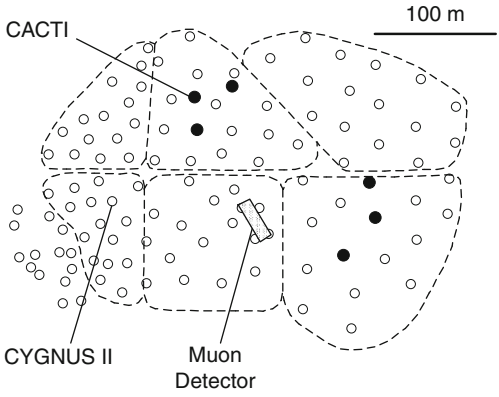

Fig. A.15 The CYGNUS II array was located near the Los Alamos National Laboratory at an altitude of 2,310 m a.s.l. (780 g cm^{-2}) and consisted of 96 scintillation detectors (○) and a 70 m^2 muon detector with a threshold of ∼2 GeV (Allen et al., 1992). The CACTI experiment consisted of 6 wide angle Cherenkov detectors (●) (Paling et al., 1997)

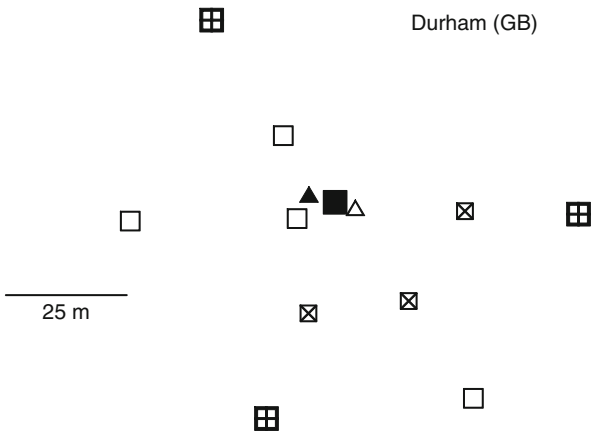

Fig. A.16 The Durham (GB) array consisted of scintillation detectors measuring 2 m^2 (⊞), 1.6 m^2 (□), 1 m^2 (⊠) and 0.75 m^2 (△). It had a solid iron magnet spectrometer (MARS) (Ayre et al., 1972a, b) (■) and a hadron chamber (▲) (Rada et al., 1977)

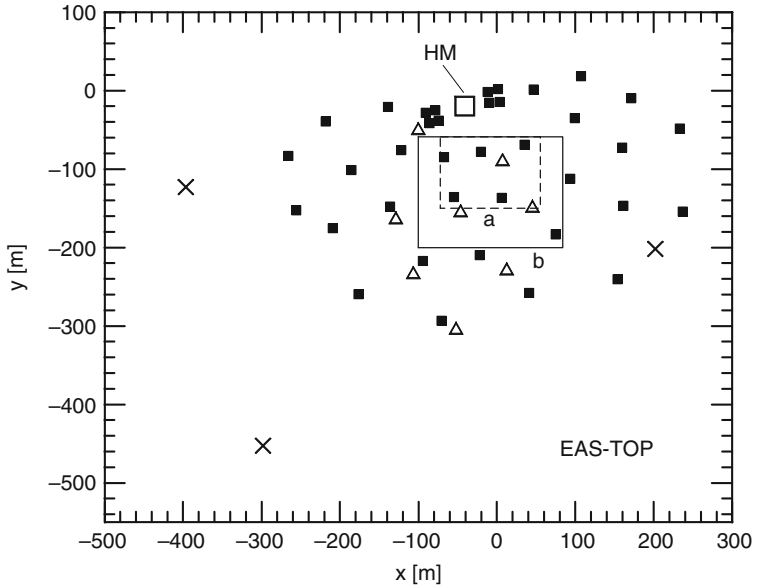

Fig. A.17 EAS-TOP air shower array (2,005 m a.s.l.) status of 1998. The symbols which indicate the location of different detector units represent the following kind of detectors: ■ scintillator module, △ wide acceptance Cherenkov telescope, × radio antennae for the detection of radio bursts associated with air showers, and □ the combined hadron calorimeter-muon detector, labeled *HM* (twin units). The two rectangular areas that are outlined with *dashed* and the *solid lines*, labeled *a* and *b*, identify the fiducial regions, i.e., the core location regions, for two sets of spectral measurements (Aglietta et al., 1989, 1999)

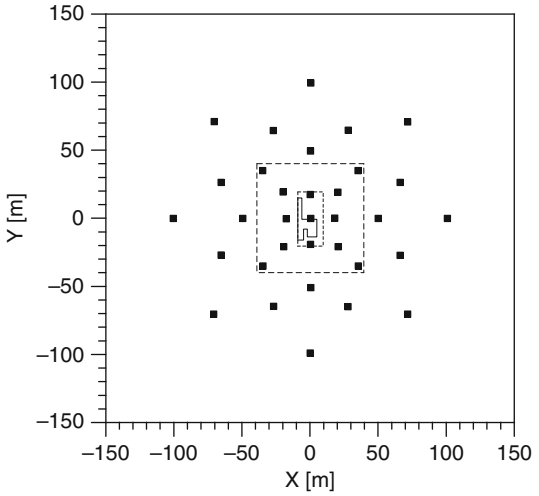

Fig. A.18 GAMMA air shower experiment at Mt. Aragats in Armenia located at an altitude of 3,200 m a.s.l. (700 g cm^{-2}). The 33 *black squares* represent scintillation detectors consisting of 3 units, each measuring 1 m^2. The *dashed contour* indicates the underground part with 150 m^2 of scintillation detectors having a muon threshold energy of $\geq$5 GeV. The *inner rectangle* is the contour of the calorimeter of the ANI project, currently under construction (Shaulov, 2007; Garyaka et al., 2007)

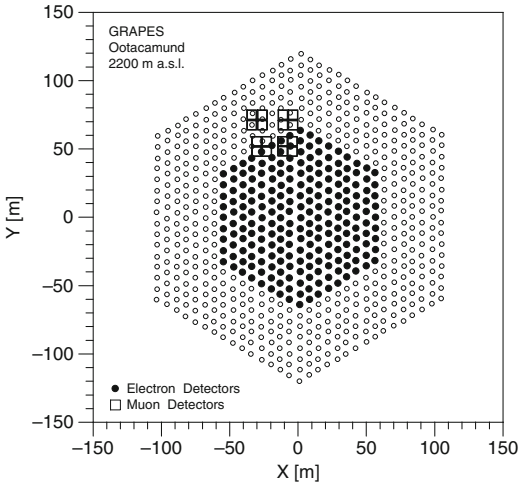

Fig. A.19 Layout of the GRAPES experiment at Ootacamund, India (2,200 m a.s.l., 800 g cm^{-2}). The muon tracking detector combination which is at present the largest of its kind has an effective area of 560 m^2 (Gupta et al., 2005). The shower detectors plotted as ● are those that were used at that epoch. The muon detector which has a threshold of 1 GeV consists of 16 modules measuring 35 m^2 each (□). The modules consist of large proportional counters (Hayashi, 2005; Hayashi et al., 2005)

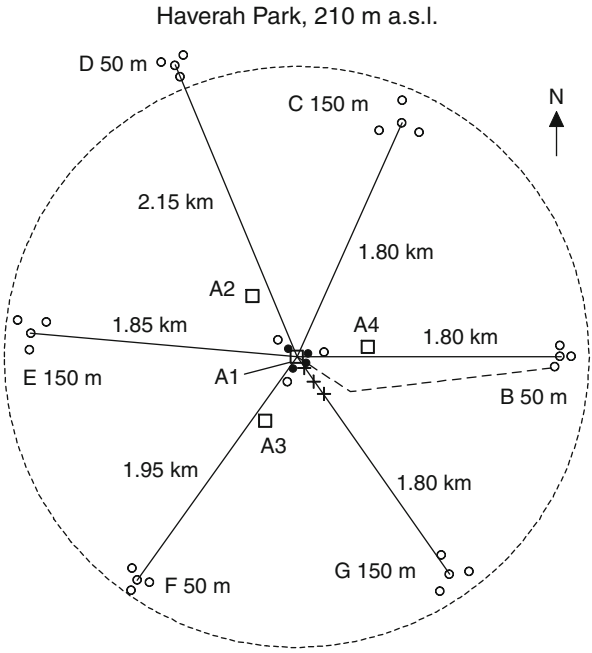

Fig. A.20 Haverah Park air shower array status of 1968 (Earnshaw et al., 1968). The *crosses* indicate the location of radio antennae for the detection of radio bursts associated with air showers (Allan, 1971)

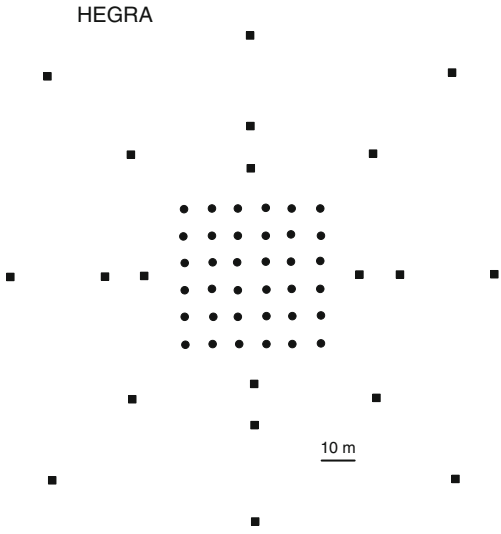

Fig. A.21 Original proposal of first HEGRA array at Roque de los Muchachos (2,250 m a.s.l.), La Palma (Canary Islands), by Allkofer (1985) who founded the project in the early 1980s, showing two kinds of 1 m^2 scintillation detectors. Up to date, the site has seen a wide variety of particle and air Cherenkov detectors and Cherenkov telescopes (for details see the HEGRA web site)

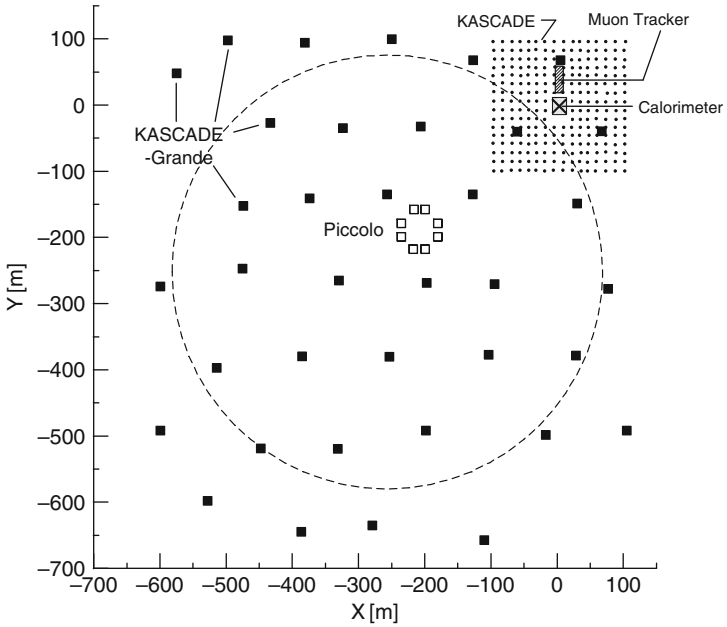

Fig. A.22 Layout of the elaborate KASCADE-Grande air shower array at the Forschungszentrum Karlsruhe (Germany) (110 m a.s.l.) (Kampert et al., 2003; Haungs et al., 2003; Navarra et al., 2004). The resolutions of the Grande array are 13 m for core location, 0.3° for arrival direction, and 15% for the shower size at a primary energy of 100 PeV (10^{17} eV). The KASCADE array has 252 stations that are distributed over an area of 200 × 200 m^2 (Antoni et al., 2003). Each station consists of liquid scintillators to measure the shower particle density ($E_{EM} \geq 5$ MeV) and shielded (10 cm Pb + 4 cm Fe) plastic scintillators underneath to measure the muon density ($E_\mu > 0.23$ GeV). The central detector consists of a 9-layer hadron calorimeter with 40,000 channels of liquid ionization chambers; it has a threshold energy of 50 GeV. Additional muon facilities are located in and under the calorimeter with threshold energies of 0.49 and 2.4 GeV, and a muon tracker in a tunnel with a threshold of 0.8 GeV. The Picolo cluster sub-array serves as a trigger. The array has a 100% trigger efficiency for events with primary energy of 10 PeV over the entire Grande collecting area (*dashed circle*). A low frequency radio antenna array (40–80 MHz) called LOPES (not shown above), a prototype of LOFAR, is also integrated in the KASCADE-Grande array to detect air shower radio pulses (Horneffer et al., 2003)

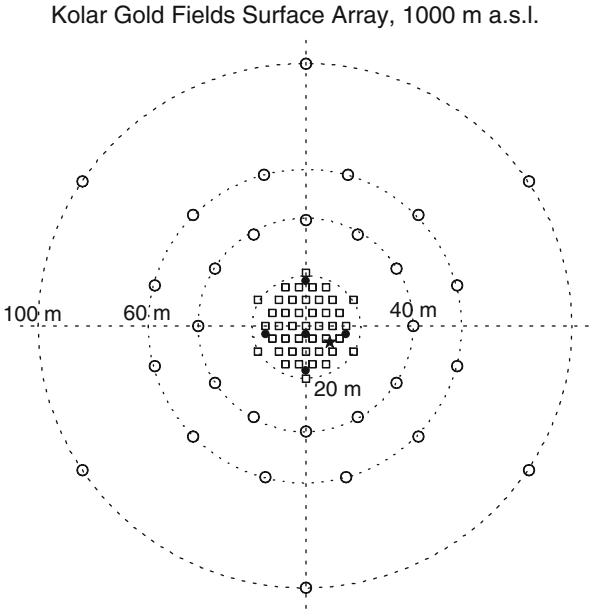

Fig. A.23 Air shower array at the Kolar Gold Fields, status 1977 (Acharya et al., 1977). The *squares* and *circles* are 2.25 and 1 m^2 plastic scintillation detectors, respectively, the *full circles* 1.15 m^2 liquid scintillation detectors used for fast timing. The symbol ⋆ marks the intersection of a perpendicular from the center of the $2 \times 1 \times 2$ m^3 neon flash tube telescope, located at a depth of 266 m underground (muon threshold $\simeq$220 GeV). A cross-sectional view of the abandoned underground installations is shown in Fig. A.40

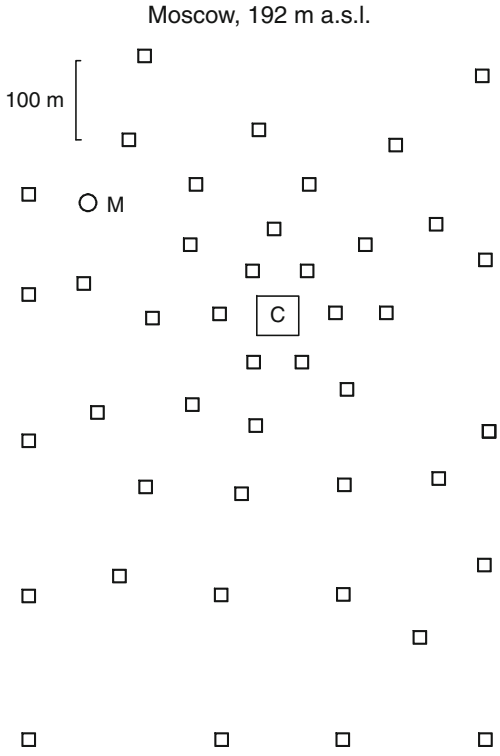

Fig. A.24 Air shower array at the Moscow State University (Vernov et al., 1979). The *open squares* are charged particle detectors, the central system (*C*) contains 3,000 hodoscope counters. A total of 8,160 Geiger counters are used. At each detector location which is 60 m or more from the center of the array a 0.5 m^2 scintillation detector is installed. Muon detectors of area 18 m^2 and threshold 10 GeV are located at 180, 250 and 280 m from the *center*. In addition a 32 m^2 muon detector and a solid iron magnetic muon spectrometer are located at the *center*, at a depth of 40 m.w.e

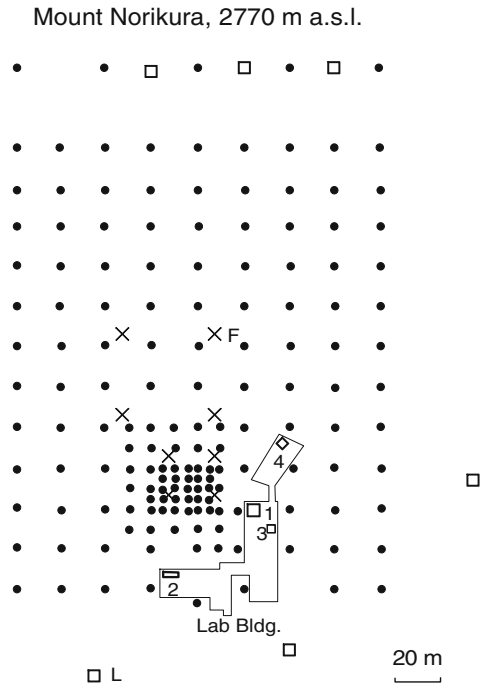

Fig. A.25 One of many air shower array configurations used at Mt. Norikura in Japan (Miyake et al., 1979). The figure shows a total of 152 scintillation detectors of area 0.25 m^2 (•) each, arranged in a lattice as shown, and 6 additional detectors of area 1 m^2 (□) in the outer area. × identifies fast timing detectors. A 25 m^2 proportional counter array shielded with 2 cm of Pb located under a 6 m by 5.5 m water tank of height 2 m (*1*) was used to observe high energy gamma rays. During a certain period the proportional counters were replaced by 48 plastic scintillators above and 48 below the tank. This arrangement served as core detector. In addition a cloud chamber (2) was used occasionally. Two neon hodoscopes of 6 and 4 m^2 (3 and 4) shielded by 35 cm of lead were also incorporated. For details of special apparatuses see Sasaki et al. (1979); for earlier array layouts see Miyake et al. (1968, 1973) and Kino et al. (1975)

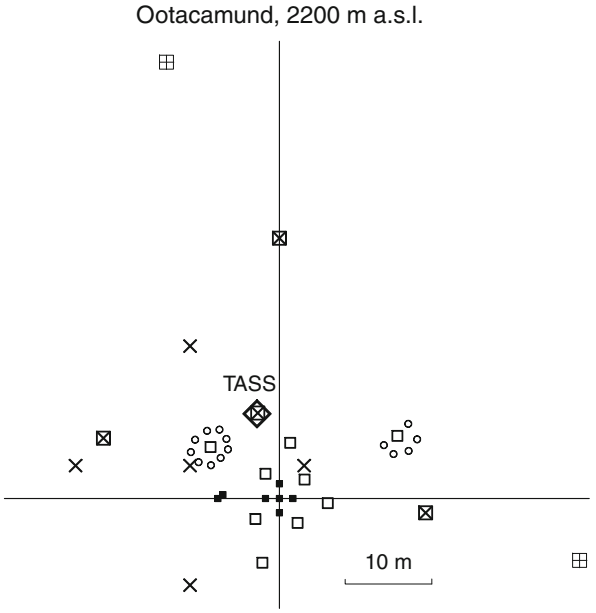

Fig. A.26 One of several arrangements used for the air shower array at Ootacamund, India (Chatterjee et al., 1965b). The different *symbols* identify the following detectors: ■, □ and ⊞ represent 0.36, 1.0 and 1.44 m^2 scintillators, respectively; ⊠ 1.0 m^2 muon detectors consisting of Pb-shielded Geiger-Mueller hodoscope arrays, × fast timing scintillators, ○ BF_3 neutron detectors, and ◇ the 1 m^2 total absorption scintillation spectrometer (TASS) to record nuclear interacting particles of energy >100 GeV, with a muon detector underneath. In addition there was a 4 m^2 combination of energy flow detectors for the soft and hadronic components

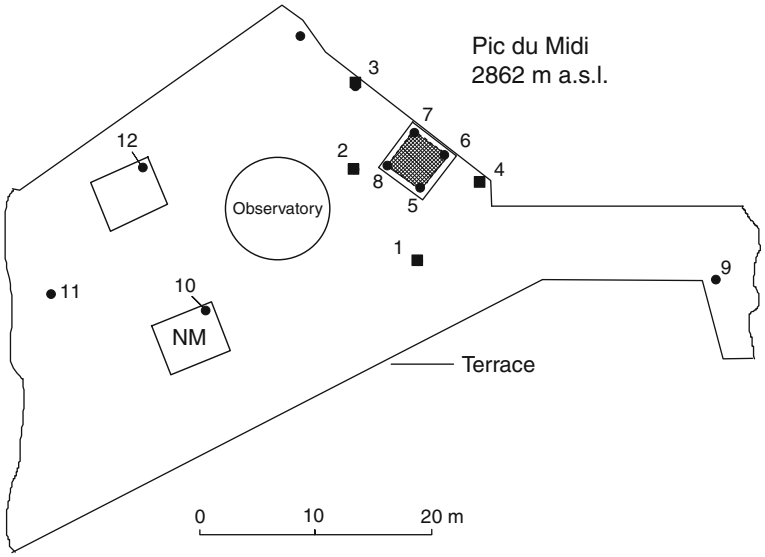

Fig. A.27 Air shower array of the University of Kiel at the terrace of Pic du Midi, France, located at an altitude of 2,862 m. (Van Staa et al., 1973, 1974). The full symbols *1–13* represent 0.25 m^2 scintillation detectors. Detectors 1–4 were equipped for fast timing, and NM indicated a neutron monitor. The *square* containing the four scintillators *5–8* that serve as trigger detectors represents the hadron detector and the hatched area within it is the 14 m^2 neon hodoscope with approximately 80,000 neon tubes that serves as burst detector. The hadron target consists of a layer of 100 cm of sand and 25 cm of concrete, topped with a 10 cm thick layer of lead to absorb the photon-electron component

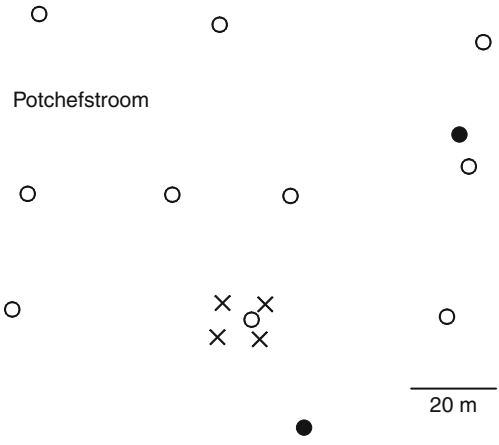

Fig. A.28 The Potchefstroom array was very small and consisted of 10 scintillation detectors and 2 muon detectors (De Villiers et al., 1979)

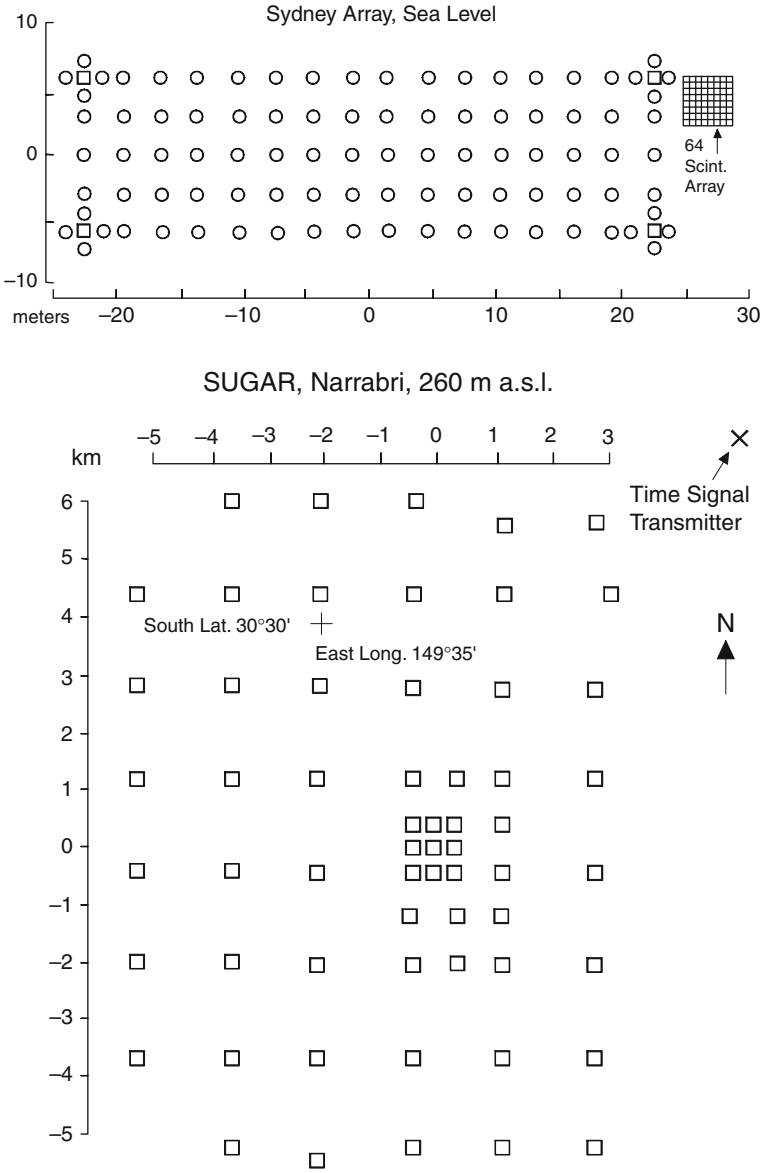

Fig. A.29 *Upper figure*: Sydney air shower array, status 1965 (Bray et al., 1965). *Circles* represent trays with 3 Geiger counters, the four *boxes* at the corners hold 48 Geiger counters each. In the *upper right corner* is the 64 scintillator array. *Lower figure*: Layout of early status of the Sydney University Giant air shower Array (SUGAR) at Narrabri (Brownlee et al., 1970). Except for the central section the counters are underground and record chiefly muons

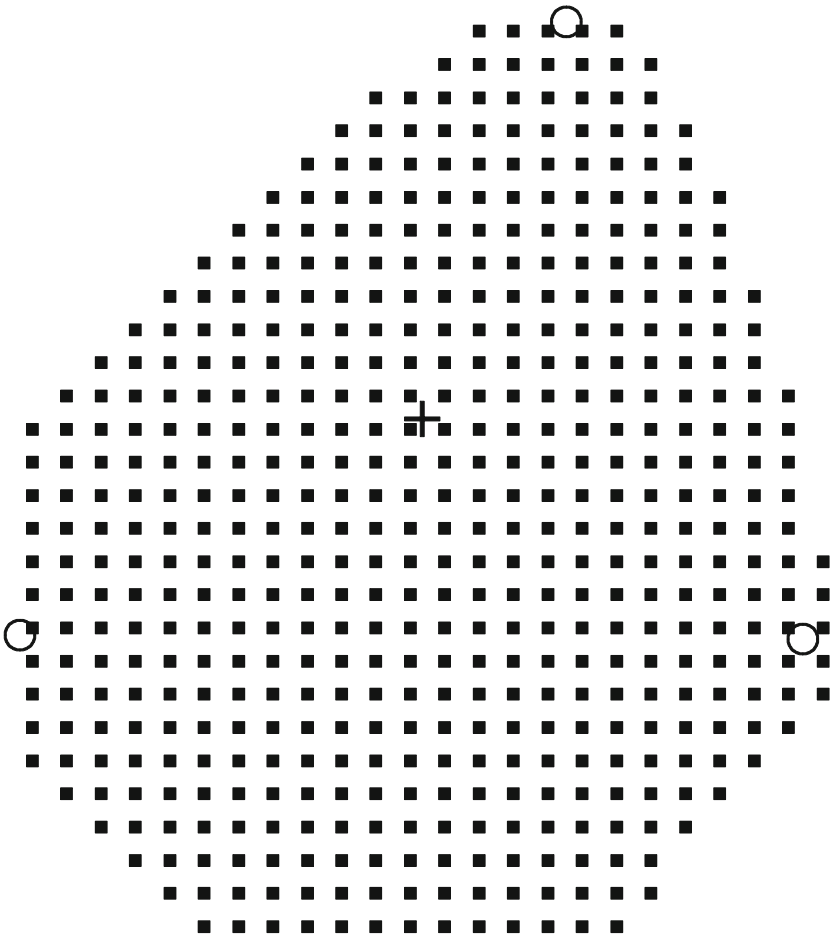

Fig. A.30 Layout of the giant Telescope Array located at Dugway, Utah (USA), 1,400 m a.s.l., 39.3° N, long. 112.9° W (Kasahara et al., 2007). It consists of 3 fluorescence stations, each having 12 identical telescopes, and 512 plastic scintillation detectors. The aperture of the surface detectors is 1,900 km^2sr and the fluorescence detectors have a stereoscopic aperture of 860 km^2sr at 10^{20} eV with a duty factor of ∼10%. Participating in this joint venture project are mainly Japanese universities and institutions, some American and a few Korean universities, and a German institution. The approximate linear dimensions of the array are 17 km by 20 km (courtesy of Ken Honda and the Telescope Array Collaboration)

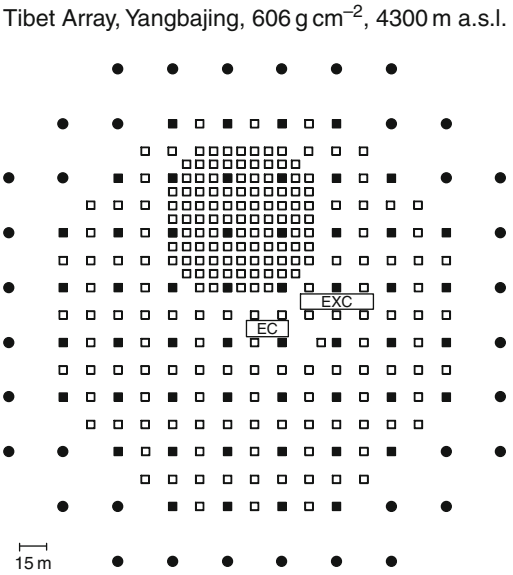

Fig. A.31 Layout of Tibet II Array located at Yangbajing (606 g cm^{-2}, 4,300 m a.s.l.). The array consists of 221 scintillation detectors that are placed 15 m apart and has a threshold for particles and gamma rays of 10 TeV. Its angular resolution is about 1° (Amenomori et al., 1997a, b). For the layout of the Tibet III array see Amenomori et al. (2003, 2006)

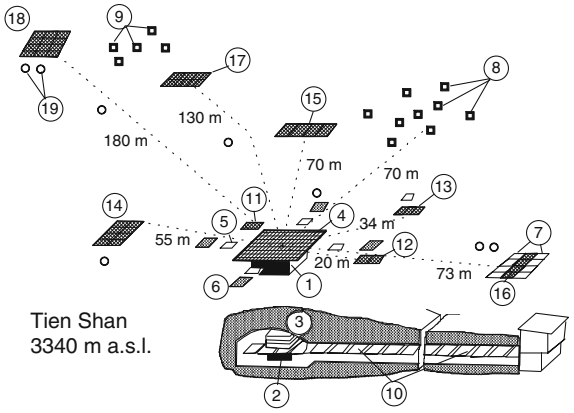

Fig. A.32 Layout of the complex air shower array at Tien Shan (Kazakhstan) (690 g cm^{-2}, 3,340 m a.s.l.) (Abdrashitov et al., 1981). This array was for many years the worldwide best equipped air shower installation. It consisted of a 6 m by 6 m (36 m^2) central ionization chamber calorimeter (*1*) that was interlaced with 15 rows of ionization chambers, each measuring $10 \times 15 \times 300$ cm^3, that were separated by layers of 2.5 cm and 5 cm of Pb, totaling 850 g cm^{-2} of Pb. The accuracy of the hadron spatial resolution was 25–30 cm, that of the energy measurement 15%. The chamber was covered with an carpet of 64 scintillation detectors of 0.25 m^2 area each that were uniformly distributed about the chamber center over an area measuring 11 m by 11 m (121 m^2). The shower detection array comprised 115 scintillation detectors, partly arranged in clusters (*4, 5, 7, 8*, and *9*) with a total effective area of 53 m^2, distributed out to 130 m from the *center* of the ionization chamber. The four detectors of type (*5*) of 1 m^2 area were used to determine the shower axis location and direction. The circular symbols (*19*) represent air Cherenkov detectors. A total of 9 Geiger-Müller hodoscope detector trays (*6, 11, 12, 13, 14, 15, 16, 17*, and *18*) with an effective area of 38.4 m^2, located at distances of 5, 10, 20, 34, 55, 70, 73, 130 and 180 m from the *center* (see labels attached to the *thin dotted lines*) permitted reliable muon measurements. In addition, a 45 m^2 muon detector hodoscope was operated in a tunnel (*10*) at a depth of 20 m w.e., having a muon energy threshold of $\geq$5 GeV. An underground calorimeter of 9 m^2 effective area (*2, 3*) below the larger surface unit with 15 trays of ionization chambers, separated by 5 cm of Pb, served to analyze the high energy muon component in the shower core. (For earlier layout versions see Erlykin et al., 1965; Aseikin et al., 1971; Betev et al., 1977.) Note that the new Tien Shan installation is at a slightly different location and consists mainly of air Cherenkov detectors for gamma ray astronomy purposes. For a recent layout see Slavatinsky (2001)

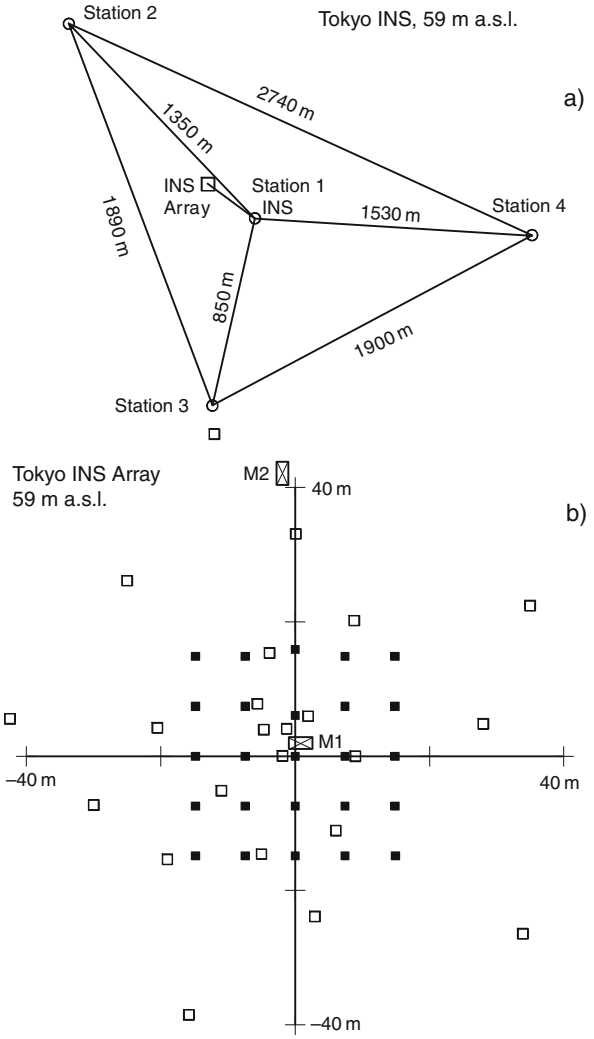

Fig. A.33 (**a**) Air shower array at the Institute for Nuclear Studies (INS) of the University of Tokyo, status 1973 (Kawaguchi et al., 1973). *Stations 1–4* have a pair of scintillation detectors of area 2 m^2 each that are 50 m apart. (See also Suga et al., 1971). (**b**) Details of local INS array. *M1* and *M2* are muon detectors having a threshold of 5 and 15 GeV, respectively. The *open squares* represent 1 m^2 scintillation detectors, the *full squares* are a later addition. For further details see Matano et al. (1971). For earlier arrangements see Hara et al. (1970)

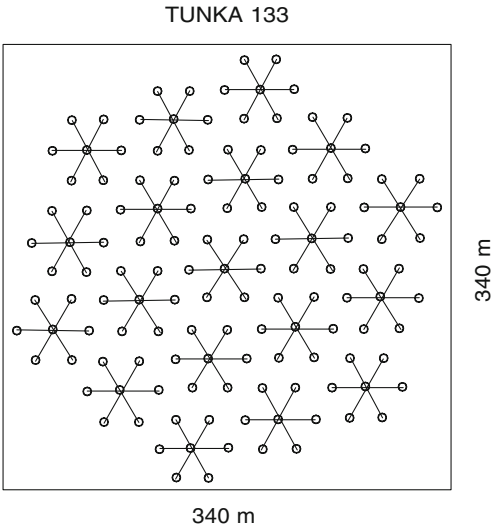

Fig. A.34 Layout of the TUNKA-133 optical Cherenkov array, located in the Tunka valley (675 m a.s.l.) in Russia, near lake Baikal (Budnev et al., 2005, 2007). The array was operated at earlier stages with much fewer detector units while it was under construction and systematically enlarged

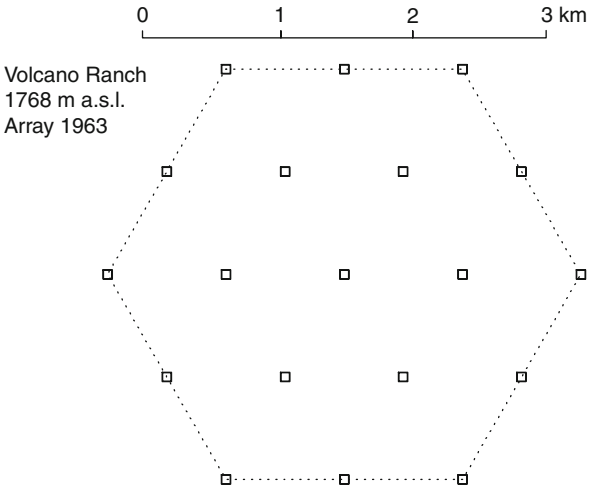

Fig. A.35 Layout of Volcano Ranch air shower array, status 1963 (Linsley, 1963a, b)

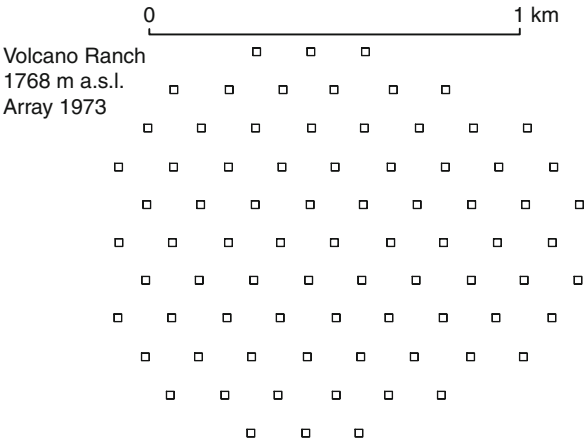

Fig. A.36 Layout of Volcano Ranch array 1973 (Linsley, 1973)

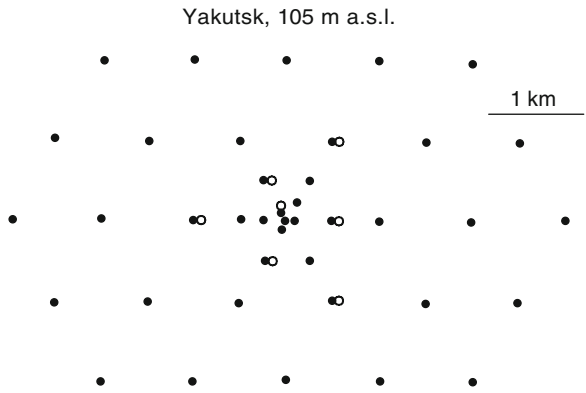

Fig. A.37 Layout of Yakutsk air shower array, status 1973 (Diminstein et al., 1973). For an earlier layout see Egorov et al. (1971); further details are also given by Kozlov et al. (1979), Diminstein et al. (1979) and Artamonov et al. (1983, 1991)

A.2 Cosmic Ray Underground Installations of Past and Present

A.2.1 Underground Muon and Neutrino Detectors

Table A.6 is a list of muon and neutrino detectors of the past and present. Most of these detectors are being operated or had been operated autonomously, but some could be used jointly with nearby air shower arrays. Those underground installations that are or were located underneath of an air shower array or in its immediate vicinity, so that components of the same shower event could be recorded simultaneous, that had been operated jointly, are marked.

Table A.6 List of major underground muon and neutrino detectors of past and present

Detector (Location)	Mass tons	Depth m.w.e.	Size m	E_μ TeV	Status
AMANDA (Antarctica)	$\sim 10^6$ m^3 IČ	$\simeq$1,000	evolving	0.4	operating
Antares (France)	WČ				constr.
Baikal (Russia)	$3{\cdot}10^7$ WĈ	1,300	200·300 0.400	0.5	operating
Baksan (Russia) [a]	85 Sc	850	16·16	0.23	operating
C.W.I. (SA)	20 ScFt	8,200	90·0.13·1.5	$\simeq$10	shut-dn.
DUMAND 1 (USA)	$3{\cdot}10^5$ WČ	4,500	70ø·70	3.5	shut-dn.
DUMAND 2 (USA)	$2{\cdot}10^6$ WČ	4,500	106ø·230	3.5	discont.
Frejus (F/I)	912 Fe	4,400	6·12	3	shut-dn.
Gallex (Italy)	110 $GaCl_3$	$\sim$3,300	54 m^3	3	shut-dn.
Homestake (USA)	615 C_2 Cl_4	4,200	390 m^3	3	shut-dn.
Homestake (USA) [a]	300 WČ	4,200	8·24	3	shut-dn.
HPW/(USA)	1,000 WČ	1,700	10ø	0.6	discont.
Icarus (Italy)	10^4 LA	3,100	–	3	discont.
ICECUBE (Antarctica) [a]	$\sim 10^9$ IČ	$\simeq$1,200	1 km^3	0.5	operating
IMB (USA)	8,000 WČ	1,570	17·23	0.6	shut-dn.
Issyk-Kul (Kyrgyzstan)	10^6 m^3 WČ	500	$\sim$1 km^2	$\geq$0.15	discont.
Kamiokande (J)	2,900 WČ	2,700	16ø·16	>1	shut-dn.
KGF (India) [a]	- Sc	730	6 m^2	0.22	shut-dn.
KGF (India) [a]	- WČ	1,590	10 m^2	0.64	shut-dn.
KGF (India)	- ScFt	2,895	6·6	1.7	shut-dn.
KGF (India)	375 Fe Pc	7,500	6·6	12	shut-dn.
LSD (Italy)	200 Sc	5,200	7·8	4	shut-dn.
LVD (Italy) [a]	3,600 Sc	3,100	31·13·12	1.3	operating
MACRO (Italy) [a]	- ScStTe	3,100	72·12·10	1.3	shut-dn.
NEMO (Italy)	WČ				planning
NESTOR (Greece) [b]	$2.8{\cdot}10^5$ WČ	3,800	34ø·400	3.0	discont.
NUSEX (Italy)	150 Fe Ft	5,000	3.5·3.5	4	shut-dn.
Ohya (Japan) [a]	- Fe	31	400 m^2	0.015	shut-dn.
SAGE (Russia)	- Ga				operating
Soudan 1 (USA)	30 FeCon	2,100	3·3	0.6	shut-dn.
Soudan 2 (USA) [a]	1,000 FeCon	2,100	8·16	0.6	operating
SNO Sudburry (CND)	- D_2				operating
Super Kamiokande (J)	32,000 WČ	2,700	38ø·40	>1	operating
Utah	1,800 WČSpMag.	>150	$12 \cdot 10 \cdot 6$	0.5	shut-dn.

[a] EAS array at surface.

[b] per tower.

E_μ – muon threshold; ø – diameter; IČ – ice Cherenkov; WČ – water Cherenkov; Sc – scintillation counters; Ft – Flash tubes; Con – concrete; LA - liquid argon; St – Streamer tubes; Te – Track etching; Sp - Spark chambers; D_2 - deuterium; Mag. – magnetized iron plates.

A.2.2 Layouts of Major Underground Detectors Associated with Air Shower Arrays

(a) Comments to Layouts

The underground detector experiments shown here had been operated autonomously but also in coincidence with an air shower array at the surface above or near the underground installation. The simultaneous acquisition of data from a surface and underground installation enriches the data and improves their interpretation significantly. Underground detectors supply complementary data that are otherwise inaccessible to surface measurements, such as data on single and multiple high energy muons in showers, on delayed penetrating particles, and other phenomena. They also offer an alternative method to determine the arrival direction of showers.

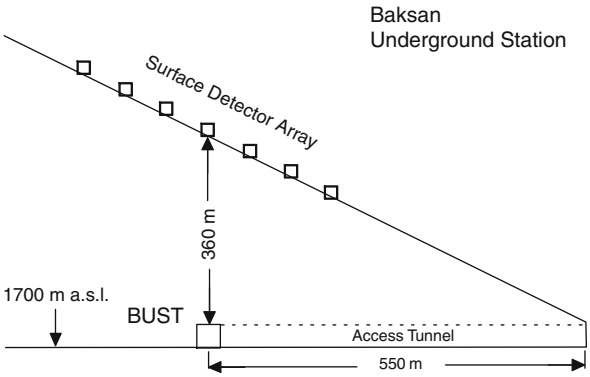

Fig. A.38 Cutaway view of the Baksan installation showing the surface array and the underground scintillation telescope BUST ($16 \times 16 \times 11\,m^3$) under an overburden of $\sim 850\,g\,cm^{-2}$. The layout of the surface array is given in Fig. A.7. (Alexeyev et al., 1979a, b, 1993; Chudakov et al., 1999)

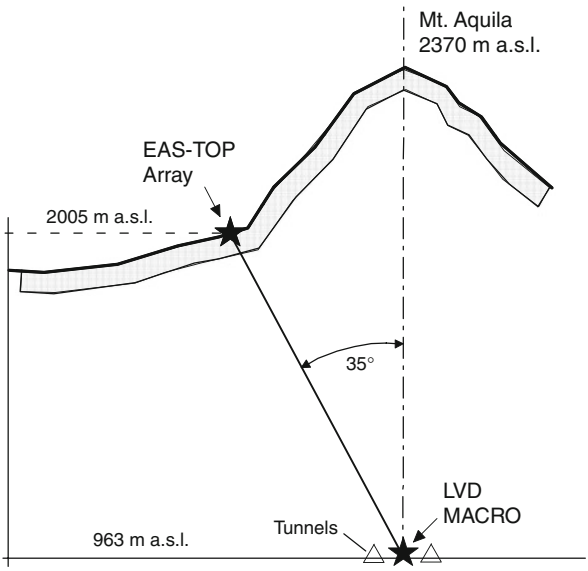

Fig. A.39 Cutaway view showing the locations of the EAS-TOP, LVD and MACRO detectors at Gran Sasso (Aglietta et al., 2004). Details of the EAS-TOP installation are shown in Fig. A.17. The minimum rock overburden in the direction of the EAS-TOP array is 3,100 m w.e. The MACRO detector measured $76.6 \times 12 \times 4.8\,m^3$ (Ahlen et al., 1992, 1993; Ambrosio et al., 2002), the LVD detector (still operating) measures $22.7 \times 13.2 \times 10\,m^3$ (Bari et al., 1989; Aglietta et al., 1992)

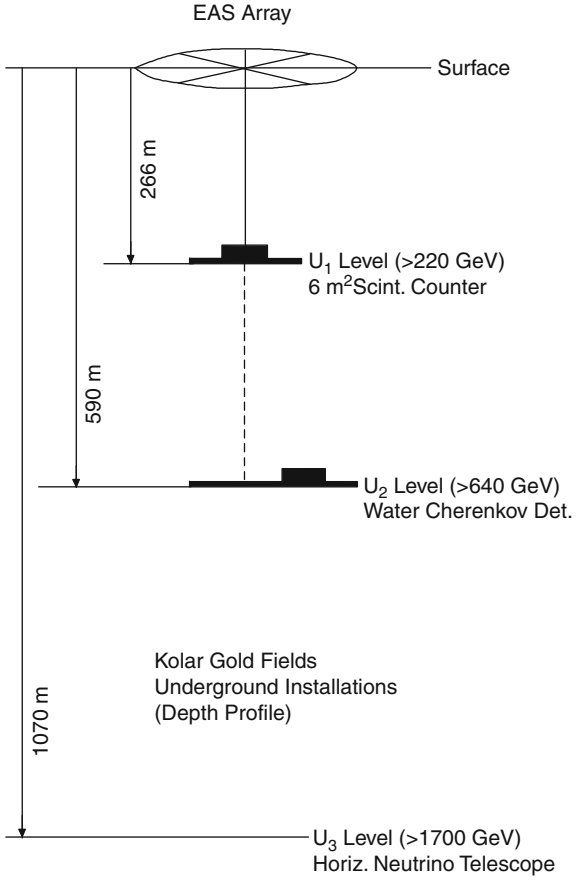

Fig. A.40 Muon and neutrino telescopes underneath the Kolar Gold Fields (KGF) air shower array, now shut-down (Chatterjee et al., 1965a). Illustrated are the experimental sites at the three different depth levels. The surface is at an altitude of 920 m a.s.l. (920 g cm^{-2}), the lowest level is 1,070 m below the surface which corresponds to a depth of approximately 7,500 m w.e. (water equivalent)

References

Abdrashitov, S.F., et al.: PICRC, 6, p. 156 (1981).
Acharya, B.S., et al.: PICRC, 8, p. 36 (1977).
Aglietta, M., et al.: Nucl. Instr. Meth., A277, p. 23 (1989).
Aglietta, M., et al.: Nuovo Cim. A, 12, p. 1793 (1992).
Aglietta, M., et al.: Astropart. Phys., 10, p. 1 (1999).
Aglietta, M., et al.: Astropart. Phys., 21, pp. 223–240 (2004).
Aguirre, C., et al.: PICRC, 8, p. 208 (1977).
Ahlen, S., et al., MACRO Collaboration: Phys. Rev. D, 46, p. 4836 (1992).
Ahlen, S., et al., MACRO Collaboration: Nucl. Instr. Meth. A, 324, p. 337 (1993).
Alexeyev, E.N., et al.: PICRC, 10, p. 276 (1979a).
Alexeyev, E.N., et al.: PICRC, 10, p. 282 (1979b).
Alexeyev, E.N., et al.: PICRC, 2, p. 474 (1993).

Allan, H.R.: Progress in Elementary Particle and Cosmic Ray Physics, North-Holland, Amsterdam, Vol. X, pp. 169–302 (1971).
Allen, R.C., et al.: Nucl. Instr. Meth. A, 311, p. 350 (1992).
Allkofer, O.C.: PICRC, 3, p. 418 (1985).
Ambrosio, M., et al.: Nucl. Instr. Meth. A, 486, p. 663 (2002).
Amenomori, M., et al.: PICRC, 5, p. 245 (1997a).
Amenomori, M., et al.: PICRC, 5, p. 249 (1997b).
Amenomori, M., et al.: Proceedings of the International Science Symposium "The Universe Viewed in Gamma Rays", University of Tokyo, Sept. 25–28, 2002, R. Enomoto, M. Mori, S. Yanagita, ed., Universal Academy Press, Inc., Japan (2003).
Amenomori, M., et al.: Adv. Space Res., 37, p. 1932 (2006).
Antoni, T., et al.: Nucl. Instr. Meth. A, 513, p. 490 (2003).
Antonov, R.A., et al.: PICRC, 6, p. 2194 (1971).
Antonov, R.A., et al.: Yadernaya Fiz. 18, p. 554 (1973) (in Russian).
Antonov, R.A., et al.: PICRC, 8, p. 137 (1977).
Artamonov, V.P., et al.: PICRC, 8, p. 196 (1983).
Artamonov, V.P., et al.: PICRC, 4, p. 375 (1991).
Aseikin, V.S., et al.: PICRC, 6, p. 2152 (1971).
Ayre, C.A., et al.: Nucl. Instr. Meth., 102, pp. 19–28 (1972a).
Ayre, C.A., et al.: Nucl. Instr. Meth., 102, pp. 29–34 (1972b).
Baillon, P.: CERN/PPE 91-12 (1991).
Bari, G., et al.: Nucl. Instr. Meth., A277, p. 11 (1989).
Betev, B., et al.: PICRC, 8, p. 123 (1977).
Bray, A.D., et al.: PICRC, 2, p. 685 (1965).
Brownlee, R.G., et al.: Acta Phys. Acad. Sci. Hung., 29, S3, p. 651 (1970).
Budnev, N.M., et al.: PICRC, 8, p. 255 (2005).
Budnev, N.M., et al.: PICRC, pre-conference edition, paper 0629, Merida, Mexico (2007).
Cassidy, M., et al.: PICRC, 5, p. 189 (1997).
Chatterjee, B.K., et al.: PICRC, 2, p. 627 (1965a).
Chatterjee, B.K., et al.: PICRC, 2, p. 734 (1965b).
Chiba, N., et al.: Nucl. Instr. Meth., A311, pp. 338–349 (1992).
Chudakov, A.E., et al.: arXiv:astro-ph/9912192v1 Dec. (1999).
Clark, G.W., et al.: Phys. Rev., 122, p. 637 (1961).
Clay, R.W., et al.: PICRC, 8, p. 3093 (1975).
De Villiers, E.J., and D.J. van der Walt: PICRC, 13, p. 277 (1979).
Diminstein, A.S., et al.: PICRC, 5, p. 3232 (1973).
Diminstein, O.S., et al.: PICRC, 8, p. 122 (1979).
Earnshaw, R.A., et al.: Can. J. Phys., 46, p. S5 (1968).
Egorov, T.A., et al.: PICRC, 6, p. 2059 (1971).
Erlykin, A.D., et al.: PICRC, 2, p. 731 (1965).
Garyaka, A.P., et al.: Astropart. Phys., 26, p. 169 (2007).
Gupta, S., et al.: Nucl. Instr. Meth. A, 540, p. 311 (2005).
Hara, T., et al.: Acta Phys. Acad. Sci. Hung., 29, S3, p. 361 (1970).
Hara, T., et al.: PICRC, 8, p. 135 (1979).
Haungs, A., et al.: PICRC, 2, p. 985 (2003).
Hayashi, Y., GRAPES Collaboration: PICRC, 10, p. 243 (2005).
Hayashi, Y., et al.: Nucl. Instr. Meth. A, 545, p. 643 (2005).
Horneffer, A., et al.: PICRC, 2, p. 696 (2003).
Kampert, K.H., et al.: Nucl. Phys. B (Proc. Suppl.), 122, p. 422 (2003).
Kasahara, K., et al.: PICRC, pre-conference edition, paper 0955, Merida, Mexico (2007).
Kawaguchi, S., et al.: PICRC, 4, p. 2562 (1973).
Kino, S., et al.: PICRC, 8, p. 2837 (1975).
Kozlov, V.G., et al.: PICRC, 8, p. 356 (1979).

Kuhlmann, J.D., et al.: PICRC, 8, p. 239 (1977).
Linsley, J.: Phys. Rev. Lett., 10, p. 146 (1963a).
Linsley, J.: PICRC, 4, p. 77 (1963b).
Linsley, J.: PICRC, 5, p. 3212 (1973).
Lorenz, E.: Nucl. Phys. B (Proc. Suppl.), 33A,B, p. 93 (1993).
Matano, T., et al.: PICRC, 7, p. 2724 (1971).
Miyake, S., et al.: Can. J. Phys., 46, p. S17 (1968).
Miyake, S., et al.: PICRC, 5, p. 3220 (1973).
Miyake, S., et al.: PICRC, 13, p. 171 (1979).
Navarra, G., et al.: Nucl. Instr. Meth. A, 518, pp. 207–209 (2004).
Ogio, S., et al.: Astrophys. J., 612, pp. 268–275 (2004).
Ong, R.A., et al., CASA-MIA Collaboration: PICRC, pre-conference edition, paper 814, Merida, Mexico (2007).
Paling, S., et al.: PICRC, 5, p. 253 (1997).
Rada, W.S., et al.: PICRC, 8, p. 13 (1977).
Sasaki, H., et al.: PICRC, 8, p. 190 (1979).
Shaulov, S., et al.: PICRC, pre-conference edition, paper 483, Merida, Mexico (2007).
Shirasaki, Y., et al.: PICRC, 4, p. 53 (1997).
Slavatinsky, S.A., Tien Shan Collaboration: Nucl. Phys. B (Proc. Suppl.), 97, p. 109 (2001).
Suga, K., et al.: PICRC, 7, p. 2742 (1971).
Toyoda, Y., et al.: PICRC, 2, p. 708 (1965).
Van Staa, R., et al.: PICRC, 4, p. 2676 (1973).
Van Staa, R., et al.: J. Phys. A, 7, p. 135 (1974).
Vernov, S.N., et al.: PICRC, 8, p. 129 (1979).

Appendix B
Miscellaneous Relations, Tables, Lists and Constants

B.1 Electromagnetic Interaction Related Constants and Parameters

Table B.1 Radiation length $\chi_\circ$, critical energy E_{crit} and density ρ of frequently used elements

Element	Z	A	$\chi_\circ$ g cm^{-2}	$\chi_\circ$ cm	E_{crit} MeV	ρ g cm^{-3}
Aluminum	13	26.98	24.1	8.9	40	2.70[a]
Carbon	6	12.01	42.7	18.8	79	2.25[b]
Copper	29	63.54	12.9	1.43	18.8	8.89[c]
Hydrogen	1	1.008	62.8	7,500 (m)	350	0.07[d]
Helium	2	4.003	93.1	5,600 (m)	250	0.15[d]
Iron	26	55.85	13.8	1.76	20.7	7.85[e]
Lead	82	207.21	6.4	0.56	7.40	11.34
Nitrogen	7	14.008	38.6	331 (m)	85	0.81[d]
Oxygen	8	16.00	34.6	258 (m)	75	1.14[d]
Silicon	14	28.09	21.8	9.36	37.5	2.35[f]

[a] drawn.
[b] graphite.
[c] hard drawn.
[d] liquid.
[e] wrought.
[f] amorphous.

Table B.2 Radiation length $\chi_\circ$ and critical energy E_{crit} of mixtures and compounds

Compound	Z	A	$\chi_\circ$ g cm^{-2}	$\chi_\circ$ cm	E_{crit} MeV
Air	7.4	14.8	37.15	304 (m)	84.4
Water	7.2	14.3	36.1	36.1	73.0
Emulsion-G5			11.4	2.98	16.4

Table B.3 Data on Ilford G-5 emulsion

Property		Composition g cm^{-3}		Z
Density	3.907 g cm^{-3}	Silver	1.85	47
Atoms cm^{-3}	$8.12 \cdot 10^{22}$	Bromine	1.36	35
Mean A	28.98	Iodine	0.024	53
Mean Z	13.17	Carbon	0.27	6
Mean Z^2	456	Hydrogen	0.056	1
Radiation Length, χ	2.93 cm	Oxygen	0.27	8
$\lambda_{\rm int}^{p,\rm Emul}$	~37 cm	Sulfur	0.010	16
		Nitrogen	0.067	7

B.2 Bethe-Bloch Ionization Loss Formula

The Bethe-Bloch equation given below includes the *density correction term* of Sternheimer et al. (1984) to account for the density effect of ionization, δ. The equation is written in the form derived by Petrukhin and Shestakov (1968) (see also Sternheimer, 1952, 1953, 1954a, b, 1956, 1959, 1961, 1971, 1984; Eidelman et al., 2004).

$$-\left(\frac{\mathrm{d}E}{\mathrm{d}x}\right) = 2\pi N_A \alpha^2 \lambda_e^2 \frac{Z m_e}{A\beta^2}\left[\ln\left(\frac{2m_e\gamma^2\beta^2 E'_m}{I^2(Z)}\right) - 2\beta^2 + \frac{E'^2_m}{4E^2} - \delta\right]. \quad \text{(B.1)}$$

The symbols stand for the following quantities:

$\alpha = 1/137.036$	fine structure constant
$N_A = 6.023 \cdot 10^{23}$	Avogadro's number
Z	atomic number of absorber
A	atomic weight of absorber
m_e	rest masses of electron
m_μ	rest masses of muon
$\beta = p/E$	
p	p muon momentum
E	E muon energy
$\gamma = E/m_\mu$	Lorentz factor of muon
$\lambda_e = 3.8616 \cdot 10^{-11}$ cm	Compton wavelength of electron
$I(Z)$	mean ionization potential of absorber and
E'_m	maximum energy transferable to electron

For E'_m we write

$$E'_m = \frac{2m_e p^2}{m_e^2 + m_\mu^2 + 2m_e\sqrt{p^2 + m_\mu^2}}, \quad \text{(B.2)}$$

and δ is the density correction term,

$$\delta(X) = 4.6052\,X + a(X_1 - X)^m + C\ , \quad \text{for } X_0 < X < X_1 \tag{B.3}$$

and

$$\delta(X) = 4.6052\,X + C\ , \quad \text{for } X > X_1\ . \tag{B.4}$$

The quantity X as used by Sternheimer et al. (1984) is expressed as

$$X = \lg\left(\frac{p}{mc}\right)\ , \tag{B.5}$$

where p is the momentum and m the rest mass of the particle, and c is the velocity of light.

Additional Physical Constants

Avogadro constant	N_A	$6.023 \cdot 10^{23}$ mol^{-1}
Boltzman constant	k	$1.380 \cdot 10^{-23}$ JK^{-1}
Classical electron radius	r_e	$2.817 \cdot 10^{-13}$ cm

B.3 The Atmosphere

B.3.1 Characteristic Data and Relations

To provide a better understanding of the secondary processes which take place in the atmosphere, some of its basic features are outlined. The Earth's atmosphere is a large volume of gas with a density of almost 10^{19} particles per cm^3 at sea level. With increasing altitude the density of air decreases and with it the number of molecules and nuclei per unit volume, too. Since the real atmosphere is a complex system we frequently use an approximate representation, a simplified model, called the *standard isothermal exponential atmosphere*, where accuracy permits it.

The atmosphere consists mainly of nitrogen and oxygen, although small amounts of other constituents are present. In the *homosphere* which is the region where thermal diffusion prevails the atmospheric composition remains fairly constant. This region extends from sea level to altitudes between 85 and 115 km, depending on thermal conditions. Beyond this boundary molecular diffusion is dominating. Table B.5 gives the number of molecules, n_i, per cm^3 of each constituent, i, at standard temperature and pressure (STP), i.e., at 273.16 K and 760 mmHg, and the relative percentage, q_i, of the constituents.

Table B.4 Parameters for Eq. (4.9) and unit radiation length of atoms, χ_0 (after Tsai, 1974) Z–Atomic Number, A–Atomic Weight, f–Coulomb Corrections

Z	A	f	χ_0 [g cm^{-2}]	Z	A	f	χ_0 [g cm^{-2}]
1	1.0080	$6.4005 \cdot 10^{-5}$	63.0470	47	107.8700	$1.2850 \cdot 10^{-1}$	8.9701
2	4.0026	$2.5599 \cdot 10^{-4}$	94.3221	48	122.4000	$1.3351 \cdot 10^{-1}$	8.9945
3	6.9390	$5.7583 \cdot 10^{-4}$	82.7559	49	114.8200	$1.3859 \cdot 10^{-1}$	8.8491
4	9.0122	$1.0234 \cdot 10^{-3}$	65.1899	50	118.6900	$1.4373 \cdot 10^{-1}$	8.8170
5	10.8110	$1.5984 \cdot 10^{-3}$	52.6868	51	121.7500	$1.4893 \cdot 10^{-1}$	8.7244
6	12.0111	$2.3005 \cdot 10^{-3}$	42.6983	52	127.6000	$1.5419 \cdot 10^{-1}$	8.8267
7	14.0067	$3.1294 \cdot 10^{-3}$	37.9879	53	126.9040	$1.5951 \cdot 10^{-1}$	8.4803
8	15.9994	$4.0845 \cdot 10^{-3}$	34.2381	54	131.3000	$1.6489 \cdot 10^{-1}$	8.4819
9	18.9984	$5.1654 \cdot 10^{-3}$	32.9303	55	132.9050	$1.7032 \cdot 10^{-1}$	8.3052
10	20.1830	$6.3715 \cdot 10^{-3}$	28.9367	56	137.3400	$1.7581 \cdot 10^{-1}$	8.3073
11	22.9898	$7.7022 \cdot 10^{-3}$	27.7362	57	138.9100	$1.8134 \cdot 10^{-1}$	8.1381
12	24.3120	$9.1566 \cdot 10^{-3}$	25.0387	58	140.1200	$1.8693 \cdot 10^{-1}$	7.9357
13	26.9815	$1.0734 \cdot 10^{-2}$	24.0111	59	140.9070	$1.9256 \cdot 10^{-1}$	7.7379
14	28.0860	$1.2434 \cdot 10^{-2}$	21.8234	60	144.2400	$1.9824 \cdot 10^{-1}$	1.7051
15	30.9738	$1.4255 \cdot 10^{-2}$	21.2053	61	145.0000	$2.0396 \cdot 10^{-1}$	7.5193
16	32.0640	$1.6196 \cdot 10^{-2}$	19.4953	62	150.3500	$2.0972 \cdot 10^{-1}$	7.5727
17	35.4530	$1.8236 \cdot 10^{-2}$	19.2783	63	151.9600	$2.1553 \cdot 10^{-1}$	7.4377
18	39.9480	$2.0435 \cdot 10^{-2}$	19.5489	64	157.2500	$2.2137 \cdot 10^{-1}$	7.4830
19	39.1020	$2.2731 \cdot 10^{-2}$	17.3167	65	158.9240	$2.2725 \cdot 10^{-1}$	7.3563
20	40.0800	$2.5142 \cdot 10^{-2}$	16.1442	66	162.5000	$2.3317 \cdot 10^{-1}$	7.3199
21	44.9560	$2.7668 \cdot 10^{-2}$	16.5455	67	164.9300	$2.3911 \cdot 10^{-1}$	7.2332
22	47.9000	$3.0308 \cdot 10^{-2}$	16.1745	68	167.2600	$2.4509 \cdot 10^{-1}$	7.1448
23	50.9420	$3.3059 \cdot 10^{-2}$	15.8425	69	168.9340	$2.5110 \cdot 10^{-1}$	7.0318
24	51.9960	$3.5921 \cdot 10^{-2}$	14.9444	70	173.0400	$2.5714 \cdot 10^{-1}$	7.0214
25	54.9380	$3.8892 \cdot 10^{-2}$	14.6398	71	174.9700	$2.6321 \cdot 10^{-1}$	6.9237
26	55.8470	$4.1971 \cdot 10^{-2}$	13.8389	72	178.4900	$2.6930 \cdot 10^{-1}$	6.8907
27	58.9332	$4.5156 \cdot 10^{-2}$	13.6174	73	180.9480	$2.7541 \cdot 10^{-1}$	6.8177
28	58.7100	$4.8445 \cdot 10^{-2}$	12.6820	74	183.8500	$2.8155 \cdot 10^{-1}$	6.7630
29	63.5400	$5.1837 \cdot 10^{-2}$	12.8616	75	186.2000	$2.8771 \cdot 10^{-1}$	6.6897
30	65.3700	$5.5331 \cdot 10^{-2}$	12.4269	76	190.2000	$2.9389 \cdot 10^{-1}$	6.6763
31	69.7200	$5.8924 \cdot 10^{-2}$	12.4734	77	192.2000	$3.0008 \cdot 10^{-1}$	6.5936
32	72.5900	$6.2615 \cdot 10^{-2}$	12.2459	78	195.0900	$3.0629 \cdot 10^{-1}$	6.5433
33	74.9216	$6.6402 \cdot 10^{-2}$	11.9401	79	196.9670	$3.1252 \cdot 10^{-1}$	6.4608
34	78.9600	$7.0284 \cdot 10^{-2}$	11.9082	80	200.5900	$3.1876 \cdot 10^{-1}$	6.4368
35	79.9090	$7.4258 \cdot 10^{-2}$	11.4230	81	204.3700	$3.2502 \cdot 10^{-1}$	6.4176
36	83.8000	$7.8323 \cdot 10^{-2}$	11.3722	82	207.1900	$3.3128 \cdot 10^{-1}$	6.3688
37	85.4700	$8.2478 \cdot 10^{-2}$	11.0272	83	208.9800	$3.3756 \cdot 10^{-1}$	6.2899
38	87.6200	$8.6719 \cdot 10^{-2}$	10.7623	84	210.0000	$3.4384 \cdot 10^{-1}$	6.1907
39	88.9050	$9.1046 \cdot 10^{-2}$	10.4101	85	210.0000	$3.5013 \cdot 10^{-1}$	6.0651
40	91.2200	$9.5456 \cdot 10^{-2}$	10.1949	86	222.0000	$3.5643 \cdot 10^{-1}$	6.2833
41	92.9060	$9.9948 \cdot 10^{-2}$	9.9225	87	223.0000	$3.6273 \cdot 10^{-1}$	6.1868
42	95.9400	$1.0452 \cdot 10^{-1}$	9.8029	88	226.0000	$3.6904 \cdot 10^{-1}$	6.1477
43	99.0000	$1.0917 \cdot 10^{-1}$	9.6881	89	227.0000	$3.7535 \cdot 10^{-1}$	6.0560
44	101.0700	$1.1389 \cdot 10^{-1}$	9.4825	90	232.0380	$3.8166 \cdot 10^{-1}$	6.0726
45	102.9050	$1.1869 \cdot 10^{-1}$	9.2654	91	231.0000	$3.8797 \cdot 10^{-1}$	5.9319
46	106.4000	$1.2356 \cdot 10^{-1}$	9.2025	92	238.0300	$3.9429 \cdot 10^{-1}$	5.9990

Table B.5 Composition of the atmosphere (STP)

Molecule	n_i [cm^{-3}]	$q_i = n_i/n_{\text{air}}$[%]
air	$2.687 \cdot 10^{19}$	100
N_2	$2.098 \cdot 10^{19}$	78.1
O_2	$5.629 \cdot 10^{18}$	20.9
Ar	$2.510 \cdot 10^{17}$	0.9
CO_2	$8.87 \cdot 10^{15}$	0.03
He	$1.41 \cdot 10^{14}$	$5.0 \cdot 10^{-4}$
Ne	$4.89 \cdot 10^{14}$	$1.8 \cdot 10^{-3}$
Kr	$3.06 \cdot 10^{13}$	$1.0 \cdot 10^{-4}$
Xe	$2.34 \cdot 10^{12}$	$9.0 \cdot 10^{-6}$

Specific regions within the atmosphere are defined according to their temperature variations. These include the *troposphere* where the processes which constitute the weather take place, the *stratosphere* which generally is without clouds, where ozone is concentrated, the *mesosphere* which lies between 50 and 80 km, where the temperature decreases with increasing altitude, and the *thermosphere* where the temperature increases with altitude up to about 130 km. The *temperature profile* of the atmosphere versus altitude is shown in Fig. B.1. The layers between the different regions are called *pauses*, i.e., *tropopause, stratopause, mesopause and thermopause.*

The variation of density with altitude in the atmosphere is a function of the barometric parameters. The variation of each component can be represented by the *barometric law*,

$$n_i(X) = n_i(X_0) \left(\frac{T(h_0)}{T(h)} \right) \exp \left(- \int_{h_0}^{h} \frac{\mathrm{d}h}{h_{s,i}} \right) , \tag{B.6}$$

where

$n_i(X)$ number of molecules of i-th component at X [molecules cm^{-3}]
$n_i(X_0)$ number of molecules of i-th component at X_0 [molecules cm^{-3}]
$h_{s,i} = RT/M_i g(h)$ scale height of i-th component [cm]
R universal gas constant ($8.313 \cdot 10^7$ [erg mole^{-1} K^{-1}])
M_i atomic or molecular mass of the i-th component [g/mole]
h altitude (height) at X [cm]
X atmospheric depth at h [g cm^{-2}]
X_0 atmospheric depth at h_0 [g cm^{-2}] (usually sea level)
h_0 altitude (height) at X_0 [cm]
$T(h)$ temperature at h [K]
$T(h_0)$ temperature at h_0 [K]
$g(h)$ gravitational acceleration [cm s^{-2}]

In a *static isothermal atmosphere*, for which complete mixing equilibrium of all constituents is assumed, Eq. (B.6) reduces to

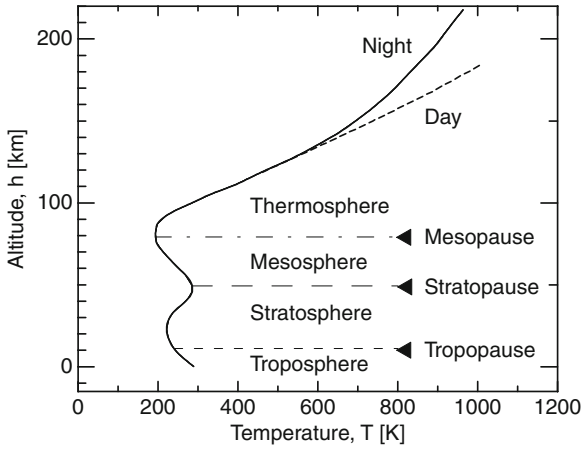

Fig. B.1 Schematic representation of the atmosphere showing its temperature profile

$$n(h) = n(h_0)\,\exp\left(-\frac{h}{h_s}\right)\,, \tag{B.7}$$

where h_s [cm] is the mean *scale height* of the mixture (see Table B.6).

Table B.6 Scale heights at different depths in the atmosphere

X [g cm^{-2}]	10	100	300	500	900
h_s [10^5cm]	6.94	6.37	6.70	7.37	8.21

For the *real atmosphere*, the same relation applies, but the scale height varies slightly with altitude. Table B.6 gives some values of h_s for different atmospheric depths. A similar relation applies to the variation of pressure with altitude.

Figure B.2 shows the relation between density and altitude in an isothermal atmosphere, in the region which is important for cosmic ray propagation and transformation processes. In an inclined direction, i.e., for non-zero zenith angles, the change of density per unit path length is less than in the vertical direction. Furthermore, for an incident particle the total thickness of atmosphere that must be traversed to reach a certain fixed altitude increases with increasing zenith angle.

For small zenith angles the *"flat Earth" approximation* can be used to compute the inclined column density (or slant depth) that follows a $\sec(\theta)$ dependence as given below,

$$X(h,\theta) = X(h,\theta=0)\cdot\sec(\theta)\ \ [\mathrm{g\,cm^{-2}}]\,. \tag{B.8}$$

However, for large zenith angles ($\theta \to 90^\circ$) this approximation diverges and the curvature of the Earth must be considered, requiring the Chapman function (Chapman, 1931), discussed in Sect. B.4, to compute the column density of a given path in the atmosphere correctly.

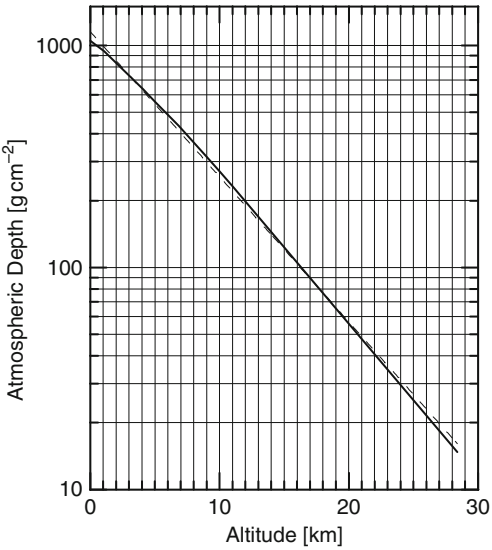

Fig. B.2 Relation between vertical depth and altitude in an isothermal atmosphere. The *dashed line* is an exponential fit to the overall data

B.3.2 Standard and Real Atmospheres

As briefly discussed before, for many applications and calculations the simple *Standard, Isothermal, Exponential Atmosphere* is adequate. However, several organizations have developed formulas to describe the density profile of the atmosphere more accurately and offer density profiles in tabulated form. One must also be aware of the fact that besides seasonal changes the atmospheric density and temperature profiles exhibit also a latitude dependence, and for special applications in-situ measurements may be required.

The relation between altitude and depth in the real atmosphere is illustrated in Fig. B.3. Frequently used tabulated density profiles are those available from COSPAR or the *Standard US Air Force Atmosphere*. In Table B.7 we present the basic data of the COSPAR International Reference Atmosphere (Barnett and Chandra,1990).

B.3.3 Special Atmospheres and Their Variations

The real average atmospheric profile manifests significant variations across the entire globe. Some of these are related to local climatic conditions, the structure of the Earth, to gravitational anomalies, and to the Earth's rotation. There is a well pronounced latitude dependence. In addition, the atmospheric profile is influenced by the ambient temperature and pressure, and is therefore subject to seasonal as

Table B.7 COSPAR international reference atmosphere: 30°N annual mean (after Barnett and Chandra, 1990)

Pressure scale height[a]	Pressure [mb]	Geometric height[b] [m]	Geopotential height[c] [m]	Temperature [K]
17.50	$2.544 \cdot 10^{-5}$	119,656	11,7361	370.1
17.25	$3.266 \cdot 10^{-5}$	116,732	11,4545	324.8
17.00	$4.194 \cdot 10^{-5}$	114,192	11,2096	287.2
16.75	$5.385 \cdot 10^{-5}$	111,965	109,948	256.9
16.50	$6.914 \cdot 10^{-5}$	109,982	108,034	233.7
16.25	$8.878 \cdot 10^{-5}$	108,161	106,275	218.1
16.00	$1.140 \cdot 10^{-4}$	106,471	104,642	207.5
15.75	$1.464 \cdot 10^{-4}$	104,861	103,085	199.6
15.50	$1.880 \cdot 10^{-4}$	103,319	101,594	194.1
15.25	$2.413 \cdot 10^{-4}$	101,823	100,146	189.9
15.00	$3.099 \cdot 10^{-4}$	100,364	98,734	187.0
14.75	$3.979 \cdot 10^{-4}$	98,931	97,345	185.0
14.50	$5.109 \cdot 10^{-4}$	97,518	95,976	183.7
14.25	$6.560 \cdot 10^{-4}$	96,118	94,619	182.8
14.00	$8.423 \cdot 10^{-4}$	94,727	93,269	182.5
13.75	$1.082 \cdot 10^{-3}$	93,340	91,924	182.5
13.50	$1.389 \cdot 10^{-3}$	91,953	90,577	183.3
13.25	$1.783 \cdot 10^{-3}$	90,562	89,226	185.2
13.00	$2.290 \cdot 10^{-3}$	89,158	87,862	187.9
12.75	$2.940 \cdot 10^{-3}$	87,733	86,477	191.2
12.50	$3.775 \cdot 10^{-3}$	86,284	85,068	194.8
12.25	$4.847 \cdot 10^{-3}$	84,804	83,628	198.6
12.00	$6.224 \cdot 10^{-3}$	83,298	8,216	201.9
11.75	$7.992 \cdot 10^{-3}$	81,766	80,670	204.4
11.50	$1.026 \cdot 10^{-2}$	80,217	79,161	206.3
11.25	$1.318 \cdot 10^{-2}$	78,662	77,646	207.8
11.00	$1.692 \cdot 10^{-2}$	77,097	76,120	209.2
10.75	$2.172 \cdot 10^{-2}$	75,521	74,581	210.8
10.50	$2.789 \cdot 10^{-2}$	73,932	73,031	212.5
10.25	$3.582 \cdot 10^{-2}$	72,333	71,469	214.3
10.00	$4.599 \cdot 10^{-2}$	70,720	69,893	216.4
9.75	$5.905 \cdot 10^{-2}$	69,087	68,296	219.2
9.50	$7.582 \cdot 10^{-2}$	67,433	66,678	222.6
9.25	$9.736 \cdot 10^{-2}$	65,754	65,035	226.4
9.00	0.1250	64,048	63,364	230.4
8.75	0.1605	62,308	61,660	234.5
8.50	0.2061	60,539	59,926	238.9
8.25	0.2647	58,739	58,160	243.6
8.00	0.3398	56,905	56,361	248.5
7.75	0.4363	55,029	54,519	253.9
7.50	0.5603	53,116	52,639	259.1
7.25	0.7194	51,170	50,726	263.5
7.00	0.9237	49,198	48,786	266.5
6.75	1.1861	47,213	46,832	267.1
6.50	1.5230	45,231	44,880	266.0
6.25	1.9556	43,265	42,942	263.0
6.00	2.5110	41,325	41,030	258.8

Table B.7 (continued)

Pressure scale height[a]	Pressure [mb]	Geometric height[b] [m]	Geopotential height[c] [m]	Temperature [K]
5.75	3.2242	39,425	39,155	253.8
5.50	4.1399	37,563	37,316	248.7
5.25	5.3157	35,737	35,513	243.7
5.00	6.8255	33,948	33,744	238.9
4.75	8.7642	32,198	32,013	234.4
4.50	11.25	30,479	30,313	230.3
4.25	14.45	28,788	28,638	226.9
4.00	18.55	27,120	26,986	223.9
3.75	23.82	25,478	25,359	221.0
3.50	30.59	23,860	23,754	218.3
3.25	39.28	22,267	22,174	215.6
3.00	50.43	20,697	20,616	212.8
2.75	64.76	19,151	19,080	210.0
2.50	83.15	17,625	17,564	207.1
2.25	106.77	16,116	16,065	205.8
2.00	137.09	14,604	14,561	208.5
1.75	176.03	13,055	13,019	214.8
1.50	226.03	11,450	11,421	223.6
1.25	290.23	9,771	9,750	234.6
1.00	372.66	8,011	7,995	247.0
0.75	478.51	6,148	6,138	259.9
0.50	614.42	4,197	4,192	272.1
0.25	788.93	2,166	2,164	283.1
0.00	1013.00	57	57	295.1

[a] The pressure scale height is minus the natural logarithm of pressure relative to the surface pressure; it is dimensionless.

[b] The geometric height or altitude of an element is its distance above the reference sea level terrestrial ellipsoid, given in meters.

[c] The geopotential height above the reference sea level ellipsoid is given in meters. It can be considered to be its geometric height plus (or minus) a correction which depends upon latitude and height. The difference between geometric and geopotential height is zero at the surface at 30°N and increases with height; the difference varies with latitude.

well as daily variations. Moreover, the profile of the polar atmospheres deviates strongly from mid-latitude or equatorial profiles and there are also remarkable differences between the arctic and Antarctic atmospheric profiles for corresponding seasons.

As an example of the seasonal variations of local atmospheres we present in Figs. B.4 and B.5 the seasonal deviation of the average atmospheric profiles measured at Stuttgart, Germany, and at Pampa Amarilla, Mendoza, Argentina, respectively (Keilhauer et al., 2004; Blümer et al., 2005), from the US Standard Atmosphere (NASA, 1976). Similar studies were carried out for the Fly's Eye site at Dugway, Utah (Wilczyńska et al., 2005) and at other locations. The consequences of these variations are discussed in Sect. 7.7 and in Chap. 17 in connection with air fluorescence measurements and longitudinal shower development (see Fig. 7.24).

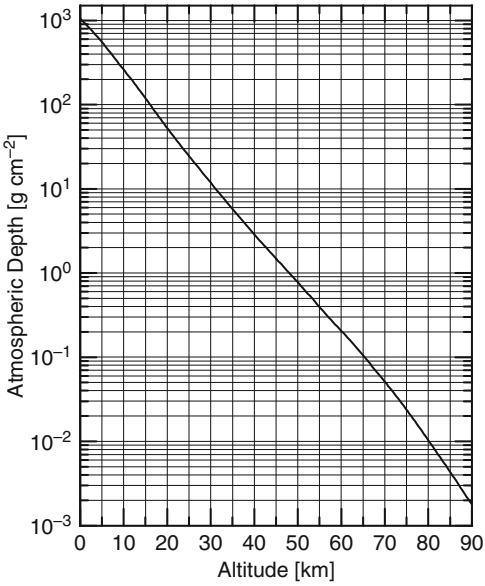

Fig. B.3 Relation between vertical depth or column density and altitude in the real atmosphere, after Cole and Kantor (1978)

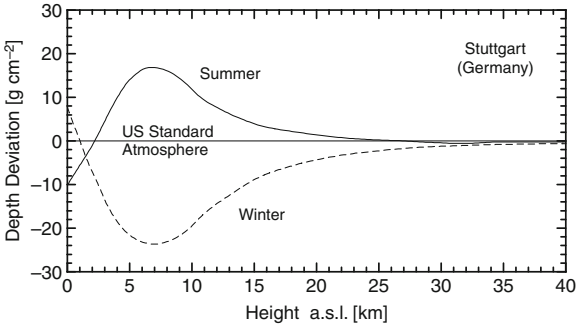

Fig. B.4 Deviation of the average seasonal atmospheric depth profiles measured at Stuttgart, Germany, from the US Standard Atmosphere (NASA, 1976; Keilhauer et al., 2004)

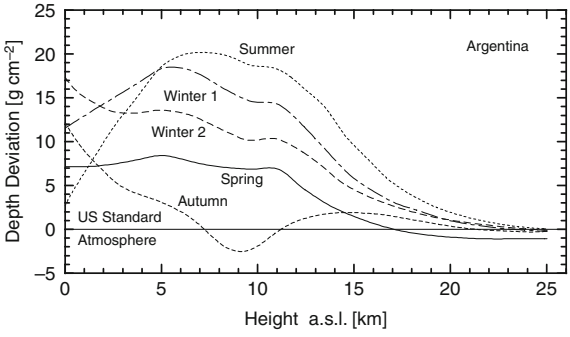

Fig. B.5 Deviation of the average seasonal atmospheric depth profiles measured at Pampa Amarilla, Argentina, from the US Standard Atmosphere (NASA, 1976). *Winter 1* and *winter 2* refer to two different atmospheric models, depending on the pressure condition (for details see Keilhauer et al., 2004)

B.4 Chapman Function

In a standard isothermal exponential atmosphere that is characterized by a constant scale height $h_s = (kT/Mg)$ [cm], where k is Boltzman's constant, T [K] the temperature in Kelvin, M [g/mole] the molecular weight and g [$\mathrm{cm^{-1}s^{-2}}$] the gravitational acceleration, the vertical column density X [$\mathrm{g\,cm^{-2}}$] of air overlaying a point P at altitude h [cm] is given by the common *barometer formula*

$$X(h) = X(h=0)e^{-(h/h_s)} \ \ [\mathrm{g\,cm^{-2}}] \ . \tag{B.9}$$

For inclined trajectories the *Chapman function* permits to compute the thickness or column density of inclined trajectories in the atmosphere accurately, taking into account the *curvature* of the Earth (Chapman, 1931). Depending on the accuracy required it should be used for trajectories whose zenith angle, θ, exceeds about 70°. Various approximate forms of the Chapman function are available (see Fitzmaurice, 1964; Swider and Gardner, 1967; Brasseur and Solomon, 1986). We give here the expression of Swider and Gardner (1967) for zenith angles $\leq (\pi/2)$ which gives the ratio of the total amount of atmosphere in the inclined direction, θ, with respect to the vertical (cf Fig. B.6).

$$Ch\left(x, \theta \leq \frac{\pi}{2}\right) = \left(\frac{\pi x}{2}\right)^{1/2} \left(1 - \mathrm{erf}\left[x^{1/2} \cos\frac{\theta}{2}\right]\right) \exp\left(x \cos^2\frac{\theta}{2}\right) \ , \tag{B.10}$$

where

$$x = \frac{R_E + h}{h_s} \ . \tag{B.11}$$

R_E is the radius of the Earth, h the altitude of observation in the atmosphere, and h_s is the appropriate scale height of the atmosphere.

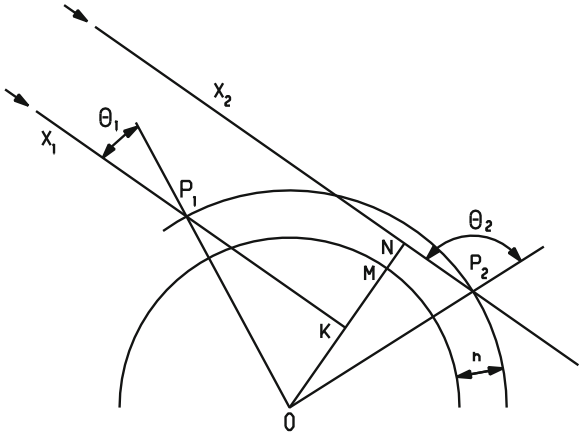

Fig. B.6 Atmospheric column density X_1 in *curved* atmosphere encountered by a cosmic ray incident under zenith angle $\theta_1 \leq \pi/2$ to reach point P_1 at altitude h. Also shown is the situation for point P_2 at $\theta > \pi/2$ and column density X_2, a situation that may arise when h is large

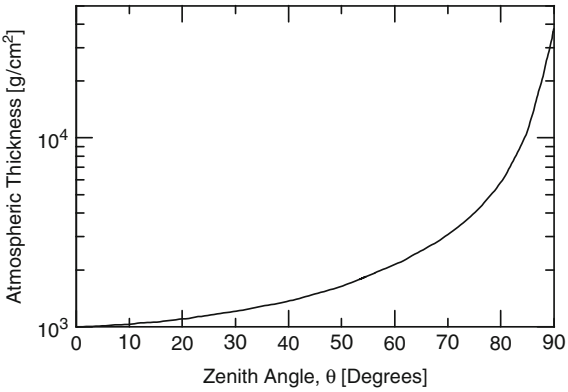

Fig. B.7 Relation between zenith angle and atmospheric thickness or column density at sea level for the "curved" Earth, as described by the Chapman function

For $\theta = \pi/2$, i.e., for horizontal direction we get

$$\mathrm{Ch}(x, \frac{\pi}{2}) = (\pi x/2)^{1/2} \ , \tag{B.12}$$

which is about equal to 40. In other words, the column density or atmospheric thickness is approximately 40 times larger than for vertical incidence ($\theta = 0^\circ$). Figure B.7 displays the atmospheric column density as a function of zenith angle as is obtained with the Chapman function.

B.5 Gross Transformation

The Gross transformation allows to transform the *altitude dependence* of the rate of air showers to the *zenith angle distribution* (Gross, 1933). Moreover, it permits to calculate the vertical intensity $R_V(X, \theta = 0)$ of air showers per unit solid angle at an atmospheric depth X in terms of the measured rate of all showers $R(X)$ at this depth. The Gross transformation can be written in different forms; it is frequently expressed as (Galbraith, 1958; Allkofer, 1975)

$$R_V(X, \theta = 0) = \frac{1}{2\pi}\left((n+1)R(X) - X\frac{\partial R(X)}{\partial X}\right) \ [\mathrm{m}^{-2}\mathrm{s}^{-1}] \tag{B.13}$$

where

$$n = 2(\gamma - 1) + (k\gamma) - \kappa \ .$$

γ is the exponent of the *density spectrum*, κ is the exponent of the *decoherence* rate, R, i.e., $R \propto d^{-\kappa}$, determined empirically, k is related to the counter geometry and response, and d is the counter separation (Galbraith, 1958; Allkofer, 1975, Khristiansen, 1980).

B.6 Energy, Particle, Photon and Magnetic Field Densities in Space

Energy and field densities in space are of great importance for the propagation of cosmic rays, irrespective whether they are of galactic or extragalactic origin. Magnetic fields in space deflect the charged particles and thus mask their origin for the observer on Earth. On the other hand radiation in space provokes interactions that degrade the original primary energy of all particles, charged and neutral.

In Table B.8 we have listed the energy and/or number densities of particles and photons in the different regions of space, i.e., in the heliosphere, the Galaxy, extragalactic (metagalactic) space and the Universe. Some of the data are rather speculative.

The anisotropy of the cosmic microwave background radiation CMBR is discussed in the article of Smoot (2000). The spectral distributions of the CMBR and of the radiation from other contributing sources are plotted in Fig. B.8. The plot shows the distribution of the power per unit frequency bandwidth per unit area and solid angle.

Table B.8 Energy and number density of particles and photons

Type of particle or photon	Energy density [eV cm^{-3}]	Number density [cm^{-3}]
Cosmic rays in Galaxy, all[a,b]	0.9	–
Cosmic rays in Galaxy, p only[a]	0.65	–
Cosmic rays near Earth, solar min.[d]	0.60	–
Cosmic rays at 1 pc from Sun[e]	0.80–1.0	–
2.7 K CMBR $< E >= 6.4 \cdot 10^{-4}$ eV [f,g]	0.24	$\simeq 410$
Starlight, $< E >= 1$ eV[h]	0.6	0.25
EG Starlight, $< E >= 2$ eV[f]	10^{-2}	$5 \cdot 10^{-3}$
Neutrinos, $E \simeq 0.03$ eV[b,c]	–	$\simeq 10^8$
Galactic magnetic field[h]	0.2	–
Local Galactic magnetic field strength $B \simeq 4 - 9\mu$G[i]		
Galactic magnetic field strength at few pc $B \simeq 1.6\mu$G[i]		
Extragalactic magnetic field strength $B \simeq 1$nG[j,k]		

[a] Ginzburg (1958).
[b] Khristiansen (1980).
[c] Fermi energy.
[d] Ginzburg and Syrovatskii (1969).
[e] Bloemen (1987).
[f] Ramana Murthy and Wolfendale (1993).
[g] Bergstrom and Goober (2004).
[h] Longair (1981).
[i] Beck (2009a, b).
[j] Kotera and Lemoine (2008).
[k] Kronberg (1994).

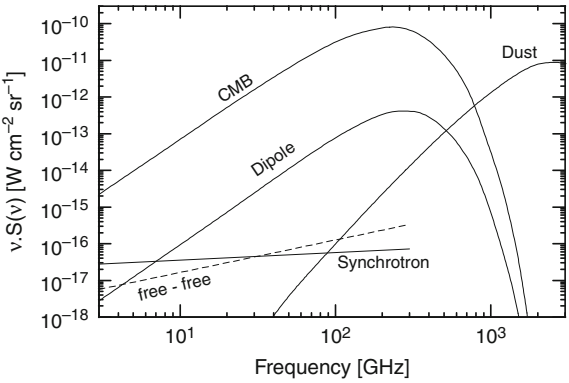

Fig. B.8 Intensity of the microwave sky from 3 to 3,000 GHz near a Galactic latitude of $b = 20°$. The ordinate is the brightness of the sky, $S(\nu)$, multiplied by the frequency, ν (Smoot, 2000)

B.7 Data on Cherenkov Radiation

B.7.1 Cherenkov Radiation in the Atmosphere

Figure B.9 is a quick reference diagram for practical applications to extract the relevant parameters of Cherenkov radiation in the atmosphere, and in Table B.9 we list the Cherenkov threshold energies in water and air (at NTP) for electrons, muons, pions and protons.

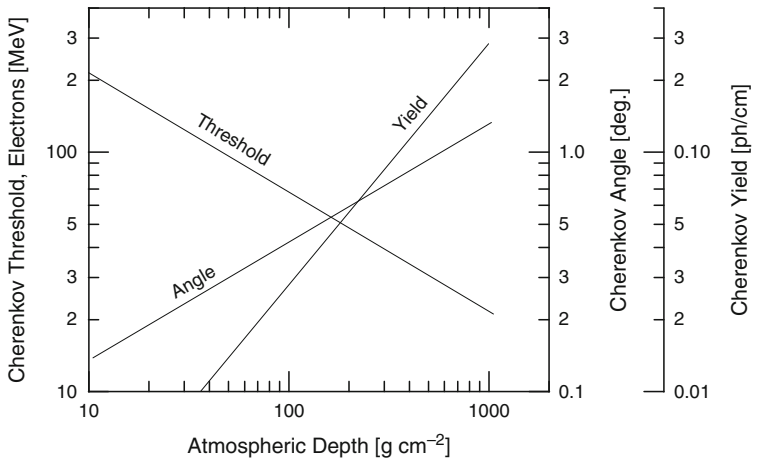

Fig. B.9 Characteristic properties of the Cherenkov radiation of electrons in the Earth's atmosphere. Shown is the threshold energy for the production of Cherenkov photons, the opening angle of the Cherenkov cone of emission with respect to the velocity vector of the electrons and the photon yield per centimeter as a function of atmospheric depth

Table B.9 Cherenkov threshold energies of particles in water and air

Particle	Kinetic energy in	
	Water	Air (NTP)
Electron	257 keV	21 MeV
Muon	53 MeV	4.4 GeV
Pion	70 MeV	5.8 GeV
Proton	475 MeV	39 GeV

References

Allkofer, O.C.: Introduction to Cosmic Radiation, Verlag Karl Thiemig, Munchen (1975).

Barnett, J.J., and S. Chandra: COSPAR International Reference Atmosphere. Adv. Space Res., 10, 12, p. 7 (1990).

Beck, R.: arXiv:0810.2923v4 [astro-ph] 12 Jan (2009a).

Beck, R.: Astrophys. Space Sci. Trans., 5, p. 43 (2009b)

Bergström, L., and A. Goobar: Cosmology and Particle Astrophysics, Springer, Berlin, 2nd ed. (2004).

Bloemen, H.: Proc. Symp. Interstellar Processes, Hollenbach, D.J., and H.A. Thronson, Jr., eds., Astrophysics and Space Science Library, D. Reidel Publ. Co. Dordrecht (1987).

Blümer, J., et al., Pierre Auger Collaboration: PICRC, 7, p. 123 (2005).

Brasseur, G., and S. Solomon: Aeronomy of the Moddle Atmosphere, D. Reidel Publishing Company, Dordrecht/Boston/Lancaster (1986).

Chapman, S.: Proc. Phys. Soc. (Lond.), 43, p. 483 (1931).

Cole, A.E., and A.J. Kantor: Air Force Reference Atmosphere, AFGL-TR-78-0051 (1978).

Eidelman, S., et al.: Particle Physics Booklet, Particle Data Group, Springer, Berlin (available from LBNL and CERN) (2004), and Phys. Lett. B, 592, p. 1 (2004).

Fitzmaurice, J.A.: Appl. Opt., 3, p. 640 (1964).

Galbraith, W.: Extensive Air Showers, Butterworths Scientific Publishers, London (1958).

Ginzburg, V.L.: Progress in Elementary and Cosmic Ray Physics, North Holland Publishing Co., Amsterdam, Vol. 4 (1958).

Ginzburg, V.L., and S.I. Syrovatskii: The Origin of Cosmic Rays, Gordon and Breach, New York (1969).

Gross, B: Zeitschr. f. Physik, 83, p. 214 (1933).

Keilhauer, B., et al.: Astropart. Phys., 22, p. 249 (2004).

Khristiansen, G.B.: Cosmic Rays of Superhigh Energies, Verlag Karl Thiemig, Munchen (1980).

Kotera, K., and M. Lemoine: arXiv:0706.1891v2 [astro-ph] 4 Jan (2008).

Kronberg, P.P.: Rep. Prog. Phys., 57, p. 325 (1994).

Longair, M.S.: High Energy Astrophysics, Cambridge University Press, Cambridge, MA (1981).

NASA, National Aeronautics and Space Administration, US Standard Atmosphere 1976, NASA-TM-X-74335 (1976).

Petrukhin, A.A., and V.V. Shestakov: Can. J. Phys., 46, part 1, p. S377 (1968).

Ramana-Murthy, P., V., and A. W. Wolfendale: Gamma Ray Astronomy, Cambridge University Press, Cambridge, MA, 2nd ed. (1993).

Smoot, G.F.: Phys. Rep., 333–334, pp. 269–308 (2000).

Sternheimer, R.M.: Phys. Rev., 88, p. 851 (1952).

Sternheimer, R.M.: Phys. Rev., 89, p. 1309 (1953), Erratum.

Sternheimer, R.M.: Phys. Rev., 93, p. 351 (1954a).

Sternheimer, R.: Phys. Rev., 93, p. 1434 (1954b), Erratum.
Sternheimer, R.: Phys. Rev., 103, p. 511 (1956).
Sternheimer, R.: Phys. Rev., 115, p. 137 (1959).
Sternheimer, R.: Phys. Rev., 124, p. 2051 (1961).
Sternheimer, R.M., and R.F. Peierls: Phys. Rev. B, 3, p. 3681 (1971).
Sternheimer, R.M., et al.: "The Density Effect for the Ionization Loss of Charged Particles in Various Substances", Atomic and Nuclear Data Tables, 30, p. 261 (1984). See also Groom, D.E., et al., ibid 78, pp. 183–356 (2001) and Ivanov, D.Yu., et al.,: Phys. Lett. B, 442, p. 453 (1998) for corrections.
Swider, W., and M.E. Gardner: Environmental Research Papers No 272, Air Force Cambridge Research, Bedford, MA (1967).
Tsai, Y.S.: Rev. Mod. Phys., 46, p. 815 (1974).
Wilczyńska, B., et al.: PICRC, 7, p. 203 (2005).

Appendix C
List of Symbols

Table C.1 Roman symbols used in this book

a	Length, distance
	Parameter
A	Area
	Atomic weight or mass
	Mass number
	Parameter
b	Length, distance
	Parameter
B	Magnetic induction
	Parameter, general constant, background
c	Velocity of light in vacuum
C	Constant, parameter
D	Distance, separation
e	Electric charge of the electron
e^-	Electron
E_0	Initial or primary energy of a particle
E_s	Scattering energy
ER	Elongation rate
$f(dN)$	Differential shower size spectrum
$F(N)$	Integral number or size spectrum
$FWHM$	Full width at half maximum of pulse
$G(\rho)$	Shower density spectrum
h	Height (vertical) or altitude in atmosphere
h_s	Scale height of atmosphere
H	Magnetic field strength
$\mathcal{H}$	Humidity
I	Intensity
$I(N)$	Differential spectrum
$I(> N)$	Integral spectrum
J	Flux, integral spectrum,
k	Constant, scale factor
K	Inelasticity
	Azimuthal asymmetry ratio (geomagnetic)
	Constant, normalizing -, scale factor
l	Length, element of
L	Distance, scattering length

Table C.1 (continued)

m_e	Rest mass of electron
M	Coincidence fold
M_0	Azimuthal asymmetry factor
	Primary mass
n	Index of refraction
	Exponent, secondary particle multiplicity
N	All-particle shower size
N_A	Avogadro's number
N_{ch}	Charged particle shower size
N_e	Electron shower size
N_μ	Muon shower size
p	Momentum
p_l	Longitudinal momentum
p_t	Transverse momentum
P	Pressure
Q	Cherenkov photon density (visible)
r	Radius, radial distance
r_e	Classical electron radius
R	Rate of events
	Radius, radius of nucleon, radial distance
	Radial distribution function (of Cherenkov photons)
s	Age parameter of air showers
	Center of mass energy squared
S	Magnetic rigidity
	Path length
	Sensitivity
t	Time
	Thickness (of target, air, etc.) in radiation units
t_d	Delay time
t_f	Fall time of a pulse
t_r	Rise time of a pulse
t_t	Top time of a pulse
T	Temperature of atmosphere, etc.
$\mathrm{ve}\mu/\mathrm{m}^2$	Vertical equivalent muons per square meter (for definition see Blake et al., ICRC 8, p. 189, 1977)
x	Distance, path length
X	Column density, atmospheric, underground, etc.
X_s	Slant depth, atmospheric, underground
X_{max}	Depth of shower maximum in atmosphere
X_0	Vertical atmosperic column density at sea level
y	Rapidity
Y	Yield
Z	Atomic number, atomic charge

Table C.2 Greek symbols used in this book

α	Fine structure constant
	Barometric coefficient of air showers
	Decoherence exponent
β	Temperature coefficient of air showers
	Velocity divided by velocity of light, v/c
χ_0	Radiation length, cascade unit
χ_a	Radiation length in air
δ	Angle
Δ	Increment
ϵ_c	Critical energy (of electrons)
η	Elasticity
ϕ	Azimuthal angle
γ	Exponent of spectra (size, number, density, etc.)
Γ	Exponent of integral primary spectrum
κ	Ratio, signal-to-noise
λ	Geomagnetic latitude
	Optical wavelength
λ_{abs}	Absorption length of shower particles
$\lambda_{\text{abs}}^{\mu}$	Absorption length of muons in showers
λ_{int}	Interaction mean free path (i.m.f.p.)
λ_{int}^{N}	Interaction mean free path of nucleons
$\lambda_{\text{int}}^{\pi}$	Interaction mean free path of pions
Λ_{att}	Attenuation length of air shower rate
μ_N	Attenuation coefficient of air shower rate
μ_p	Absorption coefficient of shower particles
ρ	Particle or photon density
	Radius of curvature of charged particle
	In magnetic field
σ	Cross section
	Standard deviation
σ_0	Total $e^{\pm}$ pair production probability
σ_{inel}	Inelastic cross section
$\sigma_{\text{inel}}^{p,\text{air}}$	Inelastic proton-air cross section
σ_{int}	Interaction cross section
θ	Zenith angle
	Angle of emission
ξ	Angle
	Function
ζ	Constant related to the cascade unit

Appendix D
Abbreviations and Acronyms

The following table contains a partial list of frequently used abbreviations and acronyms of experimental sites, installations, experiments and instruments.

Table D.1 List of abbreviations and acronyms

AGASA	Akeno Giant Air Shower Array (Japan)
AIRES	AIR shower Extended Simulation
AMANDA	Antarctic Muon and Neutrino Detector Array
ANITA	Antarctic Impulsive Transient Antenna experiment
ASICO	Air shower SImulation and COrrelation
BLANCA	Broad Lateral Non-imaging Cherenkov Array
CASA	Chicago Air Shower Array (Dugway, Utah, USA)
CERN	European Center for Particle Physics (Geneva, CH)
CMBR	Cosmic Microwave Background Radiation
CORSIKA	COsmic Ray SImulation for KAscade
CREAM	Cosmic Ray Energy And Mass experiment
DICE	Dual Imaging Cherenkov Experiment (Dugawy, USA)
DPM	Dual Parton Model
EM	Electro-Magnetic
EPOS	Energy Parton Off-shell Splitting (MC simulation)
FNAL	Fermi National Accelerator Laboratory (Chicago, USA)
FORTE	Fast On-orbit Recording of Transient Events
FWHM	Full Width at Half Maximum
GLUE	Goldstone Lunar Ultrahigh energy neutrino Experiment
GRAPES	Gamma Ray Astronomy at PeV EnergieS (Ooty, India)
GZK	Greisen-Zatsepin-Kuzmin cutoff
HAS	Horizontal Air Shower
HEGRA	High Energy Gamma Ray Astronomy (Canary Islands)
HESS	High Energy Stereoscopic System (Namibia)
HSA	Hillas Splitting Algorithm
IC	Inverse Compton scattering
ISR	Intersecting Storage Ring (CERN, Geneva, Switzerland)
KASCADE	KArlsruhe Shower Core and Array DEtector (Germany)
KNO	Koba-Nielsen-Olesen scaling
LAAS	Large Area Air Shower experiment (Japan)
LANL	Los Alamos National Laboratory (NM, USA)
LAP	Local Age Parameter, Lateral Age Parameter
LDF	Lateral Distribution Function

Table D.1 (continued)

LEP	Large Electron Positron collider (CERN, Geneva, CH)
LHC	Large Hadron Collider (CERN, Geneva, Switzerland)
LPM	Landau – Pomeranchuk – Migdal effect
LVD	Large Volume Detector (Gran Sasso, Italy)
MACRO	Monopole Astrophysics Cosmic Ray Observatory (Italy)
MC	Monte Carlo method
MIA	MIchigan Array (Dugway, Utah, USA)
MOCCA	MOnte Carlo CAscade simulation program
NKG	Nishimura – Kamata – Greisen – function
NTP	Normal Temperature and Pressure
OWL	Orbiting Wide-angle Light collector
QGS	Quark Gluon String
RHIC	Relativistic Heavy Ion Collider (Brookhaven, USA)
RICE	Radio Ice Cherenkov Experiment (Antarctica)
SHALON	Russian abbr. for "EAS from Neutrinos" (Tien Shan)
SIBYLL	MC event generator
SPS	300 GeV Super Proton Synchrotron (CERN, Switzerland)
TACTIC	TeV Atmospheric Cherenkov Telescope with Imaging Camera
TRACER	Transition Radiation Array for Cosmic Energetic Radiation
TTC	Time-Track-Complementarity
VERITAS	Very Energetic Radiation Imaging Telescope Array System (Whipple Observatory, Arizona, USA)

Appendix E
List of Cosmic Ray Conferences

1.	Cracow, Poland	1947	17.	Paris, France	1981
2.	Como, Italy	1949	18.	Bangalore, India	1983
3.	Bagneres de Bigorre, F	1953	19.	La Jolla, Ca., USA	1985
4.	Guanjuato, Mexico	1955	20.	Moscow, U.S.S.R.	1987
5.	Varenna, Italy	1957	21.	Adelaide, Australia	1990
6.	Moscow, U.S.S.R.	1959	22.	Dublin, Ireland	1991
7.	Kyoto, Japan	1961	23.	Calgary, Canada	1993
8.	Jaipur, India	1963	24.	Rome, Italy	1995
9.	London, England	1965	25.	Durban, South Africa	1997
10.	Calgary, Canada	1967	26.	Salt Lake City, USA	1999
11.	Budapest, Hungary	1969	27.	Hamburg, Germany	2001
12.	Hobart, Tasmania, Aus.	1971	28.	Tsukuba, Japan	2003
13.	Denver, Co., USA	1973	29.	Pune, India	2005
14.	Munich, Germany	1975	30.	Merida, Mexico	2007
15.	Plovdiv, Bulgaria	1977	31.	Lodz, Poland	2009
16.	Kyoto, Japan	1979	32.	Beijing, China	2011

Index

PETER GRIEDER, born 1928 in Switzerland, obtained his MS degree in physics from the Illinois Institute of Technology in Chicago in 1957. He did the research for his thesis with the Argonne group of the U.S. Atomic Energy Commission at the University of Chicago. There he took part in cosmic ray physics seminars of Professors Simpson, Schein and Chandrasekhar. In 1961 he got his PhD from the University of Bern, Switzerland, where he did his research under Prof. F.G. Houtermans in high energy cosmic ray physics.

He then worked successively as a postdoctoral scientist at the Niels Bohr Institute in Copenhagen with Prof. Bernard Peters on quark-hunt experiments, at CERN in Geneva in the experimental and later on in the theoretical physics division with Drs. R. Hagedorn and M. Jacob on models of high energy hadronic interactions and multi-particle production, in conjunction with air showers.

In 1968 he was appointed lecturer at the University of Bern, and in 1970 visiting professor for one year at the Institute for Nuclear Studies of the University of Tokyo, where he worked in the cosmic ray group of Prof. K. Suga. In 1978 he was appointed professor of physics at the University of Bern. From 1985 to 1987 he was secretary of the Swiss Physical Society.

His research activities comprise high energy phenomena, extensive air showers and neutrino astronomy. He developed the ASICO air shower simulation program system which later on was renamed CORSIKA, that is widely used today with a variety of modern event generators, developed by many different authors. He was co-initiator together with Prof. Fred Reines, Nobel Laureate, and colleagues from other institutions of the pioneering DUMAND neutrino telescope project in Hawaii, that was the template for all presently existing and planned giant neutrino telescopes. He was guest professor for many years at the University of Hawaii and is the author of numerous scientific articles and several books.

Extensive Air Showers

Peter K.F. Grieder

Extensive Air Showers

High Energy Phenomena and Astrophysical Aspects

A Tutorial, Reference Manual and Data Book

Volume I

Springer

Prof. Dr. Peter K.F. Grieder
University of Bern
Physikalisches Institut
Sidlerstr. 5
3012 Bern
Switzerland
peter.grieder@space.unibe.ch

Cover

Left: Photograph of the original KASCADE air shower array at Karlsruhe, Germany, showing part of the 252 huts, distributed over an area of 200 by 200 m, that house the combined unshielded (all charged particle) and shielded (muon) detectors, and the huge central hadron calorimeter. The latter measures 320 m^2, is 11.5 nuclear interaction lengths deep and consists of nine layers of lead, iron and concrete. In addition the experiment includes major muon tracking facilities. It was designed to study galactic cosmic rays at energies around the spectral knee region (PeV). In 2003 the experiment had been extended to KASCADE-Grande, covering an area of 700 by 700 m and an energy range up to 1 EeV. The experiment could then study the galactic-extragalactic transition region of the cosmic radiation. It was shut-off at the end of March 2009 (Courtesy of Forschungszentrum Karlsruhe, Germany).

Right: The Crab Nebula (catalogue designation M1, NGC 1952, Taurus A) in our own Galaxy is the remnant of the supernova SN-1054, discovered by Chinese astronomers in the year 1054 AD. I have chosen this picture as a symbolic representative of a galactic research object, reflecting the aims of the KASCADE project to study the galactic cosmic radiation. Recently, old documents had been found in European monasteries where the event SN-1054 is mentioned, thus confirming the Chinese observation. The Crab Nebula spans about 11 light-years across (3.4 pc) and is at a distance of approximately $6,500 \pm 1,600$ ly (2 ± 0.5 kpc) from our location. A Pulsar (rotating neutron star) is in its center. Both objects are emitters of gamma rays and are intensely studied by gamma ray astronomers (Courtesy of ESO).

Corrected 2nd Printing 2010

ISBN 978-3-540-76940-8 e-ISBN 978-3-540-76941-5
DOI 10.1007/978-3-540-76941-5
Springer Heidelberg Dordrecht London New York

Library of Congress Control Number: 2009939841

Cover design: WMXDesign GmbH, Heidelberg

Printed on acid-free paper

Springer is part of Springer Science+Business Media (www.springer.com)

To
Estelle
and our
Family

Preface

This book grew out of a personal need to carry out my work more efficiently. It was in the 60s when I began to develop the first highly structured air shower simulation program and was carrying out extensive air shower simulations on an almost industrial basis. The primary aim at that time was to study the systematics of hadronic interactions at the highest energies in conjunction with experimental air shower and accelerator data. This goal remains to date but today the determination of the primary mass, its energy dependence and questions related to the origin, acceleration and propagation of the most energetic cosmic rays are in the foreground.

The results obtained with the ever growing shower model that eventually grew into the program system named ASICO (Air shower SImulation and COrrelation), which later on became CORSIKA, were so manifold and rich, and covered essentially the full scope of air shower observables that it became necessary to build a library of experimental data for comparison and efficient analysis work; this was the beginning of this book. As the library grew it became evident that it could be of interest to a broader community, active in air shower research. A natural consequence was to add theoretical and tutorial sections to the various chapters, and to expand the book to a comprehensive reference manual for researchers that can also be used as a text book for the advanced student.

The data presented in these two volumes are not an all-inclusive collection. In view of the very large number of experiments that were carried out by so many research groups throughout the years it became unavoidable to take a selection for the presentation here, to compile the data and summarize results. Emphasis was therefore given to the historically as well as the contemporarily scientifically relevant information and data. The fast evolving field of ground based high energy gamma ray astronomy, which employs air shower detection techniques (air Cherenkov as well as particle detection), is only touched on the side, mostly in connection with wide-angle large aperture atmospheric Cherenkov detector arrays. Today, the field of gamma ray astronomy is essentially a separate discipline of its own, yet it remains closely related to cosmic ray and air shower research.

Readme

Organization of the Book: Extensive air showers consist of a superposition of extremely complex processes that involve different fundamental interactions and many aspects of particle physics, cosmic ray physics and astrophysics. Most observables are functions of many variables and parameters and all observables are more or less coupled with each other. This complexity makes it difficult to break up the vast contents of this book into self contained chapters that can be studied separately and in an easily digestible form. I have carefully reflected on how to structure the presentation of the contents of this book and I fully realize that subject oriented sectioning can be done in different ways. A clear structure is of basic importance for the reader and student. No matter how the structuring is carried out, a consequence of the complexity of the subject is that much cross referencing between the chapters is required to link the topics properly. Moreover, an extensive subject index is needed to navigate successfully through the volumes. Both of these requirements are fulfilled and I hope that the reader will be satisfied with the presentation and contents.

The book is divided into two parts that are in two separate volumes. Part I deals mainly with the basic theoretical framework of the processes that determine an air shower. Included are, after the general introduction chapters that describe the shower detection techniques and the basic shower reconstruction procedure using directly accessible shower parameters, followed by a summary of the relevant hadronic, electromagnetic and weak interactions and the cascade formation processes. Subsequently a detailed discussion of the longitudinal, lateral and temporal shower development, and an outline of the complexity and interrelationship of the indirectly observable process and parameters follows. Part I ends with a summary of ways and means to extract information from air shower observations on the primary radiation and presents a compilation of data of our current knowledge of the high energy portion of the primary spectrum and composition.

Part II contains mainly compilations of data of experimental and theoretical nature as well as predictions from simulations of individual air shower constituents, i.e., spectra and distributions of separate components in showers. Also included are chapters dedicated exclusively to special processes and detection methods. These comprise optical atmospheric Cherenkov and fluorescence phenomena that offer special observational windows and have proven to be successful alternatives to particle measurements because they yield three-dimensional insight into the shower process, and radio emission that may possibly develop into a useful future method of detection. I have also included a brief chapter that deals with correlations of shower observables, one that exposes the technique of air shower simulations, and the inevitable chapter on miscellaneous topics. Part II ends with a compilation of definitions and relations, and several appendices that offer useful information. For the benefit of the reader, extensive cross referencing is used that links different yet related topics for rapid access. The extensive subject index at the back of each volume covers both volumes.

Overviews: With the exception of Chap. 1 (Introduction, Facts and Phenomenology) each chapter is preceded with a brief *Overview* that summarizes the contents and offers directions where to find related topics that some readers may expect to find in the chapter but are discussed elsewhere.

Comments on Observation Levels: It will be noticed that sometimes different atmospheric depths or altitudes are specified for a particular site in different chapters and sections, and for different data sets of the same site. This reflects the actual situation in the literature. Most authors do not offer an explanation. Moreover, occasionally altitude and atmospheric overburden may seem to be in minor disparity. In some cases this may be due to seasonal changes of the barometric pressure. However, in some cases when data are being evaluated some authors take intentionally a somewhat larger overburden than would correspond to the vertical depth to account for the finite zenith-angular bin width and average zenith angle ($\theta > 0^\circ$) within the "vertical" angular bin. Whenever given I have listed the published site data that had been used in the particular case.

Comments on Nomenclature: There is sometimes some confusion in the literature when authors discuss the *shower size* because of inaccurate terminology, which may be a problem for students. Some authors use for the shower size the symbol N_e, which implies the *electron size*, but mean in fact the *total shower size N*, i.e., the total number of charged particles, N_{ch}, in a shower as it is deduced from common particle density measurements that include particles produced by interactions of neutrals (neutrons) and gamma rays (transition effects) in the detectors. In the cases where it is evident that the *all-particle shower size* is meant, I use the symbol N to avoid ambiguities.

On the other hand, in some experiments and in some work the authors clearly deal with electrons only, or chiefly electrons, and mean the actual *electron size* of a shower. In this case I have used the symbol N_e as is appropriate. It is evident that to isolate the electrons from the rest of the particles in a shower is not a trivial matter and a clear distinction is made only in a few experiments. As far as possible I have tried to call the readers attention to the problem whenever it surfaces. For the *muon size* the definition is unambiguous and I have used the symbol N_μ.

Confusing terminology is also frequently encountered in papers that deal with the attenuation of the shower rate or shower frequency and the absorption of the shower particles. Likewise there is no standard for the symbols representing the quantities.

Throughout the book I call the variation of the integral rate of showers of size $\geq N$ with zenith angle θ (due to the change of atmospheric slant depth) at fixed altitude of observation, h, the *shower rate* or *shower frequency attenuation*, and the corresponding attenuation length in the atmosphere the *shower rate attenuation length*, $\Lambda_{\rm att}$. Analogously I call the variation of the shower size N of given rate (fixed primary energy) with atmospheric depth, X, the *shower particle absorption*, and the corresponding absorption length in the atmosphere the *shower particle absorption length*, $\lambda_{\rm abs}$.

In the latter case, when dealing with muons I use for the *muon absorption length* the symbol $\lambda_{\mu,\rm abs}$ and, likewise, for electrons only and hadrons only the *electron absorption length* $\lambda_{e,\rm abs}$ and the *hadron absorption length* $\lambda_{h,\rm abs}$, respectively. These

quantities and their reciprocals, the *shower rate attenuation coefficient*, μ_{att}, and the *shower particle absorption coefficient*, μ_{abs}, are defined in Chap. 6. A list of symbols is included at the end of the second volume.

Comments on Hadronic Interaction Models (Event Generators): I have devoted some pages for summarizing the physics and mathematics of the early phenomenological high energy hadronic interaction models and discuss the modern models that are based on partons, quark-gluon string and Regge theory more superficially, in form of a catalogue of models, offering only a very brief description of each. However, the relevant references, some of which are very extensive papers, are listed.

The reason for discussing the early models in some detail is that the original papers describing them were published in conference proceedings and journals that are not readily available, yet the models are still of some interest to many. On the other hand, the number of modern low and high energy interaction models (event generators) has grown very rapidly in recent years and they are subject to fast evolution. A detailed description would be quickly obsolete. For this reason I do not discuss them in detail.

References: The frequently used abbreviation PICRC stands for *Proceedings of the International Cosmic Ray Conference* and is used there where the proceedings are not part of a regular scientific journal or series.

Acknowledgements

I am particularly indebted to my dear friend and colleague, Prof. Lawrence Jones (University of Michigan, Ann Arbor, USA), for so many valuable and often hour-long discussions on many of the topics which I treat in this book. Many of our discussions took place during his frequent visits to CERN in Geneva, Switzerland, but some were conducted in more exotic places when we met at conferences around the world. I am equally indebted to Prof. Jun Nishimura (Tokyo) with whom a more than three decade-long relationship has greatly enriched my knowledge, and whose comments and suggestions I sincerely treasure. Special thanks go to Prof. Suresh Tonwar (University of Maryland, USA, formerly Tata Institute of Fundamental Research, Mumbai, India) and to Prof. Jörg Hörandel (University of Nijmegen, The Netherlands, formerly Forschungszentrum (FZ) Karlsruhe, Germany), for their valuable comments on many topics. I also want to express my sincere gratitude to the many colleagues that I have listed below, in alphabetic order, for their suggestions that were often prompted by stimulating discussions at conferences, during visits, on the phone and via e-mail.

Dr. Antonella Castellina, University of Torino, Italy; Dr. Laurent Desorgher, University of Bern, Switzerland; Dr. Paul Doll, Dr. Andreas Haungs and Dr. Dieter Heck, all FZ Karlsruhe, Germany; Prof. Ken Honda, Yamanashi University, Japan;

Dr. Bianca Keilhauer, FZ Karlsruhe and University of Karlsruhe, Germany; Prof. Alexander Konopelko, MPI Heidelberg, Germany; Prof. Peter Minkowski, University of Bern, Switzerland; Prof. Motohiko Nagano, ICRR, Tokyo, Japan; Prof. Gianni Navarra, University of Torino, Italy; Prof, Heinigerd Rebel, FZ Karlsruhe and University of Heidelberg, Germany.

I greatly appreciate the support of the University of Bern, in particular the kind assistance which the staff of the Library of the Institute for Exact Sciences of the University has given me. I also acknowledge the valuable help of Dr. B. Housley and Dr. U. Jenzer who adapted the software to my needs, and the graphics support received from Mr. U. Lauterburg and Mr. T. Sémon.

I am grateful for the documentation and the numerous pre- and reprints that I was privileged to receive from colleagues all over the world. Last but not least I want to mention the valuable cooperation with the late Professors Koichi Suga and Tsuneo Matano that began many years ago, during my 1-year stay as guest professor at the Institute for Nuclear Studies of the University of Tokyo, that played a significant role in my scientific career.

Bern, May 2009 Peter K.F. Grieder

Contents

Part I

Extensive Air Showers

Peter K.F. Grieder

Extensive Air Showers

High Energy Phenomena and Astrophysical Aspects

A Tutorial, Reference Manual and Data Book

Volume II

Springer

Prof. Dr. Peter K.F. Grieder
University of Bern
Physikalisches Institut
Sidlerstr. 5
3012 Bern
Switzerland
peter.grieder@space.unibe.ch

Cover

Left: Partial map of the layout of the giant Auger air shower array, covering about 3,000 km^2, with the four Fly's Eye type air fluorescence detectors indicated. The detector combination which is located near Malargüe, in Argentina is known under the name Auger Observatory. Its aim is to study the ultrahigh energy (UHE) component of the primary cosmic radiation beyond 10^{17} eV, the spectral ankle region around about $5 \cdot 10^{18}$ eV where the extragalactic cosmic ray component is believed to become dominant, to establish the existence of the Greisen-Zatsepin-Kuzmin (GZK) spectral cutoff expected at $\sim 10^{19}$ eV, and to search for correlations between UHE cosmic ray events and astrophysical objects in an attempt to identify objects as sources of UHE cosmic rays (Courtesy of Forschungszentrum Karlsruhe, Germany).

Right: The spiral galaxy NGC 5236 (other catalogue designations are Messier 83 or Southern Pinwheel galaxy) is located in the southern constellation Hydra. It is at a distance of approximately 15 million light years ($\sim$ 4.6 Mpc) from our location. Its size is about half of the Milky Way (Courtesy of ESO). I have chosen this picture as a symbolic representative of an extragalactic research object, reflecting the aims of the Auger project to study the extragalactic component of the cosmic radiation, and to find its sources.

Corrected 2nd Printing 2010

ISBN 978-3-540-76940-8 e-ISBN 978-3-540-76941-5
DOI 10.1007/978-3-540-76941-5
Springer Heidelberg Dordrecht London New York

Library of Congress Control Number: 2009939841

Cover design: WMXDesign GmbH, Heidelberg

Printed on acid-free paper

Springer is part of Springer Science+Business Media (www.springer.com)

To
Estelle
and our
Family

Preface

This book grew out of a personal need to carry out my work more efficiently. It was in the 60s when I began to develop the first highly structured air shower simulation program and was carrying out extensive air shower simulations on an almost industrial basis. The primary aim at that time was to study the systematics of hadronic interactions at the highest energies in conjunction with experimental air shower and accelerator data. This goal remains to date but today the determination of the primary mass, its energy dependence and questions related to the origin, acceleration and propagation of the most energetic cosmic rays are in the foreground.

The results obtained with the ever growing shower model that eventually grew into the program system named ASICO (Air shower SImulation and COrrelation), which later on became CORSIKA, were so manifold and rich, and covered essentially the full scope of air shower observables that it became necessary to build a library of experimental data for comparison and efficient analysis work; this was the beginning of this book. As the library grew it became evident that it could be of interest to a broader community, active in air shower research. A natural consequence was to add theoretical and tutorial sections to the various chapters, and to expand the book to a comprehensive reference manual for researchers that can also be used as a text book for the advanced student.

The data presented in these two volumes are not an all-inclusive collection. In view of the very large number of experiments that were carried out by so many research groups throughout the years it became unavoidable to take a selection for the presentation here, to compile the data and summarize results. Emphasis was therefore given to the historically as well as the contemporarily scientifically relevant information and data. The fast evolving field of ground based high energy gamma ray astronomy, which employs air shower detection techniques (air Cherenkov as well as particle detection), is only touched on the side, mostly in connection with wide-angle large aperture atmospheric Cherenkov detector arrays. Today, the field of gamma ray astronomy is essentially a separate discipline of its own, yet it remains closely related to cosmic ray and air shower research.

Readme

Organization of the Book: Extensive air showers consist of a superposition of extremely complex processes that involve different fundamental interactions and many aspects of particle physics, cosmic ray physics and astrophysics. Most observables are functions of many variables and parameters and all observables are more or less coupled with each other. This complexity makes it difficult to break up the vast contents of this book into self contained chapters that can be studied separately and in an easily digestible form. I have carefully reflected on how to structure the presentation of the contents of this book and I fully realize that subject oriented sectioning can be done in different ways. A clear structure is of basic importance for the reader and student. No matter how the structuring is carried out, a consequence of the complexity of the subject is that much cross referencing between the chapters is required to link the topics properly. Moreover, an extensive subject index is needed to navigate successfully through the volumes. Both of these requirements are fulfilled and I hope that the reader will be satisfied with the presentation and contents.

The book is divided into two parts that are in two separate volumes. Part I deals mainly with the basic theoretical framework of the processes that determine an air shower. Included are, after the general introduction chapters that describe the shower detection techniques and the basic shower reconstruction procedure using directly accessible shower parameters, followed by a summary of the relevant hadronic, electromagnetic and weak interactions and the cascade formation processes. Subsequently a detailed discussion of the longitudinal, lateral and temporal shower development, and an outline of the complexity and interrelationship of the indirectly observable process and parameters follows. Part I ends with a summary of ways and means to extract information from air shower observations on the primary radiation and presents a compilation of data of our current knowledge of the high energy portion of the primary spectrum and composition.

Part II contains mainly compilations of data of experimental and theoretical nature as well as predictions from simulations of individual air shower constituents, i.e., spectra and distributions of separate components in showers. Also included are chapters dedicated exclusively to special processes and detection methods. These comprise optical atmospheric Cherenkov and fluorescence phenomena that offer special observational windows and have proven to be successful alternatives to particle measurements because they yield three-dimensional insight into the shower process, and radio emission that may possibly develop into a useful future method of detection. I have also included a brief chapter that deals with correlations of shower observables, one that exposes the technique of air shower simulations, and the inevitable chapter on miscellaneous topics. Part II ends with a compilation of definitions and relations, and several appendices that offer useful information. For the benefit of the reader, extensive cross referencing is used that links different yet related topics for rapid access. The extensive subject index at the back of each volume covers both volumes.

Overviews: With the exception of Chap. 1 (Introduction, Facts and Phenomenology) each chapter is preceded with a brief *Overview* that summarizes the contents and offers directions where to find related topics that some readers may expect to find in the chapter but are discussed elsewhere.

Comments on Observation Levels: It will be noticed that sometimes different atmospheric depths or altitudes are specified for a particular site in different chapters and sections, and for different data sets of the same site. This reflects the actual situation in the literature. Most authors do not offer an explanation. Moreover, occasionally altitude and atmospheric overburden may seem to be in minor disparity. In some cases this may be due to seasonal changes of the barometric pressure. However, in some cases when data are being evaluated some authors take intentionally a somewhat larger overburden than would correspond to the vertical depth to account for the finite zenith-angular bin width and average zenith angle ($\theta > 0^\circ$) within the "vertical" angular bin. Whenever given I have listed the published site data that had been used in the particular case.

Comments on Nomenclature: There is sometimes some confusion in the literature when authors discuss the *shower size* because of inaccurate terminology, which may be a problem for students. Some authors use for the shower size the symbol N_e, which implies the *electron size*, but mean in fact the *total shower size N*, i.e., the total number of charged particles, N_{ch}, in a shower as it is deduced from common particle density measurements that include particles produced by interactions of neutrals (neutrons) and gamma rays (transition effects) in the detectors. In the cases where it is evident that the *all-particle shower size* is meant, I use the symbol N to avoid ambiguities.

On the other hand, in some experiments and in some work the authors clearly deal with electrons only, or chiefly electrons, and mean the actual *electron size* of a shower. In this case I have used the symbol N_e as is appropriate. It is evident that to isolate the electrons from the rest of the particles in a shower is not a trivial matter and a clear distinction is made only in a few experiments. As far as possible I have tried to call the readers attention to the problem whenever it surfaces. For the *muon size* the definition is unambiguous and I have used the symbol N_μ.

Confusing terminology is also frequently encountered in papers that deal with the attenuation of the shower rate or shower frequency and the absorption of the shower particles. Likewise there is no standard for the symbols representing the quantities.

Throughout the book I call the variation of the integral rate of showers of size $\geq N$ with zenith angle θ (due to the change of atmospheric slant depth) at fixed altitude of observation, h, the *shower rate* or *shower frequency attenuation*, and the corresponding attenuation length in the atmosphere the *shower rate attenuation length*, $\Lambda_{\rm att}$. Analogously I call the variation of the shower size N of given rate (fixed primary energy) with atmospheric depth, X, the *shower particle absorption*, and the corresponding absorption length in the atmosphere the *shower particle absorption length*, $\lambda_{\rm abs}$.

In the latter case, when dealing with muons I use for the *muon absorption length* the symbol $\lambda_{\mu,\rm abs}$ and, likewise, for electrons only and hadrons only the *electron absorption length* $\lambda_{e,\rm abs}$ and the *hadron absorption length* $\lambda_{h,\rm abs}$, respectively. These

quantities and their reciprocals, the *shower rate attenuation coefficient*, μ_{att}, and the *shower particle absorption coefficient*, μ_{abs}, are defined in Chap. 6. A list of symbols is included at the end of the second volume.

Comments on Hadronic Interaction Models (Event Generators): I have devoted some pages for summarizing the physics and mathematics of the early phenomenological high energy hadronic interaction models and discuss the modern models that are based on partons, quark-gluon string and Regge theory more superficially, in form of a catalogue of models, offering only a very brief description of each. However, the relevant references, some of which are very extensive papers, are listed.

The reason for discussing the early models in some detail is that the original papers describing them were published in conference proceedings and journals that are not readily available, yet the models are still of some interest to many. On the other hand, the number of modern low and high energy interaction models (event generators) has grown very rapidly in recent years and they are subject to fast evolution. A detailed description would be quickly obsolete. For this reason I do not discuss them in detail.

References: The frequently used abbreviation PICRC stands for *Proceedings of the International Cosmic Ray Conference* and is used there where the proceedings are not part of a regular scientific journal or series.

Acknowledgements

I am particularly indebted to my dear friend and colleague, Prof. Lawrence Jones (University of Michigan, Ann Arbor, USA), for so many valuable and often hour-long discussions on many of the topics which I treat in this book. Many of our discussions took place during his frequent visits to CERN in Geneva, Switzerland, but some were conducted in more exotic places when we met at conferences around the world. I am equally indebted to Prof. Jun Nishimura (Tokyo) with whom a more than three decade-long relationship has greatly enriched my knowledge, and whose comments and suggestions I sincerely treasure. Special thanks go to Prof. Suresh Tonwar (University of Maryland, USA, formerly Tata Institute of Fundamental Research, Mumbai, India) and to Prof. Jörg Hörandel (University of Nijmegen, The Netherlands, formerly Forschungszentrum (FZ) Karlsruhe, Germany), for their valuable comments on many topics. I also want to express my sincere gratitude to the many colleagues that I have listed below, in alphabetic order, for their suggestions that were often prompted by stimulating discussions at conferences, during visits, on the phone and via e-mail.

Dr. Antonella Castellina, University of Torino, Italy; Dr. Laurent Desorgher, University of Bern, Switzerland; Dr. Paul Doll, Dr. Andreas Haungs and Dr. Dieter Heck, all FZ Karlsruhe, Germany; Prof. Ken Honda, Yamanashi University, Japan;

Dr. Bianca Keilhauer, FZ Karlsruhe and University of Karlsruhe, Germany; Prof. Alexander Konopelko, MPI Heidelberg, Germany; Prof. Peter Minkowski, University of Bern, Switzerland; Prof. Motohiko Nagano, ICRR, Tokyo, Japan; Prof. Gianni Navarra, University of Torino, Italy; Prof, Heinigerd Rebel, FZ Karlsruhe and University of Heidelberg, Germany.

I greatly appreciate the support of the University of Bern, in particular the kind assistance which the staff of the Library of the Institute for Exact Sciences of the University has given me. I also acknowledge the valuable help of Dr. B. Housley and Dr. U. Jenzer who adapted the software to my needs, and the graphics support received from Mr. U. Lauterburg and Mr. T. Sémon.

I am grateful for the documentation and the numerous pre- and reprints that I was privileged to receive from colleagues all over the world. Last but not least I want to mention the valuable cooperation with the late Professors Koichi Suga and Tsuneo Matano that began many years ago, during my 1-year stay as guest professor at the Institute for Nuclear Studies of the University of Tokyo, that played a significant role in my scientific career.

Bern, May 2009 Peter K.F. Grieder

Contents

Part II

Part I